Delft University of Technology

The Delft Sand, Clay & Rock Cutting Model. Family Edition.

Miedema, SA

Publication date
2015

Document Version
Final published version

Citation (APA)
Miedema, SA. (2015). *The Delft Sand, Clay & Rock Cutting Model. Family Edition.* (3 ed.) IOS Press.

Sape A. Miedema

THE DELFT SAND, CLAY & ROCK CUTTING MODEL

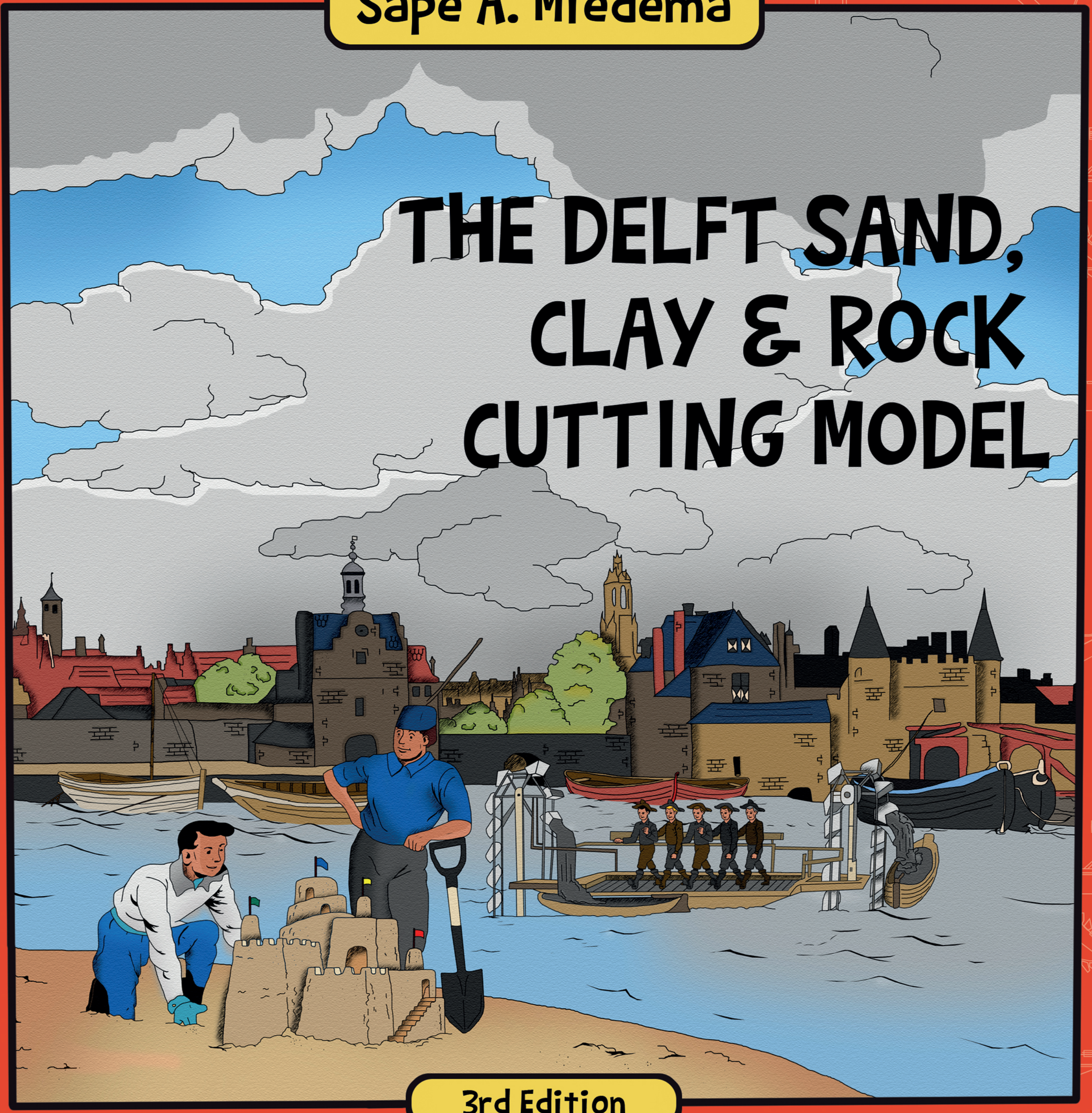

3rd Edition

The Delft Sand, Clay & Rock Cutting Model

3rd Edition

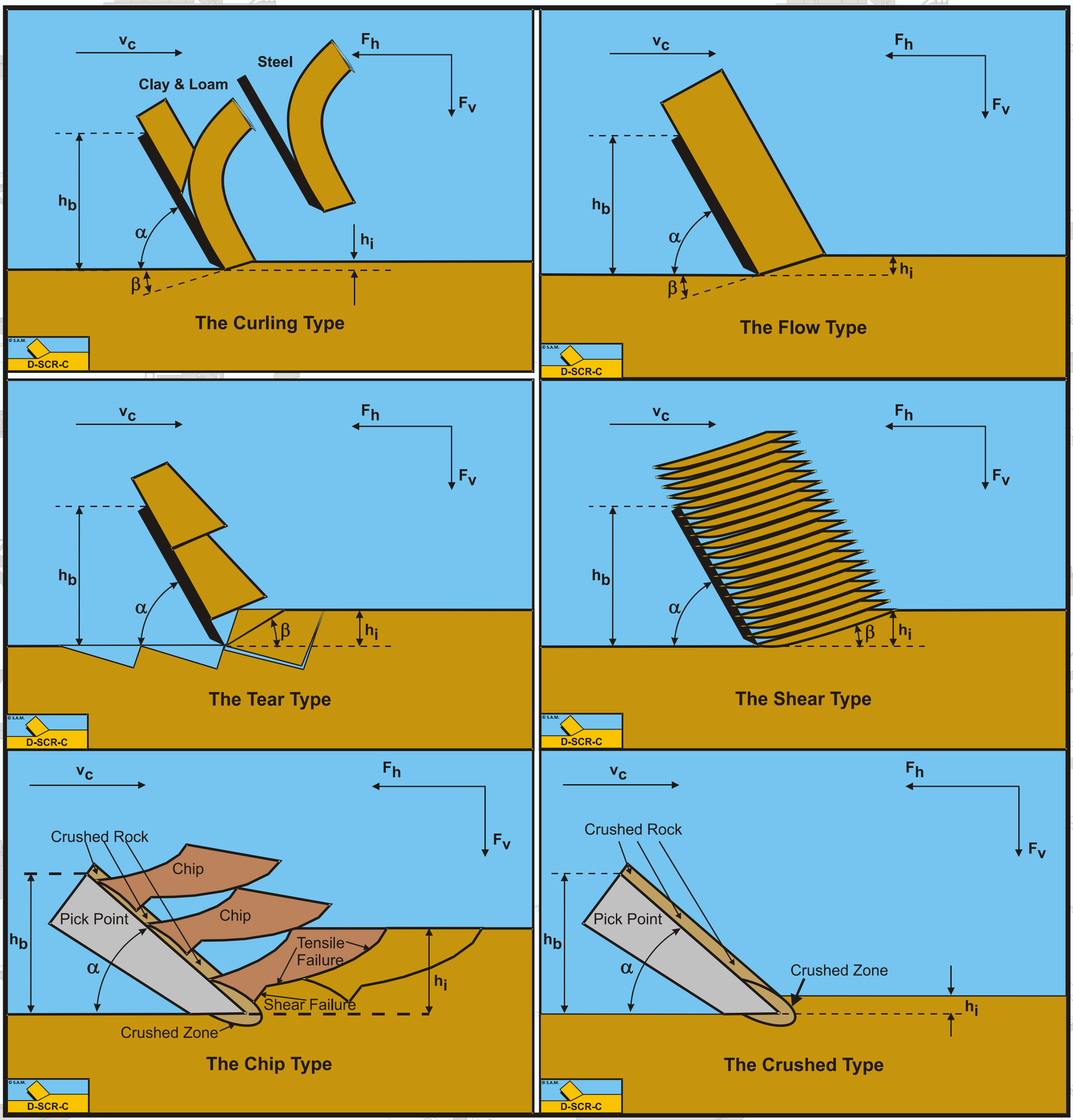

By

Sape A. Miedema

The cover shows a father and a son (or a teacher and a student) cutting sand on the beach, making a soil structure, with the city of Delft in the background and a historic dredge in the water. The cover has been designed by Riëlle van der Meijden of About Colors (www.aboutcolors.nl) and is inspired by:

The comic book Oscar & Isidoor was made by Frederic Antonin Breysse (1907-2001) in the period 1945-1955. The comics were first published in the French magazine "Coeurs Vaillants" and later in the Dutch magazine "Taptoe".

This comic book was the first comic book read by the author around 1960.

The painting "View on Delft" is an oil painting by Johannes Vermeer (1632-1675) painted in 1660-1661.

The painting shows the city of Delft, which is the residence of the author since 1974 and the location of Delft University of Technology, established in 1842.

In 1761 a dredging machine was invented by F.X. dÁrles de Liniere for the maintenance of rivers and canals in Holland. To explain the patent, he added a color drawing. The patent was accepted by the "Staten van Holland".

This drawing is used in the lectures of the author to show how dredging started.

The Delft Sand, Clay & Rock Cutting Model

Family 3rd Edition

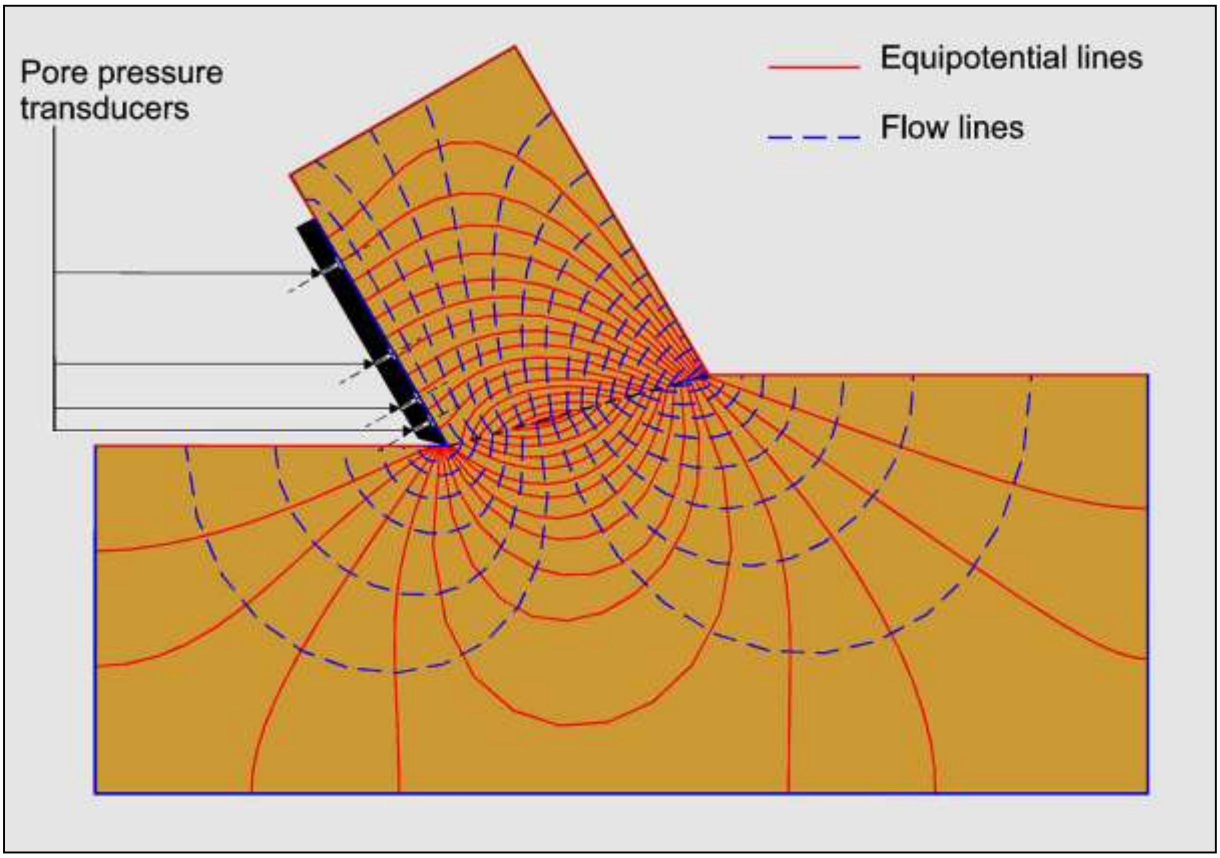

By

Sape A. Miedema

Delft University Press

Preliminary edition:
ISBN Book: 978-94-6186-249-5
ISBN EBook: 978-94-6186-252-5

1st edition, 2014:
ISBN Book: 978-1-61499-453-4
ISBN EBook: 978-1-61499-454-1
DOI: 10.3233/978-1-61499-454-1-i

2nd edition, 2015, version: Wednesday, January 27, 2016:
ISBN Book: 978-94-6186-537-3
ISBN EBook: 978-94-6186-539-7

Publisher
IOS Press BV
Nieuwe Hemweg 6b
1013 BG Amsterdam
The Netherlands
Tel: +31-20-688 3355
Fax: +31-20-687 0019
Email: order@iospress.nl
www.iospress.nl

Distributor in the USA & Canada
IOS Press, Inc.
4502 Rachael Manor Drive
Fairfax, VA 22032
USA
Fax: +1 703 323 3668
Email: iosbooks@iospress.com

PRINTED IN THE NETHERLANDS

Preface

In dredging, trenching, (deep sea) mining, drilling, tunnel boring and many other applications, sand, clay or rock has to be excavated. The productions (and thus the dimensions) of the excavating equipment range from mm^3/sec - cm^3/sec to m^3/sec. In oil drilling layers with a thickness of a magnitude of 0.2 mm are cut, while in dredging this can be of a magnitude of 0.1 m with cutter suction dredges and meters for clamshells and backhoe's. Some equipment is designed for dry soil, while others operate under water saturated conditions. Installed cutting powers may range up to 10 MW. For both the design, the operation and production estimation of the excavating equipment it is important to be able to predict the cutting forces and powers. After the soil has been excavated it is usually transported hydraulically as a slurry over a short (TSHD's) or a long distance (CSD's) or mechanically. Estimating the pressure losses and determining whether or not a bed will occur in the pipeline is of great importance. Fundamental processes of sedimentation, initiation of motion and erosion of the soil particles determine the transport process and the flow regimes. In TSHD's the soil has to settle during the loading process, where also sedimentation and erosion will be in equilibrium. In all cases we have to deal with soil and high density soil water mixtures and its fundamental behavior.

This book gives an overview of cutting theories. It starts with a generic model, which is valid for all types of soil (sand, clay and rock) after which the specifics of dry sand, water saturated sand, clay, atmospheric rock and hyperbaric rock are covered. For each soil type small blade angles and large blade angles, resulting in a wedge in front of the blade, are discussed. The failure mechanism of sand, dry and water saturated, is the so called **Shear Type**. The failure mechanism of clay is the so called **Flow Type**, but under certain circumstances also the **Curling Type** and the **Tear Type** are possible. Rock will usually fail in a brittle way. This can be brittle tensile failure, the **Tear Type** for small blade angles, but it can also be brittle shear failure, which is of the **Shear Type** of failure mechanism for larger blade angles. For practical cutting angles in dredging a combination may occur, the **Chip Type.** Under hyperbaric conditions rock may also fail in a more apparent ductile way according to the **Flow Type** or **Crushed Type** of failure mechanism. This is also called cataclastic failure.

For each case considered, the equations/model for the cutting forces, power and specific energy are given. The models are verified with laboratory research, mainly at the Delft University of Technology, but also with data from literature.

The model is named The Delft Sand, Clay & Rock Cutting Model. Up to date information (modifications and additions) and high resolution graphs and drawings can be found on the website www.dscrcm.com.

About the Author.

Dr.ir. Sape A. Miedema (November 8th 1955) obtained his M.Sc. degree in Mechanical Engineering with honours at the Delft University of Technology (DUT) in 1983. He obtained his Ph.D. degree on research into the basics of soil cutting in relation with ship motions, in 1987. From 1987 to 1992 he was Assistant Professor at the chair of Dredging Technology. In 1992 and 1993 he was a member of the management board of Mechanical Engineering & Marine Technology of the DUT. In 1992 he became Associate Professor at the DUT with the chair of Dredging Technology. From 1996 to 2001 he was appointed Head of Studies of Mechanical Engineering and Marine Technology at the DUT, but still remaining Associate Professor of Dredging Engineering. In 2005 he was appointed Head of Studies of the MSc program of Offshore & Dredging Engineering and he is also still Associate Professor of Dredging Engineering. In 2013 he was also appointed as Head of Studies of the MSc program Marine Technology of the DUT.

Dr.ir. S.A. Miedema teaches (or has taught) courses on soil mechanics and soil cutting, pumps and slurry transport, hopper sedimentation and erosion, mechatronics, applied thermodynamics related to energy, drive system design principles, mooring systems, hydromechanics and mathematics. He is (or has been) also teaching at Hohai University, Changzhou, China, at Cantho University, Cantho Vietnam, at Petrovietnam University, Baria, Vietnam and different dredging companies in the Netherlands and the USA.
His research focuses on the mathematical modeling of dredging systems like, cutter suction dredges, hopper dredges, clamshell dredges, backhoe dredges and trenchers. The fundamental part of the research focuses on the cutting processes of sand, clay and rock, sedimentation processes in Trailing Suction Hopper Dredges and the associated erosion processes. Lately the research focuses on hyperbaric rock cutting in relation with deep sea mining and on hydraulic transport of solids/liquid settling slurries.

This book is dedicated to my father

Jacob Miedema

April 7th 1928 – July 18th 2015

Table of Contents

Chapter 1: Introduction.

1.1. Approach.

This book gives an overview of cutting theories for the cutting of sand, clay and rock as applied in dredging engineering. In dredging engineering in general sand, clay and rock are excavated with buckets of bucket ladder dredges, cutter heads of cutter suction dredges, dredging wheels of wheel dredges, drag heads of trailing suction hopper dredges, clamshells, backhoes and other devices. Usually the blades have a width much larger than the layer thickness of the cut (2D process) and the blade angles of these devices are not too large in the range of 30°-60°. Although clamshells and backhoes may have blade angles around 90° when they start cutting. Other devices like drill bits of oil drilling devices, blades of tunnel boring machines, ice berg scour and the bull dozer effect in front of a drag head may have cutting angles larger than 90°. In such a case a different cutting mechanism is encountered, the so called wedge mechanism.

The book starts with some basic soil mechanics, the Mohr circle and active and passive soil failure in *Chapter 2: Basic Soil Mechanics*. These topics can also be found in any good soil mechanics book, but covering this makes the reader familiar with the use of the many trigonometrically equations and derivations as applied in the cutting theories.

A generic cutting theory for small blade angles is derived in *Chapter 3: The General Cutting Process.* This generic cutting theory assumes a 2D plane strain cutting process, where the failure lines are considered to be straight lines. The generic cutting theory takes all the possible forces into account. One can distinguish normal and friction forces, cohesive and adhesive forces, gravitational and inertial forces and pore vacuum pressure forces.
Six types of cutting mechanisms are distinguished; the **Shear Type**, the **Flow Type**, the **Curling Type,** the **Tear Type**, the **Crushed Type** and the **Chip Type**.
The **Shear Type**, the **Flow Type** and the **Crushed Type** are mathematically equivalent.
The **Chip Type** is a mix of the **Shear Type** and the **Tear Type**.
The generic theory also contains a chapter on the so called **snow plough effect**, a blade not perpendicular to the direction of the cutting velocity like a snow plough. Finally the methods for determining the shear plane angle and the specific energy are discussed.

In *Chapter 4: Which Cutting Mechanism for Which Kind of Soil?* it is discussed which terms in the generic equation are valid in which type of soil. A matrix is given to enable the reader to determine the terms and soil properties of influence.

The following chapters give the 2D theory of soil cutting with small blade angles that will enable the reader to determine the cutting forces, powers and production in different types of soil.

Dry sand cutting is dominated by gravitational and inertial forces and by the internal and external friction angles. The cutting mechanism is the **Shear Type**. This is covered in *Chapter 5: Dry Sand Cutting.*

Saturated sand cutting is dominated by pore vacuum pressure forces and by the internal and external friction angles. The cutting mechanism is the **Shear Type**. This is covered in *Chapter 6: Saturated Sand Cutting.*

Clay cutting is dominated by cohesive (internal shear strength) and adhesive (external shear strength) forces. The basic cutting mechanism is the **Flow Type**. Cutting a thin layer, combined with a high adhesive force may result in the **Curling Type** mechanism. Cutting a thick layer combined with a small adhesive force and a low tensile strength may result in the **Tear Type** mechanism. This is covered in *Chapter 7: Clay Cutting*.

Rock cutting under atmospheric conditions (normal dredging) is dominated by the internal shear strength and by the internal and external friction angles. The main cutting mechanism is the **Chip Type** a mix of the **Shear Type** and the **Tear Type**, brittle cutting**.** At small blade angles the pure **Tear Type** may occur, at large blade angle the pure **Shear Type**. Cutting a very thin layer or using large blade angles may result in the **Crushed Type.** This is covered in *Chapter 8: Rock Cutting: Atmospheric Conditions*.

Rock cutting under hyperbaric conditions (deep sea mining) is dominated by the internal shear strength, the pore vacuum pressure forces and by the internal and external friction angles. The main cutting mechanism is the **Crushed Type**, cataclastic semi-ductile cutting**.** This is covered in *Chapter 9: Rock Cutting: Hyperbaric Conditions*.

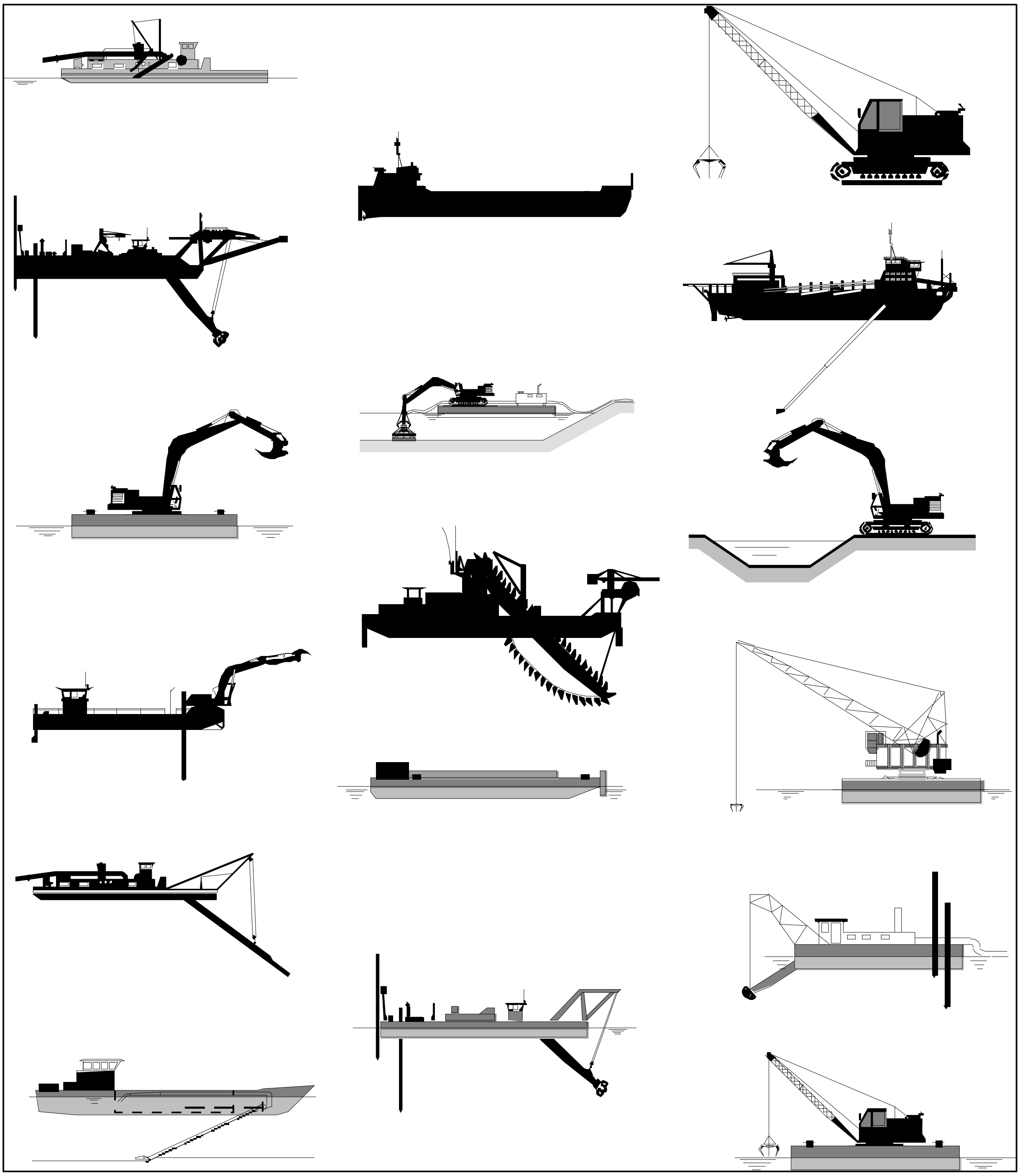

Figure 1-1: Different types of dredging equipment.

At large blade angles, the theory of the 2D cutting process at small blade angles can no longer be valid. This theory would give very large and even negative cutting forces which is physically impossible. The reason for this is a sine in the denominator of the generic cutting force equation containing the sum of the blade angle, the shear angle, the internal friction angle and the external friction angle. If the sum of these 4 angles approaches 180 degrees, the sine will become very small resulting in very high cutting forces. If the sum of these 4 angles exceeds 180 degrees, the sine is negative resulting in negative cutting forces. Nature will find another mechanism which is identified as the wedge mechanism. In front of the blade a wedge will occur, with an almost fixed wedge angle, reducing the cutting forces. *Chapter 10: The Occurrence of a Wedge* describes the generic theory for the occurrence of a wedge in front of the blade.

The following chapters give the theory of soil cutting at large blade angles that will enable the reader to determine the cutting forces, powers and production in different types of soil.

In dry sand cutting the blade angle, the shear angle, the internal friction angle and the external friction angle play a role. The issue of the sum of these 4 angles approaching or exceeding 180 degrees may occur for large blade angles. This is covered in *Chapter 11: A Wedge in Dry Sand Cutting*.

In saturated sand cutting the blade angle, the shear angle, the internal friction angle and the external friction angle play a role. The issue of the sum of these 4 angles approaching or exceeding 180 degrees may occur for large blade angles. This is covered in *Chapter 12: A Wedge in Saturated Sand Cutting*.

In clay cutting the blade angle and the shear angle play a role. The issue of the sum of these 4 angles approaching or exceeding 180 degrees may occur for very large blade angles, for example ice berg scour. This is covered in *Chapter 13: A Wedge in Clay Cutting*.

In atmospheric rock cutting the blade angle, the shear angle, the internal friction angle and the external friction angle play a role. The issue of the sum of these 4 angles approaching or exceeding 180 degrees may occur for large blade angles. This is covered in *Chapter 14: A Wedge in Atmospheric Rock Cutting*.

In hyperbaric rock cutting the blade angle, the shear angle, the internal friction angle and the external friction angle play a role. The issue of the sum of these 4 angles approaching or exceeding 180 degrees may occur for large blade angles. This is covered in *Chapter 15: A Wedge in Hyperbaric Rock Cutting*.

Appendix Y shows all the different equipment the theory can be applied to and Appendix Z gives a list of the publications this book is based on. It is the choice of the author to make each chapter self-containing, meaning that figures and basic equations may be repeated at the start of each chapter.
In the appendices many graphs, charts and tables are shown, much more than in the corresponding chapters, in order to give the reader all the information necessary to apply the theory in this book in a proper way.
Empty space and pages are filled with figures and photos illustrating different equipment for soil cutting.

The book is used for the MSc program of Offshore & Dredging Engineering at the Delft University of Technology.

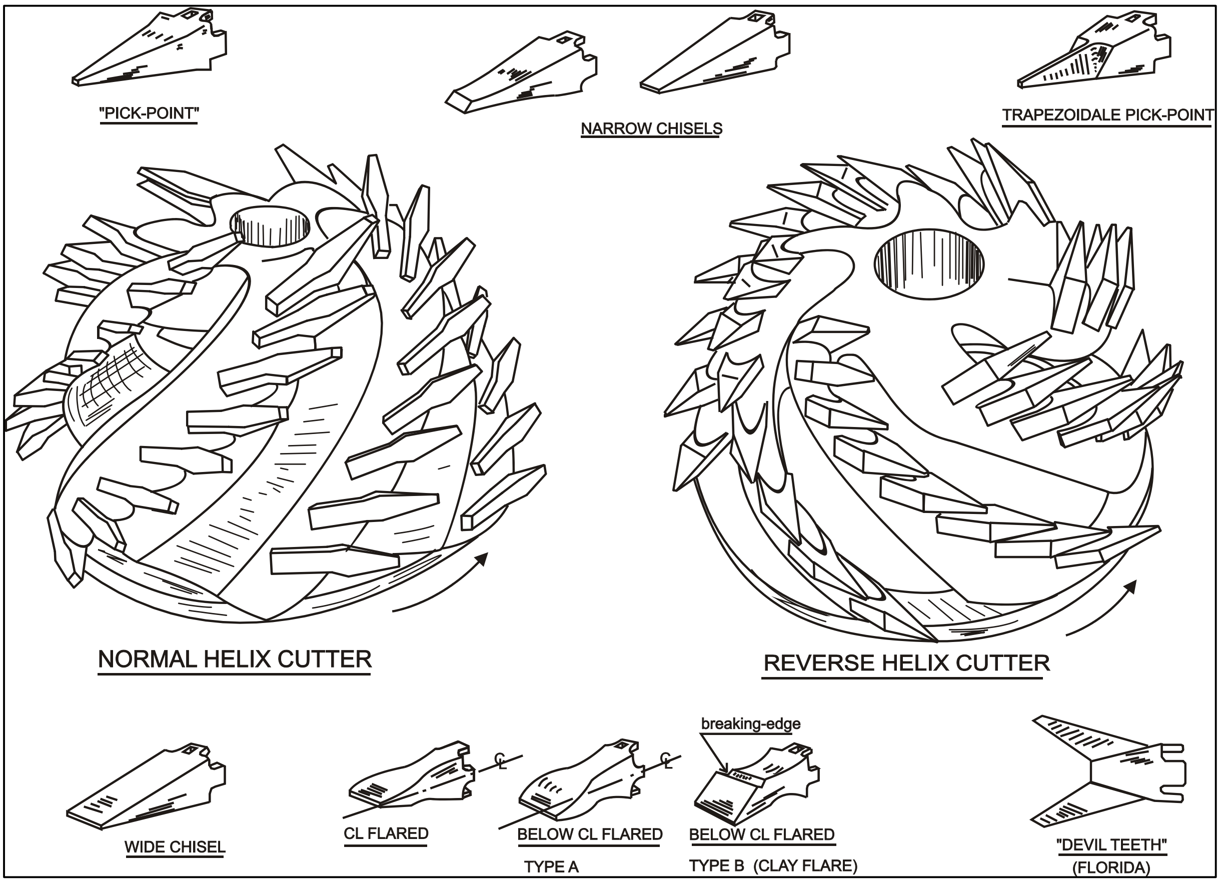

Figure 1-2: A rock cutter head with pick points.

Figure 1-3: The author on the clamshell dredge "Chicago" of Great Lakes Dredge & Dock.

Figure 1-4: The author on the backhoe dredge "New York" of Great Lakes Dredge & Dock.

Chapter 2: Basic Soil Mechanics.

2.1. Introduction.

Cutting processes of soil distinguish from the classical soil mechanics in civil engineering in the fact that:

Classical soil mechanics assume:
1. Small to very small strain rates.
2. Small to very small strains.
3. A very long time span, years to hundreds of years.
4. Structures are designed to last forever.

Cutting processes assume:
1. High to very high strain rates.
2. High to very high strains and deformations in general.
3. A very short time span, following from very high cutting velocities.
4. The soil is supposed to be excavated, the coherence has to be broken.

For the determination of cutting forces, power and specific energy the criterion for failure has to be known. In this book the failure criterion of Mohr-Coulomb will be applied in the mathematical models for the cutting of sand, clay and rock. The Mohr–Coulomb theory is named in honor of Charles-Augustin de Coulomb and Christian Otto Mohr. Coulomb's contribution was a 1773 essay entitled "*Essai sur une application des règles des maximis et minimis à quelques problèmes de statique relatifs à l'architecture*". Mohr developed a generalized form of the theory around the end of the 19th century. To understand and work with the Mohr-Coulomb failure criterion it is also necessary to understand the so called Mohr circle. The Mohr circle is a two dimensional graphical representation of the state of stress at a point. The abscissa, $\boldsymbol{\sigma}$, and ordinate, $\boldsymbol{\tau}$, of each point on the circle are the normal stress and shear stress components, respectively, acting on a particular cut plane under an angle $\boldsymbol{\alpha}$ with the horizontal. In other words, the circumference of the circle is the locus of points that represent the state of stress on individual planes at all their orientations. In this book a plane strain situation is considered, meaning a two-dimensional cutting process. The width of the blades considered $\mathbf{w}$ is always much bigger than the layer thickness $\mathbf{h_i}$ considered. In geomechanics (soil mechanics and rock mechanics) compressive stresses are considered positive and tensile stresses are considered to be negative, while in other engineering mechanics the tensile stresses are considered to be positive and the compressive stresses are considered to be negative. Here the geomechanics approach will be applied. There are two special stresses to be mentioned, the so called principal stresses. Principal stresses occur at the planes where the shear stress is zero. In the plane strain situation there are two principal stresses, which are always under an angle of 90° with each other.

In order to understand the cutting processes in sand, clay and rock, it is required to have knowledge of basic soil and rock mechanics. The next chapters 2.2-2.7 cover this knowledge and have been composed almost entirely from information from the public domain, especially internet. Most information comes from Wikipedia and Answers.com.

2.2. Soil Mechanics.

2.2.1. Definition.

McGraw-Hill Science & Technology Encyclopedia gives the following description of Soil Mechanics:
The study of the response of masses composed of soil, water, and air to imposed loads. Because both water and air are able to move through the soil pores, the discipline also involves the prediction of these transport processes. Soil mechanics provides the analytical tools required for foundation engineering, retaining wall design, highway and railway sub base design, tunneling, earth dam design, mine excavation design, and so on. Because the discipline relates to rock as well as soils, it is also known as geotechnical engineering. Soil consists of a multiphase aggregation of solid particles, water, and air.

This fundamental composition gives rise to unique engineering properties, and the description of the mechanical behavior of soils requires some of the most sophisticated principles of engineering mechanics. The terms multiphase and aggregation both imply unique properties. As a multiphase material, soil exhibits mechanical properties that show the combined attributes of solids, liquids, and gases. Individual soil particles behave as solids, and show relatively little deformation when subjected to either normal or shearing stresses. Water behaves as a liquid, exhibiting little deformation under normal stresses, but deforming greatly when subjected to shear. Being a viscous liquid, however, water exhibits a shear strain rate that is proportional to the shearing stress. Air in the soil behaves as a gas, showing appreciable deformation under both normal and shear stresses. When the three phases are combined to form a soil mass, characteristics that are an outgrowth of the interaction of the phases are manifest. Moreover, the particulate nature of the solid particles contributes other unique attributes.

Figure 2-1: Earthwork in Germany (source Wikimedia).

When dry soil is subjected to a compressive normal stress, the volume decreases nonlinearly; that is, the more the soil is compressed, the less compressible the mass becomes. Thus, the more tightly packed the particulate mass becomes, the more it resists compression. The process, however, is only partially reversible, and when the compressive stress is removed the soil does not expand back to its initial state.

When this dry particulate mass is subjected to shear stress, an especially interesting behavior owing to the particulate nature of the soil solids results. If the soil is initially dense (tightly packed), the mass will expand because the particles must roll up and over each other in order for shear deformation to occur. Conversely, if the mass is initially loose, it will compress when subjected to a shear stress. Clearly, there must also exist a specific initial density (the critical density) at which the material will display zero volume change when subjected to shear stress. The term dilatancy has been applied to the relationship between shear stress and volume change in particulate materials. Soil is capable of resisting shear stress up to a certain maximum value. Beyond this value, however, the material undergoes large, uncontrolled shear deformation.

The other limiting case is saturated soil, that is, a soil whose voids are entirely filled with water. When such a mass is initially loose and is subjected to compressive normal stress, it tends to decrease in volume; however, in order for this volume decrease to occur, water must be squeezed from the soil pores. Because water exhibits a viscous resistance to flow in the microscopic pores of fine-grained soils, this process can require considerable time, during which the pore water is under increased pressure. This excess pore pressure is at a minimum near the drainage face of the soil mass and at a maximum near the center of the soil sample. It is this gradient (or change in pore water pressure with change in position within the soil mass) that causes the outflow of water and the corresponding decrease in volume of the soil mass. Conversely, if an initially dense soil mass is subjected to shear stress, it tends to expand. The expansion, however, may be time-dependent because of the viscous resistance to water being drawn into the soil pores. During this time the pore water will be under decreased pressure. Thus, in saturated soil masses, changes in pore water pressure and time-dependent volume change can be induced by either changes in normal stress or by changes in shear stress.

2.2.2. Soil Creation.

The primary mechanism of soil creation is the weathering of rock. All rock types (igneous rock, metamorphic rock and sedimentary rock) may be broken down into small particles to create soil. Weathering mechanisms are physical weathering, chemical weathering, and biological weathering. Human activities such as excavation, blasting, and waste disposal, may also create soil. Over geologic time, deeply buried soils may be altered by pressure and temperature to become metamorphic or sedimentary rock, and if melted and solidified again, they would complete the geologic cycle by becoming igneous rock.

Physical weathering includes temperature effects, freeze and thaw of water in cracks, rain, wind, impact and other mechanisms. Chemical weathering includes dissolution of matter composing a rock and composition of soils. Physical weathering includes temperature effects, freeze and thaw of water in cracks, rain, wind, impact and other mechanisms. Chemical weathering includes dissolution of matter composing a rock and precipitation in the form of another mineral. Clay minerals, for example can be formed by weathering of feldspar, which is the most common mineral present in igneous rock. The most common mineral constituent of silt and sand is quartz, also called silica, which has the chemical name silicon dioxide. The reason that feldspar is most common in rocks but silicon is more prevalent in soils is that feldspar is much more soluble than silica. Silt, Sand, and Gravel are basically little pieces of broken rocks. According to the Unified Soil Classification System, silt particle sizes are in the range of 0.002 mm to 0.075 mm and sand particles have sizes in the range of 0.075 mm to 4.75 mm. Gravel particles are broken pieces of rock in the size range 4.75 mm to 100 mm. Particles larger than gravel are called cobbles and boulders.

Figure 2-2: Fox glacier, New Zealand (source Wikimedia).

Soil deposits are affected by the mechanism of transport and deposition to their location. Soils that are not transported are called residual soils -- they exist at the same location as the rock from which they were generated. Decomposed granite is a common example of a residual soil. The common mechanisms of transport are the actions of gravity, ice, water, and wind. Wind-blown soils include dune sands and loess. Water carries particles of different size depending on the speed of the water, thus soils transported by water are graded according to their size. Silt and clay may settle out in a lake, and gravel and sand collect at the bottom of a river bed. Wind-blown soil deposits (aeolian soils) also tend to be sorted according to their grain size. Erosion at the base of glaciers is powerful enough

to pick up large rocks and boulders as well as soil; soils dropped by melting ice can be a well graded mixture of widely varying particle sizes. Gravity on its own may also carry particles down from the top of a mountain to make a pile of soil and boulders at the base; soil deposits transported by gravity are called colluvium.
The mechanism of transport also has a major effect on the particle shape. For example, low velocity grinding in a river bed will produce rounded particles. Freshly fractured colluvium particles often have a very angular shape.

2.2.3. Soil Classification.

Soil classification deals with the systematic categorization of soils based on distinguishing characteristics as well as criteria that dictate choices in use.

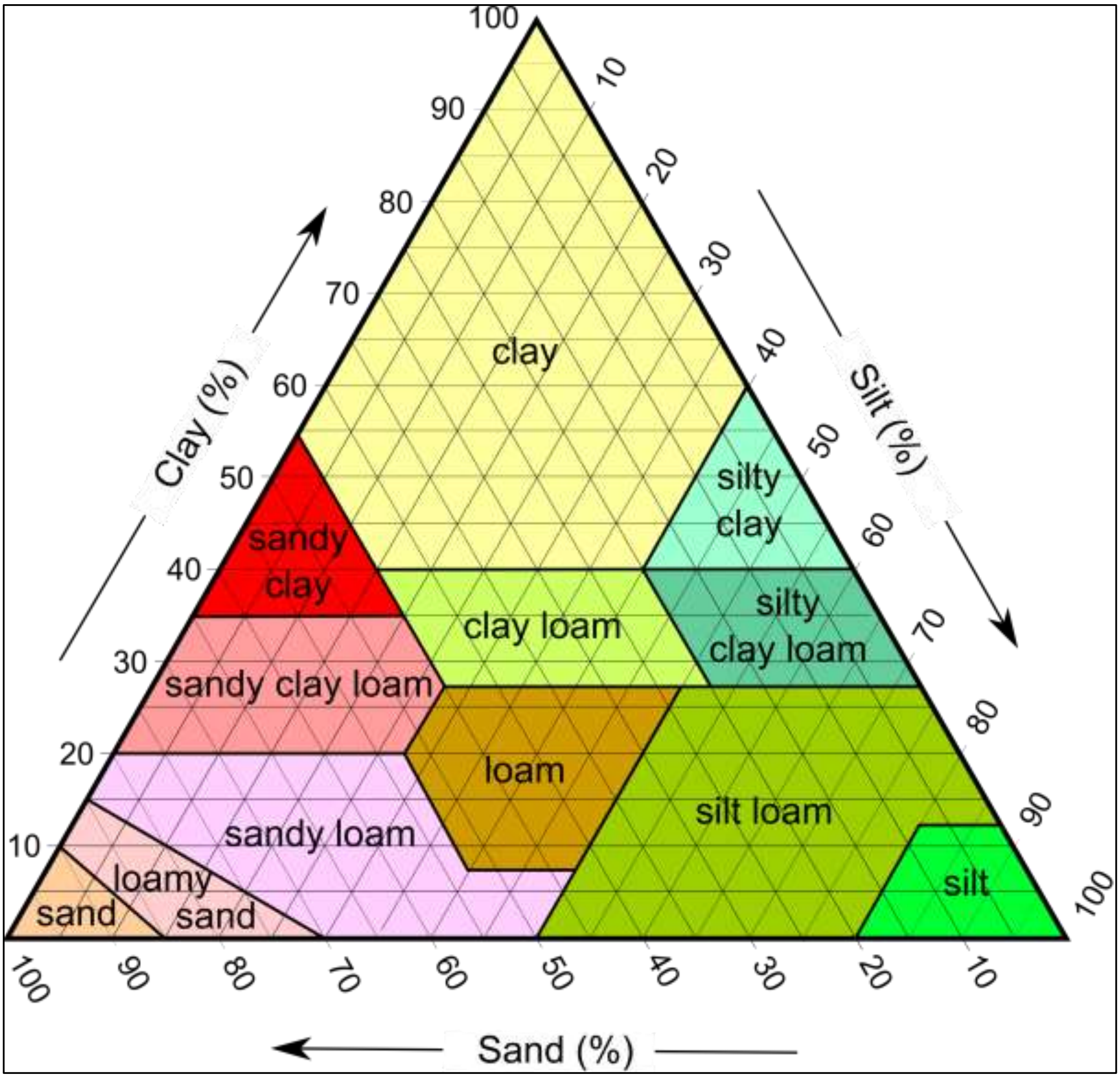

Figure 2-3: Soil naming according to USDA.

Soil texture is a qualitative classification tool used in both the field and laboratory to determine classes for agricultural soils based on their physical texture. The classes are distinguished in the field by the 'textural feel' which can be further clarified by separating the relative proportions of sand, silt and clay using grading sieves: The Particle Size Distribution (PSD). The class is then used to determine crop suitability and to approximate the soils responses to environmental and management conditions such as drought or calcium (lime) requirements. A qualitative rather than a quantitative tool it is a fast, simple and effective means to assess the soils physical characteristics. Although the U.S.D.A. system uses 12 classes whilst the U.K.-ADAS uses just 11 the systems are mutually compatible as shown in the combined soil textural triangle below.

Hand analysis, whilst an arbitrary technique, is an extremely simple and effective means to rapidly assess and classify a soils physical condition. Correctly executed the procedure allows for rapid and frequent assessment of soil characteristics with little or no equipment. It is thus an extremely useful tool for identifying spatial variation both within and between plots (fields) as well as identifying progressive changes and boundaries between soil classes and orders.

The method involves taking a small sample of soil, sufficient to roll into a ball of approximately 2.5 cm diameter, from just below the surface. Using a small drop of water or 'spit' the sample is then moisten to the sticky point (the point at which it begins to adhere to the finger). The ball is then molded to determine its workability and its class according to the steps in the chart opposite.

Soil separates are specific ranges of particle sizes. In the United States, the smallest particles are clay particles and are classified by the USDA as having diameters of less than 0.002 mm. The next smallest particles are silt particles and have diameters between 0.002 mm and 0.05 mm. The largest particles are sand particles and are larger than 0.05 mm in diameter. Furthermore, large sand particles can be described as coarse, intermediate as medium, and the smaller as fine. Other countries have their own particle size classifications.

Table 2-1: Soil Classification.

Name of Soil	Diameter Limits (mm)
Clay	<0.002
Fine silt	0.002–0.006
Medium silt	0.006-0.020
Coarse silt	0.020-0.060
Very fine sand	0.060–0.100
Fine sand	0.100–0.200
Medium sand	0.200–0.600
Coarse sand	0.600–1.000
Very coarse sand	1.000–2.000
Fine gravel	2-6
Medium gravel	6-20
Coarse gravel	20-60
Cobbles	60-200
Boulders	>200

Figure 2-4: Soil failure (www.4isfge.org).

Figure 2-5: The Wenjiagou landslide (blogs.agu.org).

Figure 2-6: Karl von Terzaghi, one of the founders of modern soil mechanics.

2.3. Soils.

2.3.1. Sand.

Sand is any material composed of loose, stony grains between 1/16 mm and 2 mm in diameter. Larger particles are categorized as gravel; smaller particles are categorized as silt or clay. Sands are usually created by the breakdown of rocks, and are transported by wind and water, before depositing to form soils, beaches, dunes, and underwater fans or deltas. Deposits of sand are often cemented together over time to form sandstones.

The most common sand-forming process is weathering, especially of granite. Granite consists of distinct crystals of quartz, feldspar, and other minerals. When exposed to water, some of these minerals (e.g., feldspar) decay chemically faster than others (especially quartz), allowing the granite to crumble into fragments. Sand formed by weathering is termed epiclastic.

Figure 2-7: Sand from the Gobi desert, Mongolia (source Wikimedia).

Where fragmentation is rapid, granite crumbles before its feldspar has fully decayed and the resulting sand contains more feldspar. If fragmentation is slow, the resulting sand contains less feldspar. Fragmentation of rock is enhanced by exposure to fast-running water, so steep mountains are often source areas for feldspar-rich sands and gentler terrains are often source areas for feldspar-poor sands. Epiclastic sands and the sandstones formed from them thus record information about the environments that produce them. A sedimentologist can deduce the existence of whole mountain ranges long ago eroded, and of mountain-building episodes that occurred millions of years ago from sandstones rich in relatively unstable minerals like feldspar.

The behavior of sand carried by flowing water can inscribe even more detailed information about the environment in sand deposits. When water is flowing rapidly over a horizontal surface, any sudden vertical drop in that surface splits the current into two layers, (1) an upper layer that continues to flow downstream and (2) a slower backflow that curls under in the lee of the drop-off. Suspended sand tends to settle out in the backflow zone, building a slope called a "slip face" that tilts downhill from the drop-off. The backflow zone adds continually to the slip face, growing it downstream, and as the slip face grows downstream its top edge continues to create a backflow zone. The result is the deposition of a lengthening bed of sand. Typically, periodic avalanches of large grains down the slip face (or other processes) coat it with thin layers of distinctive material. These closely-spaced laminations are called "cross bedding" because they angle across the main bed. Cross-bedding in sandstone records the direction of the current that deposited the bed, enabling geologists to map currents that flowed millions of years ago (paleocurrents).

Evidence of grain size, bed thickness, and cross-bedding angle, allows geologists to determine how deep and fast a paleocurrent was, and thus how steep the land was over which it flowed.

Figure 2-8: Sand in the Sahara desert (source Luca Galuzzi – www.galuzzi.it)

Ripples and dunes—probably the most familiar forms created by wind- or waterborne sand—involve similar processes. However, ripples and dunes are more typical of flow systems to which little or no sand is being added. The downstream slip faces of ripples and dunes are built from grains plucked from their upstream sides, so these structures can migrate without growing. When water or wind entering the system (e.g., water descending rapidly from a mountainous region) imports large quantities of sand, the result is net deposition rather than the mere migration of sand forms.

Grain shape, too, records history. All epiclastic grains of sand start out angular and become more rounded as they are polished by abrasion during transport by wind or water. Quartz grains, however, resist wear. One trip down a river is not enough to thoroughly round an angular grain of quartz; even a long sojourn on a beach, where grains are repeatedly tumbled by waves, does not suffice. The well-rounded state of many quartz sands can be accounted for only by crustal recycling. Quartz grains can survive many cycles of erosion, burial and cementation into sandstone, uplift, and re-erosion. Recycling time is on the order of 200 million years, so a quartz grain first weathered from granite 2.4 billion years ago may have gone through 10 or 12 cycles of burial and re-erosion to reach its present day state. An individual quartz grain's degree of roundness is thus an index of its antiquity. Feldspar grains can also survive recycling, but not as well, so sand that has been recycled a few times consists mostly of quartz.

Sand can be formed not only by weathering but by explosive volcanism, the breaking up of shells by waves, the cementing into pellets of finer-grained materials (pelletization), and the precipitation of dissolved chemicals (e.g., calcium carbonate) from solution.

Pure quartz sands are mined to make glass and the extremely pure silicon employed in microchips and other electronic components.

2.3.2. Clay.

Clay is a fine-grained (small particle size) sedimentary rock. Clay is so fine-grained it is rarely possible to see the individual mineral particles with the naked eye. The definition of clays describes rocks with particle sizes of less than 4 μm in diameter. Most sedimentary rocks are described using both mineral content and particle size. While this is also true for clays, the particle size description is most reliable and most often used.

Figure 2-9: Quaternary clay in Estonia (source Wikimedia)

The majority of common types of minerals found in clays are kaolinite (a soapy-feeling and lightweight mineral), talc, pyrophyllite, all types of micas, minerals from the chlorite group, feldspars, and a lesser amount of tectosilicates (including quartz).

The mineral content of clays is less variable than other types of sedimentary rock. This is a direct result of the way clays are formed. Water carries the bulk of sediments to their resting place where they are cemented together. The transport of sediments is directly related to the force or velocity of water carrying them. The stronger the velocity of water, the larger and heavier the particle it can move. Conversely, the weaker the flow, the smaller the particle that is carried by the water. As a result, water acts as a winnowing filter for certain types of minerals. The heavier minerals are not carried as far by water currents as are the lighter ones. When water finally comes to rest, it deposits its load of minerals. The last to be released are the lighter and smaller particles, the clay minerals.

Where rivers meet oceans, the clay minerals are so light they are usually carried far out to sea where they fall gently to the bottom forming a fine-grained sediment. These deposits cover organic materials and trap them at the edges of deltas and continental slopes. Over millions of years, the organic materials convert to petroleum and remain trapped by the clays. This relationship makes the study of clays extremely important for petroleum geologists. In addition to this important economic consideration, clays provide important economic resources for a wide variety of other industries.

Depending on the academic source, there are three or four main groups of clays: kaolinite, montmorillonite, smectite, illite, and chlorite. Chlorites are not always considered a clay, sometimes being classified as a separate group within the phyllosilicates. There are approximately 30 different types of "pure" clays in these categories, but most "natural" clays are mixtures of these different types, along with other weathered minerals.

Varve (or varved clay) is clay with visible annual layers, formed by seasonal differences in erosion and organic content. This type of deposit is common in former glacial lakes. When glacial lakes are formed there is very little movement of the water that makes the lake, and these eroded soils settle on the lake bed. This allows such an even distribution on the different layers of clay.

Figure 2-10: Varved clay, Little River State Park, Waterbury, Vermont (source www.anr.state.vt.us).

Quick clay is a unique type of marine clay indigenous to the glaciated terrains of Norway, Canada, Northern Ireland, and Sweden. It is highly sensitive clay, prone to liquefaction, which has been involved in several deadly landslides.

Clays exhibit plasticity when mixed with water in certain proportions. When dry, clay becomes firm and when fired in a kiln, permanent physical and chemical changes occur. These reactions, among other changes, cause the clay to be converted into a ceramic material. Because of these properties, clay is used for making pottery items, both utilitarian and decorative. Different types of clay, when used with different minerals and firing conditions, are used to produce earthenware, stoneware, and porcelain. Prehistoric humans discovered the useful properties of clay, and one of the earliest artifacts ever uncovered is a drinking vessel made of sun-dried clay. Depending on the content of the soil, clay can appear in various colors, from a dull gray to a deep orange-red.

Clay tablets were used as the first known writing medium, inscribed with cuneiform script through the use of a blunt reed called a stylus.

Clays sintered in fire were the first form of ceramic. Bricks, cooking pots, art objects, dishware, and even musical instruments such as the ocarina can all be shaped from clay before being fired. Clay is also used in many industrial processes, such as paper making, cement production, and chemical filtering. Clay is also often used in the manufacture of pipes for smoking tobacco. Until the late 20th century bentonite clay was widely used as a mold binder in the manufacture of sand castings.

Clay, being relatively impermeable to water, is also used where natural seals are needed, such as in the cores of dams, or as a barrier in landfills against toxic seepage (lining the landfill, preferably in combination with geotextiles).

Recent studies have investigated clay's absorption capacities in various applications, such as the removal of heavy metals from waste water and air purification.

2.3.3. Rock.

To the geologist, the term rock means a naturally occurring aggregate of minerals that may include some organic solids (e.g., fossils) and/or glass. Rocks are generally subdivided into three large classes: igneous, sedimentary, and metamorphic. These classes relate to common origin, or genesis. Igneous rocks form from cooling liquid rock or related volcanic eruptive processes. Sedimentary rocks form from compaction and cementation of sediments. Metamorphic rocks develop due to solid-state, chemical and physical changes in pre-existing rock because of elevated temperature, pressure, or chemically active fluids.

With igneous rocks, the aggregate of minerals comprising these rocks forms upon cooling and crystallization of liquid rock. As crystals form in the liquid rock, they become interconnected to one another like jigsaw puzzle pieces. After total crystallization of the liquid, a hard, dense igneous rock is the result. Also, some volcanic lavas, when extruded on the surface and cooled instantaneously, will form a natural glass.

Figure 2-11: Sample of igneous gabbro, Rock Creek Canyon, California (source Wikimedia).

Glass is a mass of disordered atoms, which are frozen in place due to sudden cooling, and is not a crystalline material like a mineral. Glass composes part of many extrusive igneous rocks (e.g., lava flows) and pyroclastic igneous rocks. Alternatively, some igneous rocks are formed from volcanic processes, such as violent volcanic eruption. Violent eruptions eject molten, partially molten, and non-molten igneous rock, which then falls in the vicinity of the eruption. The fallen material may solidify into a hard mass, called pyroclastic igneous rock. The texture of igneous rocks (defined as the size of crystals in the rock) is strongly related to cooling rate of the original liquid. Rapid cooling of liquid rock promotes formation of small crystals, usually too small to see with the unaided eye. Rocks with this cooling history are called fine-textured igneous rocks. Slow cooling (which usually occurs deep underground) promotes formation of large crystals. Rocks with this cooling history are referred to as coarse-textured igneous rocks.

The mineral composition of igneous rocks falls roughly into four groups: silicic, intermediate, mafic, and ultramafic. These groups are distinguished by the amount of silica (SiO_4), iron (Fe), and magnesium (Mg) in the constituent minerals. Mineral composition of liquid rock is related to place of origin within the body of the earth. Generally speaking, liquids from greater depths within the earth contain more Fe and Mg and less SiO_4 than those from shallow depths.

In sedimentary rocks, the type of sediment that is compacted and cemented together determines the rock's main characteristics. Sedimentary rocks composed of sediment that has been broken into pieces (i.e., clastic sediment), such as gravel, sand, silt, and clay, are clastic sedimentary rocks (e.g., conglomerate, sandstone, siltstone, and shale, respectively). Sedimentary rocks composed of sediment that is chemically derived (i.e., chemical sediment), such as dissolved elements like calcium (Ca), sodium (Na), iron (Fe), and silicon (Si), are chemical sedimentary rocks. Examples of chemical sedimentary rocks are limestone (composed of calcium carbonate), rock salt (composed of sodium chloride), rock gypsum (composed of calcium sulfate), ironstones (composed of iron oxides), and chert (composed of hydrated silica). Biochemical sedimentary rocks are a special kind of chemical sedimentary rock wherein the constituent particles were formed by organisms (typically as organic hard parts, such as shells), which then became sedimentary particles. Examples of this special kind of sedimentary rock include chalk, fossiliferous limestone, and coquina. Sedimentary rocks are formed from sediment in two stages: compaction and cementation. Compaction occurs when sediments pile up to sufficient thickness that overlying mass squeezes out water and closes much open space. Cementation occurs when water flowing through the compacted sediment deposits mineral crystals upon particles thus binding them together. The main cement minerals are calcite ($CaCO_3$), hematite (Fe_2O_3), and quartz (SiO_2).

With metamorphic rocks, the nature of the pre-existing rock (protolith) determines in large part the characteristics of the ultimate metamorphic rock. Regardless of protolith, however, almost all metamorphic rocks are harder and more dense than their protoliths. A protolith with flat or elongate mineral crystals (e.g., micas or amphiboles) will yield a metamorphic rock with preferentially aligned minerals (due to directed pressure). Such metamorphic rocks are called foliated metamorphic rocks (e.g., slate and schist). Non-foliated metamorphic rocks (e.g., marble and quartzite) come from protoliths that have mainly equidimensional mineral crystals (e.g., calcite and quartz, respectively). For example, a protolith shale will yield a foliated metamorphic rock, and a protolith limestone will yield marble, a non-foliated metamorphic rock. Metamorphic rocks possess distinctive grades or levels of metamorphic change from minimal to a maximum near total melting. Low-grade metamorphic rocks generally have fine-textured crystals and low-temperature indicator minerals like the mica chlorite. High-grade metamorphic rocks generally have coarse-textured crystals and very distinctive foliation, plus high-temperature indicator minerals like the silicate mineral staurolite.

Rock is a brittle natural solid found mainly in the outer reaches of Earth's crust and upper mantle. Material that would be brittle rock at such shallow depths becomes to one degree or another rather plastic within the body of the earth. The term "rock" is not generally applied to such non-brittle internal Earth materials. Therefore, rock is a concept related to the outer shell of the earth. The term rock may also be properly applied to brittle natural solids found on the surfaces of other planets and satellites in our solar system. Meteorites are rock. Naturally occurring ice (e.g., brittle water ice in a glacier, H_2O) is also a rock, although we do not normally think of ice this way.

Rock has been an important natural resource for people from early in human evolution. Rocks' properties are the key to their specific usefulness, now as in the past. Hard, dense rocks that could be chipped into implements and weapons were among the first useful possessions of people. Fine-textured and glassy rocks were particularly handy for these applications. Later on, rock as building stone and pavement material became very important, and this continues today in our modern world. All of Earth's natural mineral wealth, fossil energy resources, and most groundwater are contained within rocks of the earth's crust.

Rock is a natural occurrence mass of cohesive organic or inorganic material, which forms a part earth crest of which most rocks are composed of one or more minerals. Rocks can be classified in different ways. The most used classification is based on their origin, in which the following classes can be distinguished.

Igneous rock; a rock that has solidified from molten rock material (magma), which was generated within the Earth. Well known are granite and basalt

Sedimentary rock; a rock formed by the consolidation of sediment settle out in water, ice of air and accumulated on the Earth’s surface, either on dry land or under water. Examples are sandstone, lime stone and clay stone

Metamorphic rock; any class of rocks that are the result of partial or complete recrystallization in the solid state of pre-existing rocks under conditions of temperature and pressure that are significantly different from those obtaining at the surface of the Earth.

When deterring the dredge-ability of rock, distinction has to be made between the properties of intact rock and that of a rock mass. Depending on the fracture density of the rock the cutter will cut intact rock or break out rock blocks.

In the first case the strength (tensile- and compressive strength), deformation properties (E-value) and the petrography (mineralogical proposition) of the intact rock determines the production completely. The second case the fracture frequency and the weathering of the rock is more important than the strength of the intact rock. It is known that the absence of water in rock is important for the rock strength. When saturated with water the rock strength can be 30 to 90 % of the strength of dry rock. Therefore rock samples have to be sealed immediately after drilling in such a way that evaporation of or intake of water is avoided. It has to be mentioned that this does not mean that cutting forces in saturated rock are always lower than in dry rock. The petrography is important for the weir of rock cutting tools.

Figure 2-12: Sandstone formations, Vermillion Cliffs, Arizona (source www.reddit.com).

Figure 2-13: Columns of Basalt of the Scottish Island of Staffa (National Geographic).

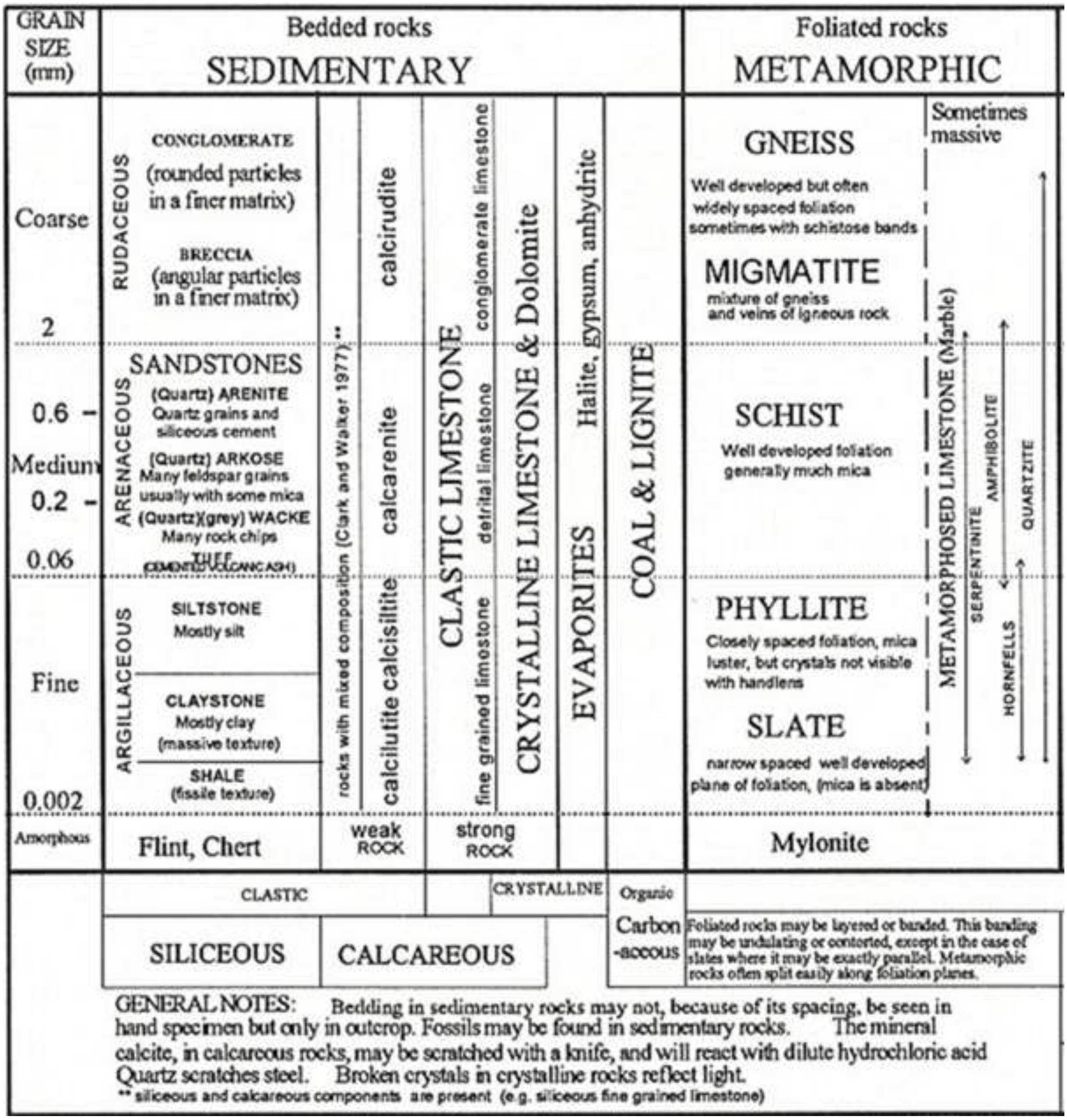

Foliated rocks may be layered or banded. This banding may be undulating or contorted, except in the case of slates where it may be exactly parallel. Metamorphic rocks often split easily along foliation planes.

GENERAL NOTES: Bedding in sedimentary rocks may not, because of its spacing, be seen in hand specimen but only in outcrop. Fossils may be found in sedimentary rocks. The mineral calcite, in calcareous rocks, may be scratched with a knife, and will react with dilute hydrochloric acid Quartz scratches steel. Broken crystals in crystalline rocks reflect light.

** siliceous and calcareous components are present (e.g. siliceous fine grained limestone)

Figure 2-14 A: Aid to identification of rock for engineering purposes (After BS 5930:1981).

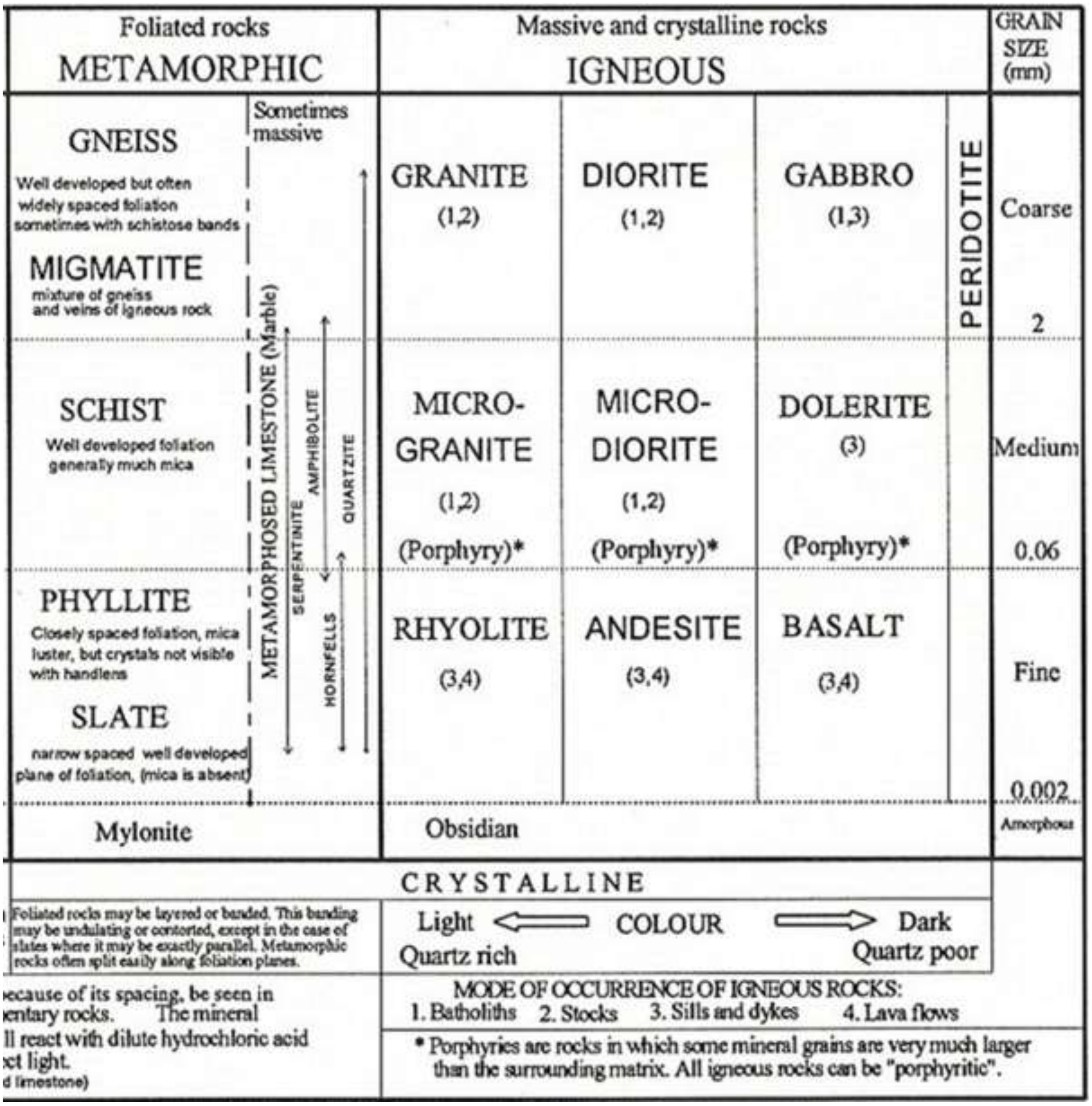

Foliated rocks METAMORPHIC		Massive and crystalline rocks IGNEOUS				GRAIN SIZE (mm)
GNEISS Well developed but often widely spaced foliation sometimes with schistose bands MIGMATITE mixture of gneiss and veins of igneous rock	Sometimes massive	GRANITE (1,2)	DIORITE (1,2)	GABBRO (1,3)	PERIDOTITE	Coarse 2
SCHIST Well developed foliation generally much mica	METAMORPHOSED LIMESTONE (Marble) SERPENTINITE AMPHIBOLITE HORNFELS QUARTZITE	MICRO-GRANITE (1,2) (Porphyry)*	MICRO-DIORITE (1,2) (Porphyry)*	DOLERITE (3) (Porphyry)*		Medium 0.06
PHYLLITE Closely spaced foliation, mica luster, but crystals not visible with handlens SLATE narrow spaced well developed plane of foliation, (mica is absent)		RHYOLITE (3,4)	ANDESITE (3,4)	BASALT (3,4)		Fine 0.002
Mylonite		Obsidian				Amorphous

CRYSTALLINE

Foliated rocks may be layered or banded. This banding may be undulating or contorted, except in the case of slates where it may be exactly parallel. Metamorphic rocks often split easily along foliation planes.

Light ⇐ COLOUR ⇒ Dark
Quartz rich Quartz poor

ecause of its spacing, be seen in
entary rocks. The mineral
ll react with dilute hydrochloric acid
ct light.
d limestone)

MODE OF OCCURRENCE OF IGNEOUS ROCKS:
1. Batholiths 2. Stocks 3. Sills and dykes 4. Lava flows

* Porphyries are rocks in which some mineral grains are very much larger than the surrounding matrix. All igneous rocks can be "porphyritic".

Figure 2-15 B: Aid to identification of rock for engineering purposes (After BS 5930:1981).

Figure 2-16: Utica Shale, Fort Plain, New York (Wikipedia).

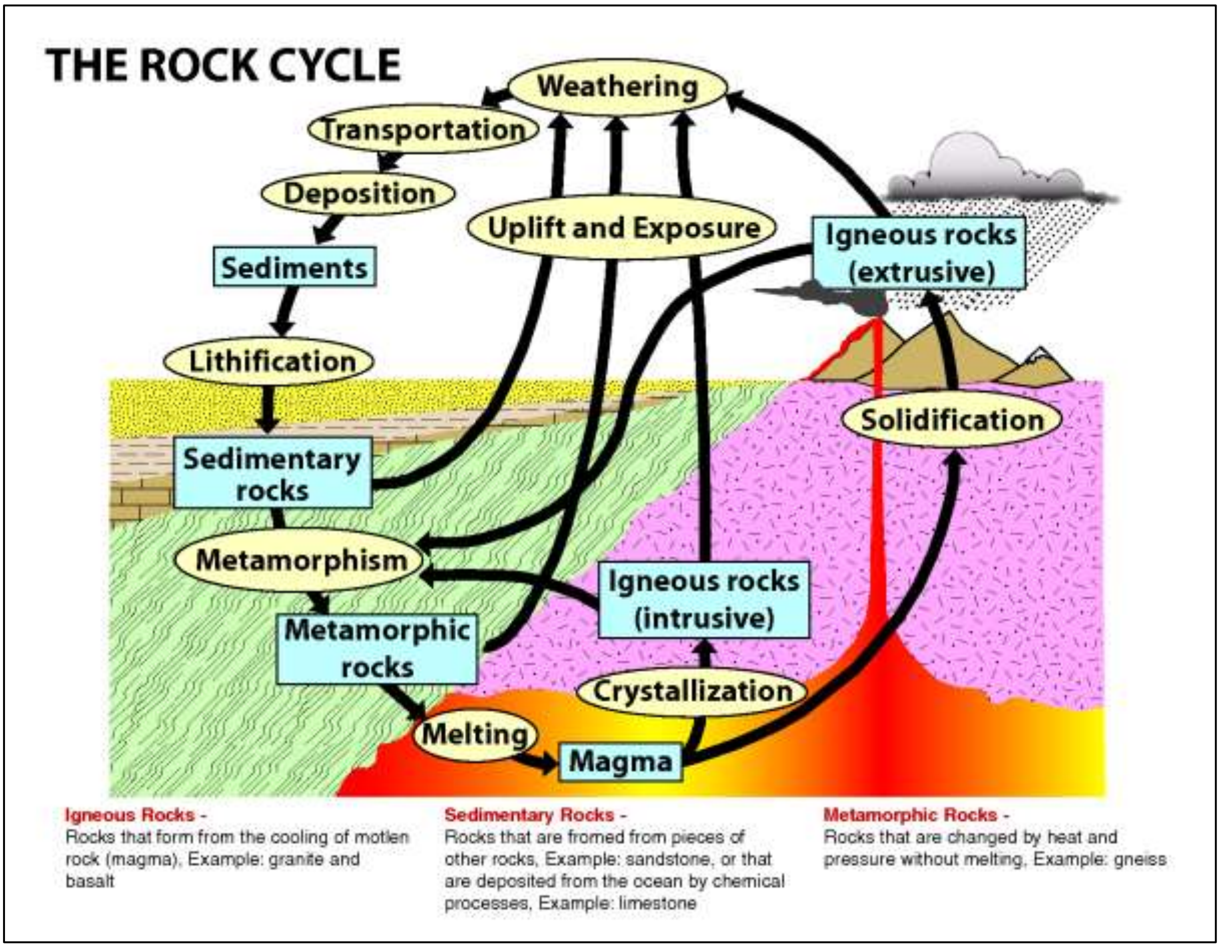

Igneous Rocks -
Rocks that form from the cooling of motlen rock (magma). Example: granite and basalt

Sedimentary Rocks -
Rocks that are fromed from pieces of other rocks, Example: sandstone, or that are deposited from the ocean by chemical processes, Example: limestone

Metamorphic Rocks -
Rocks that are changed by heat and pressure without melting, Example: gneiss

Figure 2-17: The rock formation cycle (galleryhip.com).

2.4. Soil Mechanical Parameters.

2.4.1. Grain Size Distribution/Particle Size Distribution.

Soils consist of a mixture of particles of different size, shape and mineralogy. Because the size of the particles obviously has a significant effect on the soil behavior, the grain size and grain size distribution are used to classify soils. The grain size distribution describes the relative proportions of particles of various sizes. The grain size is often visualized in a cumulative distribution graph which, for example, plots the percentage of particles finer than a given size as a function of size. The median grain size, d_{50}, is the size for which 50% of the particle mass consists of finer particles. Soil behavior, especially the hydraulic conductivity, tends to be dominated by the smaller particles; hence, the term "effective size", denoted by d_{10}, is defined as the size for which 10% of the particle mass consists of finer particles.

Sands and gravels that possess a wide range of particle sizes with a smooth distribution of particle sizes are called well graded soils. If the soil particles in a sample are predominantly in a relatively narrow range of sizes, the soil is called uniformly graded soils. If there are distinct gaps in the gradation curve, e.g., a mixture of gravel and fine sand, with no coarse sand, the soils may be called gap graded. Uniformly graded and gap graded soils are both considered to be poorly graded. There are many methods for measuring particle size distribution. The two traditional methods used in geotechnical engineering are sieve analysis and hydrometer analysis.

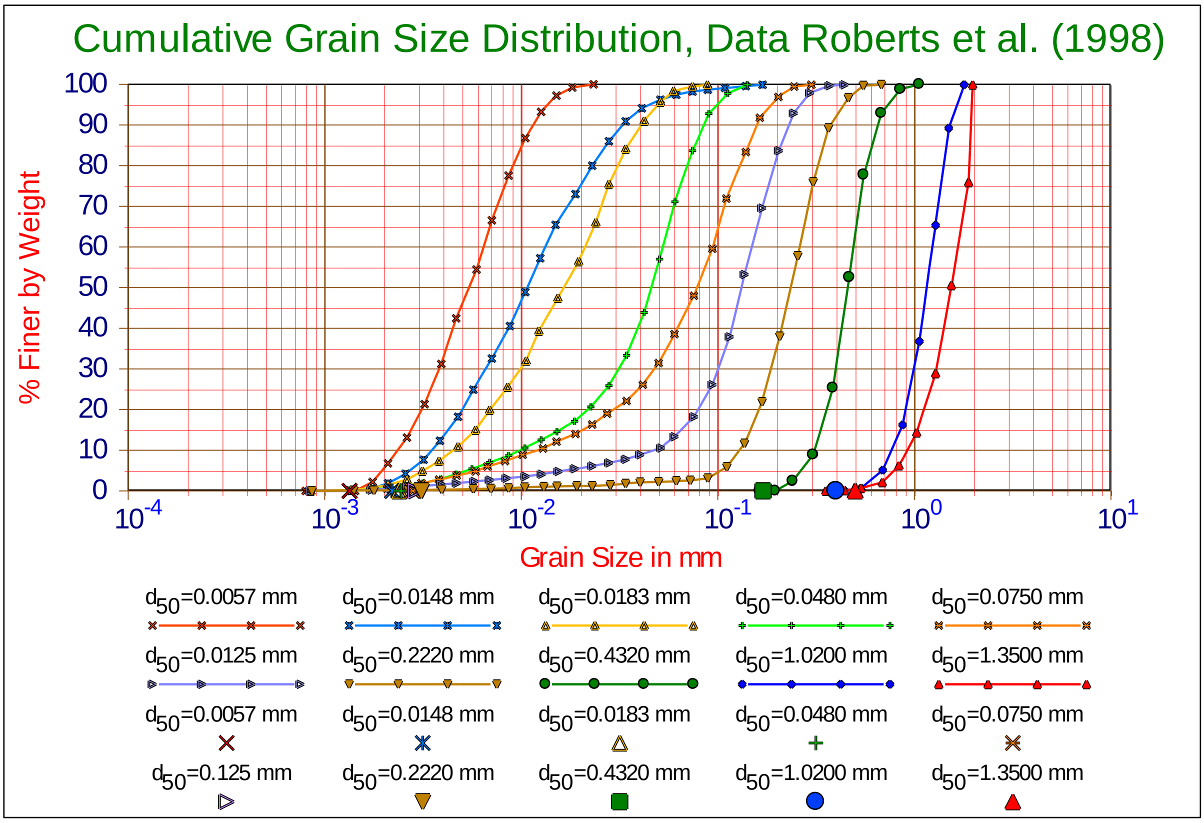

Figure 2-18: The particle size distributions of the sands used by Roberts et al. (1998).

2.4.2. Atterberg Limits.

The **Atterberg limits** are a basic measure of the nature of a fine-grained soil. Depending on the water content of the soil, it may appear in four states: solid, semi-solid, plastic and liquid. In each state the consistency and behavior of a soil is different and thus so are its engineering properties. Thus, the boundary between each state can be defined based on a change in the soil's behavior. The Atterberg limits can be used to distinguish between silt and clay, and it can distinguish between different types of silts and clays. These limits were created by Albert Atterberg, a Swedish chemist. They were later refined by Arthur Casagrande. These distinctions in soil are used in picking the soils to build structures on top of. These tests are mainly used on clayey or silty soils since these are the soils that expand and shrink due to moisture content. Clays and silts react with the water and thus change sizes and have varying shear strengths. Thus these tests are used widely in the preliminary stages of building any structure to insure that the soil will have the correct amount of shear strength and not too much change in volume as it expands and shrinks with different moisture contents.

Figure 2-19: Liquid limit device.

Figure 2-20: Liquid limit device.

2.4.2.1. Shrinkage Limit.

The shrinkage limit (SL) is the water content where further loss of moisture will not result in any more volume reduction. The test to determine the shrinkage limit is ASTM International D4943. The shrinkage limit is much less commonly used than the liquid and plastic limits.

2.4.2.2. Plastic Limit.

The plastic limit (PL) is the water content where soil transitions between brittle and plastic behavior. A thread of soil is at its plastic limit when it begins to crumble when rolled to a diameter of 3 mm. To improve test result consistency, a 3 mm diameter rod is often used to gauge the thickness of the thread when conducting the test. The Plastic Limit test is defined by ASTM standard test method D 4318.

2.4.2.3. Liquid Limit.

The liquid limit (LL) is the water content at which a soil changes from plastic to liquid behavior. The original liquid limit test of Atterberg's involved mixing a pat of clay in a round-bottomed porcelain bowl of 10-12cm diameter. A groove was cut through the pat of clay with a spatula, and the bowl was then struck many times against the palm of one hand. Casagrande subsequently standardized the apparatus and the procedures to make the measurement more repeatable. Soil is placed into the metal cup portion of the device and a groove is made down its center with a standardized tool of 13.5 millimeters (0.53 in) width. The cup is repeatedly dropped 10mm onto a hard rubber base during which the groove closes up gradually as a result of the impact. The number of blows for the groove to close is recorded. The moisture content at which it takes 25 drops of the cup to cause the groove to close over a distance of 13.5 millimeters (0.53 in) is defined as the liquid limit. The test is normally run at several moisture contents, and the moisture content which requires 25 blows to close the groove is interpolated from the test results. The Liquid Limit test is defined by ASTM standard test method D 4318. The test method also allows running the test at one moisture content where 20 to 30 blows are required to close the groove; then a correction factor is applied to obtain the liquid limit from the moisture content.
The following is when you should record the N in number of blows needed to close this 1/2-inch gap:
The materials needed to do a Liquid limit test are as follows

- Casagrande cup (liquid limit device)
- Grooving tool
- Soil pat before test
- Soil pat after test

Another method for measuring the liquid limit is the fall cone test. It is based on the measurement of penetration into the soil of a standardized cone of specific mass. Despite the universal prevalence of the Casagrande method, the fall cone test is often considered to be a more consistent alternative because it minimizes the possibility of human variations when carrying out the test.

2.4.2.4. Importance of Liquid Limit Test.

The importance of the liquid limit test is to classify soils. Different soils have varying liquid limits. Also to find the plasticity index of a soil you need to know the liquid limit and the plastic limit.

2.4.2.5. Derived Limits.

The values of these limits are used in a number of ways. There is also a close relationship between the limits and properties of a soil such as compressibility, permeability, and strength. This is thought to be very useful because as limit determination is relatively simple, it is more difficult to determine these other properties. Thus the Atterberg limits are not only used to identify the soil's classification, but it allows for the use of empirical correlations for some other engineering properties.

2.4.2.6. Plasticity Index.

The plasticity index (PI) is a measure of the plasticity of a soil. The plasticity index is the size of the range of water contents where the soil exhibits plastic properties. The PI is the difference between the liquid limit and the plastic limit (PI = LL-PL). Soils with a high PI tend to be clay, those with a lower PI tend to be silt, and those with a PI of 0 (non-plastic) tend to have little or no silt or clay.

PI and their meanings

- 0 – Non-plastic
- (1-5)- Slightly Plastic
- (5-10) - Low plasticity
- (10-20)- Medium plasticity
- (20-40)- High plasticity
- >40 Very high plasticity

2.4.2.7. Liquidity Index.

The liquidity index (LI) is used for scaling the natural water content of a soil sample to the limits. It can be calculated as a ratio of difference between natural water content, plastic limit, and plasticity index:
LI=(W-PL)/(LL-PL) where W is the natural water content.

2.4.2.8. Activity.

The activity (A) of a soil is the PI divided by the percent of clay-sized particles (less than 2 μm) present. Different types of clays have different specific surface areas which controls how much wetting is required to move a soil from one phase to another such as across the liquid limit or the plastic limit. From the activity one can predict the dominant clay type present in a soil sample. High activity signifies large volume change when wetted and large shrinkage when dried. Soils with high activity are very reactive chemically. Normally the activity of clay is between 0.75 and 1.25, and in this range clay is called normal. It is assumed that the plasticity index is approximately equal to the clay fraction (A = 1). When A is less than 0.75, it is considered inactive. When it is greater than 1.25, it is considered active.

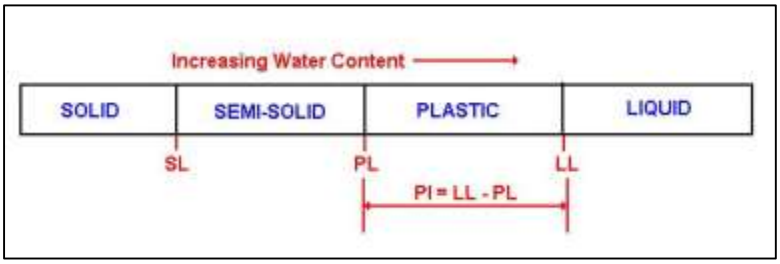

Figure 2-21: The relation between SL, PL, LL and PI.

2.4.3. Mass Volume Relations.

There are a variety of parameters used to describe the relative proportions of air (gas), water (liquid) and solids in a soil. This section defines these parameters and some of their interrelationships. The basic notation is as follows:

V_g, **V_l**, and **V_s** represent the volumes of gas, liquid and solids in a soil mixture;
W_g, **W_l**, and **W_s** represent the weights of gas, liquid and solids in a soil mixture;
M_g, **M_l**, and **M_s** represent the masses of gas, liquid and solids in a soil mixture;
ρ_g, **ρ_l**, and **ρ_s** represent the densities of the constituents (gas, liquid and solids) in a soil mixture;
Note that the weights, **W**, can be obtained by multiplying the mass, **M**, by the acceleration due to gravity, **g**; e.g., **$W_s = M_s \cdot g$**

2.4.3.1. Specific Gravity.

Specific Gravity is the ratio of the density of one material compared to the density of pure water (ρ_l = 1000 kg/m^3).

$$G_s = \frac{\rho_s}{\rho_l} \tag{2-1}$$

2.4.3.2. Density.

The terms density and unit weight are used interchangeably in soil mechanics. Though not critical, it is important that we know it. Density, Bulk Density, or Wet Density, **ρ_t**, are different names for the density of the mixture, i.e., the total mass of air, water, solids divided by the total volume of air, water and solids (the mass of air is assumed to be zero for practical purposes. To find the formula for density, divide the mass of the soil by the volume of the soil, the basic formula for density is:

$$\rho_t = \frac{M_t}{V_t} = \frac{M_s + M_l + M_g}{V_s + V_l + V_g} \tag{2-2}$$

Unit weight of a soil mass is the ratio of the total weight of soil to the total volume of soil. Unit Weight, **γ_t**, is usually determined in the laboratory by measuring the weight and volume of a relatively undisturbed soil sample obtained from a brass ring. Measuring unit weight of soil in the field may consist of a sand cone test, rubber balloon or nuclear densitometer, the basic formula for unit weight is:

$$\gamma_t = \frac{M_t \cdot g}{V_t} \tag{2-3}$$

Dry Density, **ρ_d**, is the mass of solids divided by the total volume of air, water and solids:

$$\rho_d = \frac{M_s}{V_t} = \frac{M_s}{V_s + V_l + V_g} \tag{2-4}$$

Submerged Density, **ρ_{st}**, defined as the density of the mixture minus the density of water is useful if the soil is submerged under water:

$$\rho_{sd} = \rho_t - \rho_l \tag{2-5}$$

Table 2-2: Empirical values for ρ_t, of granular soils based on the standard penetration number, (from Bowels, *Foundation Analysis*).

SPT Penetration, N-Value (blows/ foot)	**ρ_t** (kg/m^3)
0 - 4	1120 - 1520
4 - 10	1520 - 1800
10 - 30	1800 - 2080
30 - 50	2080 - 2240
>50	2240 - 2400

Table 2-3: Empirical values for ρ_s, of cohesive soils based on the standard penetration number, (From Bowels, *Foundation Analysis*).

SPT Penetration, N-Value (blows/ foot)	$\rho_{s,\,sat}$ (kg/m^3)
0 - 4	1600 - 1840
4 - 8	1840 - 2000
8 - 32	2000 - 2240

Table 2-4: Typical Soil Characteristics (From Lindeburg, Civil Engineering Reference Manual for the PE Exam, 8th edition).

Soil Type	ρ_s (kg/m^3)	$\rho_{s,\,sat}$ (kg/m^3)
Sand, loose and uniform	1440	1888
Sand, dense and uniform	1744	2080
Sand, loose and well graded	1584	1984
Sand, dense and well graded	1856	2160
Glacial clay, soft	1216	1760
Glacial clay, stiff	1696	2000

Table 2-5: Typical Values of Soil Index Properties
(From *NAVFAC 7.01*).

Soil Type	ρ_s (kg/m^3)
Sand; clean, uniform, fine or medium	1344 - 2176
Silt; uniform, inorganic	1296 - 2176
Silty Sand	1408 - 2272
Sand; Well-graded	1376 - 2368
Silty Sand and Gravel	1440 - 2480
Sandy or Silty Clay	1600 - 2352
Silty Clay with Gravel; uniform	1840 - 2416
Well-graded Gravel, Sand, Silt and Clay	2000 - 2496
Clay	1504 - 2128
Colloidal Clay	1136 - 2048
Organic Silt	1392 - 2096
Organic Clay	1296 - 2000

2.4.3.3. Relative Density.

Relative density is an index that quantifies the state of compactness between the loosest and densest possible state of coarse-grained soils. The relative density is written in the following formulas:

$$D_r = \frac{e_{max} - e}{e_{max} - e_{min}} = \frac{n_{max} - n}{n_{max} - n_{min}} \tag{2-6}$$

Table 2-6: Designation of Granular Soil Based on Relative Density.

D_r (%)	Description
0 - 20	Very loose
20 - 40	Loose
40 - 70	Medium dense
70 - 85	Dense
85 - 100	Very dense

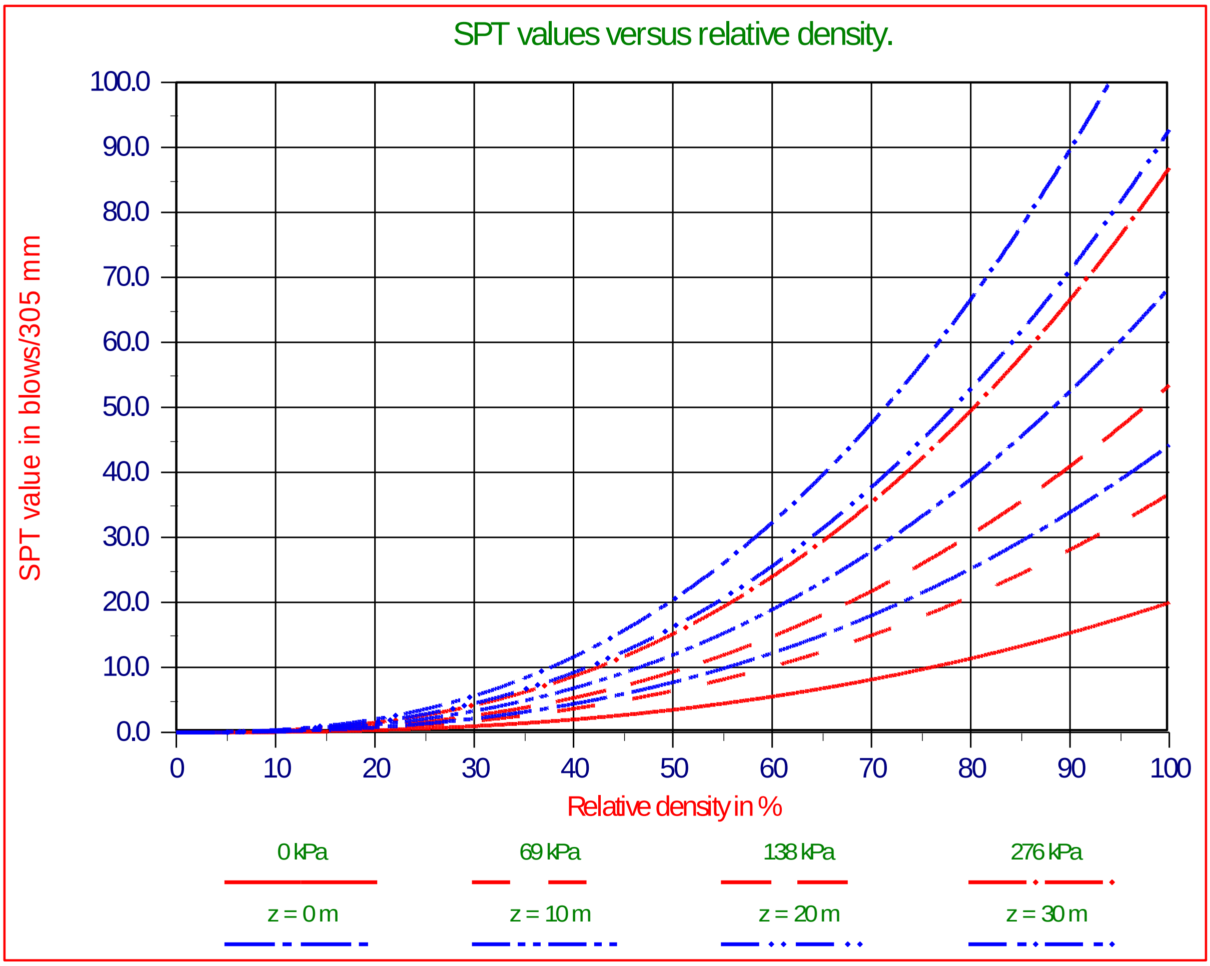

Figure 2-22: SPT values versus relative density (Miedema (1995).

Lambe & Whitman (1979), page 78 (Figure 2-22) give the relation between the SPT value, the relative density and the hydrostatic pressure in two graphs. With some curve-fitting these graphs can be summarized with the following equation (Miedema (1995)):

$$SPT = \left(1.82 + 0.221 \cdot \left(z + 10\right)\right) \cdot 10^{-4} \cdot RD^{2.52} \tag{2-7}$$

2.4.3.4. Porosity.

Porosity is the ratio of the volume of openings (voids) to the total volume of material. Porosity represents the storage capacity of the geologic material. The primary porosity of a sediment or rock consists of the spaces between the grains that make up that material. The more tightly packed the grains are, the lower the porosity. Using a box of marbles as an example, the internal dimensions of the box would represent the volume of the sample. The space surrounding each of the spherical marbles represents the void space. The porosity of the box of marbles would be determined by dividing the total void space by the total volume of the sample and expressed as a percentage.
The primary porosity of unconsolidated sediments is determined by the shape of the grains and the range of grain sizes present. In poorly sorted sediments, those with a larger range of grain sizes, the finer grains tend to fill the spaces between the larger grains, resulting in lower porosity. Primary porosity can range from less than one percent in crystalline rocks like granite to over 55% in some soils. The porosity of some rock is increased through fractures or solution of the material itself. This is known as secondary porosity.

$$\mathbf{n = \frac{V_v}{V_t} = \frac{V_v}{V_s + V_v} = \frac{e}{1+e}} \tag{2-8}$$

2.4.3.5. Void ratio.

The ratio of the volume of void space to the volume of solid substance in any material consisting of void space and solid material, such as a soil sample, a sediment, or a powder.

$$\mathbf{e = \frac{V_v}{V_s} = \frac{V_v}{V_t - V_v} = \frac{n}{1-n}} \tag{2-9}$$

The relations between void ratio **e** and porosity **n** are:

$$\mathbf{e = \frac{n}{1-n} \quad and \quad n = \frac{e}{1+e}} \tag{2-10}$$

2.4.3.6. Dilatation.

Dilation (or dilatation) refers to an enlargement or expansion in bulk or extent, the opposite of contraction. It derives from the Latin dilatare, "to spread wide". It is the increase in volume of a granular substance when its shape is changed, because of greater distance between its component particles. Suppose we have a volume **V** before the enlargement and a volume **V+dV** after the enlargement. Before the enlargement we name the porosity $\mathbf{n_i}$ (i from initial) and after the enlargement $\mathbf{n_{cv}}$ (the constant volume situation after large deformations). For the volume before the deformation we can write:

$$\mathbf{V = (1-n_i)\cdot V + n_i \cdot V} \tag{2-11}$$

The first term on the right hand side is the sand volume, the second term the pore volume. After the enlargement we get:

$$\mathbf{V + dV = (1-n_{cv})\cdot(V+dV) + n_{cv}\cdot(V+dV)} \tag{2-12}$$

Again the first term on the right hand side is the sand volume. Since the sand volume did not change during the enlargement (we assume the quarts grains are incompressible), the volume of sand in both equations should be the same, thus:

$$\mathbf{(1-n_i)\cdot V = (1-n_{cv})\cdot(V+dV)} \tag{2-13}$$

From this we can deduce that the dilatation **ε is:**

$$\mathbf{\varepsilon = \frac{dV}{V} = \frac{n_{cv} - n_i}{1-n_{cv}} = \frac{dn}{1-n_{cv}}} \tag{2-14}$$

2.4.4. Permeability.

Permeability is a measure of the ease with which fluids will flow though a porous rock, sediment, or soil. Just as with porosity, the packing, shape, and sorting of granular materials control their permeability. Although a rock may be highly porous, if the voids are not interconnected, then fluids within the closed, isolated pores cannot move. The degree to which pores within the material are interconnected is known as effective porosity. Rocks such as pumice and shale can have high porosity, yet can be nearly impermeable due to the poorly interconnected voids. In contrast, well-sorted sandstone closely replicates the example of a box of marbles cited above. The rounded sand grains provide ample, unrestricted void spaces that are free from smaller grains and are very well linked. Consequently, sandstones of this type have both high porosity and high permeability.
The range of values for permeability in geologic materials is extremely large. The most conductive materials have permeability values that are millions of times greater than the least permeable. Permeability is often directional in nature. The characteristics of the interstices of certain materials may cause the permeability to be significantly greater in one direction. Secondary porosity features, like fractures, frequently have significant impact on the permeability of the material. In addition to the characteristics of the host material, the viscosity and pressure of the fluid also affect the rate at which the fluid will flow.

Hydraulic conductivity or permeability **k** can be estimated by particle size analysis of the sediment of interest, using empirical equations relating either **k** to some size property of the sediment. Vukovic and Soro (1992) summarized several empirical methods from former studies and presented a general formula:

$$\mathbf{k=C\cdot\frac{g}{\nu_l}\cdot f(n)\cdot d_e^2} \qquad \mathbf{(2\text{-}15)}$$

The kinematic viscosity $\boldsymbol{\nu_l}$ is related to dynamic viscosity $\boldsymbol{\mu_l}$ and the fluid (water) density $\boldsymbol{\rho_l}$ as follows:

$$\boldsymbol{\nu_l=\frac{\mu_l}{\rho_l}} \qquad \mathbf{(2\text{-}16)}$$

The values of **C**, **f(n)** and $\mathbf{d_e}$ are dependent on the different methods used in the grain-size analysis. According to Vukovic and Soro (1992), porosity **n** may be derived from the empirical relationship with the coefficient of grain uniformity **U** as follows:

$$\mathbf{n=0.255\cdot\left(1+0.83^U\right)} \qquad \mathbf{(2\text{-}17)}$$

Where **U** is the coefficient of grain uniformity and is given by:

$$\mathbf{U=\left(\frac{d_{60}}{d_{10}}\right)} \qquad \mathbf{(2\text{-}18)}$$

Here, $\mathbf{d_{60}}$ and $\mathbf{d_{10}}$ in the formula represent the grain diameter in (mm) for which, 60% and 10% of the sample respectively, are finer than. Former studies have presented the following formulae which take the general form presented in equation (2-15) above but with varying **C, f(n)** and $\mathbf{d_e}$ values and their domains of applicability.

Hazen's formula (1982) was originally developed for determination of hydraulic conductivity of uniformly graded sand but is also useful for fine sand to gravel range, provided the sediment has a uniformity coefficient less than 5 and effective grain size between 0.1 and 3mm.

$$\mathbf{k=6\cdot10^{-4}\cdot\frac{g}{\nu_l}\cdot\left(1+10\cdot\left(n-0.26\right)\right)\cdot d_{10}^2} \qquad \mathbf{(2\text{-}19)}$$

The Kozeny-Carman equation is one of the most widely accepted and used derivations of permeability as a function of the characteristics of the soil medium. The Kozeny-Carman equation (or Carman-Kozeny equation) is a relation used in the field of fluid dynamics to calculate the pressure drop of a fluid flowing through a packed bed of solids. It is named after Josef Kozeny and Philip C. Carman. This equation was originally proposed by Kozeny (1927) and was then modified by Carman (1937) and (1956) to become the Kozeny-Carman equation. It is not appropriate for either soil with effective size above 3 mm or for clayey soils. The equation is only valid for laminar flow. The equation is given as:

$$k = d_e^2 \cdot \frac{\gamma_l}{\mu_l} \cdot \frac{e^3}{1+e} \cdot C \qquad \text{or} \qquad k = 8.3 \cdot 10^{-3} \cdot \frac{g}{\nu_l} \cdot \frac{n^3}{(1-n)^2} \cdot d_{10}^2 \tag{2-20}$$

$$\text{With:} \quad \nu_l = \frac{\mu_l}{\rho_l} \quad \text{and} \quad \gamma_l = \rho_l \cdot g$$

This equation holds for flow through packed beds with particle Reynolds numbers up to approximately 1.0, after which point frequent shifting of flow channels in the bed causes considerable kinetic energy losses. This equation can be expressed as "*flow is proportional to the pressure drop and inversely proportional to the fluid viscosity*", which is known as Darcy's law.

The Breyer method does not consider porosity and therefore, porosity function takes on value 1. Breyer formula is often considered most useful for materials with heterogeneous distributions and poorly sorted grains with uniformity coefficient between 1 and 20, and effective grain size between 0.06mm and 0.6mm.

$$k = 6 \cdot 10^{-4} \cdot \frac{g}{\nu_l} \cdot \log\left(\frac{500}{U}\right) \cdot d_{10}^2 \tag{2-21}$$

The Slitcher formula is most applicable for grain-sizes between 0.01 mm and 5 mm.

$$k = 1 \cdot 10^{-2} \cdot \frac{g}{\nu_l} \cdot n^{3.287} \cdot d_{10}^2 \tag{2-22}$$

The Terzaghi (1964) formula is most applicable for coarse sand. The Terzaghi equation:

$$k = C_t \cdot \frac{g}{\nu_l} \cdot \left(\frac{n - 0.13}{\sqrt[3]{1-n}}\right)^2 \cdot d_{10}^2 \tag{2-23}$$

Where the $\mathbf{C_t}$ = sorting coefficient and $6.1 \times 10^{-3} < C_t < 10.7 \times 10^{-3}$.

2.4.5. The Angle of Internal Friction.

Angle of internal friction for a given soil is the angle on the graph (Mohr's Circle) of the shear stress and normal effective stresses at which shear failure occurs. Angle of Internal Friction, **φ**, can be determined in the laboratory by the Direct Shear Test or the Triaxial Stress Test. Typical relationships for estimating the angle of internal friction, **φ**, are as follows:

Table 2-7: Empirical values for φ, of granular soils based on the standard penetration number, (From Bowels, *Foundation Analysis*).

SPT Penetration, N-Value (blows/ foot)	**φ** (degrees)
0	25 - 30
4	27 - 32
10	30 - 35
30	35 - 40
50	38 - 43

Table 2-8: Relationship between φ, and standard penetration number for sands, (From Peck 1974, *Foundation Engineering Handbook*).

SPT Penetration, N-Value (blows/ foot)	**Density of Sand**	**φ** (degrees)
<4	Very loose	<29
4 - 10	Loose	29 - 30
10 - 30	Medium	30 - 36
30 - 50	Dense	36 - 41
>50	Very dense	>41

Table 2-9: Relationship between φ, and standard penetration number for sands, (From Meyerhof 1956, *Foundation Engineering Handbook*).

SPT Penetration, N-Value (blows/ foot)	**Density of Sand**	**φ** (degrees)
<4	Very loose	<30
4 - 10	Loose	30 - 35
10 - 30	Medium	35 - 40
30 - 50	Dense	40 - 45
>50	Very dense	>45

Lambe & Whitman (1979), page 148 (Figure 2-23) give the relation between the SPT value and the angle of internal friction, also in a graph. This graph is valid up to 12 m in dry soil. With respect to the internal friction, the relation given in the graph has an accuracy of 3 degrees. A load of 12 m dry soil with a density of 1.67 ton/m^3 equals a hydrostatic pressure of 20 m.w.c. An absolute hydrostatic pressure of 20 m.w.c. equals 10 m of water depth if cavitation is considered. Measured SPT values at any depth will have to be reduced to the value that would occur at 10 m water depth. This can be accomplished with the following equation:

$$\mathrm{SPT_{10}} = \frac{1}{(0.646 + 0.0354 \cdot z)} \cdot \mathrm{SPT_z} \qquad \textbf{(2-24)}$$

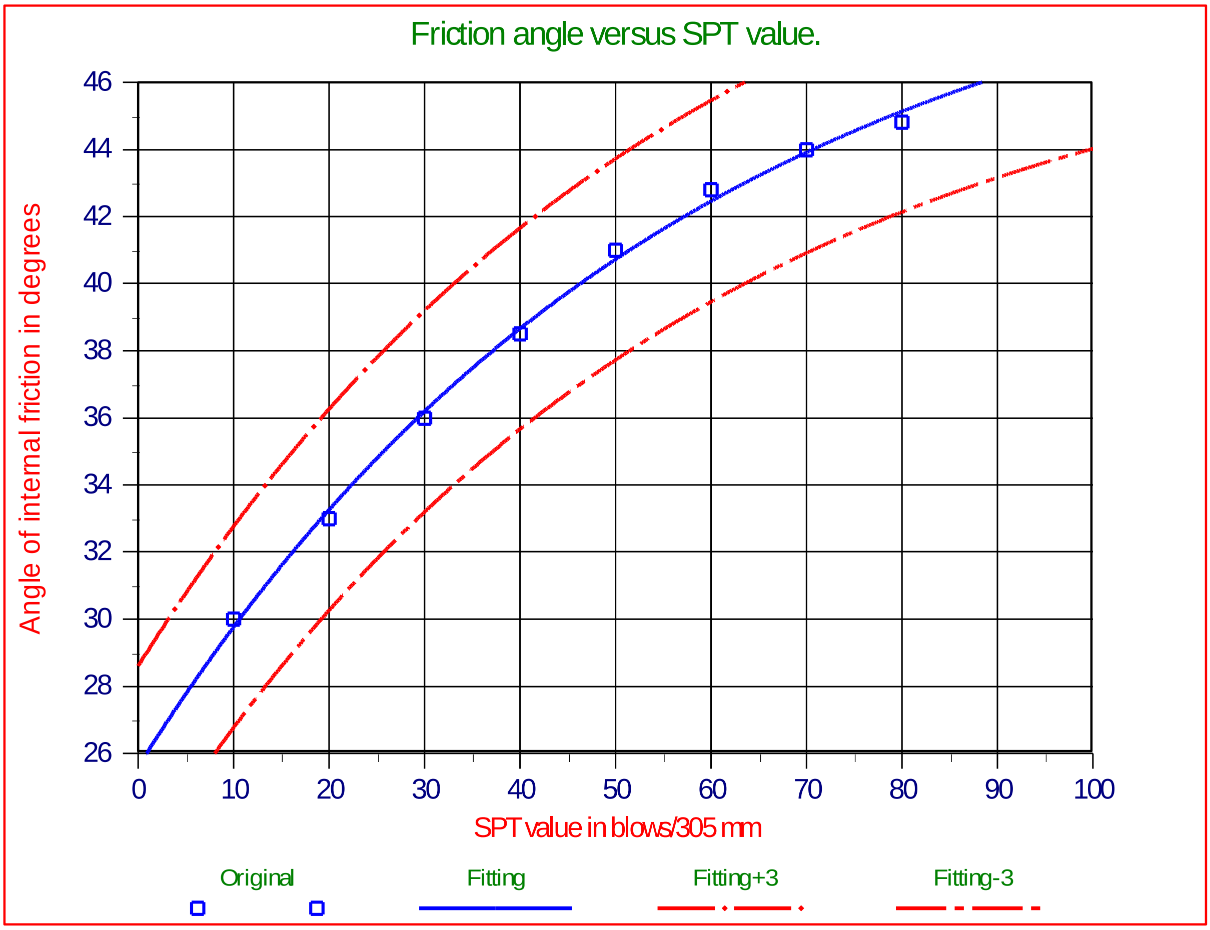

Figure 2-23: Friction angle versus SPT value (Miedema (1995).

With the aim of curve-fitting, the relation between the SPT value reduced to 10 m water depth and the angle of internal friction can be summarized to:

$$\varphi = 51.5 - 25.9 \cdot e^{-0.01753 \cdot SPT_{10}} \tag{2-25}$$

2.4.6. The Angle of External Friction.

The external friction angle, δ, or friction between a soil medium and a material such as the composition from a retaining wall or pile may be expressed in degrees as the following:

Table 2-10: External friction angle φ values.

20°	steel piles (NAVFAC)
0.67·φ-0.83·φ	USACE
20°	steel (Broms)
3/4·φ	concrete (Broms)
2/3·φ	timber (Broms)
2/3·φ	Lindeburg
2/3·φ	for concrete walls (Coulomb)

The external friction angle can be estimated as **1/3·φ** for smooth retaining walls like sheet piles or concrete surfaces against timber formwork, or as **1/2·φ** to **2/3·φ** for rough surfaces. In the absence of detailed information the assumption of **2/3·φ** is commonly made.

2.4.7. Shear Strength.

2.4.7.1. Introduction.

Shear strength is a term used in soil mechanics to describe the magnitude of the shear stress that a soil can sustain. The shear resistance of soil is a result of friction and interlocking of particles, and possibly cementation or bonding at particle contacts. Due to interlocking, particulate material may expand or contract in volume as it is subject to shear strains. If soil expands its volume, the density of particles will decrease and the strength will decrease; in this case, the peak strength would be followed by a reduction of shear stress. The stress-strain relationship levels off when the material stops expanding or contracting, and when inter-particle bonds are broken. The theoretical state at which the shear stress and density remain constant while the shear strain increases may be called the critical state, steady state, or residual strength.

The volume change behavior and inter-particle friction depend on the density of the particles, the inter-granular contact forces, and to a somewhat lesser extent, other factors such as the rate of shearing and the direction of the shear stress. The average normal inter-granular contact force per unit area is called the effective stress.

If water is not allowed to flow in or out of the soil, the stress path is called an undrained stress path. During undrained shear, if the particles are surrounded by a nearly incompressible fluid such as water, then the density of the particles cannot change without drainage, but the water pressure and effective stress will change. On the other hand, if the fluids are allowed to freely drain out of the pores, then the pore pressures will remain constant and the test path is called a drained stress path. The soil is free to dilate or contract during shear if the soil is drained. In reality, soil is partially drained, somewhere between the perfectly undrained and drained idealized conditions. The shear strength of soil depends on the effective stress, the drainage conditions, the density of the particles, the rate of strain, and the direction of the strain.

For undrained, constant volume shearing, the Tresca theory may be used to predict the shear strength, but for drained conditions, the Mohr–Coulomb theory may be used.

Two important theories of soil shear are the critical state theory and the steady state theory. There are key differences between the steady state condition and the steady state condition and the resulting theory corresponding to each of these conditions.

2.4.7.2. Undrained Shear Strength.

This term describes a type of shear strength in soil mechanics as distinct from drained strength. Conceptually, there is no such thing as the undrained strength of a soil. It depends on a number of factors, the main ones being:

- Orientation of stresses
- Stress path
- Rate of shearing
- Volume of material (like for fissured clays or rock mass)

Undrained strength is typically defined by Tresca theory, based on Mohr's circle as:

$$\sigma_1 - \sigma_3 = 2 \cdot S_u = U.C.S. \tag{2-26}$$

It is commonly adopted in limit equilibrium analyses where the rate of loading is very much greater than the rate at which pore water pressures that are generated due to the action of shearing the soil may dissipate. An example of this is rapid loading of sands during an earthquake, or the failure of a clay slope during heavy rain, and applies to most failures that occur during construction. As an implication of undrained condition, no elastic volumetric strains occur, and thus Poisson's ratio is assumed to remain 0.5 throughout shearing. The Tresca soil model also assumes no plastic volumetric strains occur. This is of significance in more advanced analyses such as in finite element analysis. In these advanced analysis methods, soil models other than Tresca may be used to model the undrained condition including Mohr-Coulomb and critical state soil models such as the modified Cam-clay model, provided Poisson's ratio is maintained at 0.5.

2.4.7.3. Drained Shear Strength.

The drained shear strength is the shear strength of the soil when pore fluid pressures, generated during the course of shearing the soil, are able to dissipate during shearing. It also applies where no pore water exists in the soil (the soil is dry) and hence pore fluid pressures are negligible. It is commonly approximated using the Mohr-Coulomb equation. (It was called "Coulomb's equation" by Karl von Terzaghi in 1942.) combined it with the principle of effective stress. In terms of effective stresses, the shear strength is often approximated by:

$$\tau = c + \sigma \cdot \tan(\varphi) \tag{2-27}$$

The coefficient of friction μ is equal to tan(φ). Different values of friction angle can be defined, including the peak friction angle, φ'_p, the critical state friction angle, φ'_{cv}, or residual friction angle, φ'_r.
c' is called cohesion, however, it usually arises as a consequence of forcing a straight line to fit through measured values of (τ,σ')even though the data actually falls on a curve. The intercept of the straight line on the shear stress axis is called the cohesion. It is well known that the resulting intercept depends on the range of stresses considered: it is not a fundamental soil property. The curvature (nonlinearity) of the failure envelope occurs because the dilatancy of closely packed soil particles depends on confining pressure.

2.4.7.4. Cohesion (Internal Shear Strength).

Cohesion (in Latin cohaerere "stick or stay together") or **cohesive attraction** or **cohesive force** is the action or property of like molecules sticking together, being mutually attractive. This is an intrinsic property of a substance that is caused by the shape and structure of its molecules which makes the distribution of orbiting electrons irregular when molecules get close to one another, creating electrical attraction that can maintain a macroscopic structure such as a water drop. Cohesive soils are clay type soils. Cohesion is the force that holds together molecules or like particles within a soil. Cohesion, **c**, is usually determined in the laboratory from the Direct Shear Test. Unconfined Compressive Strength, UCS, can be determined in the laboratory using the Triaxial Test or the Unconfined Compressive Strength Test. There are also correlations for UCS with shear strength as estimated from the field using Vane Shear Tests. With a conversion of 1 kips/ft^2=47.88 kN/m^2.

$$c = \frac{U.C.S.}{2} \tag{2-28}$$

Table 2-11: Guide for Consistency of Fine-Grained Soil, NAVFAC 7.02

SPT Penetration (blows/ foot)	**Estimated Consistency**	**UCS**(kPa)
<2	Very Soft	<24
2 - 4	Soft	24 - 48
4 - 8	Medium	48 - 96
8 - 15	Stiff	96 – 192
15 - 30	Very Stiff	192 – 388
>30	Hard	>388

Table 2-12: Empirical Values for Consistency of Cohesive Soil, (from Foundation Analysis, Bowels)

SPT Penetration (blows/ foot)	**Estimated Consistency**	**UCS** (kips/ft^2)
0 - 2	Very Soft	0 - 0.5
2 - 4	Soft	0.5 - 1.0
4 - 8	Medium	1.0 - 2.0
8 - 16	Stiff	2.0 - 4.0
16 - 32	Very Stiff	4.0 - 8.0
>32	Hard	>8

2.4.7.5. Adhesion (External Shear Strength).

Adhesion is any attraction process between dissimilar molecular species that can potentially bring them in close contact. By contrast, cohesion takes place between similar molecules.
Adhesion is the tendency of dissimilar particles and/or surfaces to cling to one another (cohesion refers to the tendency of similar or identical particles/surfaces to cling to one another). The forces that cause adhesion and cohesion can be divided into several types. The intermolecular forces responsible for the function of various kinds of stickers and sticky tape fall into the categories of chemical adhesion, dispersive adhesion, and diffusive adhesion.

2.4.8. UCS or Unconfined Compressive Strength.

UCS is one of the most basic parameters of rock strength, and the most common determination performed for bore ability predictions. It is measured in accordance with the procedures given in **ASTM D2938**, with the length to diameter ratio of 2 by using **NX**-size core samples. 3 to 5 **UCS** determinations are recommended to achieve statistical significance of the results. If the sample length to diameter ratio was greater or less than 2, ASTM recommends a correction factor that is applied to the **UCS** value determined from testing. **UCS** measurements are made using an electronic-servo controlled **MTS** stiff testing machine with a capacity of 220 kips. Loading data and other test parameters are recorded with a computer based data acquisition system, and the data is subsequently reduced and analyzed with a customized spreadsheet program.

The most important test for rock in the field of dredging is the uniaxial unconfined compressive strength (UCS). In the test a cylindrical rock sample is axial loaded till failure. Except the force needed, the deformation is measured too. So the complete stress-strain curve is measured from which the deformation modulus and the specific work of failure can be calculated. The unconfined compressive strength of the specimen is calculated by dividing the maximum load at failure by the sample cross-sectional area:

$$\sigma_{c} = \frac{F}{A} \tag{2-29}$$

Figure 2-24: A UCS test facility (Timely Engineering Soil Tests, LLC).

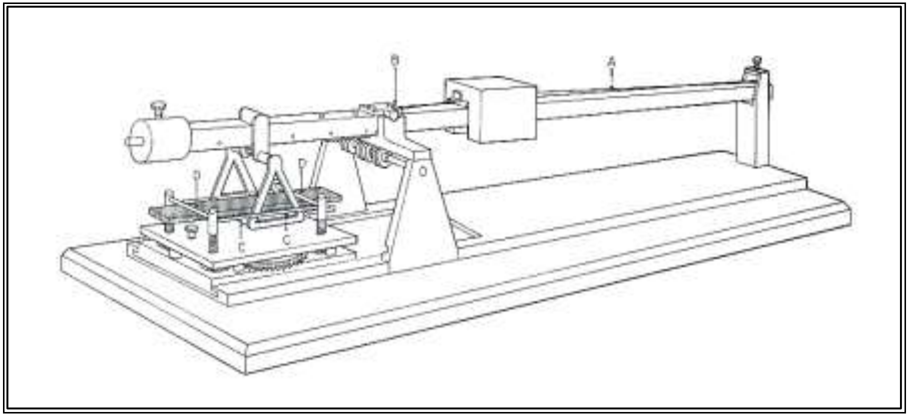

Figure 2-25: Bending (Vlasblom (2003-2007)).

2.4.9. Unconfined Tensile Strength.

The uniaxial unconfined tensile strength is defined in the same way as the compressive strength. Sample preparation and testing procedure require much effort and not commonly done. Another method to determine the tensile strength, also commonly not used, is by bending a sample.

2.4.10. BTS or Brazilian Tensile Strength.

Indirect, or **Brazilian**, tensile strength is measured using **NX**-size core samples cut to an approximate 0.5 length-to-diameter ratio, and following the procedures of **ASTM D3967**. **BTS** measurements are made using an electronic-servo controlled **MTS** stiff testing machine with a capacity of 220 kips. Loading data and other test parameters are recorded with a computer based data acquisition system, and the data is subsequently reduced and analyzed with a customized spreadsheet program. **BTS** provides a measure of rock toughness, as well as strength. The indirect tensile strength is calculated as follows (Fairhurst (1964)):

$$\sigma_T = \frac{2 \cdot F}{\pi \cdot L \cdot D} \tag{2-30}$$

In bedded/foliated rocks, particular attention needs to be given to loading direction with respect to bedding/foliation. The rock should be loaded so that breakage occurs in approximately the same direction as fracture propagation between adjacent cuts on the tunnel face. This is very important assessment in mechanical excavation by tunnel boring machines. The most common used test to estimate, in an indirect way, the tensile strength is the Brazilian split test. Here the cylindrical sample is tested radial.

The validity of BTS to determine de UTS is discussed by many researchers. In general it can be stated that the BTS over estimates the UTS. According to Pells (1993) this discussion is in most applications in practice largely academic.

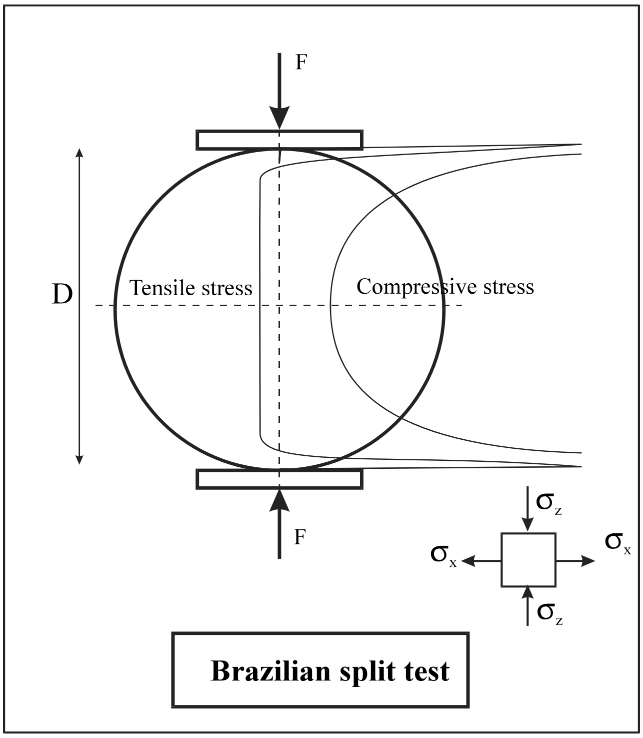

Figure 2-26: The Brazilian split test (Vlasblom (2003-2007)).

2.4.11. Hardness.

Hardness is a loosely defined term, referring the resistance to rock or minerals against an attacking tool. Hardness is determined using rebound tests (f.i. Schmidt hammer), indentation tests, (Brinell, Rockwell) or scratch tests (Mohs). The last test is based on the fact that a mineral higher in the scale can scratch a mineral lower in the scale.

Although this scale was established in the early of the 19th century it appeared that the increment of Mohs scale corresponded with a 60% increase in indentation hardness.

Table 2-13: The Mohs scale (source Wikipedia).

Mohs hardness	Mineral	Chemical formula	Absolute hardness.	Image
1	Talc	$Mg_3Si_4O_{10}(OH)_2$	1	
2	Gypsum	$CaSO_4{\cdot}2H_2O$	3	
3	Calcite	$CaCO_3$	9	
4	Fluorite	CaF_2	21	
5	Apatite	$Ca_5(PO_4)_3(OH^-,Cl^-,F^-)$	48	
6	Orthoclase	$KAlSi_3O_8$	72	
7	Quartz	SiO_2	100	
8	Topaz	$Al_2SiO_4(OH^-,F^-)_2$	200	
9	Corundum	Al_2O_3	400	
10	Diamond	C	1600	

2.5. Criteria & Concepts.

2.5.1. Failure Criteria.

After a soil reaches the critical state, it is no longer contracting or dilating and the shear stress on the failure plane τ_{crit} is determined by the effective normal stress on the failure plane σ_n' and critical state friction angle, φ_{cv}, :

$$\tau_{crit} = \sigma_n' \cdot \tan(\varphi_{cv}) \tag{2-31}$$

The peak strength of the soil may be greater, however, due to the interlocking (dilatancy) contribution. This may be stated:

$$\tau_{peak} = \sigma_n' \cdot \tan\left(\varphi_{peak}\right) \tag{2-32}$$

Where $\varphi_{peak} > \varphi_{cv}$. However, use of a friction angle greater than the critical state value for design requires care. The peak strength will not be mobilized everywhere at the same time in a practical problem such as a foundation, slope or retaining wall. The critical state friction angle is not nearly as variable as the peak friction angle and hence it can be relied upon with confidence. Not recognizing the significance of dilatancy, Coulomb proposed that the shear strength of soil may be expressed as a combination of adhesion and friction components:

$$\tau = \sigma' \cdot \tan(\varphi) + c' \tag{2-33}$$

It is now known that the **c'** and **φ** parameters in the last equation are not fundamental soil properties. In particular, **c'** and **φ** are different depending on the magnitude of effective stress. According to Schofield (2006), the longstanding use of **c'** in practice has led many engineers to wrongly believe that **c'** is a fundamental parameter. This assumption that **c'** and **φ** are constant can lead to overestimation of peak strengths.

2.5.2. The Phi=0 Concept.

When a fast triaxial test is carried out, so an unconsolidated undrained test, it is very well possible that the pore pressures will be equal to the increase of the cell pressure. If a test at high cell pressure is carried out, the only difference with a test with a low cell pressure is the value of the pore pressures. The grain pressures will be almost equal in both cases and the result is, that we will find the same critical Mohr circle. So let's consider a series of unconsolidated undrained (UU) tests. Three specimens are selected and all are consolidated to 110 kPa. This brings the specimens to the end of step 1 in the UU test program. Now the confining pressures are changed to say 70, 140 and 700 kPa, without allowing further consolidation and the sheared undrained. The result, within experimental scatter, is that the shear stress or radius of the Mohr circle is about 35 kPa for each specimen.
So what happened?
When the confining pressure was changed, the pore pressure in the fully saturated specimens changed just as much as did the confining pressure, and the effective stress remained unchanged and equal in each specimen. Thus the effective stress remained 110 kPa and each specimen behaved during shear just as did the CU specimen. The shear stress and thus the radius of the Mohr circle did not increase and apparently the specimens did not encounter internal friction. This is called the phi=0 concept. In clays with a very low permeability and at a high deformation rate, like during the cutting of clay, the clay behaves like the internal friction angle is zero. So for cutting processes the phi=0 concept will be applied.

2.5.3. Factors Controlling Shear Strength of Soils.

The stress-strain relationship of soils, and therefore the shearing strength, is affected by:

1. Soil composition (basic soil material): mineralogy, grain size and grain size distribution, shape of particles, pore fluid type and content, ions on grain and in pore fluid.
2. State (initial): Defined by the initial void ratio, effective normal stress and shear stress (stress history). State can be described by terms such as: loose, dense, over consolidated, normally consolidated, stiff, soft, contractive, dilative, etc.
3. Structure: Refers to the arrangement of particles within the soil mass; the manner the particles are packed or distributed. Features such as layers, joints, fissures, slickensides, voids, pockets, cementation, etc., are part of the structure. Structure of soils is described by terms such as: undisturbed, disturbed, remolded,

compacted, cemented; flocculent, honey-combed, single-grained; flocculated, deflocculated; stratified, layered, laminated; isotropic and anisotropic.

4. Loading conditions: Effective stress path, i.e., drained, and undrained; and type of loading, i.e., magnitude, rate (static, dynamic), and time history (monotonic, cyclic).

The shear strength and stiffness of soil determines whether or not soil will be stable or how much it will deform. Knowledge of the strength is necessary to determine if a slope will be stable, if a building or bridge might settle too far into the ground, and the limiting pressures on a retaining wall. It is important to distinguish between failure of a soil element and the failure of a geotechnical structure (e.g., a building foundation, slope or retaining wall); some soil elements may reach their peak strength prior to failure of the structure. Different criteria can be used to define the "shear strength" and the "yield point" for a soil element from a stress-strain curve. One may define the peak shear strength as the peak of a stress strain curve, or the shear strength at critical state as the value after large strains when the shear resistance levels off. If the stress-strain curve does not stabilize before the end of shear strength test, the "strength" is sometimes considered to be the shear resistance at 15% to 20% strain. The shear strength of soil depends on many factors including the effective stress and the void ratio.

The shear stiffness is important, for example, for evaluation of the magnitude of deformations of foundations and slopes prior to failure and because it is related to the shear wave velocity. The slope of the initial, nearly linear, portion of a plot of shear stress as a function of shear strain is called the shear modulus

2.5.4. Friction, Interlocking & Dilation.

Soil is an assemblage of particles that have little to no cementation while rock (such as sandstone) may consist of an assembly of particles that are strongly cemented together by chemical bonds. The shear strength of soil is primarily due to inter-particle friction and therefore, the shear resistance on a plane is approximately proportional to the effective normal stress on that plane.[3] But soil also derives significant shear resistance from interlocking of grains. If the grains are densely packed, the grains tend to spread apart from each other as they are subject to shear strain. The expansion of the particle matrix due to shearing was called dilatancy by Osborne Reynolds. If one considers the energy required to shear an assembly of particles there is energy input by the shear force, T, moving a distance, x and there is also energy input by the normal force, N, as the sample expands a distance, y. Due to the extra energy required for the particles to dilate against the confining pressures, dilatant soils have greater peak strength than contractive soils. Furthermore, as dilative soil grains dilate, they become looser (their void ratio increases), and their rate of dilation decreases until they reach a critical void ratio. Contractive soils become denser as they shear, and their rate of contraction decreases until they reach a critical void ratio.

The tendency for a soil to dilate or contract depends primarily on the confining pressure and the void ratio of the soil. The rate of dilation is high if the confining pressure is small and the void ratio is small. The rate of contraction is high if the confining pressure is large and the void ratio is large. As a first approximation, the regions of contraction and dilation are separated by the critical state line.

2.5.5. Effective Stress.

Karl von Terzaghi (1964) first proposed the relationship for effective stress in 1936. For him, the term ‘effective’ meant the calculated stress that was effective in moving soil, or causing displacements. It represents the average stress carried by the soil skeleton. Effective stress (**σ'**) acting on a soil is calculated from two parameters, total stress (**σ**) and pore water pressure (**u**) according to:

$$\sigma' = \sigma - u \tag{2-34}$$

Typically, for simple examples:

$$\sigma = \gamma_{soil} \cdot H_{soil} \quad \text{and} \quad u = \gamma_w \cdot H_w \tag{2-35}$$

Much like the concept of stress itself, the formula is a construct, for the easier visualization of forces acting on a soil mass, especially simple analysis models for slope stability, involving a slip plane. With these models, it is important to know the total weight of the soil above (including water), and the pore water pressure within the slip plane, assuming it is acting as a confined layer.

However, the formula becomes confusing when considering the true behavior of the soil particles under different measurable conditions, since none of the parameters are actually independent actors on the particles.

Consider a grouping of round quartz sand grains, piled loosely, in a classic ‘cannonball’ arrangement. As can be seen, there is a contact stress where the spheres actually touch. Pile on more spheres and the contact stresses

increase, to the point of causing frictional instability (dynamic friction), and perhaps failure. The independent parameter affecting the contacts (both normal and shear) is the force of the spheres above. This can be calculated by using the overall average density of the spheres and the height of spheres above.
If we then have these spheres in a beaker and add some water, they will begin to float a little depending on their density (buoyancy). With natural soil materials, the effect can be significant, as anyone who has lifted a large rock out of a lake can attest. The contact stress on the spheres decreases as the beaker is filled to the top of the spheres, but then nothing changes if more water is added. Although the water pressure between the spheres (pore water pressure) is increasing, the effective stress remains the same, because the concept of 'total stress' includes the weight of all the water above. This is where the equation can become confusing, and the effective stress can be calculated using the buoyant density of the spheres (soil), and the height of the soil above.

The concept of effective stress truly becomes interesting when dealing with non-hydrostatic pore water pressure. Under the conditions of a pore pressure gradient, the ground water flows, according to the permeability equation (Darcy's law). Using our spheres as a model, this is the same as injecting (or withdrawing) water between the spheres. If water is being injected, the seepage force acts to separate the spheres and reduces the effective stress. Thus, the soil mass becomes weaker. If water is being withdrawn, the spheres are forced together and the effective stress increases. Two extremes of this effect are quicksand, where the groundwater gradient and seepage force act against gravity; and the 'sandcastle effect', where the water drainage and capillary action act to strengthen the sand. As well, effective stress plays an important role in slope stability, and other geotechnical engineering and engineering geology problems, such as groundwater-related subsidence.

2.5.6. Pore Water Pressure: Hydrostatic Conditions.

If there is no pore water flow occurring in the soil, the pore water pressures will be hydrostatic. The water table is located at the depth where the water pressure is equal to the atmospheric pressure. For hydrostatic conditions, the water pressure increases linearly with depth below the water table:

$$u = \rho_w \cdot g \cdot z_w \qquad \textbf{(2-36)}$$

2.5.7. Pore Water Pressure: Capillary Action.

Due to surface tension water will rise up in a small capillary tube above a free surface of water. Likewise, water will rise up above the water table into the small pore spaces around the soil particles. In fact the soil may be completely saturated for some distance above the water table. Above the height of capillary saturation, the soil may be wet but the water content will decrease with elevation. If the water in the capillary zone is not moving, the water pressure obeys the equation of hydrostatic equilibrium, $\mathbf{u = \rho_w \cdot g \cdot z_w}$, but note that z_w, is negative above the water table. Hence, hydrostatic water pressures are negative above the water table. The thickness of the zone of capillary saturation depends on the pore size, but typically, the heights vary between a centimeter or so for coarse sand to tens of meters for a silt or clay.
The surface tension of water explains why the water does not drain out of a wet sand castle or a moist ball of clay. Negative water pressures make the water stick to the particles and pull the particles to each other, friction at the particle contacts make a sand castle stable. But as soon as a wet sand castle is submerged below a free water surface, the negative pressures are lost and the castle collapses. Considering the effective stress equation, $\boldsymbol{\sigma' = \sigma - u}$,, if the water pressure is negative, the effective stress may be positive, even on a free surface (a surface where the total normal stress is zero). The negative pore pressure pulls the particles together and causes compressive particle to particle contact forces.
Negative pore pressures in clayey soil can be much more powerful than those in sand. Negative pore pressures explain why clay soils shrink when they dry and swell as they are wetted. The swelling and shrinkage can cause major distress, especially to light structures and roads.

2.5.8. Darcy's Law.

Darcy's law states that the volume of flow of the pore fluid through a porous medium per unit time is proportional to the rate of change of excess fluid pressure with distance. The constant of proportionality includes the viscosity of the fluid and the intrinsic permeability of the soil.

$$Q = \frac{-K \cdot A}{\mu_l} \cdot \frac{(u_b - u_a)}{L} \qquad \textbf{(2-37)}$$

The negative sign is needed because fluids flow from high pressure to low pressure. So if the change in pressure is negative (in the *x*-direction) then the flow will be positive (in the *x*-direction). The above equation works well for a horizontal tube, but if the tube was inclined so that point b was a different elevation than point a, the equation would not work. The effect of elevation is accounted for by replacing the pore pressure by *excess pore pressure*, u_e defined as:

$$\mathbf{u_c = u - \rho_w \cdot g \cdot z} \tag{2-38}$$

Where z is the depth measured from an arbitrary elevation reference (datum). Replacing **u** by $\mathbf{u_e}$ we obtain a more general equation for flow:

$$\mathbf{Q = \frac{-K \cdot A}{\mu_l} \cdot \frac{\left(u_{c,b} - u_{c,a}\right)}{L}} \tag{2-39}$$

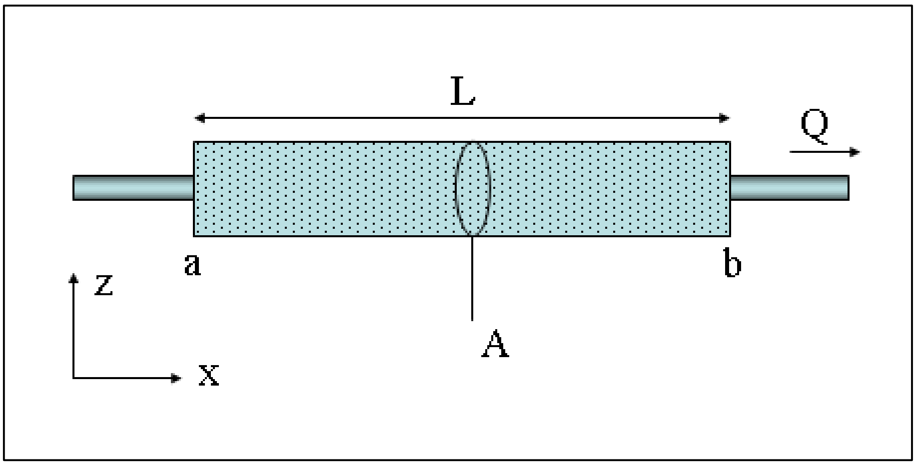

Figure 2-27: Diagram showing definitions and directions for Darcy's law.

Dividing both sides of the equation by A, and expressing the rate of change of excess pore pressure as a derivative, we obtain a more general equation for the apparent velocity in the x-direction:

$$\mathbf{q_x = \frac{-K}{\mu_l} \cdot \frac{d u_c}{d x}} \tag{2-40}$$

Where q_x has units of velocity and is called the Darcy velocity, or discharge velocity. The seepage velocity (v_{sx} = average velocity of fluid molecules in the pores) is related to the Darcy velocity, and the porosity, n:

$$\mathbf{v_{s,x} = \frac{q_x}{n}} \tag{2-41}$$

Civil engineers predominantly work on problems that involve water and predominantly work on problems on earth (in earth's gravity). For this class of problems, civil engineers will often write Darcy's law in a much simpler form:

$$\mathbf{q_x = k \cdot i_x} \tag{2-42}$$

Where k is called permeability, and is defined as:

$$\mathbf{k = K \cdot \frac{\rho_l \cdot g}{\mu_l}} \tag{2-43}$$

And **i** is called the hydraulic gradient. The hydraulic gradient is the rate of change of total head with distance. Values are for typical fresh groundwater conditions, using standard values of viscosity and specific gravity for water at 20°C and 1 atm.

Table 2-14: Typical values of the permeability k.

Soil	Permeability (m/s)	Degree of permeability
Well sorted gravel	$10^0>k>10^{-2}$	Extremely high
Gravel	$10^{-2}>k>10^{-3}$	Very high
Sandy gravel, clean sand, fine sand	$10^{-3}>k>10^{-5}$	High to Medium
Sand, dirty sand, silty sand	$10^{-5}>k>10^{-7}$	Low
Silt, silty clay	$10^{-7}>k>10^{-9}$	Very low
Clay	$<10^{-9}$	Vitually impermeable
Highly fractured rocks	$10^0>k>10^{-3}$	Very high
Oil reservoir rocks	$10^{-4}>k>10^{-6}$	Medium to Low
Fresh sandstone	$10^{-7}>k>10^{-8}$	Very low
Fresh limestone, dolomite	$10^{-9}>k>10^{-10}$	Vitually impermeable
Fresh granite	$<10^{-11}$	Vitually impermeable

Table 2-15: Some permeabilities according to Hazen's equation.

Material	Permeability (m/s)	d_{10} (mm)
Uniform coarse sand	0.0036	0.6
Uniform medium sand	0.0009	0.3
Clean, well-graded sand	0.0001	0.1
Uniform fine sand	$36\cdot10^{-6}$	0.06
Well-graded fine sand	$4\cdot10^{-6}$	0.02
Silty sand	10^{-6}	0.01
Uniform silt	$36\cdot10^{-8}$	0.006
Sandy clay	$4\cdot10^{-8}$	0.002
Silty clay	10^{-8}	0.001
Clay	$64\cdot10^{-10}$	0.0008
Colloidal clay	$9\cdot10^{-11}$	0.00003

2.5.9. Brittle versus Ductile Failure.

The terms ductile failure and brittle failure are often used in literature for the failure of materials with shear strength and tensile strength.

> *"In materials science, ductility is a solid material's ability to deform under tensile stress; this is often characterized by the material's ability to be stretched into a wire. Malleability, a similar property, is a material's ability to deform under compressive stress; this is often characterized by the material's ability to form a thin sheet by hammering or rolling. Both of these mechanical properties are aspects of plasticity, the extent to which a solid material can be plastically deformed without fracture. Ductility and malleability are not always coextensive – for instance, while gold has high ductility and malleability, lead has low ductility but high malleability. The word ductility is sometimes used to embrace both types of plasticity.*
> *A material is brittle if, when subjected to stress, it breaks without significant deformation (strain). Brittle materials absorb relatively little energy prior to fracture, even those of high strength. Breaking is often accompanied by a snapping sound. Brittle materials include most ceramics and glasses (which do not deform plastically) and some polymers, such as PMMA and polystyrene. Many steels become brittle at low temperatures (see ductile-brittle transition temperature), depending on their composition and processing. When used in materials science, it is generally applied to materials that fail when there is little or no evidence of plastic deformation before failure. One proof is to match the broken halves, which should fit exactly since no plastic deformation has occurred. Generally, the brittle strength of a material can be increased by pressure. This happens as an example in the brittle-ductile transition zone at an approximate depth of 10 kilometers in the Earth's crust, at which rock becomes less likely to fracture, and more likely to deform ductile*." (Source Wikipedia).

In rock failure a distinction is made between brittle, brittle ductile and ductile failure. Factors determining those types of failure are the ductility number (ratio compressive strength over tensile strength), the confining pressure and the temperature. During dredging the temperature will have hardly any influence, however when drilling deep oil wells temperature will play an important role. The confining pressure, where the failure transit from brittle to ductile is called $\boldsymbol{\sigma_{bp}}$.

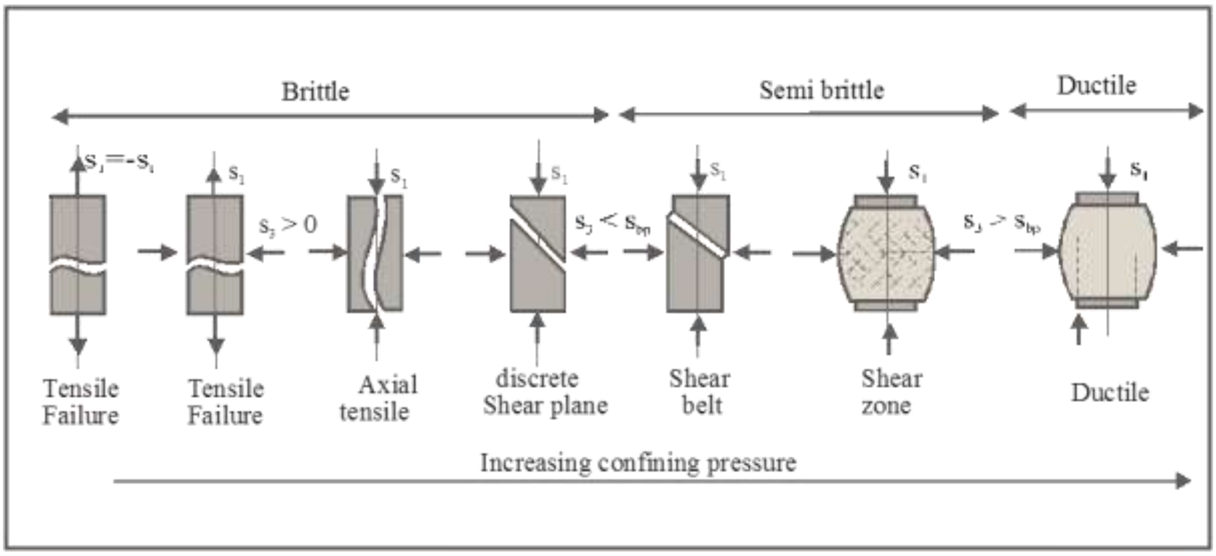

Figure 2-28: Brittle failure types (Vlasblom (2003-2007)).

Brittle failure occurs at relative low confining pressures $\boldsymbol{\sigma_3} < \boldsymbol{\sigma_{bp}}$ en deviator stress $\mathbf{q}=\boldsymbol{\sigma_1}-\boldsymbol{\sigma_3} > ½\mathbf{q_u}$. The strength increases with the confining pressure, but decreases after the peak strength to a residual value. The presence of pore water can play an important role.

Brittle failure types are:

- Pure tensile failure with or without a small confining pressure.
- Axial tensile failure
- Shear plane failure

Brittle ductile failure is also called semi brittle. In the transition area where $\boldsymbol{\sigma_3} \approx \boldsymbol{\sigma_{bp}}$, the deformations are not restricted to local shear planes or fractures but are divided over the whole area. The residual- strength is more or less equal to the peak strength.

Ductile failure. A rock fails ductile when $\boldsymbol{\sigma_3} >> \mathbf{q_u}$ and $\boldsymbol{\sigma_3} > \boldsymbol{\sigma_{bp}}$ while the force stays constant or increases some what with increasing deformation.

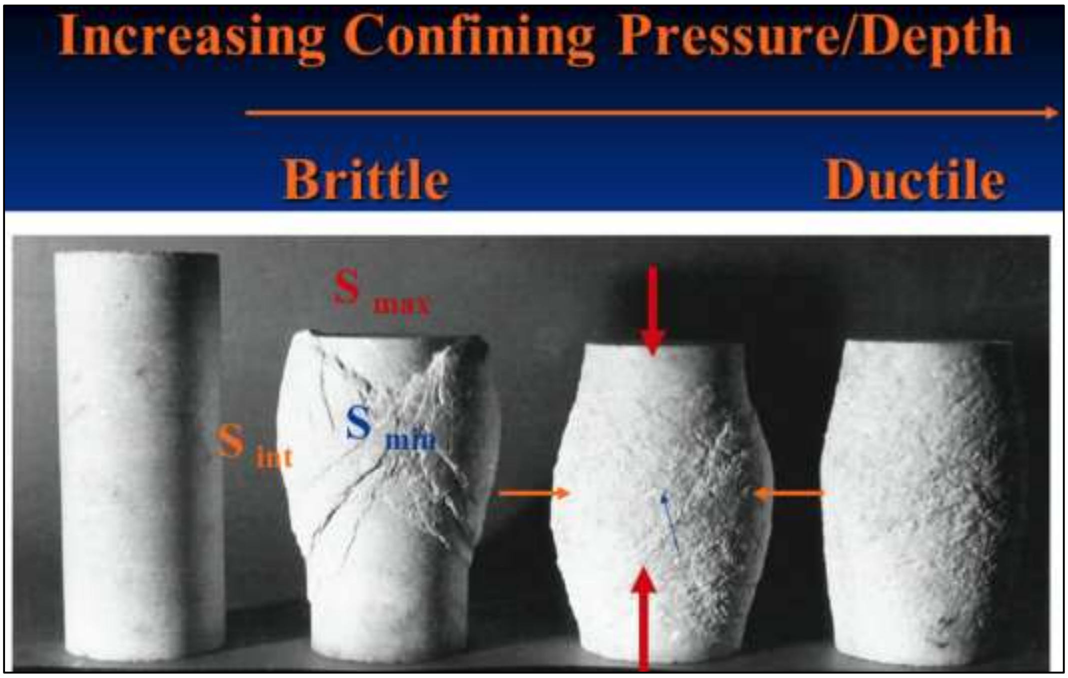

Figure 2-29: Brittle-ductile failure of marble (M.S. Patterson, Australian National University).

2.6. Soil Mechanical Tests.

2.6.1. Sieve Analysis.

The size distribution of gravel and sand particles are typically measured using sieve analysis. The formal procedure is described in ASTM D6913-04(2009). A stack of sieves with accurately dimensioned holes between a mesh of wires is used to separate the particles into size bins. A known volume of dried soil, with clods broken down to individual particles, is put into the top of a stack of sieves arranged from coarse to fine. The stack of sieves is shaken for a standard period of time so that the particles are sorted into size bins. This method works reasonably well for particles in the sand and gravel size range. Fine particles tend to stick to each other, and hence the sieving process is not an effective method. If there are a lot of fines (silt and clay) present in the soil it may be necessary to run water through the sieves to wash the coarse particles and clods through.

A variety of sieve sizes are available. The boundary between sand and silt is arbitrary. According to the Unified Soil Classification System, a #4 sieve (4 openings per inch) having 4.75mm opening size separates sand from gravel and a #200 sieve with an 0.075 mm opening separates sand from silt and clay. According to the British standard, 0.063 mm is the boundary between sand and silt, and 2 mm is the boundary between sand and gravel.

Figure 2-30: A set of sieves (Essa Australia from: www.directindustry.com).

2.6.2. Hydrometer Analysis.

The classification of fine-grained soils, i.e., soils that are finer than sand, is determined primarily by their Atterberg limits, not by their grain size. If it is important to determine the grain size distribution of fine-grained soils, the hydrometer test may be performed. In the hydrometer tests, the soil particles are mixed with water and shaken to produce a dilute suspension in a glass cylinder, and then the cylinder is left to sit. A hydrometer is used to measure the density of the suspension as a function of time. Clay particles may take several hours to settle past the depth of measurement of the hydrometer. Sand particles may take less than a second. Stoke's law provides the theoretical basis to calculate the relationship between sedimentation velocity and particle size. ASTM provides the detailed procedures for performing the Hydrometer test.

Clay particles can be sufficiently small that they never settle because they are kept in suspension by Brownian motion, in which case they may be classified as colloids.

2.6.3. Standard Penetration Test.

The standard penetration test (SPT) is an in-situ dynamic penetration test designed to provide information on the geotechnical engineering properties of soil. The test procedure is described in the British Standard BS EN ISO 22476-3, ASTM D1586 and Australian Standards AS 1289.6.3.1.

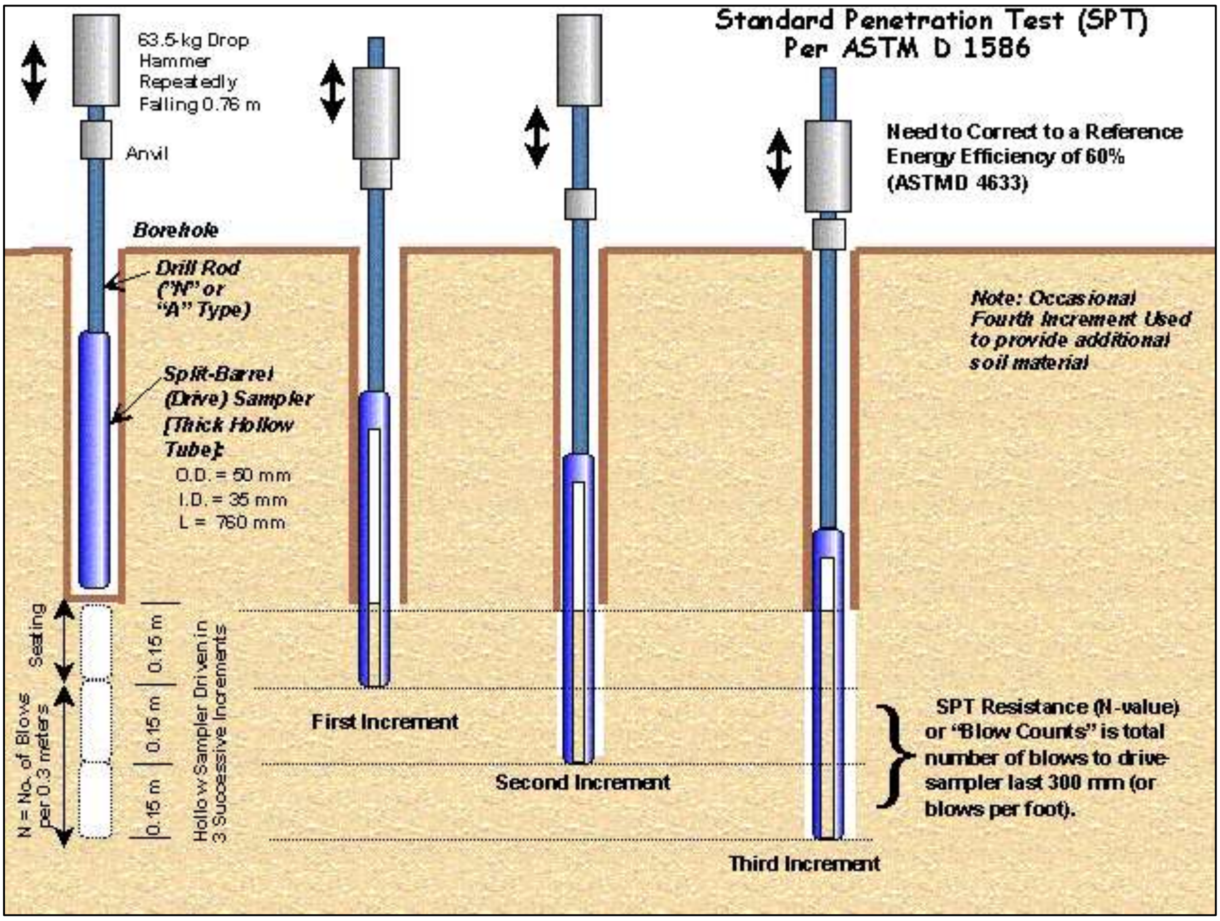

Figure 2-31: The Standard Penetration Test (www.shalviengineering.com).

The test uses a thick-walled sample tube, with an outside diameter of 50 mm and an inside diameter of 35 mm, and a length of around 650 mm. This is driven into the ground at the bottom of a borehole by blows from a slide hammer with a weight of 63.5 kg (140 lb) falling through a distance of 760 mm (30 in). The sample tube is driven 150 mm into the ground and then the number of blows needed for the tube to penetrate each 150 mm (6 in) up to a depth of 450 mm (18 in) is recorded. The sum of the number of blows required for the second and third 6 in. of penetration is termed the "standard penetration resistance" or the "N-value". In cases where 50 blows are insufficient to advance it through a 150 mm (6 in) interval the penetration after 50 blows is recorded. The blow count provides an indication of the density of the ground, and it is used in many empirical geotechnical engineering formulae.

The main purpose of the test is to provide an indication of the relative density of granular deposits, such as sands and gravels from which it is virtually impossible to obtain undisturbed samples. The great merit of the test, and the main reason for its widespread use is that it is simple and inexpensive. The soil strength parameters which can be inferred are approximate, but may give a useful guide in ground conditions where it may not be possible to obtain borehole samples of adequate quality like gravels, sands, silts, clay containing sand or gravel and weak rock. In conditions where the quality of the undisturbed sample is suspect, e.g. very silty or very sandy clays, or hard clays, it is often advantageous to alternate the sampling with standard penetration tests to check the strength. If the samples are found to be unacceptably disturbed, it may be necessary to use a different method for measuring strength like the plate test. When the test is carried out in granular soils below groundwater level, the soil may become loosened. In certain circumstances, it can be useful to continue driving the sampler beyond the distance specified, adding further drilling rods as necessary. Although this is not a standard penetration test, and should not be regarded as such, it may at least give an indication as to whether the deposit is really as loose as the standard test may indicate.

The usefulness of SPT results depends on the soil type, with fine-grained sands giving the most useful results, with coarser sands and silty sands giving reasonably useful results, and clays and gravelly soils yielding results which may be very poorly representative of the true soil conditions. Soils in arid areas, such as the Western United States, may exhibit natural cementation. This condition will often increase the standard penetration value.

The SPT is used to provide results for empirical determination of a sand layer's susceptibility to earthquake liquefaction, based on research performed by Harry Seed, T. Leslie Youd, and others.

Despite its many flaws, it is usual practice to correlate SPT results with soil properties relevant for geotechnical engineering design. The reason being that SPT results are often the only test results available, therefore the use of direct correlations has become common practice in many countries.

Different correlations are proposed for granular and cohesive soils.

2.6.4. Cone Penetration Test.

The cone penetration test (CPT) is an in situ testing method used to determine the geotechnical engineering properties of soils and delineating soil stratigraphy. It was initially developed in the 1950s at the Dutch Laboratory for Soil Mechanics in Delft to investigate soft soils. Based on this history it has also been called the "Dutch cone test". Today, the CPT is one of the most used and accepted in situ test methods for soil investigation worldwide.

The test method consists of pushing an instrumented cone, with the tip facing down, into the ground at a controlled rate (usually 2 centimeters/second). The resolution of the CPT in delineating stratigraphic layers is related to the size of the cone tip, with typical cone tips having a cross-sectional area of either 10 or 15 cm², corresponding to diameters of 3.6 and 4.4 cm.

The early applications of CPT mainly determined the soil geotechnical property of bearing capacity. The original cone penetrometers involved simple mechanical measurements of the total penetration resistance to pushing a tool with a conical tip into the soil. Different methods were employed to separate the total measured resistance into components generated by the conical tip (the "tip friction") and friction generated by the rod string. A friction sleeve was added to quantify this component of the friction and aid in determining soil cohesive strength in the 1960s (Begemann, 1965). Electronic measurements began in 1948 and improved further in the early 1970s (de Reister, 1971). Most modern electronic CPT cones now also employ a pressure transducer with a filter to gather pore water pressure data. The filter is usually located either on the cone tip (the so-called U1 position), immediately behind the cone tip (the most common U2 position) or behind the friction sleeve (U3 position). Pore water pressure data aids determining stratigraphy and is primarily used to correct tip friction values for those effects. CPT testing which also gathers this piezometer data is called CPTU testing. CPT and CPTU testing equipment generally advances the cone using hydraulic rams mounted on either a heavily ballasted vehicle or using screwed-in anchors as a counter-force. One advantage of CPT over the Standard Penetration Test (SPT) is a more continuous profile of soil parameters, with CPTU data recorded typically at 2cm intervals.

In addition to the mechanical and electronic cones, a variety of other CPT-deployed tools have been developed over the years to provide additional subsurface information. One common tool advanced during CPT testing is a geophone set to gather seismic shear wave and compression wave velocities. This data helps determine the shear modulus and Poisson's ratio at intervals through the soil column for soil liquefaction analysis and low-strain soil strength analysis. Engineers use the shear wave velocity and shear modulus to determine the soil's behavior under low-strain and vibratory loads. Additional tools such as laser-induced fluorescence, X-ray fluorescence[1], soil conductivity/resistivity, membrane interface probe and cameras for capturing video imagery are also increasingly advanced in conjunction with the CPT probe. An additional CPT deployed tool used in Britain, Netherlands, Germany, Belgium and France is a piezocone combined with a tri-axial magnetometer. This is used to attempt to ensure that tests, boreholes, and piles, do not encounter unexploded ordnance (UXB) or duds. The magnetometer in the cone detects ferrous materials of 50 kg or larger within a radius of up to about 2 m distance from the probe depending on the material, orientation and soil conditions.

CPT for geotechnical applications was standardized in 1986 by ASTM Standard D 3441 (ASTM, 2004). ISSMGE provides international standards on CPT and CPTU. Later ASTM Standards have addressed the use of CPT for various environmental site characterization and groundwater monitoring activities. Particularly for geotechnical soil investigations, CPT is gaining popularity compared to standard penetration testing as a method of geotechnical soil investigation by its increased accuracy, speed of deployment, more continuous soil profile and reduced cost over other soil testing methods. The ability to advance additional in situ testing tools using the CPT direct push drilling rig, including the seismic tools described above, are accelerating this process.

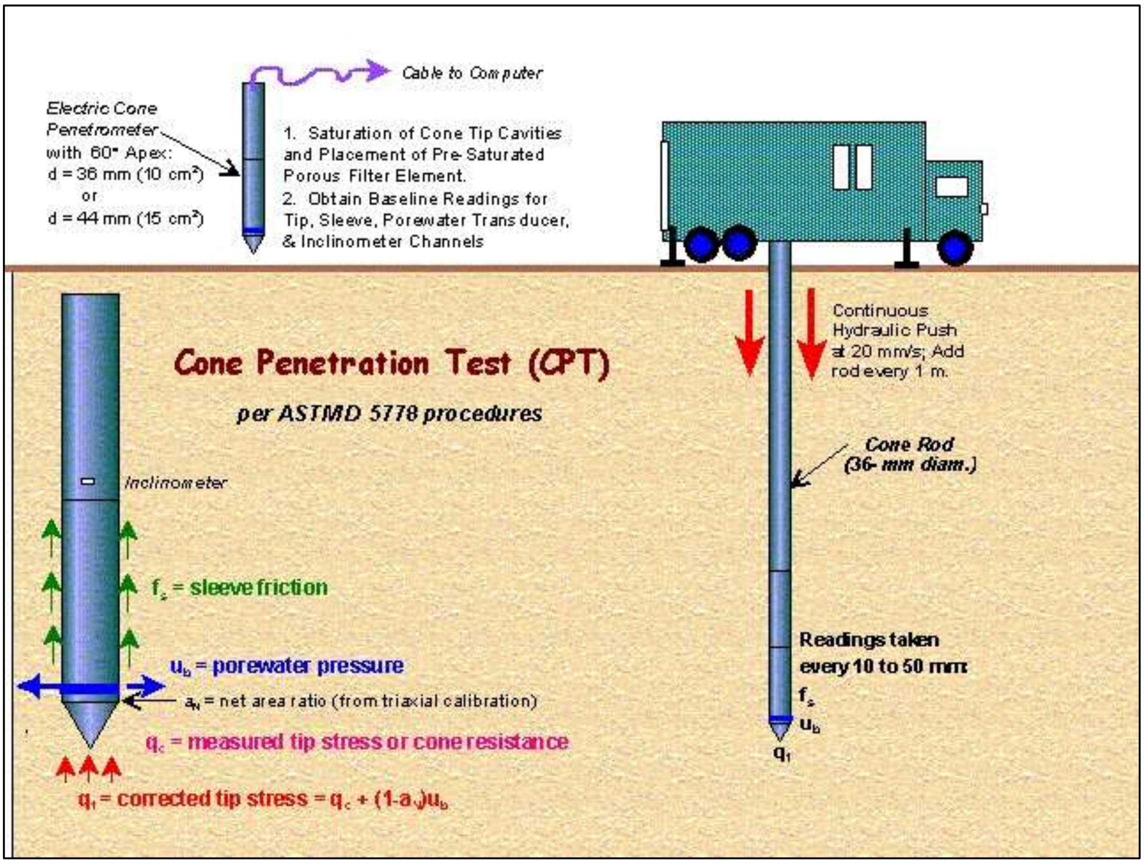

Figure 2-32: A typical CPT test setup (www.geotechdata.com).

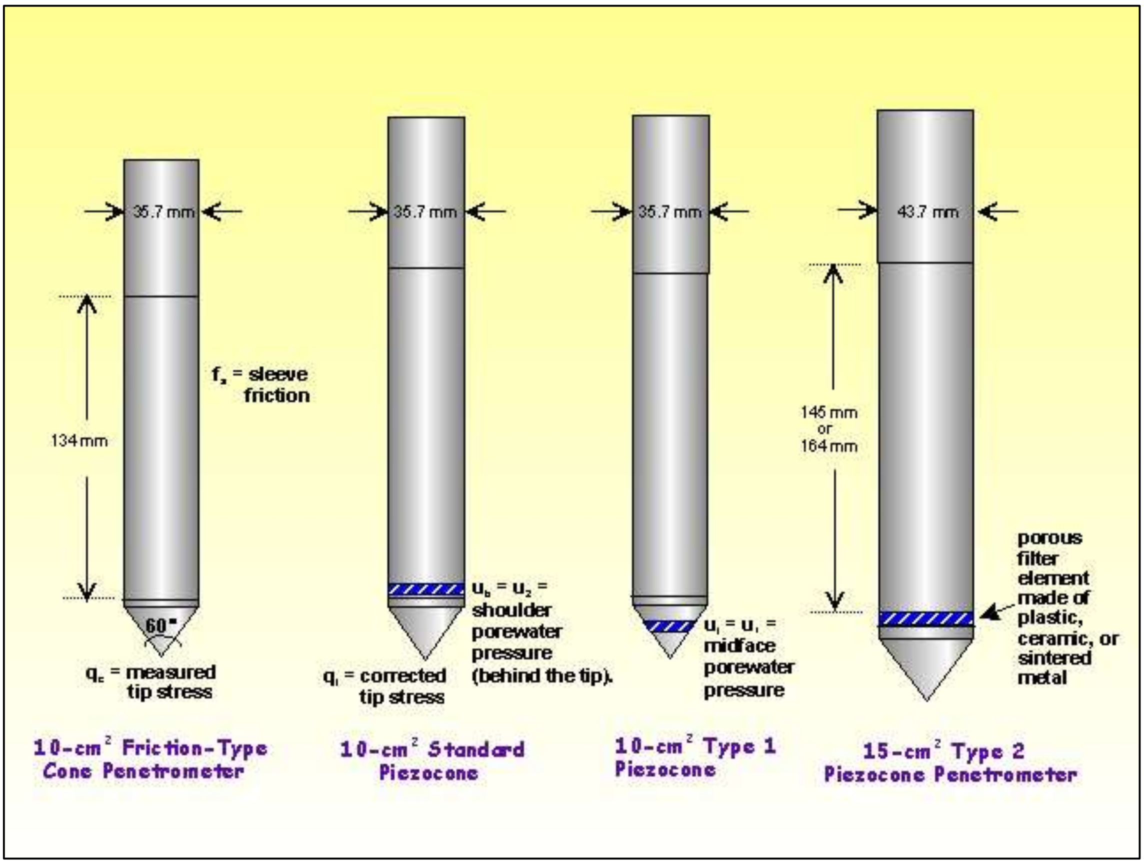

Figure 2-33: Several configurations of cones (www.geotechdata.info).

Figure 2-34: Several cone configurations.

2.6.5. Triaxial Test.

A triaxial shear test is a common method to measure the mechanical properties of many deformable solids, especially soil (e.g. sand, clay) and rock, and other granular materials or powders. There are several variations on the test. Although the name triaxial test suggests that the stresses would be different in three directions, this is not true in the test as is usually done. In this test with oil or water as confining medium, the confining pressures are equal in all directions (i.e. in terms of principal stresses: for a compression test: $\sigma_1 \neq \sigma_2 = \sigma_3$ and for tensile: $\sigma_1 = \sigma_2 \neq \sigma_3$). Only in a true triaxial test the stresses in all three directions can be different (i.e. $\sigma_1 \neq \sigma_2 \neq \sigma_3$). For loose granular materials like sand or gravel, the material is contained in a cylindrical latex sleeve with a flat, circular metal plate or platen closing off the top and bottom ends. This cylinder is placed into a bath of water (mostly water but may be any other fluid) to provide pressure along the sides of the cylinder. The top platen can then be mechanically driven up or down along the axis of the cylinder to squeeze the material. The distance that the upper platen travels is measured as a function of the force required to move it, as the pressure of the surrounding water is carefully controlled. The net change in volume of the material is also measured by how much water moves in or out of the surrounding bath. The test for cohesive (non-loose) materials (e.g. clay, rock) is similar to the test for loose granular materials. For rock testing the sleeve may be a thin metal sheeting rather than latex. Triaxial testing on rock is fairly seldom done because the high forces and pressures required to break a rock sample imply very costly and cumbersome testing equipment available at few laboratories in the world. During the test the pore pressures of fluids (e.g. water, oil) or gasses in the sample may be measured.

The principle behind a triaxial shear test is that the stress applied in the vertical direction (along the axis of the cylindrical sample) can be different from the stresses applied in the horizontal directions perpendicular to the sides of the cylinder, i.e. the confining pressure). In a homogeneous and isotropic material this produces a non-hydrostatic stress state, with shear stress that may lead to failure of the sample in shear. In non-homogeneous and anisotropic samples (e.g. bedded or jointed samples) failure may occur due to bending moments and, hence, failure may be tensile. Also combinations of bending and shear failure may happen in inhomogeneous and anisotropic material.
A solid is defined as a material that can support shear stress without moving. However, every solid has an upper limit to how much shear stress it can support. The triaxial test is designed to measure that limit. The stress on the platens is increased until the material in the cylinder fails and forms sliding regions within itself, known as shear bands. A motion where a material is deformed under shear stress is known as shearing. The geometry of the shearing in a triaxial test typically causes the sample to become shorter while bulging out along the sides. The

stress on the platen is then reduced and the water pressure pushes the sides back in, causing the sample to grow taller again. This cycle is usually repeated several times while collecting stress and strain data about the sample.
During the shearing, a granular material will typically have a net gain or loss of volume. If it had originally been in a dense state, then it typically gains volume, a characteristic known as Reynolds' dilatancy. If it had originally been in a very loose state, then contraction may occur before the shearing begins or in conjunction with the shearing.

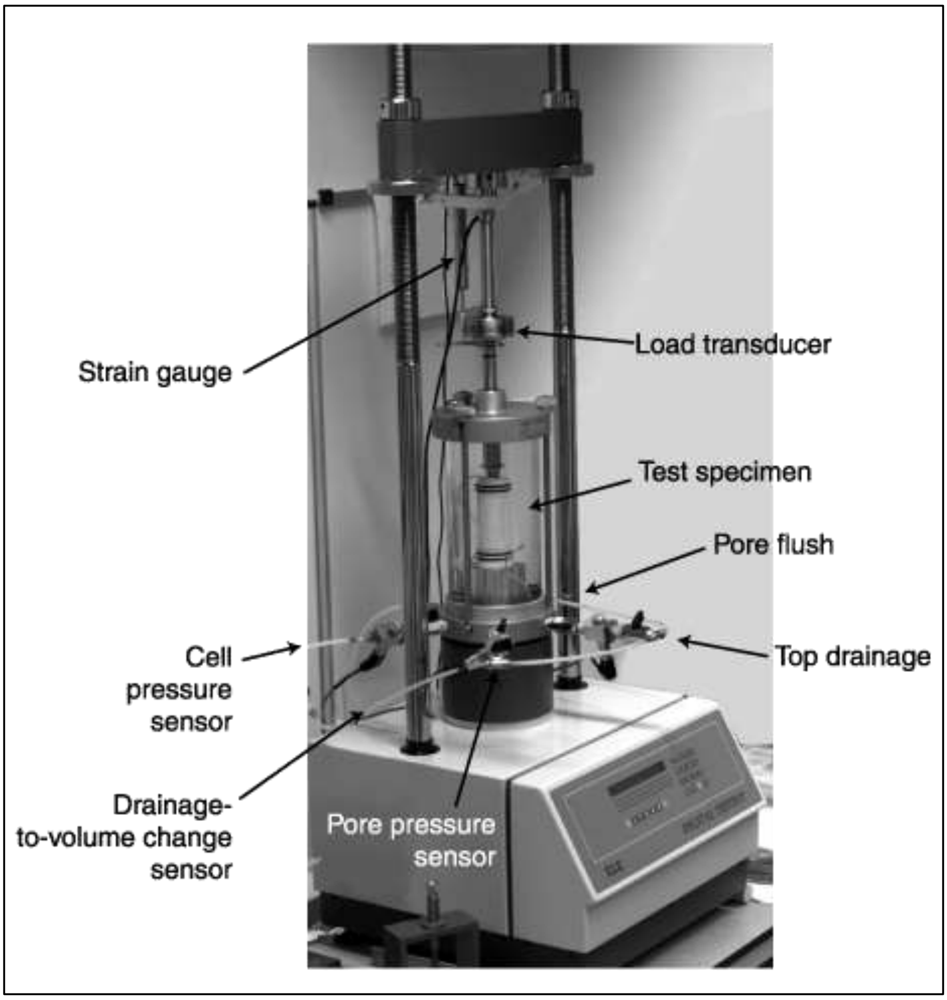

Figure 2-35: The Triaxial apparatus (www.geotechdata.info).

From the triaxial test data, it is possible to extract fundamental material parameters about the sample, including its angle of shearing resistance, apparent cohesion, and dilatancy angle. These parameters are then used in computer models to predict how the material will behave in a larger-scale engineering application. An example would be to predict the stability of the soil on a slope, whether the slope will collapse or whether the soil will support the shear stresses of the slope and remain in place. Triaxial tests are used along with other tests to make such engineering predictions.
The triaxial test can be used to determine the shear strength of a discontinuity. A homogeneous and isotropic sample (see above) fails due to shear stresses in the sample. If a sample with a discontinuity is orientated such that the discontinuity is about parallel to the plane in which maximum shear stress will be developed during the test, the sample will fail due to shear displacement along the discontinuity, and hence, the shear strength of a discontinuity can be calculated.

There are several variations of the triaxial test:

2.6.5.1. Consolidated Drained (CD).

In a consolidated drained test the sample is consolidated and sheared in compression with drainage. The rate of axial deformation is kept constant, i.e. is strain controlled. The idea is that the test allows the sample and the pore pressures to fully consolidate (i.e. adjust) to the surrounding stresses. The test may take a long time to allow the sample to adjust, in particular low permeability samples need a long time to drain and adjust stain to stress levels.

2.6.5.2. Consolidated Undrained (CU).

In a consolidated undrained test the sample is not allowed to drain. The shear characteristics are measured under undrained conditions and the sample is assumed to be fully consolidated under the stresses applied that should be similar to the field conditions. Test in particular used if a change in stress is to happen without time for further consolidation.

2.6.5.3. Unconsolidated Undrained (UU).

In an unconsolidated undrained test the sample is not allowed to drain. The sample is compressed at a constant rate (strain-controlled).

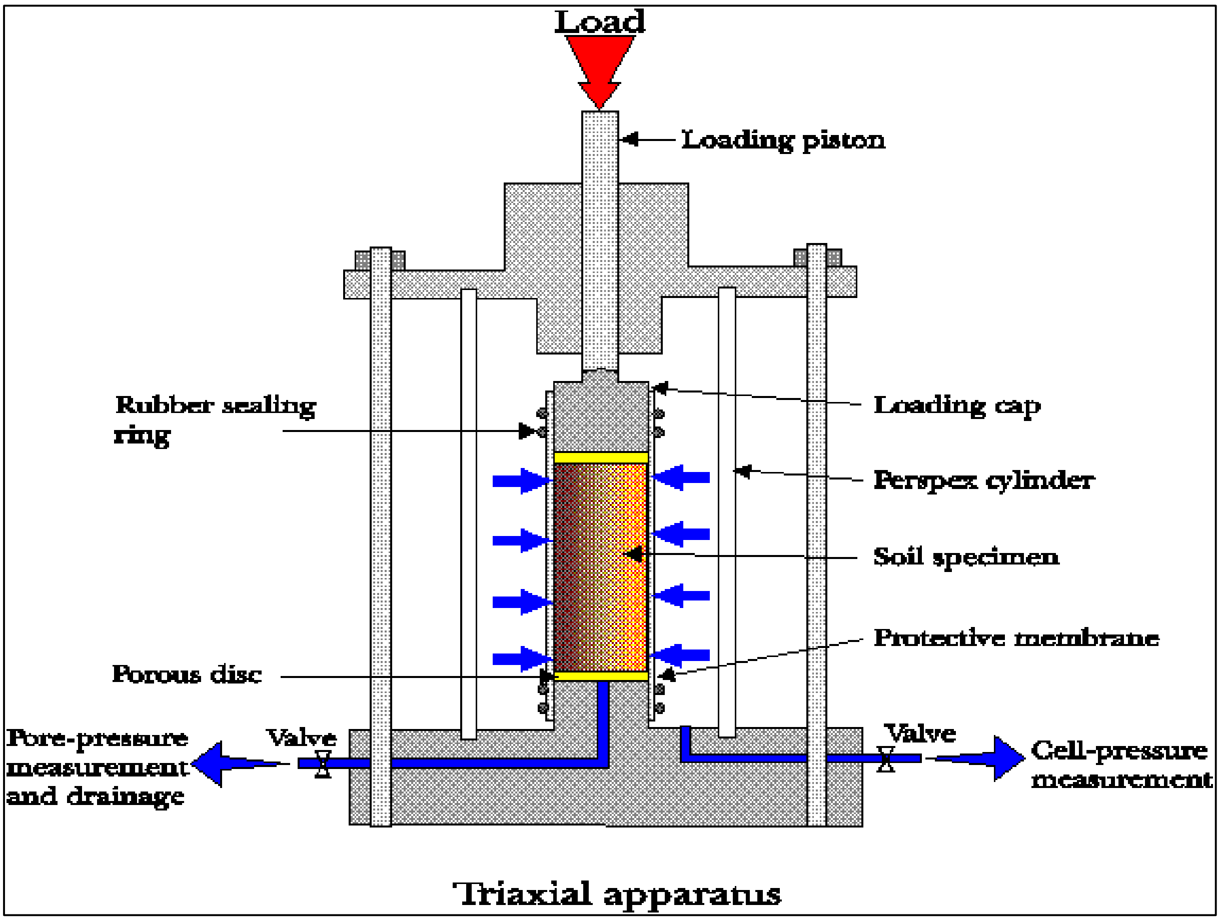

Figure 2-36: The Triaxial apparatus cross-section (civilblog.org).

2.6.6. Shear Test.

A direct shear test also known as shear box test is a laboratory or field test used by geotechnical engineers to measure the shear strength properties of soil or rock material, or of discontinuities in soil or rock masses. For soil the U.S. and U.K. standards defining how the test should be performed are ASTM D 3080 and BS 1377-7:1990 respectively to establish the shear strength properties of soil. It is also possible to estimate typical values of the shear strength parameters based on the type and classification of the soils. For rock the test is generally restricted to rock with (very) low (shear) strength. The test is, however, standard practice to establish the shear strength properties of discontinuities in rock.

The test is performed on three or four specimens from a relatively undisturbed soil sample. A specimen is placed in a shear box which has two stacked rings to hold the sample; the contact between the two rings is at approximately the mid-height of the sample. A confining stress is applied vertically to the specimen, and the upper ring is pulled laterally until the sample fails, or through a specified strain. The load applied and the strain induced is recorded at frequent intervals to determine a stress-strain curve for the confining stress.

Direct Shear tests can be performed under several conditions. The sample is normally saturated before the test is run, but can be run at the in-situ moisture content. The rate of strain can be varied to create a test of undrained or drained conditions, depending whether the strain is applied slowly enough for water in the sample to prevent pore-water pressure buildup.

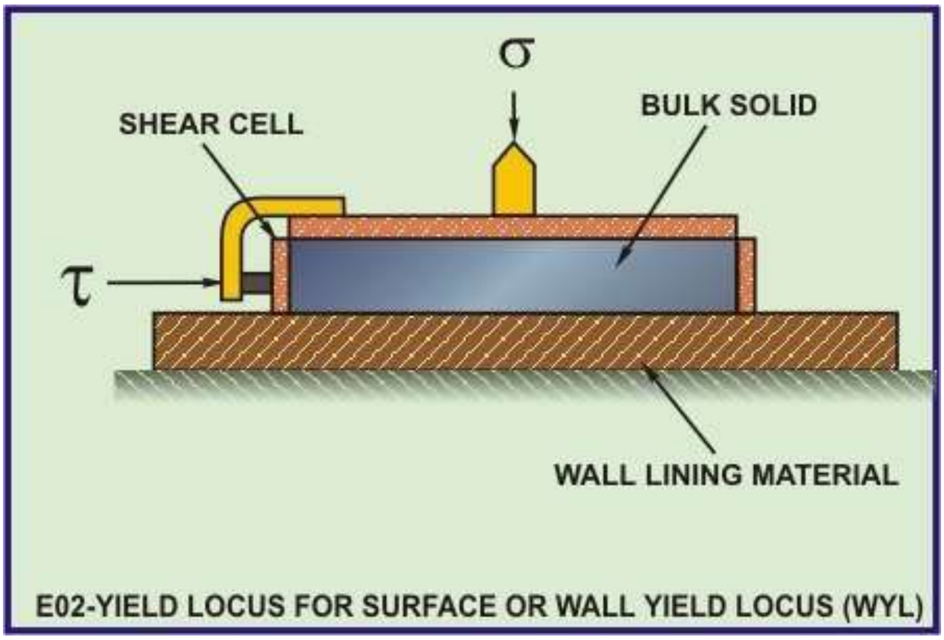

Figure 2-37: The direct shear test.

Several specimens are tested at varying confining stresses to determine the shear strength parameters, the soil cohesion (c) and the angle of internal friction (commonly friction angle) (φ). The results of the tests on each specimen are plotted on a graph with the peak (or residual) stress on the x-axis and the confining stress on the y-axis. The y-intercept of the curve which fits the test results is the cohesion, and the slope of the line or curve is the friction angle.

2.6.7. Point Load Test.

The Point Load Strength test is intended as an index test for the strength classification of rock materials. It may also be used to predict other strength parameters with which it is correlated, for example the unconfined compressive and the tensile strength. It is measured in accordance with the procedures recommended in **ASTM D5731**, usually with **NX**-size core samples. The testing machine consists of a loading frame, which measures the force required to break the sample, and a system for measuring the distance between the two platen contact points. Rock specimens in the form of either core, cut blocks, or irregular lumps are broken by application of concentrated load through a pair of spherically truncated, conical platens. The applied force at failure of the sample and distance between the platen tips are recorded in order to calculate the point load index as follows:

$$\mathbf{I_s = \frac{F}{D_e^2}} \qquad \mathbf{(2\text{-}44)}$$

Another test that is familiar with the Brazilian splitting test is the point load strength test. This test is executed either axial, diametrical or on irregular pieces. The point load test is frequently used to determine the strength when a large number of samples have to be tested. The tests give for brittle rocks, when tested under diametric loading, values reasonable close to the **BTS**. Also it is suggested that **PLS=0.8*BTS**, it is suggested to establish such a relation based on both tests.

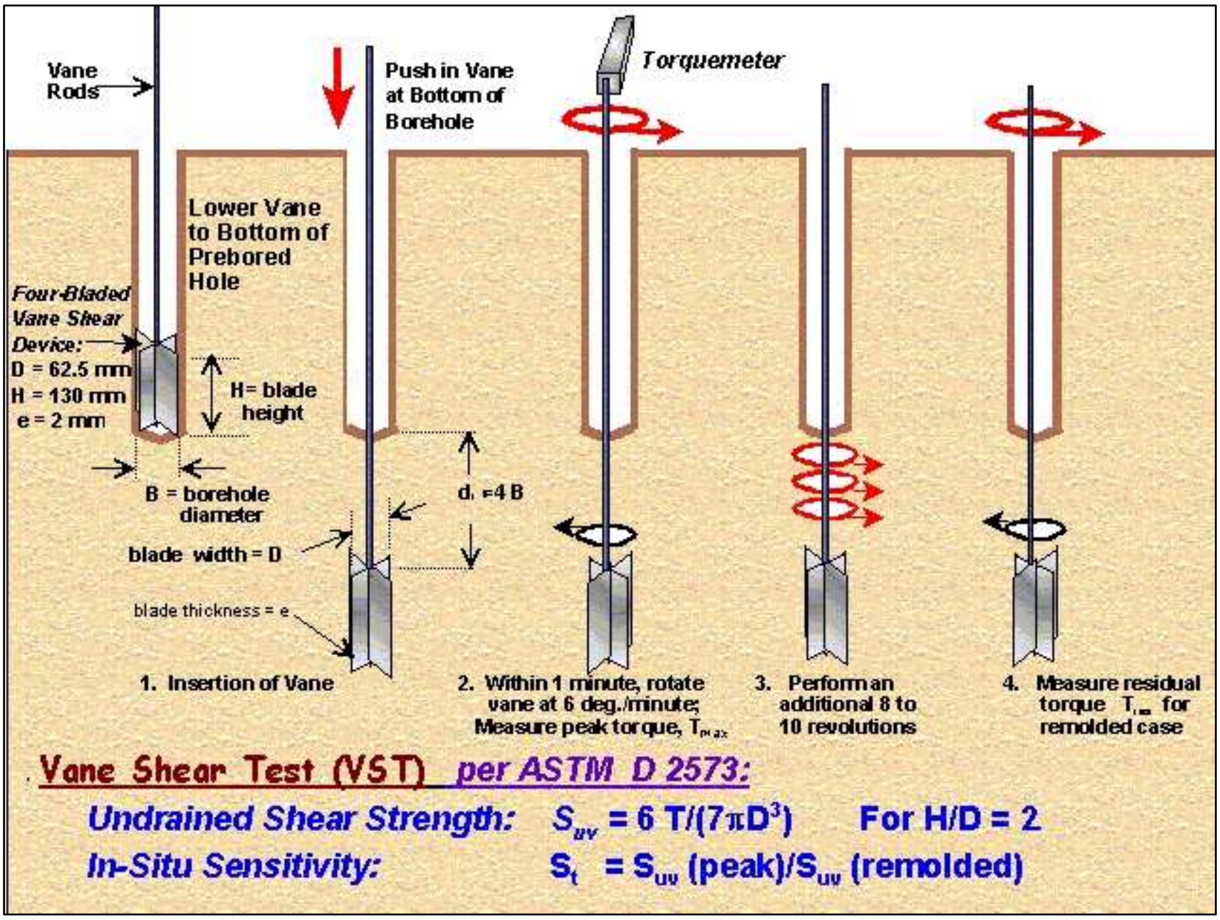

Figure 2-38: The vane shear test (English.geocpt.es).

Figure 2-39: Shear vane and Torvane for soil testing (www.humboldtmfg.com).

Figure 2-40: Point load test facility (inside.mines.edu).

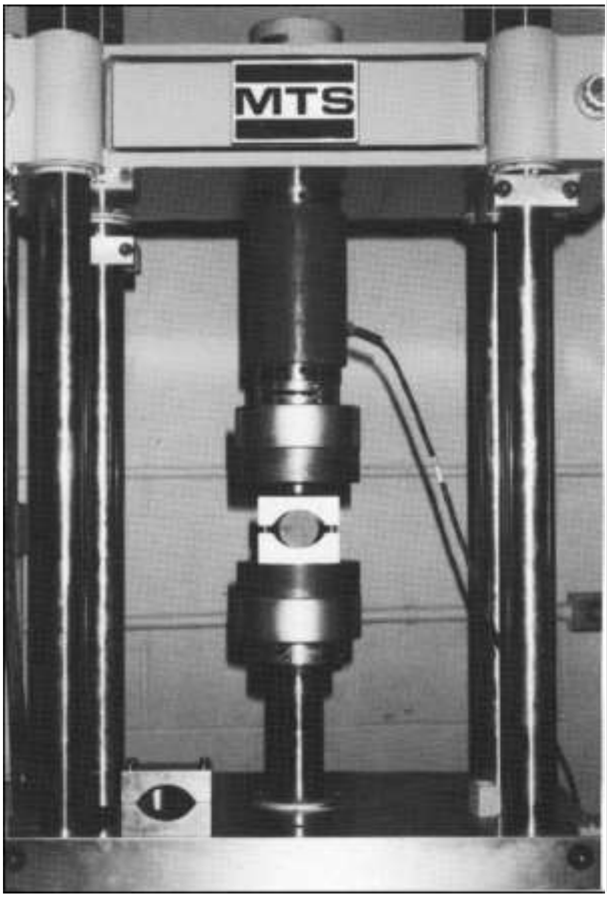

Figure 2-41: Brazilian splitting tension test.

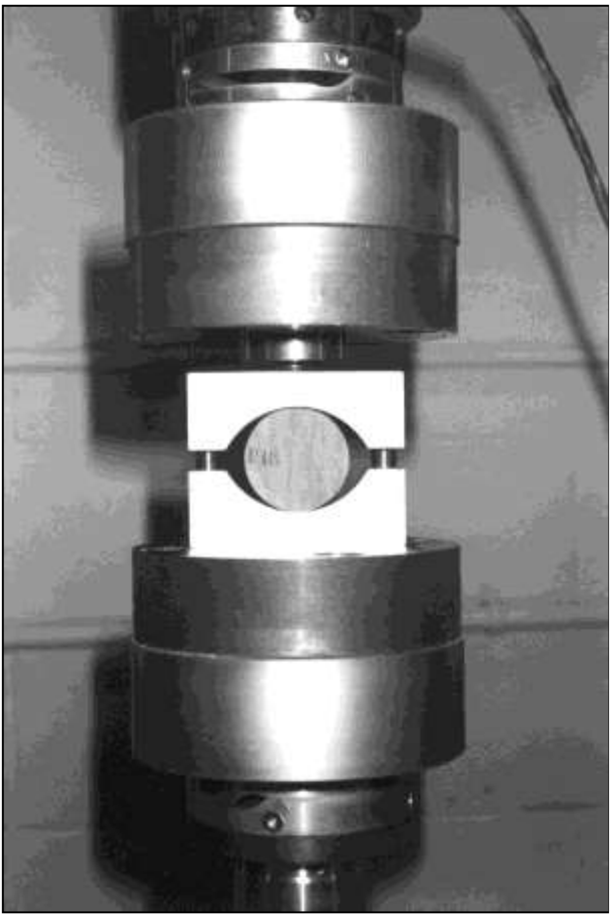

Figure 2-42: BTS zoomed.

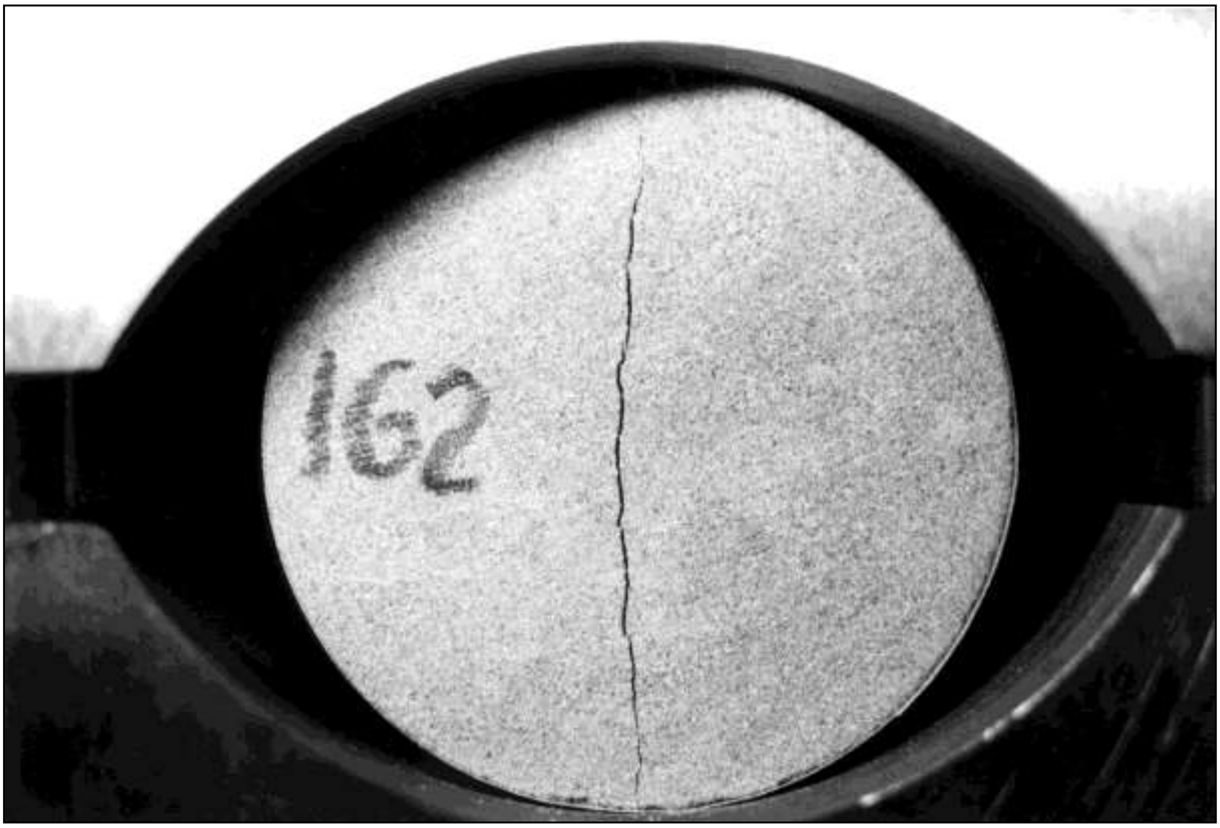

Figure 2-43: A BTS test after failure.

2.7. Nomenclature.

G_s	Specific gravity	-
ρ_s	Density of the soil	kg/m^3
ρ_w	Density of water	kg/m^3
g	Gravitational constant (9.81 m/s^2)	m/s^2
M_t	Mass of the soil, total mass	kg
M_s	Mass of the solids	kg
M_w	Mass of the water	kg
M_a	Mass of the air	kg
V_t	Volume of the soil, total volume	m^3
V_s	Volume of the solids	m^3
V_w	Volume of the water	m^3
V_a	Volume of the air	m^3
ρ_t	Density of the soil	kg/m^3
γ_t	Unit weight of the soil	N/ m^3
g	Gravitational constant (9.81 m/s^2)	m/s^2
D_r	Relative density	-
e	Current void ratio of the soil in-situ	-
e_{max}	Void ratio of the soil at its loosest condition	-
e_{min}	Void ratio of the soil at its densest condition	-
n	Porosity of the soil in-situ	-
n_{max}	Porosity of the soil at its loosest condition	-
n_{min}	Porosity of the soil in its densest condition	-
V_v	Volume of the voids/pores	m^3
V_s	Volume of the solids/grains/particles	m^3
n	Porosity	-
e	Void ratio	-
C_t	Sorting coefficient	-
C	Sorting coefficient	-
K	Hydraulic conductivity	m^2

k	Permeability	**m/s**
$f(n)$	porosity function	**-**
C	sorting coefficient	
d_e	effective grain diameter	**mm**
d_{10}	Grain diameter where 10% is smaller	**mm**
d_{60}	Grain diameter where 60% is smaller	**mm**
U	Grain uniformity coefficient	**-**
ν	kinematic viscosity	
μ	Dynamic viscosity	**Pa.s**
ρ_w	Water density	**kg/m^3**
γ_w	Unit weight of water	**N/m^3**
Q	units of volume per time	**m^3/s**
K	intrinsic permeability	**m^2**
k	permeability	**m/s**
A	cross sectional area	**m^2**
L	Length	**m**
u_a	Start excess pore pressure	**Pa**
u_b	End excess pore pressure	**Pa**
μ	dynamic viscosity of the fluid	**Pa.s**
c	Cohesion	**kPa**
UCS	Unconfined Compressive Strength	**kPa**
V	The total volume of soil	**m^3**
n_i	Initial porosity	**-**
n_{cv}	Porosity at constant volume	**-**
ε	Dilatation	**-**
σ_c	Unconfined Compressive Strength	**kPa**
F	Maximum Failure Load	**kN**
A	Cross-sectional area of the core sample	**m^2**
E	Deformation modulus	**N/m^2**
W	Specific work of failure	**J/m^3**
σ_T	Brazilian Tensile Strength (BTS)	**kPa**
D	Diameter of the core sample	**m**
F	Maximum Failure Load	**kN**
L	Length of the core sample	**m**
I_S	Point load index	**kPa**
F	Failure load	**kN**
D_e	Distance between platen tips	**m**
D_e^2	$= D^2$ for diametrical test	**m^2**
D_e^2	$= 4A/\pi =$ for axial, block and lump test	**m^2**
A	$= W.D =$ minimum cross-sectional area of a plane through the platen contact points	**m^2**
ρ_w	Density of water	**kg/m^3**
z_w	Depth below the water table	**m**
u	Hydrostatic pressure	**kPa**
g	Gravitational constant	**m/s^2**
σ_1	the major principal stress	**kPa**
σ_3	the minor principal stress	**kPa**
τ	the shear strength $\tau = S_u$ (or sometimes c_u)	**kPa**
S_u	the undrained strength	**kPa**
σ'	$(\sigma - u)$ the effective stress	**kPa**
σ	Total stress applied normal to the shear plane	**kPa**
u	Pore water pressure acting on the same plane	**kPa**
φ	Effective stress friction angle or the angle of internal friction after Coulomb friction	**deg**
c'	Cohesion	**kPa**
τ	The shear strength $\tau = S_u$ (or sometimes c_u)	**kPa**

2.8. The Mohr Circle.

In the derivation of the Mohr circle the vertical stress σ_v and the horizontal stress σ_h are assumed to be the principal stresses, but in reality these stresses could have any orientation. It should be noted here that the Mohr circle approach is valid for the stress situation in a point in the soil. Now consider an infinitesimal element of soil under plane strain conditions as is shown in Figure 2-44. On the element a vertical stress σ_v and a horizontal stress σ_h are acting. On the horizontal and vertical planes the shear stresses are assumed to be zero. Now the question is, what would the normal stress σ and shear stress τ be on a plane with an angle α with the horizontal direction? To solve this problem, the horizontal and vertical equilibriums of forces will be derived. Equilibriums of stresses do not exist. One should consider that the surfaces of the triangle drawn in Figure 2-44 are not equal. If the surface (or length) of the surface under the angle α is considered to be 1, then the surface (or length) of the horizontal side is **cos(α)** and the vertical side **sin(α)**. The stresses have to be multiplied with their surface in order to get forces and forces are required for the equilibriums of forces, see Figure 2-45. The derivation of the Mohr circle is also an exercise for the derivation of many equations in this book where equilibriums of forces and moments are applied.

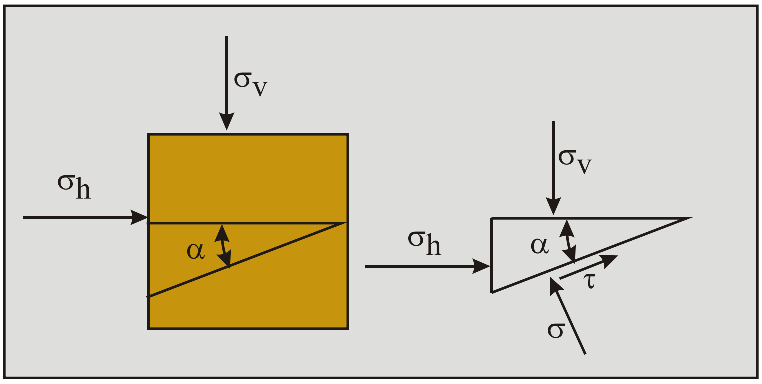

Figure 2-44: The stresses on a soil element.

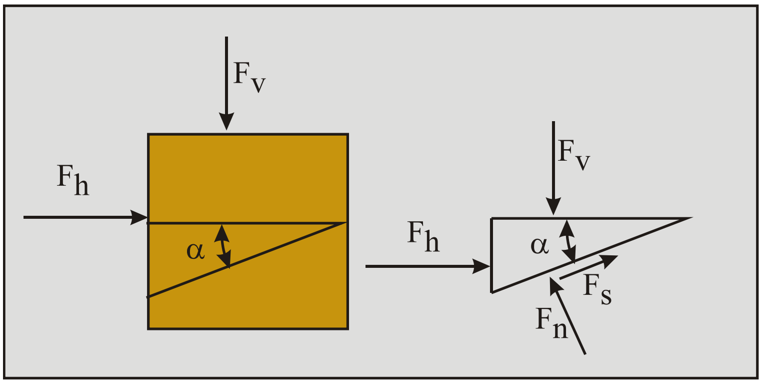

Figure 2-45: The forces on a soil element.

Since an equilibrium of stresses does not exist, only an equilibrium of forces exists, the forces on the soil element have to be known, or the ratio of the forces has to be known.
These forces are, assuming the length of the side under an angle α is 1:

$$F_h = \sigma_h \cdot \sin(\alpha) \quad \text{and} \quad F_v = \sigma_v \cdot \cos(\alpha) \tag{2-45}$$

And:

$$F_n = \sigma \quad \text{and} \quad F_s = \tau \tag{2-46}$$

The equilibrium of forces in the horizontal direction:

$$\begin{gathered} F_h = F_n \cdot \sin(\alpha) - F_s \cdot \cos(\alpha) \\ \sigma_h \cdot \sin(\alpha) = \sigma \cdot \sin(\alpha) - \tau \cdot \cos(\alpha) \end{gathered} \tag{2-47}$$

The equilibrium of forces in the vertical direction:

$$\mathbf{F_v = F_n \cdot \cos(\alpha) + F_s \cdot \sin(\alpha)}$$

$$\sigma_v \cdot \cos(\alpha) = \sigma \cdot \cos(\alpha) + \tau \cdot \sin(\alpha) \tag{2-48}$$

Equations (2-47) and (2-48) form a system of two equations with two unknowns **σ** and **τ**. The normal stresses **σ$_h$** and **σ$_v$** are considered to be known variables. To find a solution for the normal stress **σ** on the plane considered, equation (2-47) is multiplied with **sin(α)** and equation (2-48) is multiplied with **cos(α)**, this gives:

$$\sigma_h \cdot \sin(\alpha) \cdot \sin(\alpha) = \sigma \cdot \sin(\alpha) \cdot \sin(\alpha) - \tau \cdot \cos(\alpha) \cdot \sin(\alpha) \tag{2-49}$$

$$\sigma_v \cdot \cos(\alpha) \cdot \cos(\alpha) = \sigma \cdot \cos(\alpha) \cdot \cos(\alpha) + \tau \cdot \sin(\alpha) \cdot \cos(\alpha) \tag{2-50}$$

Adding up equations (2-49) and (2-50) eliminates the terms with **τ** and preserves the terms with **σ**, giving:

$$\sigma_v \cdot \cos^2(\alpha) + \sigma_h \cdot \sin^2(\alpha) = \sigma \tag{2-51}$$

Using some basic rules from trigonometry:

$$\cos^2(\alpha) = \frac{1 + \cos(2 \cdot \alpha)}{2} \tag{2-52}$$

$$\sin^2(\alpha) = \frac{1 - \cos(2 \cdot \alpha)}{2} \tag{2-53}$$

Giving for the normal stress **σ** on the plane considered:

$$\sigma = \left(\frac{\sigma_v + \sigma_h}{2}\right) + \left(\frac{\sigma_v - \sigma_h}{2}\right) \cdot \cos(2 \cdot \alpha) \tag{2-54}$$

To find a solution for the shear stress τ on the plane considered, equation (2-47) is multiplied with **-cos(α)** and equation (2-48) is multiplied with **sin(α)**, this gives:

$$-\sigma_h \cdot \sin(\alpha) \cdot \cos(\alpha) = -\sigma \cdot \sin(\alpha) \cdot \cos(\alpha) + \tau \cdot \cos(\alpha) \cdot \cos(\alpha) \tag{2-55}$$

$$\sigma_v \cdot \cos(\alpha) \cdot \sin(\alpha) = \sigma \cdot \cos(\alpha) \cdot \sin(\alpha) + \tau \cdot \sin(\alpha) \cdot \sin(\alpha) \tag{2-56}$$

Adding up equations (2-55) and (2-56) eliminates the terms with **σ** and preserves the terms with **τ**, giving:

$$\left(\sigma_v - \sigma_h\right) \cdot \sin(\alpha) \cdot \cos(\alpha) = \tau \tag{2-57}$$

Using the basic rules from trigonometry, equations (2-52) and (2-53), gives for **τ** on the plane considered:

$$\tau = \left(\frac{\sigma_v - \sigma_h}{2}\right) \cdot \sin(2 \cdot \alpha) \tag{2-58}$$

Squaring equations (2-54) and (2-58) gives:

$$\left(\sigma - \left(\frac{\sigma_v + \sigma_h}{2}\right)\right)^2 = \left(\frac{\sigma_v - \sigma_h}{2}\right)^2 \cdot \cos^2(2 \cdot \alpha) \tag{2-59}$$

And:

$$\tau^2 = \left(\frac{\sigma_v - \sigma_h}{2}\right)^2 \cdot \sin^2(2\cdot\alpha) \tag{2-60}$$

Adding up equations (2-59) and (2-60) gives:

$$\left(\sigma - \left(\frac{\sigma_v + \sigma_h}{2}\right)\right)^2 + \tau^2 = \left(\frac{\sigma_v - \sigma_h}{2}\right)^2 \cdot \left(\sin^2(2\cdot\alpha) + \cos^2(2\cdot\alpha)\right) \tag{2-61}$$

This can be simplified to the following circle equation:

$$\left(\sigma - \left(\frac{\sigma_v + \sigma_h}{2}\right)\right)^2 + \tau^2 = \left(\frac{\sigma_v - \sigma_h}{2}\right)^2 \tag{2-62}$$

If equation (2-62) is compared with the general circle equation from mathematics, equation (2-63):

$$\left(x - x_C\right)^2 + \left(y - y_C\right)^2 = R^2 \tag{2-63}$$

The following is found:

$$\begin{aligned} x &= \sigma \\ x_C &= \left(\frac{\sigma_v + \sigma_h}{2}\right) \\ y &= \tau \\ y_C &= 0 \\ R &= \left(\frac{\sigma_v - \sigma_h}{2}\right) \end{aligned} \tag{2-64}$$

Figure 2-46 shows the resulting Mohr circle with the Mohr-Coulomb failure criterion:

$$\tau = c + \sigma \cdot \tan(\varphi) \tag{2-65}$$

The variable **c** is the cohesion or internal shear strength of the soil. In Figure 2-46 it is assumed that the cohesion **c=0**, which describes the behavior of a cohesion less soil, sand. Further it is assumed that the vertical stress $\boldsymbol{\sigma_v}$ (based on the weight of the soil above the point considered) is bigger than the horizontal stress $\boldsymbol{\sigma_h}$. So in this case the horizontal stress at failure follows the vertical stress. The angle $\boldsymbol{\alpha}$ of the plane considered, appears as an angle of $\boldsymbol{2\cdot\alpha}$ in the Mohr circle. Figure 2-47: shows how the internal friction angle can be determined from a number of tri-axial tests for a cohesion less soil (sand). The 3 circles in this figure will normally not have the failure line as a tangent exactly, but one circle will be a bit too big and another a bit too small. The failure line found will be a best fit. Figure 2-48 and Figure 2-49 show the Mohr circles for a soil with an internal friction angle and cohesion. In such a soil, the intersection point of the failure line with the vertical axis is considered to be the cohesion.

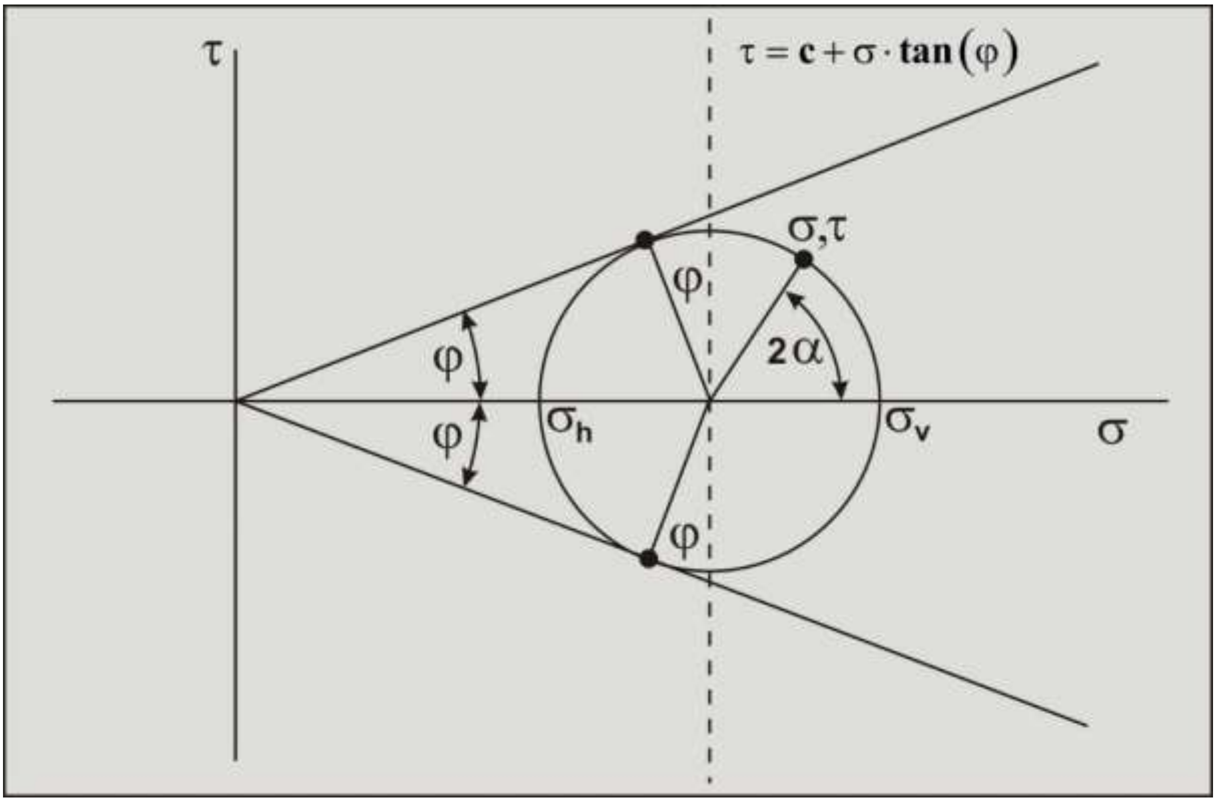

Figure 2-46: The resulting Mohr circle for cohesion less soil.

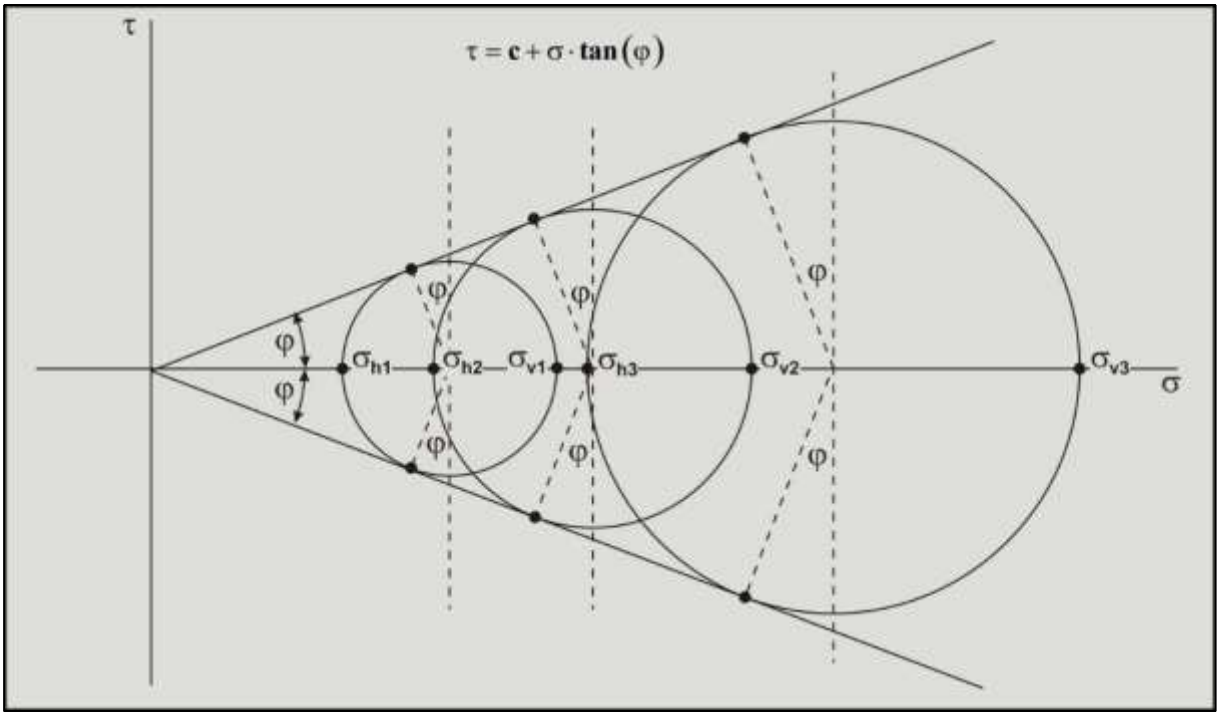

Figure 2-47: Determining the angle of internal friction from tri-axial tests of cohesion less soil.

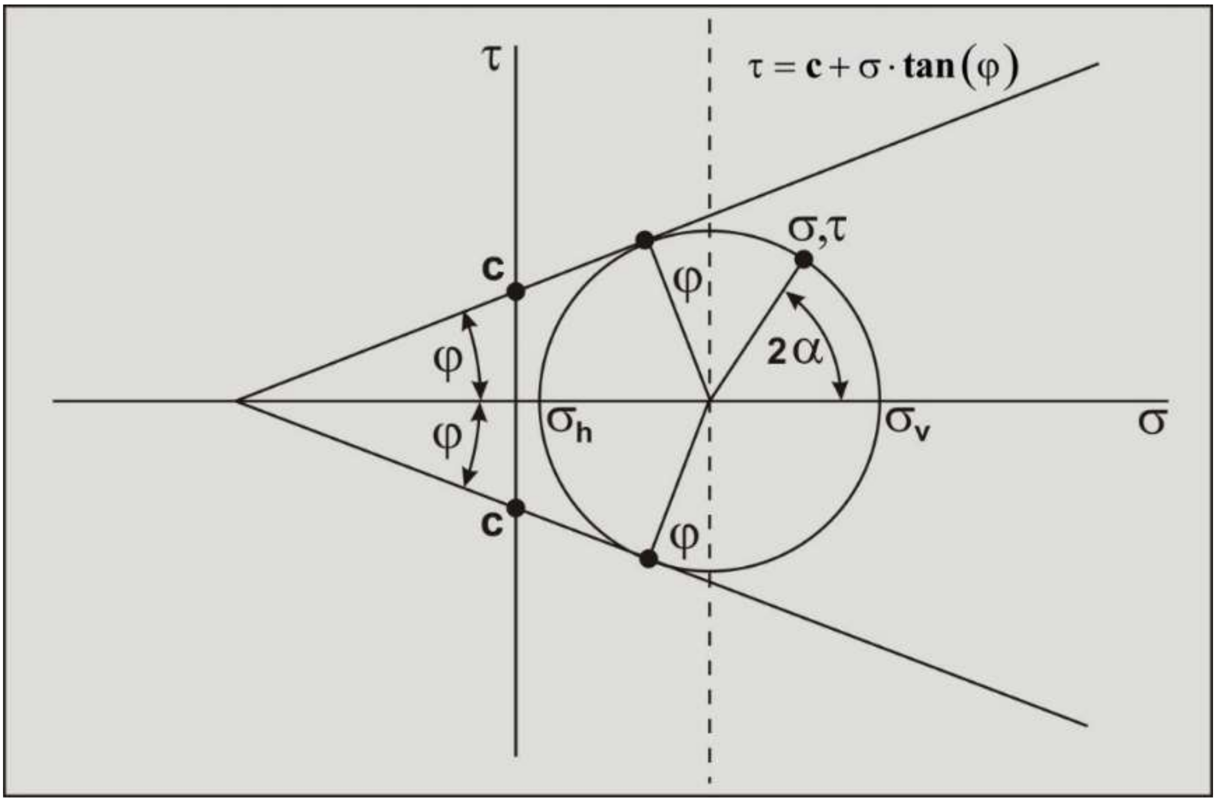

Figure 2-48: The Mohr circle for soil with cohesion.

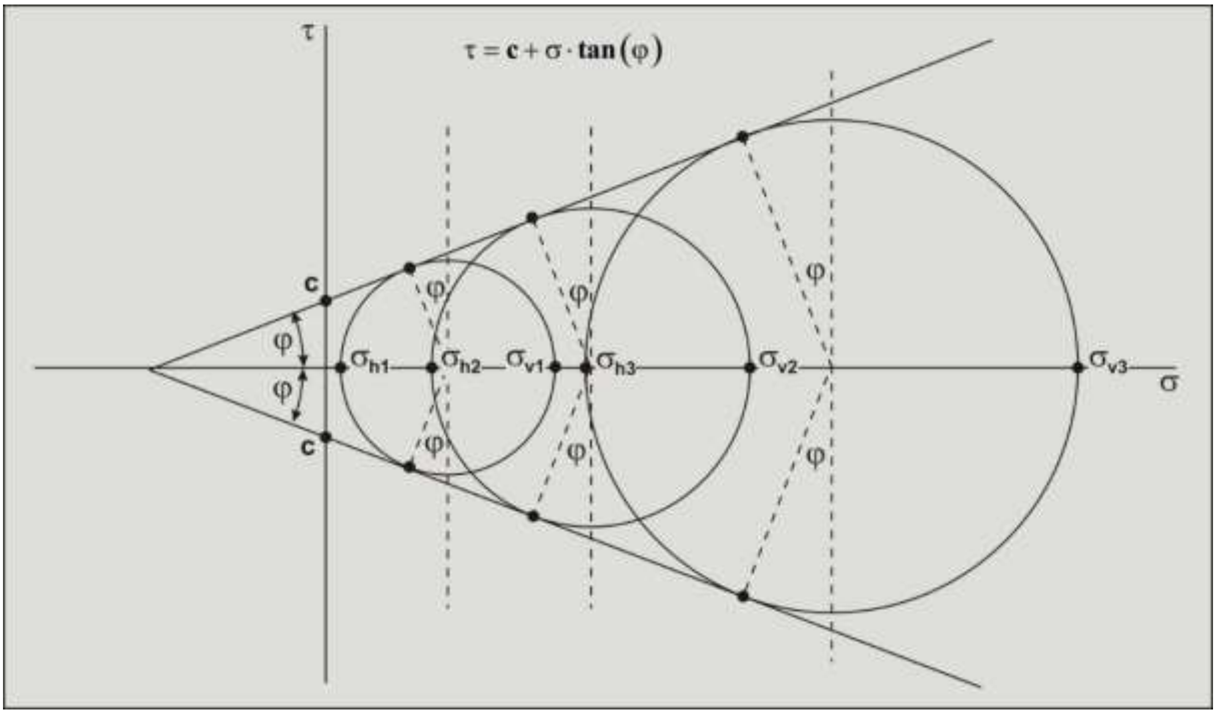

Figure 2-49: Determining the angle of internal friction from tri-axial tests of soil with cohesion.

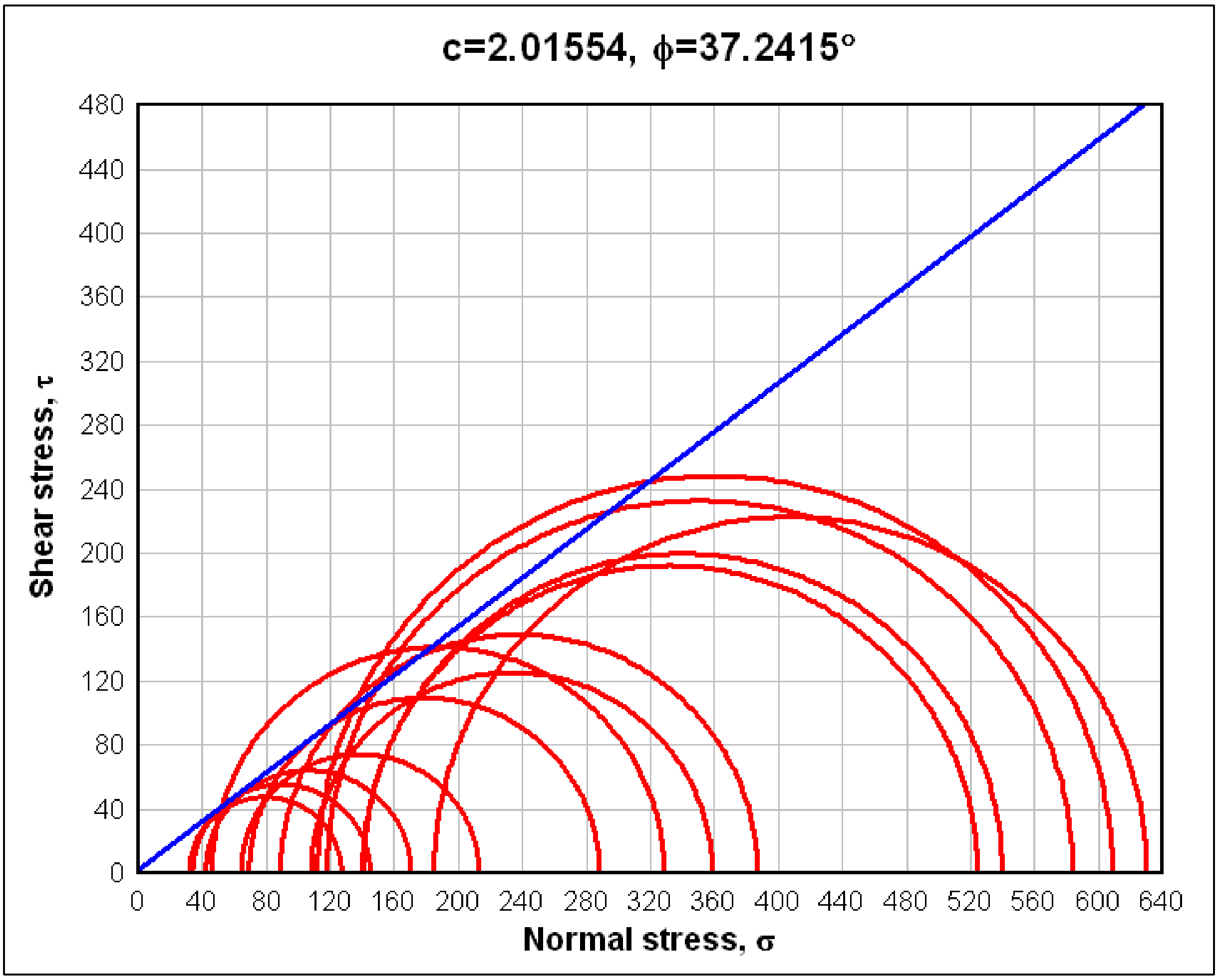

Figure 2-50: An example of Mohr circles resulting in an internal friction angle and cohesion (www.dplot.com).

2.9. Active Soil Failure.

Active soil failure is failure of the soil where the soil takes action, normally because of gravity. The standard example of active soil failure is illustrated by the retaining wall example. A retaining wall has to withstand the forces exerted on it by the soil, in this case a sand with an internal friction angle **φ**. The retaining wall has to be strong enough to withstand the maximum possible occurring force. The height of the retaining wall is **h**. The problem has 4 unknowns; the force on the retaining wall **F**, the normal force on the shear plane **N**, the shear force on the shear plane **S** and the angle of the shear plane with the horizontal **β**. To solve this problem, 4 conditions (equations) have to be defined. The first equation is the relation between the normal force **N** and the shear force **S**. The second and third equations follow from the horizontal and vertical equilibrium of forces on the triangular wedge that will move downwards when the retaining wall fails to withstand the soil forces. The fourth condition follows from the fact that we search for the maximum possible force, a maximum will occur if the derivative of the force with respect to the angle of the shear plane is zero and the second derivative is negative. It should be mentioned that the direction of the shear force is always opposite to the possible direction of motion of the soil. Since the soil will move downwards because of gravity, the shear force is directed upwards.

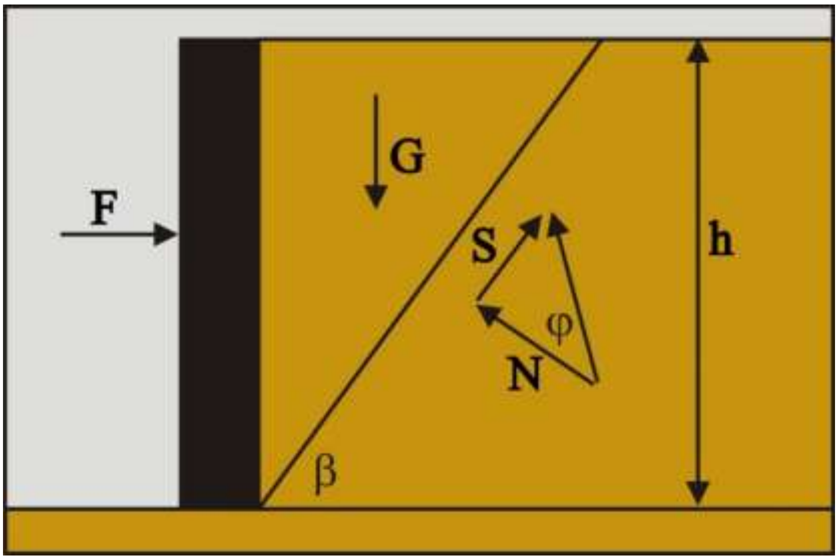

Figure 2-51: Active soil failure.

To start solving the problem, first the weight of the triangular wedge of soil is determined according to:

$$G = \frac{1}{2}\cdot\rho_s\cdot g\cdot h^2\cdot\cot(\beta)\cdot w \qquad \textbf{(2-66)}$$

The first relation necessary to solve the problem, the relation between the normal force and the shear force on the shear plane is:

$$S = N\cdot\tan(\varphi) \qquad \textbf{(2-67)}$$

Further it is assumed that the soil consists of pure sand without cohesion and adhesion and it is assumed that the retaining wall is smooth, so no friction between the sand and the wall.

$$\begin{aligned}&\text{No cohesion} &&\Rightarrow c=0\\ &\text{No adhesion} &&\Rightarrow a=0\\ &\text{Smooth wall} &&\Rightarrow \delta=0\end{aligned} \qquad \textbf{(2-68)}$$

This gives for the horizontal and vertical equilibrium equations on the triangular wedge:

$$\begin{aligned}&\text{Horizontal} &&\Rightarrow F+S\cdot\cos(\beta)-N\cdot\sin(\beta)=0\\ &\text{Vertical} &&\Rightarrow G-N\cdot\cos(\beta)-S\cdot\sin(\beta)=0\end{aligned} \qquad \textbf{(2-69)}$$

Substituting equation (2-67) gives:

$$\begin{aligned} & F + N \cdot \tan(\varphi) \cdot \cos(\beta) - N \cdot \sin(\beta) = 0 \\ & G - N \cdot \cos(\beta) - N \cdot \tan(\varphi) \cdot \sin(\beta) = 0 \end{aligned} \tag{2-70}$$

Writing the full tangent and multiplying with **cos(φ)** gives:

$$\begin{aligned} & F \cdot \cos(\varphi) + N \cdot \sin(\varphi) \cdot \cos(\beta) - N \cdot \sin(\beta) \cdot \cos(\varphi) = 0 \\ & G \cdot \cos(\varphi) - N \cdot \cos(\beta) \cdot \cos(\varphi) - N \cdot \sin(\varphi) \cdot \sin(\beta) = 0 \end{aligned} \tag{2-71}$$

Now the terms with the normal force **N** can be combined to:

$$\begin{aligned} & F \cdot \cos(\varphi) + N \cdot \sin(\varphi - \beta) = 0 \\ & G \cdot \cos(\varphi) - N \cdot \cos(\varphi - \beta) = 0 \end{aligned} \tag{2-72}$$

Cross multiplying with sine and cosine to give the normal force the same terms:

$$\begin{aligned} & F \cdot \cos(\varphi) \cdot \cos(\varphi - \beta) + N \cdot \sin(\varphi - \beta) \cdot \cos(\varphi - \beta) = 0 \\ & G \cdot \cos(\varphi) \cdot \sin(\varphi - \beta) - N \cdot \cos(\varphi - \beta) \cdot \sin(\varphi - \beta) = 0 \end{aligned} \tag{2-73}$$

Adding up the two equations gives:

$$F \cdot \cos(\varphi) \cdot \cos(\varphi - \beta) = -G \cdot \cos(\varphi) \cdot \sin(\varphi - \beta) \tag{2-74}$$

Solving the first 3 equations with the first 3 unknowns gives for the force on the retaining wall:

$$F = -G \cdot \tan(\varphi - \beta) \tag{2-75}$$

With the equation for the weight of the sand.

$$G = \frac{1}{2} \cdot \rho_s \cdot g \cdot h^2 \cdot \cot(\beta) \cdot w \tag{2-76}$$

The equation for the force on the retaining wall is found.

$$F = -\frac{1}{2} \cdot \rho_s \cdot g \cdot h^2 \cdot \frac{\cos(\beta) \cdot \sin(\varphi - \beta)}{\sin(\beta) \cdot \cos(\varphi - \beta)} \cdot w \tag{2-77}$$

This equation still contains the angle of the shear plane as an unknown. Since we are looking for the maximum possible force, a value for **β** has to be found where this force reaches a maximum. The derivative of the force and the second derivative have to be determined.

$$\frac{dF}{d\beta} = 0 \tag{2-78}$$

$$\frac{d^2F}{d\beta^2} < 0 \tag{2-79}$$

Since the equation of the force on the retaining wall contains this angle both in the nominator and the denominator, determining the derivative may be complicated. It is easier to simplify the equation with the following trick:

$$-\frac{\cos(\beta)\cdot\sin(\varphi-\beta)}{\sin(\beta)\cdot\cos(\varphi-\beta)}=-\frac{\cos(\beta)\cdot\sin(\varphi-\beta)}{\sin(\beta)\cdot\cos(\varphi-\beta)}-1+1=$$

$$-\frac{\cos(\beta)\cdot\sin(\varphi-\beta)}{\sin(\beta)\cdot\cos(\varphi-\beta)}-\frac{\sin(\beta)\cdot\cos(\varphi-\beta)}{\sin(\beta)\cdot\cos(\varphi-\beta)}+1=1-\frac{\sin(\varphi)}{\sin(\beta)\cdot\cos(\varphi-\beta)} \tag{2-80}$$

Substituting this result in the equation for the force on the retaining wall gives:

$$F=\frac{1}{2}\cdot\rho_s\cdot g\cdot h^2\cdot\left(1-\frac{\sin(\varphi)}{\sin(\beta)\cdot\cos(\varphi-\beta)}\right)\cdot w \tag{2-81}$$

When the denominator in the term between brackets has a maximum, also the whole equation has a maximum. So we have to find the maximum of this denominator.

$$f=\sin(\beta)\cdot\cos(\beta-\varphi)\Rightarrow \text{F maximum if f maximum} \tag{2-82}$$

The first derivative of this denominator with respect to the shear angle is:

$$\frac{df}{d\beta}=\cos(2\cdot\beta-\varphi) \tag{2-83}$$

The second derivative of this denominator with respect to the shear angle is:

$$\frac{d^2f}{d\beta^2}=-2\cdot\sin(2\cdot\beta-\varphi) \tag{2-84}$$

The first derivative is zero when the shear angle equals 45 degrees plus half the internal friction angle:

$$\frac{df}{d\beta}=0 \Rightarrow \beta=\frac{\pi}{4}+\frac{1}{2}\cdot\varphi \tag{2-85}$$

Substituting this solution in the equation for the second derivative gives a negative second derivative which shows that a maximum has been found.

$$\frac{d^2f}{d\beta^2}=-2 \text{ for } \beta=\frac{\pi}{4}+\frac{1}{2}\cdot\varphi \tag{2-86}$$

Substituting this solution for the shear plane angle in the equation for the force on the retaining wall gives:

$$F=\frac{1}{2}\cdot\rho_s\cdot g\cdot h^2\cdot\left(\frac{1-\sin(\varphi)}{1+\sin(\varphi)}\right)\cdot w=\frac{1}{2}\cdot\rho_s\cdot g\cdot h^2\cdot w\cdot K_a \tag{2-87}$$

The factor **K_a** is often referred to as the coefficient of active failure, which is smaller than 1. In the case of a 30 degrees internal friction angle, the value is 1/3.

$$K_A=\frac{1-\sin\varphi}{1+\sin\varphi}=\tan^2(45-\varphi/2) \tag{2-88}$$

The horizontal stresses equal the vertical stresses times the factor of active failure, which means that the horizontal stresses are smaller than the vertical stresses.

$$\sigma_h=K_A\cdot\sigma_v \tag{2-89}$$

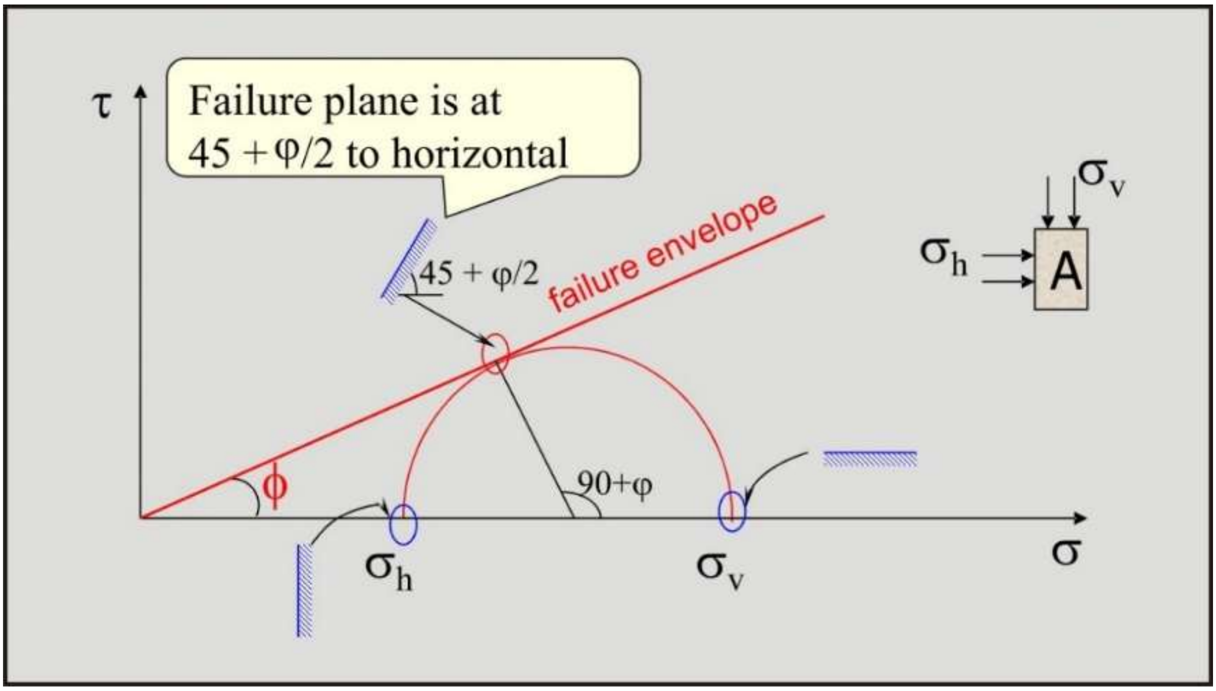

Figure 2-52: The Mohr circle for active soil failure.

Figure 2-53: An example of active soil failure, Utah copper mine landslide (photoblog.nbcnews.com).

2.10. Passive Soil Failure.

Passive soil failure is failure of the soil where the outside world takes action, for example a bulldozer. The standard example of passive soil failure is illustrated by the retaining wall example. A retaining wall has to push to supersede the forces exerted on it by the soil, in this case a sand with an internal friction angle **φ**. The retaining wall has to push strong enough to overcome the minimum possible occurring force. The height of the retaining wall is **h**. The problem has 4 unknowns; the force on the retaining wall **F**, the normal force on the shear plane **N**, the shear force on the shear plane **S** and the angle of the shear plane with the horizontal **β**. To solve this problem, 4 conditions (equations) have to be defined. The first equation is the relation between the normal force **N** and the shear force **S**. The second and third equations follow from the horizontal and vertical equilibrium of forces on the triangular wedge that will move upwards when the retaining wall pushes and the soil fails. The fourth condition follows from the fact that we search for the minimum possible force, a minimum will occur if the derivative of the force with respect to the angle of the shear plane is zero and the second derivative is positive. It should be mentioned that the direction of the shear force is always opposite to the possible direction of motion of the soil. Since the soil will move upwards because of the pushing retaining wall, the shear force is directed downwards.

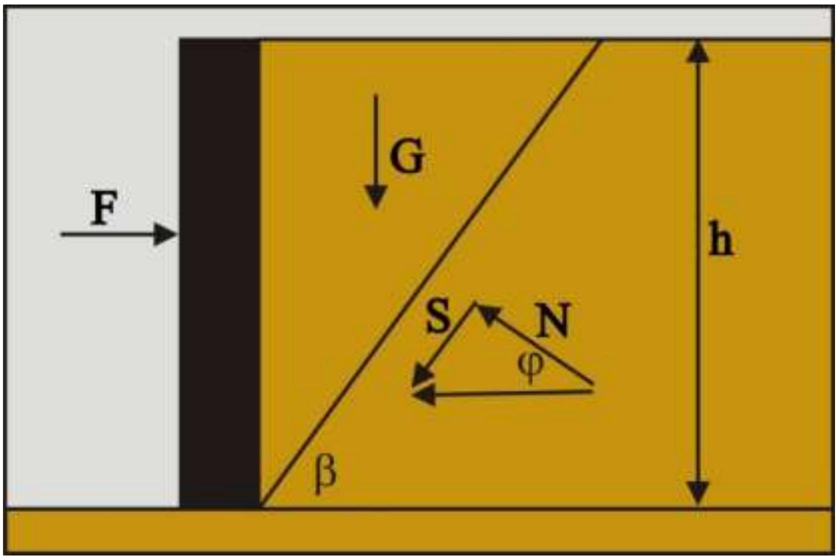

Figure 2-54: Passive soil failure.

To start solving the problem, first the weight of the triangular wedge of soil is determined according to:

$$G = \frac{1}{2} \cdot \rho_s \cdot g \cdot h^2 \cdot \cot(\beta) \cdot w \qquad \textbf{(2-90)}$$

The first relation necessary to solve the problem, the relation between the normal force and the shear force on the shear plane is:

$$S = N \cdot \tan(\varphi) \qquad \textbf{(2-91)}$$

Further it is assumed that the soil consists of pure sand without cohesion and adhesion and it is assumed that the retaining wall is smooth, so no friction between the sand and the wall.

$$\begin{aligned} &\text{No cohesion} \Rightarrow c = 0 \\ &\text{No adhesion} \Rightarrow a = 0 \\ &\text{Smooth wall} \Rightarrow \delta = 0 \end{aligned} \qquad \textbf{(2-92)}$$

This gives for the horizontal and vertical equilibrium equations on the triangular wedge:

$$\begin{aligned} &\text{Horizontal} \Rightarrow F - S \cdot \cos(\beta) - N \cdot \sin(\beta) = 0 \\ &\text{Vertical} \Rightarrow G - N \cdot \cos(\beta) + S \cdot \sin(\beta) = 0 \end{aligned} \qquad \textbf{(2-93)}$$

Substituting equation (2-91) gives:

$$\begin{aligned} & F - N \cdot \tan(\varphi) \cdot \cos(\beta) - N \cdot \sin(\beta) = 0 \\ & G - N \cdot \cos(\beta) + N \cdot \tan(\varphi) \cdot \sin(\beta) = 0 \end{aligned} \tag{2-94}$$

Writing the full tangent and multiplying with **cos(φ)** gives:

$$\begin{aligned} & F \cdot \cos(\varphi) - N \cdot \sin(\varphi) \cdot \cos(\beta) - N \cdot \sin(\beta) \cdot \cos(\varphi) = 0 \\ & G \cdot \cos(\varphi) - N \cdot \cos(\beta) \cdot \cos(\varphi) + N \cdot \sin(\varphi) \cdot \sin(\beta) = 0 \end{aligned} \tag{2-95}$$

Now the terms with the normal force **N** can be combined to:

$$\begin{aligned} & F \cdot \cos(\varphi) - N \cdot \sin(\varphi + \beta) = 0 \\ & G \cdot \cos(\varphi) - N \cdot \cos(\varphi + \beta) = 0 \end{aligned} \tag{2-96}$$

Cross multiplying with sine and cosine to give the normal force the same terms:

$$\begin{aligned} & F \cdot \cos(\varphi) \cdot \cos(\varphi + \beta) - N \cdot \sin(\varphi + \beta) \cdot \cos(\varphi + \beta) = 0 \\ & -G \cdot \cos(\varphi) \cdot \sin(\varphi + \beta) + N \cdot \cos(\varphi + \beta) \cdot \sin(\varphi + \beta) = 0 \end{aligned} \tag{2-97}$$

Adding up the two equations gives:

$$F \cdot \cos(\varphi) \cdot \cos(\varphi + \beta) = G \cdot \cos(\varphi) \cdot \sin(\varphi + \beta) \tag{2-98}$$

Solving the first 3 equations with the first 3 unknowns gives for the force on the retaining wall:

$$F = G \cdot \tan(\varphi + \beta) \tag{2-99}$$

With the equation for the weight of the sand.

$$G = \frac{1}{2} \cdot \rho_s \cdot g \cdot h^2 \cdot \cot(\beta) \cdot w \tag{2-100}$$

The equation for the force on the retaining wall is found.

$$F = \frac{1}{2} \cdot \rho_s \cdot g \cdot h^2 \cdot \frac{\cos(\beta) \cdot \sin(\varphi + \beta)}{\sin(\beta) \cdot \cos(\varphi + \beta)} \cdot w \tag{2-101}$$

This equation still contains the angle of the shear plane as an unknown. Since we are looking for the minimum possible force, a value for **β** has to be found where this force reaches a minimum. The derivative of the force and the second derivative have to be determined.

$$\frac{dF}{d\beta} = 0 \tag{2-102}$$

$$\frac{d^2F}{d\beta^2} > 0 \tag{2-103}$$

Since the equation of the force on the retaining wall contains this angle both in the nominator and the denominator, determining the derivative may be complicated. It is easier to simplify the equation with the following trick:

$$\begin{aligned}
&\frac{\cos(\beta)\cdot\sin(\varphi+\beta)}{\sin(\beta)\cdot\cos(\varphi+\beta)}=\frac{\cos(\beta)\cdot\sin(\varphi+\beta)}{\sin(\beta)\cdot\cos(\varphi+\beta)}-1+1\\
&=\frac{\cos(\beta)\cdot\sin(\varphi+\beta)}{\sin(\beta)\cdot\cos(\varphi+\beta)}-\frac{\sin(\beta)\cdot\cos(\varphi+\beta)}{\sin(\beta)\cdot\cos(\varphi+\beta)}+1\\
&=\frac{\cos(-\beta)\cdot\sin(\varphi+\beta)}{\sin(\beta)\cdot\cos(\varphi+\beta)}+\frac{\sin(-\beta)\cdot\cos(\varphi+\beta)}{\sin(\beta)\cdot\cos(\varphi+\beta)}+1\\
&=1+\frac{\sin(\varphi)}{\sin(\beta)\cdot\cos(\varphi+\beta)}
\end{aligned}\tag{2-104}$$

Substituting this result in the equation for the force on the retaining wall gives:

$$F=\frac{1}{2}\cdot\rho_s\cdot g\cdot h^2\cdot\left(1+\frac{\sin(\varphi)}{\sin(\beta)\cdot\cos(\varphi+\beta)}\right)\cdot w\tag{2-105}$$

When the denominator in the term between brackets has a maximum, also the whole equation has a minimum. So we have to find the maximum of this denominator.

$$f=\sin(\beta)\cdot\cos(\beta+\varphi)\quad\Rightarrow\quad F\ \text{minimum if}\ f\ \text{maximum}\tag{2-106}$$

The first derivative of this denominator with respect to the shear angle is:

$$\frac{df}{d\beta}=\cos(2\cdot\beta+\varphi)\tag{2-107}$$

The second derivative of this denominator with respect to the shear angle is:

$$\frac{d^2f}{d\beta^2}=-2\cdot\sin(2\cdot\beta+\varphi)\tag{2-108}$$

The first derivative is zero when the shear angle equals 45 degrees minus half the internal friction angle:

$$\frac{df}{d\beta}=0\quad\Rightarrow\quad\beta=\frac{\pi}{4}-\frac{1}{2}\cdot\varphi\tag{2-109}$$

Substituting this solution in the equation for the second derivative gives a negative second derivative which shows that a maximum has been found.

$$\frac{d^2f}{d\beta^2}=-2\ \text{for}\ \beta=\frac{\pi}{4}-\frac{1}{2}\cdot\varphi\tag{2-110}$$

Substituting this solution for the shear plane angle in the equation for the force on the retaining wall gives:

$$F=\frac{1}{2}\cdot\rho_s\cdot g\cdot h^2\cdot\left(\frac{1+\sin(\varphi)}{1-\sin(\varphi)}\right)\cdot w=\frac{1}{2}\cdot\rho_s\cdot g\cdot h^2\cdot w\cdot K_p\tag{2-111}$$

The factor $\mathbf{K_p}$ is often referred to as the coefficient of passive failure, which is larger than 1. In the case of a 30 degrees internal friction angle, the value is 3.

$$K_p = \frac{1+\sin\varphi}{1-\sin\varphi} = \tan^2(45+\varphi/2) \tag{2-112}$$

The horizontal stresses equal the vertical stresses times the factor of passive failure, which means that the horizontal stresses are larger than the vertical stresses.

$$\sigma_h = K_p \cdot \sigma_v \tag{2-113}$$

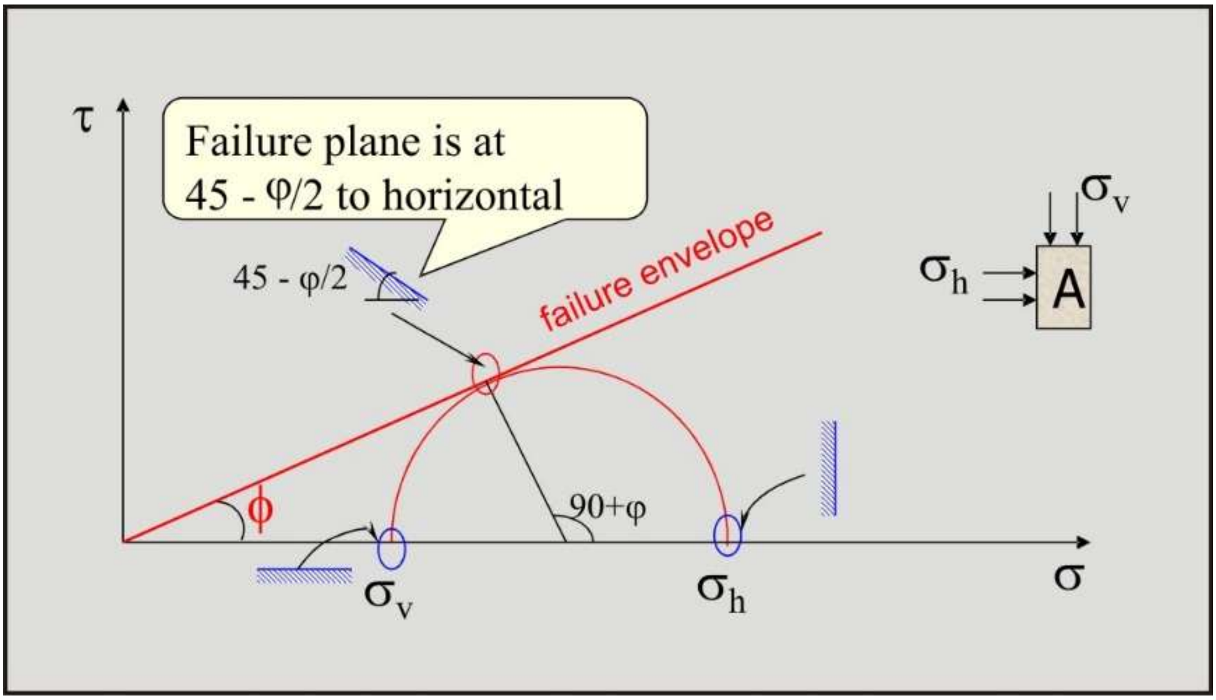

Figure 2-55: The Mohr circle for passive soil failure.

Figure 2-56: An example of passive soil failure, the Komatsu D65PX-15 (www.youtube.com).

2.11. Summary.

Figure 2-57 gives a summary of the Mohr circles for **Active** and **Passive** failure of a cohesion less soil.

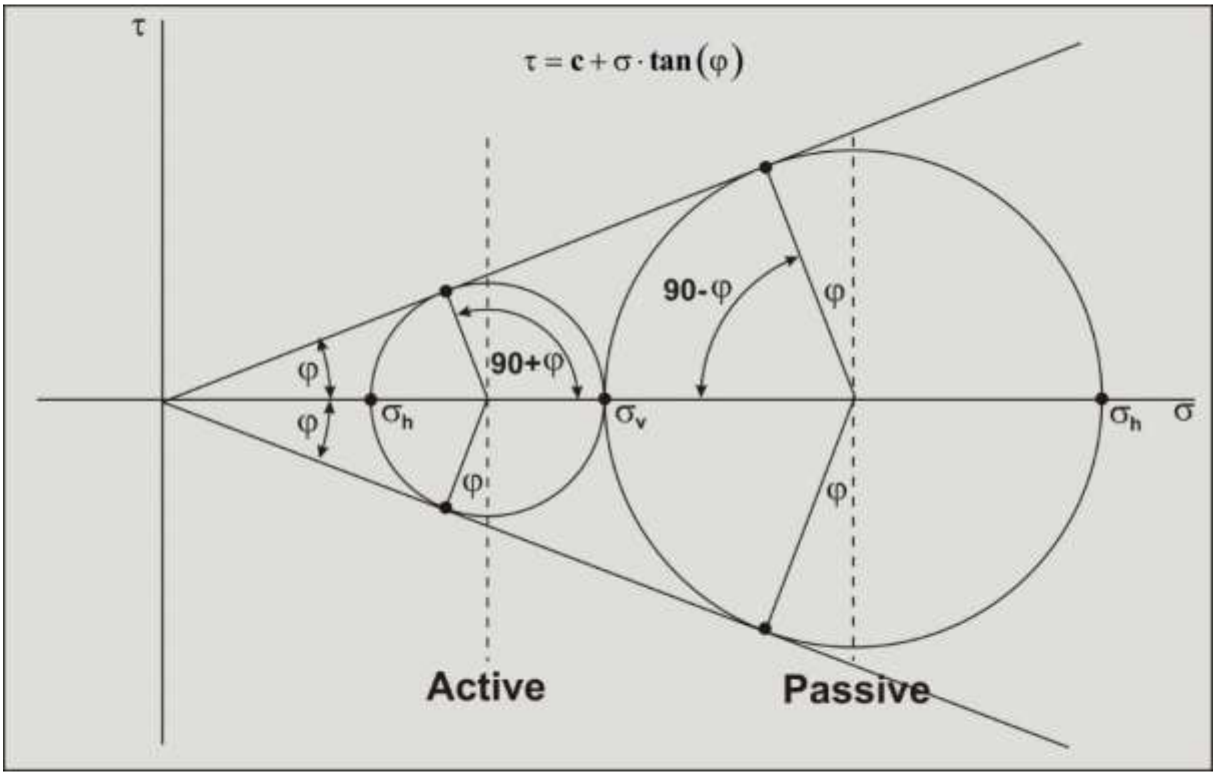

Figure 2-57: The Mohr circles for active and passive failure for a cohesion less soil.

Some equations for a cohesion less soil in the active state:

Failure will occur if:

$$\sin(\varphi) = \frac{\frac{1}{2} \cdot (\sigma_v - \sigma_h)}{\frac{1}{2} \cdot (\sigma_v + \sigma_h)} \qquad \textbf{(2-114)}$$

This can also be written as:

$$\left(\frac{\sigma_v - \sigma_h}{2}\right) - \left(\frac{\sigma_v + \sigma_h}{2}\right) \cdot \sin(\varphi) = 0 \qquad \textbf{(2-115)}$$

Using this equation the value of $\boldsymbol{\sigma_h}$ can be expressed into $\boldsymbol{\sigma_v}$:

$$\sigma_h = \sigma_v \frac{1 - \sin(\varphi)}{1 + \sin(\varphi)} = K_a \cdot \sigma_v \qquad \textbf{(2-116)}$$

On the other hand, the value of $\boldsymbol{\sigma_v}$ can also be expressed into $\boldsymbol{\sigma_h}$:

$$\sigma_v = \sigma_h \frac{1 + \sin(\varphi)}{1 - \sin(\varphi)} = K_p \cdot \sigma_h \qquad \textbf{(2-117)}$$

For the passive state the stresses $\boldsymbol{\sigma_v}$ and $\boldsymbol{\sigma_h}$ should be reversed.

Figure 2-58 gives a summary of the Mohr circles for **Active** and **Passive** failure for a soil with cohesion.

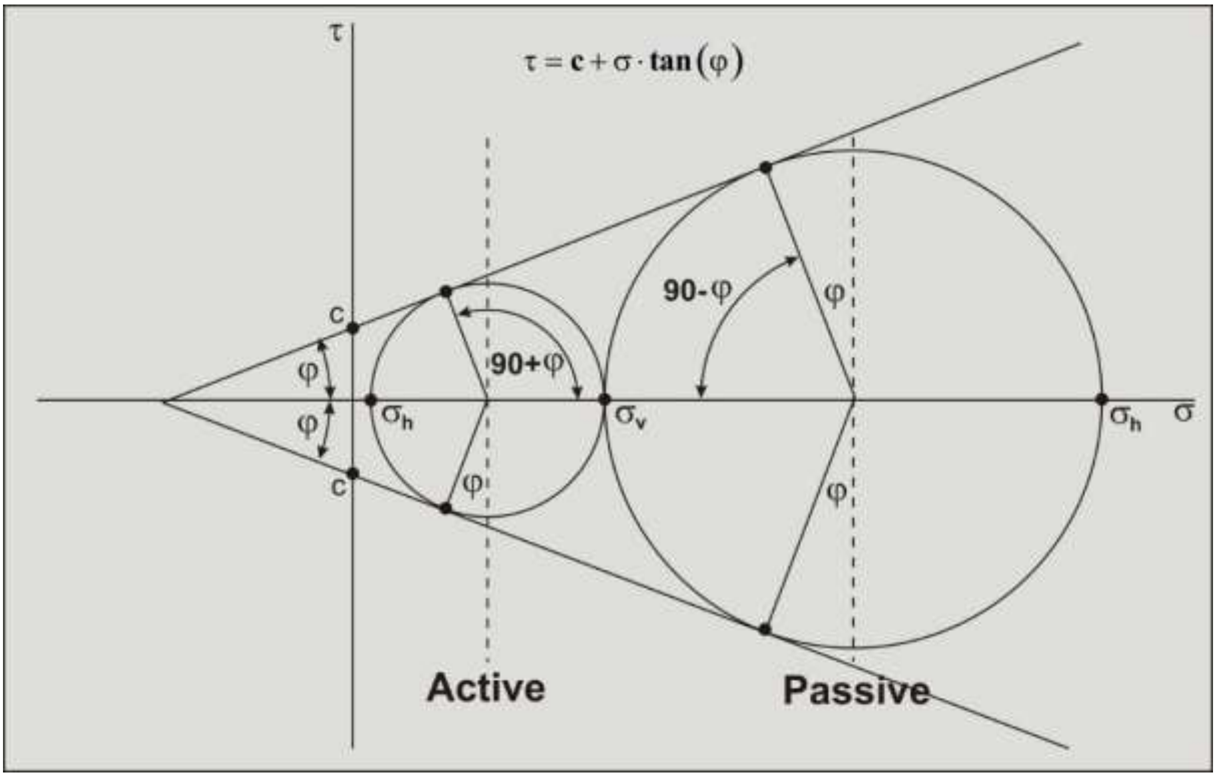

Figure 2-58: The Mohr circles for active and passive failure for a soil with cohesion.

Some equations for a soil with cohesion in the active state:

Failure will occur if:

$$\sin(\varphi) = \frac{\frac{1}{2} \cdot (\sigma_v - \sigma_h)}{c \cdot \cot(\varphi) + \frac{1}{2} \cdot (\sigma_v + \sigma_h)} \tag{2-118}$$

This can also be written as:

$$\left(\frac{\sigma_v - \sigma_h}{2}\right) - \left(\frac{\sigma_v + \sigma_h}{2}\right) \cdot \sin(\varphi) - c \cdot \cos(\varphi) = 0 \tag{2-119}$$

Using this equation the value of σ_h can be expressed into σ_v:

$$\sigma_h = \sigma_v \frac{1 - \sin(\varphi)}{1 + \sin(\varphi)} - 2 \cdot c \cdot \frac{\cos(\varphi)}{1 + \sin(\varphi)} = K_a \cdot \sigma_v - 2 \cdot c \cdot \sqrt{K_a} \tag{2-120}$$

On the other hand, the value of σ_v can also be expressed into σ_h:

$$\sigma_v = \sigma_h \frac{1 + \sin(\varphi)}{1 - \sin(\varphi)} + 2 \cdot c \cdot \frac{\cos(\varphi)}{1 - \sin(\varphi)} = K_p \cdot \sigma_h + 2 \cdot c \cdot \sqrt{K_p} \tag{2-121}$$

For the passive state the stresses σ_v and σ_h should be reversed.

2.12. Shear Strength versus Friction.

To avoid confusion between cohesion and adhesion on one side and internal and external friction on the other side, internal and external friction, also named Coulomb friction, depend linearly on normal stresses, internal friction depends on the normal stress between the sand grains and external friction on the normal stress between the sand grains and another material, for example steel. In civil engineering internal and external friction are denoted by the angle of internal friction and the angle of external friction, also named the soil/interface friction angle. In mechanical engineering the internal and external friction angles are denoted by the internal and external friction coefficient. If there is no normal stress, there is no shear stress resulting from normal stress, so the friction is zero. Adhesion and cohesion are considered to be the sticky effect between two surfaces. Cohesion is the sticky effect between two surfaces of the same material before any failure has occurred and adhesion is the sticky effect between two different materials, for example adhesive tape. Adhesion and cohesion could be named the external and internal shear strength which are independent from normal stresses. The equations for the resulting shear stresses are:

$$\tau_{in}=\tau_c+\sigma_{in}\cdot\tan(\varphi) \quad \text{or} \quad \tau_{in}=\tau_c+\sigma_{in}\cdot\mu_{in} \tag{2-122}$$

$$\tau_{ex}=\tau_a+\sigma_{ex}\cdot\tan(\delta) \quad \text{or} \quad \tau_{ex}=\tau_a+\sigma_{ex}\cdot\mu_{ex} \tag{2-123}$$

Or

$$\tau_{in}=c+\sigma_{in}\cdot\tan(\varphi) \quad \text{or} \quad \tau_{in}=c+\sigma_{in}\cdot\mu_{in} \tag{2-124}$$

$$\tau_{ex}=a+\sigma_{ex}\cdot\tan(\delta) \quad \text{or} \quad \tau_{ex}=a+\sigma_{ex}\cdot\mu_{ex} \tag{2-125}$$

With:

$$\mu_{in}=\tan(\varphi) \tag{2-126}$$

$$\mu_{ex}=\tan(\delta) \tag{2-127}$$

The values of the internal friction angle **φ** and the external friction angle **δ** not only depend on the soil properties like the density and the shape of the particles, but may also depend on the deformation history.

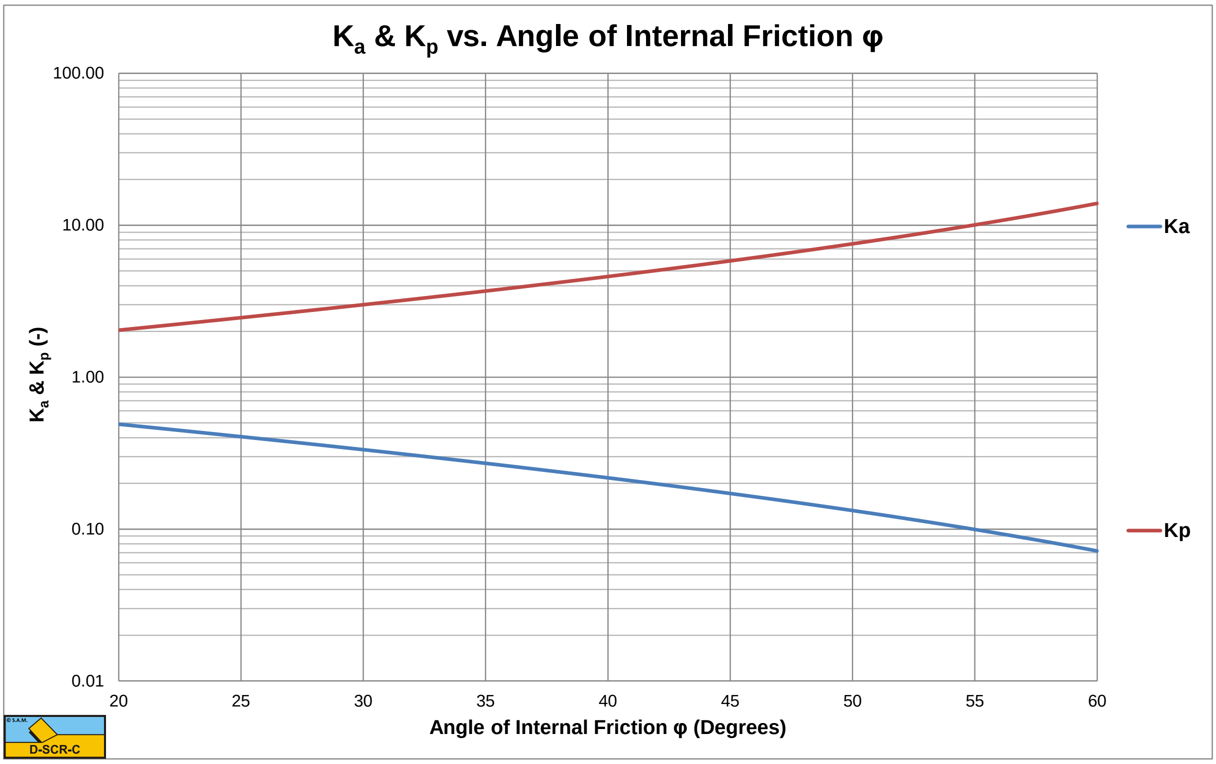

Figure 2-59: The coefficients of active and passive soil failure K_a & K_p.

Figure 2-59, Figure 2-60 and Figure 2-61 show the $\mathbf{K_a}$ and $\mathbf{K_p}$ coefficients as a function of the internal friction angle.

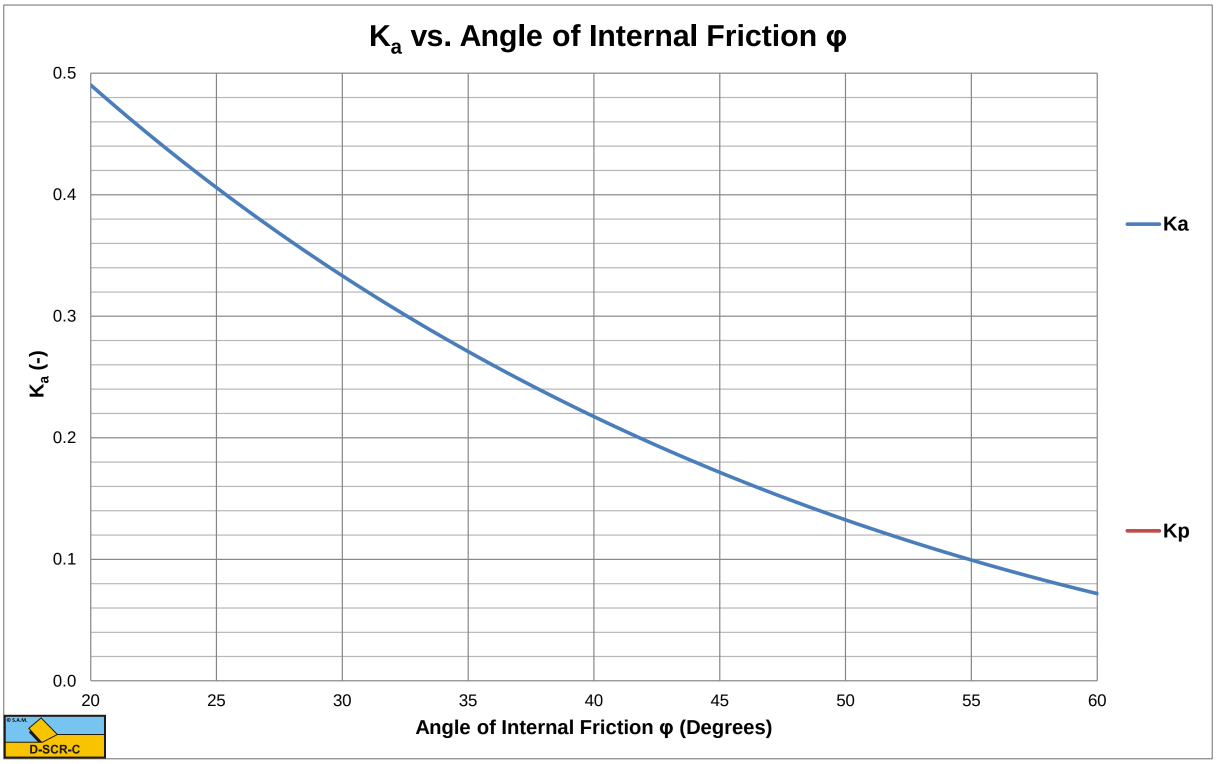

Figure 2-60: The coefficient of active soil failure K_a.

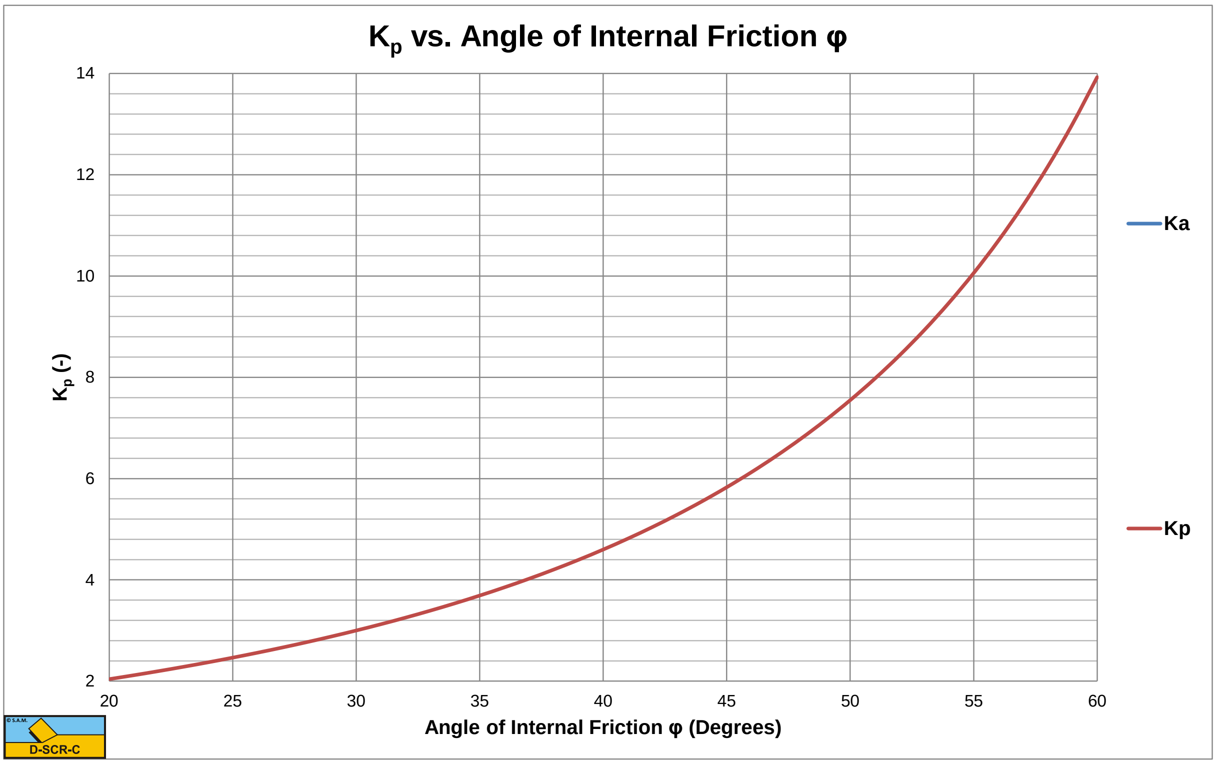

Figure 2-61: The coefficient of passive soil failure K_p.

2.13. Nomenclature.

a, τ_a	Adhesion or external shear strength	**kPa**
c, τ_c	Cohesion or internal shear strength	**kPa**
f	Function	**-**
F	Horizontal force	**kN**
F_h	Horizontal force on soil element	**kN**
F_v	Verical force on soil element	**kN**
F_n	Normal force on soil element	**kN**
F_s	Shear force on soil element	**kN**
g	Gravitational constant (9.81)	**m/s^2**
G	Gravitational vertical force	**kN**
h	Height of the dam/soil	**m**
K_a	Coefficient of active failure	**-**
K_p	Coefficient of passive failure	**-**
N	Force normal to the shear plane	**kN**
S	Shear force on the shear plane	**kN**
α	Orientation of shear plane (Mohr circle)	**rad**
β	Angle of the shear plane (active & passive failure)	**rad**
δ	External friction angle or soil/interface friction angle	**rad**
φ	Internal friction angle	**rad**
σ	Normal stress	**kPa**
σ_h	Horizontal normal stress (principal stress)	**kPa**
σ_v	Vertical normal stress (principal stress)	**kPa**
σ_{in}	Internal normal stress	**kPa**
σ_{ex}	External normal stress or soil interface normal stress	**kPa**
τ	Shear stress	**kPa**
τ_{in}	Internal shear stress	**kPa**
τ_{ex}	External shear stress or soil interface shear stress	**kPa**
ρ_g	Density of the soil	**ton/m^3**
μ_{in}	Internal friction coefficient	**-**
μ_{ex}	External friction coefficient	**-**

Chapter 3: The General Cutting Process.

3.1. Cutting Mechanisms.

Hatamura and Chijiiwa (1975), (1976A), (1976B), (1977A) and (1977B) distinguished three failure mechanisms in soil cutting. The **Shear Type**, the **Flow Type** and the **Tear Type**. The **Flow Type** and the **Tear Type** occur in materials without an angle of internal friction. The **Shear Type** occurs in materials with an angle of internal friction like sand.

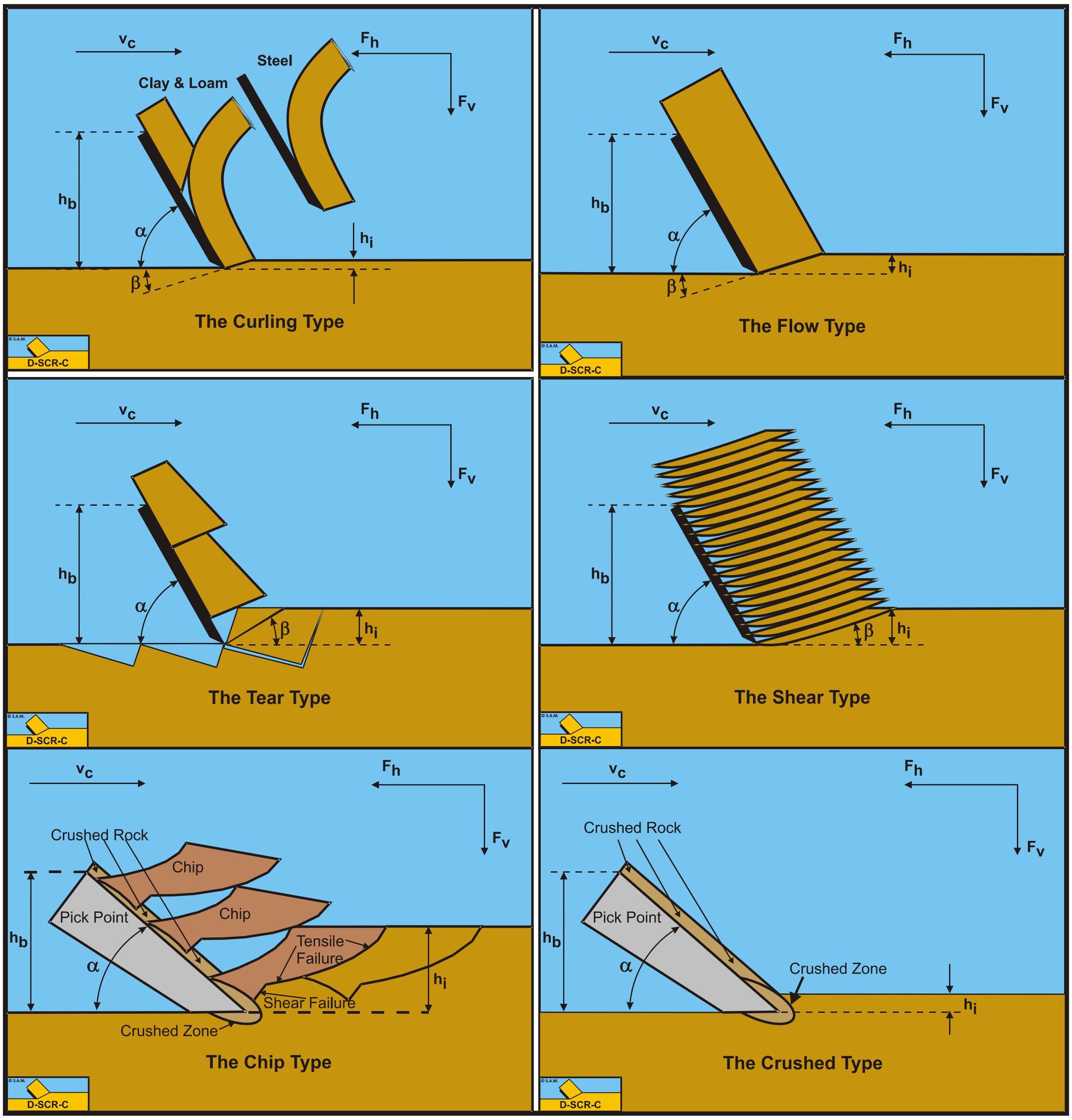

Figure 3-1: The Curling Type, the Flow Type, the Tear Type, the Shear Type, the Crushed Type and the Chip Type.

A fourth failure mechanism can be distinguished (Miedema (1992)), the **Curling Type**, as is known in metal cutting. Although it seems that the curling of the chip cut is part of the flow of the material, whether the **Curling Type** or the **Flow Type** occurs depends on several conditions. The **Curling Type** in general will occur if the adhesive force on the blade is large with respect to the normal force on the shear plane. Whether the **Curling Type** results in pure curling or buckling of the layer cut giving obstruction of the flow depends on different parameters. In rock or stone two additional cutting mechanisms may occur, the **Crushed Type** and the **Chip Type**. The

Crushed Type will occur if a thin layer of rock is scraped or cut like in oil and gas drilling. The mechanism of the **Crushed Type** is similar to the **Shear Type**, only first the rock material has to be crushed. The **Chip Type** will occur when cutting thicker layers of rock or stone. This type is similar to the **Tear Type**.

Figure 3-1 illustrates the **Curling Type**, the **Flow Type** and the **Tear Type** mechanisms as they might occur when cutting clay, the **Shear Type** mechanism as it might occur when cutting sand and the **Crushed Type** and **Chip Type** as they might occur when cutting rock or stone. Of course also mixed types may occur.
To predict which type of failure mechanism will occur under given conditions with specific soil, a formulation for the cutting forces has to be derived. The derivation is made under the assumption that the stresses on the shear plane and the blade are constant and equal to the average stresses acting on the surfaces. Figure 3-2 gives some definitions regarding the cutting process. The line A-B is considered to be the shear plane, while the line A-C is the contact area between the blade and the soil. The blade angle is named $\boldsymbol{\alpha}$ and the shear angle $\boldsymbol{\beta}$. The blade is moving from left to right with a cutting velocity $\mathbf{v_c}$. The thickness of the layer cut is $\mathbf{h_i}$ and the vertical height of the blade $\mathbf{h_b}$. The horizontal force on the blade $\mathbf{F_h}$ is positive from right to left always opposite to the direction of the cutting velocity $\mathbf{v_c}$. The vertical force on the blade $\mathbf{F_v}$ is positive downwards.
The shear angle $\boldsymbol{\beta}$ is determined based on the minimum energy principle. It is assumed that failure will occur at a shear angle where the cutting energy is at a minimum. The cutting power is the cutting energy per unit of time, so the cutting power also has to be at the minimum level.
Since the vertical force is perpendicular to the cutting velocity, the vertical force does not contribute to the cutting power, which is equal to the horizontal cutting force times the cutting velocity:

$$\mathbf{P_c = F_h \cdot v_c} \tag{3-1}$$

Whether the minimum energy principle is true and whether the approach of using straight failure planes is right has been validated with experiments. The experimental data, usually measurements of the horizontal and vertical cutting forces and pore pressures, shows that the approach in this book gives a good prediction of the cutting forces.

3.2. Definitions.

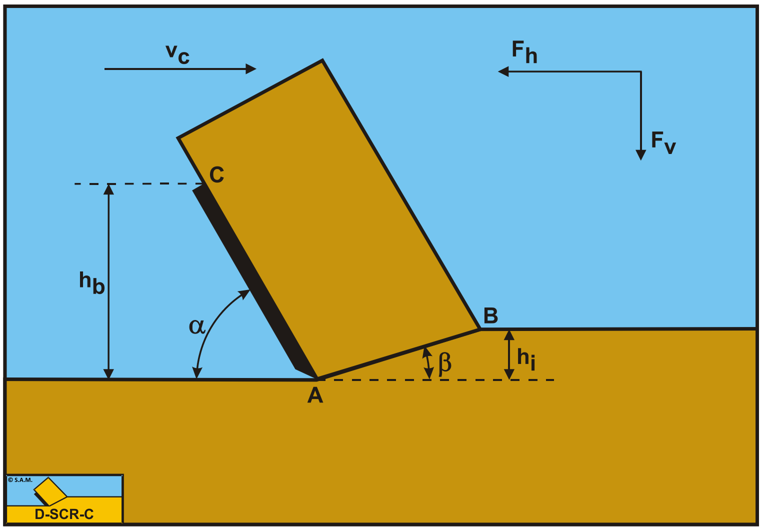

Figure 3-2: The cutting process, definitions.

Definitions:
1. **A**: The blade tip.
2. **B**: End of the shear plane.
3. **C**: The blade top.
4. **A-B**: The shear plane.
5. **A-C**: The blade surface.
6. $\mathbf{h_b}$: The height of the blade.
7. $\mathbf{h_i}$: The thickness of the layer cut.
8. $\mathbf{v_c}$: The cutting velocity.
9. $\boldsymbol{\alpha}$: The blade angle.

10. **β**: The shear angle.
11. **F_h**: The horizontal force, the arrow gives the positive direction.
12. **F_v**: The vertical force, the arrow gives the positive direction.

3.3. The Flow/ Shear/Crushed Type.

Figure 3-3 and Figure 3-4 show the **Flow Type** and the **Shear Type** of cutting process. The **Shear Type** is modeled as the **Flow Type**. The difference is that in dry soil the forces calculated for the **Flow Type** are constant forces because the process is ductile. For the **Shear Type** the forces are the peak forces, because the process is assumed to be brittle (shear). The average forces can be determined by multiplying the peak forces with a factor of ¼ to ½.

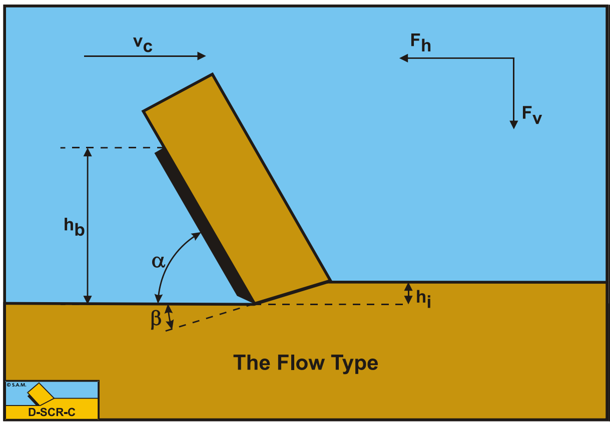

Figure 3-3: The Flow Type

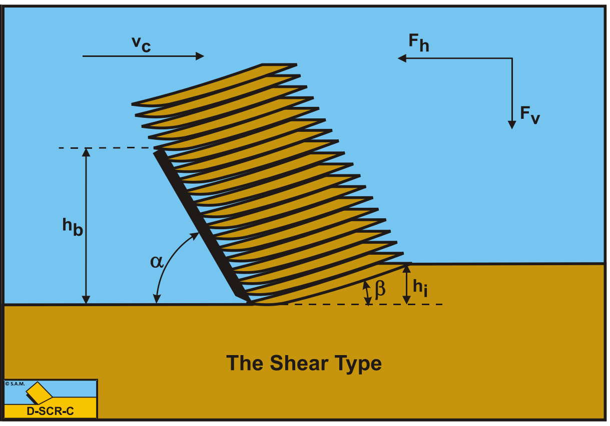

Figure 3-4: The Shear Type

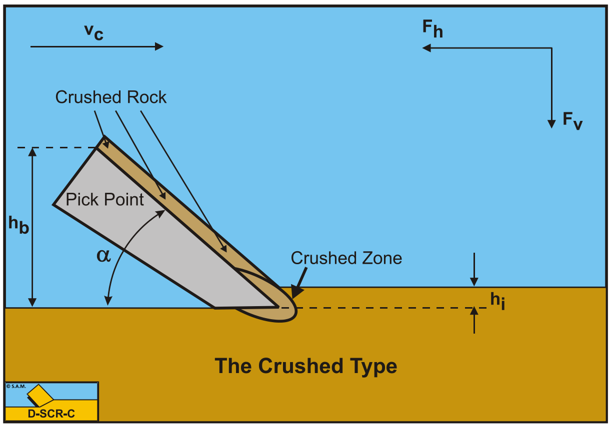

Figure 3-5: The Crushed Type.

3.3.1. The Equilibrium of Forces.

Figure 3-6 illustrates the forces on the layer of soil cut. The forces shown are valid in general. The forces acting on this layer are:

1. A normal force acting on the shear surface **N_1** resulting from the effective grain stresses.
2. A shear force **S_1** as a result of internal friction **$N_1 \cdot \tan(\phi)$**.
3. A force **W_1** as a result of water under pressure in the shear zone.
4. A shear force **C** as a result of pure cohesion τ_c. This force can be calculated by multiplying the cohesive shear strength τ_c with the area of the shear plane.
5. A gravity force **G** as a result of the (under water) weight of the layer cut.
6. An inertial force **I**, resulting from acceleration of the soil.
7. A force normal to the blade **N_2**, resulting from the effective grain stresses.
8. A shear force **S_2** as a result of the external friction angle **$N_2 \cdot \tan(\delta)$**.
9. A shear force **A** as a result of pure adhesion between the soil and the blade τ_a. This force can be calculated by multiplying the adhesive shear strength τ_a of the soil with the contact area between the soil and the blade.
10. A force **W_2** as a result of water under pressure on the blade

The normal force **N₁** and the shear force **S₁** can be combined to a resulting grain force **K₁**.

$$K_1 = \sqrt{N_1^2 + S_1^2} \tag{3-2}$$

The forces acting on a straight blade when cutting soil, can be distinguished as:

11. A force normal to the blade **N₂**, resulting from the effective grain stresses.
12. A shear force **S₂** as a result of the external friction angle **N₂·tan(δ)**.
13. A shear force **A** as a result of pure adhesion between the soil and the blade τ_a. This force can be calculated by multiplying the adhesive shear strength τ_a of the soil with the contact area between the soil and the blade.
14. A force **W₂** as a result of water under pressure on the blade.

These forces are shown in Figure 3-7. If the forces **N₂** and **S₂** are combined to a resulting force **K₂** and the adhesive force **A** and the water under pressures forces **W₁** and **W₂** are known, then the resulting force **K₂** is the unknown force on the blade. By taking the horizontal and vertical equilibrium of forces an expression for the force **K₂** on the blade can be derived.

$$K_2 = \sqrt{N_2^2 + S_2^2} \tag{3-3}$$

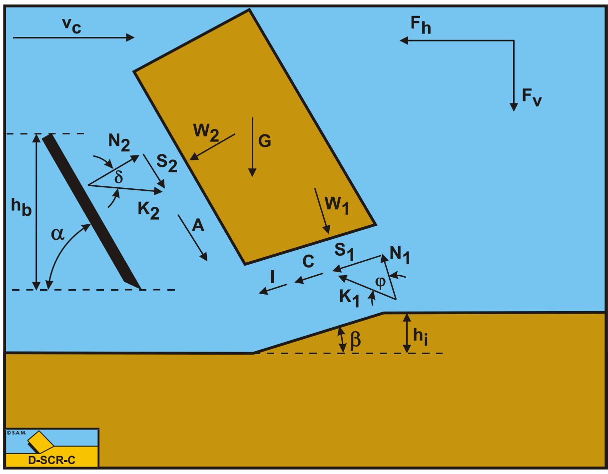

Figure 3-6: The forces on the layer cut.

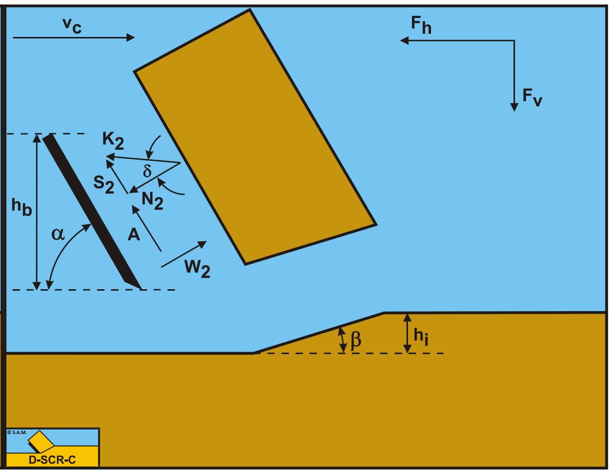

Figure 3-7: The forces on the blade.

The horizontal equilibrium of forces:

$$\begin{gathered}\sum F_h = K_1 \cdot \sin(\beta + \varphi) - W_1 \cdot \sin(\beta) + C \cdot \cos(\beta) + I \cdot \cos(\beta) \\ - A \cdot \cos(\alpha) + W_2 \cdot \sin(\alpha) - K_2 \cdot \sin(\alpha + \delta) = 0\end{gathered} \tag{3-4}$$

The vertical equilibrium of forces:

$$\begin{gathered}\sum F_v = - K_1 \cdot \cos(\beta + \varphi) + W_1 \cdot \cos(\beta) + C \cdot \sin(\beta) + I \cdot \sin(\beta) \\ + G + A \cdot \sin(\alpha) + W_2 \cdot \cos(\alpha) - K_2 \cdot \cos(\alpha + \delta) = 0\end{gathered} \tag{3-5}$$

The force **K₁** on the shear plane is now:

$$\begin{gathered}K_1 = \frac{W_2 \cdot \sin(\delta) + W_1 \cdot \sin(\alpha + \beta + \delta) + G \cdot \sin(\alpha + \delta)}{\sin(\alpha + \beta + \delta + \varphi)} \\ + \frac{- I \cdot \cos(\alpha + \beta + \delta) - C \cdot \cos(\alpha + \beta + \delta) + A \cdot \cos(\delta)}{\sin(\alpha + \beta + \delta + \varphi)}\end{gathered} \tag{3-6}$$

The force **K₂** on the blade is now:

$$K_2 = \frac{W_2 \cdot \sin(\alpha+\beta+\varphi) + W_1 \cdot \sin(\varphi) + G \cdot \sin(\beta+\varphi)}{\sin(\alpha+\beta+\delta+\varphi)} + \frac{+I \cdot \cos(\varphi) + C \cdot \cos(\varphi) - A \cdot \cos(\alpha+\beta+\varphi)}{\sin(\alpha+\beta+\delta+\varphi)} \tag{3-7}$$

From equation (3-7) the forces on the blade can be derived. On the blade a force component in the direction of cutting velocity F_h and a force perpendicular to this direction F_v can be distinguished.

$$F_h = -W_2 \cdot \sin(\alpha) + K_2 \cdot \sin(\alpha+\delta) + A \cdot \cos(\alpha) \tag{3-8}$$

$$F_v = -W_2 \cdot \cos(\alpha) + K_2 \cdot \cos(\alpha+\delta) - A \cdot \sin(\alpha) \tag{3-9}$$

The normal force on the shear plane is now:

$$N_1 = \frac{W_2 \cdot \sin(\delta) + W_1 \cdot \sin(\alpha+\beta+\delta) + G \cdot \sin(\alpha+\delta)}{\sin(\alpha+\beta+\delta+\varphi)} \cdot \cos(\varphi) + \frac{-I \cdot \cos(\alpha+\beta+\delta) - C \cdot \cos(\alpha+\beta+\delta) + A \cdot \cos(\delta)}{\sin(\alpha+\beta+\delta+\varphi)} \cdot \cos(\varphi) \tag{3-10}$$

The normal force on the blade is now:

$$N_2 = \frac{W_2 \cdot \sin(\alpha+\beta+\varphi) + W_1 \cdot \sin(\varphi) + G \cdot \sin(\beta+\varphi)}{\sin(\alpha+\beta+\delta+\varphi)} \cdot \cos(\delta) + \frac{+I \cdot \cos(\varphi) + C \cdot \cos(\varphi) - A \cdot \cos(\alpha+\beta+\varphi)}{\sin(\alpha+\beta+\delta+\varphi)} \cdot \cos(\delta) \tag{3-11}$$

If the equations (3-10) and (3-11) give a positive result, the normal forces are compressive forces. It can be seen from these equations that the normal forces can become negative, meaning that a tensile rupture might occur, depending on values for the adhesion and cohesion and the angles involved. The most critical direction where this might occur can be found from the Mohr circle.

3.3.2. The Individual Forces.

If there is no cavitation the water pressures forces **W₁** and **W₂** can be written as:

$$W_1 = \frac{p_{1m} \cdot \rho_w \cdot g \cdot v_c \cdot \varepsilon \cdot h_i^2 \cdot w}{\left(a_1 \cdot k_i + a_2 \cdot k_{max}\right) \cdot \sin(\beta)} = \frac{p_{1m} \cdot \rho_w \cdot g \cdot v_c \cdot \varepsilon \cdot h_i^2 \cdot w}{k_m \cdot \sin(\beta)} \tag{3-12}$$

$$W_2 = \frac{p_{2m} \cdot \rho_w \cdot g \cdot v_c \cdot \varepsilon \cdot h_i \cdot w}{\left(a_1 \cdot k_i + a_2 \cdot k_{max}\right) \cdot \sin(\alpha)} = \frac{p_{2m} \cdot \rho_w \cdot g \cdot v_c \cdot \varepsilon \cdot h_i \cdot w}{k_m \cdot \sin(\alpha)} \tag{3-13}$$

In case of cavitation **W₁** and **W₂** become:

$$W_1 = \frac{\rho_w \cdot g \cdot (z+10) \cdot h_i \cdot w}{\sin(\beta)} \tag{3-14}$$

$$W_2 = \frac{\rho_w \cdot g \cdot (z+10) \cdot h_b \cdot w}{\sin(\alpha)} \tag{3-15}$$

Wismer and Luth (1972A) and (1972B) investigated the inertia forces term **I** of the total cutting forces. The following equation is derived:

$$\mathrm{I} = \rho_s \cdot v_c^2 \cdot \frac{\sin(\alpha)}{\sin(\alpha+\beta)} \cdot h_i \cdot w \tag{3-16}$$

The cohesive and the adhesive forces **C** and **A** can be determined with soil mechanical experiments. For the cohesive and adhesive forces the following equations are valid:

$$\mathrm{C} = \frac{c \cdot h_i \cdot w}{\sin(\beta)} \tag{3-17}$$

$$\mathrm{A} = \frac{a \cdot h_b \cdot w}{\sin(\alpha)} \tag{3-18}$$

The gravitational force **G** (weight submerged) follows from:

$$\mathrm{G} = \left(\rho_s - \rho_w\right) \cdot g \cdot h_i \cdot w \cdot \frac{\sin(\alpha+\beta)}{\sin(\beta)} \cdot \left\{ \frac{\left(h_b + h_i \cdot \sin(\alpha)\right)}{\sin(\alpha)} + \frac{h_i \cdot \cos(\alpha+\beta)}{2 \cdot \sin(\beta)} \right\} \tag{3-19}$$

The gravitational force **G** (dry weight) follows from:

$$\mathrm{G} = \rho_s \cdot g \cdot h_i \cdot w \cdot \frac{\sin(\alpha+\beta)}{\sin(\beta)} \cdot \left\{ \frac{\left(h_b + h_i \cdot \sin(\alpha)\right)}{\sin(\alpha)} + \frac{h_i \cdot \cos(\alpha+\beta)}{2 \cdot \sin(\beta)} \right\} \tag{3-20}$$

This is in accordance with the area that is used for the water pore pressure calculations in the case of water saturated sand (see Figure 6-7).

3.4. The Curling Type.

In some soils it is possible that the **Curling Type** of cutting mechanism occurs. This will happen when the layer cut is relatively thin and there is a force on the blade of which the magnitude depends on the blade height, like the adhesive force or the pore pressure force in the case of a cavitating cutting process. In soils like clay and loam, but also in rock under hyperbaric conditions this may occur. Figure 3-8 shows this **Curling Type**. The question now is, what is the effective blade height $\mathbf{h_{b,m}}$ where the soil is in contact with the blade. To solve this problem, an additional equation is required. There is only one equation available and that is the equilibrium equation of moments on the layer cut. Figure 3-9 shows the moments acting on the layer cut. In the case of clay, loam or hyperbaric rock, the contribution of gravity can be neglected.

The equilibrium of moments when the gravity moment is neglected is:

$$(N_1 - W_1) \cdot R_1 = (N_2 - W_2) \cdot R_2 \tag{3-21}$$

The arms of the 2 moments are:

$$R_1 = \frac{\lambda_1 \cdot h_i}{\sin(\beta)}, \quad R_2 = \frac{\lambda_2 \cdot h_{b,m}}{\sin(\alpha)} \tag{3-22}$$

This gives the equilibrium equation of moments on the layer cut:

$$\left(\begin{array}{l}\dfrac{W_2\cdot\sin(\delta)+W_1\cdot\sin(\alpha+\beta+\delta)}{\sin(\alpha+\beta+\delta+\varphi)}\cdot\cos(\varphi)\\[2ex] +\dfrac{-C\cdot\cos(\alpha+\beta+\delta)+A\cdot\cos(\delta)}{\sin(\alpha+\beta+\delta+\varphi)}\cdot\cos(\varphi)\\[2ex] -W_1\end{array}\right)\cdot\frac{\lambda_1\cdot h_i}{\sin(\beta)}=\left(\begin{array}{l}\dfrac{W_2\cdot\sin(\alpha+\beta+\varphi)+W_1\cdot\sin(\varphi)}{\sin(\alpha+\beta+\delta+\varphi)}\cdot\cos(\delta)\\[2ex] +\dfrac{+C\cdot\cos(\varphi)-A\cdot\cos(\alpha+\beta+\varphi)}{\sin(\alpha+\beta+\delta+\varphi)}\cdot\cos(\delta)\\[2ex] -W_2\end{array}\right)\cdot\frac{\lambda_2\cdot h_{b,m}}{\sin(\alpha)}$$

(3-23)

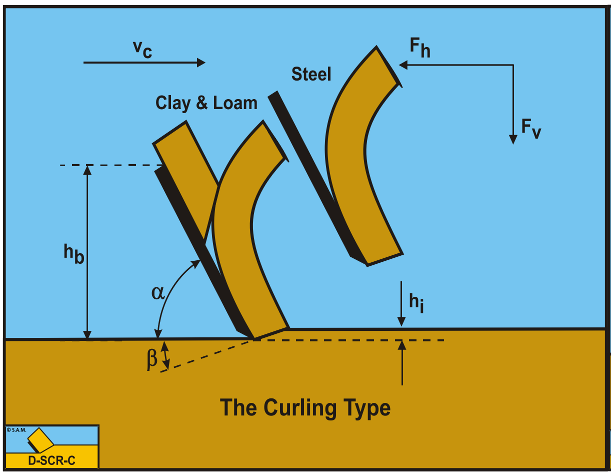

Figure 3-8: The Curling Type of cutting mechanism.

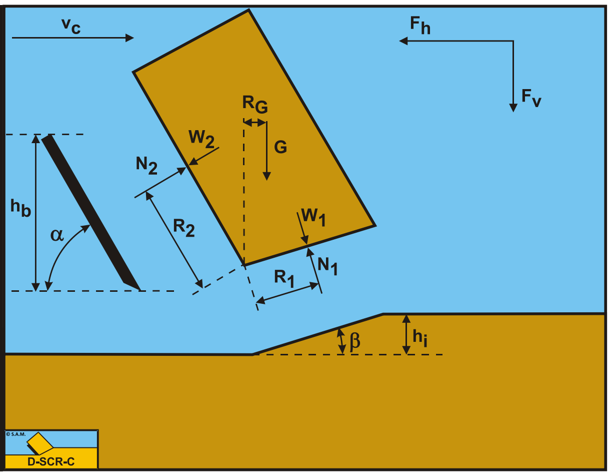

Figure 3-9: The general equilibrium of moments.

When the equations for **W**$_1$, **W**$_2$, **C** and **A** as mentioned before are substituted, the resulting equation is a second degree equation with **h**$_{b,m}$ as the variable.
This can be solved using the following set of equations:

$$A\cdot x^2+B\cdot x+C=0 \quad \text{and} \quad h_{b,m}=x=\frac{-B\pm\sqrt{B^2-4\cdot A\cdot C}}{2\cdot A}$$

$$A=\frac{\lambda_2\cdot p_{2m}\cdot\sin(\alpha+\beta+\delta+\varphi)-\lambda_2\cdot p_{2m}\cdot\sin(\alpha+\beta+\varphi)\cdot\cos(\delta)}{\sin(\alpha)\cdot\sin(\alpha)}$$
$$+\frac{+a\cdot\lambda_2\cdot\cos(\alpha+\beta+\varphi)\cdot\cos(\delta)}{\sin(\alpha)\cdot\sin(\alpha)}$$

$$B=\frac{\lambda_1\cdot p_{2m}\cdot\sin(\delta)\cdot\cos(\varphi)-\lambda_2\cdot p_{1m}\cdot\cos(\delta)\cdot\sin(\varphi)}{\sin(\alpha)\cdot\sin(\beta)}\cdot h_i$$
$$+\frac{-c\cdot\lambda_2\cdot\cos(\delta)\cdot\cos(\varphi)+a\cdot\lambda_1\cdot\cos(\varphi)\cdot\cos(\delta)}{\sin(\alpha)\cdot\sin(\beta)}\cdot h_i$$

(3-24)

$$C=\frac{\lambda_1\cdot p_{1m}\cdot\sin(\alpha+\beta+\delta)\cdot\cos(\varphi)-\lambda_1\cdot p_{1m}\cdot\sin(\alpha+\beta+\delta+\varphi)}{\sin(\beta)\cdot\sin(\beta)}\cdot h_i\cdot h_i$$
$$+\frac{-c\cdot\lambda_1\cdot\cos(\alpha+\beta+\delta)\cdot\cos(\varphi)}{\sin(\beta)\cdot\sin(\beta)}\cdot h_i\cdot h_i$$

The usage is now as follows:

$$\text{if } h_{b,m} < h_b \text{ then use } h_{b,m}$$
$$\text{if } h_{b,m} \geq h_b \text{ then use } h_b \tag{3-25}$$

3.5. The Tear Type and Chip Type.

The **Tear Type** of cutting process has a failure mechanism based on tensile failure. For such a failure mechanism to occur it is required that negative stresses may occur. In sand this is not the case, because in sand the failure lines according to the Mohr-Coulomb criterion will pass through the origin as is shown in Figure 2-46 and Figure 2-47. For the failure lines not to pass through the origin it is required that the soil has a certain cohesion or shear strength like with clay and rock. In clay and rock, normally, the inertial forces and the gravity can be neglected and also the water pore pressures do not play a role. Only with hyperbaric rock cutting the water pore pressures will play a role, but there the **Tear Type** will not occur. This implies that for the **Tear Type** and **Chip Type** a soil with cohesion and adhesion and internal and external friction will be considered.

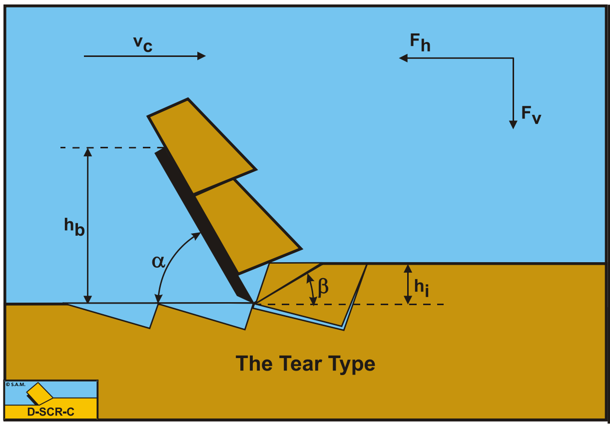

Figure 3-10: The Tear Type cutting mechanism in clay.

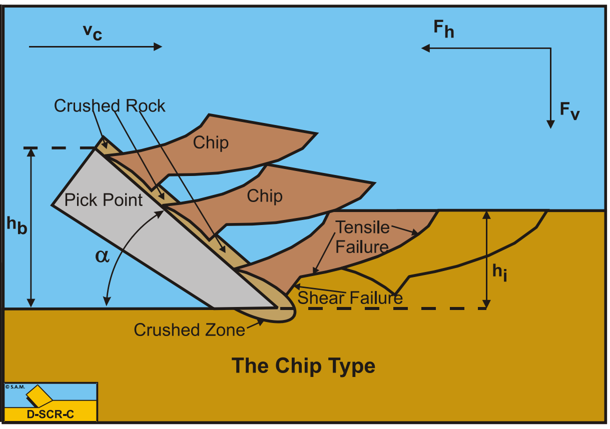

Figure 3-11: The Chip Type cutting mechanism in rock.

If clay or rock is considered, the following condition can be derived with respect to tensile rupture:

With the relations for the cohesive force **C**, the adhesive force **A** and the adhesion/cohesion ratio **r** (the ac ratio **r**):

$$C = \frac{\lambda_s \cdot c \cdot h_i \cdot w}{\sin(\beta)} \tag{3-26}$$

$$A = \frac{\lambda_s \cdot a \cdot h_b \cdot w}{\sin(\alpha)} \tag{3-27}$$

$$r = \frac{a \cdot h_b}{c \cdot h_i} \tag{3-28}$$

The horizontal $\mathbf{F_h}$ and vertical $\mathbf{F_v}$ cutting forces can be determined according to:

$$F_h = \lambda_s \cdot c \cdot h_i \cdot w \cdot \frac{\frac{\sin(\alpha+\delta)}{\sin(\beta)} \cdot \cos(\varphi) + r \cdot \frac{\sin(\beta+\varphi)}{\sin(\alpha)} \cdot \cos(\delta)}{\sin(\alpha+\beta+\delta+\varphi)} \tag{3-29}$$

$$F_v = \lambda_s \cdot c \cdot h_i \cdot w \cdot \frac{\frac{\cos(\alpha+\delta)}{\sin(\beta)} \cdot \cos(\varphi) - r \cdot \frac{\cos(\beta+\varphi)}{\sin(\alpha)} \cdot \cos(\delta)}{\sin(\alpha+\beta+\delta+\varphi)} \tag{3-30}$$

The shear angle β is determined in the case where the horizontal cutting force F_h is at a minimum, based on the minimum energy principle.

$$\frac{\partial F_h}{\partial \beta}=\frac{r\cdot\cos(\delta)\cdot\sin(2\cdot\beta+\varphi)\cdot\sin(\alpha)\cdot\sin(\beta)\cdot\sin(\alpha+\beta+\delta+\varphi)}{\sin^2(\alpha+\beta+\delta+\varphi)\cdot\sin^2(\alpha)\cdot\sin^2(\beta)}$$

$$+\frac{-\sin(\alpha)\cdot\sin(\alpha+2\cdot\beta+\delta+\varphi)\cdot\left(\sin(\alpha)\cdot\sin(\alpha+\delta)\cdot\cos(\varphi)\right)}{\sin^2(\alpha+\beta+\delta+\varphi)\cdot\sin^2(\alpha)\cdot\sin^2(\beta)} \tag{3-31}$$

$$+\frac{-\sin(\alpha)\cdot\sin(\alpha+2\cdot\beta+\delta+\varphi)\cdot\left(r\cdot\sin(\beta)\cdot\sin(\beta+\varphi)\cdot\cos(\delta)\right)}{\sin^2(\alpha+\beta+\delta+\varphi)\cdot\sin^2(\alpha)\cdot\sin^2(\beta)}=0$$

In the special case where there is no adhesion, $r=0$, the shear angle is:

$$\frac{\partial F_h}{\partial \beta}=\frac{-\sin(\alpha+2\cdot\beta+\delta+\varphi)\cdot\sin(\alpha+\delta)\cdot\cos(\varphi)}{\sin^2(\alpha+\beta+\delta+\varphi)\cdot\sin^2(\beta)}=0 \tag{3-32}$$

So:

$$\sin(\alpha+2\cdot\beta+\delta+\varphi)=0 \text{ for } \alpha+2\cdot\beta+\delta+\varphi=\pi \text{ giving } \beta=\frac{\pi}{2}-\frac{\alpha+\delta+\varphi}{2} \tag{3-33}$$

The cohesion **c** can be determined from the UCS value and the angle of internal friction **φ** according to (as is shown in Figure 3-12):

$$c=\frac{UCS}{2}\cdot\left(\frac{1-\sin(\varphi)}{\cos(\varphi)}\right) \tag{3-34}$$

According to the Mohr-Coulomb failure criterion, the following is valid for the shear stress on the shear plane, as is shown in Figure 3-13.

$$\tau_{S1}=c+\sigma_{N1}\cdot\tan(\varphi) \tag{3-35}$$

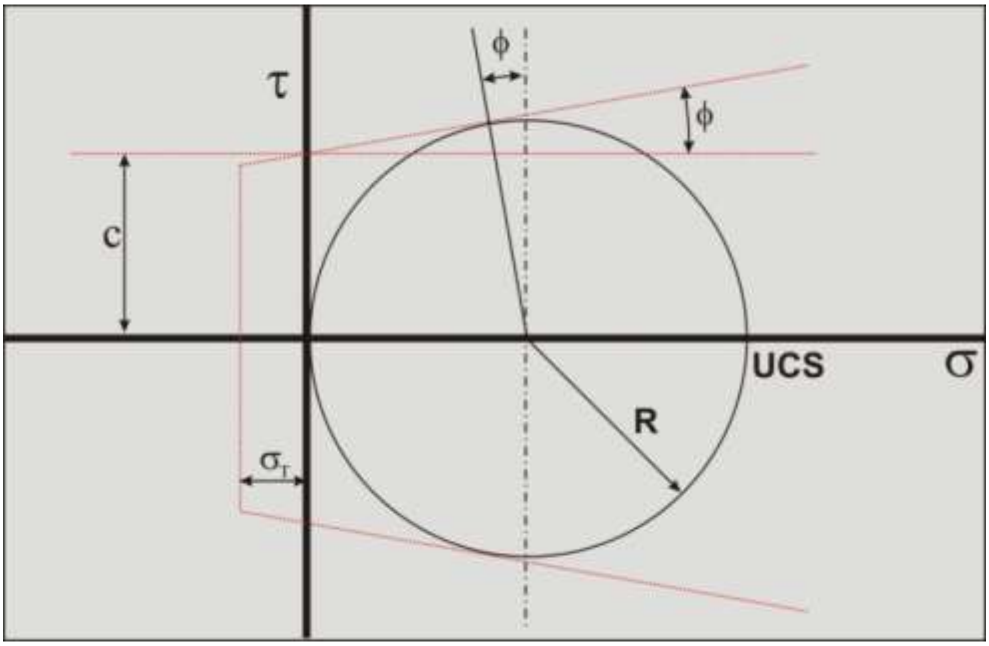

Figure 3-12: The Mohr circle for UCS and cohesion.

The average stress condition on the shear plane is now σ_{N1}, τ_{S1} as is show in Figure 3-13. A Mohr circle (Mohr circle 1) can be drawn through this point, resulting in a minimum stress σ_{min} which is negative, so tensile. If this minimum normal stress is smaller than the tensile strength σ_T tensile fracture will occur, as is the case in the figure. Now Mohr circle 1 can never exist, but a smaller circle (Mohr circle 2) can, just touching the tensile strength σ_T. The question is now, how to get from Mohr circle 1 to Mohr circle 2. To find Mohr circle 2 the following steps have to be taken.

The radius **R** of the Mohr circle 1 can be found from the shear stress τ_{S1} by:

$$\mathbf{R}=\frac{\tau_{S1}}{\cos(\varphi)} \tag{3-36}$$

The center of the Mohr circle 1, σ_C, now follows from:

$$\begin{aligned}\sigma_C&=\sigma_{N1}+\mathbf{R}\cdot\sin(\varphi)=\sigma_{N1}+\tau_{S1}\cdot\tan(\varphi)\\&=\sigma_{N1}+c\cdot\tan(\varphi)+\sigma_{N1}\cdot\tan^2(\varphi)\end{aligned} \tag{3-37}$$

The normal force **N₁** on the shear plane is now:

$$\begin{aligned}N_1&=\frac{-C\cdot\cos(\alpha+\beta+\delta)+A\cdot\cos(\delta)}{\sin(\alpha+\beta+\delta+\varphi)}\cdot\cos(\varphi)\\&=\lambda_s\cdot c\cdot h_i\cdot w\cdot\frac{-\dfrac{\cos(\alpha+\beta+\delta)}{\sin(\beta)}+r\cdot\dfrac{\cos(\delta)}{\sin(\alpha)}}{\sin(\alpha+\beta+\delta+\varphi)}\cdot\cos(\varphi)\end{aligned} \tag{3-38}$$

The normal stress σ_{N1} on the shear plane is:

$$\begin{aligned}\sigma_{N1}&=\frac{N_1\cdot\sin(\beta)}{h_i\cdot w}\\&=\lambda_s\cdot c\cdot\frac{-\dfrac{\sin(\beta)\cdot\cos(\alpha+\beta+\delta)}{\sin(\beta)}+r\cdot\dfrac{\sin(\beta)\cdot\cos(\delta)}{\sin(\alpha)}}{\sin(\alpha+\beta+\delta+\varphi)}\cdot\cos(\varphi)\end{aligned} \tag{3-39}$$

The minimum principal stress σ_{min} equals the normal stress in the center of the Mohr circle σ_C minus the radius of the Mohr circle **R**:

$$\sigma_{min}=\sigma_C-\mathbf{R}=\sigma_{N1}+c\cdot\tan(\varphi)+\sigma_{N1}\cdot\tan^2(\varphi)-\frac{c}{\cos(\varphi)}-\frac{\sigma_{N1}\cdot\tan(\varphi)}{\cos(\varphi)} \tag{3-40}$$

Rearranging this gives:

$$\sigma_{min}=\sigma_{N1}\cdot\left(1+\tan^2(\varphi)-\frac{\tan(\varphi)}{\cos(\varphi)}\right)+c\cdot\left(\tan(\varphi)-\frac{1}{\cos(\varphi)}\right) \tag{3-41}$$

$$\sigma_{min} = \frac{\sigma_{N1}}{\cos(\varphi)} \cdot \left(\frac{\cos^2(\varphi) + \sin^2(\varphi) - \sin(\varphi)}{\cos(\varphi)} \right) - c \cdot \left(\frac{1 - \sin(\varphi)}{\cos(\varphi)} \right)$$

$$= \left(\frac{\sigma_{N1}}{\cos(\varphi)} - c \right) \cdot \left(\frac{1 - \sin(\varphi)}{\cos(\varphi)} \right) \qquad \textbf{(3-42)}$$

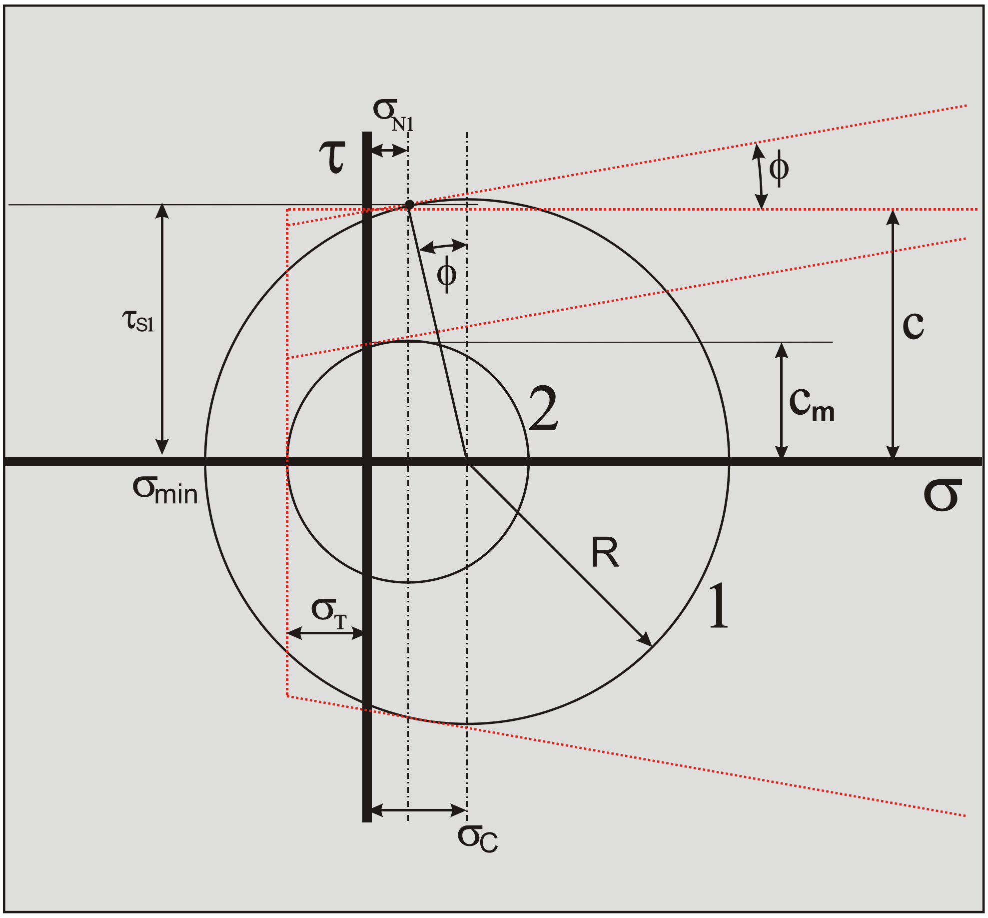

Figure 3-13: The Mohr circles of the Tear Type.

Now ductile failure will occur if the minimum principal stress $\boldsymbol{\sigma_{min}}$ is bigger than then tensile strength $\boldsymbol{\sigma_T}$, thus:

$$\sigma_{min} > \sigma_T \qquad \textbf{(3-43)}$$

If equation (3-43) is true, ductile failure will occur. Keep in mind however, that the tensile strength $\boldsymbol{\sigma_T}$ is a negative number. Of course if the minimum normal stress σ_{min} is positive, brittle tensile failure can never occur. Substituting equation (3-39) for the normal stress on the shear plane gives the following condition for the **Tear Type**:

$$c \cdot \left(\frac{r \cdot \dfrac{\sin(\beta) \cdot \cos(\delta)}{\sin(\alpha)} - \cos(\alpha + \beta + \delta) - \sin(\alpha + \beta + \delta + \varphi)}{\sin(\alpha + \beta + \delta + \varphi)} \right) \cdot \left(\frac{1 - \sin(\varphi)}{\cos(\varphi)} \right) > \sigma_T \qquad \textbf{(3-44)}$$

In clay it is assumed that the internal and external friction angles are zero, while in rock it is assumed that the adhesion is zero. This will be explained in detail in the chapters on clay and rock cutting.
The ratios between the pore pressures and the cohesive shear strength, in the case of hyperbaric rock cutting, can be found according to:

$$r = \frac{a \cdot h_b}{c \cdot h_i},\ r_1 = \frac{p_{1m} \cdot h_i}{c \cdot h_i} \ \text{or}\ r_1 = \frac{\rho_w \cdot g \cdot (z+10) \cdot h_i}{c \cdot h_i},$$

$$r_2 = \frac{p_{2m} \cdot h_b}{c \cdot h_i} \ \text{or}\ r_2 = \frac{\rho_w \cdot g \cdot (z+10) \cdot h_b}{c \cdot h_i} \tag{3-45}$$

Equation (3-46) can be derived for the occurrence of tensile failure under hyperbaric conditions. Under hyperbaric conditions equation (3-46) will almost always be true, because of the terms with **r₁** and **r₂** which may become very big (positive). So tensile failure will not be considered for hyperbaric conditions.

$$c \cdot \left(\frac{r \cdot \frac{\sin(\beta) \cdot \cos(\delta)}{\sin(\alpha)} + r_2 \cdot \frac{\sin(\beta) \cdot \sin(\delta)}{\sin(\alpha)} + r_1 \cdot \sin(\alpha+\beta+\delta)}{\sin(\alpha+\beta+\delta+\varphi)} + \frac{-\cos(\alpha+\beta+\delta) - \sin(\alpha+\beta+\delta+\varphi)}{\sin(\alpha+\beta+\delta+\varphi)} \right) \cdot \left(\frac{1-\sin(\varphi)}{\cos(\varphi)} \right) > \sigma_T \tag{3-46}$$

Analyzing equations (3-44) and (3-46) gives the following conclusions:

1. The first term of equations (3-44) and (3-46) is always positive.
2. If the sum of **$\alpha+\beta+\delta>\pi/2$**, in the second term of equation (3-44) and the fourth term of equation (3-46), these terms are positive, which will be the case for normal cutting angles.
3. The second and third terms of equation (3-46) are always positive.
4. The last term in equations (3-44) and (3-46) is always negative.
5. Equation (3-44) may become negative and fulfill the condition for the **Tear Type**.
6. Equation (3-46) will never become negative under normal conditions, so under hyperbaric conditions the **Tear Type** will never occur.
7. The **Tear Type** may occur with clay and rock under atmospheric conditions.

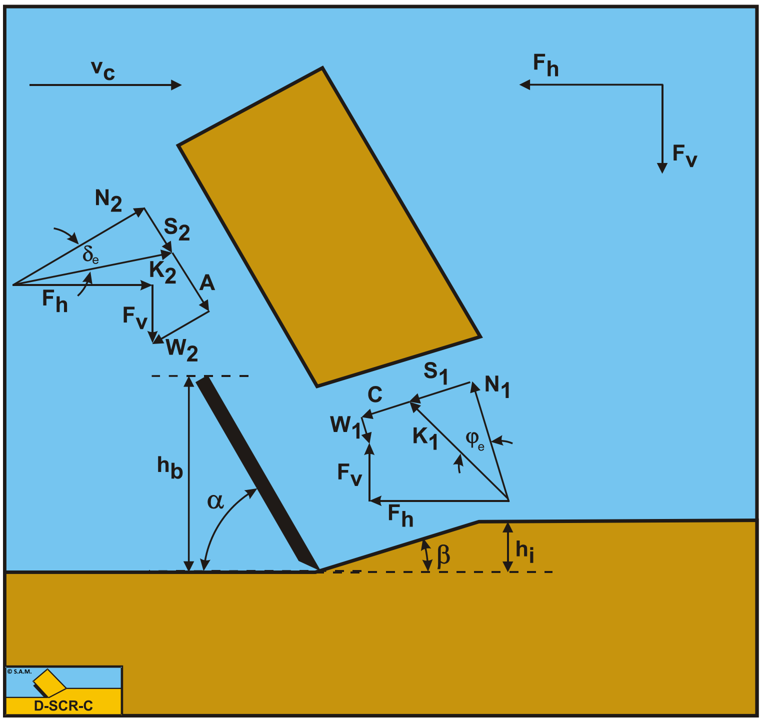

Figure 3-14: The forces on the layer cut.

3.6. The Snow Plough Effect.

3.6.1. The Normal and Friction Forces on the Shear Surface and Blade.

On a cutter head, the blades can be divided into small elements, at which a two dimensional cutting process is considered. However, this is correct only when the cutting edge of this element is perpendicular to the direction of the velocity of the element. For most elements this will not be the case. The cutting edge and the absolute velocity of the cutting edge will not be perpendicular. This means the elements can be considered to be deviated with respect to the direction of the cutting velocity. A component of the cutting velocity perpendicular to the cutting edge and a component parallel to the cutting edge can be distinguished. This second component results in a deviation force on the blade element, due to the friction between the soil and the blade. This force is also the cause of the transverse movement of the soil, the snow plough effect.

To predict the deviation force and the direction of motion of the soil on the blade, the equilibrium equations of force will have to be solved in three directions. Since there are four unknowns, three forces and the direction of the velocity of the soil on the blade, one additional equation is required. This equation follows from an equilibrium equation of velocity between the velocity of grains in the shear zone and the velocity of grains on the blade. Since the four equations are partly non-linear and implicit, they have to be solved iteratively. The results of solving these equations have been compared with the results of laboratory tests on sand. The correlation between the two was very satisfactory, with respect to the magnitude of the forces and with respect to the direction of the forces and the flow of the soil on the blade.

Although the normal and friction forces as shown in Figure 3-14 are the basis for the calculation of the horizontal and vertical cutting forces, the approach used, requires the following equations to derive these forces by using equations (3-8) and (3-9). The index 1 points to the shear surface, while the index 2 points to the blade.

$$\mathbf{F_{n1} = F_h \cdot \sin(\beta) - F_v \cdot \cos(\beta)} \tag{3-47}$$

$$\mathbf{F_{f1} = F_h \cdot \cos(\beta) + F_v \cdot \sin(\beta)} \tag{3-48}$$

$$\mathbf{F_{n2} = F_h \cdot \sin(\alpha) + F_v \cdot \cos(\alpha)} \tag{3-49}$$

$$\mathbf{F_{f2} = F_h \cdot \cos(\alpha) - F_v \cdot \sin(\alpha)} \tag{3-50}$$

3.6.2. The 3D Cutting Theory.

The previous paragraphs summarized the two-dimensional cutting theory. However, as stated in the introduction, in most cases the cutting process is not two-dimensional, because the drag velocity is not perpendicular to the cutting edge of the blade. Figure 3-16 shows this phenomenon. As with snow-ploughs, the soil will flow to one side while the blade is pushed to the opposite side. This will result in a third cutting force, the deviation force $\mathbf{F_d}$. To determine this force, the flow direction of the soil has to be known. Figure 3-17 shows a possible flow direction.

3.6.3. Velocity Conditions.

For the velocity component perpendicular to the blade $\mathbf{v_c}$, if the blade has a deviation angle $\boldsymbol{\iota}$ and a drag velocity $\mathbf{v_d}$ according to Figure 3-17, it yields:

$$\mathbf{v_c = v_d \cdot \cos(\iota)} \tag{3-51}$$

The velocity of grains in the shear surface perpendicular to the cutting edge $\mathbf{v_{r1}}$ is now:

$$\mathbf{v_{r1} = v_c \cdot \frac{\sin(\alpha)}{\sin(\alpha+\beta)}} \tag{3-52}$$

The relative velocity of grains with respect to the blade $\mathbf{v_{r2}}$, perpendicular to the cutting edge is:

$$v_{r2} = v_c \cdot \frac{\sin(\beta)}{\sin(\alpha+\beta)} \qquad (3\text{-}53)$$

The grains will not only have a velocity perpendicular to the cutting edge, but also parallel to the cutting edge, the deviation velocity components $\mathbf{v_{d1}}$ on the shear surface and $\mathbf{v_{d2}}$ on the blade.

Figure 3-15: Urban winter service vehicle with snowplow (commons.wikimedia.org).

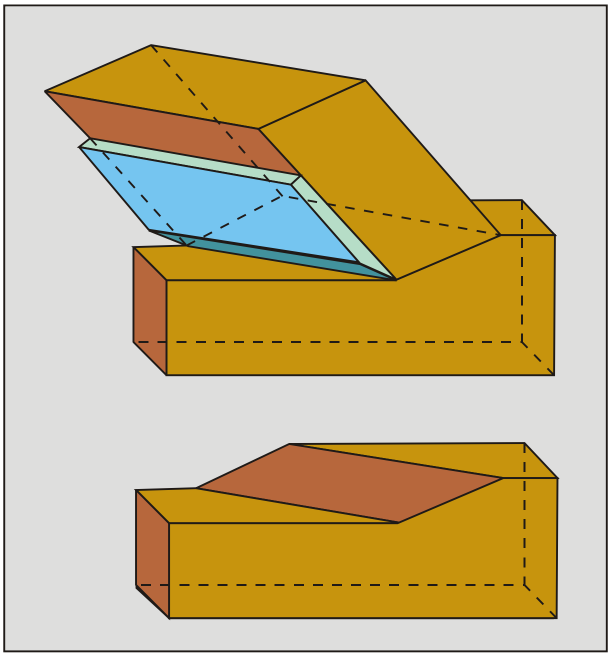

Figure 3-16: The 3D cutting process.

The velocity components of a grain in **x**, **y** and **z** direction can be determined by considering the absolute velocity of grains in the shear surface, this leads to:

$$\vec{v}_{r2} + \vec{v}_{d2} + \vec{v}_{d} = \vec{v}_{r1} + \vec{v}_{d1} \qquad \textbf{(3-54)}$$

$$v_{x1} = v_{r1} \cdot \cos(\beta) \cdot \cos(\iota) + v_{d1} \cdot \sin(\iota) \qquad \textbf{(3-55)}$$

$$v_{y1} = v_{r1} \cdot \cos(\beta) \cdot \sin(\iota) - v_{d1} \cdot \cos(\iota) \qquad \textbf{(3-56)}$$

$$v_{z1} = v_{r1} \cdot \sin(\beta) \qquad \textbf{(3-57)}$$

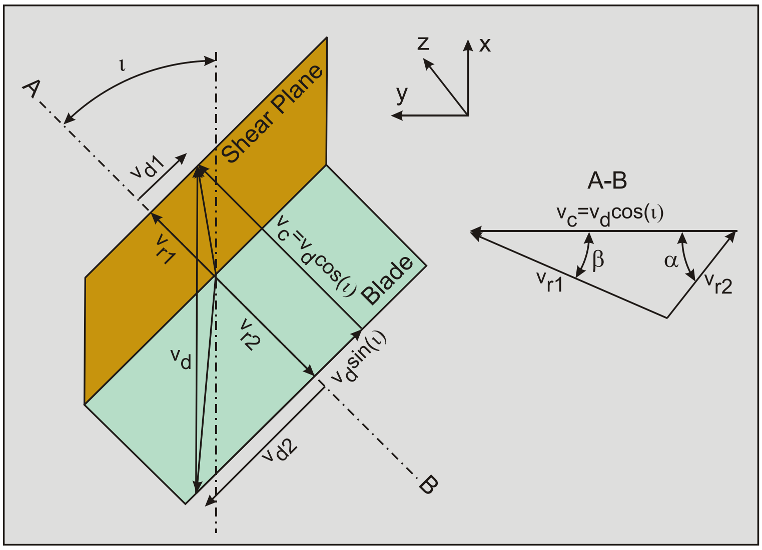

Figure 3-17: Velocity conditions.

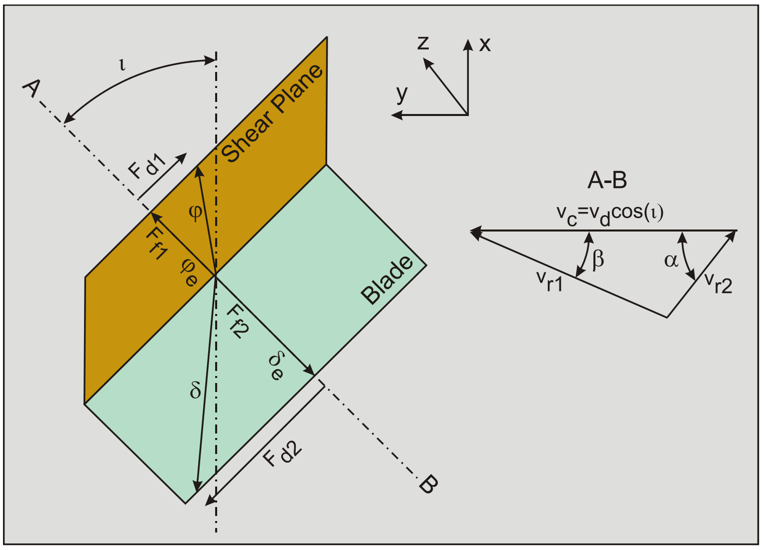

Figure 3-18: Force directions.

The velocity components of a grain can also be determined by a summation of the drag velocity of the blade and the relative velocity between the grains and the blade, this gives:

$$v_{x2} = v_{d} - v_{r2} \cdot \cos(\alpha) \cdot \cos(\iota) - v_{d2} \cdot \sin(\iota) \qquad \textbf{(3-58)}$$

$$v_{y2} = -v_{r2} \cdot \cos(\alpha) \cdot \sin(\iota) + v_{d2} \cdot \cos(\iota) \qquad \textbf{(3-59)}$$

$$v_{z2} = v_{r2} \cdot \sin(\alpha) \tag{3-60}$$

Since both approaches will have to give the same resulting velocity components, the following condition for the transverse velocity components can be derived:

$$v_{x1} = v_{x2} \implies v_{d1} + v_{d2} = v_d \cdot \sin(\iota) \tag{3-61}$$

$$v_{y1} = v_{y2} \implies v_{d1} + v_{d2} = v_d \cdot \sin(\iota) \tag{3-62}$$

$$v_{z1} = v_{z2} \tag{3-63}$$

3.6.4. The Deviation Force.

Since a friction force always has a direction matching the direction of the relative velocity between two bodies, the fact that a deviation velocity exists on the shear surface and on the blade, implies that also deviation forces must exist. To match the direction of the relative velocities, the following equations can be derived for the deviation force on the shear surface and on the blade (Figure 3-18):

$$F_{d1} = F_{f1} \cdot \frac{v_{d1}}{v_{r1}} \tag{3-64}$$

$$F_{d2} = F_{f2} \cdot \frac{v_{d2}}{v_{r2}} \tag{3-65}$$

Since perpendicular to the cutting edge, an equilibrium of forces exists, the two deviation forces must be equal in magnitude and have opposite directions.

$$F_{d1} = \left| F_{d2} \right| \tag{3-66}$$

By substituting equations (3-64) and (3-65) in equation (3-66) and then substituting equations (3-48) and (3-50) for the friction forces and equations (3-52) and (3-53) for the relative velocities, the following equation can be derived, giving a second relation between the two deviation velocities:

$$\lambda = \frac{v_{d1}}{v_{d2}} = \left(\frac{F_{f2}}{F_{f1}} \right) \cdot \left(\frac{v_{r1}}{v_{r2}} \right) = \left(\frac{F_h \cdot \cos(\alpha) - F_v \cdot \sin(\alpha)}{F_h \cdot \cos(\beta) + F_v \cdot \sin(\beta)} \right) \cdot \left(\frac{\sin(\alpha)}{\sin(\beta)} \right) \tag{3-67}$$

To determine $\mathbf{F_h}$ and $\mathbf{F_v}$ perpendicular to the cutting edge, the angle of internal friction $\boldsymbol{\varphi_e}$ and the external friction angle $\boldsymbol{\delta_e}$ mobilized perpendicular to the cutting edge, have to be determined by using the ratio of the transverse velocity and the relative velocity, according to:

$$\tan(\varphi_e) = \tan(\varphi) \cdot \cos\left(\operatorname{atn}\left(\frac{v_{d1}}{v_{r1}} \right) \right) \tag{3-68}$$

$$\tan(\delta_e) = \tan(\delta) \cdot \cos\left(\operatorname{atn}\left(\frac{v_{d2}}{v_{r2}} \right) \right) \tag{3-69}$$

For the cohesion **c** and the adhesion **a** this gives:

$$c_e = c \cdot \cos\left(\operatorname{atn}\left(\frac{v_{d1}}{v_{r1}} \right) \right) \tag{3-70}$$

$$a_e = a \cdot \cos\left(\operatorname{atn}\left(\frac{v_{d2}}{v_{r2}} \right) \right) \tag{3-71}$$

3.6.5. The Resulting Cutting Forces.

The resulting cutting forces in **x**, **y** and **z** direction can be determined once the deviation velocity components are known. However, it can be seen that the second velocity condition equation (3-67) requires the horizontal and vertical cutting forces perpendicular to the cutting edge, while these forces can only be determined if the mobilized internal and external friction angles and the mobilized cohesion and adhesion (equations (3-68), (3-69), (3-70) and (3-71)) are known. This creates an implicit set of equations that will have to be solved by means of an iteration process. For the cutting forces on the blade the following equation can be derived:

$$F_{x2} = F_h \cdot \cos(\iota) + F_{d2} \cdot \sin(\iota) \tag{3-72}$$

$$F_{y2} = F_h \cdot \sin(\iota) - F_{d2} \cdot \cos(\iota) \tag{3-73}$$

$$F_{z2} = F_v \tag{3-74}$$

The problem of the model being implicit can be solved in the following way:

A new variable **λ** is introduced in such a way that:

$$v_{d1} = \frac{\lambda}{1+\lambda} \cdot v_d \cdot \sin(\iota) \tag{3-75}$$

$$v_{d2} = \frac{1}{1+\lambda} \cdot v_d \cdot \sin(\iota) \tag{3-76}$$

This satisfies the condition from equations (3-61) and (3-62) for the sum of these 2 velocities:

$$v_{d1} + v_{d2} = v_d \cdot \sin(\iota) \tag{3-77}$$

The procedure starts with a starting value for **λ=1**. Based on the velocities found with equations (3-75), (3-76), (3-52) and (3-53), the mobilized internal φ_e and external δ_e friction angles and the cohesion c_e and adhesion a_e can be determined using the equations (3-68), (3-69), (3-70) and (3-71). Once these are known, the horizontal F_h and vertical F_v cutting forces in the plane perpendicular to the cutting edge can be determined with equations (3-8) and (3-9). With the equations (3-48), (3-50), (3-64) and (3-65) the friction and deviation forces on the blade and the shear plane can be determined. Now with equation (3-67) the value of the variable **λ** can be determined and if the starting value is correct, this value should be found. In general this will not be the case after one iteration. But repeating this procedure 3 or 4 times should give enough accuracy.

3.7. Example Program in Visual Basic 6.

```
Start:
  Labda = 1
  'In case of deviation angle
  If Iota <> 0 Then
    Vr1 = Vd * cos(Iota) * sin(Alpha) / sin(Alpha + Beta)    (3-52)
    Vr2 = Vd * cos(Iota) * sin(Beta) / sin(Alpha + Beta)     (3-53)
    Vd1 = Vd * sin(Iota) * Labda / (1 + Labda)               (3-75)
    Vd2 = Vd * sin(Iota) / (1 + Labda)                       (3-76)
    'So Vd1+Vd2 = Vd * sin(Iota)
    Phi_e = atn(Tan(Phi) * cos(atn(Vd1 / Vr1)))              (3-68)
    Delta_e = atn(Tan(Delta) * cos(atn(Vd2 / Vr2)))          (3-69)
    Cohesion_e = Cohesion * cos(atn(Vd1 / Vr1))              (3-70)
    Adhesion_e = Adhesion * cos(atn(Vd2 / Vr2))              (3-71)
  End If
```

Insert here the force calculation (F_h and F_v)

```
'In case of deviation angle                  (3-48)
If Iota <> 0 Then                            (3-50)
  Ff1 = Fh * cos(Beta) + Fv * sin(Beta)      (3-64)
  Ff2 = Fh * cos(Alpha) - Fv * sin(Alpha)    (3-65)
  Fd1 = abs(Ff1 * (Vd1 / Vr1))               (3-67)
  Fd2 = abs(Ff2 * (Vd2 / Vr2))
  Labda2 = (Vr1 / Vr2) * (Ff2 / Ff1)         (3-72)
  Fd = (Fd1 + Fd2) / 2                       (3-73)
  Fx2 = Fh * cos(Iota) + Fd * sin(Iota)      (3-74)
  Fy2 = Fh * sin(Iota) - Fd * cos(Iota)
  Fz2 = Fv
End If

 If Abs(Labda – Labda2) > 0.001 Then Goto Start
```

Figure 3-19: A piece of a program showing the iteration scheme.

3.8. Finding the Shear Angle.

The unknown in all the mechanisms is the shear angle **β**. With the assumption that nature will choose the mechanism configuration that requires the least energy and this energy equals the horizontal force $\mathbf{F_h}$ times the cutting velocity $\mathbf{v_c}$ times time, the shear angle **β** should be chosen where the horizontal force $\mathbf{F_h}$ is at a minimum. In some cases an analytical solution exists by taking the derivative of the horizontal force $\mathbf{F_h}$ with respect to the shear angle **β** and making it equal to zero. The second derivative has to be positive in this case. In other cases it is more convenient to determine the minimum numerically. This minimum value depends strongly on the blade angle **α** and the blade height – layer thickness ratio $\mathbf{h_b/h_i}$. This minimum also depends strongly on the soil properties and thus the type of soil. Different soils will have shear angles in a different range. Different cutting mechanisms will also have shear angles in different ranges. For saturated sand with blade angles **α** from 30° to 60°, the shear angle **β** will range from 30° to 20°. For clay, the shear angle depends strongly on the ratio of the adhesion to the cohesion. For very strong clays with a low relative adhesion the shear angle can be in the range of 60° to 75° for blade angles **α** from 30° to 60°. For soft clays with a high relative adhesion the shear angle is much smaller, from 30° to 40°. In general one can say that the shear angle decreases with increasing blade angle, internal/external friction angle and adhesion.

The criterion of least energy is arbitrary but reasonable. Other criteria may be applied to find the shear angle. Also other mechanisms may be applied leading to slightly different shear angles. In this book it is assumed that the shear plane is a straight line, which is questionable. First of all, the shear plane does not have to be a line without thickness. An area with a certain thickness is also possible. Secondly, the shape of the shear plane could be curved, like a circle segment. The advantage of the approach chosen is, that one can compare the different mechanisms more easily and the models derived give more insight in the basic parameters.

3.9. Specific Cutting Energy E_{sp}.

In the dredging industry, the specific cutting energy is described as:

The amount of energy, that has to be added to a volume unit of soil (e.g. sand, clay or rock) to excavate the soil.

The dimension of the specific cutting energy is: kN/m² or kPa for sand and clay, while for rock often MN/m² or MPa is used.

For the case as described above, cutting with a straight blade, the specific cutting energy can be written as:

$$E_{sp} = \frac{P_c}{Q_c} = \frac{F_h \cdot v_c}{h_i \cdot w \cdot v_c} = \frac{F_h}{h_i \cdot w} \qquad \mathbf{(3\text{-}78)}$$

So the specific cutting energy equals the cutting power divided by the cutting volumetric production. Once the specific cutting energy is known and the installed cutting power is known, this can be used to determine the theoretical cutting production according to:

$$Q_c = \frac{P_c}{E_{sp}} \qquad (3\text{-}79)$$

It should be noted here that there may be other factors limiting the production, like the hydraulic transport system of a cutter suction dredge, the throughput between the blades of a cutter head or the capacity of the swing winches.

3.10. Nomenclature.

a_1, a_2	Coefficients for weighted permeability	-
a, τ_a	Adhesion or external shear strength	kPa
A	Adhesive force on the blade	kN
c, τ_c	Cohesion or internal shear strength	kPa
C, C_1	Force due to cohesion in the shear plane	kN
C_2	Force due to cohesion on the front of the wedge	kN
C_3	Force due to cohesion at the bottom of the wedge	kN
F_h	Horizontal cutting force	kN
F_{f1}	Friction force on the shear surface	kN
F_{f2}	Friction force on the blade	kN
F_{n1}	Normal force on the shear surface	kN
F_{n2}	Normal force on the blade	kN
F_v	Vertical cutting force	kN
F_{d1}	Deviation force on the shear surface	kN
$F_{d,\ d2}$	Deviation force on the blade	kN
$F_{x1,\ 2}$	Cutting force in x-direction	kN
$F_{y1,\ 2}$	Cutting force in y-direction	kN
$F_{z1,\ 2}$	Cutting force in z-direction	kN
g	Gravitational constant (9.81)	m/s²
G, G_1	Gravitational force on the layer cut	kN
G_2	Gravitational force on the wedge	kN
h_i	Initial thickness of layer cut	m
h_b	Height of blade	m
$h_{b,m}$	Effective height of the blade in case **Curling Type**	m
I	Inertial force on the shear plane	kN
k_i	Initial permeability	m/s
k_{max}	Maximum permeability	m/s
k_m	Average permeability	m/s
K_1	Grain force on the shear plane	kN
K_2	Grain force on the blade or the front of the wedge	kN
K_3	Grain force on the bottom of the wedge	kN
K_4	Grain force on the blade (in case a wedge exists)	kN
n_i	Initial porosity	%
n_{max}	Maximum porosity	%
N_1	Normal force on the shear plane	kN
N_2	Normal force on the blade or the front of the wedge	kN
N_3	Normal force on the bottom of the wedge	kN
N_4	Normal force on the blade (in case a wedge exists)	kN
p_{1m}	Average pore pressure on the shear surface	kPa
p_{2m}	Average pore pressure on the blade	kPa
P_c	Cutting power	kW
R_1	Acting point of resulting forces on the shear plane	m
R_2	Acting point of resulting forces on the blade	m
R_3	Acting point of resulting forces on the bottom of the wedge	m
R_4	Acting point of resulting forces on the blade (in case a wedge exists)	m

S_1	Shear force due to friction on the shear plane	kN
S_2	Shear force due to friction on the blade or the front of the wedge	kN
S_3	Shear force due to friction at the bottom of the wedge	kN
S_4	Shear force due to friction on the blade (in case a wedge exists)	kN
v_c	Cutting velocity component perpendicular to the blade	m/s
v_d	Cutting velocity, drag velocity	m/s
v_{r1}	Velocity of grains in the shear surface	m/s
v_{r2}	Relative velocity of grains on the blade	m/s
v_{d1}	Deviation velocity of grains in the shear surface	m/s
v_{d2}	Deviation velocity of grains on the blade	m/s
$v_{x1,2}$	Velocity of grains in the x-direction	m/s
$v_{y1,2}$	Velocity of grains in the y-direction	m/s
$v_{z1,2}$	Velocity of grains in the z-direction	m/s
w	Width of blade	m
W_1	Force resulting from pore under pressure on the shear plane	kN
W_2	Force resulting from pore under pressure on the blade/ front wedge	kN
W_3	Force resulting from pore under pressure on the bottom of the wedge	kN
W_4	Force resulting from pore under pressures on the blade, wedge	kN
z	Water depth	m
α	Cutting angle blade	rad
β	Shear angle	rad
ε	Dilatation	-
ϕ	Angle of internal friction	rad
ϕ_e	Angle of internal friction perpendicular to the cutting edge	rad
λ_s	Strengthening factor	-
λ_1	Acting point factor for resulting forces on the shear plane	-
λ_2	Acting point factor for resulting forces on the blade or front of wedge	-
λ_3	Acting point factor for resulting forces on the bottom of the wedge	-
λ_4	Acting point factor for resulting forces on the blade	-
δ	External friction angle	rad
δ_e	External friction angle perpendicular to the cutting edge	rad
ι	Deviation angle blade	rad
ρ_s	Density of the soil	ton/m^3
ρ_l	Density water	ton/m^3
θ	Wedge angle	rad

Chapter 4: Which Cutting Mechanism for Which Kind of Soil?

4.1. Cutting Dry Sand.

In dry sand the cutting processes are governed by gravity and by inertial forces. Pore pressure forces, cohesion and adhesion are not present or can be neglected. Internal and external friction are present. The cutting process is of the **Shear Type** with discrete shear planes, but this can be modeled as the **Flow Type**, according to Merchant (1944). This approach will give an estimate of the maximum cutting forces. The average cutting forces may be 30%-50% of the maximum cutting forces.
Dry sand cutting is dominated by gravitational and inertial forces and by the internal and external friction angles. The cutting mechanism is the **Shear Type**. This is covered in *Chapter 5: Dry Sand Cutting*.

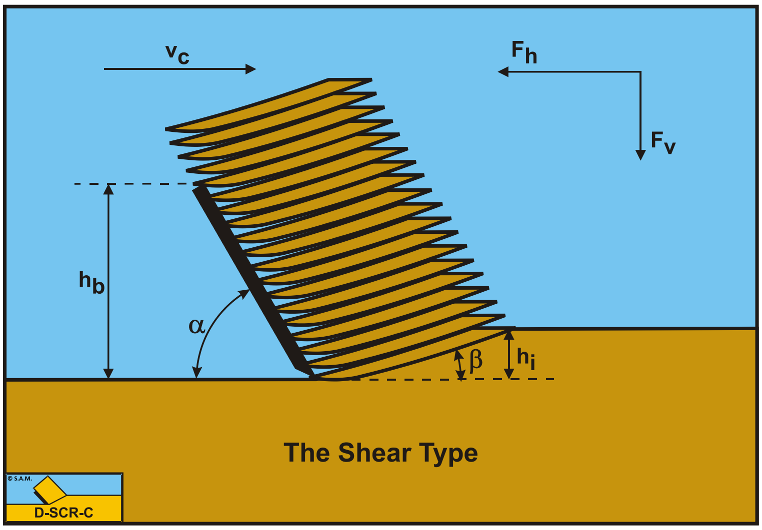

Figure 4-1: The Shear Type in dry sand cutting.

The forces $\mathbf{K_1}$ and $\mathbf{K_2}$ on the blade, chisel or pick point are now:

$$K_1 = \frac{W_2 \cdot \sin(\delta) + W_1 \cdot \sin(\alpha+\beta+\delta) + G \cdot \sin(\alpha+\delta)}{\sin(\alpha+\beta+\delta+\varphi)} + \frac{-I \cdot \cos(\alpha+\beta+\delta) - C \cdot \cos(\alpha+\beta+\delta) + A \cdot \cos(\delta)}{\sin(\alpha+\beta+\delta+\varphi)} \qquad (4\text{-}1)$$

$$K_2 = \frac{W_2 \cdot \sin(\alpha+\beta+\varphi) + W_1 \cdot \sin(\varphi) + G \cdot \sin(\beta+\varphi)}{\sin(\alpha+\beta+\delta+\varphi)} + \frac{+I \cdot \cos(\varphi) + C \cdot \cos(\varphi) - A \cdot \cos(\alpha+\beta+\varphi)}{\sin(\alpha+\beta+\delta+\varphi)} \qquad (4\text{-}2)$$

The normal forces $\mathbf{N_1}$ on the shear plane and $\mathbf{N_2}$ on the blade are:

$$N_1 = K_1 \cdot \cos(\varphi) \quad \text{and} \quad N_2 = K_2 \cdot \cos(\delta) \qquad (4\text{-}3)$$

The horizontal and vertical forces on the blade, chisel or pick point are:

$$F_h = -W_2 \cdot \sin(\alpha) + K_2 \cdot \sin(\alpha+\delta) + A \cdot \cos(\alpha) \qquad (4\text{-}4)$$

$$F_v = -W_2 \cdot \cos(\alpha) + K_2 \cdot \cos(\alpha+\delta) - A \cdot \sin(\alpha) \qquad (4\text{-}5)$$

The equilibrium of moments around the blade tip is:

$$(N_1 - W_1) \cdot R_1 - G \cdot R_3 = (N_2 - W_2) \cdot R_2 \qquad (4\text{-}6)$$

Analyzing these equations results in the following conclusions:

- Since the argument in the cosine of the inertial term in the force **K₁** is always greater than 90 degrees, the cosine is negative and the term as a whole is positive. This results in positive forces on the blade, chisel or pick point and also positive normal forces.
- There are no forces directly proportional to the (mobilized) blade height or the length of the shear plane, so the equilibrium of moments does not play a role. The **Curling Type** and the **Tear Type** will not occur. The acting points of the forces **R₁** and **R₂** will be adjusted by nature to form an equilibrium of moments.
- When the argument of the sine in the denominator gets close to 180 degrees, the forces become very large. If the argument is greater than 180 degrees, the forces would become negative. Since both conditions will not happen in nature, nature will find another cutting mechanism, the wedge mechanism.

4.2. Cutting Water Saturated Sand.

From literature it is known that, during the cutting process, the sand increases in volume. This increase in volume is accredited to dilatancy. Dilatancy is the change of the pore volume as a result of shear in the sand. This increase of the pore volume has to be filled with water. The flowing water experiences a certain resistance, which causes sub-pressures in the pore water in the sand. As a result the grain stresses increase and therefore the required cutting forces. The rate of the increase of the pore volume in the dilatancy zone, the volume strain rate, is proportional to the cutting velocity. If the volume strain rate is high, there is a chance that the pore pressure reaches the saturated water vapor pressure and cavitation occurs. A further increasing volume strain rate will not be able to cause a further decrease of the pore pressure. This also implies that, with a further increasing cutting velocity, the cutting forces cannot increase as a result of the dilatancy properties of the sand. The cutting forces can, however, still increase with an increasing cutting velocity as a result of the inertia forces and the flow resistance.

The cutting process can be subdivided in 5 areas in relation with the cutting forces:

- Very low cutting velocities, a quasi-static cutting process. The cutting forces are determined by gravitation.
- The volume strain rate is high in relation to the permeability of the sand. The volume strain rate is however so small that inertia forces can be neglected. The cutting forces are dominated by the dilatancy properties of the sand.
- A transition region, with local cavitation. With an increasing volume strain rate, the cavitation area will increase so that the cutting forces increase slightly as a result of dilatancy.
- Cavitation occurs almost everywhere around and on the blade. The cutting forces do not increase anymore as a result of the dilatancy properties of the sand.
- Very high cutting velocities. The inertia forces part in the total cutting forces can no longer be neglected but form a substantial part.

Under normal conditions in dredging, the cutting process in sand will be governed by the effects of dilatation. Gravity, inertia, cohesion and adhesion will not play a role. Internal and external friction are present.
Saturated sand cutting is dominated by pore vacuum pressure forces and by the internal and external friction angles. The cutting mechanism is the **Shear Type**. This is covered in *Chapter 6: Saturated Sand Cutting.*

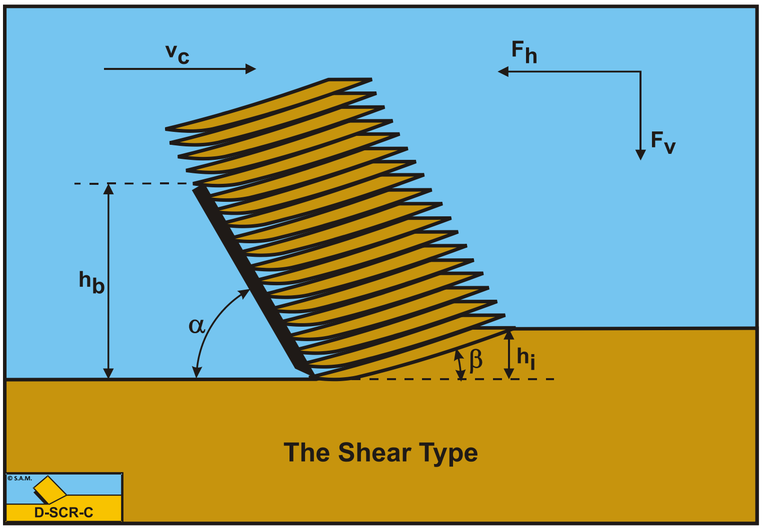

Figure 4-2: The Shear Type in saturated sand cutting.

The forces **K₁** and **K₂** on the blade, chisel or pick point are now:

$$\mathrm{K_1 = \frac{W_2 \cdot \sin(\delta) + W_1 \cdot \sin(\alpha+\beta+\delta) + G \cdot \sin(\alpha+\delta)}{\sin(\alpha+\beta+\delta+\varphi)} + \frac{-I \cdot \cos(\alpha+\beta+\delta) - C \cdot \cos(\alpha+\beta+\delta) + A \cdot \cos(\delta)}{\sin(\alpha+\beta+\delta+\varphi)}} \qquad \text{(4-7)}$$

$$\mathrm{K_2 = \frac{W_2 \cdot \sin(\alpha+\beta+\varphi) + W_1 \cdot \sin(\varphi) + G \cdot \sin(\beta+\varphi)}{\sin(\alpha+\beta+\delta+\varphi)} + \frac{+I \cdot \cos(\varphi) + C \cdot \cos(\varphi) - A \cdot \cos(\alpha+\beta+\varphi)}{\sin(\alpha+\beta+\delta+\varphi)}} \qquad \text{(4-8)}$$

The normal forces **N$_1$** on the shear plane and **N$_2$** on the blade are:

$$\mathrm{N_1 = K_1 \cdot \cos(\varphi) \quad and \quad N_2 = K_2 \cdot \cos(\delta)} \qquad \text{(4-9)}$$

The horizontal and vertical forces on the blade, chisel or pick point are:

$$\mathrm{F_h = -W_2 \cdot \sin(\alpha) + K_2 \cdot \sin(\alpha+\delta) + A \cdot \cos(\alpha)} \qquad \text{(4-10)}$$

$$\mathrm{F_v = -W_2 \cdot \cos(\alpha) + K_2 \cdot \cos(\alpha+\delta) - A \cdot \sin(\alpha)} \qquad \text{(4-11)}$$

The equilibrium of moments around the blade tip is:

$$\mathrm{(N_1 - W_1) \cdot R_1 - G \cdot R_3 = (N_2 - W_2) \cdot R_2} \qquad \text{(4-12)}$$

Analyzing these equations results in the following conclusions:

- The pore pressure forces **W$_1$** and **W$_2$** are limited by the occurrence of cavitation.
- All the terms are positive, resulting in positive forces on the blade and also positive normal forces.
- In the non-cavitating case the pore pressure forces are related to the (mobilized) blade height or the length of the shear plane. In the cavitating case the pore pressure forces are proportional to the (mobilized) blade height or the length of the shear plane. Theoretically the **Curling Type** and the **Tear Type** may occur. This has however never been observed with in dredging normal blade heights and layer thicknesses.
- When the argument of the sine in the denominator gets close to 180 degrees, the forces become very large. If the argument is greater than 180 degrees, the forces would become negative. Since both conditions will not happen in nature, nature will find another cutting mechanism, the wedge mechanism.

4.3. Cutting Clay.

In clay the cutting processes are dominated by cohesion and adhesion (internal and external shear strength). Because of the **φ=0** concept, the internal and external friction angles are set to 0. Gravity, inertial forces and pore pressures are also neglected. This simplifies the cutting equations. Clay however is subject to strengthening, meaning that the internal and external shear strength increase with an increasing strain rate.

The reverse of strengthening is creep, meaning that under a constant load the material will continue deforming with a certain strain rate. Under normal circumstances clay will be cut with the **Flow Type** mechanism, but under certain circumstances the **Curling Type** or the **Tear Type** may occur. The **Curling Type** will occur when the blade height is large with respect to the layer thickness, **h$_b$/h$_i$**, the adhesion is high compared to the cohesion **a/c** and the blade angle **α** is relatively big. The **Tear Type** will occur when the blade height is small with respect to the layer thickness, **h$_b$/h$_i$**, the adhesion is small compared to the cohesion **a/c** and the blade angle **α** is relatively small.
Clay cutting is dominated by cohesive (internal shear strength) and adhesive (external shear strength) forces. The basic cutting mechanism is the **Flow Type**. Cutting a thin layer, combined with a high adhesive force may result in the **Curling Type** mechanism. Cutting a thick layer combined with a small adhesive force and a low tensile strength may result in the **Tear Type** mechanism. This is covered in *Chapter 7: Clay Cutting*.

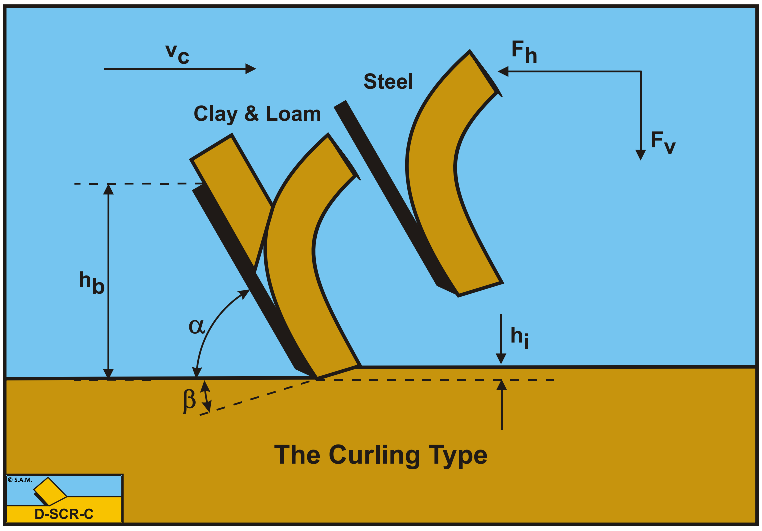

Figure 4-3: The Curling Type in clay and loam cutting.

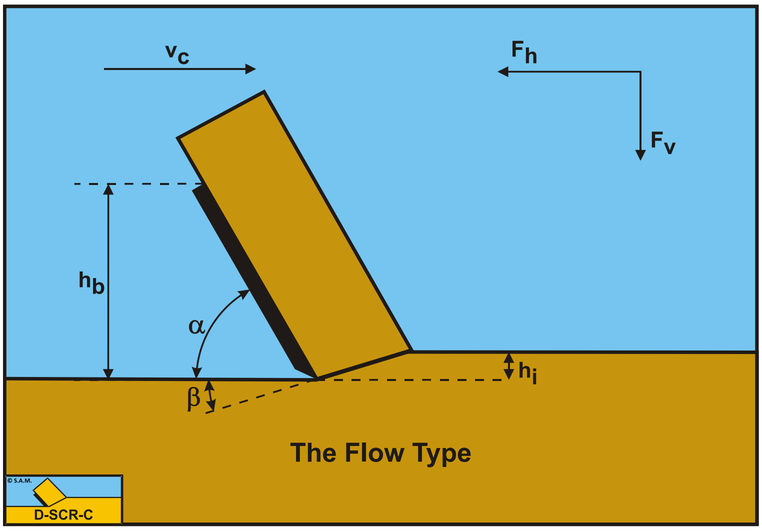

Figure 4-4: The Flow Type in clay and loam cutting.

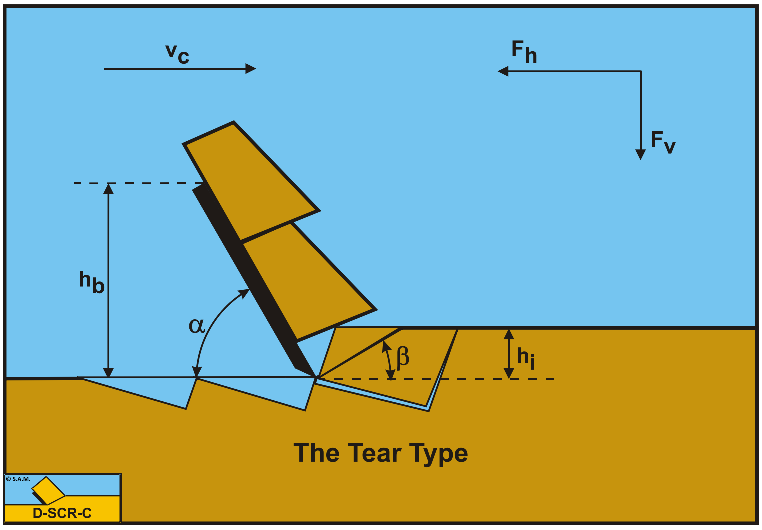

Figure 4-5: The Tear Type in clay and loam cutting.

The forces **K₁** and **K₂** on the blade, chisel or pick point are now:

$$K_1 = \frac{W_2 \cdot \sin(\delta) + W_1 \cdot \sin(\alpha+\beta+\delta) + G \cdot \sin(\alpha+\delta)}{\sin(\alpha+\beta+\delta+\varphi)} + \frac{-I \cdot \cos(\alpha+\beta+\delta) - C \cdot \cos(\alpha+\beta+\delta) + A \cdot \cos(\delta)}{\sin(\alpha+\beta+\delta+\varphi)} \tag{4-13}$$

$$K_2 = \frac{W_2 \cdot \sin(\alpha+\beta+\varphi) + W_1 \cdot \sin(\varphi) + G \cdot \sin(\beta+\varphi)}{\sin(\alpha+\beta+\delta+\varphi)} + \frac{+I \cdot \cos(\varphi) + C \cdot \cos(\varphi) - A \cdot \cos(\alpha+\beta+\varphi)}{\sin(\alpha+\beta+\delta+\varphi)} \tag{4-14}$$

The normal forces **N₁** on the shear plane and **N₂** on the blade are:

$$N_1 = K_1 \cdot \cos(\varphi) \quad \text{and} \quad N_2 = K_2 \cdot \cos(\delta) \tag{4-15}$$

The horizontal and vertical forces on the blade, chisel or pick point are:

$$F_h = -W_2 \cdot \sin(\alpha) + K_2 \cdot \sin(\alpha+\delta) + A \cdot \cos(\alpha) \tag{4-16}$$

$$F_v = -W_2 \cdot \cos(\alpha) + K_2 \cdot \cos(\alpha+\delta) - A \cdot \sin(\alpha) \tag{4-17}$$

The equilibrium of moments around the blade tip is:

$$(N_1 - W_1) \cdot R_1 - G \cdot R_3 = (N_2 - W_2) \cdot R_2 \tag{4-18}$$

Analyzing these equations results in the following conclusions:

- At normal cutting angles in dredging, the argument of the cosine in the cohesive term of **K₁** is greater than 90 degrees, resulting in a small positive term as a whole. Together with the adhesive term, this gives a positive normal stress on the shear plane. The minimum normal stress however equals the normal stress on the shear plane, minus the radius of the Mohr circle, which is the cohesion. The result may be a negative minimum normal stress. If this negative minimum normal stress is smaller than the negative tensile strength, the **Tear Type** will occur. This occurrence depends on the ratio between the adhesive force to the cohesive force. A large ratio will suppress the **Tear Type**.
- The adhesive force on the blade is proportional to the (mobilized) length of the blade, so the **Curling Type** may occur. The cohesive force on the shear plane is proportional to the (mobilized) cohesion, so the **Tear Type** may occur. The occurrence of the **Curling Type** or **Tear Type** depends on the ratio of the adhesive force to the cohesive force. A large ratio results in the **Curling Type**, a small ratio in the **Tear Type**.
- When the argument of the sine in the denominator gets close to 180 degrees, the forces become very large. If the argument is greater than 180 degrees, the forces would become negative. Since both conditions will not happen in nature, nature will find another cutting mechanism, the wedge mechanism. In clay this is not likely to occur, since there are only two angles in the argument of the sine in the denominator. It would require very large blade angles to occur.

4.4. Cutting Rock Atmospheric.

Rock is the collection of materials where the grains are bonded chemically from very stiff clay, sandstone to very hard basalt. It is difficult to give one definition of rock or stone and also the composition of the material can differ strongly. Still it is interesting to see if the model used for sand and clay, which is based on the Coulomb model, can be used for rock as well. Typical parameters for rock are the compressive strength UCS and the tensile strength BTS and specifically the ratio between those two, which is a measure for how fractured the rock is. Rock also has shear strength and because it consists of bonded grains it will have an internal friction angle and an external friction angle. It can be assumed that the permeability of the rock is very low, so initially the pore pressures do no play a role under atmospheric conditions. Since the absolute hydrostatic pressure, which would result in a cavitation under pressure of the same magnitude can be neglected with respect to the compressive strength of the rock; the pore pressures are usually neglected. This results in a material where gravity, inertia, pore pressures and adhesion can be neglected.

Rock cutting under atmospheric conditions (normal dredging) is dominated by the internal shear strength and by the internal and external friction angles. The main cutting mechanism is the **Chip Type**, brittle cutting**.** Cutting a very thin layer or using large blade angles may result in the **Crushed Type.** This is covered in *Chapter 8: Rock Cutting: Atmospheric Conditions*.

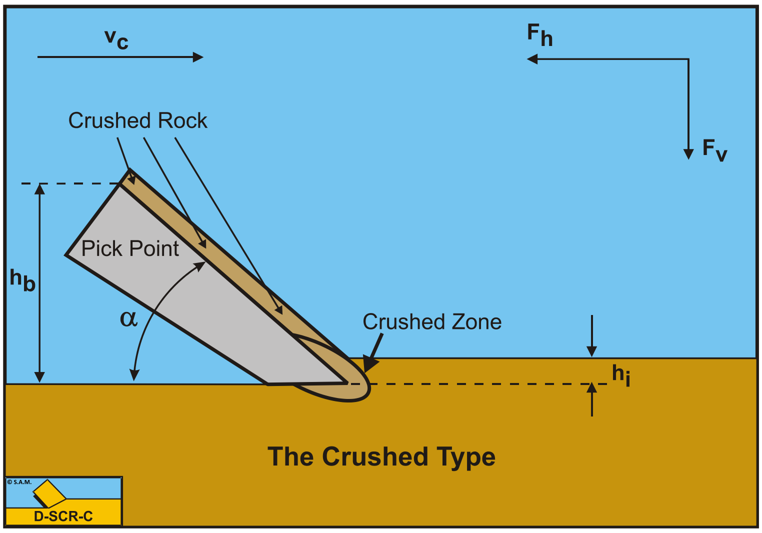

Figure 4-6: The Crushed Type in atmospheric rock cutting.

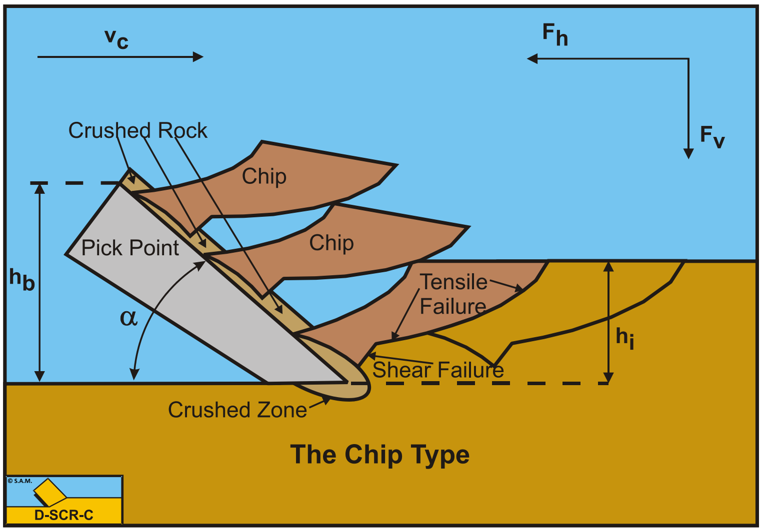

Figure 4-7: The Chip Type in atmospheric rock cutting.

The forces $\mathbf{K_1}$ and $\mathbf{K_2}$ on the blade, chisel or pick point are now:

$$K_1 = \frac{W_2 \cdot \sin(\delta) + W_1 \cdot \sin(\alpha+\beta+\delta) + G \cdot \sin(\alpha+\delta)}{\sin(\alpha+\beta+\delta+\varphi)} + \frac{-I \cdot \cos(\alpha+\beta+\delta) - C \cdot \cos(\alpha+\beta+\delta) + A \cdot \cos(\delta)}{\sin(\alpha+\beta+\delta+\varphi)} \tag{4-19}$$

$$K_2 = \frac{W_2 \cdot \sin(\alpha+\beta+\varphi) + W_1 \cdot \sin(\varphi) + G \cdot \sin(\beta+\varphi)}{\sin(\alpha+\beta+\delta+\varphi)} + \frac{+I \cdot \cos(\varphi) + C \cdot \cos(\varphi) - A \cdot \cos(\alpha+\beta+\varphi)}{\sin(\alpha+\beta+\delta+\varphi)} \tag{4-20}$$

The normal forces $\mathbf{N_1}$ on the shear plane and $\mathbf{N_2}$ on the blade are:

$$N_1 = K_1 \cdot \cos(\varphi) \quad \text{and} \quad N_2 = K_2 \cdot \cos(\delta) \tag{4-21}$$

The horizontal and vertical forces on the blade, chisel or pick point are:

$$F_h = -W_2 \cdot \sin(\alpha) + K_2 \cdot \sin(\alpha + \delta) + A \cdot \cos(\alpha) \tag{4-22}$$

$$F_v = -W_2 \cdot \cos(\alpha) + K_2 \cdot \cos(\alpha + \delta) - A \cdot \sin(\alpha) \tag{4-23}$$

The equilibrium of moments around the blade tip is:

$$(N_1 - W_1) \cdot R_1 - G \cdot R_3 = (N_2 - W_2) \cdot R_2 \tag{4-24}$$

Analyzing these equations results in the following conclusions:

- Since the argument in the cosine of the cohesive term in the force **K_1** is always greater than 90 degrees, the cosine is negative and the term as a whole is positive. This results in positive forces on the blade, chisel or pick point and also positive normal forces. The minimum normal stress however equals the normal stress on the shear plane, minus about the radius of the Mohr circle. The result may be a negative minimum normal stress. If this negative minimum normal stress is smaller than the negative tensile strength, brittle tensile failure will occur. Otherwise brittle shear failure will occur. In both cases the forces calculated are peak forces. The average forces are somewhere between 50% and 100% of the peak forces.
- On the blade the normal stresses are always high enough to avoid the occurrence of the **Curling Type**. In fact the forces on the blade do not depend on the length of the blade. The cohesive force on the shear plane however depends on the (mobilized) cohesion or shear strength, so the **Tear Type**, here named the **Chip Type** may occur.
- When the argument of the sine in the denominator gets close to 180 degrees, the forces become very large. If the argument is greater than 180 degrees, the forces would become negative. Since both conditions will not happen in nature, nature will find another cutting mechanism, the wedge mechanism.

4.5. Cutting Rock Hyperbaric.

In the case of hyperbaric rock cutting, the pore pressures cannot be neglected anymore. Gravity and inertial forces can still be neglected. Usually rock has no adhesion. When the hydrostatic pressure is larger than or approaching the UCS value of the rock, the rock tends to fail in a semi-ductile manner, named cataclastic failure. It is almost like the hydrostatic pressure can be added to the tensile strength of the rock.

Rock cutting under hyperbaric conditions (deep sea mining) is dominated by the internal shear strength, the pore vacuum pressure forces and by the internal and external friction angles. The main cutting mechanism is the **Crushed Type**, cataclastic semi-ductile cutting**.** This is covered in *Chapter 9: Rock Cutting: Hyperbaric Conditions*.

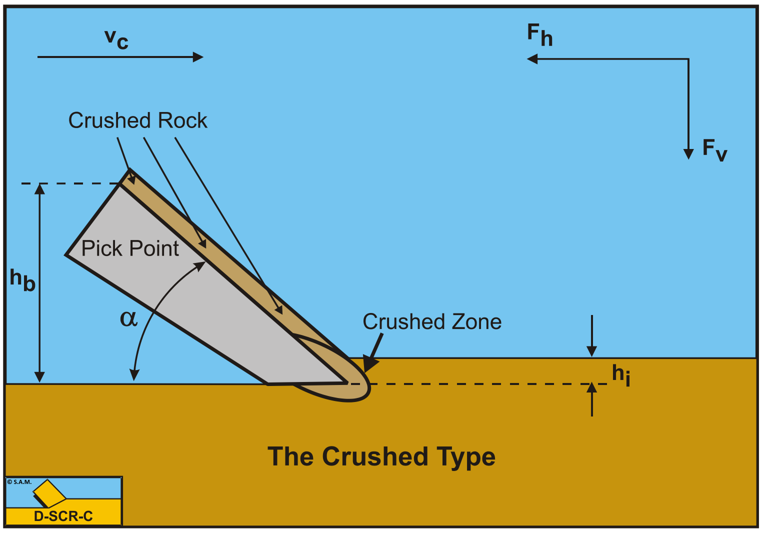

Figure 4-8: The Crushed Type in hyperbaric rock cutting.

The forces **K_1** and **K_2** on the blade, chisel or pick point are now:

$$K_1 = \frac{W_2 \cdot \sin(\delta) + W_1 \cdot \sin(\alpha+\beta+\delta) + G \cdot \sin(\alpha+\delta)}{\sin(\alpha+\beta+\delta+\varphi)} + \frac{-I \cdot \cos(\alpha+\beta+\delta) - C \cdot \cos(\alpha+\beta+\delta) + A \cdot \cos(\delta)}{\sin(\alpha+\beta+\delta+\varphi)} \quad \textbf{(4-25)}$$

$$K_2 = \frac{W_2 \cdot \sin(\alpha+\beta+\varphi) + W_1 \cdot \sin(\varphi) + G \cdot \sin(\beta+\varphi)}{\sin(\alpha+\beta+\delta+\varphi)} + \frac{+I \cdot \cos(\varphi) + C \cdot \cos(\varphi) - A \cdot \cos(\alpha+\beta+\varphi)}{\sin(\alpha+\beta+\delta+\varphi)} \quad \textbf{(4-26)}$$

The normal forces $\mathbf{N_1}$ on the shear plane and $\mathbf{N_2}$ on the blade are:

$$N_1 = K_1 \cdot \cos(\varphi) \quad \text{and} \quad N_2 = K_2 \cdot \cos(\delta) \quad \textbf{(4-27)}$$

The horizontal and vertical forces on the blade, chisel or pick point are:

$$F_h = -W_2 \cdot \sin(\alpha) + K_2 \cdot \sin(\alpha+\delta) + A \cdot \cos(\alpha) \quad \textbf{(4-28)}$$

$$F_v = -W_2 \cdot \cos(\alpha) + K_2 \cdot \cos(\alpha+\delta) - A \cdot \sin(\alpha) \quad \textbf{(4-29)}$$

The equilibrium of moments around the blade tip is:

$$(N_1 - W_1) \cdot R_1 - G \cdot R_3 = (N_2 - W_2) \cdot R_2 \quad \textbf{(4-30)}$$

Analyzing these equations results in the following conclusions:

- Since the argument in the cosine of the cohesive term in the force $\mathbf{K_1}$ is always greater than 90 degrees, the cosine is negative and the term as a whole is positive. This results in positive forces on the blade, chisel or pick point and also positive normal forces. The minimum normal stress however equals the normal stress on the shear plane, minus about the radius of the Mohr circle. The result will always be a positive minimum normal stress because of the influence of the large pore under pressure forces.
- On the blade the **Curling Type** may occur based on the equilibrium of moments, because the pore pressure force depends on the length of the blade. When cutting a very thin layer of rock, compared to the height of the blade, as in oil drilling, this will occur. On the shear plane, both the pore pressure force and the cohesive force depend on the length of the shear plane, which may result in brittle tensile failure, the **Tear Type**, here named the **Chip Type**. Usually this is suppressed by the very large pore under pressures in relation to the strength of the rock.
- When the argument of the sine in the denominator gets close to 180 degrees, the forces become very large. If the argument is greater than 180 degrees, the forces would become negative. Since both conditions will not happen in nature, nature will find another cutting mechanism, the wedge mechanism.

4.6. Summary.

The cutting forces for sand, clay and rock can be described by a generic equation, where a number of terms dominate for each individual type of soil. Here dry sand, water saturated sand, clay, atmospheric rock and hyperbaric rock are distinguished. The influences of the different forces for each type of soil are summarized in Table 4-1. The general cutting mechanism is the **Flow Type**, which is mathematically the same as the **Shear Type** and the **Crushed Type**. If the forces on the blade depend on the length of the blade, such as the adhesive force **A** or the pore under pressure force $\mathbf{W_2}$, the **Curling Type** may occur if the layer thickness is very small compared to the blade length. A mobilized blade length (height) is introduced. If the forces on the shear plane depend on the length of the shear plane, such as the cohesive force **C** and the pore under pressure force $\mathbf{W_1}$, the **Tear Type** (or **Chip Type**) may occur if the layer thickness is large compared to the blade length. A mobilized shear strength is introduced.

However there may also be mixed soils like clay mixed with sand, resulting in a clay with internal friction. Or sand mixed with clay, resulting in a very low permeability. For clay the ratio of the adhesion to the cohesion is very important and little is known about this. Very weak clays may have an adhesion almost equal to the cohesion, but when the cohesion increases the ratio between adhesion and cohesion decreases. A 100 kPa clay may have an adhesion of just 5-10 kPa. For even harder clays the adhesion may drop to zero. The harder clays however seem to have some internal and external friction, increasing with the strength of the clay. A new topic is the cutting of permafrost, frozen clay. From preliminary research it appears that permafrost behaves more like rock, but how exactly is still a question. Future research will give an answer to these questions and hopefully the generic equations will also be applicable for these soils.

Table 4-1: The influences for each type of soil.

	Gravity	Inertia	Pore Pressure	Cohesion	Adhesion	Friction
Dry sand	🟩	🟩				🟩
Saturated sand			🟩			🟩
Clay				🟩	🟩	
Atmospheric rock				🟩		🟩
Hyperbaric rock			🟩	🟩		🟩

4.7. Nomenclature.

a, τ_a	Adhesion or external shear strength	**kPa**
A	Adhesive force on the blade	**kN**
c, τ_c	Cohesion or internal shear strength	**kPa**
c_m	Mobilized cohesion in case of **Tear Type** or **Chip Type**	**m**
C	Force due to cohesion in the shear plane	**kN**
F_h	Horizontal cutting force	**kN**
F_v	Vertical cutting force	**kN**
g	Gravitational constant (9.81)	**m/s^2**
G	Gravitational force on the layer cut	**kN**
h_i	Initial thickness of layer cut	**m**
h_b	Height of blade	**m**
$h_{b,m}$	Mobilized height of the blade in case **Curling Type**	**m**
I	Inertial force on the shear plane	**kN**
K_1	Grain force on the shear plane	**kN**
K_2	Grain force on the blade	**kN**
N_1	Normal force on the shear plane	**kN**
N_2	Normal force on the blade	**kN**
R_1	Acting point forces on the shear plane	**m**
R_2	Acting point forces on the blade	**m**
R_3	Acting point gravity force	**m**
S_1	Shear force due to friction on the shear plane	**kN**
S_2	Shear force due to friction on the blade or the front of the wedge	**kN**
v_c	Cutting velocity	**m/s**
w	Width of blade	**m**
W_1	Force resulting from pore under pressure on the shear plane	**kN**
W_2	Force resulting from pore under pressure on the blade/ front wedge	**kN**
z	Water depth	**m**
α	Cutting angle blade	**rad**
β	Shear angle	**rad**
ϕ	Angle of internal friction	**rad**
δ	External friction angle	**rad**
ρ_s	Density of the soil	**ton/m^3**
ρ_l	Density water	**ton/m^3**

Chapter 5: Dry Sand Cutting.

5.1. Introduction.

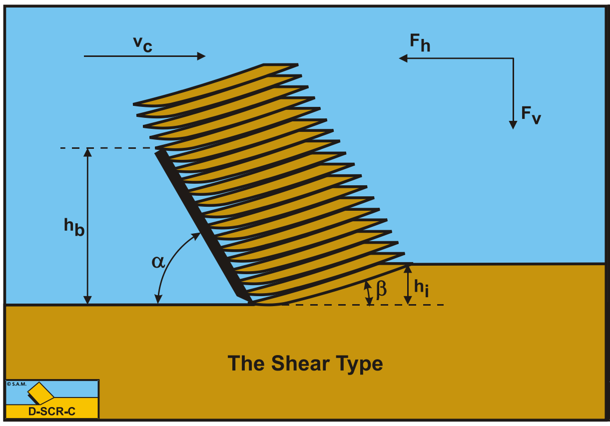

Figure 5-1: The cutting mechanism in dry sand, the Shear Type.

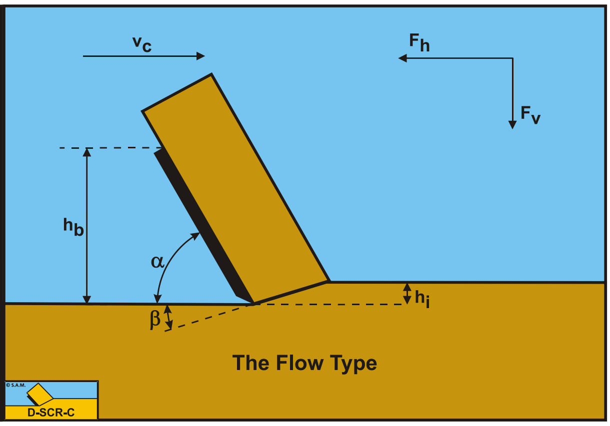

Figure 5-2: Dry sand modeled according to the Flow Type.

In literature most cutting theories are based on one time failure of the sand. Here a continuous cutting process is considered. In dry sand the cutting processes are governed by gravity and by inertial forces. Pore pressure forces, cohesion and adhesion are not present or can be neglected. Internal and external friction are present. The cutting process is of the **Shear Type** with discrete shear planes (see Figure 5-1), but this can be modeled as the **Flow Type** (see Figure 5-2), according to Merchant (1944). This approach will give an estimate of the maximum cutting forces. The average cutting forces may be 30%-50% of the maximum cutting forces.

5.2. Definitions.

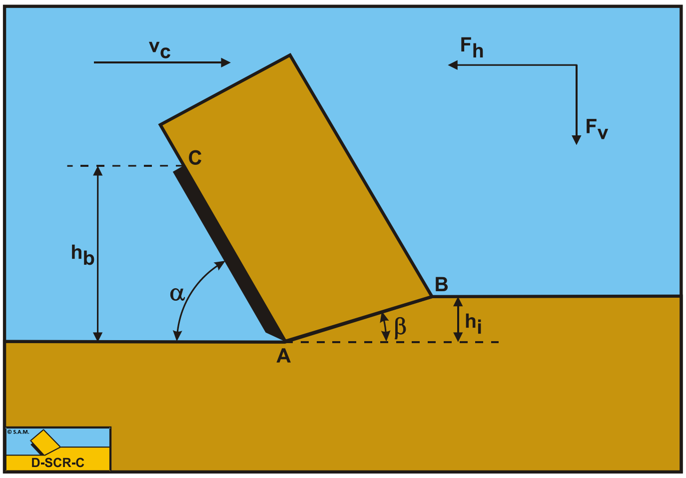

Figure 5-3: The cutting process, definitions.

Definitions:

1. **A**: The blade tip.
2. **B**: End of the shear plane.
3. **C**: The blade top.
4. **A-B**: The shear plane.
5. **A-C**: The blade surface.
6. **h_b**: The height of the blade.
7. **h_i**: The thickness of the layer cut.
8. **v_c**: The cutting velocity.
9. **α**: The blade angle.
10. **β**: The shear angle.
11. **F_h**: The horizontal force, the arrow gives the positive direction.
12. **F_v**: The vertical force, the arrow gives the positive direction.

5.3. The Equilibrium of Forces.

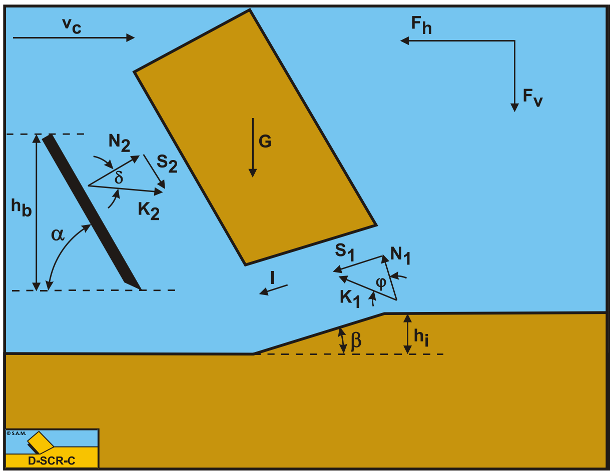

Figure 5-4: The forces on the layer cut in dry sand.

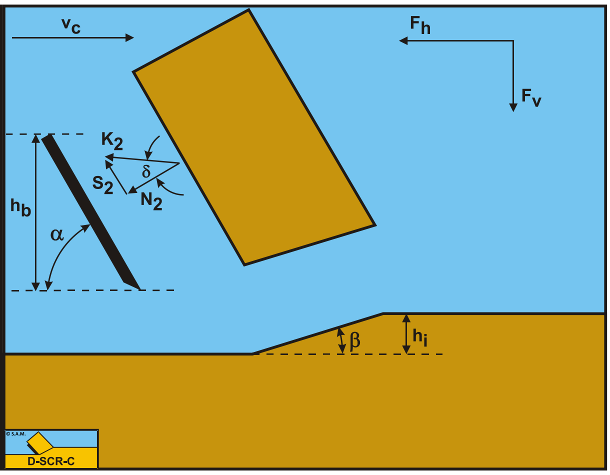

Figure 5-5: The forces on the blade in dry sand.

Figure 5-4 illustrates the forces on the layer of soil cut. The forces shown are valid in general. The forces acting on this layer are:

1. A normal force acting on the shear surface $\mathbf{N_1}$, resulting from the effective grain stresses.
2. A shear force $\mathbf{S_1}$ as a result of internal friction, $\mathbf{N_1 \cdot tan(\phi)}$.
3. A gravity force **G** as a result of the weight of the layer cut.
4. An inertial force **I**, resulting from acceleration of the soil.
5. A force normal to the blade $\mathbf{N_2}$, resulting from the effective grain stresses.
6. A shear force $\mathbf{S_2}$ as a result of the soil/steel friction $\mathbf{N_2 \cdot tan(\delta)}$.

The normal force $\mathbf{N_1}$ and the shear force $\mathbf{S_1}$ can be combined to a resulting grain force $\mathbf{K_1}$.

$$K_1 = \sqrt{N_1^2 + S_1^2} \tag{5-1}$$

The forces acting on a straight blade when cutting soil, can be distinguished as:

7. A force normal to the blade $\mathbf{N_2}$, resulting from the effective grain stresses.
8. A shear force $\mathbf{S_2}$ as a result of the soil/steel friction $\mathbf{N_2 \cdot tan(\delta)}$.

These forces are shown in Figure 5-5. If the forces $\mathbf{N_2}$ and $\mathbf{S_2}$ are combined to a resulting force $\mathbf{K_2}$ and the adhesive force and the water under pressures are known, then the resulting force $\mathbf{K_2}$ is the unknown force on the blade. By taking the horizontal and vertical equilibrium of forces an expression for the force $\mathbf{K_2}$ on the blade can be derived.

$$K_2 = \sqrt{N_2^2 + S_2^2} \tag{5-2}$$

Pure sand is supposed to be cohesion less, meaning it does not have shear strength or the shear strength is zero and the adhesion is also zero. The shear stresses, internal and external, depend completely on the normal stresses. In dry sand the pores between the sand grains are filled with air and although dilatation will occur due to shearing, Miedema (1987 September), there will be hardly any generation of pore under pressures because the permeability for air flowing through the pores is high. This means that the cutting forces do not depend on pore pressure forces, nor on adhesion and cohesion, but only on gravity and inertia, resulting in the following set of equations:

The horizontal equilibrium of forces:

$$\sum F_h = K_1 \cdot \sin(\beta + \varphi) + I \cdot \cos(\beta) - K_2 \cdot \sin(\alpha + \delta) = 0 \tag{5-3}$$

The vertical equilibrium of forces:

$$\sum F_v = -K_1 \cdot \cos(\beta + \varphi) + I \cdot \sin(\beta) + G - K_2 \cdot \cos(\alpha + \delta) = 0 \tag{5-4}$$

The force **K₁** on the shear plane is now:

$$K_1 = \frac{G \cdot \sin(\alpha + \delta) - I \cdot \cos(\alpha + \beta + \delta)}{\sin(\alpha + \beta + \delta + \varphi)} \qquad \textbf{(5-5)}$$

The force **K₂** on the blade is now:

$$K_2 = \frac{G \cdot \sin(\beta + \varphi) + I \cdot \cos(\varphi)}{\sin(\alpha + \beta + \delta + \varphi)} \qquad \textbf{(5-6)}$$

Wismer and Luth (1972A) and (1972B) researched the inertia forces part of the total cutting forces. The following equation is derived:

$$I = \rho_s \cdot v_c^2 \cdot \frac{\sin(\alpha)}{\sin(\alpha + \beta)} \cdot h_i \cdot w \qquad \textbf{(5-7)}$$

The gravitational force (weight dry) follows, based on Figure 5-2, from:

$$G = \rho_s \cdot g \cdot h_i \cdot w \cdot \frac{\sin(\alpha + \beta)}{\sin(\beta)} \cdot \left\{ \frac{\left(h_b + h_i \cdot \sin(\alpha)\right)}{\sin(\alpha)} + \frac{h_i \cdot \cos(\alpha + \beta)}{2 \cdot \sin(\beta)} \right\} \qquad \textbf{(5-8)}$$

In reality the shape of the layer cut may be different since there is no force to keep the sand together and the maximum slope of the sand will be dependent on the angle of natural repose. For the calculations the above equation is applied, since this equation is used for all soil types. Other formulations for the weight of the soil may be used. From equation (5-6) the forces on the blade can be derived. On the blade a force component in the direction of cutting velocity **Fₕ** and a force perpendicular to this direction **Fᵥ** can be distinguished.

$$F_h = K_2 \cdot \sin(\alpha + \delta) \qquad \textbf{(5-9)}$$

$$F_v = K_2 \cdot \cos(\alpha + \delta) \qquad \textbf{(5-10)}$$

The normal force on the shear plane is now:

$$N_1 = \frac{G \cdot \sin(\alpha + \delta) - I \cdot \cos(\alpha + \beta + \delta)}{\sin(\alpha + \beta + \delta + \varphi)} \cdot \cos(\varphi) \qquad \textbf{(5-11)}$$

The normal force on the blade is now:

$$N_2 = \frac{G \cdot \sin(\beta + \varphi) + I \cdot \cos(\varphi)}{\sin(\alpha + \beta + \delta + \varphi)} \cdot \cos(\delta) \qquad \textbf{(5-12)}$$

Equations (5-11) and (5-12) show that the normal force on the shear plane **N₁** can become negative at very high velocities, which are physically impossible, while the normal force on the blade **N₂** will always be positive. Under normal conditions the sum of **α+β+δ** will be greater than 90 degrees in which case the cosine of this sum is negative, resulting in a normal force on the shear plane that is always positive. Only in the case of a small blade angle **α**, shear angle **β** and angle of external friction **δ**, the sum of these angles could be smaller than 90°, but still close to 90° degrees. For example a blade angle of 30° would result in a shear angle of about 30°. Loose sand could have an external friction angle of 20°, so the sum would be 80°. But this is a lower limit for **α+β+δ**. A more realistic example is a blade with an angle of 60°, resulting in a shear angle of about 20° and a medium to hard sand with an external friction angle of 30°, resulting in **α+β+δ=110°.** So for realistic cases the normal force on the shear plane **N₁** will always be positive. In dry sand, always the shear type of cutting mechanism will occur.

Based on the weight only of the soil, the forces can also be expressed as:

$$F_h = \rho_s \cdot g \cdot h_i^2 \cdot w \cdot \lambda_{HD}$$

With : **(5-13)**

$$\lambda_{HD} = \frac{\sin(\alpha+\beta)}{\sin(\beta)} \cdot \left\{ \frac{\left(h_b / h_i + \sin(\alpha)\right)}{\sin(\alpha)} + \frac{\cos(\alpha+\beta)}{2 \cdot \sin(\beta)} \right\} \cdot \frac{\sin(\beta+\varphi) \cdot \sin(\alpha+\delta)}{\sin(\alpha+\beta+\delta+\varphi)}$$

$$F_v = \rho_s \cdot g \cdot h_i^2 \cdot w \cdot \lambda_{VD}$$

With : **(5-14)**

$$\lambda_{VD} = \frac{\sin(\alpha+\beta)}{\sin(\beta)} \cdot \left\{ \frac{\left(h_b / h_i + \sin(\alpha)\right)}{\sin(\alpha)} + \frac{\cos(\alpha+\beta)}{2 \cdot \sin(\beta)} \right\} \cdot \frac{\sin(\beta+\varphi) \cdot \cos(\alpha+\delta)}{\sin(\alpha+\beta+\delta+\varphi)}$$

Figure 5-6, Figure 5-7 and Figure 5-8 show the shear angle **β**, the horizontal cutting force coefficient **λ_{HD}** and the vertical cutting force coefficient **λ_{VD}**. It should be mentioned here that choosing another shape of the layer cut will result in different values for the shear angle and the cutting force coefficients.

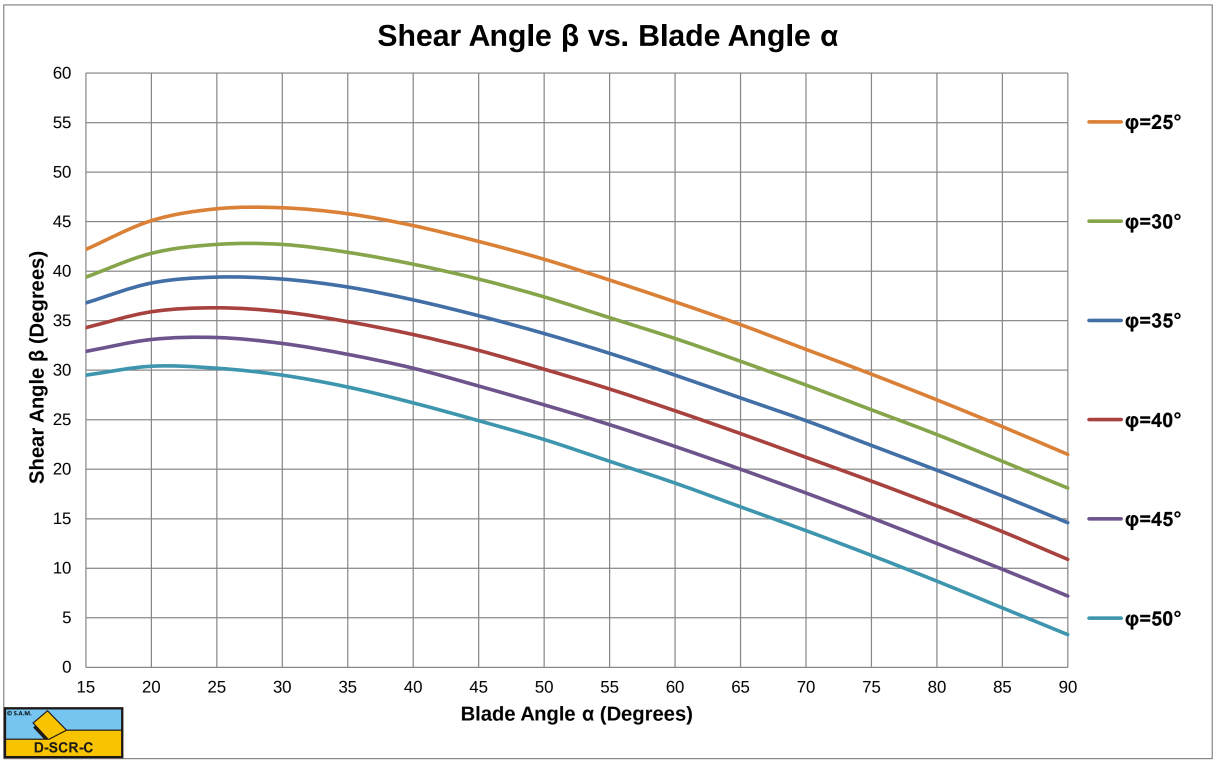

Figure 5-6: The shear angle β as a function of the blade angle α for h_b/h_i=2.

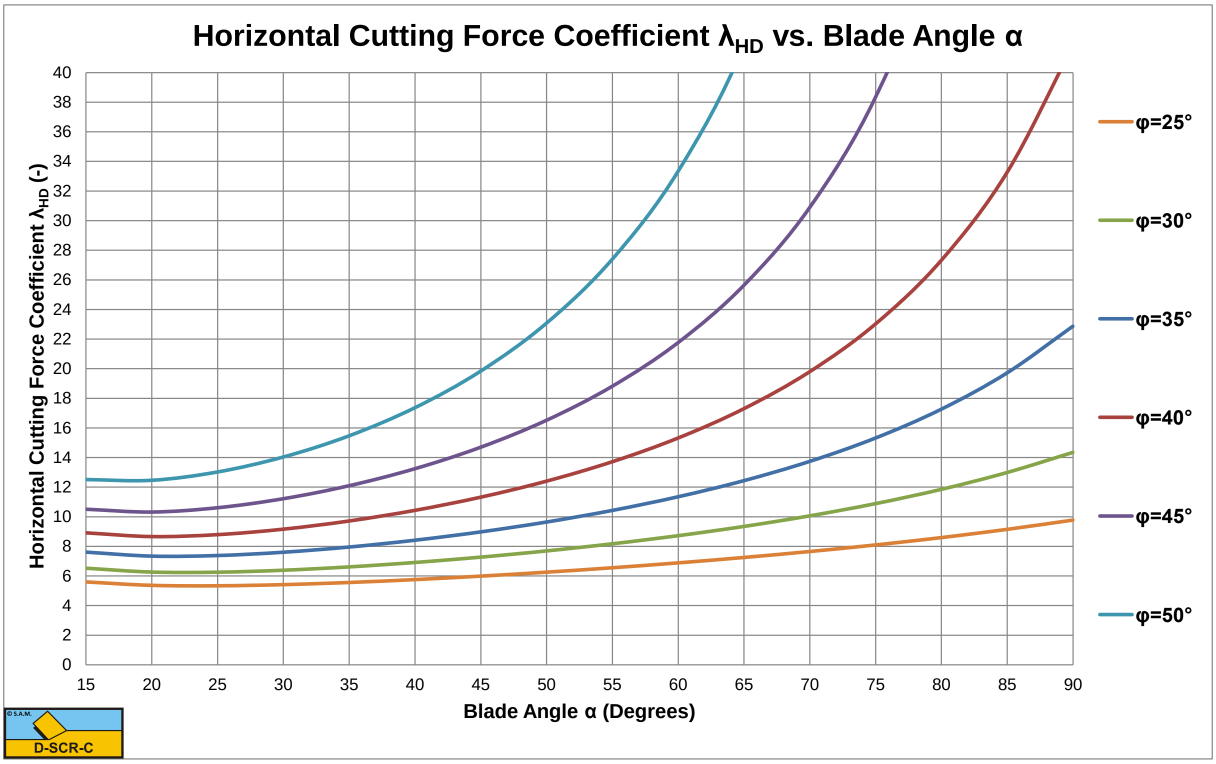

Figure 5-7: The horizontal cutting force coefficient λ_{HD} as a function of the blade angle α for $h_b/h_i=2$.

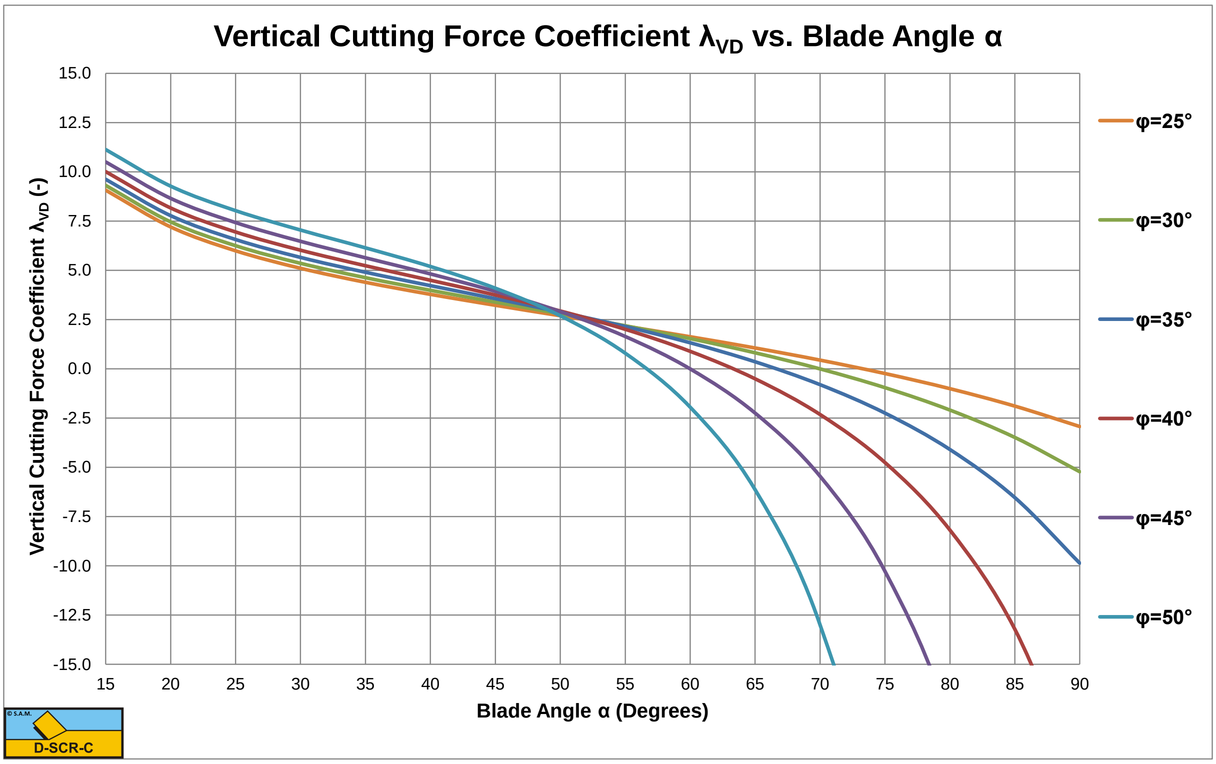

Figure 5-8: The vertical cutting force coefficient λ_{VD} as a function of the blade angle α for $h_b/h_i=2$.

For blade angles up to 60°, there is not much influence of the angle of internal friction on the vertical force. The horizontal force and the shear angle however depend strongly on the angle of internal friction. At large blade angles, the horizontal force becomes very large, while the vertical force changes sign and becomes very large negative (upwards directed). The shear angle decreases with increasing blade angle and angle of internal friction.

At large blade angles nature will look for an alternative mechanism, the wedge mechanism, which is discussed in later chapters.

5.4. An Alternative Shape of the Layer Cut.

The shape of the layer cut will most probably be different with dry sand cutting compared to saturated sand cutting or clay and rock cutting. First of all with dry sand cutting the cutting forces are determined by the weight of the layer cut while with the other types of soil the weight can be neglected. Secondly in dry sand there are no forces to keep the layer cut together, so the sand will move down if possible and the maximum slopes will be under the angle of natural repose φ_{nr} (usually about 30°). Figure 5-9 shows this alternative shape of the layer cut. The line **D-E-F** is the top of the sand, where the two marked areas have the same cross section.

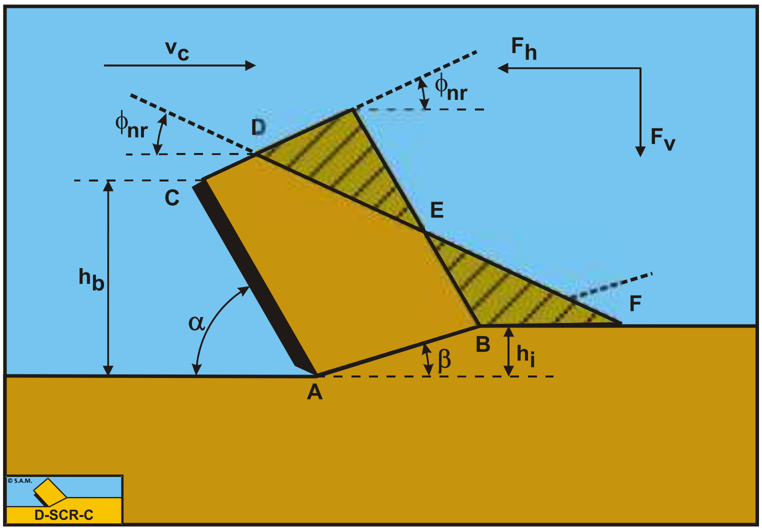

Figure 5-9: The alternative shape of the layer cut.

The gravitational force (weight dry) follows, based on Figure 5-9, from:

$$G = \rho_s \cdot g \cdot h_i \cdot w \cdot \frac{\sin(\alpha+\beta)}{\sin(\beta)} \cdot \left\{ \frac{h_b}{\sin(\alpha)} + \frac{h_i \cdot \cos(\alpha+\beta)}{2 \cdot \sin(\beta)} - \frac{h_i \cdot \sin(\alpha+\beta)}{2 \cdot \sin(\beta)} \cdot \frac{\cos\left(\alpha+\varphi_{nr}\right)}{\sin\left(\alpha+\varphi_{nr}\right)} \right\} \tag{5-15}$$

Based on the weight only of the soil, the forces can now be expressed as:

$$F_h = \rho_s \cdot g \cdot h_i^2 \cdot w \cdot \lambda_{HD}$$

$$\text{With:} \quad \lambda_{HD} = \frac{\sin(\alpha+\beta)}{\sin(\beta)} \cdot \frac{\sin(\beta+\varphi) \cdot \sin(\alpha+\delta)}{\sin(\alpha+\beta+\delta+\varphi)} \cdot \left\{ \frac{h_b / h_i}{\sin(\alpha)} + \frac{\cos(\alpha+\beta)}{2 \cdot \sin(\beta)} - \frac{\sin(\alpha+\beta)}{2 \cdot \sin(\beta)} \cdot \frac{\cos\left(\alpha+\varphi_{nr}\right)}{\sin\left(\alpha+\varphi_{nr}\right)} \right\} \tag{5-16}$$

$$F_v = \rho_s \cdot g \cdot h_i^2 \cdot w \cdot \lambda_{VD}$$

$$\text{With:} \quad \lambda_{VD} = \frac{\sin(\alpha+\beta)}{\sin(\beta)} \cdot \frac{\sin(\beta+\varphi)\cdot\cos(\alpha+\delta)}{\sin(\alpha+\beta+\delta+\varphi)} \tag{5-17}$$

$$\cdot\left\{\frac{h_b/h_i}{\sin(\alpha)} + \frac{\cos(\alpha+\beta)}{2\cdot\sin(\beta)} - \frac{\sin(\alpha+\beta)}{2\cdot\sin(\beta)} \cdot \frac{\cos\left(\alpha+\varphi_{nr}\right)}{\sin\left(\alpha+\varphi_{nr}\right)}\right\}$$

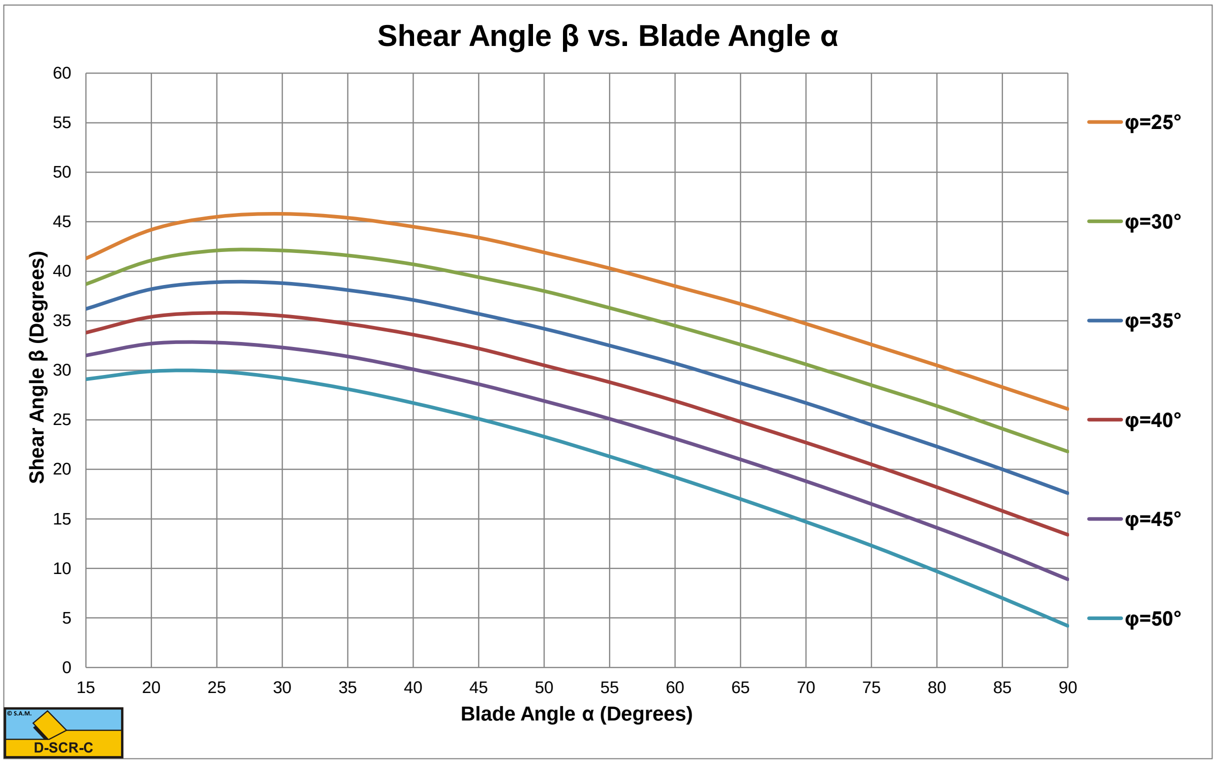

Figure 5-10: The shear angle β as a function of the blade angle α for h_b/h_i=2.

Figure 5-10, Figure 5-11 and Figure 5-12 show the shear angle and the cutting force coefficients for the alternative shape of the layer cut. The difference with the standard configuration is small. Other configurations may exist, but no big differences are expected. The model for dry sand or gravel can also be used for saturated sand, if the cutting process is completely drained and there are no pore vacuum pressures. This only occurs if the permeability is very high, which could be the case in gravel. Of course the dry density of the sand or gravel has to be replaced by the submerged density of the sand or gravel, which is usually close to unity.

The shapes of the curves between the standard configuration and the alternative configuration are very similar. The shear angle first increases with an increasing blade angle up to a maximum after which the shear angle decreases with a further increasing shear angle. The shear angle also decreases with an increasing angle of internal friction. It should be noted here that the external friction angle is assumed to be 2/3 of the internal friction angle.

The cutting forces become very high at large blade angles (close to 90°). Nature will find an alternative cutting mechanism in this case which has been identified as the wedge mechanism. At which blade angle the wedge mechanism will start to occur depends on the internal and external friction angles, but up to a blade angle of 60° the model as described here can be applied. See Chapter 11: A Wedge in Dry Sand Cutting. for detailed information on the wedge mechanism.

5.5. The Influence of Inertial Forces.

In the previous chapter the shear angle and the cutting forces are given for the influence of the weight only. This will be appropriate for very small cutting velocities, but the question is of course; what is a very low cutting speed.

Analyzing the equations for the influence of the weight (gravity) and the influence of the inertial forces shows a significant difference. The gravitational forces are proportional to the density of the soil ρ_s, the gravitational constant g, the thickness of the layer cut h_i squared and the width of the blade w. The inertial forces are proportional to the density of the soil ρ_s, the cutting velocity v_c squared, the thickness of the layer cut h_i and the width of the blade w. This implies that the ratio between these two forces does not only depends on the geometry, but even stronger on the layer thickness h_i and the cutting velocity v_c. The thicker the layer cut, the higher the influence of gravity and the higher the cutting velocity, the higher the influence of inertia. One cannot say simply the higher the cutting velocity the higher the influence of inertia.

$$\text{Gravitation}: \quad F \propto \rho_s \cdot g \cdot h_i^2 \cdot w \tag{5-18}$$

$$\text{Inertia}: \quad F \propto \rho_s \cdot v_c^2 \cdot h_i \cdot w \tag{5-19}$$

The contribution of the inertial forces is determined by the following dimensionless parameter:

$$\lambda_i = \frac{v_c^2}{g \cdot h_i} \tag{5-20}$$

In dredging a layer thickness of the magnitude of centimeters is common, while for a bulldozer a layer thickness of a magnitude of a meter is not strange. At the same cutting velocity, the relative influence of inertial forces will differ between dredging applications and the operation of bulldozers. If inertial forces dominate the cutting process, the cutting forces can be expressed as:

$$\begin{gathered} F_h = \rho_s \cdot v_c^2 \cdot h_i \cdot w \cdot \lambda_{HI} \\ \text{With}: \quad \lambda_{HI} = \frac{\sin(\alpha)}{\sin(\alpha+\beta)} \cdot \frac{\cos(\varphi)}{\sin(\alpha+\beta+\delta+\varphi)} \cdot \sin(\alpha+\delta) \end{gathered} \tag{5-21}$$

$$\begin{gathered} F_v = \rho_s \cdot v_c^2 \cdot h_i \cdot w \cdot \lambda_{VI} \\ \text{With}: \quad \lambda_{VI} = \frac{\sin(\alpha)}{\sin(\alpha+\beta)} \cdot \frac{\cos(\varphi)}{\sin(\alpha+\beta+\delta+\varphi)} \cdot \cos(\alpha+\delta) \end{gathered} \tag{5-22}$$

These equations are derived from equations (5-6), (5-7), (5-9) and (5-10). The shear angle β can be derived analytically for the inertial forces, giving:

$$\beta = \frac{\pi}{2} - \frac{2 \cdot \alpha + \delta + \varphi}{2} \tag{5-23}$$

Figure 5-13 shows the percentage of the contribution of the inertial forces to the horizontal cutting force for a layer thickness h_i of 1.0 m at a cutting velocity of 0.5 m/sec, giving λ_i**=0.025**. Figure 5-14 shows the percentage of the contribution of the inertial forces to the horizontal cutting force for a layer thickness h_i of 0.1 m at a cutting velocity of 15.7 m/sec, giving λ_i**=250**.

Table 5-1 shows the inertial effect for the dimensionless inertial effect parameter λ_i ranging from 0.025 to 250. The percentage contribution of the inertial effect on the horizontal force is given as well as the shear angle, both horizontal and vertical cutting force coefficients based on equations (5-21) and (5-22) and both horizontal and vertical cutting force coefficients based on equations (5-13) and (5-14) for the case where the blade height h_b equals the layer thickness h_i. The table shows that the inertial effect can be neglected at very small values of the dimensionless inertial effect parameter λ_i, while at large values the gravitational effect can be neglected. The shear angle β decreases with an increasing dimensionless inertial effect parameter λ_i. Since the inertial forces are not influenced by the blade height h_b, the cutting forces are not dependent on the blade height at high cutting velocities. At low cutting velocities there will be an effect of the blade height.

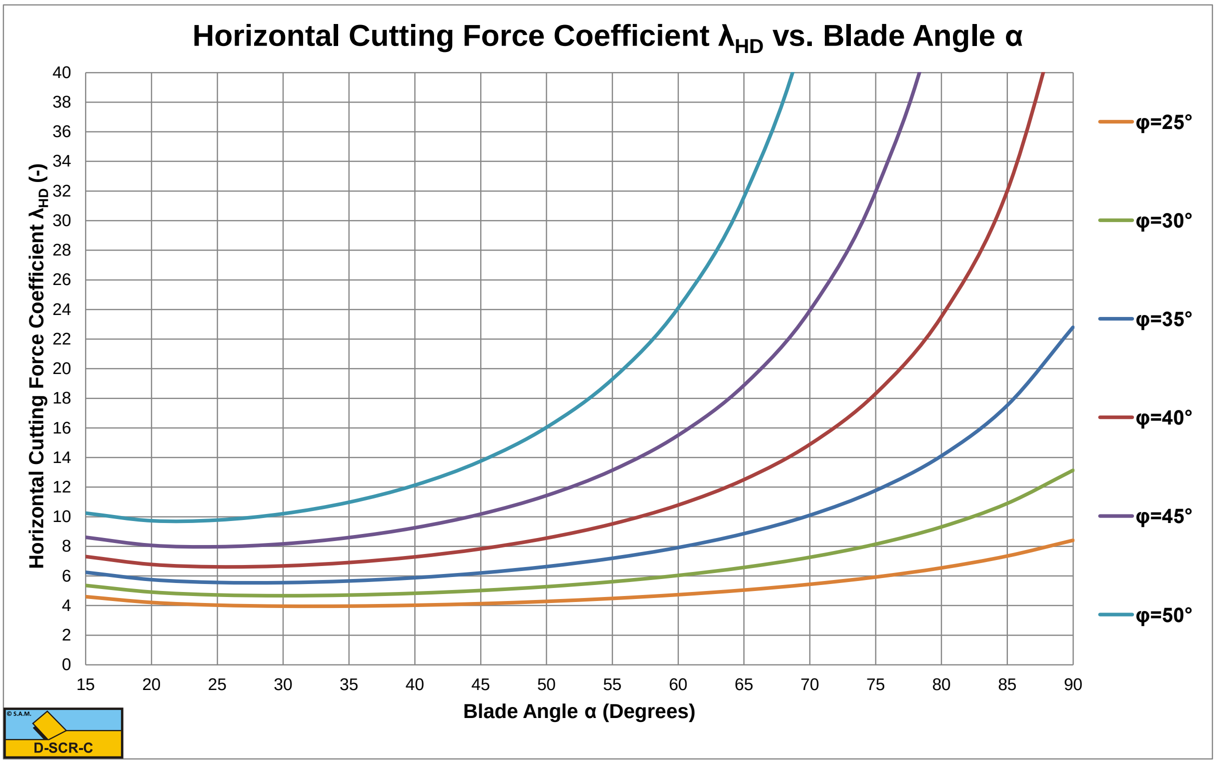

Figure 5-11: The horizontal cutting force coefficient λ_{HD} as a function of the blade angle α for h_b/h_i=2.

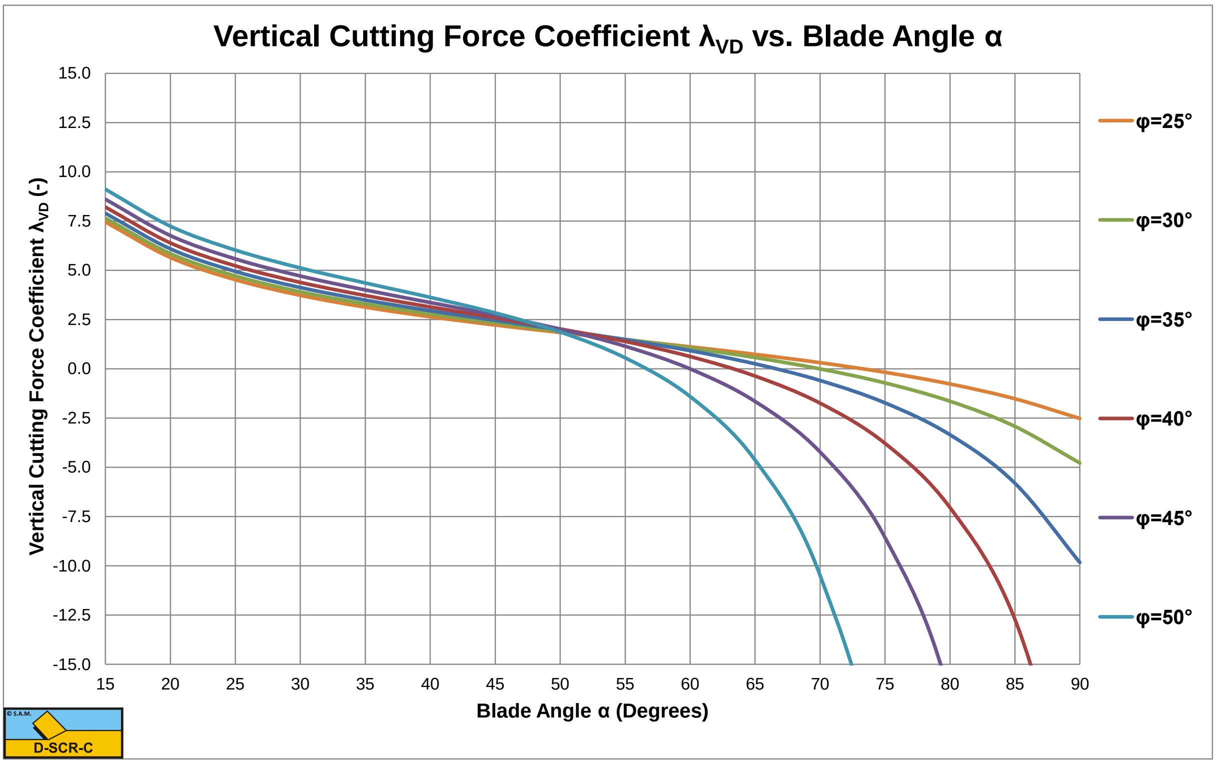

Figure 5-12: The vertical cutting force coefficient λ_{VD} as a function of the blade angle α for h_b/h_i=2.

The contribution of the inertial effect only depends on the dimensionless inertial effect parameter $\boldsymbol{\lambda_i}$ and not on the cutting velocity or layer thickness individually. The dimensionless inertial effect parameter $\boldsymbol{\lambda_i}$ in fact is a Froude number of the cutting process. Figure 5-15, Figure 5-16 and Figure 5-17 show the shear angle and both horizontal and vertical cutting force coefficients at very high values of the dimensionless inertial effect parameter $\boldsymbol{\lambda_i}$ ($\boldsymbol{\lambda_i}$=**250**). The shear angles are considerably smaller than in the case where inertial forces can be neglected. Also in the case where the inertial forces dominate, the cutting forces become very high at large blade angles (close to 90°). Nature will find an alternative cutting mechanism in this case which has been identified as the wedge mechanism. At which blade angle the wedge mechanism will start to occur depends on the internal and external friction angles, but up to a blade angle of 60° the model as described here can be applied. See Chapter 11: A Wedge in Dry SandCutting for detailed information on the wedge mechanism.

Figure 5-13: The percentage inertial force for a layer thickness h_i=1.0 m, blade height h_b=1.0 m and a cutting velocity v_c=0.5 m/sec.

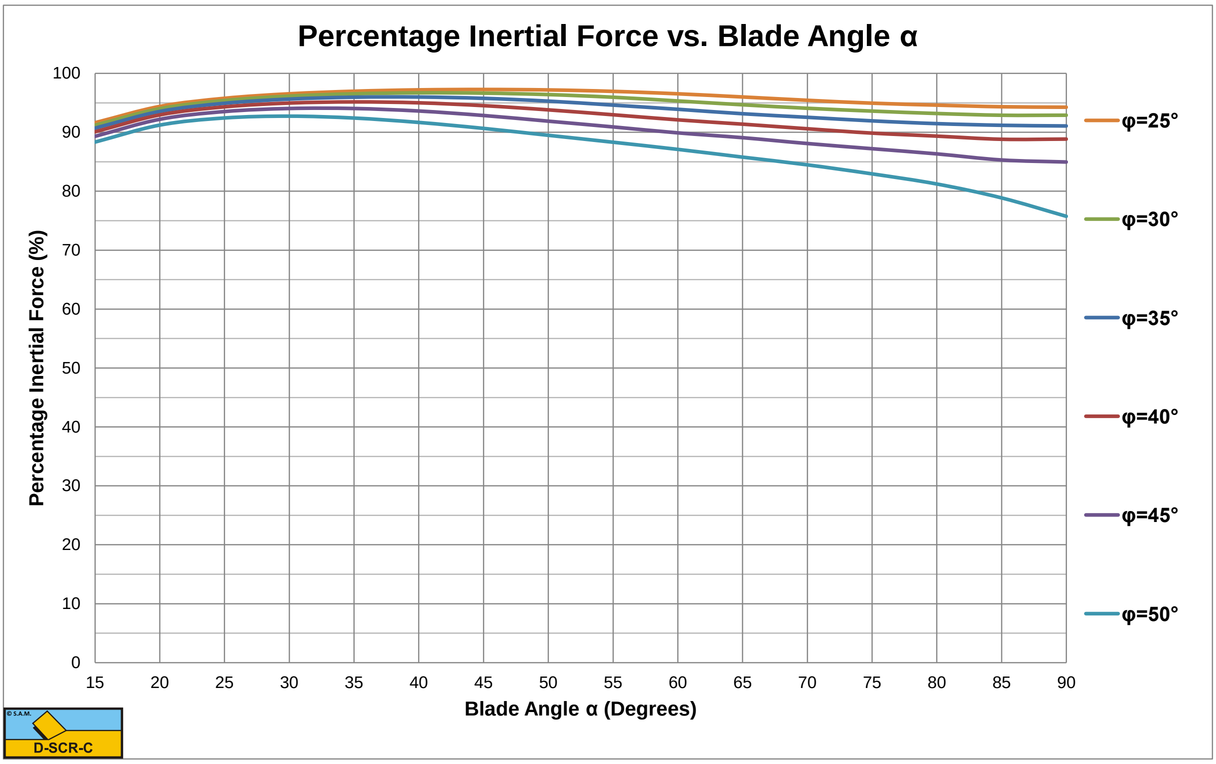

Figure 5-14: The percentage inertial force for a layer thickness h_i=1.0 m, blade height h_b=1.0 m and a cutting velocity v_c=15.7 m/sec.

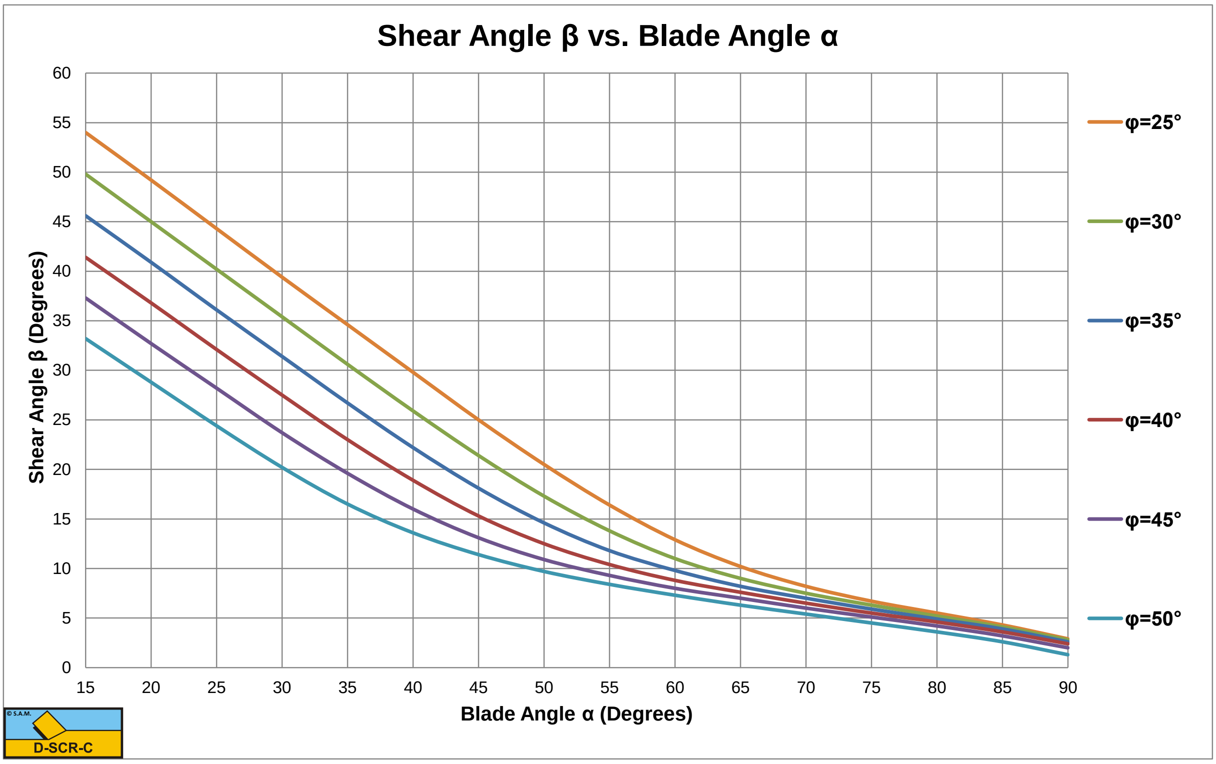

Figure 5-15: The shear angle β, including the effect of inertial forces.

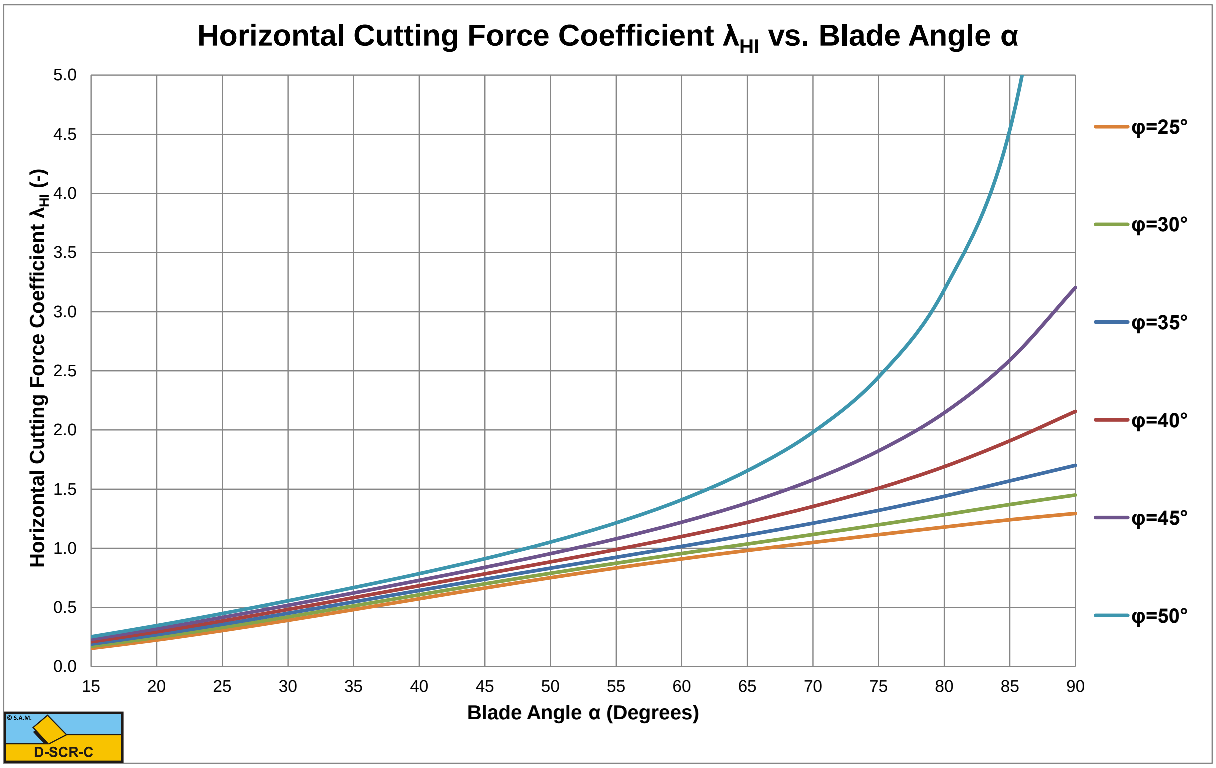

Figure 5-16: The horizontal cutting force coefficient λ_{HI}.

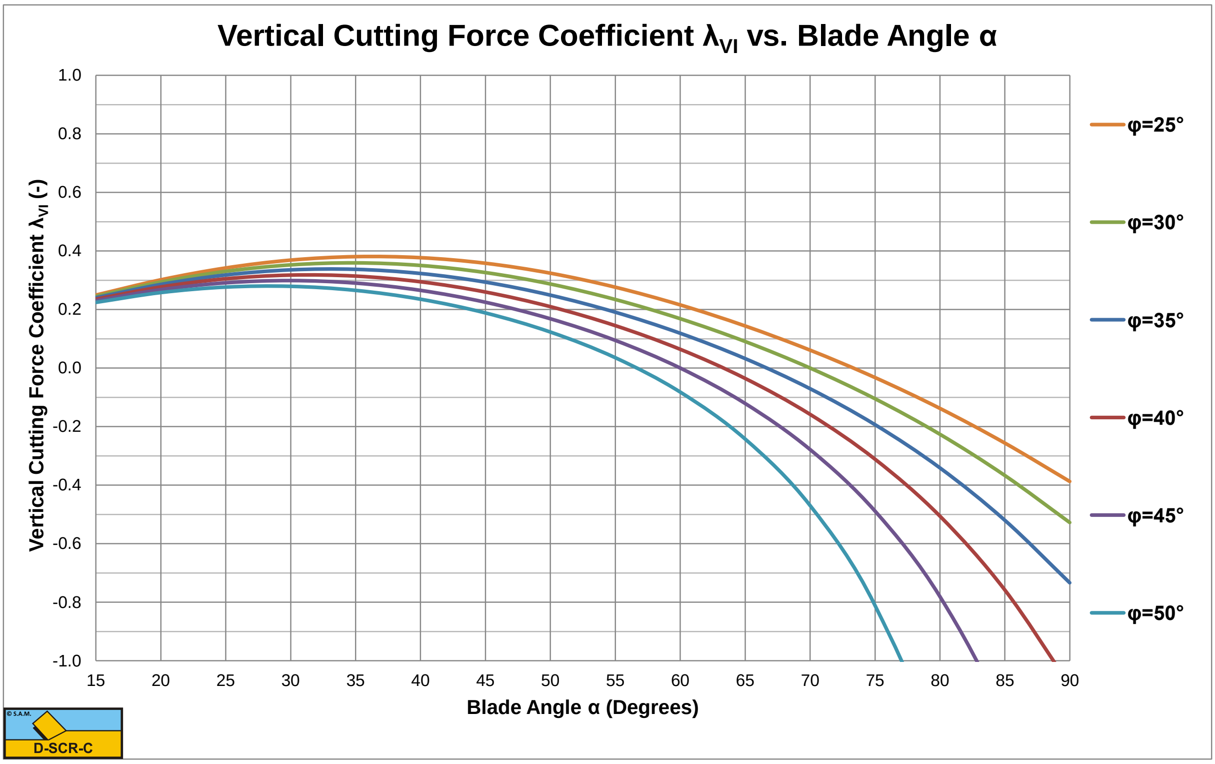

Figure 5-17: The vertical cutting force coefficient λ_{VI}.

Table 5-1: The inertial effect.

λ_i	%	β	λ_{HI}	λ_{VI}	λ_{HD}	λ_{HV}
0.025	0.74	31.6	187.68	27.49	4.78	0.70
0.250	6.65	30.8	20.26	2.97	5.09	0.75
2.500	37.69	26.0	3.12	0.46	7.95	1.16
25.00	78.98	16.9	1.25	0.18	31.40	4.60
250.0	94.98	9.6	0.96	0.14	245.36	35.94

5.6. Specific Energy.

In the dredging industry, the specific cutting energy is described as: The amount of energy, that has to be added to a volume unit of soil (e.g. sand, clay or rock) to excavate the soil. The dimension of the specific cutting energy is: kN/m² or kPa for sand and clay, while for rock often MN/m^2 or MPa is used.

For the case as described above, cutting with a straight blade, the specific cutting energy can be written as:

$$\mathbf{E_{sp}=\frac{P_c}{Q_c}=\frac{F_h\cdot v_c}{h_i\cdot w\cdot v_c}=\frac{F_h}{h_i\cdot w}} \tag{5-24}$$

At low cutting velocities this gives for the specific cutting energy:

$$\mathbf{E_{sp}=\frac{P_c}{Q_c}=\frac{F_h\cdot v_c}{h_i\cdot w\cdot v_c}=\frac{\rho_s\cdot g\cdot h_i^2\cdot w\cdot\lambda_{HD}}{h_i\cdot w}=\rho_s\cdot g\cdot h_i\cdot\lambda_{HD}} \tag{5-25}$$

At high cutting velocities this gives for the specific cutting energy:

$$\mathbf{E_{sp}=\frac{P_c}{Q_c}=\frac{F_h\cdot v_c}{h_i\cdot w\cdot v_c}=\frac{\rho_s\cdot v_c^2\cdot h_i\cdot w\cdot\lambda_{HI}}{h_i\cdot w}=\rho_s\cdot v_c^2\cdot\lambda_{HI}} \tag{5-26}$$

At medium cutting velocities a weighted average of both has to be used.

5.7. Usage of the Model for Dry Sand.

To use the model for dry sand, first the dry density $\boldsymbol{\rho_s}$ of the sand and the internal friction angle $\boldsymbol{\varphi}$ have to be known. The external friction angle $\boldsymbol{\delta}$ is assumed to be 2/3 of the internal friction angle $\boldsymbol{\varphi}$. Secondly the geometry of the blade, the cutting angle $\boldsymbol{\alpha}$, the blade height $\mathbf{h_b}$ and the blade width $\mathbf{w}$ have to be chosen. Thirdly the operational parameters, the layer thickness $\mathbf{h_i}$ and the cutting velocity $\mathbf{v_c}$ have to be chosen. Based on the dimensionless inertial effect parameter $\boldsymbol{\lambda_i}$ the fraction of the contribution of the inertial force to the total horizontal force can be determined with:

$$\mathbf{f_i=\frac{1}{1+e^{-2\cdot\log(\lambda_i/5)}}} \tag{5-27}$$

This equation is empirically derived for a 60° blade and a 40° internal friction angle and may differ for other values of the blade angle and the internal friction angle.

$$\begin{aligned}\mathbf{F_h}&\mathbf{=\left(1-f_i\right)\cdot\rho_s\cdot g\cdot h_i^2\cdot w\cdot\lambda_{HD}+f_i\cdot\rho_s\cdot v_c^2\cdot h_i\cdot w\cdot\lambda_{HI}}\\&\mathbf{=\rho_s\cdot g\cdot h_i^2\cdot w\cdot\left(\left(1-f_i\right)\cdot\lambda_{HD}+f_i\cdot\lambda_i\cdot\lambda_{HI}\right)}\end{aligned} \tag{5-28}$$

$$\begin{aligned}\mathbf{F_v}&\mathbf{=\left(1-f_i\right)\cdot\rho_s\cdot g\cdot h_i^2\cdot w\cdot\lambda_{VD}+f_i\cdot\rho_s\cdot v_c^2\cdot h_i\cdot w\cdot\lambda_{VI}}\\&\mathbf{=\rho_s\cdot g\cdot h_i^2\cdot w\cdot\left(\left(1-f_i\right)\cdot\lambda_{VD}+f_i\cdot\lambda_i\cdot\lambda_{VI}\right)}\end{aligned} \tag{5-29}$$

The specific energy is now:

$$\mathbf{E_{sp}=\rho_s\cdot g\cdot h_i\cdot\left(\left(1-f_i\right)\cdot\lambda_{HD}+f_i\cdot\lambda_i\cdot\lambda_{HI}\right)} \tag{5-30}$$

In the case of saturated sand or gravel with a very high permeability (in general coarse gravel), the equations change slightly, since the weight of the soil cut is determined by the submerged weight, while the mass of the soil cut also includes the mass of the pore water. The wet density of saturated sand or gravel is usually close to $\boldsymbol{\rho_s=2}$ **ton/m³**, while the submerged weight is close to $\boldsymbol{(\rho_s-\rho_w)\cdot g=10}$ **kN/m³** (a porosity of 40% and a quarts density of $\boldsymbol{\rho_q=2.65}$ **ton/m³** are assumed). This will double the contribution of the inertial forces as determined by the following dimensionless parameter:

$$\lambda_i=\frac{v_c^2}{g\cdot h_i}\cdot\frac{(\rho_s-\rho_w)}{\rho_s}\approx\frac{2\cdot v_c^2}{g\cdot h_i} \tag{5-31}$$

Using this dimensionless inertial effect parameter $\boldsymbol{\lambda_i}$, the cutting forces can be determined by:

$$F_h=(\rho_s-\rho_w)\cdot g\cdot h_i^2\cdot w\cdot\left((1-f_i)\cdot\lambda_{HD}+f_i\cdot\lambda_i\cdot\lambda_{HI}\right) \tag{5-32}$$

$$F_v=(\rho_s-\rho_w)\cdot g\cdot h_i^2\cdot w\cdot\left((1-f_i)\cdot\lambda_{VD}+f_i\cdot\lambda_i\cdot\lambda_{VI}\right) \tag{5-33}$$

The specific energy is now:

$$E_{sp}=(\rho_s-\rho_w)\cdot g\cdot h_i\cdot\left((1-f_i)\cdot\lambda_{HD}+f_i\cdot\lambda_i\cdot\lambda_{HI}\right) \tag{5-34}$$

Under water at high cutting velocities there may also be a drag force which has not been taken into account here.

The horizontal cutting force coefficients $\boldsymbol{\lambda_{HD}}$ and $\boldsymbol{\lambda_{HI}}$ can be found in Figure 5-11 and Figure 5-16. The vertical cutting force coefficients $\boldsymbol{\lambda_{VD}}$ and $\boldsymbol{\lambda_{VI}}$ can be found in Figure 5-12 and Figure 5-17.

The cutting forces calculated are for a plane strain 2D cutting process, so 3D side effects are not included.

Figure 5-18: A dredging wheel used in the German braunkohl mines (www.wikiwand.com).

5.8. Experiments in Dry Sand.

5.8.1. Hatamura & Chijiiwa (1977B).

Hatamura & Chijiiwa (1977B) carried out very good and extensive research into the cutting of sand, clay and loam. They did not only measure the cutting forces, but also the stresses on the blade, the shear angles and velocity distributions in the sand cut. For their experiments they used a blade with a width of **w=0.33 m**, a length of **L=0.2 m**, blade angles of **α=30°, 45°, 60°, 75° and 90°**, layer thicknesses of **h_i=0.05 m, 0.10 m and 0.15 m** and cutting velocities of **v_c=0.05 m/sec, 0.10 m/sec and 0.14 m/sec**. The sand they used had an internal friction angle **φ=38°** and an external friction angle **δ=26.6°** (almost 2/3·φ). The dry density of the sand was **ρ_s=1.46 ton/m^3**.

Figure 5-19 shows the shear angles measured versus the shear angles calculated with the current model based on the minimum cutting energy criterion. In general there is a good match, especially for the experiments with a layer thickness of 0.1 m. For the experiments with a layer thickness of 0.05 m the theory overestimates the experimental value while for the layer thickness of 0.15 m, the theory underestimates the experimental value. Now the number of experiments is very limited and more experiments are required to get a better validation.
Figure 5-20 shows the total cutting force measured versus the total cutting force calculated. The total cutting force is the vectorial sum of the horizontal and the vertical cutting force. Hatamura & Chijiiwa (1977B) did not give the horizontal and vertical cutting forces, but the total cutting force and the direction of this force. For blade angles up to 60° there is a good match between experiments and theory. However at larger blade angles the theory overestimates the total cutting force strongly. This is most probably caused by the occurrence of a wedge in front of the blade at large blade angles. The occurrence of a wedge will strongly reduce the cutting forces in that case. See also Chapter 11: A Wedge in Dry Sand Cutting.

Figure 5-21 shows the direction of the total cutting force, measured versus calculated. There is an almost perfect match, also for the large blade angles where the forces are overestimated.

The conclusion is that the model developed here matches the experiments well for small blade angles, both in magnitude and direction, for large blade angles the wedge theory has to be applied. Hatamura & Chijiiwa (1977B) also carried out some tests with different cutting velocities, but the velocities were so small that there was hardly any inertial effect.

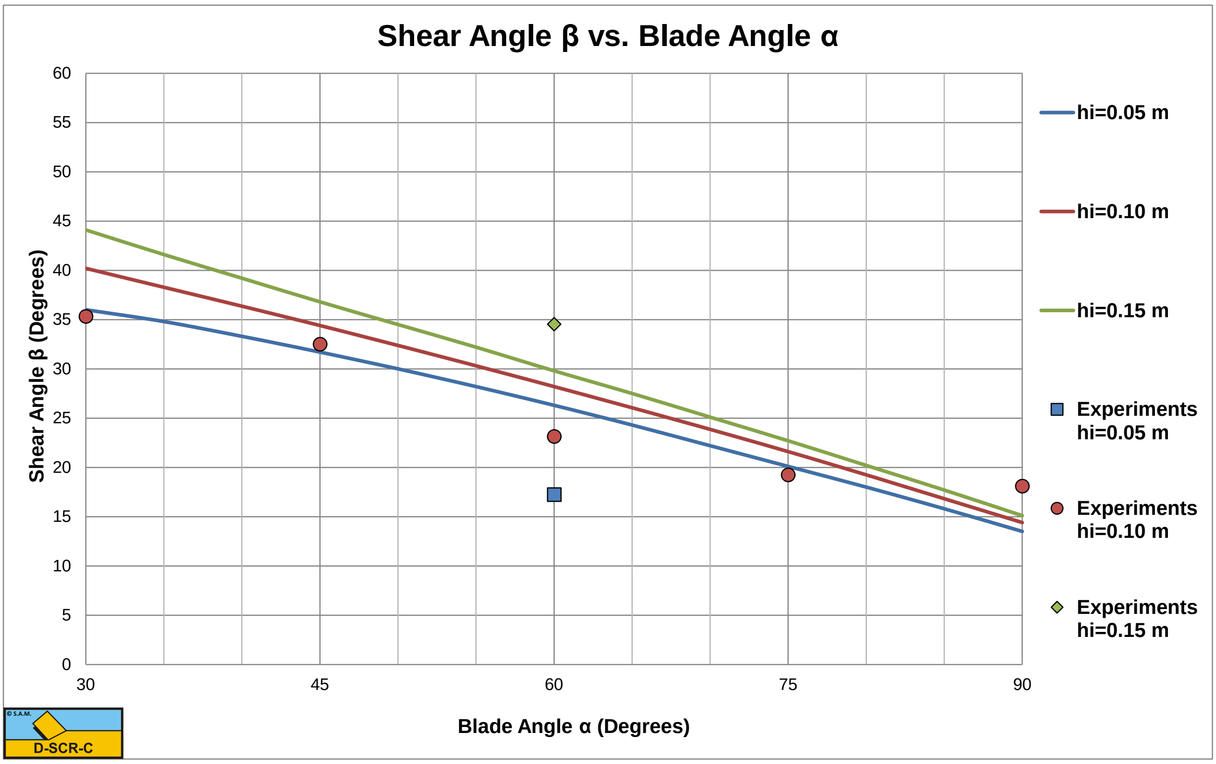

Figure 5-19: The shear angle versus the blade angle.

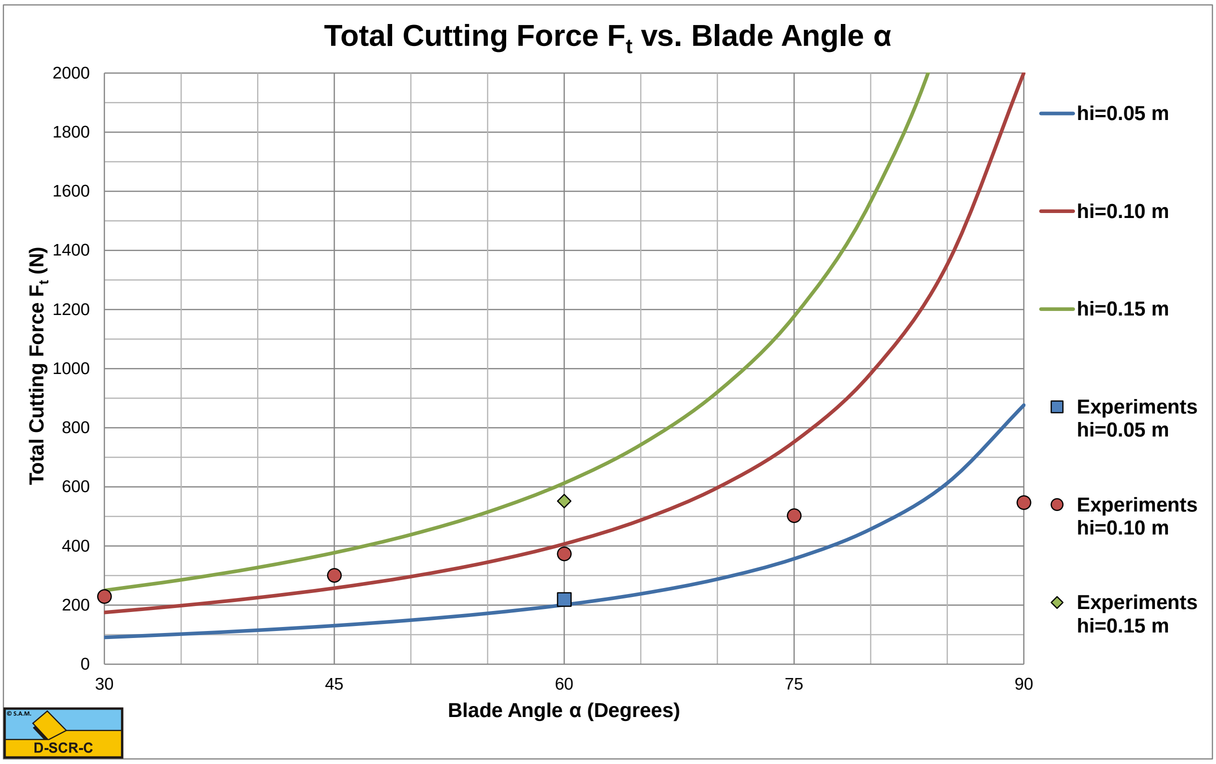

Figure 5-20: The total cutting force versus the blade angle.

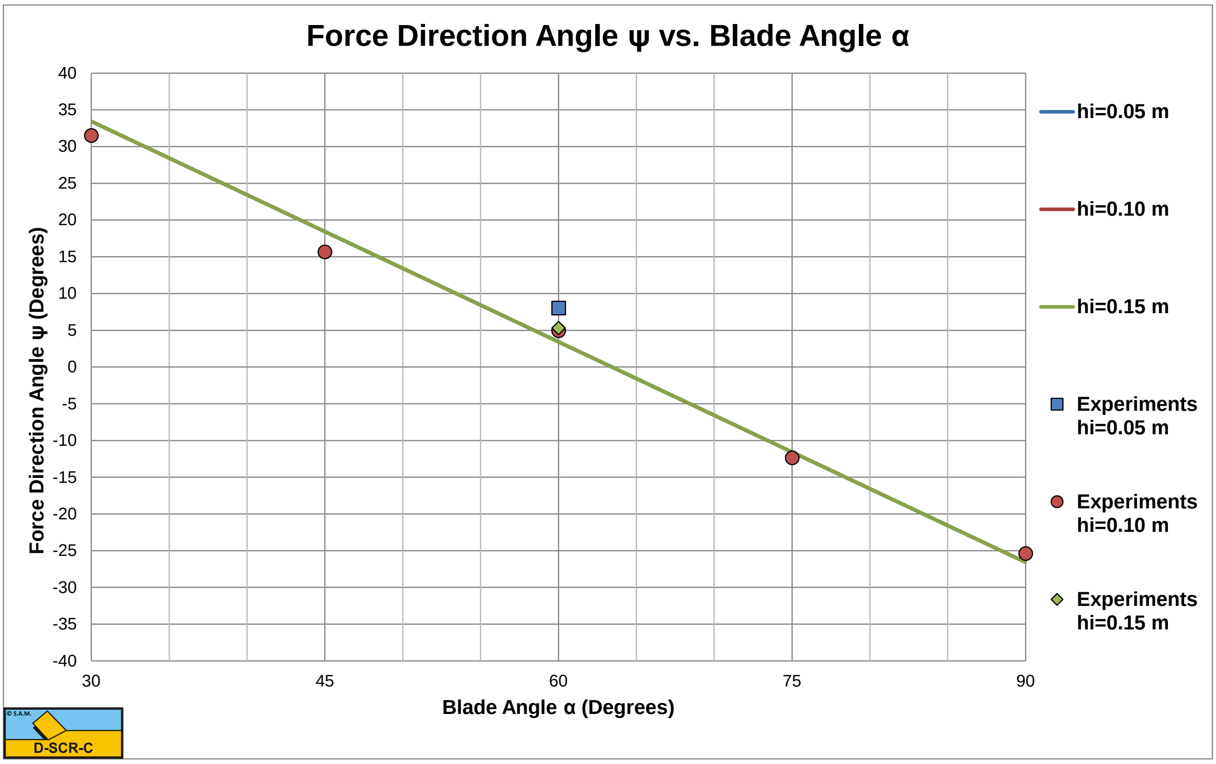

Figure 5-21: The direction of the total cutting force versus the blade angle.

5.8.2. Wismer & Luth (1972B).

Wismer & Luth (1972B) investigated rate effects in soil cutting in dry sand, clay and loam. They found that in dry quarts sand the cutting forces consist of two components, a static component and a dynamic component. The static component depends on the cutting geometry, like the blade angle and the blade height. The static component also depends on the layer thickness and the soil mechanical parameters, in this case the dry soil density, the internal friction angle and the external friction angle. The dynamic component also depends on the cutting geometry and the soil mechanical properties, but also on the cutting velocity squared. In fact their findings match equations (5-6), (5-7), (5-9) and (5-10), but they use a different formulation for equation (5-8) or (5-15), the cross section of the layer cut. One of the reasons for the latter is that they use a fixed shear angle of **β=45-φ/2** resulting in a different weight of the soil cut compared with the theory described here. In the current theory the shear angle depends on the geometry, the operational parameters and the soil mechanical parameters. The test carried out by Wismer & Luth (1972B) were with an α=30° blade with a blade height **h_b=0.0969 m** and a width of **w=0.1262 m**. The layer thickness was **h_i=0.098 m**. In order to validate the rate effect, first they calibrated the soil mechanical properties, so the cutting forces at zero cutting velocity would match the experiments. This requires an internal friction angle **φ=41°** and an external friction angle **δ=27.3°** (**δ=2/3·φ**), to have the correct ratio between the horizontal and the vertical force. Further, the theoretical cutting forces have to be multiplied by a factor 1.23 in order to match quantitatively. This may be the result of 3D side effects, since the blade used was not very wide compared to the layer thickness and/or the cross section of the layer cut was larger than the here assumed cross section. Both explanations seem to be reasonable. After applying these corrections and calibrations, the cutting forces are determined and plotted in Figure 5-22. The correlation between the theoretical lines and the measured data points is remarkable, resulting in the conclusion that the approach of Wismer & Luth (1972B) to quantify the rate effects for dry sand is a good approach.

Wismer & Luth (1972B) used a fixed shear angle of **β=45-φ/2** resulting in **β=24.5°**. The values found here, based on the minimum energy principle range from **β=38.8°** at zero cutting velocity to **β=32.2°** at a cutting velocity **v_c=3 m/sec**, taking into account the effect of the inertial forces on the shear angle.

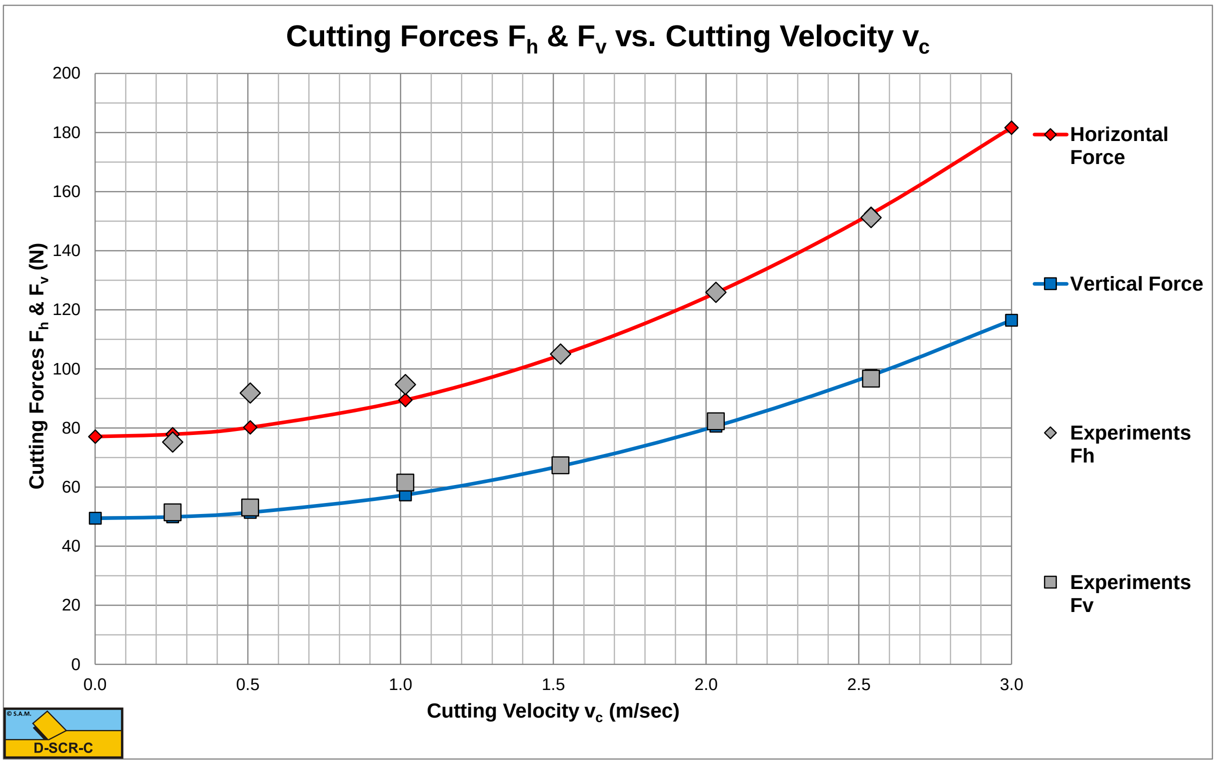

Figure 5-22: Cutting forces versus cutting velocity.

5.9. Nomenclature.

F_h	Horizontal cutting force	kN
F_v	Vertical cutting force	kN
g	Gravitational constant (9.81)	m/s^2
G	Gravitational force on the layer cut	kN
h_i	Initial thickness of layer cut	m
h_b	Height of blade	m
I	Inertial force on the shear plane	kN
K_1	Grain force on the shear plane	kN
K_2	Grain force on the blade or the front of the wedge	kN
N_1	Normal force on the shear plane	kN
N_2	Normal force on the blade or the front of the wedge	kN
Pc	Cutting power	kW
S_1	Shear force due to friction on the shear plane	kN
S_2	Shear force due to friction on the blade or the front of the wedge	kN
v_c	Cutting velocity component perpendicular to the blade	m/s
w	Width of blade	m
W_1	Force resulting from pore under pressure on the shear plane	kN
W_2	Force resulting from pore under pressure on the blade or on the front of the wedge	kN
α	Cutting angle blade	rad
β	Shear angle	rad
ϕ	Angle of internal friction	rad
δ	External friction angle	rad
ρ_s	Density of the soil	ton/m^3
ρ_w	Density water	ton/m^3

Figure 5-23: A bulldozer pushing sand (commons.wikimedia.org).

Chapter 6: Saturated Sand Cutting.

6.1. Introduction.

Although calculation models for the determination of the cutting forces for dry soil, based on agriculture, were available for a long time (Hettiaratchi & Reece (1965), (1966), (1967A), (1967B), (1974), (1975) and Hatamura & Chijiiwa (1975), (1976A), (1976B), (1977A) and (1977B)) it is only since the seventies and the eighties that the cutting process in saturated sand is extensively researched at the Delft Hydraulics Laboratory, at the Delft University of Technology and at the Mineraal Technologisch Instituut (MTI, IHC).

First the process is described, for a good understanding of the terminology used in the literature discussion.

From literature it is known that, during the cutting process, the sand increases in volume (see Figure 6-7). This increase in volume is accredited to dilatancy. Dilatancy is the change of the pore volume as a result of shear in the sand package. This increase of the pore volume has to be filled with water. The flowing water experiences a certain resistance, which causes sub-pressures in the pore water in the sand package. As a result the grain stresses increase and therefore the required cutting forces. The rate of the increase of the pore volume in the dilatancy zone, the volume strain rate, is proportional to the cutting velocity. If the volume strain rate is high, there is a chance that the pore pressure reaches the saturated water vapor pressure and cavitation occurs. A further increasing volume strain rate will not be able to cause a further decrease of the pore pressure. This also implies that, with a further increasing cutting velocity, the cutting forces cannot increase as a result of the dilatancy properties of the sand. The cutting forces can, however, still increase with an increasing cutting velocity as a result of the inertia forces and the flow resistance.
The cutting process can be subdivided in 5 areas in relation with the cutting forces:

- Very low cutting velocities, a quasi-static cutting process. The cutting forces are determined by the gravitation, cohesion and adhesion.
- The volume strain rate is high in relation to the permeability of the sand. The volume strain rate is however so small that inertia forces can be neglected. The cutting forces are dominated by the dilatancy properties of the sand.
- A transition region, with local cavitation. With an increasing volume strain rate, the cavitation area will increase so that the cutting forces increase slightly as a result of dilatancy.
- Cavitation occurs almost everywhere around and on the blade. The cutting forces do not increase anymore as a result of the dilatancy properties of the sand.
- Very high cutting velocities. The inertia forces part in the total cutting forces can no longer be neglected but form a substantial part.

Under normal conditions in dredging, the cutting process in sand will be governed by the effects of dilatation. Gravity, inertia, cohesion and adhesion will not play a role.

6.2. Definitions.

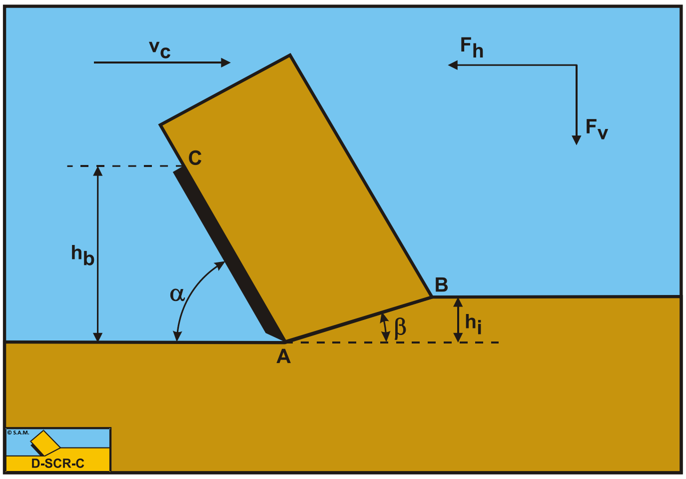

Figure 6-1: The cutting process definitions.

Definitions:

1. **A**: The blade tip.
2. **B**: End of the shear plane.
3. **C**: The blade top.
4. **A-B**: The shear plane.
5. **A-C**: The blade surface.
6. **h_b**: The height of the blade.
7. **h_i**: The thickness of the layer cut.
8. **v_c**: The cutting velocity.
9. **α**: The blade angle.
10. **β**: The shear angle.
11. **F_h**: The horizontal force, the arrow gives the positive direction.
12. **F_v**: The vertical force, the arrow gives the positive direction.

6.3. Cutting Theory Literature.

In the seventies extensive research is carried out on the forces that occur while cutting sand under water. A conclusive cutting theory has however not been published in this period. However qualitative relations have been derived by several researchers, with which the dependability of the cutting forces with the soil properties and the blade geometry are described (Joanknecht (1974), van Os (1977A), (1976) and (1977B)).

A process that has a lot of similarities with the cutting of sand as far as water pressure development is concerned, is the, with uniform velocity, forward moving breach. Meijer and van Os (1976) and Meijer (1981) and (1985) have transformed the storage equation for the, with the breach, forward moving coordinate system.

$$\left|\frac{\partial^2 p}{\partial x^2}\right| + \left|\frac{\partial^2 p}{\partial y^2}\right| = \frac{\rho_w \cdot g \cdot v_c}{k} \cdot \left|\frac{\partial e}{\partial x}\right| - \frac{\rho_w \cdot g}{k} \cdot \left|\frac{\partial e}{\partial t}\right| \tag{6-1}$$

In the case of a stationary process, the second term on the right is zero, resulting:

$$\left|\frac{\partial^2 p}{\partial x^2}\right| + \left|\frac{\partial^2 p}{\partial y^2}\right| = \frac{\rho_w \cdot g \cdot v_c}{k} \cdot \left|\frac{\partial e}{\partial x}\right| \tag{6-2}$$

Van Os (1977A), (1976) and (1977B) describes the basic principles of the cutting process, with special attention for the determination of the water sub-pressures and the cavitation. Van Os uses the non-transformed storage equation for the determination of the water sub-pressures.

$$\left|\frac{\partial^2 p}{\partial x^2}\right| + \left|\frac{\partial^2 p}{\partial y^2}\right| = \frac{\rho_w \cdot g}{k} \cdot \left|\frac{\partial e}{\partial t}\right| \tag{6-3}$$

The average volume strain rate has to be substituted in the term **∂e/∂t** on the right. The average volume strain rate is the product of the average volume strain of the sand package and the cutting velocity and arises from the volume balance over the shear zone. Van Os gives a qualitative relation between the water sub-pressures and the average volume strain rate:

$$p :: \frac{v_c \cdot h_i \cdot \varepsilon}{k} \tag{6-4}$$

The problem of the solution of the storage equation for the cutting of sand under water is a mixed boundary value problem, for which the water sub-pressures along the boundaries are known (hydrostatic).

Joanknecht (1973) and (1974) assumes that the cutting forces are determined by the sub-pressure in the sand package. A distinction is made between the parts of the cutting force caused by the inertia forces, the sub-pressure behind the blade and the soil mechanical properties of the sand. The influence of the geometrical parameters gives the following qualitative relation:

$$F_{ci} :: v_c \cdot h_i^2 \cdot w \tag{6-5}$$

The cutting force is proportional to the cutting velocity, the blade width and the square of the initial layer-thickness. A relation with the pore percentage and the permeability is also mentioned. A relation between the cutting force and these soil mechanical properties is however not given. It is observed that the cutting forces increase with an increasing blade angle.

In the eighties research has led to more quantitative relations. Van Leussen and Nieuwenhuis (1984) discuss the soil mechanical aspects of the cutting process. The forces models of Miedema (1984B), (1985B), (1985A), (1986B) and (1987 September), Steeghs (1985A) and (1985B) and the CSB (Combinatie Speurwerk Baggertechniek) model (van Leussen and van Os (1987 December)) are published in the eighties.

Brakel (1981) derives a relation for the determination of the water sub-pressures based upon, over each other rolling, round grains in the shear zone. The force part resulting from this is added to the model of Hettiaratchi and Reece (1974).

Miedema (1984B) has combined the qualitative relations of Joanknecht (1973) and (1974) and van Os (1976), (1977A) and (1977B) to the following relation:

$$F_{ci} :: \frac{\rho_w \cdot g \cdot v_c \cdot h_i^2 \cdot w \cdot \varepsilon}{k_m} \tag{6-6}$$

With this basic equation calculation models are developed for a cutter head and for the periodical moving cutter head in the breach. The proportionality constants are determined empirically.
Van Leussen and Nieuwenhuis (1984) discuss the soil mechanical aspects of the cutting process. Important in the cutting process is the way shear takes place and the shape or angle of the shear plane, respectively shear zone. In literature no unambiguous image could be found. Cutting tests along a windowpane gave an image in which the shape of the shear plane was more in accordance with the so-called "stress characteristics" than with the so-called "zero-extension lines". Therefore, for the calculation of the cutting forces, the "stress characteristics method" is used (Mohr-Coulomb failure criterion). For the calculation of the water sub-pressures, however, the "zero-extension lines" are used, which are lines with a zero linear strain. A closer description has not been given for both calculations.

Although the cutting process is considered as being two-dimensional, Van Leussen and Nieuwenhuis found, that the angle of internal friction, measured at low deformation rates in a tri-axial apparatus, proved to be sufficient for dredging processes. Although the cutting process can be considered as a two-dimensional process and therefore it should be expected that the angle of internal friction has to be determined with a "plane deformation test". A sufficient explanation has not been found.

Little is known about the value of the angle of friction between sand and steel. Van Leussen and Nieuwenhuis don't give an unambiguous method to determine this soil mechanical parameter. It is, however, remarked that at low cutting velocities (0.05 mm/s), the soil/steel angle of friction can have a statistical value which is 1.5 to 2 times larger than the dynamic soil/steel angle of friction. The influence of the initial density on the resulting angle of friction is not clearly present, because loosely packed sand moves over the blade. The angles of friction measured on the blades are much larger than the angles of friction measured with an adhesion cell, while also a dependency with the blade angle is observed.

With regard to the permeability of the sand, Van Leussen and Nieuwenhuis found that no large deviations of Darcy's law occur with the water flow through the pores. The found deviations are in general smaller than the accuracy with which the permeability can be determined in situ.

The size of the area where $\partial e/\partial t$ from equation (6-1) is zero can be clarified by the figures published by van Leussen and Nieuwenhuis. The basis is formed by a cutting process where the density of the sand is increased in a shear band with a certain width. The undisturbed sand has the initial density while the sand after passage of the shear band possesses a critical density. This critical density appeared to be in good accordance with the wet critical density of the used types of sand. This implies that outside the shear band the following equation (Biot (1941)) is valid:

$$\left|\frac{\partial^2 p}{\partial x^2}\right| + \left|\frac{\partial^2 p}{\partial y^2}\right| = 0 \tag{6-7}$$

Values for the various densities are given for three types of sand. Differentiation of the residual density as a function of the blade angle is not given. A verification of the water pressures calculations is given for a 60° blade with a blade-height/layer-thickness ratio of 1.

Miedema (1984A) and (1984B) gives a formulation for the determination of the water sub-pressures. The deformation rate is determined by taking the volume balance over the shear zone, as van Os (1977A), (1976) and (1977B) did. The deformation rate is modeled as a boundary condition in the shear zone , while the shear zone is modeled as a straight line instead of a shear band as with van Os (1976), (1977A), (1977B), van Leussen and Nieuwenhuis (1984) and Hansen (1958). The influence of the water depth on the cutting forces is clarified. Steeghs (1985A) and (1985B) developed a theory for the determination of the volume strain rate, based upon a cyclic deformation of the sand in a shear band. This implies that not an average value is taken for the volume strain rate but a cyclic, with time varying, value, based upon the dilatancy angle theory.

Miedema (1985A) and (1985B) derives equations for the determination of the water sub-pressures and the cutting forces, based upon Miedema (1982), (1984A) and (1984B). The water sub-pressures are determined with a finite element method. Explained are the influences of the permeability of the disturbed and undisturbed sand and the determination of the shear angle. The derived theory is verified with model tests. On basis of this research $\mathbf{n_{max}}$ is chosen for the residual pore percentage instead of the wet critical density.

Steeghs (1985A) and (1985B) derives equations for the determination of the water sub-pressures according to an analytical approximation method. With this approximation method the water sub-pressures are determined with a modification of equation (6-4) derived by van Os (1976), (1977A), (1977B) and the storage equation (6-7). Explained is how cutting forces can be determined with the force equilibrium on the cut layer. Also included are the gravity force, the inertia forces and the sub-pressure behind the blade. For the last influence factor no formulation is given. Discussed is the determination of the shear angle. Some examples of the cutting forces are given as a function of the cutting velocity, the water depth and the sub-pressure behind the blade. A verification of this theory is not given.

Miedema (1986A) develops a calculation model for the determination of the cutting forces on a cutter-wheel based upon (1985A) and (1985B). This will be discussed in the appropriate section. Also nomograms are published with which the cutting forces and the shear angle can be determined in a simple way. Explained is the determination of the weighted average permeability from the permeability of the disturbed and undisturbed sand. Based upon the calculations it is concluded that the average permeability forms a good estimation.

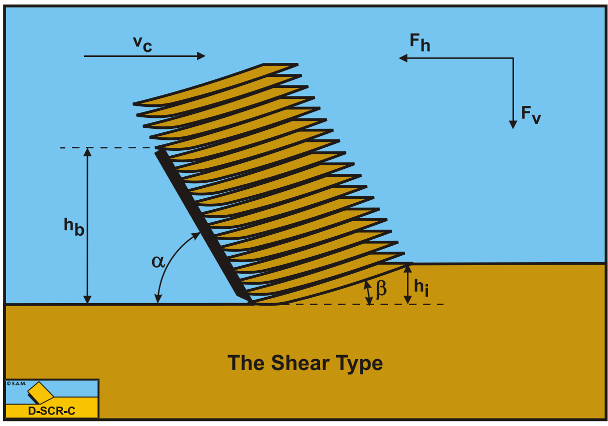

Figure 6-2: The cutting mechanism in water saturated sand, the Shear Type.

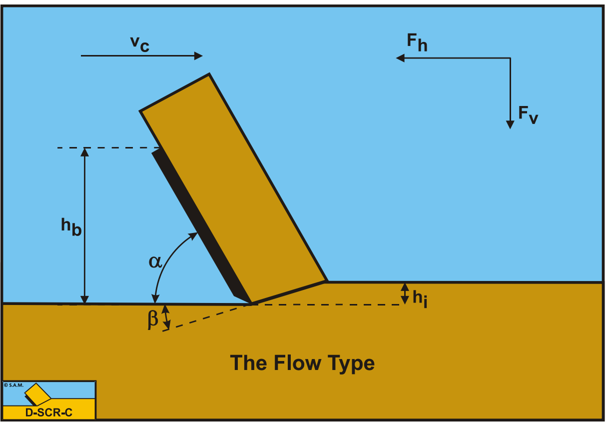

Figure 6-3: Water saturated sand modeled according to the Flow Type.

Miedema (1986B) extends the theory with adhesion, cohesion, inertia forces, gravity, and sub-pressure behind the blade. The method for the calculation of the coefficients for the determination of a weighted average permeability are discussed. It is concluded that the additions to the theory lead to a better correlation with the tests results.

Van Os and van Leussen (1987 December) summarize the publications of van Os (1976), (1977A), (1977B) and of Van Leussen and Nieuwenhuis (1984) and give a formulation of the theory developed in the early seventies at the Waterloopkundig Laboratorium. Discussed are the water pressures calculation, cavitation, the weighted average permeability, the angle of internal friction, the soil/steel angle of friction, the permeability, the volume strain and the cutting forces. Verification is given of a water pressures calculation and the cutting forces. The water sub-pressures are determined with equation (6-4) derived by van Os (1976), (1977A) and (1977B). The water pressures calculation is performed with the finite difference method, in which the height of the shear band is equal to the mesh width of the grid. The size of this mesh width is considered to be arbitrary. From an example, however, it can be seen that the shear band has a width of 13% of the layer-thickness. Discussed is the determination of a weighted average permeability. The forces are determined with Coulomb's method.

6.4. The Equilibrium of Forces.

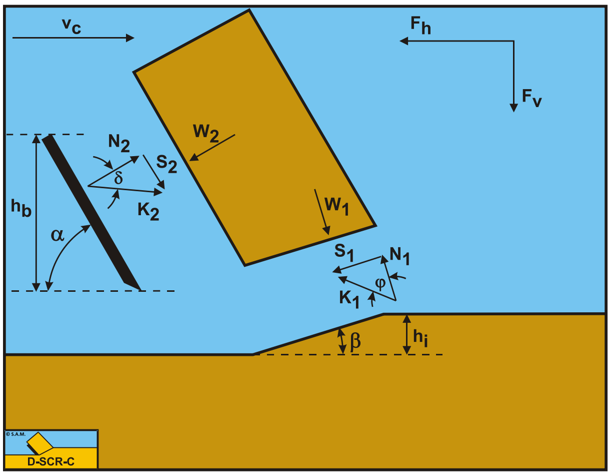

Figure 6-4: The forces on the layer cut in water saturated sand.

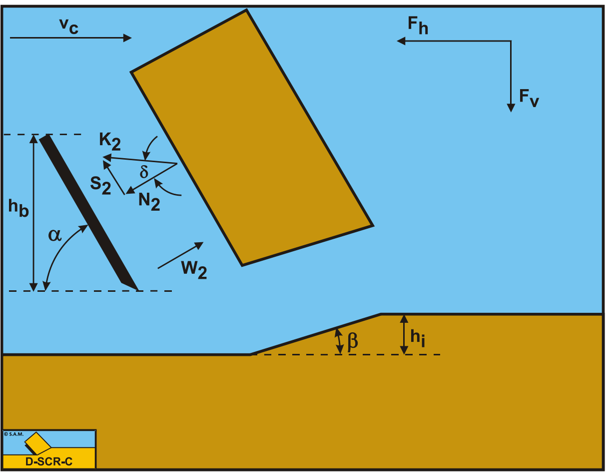

Figure 6-5: The forces on the blade in water saturated sand.

Figure 6-4 illustrates the forces on the layer of soil cut. The forces shown are valid in general. The forces acting on this layer are:

1. A normal force acting on the shear surface **N_1**.
2. A shear force **S_1** as a result of internal friction **$N_1 \cdot \tan(\phi)$**.
3. A force **W_1** as a result of water under pressure in the shear zone.
4. A force normal to the blade **N_2**.
5. A shear force **S_2** as a result of the soil/steel friction **$N_2 \cdot \tan(\delta)$**.
6. A force **W_2** as a result of water under pressure on the blade.

The normal force **N_1** and the shear force **S_1** can be combined to a resulting grain force **K_1**.

$$K_1 = \sqrt{N_1^2 + S_1^2} \tag{6-8}$$

The forces acting on a straight blade when cutting soil, can be distinguished as:

7. A force normal to the blade **N_2**.
8. A shear force **S_2** as a result of the soil/steel friction **$N_2 \cdot \tan(\delta)$**.
9. A force **W_2** as a result of water under pressure on the blade.

These forces are shown in Figure 6-5. If the forces **N_2** and **S_2** are combined to a resulting force **K_2** and the adhesive force and the water under pressures are known, then the resulting force **K_2** is the unknown force on the blade. By taking the horizontal and vertical equilibrium of forces an expression for the force **K_2** on the blade can be derived.

$$K_2 = \sqrt{N_2^2 + S_2^2} \tag{6-9}$$

Water saturated sand is also cohesionless, although in literature the phenomenon of water under pressures is sometimes referred to as apparent cohesion. It should be stated however that the water under pressures have nothing to do with cohesion or shear strength. The shear stresses still follow the rules of Coulomb friction. Due to dilatation, a volume increase of the pore volume caused by shear stresses, under pressures develop around the shear plane as described by Miedema (1987 September), resulting in a strong increase of the grain stresses. Because the permeability of the flow of water through the pores is very low, the stresses and thus the forces are dominated by the phenomenon of dilatancy and gravitation, inertia, adhesion and cohesion can be neglected.

The horizontal equilibrium of forces is:

$$\sum F_h = K_1 \cdot \sin(\beta+\varphi) - W_1 \cdot \sin(\beta) + W_2 \cdot \sin(\alpha) - K_2 \cdot \sin(\alpha+\delta) = 0 \qquad \textbf{(6-10)}$$

The vertical equilibrium of forces is:

$$\sum F_v = - K_1 \cdot \cos(\beta+\varphi) + W_1 \cdot \cos(\beta) + W_2 \cdot \cos(\alpha) - K_2 \cdot \cos(\alpha+\delta) = 0 \qquad \textbf{(6-11)}$$

The force **K₁** on the shear plane is now:

$$K_1 = \frac{W_2 \cdot \sin(\delta) + W_1 \cdot \sin(\alpha+\beta+\delta)}{\sin(\alpha+\beta+\delta+\varphi)} \qquad \textbf{(6-12)}$$

The force **K₂** on the blade is now:

$$K_2 = \frac{W_2 \cdot \sin(\alpha+\beta+\varphi) + W_1 \cdot \sin(\varphi)}{\sin(\alpha+\beta+\delta+\varphi)} \qquad \textbf{(6-13)}$$

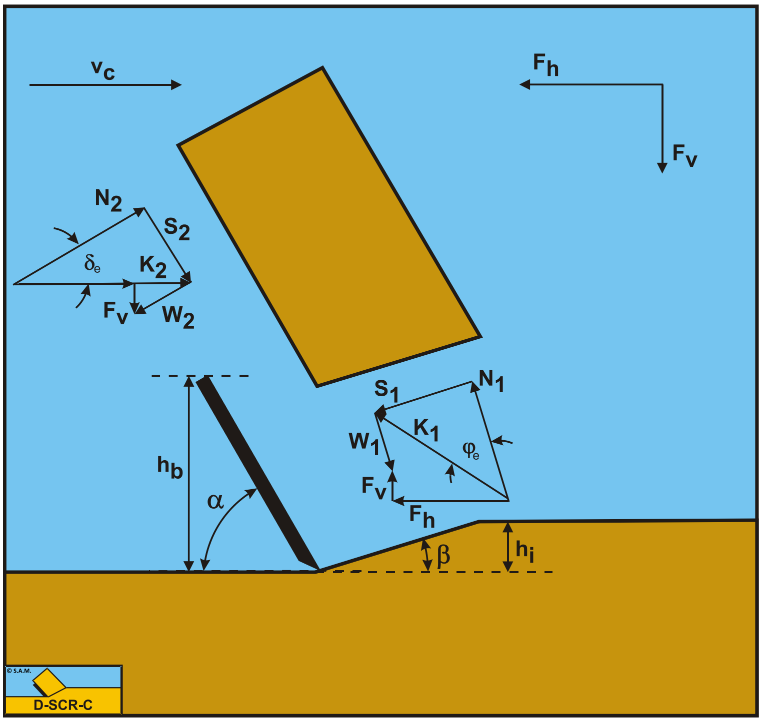

Figure 6-6: The forces on the blade when cutting water saturated sand.

From equation (6-13) the forces on the blade can be derived. On the blade a force component in the direction of cutting velocity **Fₕ** and a force perpendicular to this direction **Fᵥ** can be distinguished.

$$F_h = -W_2 \cdot \sin(\alpha) + K_2 \cdot \sin(\alpha+\delta) \qquad \textbf{(6-14)}$$

$$F_v = -W_2 \cdot \cos(\alpha) + K_2 \cdot \cos(\alpha+\delta) \qquad \textbf{(6-15)}$$

The normal force on the shear plane is now:

$$N_1 = \frac{W_2 \cdot \sin(\delta) + W_1 \cdot \sin(\alpha+\beta+\delta)}{\sin(\alpha+\beta+\delta+\varphi)} \cdot \cos(\varphi) \tag{6-16}$$

The normal force on the blade is now:

$$N_2 = \frac{W_2 \cdot \sin(\alpha+\beta+\varphi) + W_1 \cdot \sin(\varphi)}{\sin(\alpha+\beta+\delta+\varphi)} \cdot \cos(\delta) \tag{6-17}$$

Equations (6-16) and (6-17) show, that the normal forces on the shear plane and the blade are always positive. Positive means compressive stresses. In water saturated sand, always the shear type of cutting mechanism will occur. Figure 6-6 shows these forces on the layer cut.

6.5. Determination of the Pore Pressures.

The cutting process can be modeled as a two-dimensional process, in which a straight blade cuts a small layer of sand (Figure 6-7). The sand is deformed in the shear zone, also called deformation zone or dilatancy zone. During this deformation the volume of the sand changes as a result of the shear stresses in the shear zone. In soil mechanics this phenomenon is called dilatancy. In hard packed sand the pore volume is increased as a result of the shear stresses in the deformation zone. This increase in the pore volume is thought to be concentrated in the deformation zone, with the deformation zone modeled as a straight line. Water has to flow to the deformation zone to fill up the increase of the pore volume in this zone. As a result of this water flow the grain stresses increase and the water pressures decrease. Therefore there are water under-pressures.

This implies that the forces necessary for cutting hard packed sand under water will be determined for an important part by the dilatancy properties of the sand. At low cutting velocities these cutting forces are also determined by the gravity, the cohesion and the adhesion for as far as these last two soil mechanical parameters are present in the sand. Is the cutting at high velocities, then the inertia forces will have an important part in the total cutting forces especially in dry sand.

If the cutting process is assumed to be stationary, the water flow through the pores of the sand can be described in a blade motions related coordinate system. The determination of the water under-pressures in the sand around the blade is then limited to a mixed boundary conditions problem. The potential theory can be used to solve this problem. For the determination of the water under-pressures it is necessary to have a proper formulation of the boundary condition in the shear zone. Miedema (1984B) derived the basic equation for this boundary condition.

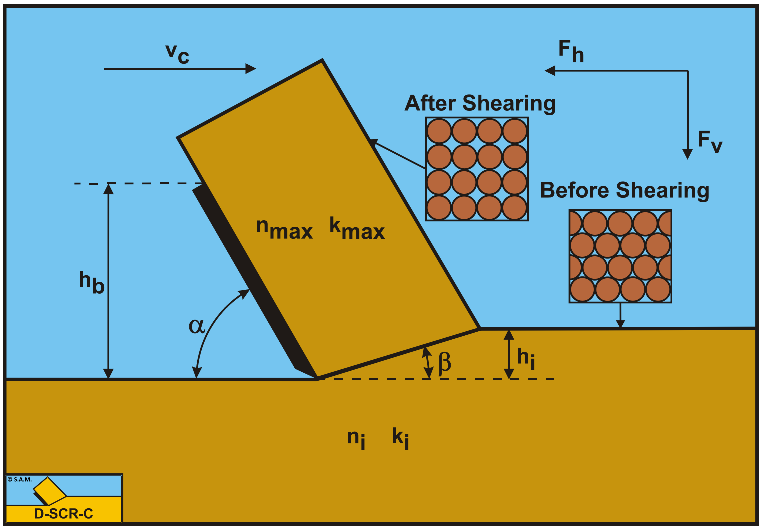

Figure 6-7: The cutting process modeled as a continuous process.

In (1985A) and (1985B) a more extensive derivation is published by Miedema. If it is assumed that no deformations take place outside the deformation zone, then the following equation applies for the sand package around the blade:

$$\left|\frac{\partial^2 p}{\partial x^2}\right| + \left|\frac{\partial^2 p}{\partial y^2}\right| = 0 \tag{6-18}$$

The boundary condition is in fact a specific flow rate (Figure 6-8) that can be determined with the following hypothesis. For a sand element in the deformation zone, the increase in the pore volume per unit of blade length is:

$$\Delta V = \varepsilon \cdot \Delta A = \varepsilon \cdot \Delta x \cdot \Delta h_i = \varepsilon \cdot \Delta x \cdot \Delta l \cdot \sin(\beta) \tag{6-19}$$

$$\varepsilon = \frac{n_{max} - n_i}{1 - n_{max}} \tag{6-20}$$

It should be noted that in this book the symbol **ε** is used for the dilatation, while in previous publications the symbol **e** is often used. This is to avoid confusion with the symbol **e** for the void ratio.
For the residual pore percentage $\mathbf{n_{max}}$ is chosen on the basis of the ability to explain the water under-pressures, measured in laboratory tests. The volume flow rate flowing to the sand element is equal to:

$$\Delta Q = \frac{\partial V}{\partial t} = \varepsilon \cdot \frac{\partial x}{\partial t} \cdot \Delta l \cdot \sin(\beta) = \varepsilon \cdot v_c \cdot \Delta l \cdot \sin(\beta) \tag{6-21}$$

With the aid of Darcy's law the next differential equation can be derived for the specific flow rate perpendicular to the deformation zone:

$$q = \frac{\partial Q}{\partial l} = q_1 + q_2 = \frac{k_i}{\rho_w \cdot g} \cdot \left|\frac{\partial p}{\partial n}\right|_1 + \frac{k_{max}}{\rho_w \cdot g} \cdot \left|\frac{\partial p}{\partial n}\right|_2 = \varepsilon \cdot v_c \cdot \sin(\beta) \tag{6-22}$$

The partial derivative **∂p/∂n** is the derivative of the water under-pressures perpendicular on the boundary of the area, in which the water under-pressures are calculated (in this case the deformation zone). The boundary conditions on the other boundaries of this area are indicated in Figure 6-8. A hydrostatic pressure distribution is assumed on the boundaries between sand and water. This pressure distribution equals zero in the calculation of the water under-pressures, if the height difference over the blade is neglected.

The boundaries that form the edges in the sand package are assumed to be impenetrable. Making equation (6-22) dimensionless is similar to that of the breach equation of Meijer and van Os (1976). In the breach problem the length dimensions are normalized by dividing them by the breach height, while in the cutting of sand they are normalized by dividing them by the cut layer thickness.
Equation (6-22) in normalized format:

$$\frac{k_i}{k_{max}} \cdot \left|\frac{\partial p}{\partial n'}\right|_1 + \left|\frac{\partial p}{\partial n'}\right|_2 = \frac{\rho_w \cdot g \cdot v_c \cdot \varepsilon \cdot h_i \cdot \sin(\beta)}{k_{max}} \qquad \text{with:} \quad n' = \frac{n}{h_i} \tag{6-23}$$

This equation is made dimensionless with:

$$\left|\frac{\partial p}{\partial n}\right|' = \frac{\left|\frac{\partial p}{\partial n'}\right|}{\rho_w \cdot g \cdot v_c \cdot \varepsilon \cdot h_i / k_{max}} \tag{6-24}$$

The accent indicates that a certain variable or partial derivative is dimensionless. The next dimensionless equation is now valid as a boundary condition in the deformation zone:

$$\frac{k_i}{k_{max}} \cdot \left|\frac{\partial p}{\partial n}\right|_1' + \left|\frac{\partial p}{\partial n}\right|_2' = \sin(\beta) \tag{6-25}$$

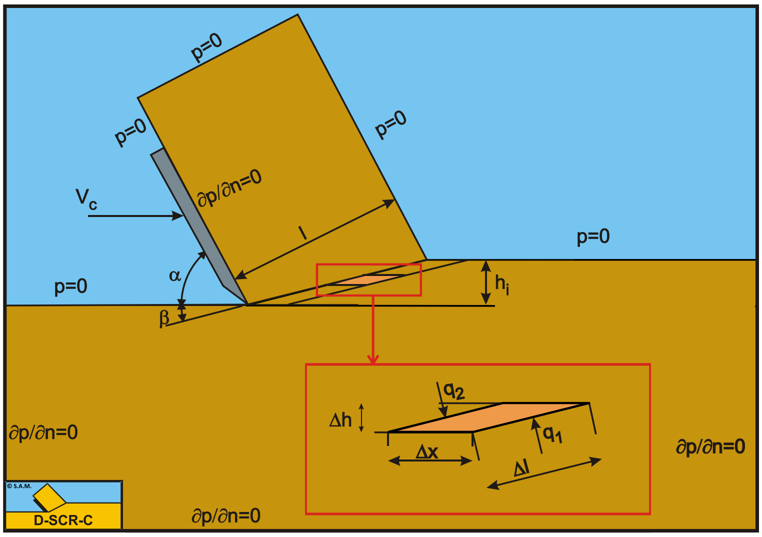

Figure 6-8: The volume balance over the shear zone.

The storage equation also has to be made dimensionless, which results in the next equation:

$$\left|\frac{\partial^2 p}{\partial x^2}\right|' + \left|\frac{\partial^2 p}{\partial y^2}\right|' = 0 \qquad \textbf{(6-26)}$$

Because this equation equals zero, it is similar to equation (6-18). The water under-pressures distribution in the sand package can now be determined using the storage equation and the boundary conditions. Because the calculation of the water under-pressures is dimensionless the next transformation has to be performed to determine the real water under-pressures. The real water under-pressures can be determined by integrating the derivative of the water under-pressures in the direction of a flow line, along a flow line, so:

$$P_{calc} = \int_{s'} \left|\frac{\partial p}{\partial s}\right|' \cdot ds' \qquad \textbf{(6-27)}$$

This is illustrated in Figure 6-9. Using equation (6-30) this is written as:

$$P_{real} = \int_{s} \left|\frac{\partial p}{\partial s}\right| \cdot ds = \int_{s'} \frac{\rho_w \cdot g \cdot v_c \cdot \varepsilon \cdot h_i}{k_{max}} \cdot \left|\frac{\partial p}{\partial s}\right|' \cdot ds' \quad \text{with:} \quad s' = \frac{s}{h_i} \qquad \textbf{(6-28)}$$

This gives the next relation between the real emerging water under-pressures and the calculated water under-pressures:

$$P_{real} = \frac{\rho_w \cdot g \cdot v_c \cdot \varepsilon \cdot h_i}{k_{max}} \cdot P_{calc} \qquad \textbf{(6-29)}$$

To be independent of the ratio between the initial permeability $\mathbf{k_i}$ and the maximum permeability $\mathbf{k_{max}}$, $\mathbf{k_{max}}$ has to be replaced with the weighted average permeability $\mathbf{k_m}$ before making the measured water under-pressures dimensionless.

6.6. Numerical Water Pore Pressure Calculations.

The water under-pressures in the sand package on and around the blade are numerically determined using the finite element method. The solution of such a calculation is however not only dependent on the physical model of the problem, but also on the next points:

1. The size of the area in which the calculation takes place.
2. The size and distribution of the elements.

3. The boundary conditions.

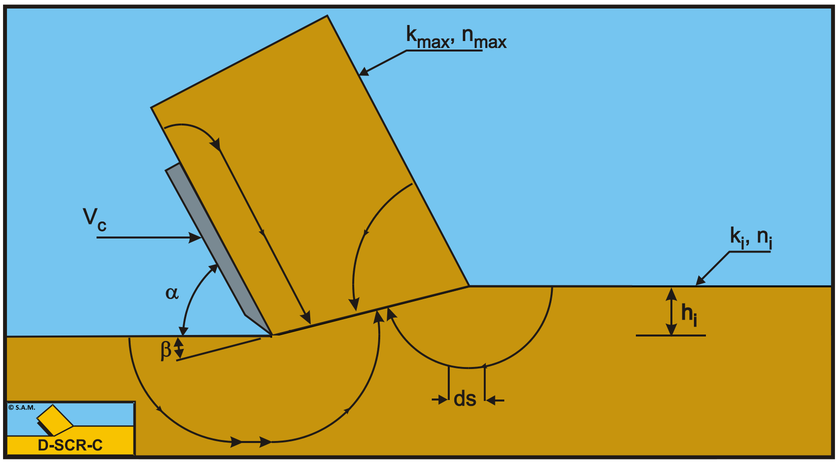

Figure 6-9: Flow of the pore water to the shear zone.

The choices for these three points have to be evaluated with the problem that has to be solved in mind. These calculations are about the values and distribution of the water under-pressures in the shear zone and on the blade. A variation of the values for point 1 and 2 may therefore not influence this part of the solution. This is achieved by on the one hand increasing the area in which the calculations take place in steps and on the other hand by decreasing the element size until the variation in the solution was less than 1%. The distribution of the elements is chosen such that a finer mesh is present around the blade tip, the shear zone and on the blade, also because of the blade tip problem. A number of boundary conditions follow from the physical model of the cutting process, these are:

1. The boundary condition in the shear zone. This is described by equation (6-23).
2. The boundary condition along the free sand surface. The hydrostatic pressure at which the process takes place, can be chosen, when neglecting the dimensions of the blade and the layer in relation to the hydrostatic pressure head. Because these calculations are meant to obtain the difference between the water under-pressures and the hydrostatic pressure it is valid to take a zero pressure as the boundary condition.

The boundary conditions, along the boundaries of the area where the calculation takes place that are located in the sand package are not determined by the physical process. For this boundary condition there is a choice between:

1. A hydrostatic pressure along the boundary.
2. A boundary as an impenetrable wall.
3. A combination of a known pressure and a known specific flow rate.

None of these choices complies with the real process. Water from outside the calculation area will flow through the boundary. This also implies, however, that the pressure along this boundary is not hydrostatic. If, however, the boundary is chosen with enough distance from the real cutting process the boundary condition may not have an influence on the solution. The impenetrable wall is chosen although this choice is arbitrary. Figure 6-8 gives an impression of the size of the area and the boundary conditions, while Figure 6-10 shows the element mesh. Figure 6-12 shows the two-dimensional distribution of the water under-pressures. A table with the dimensionless pore pressures can be found in Miedema (1987 September), Miedema & Yi (2001) and in Appendix C: and Appendix R:

The following figures give an impression of how the FEM calculations are carried out:
Figure 6-10 and Figure 6-11: Show how the mesh has been varied in order to get a 1% accuracy.
Figure 6-12: Shows both the equipotential lines and the flow lines (stream function).
Figure 6-14 and Figure 6-15: Show the equipotential lines both as lines and as a color plot. This shows clearly where the largest under pressures occur on the shear plane.
Figure 6-13 shows the pressure distribution on both the shear plane and the blade. From these pressure distributions the average dimensionless pressures $\mathbf{p_{1m}}$ and $\mathbf{p_{2m}}$ are determined.
Figure 6-16 and Figure 6-17: Show the streamlines both as lines and as a color plot. This shows the paths of the pore water flow.

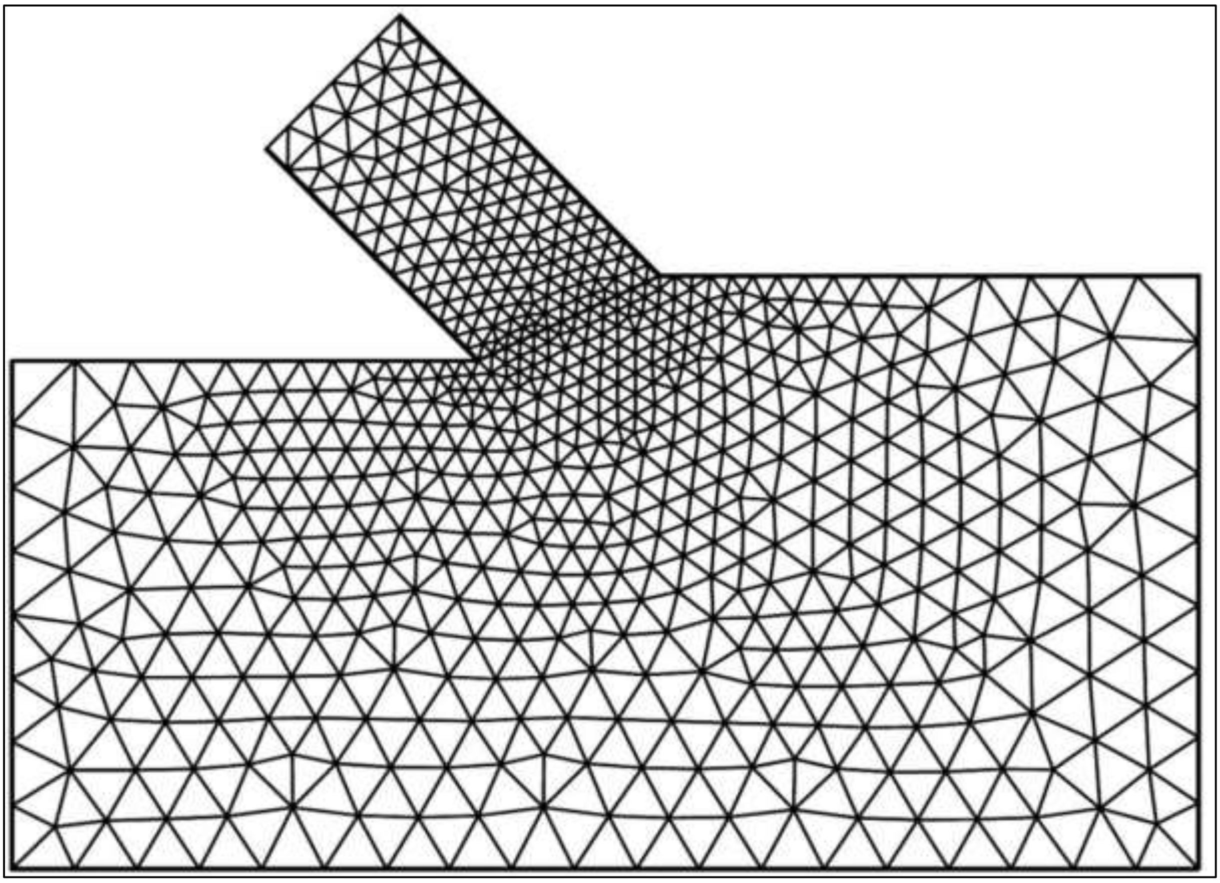

Figure 6-10: The coarse mesh as applied in the pore pressure calculations.

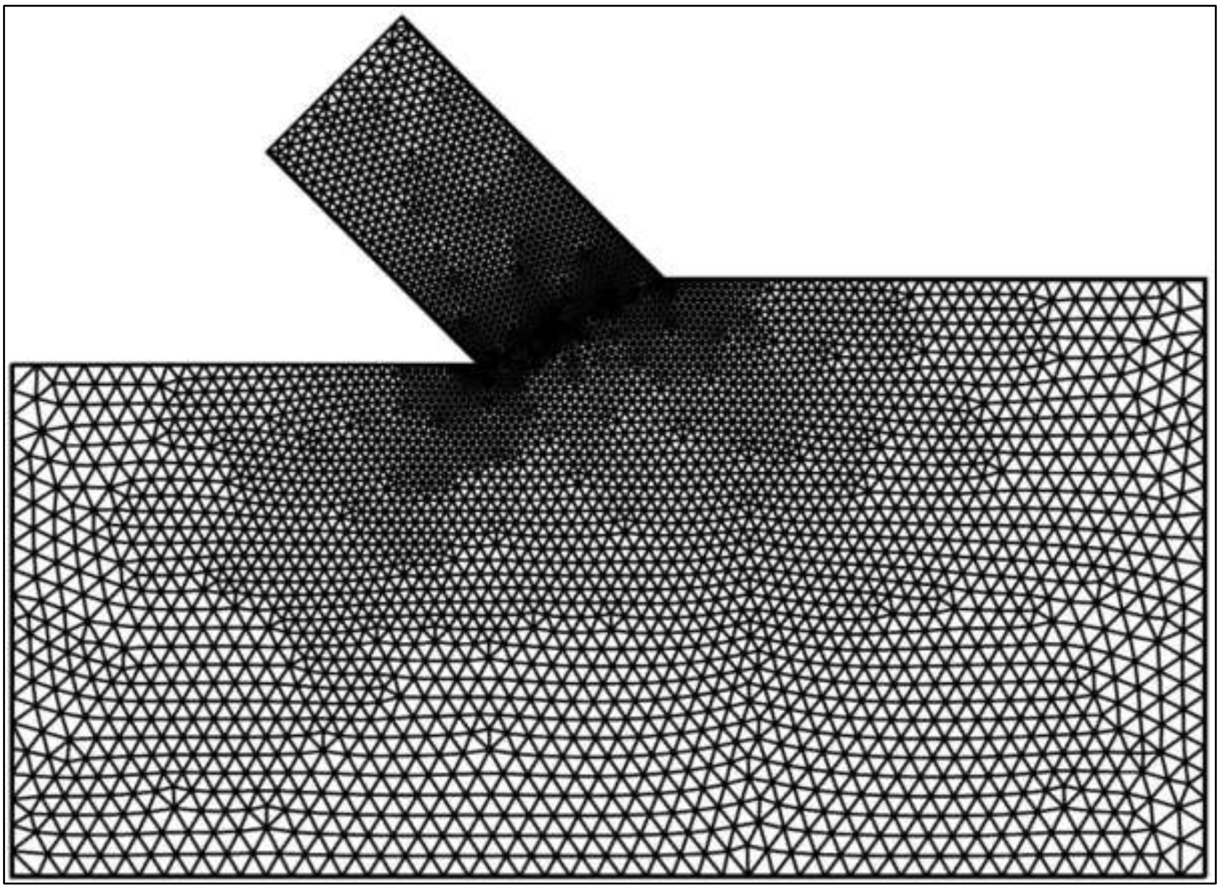

Figure 6-11: The fine mesh as applied in the pore pressure calculations.

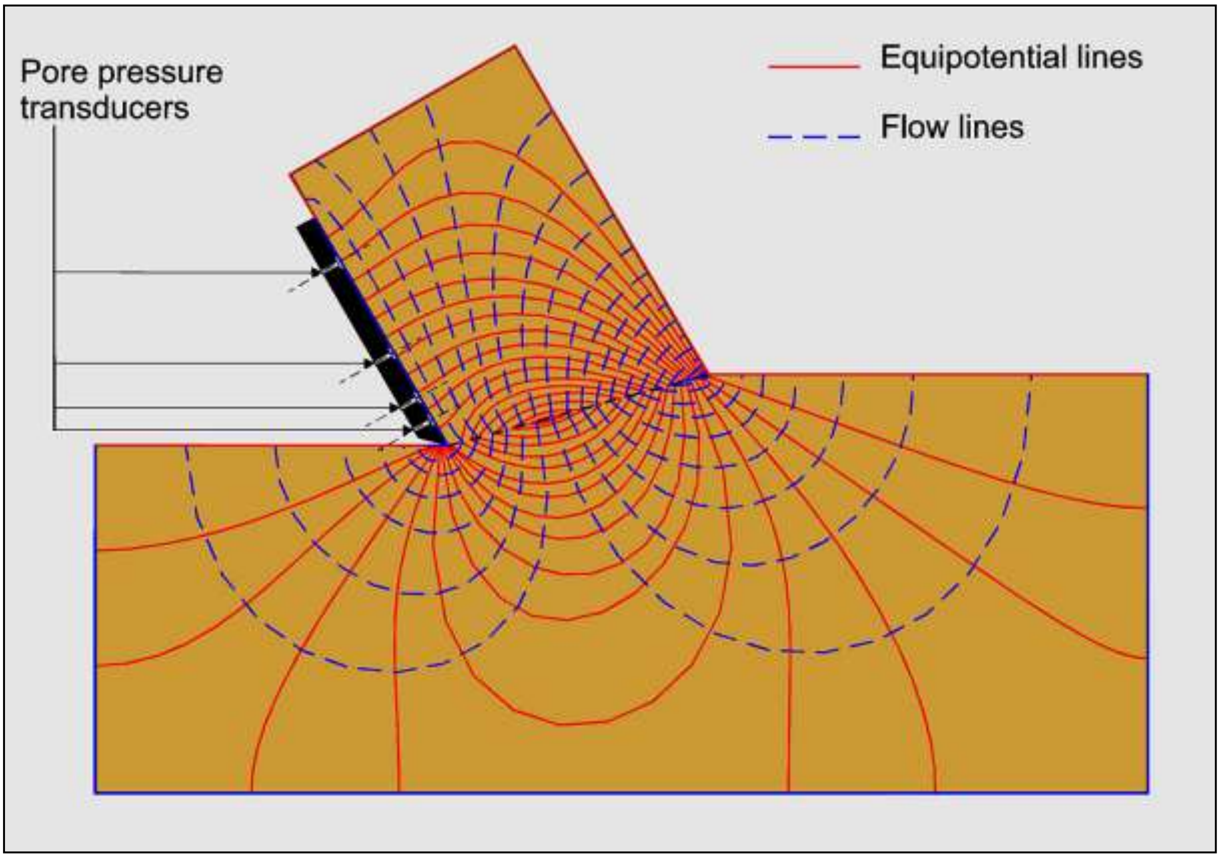

Figure 6-12: The water under-pressures distribution in the sand package around the blade.

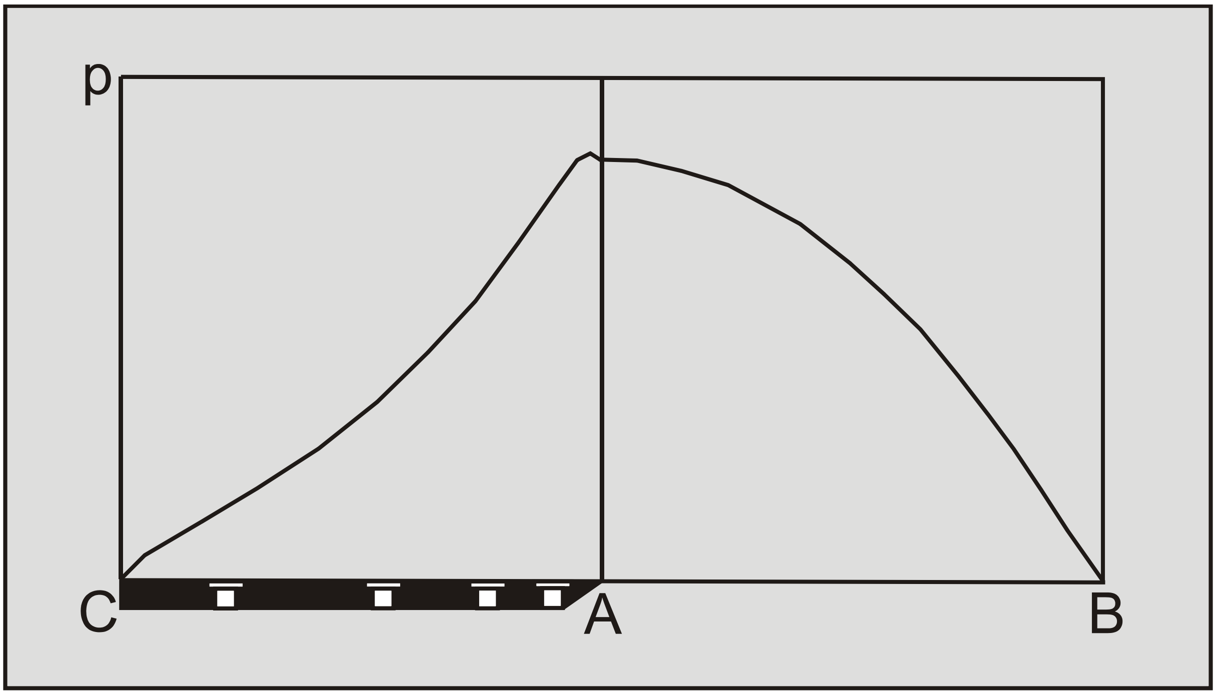

Figure 6-13: The pore pressure distribution on the blade A-C and in the shear zone A-B.

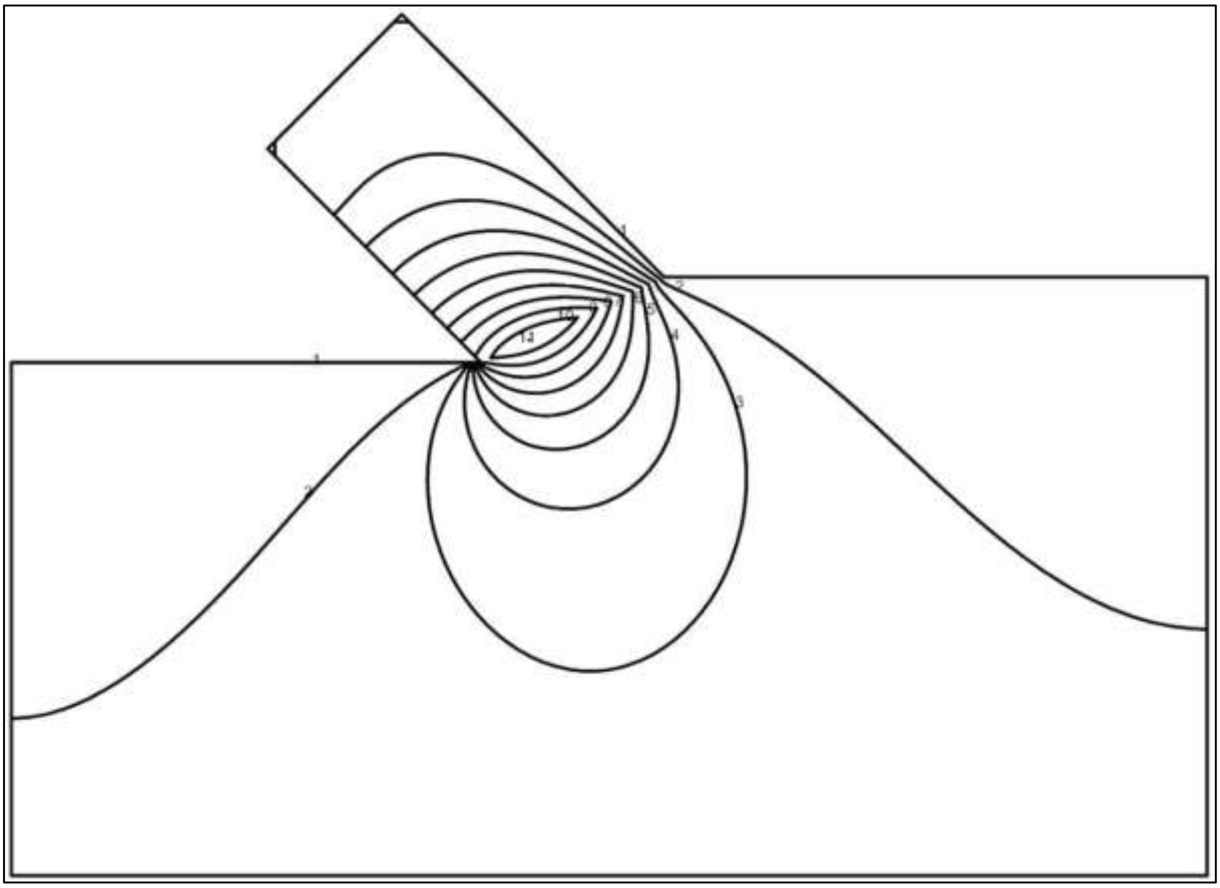

Figure 6-14: The equipotential lines.

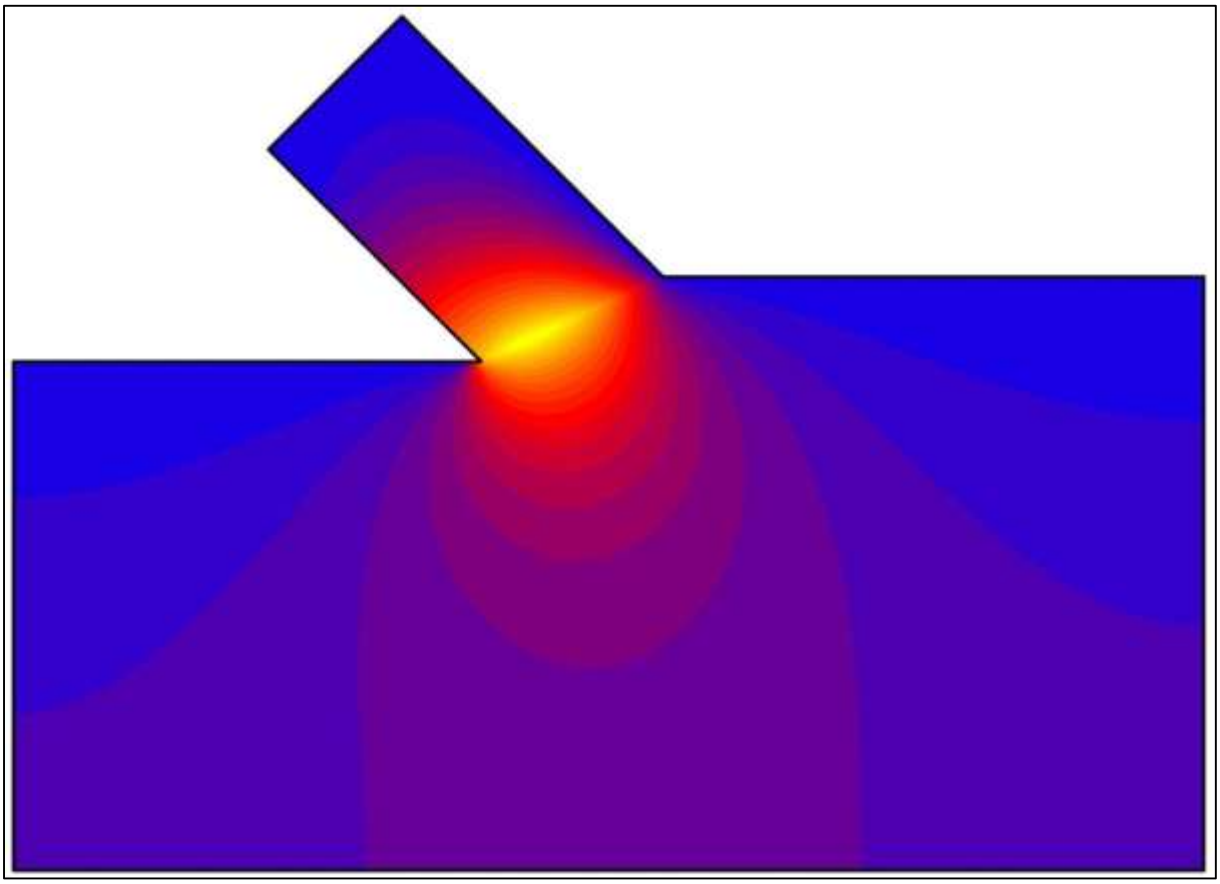

Figure 6-15: The equipotential lines in color.

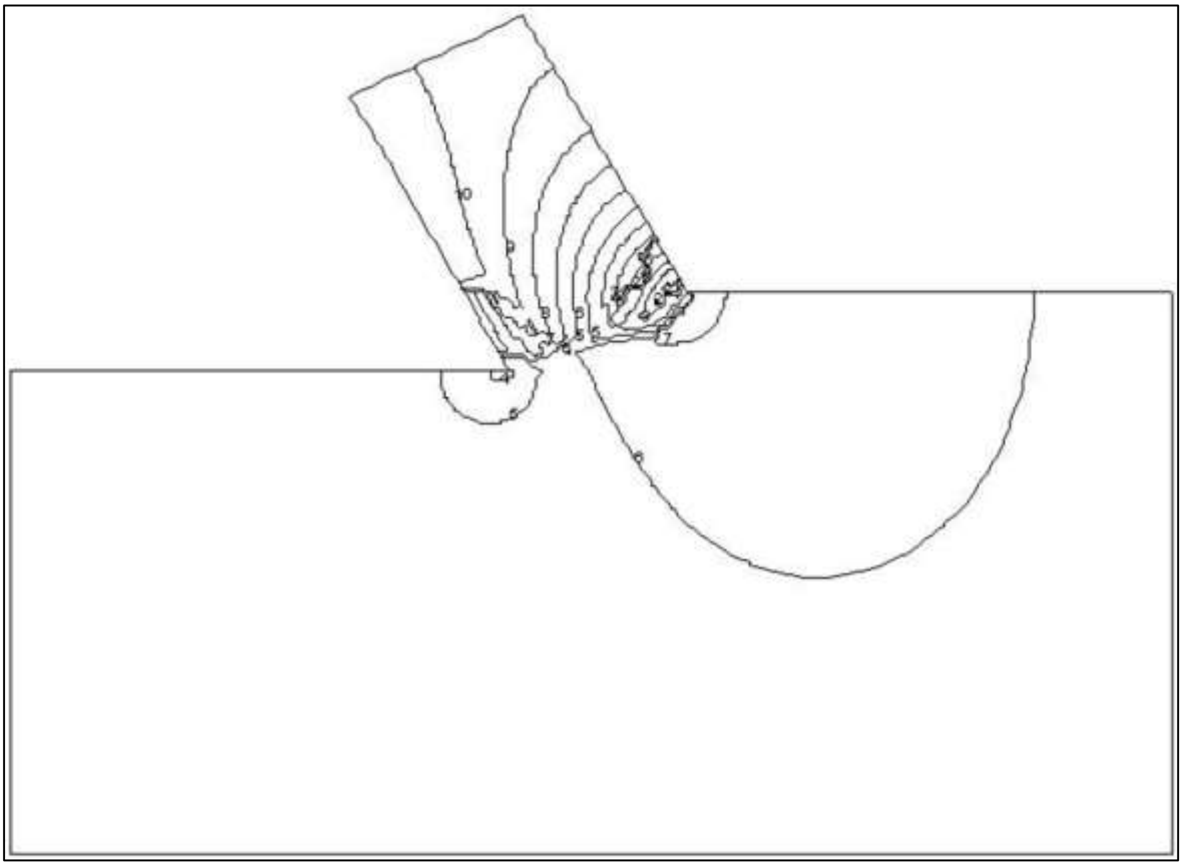

Figure 6-16: Flow lines or stream function.

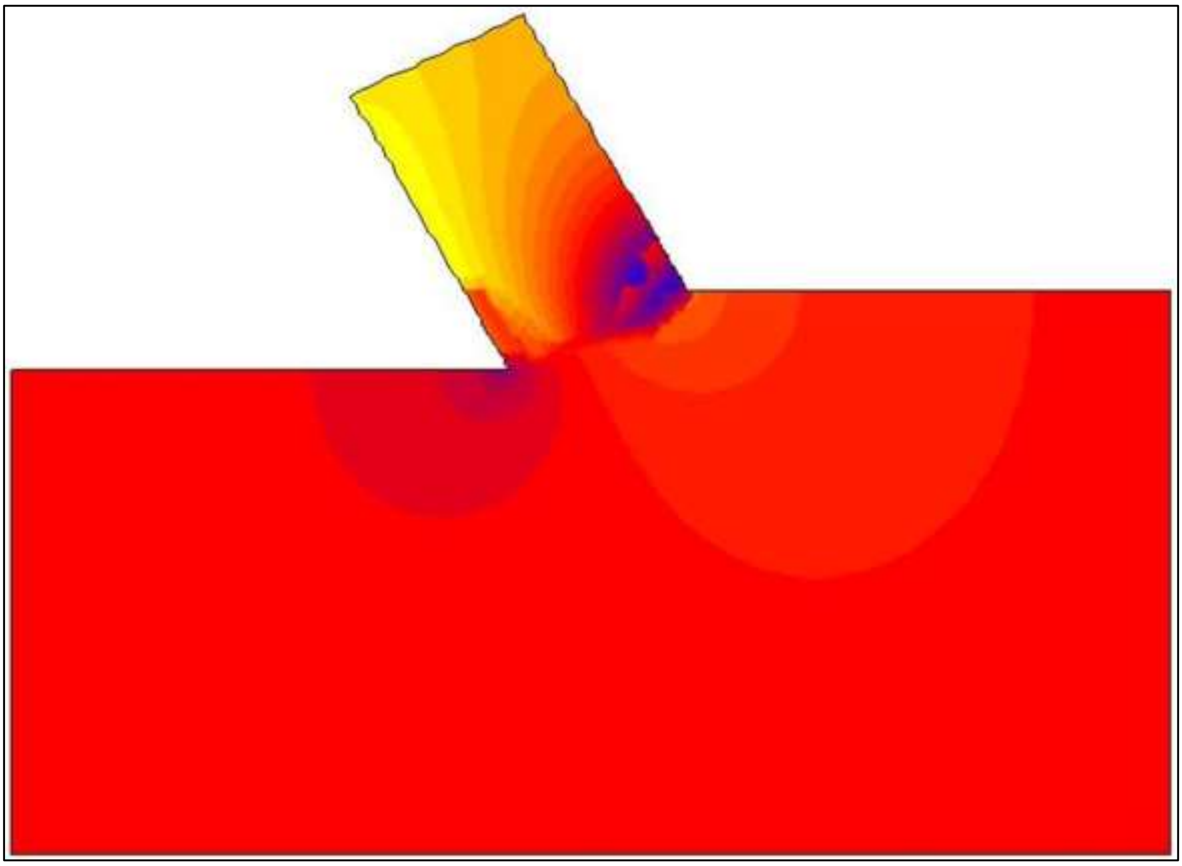

Figure 6-17: The stream function in colors.

6.7. The Blade Tip Problem.

During the physical modeling of the cutting process it has always been assumed that the blade tip is sharp. In other words, that in the numerical calculation, from the blade tip, a hydrostatic pressure can be introduced as the boundary condition along the free sand surface behind the blade. In practice this is never valid, because of the following reasons:

1. The blade tip always has a certain rounding, so that the blade tip can never be considered really sharp.
2. Through wear of the blade a flat section develops behind the blade tip, which runs against the sand surface (clearance angle ≤ zero)
3. If there is also dilatancy in the sand underneath the blade tip it is possible that the sand runs against the flank after the blade has passed.
4. There will be a certain under-pressure behind the blade as a result of the blade speed and the cutting process.

A combination of these factors determines the distribution of the water under-pressures, especially around the blade tip. The first three factors can be accounted for in the numerical calculation as an extra boundary condition behind the blade tip. Along the free sand surface behind the blade tip an impenetrable line element is put in, in the calculation. The length of this line element is varied with $\mathbf{0.0 \cdot h_i}$, $\mathbf{0.1 \cdot h_i}$ and $\mathbf{0.2 \cdot h_i}$. It showed from these calculations that especially the water under-pressures on the blade are strongly determined by the choice of this boundary condition as indicated in Figure 6-18 and Figure 6-19.

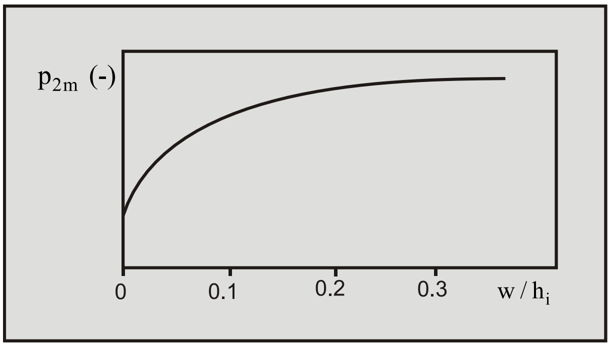

Figure 6-18: The water pore pressures on the blade as function of the length of the wear section w.

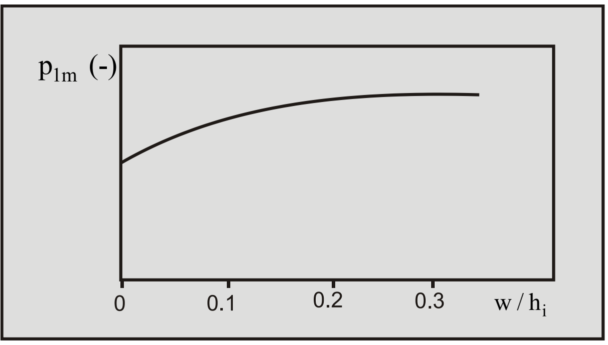

Figure 6-19: The water pore pressure in the shear zone as function of the length of the wear section w.

It is hard to estimate to what degree the influence of the under-pressure behind the blade on the water under-pressures around the blade tip can be taken into account with this extra boundary condition. Since there is no clear formulation for the under-pressure behind the blade available, it will be assumed that the extra boundary condition at the blade tip describes this influence. If there is no cavitation the water pressures forces $\mathbf{W_1}$ and $\mathbf{W_2}$ can be written as:

$$W_1 = \frac{p_{1m} \cdot \rho_w \cdot g \cdot v_c \cdot \varepsilon \cdot h_i^2 \cdot w}{k_{max} \cdot \sin(\beta)} \tag{6-30}$$

And

$$W_2 = \frac{p_{2m} \cdot \rho_w \cdot g \cdot v_c \cdot \varepsilon \cdot h_i \cdot h_b \cdot w}{k_{max} \cdot \sin(\alpha)} \tag{6-31}$$

In case of cavitation $\mathbf{W_1}$ and $\mathbf{W_2}$ become:

$$W_1 = \frac{\rho_w \cdot g \cdot (z+10) \cdot h_i \cdot w}{\sin(\beta)} \tag{6-32}$$

And

$$W_2 = \frac{\rho_w \cdot g \cdot (z+10) \cdot h_b \cdot w}{\sin(\alpha)} \tag{6-33}$$

6.8. Analytical/Numerical Water Pore Pressure Calculations.

As is shown in Figure 6-9, the water can flow from 4 directions to the shear zone where the dilatancy takes place. Two of those directions go through the sand which has not yet been deformed and thus have a permeability of $\mathbf{k_i}$, while the other two directions go through the deformed sand and thus have a permeability of $\mathbf{k_{max}}$. Figure 6-12 shows that the flow lines in 3 of the 4 directions have a more or less circular shape, while the flow lines coming from above the blade have the character of a straight line. If a point on the shear zone is considered, then the water will flow to that point along the 4 flow lines as mentioned above. Along each flow line, the water will encounter a certain resistance. One can reason that this resistance is proportional to the length of the flow line and reversibly proportional to the permeability of the sand. Figure 6-20 shows a point on the shear zone and it shows the 4 flow lines. The length of the flow lines can be determined with the equations (6-36), (6-37), (6-38) and (6-39). The variable $\mathbf{L_{max}}$ in these equations is the length of the shear zone, which is equal to $\mathbf{h_i/\sin(\beta)}$, while the variable $\mathbf{L}$ starts at the free surface with a value zero and ends at the blade tip with a value $\mathbf{L_{max}}$.

According to the law of Darcy, the specific flow **q** is related to the pressure difference **Δp** according to:

$$q = k \cdot i = k \cdot \frac{\Delta p}{\rho_w \cdot g \cdot \Delta s} \tag{6-34}$$

The total specific flow coming through the 4 flow lines equals the total flow caused by the dilatation, so:

$$\begin{aligned} q &= \varepsilon \cdot v_c \cdot \sin(\beta) \\ &= k_{max} \cdot \frac{\Delta p}{\rho_w \cdot g \cdot s_1} + k_{max} \cdot \frac{\Delta p}{\rho_w \cdot g \cdot s_2} + k_i \cdot \frac{\Delta p}{\rho_w \cdot g \cdot s_3} + k_i \cdot \frac{\Delta p}{\rho_w \cdot g \cdot s_4} \end{aligned} \tag{6-35}$$

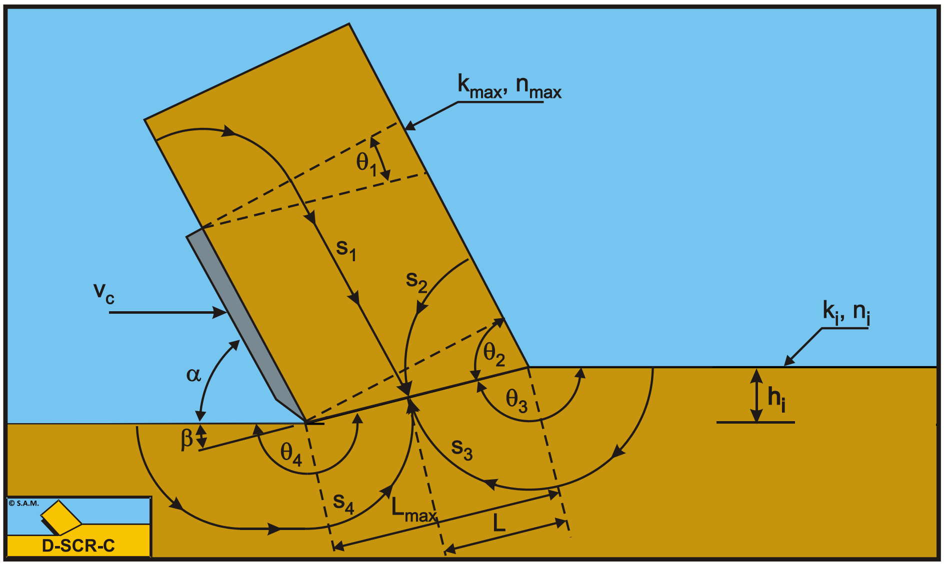

Figure 6-20: The flow lines used in the analytical method.

For the lengths of the 4 flow lines, where $\mathbf{s_2}$ and $\mathbf{s_3}$ have a correction factor of 0.8 based on calibration with the experiments:

$$\begin{aligned} s_1 &= \left(L_{max} - L\right) \cdot \left(\frac{\pi}{2} + \theta_1\right) + \frac{h_b}{\sin(\alpha)} \\ \text{With: } \theta_1 &= \frac{\pi}{2} - (\alpha + \beta) \end{aligned} \tag{6-36}$$

$$s_2 = 0.8 \cdot L \cdot \theta_2$$

$$\text{With: } \theta_2 = \alpha + \beta \tag{6-37}$$

$$s_3 = 0.8 \cdot L \cdot \theta_3$$

$$\text{With: } \theta_3 = \pi - \beta \tag{6-38}$$

$$s_4 = \left(L_{max} - L\right) \cdot \theta_4 + 0.9 \cdot h_i \cdot \left(\frac{h_i}{h_b}\right)^{0.5} \cdot \left(1.85 \cdot \alpha\right)^2 \cdot \left(\frac{k_i}{k_{max}}\right)^{0.4} \tag{6-39}$$

$$\text{With: } \theta_4 = \pi + \beta$$

The equation for the length **s₄** has been determined by calibrating this equation with the experiments and with the FEM calculations. This length should not be interpreted as a length, but as the influence of the flow of water around the tip of the blade. The total specific flow can also be written as:

$$\rho_w \cdot g \cdot q = \rho_w \cdot g \cdot \varepsilon \cdot v_c \cdot \sin\left(\beta\right)$$

$$= \frac{\Delta p}{\left(\frac{s_1}{k_{max}}\right)} + \frac{\Delta p}{\left(\frac{s_2}{k_{max}}\right)} + \frac{\Delta p}{\left(\frac{s_3}{k_i}\right)} + \frac{\Delta p}{\left(\frac{s_4}{k_i}\right)} = \frac{\Delta p}{R_1} + \frac{\Delta p}{R_2} + \frac{\Delta p}{R_3} + \frac{\Delta p}{R_4} = \frac{\Delta p}{R_t} \tag{6-40}$$

The total resistance on the flow lines can be determined by dividing the length of a flow line by the permeability of the flow line. The equations (6-41), (6-42), (6-43) and (6-44) give the resistance of each flow line.

$$R_1 = \frac{s_1}{k_{max}} \tag{6-41}$$

$$R_2 = \frac{s_2}{k_{max}} \tag{6-42}$$

$$R_3 = \frac{s_3}{k_i} \tag{6-43}$$

$$R_4 = \frac{s_4}{k_i} \tag{6-44}$$

Since the 4 flow lines can be considered as 4 parallel resistors, the total resulting resistance can be determined according to the rule for parallel resistors. Equation (6-45) shows this rule.

$$\frac{1}{R_t} = \frac{1}{R_1} + \frac{1}{R_2} + \frac{1}{R_3} + \frac{1}{R_4} \tag{6-45}$$

The resistance **R_t** in fact replaces the **h_i/k_{max}** part of the equations (6-23), (6-24), (6-28) and (6-29), resulting in equation (6-46) for the determination of the pore vacuum pressure of the point on the shear zone.

$$\Delta p = \rho_w \cdot g \cdot v_c \cdot \varepsilon \cdot \sin\left(\beta\right) \cdot R_t \tag{6-46}$$

The average pore vacuum pressure on the shear zone can be determined by summation or integration of the pore vacuum pressure of each point on the shear zone. Equation (6-47) gives the average pore vacuum pressure by summation.

$$p_{1m} = \frac{1}{n} \cdot \sum_{i=0}^{n} \Delta p_i \tag{6-47}$$

The determination of the pore pressures on the blade requires a different approach, since there is no dilatation on the blade. However, from the determination of the pore pressures on the shear plane, the pore pressure at the tip of the blade is known. This pore pressure can also be determined directly from:

For the lengths of the 4 flow lines the following is valid at the tip of the blade:

$$s_1 = \frac{h_b}{\sin(\alpha)} \tag{6-48}$$

$$s_2 = 0.8 \cdot L_{max} \cdot \theta_2 \quad \text{with:} \quad \theta_2 = \alpha + \beta \tag{6-49}$$

$$s_3 = 0.8 \cdot L_{max} \cdot \theta_3 \quad \text{with:} \quad \theta_3 = \pi - \beta \tag{6-50}$$

$$s_4 = 0.9 \cdot h_i \cdot \left(\frac{h_i}{h_b}\right)^{0.5} \cdot (1.85 \cdot \alpha)^2 \cdot \left(\frac{k_i}{k_{max}}\right)^{0.4} \tag{6-51}$$

The resistances can be determined with equations (6-41), (6-42), (6-43) and (6-44) and the pore pressure with equation (6-46). Now a linear distribution of the pore pressure on the blade could be assumed, resulting in an average pressure of half the pore pressure at the tip of the blade, but it is not that simple. If the surface of the blade is considered to be a flow line, water will flow from the top of the blade to the tip of the blade. However there will also be some entrainment from the pore water in the sand above the blade, due to the pressure gradient, although the pressure gradient on the blade is considered zero (an impermeable wall). This entrainment flow of water will depend on the ratio of the length of the shear plane to the length of the blade in some way. A high entrainment will result in smaller pore vacuum pressures. When the blade is divided into N intervals, the entrainment per interval will be 1/N times the total entrainment. The two required resistances are now, using i as the counter:

$$R_{1,i} = \frac{s_{1,i}}{k_{max}} \cdot \left(1 - \frac{i}{N}\right) \tag{6-52}$$

$$R_2 = \frac{s_2}{k_{max}} \tag{6-53}$$

The number of intervals for entrainment and the geometry are taken into account in the constant assumed resistance **R_2** according to:

$$R_2' = N \cdot 1.75 \cdot \left(\frac{h_i}{\sin(\beta)} \cdot \frac{\sin(\alpha)}{h_b}\right) \cdot R_2 \tag{6-54}$$

The total resistance is now:

$$\frac{1}{R_{t,i}} = \frac{1}{R_{1,i}} + \frac{1}{R_2'} \tag{6-55}$$

Now starting from the tip of the blade, the initial flows over the blade are determined.

$$q_0 = \frac{\Delta p_{tip}}{\rho_w \cdot g \cdot R_{t,0}}, \quad q_{1,0} = \frac{\Delta p_{tip}}{\rho_w \cdot g \cdot R_{1,0}}, \quad q_{2,0} = \frac{\Delta p_{tip}}{\rho_w \cdot g \cdot R_2^{'}} \tag{6-56}$$

However Figure 6-13 (left graph) shows that the pore vacuum pressure distribution is not linear. Going from the tip (edge) of the blade to the top of the blade, first the pore vacuum pressure increases until it reaches a maximum and then it decreases (non-linear) until it reaches zero at the top of the blade. In this graph, the top of the blade is left and the tip of the blade is right. The graph on the right side of Figure 6-13 shows the pore vacuum pressure on the shear zone. In this graph, the tip of the blade is on the left side, while the right side is the point where the shear zone reaches the free water surface. Thus the pore vacuum pressure equals zero at the free water surface (most right point of the graph). Because the distribution of the pore vacuum pressure is non-linear, entrainment used. From the FEM calculations of Miedema (1987 September) and Yi (2000) it is known, that the shape of the pore vacuum pressure distribution on the blade depends strongly on the ratio of the length of the shear zone and the length of the blade, and on the length of the flat wear zone (as shown in Figure 6-18 and Figure 6-19).

The tip effect is taken into account by letting the total flow over the blade increase the first few iteration steps (**Int(0.05·N·α)**) and then decrease the total flow, so first:

$$q_i = q_{i-1} + q_{2,i-1}, \quad q_{1,i} = q_i \cdot \frac{R_{t,i}}{R_{1,i}}, \quad q_{2,i} = q_i \cdot \frac{R_{t,i}}{R_2^{'}},$$
$$\Delta p_i = \rho_w \cdot g \cdot q_i \cdot R_{t,i} \tag{6-57}$$

In each subsequent iteration step the flow over the blade and the pore vacuum pressure on the blade are determined according to:

$$q_i = q_{i-1} - q_{2,i-1}, \quad q_{1,i} = q_i \cdot \frac{R_{t,i}}{R_{1,i}}, \quad q_{2,i} = q_i \cdot \frac{R_{t,i}}{R_2^{'}},$$
$$\Delta p_i = \rho_w \cdot g \cdot q_i \cdot R_{t,i} \tag{6-58}$$

The average pore vacuum pressure on the blade can be determined by integration or summation.

$$p_{2m} = \frac{1}{n} \cdot \sum_{i=0}^{n} \Delta p_i \tag{6-59}$$

In the past decades many research has been carried out into the different cutting processes. The more fundamental the research, the less the theories can be applied in practice. The analytical method as described here, gives a method to use the basics of the sand cutting theory in a very practical and pragmatic way.

One has to consider that usually the accuracy of the output of a complex calculation is determined by the accuracy of the input of the calculation, in this case the soil mechanical parameters. Usually the accuracy of these parameters is not very accurate and in many cases not available at all. The accuracy of less than 10% of the analytical method described here is small with regard to the accuracy of the input. This does not mean however that the accuracy is not important, but this method can be applied for a quick first estimate.

By introducing some shape factors to the shape of the streamlines, the accuracy of the analytical model has been improved.

Table 6-1: A comparison between the numerical and analytical dimensionless pore vacuum pressures.

k_i/k_{max}=0.25	p_{1m}	p_{2m}	p_{1m} (analytical)	p_{2m} (analytical)
α=30°, β=30°, h_b/h_i=2	0.294	0.085	0.333	0.072
α=45°, β=25°, h_b/h_i=2	0.322	0.148	0.339	0.140
α=60°, β=20°, h_b/h_i=2	0.339	0.196	0.338	0.196

Table 6-1 was determined by Miedema & Yi (2001). Since then the algorithm has been improved, resulting in the program listing of Figure 6-21. With this new program listing also the pore vacuum pressure distribution on the blade can be determined.

```
'Determine the pore vacuum pressure on the shear plane
Teta1 = Pi/2 - Alpha - Beta
Teta2 = Alpha + Beta
Teta3 = Pi - Beta
Teta4 = Pi + Beta

Lmax = Hi / Sin(Beta)
L1 = Hb / Sin(Alpha)
L4 = 0.9 * Hi *(Hi/Hb)^0.5*(1.85*Alpha)^2*(Ki/Kmax)^0.4

N = 100
StepL = Lmax / N
P = 0
DPMax = RhoW * G * (Z + 10)

For I = 0 To N
  L = I * StepL + 0.0000000001
  'Determine the 4 lengths
  S1 = (Lmax - L) * (Pi/2+Teta1) + L1
  S2 = 0.8*L * Teta2
  S3 = 0.8*L * Teta3
  S4 = (Lmax - L) * Teta4 + L4
  'Determine the 4 resistances
  R1 = S1 / Kmax
  R2 = S2 / Kmax
  R3 = S3 / Ki
  R4 = S4 / Ki
  'Determine the total resistance
  Rt = 1 / (1 / R1 + 1 / R2 + 1 / R3 + 1 / R4)
  'Determine the pore vacuum pressure in point I
  DP = RhoW * G * Vc * E * Sin(Beta) * Rt
  'Integrate the pore vacuum pressure
  P = P + DP
  'Store the pore vacuum pressure in point I
  P1(I)=DP
Next I
'Store the pore vacuum pressure at the tip of the blade
Ptip=DP
'Determine the average pore vacuum pressure with correction for integration
P1m = (P - Ptip / 2) / N
'Determine the pore vacuum pressure on the blade
'Determine the 2 lengths
S1=L1
S2=0.8*Lmax*Teta2
'Determine the 2 resistances
R1=S1/Kmax
R2=S2/Kmax
'Compensate R2 for the number of intervals and the geometry
R2=R2*N*1.75*(Hi*Sin(Alpha)/(Hb*Sin(Beta))
'Determine the effective resistance
Rt=1/(1/R1+1/R2)
'Determine the total flow over the blade at the tip of the blade
Q=Ptip/(RhoW*G*Rt)
'Determine the two flows, Q1 over the blade and Q2 from entrainment
Q1=Ptip/(Rhow*G*R1)
Q2=Ptip/(Rhow*G*R2)
```

```
'Determine the pressure effect near the tip of the blade
TipEffect=Int(0.05*N*Alpha)
'Now determine the pore vacuum pressure distribution on the blade
P=0
For I = 1 To N
    'Determine the length of the top of the blade to point I
    S1=L1*(1-I/N)
    'Determine the resistance of the top of the blade to point I
    R1=S1/Kmax
    'Determine the effective resistance in point I
    Rt=1/(1/R1+1/R2)
    'Determine the flow at the tip of the blade
    IF I>TipEffect THEN
      Q=Q-Q2
    ELSE
      Q=Q+Q2
    END IF
    'Determine the 2 flows
    Q1=Q*Rt/R1
    Q2=Q*Rt/R2
    'Determine the pore vacuum pressure in point I
    DP=Rhow*G*Q*Rt
    'Integrate the pore vacuum pressure
    P = P + DP
    'Store the pore vacuum pressure in point I
    P2(I)=DP
Next I
'Determine the average pore vacuum pressure with correction for integration
P2m = (P - Ptip / 2) / N
```

Figure 6-21: A small program to determine the pore pressures.

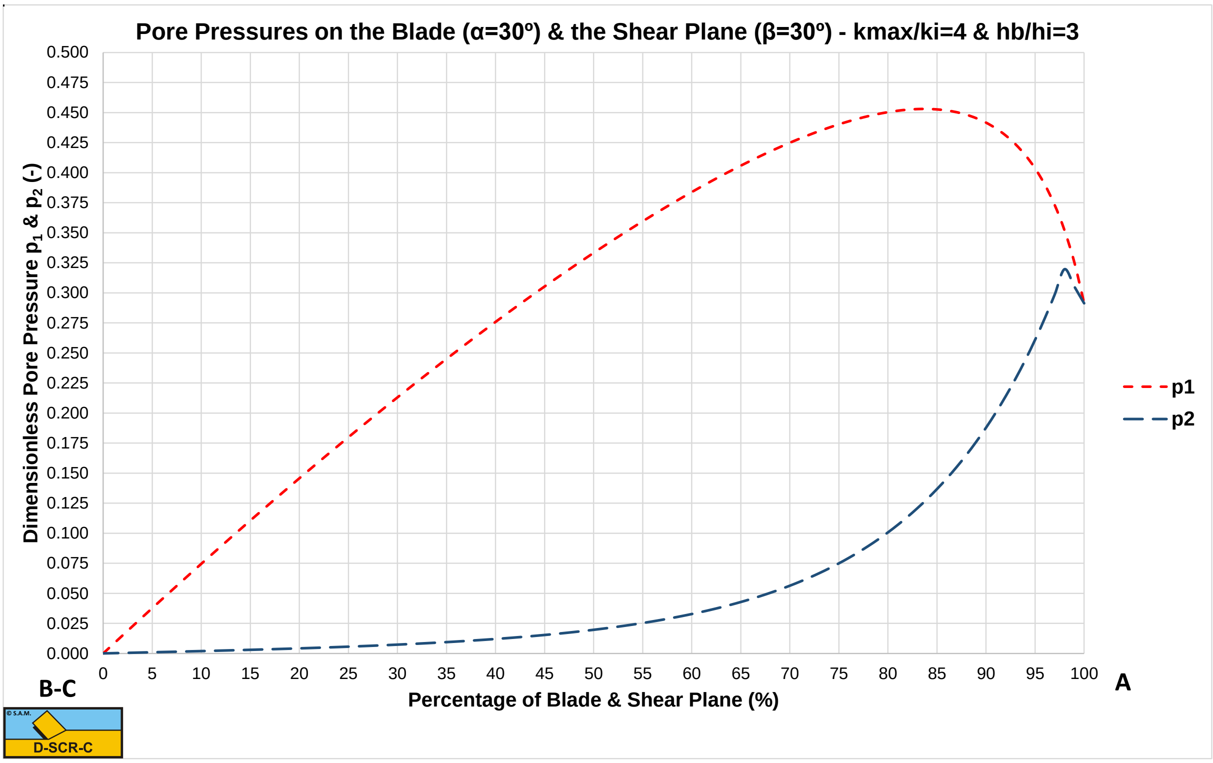

Figure 6-22: The dimensionless pressures on the blade and the shear plane, α=30°, β=30°, k_i/k_{max}=0.25, h_i/h_b=1/3.

Figure 6-21 shows a program listing to determine the pore pressures with the analytical/numerical method. Figure 6-22, Figure 6-23 and Figure 6-24 show the resulting pore vacuum pressure curves on the shear plane and on the blade for 30, 45 and 60 degree blades with a **h_i/h_b** ratio of 1/3 and a **k_i/k_{max}** ratio of 1/4. The curves match both the FEM calculations and the experiments very well.

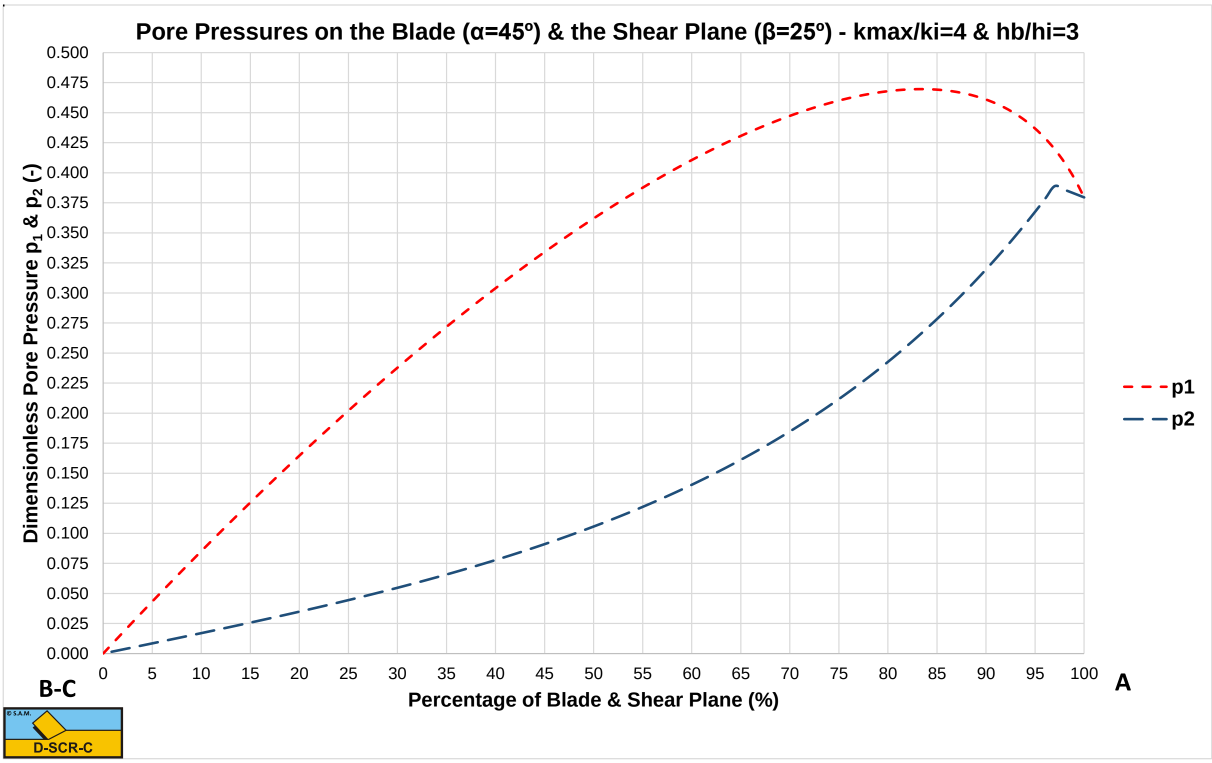

Figure 6-23: The dimensionless pressures on the blade and the shear plane, α=45°, β=25°, k_i/k_{max}=0.25, h_i/h_b=1/2.

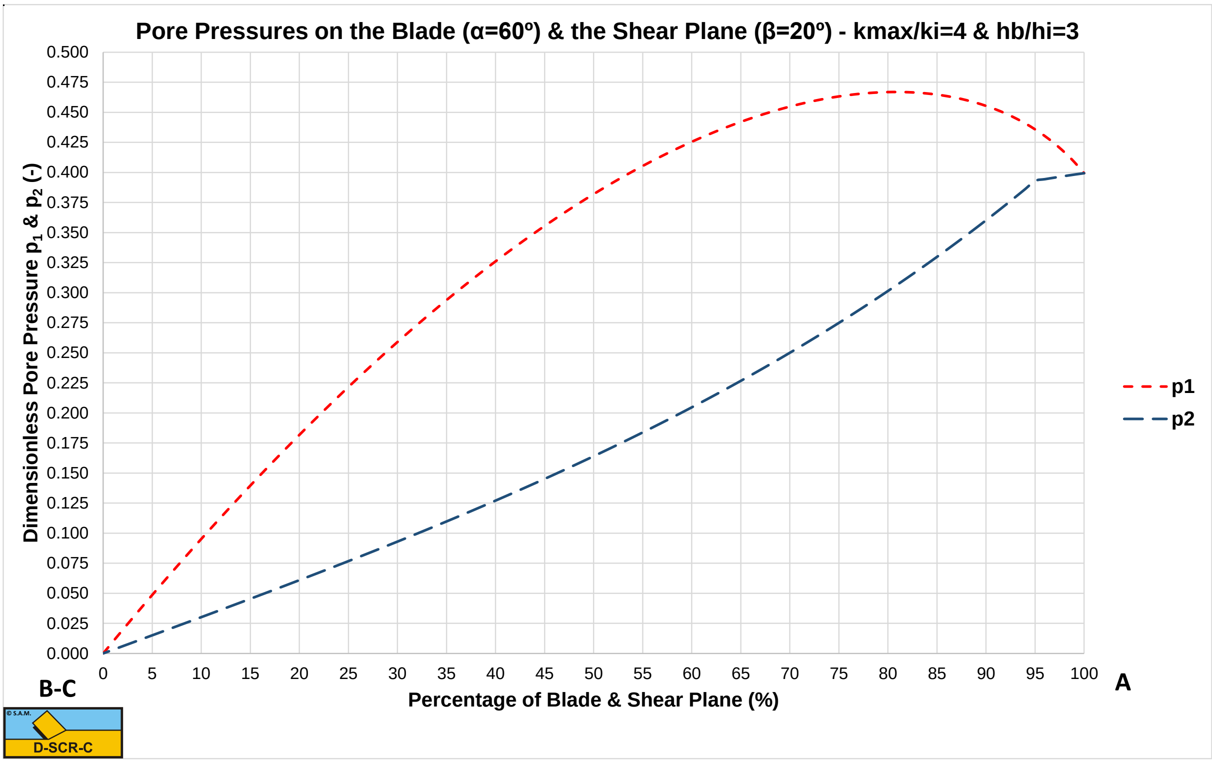

Figure 6-24: The dimensionless pressures on the blade and the shear plane, α=60°, β=20°, k_i/k_{max}=0.25, h_i/h_b=1/1.

6.9. Determination of the Shear Angle β.

The equations are derived with which the forces on a straight blade can be determined according to the method of Coulomb (see Verruyt (1983)). Unknown in these equations is the shear angle **β**. In literature several methods are used to determine this shear angle.
The oldest is perhaps the method of Coulomb (see Verruyt (1983)). This method is widely used in sheet pile wall calculations. Since passive earth pressure is the cause for failure here, it is necessary to find the shear angle at which the total, on the earth, exerted force by the sheet pile wall is at a minimum.

When the water pressures are not taken into account, an analytical solution for this problem can be found.
Another failure criterion is used by Hettiaratchi and Reece (1966), (1967A), (1967B), (1974) and (1975). This principle is based upon the cutting of dry sand. The shear plane is not assumed to be straight as in the method of Coulomb, but the shear plane is composed of a logarithmic spiral from the blade tip that changes into a straight shear plane under an angle of **45º - φ/2** with the horizontal to the sand surface. The straight part of the shear plane is part of the so-called passive Rankine zone. The origin of the logarithmic spiral is chosen such that the total force on the blade is minimal.

There are perhaps other failure criterions for sheet pile wall calculations known in literature, but these mechanisms are only suited for a one-time failure of the earth. In the cutting of soil the process of building up stresses and next the collapse of the earth is a continuous process.

Another criterion for the collapse of earth is the determination of those failure conditions for which the total required strain energy is minimal. Rowe (1962) and Josselin de Jong (1976) use this principle for the determination of the angle under which local shear takes place. From this point of view it seems plausible to assume that those failure criterions for the cutting of sand have to be chosen, for which the cutting work is minimal. This implies that the shear angle **β** has to be chosen for which the cutting work and therefore the horizontal force, exerted by the blade on the soil, is minimal. Miedema (1985B) and (1986B) and Steeghs (1985A) and (1985B) have chosen this method.
Assuming that the water pressures are dominant in the cutting of packed water saturated sand, and thus neglecting adhesion, cohesion, gravity, inertia forces, flow resistance and under-pressure behind the blade, the force $\mathbf{F_h}$ (equation (6-14)) becomes for the non-cavitating situation:

$$\mathbf{F_h}=\left(\begin{array}{l}-\mathbf{p_{2m}}\cdot\mathbf{h_b}\cdot\dfrac{\sin(\alpha)}{\sin(\alpha)}\\ \\ +\mathbf{p_{2m}}\cdot\mathbf{h_b}\cdot\dfrac{\sin(\alpha+\beta+\varphi)\cdot\sin(\alpha+\delta)}{\sin(\alpha+\beta+\delta+\varphi)\cdot\sin(\alpha)}\\ \\ +\mathbf{p_{1m}}\cdot\mathbf{h_i}\cdot\dfrac{\sin(\varphi)\cdot\sin(\alpha+\delta)}{\sin(\alpha+\beta+\delta+\varphi)\cdot\sin(\beta)}\end{array}\right)\cdot\frac{\rho_w\cdot\mathbf{g}\cdot\mathbf{v_c}\cdot\varepsilon\cdot\mathbf{h_i}\cdot\mathbf{w}}{(\mathbf{a_1}\cdot\mathbf{k_i}+\mathbf{a_2}\cdot\mathbf{k_{max}})}\cdot \qquad \textbf{(6-60)}$$

With the following simplification:

$$\mathbf{F_h'}=\frac{\mathbf{F_h}}{\dfrac{\rho_w\cdot\mathbf{g}\cdot\mathbf{v_c}\cdot\varepsilon\cdot\mathbf{h_i}\cdot\mathbf{w}}{(\mathbf{a_1}\cdot\mathbf{k_i}+\mathbf{a_2}\cdot\mathbf{k_{max}})}} \qquad \textbf{(6-61)}$$

Since the value of the shear angle **β**, for which the horizontal force is minimal, has to be found, equations (6-62) and (6-65) are set equal to zero. It is clear that this problem has to be solved iterative, because an analytical solution is impossible.

The Newton-Rhapson method works very well for this problem. In Miedema (1987 September) and 0 and 0 the resulting shear angles **β**, calculated with this method, can be found for several values of **δ**, **φ**, **α**, several ratios of $\mathbf{h_b/h_i}$ and for the non-cavitating and cavitating cutting process.

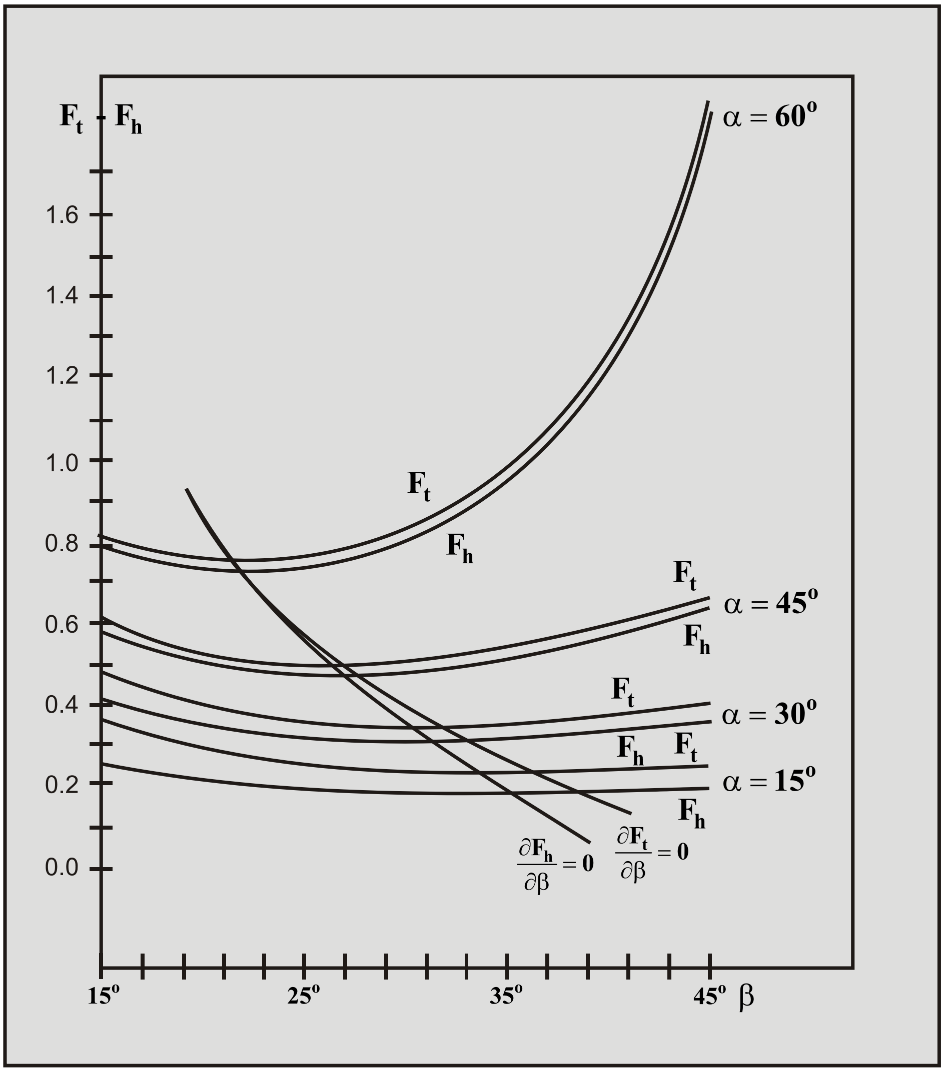

Figure 6-25: The forces F_h and F_t as function of the shear angle β and the blade angle α.

Interesting are now the results if another method is used. To check this, the shear angles have also been determined according Coulomb's criterion: there is failure at the shear angle for which the total force, exerted by the blade on the soil, is minimal. The maximum deviation of these shear angles with the shear angles according Miedema (1987 September) has a value of only 3° at a blade angle of 15°. The average deviation is approximately 1.5° for blade angles up to 60°.

The forces have a maximum deviation of less than 1%. It can therefore be concluded that it does not matter if the total force, exerted by the soil on the blade, is minimized, or the horizontal force. Next these calculations showed that the cutting forces, as a function of the shear angle, vary only slightly with the shear angles, found using the above equation. This sensitivity increases with an increasing blade angle. Figure 6-25 shows this for the following conditions:
The forces are determined by minimizing the specific cutting energy and minimizing the total cutting force $\mathbf{F_t}$. **(**$\boldsymbol{\alpha = 15°}$, **30°**, **45°** and **60°**, $\boldsymbol{\delta = 24°}$, $\boldsymbol{\varphi = 42°}$, $\mathbf{h_b/h_i = 1}$ and a non-cavitating cutting process).

The derivative of the force $\mathbf{F'_h}$ to the shear angle $\boldsymbol{\beta}$ becomes:

$$\begin{aligned}\frac{\partial F_h^{'}}{\partial \beta} = & -p_{1m}\cdot h_i\cdot\frac{\sin(\varphi)\cdot\sin(\alpha+2\cdot\beta+\delta+\varphi)\cdot\sin(\alpha+\delta)}{\sin^2(\beta)\cdot\sin(\alpha+\beta+\delta+\varphi)^2}\\ & +p_{2m}\cdot h_b\cdot\frac{\sin(\delta)\cdot\sin(\alpha+\delta)}{\sin(\alpha)\cdot\sin(\alpha+\beta+\delta+\varphi)^2}\\ & +\frac{\partial p_{1m}}{\partial\beta}\cdot h_i\cdot\frac{\sin(\varphi)\cdot\sin(\alpha+\delta)}{\sin(\beta)\cdot\sin(\alpha+\beta+\delta+\varphi)}\\ & +\frac{\partial p_{2m}}{\partial\beta}\cdot h_b\cdot\left\{\frac{\sin(\alpha+\beta+\varphi)\cdot\sin(\alpha+\delta)}{\sin(\alpha)\cdot\sin(\alpha+\beta+\delta+\varphi)}-1\right\}=0\end{aligned} \tag{6-62}$$

For the cavitating situation this gives for the force **F_h**:

$$F_h=\left(\begin{array}{l}-h_b\cdot\frac{\sin(\alpha)}{\sin(\alpha)}+h_b\cdot\frac{\sin(\alpha+\beta+\varphi)\cdot\sin(\alpha+\delta)}{\sin(\alpha+\beta+\delta+\varphi)\cdot\sin(\alpha)}\\ \\ +h_i\cdot\frac{\sin(\varphi)\cdot\sin(\alpha+\delta)}{\sin(\alpha+\beta+\delta+\varphi)\cdot\sin(\beta)}\end{array}\right)\cdot\rho_w\cdot g\cdot(z+10)\cdot w \tag{6-63}$$

With the following simplification:

$$F_h^{'}=\frac{F_h}{\rho_w\cdot g\cdot(z+10)\cdot w} \tag{6-64}$$

The derivative of the force **F'_h** to the shear angle **β** becomes:

$$\begin{aligned}\frac{\partial F_h^{'}}{\partial\beta}= & -h_i\cdot\frac{\sin(\varphi)\cdot\sin(\alpha+2\cdot\beta+\delta+\varphi)\cdot\sin(\alpha+\delta)}{\sin^2(\beta)\cdot\sin(\alpha+\beta+\delta+\varphi)^2}\\ & +h_b\cdot\frac{\sin(\delta)\cdot\sin(\alpha+\delta)}{\sin(\alpha)\cdot\sin(\alpha+\beta+\delta+\varphi)^2}=0\end{aligned} \tag{6-65}$$

For the cavitating cutting process equation (6-65) can be simplified to:

$$h_b\cdot\sin(\delta)\cdot\sin^2(\beta)=h_i\cdot\sin(\alpha)\cdot\sin(\phi)\cdot\sin(\alpha+2\cdot\beta+\delta+\varphi) \tag{6-66}$$

The iterative results can be approximated by:

$$\beta=61.29^{\circ}+0.345\cdot\frac{h_b}{h_i}-0.3068\cdot\alpha-0.4736\cdot\delta-0.248\cdot\varphi \tag{6-67}$$

6.10. The Coefficients a_1 and a_2.

In the derivation of the calculation of the water under-pressures around the blade for the non-cavitating cutting process, resulting in equations (6-30) and (6-31), it already showed that the water under-pressures are determined by the permeability of the undisturbed sand $\mathbf{k_i}$ and the permeability of the disturbed sand $\mathbf{k_{max}}$. Equation (6-25) shows this dependence. The water under-pressures are determined for several ratios of the initial permeability of the undisturbed sand to the maximum permeability of the disturbed sand:

$\mathbf{k_i/k_{max} = 1}$

$\mathbf{k_i/k_{max} = 0.5}$

$\mathbf{k_i/k_{max} = 0.25}$

The average water under-pressures $\mathbf{p_{1m}}$ and $\mathbf{p_{2m}}$ can be put against the ratio $\mathbf{k_i/k_{max}}$, for a certain shear angle $\boldsymbol{\beta}$. A hyperbolic relation emerges between the average water under-pressures and the ratio of the permeabilities. If the reciprocal values of the average water under-pressures are put against the ratio of the permeabilities a linear relation emerges.

The derivatives of $\mathbf{p_{1m}}$ and $\mathbf{p_{2m}}$ to the ratio $\mathbf{k_i/k_{max}}$ are, however, not equal to each other. This implies that a relation for the forces as a function of the ratio of permeabilities cannot be directly derived from the found average water under-pressures.

This is in contrast with the method used by Van Leussen and Van Os (1987 December). They assume that the average pore pressure on the blade has the same dependability on the ratio of permeabilities as the average pore pressure in the shear zone. No mathematical background is given for this assumption.

For the several ratios of the permeabilities it is possible with the shear angles determined, to determine the dimensionless forces $\mathbf{F_h}$ and $\mathbf{F_v}$. If these dimensionless forces are put against the ratio of the permeabilities, also a hyperbolic relation is found (Miedema (1987 September)), shown in Figure 6-26 and Figure 6-27.
A linear relation can therefore also be found if the reciprocal values of the dimensionless forces are taken. This relation can be represented by:

$$\frac{1}{F_h} = a + b \cdot \frac{k_i}{k_{max}} \tag{6-68}$$

With the next transformations an equation can be derived for a weighted average permeability $\mathbf{k_m}$:

$$a_1 = \frac{b}{a+b} \quad \& \quad a_2 = \frac{a}{a+b} \tag{6-69}$$

So:

$$k_m = a_1 \cdot k_i + a_2 \cdot k_{max} \quad \text{with: } a_1 + a_2 = 1 \tag{6-70}$$

Since the sum of the coefficients $\mathbf{a_1}$ and $\mathbf{a_2}$ is equal to 1 only coefficient $\mathbf{a_1}$ is given in Miedema (1987) and 0. It also has to be remarked that this coefficient is determined on the basis of the linear relation of $\mathbf{F_h}$ (dimensionless $\mathbf{c_1}$), because the horizontal force gives more or less the same relation as the vertical force, but has besides a much higher value. Only for the 60° blade, where the vertical force is very small and can change direction, differences occur between the linear relations of the horizontal and the vertical force as function of the ratio of the permeabilities.
The influence of the undisturbed soil increases when the blade-height/layer-thickness ratio increases. This can be explained by the fact that the water that flows to the shear zone over the blade has to cover a larger distance with an increasing blade height and therefore has to overcome a higher resistance. Relatively more water will have to flow through the undisturbed sand to the shear zone with an increasing blade height.

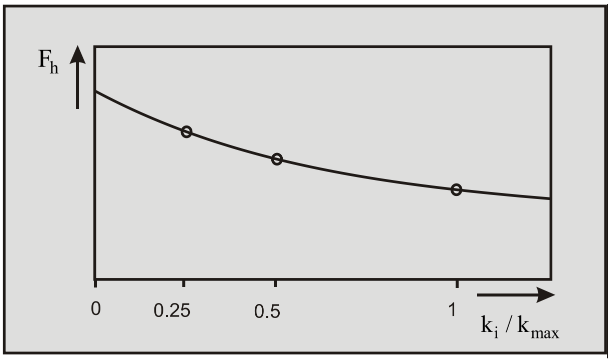

Figure 6-26: The force F_h as function of the ratio between k_i and k_{max}.

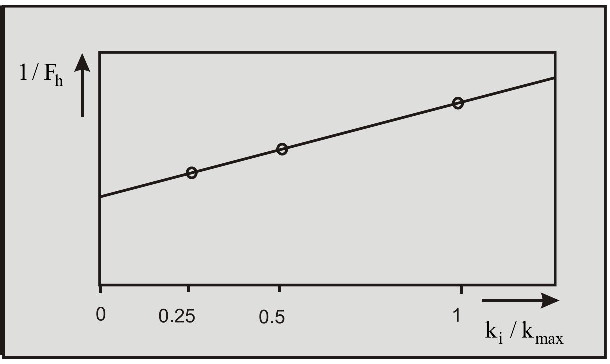

Figure 6-27: The reciprocal of the force F_h as function of the ratio between k_i and k_{max}.

6.11. Determination of the Coefficients c_1, c_2, d_1 and d_2.

If only the influence of the water under-pressures on the forces that occur with the cutting of saturated packed sand under water is taken in to account, equations (6-14) and (6-15) can be applied. It will be assumed that the non-cavitating process switches to the cavitating process for that cutting velocity $\mathbf{v_c}$, for which the force in the direction of the cutting velocity $\mathbf{F_h}$ is equal for both processes. In reality, however, there is a transition region between both processes, where locally cavitation starts in the shear zone. Although this transition region starts at about 65% of the cutting velocity at which, theoretically, full cavitation takes place, it shows from the results of the cutting tests that for the determination of the cutting forces the existence of a transition region can be neglected. In the simplified equations the coefficients $\mathbf{c_1}$ and $\mathbf{d_1}$ represent the dimensionless horizontal force (or the force in the direction of the cutting velocity) in the non-cavitating and the cavitating cutting process. The coefficients $\mathbf{c_2}$ and $\mathbf{d_2}$ represent the dimensionless vertical force or the force perpendicular to the direction of the cutting velocity in the non-cavitating and the cavitating cutting process. For the non-cavitating cutting process:

$$F_{ci} = \frac{c_i \cdot \rho_w \cdot g \cdot v_c \cdot h_i^2 \cdot \varepsilon \cdot w}{k_m} \tag{6-71}$$

In which:

$$c_1 = \left(\frac{\left(p_{1m} \cdot \frac{\sin(\phi)}{\sin(\beta)} + p_{2m} \cdot \frac{h_b}{h_i} \cdot \frac{\sin(\alpha+\beta+\phi)}{\sin(\alpha)} \right) \cdot \sin(\alpha+\delta)}{\sin(\alpha+\beta+\delta+\phi)} - p_{2m} \cdot \frac{h_b}{h_i} \cdot \frac{\sin(\alpha)}{\sin(\alpha)} \right) \cdot \frac{(a_1 \cdot k_i + a_2 \cdot k_{max})}{k_{max}} \tag{6-72}$$

And:

$$c_2 = \left(\frac{\left(p_{1m} \cdot \frac{\sin(\phi)}{\sin(\beta)} + p_{2m} \cdot \frac{h_b}{h_i} \cdot \frac{\sin(\alpha+\beta+\phi)}{\sin(\alpha)} \right) \cdot \cos(\alpha+\delta)}{\sin(\alpha+\beta+\delta+\phi)} - p_{2m} \cdot \frac{h_b}{h_i} \cdot \frac{\cos(\alpha)}{\sin(\alpha)} \right) \cdot \frac{(a_1 \cdot k_i + a_2 \cdot k_{max})}{k_{max}} \tag{6-73}$$

And for the cavitating cutting process:

$$F_{ci}=d_i\cdot\rho_w\cdot g\cdot(z+10)\cdot h_i\cdot w \tag{6-74}$$

In which:

$$d_1=\frac{\left(\dfrac{\sin(\phi)}{\sin(\beta)}+\dfrac{h_b}{h_i}\cdot\dfrac{\sin(\alpha+\beta+\phi)}{\sin(\alpha)}\right)\cdot\sin(\alpha+\delta)}{\sin(\alpha+\beta+\delta+\phi)}-\frac{h_b}{h_i}\cdot\frac{\sin(\alpha)}{\sin(\alpha)} \tag{6-75}$$

And:

$$d_2=\frac{\left(\dfrac{\sin(\phi)}{\sin(\beta)}+\dfrac{h_b}{h_i}\cdot\dfrac{\sin(\alpha+\beta+\phi)}{\sin(\alpha)}\right)\cdot\cos(\alpha+\delta)}{\sin(\alpha+\beta+\delta+\phi)}-\frac{h_b}{h_i}\cdot\frac{\cos(\alpha)}{\sin(\alpha)} \tag{6-76}$$

The values of the 4 coefficients are determined by minimizing the cutting work that is at that shear angle **β** where the derivative of the horizontal force to the shear angle is zero. The coefficients **c_1, c_2, d_1** and **d_2** are given in Miedema (1987 September) and in 0 and 0 for the non-cavitating cutting process and 0 and 0 for the cavitating cutting process as functions of **α, δ, φ** and the ratio **h_b/h_i**.

6.11.1. Approximations.

Assuming δ=2/3·φ the coefficients can be approximated by:

α=30° and **h_b/h_i=1**:

$$c_1=0.0427\cdot e^{0.0509\cdot\varphi}\quad\text{and}\quad c_2=0.0343\cdot e^{0.0341\cdot\varphi}$$

$$d_1=0.3027\cdot e^{0.0516\cdot\varphi}\quad\text{and}\quad d_2=-0.3732+0.0219\cdot\varphi \tag{6-77}$$

α=30° and **h_b/h_i=2**:

$$c_1=0.0455\cdot e^{0.0511\cdot\varphi}\quad\text{and}\quad c_2=0.0304\cdot e^{0.0356\cdot\varphi}$$

$$d_1=0.4795\cdot e^{0.0490\cdot\varphi}\quad\text{and}\quad d_2=-0.5380+0.0159\cdot\varphi \tag{6-78}$$

α=30° and **h_b/h_i=3**:

$$c_1=0.0457\cdot e^{0.0512\cdot\varphi}\quad\text{and}\quad c_2=0.0312\cdot e^{0.0348\cdot\varphi}$$

$$d_1=0.6418\cdot e^{0.0478\cdot\varphi}\quad\text{and}\quad d_2=-0.7332+0.0094\cdot\varphi \tag{6-79}$$

α=45° and **h_b/h_i=1**:

$$c_1=0.0485\cdot e^{0.0577\cdot\varphi}\quad\text{and}\quad c_2=0.0341\cdot e^{0.0255\cdot\varphi}$$

$$d_1=0.2618\cdot e^{0.0603\cdot\varphi}\quad\text{and}\quad d_2=-0.0287+0.0081\cdot\varphi \tag{6-80}$$

α=45° and **h$_b$/h$_i$=2**:

$$\begin{gathered}c_1 = 0.0545 \cdot e^{0.0580 \cdot \varphi} \quad \text{and} \quad c_2 = 0.0281 \cdot e^{0.0238 \cdot \varphi} \\ d_1 = 0.3764 \cdot e^{0.0577 \cdot \varphi} \quad \text{and} \quad d_2 = -0.0192 - 0.0017 \cdot \varphi\end{gathered} \tag{6-81}$$

α=45° and **h$_b$/h$_i$=3**:

$$\begin{gathered}c_1 = 0.0551 \cdot e^{0.0589 \cdot \varphi} \quad \text{and} \quad c_2 = 0.0286 \cdot e^{0.0199 \cdot \varphi} \\ d_1 = 0.4814 \cdot e^{0.0563 \cdot \varphi} \quad \text{and} \quad d_2 = -0.0295 - 0.0116 \cdot \varphi\end{gathered} \tag{6-82}$$

α=60° and **h$_b$/h$_i$=1**:

$$\begin{gathered}c_1 = 0.0474 \cdot e^{0.0688 \cdot \varphi} \quad \text{and} \quad c_2 = -0.2902 + 0.0203 \cdot \varphi - 0.000334 \cdot \varphi^2 \\ d_1 = 0.2342 \cdot e^{0.0722 \cdot \varphi} \quad \text{and} \quad d_2 = +1.0548 - 0.0343 \cdot \varphi\end{gathered} \tag{6-83}$$

α=60° and **h$_b$/h$_i$=2**:

$$\begin{gathered}c_1 = 0.0562 \cdot e^{0.0686 \cdot \varphi} \quad \text{and} \quad c_2 = -0.3550 + 0.0235 \cdot \varphi - 0.000403 \cdot \varphi^2 \\ d_1 = 0.3148 \cdot e^{0.0695 \cdot \varphi} \quad \text{and} \quad d_2 = +1.2737 - 0.0516 \cdot \varphi\end{gathered} \tag{6-84}$$

α=60° and **h$_b$/h$_i$=3**:

$$\begin{gathered}c_1 = 0.0593 \cdot e^{0.0692 \cdot \varphi} \quad \text{and} \quad c_2 = -0.3785 + 0.0250 \cdot \varphi - 0.000445 \cdot \varphi^2 \\ d_1 = 0.3889 \cdot e^{0.0680 \cdot \varphi} \quad \text{and} \quad d_2 = +1.4708 - 0.0685 \cdot \varphi\end{gathered} \tag{6-85}$$

The shear angle **β** can be approximated by, for the non-cavitating case:

$$\beta = \frac{\pi - \alpha - \varphi - \delta}{3} - 0.0037 \cdot \frac{h_b}{h_i} \tag{6-86}$$

The shear angle **β** can be approximated by, for the cavitating case:

$$\beta = 1 - \frac{1}{6} \cdot \alpha - \frac{2}{7} \cdot (\varphi + \delta) - 0.057 \cdot \frac{h_b}{h_i} \tag{6-87}$$

6.12. Specific Cutting Energy.

In the dredging industry, the specific cutting energy is described as:

The amount of energy, that has to be added to a volume unit of soil (e.g. sand) to excavate the soil.

The dimension of the specific cutting energy is: kN/m² or kPa for sand and clay, while for rock often MN/m^2 or MPa is used.

Adhesion, cohesion, gravity and the inertia forces will be neglected in the determination of the specific cutting energy. For the case as described above, cutting with a straight blade with the direction of the cutting velocity perpendicular to the blade (edge of the blade) and the specific cutting energy can be written:

$$\mathbf{E_{sp}=\frac{F_h\cdot v_c}{h_i\cdot w\cdot v_c}=\frac{F_h}{h_i\cdot w}} \tag{6-88}$$

The method, with which the shear angle β is determined, is therefore equivalent with minimizing the specific cutting energy, for certain blade geometry and certain soil mechanical parameters. For the specific energy, for the non-cavitating cutting process, it can now be derived from equations (6-71) and (6-88), that:

$$\mathbf{E_{nc}=c_1\cdot\rho_w\cdot g\cdot v_c\cdot h_i\cdot\frac{\varepsilon}{k_m}} \tag{6-89}$$

For the specific energy, for the fully cavitating cutting process, can be written from equations (6-74) and (6-88):

$$\mathbf{E_{ca}=d_1\cdot\rho_w\cdot g\cdot(z+10)} \tag{6-90}$$

From these equations can be derived that the specific cutting energy, for the non-cavitating cutting process is proportional to the cutting velocity, the layer-thickness and the volume strain and inversely proportional to the permeability. For the fully cavitating process the specific cutting energy is only dependent on the water depth.

Therefore it can be posed, that the specific cutting energy, for the fully cavitating cutting process is an upper limit, provided that the inertia forces, etc., can be neglected. At very high cutting velocities, however, the specific cutting energy, also for the cavitating process will increase as a result of the inertia forces and the water resistance.

6.12.1. Specific Energy and Production in Sand.

As discussed previously, the cutting process in sand can be distinguished in a non-cavitating and a cavitating process, in which the cavitating process can be considered to be an upper limit to the cutting forces. Assuming that during an SPT test in water-saturated sand, the cavitating process will occur, because of the shock wise behavior during the SPT test, the SPT test will give information about the cavitating cutting process. Whether in practice, the cavitating cutting process will occur, depends on the soil mechanical parameters, the geometry of the cutting process and the operational parameters. The cavitating process gives an upper limit to the forces, power and thus the specific energy and a lower limit to the production and will therefore be used as a starting point for the calculations. For the specific energy of the cavitating cutting process, the following equation can be derived according to Miedema (1987 September):

$$E_{sp} = \rho_w \cdot g \cdot (z+10) \cdot d_1 \qquad \textbf{(6-91)}$$

The production, for an available power **P_a**, can be determined by:

$$Q = \frac{P_a}{E_{sp}} = \frac{P_a}{\rho_w \cdot g \cdot (z+10) \cdot d_1} \qquad \textbf{(6-92)}$$

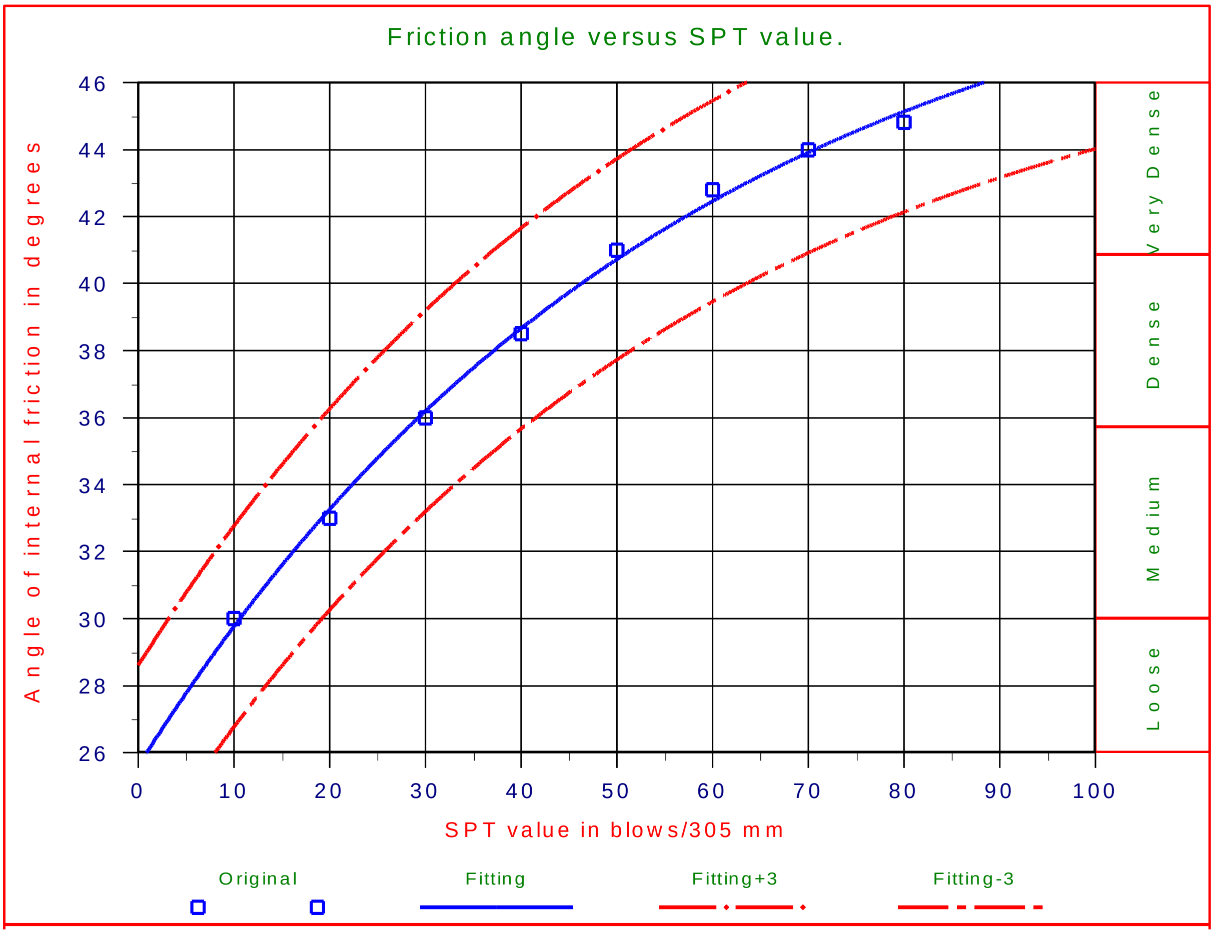

Figure 6-28: Friction angle versus SPT value (Lambe & Whitman (1979), page 148) and Miedema (1995)).

The coefficient $\mathbf{d_1}$ is the only unknown in the above equation. A relation between $\mathbf{d_1}$ and the SPT value of the sand and between the SPT value and the water depth has to be found. The dependence of $\mathbf{d_1}$ on the parameters $\boldsymbol{\alpha}$, $\mathbf{h_i}$ and $\mathbf{h_b}$ can be estimated accurately. For normal sands there will be a relation between the angle of internal friction and the soil interface friction. Assume blade angles of 30, 45 and 60 degrees, a ratio of 3 for $\mathbf{h_b / h_i}$ and a soil/interface friction angle of 2/3 times the internal friction angle. For the coefficient $\mathbf{d_1}$ the following equations are found by regression:

$$\mathbf{d_1 = (0.64 + 0.56 \cdot h_b / h_i) + (0.0164 + 0.0085 \cdot h_b / h_i) \cdot SPT_{10}} \quad (\alpha = 30 \text{ degrees}) \tag{6-93}$$

$$\mathbf{d_1 = (0.83 + 0.45 \cdot h_b / h_i) + (0.0268 + 0.0085 \cdot h_b / h_i) \cdot SPT_{10}} \quad (\alpha = 45 \text{ degrees}) \tag{6-94}$$

$$\mathbf{d_1 = (0.99 + 0.39 \cdot h_b / h_i) + (0.0503 + 0.0099 \cdot h_b / h_i) \cdot SPT_{10}} \quad (\alpha = 60 \text{ degrees}) \tag{6-95}$$

With: $\mathbf{SPT_{10}}$ = the SPT value normalized to 10 m water depth.

Lambe & Whitman (1979), page 78) and Miedema (1995) give the relation between the SPT value, the relative density **RD** (0-1) and the hydrostatic pressure in two graphs, see Figure 6-29. With some curve-fitting these graphs can be summarized with the following equation:

$$\mathbf{SPT = 0.243 \cdot \left(82.5 + \rho_l \cdot g \cdot (z + 10)\right) \cdot RD^{2.52}} \tag{6-96}$$

And:

$$\mathbf{RD = \left(\frac{4.12 \cdot SPT}{\left(82.5 + \rho_l \cdot g \cdot (z + 10)\right)}\right)^{0.397}} \tag{6-97}$$

Lambe & Whitman (1979), (page 148) and Miedema (1995) give the relation between the SPT value and the angle of internal friction, also in a graph, see Figure 6-28. This graph is valid up to 12 m in dry soil. With respect to the internal friction, the relation given in the graph has an accuracy of 3 degrees. A load of 12 m dry soil with a density of 1.67 ton/m^3 equals a hydrostatic pressure of 20 m.w.c. An absolute hydrostatic pressure of 20 m.w.c. equals 10 m of water depth if cavitation is considered. Measured SPT values at any depth will have to be reduced to the value that would occur at 10 m water depth. This can be accomplished with the following equation (see Figure 6-30):

$$\mathbf{SPT_{10} = \frac{282.5}{\left(82.5 + \rho_l \cdot g \cdot (z + 10)\right)} \cdot SPT_z} \tag{6-98}$$

With the aim of curve-fitting, the relation between the SPT value reduced to 10 m water depth and the angle of internal friction can be summarized to:

$$\mathbf{\varphi = 51.5 - 25.9 \cdot e^{-0.01753 \cdot SPT_{10}}} \quad (+/- \text{ 3 degrees}) \tag{6-99}$$

For water depths of 0, 5, 10, 15, 20, 25 and 30 m and an available power of 100 kW the production is shown graphically for SPT values in the range of 0 to 100 SPT. Figure 6-31 shows the specific energy and Figure 6-32 the production for a 45 degree blade angle.

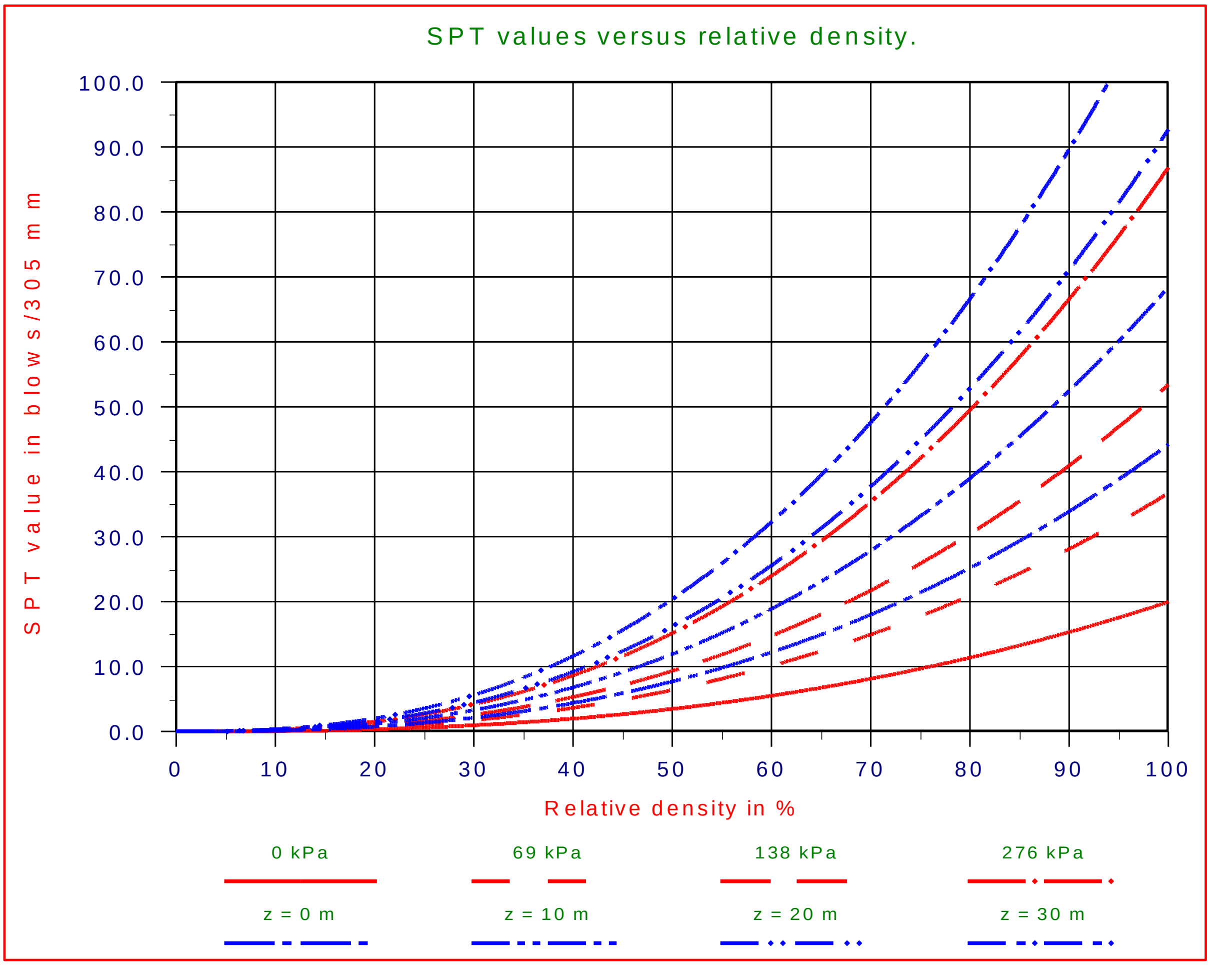

Figure 6-29: SPT values versus relative density (Lambe & Whitman (1979), page 78) and Miedema (1995)).

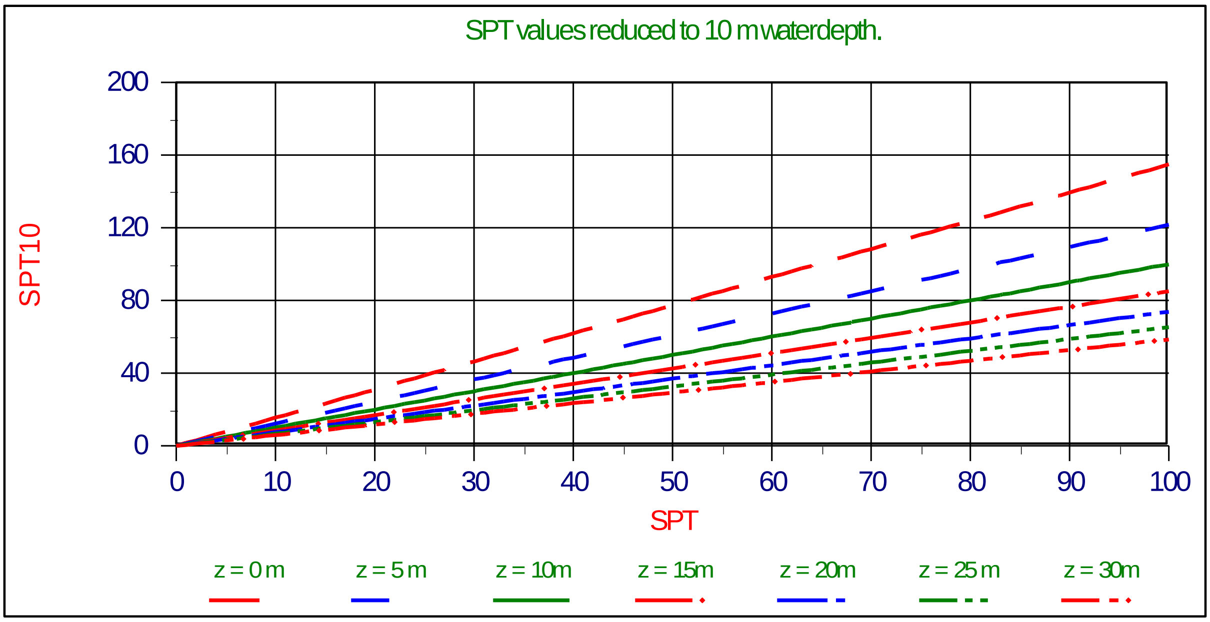

Figure 6-30: SPT values reduced to 10m water depth.

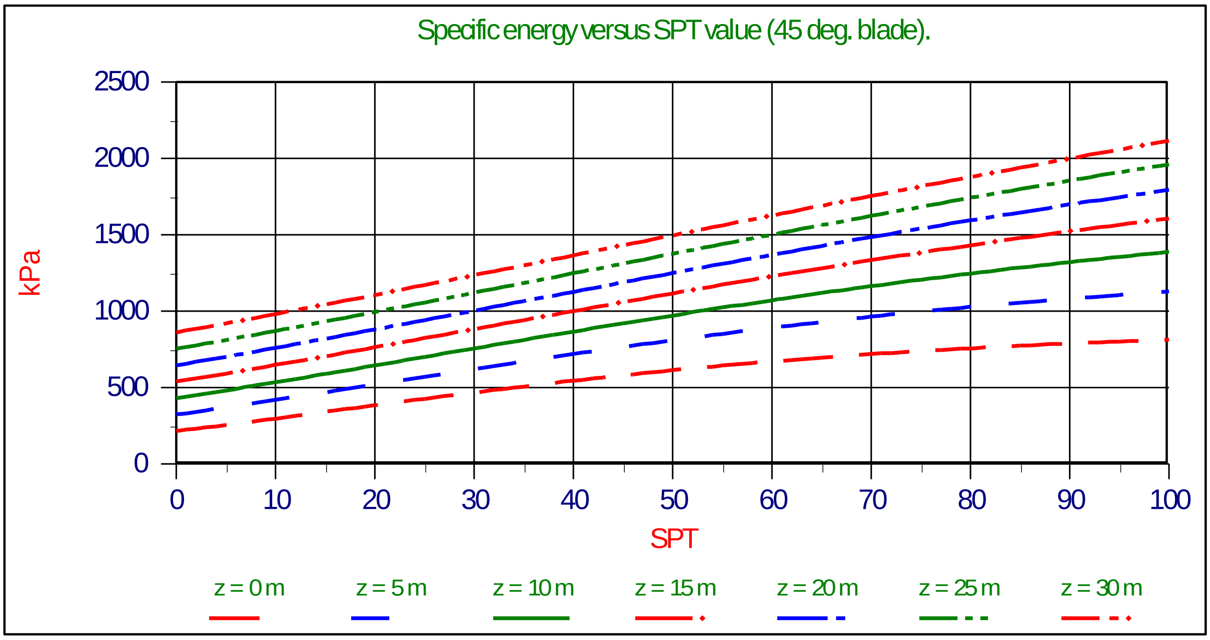

Figure 6-31: Specific energy versus SPT value (45 deg. blade).

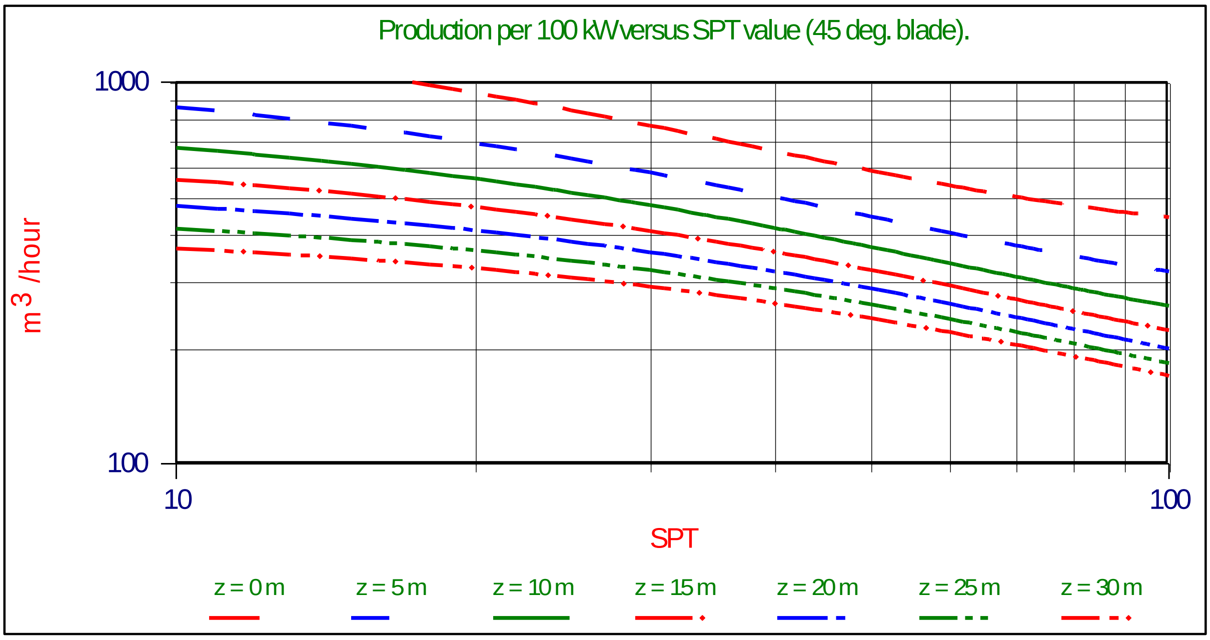

Figure 6-32: Production per 100kW versus SPT value (45 deg. blade).

6.12.2. The Transition Cavitating/Non-Cavitating.

Although the SPT value only applies to the cavitating cutting process, it is necessary to have a good understanding of the transition between the non-cavitating and the cavitating cutting process. Based on the theory in Miedema (1987 September), an equation has been derived for this transition. If this equation is valid, the cavitating cutting process will occur.

$$v_c > \frac{d_1 \cdot (z+10) \cdot k_m}{c_1 \cdot h_i \cdot \varepsilon} \tag{6-100}$$

The ratio $\mathbf{d_1/c_1}$ appears to have an almost constant value for a given blade angle, independent of the soil mechanical properties. For a blade angle of 30 degrees this ratio equals 11.9. For a blade angle of 45 degrees this ratio equals 7.72 and for a blade angle of 60 degrees this ratio equals 6.14. The ratio $\mathbf{\varepsilon/k_m}$ has a value in the range of 1000 to 10000 for medium to hard packed sands. At a given layer thickness and water depth, the transition cutting velocity can be determined using the above equation. At a given cutting velocity and water depth, the transition layer thickness can be determined.

6.12.3. Conclusions Specific Energy

To check the validity of the above derived theory, research has been carried out in the laboratory of the chair of Dredging Technology of the Delft University of Technology. The tests are carried out in hard packed water saturated sand, with a blade of 0.3 m by 0.2 m. The blade had cutting angles of 30, 45 and 60 degrees and deviation angles of 0, 15, 30 and 45 degrees. The layer thicknesses were 2.5, 5 and 10 cm and the drag velocities 0.25, 0.5 and 1 m/s. Figure 6-57 shows the results with a deviation angle of 0 degrees, while Figure 6-58 shows the results with a deviation angle of 45 degrees. The lines in this figure show the theoretical forces. As can be seen, the measured forces match the theoretical forces well.

Based on two graphs from Lambe & Whitman (1979) and an equation for the specific energy from Miedema (1987 September) and (1995), relations are derived for the SPT value as a function of the hydrostatic pressure and of the angle of internal friction as a function of the SPT value. With these equations also the influence of water depth on the production can be determined. The specific energies as measured from the tests are shown in Figure 6-57 and Figure 6-58. It can be seen that the deviated blade results in a lower specific energy. These figures also show the upper limit for the cavitating cutting process. For small velocities and/or layer thicknesses, the specific energy ranges from 0 to the cavitating value. The tests are carried out in sand with an angle of internal friction of 40 degrees. According to Figure 6-28 this should give an SPT value of 33. An SPT value of 33 at a water depth of about 0 m, gives according to Figure 6-31, a specific energy of about 450-500 kPa. This matches the specific energy as shown in Figure 6-57.

All derivations are based on a cavitating cutting process. For small SPT values it is however not sure whether cavitation will occur. A non-cavitating cutting process will give smaller forces and power and thus a higher production. At small SPT values however the production will be limited by the bull-dozer effect or by the possible range of the operational parameters such as the cutting velocity.
The calculation method used remains a lower limit approach with respect to the production and can thus be considered conservative. For an exact prediction of the production all of the required soil mechanical properties will have to be known. As stated, limitations following from the hydraulic system are not taken into consideration.

6.12.4. Wear and Side Effects.

In the previous chapters the blades are assumed to have a reasonable sharp blade tip and a positive clearance angle. A two dimensional cutting process has also been assumed. In dredging practice these circumstances are hardly encountered. It is however difficult to introduce a concept like wear in the theoretical model, because for every wear stage the water pressures have to be determined numerically again.

Also not clear is, if the assumption that the sand shears along a straight line will also lead to a good correlation with the model tests with worn blades. Only for the case with a sharp blade and a clearance angle of -1° a model test is performed.

It is however possible to introduce the wear effects and the side effects simply in the theory with empirical parameters. To do this the theoretical model is slightly modified. No longer are the horizontal and the vertical forces used, but the total cutting force and its angle with the direction of the velocity component perpendicular to the blade edge are used. Figure 6-33 shows the dimensionless forces $\mathbf{c_1}$, $\mathbf{c_2}$, and $\mathbf{c_t}$ for the non-cavitating cutting process and the dimensionless forces $\mathbf{d_1}$, $\mathbf{d_2}$ and $\mathbf{d_t}$ for the cavitating process.
For the total dimensionless cutting forces it can be written:

non-cavitating **cavitating**

$$c_t = \sqrt{\left(c_1 \cdot c_1 + c_2 \cdot c_2\right)} \qquad d_t = \sqrt{\left(d_1 \cdot d_1 + d_2 \cdot d_2\right)} \tag{6-101}$$

For the angle the force makes with the direction of the velocity component perpendicular to the blade edge:

$$\theta_t = \operatorname{atn}\left(\frac{c_2}{c_1}\right) \qquad \Theta_t = \operatorname{atn}\left(\frac{d_2}{d_1}\right) \tag{6-102}$$

It is proposed to introduce the wear and side effects, introducing a wear factor $\mathbf{c_s}$ ($\mathbf{d_s}$) and a wear angle $\boldsymbol{\theta_s}$ ($\boldsymbol{\Theta_s}$), according to:

$$c_{ts} = c_t \cdot c_s \qquad d_{ts} = d_t \cdot d_s \tag{6-103}$$

And

$$\theta_{ts} = \theta_t + \theta_s \qquad \Theta_{ts} = \Theta_t + \Theta_s \tag{6-104}$$

For the side effects, introducing a factor $\mathbf{c_r}$ ($\mathbf{d_r}$) and an angle $\boldsymbol{\theta_r}$ ($\boldsymbol{\Theta_r}$), we can now write:

$$c_{tr} = c_t \cdot c_r \qquad d_{tr} = d_t \cdot d_r \tag{6-105}$$

And

$$\theta_{tr} = \theta_t + \theta_r \qquad \Theta_{tr} = \Theta_t + \Theta_r \tag{6-106}$$

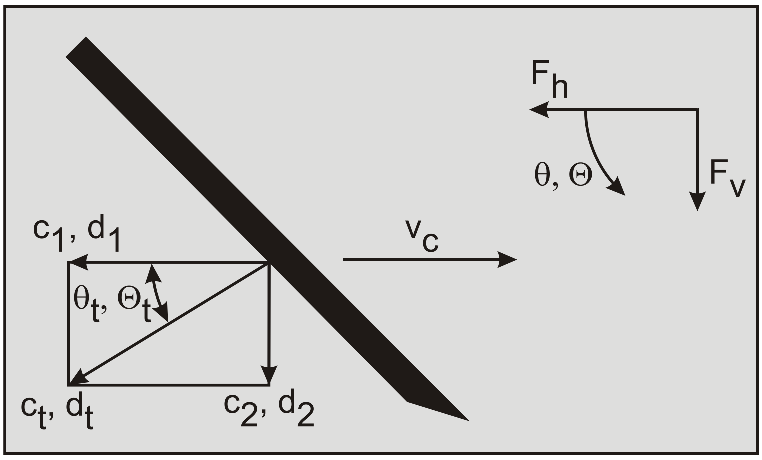

Figure 6-33: The total dimensionless cutting force c_t, d_t.

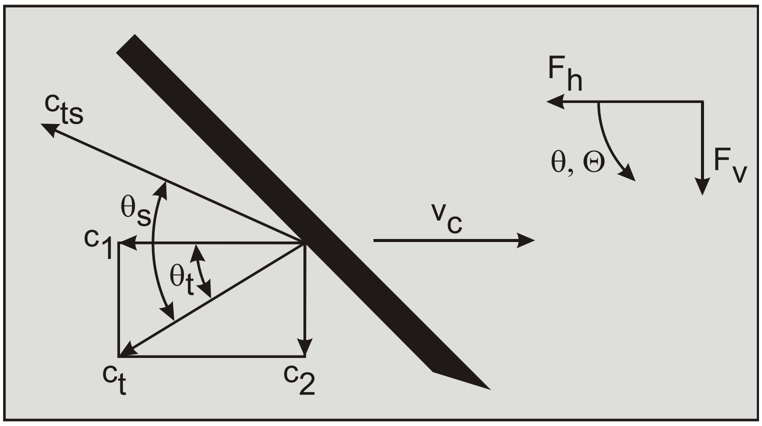

Figure 6-34: The influence of wear.

In particular the angle of rotation of the total cutting force as a result of wear, has a large influence on the force needed for the haul motion of cutter-suction and cutter-wheel dredgers. Figure 6-34 and Figure 6-35 give an impression of the expected effects of the wear and the side effects.

The angle the forces make with the velocity direction θ_t, Θ_t, where this angle is positive when directed downward.

The influence of wear on the magnitude and the direction of the dimensionless cutting forces c_t or d_t for the non-cavitating cutting process.

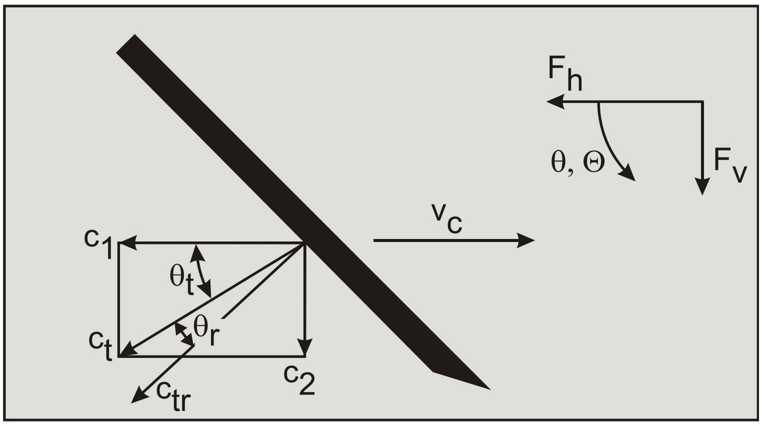

Figure 6-35: The influence of side effects.

The influence of side effects on the magnitude and the direction of the dimensionless cutting forces c_t or d_t for the non-cavitating cutting process.

6.13. Experiments.

6.13.1. Description of the Test Facility.

The tests with the straight blades are performed on two locations:

1. The old laboratory of Dredging Engineering, which will be called the old laboratory DE.

2. The new laboratory of Dredging Engineering, which will be called the new laboratory DE.

The test stand in the old laboratory DE consists of a concrete tank, 30 m long, 2.5 m wide and 1.35 m high, filled with a layer of 0.5 m sand with a $\mathbf{d_{50}}$ of 200 μm and above the sand 0.6 m water. The test stand in the new laboratory DE consists of a concrete tank, 33 m long, 3 m wide and internally 1.5 m high, with a layer of 0.7 m sand with a $\mathbf{d_{50}}$ of 105 μm and above the sand 0.6 m water. In both laboratories a main carriage can ride over the full length of the tank, pulled by two steel cables. These steel cables are winded on the drums of a hydraulic winch, placed in the basement and driven by a squirrel-cage motor of 35 kW in the old laboratory DE and 45 kW in the new laboratory DE.

In the old laboratory DE the velocity of the carriage could be infinitely variable controlled from 0.05 m/s to 2.50 m/s, with a pulling force of 6 kN. In the new laboratory DE the drive is equipped with a hydraulic two-way valve, which allows for the following speed ranges:

1. A range from 0.05 m/s to 1.40 m/s, with a maximum pulling force of 15 kN.

2. A range from 0.05 m/s to 2.50 m/s, with a maximum pulling force of 7.5 kN.

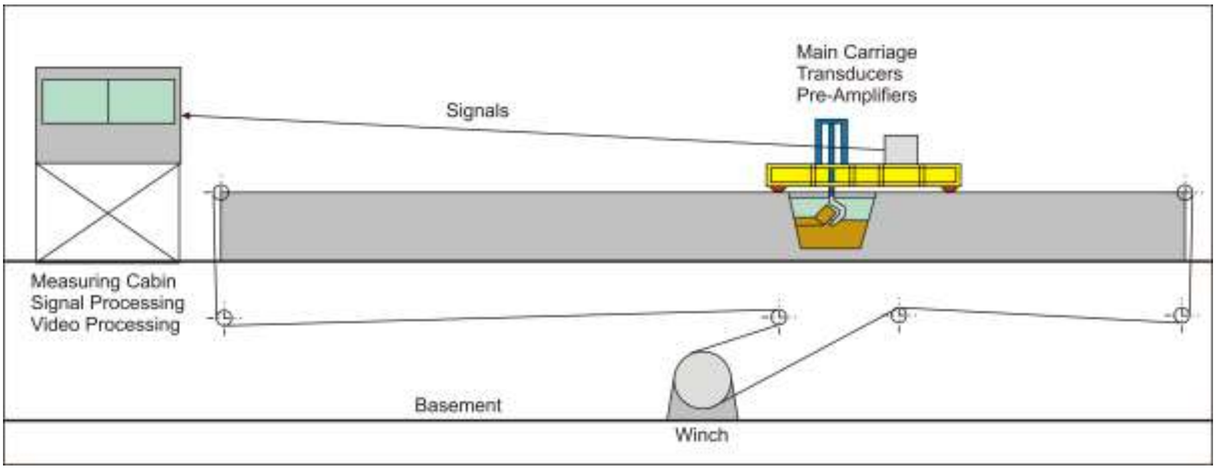

Figure 6-36: Side view of the old laboratory.

An auxiliary carriage, on which the blades are mounted, can be moved transverse of the longitudinal direction on the main carriage. Hydraulic cylinders are used to adjust the cutting depth and to position the blades in the transverse direction of the tank. Figure 6-36 shows a side view of the concrete tank with the winch drive in the basement and Figure 6-37 shows a cross section with the mounting of cutter heads or the blades underneath the auxiliary carriage (in the new laboratory DE). The main difference between the two laboratories is the side tank, which was added to dump the material excavated. This way the water stays clean and under water video recordings are much brighter. After a test the material excavated is sucked up by a dustpan dredge and put back in the main tank. The old laboratory DE was removed in 1986, when the new laboratory was opened for research. Unfortunately, the new laboratory stopped existing in 2005. Right now there are two such laboratories in the world, one at Texas A&M University in College Station, Texas, USA and one at Hohai University, Changzhou, China. Both laboratories were established around 2005.

Figure 6-38 and Figure 6-39 give an overview of both the old and the new laboratories DE, while Figure 6-40 shows a side view of the carriage, underneath which the blades are mounted.

Removing the spoil tank (3) from this figure gives a good impression of the cutting tank in the old laboratory DE. Instead of a cutter head, blades are mounted under the frame (6) during the cutting tests.

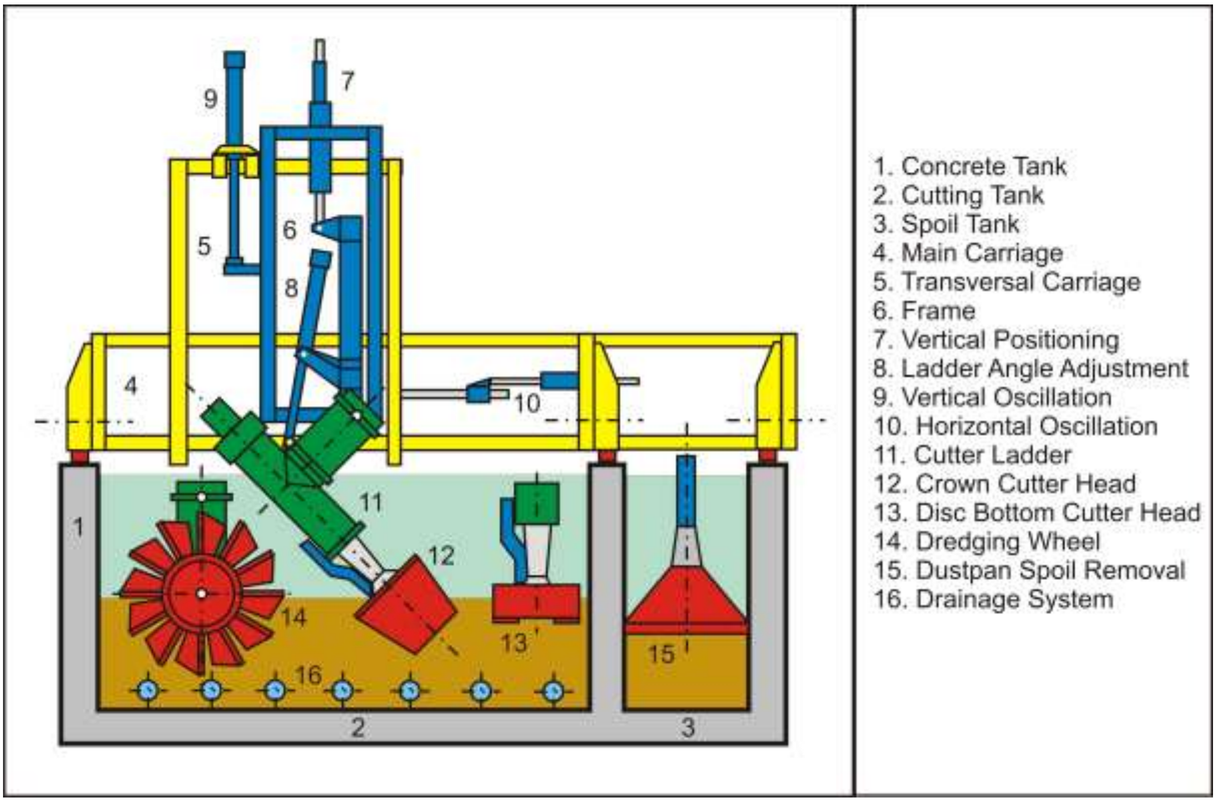

Figure 6-37: The cross section of the new laboratory DE.

Figure 6-38: An overview of the old laboratory DE.

The tests are carried out using a middle blade, flanked on both sides by a side blade, in order to establish a two-dimensional cutting process on the middle blade. The middle blade (center blade) is mounted on a dynamometer, with which the following loads can be measured:

1. The horizontal force
2. The vertical force
3. The transverse force
4. The bending moment

The side blades are mounted in a fork-like construction, attached to some dynamometers, with which the following loads can be measured:

1. The horizontal force
2. The vertical force

Figure 6-41 and Figure 6-42 show the mounting construction of the blades.

Figure 6-39: An overview of the new laboratory DE.

In the middle blade, four pore pressure transducers are mounted, with which the pore pressure distribution on the blade can be measured. However no tests are performed in which the forces on the side blades and the pore pressures are measured at the same time. The measuring signals of the dynamometers and the pressure transducers are transmitted to a measurement compartment through pre-amplifiers on the main carriage. In this measurement compartment the measuring signals are suited by 12 bit, 400 Hz A/D converters for processing on a P.C. (personal computer), after which the signals are stored on a flexible disk. Next to the blades, under water, an underwater video camera is mounted to record the cutting process. This also gives a good impression of the shear angles occurring.

Figure 6-40: A side view of the carriage.

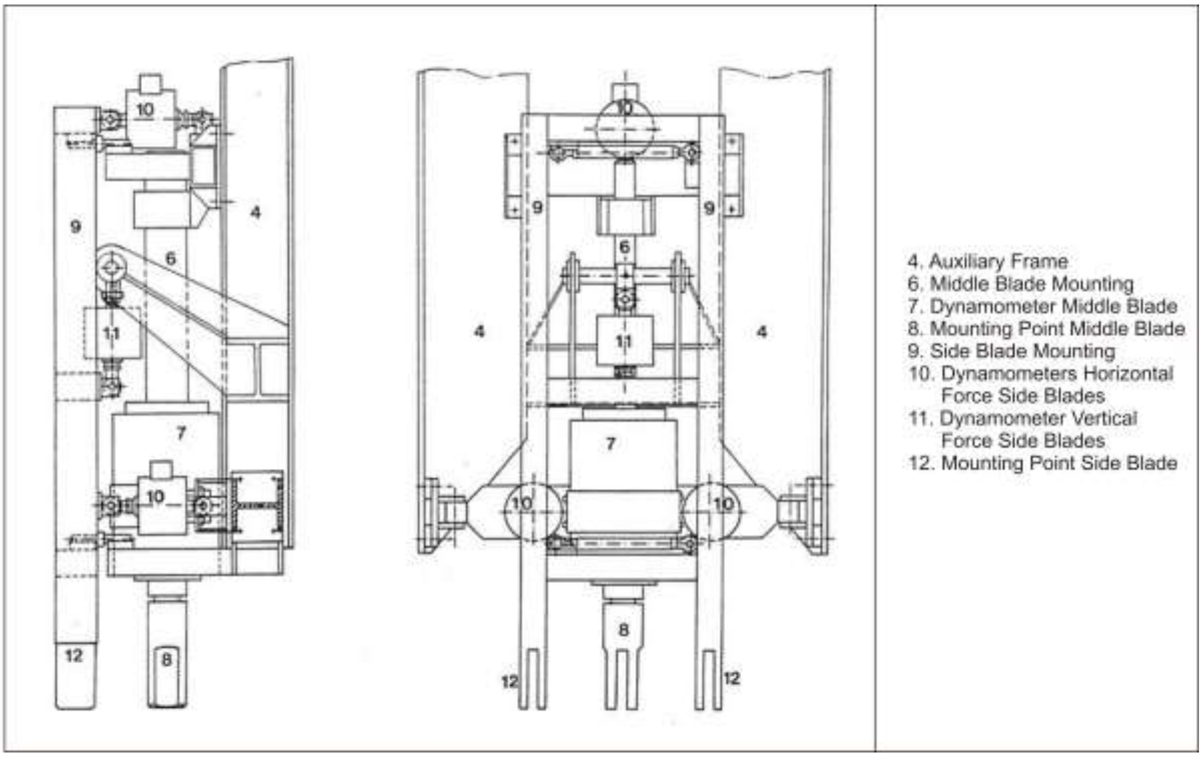

Figure 6-41: The construction in which the blades are mounted.

Figure 6-44 shows how a blade is mounted under the carriage in the new laboratory DE, in this case for so called snow-plough research. Figure shows the center blade and the two side blades mounted under the carriage in the old laboratory DE. In the center blade the 4 pore pressure transducers can be identified (the white circles) with which the pore pressures are measured.

Figure 6-47 shows the signal processing unit on the carriage, including pre-amplifiers and filters. The pre-amplifiers are used to reduce the noise on the signals that would occur transporting the signals over long distance to the measurement cabin.

Figure 6-46 shows the device used to measure the cone resistance of the sand before every experiment. The cone resistance can be related to the porosity of the sand, where the porosity relates to both the internal and external friction angle and to the permeability.

Figure 6-48 shows the measurement cabin with a PC for data processing and also showing the video screen and the tape recorder to store the video images of all the experiments.

Figure 6-45 shows a side view of the center blades. These blades could also be equipped with a wear flat to measure the influence of worn blades.

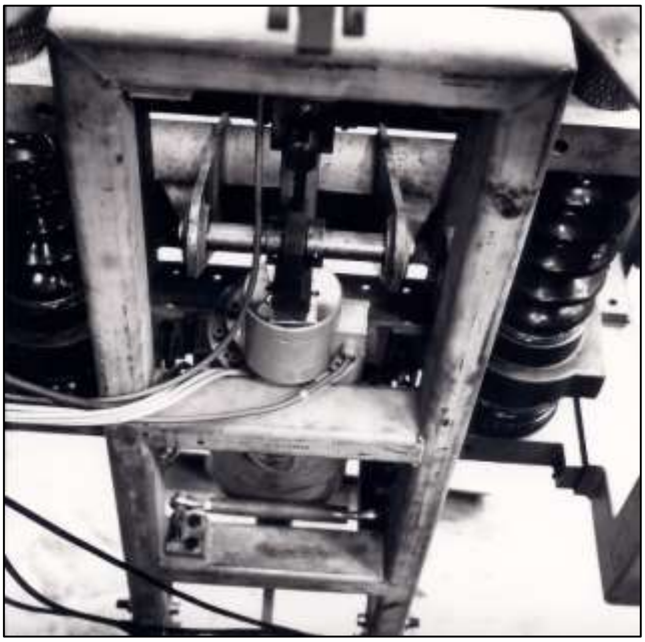

Figure 6-42: The blades are mounted in a frame with force and torque transducers.

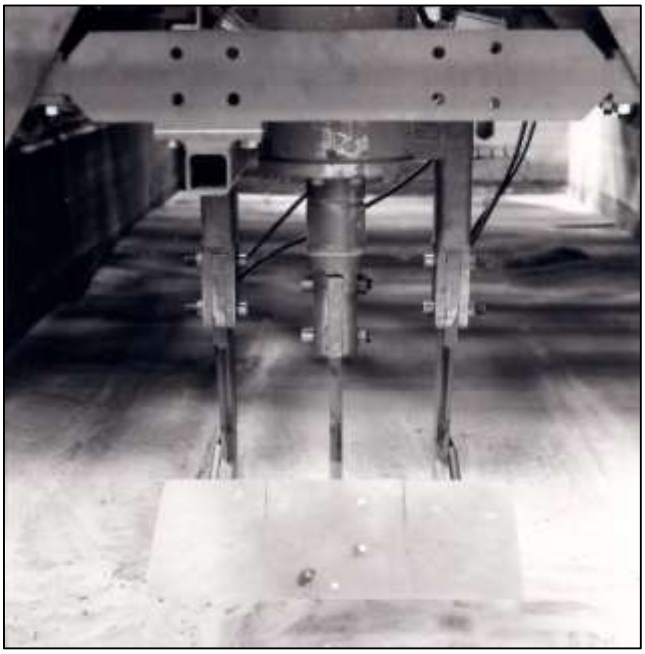

Figure 6-43: The center blade and the side blades, with the pore pressure transducers in the center blade.

Figure 6-44: A blade mounted under the carriage in the new laboratory DE.

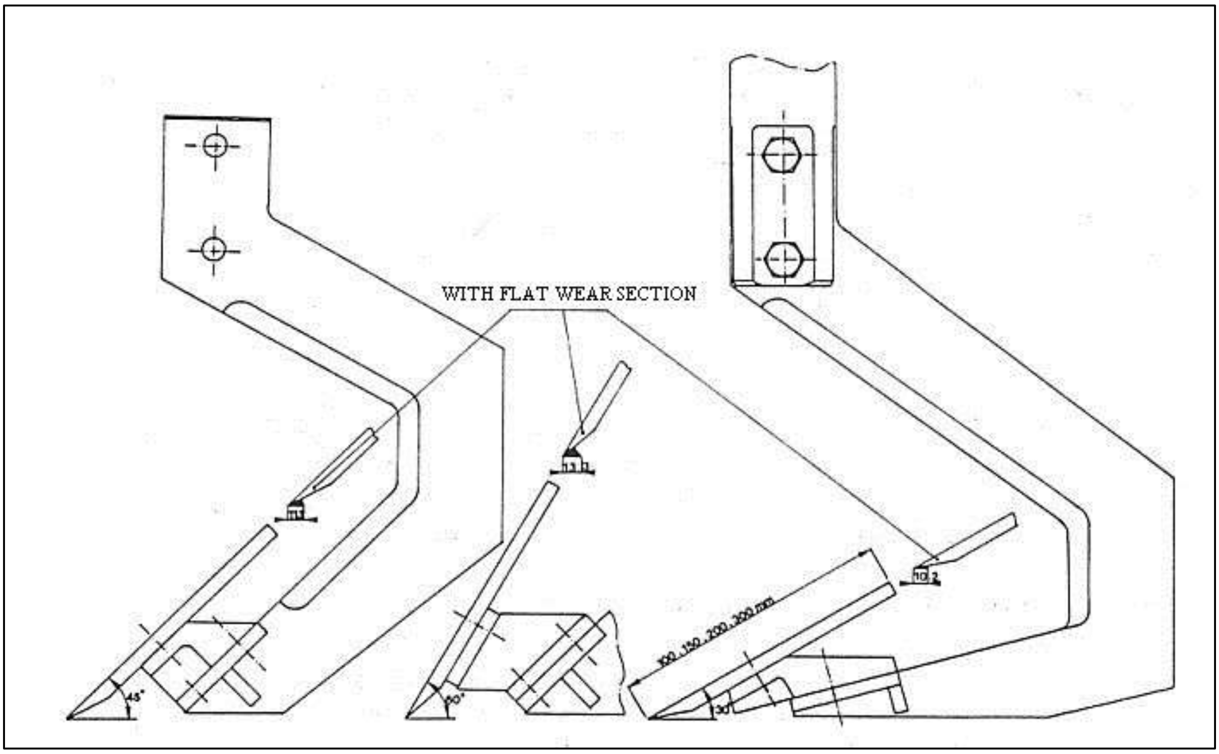

Figure 6-45: The center blade of 30º, 45º and 60º, with and without wear flat.

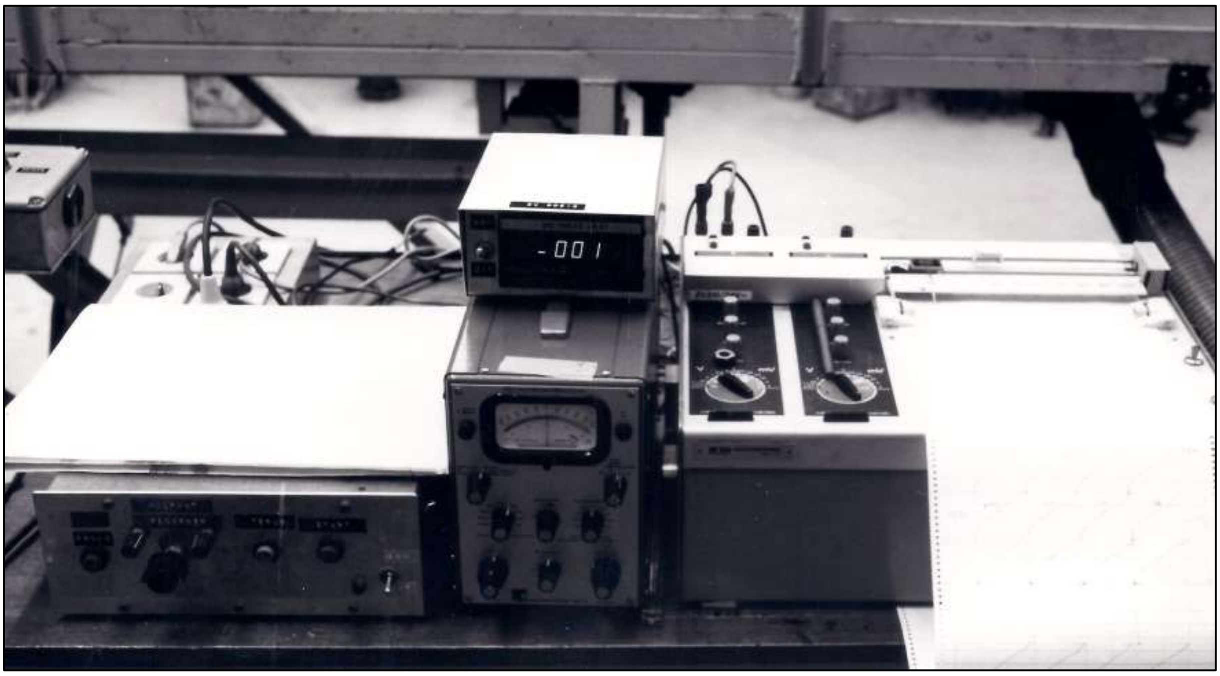

Figure 6-46: Measuring the cone resistance of the sand.

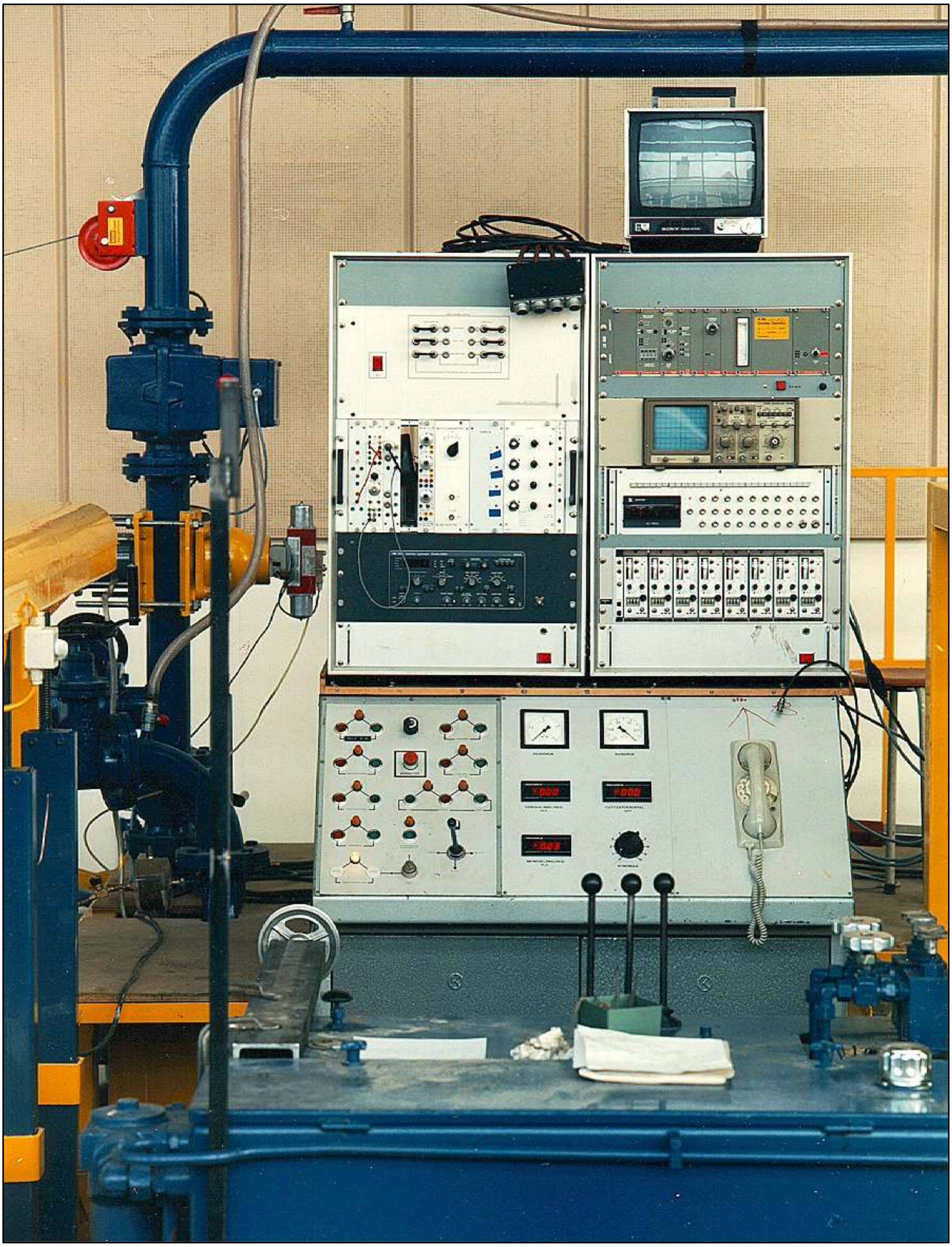

Figure 6-47: The pre-amplifiers and filters on the carriage.

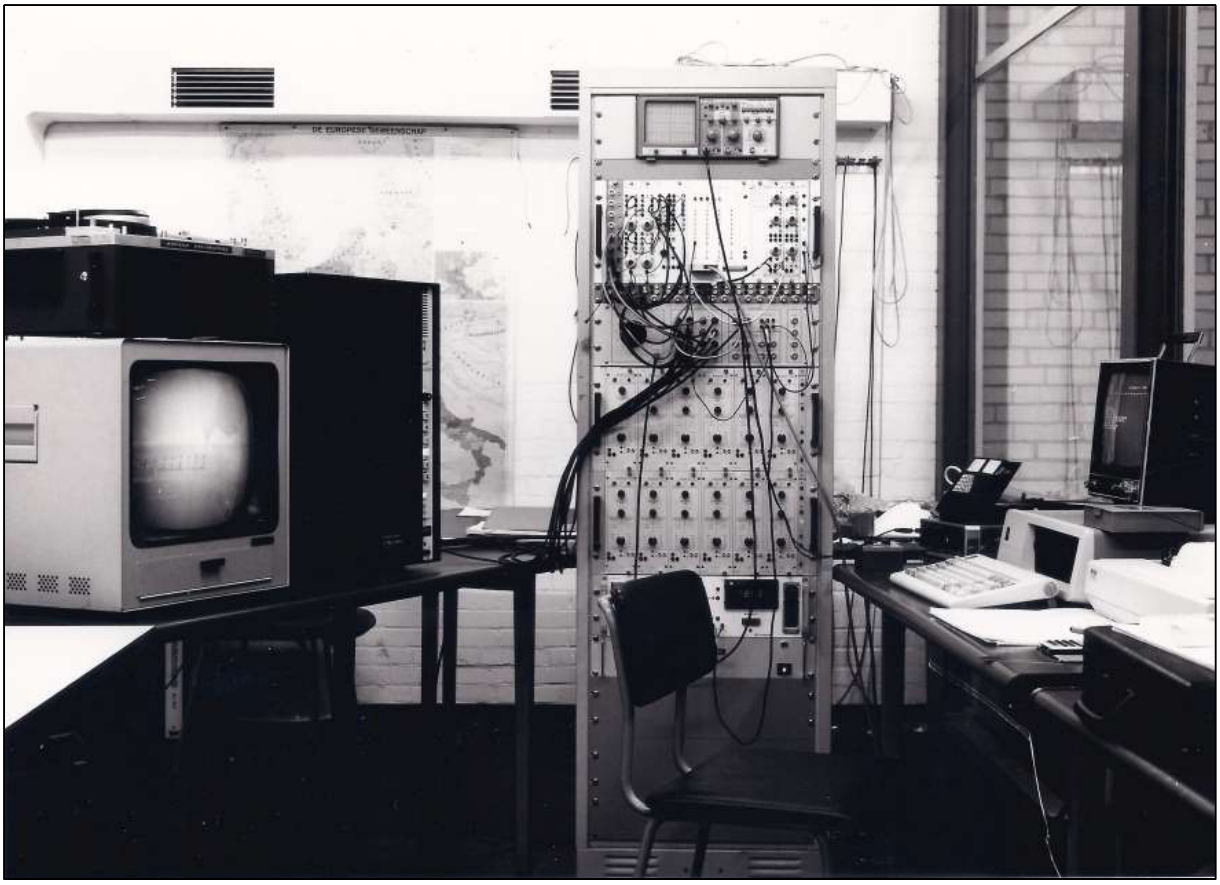

Figure 6-48: A view of the measurement cabin.

6.13.2. Test Program.

The theory for the determination of the forces that occur during the cutting of fully water saturated sand with straight blades is verified in two types of sand, sand with a $\mathbf{d_{50}}$ of 200 μm and sand with a $\mathbf{d_{50}}$ of 105 μm. The soil mechanical parameters of these two types of sand can be found in 0 and 0

The research can be subdivided in a number of studies:

1. Research of the water resistance of the blades
2. Research of the accuracy of the assumed two-dimensional character of the cutting process on the middle blade by changing the width of the middle blade with a total width of the middle blade and the side blades of 520 mm. This research is performed in the 200 μm sand.
3. Research of the quantitative character of the side effects in relation to the size and the direction of the cutting forces. This research is performed in the 200 μm sand.
4. Research of the in the theory present scale rules. This research is performed in the 200 μm sand.
5. Research of the accuracy of the theory of the cutting forces and the water sub-pressures in the non-cavitating cutting process. This research is performed in the 200 μm sand.
6. Research of the accuracy of the theory of the forces and the water sub-pressures in the non-cavitating and the partly cavitating cutting process. This research is performed in the 105 μm sand.

From points 4 and 5 it has also been established that the maximum pore percentage of the sand can be chosen for the residual pore percentage. In the 200 μm the dry critical density, the wet critical density and the minimal density are determined, while in the 105 μm sand the wet critical density and the minimal density are determined. These pore values can be found in Appendix K and Appendix L

For both type of sand only the minimal density (maximum pore percentage n_{max}) gives a large enough increase in volume to explain the measured water sub-pressures. This is in contrast to Van Leussen and Nieuwenhuis (1984) and Van Leussen and Van Os (1987 December), where for the residual density the wet critical density is chosen.

6.13.3. Water Resistance.

The water resistance is investigated under circumstances comparable with the cutting tests as far as scale; blade width and cutting velocity are concerned. Since the water resistance during all these tests could be neglected in comparison with the cutting forces, performed under the same conditions (maximum 2%), the water resistance terms are neglected in the further verification. The water resistance could however be more significant at higher cutting velocities above 2 m/s. It should be noted that at higher cutting velocities also the cutting forces will be higher, especially for the non-cavitating cutting process. Further, the inertial force, which is neglected in this research, may also play a role at very high cutting velocities.

6.13.4. The Influence of the Width of the Blade.

The blade on which the cutting forces are measured is embedded between two side blades. These side blades have to take care of the three-dimensional side effects, so that on the middle blade a two-dimensional cutting process takes place. The question now is how wide the side blades need to be, at a certain cutting depth, to avoid a significant presence of the side effects on the middle blade. Essential is, that at the deepest cutting depth the side effects on the middle blade are negligible. For this research the following blade configurations are used:

1. A middle blade of 150 mm and two side blades of 185 mm each.
2. A middle blade of 200 mm and two side blades of 160 mm each.
3. A middle blade of 250 mm and two side blades of 135 mm each.

The total blade width in each configuration is therefore 520 mm. The results of this research are, scaled to a middle blade of 200 mm wide, shown in Table 6-2, in which every value is the average of a number of tests. In this table the forces on the 0.20 m and the 0.25 m wide blade are listed in proportion to the 0.15 m wide blade. The change of the direction of the forces in relation to the 0.15 m wide blade is also mentioned. From this table the following conclusions can be drawn:

1. There is no clear tendency to assume that the side effects influence the cutting forces in magnitude.
2. The widening of the middle blade and thus narrowing the side blades, gives slightly more downward aimed forces on the middle blade at a blade angle of 30°. At a blade angle of 45° this tendency can be seen at a blade-height/layer-thickness ratio of 1 and 2, while at a blade-height/ layer-thickness ratio of 3 the forces are just slightly aimed upward. The 60° blade angle gives the same image as the 45° blade angle, however with smaller differences in proportion to the 0.15 m wide blade.

Table 6-2: The influence of the width ratio between the center blade and the side blades.

		w=0.20 m (2)		w=0.25 m (3)	
α	h_b/h_i	c_{t2}/c_{t1}	$\theta_{t2}-\theta_{t1}$	c_{t3}/c_{t1}	$\theta_{t3}-\theta_{t1}$
30°	**1**	0.95	+1.0°	1.02	+1.0°
30°	**2**	1.10	+2.0°	0.93	+4.0°
30°	**3**	0.96	+5.0°	1.05	+7.0°
45°	**1**	1.08	+3.0°	1.01	+5.0°
45°	**2**	0.93	+3.0°	0.93	+5.0°
45°	**3**	0.93	-8.0°	1.07	-5.0°
60°	**1**	1.09	+0.0°	1.00	+1.0°
60°	**2**	0.90	+1.0°	0.92	+2.0°
60°	**3**	1.04	-5.0°	0.99	-4.0°

The total measured cutting force $\mathbf{c_t}$ and the force direction $\boldsymbol{\theta_t}$, at a blade width of 0.20 m ($\mathbf{c_{t2}}$, $\boldsymbol{\theta_{t2}}$) (2) and a blade width of 0.25 m ($\mathbf{c_{t3}}$, $\boldsymbol{\theta_{t3}}$) (3) in proportion to the total cutting force and direction at a blade width of 0.15 m ($\mathbf{c_{t1}}$, $\boldsymbol{\theta_{t1}}$) (1), according the blade configurations mentioned here.

6.13.5. Side Effects.

On the outside of the side blades a three-dimensional cutting process acts, in a sense that the shear zone here is three-dimensional, but on top of that the water flows three-dimensional to the shear zone. This makes the cutting forces differ, in magnitude and direction, from the two-dimensional cutting process. Additionally it is imaginable that also forces will act on the blade in the transversal direction (internal forces in the blade). The influence of the side effects is researched by measuring the forces on both the middle blade as on the side blades. Possible present transversal forces are researched by omitting one side blade in order to be able to research the transversal forces due to the three-dimensional side effects. For this research the following blade configurations are used:

1. A middle blade of 150 mm and two side blades of 185 mm each.
2. A middle blade of 200 mm and two side blades of 160 mm each.
3. A middle blade of 250 mm and two side blades of 135 mm each.
4. A middle blade of 200 mm and one side blade of 160 mm

The results of this research can be found in Table 6-3, where every value represents the average of a number of tests. The cutting forces in this table are scaled to the 200 mm blade to simulate a middle blade without side blades.

Table 6-3: The cutting forces on the side blades.

		w=.15 m (1)		**w=.20 m (2)**		**w=.25 m (3)**		**w=.20 m (4)**	
α	**h_b/h_i**	**c_r**	**θ_r**	**c_r**	**θ_r**	**c_r**	**θ_r**	**c_r**	**θ_r**
30°	**1**	1.06	+26°	1.23	+14°	1.17	+11°	1.01	+13°
30°	**2**	0.78	+18°	0.87	+16°	0.83	+10°	1.14	+10°
30°	**3**	0.74	+22°	0.56	+22°	0.53	+11°	1.45	+ 6°
45°	**1**	1.13	+23°	1.10	+14°	1.26	+ 9°	1.04	+ 5°
45°	**2**	0.94	+19°	0.94	+11°	0.93	+ 7°	0.92	+ 7°
45°	**3**	0.79	+14°	1.10	+17°	0.98	+11°	0.85	+ 6°
60°	**1**	1.10	+ 8°	1.10	+ 6°	1.10	+ 5°	1.04	+ 2°
60°	**2**	0.94	+12°	1.10	+ 8°	1.06	+ 6°	0.91	+ 2°
60°	**3**	0.77	+ 8°	0.99	+15°	1.02	+11°	0.86	+ 3°

The cutting force on the side blades in ratio to the cutting force on the middle blade $\mathbf{c_r}$, assuming that the cutting process on the middle blade is two-dimensional. Also shown is the change of direction of the total cutting force $\boldsymbol{\theta_r}$. The cutting forces are scaled to the width of the middle blade for the blade widths 0.15 m (1), 0.20 m (2) and 0.25 m (3). The second column for w=.20 m (4) contains the results of the tests with only one side blade to measure the side effects on the middle blade. The measured cutting forces are compared to the similar tests where two side blades are used. The blade configurations are according to chapter 6.13.4. From this research the following conclusions can be drawn:

1. For all blade angles the cutting force on the edge is larger than follows from the two-dimensional process, for a blade-height / layer-thickness ratio of 1.
2. A blade-height / layer-thickness ratio of 2 or 3 shows a somewhat smaller cutting force with a tendency to smaller forces with a higher blade-height / layer-thickness ratio.
3. The direction of the cutting force is, for all four blade configurations, aimed more downwards on the sides than in the middle, where the differences with the middle blade decrease with a wider middle blade and therefore less wide side blades. This implies that, with the widening of the middle blade, the influence of the three-dimensional cutting process on the middle blade increases with a constant total blade width. This could be expected. It also explains that the cutting force in the middle blade is directed more downwards with an increasing middle blade width.
4. Blade configuration 4 differs slightly, as far as the magnitude of the forces is concerned, from the tendency seen in the other three configurations with the 30° blade. The direction of the cutting forces match with the other configurations. It has to be remarked that in this blade configuration the side effects occur only on one side of the blade, which explains the small change of the cutting forces.
5. The measured transverse forces for blade configuration 4 are in the magnitude of 1% of the vector sum of the horizontal and the vertical cutting forces and therefore it can be concluded that the transverse forces are negligible for the used sand.

The conclusions found are in principle only valid for the sand used. The influence of the side effects on the magnitude and the direction of the expected cutting forces will depend on the ratio between the internal friction of the sand and the soil/steel friction. This is because the two-dimensional cutting process is dominated by both angles of friction, while the forces that occur on the sides of the blade, as a result of the three-dimensional shear plane, are dominated more by the internal friction of the sand.

6.13.6. Scale Effects.

The soil mechanical research showed that the density of the sand increases slightly with the depth. Since both the permeability and the volume strain, and less significant the other soil mechanical parameters, are influenced by the density, it is important to know the size of this influence on the cutting forces (assuming that the two-dimensional cutting theory is a valid description of the process). If the two-dimensional cutting theory is a valid description of the process, the dimensionless cutting forces will have to give the same results for similar geometric ratios, independent of the dimensions and the layer-thickness, according to the equations for the non-cavitating cutting process and the cavitating cutting process. The following blade configurations are used to research the scaling influence:

1. A blade with a width of 150 mm wide and a height of 100 mm.
2. A blade with a width of 150 mm wide and a height of 150 mm.
3. A blade with a width of 150 mm wide and a height of 200 mm.
4. A blade with a width of 150 mm wide and a height of 300 mm.

The results of this research can be found in Table 6-4, where every value represents the average value of a number of tests.

Table 6-4: Influence of the scale factor.

Configuration		**1**	**2**	**3**	**4**
α	**h_b/h_i**	**h = 0.10**	**0.15**	**0.20**	**0.30**
30°	**1**	0.93	1.00	0.94	1.18
30°	**2**	1.23	1.00	1.06	1.13
30°	**3**	----	1.00	0.89	0.90
45°	**1**	0.95	1.00	1.13	----
45°	**2**	0.89	1.00	1.05	1.30
45°	**3**	----	1.00	1.02	1.13
60°	**1**	0.91	1.00	----	----
60°	**2**	0.90	1.00	1.19	1.04
60°	**3**	1.02	1.00	1.13	1.21

The total cutting force $\mathbf{c_t}$ with blade heights of 0.10 m (1), 0.15 m (2), 0.20 m (3) and 0.30 m (4) in proportion to the cutting force at a blade height 0.15 m (2). The blade configurations are according chapter 6.13.4. Because the influences of the gravity and inertia forces can disturb the character of the dimensionless forces compared to 0 to 0, the measured forces are first corrected for these influences. The forces in the table are in proportion to the forces that occurred with blade configuration 2. The following conclusions can be drawn from the table:

1. There is a slight tendency to larger dimensionless forces with increasing dimensions of the blades and the layer-thickness, which could be expected with the slightly increasing density.
2. For a blade angle of 30° and a blade-height / layer-thickness ratio of 2, large dimensionless forces are measured for blade configuration 1. These are the tests with the thinnest layer-thickness of 25 mm. A probable cause can be that the rounding of the blade tip in proportion with the layer-thickness is relatively large, leading to a relatively large influence of this rounding on the cutting forces. This also explains the development of the dimensionless forces at a blade angle of 30° and a blade-height / layer-thickness ratio of 3.

6.13.7. Comparison of Measurements versus Theory.

The results of the preceding three investigations are collected in Table 6-5, compared with the theory. Every value is the average of a number of tests. In the table it can be found:

1. The dimensionless forces, the average from the several scales and blade widths.
2. As 1, but corrected for the gravity and inertia forces.
3. The theoretical dimensionless forces according to Appendix D to Appendix J.

Table 6-5: The total cutting force measured.

		measured				**calculated**	
		not-corrected		**corrected**		**theoretical**	
α	**h_b/h_i**	c_t	θ_t	c_t	θ_t	c_t	θ_t
30°	**1**	0.52	+13.3°	0.48	+17.1°	0.39	+28.3°
30°	**2**	0.56	+17.0°	0.53	+20.1°	0.43	+27.4°
30°	**3**	0.56	+24.8°	0.53	+28.2°	0.43	+27.3°
45°	**1**	0.71	+ 4.9°	0.63	+ 7.5°	0.49	+12.9°
45°	**2**	0.75	+ 6.0°	0.66	+ 8.0°	0.57	+10.7°
45°	**3**	0.76	+ 5.1°	0.70	+ 6.9°	0.61	+ 9.9°
60°	**1**	1.06	+ 1.2°	0.88	+ 1.9°	0.69	- 0.7°
60°	**2**	1.00	- 2.4°	0.84	- 3.4°	0.83	- 3.2°
60°	**3**	0.99	- 3.4°	0.85	- 4.2°	0.91	- 4.6°

The total cutting force measured (not-corrected and corrected for the gravity and inertia forces) and the theoretical total cutting forces (all dimensionless). The theoretical values for $\mathbf{c_t}$ and $\boldsymbol{\theta_t}$ are based on an angle of internal friction of 38°, a soil/steel angle of friction of 30° and a weighted average permeability of approximately 0.000242 m/s dependent on the weigh factor a_1. The total cutting force $\mathbf{c_t}$ and the force direction $\boldsymbol{\theta_t}$ are determined according chapter 6.12.4. The following conclusions can be drawn from this table:

1. The measured and corrected cutting forces are larger than the, according to the theory, calculated cutting forces, at blade angles of 30° and 45°. The differences become smaller with an increase in the blade angle and when the blade-height / layer-thickness ratio increases.
2. For a blade angle of 60° the corrected measure forces agree well with the calculated forces.
3. The tendency towards larger forces with a larger blade-height / layer-thickness ratio (theory) is clearly present with blade angles 30° and 45°.
4. At a blade angle of 60° the forces seem to be less dependent of the blade-height / layer-thickness ratio.
5. The direction of the measured cutting forces agrees well with the theoretical determined direction. Only at the blade angle of 30° the forces are slightly aimed more upward for the blade-height / layer-thickness ratios 1 and 2.
6. Neglecting the inertia forces, gravity, etc. introduces an error of at least 15% within the used velocity range. This error occurs with the 60° blade, where the cutting velocity is the lowest of all cutting tests and is mainly due to the gravity.

Considering that the sand, in the course of the execution of the tests, as a result of segregation, has obtained a slightly coarser grain distribution and that the tests are performed with an increasing blade angle, can be concluded that the test results show a good correlation with the theory. It has to be remarked, however, that the scale and side effects can slightly disturb the good correlation between the theory and the measurements.

6.13.8. Location of the Resulting Cutting Force.

A quantity that is measured but has not been integrated in the theory is the location of the resulting cutting force. This quantity can be of importance for the determination of the equilibrium of a drag head. The locations, of the in this chapter performed tests, are listed in Table 6-6. Table 6-7 lists the dimensionless locations of the resulting cutting force, in relation with the layer-thickness.

Table 6-6: The location of the resulting cutting force.

Configuration		**1**	**2**	**3**	**4**
α	**h_b/h_i**	**h = 0.10**	**0.15**	**0.20**	**0.30**
30°	**1**	51.25	63.1	96.7	157.2
30°	**2**	76.00	55.7	61.3	84.8
30°	**3**	----	50.5	54.3	71.5
45°	**1**	66.38	87.5	128.0	----
45°	**2**	55.13	56.9	73.4	128.6
45°	**3**	----	62.0	56.0	82.1
60°	**1**	69.88	99.5	----	----
60°	**2**	50.00	68.4	86.1	123.9
60°	**3**	46.25	55.0	66.3	95.1

The location of the resulting cutting force in mm from the blade tip, for the blade configurations of chapter 6.13.4.

Table 6-7: The location of the resulting cutting force.

Configuration		**1**	**2**	**3**	**4**
α	**h_b/h_i**	**h = 0.10**	**0.15**	**0.20**	**0.30**
30°	**1**	0.51	0.42	0.48	0.59
30°	**2**	1.52	0.75	0.61	0.56
30°	**3**	----	1.01	0.82	0.71
45°	**1**	0.67	0.58	0.64	----
45°	**2**	1.11	0.76	0.63	0.73
45°	**3**	----	1.25	0.84	0.83
60°	**1**	0.70	0.66	----	----
60°	**2**	1.01	0.91	0.86	0.83
60°	**3**	1.38	1.11	0.99	0.95

The location of the resulting cutting force from the blade tip, along the blade, made dimensionless by dividing with the layer-thickness, for the blade configurations of chapter 6.13.4. From these tables the following conclusions can be drawn:

1. The location of the resulting cutting force is closer to the blade tip with larger blade dimensions.
2. The location of the resulting cutting force is closer to the blade tip with a smaller blade-height / layer-thickness ratio.

The first conclusion can be based upon the fact that a possible present adhesion, on a larger scale (and therefore layer-thickness) causes, in proportion, a smaller part of the cutting force. For the second conclusion this can also be a cause, although the blade-height / layer-thickness ratio must be seen as the main cause.

6.13.9. Verification of the Theory in 200 μm Sand.

The linear cutting theory is researched on three points:

1. The distribution of the water sub-pressures on the blade for a blade with a radius of rounding of 1 mm.
2. The distribution of the water sub-pressures on the blade for a blade with a flat wear face of approximately 10 mm and a clearance angle of 1°.
3. The correlation between the measured cutting forces and the theoretical cutting forces.

The dimensions of the blades and the wear faces can be found in Figure 6-45. In Table 6-10 the ratios of the wear face length and the layer-thickness are listed. In the preceding paragraph already a few conclusions are drawn upon the correlation between the measured and the calculated cutting forces. In this research both the forces and the water pressures are measured to increase the knowledge of the accuracy of the theory. Also it has to be mentioned that the soil mechanical parameters are determined during this research.
In Figure 6-56 the results of a test are shown. The results of the whole research of the forces are listed in Table 6-8 for the blade with the radius of rounding of 1 mm and in Table 6-9 for the blade with the wear flat. The dimensionless measured water sub-pressures are shown in Appendix M: Experiments in Water Saturated Sand, in

which the theoretical distribution is represented by the solid line. The water sub-pressures are made dimensionless, although the weighted average permeability k_m is used instead of the permeability k_{max} used in the equations. From this research the following conclusions can be drawn:

1. The measured forces and water sub-pressures show, in general, a good correlation with the theory.
2. The tendency towards increasing and more upward aimed forces with increasing blade angles can be observed clearly in the Table 6-8 and Table 6-9.
3. The ratio between the measured and calculated forces becomes smaller when the blade angle and the blade-height / layer-thickness ratio increase.
4. The cutting forces on the blade with the wear face are almost equal to the cutting forces on the blade with the radius of rounding, but are slightly aimed more upward.
5. The ratio between the measured and calculated water sub-pressures is, in general, smaller than the ratio between the measured and calculated cutting forces.
6. The measured water sub-pressures on the blade with the wear face and the blade with the radius of rounding differ slightly (Table 6-10) from the water sub-pressures on the blade with the radius of rounding. On the 30° and the 45° blade, the water sub-pressures tends to smaller values for the blade with the wear face, although the differences are very small. On the 60° blade these water sub-pressures are slightly higher. Therefore it can be concluded that, for water pressures calculations, the wear-section-length / layer-thickness ratio w/h_i has to be chosen dependent of the blade angle. Which was already clear during the tests because the clearance angle increased with a larger blade angle. For the determination of Appendix H to Appendix J, however, the ratio used was $w/h_i=0.2$, which is a good average value.

Table 6-8: Measured dimensionless forces.

		measured				**calculated**	
		not-corrected		**corrected**		**theoretical**	
α	**h_b/h_i**	**c_t**	**θ_t**	**c_t**	**θ_t**	**c_t**	**θ_t**
30°	**1**	0.54	+29.3°	0.49	+29.0°	0.39	+28.3°
30°	**2**	0.48	+27.5°	0.46	+27.2°	0.43	+27.4°
30°	**3**	0.49	+27.6°	0.46	+27.3°	0.43	+27.3°
45°	**1**	0.78	+15.1°	0.58	+13.9°	0.49	+12.9°
45°	**2**	0.64	+12.3°	0.59	+11.6°	0.57	+10.7°
45°	**3**	0.60	+11.0°	0.55	+10.5°	0.61	+ 9.9°
60°	**1**	1.16	+ 0.7°	0.77	- 0.6°	0.69	+ 0.7°
60°	**2**	0.95	- 1.4°	0.79	- 2.2°	0.83	- 3.2°
60°	**3**	0.93	- 3.4°	0.82	- 4.0°	0.91	- 4.6°
60°	**6**	0.70	- 4.8°	0.64	- 5.7°	1.14	- 7.4°

Measured dimensionless forces, not-corrected and corrected for gravity and inertia forces and theoretical values according to Appendix H to Appendix J for the blade with the radius of rounding and the sub-pressure behind the blade. The theoretical values for c_t and θ_t are determined based on values for the angle of internal friction of 38°, a soil/steel angle of friction of 30° and a weighted average permeability of 0.000242 m/s, dependent on the weigh factor a_1.

Table 6-9: Measured dimensionless forces.

		measured				**calculated**	
		not-corrected		**corrected**		**theoretical**	
α	**h_b/h_i**	**c_t**	**θ_t**	**c_t**	**θ_t**	**c_t**	**θ_t**
30°	**1**	0.53	+26.2°	0.48	+25.9°	0.39	+28.3°
30°	**2**	0.48	+24.0°	0.46	+23.7°	0.43	+27.4°
30°	**3**	0.49	+24.7°	0.46	+24.3°	0.43	+27.3°
45°	**1**	0.72	+11.9°	0.57	+11.0°	0.49	+12.9°
45°	**2**	0.66	+ 8.8°	0.60	+ 8.3°	0.57	+10.7°
45°	**3**	0.63	+ 7.8°	0.60	+ 7.3°	0.61	+ 9.9°
60°	**1**	-----	-----	-----	-----	-----	-----
60°	**2**	0.90	- 5.6°	0.80	- 6.2°	0.83	- 3.2°
60°	**3**	0.95	- 7.3°	0.87	- 8.0°	0.91	- 4.6°
60°	**6**	0.70	- 9.2°	0.64	-10.1°	1.14	- 7.4°

Measured dimensionless forces, not-corrected and corrected for gravity and inertia forces and theoretical values according to Appendix H to Appendix J for the blade with the flat wear face and the sub-pressure behind the blade. The theoretical values for $\mathbf{c_t}$ and $\boldsymbol{\theta_t}$ are determined according chapter 6.12.4. They are based on values for the angle of internal friction of 38°, a soil/steel angle of friction of 30° and a weighted average permeability of 0.000242 m/s, dependent on the weigh factor $\mathbf{a_1}$.

Table 6-10: Average dimensionless pore pressures on the blade.

α	h_b/h_i	w	h_i	w/h_i	p_{2ma}	p_{2ms}	p_{2m}	p_{2ms}/p_{2ma}
30°	**1**	10.2	100	0.102	0.076	0.073	0.076	0.96
30°	**2**	10.2	50	0.204	0.051	0.050	0.049	0.98
30°	**3**	10.2	33	0.308	0.034	0.030	0.034	0.88
45°	**1**	11.1	141	0.079	0.090	0.080	0.097	0.89
45°	**2**	11.1	70	0.159	0.069	0.068	0.082	0.99
45°	**3**	11.1	47	0.236	0.052	0.051	0.065	0.98
60°	**1**	13.3	173	0.077	0.107	-----	0.091	----
60°	**2**	13.3	87	0.153	0.083	0.090	0.100	1.08
60°	**3**	13.3	58	0.229	0.075	0.081	0.094	1.08
60°	**6**	13.3	30	0.443	0.035	0.038	0.061	1.09

The average dimensionless pore pressures on the blade, on the blade with the radius of rounding $\mathbf{p_{2ma}}$ and the blade with the wear face $\mathbf{p_{2ms}}$, the theoretical values $\mathbf{p_{2m}}$ and the ratio between the sub-pressures $\mathbf{p_{2ms}}$ and $\mathbf{p_{2ma}}$, as a function of the length of the wear face **w** (mm), the layer-thickness $\mathbf{h_i}$ (mm) and the wear-section-length / layer-thickness ratio.

6.13.10. Verification of the Theory in 105 μm Sand.

The linear cutting theory for the 105 μm is investigated on three points:

1. The distribution of the water sub-pressures on the blade in a non-cavitating cutting process.
2. The distribution of the water sub-pressures on the blade in the transition region between the non-cavitating and the cavitating cutting process.
3. The correlation between the measured cutting forces and the theoretical calculated cutting forces.

The dimensions of the blades can be found in Figure 6-45. In this research only a 30° blade with a layer-thickness of 100 mm, a 45° blade with a layer-thickness of 70 mm and a 60° with a layer-thickness of 58 mm, are used, at a blade height h of 200 mm. The soil mechanical parameters of the used sand are listed in Appendix L. The results of the research regarding the cutting forces can be found in Table 6-11.

Table 6-11: Measured dimensionless forces.

		measured				**calculated**	
α	h_b/h_i	c_t	θ_t	c_t	θ_t	c_t	θ_t
no cavitation		**not-corrected**		**corrected**		**theoretical**	
30°	**1**	.45	+16.5°	.45	+25.6°	.41	+25.1°
45°	**2**	.50	- 3.5°	.47	+ 7.2°	.62	+ 7.6°
60°	**3**	.60	- 8.8°	.58	- 6.3°	1.02	- 7.5°
cavitation		**not-corrected**		**corrected**		**theoretical**	
30°	**1**	3.4	+13.1°	3.4	+24.2°	3.3	+21.6°
45°	**2**	4.7	-10.3°	4.2	+ 5.7°	4.6	+ 2.6°
60°	**3**	4.9	- 9.0°	4.8	- 7.8°	6.8	-12.1°

Measured dimensionless forces, not-corrected and corrected for gravity and inertia forces and the theoretical values according to Appendix C to Appendix G for the non-cavitating cutting process and according to Appendix H to Appendix J for the cavitating cutting process, calculated with a sub-pressure behind the blade. The values of $\mathbf{c_t}$ and $\boldsymbol{\theta_t}$ are calculated according chapter 6.12.4. They are based on values for the angle of internal friction of 38°, a soil/steel angle of friction of 30° and a weighted average permeability between 0.00011 m/s and 0.00012 m/s, dependent on the weigh factor $\mathbf{a_1}$ and the initial pore percentage of the sand bed.

The dimensionless measured water sub-pressures of the non-cavitating cutting process are presented in Appendix M, in which the solid line represents the theoretical distribution. The dimensionless measured water sub-pressures in the transition region are also presented in Appendix M. The figures in Appendix M show the measured horizontal forces $\mathbf{F_h}$, in which the solid line represents the theoretical distribution. Other figures show the measured vertical forces $\mathbf{F_v}$, in which the solid line represents the theoretical distribution. Also shown in is the distribution of the forces, for several water depths, during a fully cavitating cutting process (the almost horizontal lines). From this research the following conclusions can be drawn:

1. The tests with the 30° blade give a good correlation with the theory, both for the forces as for the water sub-pressures. For the 45° blade both the forces and the water sub-pressures are lower than the theoretical calculated values with even larger deviations for the 60° blade. For the 60° blade the forces and the water sub-pressures values are approximately 60% of the calculated values.
2. The direction of the cutting forces agrees reasonably well with the theory for all blade angles, after correction for the gravity and the inertia forces.
3. The figures in Appendix M show that the profile of the water sub-pressures on the blade, clearly changes shape when the peak stress close to the blade tip (sub-pressure) has a value of approximately 65% of the absolute pressure. An increase of the cutting velocity results in a more flattening profile, with a translation of the peak to the middle of the blade. No cavitation is observed but rather an asymptotic approach of the cavitation pressure with an increasing cutting velocity. For the 60° blade the flattening only appears near the blade tip. This can be explained with the large blade-height / layer-thickness ratio. This also explains the low cutting forces in the range where cavitation is expected. There is some cavitation but only locally in the shear zone; the process is not yet fully cavitated.
4. Since, according to the theory, the highest sub-pressures will appear in the shear zone, cavitation will appear there first. The theoretical ratio between the highest sub-pressure in the shear zone and the highest sub-pressure on the blade is approximately 1.6, which is in accordance with conclusion 3. Obviously there is cavitation in the shear zone in these tests, during which the cavitation spot expands to above the blade and higher above the blade with higher cutting velocities.

In Appendix M the pore pressure graphs show this relation between the cavitation spot and the water pressures profile on the blade. The water sub-pressures will become smaller where the cavitation spot ends. This also implies that the measurements give an impression of the size of the cavitation spot.

As soon as cavitation occurs locally in the sand package, it becomes difficult to determine the dimensionless coefficients $\mathbf{c_1}$ and $\mathbf{c_2}$ or $\mathbf{d_1}$ and $\mathbf{d_2}$. This is difficult because the cutting process in the transition region varies between a cavitating and a non-cavitating cutting process. The ratio between the average water pressure in the shear zone and the average water pressure on the blade surface changes continuously with an increasing cutting velocity. On top of that the shape and the size of the area where cavitation occurs are unknown. However, to get an impression of the cutting process in the transition region, a number of simplifications regarding the water flow through the pores are carried out.

1. The flow from the free sand surface to the shear zone takes place along circular flow lines (see equations (6-37) and (6-38)), both through the packed sand as through the cut sand. With this assumption the distance from the free sand surface to the cavitation area can be determined, according:

$$\xi_0 = \frac{(z+10)}{v_c \cdot \varepsilon \cdot \sin(\beta)} \cdot \left(\frac{k_{max}}{\alpha + \beta} + \frac{k_i}{\pi - \beta} \right) \cdot \sin(\alpha + \beta) \qquad \mathbf{(6\text{-}107)}$$

2. The flow in the cut sand is perpendicular to the free sand surface, from the breakpoint where the shear plane reaches the free sand surface. This flow fills the water vapor bubbles with water. The distance from the free sand surface to the cavitating area can now be determined, under the assumption that the volume flow rate of the vapor bubbles equals the volume flow rate of the dilatancy, according:

$$\frac{k_{max} \cdot (z+10)}{\xi} \cdot d\psi = v_c \cdot \varepsilon \cdot \frac{\sin(\beta)}{\sin(\alpha+\beta)} \cdot d\xi \qquad \mathbf{(6\text{-}108)}$$

3. In which the right term represents the volume flow rate of the vapor bubbles from the dilatancy zone, while the left term represents the supply of water from the free sand surface. This is shown in Appendix M the pore pressure graphs. With the initial value from equation (6-107) the following solution can be found:

$$\xi = \sqrt{\xi_0^2 + 2 \cdot \frac{k_{max} \cdot (z+10)}{\left(v_c \cdot \frac{\sin(\beta)}{\sin(\alpha+\beta)} \cdot \varepsilon \right)} \cdot \psi} \tag{6-109}$$

The distance from the blade to the cavitation spot is considered to be constant over the blade. The magnitude of this distance is however unknown.

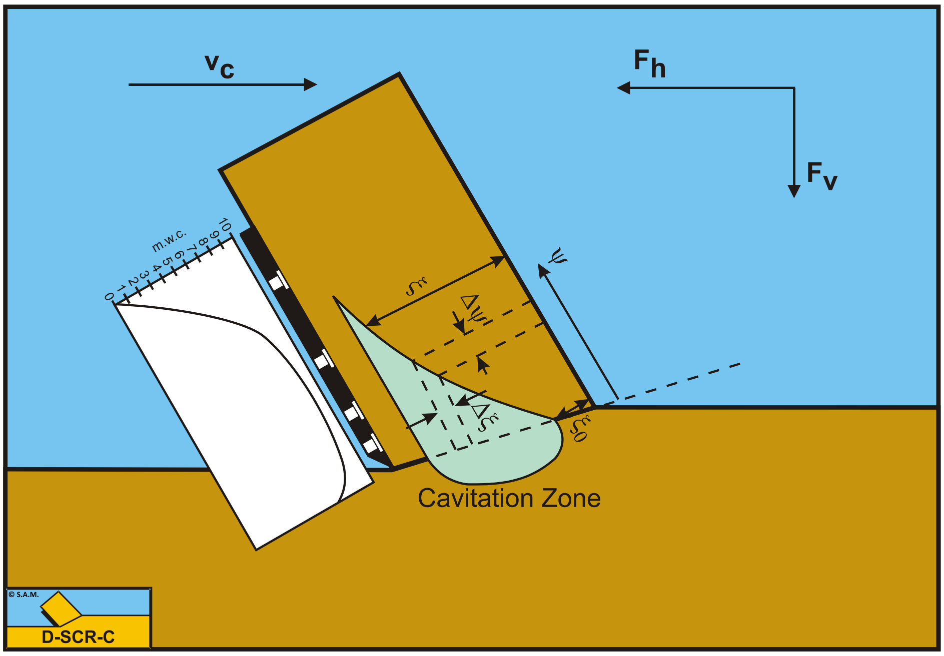

Figure 6-49: The development of cavitation over the blade.

The relation between the dimensions of the cavitation spot, and the water pressure profile on the blade.

The progressive character of the cavitation spot development results from equation (6-109). If, at a certain cutting velocity, cavitation occurs locally in the cavitation zone, then the resulting cavitation spot will always expand immediately over a certain distance above the blade as a result of the fact that a certain time is needed to fill the volume flow rate of the vapor bubbles. The development of the water sub-pressures will, in general, be influenced by the ever in the pore water present dissolved air. As soon as water sub-pressures are developing as a result of the increase in volume in the shear zone, part of the dissolved air will form air bubbles. Since these air bubbles are compressible, a large part of the volume strain will be taken in by the expansion of the air bubbles, which results in a less fast increase of the water sub-pressures with an increasing cutting velocity. The maxima of the water sub-pressures will also be influenced by the present air bubbles. This can be illustrated with the following example: Assume the sand contains 3 volume percent air, which takes up the full volume strain in the dilatancy zone. With a volume strain of 16%, this implies that after expansion, the volume percentage air is 19%. Since it is a quick process, it may be assumed that the expansion is adiabatic, which amounts to maximum water sub-pressures of 0.925 times the present hydrostatic pressure. In an isothermal process the maximum water sub-pressures are 0.842 times the present hydrostatic pressure. From this simple example it can be concluded that the, in the pore water present (either dissolved or not) air, has to be taken into account. In the verification of the water sub-pressures, measured during the cutting tests in the 105 μm sand, the possibility of a presence of dissolved air is recognized but it appeared to be impossible to quantify this influence. It is however possible that the maximum water sub-pressures reached (Appendix M the pore pressure graphs) are limited by the in the pore water present dissolved air.

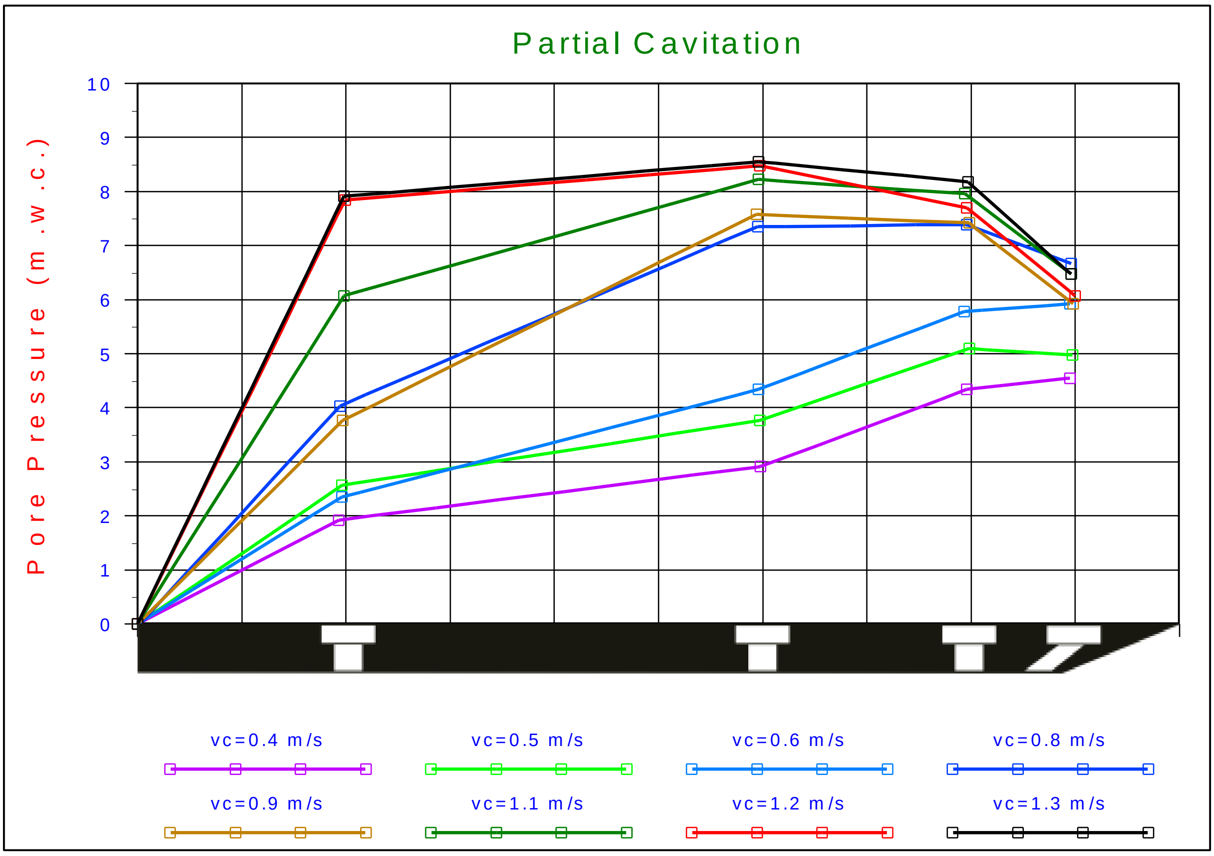

Figure 6-50: Partial cavitation limited by dissolved air, α=45°, h_i=7cm.

6.13.11. Determination of ϕ and δ from Measurements.

The soil/steel friction angle **δ** and the angle of internal friction **φ** can be determined from cutting tests. Sand without cohesion or adhesion is assumed in the next derivations, while the mass of the cut layer has no influence on the determination of the soil/steel friction angle. In Figure 6-51 it is indicated which forces, acting on the blade, have to be measured to determine the soil/steel friction angle **δ**.

The forces $\mathbf{F_h}$ and $\mathbf{F_v}$ can be measured directly. Force $\mathbf{W_2}$ results from the integration of the measured water pressures on the blade. From this figure the normal force on the blade, resulting from the grain stresses on the blade, becomes:

$$F_n = W_2 - W_3 + F_h \cdot \sin(\alpha) + F_v \cdot \cos(\alpha) \qquad \textbf{(6-110)}$$

The friction force, resulting from the grain stresses on the blade, becomes:

$$F_w = F_h \cdot \cos(\alpha) - F_v \cdot \sin(\alpha) \qquad \textbf{(6-111)}$$

The soil/steel angle of friction now becomes:

$$\delta = \arctan\left(\frac{F_w}{F_n}\right) \qquad \textbf{(6-112)}$$

Determination of the angle of internal friction from the cutting tests is slightly more complicated. In Figure 6-52 it is indicated which forces, acting on the cut layer, have to be measured to determine this angle. Directly known are the measured forces $\mathbf{F_h}$ and $\mathbf{F_v}$. The force $\mathbf{W_1}$ is unknown and impossible to measure. However from the numerical water pressures calculations the ratio between $\mathbf{W_1}$ and $\mathbf{W_2}$ is known. By multiplying the measured force $\mathbf{W_2}$ with this ratio an estimation of the value of the force $\mathbf{W_1}$ can be obtained, so:

$$W_1 = \left(\frac{W_1}{W_2}\right)_{calc} \cdot W_{2mean} \qquad (6\text{-}113)$$

For the horizontal and the vertical force equilibrium of the cut layer can now be written:

$$F_h - W_3 \cdot \sin(\alpha) = K_1 \cdot \sin(\beta + \phi) - W_1 \cdot \sin(\beta) + I \cdot \cos(\beta) \qquad (6\text{-}114)$$

$$F_v - W_3 \cdot \cos(\alpha) = -K_1 \cdot \cos(\beta + \phi) + W_1 \cdot \cos(\beta) + I \cdot \sin(\beta) + G \qquad (6\text{-}115)$$

The angle of internal friction:

$$\phi = \arctan\left(\frac{F_h - W_3 \cdot \sin(\alpha) + W_1 \cdot \sin(\beta) - I \cdot \cos(\beta)}{-F_v + W_3 \cdot \cos(\alpha) + W_1 \cdot \cos(\beta) + I \cdot \sin(\beta) + G}\right) - \beta \qquad (6\text{-}116)$$

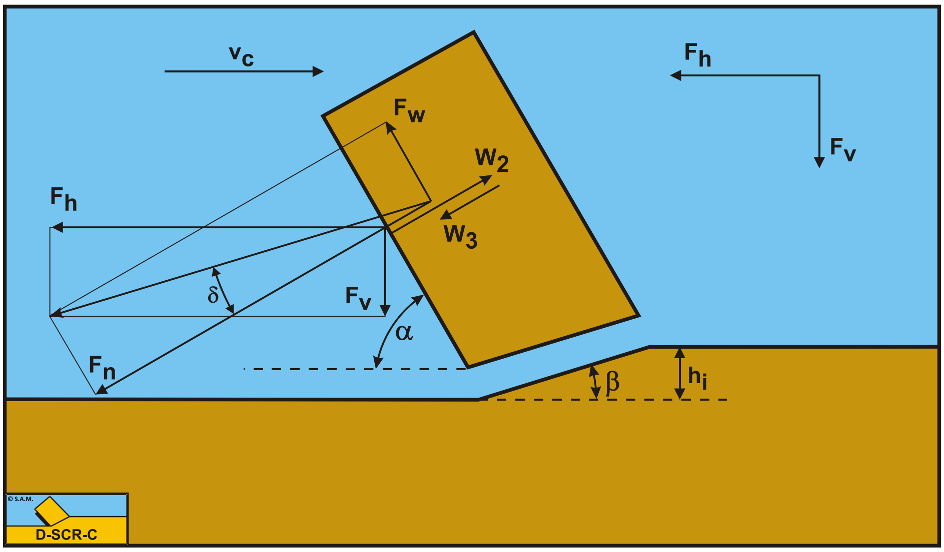

Figure 6-51: The forces from which the soil/steel friction angle δ can be determined.

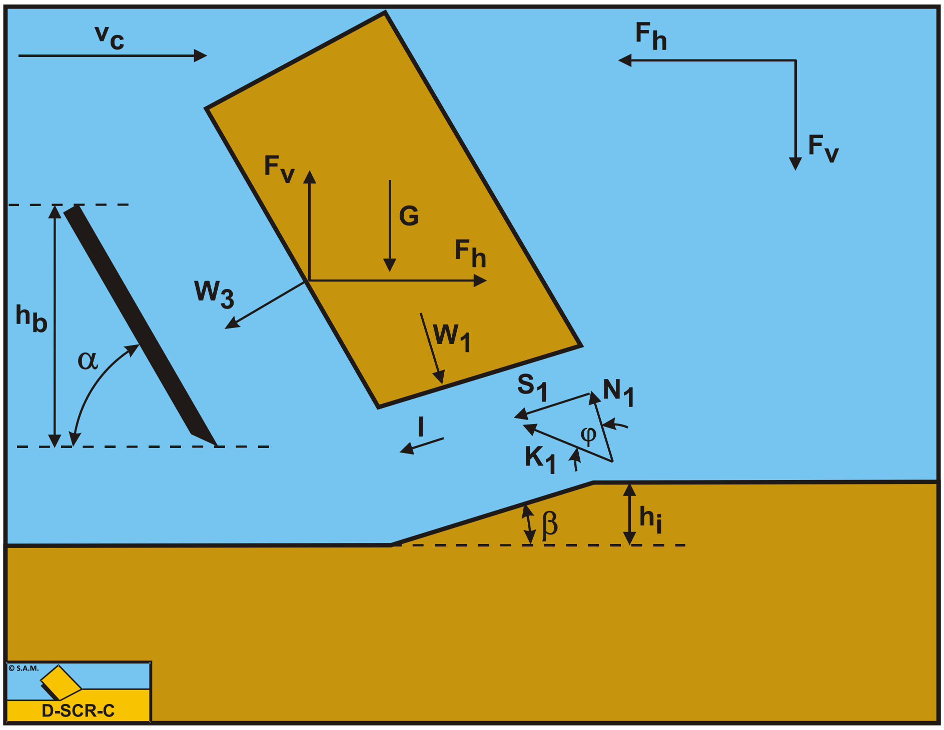

Figure 6-52: The forces from which the angle of internal friction φ of the sand can be determined.

The equations derived (6-112) and (6-116) are used to determine the values of φ and δ from the cutting tests carried out. The soil/steel friction angle can quite easily be determined, with the remark that the side and wear effects can influence the results from this equation slightly. The soil/steel friction angle, determined with this method, is therefore a gross value. This value, however, is of great practical importance, because the side and wear effects that occur in practice are included in this value.

The soil/steel friction angle **δ**, determined with this method, varied between 24° and 35°, with an average of approximately 30°. For both types of sand almost the same results were found for the soil/steel friction angle. A clear tendency towards stress or blade angle dependency of the soil/steel angle of friction is not observed. This in contrast to Van Leussen and Nieuwenhuis (1984), who found a blade angle dependency according Hettiaratchi and Reece (1974).

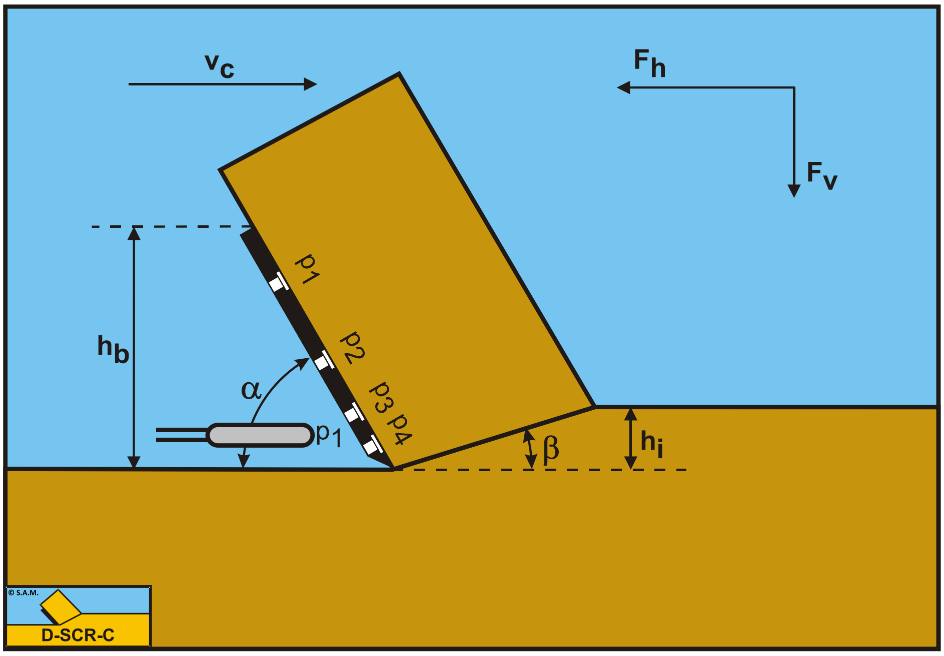

Figure 6-53: The location of the pressure transducer behind the blade.

Harder to determine is the angle of internal friction. The following average values for the angle of internal friction are found, for the 200 μm sand:

- **α = 30° » φ = 46.7°**
- **α = 45° » φ = 45.9°**
- **α = 60° » φ = 41.0°**

These values are high above the angle of internal friction that is determined with soil mechanical research according to Appendix K, for a pore percentage of 38.5%. From equation (6-116) it can be derived that the presence of sub-pressure behind the blade makes the angle of internal friction smaller and also that this reduction is larger when the blade angle is smaller. Within the test program space is created to perform experiments where the sub-pressure is measured both on and behind the blade (Figure 6-53). Pressure transducer p_1 is removed from the blade and mounted behind the blade tip. Although the number of measurements was too limited to base a theoretical or empirical model on, these measurements have slightly increased the understanding of the sub-pressure behind the blade. Behind the blade tip sub-pressures are measured, with a value of 30% to 60% of the peak pressure on the blade. The highest sub-pressure behind the blade was measured with the 30° blade. This can be explained by the wedge shaped space behind the blade. The following empirical equation gives an estimate of the force $\mathbf{W_3}$ based on these measurements:

$$\mathbf{W_3 = 0.3 \cdot \cot(\alpha) \cdot W_2} \tag{6-117}$$

The determination of the angle of internal friction corrected for under pressure behind the blade $\mathbf{W_3}$ led to the following values:

- **α = 30° » φ = 36.6°**
- **α = 45° » φ = 39.7°**
- **α = 60° » φ = 36.8°**

For the verification of the cutting tests an average value of 38° for the internal angle of friction is assumed. These values are also more in accordance with the values of internal friction mentioned in Appendix K, where a value of approximate 35° can be found with a pore percentage of 38.5%.

The same phenomena are observed in the determination of the angle of internal friction of the 105 μm sand. The assumption of a hydrostatic pressure behind the blade resulted also in too large values for the angle of internal friction, analogously to the calculations of the 200 μm sand. Here the following values are determined:

- **α = 30° » φ = 46.2°**
- **α = 45° » φ = 38.7°**
- **α = 60° » φ = 40.3°**

The determination of the angle of internal friction corrected for under pressure behind the blade $\mathbf{W_3}$ led to the following values:

- **α = 30° » φ = 38.7°**
- **α = 45° » φ = 34.0°**
- **α = 60° » φ = 38.4°**

The low value of the angle of internal friction for the 45° blade can be explained by the fact that these tests are performed for the first time in the new laboratory DE in a situation where the sand was not homogenous from top to bottom. For the verification of the cutting forces and the water pressures is, for both sand types, chosen for a soil/steel friction angle of 30° and an angle of internal friction of 38°, as average values.

6.14. General Conclusions.

From the performed research the following general conclusions can be drawn:

1. Both the measured cutting forces as the measured water sub-pressures agree reasonably with the theory. For both sand types is observed that the cutting forces and the water sub-pressures become smaller in comparison with the theory, when the blade angle becomes larger. For the 30° blade the cutting forces and the water sub-pressures are larger or equal to theoretical derived values, while for the 60° blade the theory can overestimate the measurements with a factor 1.6. This can be explained by assuming that with an increasing blade angle the cutting process becomes more discontinuous and therefore decreases the average volume strain rate. Slices of sand shear off with dilatancy around the shear planes, while the dilatancy is less in the sand between the shear planes. The theory can still be pretty useful since in dredging practice the used blade angles are between 30° and 45°.
2. Side effects can considerably influence the direction of the cutting forces, although the magnitude of the cutting forces is less disturbed. As a result of the side effects the cutting forces are aimed more downward.
3. Wear effects can also influence the direction of the cutting forces considerably, while also the magnitude of the cutting forces is less disturbed. As a result of the wear the cutting forces are, however, aimed more upwards.

6.15. The Snow Plough Effect.

To check the validity of the above derived theory, research has been carried out in the new laboratory DE. The tests are carried out in hard packed water saturated sand, with a blade of 0.3 m by 0.2 m. The blade had a cutting angle of 45 degrees and inclination angles of 0, 15, 30 and 45 degrees. The layer thicknesses were 2.5, 5 and 10 cm and the drag velocities 0.25, 0.5 and 1 m/s. Figure 6-57 and Figure 6-58 show the results with and without an inclination angle of 45 degrees. The lines in this figure show the theoretical forces. As can be seen, the measured forces match the theoretical forces well. Since the research is still in progress, further publications on this subject will follow.

More results of measurements can be found in Appendix M and Appendix N

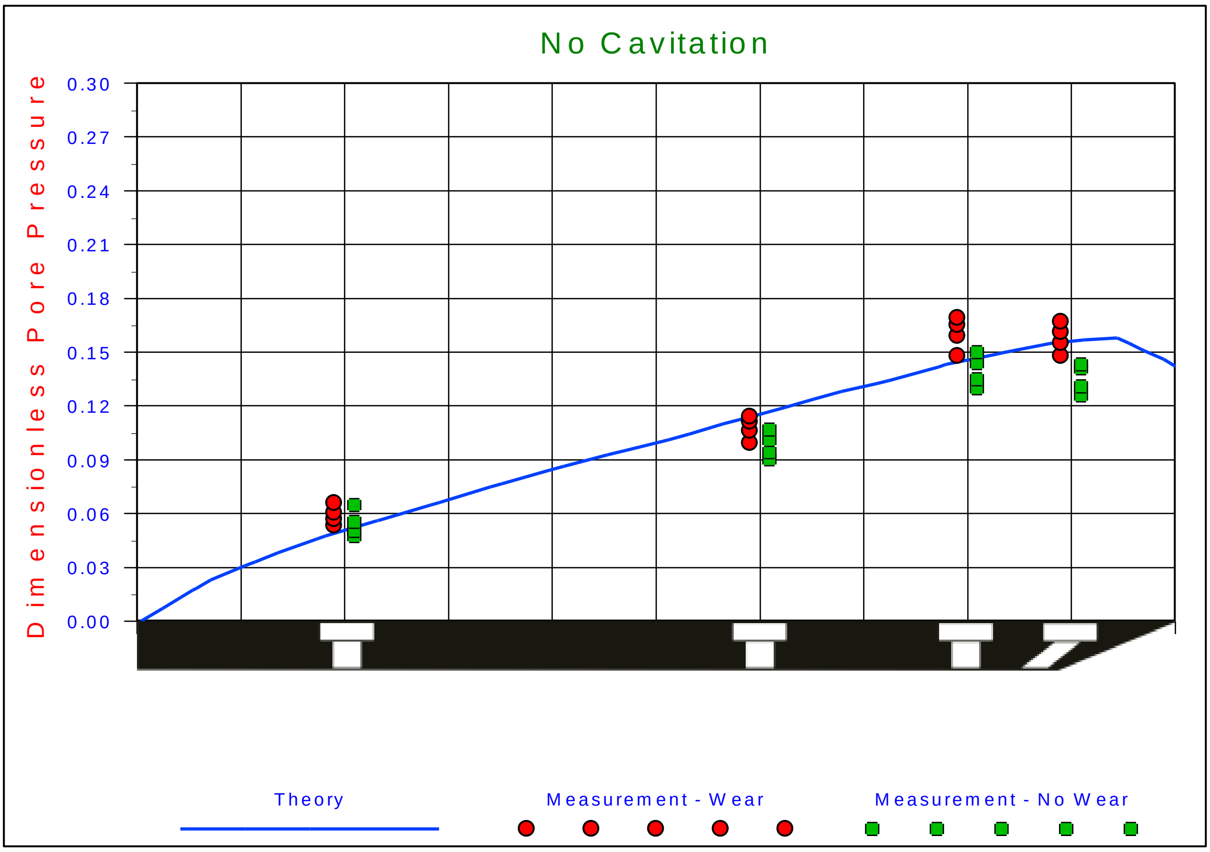

Figure 6-54: An example of pore pressure measurements versus the theory.

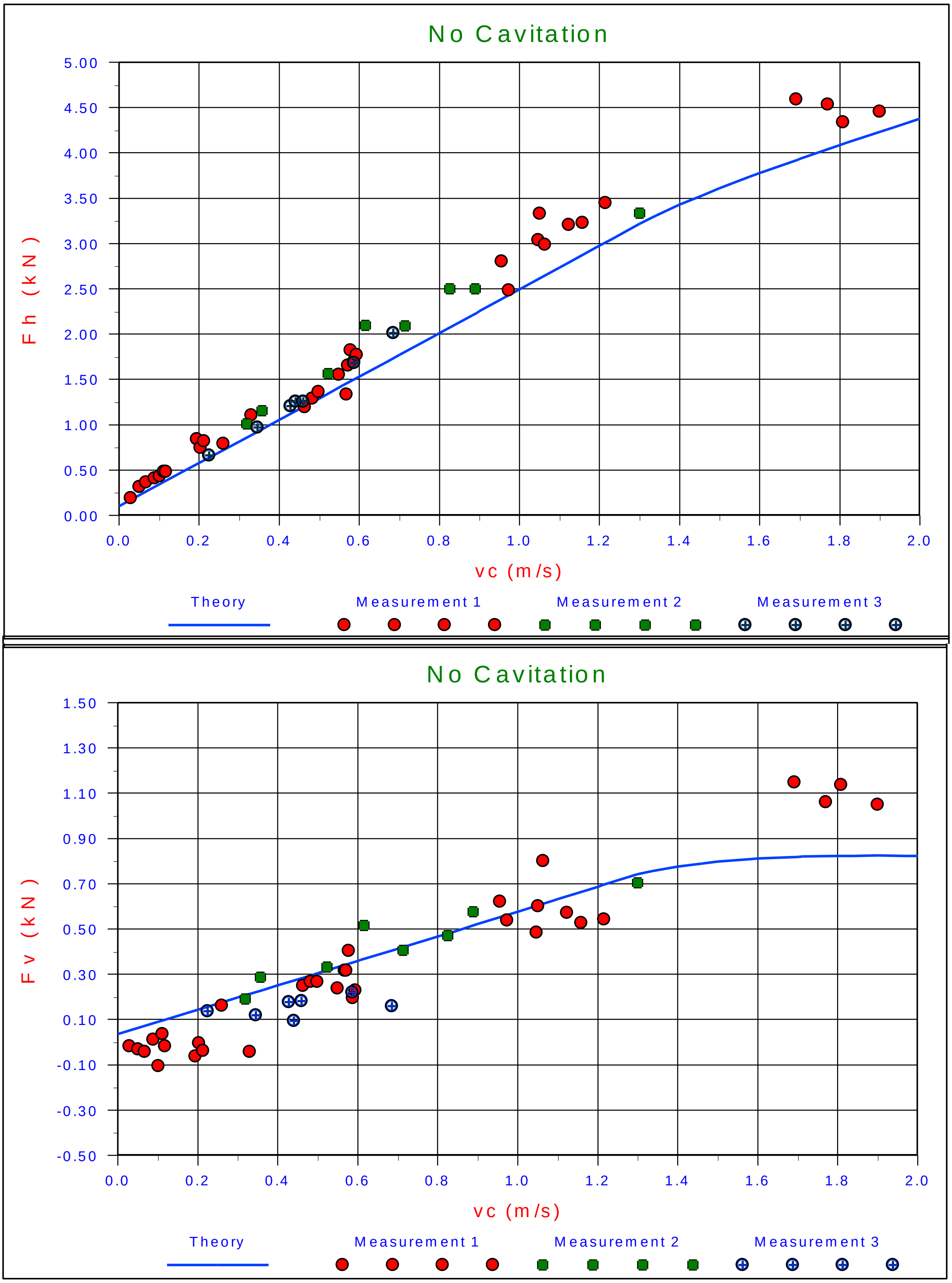

Figure 6-55: An example of the forces measured versus the theory.

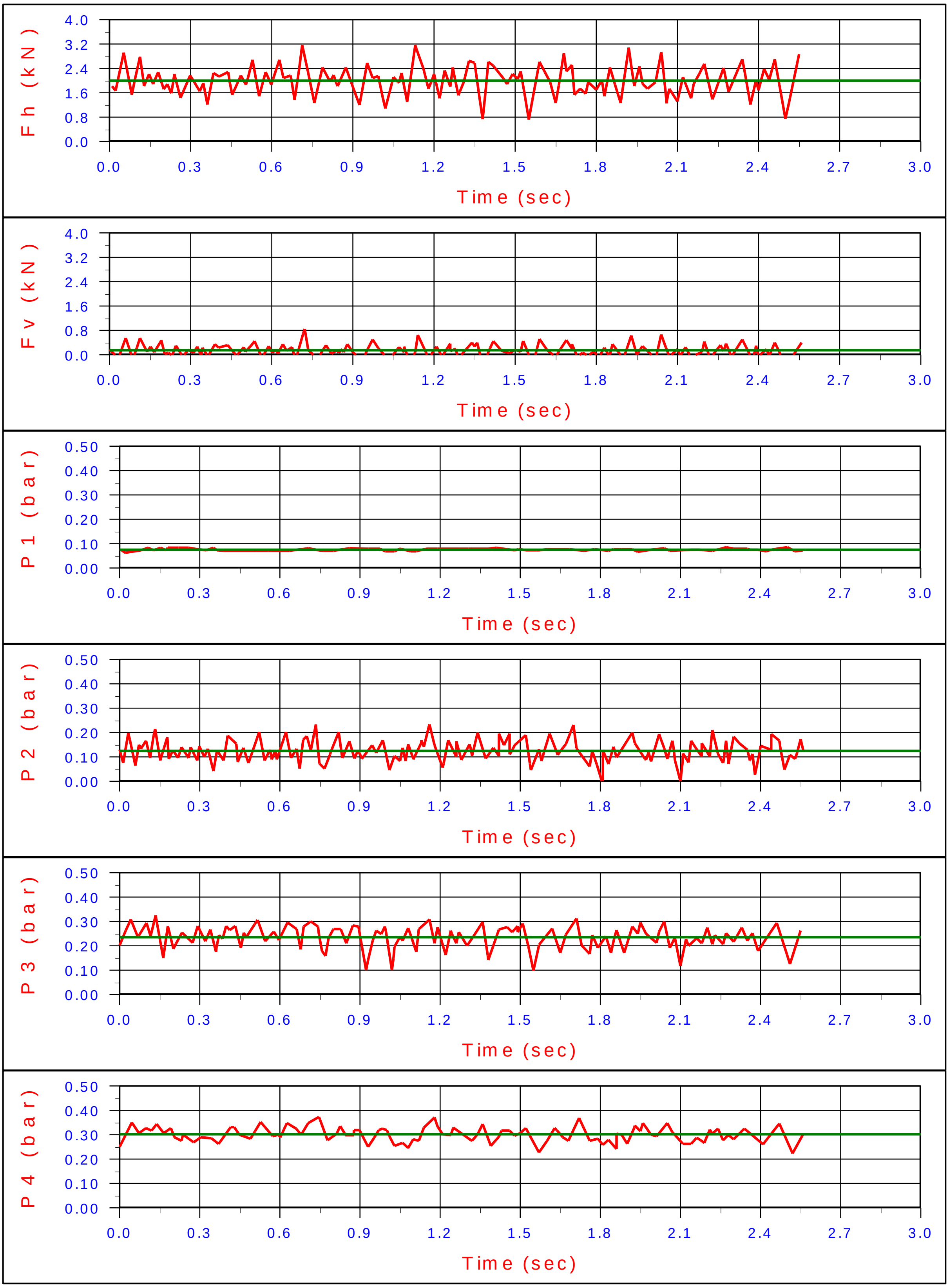

Figure 6-56: An example of the measured signals (forces and pore pressures).

The result of a cutting test graphically. In this figure the horizontal force $\mathbf{F_h}$, the vertical force $\mathbf{F_v}$ and the water pore-pressures on the blade **P1, P2, P3** and **P4** are shown. The test is performed with a blade angle $\boldsymbol{\alpha}$ of 45°, a layer thickness $\mathbf{h_i}$ of 70 mm and a cutting velocity $\mathbf{v_c}$ of 0.68 m/s in the 200 μm sand.

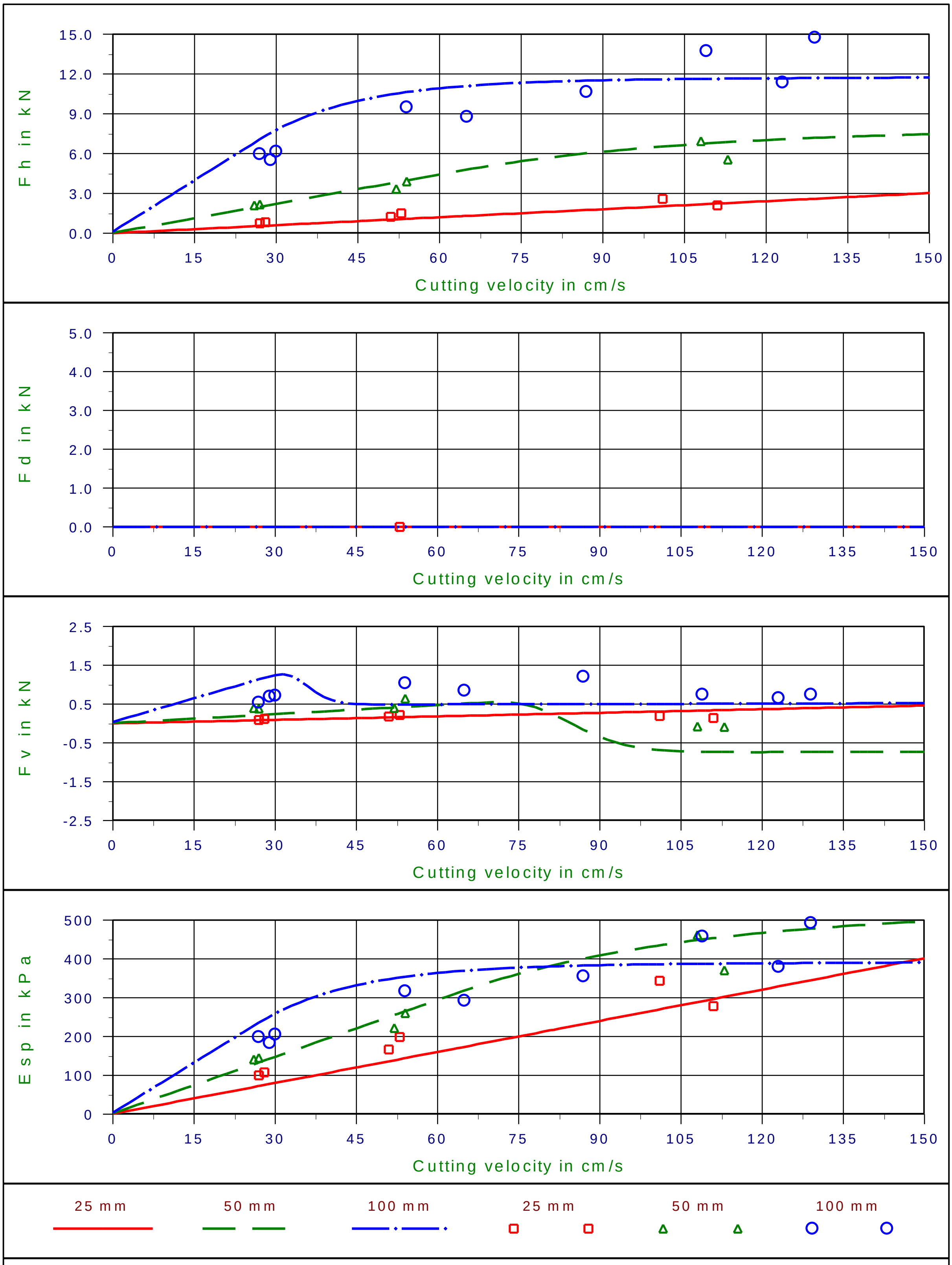

Snow-plough effect research, theory versus measurements.
Blade width 0.3 m, blade height 0.2 m, cutting angle 45 degrees, deviation angle 0 degrees.

Figure 6-57: F_h, F_v, F_d and E_{sp} as a function of the cutting velocity and the layer thickness, without deviation.

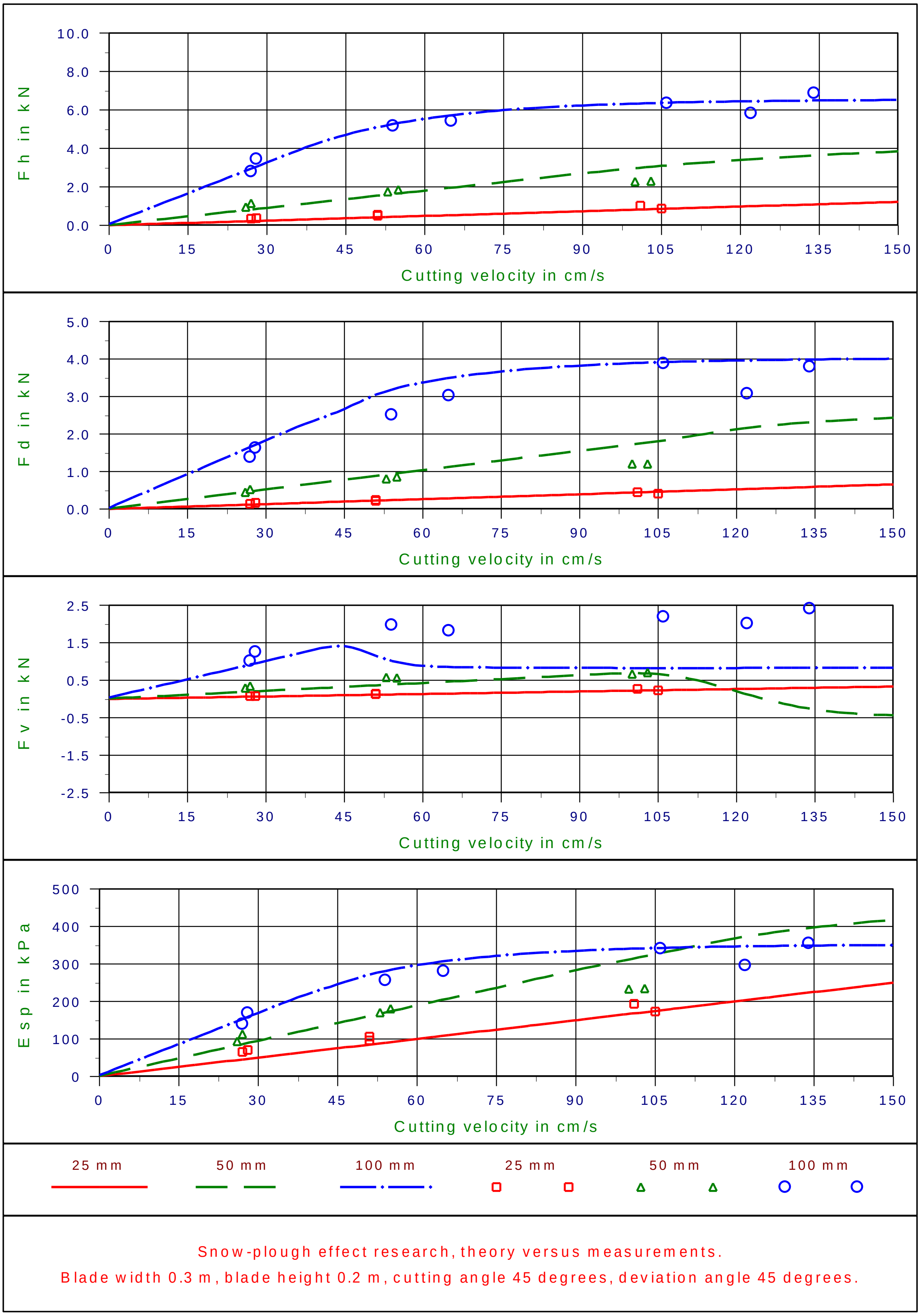

Snow-plough effect research, theory versus measurements.

Blade width 0.3 m, blade height 0.2 m, cutting angle 45 degrees, deviation angle 45 degrees.

Figure 6-58: F_h, F_v, F_d and E_{sp} as a function of the cutting velocity and the layer thickness, with deviation.

6.16. Nomenclature.

a_1,a_2	Weight factors k-value (permeability)	-
A	Surface	m^2
b_{pr}	Projected width of the blade perpendicular to the velocity direction	m
c_i ,c_1 ,c_2	Coefficients (non-cavitating cutting process)	-
c_r	Coefficient side effects	-
c_s	Wear coefficient	-
c_t	Coefficient total cutting force (non-cavitating cutting process)	-
c_{ts}	Coefficient total cutting force including wear effects	-
c_{tr}	Coefficient total cutting force including side effects	-
d_i ,d_1 ,d_2	Coefficients (cavitating cutting process)	-
d_r	Coefficient side effects	-
d_s	Wear coefficient	-
d_t	Coefficient total cutting force (cavitating cutting process)	-
d_{ts}	Coefficient total cutting force including wear	-
d_{tr}	Coefficient total cutting force including side effects	-
E_{sp}	Specific cutting energy	kN/m^2
E_{gc}	Specific cutting energy (no cavitation)	kN/m^2
E_{ca}	Specific cutting energy (full cavitation)	kN/m^2
F_{ci}	Cutting force (general)	kN
F_{cit}	Total cutting force (general)	kN
F_h	Horizontal cutting force (parallel to the cutting speed)	kN
F_l	Cutting force parallel to the edge of the blade	kN
F_n	Normal force	kN
F_v	Vertical cutting force (perpendicular to the cutting velocity)	kN
F_w	Friction force	kN
F_x	Cutting force in x-direction (longitudinal)	kN
F_{xt}	Total cutting force in x-direction (longitudinal)	kN
F_y	Cutting force in y-direction (transversal)	kN
F_{yt}	Total cutting force in y-direction (transversal)	kN
F_z	Cutting force in z-direction (vertical)	kN
g	Gravitational acceleration	m/s^2
h_i	Initial layer thickness	m
h_b	Blade height	m
k	Permeability	m/s
k_i	Initial permeability	m/s
k_{max}	Maximum permeability	m/s
k_m	Effective permeability	m/s
K_1	Grain force on the shear zone	kN
K_2	Grain force on the blade	kN
l	Length of the shear zone	m
n	Normal on an edge	m
n	Porosity	-
n_i	Initial pore percentage	%
n_{max}	Maximum pore percentage	%
N_1	Normal force on the shear zone	kN
N_2	Normal force on the blade	kN
p	Number of blades excavating element	-
p	Pressure (water pressure)	kPa
p_{atm}	Atmospheric pressure	kPa
P_{calc}	Calculated dimensionless pressure (water pore pressure)	-
p_{damp}	Saturated water pore pressure (12 cm.w.c.)	kPa

$\mathbf{P_{real}}$	Real pore pressure (water pore pressure)	kPa
$\mathbf{p_{1m}}$	Average pore pressure in the shear zone	-
$\mathbf{p_{2m}}$	Average pore pressure on the blade	-
$\mathbf{P_c}$	Drive power excavating element	kW
$\mathbf{q, q_1, q_2}$	Specific flow	m/s
$\mathbf{Q}$	Flow per unit of blade width	m^2/s
$\mathbf{s}$	Length of a stream line	m
$\mathbf{s}$	Measure for the layer thickness	m
$\mathbf{S_1}$	Shear force on the shear zone	kN
$\mathbf{S_2}$	Shear force on the blade	kN
$\mathbf{v_c}$	Cutting velocity perpendicular to the edge of the blade	m/s
$\mathbf{V}$	Volume strain per unit of blade width	m^2
$\mathbf{w}$	Width of blade of blade element	m
$\mathbf{W_1}$	Pore pressure force on the shear zone	kN
$\mathbf{W_2}$	Pore pressure force on the blade	kN
$\mathbf{x}$	Coordinate	m
$\mathbf{y}$	Coordinate	m
$\mathbf{z}$	Coordinate	m
$\mathbf{z}$	Water depth	m
$\boldsymbol{\alpha}$	Blade angle	rad
$\boldsymbol{\beta}$	Shear angle	rad
$\boldsymbol{\varepsilon}$	Volume strain	-
$\boldsymbol{\varphi}$	Angle of internal friction	rad
$\boldsymbol{\delta}$	Soil/steel interface friction angle	rad
$\boldsymbol{\rho_g}$	Wet density of the sand	ton/m^3
$\boldsymbol{\rho_s}$	Dry density of the sand	ton/m^3
$\boldsymbol{\rho_w}$	Density of water	ton/m^3
$\boldsymbol{\theta_r}$	Angular displacement force vector as a result of side effects	rad
$\boldsymbol{\theta_s}$	Angular displacement force vector as a result of wear	rad
$\boldsymbol{\theta_t}$	Angle force vector angle in relation to cutting velocity vector	rad
$\boldsymbol{\theta_{ts}}$	Angle force vector angle in relation to velocity vector including wear	rad
$\boldsymbol{\theta_{tr}}$	Angle force vector angle in relation to velocity vector including side effects	rad
$\boldsymbol{\Theta_r}$	Angular displacement force vector as a result of side effects	rad
$\boldsymbol{\Theta_s}$	Angular displacement force vector as a result of wear	rad
$\boldsymbol{\Theta_t}$	Angle force vector angle in relation to cutting velocity vector	rad
$\boldsymbol{\Theta_{ts}}$	Angle force vector angle in relation to velocity vector including wear	rad
$\boldsymbol{\Theta_{tr}}$	Angle force vector angle in relation to velocity vector including side effects	rad

Chapter 7: Clay Cutting.

7.1. Definitions.

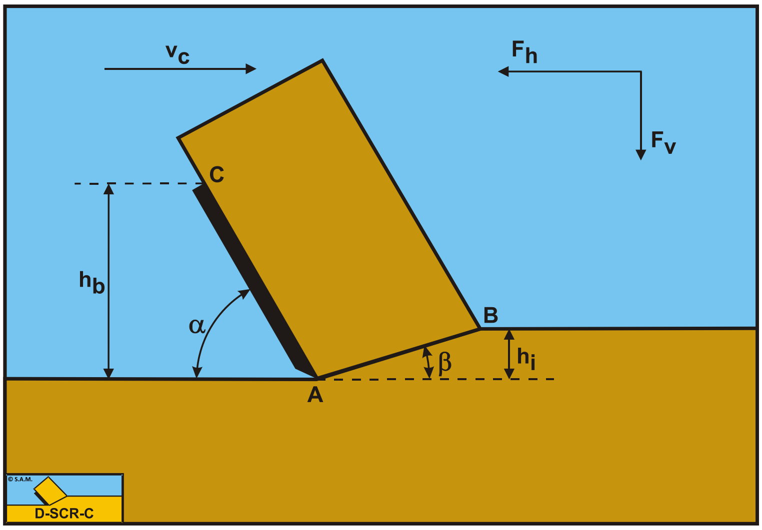

Figure 7-1: The cutting process, definitions.

Definitions:

1. **A**: The blade tip.
2. **B**: End of the shear plane.
3. **C**: The blade top.
4. **A-B**: The shear plane.
5. **A-C**: The blade surface.
6. **h_b**: The height of the blade.
7. **h_i**: The thickness of the layer cut.
8. **v_c**: The cutting velocity.
9. **α**: The blade angle.
10. **β**: The shear angle.
11. **F_h**: The horizontal force, the arrow gives the positive direction.
12. **F_v**: The vertical force, the arrow gives the positive direction.

7.2. Introduction.

Hatamura and Chijiiwa (1975), (1976A), (1976B), (1977A) and (1977B) distinguished three failure mechanisms in soil cutting. The **Shear Type**, the **Flow Type** and the **Tear Type**. The **Flow Type** and the **Tear Type** occur in materials without an angle of internal friction. The **Shear Type** occurs in materials with an angle of internal friction like sand. A fourth failure mechanism can be distinguished (Miedema (1992)), the **Curling Type**, as is known in metal cutting. Although it seems that the curling of the chip cut is part of the flow of the material, whether the **Curling Type** or the **Flow Type** occurs depends on several conditions. The **Curling Type** in general will occur if the adhesive force on the blade is large with respect to the normal force on the shear plane. Whether the **Curling Type** results in pure curling or buckling of the layer cut giving obstruction of the flow depends on different parameters.

Figure 7-2 illustrates the **Curling Type** mechanism, Figure 7-3 the **Flow Type** mechanism and Figure 7-4 the **Tear Type** mechanism as they occur when cutting clay or loam. To predict which type of failure mechanism will occur under given conditions with specific soil, a formulation for the cutting forces has to be derived. The derivation is made under the assumption that the stresses on the shear plane and the blade are constant and equal to the average stresses acting on the surfaces. Figure 7-1 gives some definitions regarding the cutting process. The line A-B is considered to be the shear plane, while the line A-C is the contact area between the blade and the soil. The blade angle is named **α** and the shear angle **β**. The blade is moving from left to right with a cutting velocity **v_c**. The thickness of the layer cut is **h_i** and the vertical height of the blade **h_b**. The horizontal force on the blade **F_h** is positive from right to left always opposite to the direction of the cutting velocity **v_c**. The vertical force on the blade **F_v** is positive downwards.

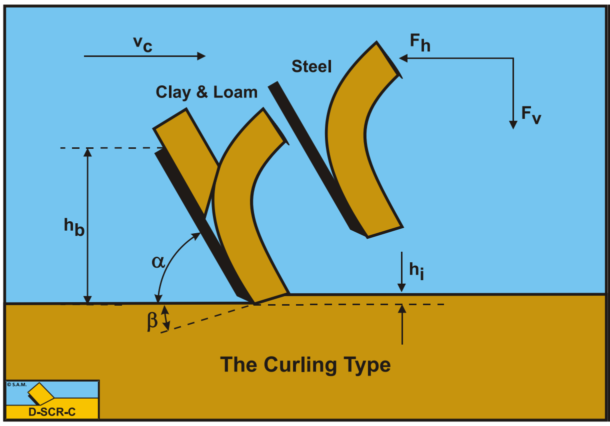

Figure 7-2: The Curling Type in clay.

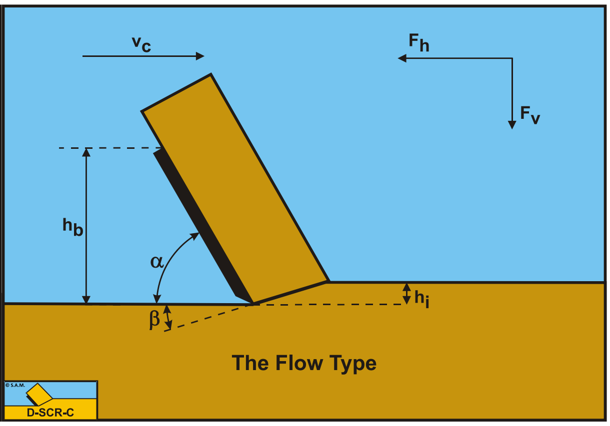

Figure 7-3: The Flow Type in clay.

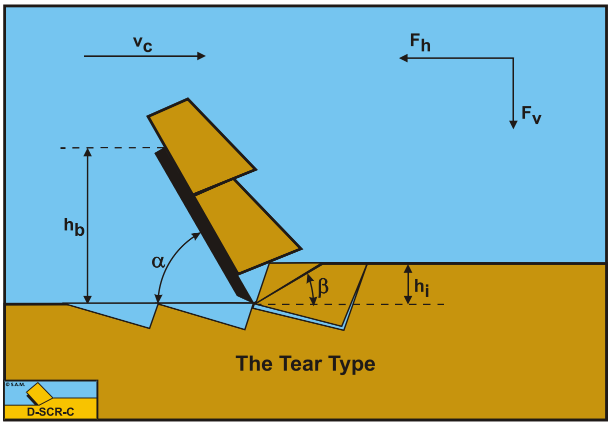

Figure 7-4: The Tear Type in clay.

Since the vertical force is perpendicular to the cutting velocity, the vertical force does not contribute to the cutting power, which is equal to:

$$\mathbf{P_c = F_h \cdot v_c} \tag{7-1}$$

In clay the cutting processes are dominated by cohesion and adhesion (internal and external shear strength). Because of the **φ=0** concept, the internal and external friction angles are set to 0. Gravity, inertial forces and pore pressures are also neglected. This simplifies the cutting equations. Clay however is subject to strengthening, meaning that the internal and external shear strength increase with an increasing strain rate. The reverse of strengthening is creep, meaning that under a constant load the material will continue deforming with a certain strain rate.

Under normal circumstances clay will be cut with the flow mechanism, but under certain circumstances the **Curling Type** or the **Tear Type** may occur.

The **Curling Type** will occur when the blade height is big with respect to the layer thickness, $\mathbf{h_b/h_i}$, the adhesion is high compared to the cohesion **a/c** and the blade angle **α** is relatively big.

The **Tear Type** will occur when the blade height is small with respect to the layer thickness, $\mathbf{h_b/h_i}$, the adhesion is small compared to the cohesion **a/c** and the blade angle **α** is relatively small.

This chapter is based on Miedema (1992), (2009) and (2010).

7.3. The Influence of Strain Rate on the Cutting Process.

7.3.1. Introduction.

Previous researchers, especially Mitchell (1976), have derived equations for the strain rate dependency of the cohesion based on the "rate process theory". However the resulting equations did not allow pure cohesion and adhesion. In many cases the equations derived resulted in a yield stress of zero or minus infinity for a material at rest. Also empirical equations have been derived giving the same problems.
Based on the "rate process theory" with an adapted Boltzman probability distribution, the Mohr-Coulomb failure criteria will be derived in a form containing the influence of the deformation rate on the parameters involved. The equation derived allows a yield stress for a material at rest and does not contradict the existing equations, but confirms measurements of previous researchers. The equation derived can be used for silt and for clay, giving both materials the same physical background. Based on the equilibrium of forces on the chip of soil cut, as derived by Miedema (1987 September) for soil in general, criteria are formulated to predict the failure mechanism when cutting clay. A third failure mechanism can be distinguished, the "curling type". Combining the equation for the deformation rate dependency of cohesion and adhesion with the derived cutting equations, allows the prediction of the failure mechanism and the cutting forces involved. The theory developed has been verified by using data obtained by Hatamura and Chijiiwa (1975), (1976A), (1976B), (1977A) and (1977B) with respect to the adapted rate process theory and data obtained by Stam (1983) with respect to the cutting forces. However since the theory developed confirms the work carried out by previous researchers its validity has been proven in advance. In this chapter simplifications have been applied to allow a clear description of the phenomena involved.
The theory in this chapter has been published by Miedema (1992) and later by Miedema (2009) and (2010).

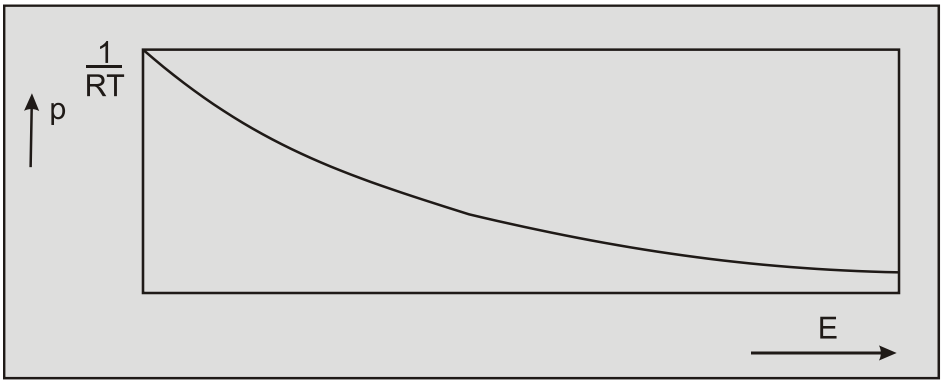

Figure 7-5: The Boltzman probability distribution.

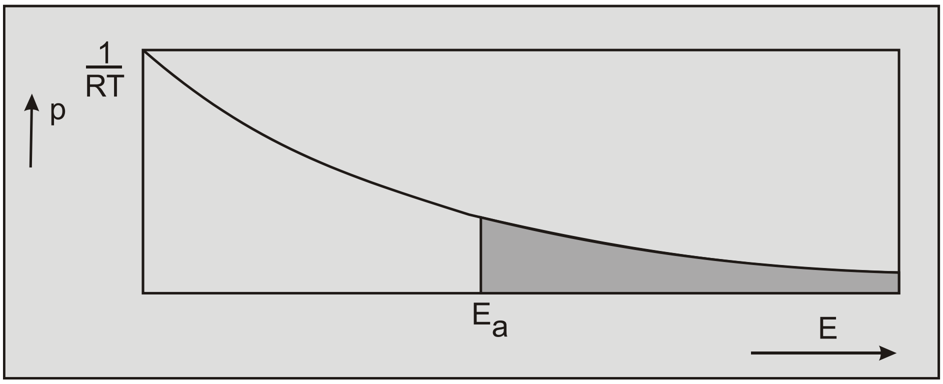

Figure 7-6: The probability of exceeding an energy level Ea.

7.3.2. The Rate Process Theory.

It has been noticed by many researchers that the cohesion and adhesion of clay increase with an increasing deformation rate. It has also been noticed that the failure mechanism of clay can be of the "flow type" or the "tear type", similar to the mechanisms that occur in steel cutting. The rate process theory can be used to describe the phenomena occurring in the processes involved. This theory, developed by Glasstone, Laidler and Eyring (1941) for the modeling of absolute reaction rates, has been made applicable to soil mechanics by Mitchell (1976). Although there is no physical evidence of the validity of this theory it has proved valuable for the modeling of many processes such as chemical reactions. The rate process theory, however, does not allow strain rate independent stresses such as real cohesion and adhesion. This connects with the starting point of the rate process theory that the probability of atoms, molecules or particles, termed flow units having a certain thermal vibration energy is in accordance with the Boltzman distribution (Figure 7-5):

$$p(E) = \frac{1}{R \cdot T} \cdot \exp\left(\frac{-E}{R \cdot T}\right) \tag{7-2}$$

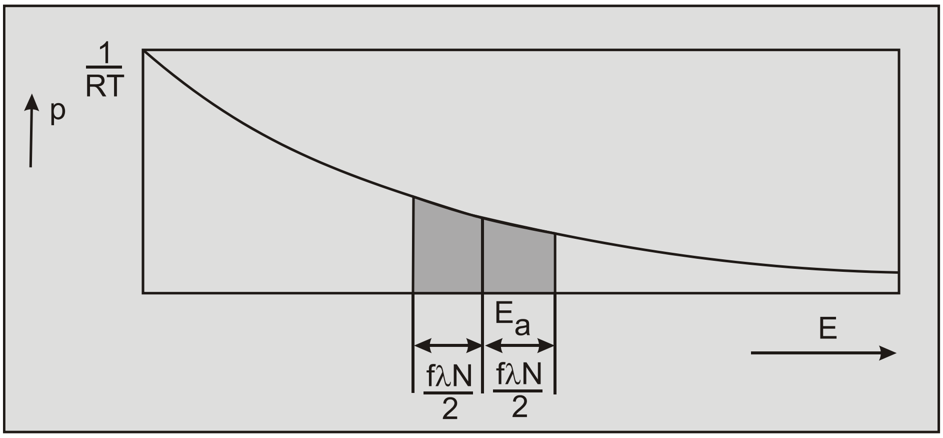

Figure 7-7: The probability of net activation in direction of force.

The movement of flow units participating in a time dependent flow is constrained by energy barriers separating adjacent equilibrium positions. To cross such an energy barrier, a flow unit should have an energy level exceeding certain activation energy $\mathbf{E_a}$. The probability of a flow unit having an energy level greater than a certain energy level $\mathbf{E_a}$ can be calculated by integrating the Boltzman distribution from the energy level $\mathbf{E_a}$ to infinity, as depicted in Figure 7-6, this gives:

$$p_{E>E_a} = \exp\left(\frac{-E_a}{R \cdot T}\right) \tag{7-3}$$

The value of the activation energy $\mathbf{E_a}$ depends on the type of material and the process involved. Since thermal vibrations occur at a frequency given by **kT/h**, the frequency of activation of crossing energy barriers is:

$$\nu = \frac{k.T}{h} \cdot \exp\left(\frac{-E_a}{R \cdot T}\right) \tag{7-4}$$

In a material at rest the barriers are crossed with equal frequency in all directions. If however a material is subjected to an external force resulting in directional potentials on the flow units, the barrier height in the direction of the force is reduced by (**f•λ/2**) and raised by the same amount in the opposite direction. Where f represents the force acting on a flow unit and **λ** represents the distance between two successive equilibrium positions. From this it can be derived that the net frequency of activation in the direction of the force **f** is as illustrated in Figure 7-7:

$$\nu = \frac{k \cdot T}{h} \cdot \exp\left(\frac{-E_a}{R \cdot T}\right) \cdot \left\{\exp\left(\frac{+f \cdot \lambda}{2 \cdot k \cdot T}\right) - \exp\left(\frac{-f \cdot \lambda}{2 \cdot k \cdot T}\right)\right\} \tag{7-5}$$

If a shear stress **τ** is distributed uniformly along **S** bonds between flow units per unit area then **f=τ/S** and if the strain rate is a function **X** of the proportion of successful barrier crossings and the displacement per crossing according to **dε/dt=X·ν** then:

$$\dot{\varepsilon} = 2 \cdot X \cdot \frac{k \cdot T}{h} \cdot \exp\left(\frac{-E_a}{R \cdot T}\right) \cdot \sinh\left(\frac{\tau \cdot \lambda \cdot N}{2 \cdot S \cdot R \cdot T}\right) \qquad \text{with} : R = N \cdot k \tag{7-6}$$

From this equation, simplified equations can be derived to obtain dashpot coefficients for theological models, to obtain functional forms for the influences of different factors on strength and deformation rate, and to study deformation mechanisms in soils. For example:

$$\text{if}\quad \left(\frac{\tau\cdot\lambda\cdot N}{2\cdot S\cdot R\cdot T}\right)<1\quad\text{then}\quad \sinh\left(\frac{\tau\cdot\lambda\cdot N}{2\cdot S\cdot R\cdot T}\right)\approx\left(\frac{\tau\cdot\lambda\cdot N}{2\cdot S\cdot R\cdot T}\right)\tag{7-7}$$

Resulting in the mathematical description of a Newtonian fluid flow, and:

$$\text{if}\quad \left(\frac{\tau\cdot\lambda\cdot N}{2\cdot S\cdot R\cdot T}\right)>1\quad\text{then}\quad \sinh\left(\frac{\tau\cdot\lambda\cdot N}{2\cdot S\cdot R\cdot T}\right)\approx\frac{1}{2}\cdot\exp\left(\frac{\tau\cdot\lambda\cdot N}{2\cdot S\cdot R\cdot T}\right)\tag{7-8}$$

Resulting in a description of the Mohr-Coulomb failure criterion for soils as proposed by Mitchell et al. (1968). Zeng and Yao (1988) and (1991) used the first simplification (7-7) to derive a relation between soil shear strength and shear rate and the second simplification (7-8) to derive a relation between soil-metal friction and sliding speed.

7.3.3. Proposed Rate Process Theory.

The rate process theory does not allow shear strength if the deformation rate is zero. This implies that creep will always occur since any material is always exposed to its own weight. This results from the starting point of the rate process theory, the Boltzman distribution of the probability of a flow unit exceeding a certain energy level of thermal vibration. According to the Boltzman distribution there is always a probability that a flow unit exceeds an energy level, between an energy level of zero and infinity, this is illustrated in Figure 7-6.
Since the probability of a flow unit having an infinite energy level is infinitely small, the time-span between the occurrences of flow units having an infinite energy level is also infinite, if a finite number of flow units is considered. From this it can be deduced that the probability that the energy level of a finite number of flow units does not exceed a certain limiting energy level in a finite time-span is close to 1. This validates the assumption that for a finite number of flow units in a finite time-span the energy level of a flow unit cannot exceed a certain limiting energy level $\mathbf{E_l}$. The resulting adapted Boltzman distribution is illustrated in Figure 7-8. The Boltzman distribution might be a good approximation for atoms and molecules but for particles consisting of many atoms and/or molecules the distribution according to Figure 7-8 seems more reasonable, since it has never been noticed that sand grains in a layer of sand at rest, start moving because of their internal energy. In clay some movement of the clay particles seems probable since the clay particles are much smaller than the sand particles. Since particles consist of many atoms, the net vibration energy in any direction will be small, because the atoms vibrate thermally with equal frequency in all directions.

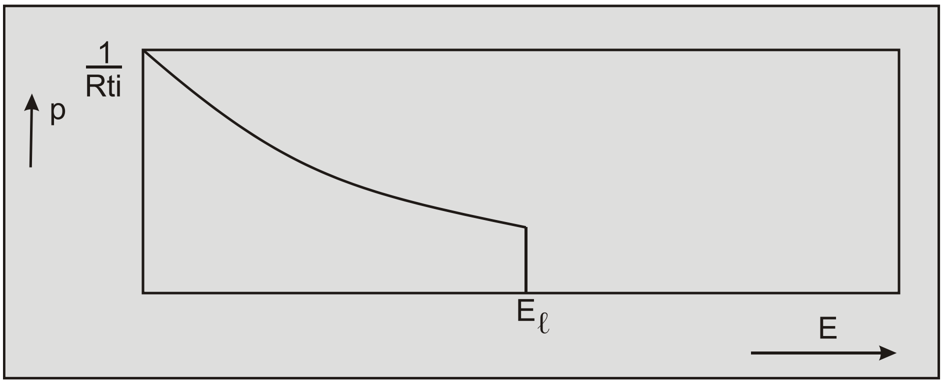

Figure 7-8: The adapted Boltzman probability distribution.

If a probability distribution according to Figure 7-8 is considered, the probability of a particle exceeding a certain activation energy $\mathbf{E_a}$ becomes:

$$p_{E>E_a}=\frac{\exp\left(\frac{-E_a}{R\cdot T}\right)-\exp\left(\frac{-E_\ell}{R\cdot T}\right)}{1-\exp\left(\frac{-E_\ell}{R\cdot T}\right)}\quad\text{if } E_a<E_\ell\ \text{and}\ p_{E>E_a}=0\quad\text{if } E_a>E_\ell\tag{7-9}$$

If the material is now subjected to an external shear stress, four cases can be distinguished with respect to the strain rate.

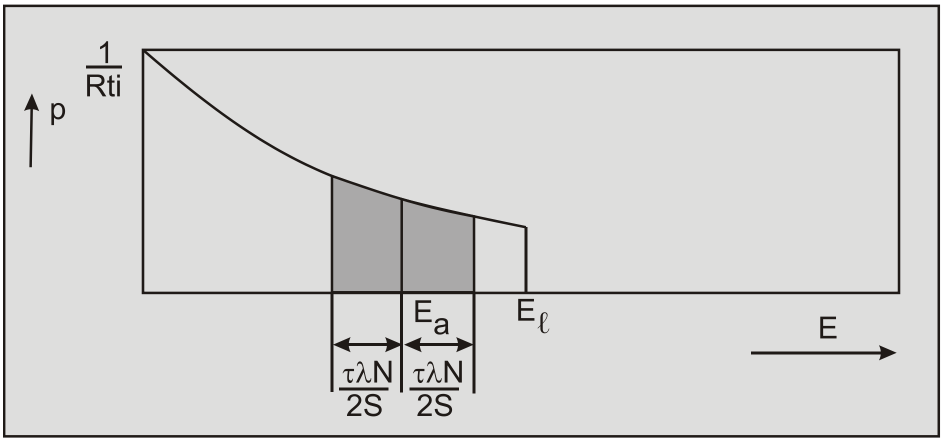

Figure 7-9: The probability of net activation in case 1.

Case 1:

The energy level $\mathbf{E_a + \tau\lambda N/2S}$ is smaller than the limiting energy level $\mathbf{E_l}$ (Figure 7-9). The strain rate equation is now:

$$\dot{\varepsilon} = 2\cdot X\cdot\frac{k\cdot T}{h\cdot i}\cdot\exp\left(\frac{-E_a}{R\cdot T}\right)\cdot\sinh\left(\frac{\tau\cdot\lambda\cdot N}{2\cdot S\cdot R\cdot T}\right) \tag{7-10}$$

with: $i = 1-\exp\left(\frac{-E_\ell}{R\cdot T}\right)$

Except for the coefficient **i**, necessary to ensure that the total probability remains 1, equation (7-10) is identical to equation (7-6).

Case 2:

The activation energy $\mathbf{E_a}$ is less than the limiting energy $\mathbf{E_l}$, but the energy level $\mathbf{E+\tau\lambda N/2S}$ is greater than the limiting energy level $\mathbf{E_l}$ (Figure 7-10).

The strain rate equation is now:

$$\dot{\varepsilon} = X\cdot\frac{k\cdot T}{h\cdot i}\cdot\left\{\exp\left(-\left(\frac{E_a}{R\cdot T}-\frac{\tau\cdot\lambda\cdot N}{2\cdot S\cdot R\cdot T}\right)\right)-\exp\left(\frac{-E_\ell}{R\cdot T}\right)\right\} \tag{7-11}$$

Case 3:

The activation energy $\mathbf{E_a}$ is greater than the limiting energy $\mathbf{E_l}$, but the energy level $\mathbf{E_a -\tau\lambda N/2S}$ is less than the limiting energy level $\mathbf{E_l}$ (Figure 7-11). The strain rate equation is now:

$$\dot{\varepsilon} = X\cdot\frac{k\cdot T}{h\cdot i}\cdot\left\{\exp\left(-\left(\frac{E_a}{R\cdot T}-\frac{\tau\cdot\lambda\cdot N}{2\cdot S\cdot R\cdot T}\right)\right)-\exp\left(\frac{-E_\ell}{R\cdot T}\right)\right\} \tag{7-12}$$

Equation (7-12) appears to be identical to equation (7-11), but the boundary conditions differ.

Case 4:

The activation energy $\mathbf{E_a}$ is greater than the limiting energy $\mathbf{E_l}$ and the energy level $\mathbf{E_a -\tau\lambda N/2S}$ is greater than the limiting energy level $\mathbf{E_l}$ (Figure 7-12). The strain rate will be equal to zero in this case.

The cases 1 and 2 are similar to the case considered by Mitchell (1976) and still do not permit true cohesion and adhesion. Case 4 considers particles at rest without changing position within the particle matrix. Case 3 considers a material on which an external shear stress of certain magnitude must be applied to allow the particles to cross energy barriers, resulting in a yield stress (true cohesion or adhesion).

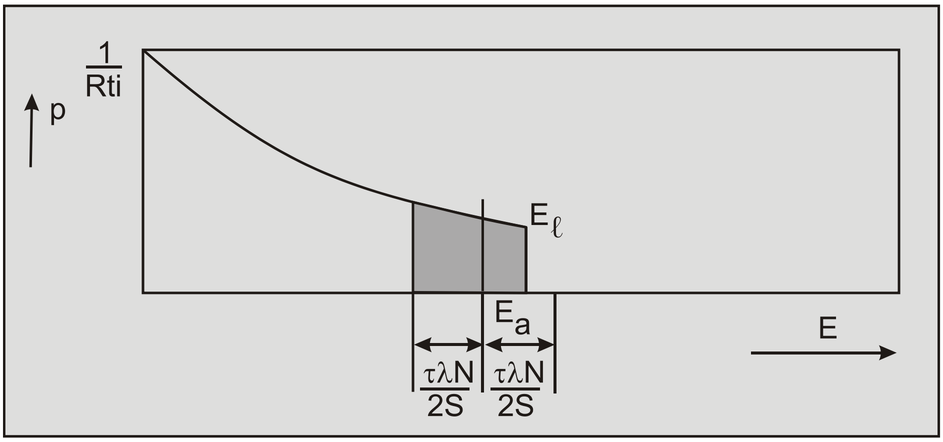

Figure 7-10: The probability of net activation in case 2.

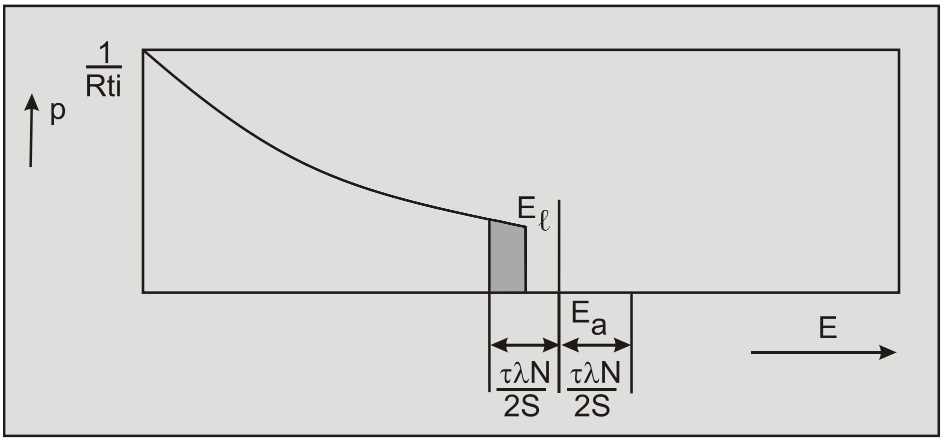

Figure 7-11: The probability of net activation in case 3.

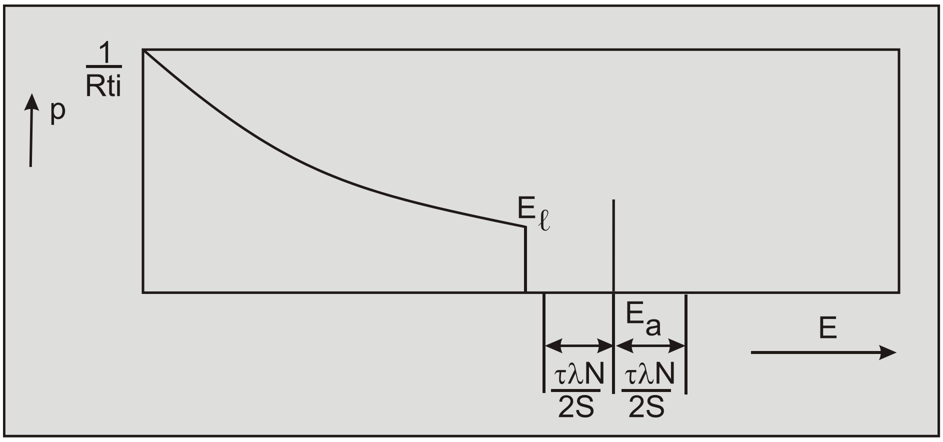

Figure 7-12: The probability of net activation in case 4.

From equation (7-12) the following equation for the shear stress can be derived:

$$\tau = (E_a - E_\ell) \cdot \frac{2 \cdot S}{\lambda \cdot N} + R \cdot T \cdot \frac{2 \cdot S}{\lambda \cdot N} \cdot \ln\left(1 + \frac{\dot{\varepsilon}}{\dot{\varepsilon}_0}\right) \qquad \textbf{(7-13)}$$

$$\text{with: } \dot{\varepsilon}_0 = \frac{X \cdot k \cdot T}{h \cdot i} \cdot \exp\left(\frac{-E_\ell}{R \cdot T}\right)$$

According to Mitchell (1976), if no shattering of particles occurs, the relation between the number of bonds **S** and the effective stress $\boldsymbol{\sigma_e}$ can be described by the following equation:

$$S = a + b.\sigma_e \tag{7-14}$$

Lobanov and Joanknecht (1980) confirmed this relation implicitly for pressures up to 10 bars for clay and paraffin wax. At very high pressures they found an exponential relation that might be caused by internal failure of the particles. For the friction between soil and metal Zeng and Yao (1988) also used equation (7-14), but for the internal friction Zeng and Yao (1991) used a logarithmic relationship, which contradicts Lobanov and Joanknecht and Mitchell, although it can be shown by Taylor series approximation that a logarithmic relation can be transformed into a linear relation for values of the argument of the logarithm close to 1. Since equation (7-14) contains the effective stress it is necessary that the clay used, is fully consolidated. Substituting equation (7-14) in equation (7-13) gives:

$$\begin{aligned}\tau = {} & a \cdot \left\{ (E_a - E_\ell) \cdot \frac{2}{\lambda \cdot N} + R \cdot T \cdot \frac{2}{\lambda \cdot N} \cdot \ln\left(1 + \frac{\dot{\varepsilon}}{\dot{\varepsilon}_0}\right) \right\} \\ & + b \cdot \left\{ \left(E_a - E_\ell\right) \cdot \frac{2}{\lambda \cdot N} + R \cdot T \cdot \frac{2}{\lambda \cdot N} \cdot \ln\left(1 + \frac{\dot{\varepsilon}}{\dot{\varepsilon}_0}\right) \right\} \cdot \sigma_e\end{aligned} \tag{7-15}$$

Equation (7-15) is of the same form as the Mohr-Coulomb failure criterion:

$$\tau = \tau_c + \sigma_e.\tan(\varphi) \tag{7-16}$$

Equation (7-15), however, allows the strain rate to become zero, which is not possible in the equation derived by Mitchell (1976). The Mitchell equation and also the equations derived by Zeng and Yao (1988) and (1991) will result in a negative shear strength at small strain rates.

7.3.4. The Proposed Theory versus some other Theories.

The proposed new theory is in essence similar to the theory developed by Mitchell (1976) which was based on the "rate process theory" as proposed by Eyring (1941). It was, however, necessary to use simplifications to obtain the equation in a useful form. The following formulation for the shear stress as a function of the strain rate has been derived by Mitchell by simplification of equation (7-6):

$$\tau = a \cdot \left\{ E_a \cdot \frac{2}{\lambda \cdot N} + R \cdot T \cdot \frac{2}{\lambda \cdot N} \cdot \ln\left(\frac{\dot{\varepsilon}}{B}\right) \right\}$$

$$+ b \cdot \left\{ E_a \cdot \frac{2}{\lambda \cdot N} + R \cdot T \cdot \frac{2}{\lambda \cdot N} \cdot \ln\left(\frac{\dot{\varepsilon}}{B}\right) \right\} \cdot \sigma_e \tag{7-17}$$

with: $B = \frac{X.k.T}{h}$

This equation is not valid for very small strain rates, because this would result in a negative shear stress. It should be noted that for very high strain rates the equations (7-15) and (7-17) will have exactly the same form. Zeng and Yao (1991) derived the following equation by simplification of equation (7-6) and by adding some empirical elements:

$$\ln(\tau) = C_1 + C_2 \cdot \ln(\dot{\varepsilon}) + C_3 \cdot \ln(1 + C_4 \cdot \sigma_e) \tag{7-18}$$

Rewriting equation (7-18) in a more explicit form gives:

$$\tau = \exp(C_1) \cdot (\dot{\varepsilon})^{C_2} \cdot (1 + C_4 \cdot \sigma_e)^{C_3} \tag{7-19}$$

Equation (7-19) is valid for strain rates down to zero, but not for a yield stress. With respect to the strain rate, equation (7-19) is the equation of a fluid behaving according to the power law named "power law fluids". It should be noted however that equation (7-19) cannot be derived from equation (7-6) directly and thus should be considered as an empirical equation. If the coefficient **C_3** equals 1, the relation between shear stress and effective stress is similar to the relation found by Mitchell (1976). For the friction between the soil (clay and loam) and metal Zeng and Yao (1988) derived the following equation by simplification of equation (7-6):

$$\tau_b = \tau_{ya} + C_5 \cdot \ln(\dot{\varepsilon}) + \sigma_e \cdot \tan(\delta) = \tau_a + \sigma_e \cdot \tan(\delta) \tag{7-20}$$

Equation (7-20) allows a yield stress, but does not allow the sliding velocity to become zero. An important conclusion of Yao and Zeng is that pasting soil on the metal surface slightly increases the friction meaning that the friction between soil and metal almost equals the shear strength of the soil.

The above-mentioned researchers based their theories on the rate process theory, other researchers derived empirical equations. Turnage and Freitag (1970) observed that for saturated clays the cone resistance varied with the penetration rate according to:

$$F = a.v^b \tag{7-21}$$

With values for the exponent ranging from 0.091 to 0.109 Wismer and Luth (1972B) and (1972A) confirmed this relation and found a value of 0.100 for the exponent, not only for cone penetration tests but also for the relation between the cutting forces and the cutting velocity when cutting clay with straight blades. Hatamura and Chijiiwa (1975), (1976A), (1976B), (1977A) and (1977B) also confirmed this relation for clay and loam cutting and found an exponent of 0.089.

Soydemir (1977) derived an equation similar to the Mitchell equation. From the data measured by Soydemir a relation according to equation (7-21) with an exponent of 0.101 can be derived. This confirms both the Mitchell approach and the power law approach.

7.3.5. Verification of the Theory Developed.

The theory developed differs from the other theories mentioned in the previous paragraph, because the resulting equation (7-15) allows a yield strength (cohesion or adhesion). At a certain consolidation pressure level equation (7-15) can be simplified to:

$$\tau = \tau_y + \tau_0 \cdot \ln\left(1 + \frac{\dot{\varepsilon}}{\dot{\varepsilon}_0}\right) \tag{7-22}$$

If **(dε/dt)/(dε₀/dt) << 1**, equation (7-22) can be approximated by:

$$\tau = \tau_y + \tau_0 \cdot \frac{\dot{\varepsilon}}{\dot{\varepsilon}_0} \tag{7-23}$$

This approximation gives the formulation of a Bingham fluid. If the yield strength τ_y is zero, equation (7-23) represents a Newtonian fluid. If **(dε/dt)/(dε₀/dt) >> 1**, equation (7-22) can be approximated by:

$$\tau = \tau_y + \tau_0 \cdot \ln\left(\frac{\dot{\varepsilon}}{\dot{\varepsilon}_0}\right) \tag{7-24}$$

This approximation is similar to equation (7-17) as derived by Mitchell.
If **(dε/dt)/(dε₀/dt) >> 1** and **$\tau - \tau_y$** $<< \tau_y$, equation (7-22) can be approximated by:

$$\tau = \tau_y \cdot \left(\frac{\dot{\varepsilon}}{\dot{\varepsilon}_0}\right)^{\tau_0/\tau_y} \tag{7-25}$$

This approximation is similar to equation (7-21) as found empirically by Wismer and Luth (1972B) and many other researchers. The equation (7-15) derived in this paper, the equation (7-17) derived by Mitchell and the empirical equation (7-21) as used by many researchers have been fitted to data obtained by Hatamura and Chijiiwa (1975), (1976A), (1976B), (1977A) and (1977B). This is illustrated in Figure 7-13 with a logarithmic horizontal axis. Figure 7-14 gives an illustration with both axis logarithmic. These figures show that the data obtained by Hatamura and Chijiiwa fit well and that the above described approximations are valid.

The values used are **τ_y = 28 kPa, τ_0 = 4 kPa** and **ε_0 = 0.03 /s**.

It is assumed that adhesion and cohesion can both be modeled according to equation (7-22). The research carried out by Zeng and Yao (1991) validates the assumption that this is true for adhesion. In more recent research Kelessidis et al. (2007) and (2008) utilize two rheological models, the Herschel-Bulkley model and the Casson model. The Herschel Bulkley model can be described by the following equation:

$$\tau = \tau_{y,HB} + K \cdot \left(\dot{\varepsilon}\right)^n \tag{7-26}$$

The Casson model can be described with the following equation:

$$\sqrt{\tau} = \sqrt{\tau_{y,Ca}} + \sqrt{\mu_{Ca} \cdot \dot{\varepsilon}} \tag{7-27}$$

Figure 7-15 compares these models with the model as derived in this paper. It is clear that for the high strain rates the 3 models give similar results. These high strain rates are relevant for cutting processes in dredging and offshore applications.

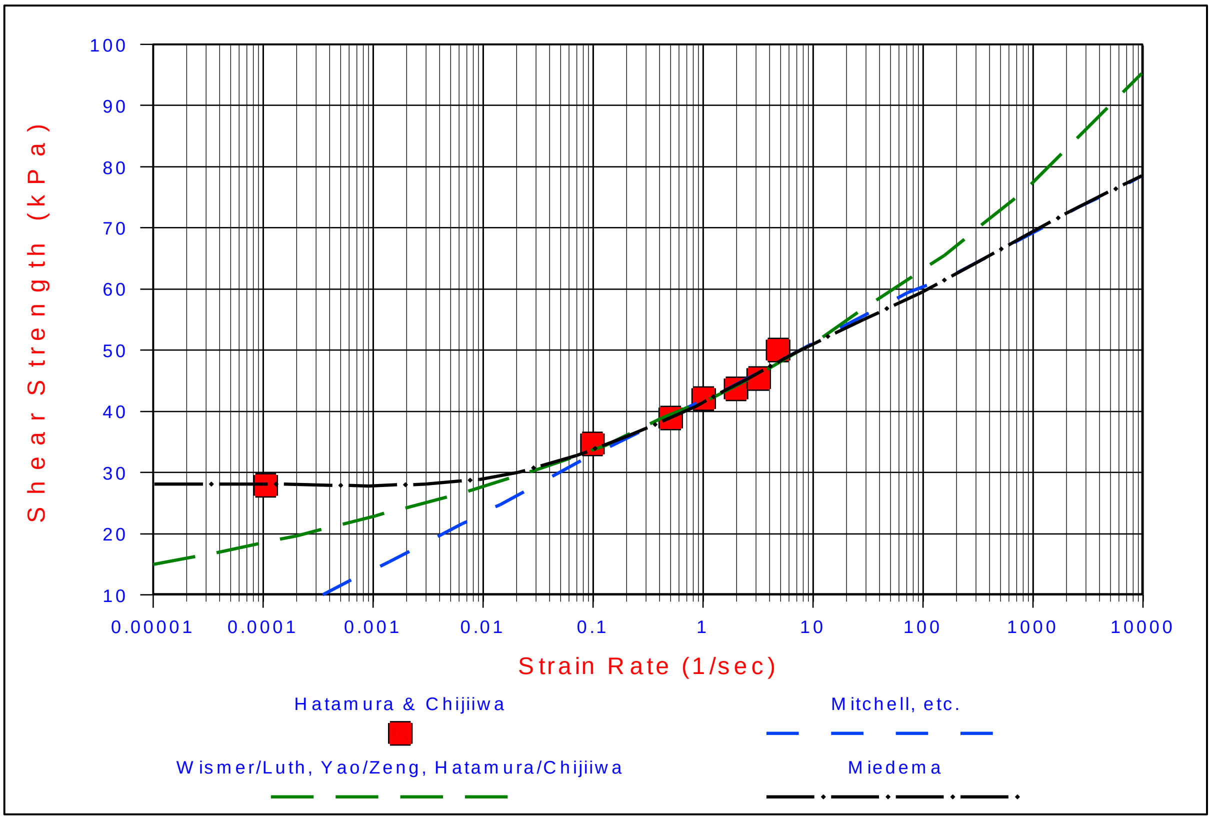

Figure 7-13: Shear stress as a function of strain rate with the horizontal axis logarithmic.

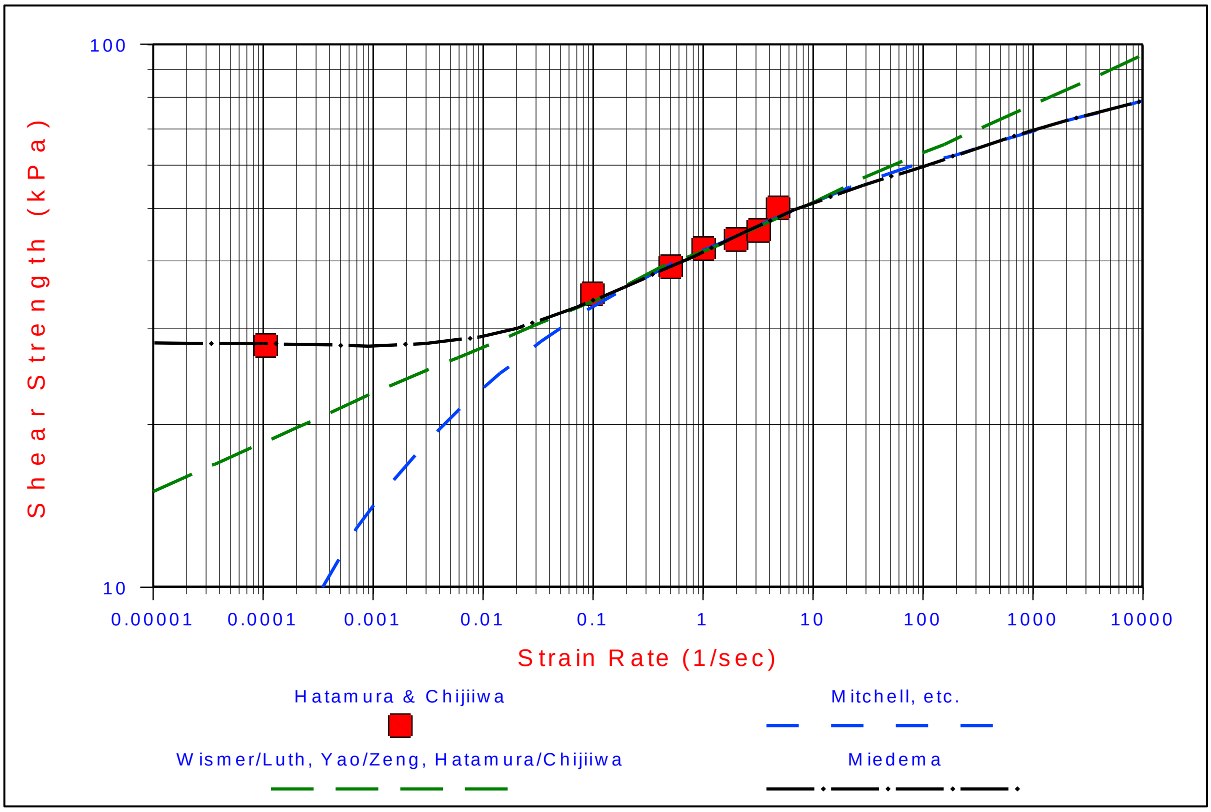

Figure 7-14: Shear stress as a function of strain rate with logarithmic axis.

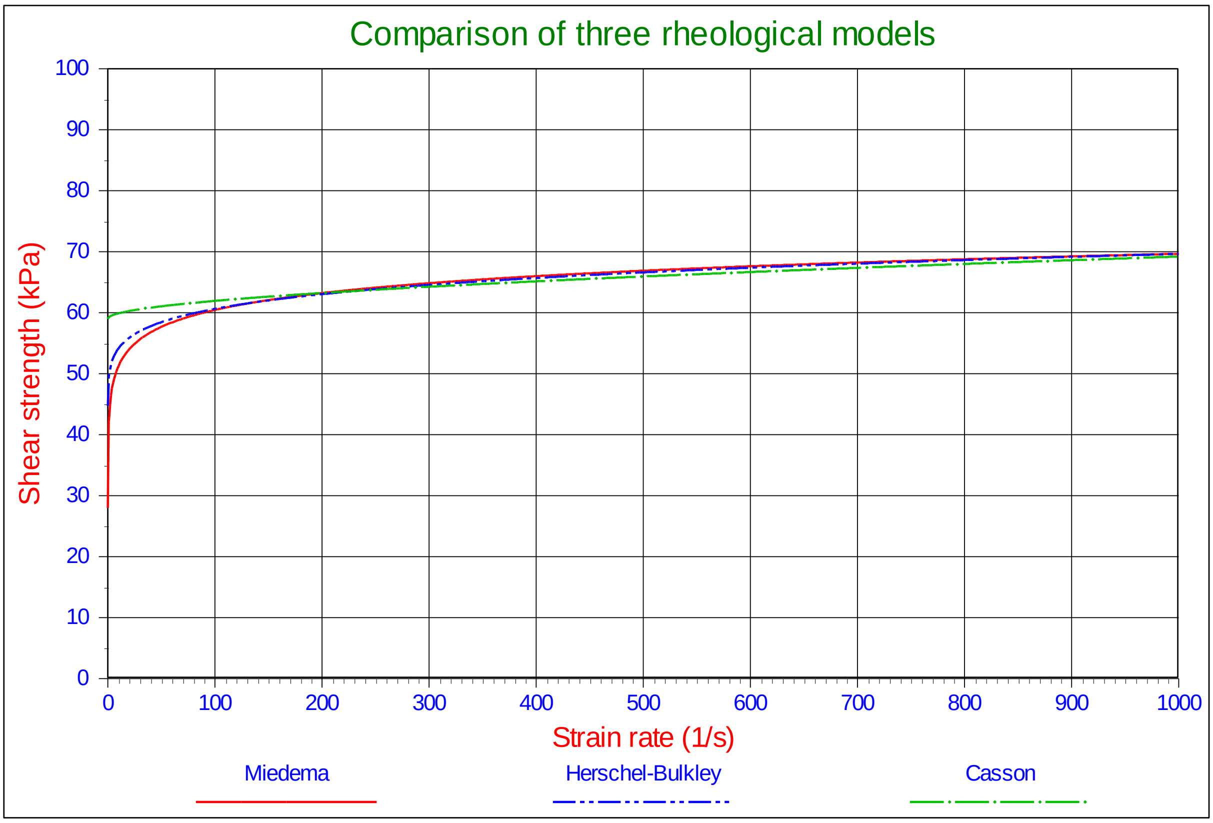

Figure 7-15: Comparison of 3 rheological models.

7.3.6. Abelev & Valent (2010).

Abelev & Valent (2010) investigated the strain rate dependency of the strength of soft marine deposits of the Gulf of Mexico. They used a precision rheometer with rotational rates from 0.25 up to 1000 1/min and water contents of 55% to 95%. They describe several models like an inverse hyperbolic sine:

$$\tau = \tau_y + \tau_0 \cdot \mathrm{arcsin}\left(\frac{\dot{\varepsilon}}{\dot{\varepsilon}_0}\right) \tag{7-28}$$

A logarithmic law and a power law:

$$\tau = \tau_y + \tau_0 \cdot \log_{10}\left(\frac{\dot{\varepsilon}}{\dot{\varepsilon}_0}\right) \quad \text{and} \quad \tau = \tau_y \cdot \left(\frac{\dot{\varepsilon}}{\dot{\varepsilon}_0}\right)^{\beta} \tag{7-29}$$

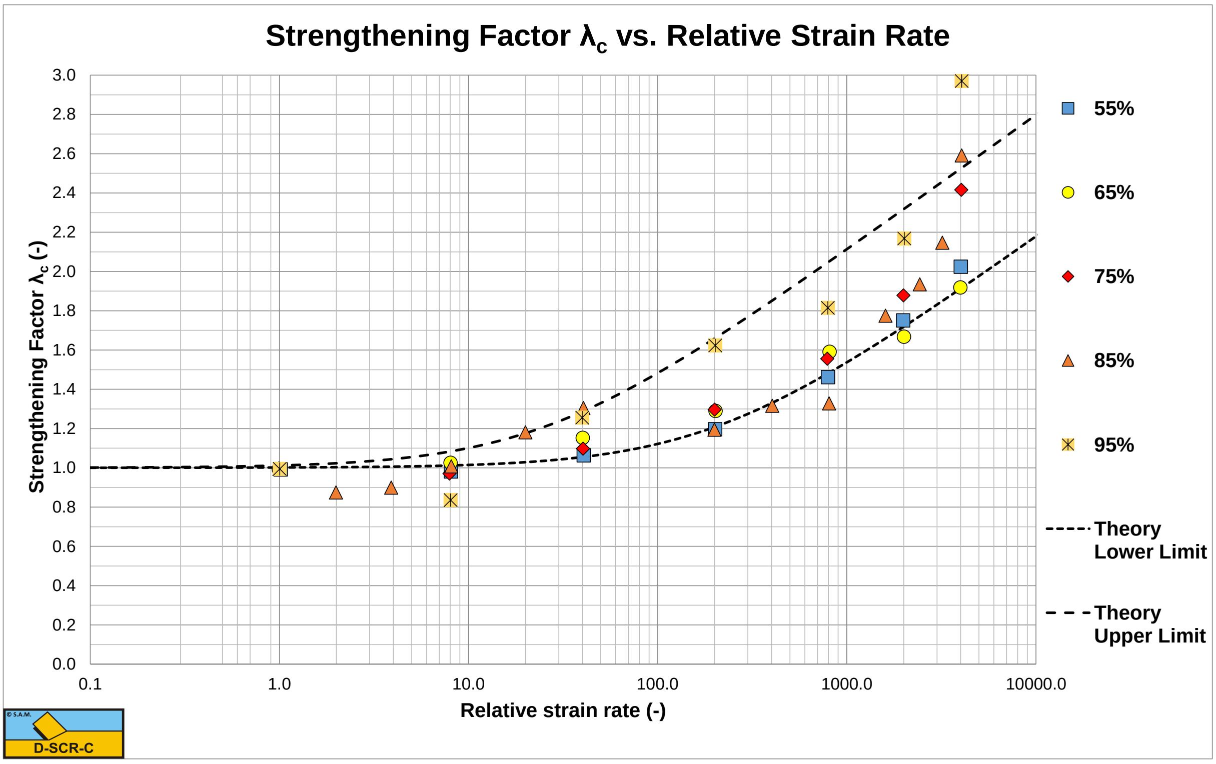

Figure 7-16: Abelev & Valent (2010) data.

The data of Abelev & Valent (2010) are shown in Figure 7-16, together with a lower limit and an upper limit based on the equation derived in this chapter. Based on their experiments they suggest a modified power law:

$$\tau = \tau_y + \tau_0 \cdot \left(\frac{\dot{\varepsilon}}{\dot{\varepsilon}_0}\right)^{\beta} \tag{7-30}$$

The use of the equation derived in this chapter however gives even better results.

$$\tau = \tau_y + \tau_0 \cdot \ln\left(1 + \frac{\dot{\varepsilon}}{\dot{\varepsilon}_0}\right) \tag{7-31}$$

One can see some dependency of the strengthening effect on the water content. It seems that the higher the water content, the larger the strengthening effect.

7.3.7. Resulting Equations for the Cutting Process.

The strain rate is the rate of change of the strain with respect to time and can be defined as a velocity divided by a characteristic length. For the cutting process it is important to relate the strain rate to the cutting (deformation) velocity $\mathbf{v_c}$ and the layer thickness $\mathbf{h_i}$. Since the deformation velocity is different for the cohesion in the shear plane and the adhesion on the blade, two different equations are found for the strain rate as a function of the cutting velocity.

$$\dot{\varepsilon}_c = 1.4 \cdot \frac{v_c}{h_i} \cdot \frac{\sin(\alpha)}{\sin(\alpha+\beta)} \tag{7-32}$$

$$\dot{\varepsilon}_a = 1.4 \cdot \frac{v_c}{h_i} \cdot \frac{\sin(\beta)}{\sin(\alpha+\beta)} \tag{7-33}$$

This results in the following two equations for the multiplication factor for cohesion (internal shear strength) and adhesion (external shear strength). With $\boldsymbol{\tau_y}$ the cohesion at zero strain rate.

$$\lambda_c = 1 + \frac{\tau_0}{\tau_y} \cdot \ln\left(1 + \frac{1.4 \cdot \frac{v_c}{h_i} \cdot \frac{\sin(\alpha)}{\sin(\alpha+\beta)}}{\dot{\varepsilon}_0}\right) \tag{7-34}$$

$$\lambda_a = 1 + \frac{\tau_0}{\tau_y} \cdot \ln\left(1 + \frac{1.4 \cdot \frac{v_c}{h_i} \cdot \frac{\sin(\beta)}{\sin(\alpha+\beta)}}{\dot{\varepsilon}_0}\right) \tag{7-35}$$

With:

$$\tau_0 / \tau_y = 0.1428, \quad \dot{\varepsilon}_0 = 0.03 \tag{7-36}$$

Van der Schrieck (1996) published a graph showing the effect of the deformation rate on the specific energy when cutting clay. Although the shape of the curves found are a bit different from the shape of the curves found with equations (7-34) and (7-35), the multiplication factor for, in dredging common deformation rates, is about 2. This factor matches the factor found with the above equations.

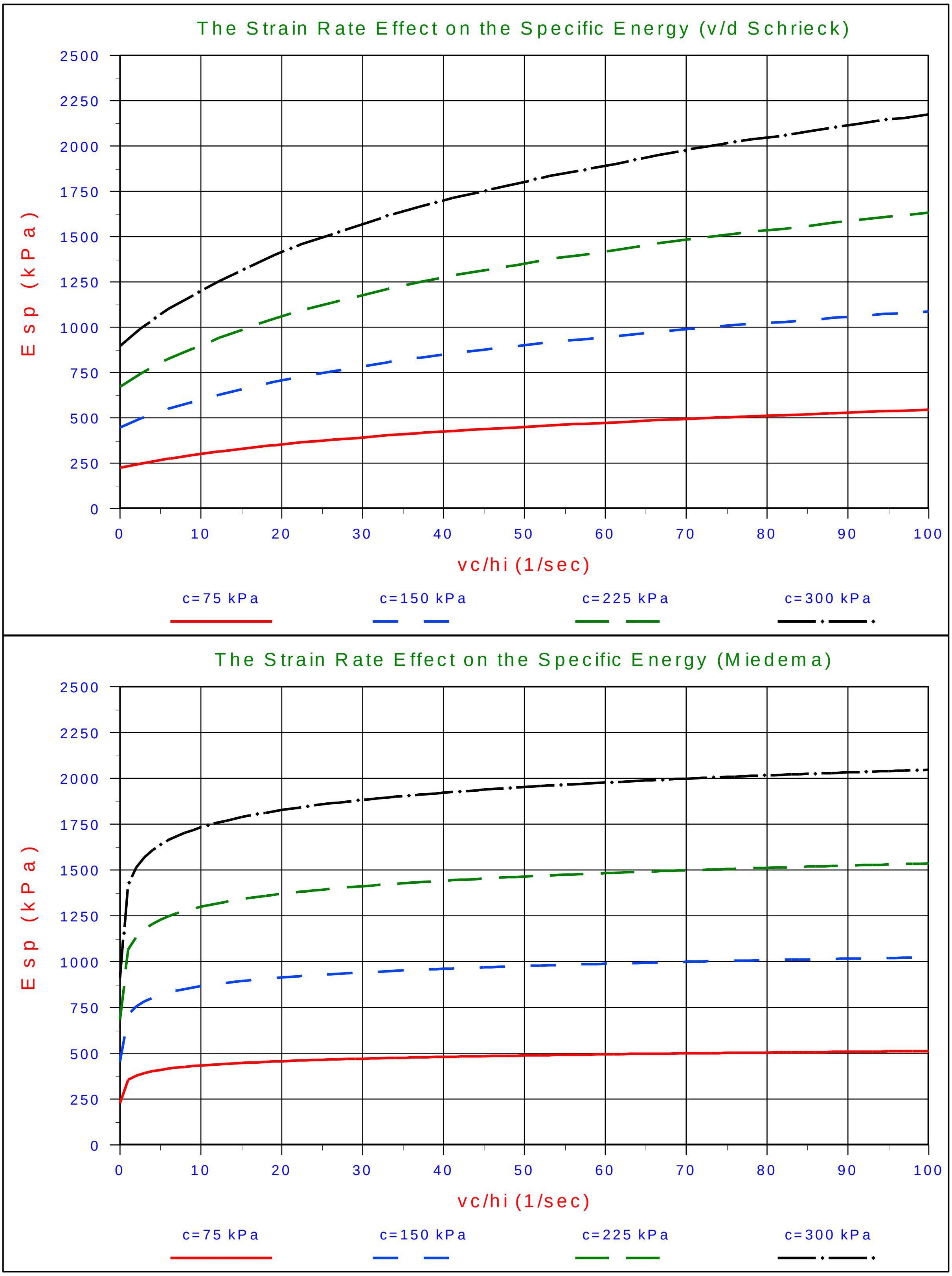

Figure 7-17: Comparison of the model developed with the v/d Schrieck (1996) model.

7.4. The Flow Type.

7.4.1. The Forces.

The most common failure mechanism in clay is the **Flow Type** as is shown in Figure 7-18, which will be considered first. The **Curling Type** and the **Tear Type** may occur under special circumstances and will be derived from the equations of the **Flow Type**.

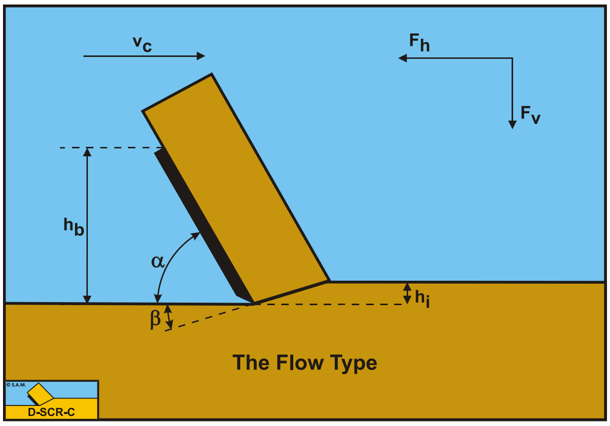

Figure 7-18: The Flow Type cutting mechanism when cutting clay.

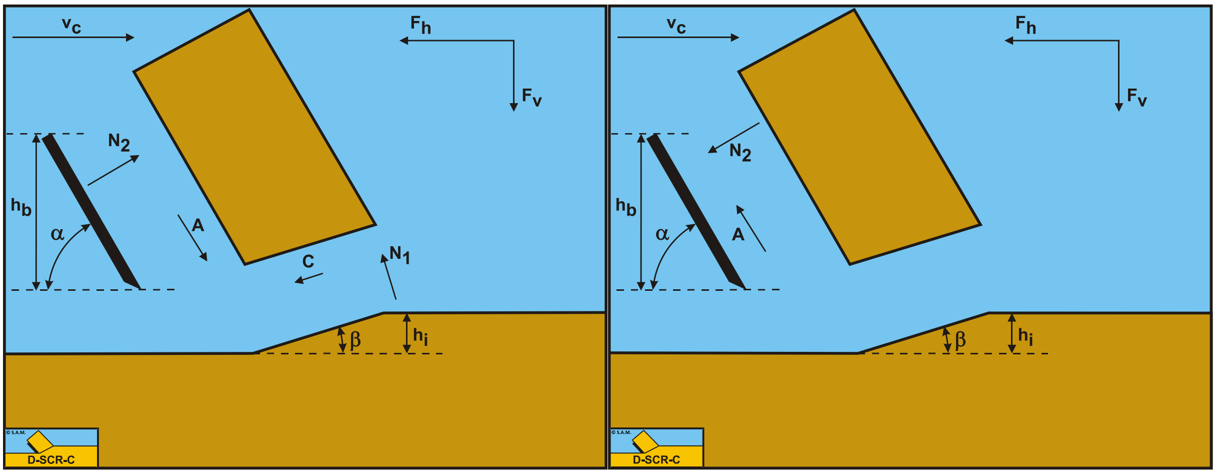

Figure 7-19: The forces on the layer cut in clay. Figure 7-20: The forces on the blade in clay.

Figure 7-19 illustrates the forces on the layer of soil cut. The forces shown are valid in general. The forces acting on this layer are:

1. A normal force acting on the shear surface $\mathbf{N_1}$ resulting from the effective grain stresses.
2. A shear force **C** as a result of pure cohesion τ_c. This force can be calculated by multiplying the cohesion **c**/cohesive shear strength τ_c with the area of the shear plane.
3. A force normal to the blade $\mathbf{N_2}$ resulting from the effective grain stresses.
4. A shear force **A** as a result of pure adhesion between the soil and the blade τ_a. This force can be calculated by multiplying the adhesion **a** (adhesive shear strength τ_a) of the soil with the contact area between the soil and the blade.

The forces acting on a straight blade when cutting soil, can be distinguished as:

5. A force normal to the blade $\mathbf{N_2}$ resulting from the effective grain stresses.
6. A shear force **A** as a result of pure adhesion between the soil and the blade τ_a. This force can be calculated by multiplying the adhesive shear strength τ_a of the soil with the contact area between the soil and the blade.

These forces are shown in Figure 7-20.

Pure clay under undrained conditions follows the **φ=0** concept, meaning that effectively there is no internal friction and thus there is also no external friction. Under drained conditions clay will have some internal friction, although smaller than sand. The reason for this is the very low permeability of the clay. If the clay is compressed with a high strain rate, the water in the pores cannot flow away resulting in the pore water carrying the extra pressure, the grain stresses do not change. If the grain stresses do not change, the shear stresses according to Coulomb friction do not change and effectively there is no relation between the extra normal stresses and the shear stresses, so apparently **$\varphi=0$**. At very low strain rates the pore water can flow out and the grains have to carry the extra normal stresses, resulting in extra shear stresses. During the cutting of clay, the strain rates, deformation rates, are so big that the internal and external friction angles can be considered to be zero. The adhesive and cohesive forces play a dominant role, so that gravity and inertia can be neglected.

The horizontal equilibrium of forces:

$$\sum F_h = N_1 \cdot \sin(\beta) + C \cdot \cos(\beta) - A \cdot \cos(\alpha) - N_2 \cdot \sin(\alpha) = 0 \tag{7-37}$$

The vertical equilibrium of forces:

$$\sum F_v = -N_1 \cdot \cos(\beta) + C \cdot \sin(\beta) + A \cdot \sin(\alpha) - N_2 \cdot \cos(\alpha) = 0 \tag{7-38}$$

The force **K_1** on the shear plane is now:

$$N_1 = \frac{-C \cdot \cos(\alpha+\beta) + A}{\sin(\alpha+\beta)} \tag{7-39}$$

The force **K_2** on the blade is now:

$$N_2 = \frac{C - A \cdot \cos(\alpha+\beta)}{\sin(\alpha+\beta)} \tag{7-40}$$

From equation (7-40) the forces on the blade can be derived. On the blade a force component in the direction of cutting velocity **F_h** and a force perpendicular to this direction **F_v** can be distinguished.

$$F_h = N_2 \cdot \sin(\alpha) + A \cdot \cos(\alpha) \tag{7-41}$$

$$F_v = N_2 \cdot \cos(\alpha) - A \cdot \sin(\alpha) \tag{7-42}$$

Since λ_c and λ_a are almost identical, an average value **λ_s** is used in the following equations. With the relations for the cohesive force **C**, the adhesive force **A** and the adhesion/cohesion ratio **r** (the ac ratio **r**):

$$C = \frac{\lambda_s \cdot c \cdot h_i \cdot w}{\sin(\beta)} \tag{7-43}$$

$$A = \frac{\lambda_s \cdot a \cdot h_b \cdot w}{\sin(\alpha)} \tag{7-44}$$

$$r = \frac{a \cdot h_b}{c \cdot h_i} \tag{7-45}$$

The horizontal **F_h** and vertical **F_v** cutting forces can be determined according to:

$$F_h = \frac{C \cdot \sin(\alpha) + A \cdot \sin(\beta)}{\sin(\alpha+\beta)} = \frac{\dfrac{\lambda_s \cdot c \cdot h_i \cdot w}{\sin(\beta)} \cdot \sin(\alpha) + \dfrac{\lambda_s \cdot a \cdot h_b \cdot w}{\sin(\alpha)} \cdot \sin(\beta)}{\sin(\alpha+\beta)}$$

$$= \lambda_s \cdot c \cdot h_i \cdot w \cdot \frac{\dfrac{\sin(\alpha)}{\sin(\beta)} + r \cdot \dfrac{\sin(\beta)}{\sin(\alpha)}}{\sin(\alpha+\beta)} \tag{7-46}$$

$$F_v = \frac{C \cdot \cos(\alpha) - A \cdot \cos(\beta)}{\sin(\alpha + \beta)} = \frac{\dfrac{\lambda_s \cdot c \cdot h_i \cdot w}{\sin(\beta)} \cdot \cos(\alpha) - \dfrac{\lambda_s \cdot a \cdot h_b \cdot w}{\sin(\alpha)} \cdot \cos(\beta)}{\sin(\alpha + \beta)}$$

$$= \lambda_s \cdot c \cdot h_i \cdot w \cdot \frac{\dfrac{\cos(\alpha)}{\sin(\beta)} - r \cdot \dfrac{\cos(\beta)}{\sin(\alpha)}}{\sin(\alpha + \beta)} \tag{7-47}$$

The normal force on the shear plane is now equal to the force **K₁** as is used in sand cutting, because the internal friction angle **φ** is zero:

$$N_1 = \frac{-C \cdot \cos(\alpha + \beta) + A}{\sin(\alpha + \beta)} \tag{7-48}$$

The normal force on the blade is now equal to the force **K₂** as is used in sand cutting, because the external friction angle **δ** is zero:

$$N_2 = \frac{C - A \cdot \cos(\alpha + \beta)}{\sin(\alpha + \beta)} \tag{7-49}$$

Equations (7-48) and (7-49) show that both the normal force on the shear plane **N₁** and the normal force on the blade **N₂** may become negative. This depends on the **ac** ratio between the adhesive and the cohesive forces **r** and on the blade angle **α** and shear angle **β**. A negative normal force on the blade will result in the **Curling Type** of cutting mechanism, while a negative normal force on the shear plane will result in the **Tear Type** of cutting mechanism. If both normal forces are positive, the **Flow Type** of cutting mechanism will occur.

7.4.2. Finding the Shear Angle.

There is one unknown in the equations and that is the shear angle **β.** This angle has to be known to determine cutting forces, specific energy and power.

$$F_h = \lambda_s \cdot c \cdot h_i \cdot w \cdot \left(\frac{\dfrac{\sin(\alpha)}{\sin(\beta)} + r \cdot \dfrac{\sin(\beta)}{\sin(\alpha)}}{\sin(\alpha + \beta)} \right) \quad \text{with: } r = \frac{a \cdot h_b}{c \cdot h_i} \tag{7-50}$$

Equation (7-50) for the horizontal cutting force **F_h** can be rewritten as:

$$F_h = \lambda_s \cdot c \cdot h_i \cdot w \cdot \left(\frac{\sin^2(\alpha) + r \cdot \sin^2(\beta)}{\sin(\alpha + \beta) \cdot \sin(\beta) \cdot \sin(\alpha)} \right) = \lambda_s \cdot c \cdot h_i \cdot w \cdot \lambda_{HF} \tag{7-51}$$

Equation (7-47) for the vertical cutting force **F_v** can be rewritten as:

$$F_v = \lambda_s \cdot c \cdot h_i \cdot w \cdot \left(\frac{\sin(\alpha) \cdot \cos(\alpha) - r \cdot \sin(\beta) \cdot \cos(\beta)}{\sin(\alpha + \beta) \cdot \sin(\beta) \cdot \sin(\alpha)} \right) = \lambda_s \cdot c \cdot h_i \cdot w \cdot \lambda_{VF} \tag{7-52}$$

The strengthening factor **λ_s,** which is not very sensitive for **β** in the range of cutting velocities **v_c** as applied in dredging, can be determined by:

$$\lambda_s = \left(1 + \frac{\tau_0}{\tau_y} \cdot \ln\left(1 + \frac{1.4 \cdot \frac{v_c}{h_i} \cdot \frac{\sin(\alpha)}{\sin(\alpha+\beta)}}{\dot{\varepsilon}_0}\right)\right) \tag{7-53}$$

$$\text{With : } \tau_0 / \tau_y = 0.1428 \text{ and } \dot{\varepsilon}_0 = 0.03$$

The shear angle **β** is determined by the case where the horizontal cutting force **F_h** is at a minimum, based on the minimum energy principle (omitting the strengthening factor **λ_s**).

$$\frac{\partial F_h}{\partial \beta} = \frac{2 \cdot r \cdot \sin^2(\beta) \cdot \cos(\beta) \cdot \sin(\alpha+\beta) \cdot \sin(\alpha)}{\sin^2(\alpha+\beta) \cdot \sin^2(\alpha) \cdot \sin^2(\beta)}$$

$$+ \frac{-\sin(\alpha) \cdot \sin(\alpha + 2 \cdot \beta) \cdot \left(\sin^2(\alpha) + r \cdot \sin^2(\beta)\right)}{\sin^2(\alpha+\beta) \cdot \sin^2(\alpha) \cdot \sin^2(\beta)} = 0 \tag{7-54}$$

In the special case where there is no adhesion **a=0**, **r=0**, the shear angle **β** is:

$$\sin(\alpha + 2 \cdot \beta) = 0 \text{ for } \alpha + 2 \cdot \beta = \pi \text{ giving } \beta = \frac{\pi}{2} - \frac{\alpha}{2} \tag{7-55}$$

An approximation equation for **β** based on curve fitting on equation (7-54) for the range **0.5<r<2** gives:

$$\beta = 1.26 \cdot e^{(-0.174 \cdot \alpha - 0.3148 \cdot r)} \text{ in radians or}$$

$$\beta = 72.2 \cdot e^{(-0.003 \cdot \alpha - 0.3148 \cdot r)} \text{ in degrees} \tag{7-56}$$

For a clay, with shear strength **c=1 kPa**, a layer thickness of **h_i=0.1 m** and a blade width of **w=1 m** Figure 7-21, Figure 7-23 and Figure 7-24 give the values of the shear angle **β**, the horizontal cutting force **F_h** and the vertical cutting force **F_v** for different values of the adhesion/cohesion (ac) ratio **r** and as a function of the blade angle **α**. The use of the **ac** ratio **r** makes the graphs independent of individual values of **h_b** and **a**. In these calculations the strain rate factor **λ_s** is set to 1. For different values of the strain rate factor **λ**, the cohesion **c**, the blade with **w** and the layer thickness **h_i**, the values found in Figure 7-23 and Figure 7-24 can be multiplied by the corresponding factors.

The horizontal cutting force **F_h** is at an absolute minimum when:

$$\alpha + \beta = \frac{\pi}{2} \tag{7-57}$$

This is however only useful if the blade angle **α** can be chosen freely. For a worst case scenario with an **ac** ratio **r=2**, meaning a high adhesion, a blade angle **α** of about 55° is found (see Figure 7-23), which matches blade angles as used in dredging. The fact that this does not give an optimum for weaker clays (clays with less adhesion) is not so relevant.

Figure 7-21, Figure 7-23 and Figure 7-24 show that the shear angle **β** is decreasing with an increasing blade angle **α** and an increasing **ac** ratio **r**. For practical blade angles between 45 and 60 degrees, the shear angle may vary between 35 and 60-70 degrees, depending on the **ac** ratio **r**. The horizontal force first decreases to a minimum with an increasing blade angle, after which it increases. At very large blade angles the horizontal force increases strongly to values that are not reasonable anymore. Nature will find another mechanism with smaller forces, the wedge mechanism, which will be described in Chapter 13: A Wedge in Clay Cutting. The vertical force (positive is downwards directed) is first increasing with an increasing blade angle to a maximum value, after which it is decreasing to very large negative (upwards directed) values at very large blade angles.

Figure 7-22 shows the sum of the blade angle and the shear angle. When this sum is 90 degrees, the minimum of the horizontal force is found. The graph shows clearly that this is the case for a 55 degree blade and an **ac** ratio **r=2**.

See Appendix V: Clay Cutting Charts for more and higher resolution charts.

7.4.3. Specific Energy.

In the dredging industry, the specific cutting energy $\mathbf{E_{sp}}$ is described as:

The amount of energy, that has to be added to a volume unit of soil (e.g. clay) to excavate the soil.

The dimension of the specific cutting energy is: kN/m² or kPa for sand and clay, while for rock often MN/m^2 or MPa is used. For the case as described above, cutting with a straight blade with the direction of the cutting velocity $\mathbf{v_c}$ perpendicular to the blade (edge of the blade), the specific cutting energy $\mathbf{E_{sp}}$ is:

$$E_{sp}=\frac{F_h\cdot v_c}{h_i\cdot w\cdot v_c}=\frac{F_h}{h_i\cdot w} \tag{7-58}$$

With the following equation for the horizontal cutting force $\mathbf{F_h}$:

$$F_h=\lambda_s\cdot c\cdot h_i\cdot w\cdot\left(\frac{\sin^2(\alpha)+r\cdot\sin^2(\beta)}{\sin(\alpha+\beta)\cdot\sin(\beta)\cdot\sin(\alpha)}\right)=\lambda_s\cdot c\cdot h_i\cdot w\cdot\lambda_{HF} \tag{7-59}$$

This gives for the specific cutting energy $\mathbf{E_{sp}}$:

$$E_{sp}=\frac{F_h\cdot v_c}{h_i\cdot w\cdot v_c}=\lambda_s\cdot c\cdot\left(\frac{\sin^2(\alpha)+r\cdot\sin^2(\beta)}{\sin(\alpha+\beta)\cdot\sin(\beta)\cdot\sin(\alpha)}\right)=\lambda_s\cdot c\cdot\lambda_{HF} \tag{7-60}$$

The cohesion **c** is half the UCS value, which can be related to the SPT value of the clay by a factor 12, so the cohesion is related by a factor 6 to the SPT value (see Table 7-1), further, the strengthening **λ** factor will have a value of about 2 at normal cutting velocities of meters per second, this gives:

$$\lambda_s\cdot c\approx 2\cdot 6\cdot SPT=12\cdot SPT \tag{7-61}$$

Now a simplified equation for the specific energy $\mathbf{E_{sp}}$ is found by:

$$E_{sp}=12\cdot SPT\cdot\left(\frac{\sin^2(\alpha)+r\cdot\sin^2(\beta)}{\sin(\alpha+\beta)\cdot\sin(\beta)\cdot\sin(\alpha)}\right)=12\cdot SPT\cdot\lambda_{HF} \tag{7-62}$$

Figure 7-25 shows the specific energy $\mathbf{E_{sp}}$ and the production $\mathbf{P_c}$ per 100 kW installed cutting power as a function of the SPT value.

Table 7-1: Guide for Consistency of Fine-Grained Soil (Lambe & Whitman (1979)).

SPT Penetration (blows/ foot)	**Estimated Consistency**	**UCS** (kPa)
<2	Very Soft Clay	<24
2 - 4	Soft Clay	24 - 48
4 - 8	Medium Clay	48 - 96
8 - 16	Stiff Clay	96 – 192

16 - 32	Very Stiff Clay	192 – 384
>32	Hard Clay	>384

See Appendix U: Specific Energy in Clay for more graphs on the specific energy in clay.

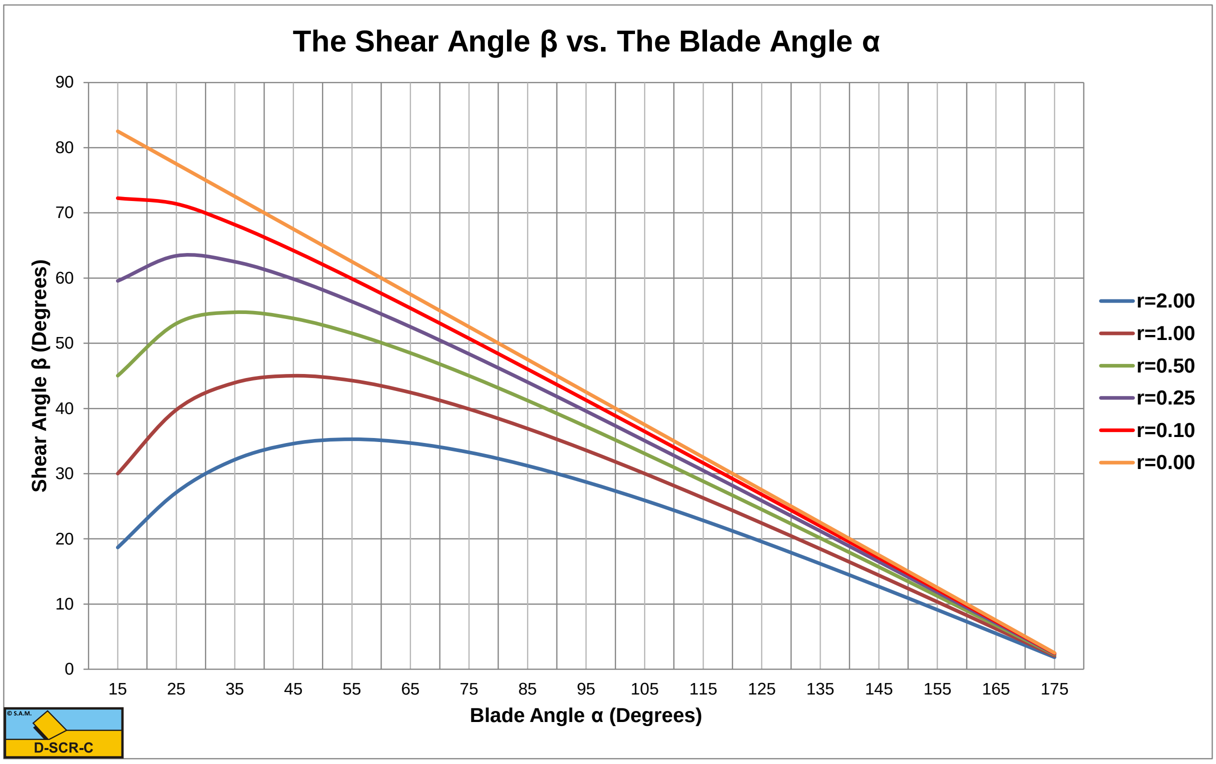

Figure 7-21: The shear angle as a function of the blade angle and the ac ratio r.

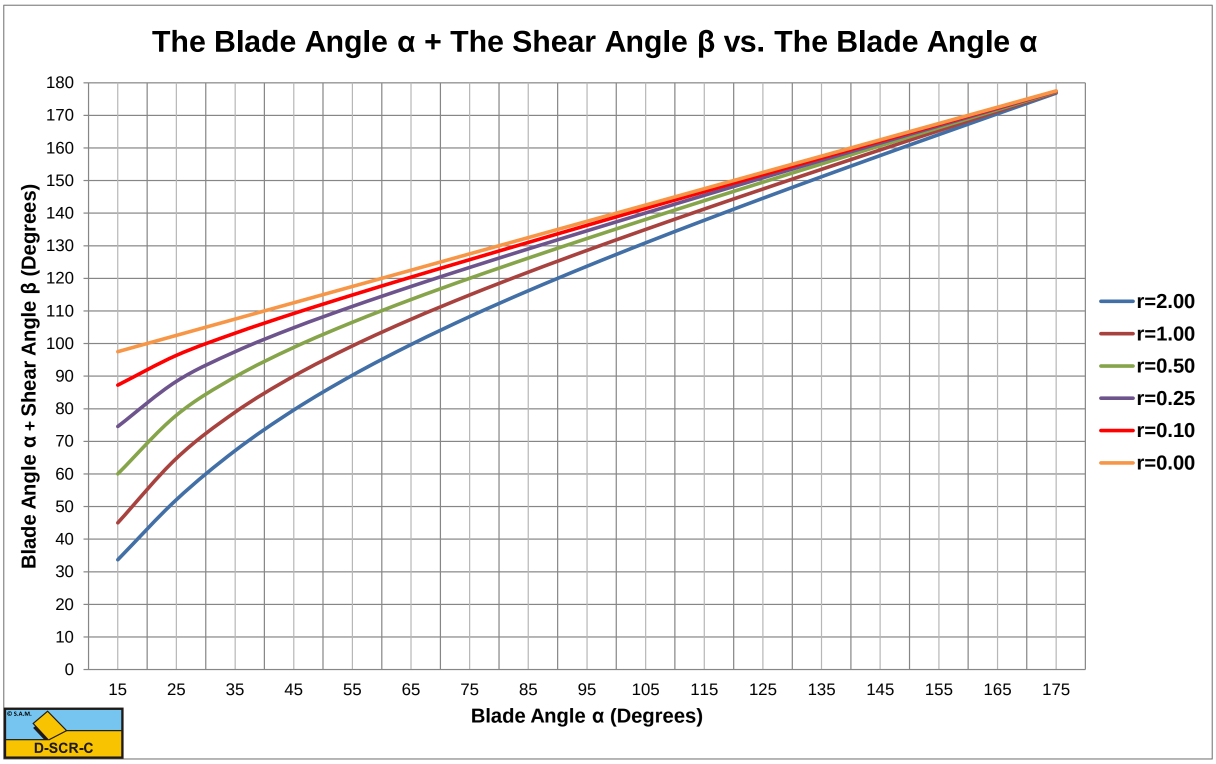

Figure 7-22: The blade angle α + the shear angle β.

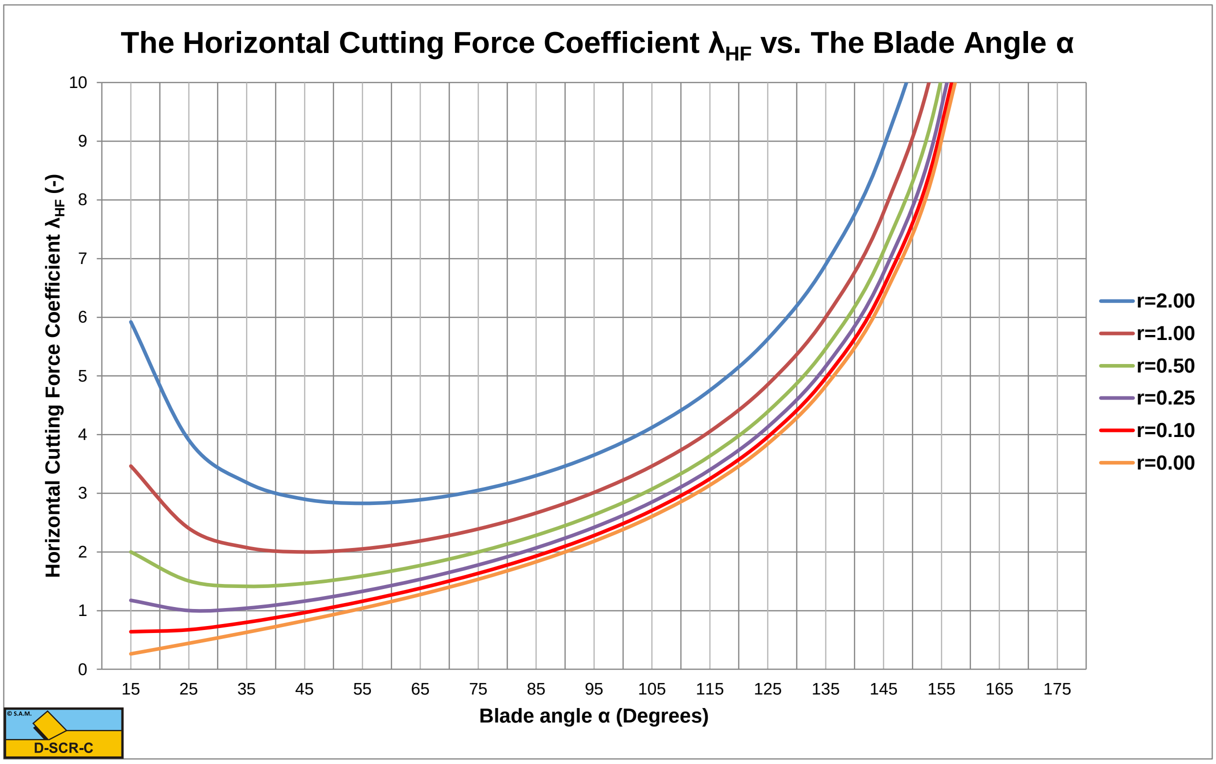

Figure 7-23: The horizontal cutting force coefficient λ_{HF} as a function of the blade angle and the ac ratio r.

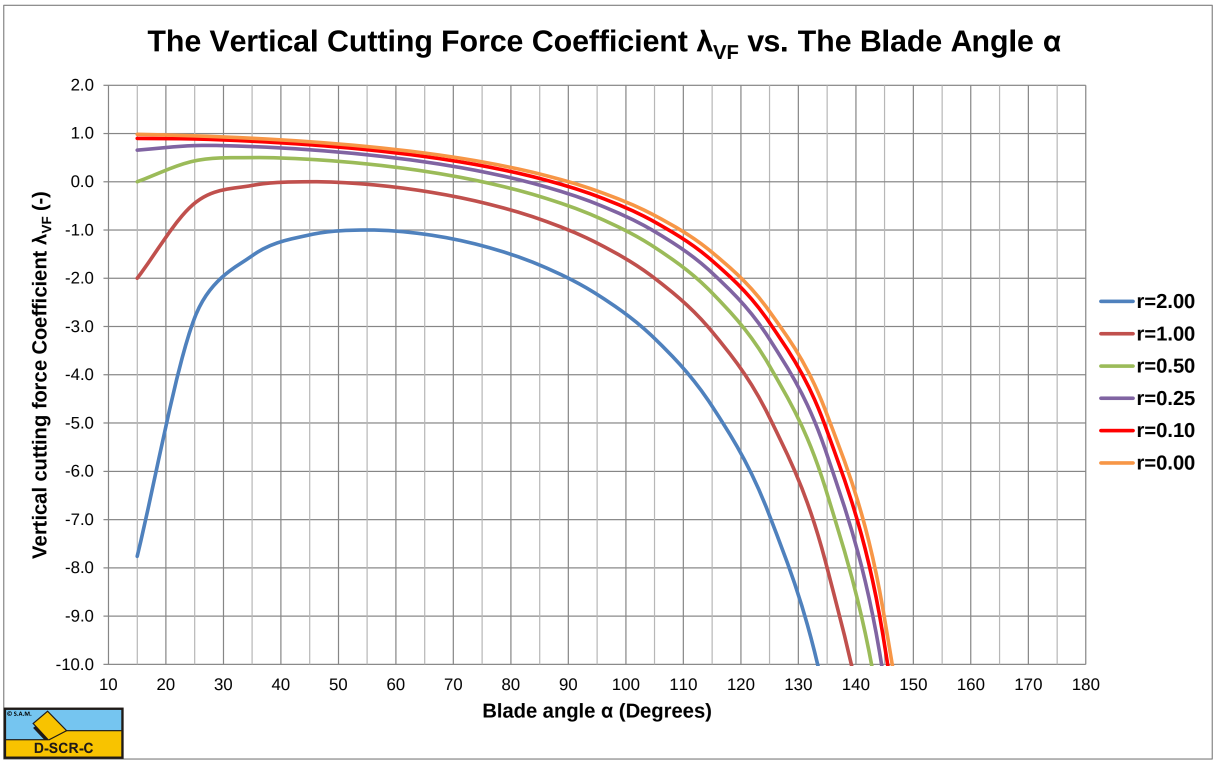

Figure 7-24: The vertical cutting force coefficient λ_{VF} as a function of the blade angle and the ac ratio r.

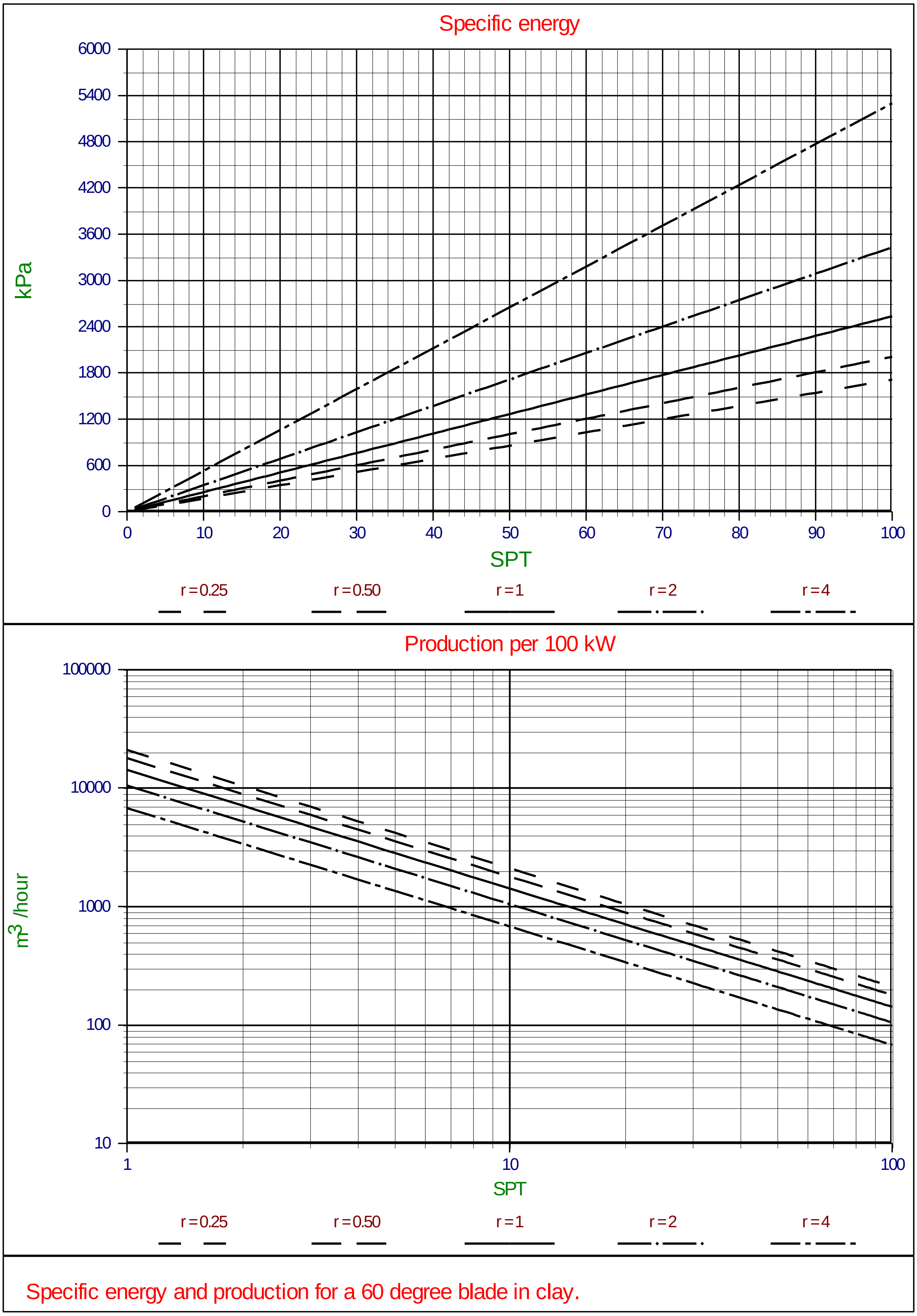

Figure 7-25: Specific energy and production in clay for a 60 degree blade.

7.5. The Tear Type.

7.5.1. Introduction.

In the previous chapter, the equations for the cutting forces of the **Flow Type** cutting mechanism have been derived. These equation however do not take into consideration that normal forces and thus stresses may become negative and may exceed the tensile strength of the clay. If the tensile stresses exceed the tensile strength, tensile failure will occur and the clay will not fail by plastic shear failure, but by tensile failure. The failure mechanism in this case is named the **Tear Type** mechanism. Based on the Mohr circle, tensile cracks will occur under and angle of 45 degrees downwards with respect of the shear angle as is shown in Figure 7-26. When the blade is progressing with the cutting velocity, after a short while a so called secondary crack will occur under 90 degrees with the first (primary) crack. The model as derived in this chapter, does not assume that the tensile strength is exceeded at the moment of tensile crack forming over the full length of the tensile crack. The model assumes that the tensile strength is exceeded at the start of the tensile crack only. In order to determine whether the tensile strength is exceeded, the average shear stress in the shear plane is used. Of course there may be a stress distribution in the shear plane, leading to locally higher and lower shear stresses and thus normal stresses, but these cannot be determined with the methodology used. Only average stresses can be determined. The methodology applied however gives reasonable and practical tools to determine whether the **Tear Type** cutting mechanism will occur or not.

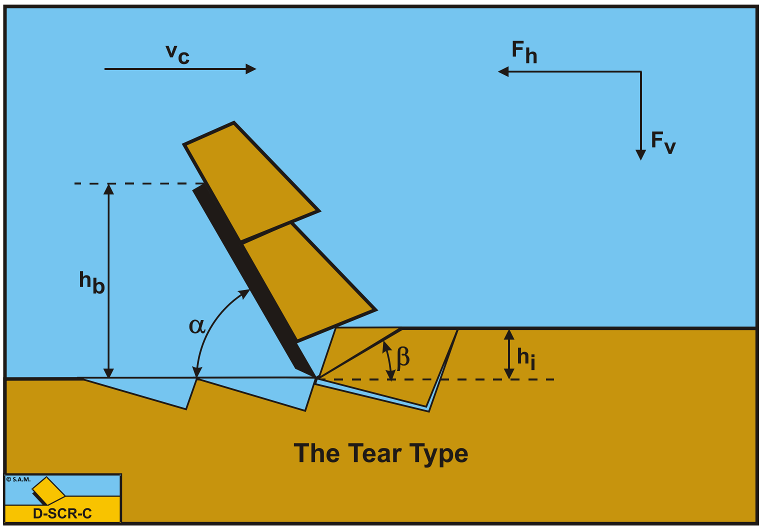

Figure 7-26: The Tear Type cutting mechanism in clay.

7.5.2. The Normal Force on the Shear Plane.

In order to determine the normal (possibly tensile) stresses on the shear plane, first the normal force on the shear plane has to be determined.

$$N_1 = \frac{-C \cdot \cos(\alpha+\beta) + A}{\sin(\alpha+\beta)} \qquad \textbf{(7-63)}$$

Substituting the equations for the cohesive force **C** and the adhesive force **A** gives:

$$N_1 = \frac{-\dfrac{\lambda_s \cdot c \cdot h_i \cdot w}{\sin(\beta)} \cdot \cos(\alpha+\beta) + \dfrac{\lambda_s \cdot a \cdot h_b \cdot w}{\sin(\alpha)}}{\sin(\alpha+\beta)} \qquad \textbf{(7-64)}$$

The average normal stress on the shear plane equals the normal force on the shear plane **N₁**, divided by the cross sectional area of the shear plane, giving:

$$\sigma_{N1} = \frac{N_1 \cdot \sin(\beta)}{h_i \cdot w} \qquad \textbf{(7-65)}$$

Substituting equation (7-64) in equation (7-65) gives for the normal stress on the shear plane:

$$\begin{aligned}\sigma_{N1} &= \frac{\sin(\beta)}{h_i \cdot w} \cdot \frac{-\dfrac{\lambda_s \cdot c \cdot h_i \cdot w}{\sin(\beta)} \cdot \cos(\alpha+\beta) + \dfrac{\lambda_s \cdot a \cdot h_b \cdot w}{\sin(\alpha)}}{\sin(\alpha+\beta)} \\ &= \lambda_s \cdot c \cdot \frac{-\cos(\alpha+\beta) + r \cdot \dfrac{\sin(\beta)}{\sin(\alpha)}}{\sin(\alpha+\beta)}\end{aligned} \qquad \textbf{(7-66)}$$

Assuming a fixed strain rate factor λ_s for cohesion and tensile strength, the normal stress minus the shear strength (cohesion) has to be bigger than the tensile strength, where the tensile strength is negative (compressive stresses are positive).

$$\sigma_{N1} - \lambda_s \cdot c \geq \lambda_s \cdot \sigma_T \qquad \textbf{(7-67)}$$

Substituting equation (7-66) into equation (7-67) gives the condition for ductile failure:

$$\lambda_s \cdot c \cdot \frac{-\cos(\alpha+\beta) + r \cdot \dfrac{\sin(\beta)}{\sin(\alpha)}}{\sin(\alpha+\beta)} - \lambda_s \cdot c \geq \lambda_s \cdot \sigma_T \qquad \textbf{(7-68)}$$

The transition from the **Flow Type** mechanism to the **Tear Type** mechanism is at the moment where the equal sign is used in the above equation, resulting in a critical ratio between the tensile strength and the shear strength, still also depending on the **ac** ratio **r** according to:

$$\frac{\sigma_T}{c} = \left(\frac{r \cdot \dfrac{\sin(\beta)}{\sin(\alpha)} - \cos(\alpha+\beta) - \sin(\alpha+\beta)}{\sin(\alpha+\beta)} \right) \qquad \textbf{(7-69)}$$

Figure 7-27 shows the critical ratio curves of the ratio of the tensile strength to the shear strength (cohesion) of the transition of the **Flow Type** mechanism to the **Tear Type** mechanism. Since the tensile strength is considered to be negative, the more negative this ratio, the higher the relative tensile strength. Below a curve the **Flow Type** may be expected, above a curve the **Tear Type**. Only negative ratios should be considered, since the tensile strength cannot be positive. The figure shows that for **r=1** (high adhesive forces) the curve just touches a ratio of zero, but never becomes negative, meaning the **Tear Type** will never occur. For smaller **r** values the curves are more negative for a decreasing **r** value. The minimum for **r** is zero (no adhesion). The figure also shows that all curves (except the **r=0** curve) start with a positive value, then decrease with an increasing blade angle to a minimum value and with a further increasing blade angle increase again to positive values. For blade angles larger than 90 degrees tensile failure will never occur. Because of the choice of the parameter $\mathbf{h_b}$, the blade height, at constant blade height the length of the blade is increasing with a decreasing blade angle. This means that the adhesive force on the blade increases with a decreasing blade angle, resulting in increasing normal stresses on the shear plane. Higher normal stresses suppress tensile failure. On the other hand, an increasing blade angle will increase the normal stress on the shear plane because of the force equilibrium. So we have two effects, the normal stresses on the shear plane will decrease with an increasing blade angle because of the decrease of the adhesive force and the normal stresses will increase with an increases blade angle because of the force equilibrium. The result is a curve with a minimum.

7.5.3. The Mobilized Shear Strength.

Assuming a mobilized shear stress $\mathbf{c_m}$ in the shear plane at the moment of tensile failure, gives:

$$c_m \cdot \left(\frac{r_m \cdot \frac{\sin(\beta)}{\sin(\alpha)} - \cos(\alpha+\beta) - \sin(\alpha+\beta)}{\sin(\alpha+\beta)} \right) = \sigma_T \tag{7-70}$$

Or:

$$c_m = \sigma_T \cdot \left(\frac{\sin(\alpha+\beta)}{r_m \cdot \frac{\sin(\beta)}{\sin(\alpha)} - \cos(\alpha+\beta) - \sin(\alpha+\beta)} \right) \tag{7-71}$$

Since the mobilized shear stress $\mathbf{c_m}$ is smaller than the shear strength $\mathbf{c}$, also the ac ratio $\mathbf{r_m}$ will be different from the ac ratio $\mathbf{r}$ when the shear stress is fully mobilized up to the shear strength. This gives for the mobilized ac ratio $\mathbf{r_m}$:

$$r_m = \frac{a \cdot h_b}{c_m \cdot h_i} = \frac{a \cdot h_b}{\sigma_T \cdot h_i} \cdot \left(\frac{r_m \cdot \frac{\sin(\beta)}{\sin(\alpha)} - \cos(\alpha+\beta) - \sin(\alpha+\beta)}{\sin(\alpha+\beta)} \right) \tag{7-72}$$

The mobilized ac ratio $\mathbf{r_m}$ is present on both sides of the equal sign. This gives for the mobilized ac ratio $\mathbf{r_m}$:

$$r_m = \frac{r_T \cdot \left(1 + \frac{\cos(\alpha+\beta)}{\sin(\alpha+\beta)} \right)}{\left(r_T \cdot \frac{\sin(\beta)}{\sin(\alpha) \cdot \sin(\alpha+\beta)} - 1 \right)} \tag{7-73}$$

$$\text{With: } \quad r_T = \frac{a \cdot h_b}{\sigma_T \cdot h_i}$$

The normal stress on the shear plane is now:

$$\sigma_{N1,m} = \lambda_s \cdot c_m \cdot \frac{-\cos(\alpha+\beta) + r_m \cdot \frac{\sin(\beta)}{\sin(\alpha)}}{\sin(\alpha+\beta)} \tag{7-74}$$

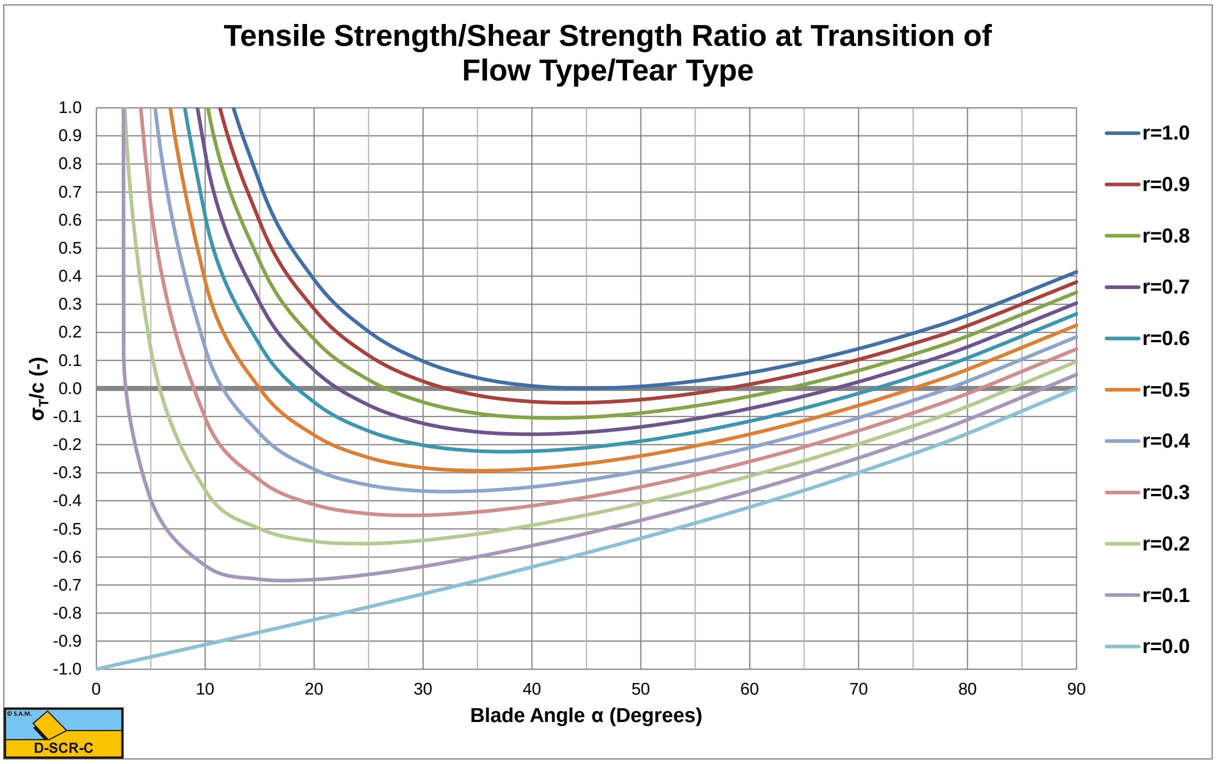

Figure 7-27: The transition Flow Type vs. Tear Type.

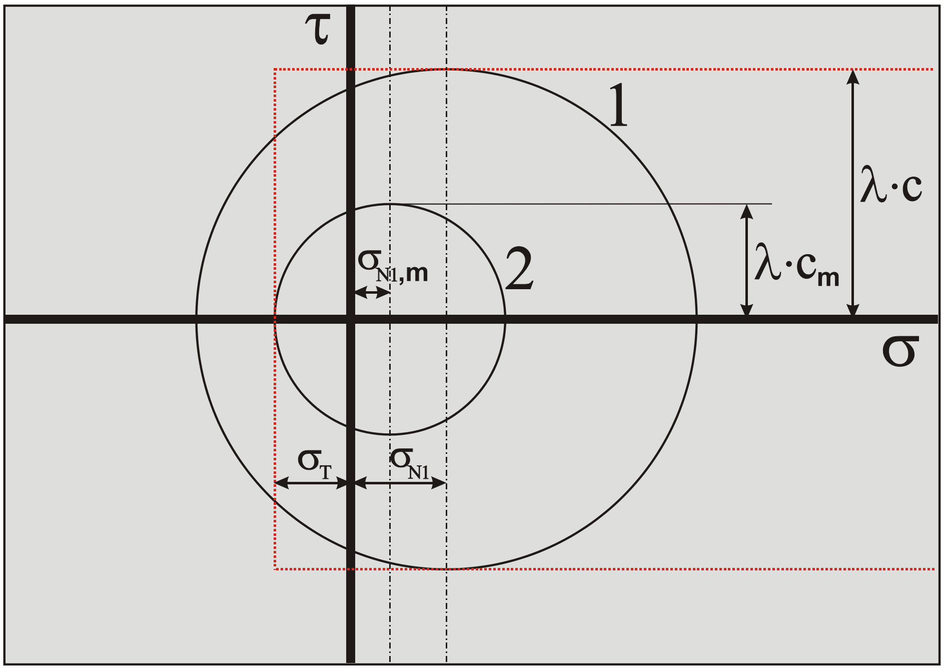

Figure 7-28: The Mohr circles when cutting clay.

7.5.4. The Resulting Cutting Forces.

Substituting the mobilized shear strength $\mathbf{c_m}$ and the mobilized ac ratio $\mathbf{r_m}$ gives the horizontal and vertical forces in the case of brittle failure, the **Tear Type** cutting mechanism:

$$F_h = \lambda_s \cdot \sigma_T \cdot h_i \cdot w \cdot \frac{\dfrac{\sin(\alpha)}{\sin(\beta)} + r_m \cdot \dfrac{\sin(\beta)}{\sin(\alpha)}}{r_m \cdot \dfrac{\sin(\beta)}{\sin(\alpha)} - \cos(\alpha+\beta) - \sin(\alpha+\beta)}$$

$$= \lambda_s \cdot \sigma_T \cdot h_i \cdot w \cdot r_T \cdot \frac{\lambda_{HT}}{r_T} \tag{7-75}$$

$$F_v = \lambda_s \cdot \sigma_T \cdot h_i \cdot w \cdot \frac{\dfrac{\cos(\alpha)}{\sin(\beta)} - r_m \cdot \dfrac{\cos(\beta)}{\sin(\alpha)}}{r_m \cdot \dfrac{\sin(\beta)}{\sin(\alpha)} - \cos(\alpha+\beta) - \sin(\alpha+\beta)} \tag{7-76}$$

$$= \lambda_s \cdot \sigma_T \cdot h_i \cdot w \cdot r_T \cdot \frac{\lambda_{VT}}{r_T}$$

The cutting forces are not dependent on the shear strength anymore, but completely dependent on the tensile strength and the adhesion.

Figure 7-29, Figure 7-30, Figure 7-31 and Figure 7-32 show the shear angle $\boldsymbol{\beta}$, the horizontal cutting force coefficient $\boldsymbol{\lambda_{HT}/r_T}$, the vertical cutting force coefficient $\boldsymbol{\lambda_{VT}/r_T}$ and the last one zoomed for the **Tear Type** of cutting mechanism. The figures show that for large values of $\mathbf{r_T}$, the shear angle and the cutting force coefficients hardly depend on the factor $\mathbf{r_T}$. It should be mentioned that the graphs show $\boldsymbol{\lambda_{HT}/r_T}$ and $\boldsymbol{\lambda_{VT}/r_T}$ and not $\boldsymbol{\lambda_{HT}}$ and $\boldsymbol{\lambda_{VT}}$. A large or very large value of $\mathbf{r_T}$ means a very small tensile strength compared to the adhesion. Equations (8-112) and (8-113) can be rewritten for the case of a very small relative tensile strength according to:

$$F_h = \lambda_s \cdot \sigma_T \cdot h_i \cdot w \cdot r_T \cdot \frac{\lambda_{HT}}{r_T} = \lambda_s \cdot \sigma_T \cdot h_i \cdot w \cdot \frac{a \cdot h_b}{\sigma_T \cdot h_i} \cdot \frac{\lambda_{HT}}{r_T} \tag{7-77}$$

$$= \lambda_s \cdot a \cdot h_b \cdot w \cdot \frac{\lambda_{HT}}{r_T}$$

$$F_v = \lambda_s \cdot \sigma_T \cdot h_i \cdot w \cdot r_T \cdot \frac{\lambda_{VT}}{r_T} = \lambda_s \cdot \sigma_T \cdot h_i \cdot w \cdot \frac{a \cdot h_b}{\sigma_T \cdot h_i} \cdot \frac{\lambda_{VT}}{r_T} \tag{7-78}$$

$$= \lambda_s \cdot a \cdot h_b \cdot w \cdot \frac{\lambda_{VT}}{r_T}$$

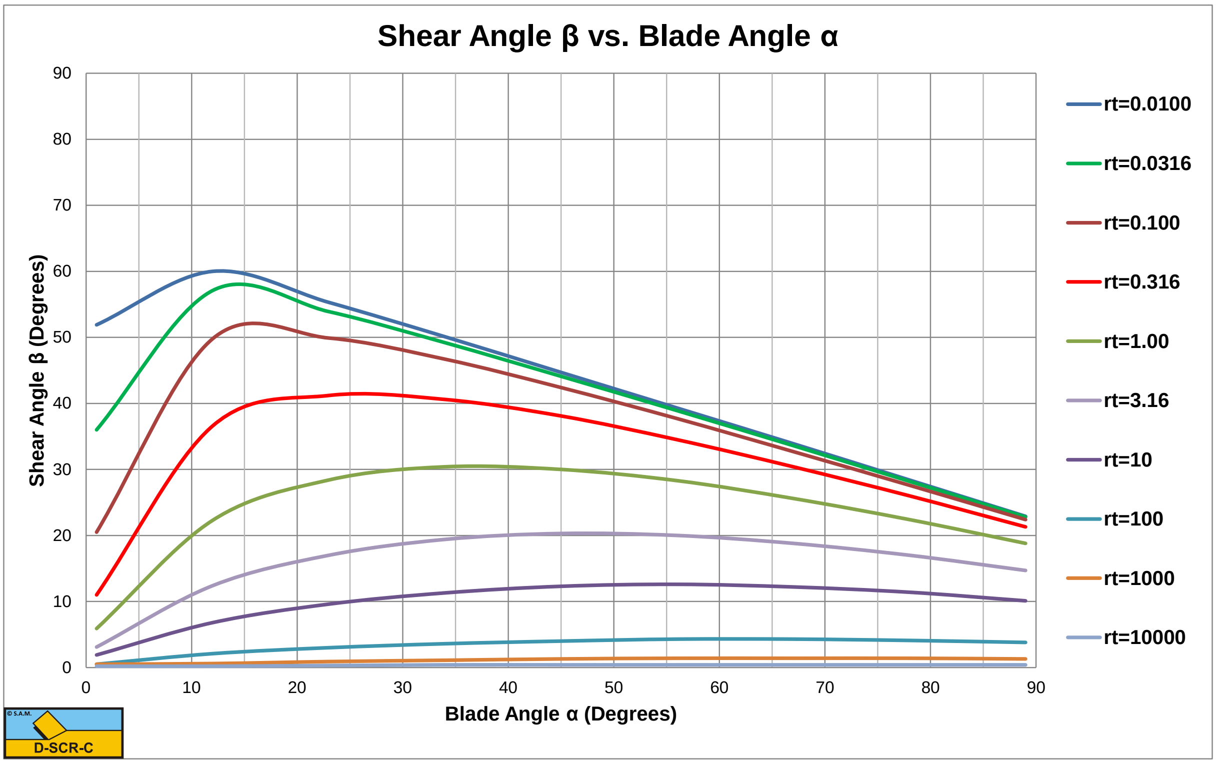

Figure 7-29: The shear angle β vs. the blade angle α for the Tear Type.

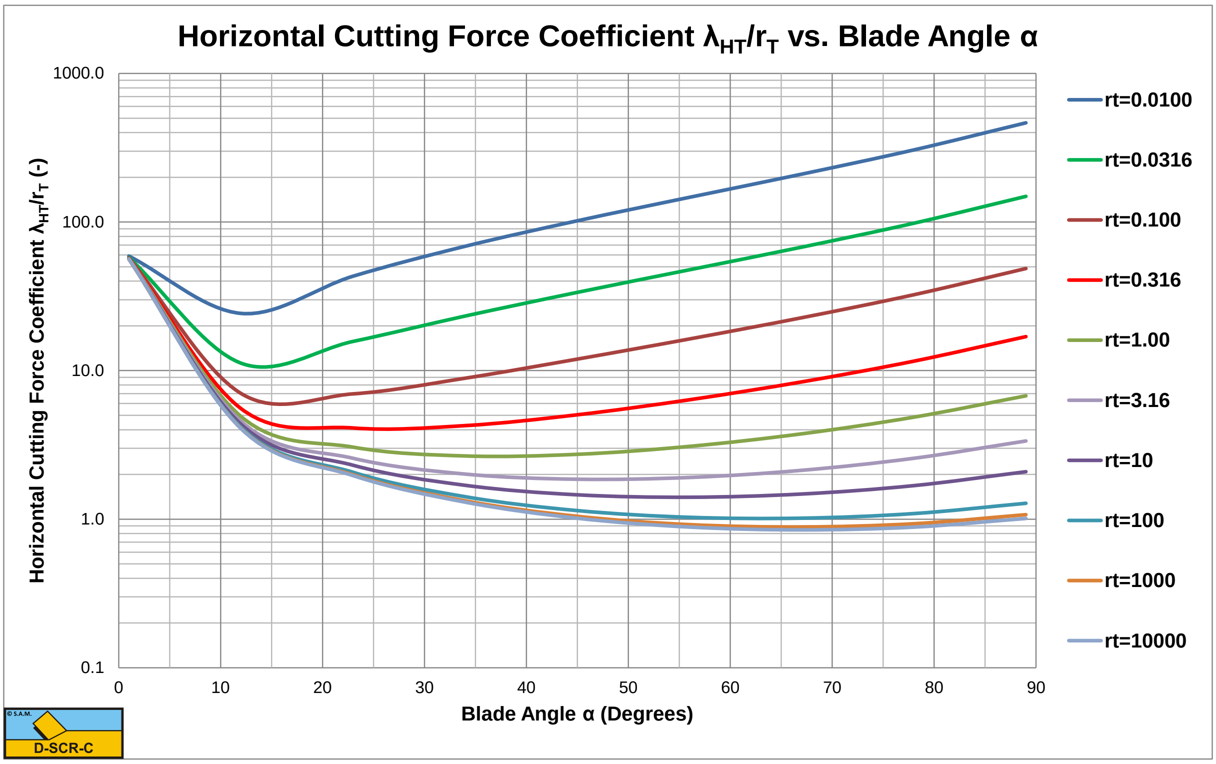

Figure 7-30: The horizontal cutting force coefficient λ_{HT}/r_T.

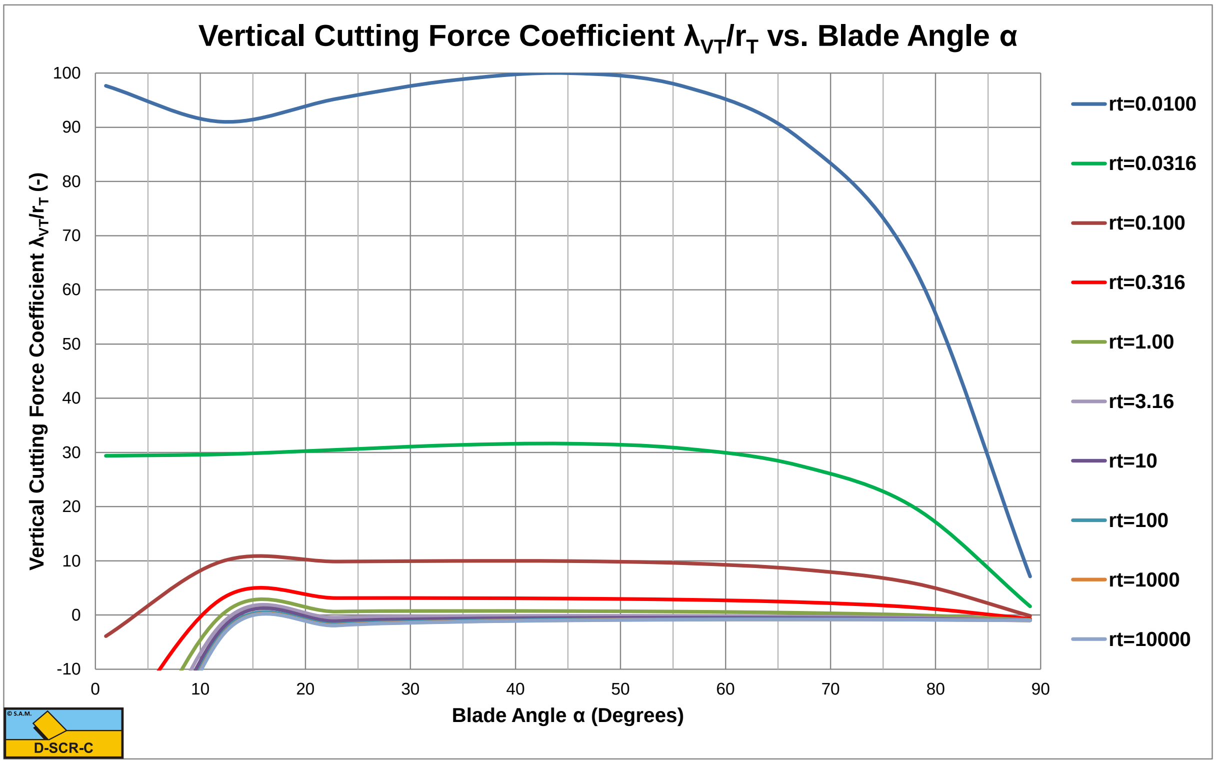

Figure 7-31: The vertical cutting force coefficient λ_{VT}/r_T.

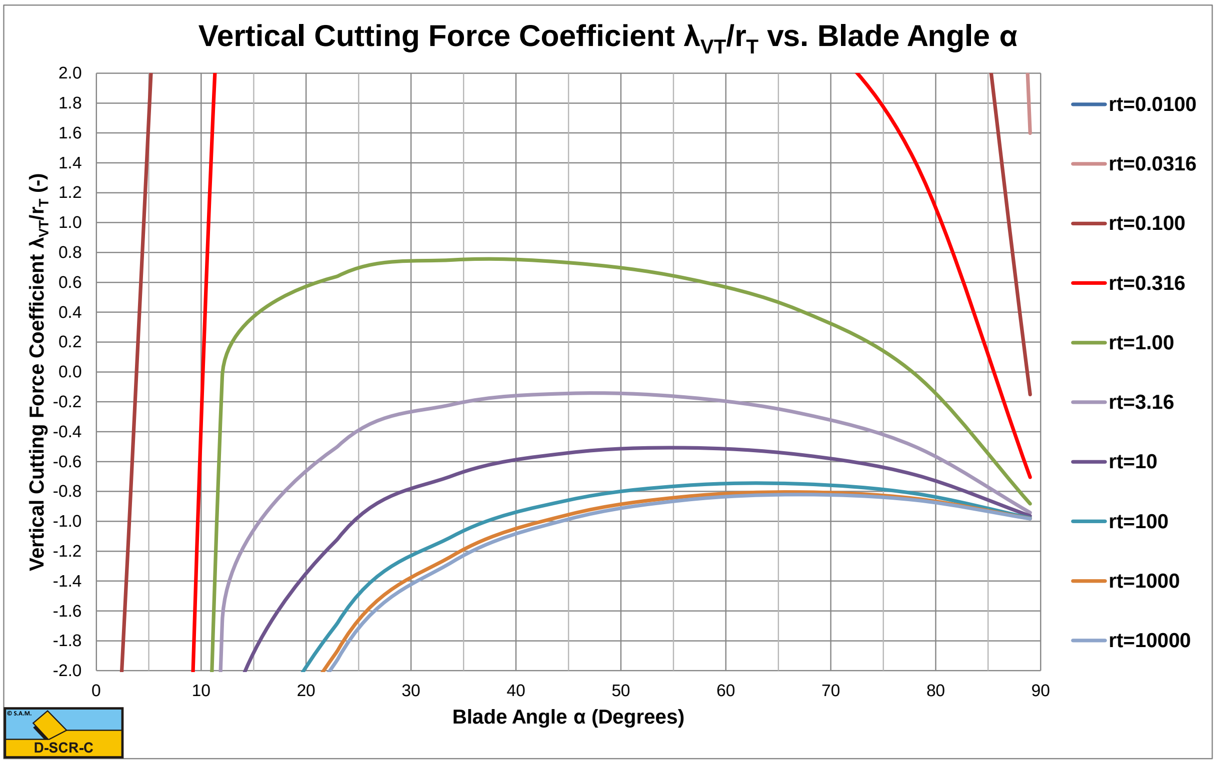

Figure 7-32: The vertical cutting force coefficient λ_{VT}/r_T zoomed.

7.6. The Curling Type.

7.6.1. Introduction.

When the layer thickness becomes very small, two things can happen. The normal force on the blade may become negative or there is no equilibrium of moments. In both cases the contact length between the clay and the blade has to be reduced. There can be different mechanisms for this. In steel cutting the curling of the chip cut is well known, but there could also be buckling or breaking of the layer cut. The result is the same, the clay will have a reduced contact length with the blade. This type of cutting mechanism is named the **Curling Type**. Both the normal force not becoming negative and the equilibrium of moments will be investigated. The mechanism with the smallest cutting forces is assumed to be the correct mechanism.

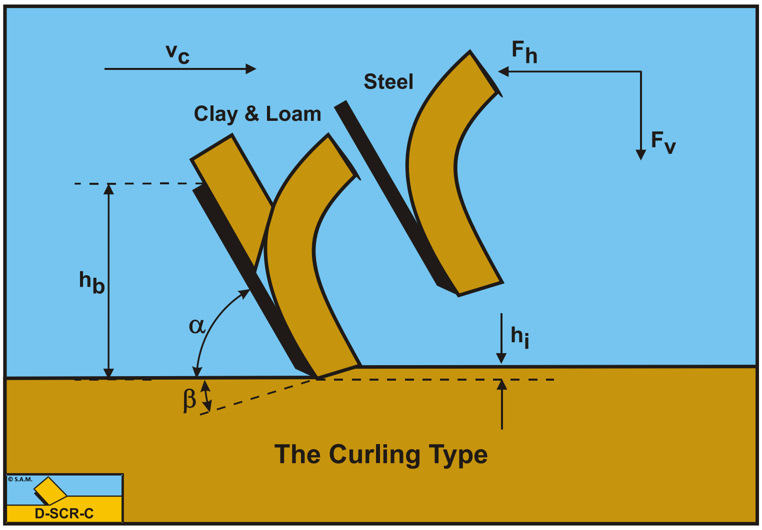

Figure 7-33: The Curling Type cutting mechanism when cutting clay.

7.6.2. The Normal Force on the Blade.

From the **Flow Type** of cutting mechanism the following equation is derived for the normal force on the blade:

$$N_2 = \frac{C - A \cdot \cos(\alpha+\beta)}{\sin(\alpha+\beta)} \tag{7-79}$$

Substituting the equations (7-43) and (7-44) gives:

$$\begin{aligned} N_2 &= \frac{\dfrac{\lambda_s \cdot c \cdot h_i \cdot w}{\sin(\beta)} - \dfrac{\lambda_s \cdot a \cdot h_b \cdot w}{\sin(\alpha)} \cdot \cos(\alpha+\beta)}{\sin(\alpha+\beta)} \\ &= \lambda_s \cdot c \cdot h_i \cdot w \cdot \frac{\dfrac{1}{\sin(\beta)} - \dfrac{r}{\sin(\alpha)} \cdot \cos(\alpha+\beta)}{\sin(\alpha+\beta)} \end{aligned} \tag{7-80}$$

Dividing the normal force by the surface of the blade gives the average normal stress on the blade:

$$\sigma_{N2} = \frac{N_2 \cdot \sin(\alpha)}{h_b \cdot w} \tag{7-81}$$

This gives for the normal stress on the blade:

$$\sigma_{N2}=\frac{\sin(\alpha)}{h_b\cdot w}\cdot\frac{\dfrac{\lambda_s\cdot c\cdot h_i\cdot w}{\sin(\beta)}-\dfrac{\lambda_s\cdot a\cdot h_b\cdot w}{\sin(\alpha)}\cdot\cos(\alpha+\beta)}{\sin(\alpha+\beta)}$$

(7-82)

$$=\lambda_s\cdot a\cdot\frac{\dfrac{1}{r}\cdot\dfrac{\sin(\alpha)}{\sin(\beta)}-\cos(\alpha+\beta)}{\sin(\alpha+\beta)}$$

As stated before this normal stress should have a value greater than zero, since it is assumed that there is no tensile strength between the clay and the blade.

$$\sigma_{N2}\geq 0 \tag{7-83}$$

In details this gives for the condition of no negative normal stress on the blade:

$$\lambda_s\cdot a\cdot\frac{\dfrac{1}{r}\cdot\dfrac{\sin(\alpha)}{\sin(\beta)}-\cos(\alpha+\beta)}{\sin(\alpha+\beta)}\geq 0 \tag{7-84}$$

At the critical condition where the normal stress equals zero this gives:

$$\frac{1}{r}\cdot\frac{\sin(\alpha)}{\sin(\beta)}=\cos(\alpha+\beta) \tag{7-85}$$

In the case of the **Curling Type**, the **ac** ratio **r** is not fully mobilized giving:

$$r_m=\frac{\sin(\alpha)}{\sin(\beta)}\cdot\frac{1}{\cos(\alpha+\beta)} \tag{7-86}$$

Substituting this mobilized **ac** ratio $\mathbf{r_m}$ in equations (7-46) and (7-47) gives for the cutting forces:

$$F_h=\lambda_s\cdot c\cdot h_i\cdot w\cdot\frac{\dfrac{\sin(\alpha)}{\sin(\beta)}+r_m\cdot\dfrac{\sin(\beta)}{\sin(\alpha)}}{\sin(\alpha+\beta)}=\lambda_s\cdot c\cdot h_i\cdot w\cdot\frac{\dfrac{\sin(\alpha)}{\sin(\beta)}+\dfrac{1}{\cos(\alpha+\beta)}}{\sin(\alpha+\beta)}$$

(7-87)

$$=\lambda_s\cdot c\cdot h_i\cdot w\cdot\frac{\dfrac{\cos(\alpha)}{\sin(\beta)}}{\cos(\alpha+\beta)}$$

$$F_v=\lambda_s\cdot c\cdot h_i\cdot w\cdot\frac{\dfrac{\cos(\alpha)}{\sin(\beta)}-r_m\cdot\dfrac{\cos(\beta)}{\sin(\alpha)}}{\sin(\alpha+\beta)}=\lambda_s\cdot c\cdot h_i\cdot w\cdot\frac{\dfrac{\cos(\alpha)}{\sin(\beta)}-\dfrac{\cos(\beta)}{\sin(\beta)}\cdot\dfrac{1}{\cos(\alpha+\beta)}}{\sin(\alpha+\beta)}$$

(7-88)

$$=-\lambda_s\cdot c\cdot h_i\cdot w\cdot\frac{\dfrac{\sin(\alpha)}{\sin(\beta)}}{\cos(\alpha+\beta)}$$

This method is simple and straightforward, but does not take a normal stress distribution on the blade into account. It does however give a prediction of the cutting forces and the reduced contact length on the blade. The unknown in the equations is the shear angle **β**. Assuming that the mechanism will choose a shear angle where the cutting energy is at a minimum, a shear angle **β** is found according to:

$$\beta = \frac{\pi}{4} - \frac{\alpha}{2} \tag{7-89}$$

If we substitute this solution in the cutting force equations we find:

$$F_h = 2 \cdot \lambda_s \cdot c \cdot h_i \cdot w \cdot \frac{\cos(\alpha)}{1 - \sin(\alpha)} \tag{7-90}$$

$$F_v = -2 \cdot \lambda_s \cdot c \cdot h_i \cdot w \cdot \frac{\sin(\alpha)}{1 - \sin(\alpha)} \tag{7-91}$$

The horizontal force will increase with an increasing blade angle, the vertical force also, but upwards directed. In the case of the **Curling Type**, the **ac** ratio **r** is not fully mobilized giving:

$$r_m = 2 \cdot \frac{\sin(\alpha)}{1 - \sin(\alpha)} \tag{7-92}$$

The condition of having a normal force of zero on the blade can never fulfill the condition of having an equilibrium of moments on the layer cut, since the normal force on the blade is zero and is therefore rejected. Still this condition gives insight in the behavior of the equations of clay cutting and is therefore mentioned here.

7.6.3. The Equilibrium of Moments.

As mentioned in the previous paragraph, the equilibrium of moments on the layer cut has to be fulfilled. If we take the equilibrium of moments around the tip of the blade, there are only two forces participating in the equilibrium of moments, the normal force on the shear plane $\mathbf{N_1}$ and the normal force on the blade $\mathbf{N_2}$. These forces have acting points $\mathbf{R_1}$ and $\mathbf{R_2}$ on the shear plane and on the blade. If the normal stresses are uniformly distributed, both acting points will be at the center (half way) the corresponding planes. The acting point of the normal force on the shear plane will be at half the length of the shear plane and the acting point of the normal force on the blade will be at half the (mobilized) length of the blade. Two factors are introduced to give the exact location of these acting points, $\boldsymbol{\lambda_1}$ on the shear plane and $\boldsymbol{\lambda_2}$ on the blade. When the moment $\mathbf{N_2 \cdot R_2}$ on the blade is greater than the moment $\mathbf{N_1 \cdot R_1}$ on the blade curling will occur in such a way that both moments are equal. The contact length between the clay and the blade will be reduced to a mobilized contact length $\mathbf{h_{b,m}}$.

The normal force on the shear plane is now equal to the force $\mathbf{N_1}$, because the internal friction angle is zero:

$$N_1 = \frac{-C \cdot \cos(\alpha + \beta) + A}{\sin(\alpha + \beta)} \tag{7-93}$$

The normal force on the blade is now equal to the force $\mathbf{N_2}$, because the external friction angle is zero:

$$N_2 = \frac{C - A \cdot \cos(\alpha + \beta)}{\sin(\alpha + \beta)} \tag{7-94}$$

This gives for the equilibrium of moments:

$$N_1 \cdot R_1 = N_2 \cdot R_2 \tag{7-95}$$

For both acting points we can write:

$$R_1 = \frac{\lambda_1 \cdot h_i}{\sin(\beta)}, \quad R_2 = \frac{\lambda_2 \cdot h_{b,m}}{\sin(\alpha)} \tag{7-96}$$

Substituting equations (7-93), (7-94) and (7-96) in equation (7-95) gives:

$$\left(\frac{A - C \cdot \cos(\alpha+\beta)}{\sin(\alpha+\beta)}\right) \cdot \frac{\lambda_1 \cdot h_i}{\sin(\beta)} = \left(\frac{C - A \cdot \cos(\alpha+\beta)}{\sin(\alpha+\beta)}\right) \cdot \frac{\lambda_2 \cdot h_{b,m}}{\sin(\alpha)} \tag{7-97}$$

Substituting equations (7-45) and (7-46) for the cohesive and adhesive forces gives:

$$\begin{aligned} &\left(\frac{a \cdot h_{b,m}}{\sin(\alpha)} - \frac{c \cdot h_i}{\sin(\beta)} \cdot \cos(\alpha+\beta)\right) \cdot \frac{\lambda_1 \cdot h_i}{\sin(\beta)} \\ &= \left(\frac{c \cdot h_i}{\sin(\beta)} - \frac{a \cdot h_{b,m}}{\sin(\alpha)} \cdot \cos(\alpha+\beta)\right) \cdot \frac{\lambda_2 \cdot h_{b,m}}{\sin(\alpha)} \end{aligned} \tag{7-98}$$

Rewriting this term by term gives:

$$\begin{aligned} &\frac{a \cdot h_{b,m}}{\sin(\alpha)} \cdot \frac{\lambda_1 \cdot h_i}{\sin(\beta)} - \frac{c \cdot h_i}{\sin(\beta)} \cdot \frac{\lambda_1 \cdot h_i}{\sin(\beta)} \cdot \cos(\alpha+\beta) \\ &= \frac{c \cdot h_i}{\sin(\beta)} \cdot \frac{\lambda_2 \cdot h_{b,m}}{\sin(\alpha)} - \frac{a \cdot h_{b,m}}{\sin(\alpha)} \cdot \frac{\lambda_2 \cdot h_{b,m}}{\sin(\alpha)} \cdot \cos(\alpha+\beta) \end{aligned} \tag{7-99}$$

Moving the terms with adhesion to the left side and the terms with cohesion to the right side gives:

$$\begin{aligned} &\frac{a \cdot h_{b,m}}{\sin(\alpha)} \cdot \frac{\lambda_1 \cdot h_i}{\sin(\beta)} + \frac{a \cdot h_{b,m}}{\sin(\alpha)} \cdot \frac{\lambda_2 \cdot h_{b,m}}{\sin(\alpha)} \cdot \cos(\alpha+\beta) \\ &= \frac{c \cdot h_i}{\sin(\beta)} \cdot \frac{\lambda_2 \cdot h_{b,m}}{\sin(\alpha)} + \frac{c \cdot h_i}{\sin(\beta)} \cdot \frac{\lambda_1 \cdot h_i}{\sin(\beta)} \cdot \cos(\alpha+\beta) \end{aligned} \tag{7-100}$$

This gives a second degree function of the mobilized blade height according to:

$$\begin{aligned} &\frac{\lambda_2 \cdot a \cdot \cos(\alpha+\beta)}{\sin(\alpha) \cdot \sin(\alpha)} \cdot h_{b,m} \cdot h_{b,m} + \frac{\lambda_1 \cdot a - \lambda_2 \cdot c}{\sin(\alpha) \cdot \sin(\beta)} \cdot h_i \cdot h_{b,m} \\ &- \frac{\lambda_1 \cdot c \cdot \cos(\alpha+\beta)}{\sin(\beta) \cdot \sin(\beta)} \cdot h_i \cdot h_i = 0 \end{aligned} \tag{7-101}$$

This second degree function can be solved with the A, B, C formula and has two solutions.

$$\mathbf{A \cdot x^2 + B \cdot x + C = 0}$$

$$\mathbf{h_{b,m} = x = \frac{-B \pm \sqrt{B^2 - 4 \cdot A \cdot C}}{2 \cdot A} \quad with: r_m = \frac{a \cdot h_{b,m}}{c \cdot h_i}}$$

$$\mathbf{A = \frac{\lambda_2 \cdot a \cdot \cos(\alpha + \beta)}{\sin(\alpha) \cdot \sin(\alpha)}} \tag{7-102}$$

$$\mathbf{B = \frac{\lambda_1 \cdot a - \lambda_2 \cdot c}{\sin(\alpha) \cdot \sin(\beta)} \cdot h_i}$$

$$\mathbf{C = -\frac{\lambda_1 \cdot c \cdot \cos(\alpha + \beta)}{\sin(\beta) \cdot \sin(\beta)} \cdot h_i \cdot h_i}$$

The following criteria are valid for the use of this method.

$$\begin{aligned} &\mathbf{if\ \ h_{b,m} < h_b\ \ then\ use\ h_{b,m}} \\ &\mathbf{if\ \ h_{b,m} \geq h_b\ \ then\ use\ h_{b,m}} \end{aligned} \tag{7-103}$$

To see which solution is valid, the terms of the equation have to be analyzed. For **α+β<π/2** the term **A>0** and **C<0** because of the minus sign. The term **B** is always positive. This will only result in a positive solution if the + sign is applied. For **α+β>π/2** the term **A<0** and **C>0** because of the minus sign. This will only result in a positive solution if the – sign is applied. So at small blade angles the plus sign gives the correct solution, while large blade angles require the minus sign solution.

Figure 7-35, Figure 7-36 and Figure 7-37 show the shear angle and the horizontal cutting force coefficient and the vertical cutting force coefficient for the **Curling Type**. At large blade angles, both the horizontal and vertical forces become very large. In cases of large blade angles the **Curling Type** will hardly occur because the **Flow Type** results in smaller forces.

$$\mathbf{F_h = \lambda_s \cdot c \cdot h_i \cdot w \cdot \frac{\dfrac{\sin(\alpha)}{\sin(\beta)} + r_m \cdot \dfrac{\sin(\beta)}{\sin(\alpha)}}{\sin(\alpha + \beta)} = \lambda_s \cdot c \cdot h_i \cdot w \cdot \lambda_{HC}} \tag{7-104}$$

$$\mathbf{F_v = \lambda_s \cdot c \cdot h_i \cdot w \cdot \frac{\dfrac{\cos(\alpha)}{\sin(\beta)} - r_m \cdot \dfrac{\cos(\beta)}{\sin(\alpha)}}{\sin(\alpha + \beta)} = \lambda_s \cdot c \cdot h_i \cdot w \cdot \lambda_{VC}} \tag{7-105}$$

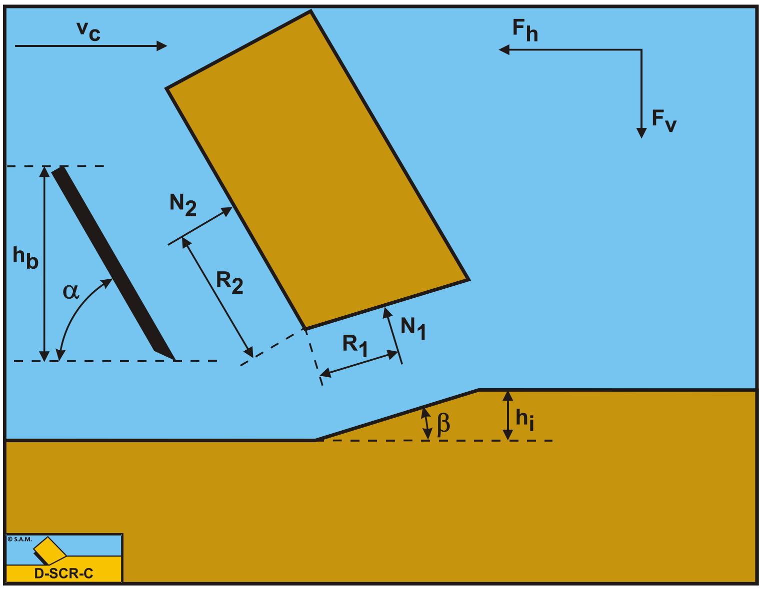

Figure 7-34: The equilibrium of moments on the layer cut in clay.

Figure 7-35, Figure 7-36 and Figure 7-37 clearly show the transition from the plus root solution to the minus root solution. This transition results in a discontinuity. How exactly this transition will take place in nature is still subject for further research. Confidential tests in clay with blade angles of 20, 30 and 40 degrees have shown that the plus root solution is valid at small blade angles, tests in hyperbaric rock cutting with a blade angle of 110 degrees have shown that the minus root solution is valid at large blade angles (see Chapter 9:). One should consider that the **Curling Type** only occurs with thin layers. Once the required mobilized blade height exceeds the actual blade height, the **Flow Type** will occur. So for example, if blade height and layer thickness are equal, the ratio cannot exceed 1 and depending on the a/c ratio, the **Flow Type** will occur above a certain blade angle.

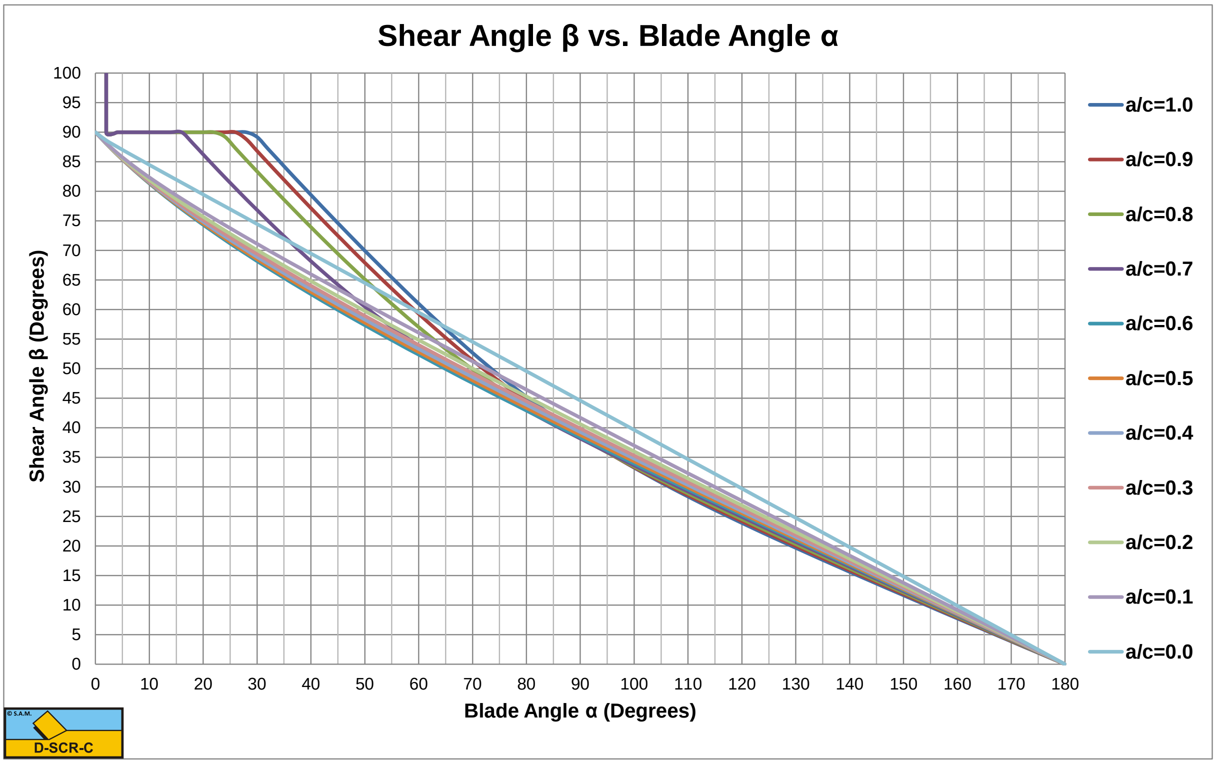

Figure 7-35: The shear angle β for the Curling Type.

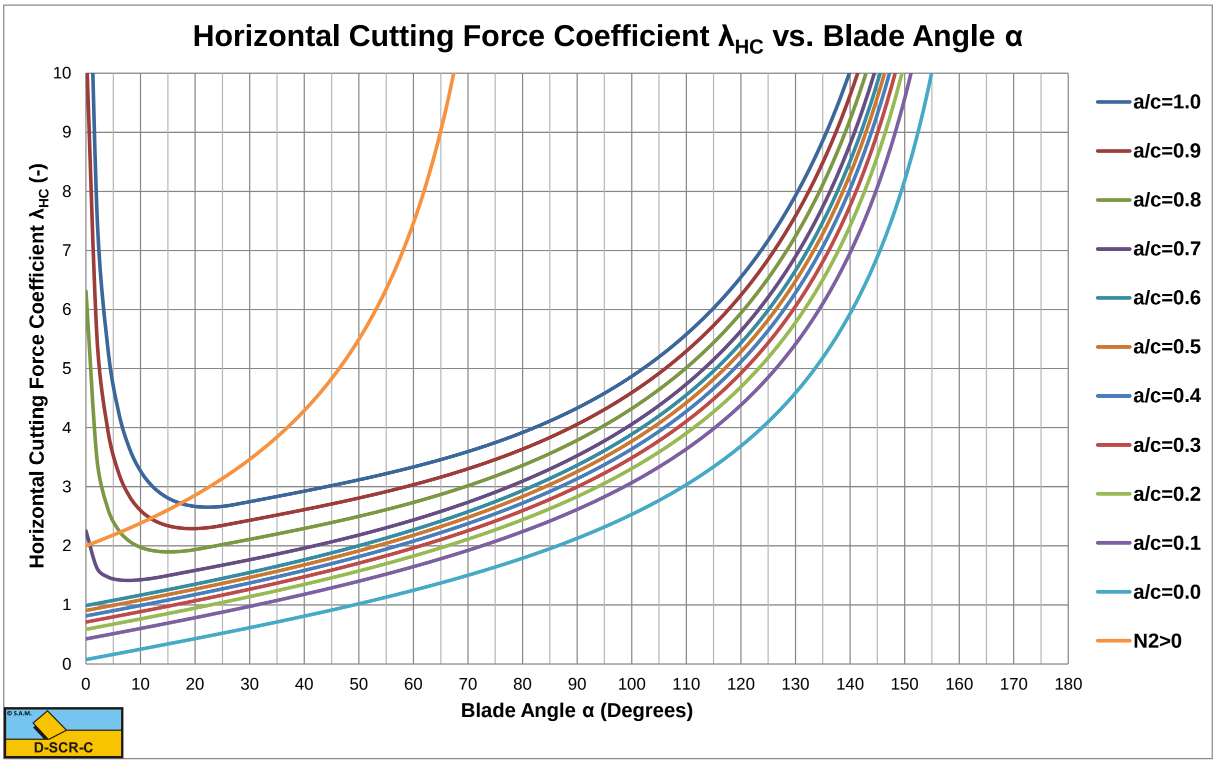

Figure 7-36: The horizontal cutting force coefficient λ_{HC}.

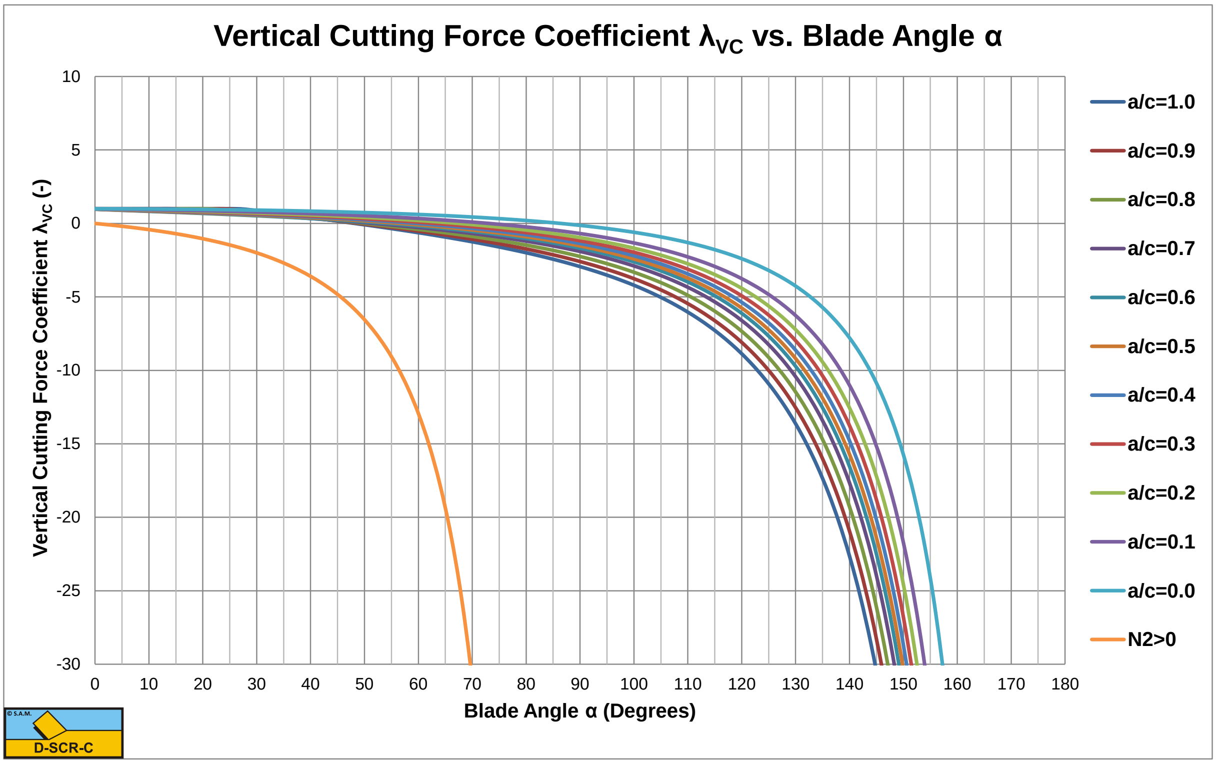

Figure 7-37: The vertical cutting force coefficient λ_{VC}.

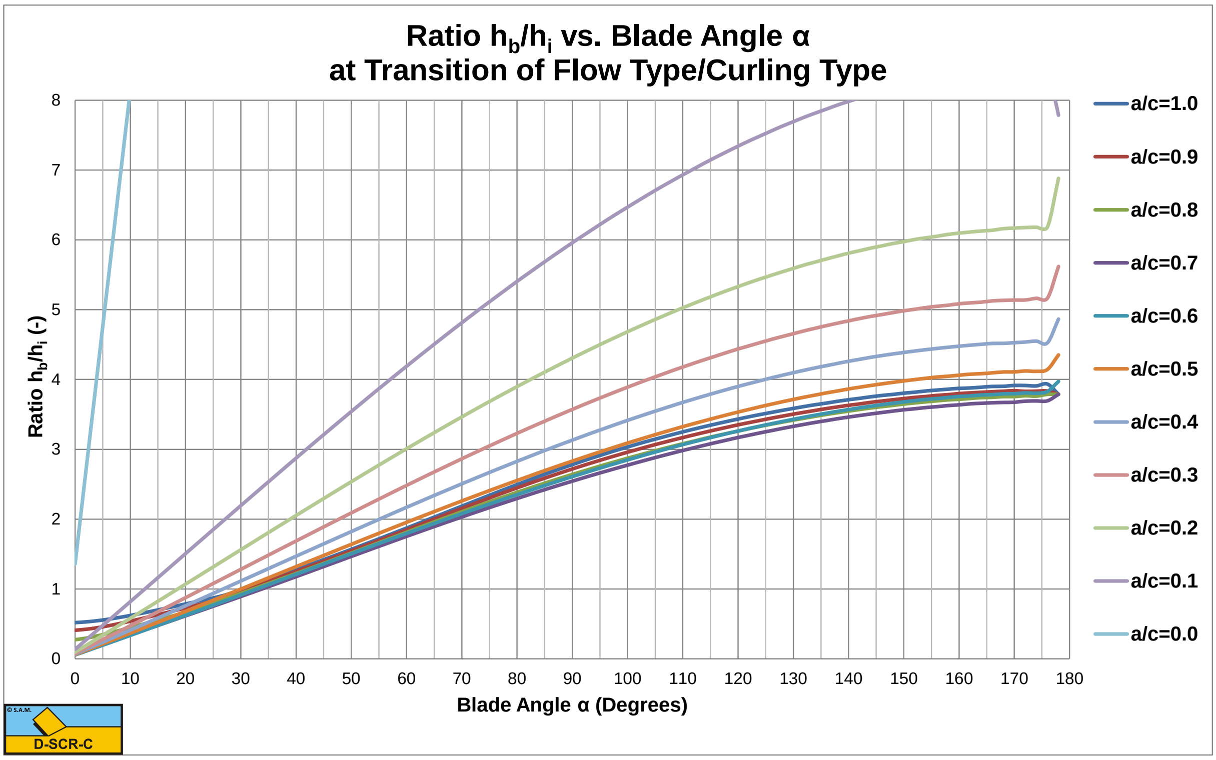

Figure 7-38: The ratio h_b/h_i at the transition Flow Type/Curling Type.

7.7. Resulting Forces.

Now the question is, when do we have a **Flow Type**, **Curling Type** or **Tear Type** and how does this depend on the different parameters. This is explained by a number of examples.

Example 1: Cohesion **c=1 kPa**, adhesion **a=1 kPa**, tensile strength **σ_T=-0.3 kPa**, blade height **h_b=0.1 m**, blade angle **α=55°,** forces per unit width of the blade**.**

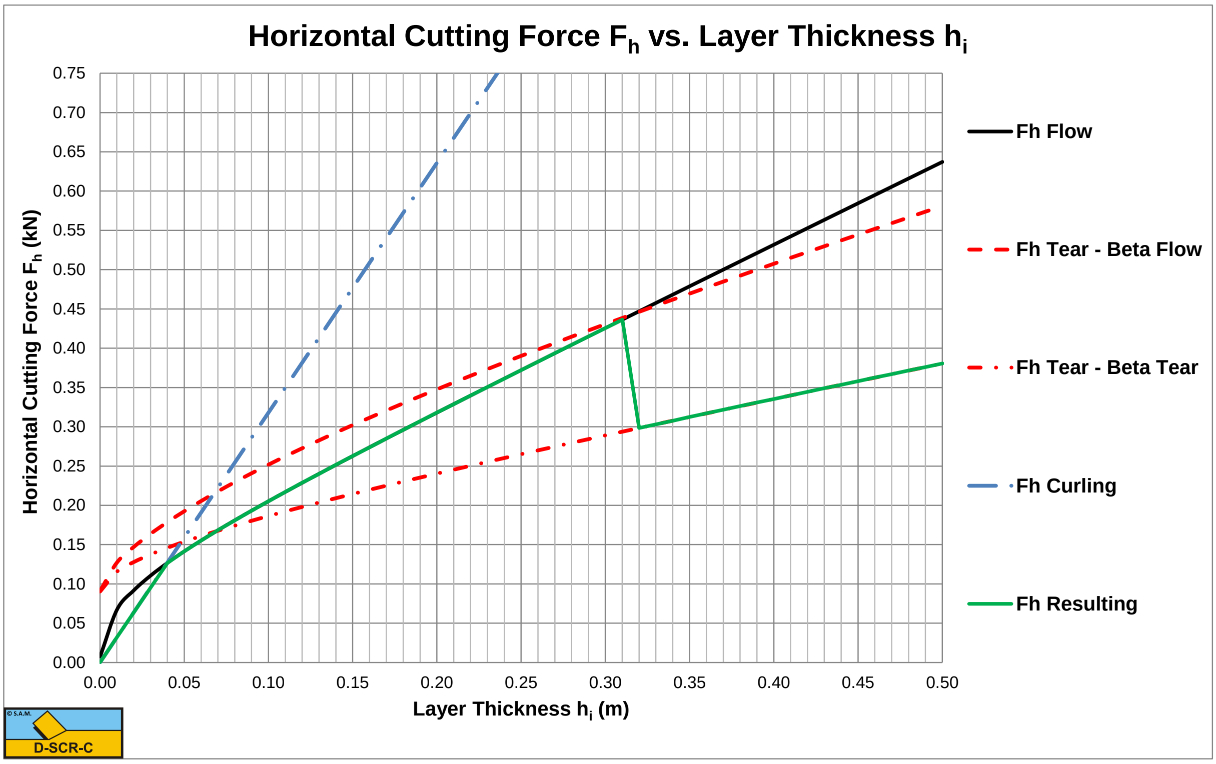

Figure 7-39: Horizontal force; cohesion c=1 kPa, adhesion a=1 kPa, tensile strength σ_T=-0.3 kPa, blade height h_b=0.1 m, blade angle α=55°

According to Figure 7-27 (see also Figure 7-40) there will be a transition from the **Flow Type** to the **Tear Type** at **r=0.3**, so a layer thickness **h_i=0.32 m**. But will this really happen? Suppose we investigate the undercutting process of a cutter head, where the layer thickness increases from zero to a maximum during the rotation of a blade. When the blade starts cutting the layer thickness is zero and increases in time. First the cutting process is of the **Curling Type** up to a layer thickness of about **h_i=0. 65 m**. At this layer thickness the mobilized blade height equals the actual blade height and there is a transition from the **Curling Type** to the **Flow Type**. When the layer thickness is increased further, at a layer thickness of about **h_i=0.32 m** the normal stresses on the shear plane result in normal stresses more negative than the tensile strength under an angle of **45°** downwards with respect to the direction of the shear plane, so there is a transition from the **Flow Type** to the **Tear Type**. However, once the **Tear Type** of cutting mechanism occurs, this mechanism will search for a shear angle, resulting in a minimum cutting force. This shear angle tends not to be equal to the optimum shear angle of the **Flow Type**. Figure 7-21 shows the optimum shear angle of the **Flow Type**, while Figure 7-29 shows the optimum shear angle of the **Tear Type**. The result is a discontinuity in the cutting force, the cutting force is reduced (the beta real curve) at the moment the **Tear Type** is the cutting mechanism. Another reduction may occur, because the force calculated is the force at the start of a tensile crack. When the blade continues moving forward, the horizontal force will probably be smaller than the force at the initiation of the tensile crack, resulting in a lower average force.

Now suppose we are overcutting with our cutter head. This means we start with some maximum layer thickness thick enough to cause the **Tear Type** to occur. When the blade progresses, the layer thickness decreases. But since the curve of the real beta is followed, the **Tear Type** will continue until a layer thickness of about **h_i=0.065 m** is reached. In fact, each time a block of clay breaks out of the clay and the cutting process starts again. At the layer thickness of about **h_i=0.065 m** there is a transition directly from the **Tear Type** to the **Flow Type**.

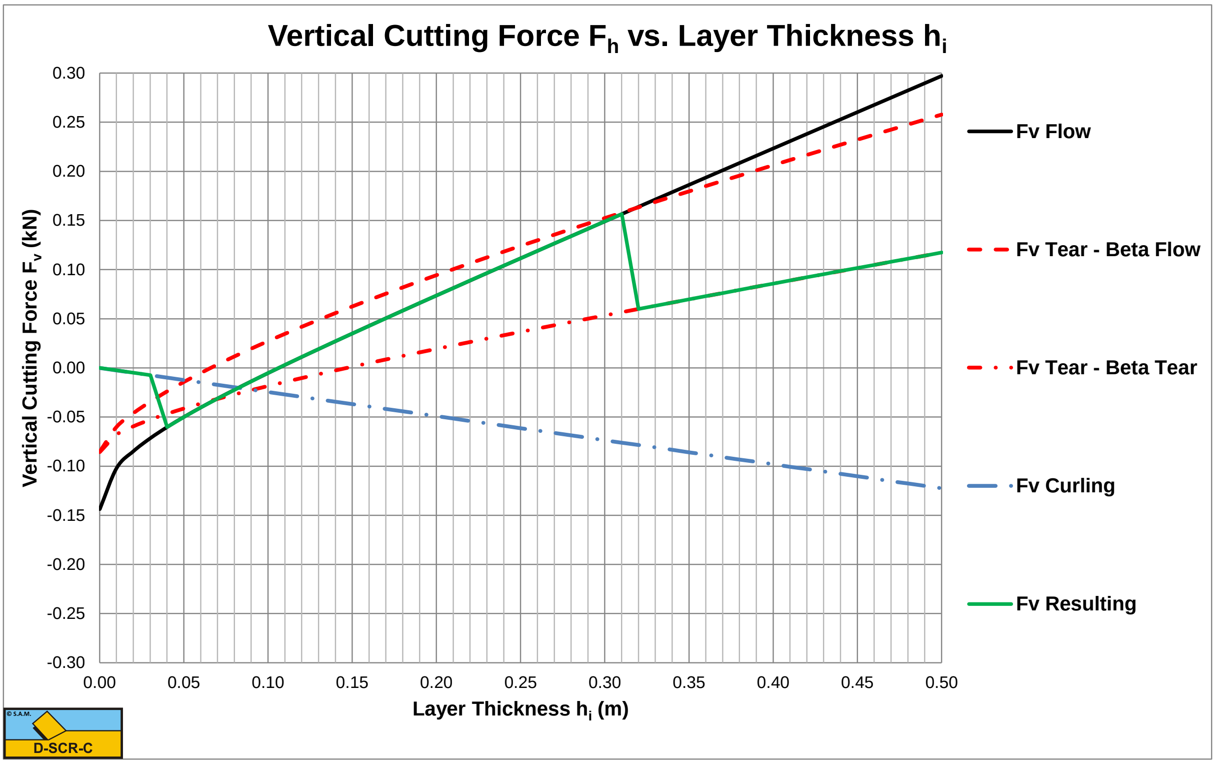

Figure 7-40: Vertical force; Cohesion c=1 kPa, adhesion a=1 kPa, tensile strength σ_T=-0.3 kPa, blade height h_b=0.1 m, blade angle α=55°

Figure 7-41 shows the Mohr circles for the **Flow Type** and the **Tear Type** for a layer thickness of **h_i=0.1 m**. Both mechanisms are possible. Which one occurs depends on the history, since both only touch one failure criterion. Figure 7-42 shows the Mohr circles for the **Flow Type** and the **Tear Type** for a layer thickness of **h_i=0.5 m**. The Mohr circle for shear failure (**Flow Type**) crosses the tensile failure criterion and thus cannot exist. Only one mechanism is possible, the **Tear Type**.

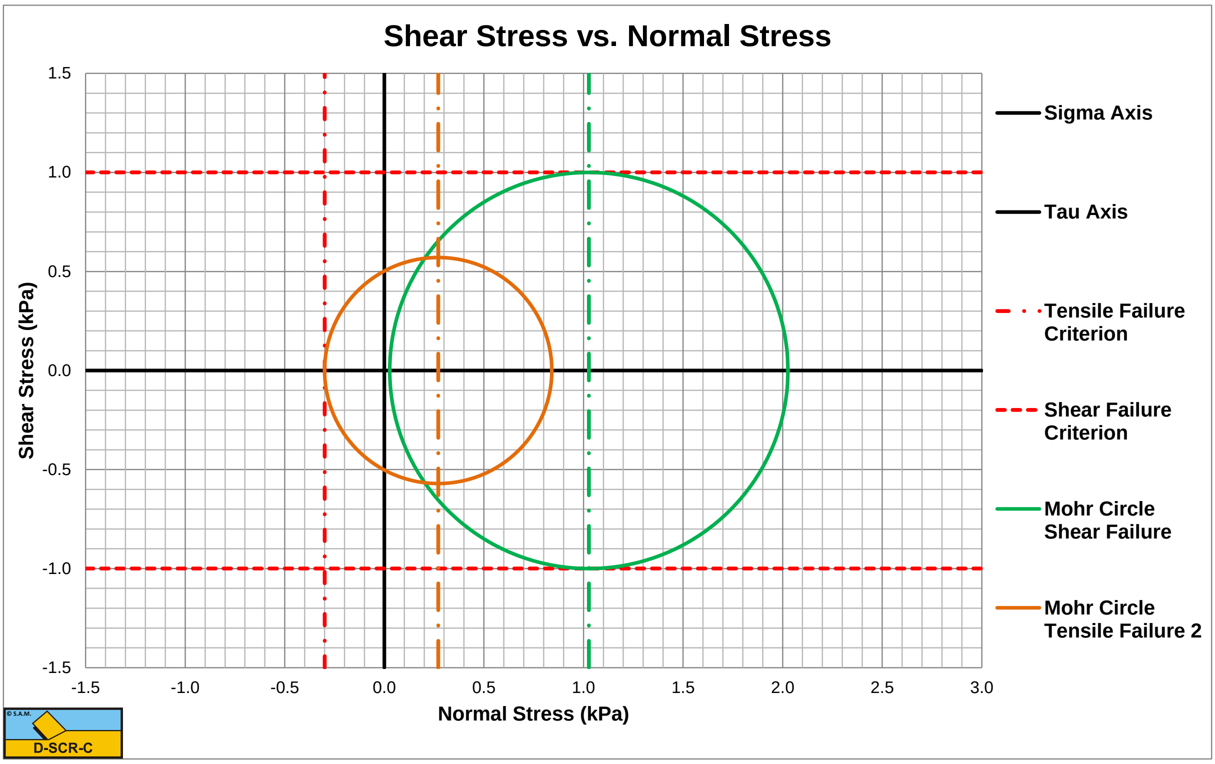

Figure 7-41: The Mohr circles for h_i=0.1 m, two possibilities.

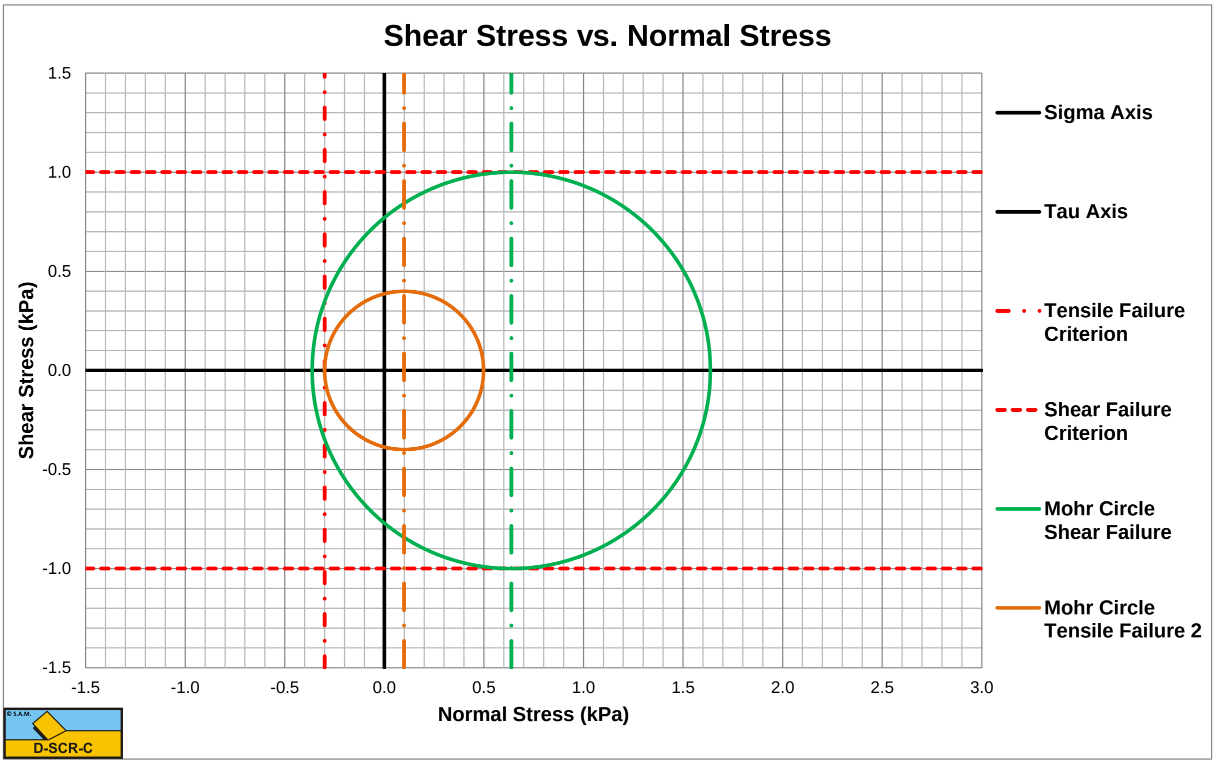

Figure 7-42: The Mohr circles for h_i=0.5 m, only tensile failure possible.

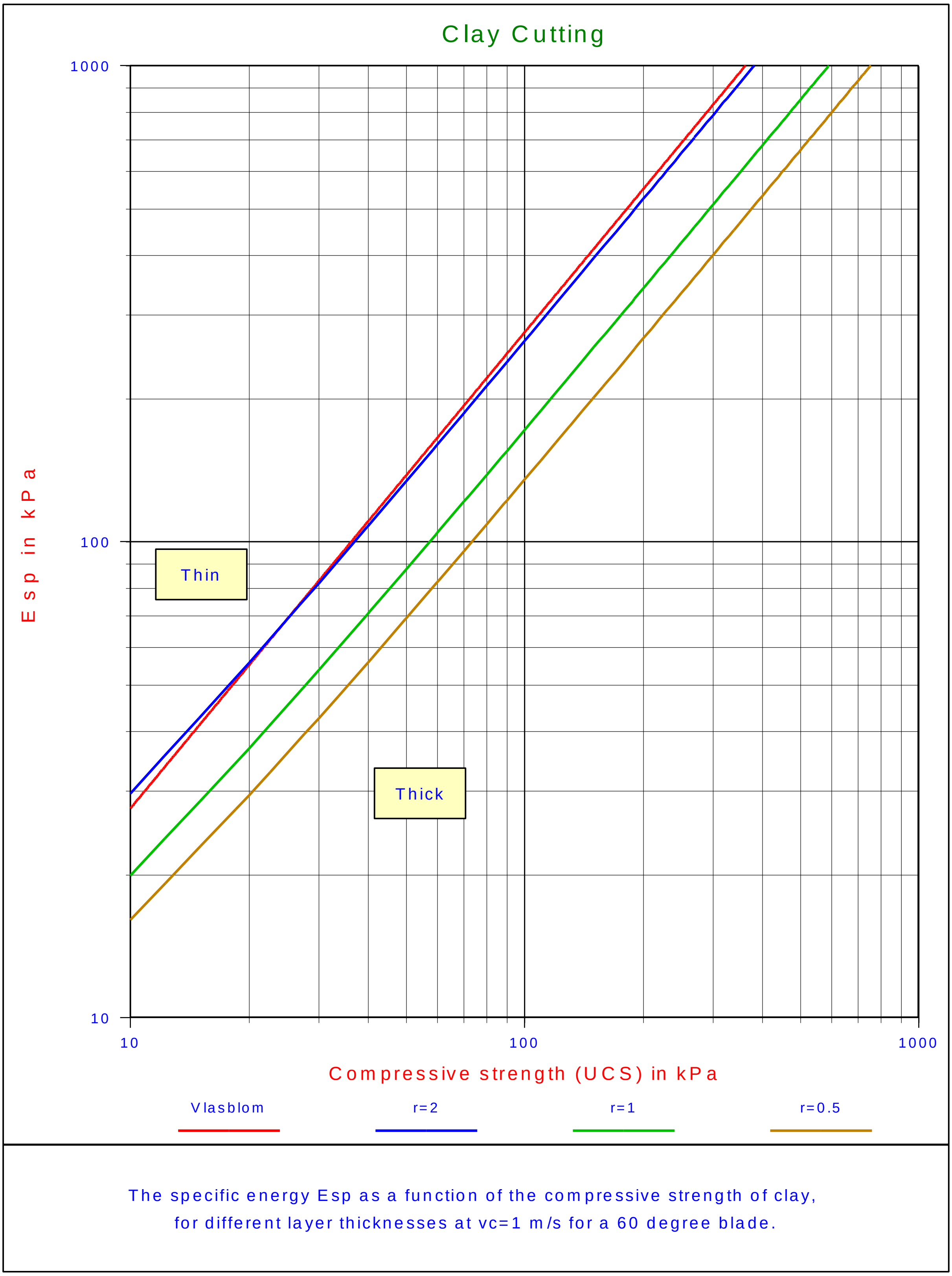

Figure 7-43: The specific energy E_{sp} in clay as a function of the compressive strength (UCS).

7.8. Experiments in Clay.

7.8.1. Experiments of Hatamura & Chijiiwa (1977B).

Hatamura & Chijiiwa (1977B) carried out experiments in sand, clay and loam. The experiments were carried out with blade angles **α** of 30°, 45°, 60°, 75° and 90°, layer thicknesses $\mathbf{h_i}$ of 0.05, 0.10 and 0.15 m and cutting velocities $\mathbf{v_c}$ of 0.05, 0.10 and 0.14 m/sec. The blade had a fixed length $\mathbf{L_4}$ of 0.2 m and a fixed width **w** of 0.33 m. The clay/loam had a dynamic cohesion **c** of 27.9 kPa and a dynamic adhesion **a** of 13.95 kPa. Hatamura & Chijiiwa (1977B) only give the dynamic cohesion and adhesion, not the static ones. Based on equation (7-53) an average strengthening factor of about 1.5 can be determined. This factor may however vary with the blade angle and layer thickness. Hatamura & Chijiiwa (1977B) measured the shear angle **β**, the total cutting force and the direction of the total cutting force. The also determined the location of the acting points of the different forces. In the model they derived they used the horizontal and vertical force equilibrium equations and the equilibrium of moments equation combined with their measured acting points. By solving the 3 equilibrium equations, they solved the horizontal cutting force, the vertical cutting force and the shear angle, based on 3 equations with 3 unknowns. The theory as derived here assumes a shear angle where there is a minimum horizontal force, based on the minimum cutting energy principle. So the two approaches are different. Hatamura & Chijiiwa (1977B) found that cutting tests with cutting angles of 30° and 45° were according to the **Tear Type**, while the larger cutting angles followed the **Flow Type** of cutting mechanism. This tells something about the tensile strength of the material. Based on the above an ac ratio **r** of 0.5-0.7 can be derived. Figure 7-27 shows that a tensile strength to cohesion $\mathbf{\sigma_T/c}$ ratio of about 0.2 may explain this. So it is assumed that the tensile strength is 20% of the cohesion.

Figure 7-44, Figure 7-45 and Figure 7-46 show the results of the experiments and the calcultations. The calculations are carried out for both the **Flow Type** and the **Tear Type**. The shear angles predicted are 5°-10° larger than the ones measured, however the tendency is the same.

The measured total cutting forces match the predicted cutting forces very well for the **Tear Type** for blade angles of 30° and 45° and for the **Flow Type** for blade angles of 60°, 75° and 90°. The theory does predict the **Tear Type** and the **Flow Type** for the corresponding blade angles. The directions measured of the total cutting force also match the theory very well if the correct cutting mechanism is considered. So apparently the total cutting forces and the direction of these forces can be predicted well, but the shear angle gives differences. We should consider that the shear angle as used in the theory here is a straight line, a simplification. In reality the shear plane may be curved, leading to different values of the shear angle measured. For the **Tear Type** it is not clear what definition Hatamura & Chijiiwa (1977B) used to determine the shear angle. Is it the point where the secondary tensile crack reaches the surface? This explains some of the differences between the measured and calculated shear angles. Overall, the theory as developed here predicts the cutting forces and the direction of these forces very well.

The force for a 60° blade and 0.05 m layer thickness is smaller than expected based on the **Flow Type** of cutting process. This is caused by the **Curling Type** as shown below.

Figure 7-45 shows that the experiment with a layer thickness of 0.05 m with a blade angle of 60° gives a smaller cutting force than estimated. Analyzing the 60° experiments as a function of the layer thickness gives Figure 7-47. This figure shows that up to a layer thickness of about 0.08 m there will be a **Curling Type** of cutting process. Above 0.08 m there will be a **Flow Type** of cutting process, while above about 0.20 m there will be a **Tear Type** of cutting process. Once the **Tear Type** is present, the force will drop to the lower **Tear Type** curve as is visible in the 30° and 45° experiments. Since all 3 cutting mechanisms were present in the experiments of Hatamura & Chijiiwa (1977B), it is not possible to find just one equation for the cutting forces. Each of the 3 cutting mechanisms has its own model or equation. Figure 7-48 shows the 30° experiment. It is clear from the figure that at 0.10 m layer thickness the cutting mechanism of of the **Tear Type**.

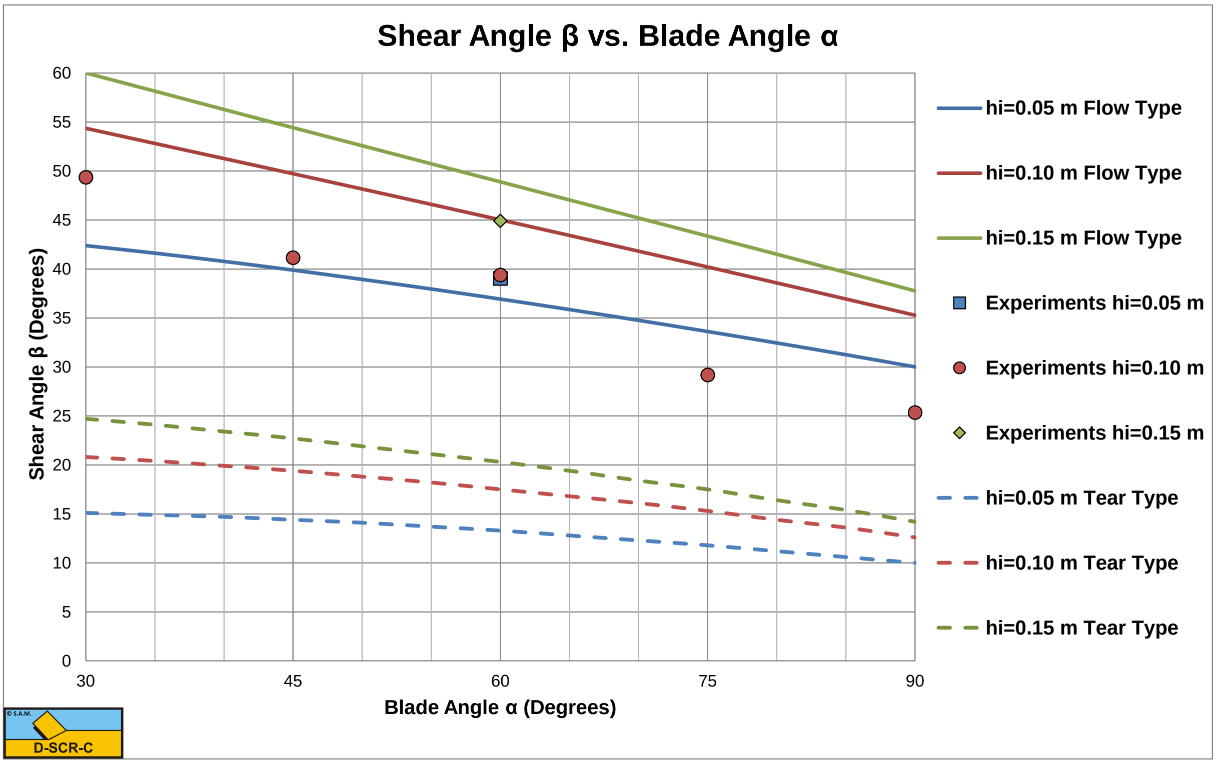

Figure 7-44: The shear angles measured and calculated.

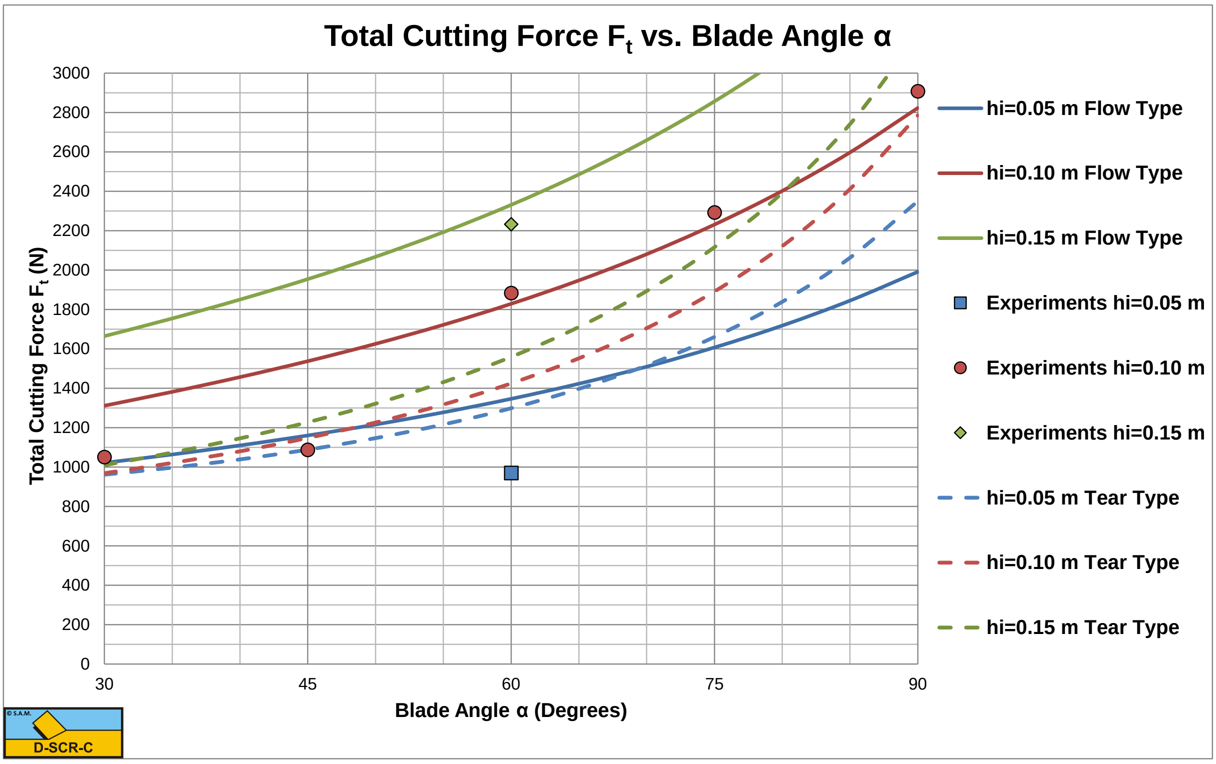

Figure 7-45: The total cutting force measured and calculated.

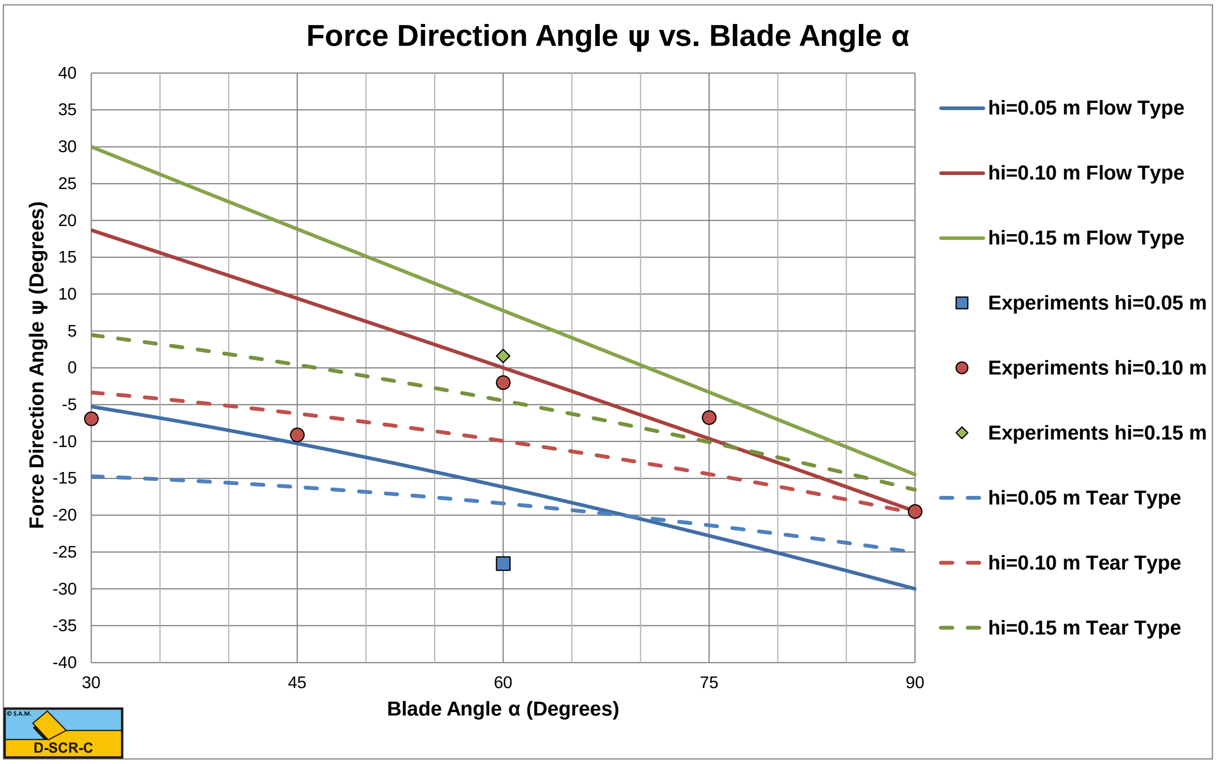

Figure 7-46: The direction of the total cutting force measured and calculated.

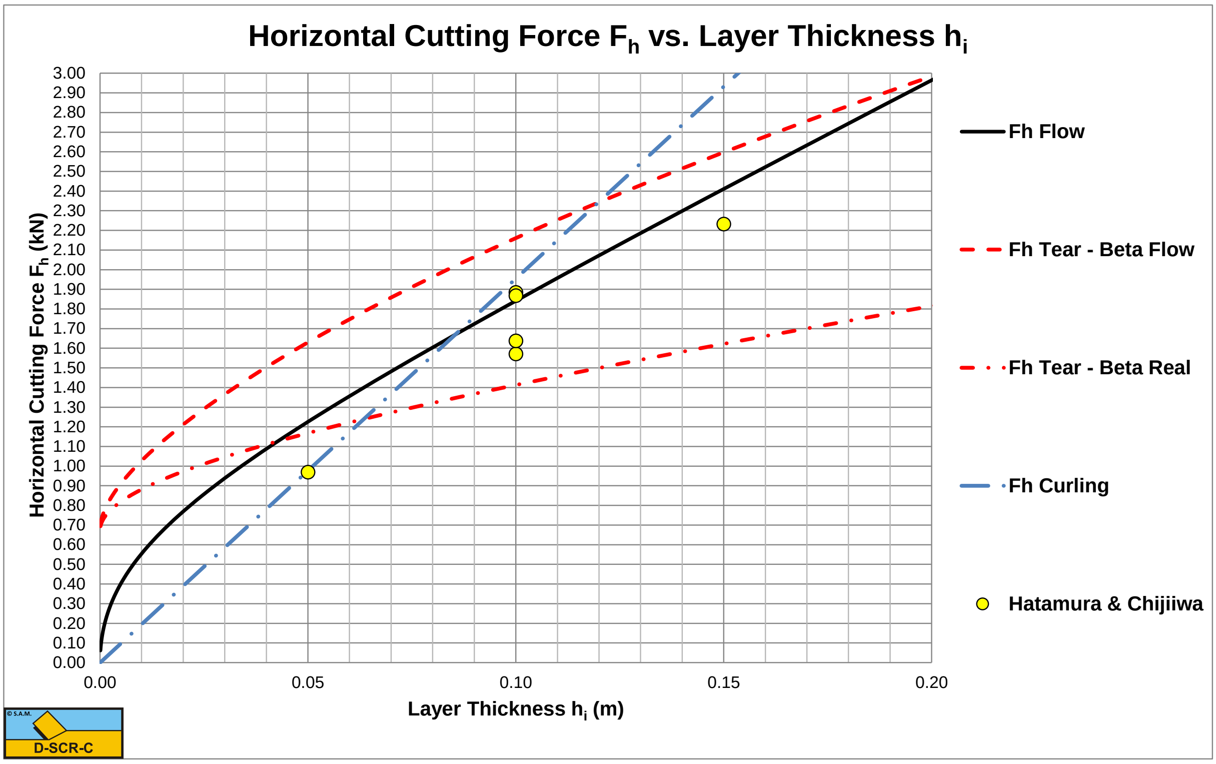

Figure 7-47: The 60 degree experiments.

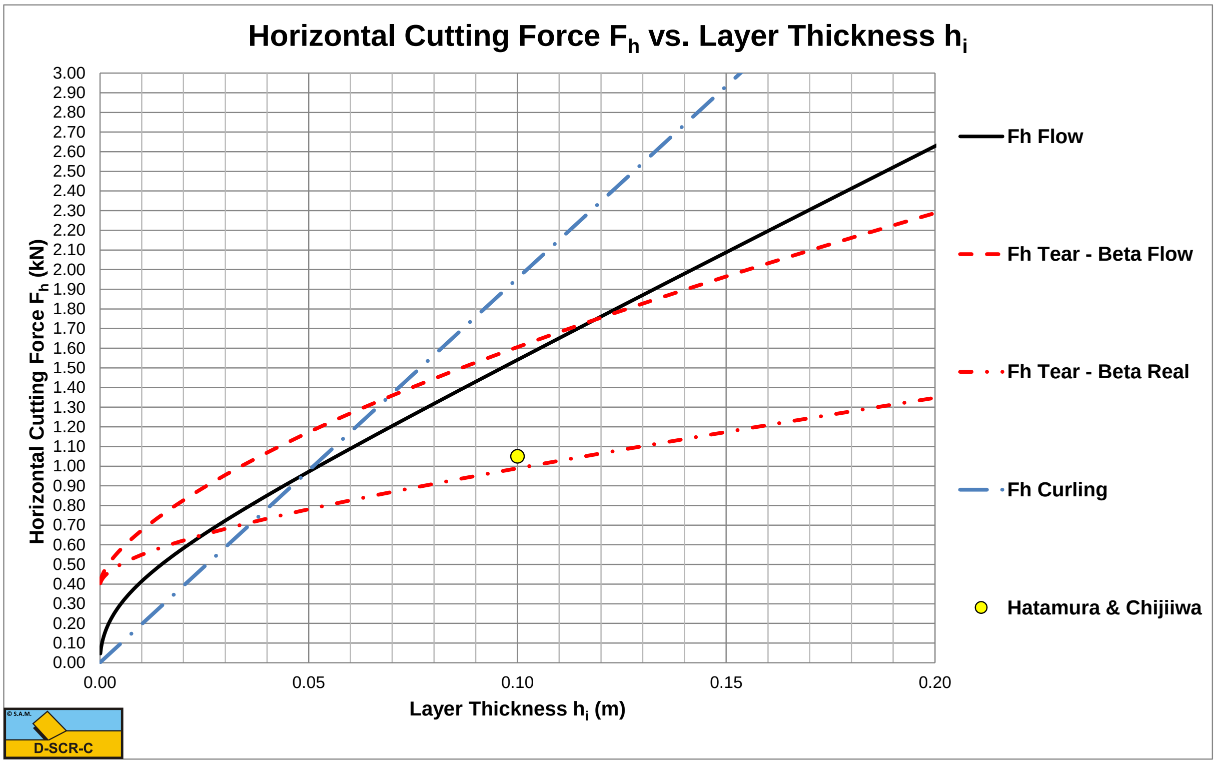

Figure 7-48: The 30 degree experiment.

7.8.2. Wismer & Luth (1972B).

Wismer & Luth (1972B) investigated rate effects in soil cutting in dry sand, clay and loam. For clay and loam they distinguished two rate effects, the inertial forces and the strengthening effect. For cutting velocities as known in dredging (up to 5-6 m/sec), the inertial forces can be neglected compared to the static cutting forces (low cutting velocities) and compared to the strengthening effect. Wismer & Luth (1972B) carried out experiments with blade angles of 30°, 60° and 90°, blades of 0.19·0.29 m, 0.127·0.193 m and 0.0762·0.117 m (7.5·11.45 inch, 5.0·7.6 inch and 3.0·4.59 inch) and layer thicknesses from 0.0225-0.0762 m (0.9-3.0 inch). They did the experiments in two types of clay. Unfortunately they did not mention the cohesion and adhesion, but the mentioned a cone resistance. However, based on their graphs the cohesion could be deducted. The cone index 27 clay should have had a cohesion of about 22.5 kPa and an adhesion of 11.25 kPa, the cone index 42 clay a cohesion of 34 kPa and an adhesion of 17 kPa. The strengthening factor of Wismer & Luth (1972B) can be rewritten in SI Units, using the reference strain rate of 0.03/sec, giving the following equation for the strengthening factor.

$$\tau = \tau_y \cdot \lambda_s \qquad \text{with:} \qquad \lambda_s = \left(\frac{\dfrac{v_c}{h_i}}{0.03} \right)^{0.1} \tag{7-106}$$

Figure 7-49 shows the theoretical strengthening factors based on the average of equations (7-34) and (7-35) and for the above equation for the minimum and maximum layer thickness, giving a range for the strengthening factor and comparing the Miedema (1992) equation with the Wismer & Luth (1972B) equation. The figure also shows the results of 5 series of tests as carried out by Wismer & Luth (1972B) with a 30° blade. The two equations match well up to cutting velocities of 1.5 m/sec, but this may differ for other configurations. At high cutting velocities the Wismer & Luth (1972B) equation gives larger strengthening factors. Both equations give a good correlation with the experiments, but of course the number of experiments is limited. A realistic strengthening factor for practical cutting velocities in dredging is a factor 2. In other words, a factor of about 2 should be used to multiply the static measured cohesion, adhesion and tensile strength.

It should be mentioned that the above equation is modified compared with the original Wismer & Luth (1972B) equation. They used the ratio cutting velocity to blade width to get the correct dimension for strain rate, here the ratio cutting velocity to layer thickness is used, which seems to be more appropriate. The constant of 0.03 is the constant found from the experiments of Hatamura & Chijiiwa (1977B).

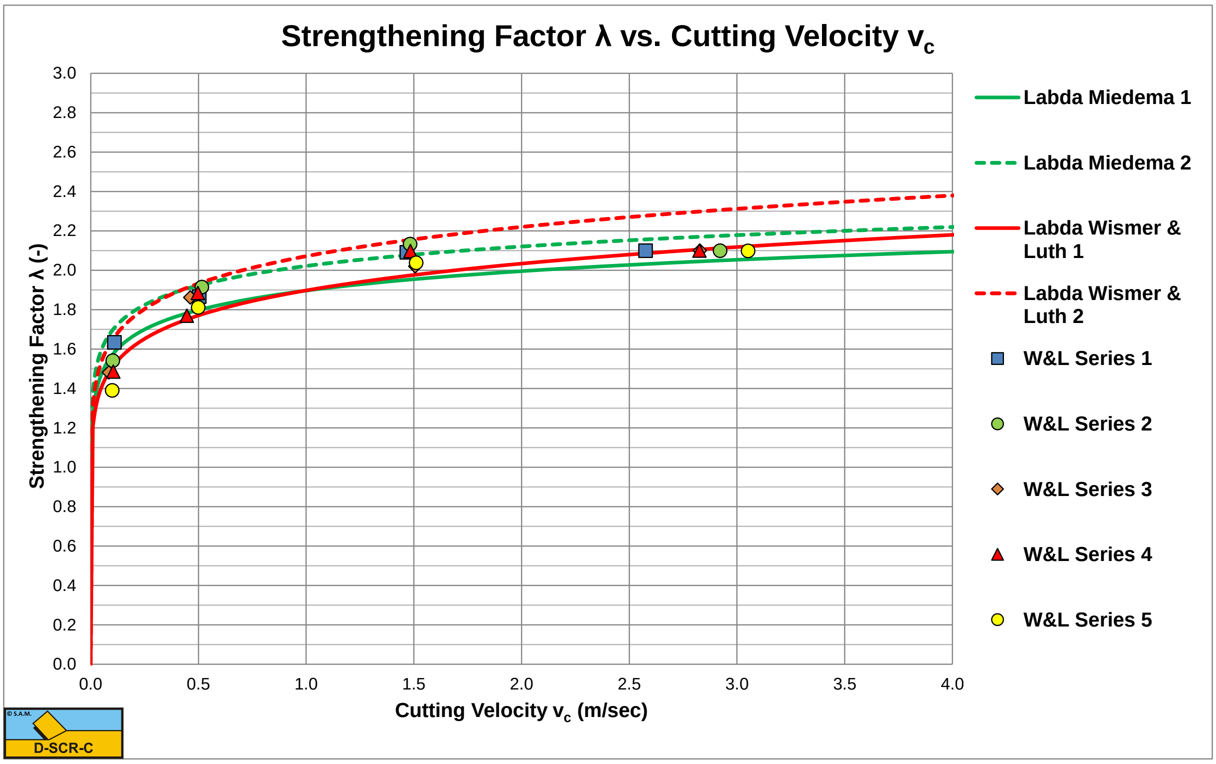

Figure 7-49: The strengthening factor.

7.9. Nomenclature.

a	Adhesion	kPa
A	Adhesive force on the blade	kN
B	Frequency (material property)	1/s
c	Cohesion	kPa
c_m	Mobilized shear strength	kPa
C	Cohesive force on shear plane	kN
E	Energy level	J/kmol
E_a	Activation energy level	J/kmol
E_l	Limiting (maximum) energy level	J/kmol
E_{sp}	Specific cutting energy	kPa
f	Shear force on flow unit	N
F	Cutting force	kN
F_h	Horizontal cutting force	kN
F_v	Vertical cutting force	kN
G	Gravitational force	kN
h	Planck constant ($6.626 \cdot 10^{-34}$ J·s)	J·s
h_b	Blade height	m
$h_{b,m}$	Mobilized blade height	m
h_i	Layer thickness	m
k	Boltzman constant ($1.3807 \cdot 10^{-23}$ J/K)	J/K
K	Constant Herschel Bulkley equation	-
K_1	Grain force on the shear plane	kN
K_2	Grain force on the blade	kN
i	Coefficient	-
I	Inertial force on the shear plane	kN
n	Power of strain rate equation	-
N	Avogadro constant ($6.02 \cdot 10^{26}$ 1/kmol)	-
N_1	Normal force on shear plane	kN
N_2	Normal force on blade	kN
p	Probability	-
P_c	Cutting power	kW
r	Ratio adhesive force to cohesive force	-
r_m	Mobilized ratio adhesive force to cohesive force	-
r_T	Ratio adhesive force to tensile force	-
R	Universal gas constant (8314 J/kmol/K)	J/kmol/K
R_1	Acting point on shear plane	m
R_2	Acting point on blade	m
S	Number of bonds per unit area	1/m²
S_1	Shear force due to internal friction on the shear surface	kN
S_2	Shear force due to soil/steel friction on the blade	kN
SPT	Standard Penetration Test	Blows/foot
T	Absolute temperature	K
T	Tensile force	kN
v_c	Cutting velocity	m/s
w	Blade width	m
W_1	Force resulting from pore under pressure on the shear plane	kN
W_2	Force resulting from pore under pressure on the blade	kN
X	Function	-
α	Blade angle	rad
β	Angle of the shear plane with the direction of cutting velocity	rad
$\dot{\varepsilon}_a$	Strain rate adhesion	1/s
$\dot{\varepsilon}_c$	Strain rate cohesion	1/s
$\dot{\varepsilon}_0$	Strain rate from triaxial test	1/s
ν	frequency of activation	1/s
λ	Distance between equilibrium positions	m

λ_a	Strain rate factor adhesive force	-
λ_c	Strain rate factor cohesive force	-
λ_s	Strain rate factor average adhesion and cohesion (usually 2)	-
λ_1	Acting point factor on shear plane	-
λ_2	Acting point factor on blade	-
λ_{HF}	Horizontal cutting force coefficient **Flow Type**	-
λ_{VF}	Vertical cutting force coefficient **Flow Type**	-
λ_{HT}	Horizontal cutting force coefficient **Tear Type**	-
λ_{VT}	Vertical cutting force coefficient **Tear Type**	-
λ_{HC}	Horizontal cutting force coefficient **Curling Type**	-
λ_{VC}	Vertical cutting force coefficient **Curling Type**	-
$d\varepsilon/dt$	Strain rate	1/s
$d\varepsilon_0/dt$	Frequency (material property)	1/s
τ	Shear stress	kPa
τ_a, a	Adhesive shear strength (strain rate dependent)	kPa
τ_c, c	Cohesive shear strength (strain rate dependent)	kPa
τ_y	Shear strength (yield stress, material property)	kPa
τ_{ya}	Adhesive shear strength (material property)	kPa
τ_{yc}	Cohesive shear strength (material property)	kPa
τ_0	Dynamical shearing resistance factor (material property)	kPa
σ_e	Effective stress	kPa
σ_n	Normal stress	kPa
σ_{N1}	Normal stress on shear plane	kPa
σ_{N2}	Normal stress on blade	kPa
σ_t	Tensile strength	kPa
ϕ	Angle of internal friction	rad
δ	Soil/steel friction angle	rad

Chapter 8: Rock Cutting: Atmospheric Conditions.

8.1. Introduction.

As mentioned in chapter 2, rock is a natural occurrence of cohesive organic or inorganic material, which forms a part of the earth crest. Most rocks are composed of one or more minerals.

Rocks can be classified in different ways. The most used classification is based on their origin, distinguishing the following 3 main classes:
Igneous rock. A rock that consists of solidified molten rock material (magma), which has been generated within the earth. Well known are granite and basalt.
Sedimentary rock. Rock formed by the consolidation of sediment as settled in water, ice or air and accumulated on the earth's surface, either on dry land or under water. Examples are sandstone, limestone and claystone.
Metamorphic rock. Any class of rocks that are the result of partial or complete recrystallization in the solid state of pre-existing rocks under conditions of temperature and pressure that are significantly different from thos obtaining at the surface of the earth.

For the atmospheric cutting of rock models, the unconfined compressive strength (UCS), the unconfined tensile strength (UTS), the Brazilian tensile strength (BTS), the angle of internal friction and the angle of external friction are the dominant material properties.

When cutting rock different types of failure may occur. A distinction is made between brittle, brittle ductile and ductile failure, where brittle can be brittle shear failure, brittle tensile failure or a combination of both. The type of failure is mainly determined by the so called ductility number being the ratio of the compressive strength over the tensile strength (UCS/BTS).

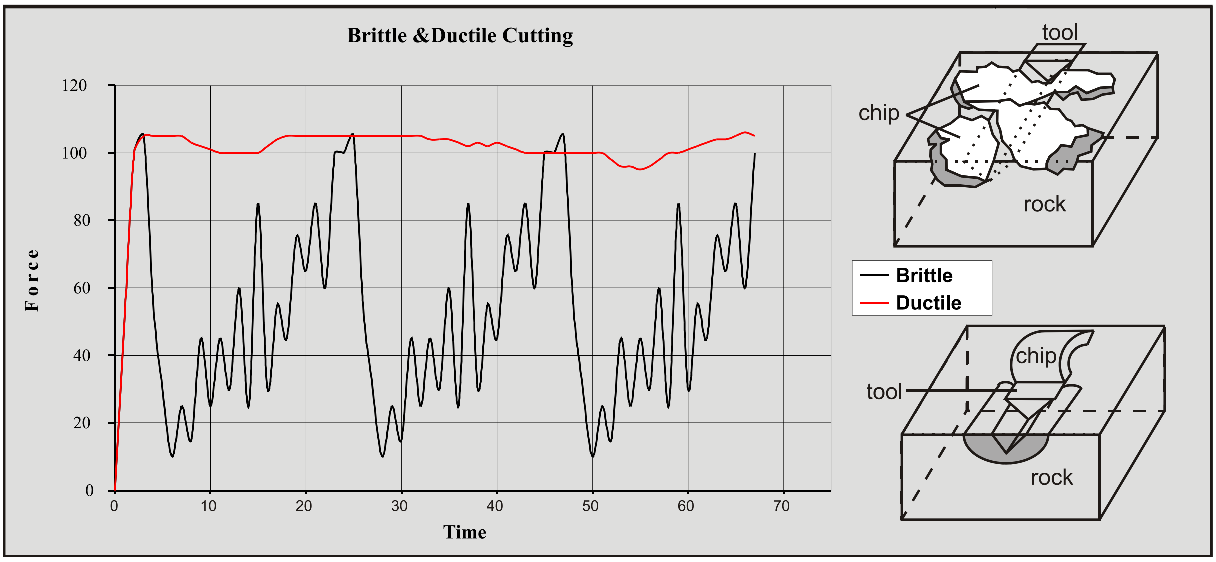

Figure 8-1: Ductile and brittle cutting Verhoef (1997).

The confining pressure and the temperature may also play a role. Figure 8-1 shows a recording of the cutting forces during brittle and ductile failure, where brittle failure shows strongly fluctuating cutting forces, while ductile failure shows a more constant force. In fact in brittle failure there is a force build up, where failure occurs if the force and thus the stresses exceed a certain limit, after which the rock instantly collapses and the force decreases rapidly. Brittle failure is always destructive, meaning that the structure of the rock changes during failure in an irreversible way. Ductile failure in its pure form is plastic deformation and is reversible. In rock ductile failure is usually cataclastic failure, meaning that the microstructure is destroyed, which is also irreversible. Figure 8-2 shows corresponding stress-strain curves.

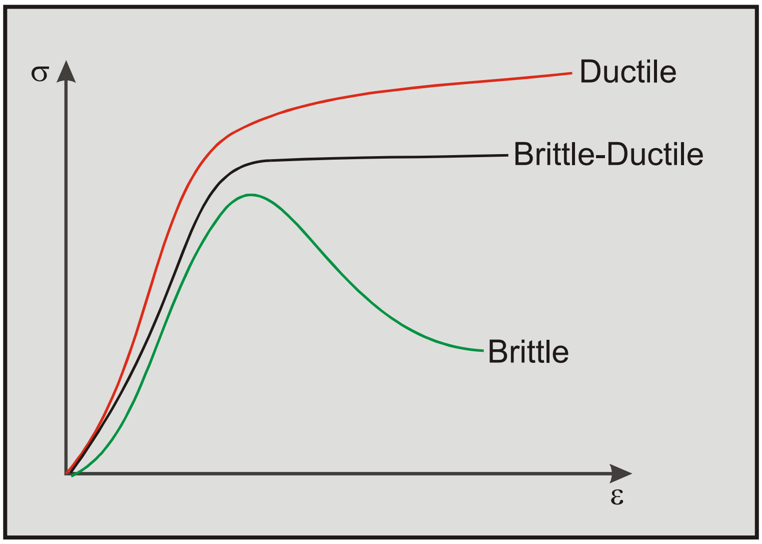

Figure 8-2: The stress-strain curves for ductile and brittle failure.

8.2. Cutting Process & Failure Criteria.

In granular materials a number of failure mechanisms can be distinguished. For clarity of definitions, the following definitions are used:

- **Flow Type**. Failure is based on plastic shear failure. Non-destructive, continues. Both the stress-strain curve according to Figure 8-2 and the non-destructive plastic deformation show ductile behavior. This type of failure will only occur at very high pressures and/or temperatures. The flow of magma is an example of this.
- **Tear Type**: **UCS/BTS=large**. Failure based on 100% tensile failure. This type of failure will occur when the **UTS-BTS** absolute value is small compared to the UCS value. This is a discontinues mechanism.
- **Chip Type**: **UCS/BTS=medium**. Failure based on a combination of shear failure and tensile failure, with a crushed zone near the tool tip. The fractions of shear failure and tensile failure depend on the **UCS/BTS** ratio. A large ratio results in more tensile failure, a small ratio in more shear failure. This is a discontinues mechanism.
- **Shear Type**: **UCS/BTS=small**. Failure based on 100% shear failure. This type of failure occurs when the **UTS-BTS** value is larger and the normal stresses in the shear plane are high, usually at larger blade angles. This is a discontinues mechanism.
- **Crushed Type**: Cataclastic failure based on shear, similar to the **Flow Type** and the **Shear Type** like in sand. The **Crushed Type** is based on cataclastic failure, disintegration of the grain matrix. This mechanism will be identified as pseudo-ductile since it shows ductile behavior in the stress-strain curve of Figure 8-2, but it is destructive and not plastic.

When cutting in dredging practice, blade or pick point angles of about 60 degrees are used. With these blade angles often the **Chip Type** of cutting mechanism occurs. Smaller blade angles may show the **Tear Type** cutting mechanisms, while larger blade angles often show the **Shear Type** of cutting mechanism. The higher the normal stresses in the rock cut, the less likely the occurrence of tensile failure.
When the pick point starts penetrating the rock, usually very high normal stresses occur in front and below the tip of the pick point, resulting in crushing of the rock. Destroying the grain matrix. In a stress-strain diagram this behavior is ductile, but since its also destructive its named pseudo-ductile. Now if the layer thickness is very small, like in oil drilling, the crushed zone may reach the surface and the whole process is of the **Crushed Type**. If the layer cut is thicker, like in dredging, the **Chip Type** cutting mechanism may occur, a combination of mechanisms. In the crushed zone and the intact rock a shear plane can be identified based on the minimum deformation work principle. When the pick point progresses, the shear stress on this shear plane increases. When the shear stress exceeds the shear strength (cohesion) a brittle shear crack will occur. It is not necessary that the shear stress exceeds the shear strength over the full length of the shear plane, it only has to exceed the shear strength at the beginning of the shear crack as in the Nishimatsu (1972) approach. When the pick point progresses, the normal and shear stresses increase, resulting in a Mohr circle with increasing radius. Now if the radius increases faster than the normal stress at the center of the Mohr circle, the minimum principal stress decreases and may even become negative. When it becomes negative it may become smaller than the negative tensile strength, resulting in tensile failure.

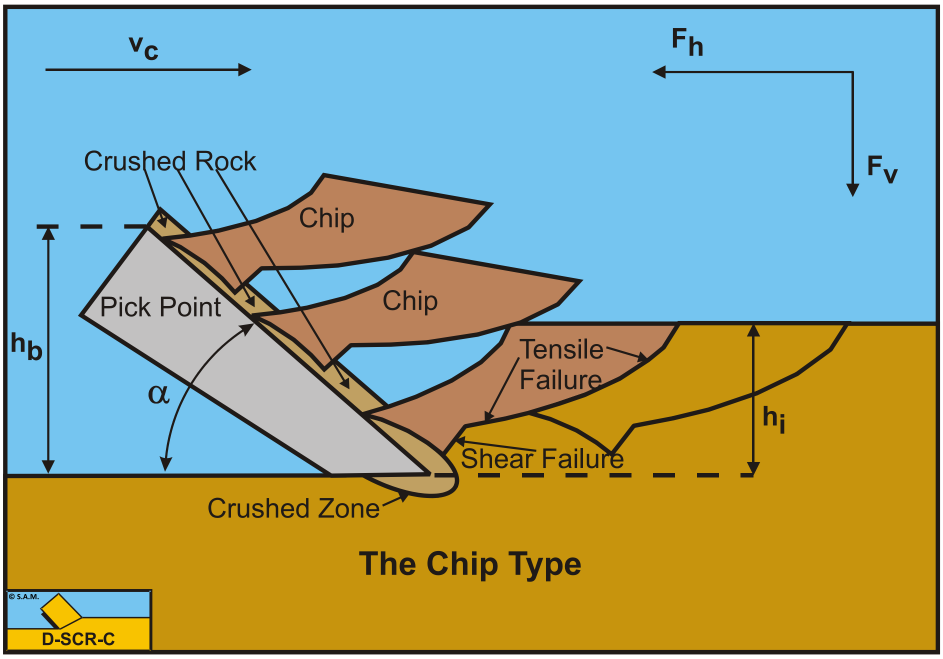

Figure 8-3: The Chip Type.

So in time it starts with a crushed zone, then a shear plane with possibly shear failure and than possibly tensile failure. If the tensile strength is large, it is possible that only shear failure occurs. If the tensile strength is small, it is possible that only tensile failure occurs. Crushing will start if locally a certain criterion is exceeded. Often the Mogi (1966) criterion is applied, giving a certain ratio between the maximum principal stress and the minimum principal stress. Ratio's used are 3.4 for sandstone and 4.2 for limestone, while Verhoef (1997) found 6 for limestone. Of course crushing does not start instantly, but gradually, based on the structure of the rock, especially the distribution of the microcracks and the skeleton. With the hypothesis that crushing starts where the rock is the weakest, one may assume that crushing starts at the scale of the microcracks, giving relatively large particles still consisting of many grains. With increasing normal stress these particles will also be fragmented into smaller particles. This process will go on until the smallest possible particles, the rock grains, result. Up to the Mogi (1966) criterion intact rock is assumed, however some fracturing or crushing may already have taken place.

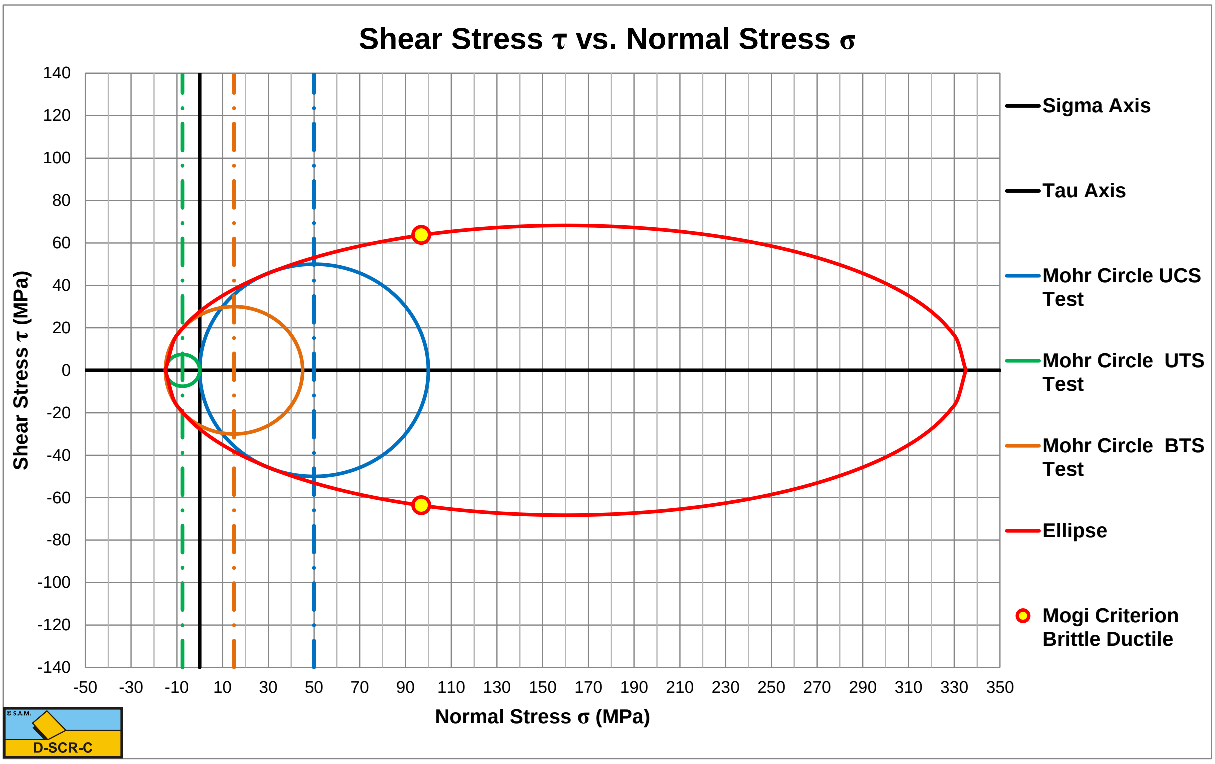

Figure 8-4: Failure envelopre according to Verhoef (1997) (Figure 9.4) of intact rock.

From the perspective of the angle of internal friction, one may assume that the angle of internal friction is based on the internal structure of the rock, and as long as the rock is intact, the angle of internal friction may change slightly based on the stress situation, but not to much. However, when fracturing and crushing starts, the internal structure of the rock is changing and this will result in a decreasing angle of internal friction. Decreasing until the angle of internal friction of the smallest particles, the rock grains is reached at high confining pressures.

Verhoef (1997) shows a complete failure envelope of intact rock, including Mogi's brittle-ductile transition. Vlasblom (2003-2007) refers to this failure envelope. Figure 8-4 shows this failure envelope, where the maximum normal stress is based on a hydrostatic compression test. So based on hydrostatic pressure, the material is crushed, without the presence of shear. This hydrostatic compressive strength (**HCS**) is a few times the **UCS** value of the rock. In the figure **HCS+UTS=3.5·UCS**. Not all rocks show this kind of behavior however. It is important to know that this envelope is based on tri-axial tests on intact rock.
Verhoef (1997) also shows in figure D3 a different failure envelope beyond the brittle-ductile transition point, which is more related to the cutting process. Beyond this transition point the crushed rock still has a certain internal friction angle, which will be discussed later and is shown in Figure 8-14 and Figure 8-15.
It is thus very important to determine the failure criterion envelope based on tests where shear failure occurs.

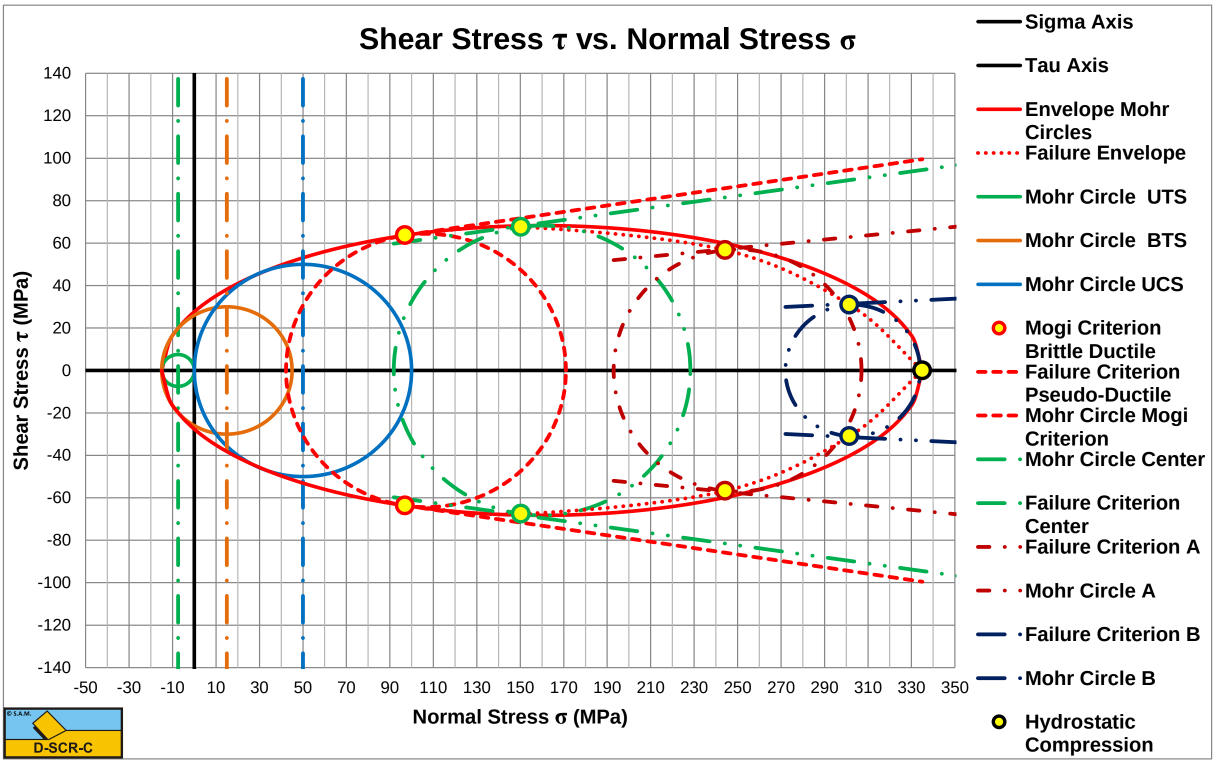

Figure 8-5: Constructing the failure envelope.

Figure 8-5 shows how a failure envelope can be constructed by connecting failure points of different stress situations. The figure shows the UTS, BTS and UCS Mohr circles, the Mohr circle at the Mogi criterion, the Mohr circle of a hydrostatic compression test and three additional Mohr circles. Connecting the failure points gives the failure curve. Surrounding the Mohr circles gives the envelope where Mohr circles have to stay inside to prevent failure. At confining stresses exceeding the Mogi point the two envelopes are slightly different.
As mentioned, the apparent shear strength and the internal friction angle of the intact and the crushed rock may differ. In the case where the Mogi criterion describes the shear strength and the angle of internal friction of the crushed rock, the failure curve for higher normal stresses may be a straight line tangent to the Mogi criterion point. Figure 8-6 shows this type of behavior. The Zijsling (1987) experiments at very high confining pressures show this type of behavior for cutting loads in Mancos Shale. The experiments of Zijsling (1987) will be discussed in chapter 9.

It is however also possible that the shear strength and the internal friction angle of the crushed rock decrease to a certain minimum with increasing normal stresses larger than the Mogi point to a point A or B in Figure 8-7. For higher normal stresses the failure curve will follow a straight line as is shown in the figure. The Zijsling (1987) experiments at very high confining pressures show this type of behavior for cutting loads in Pierre Shale.

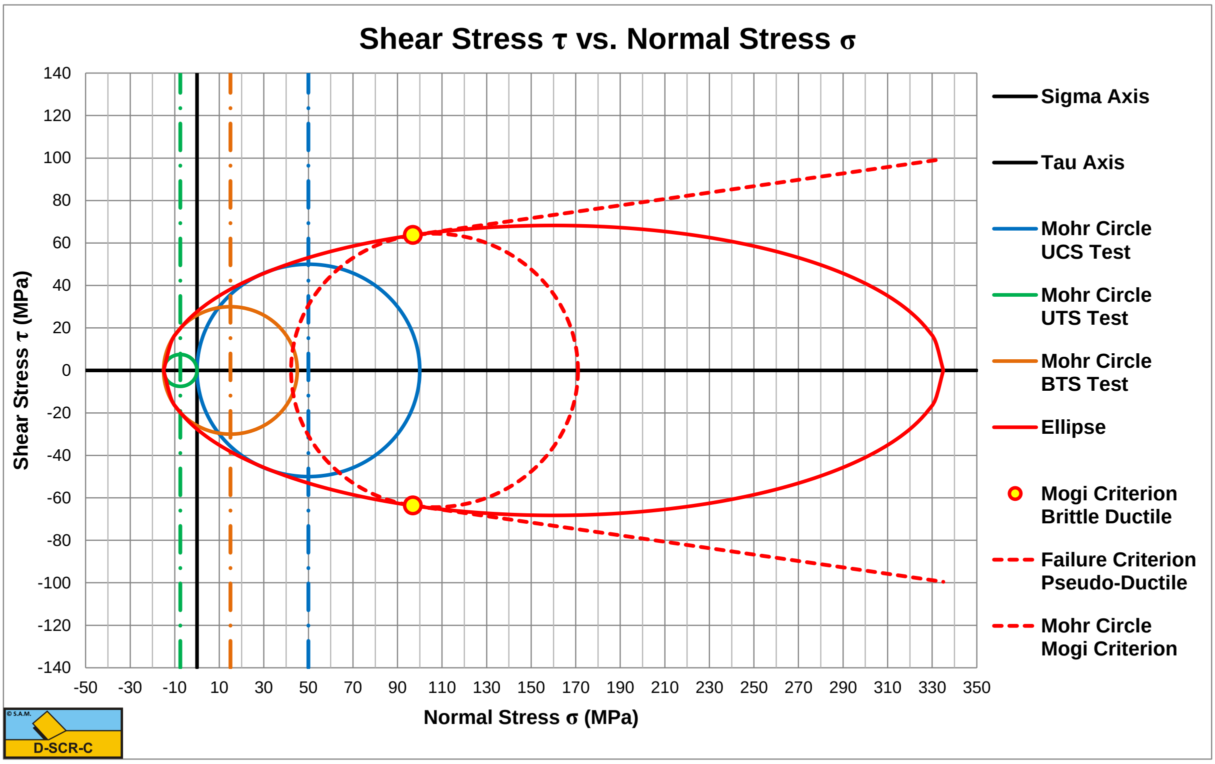

Figure 8-6: Resulting failure curve for Mancos Shale like rocks.

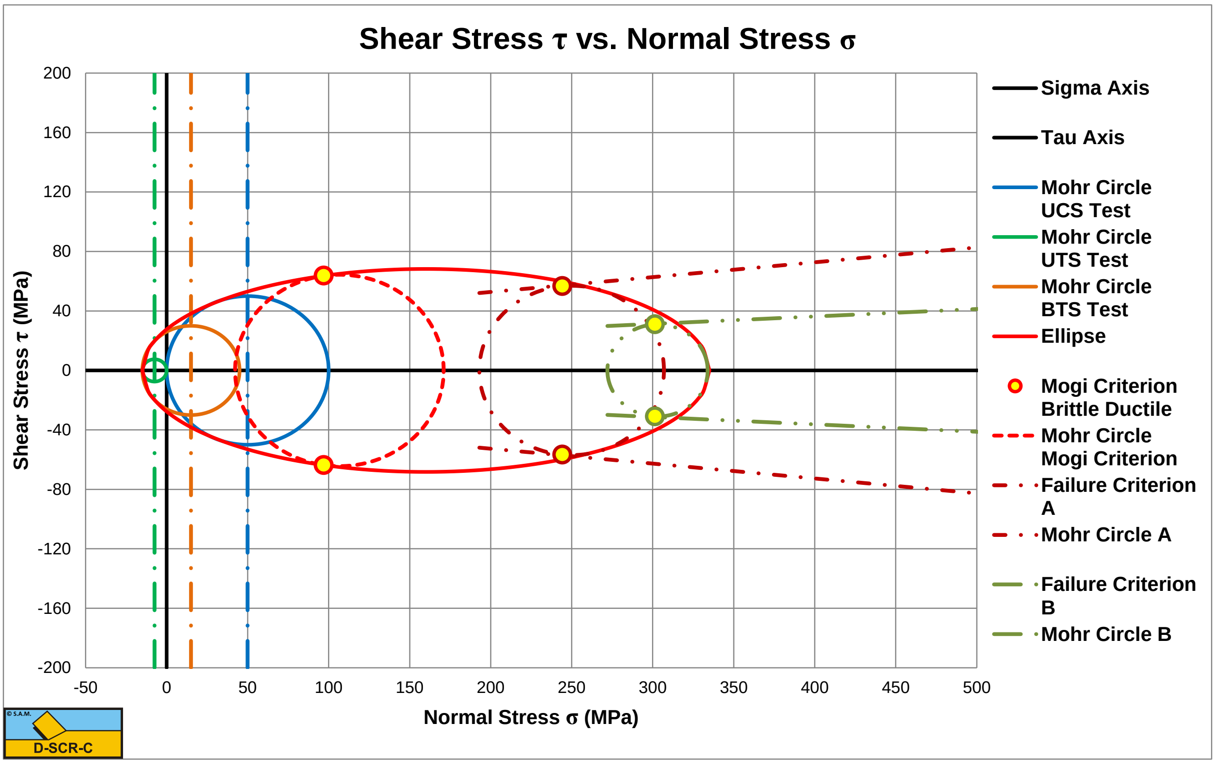

Figure 8-7: Resulting failure curves for Pierre Shale like rocks.

When increasing the bottomhole pressure (confining pressure) from 0 MPa to 50 MPa, first the cutting forces and thus the normal stresses and shear stresses increase up to a maximum, after which the cutting forces decrease, but at a certain bottomhole pressure this decrease stops and the cutting forces increase slightly with further increasing bottomhole pressure. So there was still an internal friction angle, but very small. The bottomhole pressure is a good indication of the confining pressure. The Zijsling (1987) experiments did show that the material was crushed.

It should be mentioned that the layer thickness was very small in these experiments, resulting in a crushed zone reaching to the surface. In other words, the rock was crushed completely.

8.2.1. Some Relations.

The relation between shear strength (cohesion) c, internal friction angle φ and the minimum and maximum principal stresses can be derived according to, using the basic Mohr-Coulomb relations:

$$\tau = c + \sigma \cdot \tan(\varphi) \tag{8-1}$$

And:

$$\tau = \frac{\sigma_{max} - \sigma_{min}}{2} \cdot \cos(\varphi) \qquad \sigma = \frac{\sigma_{max} + \sigma_{min}}{2} - \frac{\sigma_{max} - \sigma_{min}}{2} \cdot \sin(\varphi) \tag{8-2}$$

This gives:

$$\frac{\sigma_{max} - \sigma_{min}}{2} \cdot \cos(\varphi) = c + \left(\frac{\sigma_{max} + \sigma_{min}}{2} - \frac{\sigma_{max} - \sigma_{min}}{2} \cdot \sin(\varphi)\right) \cdot \tan(\varphi) \tag{8-3}$$

Multiplying with **cos(φ)** and reorganizing gives:

$$\frac{\sigma_{max} - \sigma_{min}}{2} \cdot \sin^2(\varphi) + \frac{\sigma_{max} - \sigma_{min}}{2} \cdot \cos^2(\varphi)$$

$$= c \cdot \cos(\varphi) + \frac{\sigma_{max} + \sigma_{min}}{2} \cdot \sin(\varphi)$$

$$\frac{\sigma_{max} - \sigma_{min}}{2} = c \cdot \cos(\varphi) + \frac{\sigma_{max} + \sigma_{min}}{2} \cdot \sin(\varphi) \tag{8-4}$$

$$\sigma_{max} \cdot (1 - \sin(\varphi)) = 2 \cdot c \cdot \cos(\varphi) + \sigma_{min} \cdot (1 + \sin(\varphi))$$

$$\sigma_{max} = \frac{2 \cdot c \cdot \cos(\varphi) + \sigma_{min} \cdot (1 + \sin(\varphi))}{(1 - \sin(\varphi))}$$

This equation can also be written as:

$$\sigma_{max} = \sigma_{min} \cdot \tan^2\left(\frac{\pi}{4} + \frac{\varphi}{2}\right) + 2 \cdot c \cdot \tan\left(\frac{\pi}{4} + \frac{\varphi}{2}\right) \tag{8-5}$$

This relation is valid for all linear failure criteria with a cohesion **c** and an internal friction angle **φ**. Now if two Mohr circles are found with index 1 and 2. Index 1 for the smallest circle and index 2 for the largest circle, the following relation is valid in relation to the failure curve and internal friction angle:

$$\frac{1 + \sin(\varphi)}{1 - \sin(\varphi)} = \frac{\sigma_{max,2} - \sigma_{max,1}}{\sigma_{min,2} - \sigma_{min,1}} = r \tag{8-6}$$

This gives:

$$\sin(\varphi) = \frac{r - 1}{r + 1} \quad \text{and} \quad \cos(\varphi) = \frac{2 \cdot \sqrt{r}}{r + 1} \quad \text{and} \quad \tan(\varphi) = \frac{r - 1}{2 \cdot \sqrt{r}} \tag{8-7}$$

Once the internal friction angle is found, the cohesion can be determined as:

$$c = \frac{UCS}{2}\cdot\left(\frac{1-\sin(\varphi)}{\cos(\varphi)}\right) = \frac{UCS}{2\cdot\sqrt{r}} \tag{8-8}$$

So the Mohr-Coulomb relation is:

$$\tau = \frac{UCS}{2\cdot\sqrt{r}} + \sigma\cdot\frac{r-1}{2\cdot\sqrt{r}} = \frac{UCS+\sigma\cdot(r-1)}{2\cdot\sqrt{r}} \tag{8-9}$$

8.2.2. Brittle versus Ductile.

The terms ductile failure and brittle failure are often used in literature for the failure of materials with shear strength and tensile strength, but what do the words ductile and brittle mean?

> *In materials science, ductility is a solid material's ability to deform under tensile stress; this is often characterized by the material's ability to be stretched into a wire. Malleability, a similar property, is a material's ability to deform under compressive stress; this is often characterized by the material's ability to form a thin sheet by hammering or rolling. Both of these mechanical properties are aspects of plasticity, the extent to which a solid material can be plastically deformed without fracture. Ductility and malleability are not always coextensive – for instance, while gold has high ductility and malleability, lead has low ductility but high malleability. The word ductility is sometimes used to embrace both types of plasticity.*
> *A material is brittle if, when subjected to stress, it breaks without significant deformation (strain). Brittle materials absorb relatively little energy prior to fracture, even those of high strength. Breaking is often accompanied by a snapping sound. Brittle materials include most ceramics and glasses (which do not deform plastically) and some polymers, such as PMMA and polystyrene. Many steels become brittle at low temperatures (see ductile-brittle transition temperature), depending on their composition and processing. When used in materials science, it is generally applied to materials that fail when there is little or no evidence of plastic deformation before failure. One proof is to match the broken halves, which should fit exactly since no plastic deformation has occurred. Generally, the brittle strength of a material can be increased by pressure. This happens as an example in the brittle-ductile transition zone at an approximate depth of 10 kilometers in the Earth's crust, at which rock becomes less likely to fracture, and more likely to deform ductile.*” (Source Wikipedia).

Rock has both shear strength and tensile strength and normally behaves brittle. If the tensile strength is high the failure is based on brittle shear, but if the tensile strength is low the failure is brittle tensile. In both cases chips break out giving it the name **Chip Type**. So rock has true brittle behavior. Under hyperbaric conditions however, the pore under pressures will be significant, helping the tensile strength to keep cracks closed. The result is a much thicker crushed zone that may even reach the surface. Crushing the rock is called cataclastic behavior. Since the whole cutting process is dominated by the crushed zone, this is named the **Crushed Type**. Due to the high pore under pressures the crushed material sticks together and visually looks like a ductile material. That’s the reason why people talk about ductile behavior of hyperbaric rock. In reality it is cataclastic behavior, which could also be named pseudo-ductile behavior.
Now whether the high confining pressure result from a high hyperbaric pressure or from the cutting process itself is not important, in both cases the pseudo-ductile behavior may occur. Figure 8-2 shows the stress-strain behavior typical for brittle and ductile behavior. Based on this stress-strain behavior the term ductile is often used for rock, but as mentioned before this is the result of cataclastic failure.

Gehking (1987) stated that pseudo-ductile behavior will occur when the ratio **UCS/BTS<9**. Brittle behavior will occur when the ratio **UCS/BTS>15**. For **9<UCS/BTS<15** there is a transition between brittle and pseudo-ductile. The geometry of the cutting equipment and the operational conditions are not mentioned by Gehking (1987).

Mogi (1966) found a linear relation between the minimum and maximum principal stress at the transition brittle to pseudo-ductile failure. For sandstone he found $\sigma_{max}=3.4\cdot\sigma_{min}$, and for limestone $\sigma_{max}=4.2\cdot\sigma_{min}$. Those values give an indication, since other researchers found $\sigma_{max}>6\cdot\sigma_{min}$ (Verhoef, 1997). Now assuming $\sigma_{max}=\alpha\cdot\sigma_{min}$ and combining this with Hoek & Brown (1988), gives:

$$\sigma_{\min} = UCS \cdot \frac{m + \sqrt{m^2 + 4 \cdot (\alpha - 1)^2}}{2 \cdot (\alpha - 1)^2}$$

$$\sigma_{\max} = \alpha \cdot UCS \cdot \frac{m + \sqrt{m^2 + 4 \cdot (\alpha - 1)^2}}{2 \cdot (\alpha - 1)^2} \tag{8-10}$$

This gives for the center of the Mohr circle:

$$\sigma_{center} = (\alpha + 1) \cdot \frac{UCS}{2} \cdot \frac{m + \sqrt{m^2 + 4 \cdot (\alpha - 1)^2}}{2 \cdot (\alpha - 1)^2}$$

$$\tau_{\max} = (\alpha - 1) \cdot \frac{UCS}{2} \cdot \frac{m + \sqrt{m^2 + 4 \cdot (\alpha - 1)^2}}{2 \cdot (\alpha - 1)^2} \tag{8-11}$$

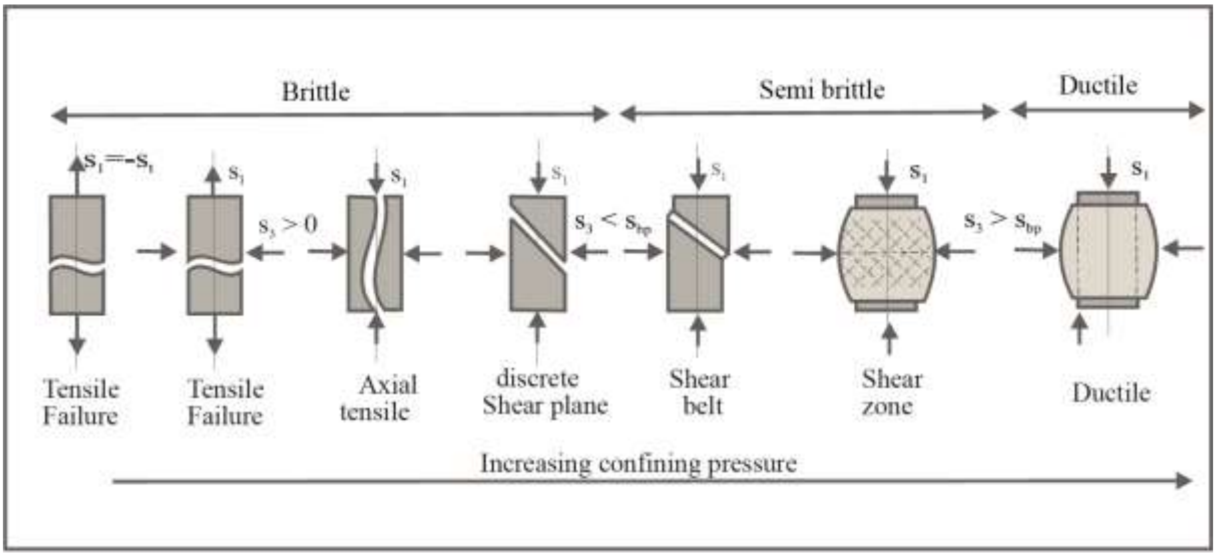

Figure 8-8: Brittle, semi brittle and ductile failure.

Figure 8-17 shows the Mogi criterion both for the top of the Mohr circle curve and the failure curve. Left of the Mogi criterion point there will be brittle failure, on the right there will be pseudo-ductile failure. When the coefficient **α** increases, the Mogi points move to the left.

In the case of a straight failure plane this gives for the normal and shear stress:

$$\sigma = \frac{\frac{c}{\cos(\varphi)} \cdot \left(\frac{\alpha + 1}{\alpha - 1} - \sin(\varphi) \right)}{1 - \frac{\tan(\varphi)}{\cos(\varphi)} \cdot \left(\frac{\alpha + 1}{\alpha - 1} - \sin(\varphi) \right)} \quad \text{and} \quad \tau = c + \sigma \cdot \tan(\varphi) \tag{8-12}$$

Which is also shown in Figure 8-17. If the angle of internal friction is to high, the brittle-ductile transition will never be reached. The criterion for this is:

$$\frac{\alpha - 1}{\alpha + 1} > \sin(\varphi) \tag{8-13}$$

8.2.3. Based on UTS and UCS.

Here a linear envelope tangent to the **UTS** and the **UCS** Mohr circles is assumed, based on the assumption that the failure curve always has to be tangent to at least two Mohr Coulomb circles. This gives for the principal stresses:

$$\sigma_{\min,1} = -\mathbf{UTS}$$

$$\sigma_{\max,1} = 0$$

$$\sigma_{\min,2} = 0 \tag{8-14}$$

$$\sigma_{\max,2} = \mathbf{UCS}$$

$$\mathbf{r} = \frac{\mathbf{UCS} - 0}{0 - -\mathbf{UTS}} = \frac{\mathbf{UCS}}{\mathbf{UTS}} = \mathbf{m}$$

This method results in a rather high value for the internal friction angle and consequently a rather low value for the shear strength (cohesion). To find a good estimate for the internal friction angle, there should be two Mohr circles based on shear failure. In this case one circle is based on shear failure, but the other circle is based on tensile failure. So this method is rejected.

Figure 8-9 shows the Mohr circles for **UTS**, **BTS** and **UCS** for **UCS=100 MPa**, **UTS=BTS=15 MPa**. The resulting angle of internal friction **φ=47.7º**. The transition brittle-ductile according to Mogi (1966) does not exist, the angle of internal friction is too high.

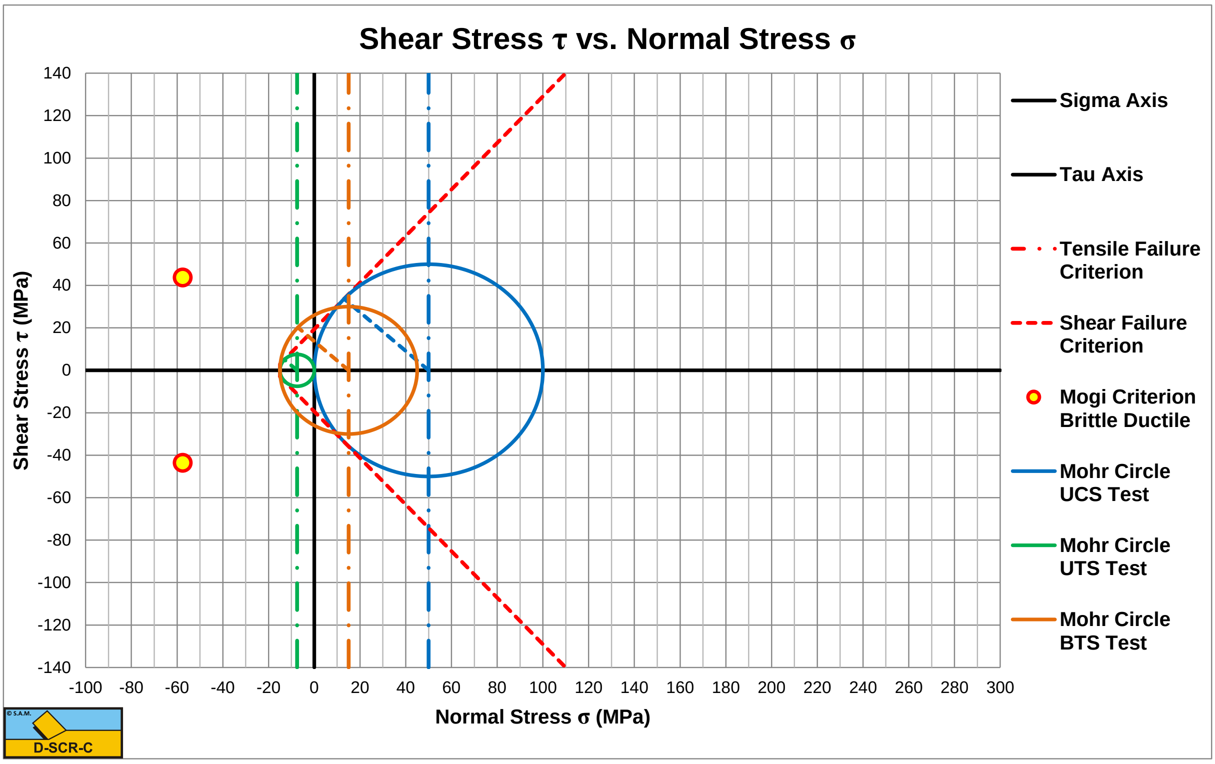

Figure 8-9: Construction of the angle of internal friction UTS-UCS based.

8.2.4. Based on BTS and UCS.

Here a linear envelope tangent to the **BTS** and the **UCS** Mohr circles is assumed, based on the assumption that the failure curve always has to be tangent to at least two Mohr Coulomb circles. This gives for the principal stresses:

$$\sigma_{\min,1} = -\mathbf{BTS}$$

$$\sigma_{\max,1} = 3 \cdot \mathbf{BTS}$$

$$\sigma_{\min,2} = 0 \qquad \textbf{(8-15)}$$

$$\sigma_{\max,2} = \mathbf{UCS}$$

$$\mathbf{r} = \frac{\mathbf{UCS} - 3 \cdot \mathbf{BTS}}{0 - -\mathbf{BTS}} = \frac{\mathbf{UCS} - 3 \cdot \mathbf{BTS}}{\mathbf{BTS}} = \frac{\mathbf{UCS}}{\mathbf{BTS}} - 3 = \mathbf{m} - 3$$

This method results in a rather high value for the internal friction angle and consequently a rather low value for the shear strength (cohesion), although the internal friction angle will be lower than from the first method. To find a good estimate for the internal friction angle, there should be two Mohr circles based on shear failure. In this case one circle is based on shear failure, but the other circle is based on tensile failure. So this method is rejected. Figure 8-10 shows the Mohr circles for **UTS**, **BTS** and **UCS** for **UCS=100 MPa**, **UTS=BTS=15 MPa**. The resulting angle of internal friction **φ=34.8°**. The transition brittle-ductile according to Mogi (1966) is at a normal stress of 316 MPa.

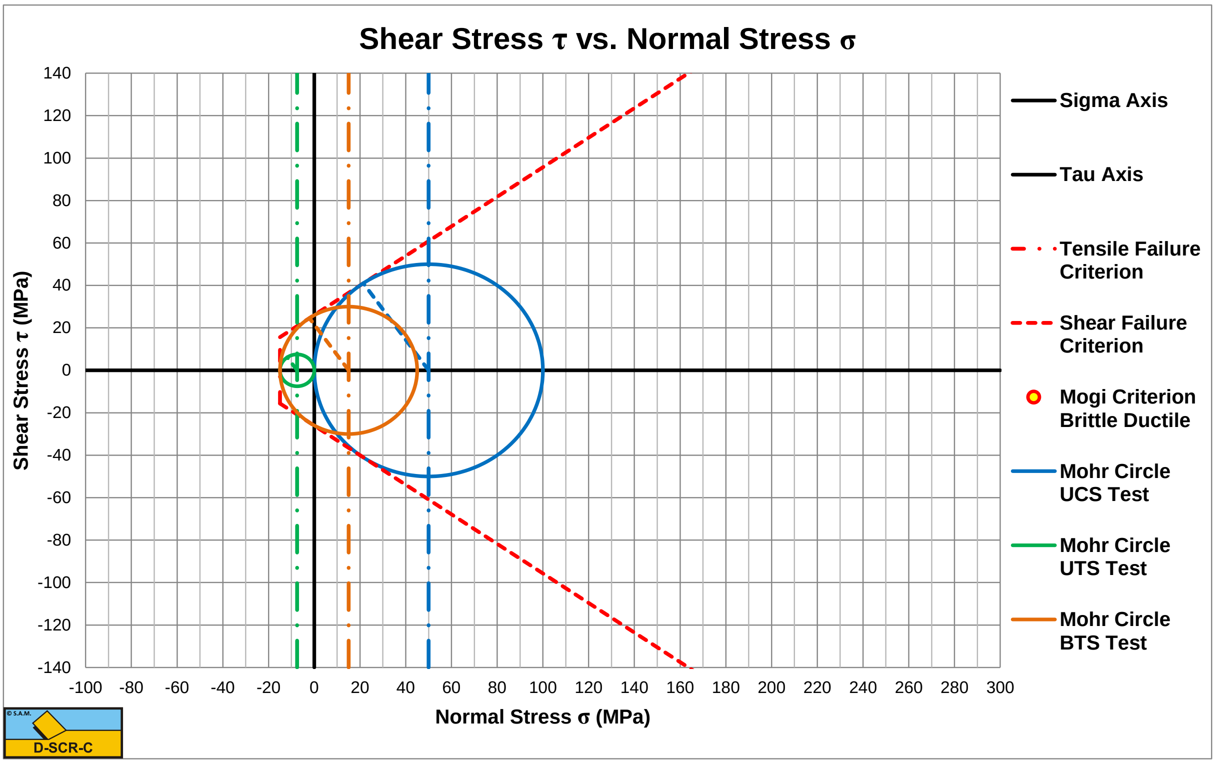

Figure 8-10: Construction of the angle of internal friction BTS-UCS based.

8.2.5. Hoek & Brown (1988).

Over the years Hoek & Brown (1988) developed a failure criterion for rock, based on the **UCS** and **BTS** values of the specific rock. The generalised criterion is empirical and yields:

$$\sigma_{max} = \sigma_{min} + UCS \cdot \left(m \cdot \frac{\sigma_{min}}{UCS} + s \right)^{a} \quad \text{with} \quad \frac{a=0.5}{s=1.0} \quad \text{for intact rock} \tag{8-16}$$

The parameters **m** and **s** are material properties. The parameter **m** is related to the ratio of the **UCS** value to the **BTS** value according to:

$$m = \frac{UCS^{2} - BTS^{2}}{UCS \cdot BTS} \quad \text{for} \quad \frac{BTS}{UCS} \ll 1 \quad m = \frac{UCS}{BTS} \tag{8-17}$$

The parameter **s** is a measure for the amount of fractures in the rock and equals 1 for intact rock. The stresses $\boldsymbol{\sigma_{min}}$ and $\boldsymbol{\sigma_{max}}$ are the minimum and maximum principal stresses of the Mohr circle considered. The **BTS** value can also be represented as a function of **m** and **s** according to:

$$BTS = \frac{UCS}{2} \cdot \left(m - \sqrt{m^{2} + 4 \cdot s} \right) \tag{8-18}$$

Based on:

$$\sigma_{center} = \frac{\sigma_{max} + \sigma_{min}}{2} \quad \text{and} \quad \tau_{max} = \frac{\sigma_{max} - \sigma_{min}}{2} \tag{8-19}$$

An equation can be derived relating the maximum shear stress $\boldsymbol{\tau_{max}}$ (the top of the Mohr circle) to the normal stress at the center of the Mohr circle $\boldsymbol{\sigma_{center}}$.

$$\tau_{max} = \frac{1}{8} \cdot \left(-m \cdot UCS + \sqrt{\left(m \cdot UCS \right)^{2} + 16 \cdot \left(m \cdot UCS \cdot \sigma_{center} + UCS^{2} \right)} \right) \tag{8-20}$$

This equation results in a curve through the tops of the Mohr circles and is not yet a failure criterion. For the failure criterion Hoek & Brown (1988) give the following method; First determine a variable **h** according to:

$$h = 1 + \frac{16 \cdot \left(m \cdot \sigma + s \cdot UCS \right)}{3 \cdot m^{2} \cdot UCS} \tag{8-21}$$

Now an angle **θ** can be determined:

$$\theta = \frac{1}{3} \cdot \left(\frac{\pi}{2} + \operatorname{atan}\left(\frac{1}{\sqrt{h^{3} - 1}} \right) \right) \tag{8-22}$$

Based on the angle **θ** the instantaneous internal friction angle can be determined, which is also the tangent to the failure criterion:

$$\varphi = \operatorname{atan}\left(\frac{1}{\sqrt{4 \cdot h \cdot \cos^{2}(\theta) - 1}} \right) \tag{8-23}$$

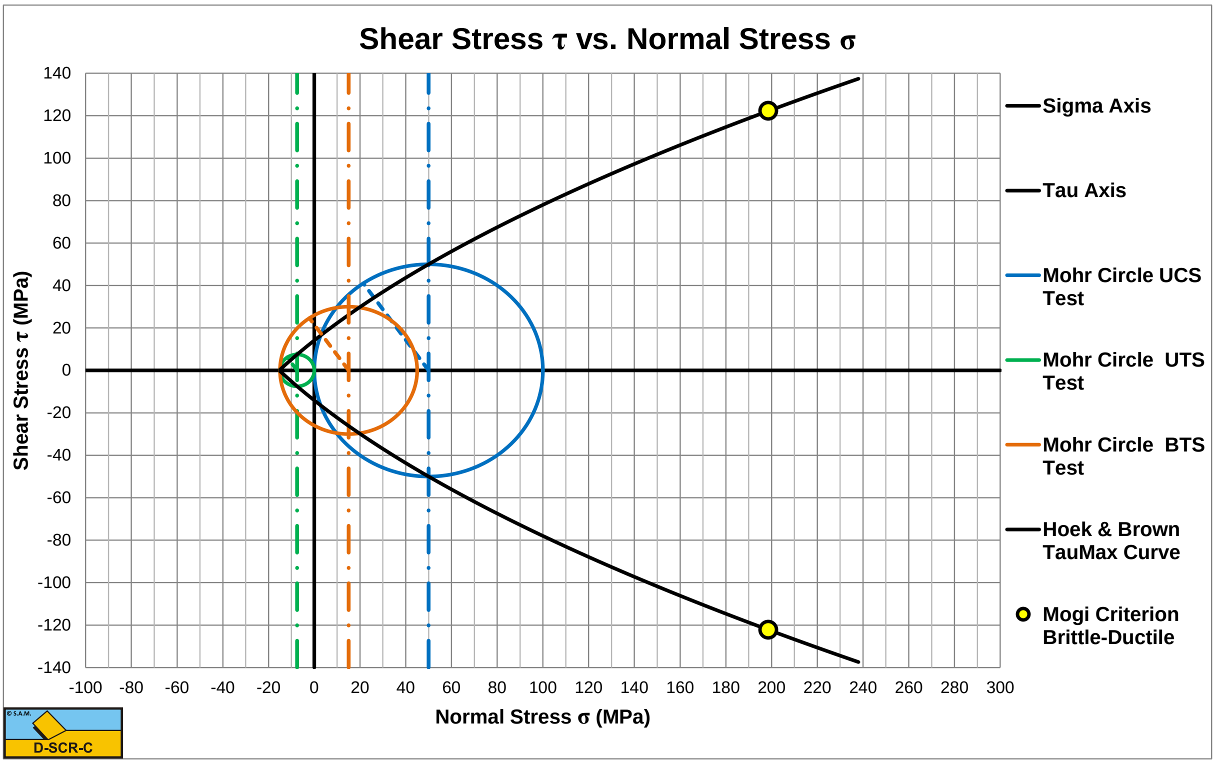

Figure 8-11: Construction Hoek & Brown failure criterion Mohr circles.

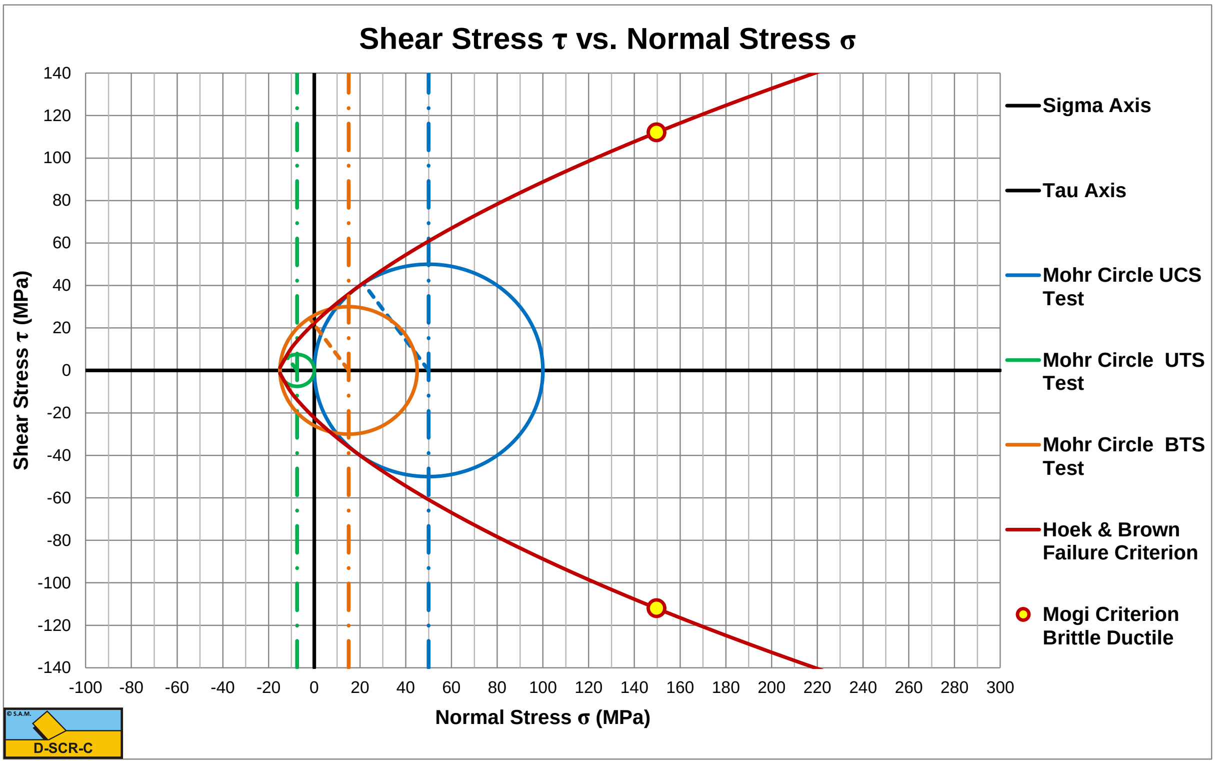

Figure 8-12: Construction Hoek & Brown failure criterion.

Table 8-1: Some m values of Hoek & Brown.

Rock Type	Class	Group	Texture			
			Coarse	Medium	Fine	Very Fine
Sedimentary	Clastic		Conglomerates (21±3) Breccias (19±5)	Sand-Stones (17±4)	Silt-Stones (7±2) Greywackes (18±3)	Clay-Stones (4±2) Shales (6±2) Marls (7±2)
	Non-clastic	Carbonates	Crystalline Limestone (12±3)	Sparitic Limestone (10±2)	Micritic Limestone (9±2)	Dolomites (9±3)
		Evapo-rites		Gypsum (8±2)	Anhy-drite (12±2)	
		Organic				Chalk (7±2)
Metamorphic	Non Foliated		Marble (9±3)	Hornfels (19±4) Meta Sandstone (19±3)	Quartzite (20±3)	
	Slightly Foliated		Migmatites (29±3)	Amphibolites (26±6)		
	Foliated		Gneiss (28±5)	Schists (12±3)	Phyllites (7±3)	Slates (7±4)
Igneous	Pluto-nic	Light	Granite (32±3) Grano-diorite (29±3)	Diorite (25±5)		
		Dark	Gabbro (27±3) Norite (20±5)	Dolerite (16±5)		
	Hypabyssal		Porphyries (20±5)		Diabase (15±5)	Peri-dotite (25±5)
	Volcanic	Lava		Rhyolite (25±5) Andesite (25±5)	Dacite (25±3) Basalt (25±5)	Obsidian (19±3)
		Pyroclastic	Agglo-merate (19±3)	Breccia (19±5)	Tuff (13±5)	

Last but not least, the shear stress **τ**, matching the normal stress **σ** can be determined:

$$\tau = \left(\cot(\varphi) - \cos(\varphi)\right) \cdot \frac{m \cdot UCS}{8} \tag{8-24}$$

A second way of determining the failure criterion curve is with the following two equations, based on the minimum principal stress:

$$\sigma = \sigma_{min} + \frac{UCS}{2} \cdot \sqrt{m \cdot \frac{\sigma_{min}}{UCS} + s} \cdot \left(1 - \frac{m}{m + 4 \cdot \sqrt{m \cdot \frac{\sigma_{min}}{UCS} + s}}\right) \tag{8-25}$$

$$\tau = \frac{UCS}{2} \cdot \sqrt{m \cdot \frac{\sigma_{min}}{UCS} + s} \cdot \sqrt{\left(1 - \left(\frac{m}{m + 4 \cdot \sqrt{m \cdot \frac{\sigma_{min}}{UCS} + s}}\right)^2\right)} \qquad \text{(8-26)}$$

Figure 8-11 and Figure 8-12 show the Hoek & Brown failure criterion for the top of the Mohr circles (A) and for the real failure condition (B). Although still based on **UTS** or **BTS** and **UCS** and not on two tests with shear failure, the resulting failure curve seems more realistic, which seems logic since it is based on many experiments. The Mohr circles for **UTS**, **BTS** and **UCS** are determined for **UCS=100 MPa**, **UTS=BTS=15 MPa**. The transition brittle-ductile according to Mogi (1966) is at a normal stress of 150 MPa.
Taking an average internal friction angle from a normal stress of zero to a normal stress of 240 MPa gives **φ=27.1º**.

8.2.6. Parabolic Envelope UTS and UCS.

Based on the **UTS** or **BTS** and the **UCS** a parabole can be constructed of the normal stress as a function of the shear stress, with boundary conditions that the parabole goes through the **UTS** or **BTS** point (shear stress equals zero, normal stress equals **-UTS** or **-BTS** and derivative **dσ/dτ** equals zero) and touches the UCS Mohr circle as a tangent. With **m=UCS/UTS** or **m=UCS/BTS** the equation of this parabole is:

$$\sigma = \frac{1}{UTS \cdot \left(\sqrt{m+1}-1\right)^{2}} \cdot \tau^{2} - UTS \tag{8-27}$$

It is more convenient to write this equation in the form where the shear stress is a function of the normal stress, giving:

$$\tau^{2} = UTS \cdot \left(\sqrt{m+1}-1\right)^{2} \cdot \left(\sigma + UTS\right) \tag{8-28}$$

Figure 8-13 shows the resulting parabole. Although still based on **UTS** or **BTS** and **UCS** and not on two tests with shear failure, the resulting failure curve seems more realistic. The Mohr circles for **UTS**, **BTS** and **UCS** are determined for **UCS=100 MPa**, **UTS=BTS=15 MPa**. The transition brittle-ductile according to Mogi (1966) is at a normal stress of 104 MPa. Taking an average internal friction angle from a normal stress of zero to a normal stress of 240 MPa gives **φ=18.6º**.

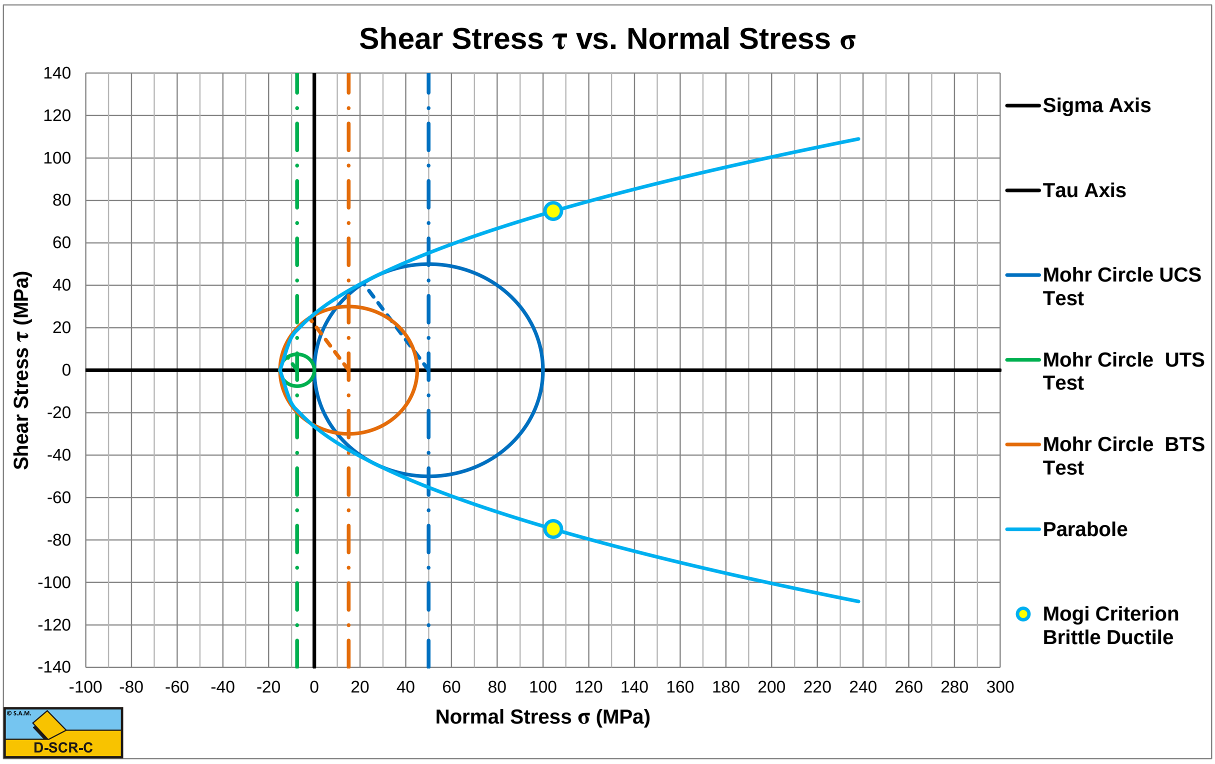

Figure 8-13: The parabolic failure criterion.

8.2.7. Ellipsoid Envelope UTS and UCS.

Instead of a parabole, also an ellipse can be used. The advantage of an ellipse is that it gives more flexibility for the shape of the failure envelope. The general equation for an ellipse is:

$$\frac{\left(\sigma-\left(a-UTS\right)\right)^{2}}{a^{2}}+\frac{\tau^{2}}{b^{2}}=1 \tag{8-29}$$

In order to find an estimate for the radii **a** and **b**, it is assumed that the ellipse also touches the **UCS** Mohr circle in the same point as the parabole. With:

$$f=\frac{1}{UTS\cdot\left(\sqrt{m+1}-1\right)^{2}} \tag{8-30}$$

This gives for the normal stress of the parabole to Mohr circle tangent point:

$$\sigma_{p}=\frac{-\left(1-f\cdot UCS\right)+\sqrt{\left(1-f\cdot UCS\right)^{2}+4\cdot f\cdot UTS}}{2\cdot f} \tag{8-31}$$

And for the shear stress at the tangent point:

$$\tau_{p}^{2}=UTS\cdot\left(\sqrt{m+1}-1\right)^{2}\cdot\left(\sigma_{p}+UTS\right) \tag{8-32}$$

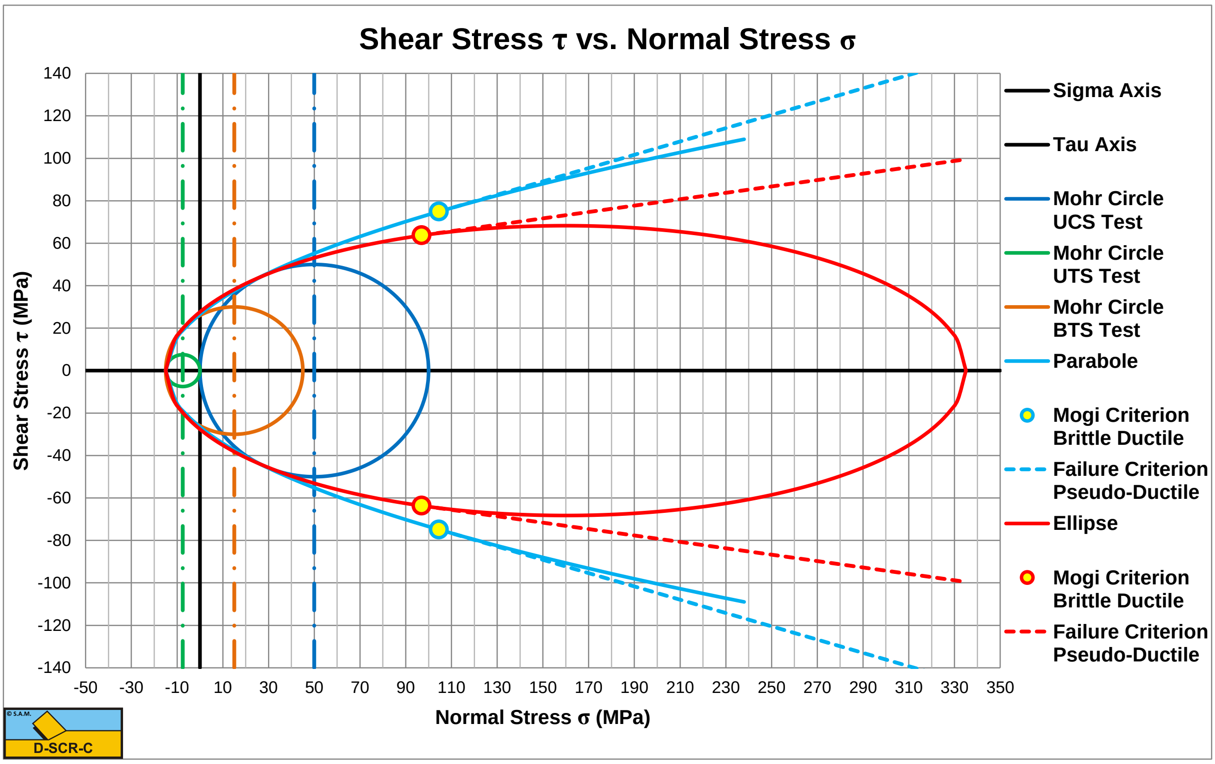

Figure 8-14: The Parabolic and Ellipsoid failure envelopes, with a=1.75·UCS.

Comment: For sandstone a residual internal friction angle of 15 degrees and for limestone 25 degrees have been found at the brittle-ductile transition points.

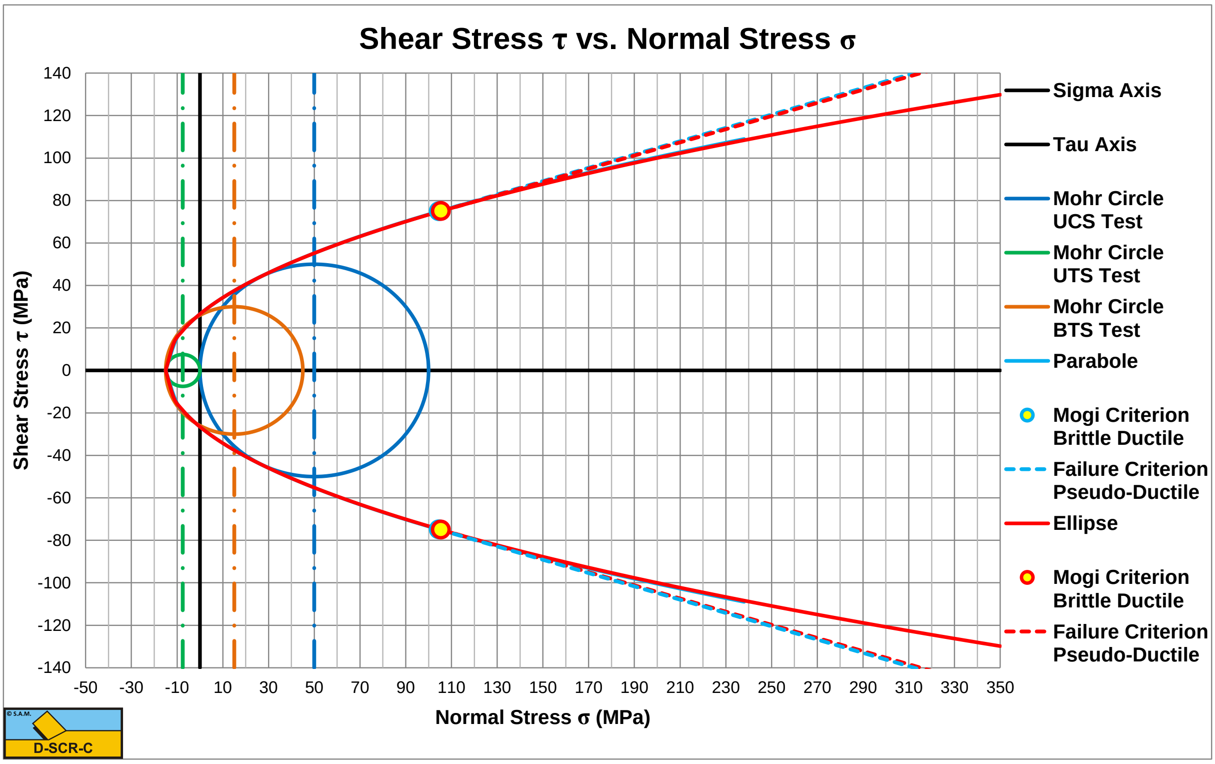

Figure 8-15 The Parabolic and Ellipsoid failure envelopes, with a=100·UCS.

For a given radius **a** this gives:

$$\mathbf{b^2 = \frac{\tau_p^2}{\left(1 - \frac{\left(\sigma_p - (a - UTS)\right)^2}{a^2}\right)}} \qquad \mathbf{(8\text{-}33)}$$

Figure 8-14 shows both the parabolic and the ellipsoid failure envelopes. The ellipsoid failure envelope is determined for **a=1.75·UCS**. The Mohr circles for **UTS**, **BTS** and **UCS** are determined for **UCS=100 MPa**, **UTS=BTS=15 MPa**. At low normal stresses the parabolic and ellipsoid failure envelopes behave almost identical. Also the Mogi brittle-ductile transition points are very close. Chosing **a>10·UCS** gives about identical envelopes in the normal stress range considered.

8.2.8. Linear Failure Criterion.

The best way to determine the angle of internal friction is to execute at least two tests with different confining pressures in the range of normal stresses the cutting process is expected to operate. Figure 8-16 shows this for a **φ=20º** internal friction angle. The Mohr circles for **UTS**, **BTS** and **UCS** are determined for **UCS=100 MPa**, **UTS=BTS=15 MPa**. The transition brittle-ductile according to Mogi (1966) is at a normal stress of 95 MPa.

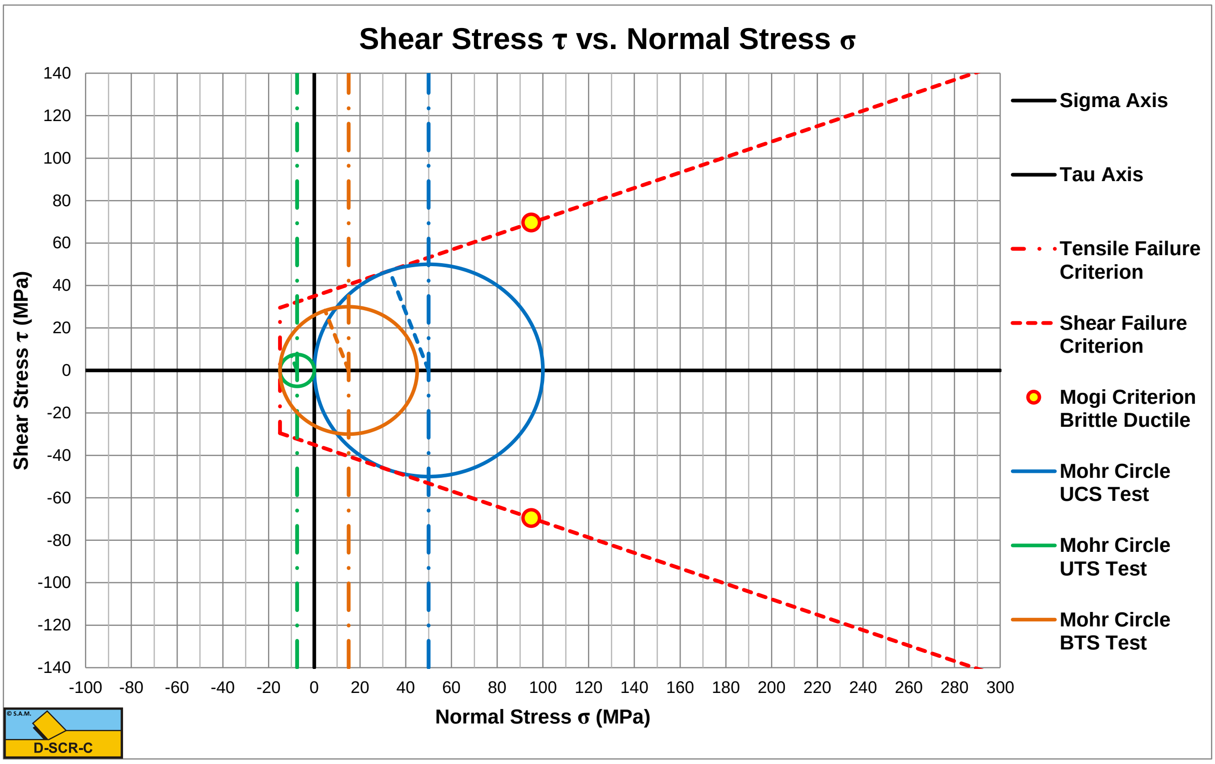

Figure 8-16: The linear failure criterion.

8.2.9. The Griffith (Fairhurst, 1964) Criterion.

Griffith (Fairhurst, 1964) has derived a criterion for brittle failure. His hypothesis aasumes that fracture occurs by rapid extension of sub-microscopic. Pre-existing flaws, randomly distributed throughout the material. He defined two criteria. The first criterion is:

$$3 \cdot \sigma_{min} + \sigma_{max} \le 0$$

$$-3 \cdot UTS + \sigma_{max} \le 0 \quad or \quad \sigma_{max} \le 3 \cdot UTS \tag{8-34}$$

$$-3 \cdot BTS + \sigma_{max} \le 0 \quad or \quad \sigma_{max} \le 3 \cdot BTS$$

Failure will occur when **σ_{min}=-UTS** or **σ_{min}=-BTS**, which is satisfied in the Brazilian split test. However when:

$$3 \cdot \sigma_{min} + \sigma_{max} > 0 \tag{8-35}$$

Failure will occur when:

$$\left(\sigma_{max} - \sigma_{min}\right)^2 - 8 \cdot UTS \cdot \left(\sigma_{max} + \sigma_{min}\right) = 0 \tag{8-36}$$

With:

$$\left(\frac{\sigma_{max}-\sigma_{min}}{2}\right)^2 = 4 \cdot UTS \cdot \left(\frac{\sigma_{max}+\sigma_{min}}{2}\right) \tag{8-37}$$

This can be written as a parabole for the center of the Mohr circles:

$$\tau_{max}^2 = 4 \cdot UTS \cdot \sigma_{center} \tag{8-38}$$

For a **UCS** test this gives:

$$\left(\frac{UCS}{2}\right)^2 = 4 \cdot UTS \cdot \frac{UCS}{2} \quad \text{or} \quad \frac{UCS}{UTS} = 8 \tag{8-39}$$

If the **UCS/UTS** or **UCS/BTS** ratio is larger than 8, brittle failure will occur.

The Griffith criterion as mentioned here is not the failure curve, but the curve connecting the tops of the Mohr circles.
In the original articles tensile is positive and compression negative, resulting in a sign change compared with the equations mentioned here. Als the minimum and maximum principal stresses were reversed.

8.2.10. Conclusions & Discussion.

6 concepts for the angle of internal friction and the failure criteria have been discussed. Figure 8-14 and Figure 8-17 show these criteria. To find the best failure criterion curve, many tests should be carried out at different confining pressures, resulting in shear failure and a set of Mohr circles. Since this information is not always available, The Hoek & Brown, Parabole or Ellipse approximations can be used. The preference of the author is the Ellipse Envelope method or the Linear Failure Criterion method, where the internal friction angle is based on the average of the Parabole Envelope method or measured by experiments.

Above the brittle-ductile transition normal stress, the failure curve will decrease according to Verhoef (1997), based on research of van Kesteren (1995). As mentioned before, at higher stress situations there will be fracturing and crushing. This results in a decrease of the angle of internal friction. The higher the normal stresses, the stronger the fracturing and crushing, the smaller the angle of internal friction. When this starts there is a decrease of the angle of internal friction, while the failure curve is still increasing. However at a certain stress situation the failure curve may be at a maximum, since the angle of internal friction decreases to much. This maximum is often close to the Mogi (1966) criterion. Since intact rock and crushed rock are two different materials with different properties, one has to be very carefull with the interpretation of the resulting failure curve. In fact the material has continuously changing properties from the moment is starts fracturing and crushing. First larger particles are formed, consisting of many rock grains. When the stresses increase, these particles will also be fractured or crushed, resulting in smaller particles, until the rock grains are left.

When the angle of internal friction decreases faster than the increase of normal stresses, the failure curve decreases. This does however not mean that there is negative internal friction, normally the tangent to the failure curve. Just that the angle of internal friction decreases faster than the increase of normal stresses and most probably that the shear strength of the crushed rock decreases to zero. Verhoef (1997) and Vlasblom (2003-2007) show a failure curve reducing to zero for very high normal stresses. This seems to be unlikely to happen. It would imply that at very high normal stresses the shear stress equals zero, so no friction at al, which sounds like liquid behavior. It is more likely that the crushed rock, once completely crushed, will have a residual internal friction angle and possibly a residual shear strength. The latter is possible, for example when the particles are so small that van der Waals forces start playing a role. But this will depend completely on the type and composition of the rock.
Figure 8-14 shows a residual internal friction angle for both the ellipse and the parabole, tangent to the failure envelopes at the Mogi brittle-criterion.

For the models derived in this chapter, a constant internal friction angle is assumed, where this constant internal friction angle should match the stress state of the cutting process considered.

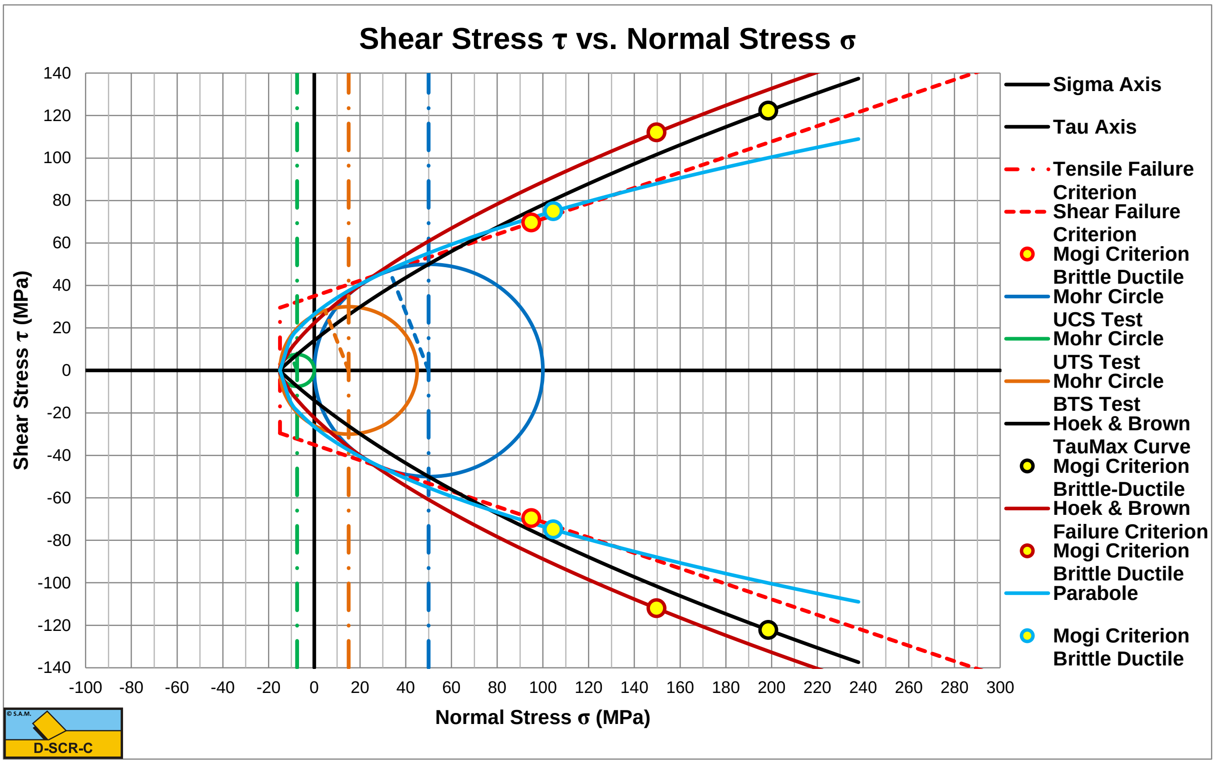

Figure 8-17: The failure criteria.

8.3. Cutting Models.

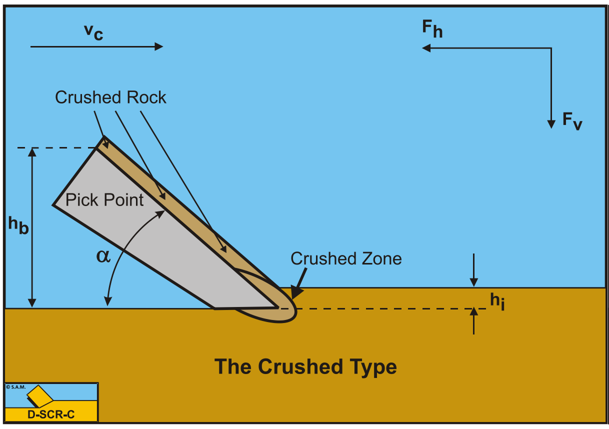

Figure 8-18: The Crushed Type.

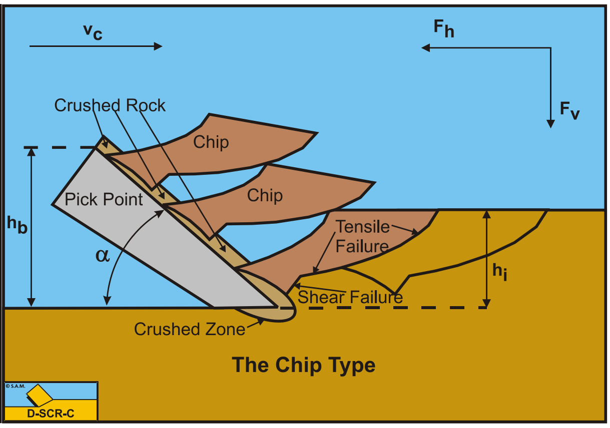

Figure 8-19: The Chip Type.

When cutting rock with a pick point, usually a crushed zone will occur in front of and under the tip of the pick point. If the cutting depth is small, this crushed zone may reach the surface and a sand like cutting process may occur. If the cutting depth is larger, the crushed material cannot escape and the stresses in the crushed zone increase strongly. According to Fairhurst (1964) the cutting forces are transmitted through particle-particle contacts. The stresses are transmitted to the intact rock as discrete point loads this way, causing micro shear cracks and finally a tensile crack. Figure 8-18 and Figure 8-19 sho this cutting mechanism.

As mentioned the type of failure depends on the UCS/BTS ratio. Geking (1987) stated that below a ratio of 9 ductile failure will occur, while above a ratio of 15 brittle failure will occur. In between these limits there is a transition between ductile and brittle failure, which is also in accordance with the findings of Fairhurst (1964).

The mechanism as described above is difficult to model. Still a method is desired to predict the cutting forces in rock cutting in order to estimate forces, power and production. In literature some models exist, like the Evans (1964) model based on tensile failure and the Nishimatsu (1972) model based on shear failure. From steel cutting also the Merchant (1944) model is known, based on plastic shear failure. The Evans (1964) model assumes a maximum tensile stress on the entire failure plane, which could match the peak forces, but overestimates the average forces. Nishimatsu (1972) build in a factor for the shear stress distribution on the failure plane, enabling the model to take into account that failure may start when the shear stress is not at a maximum everywhere in the shear plane. Both models are discussed in this chapter.

Based on the Merchant (1944) model for steel cutting and the Miedema (1987 September) model for sand cutting, a new model is developed, both for ductile cutting, ductile cataclastic cutting, brittle shear cutting and brittle tensile cutting. First a model is derived for the **Flow Type**, which is either ductile shear failure or brittle shear failure. In the case of brittle shear failure, the maximum cutting forces are calculated. For the average cutting forces the maximum cutting forces have to be reduced by 30% to 50%. Based on the **Flow Type** and the Mohr circle, the shear stress in the shear plane is determined where, on another plane (direction), tensile stresses occur equal to the tensile strength. An equivalent or mobilized shear strength is determined giving this tensile stress, leading to the **Tear Type** of failure. This approach does not require the tensile stress to be equal to the tensile strength on the whole failure plane, instead it predicts the cutting forces at the start of tensile failure.

This method can also be used for predicting the cutting forces in frozen clay, permafrost.

Roxborough (1987) derived a simple expression for the specific energy based on many experiments in different types of rock. The dimension of this equation is MPa. The two constants in the equation may vary a bit depending on the type of rock. The 0.11 is important at small UCS values, the 0.25 at large values.

$$E_{sp} = 0.25 \cdot U.C.S. + 0.11 \qquad (8\text{-}40)$$

The fact that cutting rock is irreversible, compared to the cutting of sand and clay, also means that the 4 standard cutting mechanisms cannot be applied on cutting rock. In fact the **Flow Type** looks like cataclastic ductile failure from a macroscopic point of view, but the **Flow Type** (also the **Curling Type**) are supposed to be real plastic deformation after which the material (clay) is still in tact, while cataclastic ductile failure is much more the crushing of the rock with shear falure in the crushed rock. We will name this the **Crushed Type**. When the layer cut is thicker, a crushed zone exists but not to the free surface. From the crushed zone first a shear plane is formed from which a tensile crack goes to the free surface. We will name this the **Chip Type**.

8.3.1. The Model of Evans.

For **brittle rock** the cutting theory of Evans (1964) and (1966) can be used to calculate cutting forces (Figure 8-21). The forces are derived from the geometry of the chisel (width, cutting angle and cutting depth) and the tensile strength (BTS) of the rock. Evans suggested a model on basis of observations on coal breakage by wedges. In this theory it is assumed that:

1. A force **R** is acting under an angle **δ** (external friction angle) with the normal to the surface **A-C** of the wedge.
2. A resultant force **T** of the tensile stresses acting at the center of the arc **C-D**, the line **C-D** is under an angle **β** (the shear angle) with the horizontal.
3. A third force **S** is required to maintain equilibrium in the buttock, but does not play a role in the derivation.
4. The penetration of the wedge is small compared to the layer thickness $\mathbf{h_i}$.

The action of the wedge tends to split the rock and does rotate it about point **D**. It is therefore assumed that the force **S** acts through point **D**. Along the fracture line, it is assumed that a state of plain strain is working and the equilibrium is considered per unit of width **w** of the wedge.

The force due to the tensile strength $\mathbf{\sigma_T}$ of the rock is:

$$\mathbf{T = \sigma_T \cdot r \cdot \int_{-\beta}^{\beta} \cos(\omega) \cdot d\omega \cdot w = 2 \cdot \sigma_T \cdot r \cdot \sin(\beta) \cdot w} \tag{8-41}$$

Where **r·dω** is an element of the arc **C-D** making an angle **ω** with the symmetry axis of the arc. Let $\mathbf{h_i}$ be the depth of the cut and assume that the penetration of the edge may be neglected in comparison with $\mathbf{h_i}$. This means that the force **R** is acting near point **C**. Taking moments on the chip cut about point **D** gives:

$$\mathbf{R \cdot \cos(\alpha+\beta+\delta) \cdot \frac{h_i}{\sin(\beta)} = T \cdot r \cdot \sin(\beta) = 2 \cdot \sigma_T \cdot r \cdot \sin(\beta) \cdot w \cdot r \cdot \sin(\beta)} \tag{8-42}$$

From the geometric relation it follows:

$$\mathbf{r \cdot \sin(\beta) = \frac{h_i}{2 \cdot \sin(\beta)}} \tag{8-43}$$

Hence:

$$\mathbf{R = \frac{\sigma_T \cdot h_i \cdot w}{2 \cdot \sin(\beta) \cdot \cos(\alpha+\beta+\delta)}} \tag{8-44}$$

The horizontal component of **R** is **R·sin(α+δ)** and due to the symmetry of the forces acting on the wedge the total cutting force is:

$$\mathbf{F_c = 2 \cdot R \cdot \sin(\alpha+\delta) = \sigma_T \cdot h_i \cdot w \cdot \frac{\sin(\alpha+\delta)}{\sin(\beta) \cdot \cos(\alpha+\beta+\delta)}} \tag{8-45}$$

The normal force (⊥ on cutting force) is per side:

$$\mathbf{F_n = R \cdot \cos(\alpha+\delta) = \sigma_T \cdot h_i \cdot w \cdot \frac{\cos(\alpha+\delta)}{2 \cdot \sin(\beta) \cdot \cos(\alpha+\beta+\delta)}} \tag{8-46}$$

The angle **β** can be determined by using the principle of minimum energy:

$$\mathbf{\frac{dF_c}{d\beta} = 0} \tag{8-47}$$

Giving:

$$\cos(\beta)\cdot\cos(\alpha+\beta+\delta)-\sin(\beta)\cdot\sin(\alpha+\beta+\delta)=0$$

$$\Rightarrow\quad \cos(2\cdot\beta+\alpha+\delta)=0 \qquad (8\text{-}48)$$

Resulting in:

$$\beta=\frac{1}{2}\cdot\left(\frac{\pi}{2}-\alpha-\delta\right)=\frac{\pi}{4}-\frac{\alpha+\delta}{2} \qquad (8\text{-}49)$$

With:

$$\sin(\beta)\cdot\cos(\alpha+\beta+\delta)=\frac{1-\sin(\alpha+\delta)}{2} \qquad (8\text{-}50)$$

This gives for the horizontal cutting force:

$$F_c=\sigma_T\cdot h_i\cdot w\cdot\frac{2\cdot\sin(\alpha+\delta)}{1-\sin(\alpha+\delta)}=\sigma_T\cdot h_i\cdot w\cdot\lambda_{HT} \qquad (8\text{-}51)$$

For each side of the wedge the normal force is now (the total normal/vertical force is zero):

$$F_n=\sigma_T\cdot h_i\cdot w\cdot\frac{\cos(\alpha+\delta)}{1-\sin(\alpha+\delta)}=\sigma_T\cdot h_i\cdot w\cdot\lambda_{VT} \qquad (8\text{-}52)$$

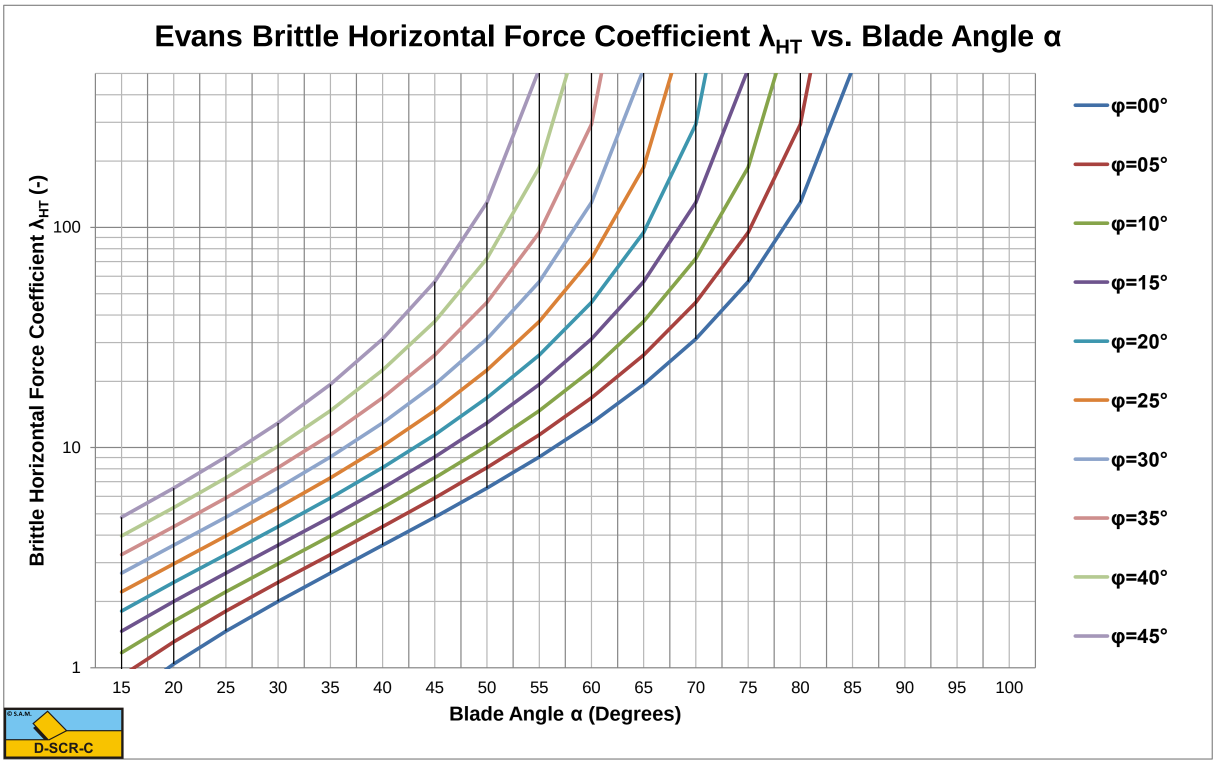

Figure 8-20: The brittle-tear horizontal force coefficient λ_{HT} (Evans).

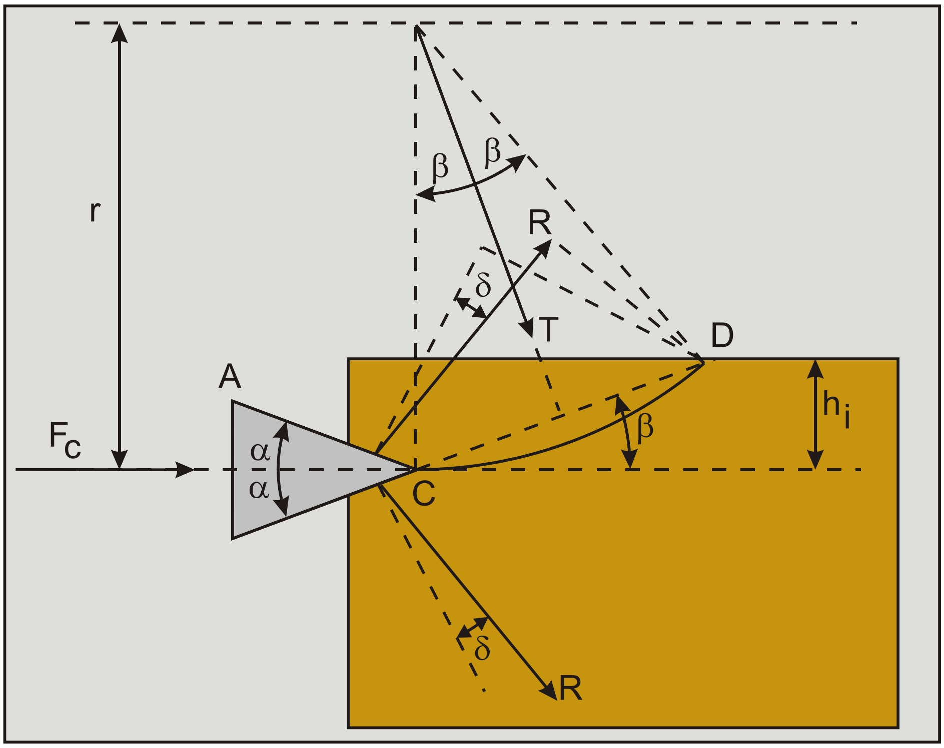

Figure 8-21: The model of Evans.

Figure 8-20 shows the brittle-tear horizontal force coefficient λ_{HT} as a function of the wedge top angle **α** and the internal friction angle **φ**. The internal friction angle **φ** does not play a role directly, but it is assumed that the external friction angle **δ** is 2/3 of the internal friction angle **φ**. Comparing Figure 8-20 with Figure 8-42 (the brittle-tear horizontal force coefficient λ_{HT} of the Miedema model) shows that the coefficient λ_{HT} of Evans is bigger than the λ_{HT} coefficient of Miedema. The Miedema model however is based on cutting with a blade, while Evans is based on the penetration with a wedge or chisel, which should give a higher cutting force. The model as is derived in chapter 8.3 assumes sharp blades however.

8.3.2. The Model of Evans under an Angle ε.

When it is assumed that the chisel enters the rock under an angle **ε** and the fracture starts in the same direction as the centerline of the chisel as is shown in Figure 8-22, the following can be derived:

$$h = 2 \cdot r \cdot \sin(\beta) \cdot \sin(\beta - \varepsilon) \quad \text{and} \quad h_i = 2 \cdot r \cdot \sin^2(\beta) \tag{8-53}$$

$$h_i = h \cdot \frac{\sin(\beta)}{\sin(\beta - \varepsilon)} \tag{8-54}$$

Substituting equation (8-53) in equation (8-45) for the cutting force gives:

$$\begin{aligned} F_c &= \sigma_T \cdot h_i \cdot w \cdot \frac{2 \cdot \sin(\alpha + \delta)}{1 - \sin(\alpha + \delta)} \\ &= \sigma_T \cdot h \cdot w \cdot \frac{\sin(\beta)}{\sin(\beta - \varepsilon)} \cdot \frac{\sin(\alpha + \delta)}{\sin(\beta) \cdot \cos(\alpha + \beta + \delta)} \\ &= \sigma_T \cdot h \cdot w \cdot \frac{\sin(\alpha + \delta)}{\sin(\beta - \varepsilon) \cdot \cos(\alpha + \beta + \delta)} \end{aligned} \tag{8-55}$$

The horizontal component of the cutting force is now:

$$F_{ch} = \sigma_T \cdot h \cdot w \cdot \frac{\sin(\alpha+\delta)}{\sin(\beta-\varepsilon)\cdot\cos(\alpha+\beta+\delta)}\cdot\cos(\varepsilon) \tag{8-56}$$

The vertical component of this cutting force is now:

$$F_{cv} = \sigma_T \cdot h \cdot w \cdot \frac{\sin(\alpha+\delta)}{\sin(\beta-\varepsilon)\cdot\cos(\alpha+\beta+\delta)}\cdot\sin(\varepsilon) \tag{8-57}$$

Note that the vertical force is not zero anymore, which makes sense since the chisel is not symmetrical with regard to the horizontal anymore. Equation (8-58) can be applied to eliminate the shear angle β from the above equations. When the denominator is at a maximum in these equations, the forces are at a minimum. The denominator is at a maximum when the first derivative of the denominator is zero and the second derivative is negative.

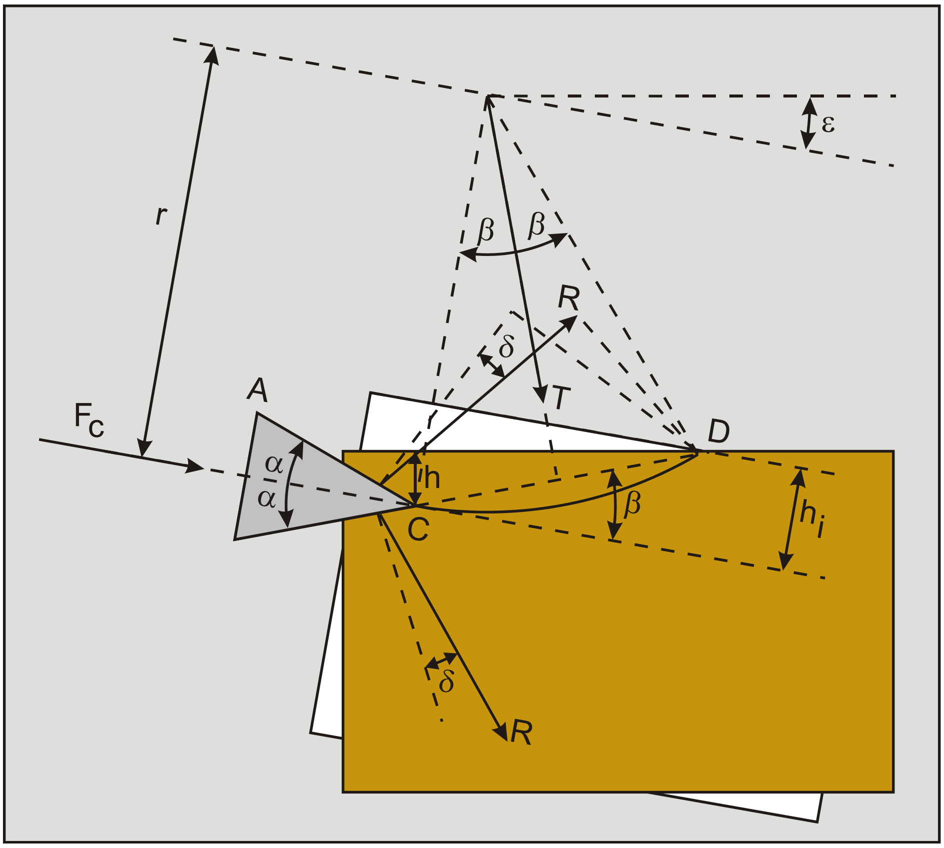

Figure 8-22: The model of Evans under an angle ε.

The angle **β** can be determined by using the principle of minimum energy:

$$\frac{dF_c}{d\beta} = 0 \tag{8-58}$$

Giving for the first derivative:

$$\begin{gathered}\cos(\beta-\varepsilon)\cdot\cos(\alpha+\beta+\delta)-\sin(\beta-\varepsilon)\cdot\sin(\alpha+\beta+\delta)=0\\ \Rightarrow\ \cos(2\cdot\beta+\alpha+\delta-\varepsilon)=0\end{gathered} \tag{8-59}$$

Resulting in:

$$\beta = \frac{1}{2}\cdot\left(\frac{\pi}{2} - \alpha - \delta + \varepsilon\right) = \frac{\pi}{4} - \frac{\alpha + \delta - \varepsilon}{2} \tag{8-60}$$

With:

$$\sin(\beta - \varepsilon)\cdot\cos(\alpha + \beta + \delta) = \frac{1 - \sin(\alpha + \delta + \varepsilon)}{2} \tag{8-61}$$

Substituting equation (8-61) in equation (8-55) gives for the force $\mathbf{F_c}$:

$$F_c = \sigma_T \cdot h \cdot w \cdot \frac{2\cdot\sin(\alpha + \delta)}{1 - \sin(\alpha + \delta + \varepsilon)} \tag{8-62}$$

The horizontal component of the cutting force $\mathbf{F_{ch}}$ is now:

$$F_{ch} = \sigma_T \cdot h \cdot w \cdot \frac{2\cdot\sin(\alpha + \delta)}{1 - \sin(\alpha + \delta + \varepsilon)}\cdot\cos(\varepsilon) \tag{8-63}$$

The vertical component of this cutting force $\mathbf{F_{cv}}$ is now:

$$F_{cv} = \sigma_T \cdot h \cdot w \cdot \frac{2\cdot\sin(\alpha + \delta)}{1 - \sin(\alpha + \delta + \varepsilon)}\cdot\sin(\varepsilon) \tag{8-64}$$

8.3.3. The Model of Evans used for a Pick point.

In the case where the angle $\boldsymbol{\varepsilon}$ equals the angle $\boldsymbol{\alpha}$, a pick point with blade angle $\mathbf{2\cdot\alpha}$ and a wear flat can be simulated as is shown in Figure 8-23. In this case the equations become:

$$F_c = \sigma_T \cdot h \cdot w \cdot \frac{2\cdot\sin(\alpha + \delta)}{1 - \sin(2\cdot\alpha + \delta)} \tag{8-65}$$

The horizontal component of the cutting force $\mathbf{F_{ch}}$ is now:

$$F_{ch} = \sigma_T \cdot h \cdot w \cdot \frac{2\cdot\sin(\alpha + \delta)}{1 - \sin(2\cdot\alpha + \delta)}\cdot\cos(\alpha) \tag{8-66}$$

The vertical component of this cutting force $\mathbf{F_{cv}}$ is now:

$$F_{cv} = \sigma_T \cdot h \cdot w \cdot \frac{2\cdot\sin(\alpha + \delta)}{1 - \sin(2\cdot\alpha + \delta)}\cdot\sin(\alpha) \tag{8-67}$$

For the force **R** (see equation (8-45)), acting on both sides of the pick point the following equation can be found:

$$R = \frac{F_c}{2\cdot\sin(\alpha + \delta)} = \sigma_T \cdot h \cdot w \cdot \frac{1}{1 - \sin(2\cdot\alpha + \delta)} \tag{8-68}$$

In the case of wear calculations the normal and friction forces on the front side and the wear flat can be interesting. According to Evans the normal and friction forces are the same on both sides, since this was the starting point of the derivation, this gives for the normal force $\mathbf{R_n}$:

$$\mathbf{R_n = \sigma_T \cdot h \cdot w \cdot \frac{1}{1 - \sin(2 \cdot \alpha + \delta)} \cdot \cos(\delta)} \tag{8-69}$$

The friction force $\mathbf{R_f}$ is now:

$$\mathbf{R_f = \sigma_T \cdot h \cdot w \cdot \frac{1}{1 - \sin(2 \cdot \alpha + \delta)} \cdot \sin(\delta)} \tag{8-70}$$

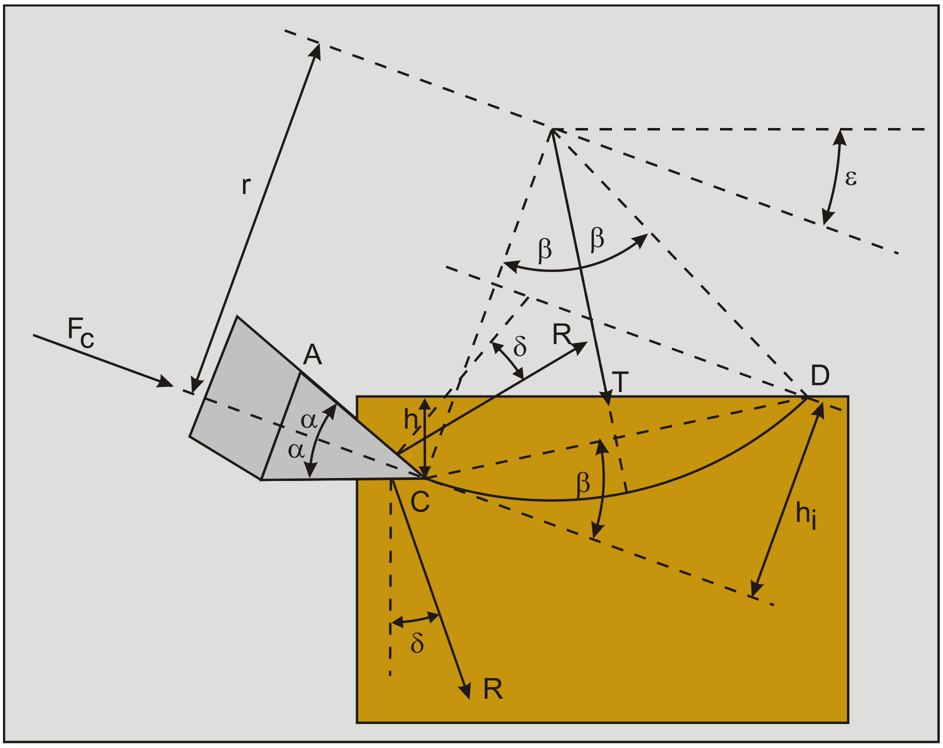

Figure 8-23: The model of Evans used for a pick point.

8.3.4. Summary of the Evans Theory.

The Evans theory has been derived for 3 cases:
1. The basic case with a horizontal moving chisel and the centerline of the chisel horizontal.
2. A horizontal moving chisel with the centerline under an angle **ε**.
3. A pick point with the centerline angle **ε** equal to half the top angle **α**, horizontally moving.

Once again it should be noted that the angle **α** as used by Evans is half the top angle of the chisel and not the blade angle as **α** is used for in most equations in this book. In case 1 the blade angle would be **α** as used by Evans, in case 2 the blade angle is **α+ε** and in case 3 the blade angle is **2·α**. In all cases it is assumed that the cutting velocity $\mathbf{v_c}$ is horizontal.

Table 8-2: Summary of the Evans theory.

Case	Cutting forces and specific energy	
1	$F_c=\sigma_T\cdot h_i\cdot w\cdot\frac{2\cdot\sin(\alpha+\delta)}{1-\sin(\alpha+\delta)}$ $F_{ch}=F_c$ $F_{cv}=0$ $E_{sp}=\frac{F_{ch}\cdot v_c}{h_i\cdot w\cdot v_c}=\sigma_T\cdot\frac{2\cdot\sin(\alpha+\delta)}{1-\sin(\alpha+\delta)}$	(8-71)
2	$F_c=\sigma_T\cdot h\cdot w\cdot\frac{2\cdot\sin(\alpha+\delta)}{1-\sin(\alpha+\delta+\varepsilon)}$ $F_{ch}=F_c\cdot\cos(\varepsilon)$ $F_{cv}=F_c\cdot\sin(\varepsilon)$ $E_{sp}=\frac{F_{ch}\cdot v_c}{h_i\cdot w\cdot v_c}=\sigma_T\cdot\frac{2\cdot\sin(\alpha+\delta)}{1-\sin(\alpha+\delta+\varepsilon)}\cdot\cos(\varepsilon)$	(8-72)
3	$F_c=\sigma_T\cdot h\cdot w\cdot\frac{2\cdot\sin(\alpha+\delta)}{1-\sin(2\cdot\alpha+\delta)}$ $F_{ch}=F_c\cdot\cos(\alpha)$ $F_{cv}=F_c\cdot\sin(\alpha)$ $E_{sp}=\frac{F_{ch}\cdot v_c}{h_i\cdot w\cdot v_c}=\sigma_T\cdot\frac{2\cdot\sin(\alpha+\delta)}{1-\sin(2\cdot\alpha+\delta)}\cdot\cos(\alpha)$	(8-73)

8.3.5. The Nishimatsu Model.

For brittle shear rock cutting we may use the equation of Nishimatsu (1972). This theory describes the cutting force of chisels by failure through shear. Figure 8-24 gives the parameters needed to calculate the cutting forces. Nishimatsu (1972) presented a theory similar to Merchant´s (1944), (1945A) and (1945B) only Nishimatsu's theory considered the normal and shear stresses acting on the failure plain (**A-B**) to be proportional to the **n**th power of the distance **λ** from point **A** to point **B**. With **n** being the so called stress distribution factor:

$$p = p_0 \cdot \left(\frac{h_i}{\sin(\beta)} - \lambda \right)^n \tag{8-74}$$

Nishumatsu made the following assumptions:

1. The rock cutting is brittle, without any accompanying plastic deformation (no ductile crushing zone).
2. The cutting process is under plain stress condition.
3. The failure is according a linear Mohr envelope.
4. The cutting speed has no effect on the processes.

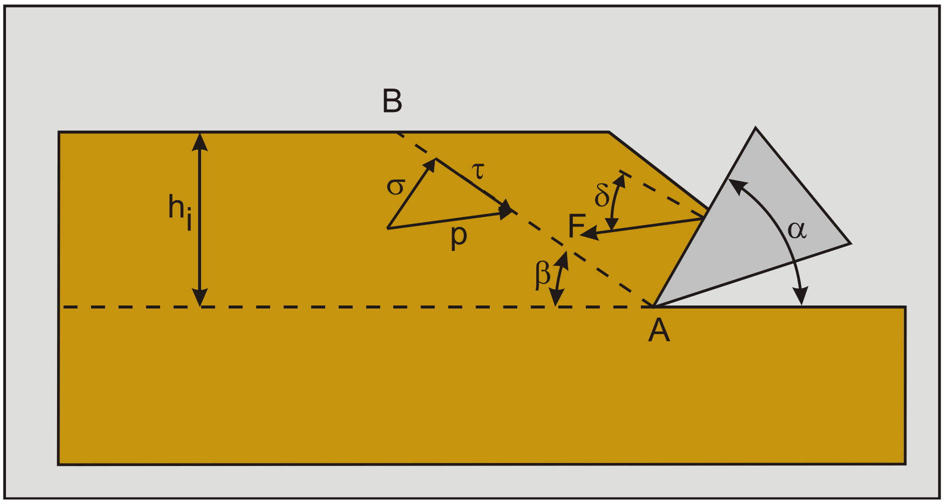

Figure 8-24: Model for shear failure by Nishimatsu (1972).

As a next assumption, let us assume that the direction of the resultant stress **p** is constant along the line **A-B**. The integration of this resultant stress **p** along the line **A-B** should be in equilibrium with the resultant cutting force **F**. Thus, we have:

$$p_0 \cdot w \cdot \int_0^{\frac{h_i}{\sin(\beta)}} \left(\frac{h_i}{\sin(\beta)} - \lambda \right)^n \cdot d\lambda = F \quad \Rightarrow \quad p_0 \cdot w \cdot \frac{1}{n+1} \cdot \left(\frac{h_i}{\sin(\beta)} \right)^{n+1} = F \tag{8-75}$$

Integrating the second term of equation (8-75) allows determining the value of the constant **p₀**.

$$p_0 \cdot w = (n+1) \cdot \left(\frac{h_i}{\sin(\beta)} \right)^{-(n+1)} \cdot F \tag{8-76}$$

Substituting this in equation (8-74) gives:

$$p \cdot w = (n+1) \cdot \left(\frac{h_i}{\sin(\beta)} \right)^{-(n+1)} \cdot \left(\frac{h_i}{\sin(\beta)} - \lambda \right)^n \cdot F \tag{8-77}$$

The maximum stress **p** is assumed to occur near the tip of the chisel, so **λ=0**, giving:

$$p \cdot w = (n+1) \cdot \left(\frac{h_i}{\sin(\beta)} \right)^{-1} \cdot F \tag{8-78}$$

For the normal stress **σ** and the shear **τ** stress this gives:

$$\sigma_0 \cdot w = -p \cdot w \cdot \cos(\alpha + \beta + \delta) = (n+1) \cdot \left(\frac{h_i}{\sin(\beta)} \right)^{-1} \cdot F \cdot \cos(\alpha + \beta + \delta) \tag{8-79}$$

$$\tau_0 \cdot w = p \cdot w \cdot \sin(\alpha + \beta + \delta) = (n+1) \cdot \left(\frac{h_i}{\sin(\beta)} \right)^{-1} \cdot F \cdot \sin(\alpha + \beta + \delta) \tag{8-80}$$

Rewriting this gives:

$$\sigma_0 \cdot h_i \cdot w = -p \cdot h_i \cdot w \cdot \cos(\alpha + \beta + \delta) = -(n+1) \cdot \sin(\beta) \cdot \cos(\alpha + \beta + \delta) \cdot F \tag{8-81}$$

$$\tau_0 \cdot h_i \cdot w = p \cdot h_i \cdot w \cdot \sin(\alpha + \beta + \delta) = (n+1) \cdot \sin(\beta) \cdot \sin(\alpha + \beta + \delta) \cdot F \tag{8-82}$$

With the Coulomb-Mohr failure criterion:

$$\tau_0 = c + \sigma_0 \cdot \tan(\varphi) \tag{8-83}$$

Substituting equations (8-81) and (8-82) in equation (8-83) gives:

$$\begin{aligned}&(n+1) \cdot \sin(\beta) \cdot \sin(\alpha + \beta + \delta) \cdot \frac{F}{h_i \cdot w} \\ &\quad = c - (n+1) \cdot \sin(\beta) \cdot \cos(\alpha + \beta + \delta) \cdot \frac{F}{h_i \cdot w} \cdot \tan(\varphi)\end{aligned} \tag{8-84}$$

This can be simplified to:

$$\begin{aligned}\frac{c \cdot h_i \cdot w \cdot \cos(\varphi)}{(n+1) \cdot \sin(\beta)} &= F \cdot \left(\sin(\alpha + \beta + \delta) \cdot \cos(\varphi) + \cos(\alpha + \beta + \delta) \cdot \sin(\varphi) \right) \\ &= F \cdot \sin(\alpha + \beta + \delta + \varphi)\end{aligned} \tag{8-85}$$

This gives for the force **F**:

$$F = \frac{1}{(n+1)} \cdot \frac{c \cdot h_i \cdot w \cdot \cos(\varphi)}{\sin(\beta) \cdot \sin(\alpha + \beta + \delta + \varphi)} \tag{8-86}$$

For the horizontal force **F$_h$** and the vertical force **F$_v$** we find:

$$F_h = \frac{1}{(n+1)} \cdot \frac{c \cdot h_i \cdot w \cdot \cos(\varphi) \cdot \sin(\alpha + \delta)}{\sin(\beta) \cdot \sin(\alpha + \beta + \delta + \varphi)} \tag{8-87}$$

$$F_v = \frac{1}{(n+1)} \cdot \frac{c \cdot h_i \cdot w \cdot \cos(\varphi) \cdot \cos(\alpha + \delta)}{\sin(\beta) \cdot \sin(\alpha + \beta + \delta + \varphi)} \tag{8-88}$$

To determine the shear angle **β** where the horizontal force **F$_h$** is at the minimum, the denominator of equation (8-86) has to be at a maximum. This will occur when the derivative of **F$_h$** with respect to **β** equals 0 and the second derivative is negative.

$$\frac{\partial \sin\left(\alpha+\beta+\delta+\varphi\right)\cdot\sin\left(\beta\right)}{\partial\beta}=\sin\left(\alpha+2\cdot\beta+\delta+\varphi\right)=0 \tag{8-89}$$

$$\beta=\frac{\pi}{2}-\frac{\alpha+\delta+\varphi}{2} \tag{8-90}$$

Using this, gives for the force **F**:

$$F=\frac{1}{\left(n+1\right)}\cdot\frac{2\cdot c\cdot h_i\cdot w\cdot\cos\left(\varphi\right)}{1+\cos\left(\alpha+\delta+\varphi\right)} \tag{8-91}$$

This gives for the horizontal force $\mathbf{F_h}$ and the vertical force $\mathbf{F_v}$:

$$F_h=\frac{1}{\left(n+1\right)}\cdot\frac{2\cdot c\cdot h_i\cdot w\cdot\cos(\varphi)\cdot\sin(\alpha+\delta)}{1+\cos(\alpha+\delta+\varphi)}=\frac{1}{\left(n+1\right)}\cdot\lambda_{HF}\cdot c\cdot h_i\cdot w \tag{8-92}$$

(8-93)

This solution is the same as the Merchant solution (equations (8-109) and (8-110)) that will be derived in the next chapter, if the value of the stress distribution factor **n=0**. In fact the stress distribution factor **n** is just a factor to reduce the forces. From tests it appeared that in a type of rock the value of **n** depends on the rake angle. It should be mentioned that for this particular case **n** is about 1 for a large cutting angle. In that case tensile failure may give way to a process of shear failure, which is observed by other researches as well. For cutting angles smaller than 80 degrees **n** is more or less constant with a value of **n=0.5**. Figure 8-31 and Figure 8-32 show the coefficients $\boldsymbol{\lambda_{HF}}$ and $\boldsymbol{\lambda_{VF}}$ for the horizontal and vertical forces $\mathbf{F_h}$ and $\mathbf{F_v}$ according to equations (8-109) and (8-110) as a function of the blade angle $\boldsymbol{\alpha}$ and the internal friction angle $\boldsymbol{\varphi}$, where the external friction angle $\boldsymbol{\delta}$ is assumed to be $\mathbf{2/3\cdot\varphi}$. A positive coefficient $\boldsymbol{\lambda_{VF}}$ for the vertical force means that the vertical force $\mathbf{F_v}$ is downwards directed. Based on equation (8-97) and (8-109) the specific energy $\mathbf{E_{sp}}$ can be determined according to:

$$E_{sp}=\frac{P_c}{Q}=\frac{F_h\cdot v_c}{h_i\cdot w\cdot v_c}=\frac{F_h}{h_i\cdot w}=\frac{1}{\left(n+1\right)}\cdot\lambda_{HF}\cdot c \tag{8-94}$$

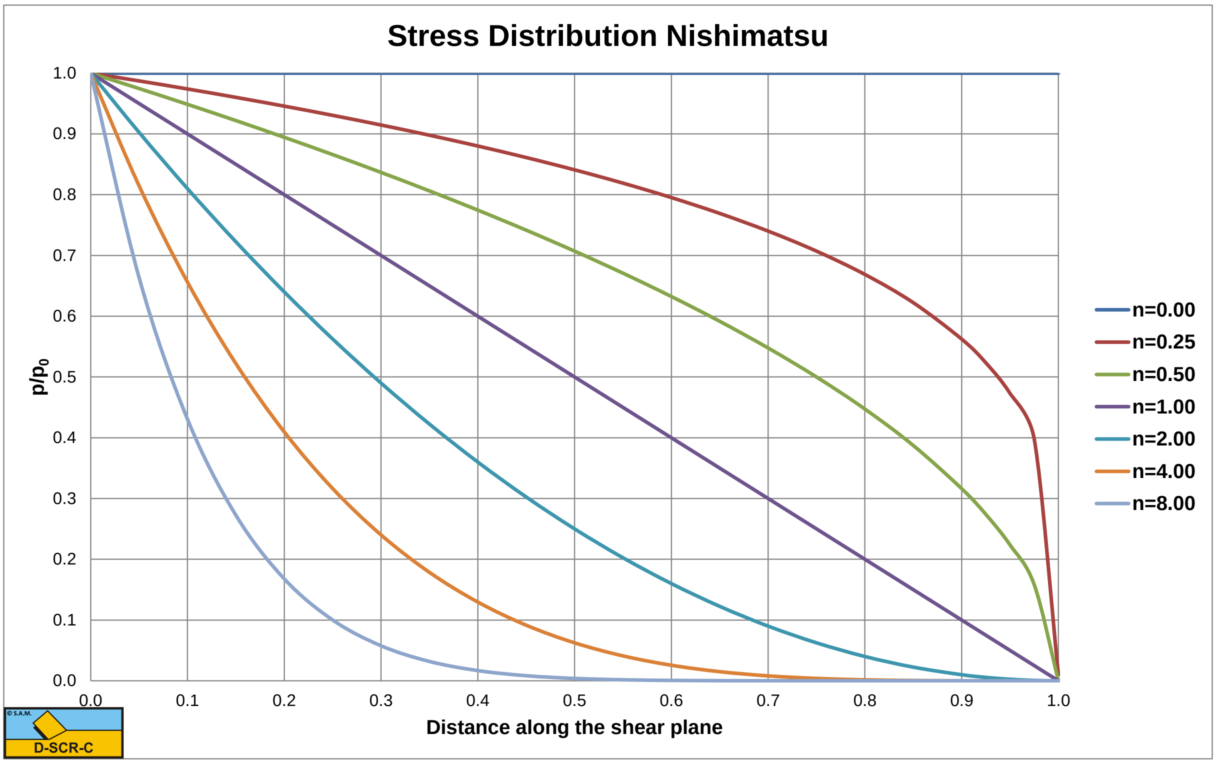

Figure 8-25: The stress distribution along the shear plane.

The difference between the Nishimatsu and the Merchant approach is that Nishimatsu assumes brittle shear failure, while Merchant assumes plastic deformation as can be seen in steel and clay cutting.

Nishimatsu uses the BTS-UCS method to determine the shear strength and the angle of internal friction. This method gives a high value for the angle of internal friction and a low value for the shear strength. For the factor **n** he found:

$$n = -4.9 + 0.18 \cdot \alpha \qquad \textbf{(8-95)}$$

With the blade angle in degrees, for blade angles from 50 to 80 degrees. With this equation **n** is about 0-1 for blade angles around 30 degrees.

8.4. The Flow Type (Based on the Merchant Model).

Rock is the collection of materials where the grains are bonded chemically from very stiff clay, sandstone to very hard basalt. It is difficult to give one definition of rock or stone and also the composition of the material can differ strongly. Still it is interesting to see if the model used for sand and clay, which is based on the Coulomb model, can be used for rock as well. Typical parameters for rock are the compressive strength UCS and the tensile strength BTS and specifically the ratio between those two, which is a measure for how fractured the rock is. Rock also has shear strength and because it consists of bonded grains it will have an internal friction angle and an external friction angle. It can be assumed that the permeability of the rock is very low, so initially the pore pressures do no play a role or cavitation will always occur under atmospheric conditions. But since the absolute hydrostatic pressure, which would result in a cavitation under pressure of the same magnitude can be neglected with respect to the compressive strength of the rock; the pore pressures are usually neglected. This results in a material where gravity, inertia, pore pressures and adhesion can be neglected.
Merchant (1944), (1945A) and (1945B) derived a model for determining the cutting forces when machining steel. The model was based on plastic deformation and a continuous chip formation (ductile cutting). The model included internal and external friction and shear strength, but no adhesion, gravity, inertia and pore pressures. Later Miedema (1987 September) extended this model with adhesion, gravity, inertial forces and pore water pressures.

Definitions:
1. **A**: The blade tip.
2. **B**: End of the shear plane.
3. **C**: The blade top.
4. **A-B**: The shear plane.
5. **A-C**: The blade surface.
6. $\mathbf{h_b}$: The height of the blade.
7. $\mathbf{h_i}$: The thickness of the layer cut.
8. $\mathbf{v_c}$: The cutting velocity.
9. $\boldsymbol{\alpha}$: The blade angle.
10. $\boldsymbol{\beta}$: The shear angle.
11. $\mathbf{F_h}$: The horizontal force, the arrow gives the positive direction.
12. $\mathbf{F_v}$: The vertical force, the arrow gives the positive direction.

Figure 8-26 gives some definitions regarding the cutting process. The line A-B is considered to be the shear plane, while the line A-C is the contact area between the blade and the soil. The blade angle is named $\boldsymbol{\alpha}$ and the shear angle $\boldsymbol{\beta}$. The blade is moving from left to right with a cutting velocity $\mathbf{v_c}$. The thickness of the layer cut is $\mathbf{h_i}$ and the vertical height of the blade $\mathbf{h_b}$. The horizontal force on the blade $\mathbf{F_h}$ is positive from right to left always opposite to the direction of the cutting velocity $\mathbf{v_c}$. The vertical force on the blade $\mathbf{F_v}$ is positive downwards. Since the vertical force is perpendicular to the cutting velocity, the vertical force does not contribute to the cutting power $\mathbf{P_c}$, which is equal to:

$$\mathbf{P_c = F_h \cdot v_c} \tag{8-96}$$

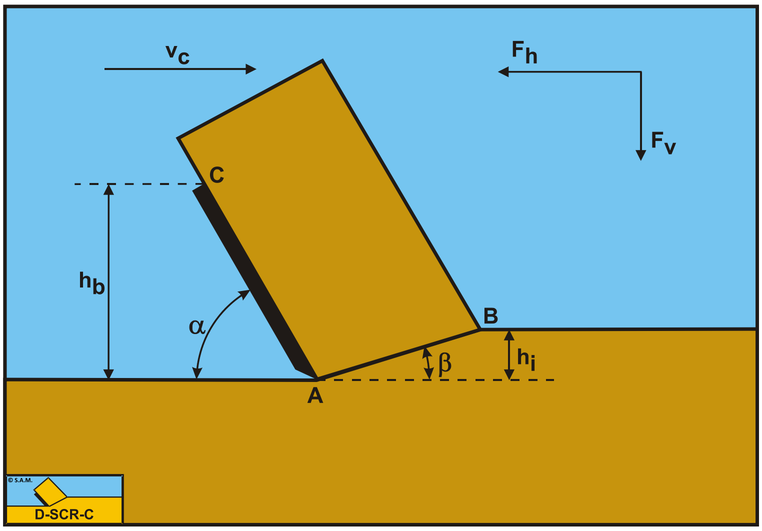

Figure 8-26: The definitions of the cutting process.

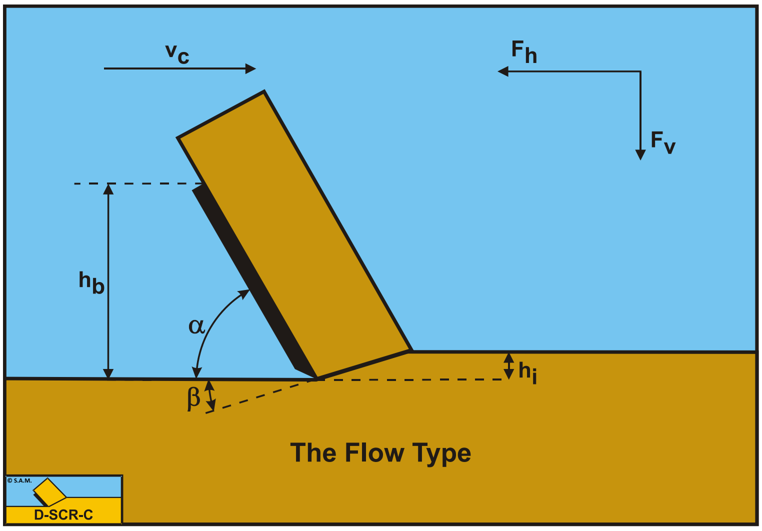

Figure 8-27: The Flow Type cutting mechanism in ductile rock cutting.

The specific energy $\mathbf{E_{sp}}$ is defined as the amount of energy used/required to excavate 1 m^3 of soil/rock. This can be determined by dividing the cutting power $\mathbf{P_c}$ by the production **Q** and results in the cutting force $\mathbf{F_h}$ in the direction of the cutting velocity $\mathbf{v_c}$, divided by the cross section cut $\mathbf{h_i \cdot w}$:

$$E_{sp} = \frac{P_c}{Q} = \frac{F_h \cdot v_c}{h_i \cdot w \cdot v_c} = \frac{F_h}{h_i \cdot w} \tag{8-97}$$

The model for rock cutting under atmospheric conditions is based on the **Flow Type** of cutting mechanism. Although in general rock will encounter a more brittle failure mechanism and the **Flow Type** considered represents the ductile failure mechanism, the **Flow Type** mechanism forms the basis for all cutting processes. The definitions of the **Flow Type** mechanism are shown in Figure 8-27.

Figure 8-28 illustrates the forces on the layer of rock cut. The forces shown are valid in general. The forces acting on this layer are:

1. A normal force acting on the shear surface $\mathbf{N_1}$ resulting from the grain stresses.
2. A shear force $\mathbf{S_1}$ as a result of internal friction $\mathbf{N_1 \cdot tan(\phi)}$.
3. A shear force **C** as a result of the shear strength (cohesion) τ_c or **c**. This force can be calculated by multiplying the cohesive shear strength τ_c with the area of the shear plane.
4. A force normal to the blade $\mathbf{N_2}$ resulting from the grain stresses.
5. A shear force $\mathbf{S_2}$ as a result of the soil/steel friction $\mathbf{N_2 \cdot tan(\delta)}$ or external friction.

The normal force $\mathbf{N_1}$ and the shear force $\mathbf{S_1}$ can be combined to a resulting grain force $\mathbf{K_1}$.

The forces acting on a straight blade when cutting rock, can be distinguished as:

6. A force normal to the blade $\mathbf{N_2}$ resulting from the grain stresses.
7. A shear force $\mathbf{S_2}$ as a result of the soil/steel friction $\mathbf{N_2 \cdot tan(\delta)}$ or external friction.

These forces are shown in Figure 8-29. If the forces $\mathbf{N_2}$ and $\mathbf{S_2}$ are combined to a resulting force $\mathbf{K_2}$ the resulting force $\mathbf{K_2}$ is the unknown force on the blade. By taking the horizontal and vertical equilibrium of forces an expression for the force $\mathbf{K_2}$ on the blade can be derived.

The horizontal equilibrium of forces:

$$\sum F_h = K_1 \cdot \sin(\beta + \varphi) + C \cdot \cos(\beta) - K_2 \cdot \sin(\alpha + \delta) = 0 \tag{8-98}$$

The vertical equilibrium of forces:

$$\sum F_v = -K_1 \cdot \cos(\beta + \varphi) + C \cdot \sin(\beta) - K_2 \cdot \cos(\alpha + \delta) = 0 \tag{8-99}$$

The force $\mathbf{K_1}$ on the shear plane is now:

$$K_1 = \frac{-C \cdot \cos(\alpha + \beta + \delta)}{\sin(\alpha + \beta + \delta + \varphi)} \tag{8-100}$$

The force $\mathbf{K_2}$ on the blade is now:

$$K_2 = \frac{C \cdot \cos(\varphi)}{\sin(\alpha + \beta + \delta + \varphi)} \tag{8-101}$$

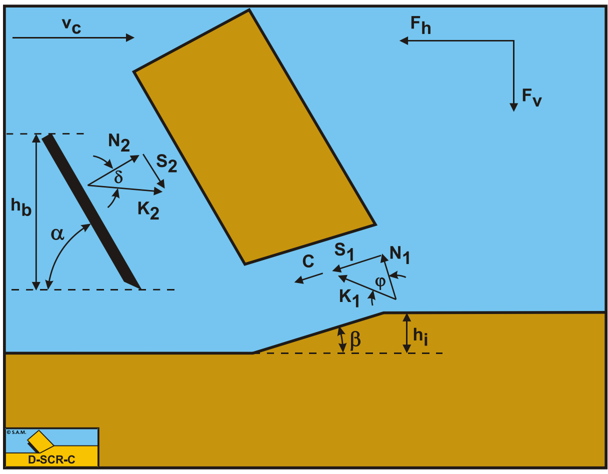

Figure 8-28: The forces on the layer cut in rock (atmospheric).

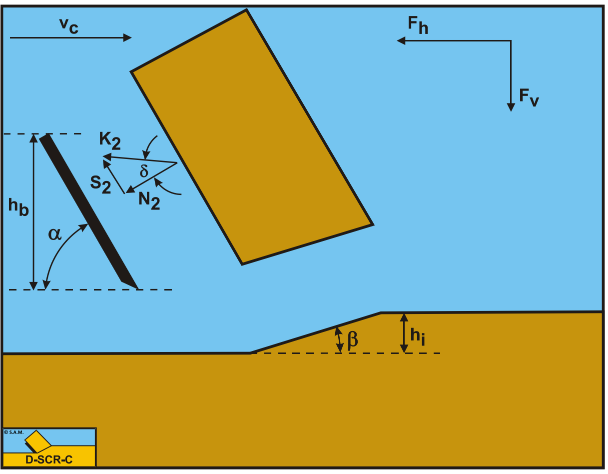

Figure 8-29: The forces on the blade in rock (atmospheric).

The force **C** due to the cohesive shear strength **c** is equal to:

$$C = \frac{\lambda_s \cdot c \cdot h_i \cdot w}{\sin(\beta)} \tag{8-102}$$

The factor λ_s in equation (8-102) is the velocity strengthening factor, which causes an increase of the cohesive shear strength. In clay (Miedema (1992) and (2010)) this factor has a value of about 2 under normal cutting conditions. In rock the strengthening effect is not reported, so a value of 1 should be used. From equation (8-101) the forces on the blade can be derived. On the blade a force component in the direction of cutting velocity $\mathbf{F_h}$ and a force perpendicular to this direction $\mathbf{F_v}$ can be distinguished.

$$F_h = K_2 \cdot \sin(\alpha + \delta) \tag{8-103}$$

$$F_v = K_2 \cdot \cos(\alpha + \delta) \tag{8-104}$$

Substituting equations (8-102) and (8-101) gives the following equations for the horizontal $\mathbf{F_h}$ and vertical $\mathbf{F_v}$ cutting forces. It should be remarked that the strengthening factor λ_s in rock is usually 1.

$$F_h = \frac{\lambda_s \cdot c \cdot h_i \cdot w \cdot \cos(\varphi) \cdot \sin(\alpha + \delta)}{\sin(\beta) \cdot \sin(\alpha + \beta + \delta + \varphi)} \tag{8-105}$$

$$F_v = \frac{\lambda_s \cdot c \cdot h_i \cdot w \cdot \cos(\varphi) \cdot \cos(\alpha + \delta)}{\sin(\beta) \cdot \sin(\alpha + \beta + \delta + \varphi)} \tag{8-106}$$

8.5. Determining the Angle β.

To determine the shear angle **β** where the horizontal force **F_h** is at the minimum, the denominator of equation (8-105) has to be at a maximum. This will occur when the derivative of **F_h** with respect to **β** equals 0 and the second derivative is negative.

$$\frac{\partial \sin(\alpha+\beta+\delta+\varphi)\cdot\sin(\beta)}{\partial\beta}=\sin(\alpha+2\cdot\beta+\delta+\varphi)=0 \qquad \textbf{(8-107)}$$

$$\beta=\frac{\pi}{2}-\frac{\alpha+\delta+\varphi}{2} \qquad \textbf{(8-108)}$$

This gives for the cutting forces:

$$F_h=\frac{2\cdot c\cdot h_i\cdot w\cdot\cos(\varphi)\cdot\sin(\alpha+\delta)}{1+\cos(\alpha+\delta+\varphi)}=\lambda_{HF}\cdot c\cdot h_i\cdot w \qquad \textbf{(8-109)}$$

$$F_v=\frac{2\cdot c\cdot h_i\cdot w\cdot\cos(\varphi)\cdot\cos(\alpha+\delta)}{1+\cos(\alpha+\delta+\varphi)}=\lambda_{VF}\cdot c\cdot h_i\cdot w \qquad \textbf{(8-110)}$$

Equations (8-109) and (8-110) are basically the same as the equations found by Merchant (1944), (1945A) and (1945B). The normal force **N_1** and the normal stress **σ_{N1}** on the shear plane are now (with **λ_s=1**):

$$N_1=\frac{-C\cdot\cos(\alpha+\beta+\delta)}{\sin(\alpha+\beta+\delta+\varphi)}\cdot\cos(\varphi)$$

$$\sigma_{N1}=\frac{-c\cdot\cos(\alpha+\beta+\delta)}{\sin(\alpha+\beta+\delta+\varphi)}\cdot\cos(\varphi) \qquad \textbf{(8-111)}$$

The normal force **N_2** and the normal stress **σ_{N2}** on the blade are now:

$$N_2=\frac{C\cdot\cos(\varphi)}{\sin(\alpha+\beta+\delta+\varphi)}\cdot\cos(\delta)$$

$$\sigma_{N2}=c\cdot\frac{h_i\cdot\sin(\alpha)}{h_b\cdot\sin(\beta)}\cdot\frac{\cos(\varphi)}{\sin(\alpha+\beta+\delta+\varphi)}\cdot\cos(\delta) \qquad \textbf{(8-112)}$$

Equations (8-111) and (8-112) show that the normal force on the shear plane tends to be negative, unless the sum of the angles **α+β+δ** is greater than 90°. With the use of equation (8-108) the following condition is found:

$$\alpha+\beta+\delta=\alpha+\delta+\left(\frac{\pi}{2}-\frac{\alpha+\delta+\varphi}{2}\right)=\frac{\pi}{2}+\frac{\alpha+\delta-\varphi}{2}>\frac{\pi}{2}$$

$$\text{so:}\quad\frac{\alpha+\delta-\varphi}{2}>0 \qquad \textbf{(8-113)}$$

Because for normal blade angles this condition is always valid, the normal force is always positive. Figure 8-31 and Figure 8-32 show the coefficients **λ_{HF}** and **λ_{VF}** for the horizontal and vertical forces **F_h** and **F_v** according to equations (8-109) and (8-110) as a function of the blade angle **α** and the internal friction angle **φ**, where the external friction angle **δ** is assumed to be **2/3·φ**. A positive coefficient **λ_{VF}** for the vertical force means that the vertical force **F_v** is downwards directed.

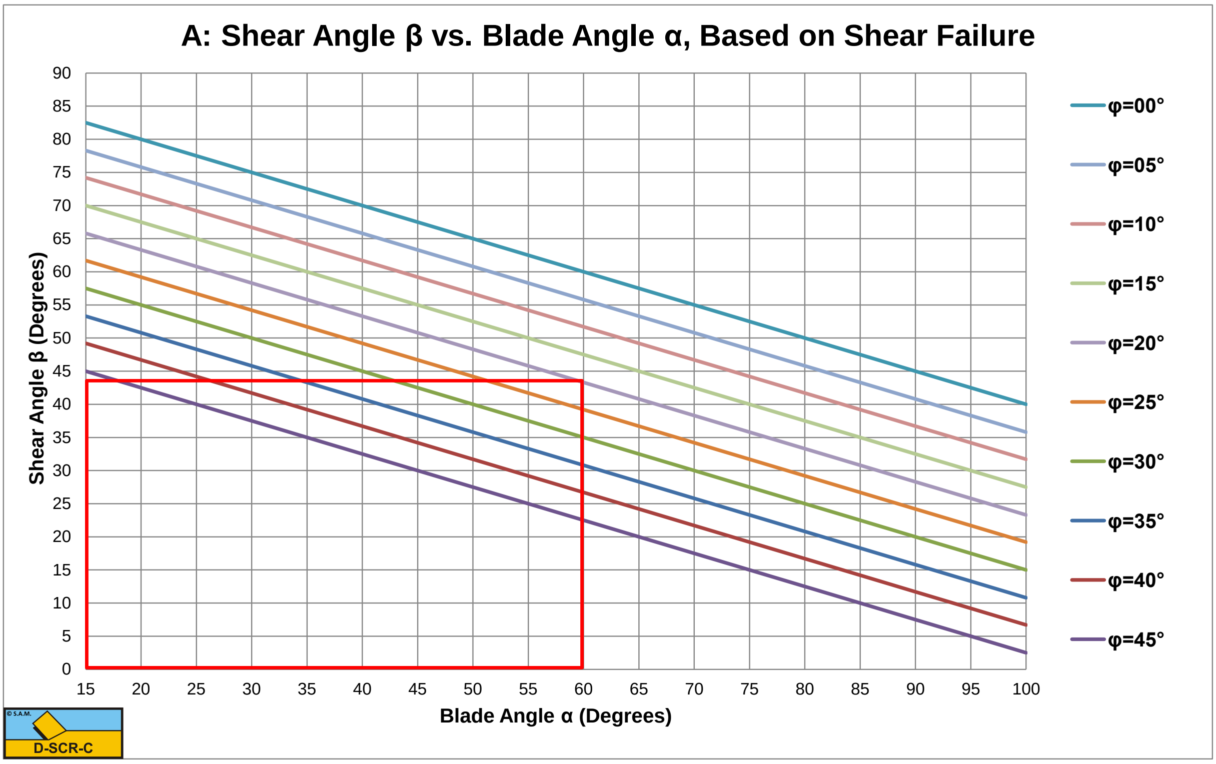

Figure 8-30: The shear angle β as a function of the blade angle α and the angle of internal friction φ.

Based on equation (8-97) and (8-109) the specific energy $\mathbf{E_{sp}}$ can be determined according to:

$$E_{sp} = \frac{P_c}{Q} = \frac{F_h \cdot v_c}{h_i \cdot w \cdot v_c} = \frac{F_h}{h_i \cdot w} = \lambda_{HF} \cdot c \tag{8-114}$$

The cohesive shear strength c is a function of the Unconfined Compressive Strength UCS and the angle of internal friction **φ** according to (see Figure 8-36):

$$c = \frac{UCS}{2} \cdot \left(\frac{1 - \sin(\varphi)}{\cos(\varphi)} \right) \tag{8-115}$$

This gives for the specific energy $\mathbf{E_{sp}}$:

$$E_{sp} = \lambda_{HF} \cdot c = \lambda_{HF} \cdot \frac{UCS}{2} \cdot \left(\frac{1 - \sin(\varphi)}{\cos(\varphi)} \right) \tag{8-116}$$

Figure 8-33 shows the specific energy $\mathbf{E_{sp}}$ to UCS ratio. In Figure 8-30, Figure 8-31, Figure 8-32 and Figure 8-33 an example is given for an **α=60º** blade and an internal friction angle of **φ=20º**.
It should be noted again that the forces and the specific energy are based on peak values. For the average this should be multiplied with a factor between 0.5 and 1.0, but closer to 0.5.

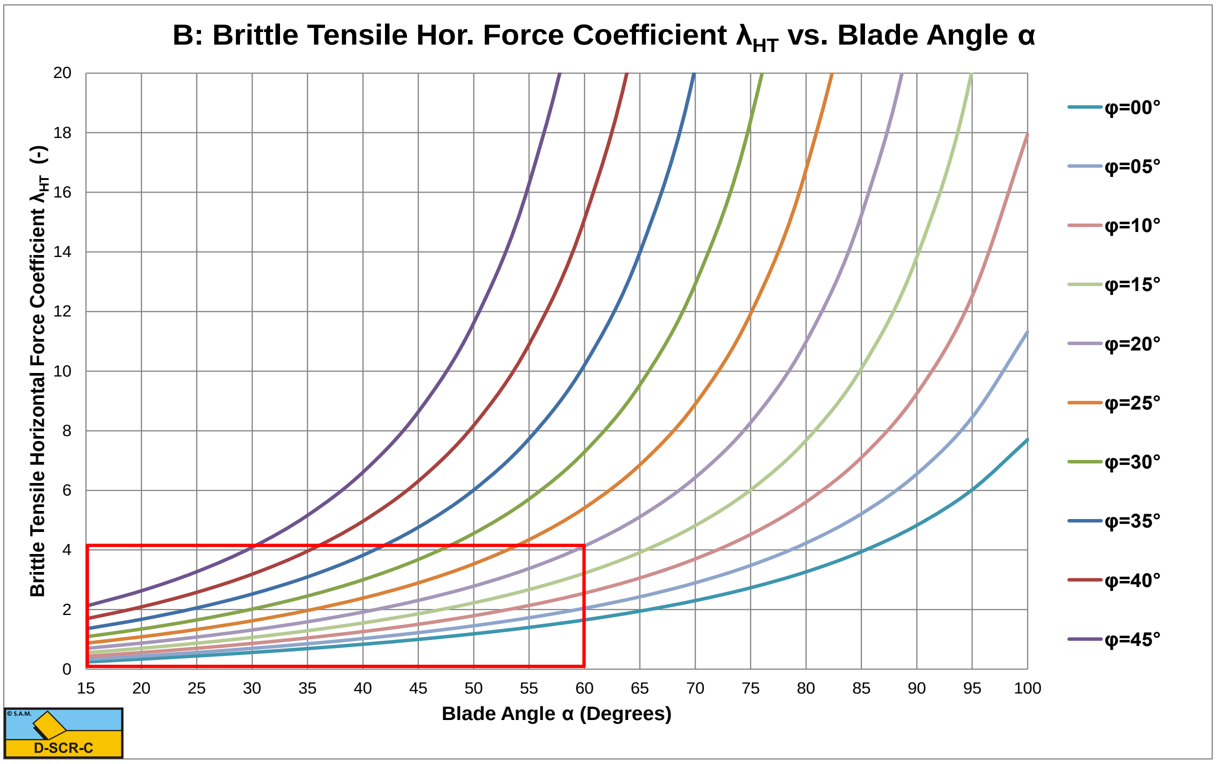

Figure 8-31: The brittle (shear failure) horizontal force coefficient λ_{HF}.

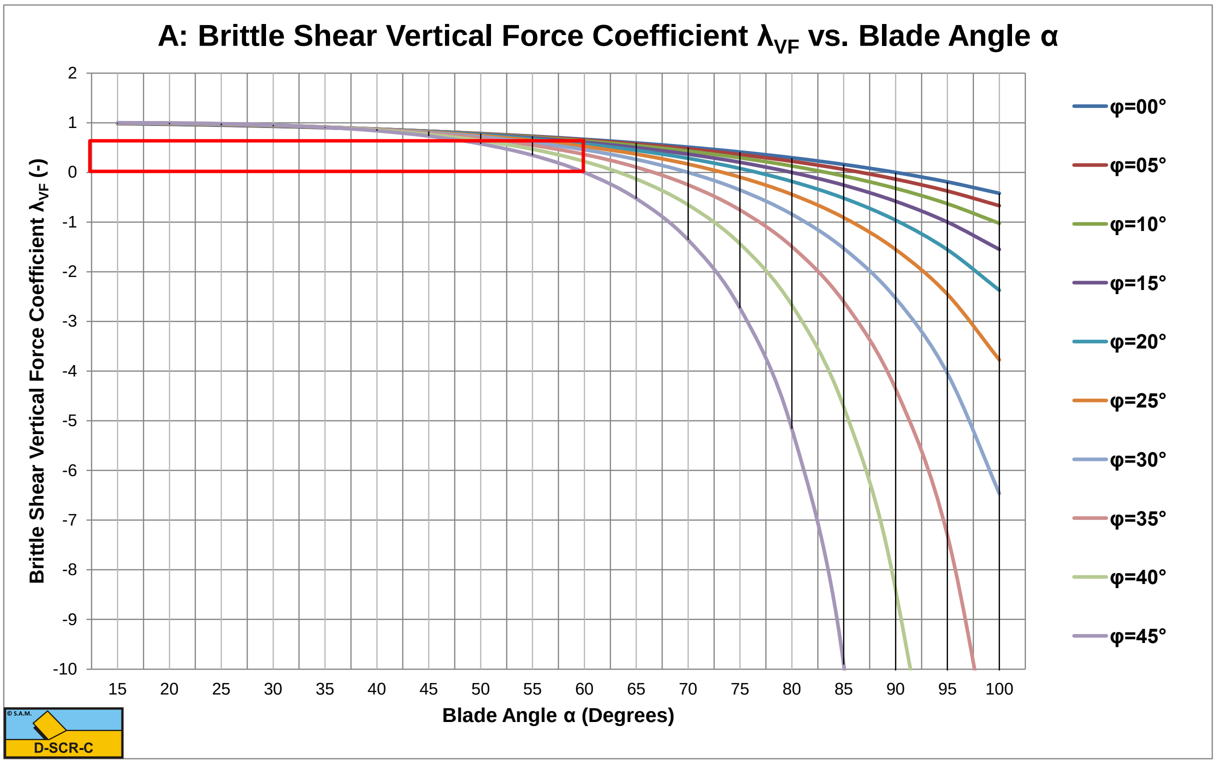

Figure 8-32: The brittle (shear failure) vertical force coefficient λ_{VF}.

If the forces become to high another mechanism will occur, for example the wedge mechanism.

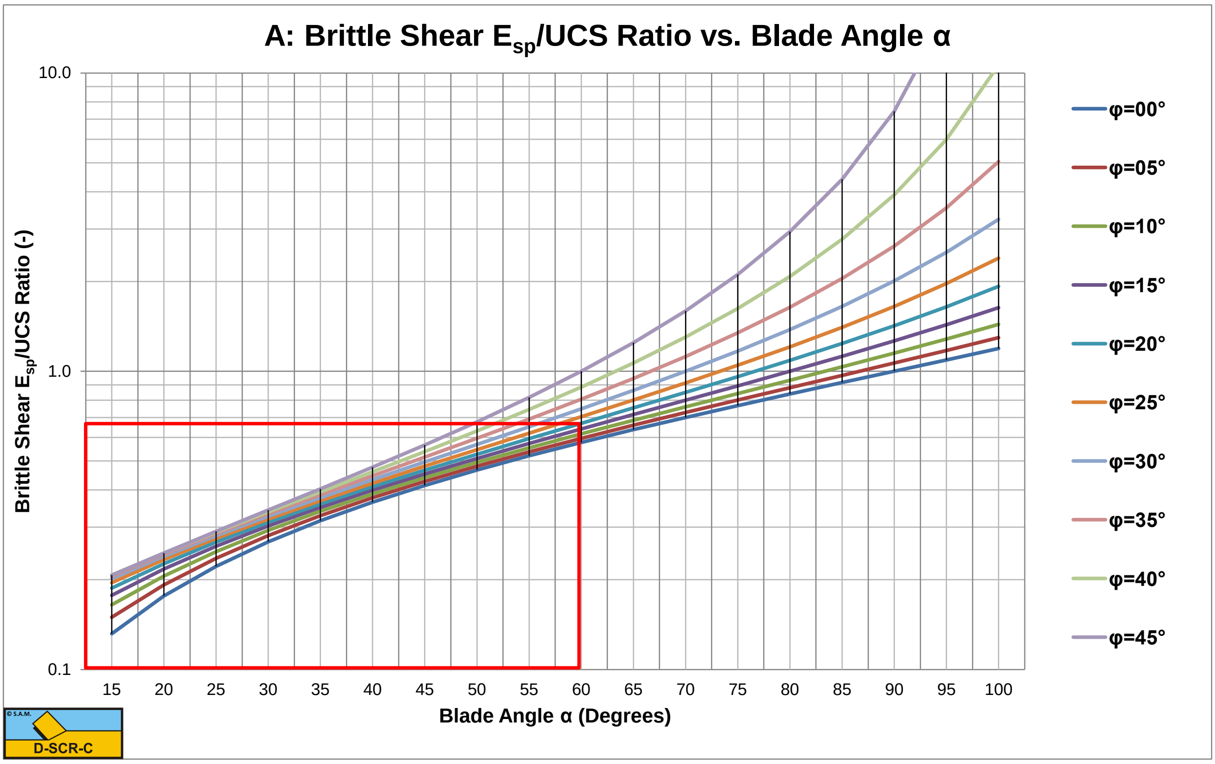

Figure 8-33: The specific energy E_{sp} to UCS ratio.

8.6. The Shear Type, Tear Type and the Chip Type.

Until now only the total normal force on the shear plane $\mathbf{N_1}$ has been taken into consideration, but of course this normal force is the result of integration of the normal stresses $\boldsymbol{\sigma_{N1}}$ on the shear plane. One could consider that cutting is partly bending the material and it is known that with bending a bar, at the inside (the smallest bending radius) compressive stresses will be developed, while at the outside (the biggest bending radius), tensile stresses are developed. So if the normal force $\mathbf{N_1}$ equals zero, this must mean that near the edge of the blade tensile stresses (negative) stresses develop, while at the outside compressive (positive) stresses develop. So even when the normal force would be slightly positive, still, tensile stresses develop in front of the edge of the blade. The normal force on the blade however is always positive, meaning that the **Curling Type** of cutting process will never occur in rock under atmospheric conditions. The previous derivations of the cutting forces are based on the **Flow Type**, but in reality rock will fail brittle with either the **Shear Type** or the **Tear Type** or a combination the **Chip Type**. For the **Shear Type** the equations (8-109) and (8-110) can still be used, considering these equations give peak forces. The average forces and thus the average cutting power $\mathbf{P_c}$ and the specific energy $\mathbf{E_{sp}}$ may be 30%-60% of the peak values. The occurrence of the **Tear Type** depends on the tensile stress. If somewhere in the rock the tensile stress $\boldsymbol{\sigma_{min}}$ is smaller than the tensile strength $\boldsymbol{\sigma_T}$, a tensile fracture may occur. One should note here that compressive stresses are positive and tensile stresses are negative. So tensile fracture/rupture will occur if the absolute value of the tensile stress $\boldsymbol{\sigma_{min}}$ is larger than the tensile strength $\boldsymbol{\sigma_T}$.

If rock is considered, the following condition can be derived with respect to tensile rupture:

The cohesion **c** can be determined from the UCS value and the angle of internal friction according to, as is shown in Figure 8-36:

$$c = \frac{UCS}{2} \cdot \left(\frac{1 - \sin(\varphi)}{\cos(\varphi)} \right) \qquad \textbf{(8-117)}$$

According to the Mohr-Coulomb failure criterion, the following is valid for the shear stress on the shear plane, as is shown in Figure 8-37.

$$\tau_{S1} = c + \sigma_{N1} \cdot \tan(\varphi) \qquad \textbf{(8-118)}$$

The average stress condition on the shear plane is now σ_{N1}, τ_{S1} as is shown in Figure 8-37. A Mohr circle (Mohr circle 1) can be drawn through this point, resulting in a minimum stress σ_{min} which is negative, so tensile. If this minimum normal stress is smaller than the tensile strength σ_T tensile fracture will occur, as is the case in the figure. Now Mohr circle 1 can never exist, but a smaller circle (Mohr circle 2) can, just touching the tensile strength σ_T. The question is now, how to get from Mohr circle 1 to Mohr circle 2. To find Mohr circle 2 the following steps have to be taken.

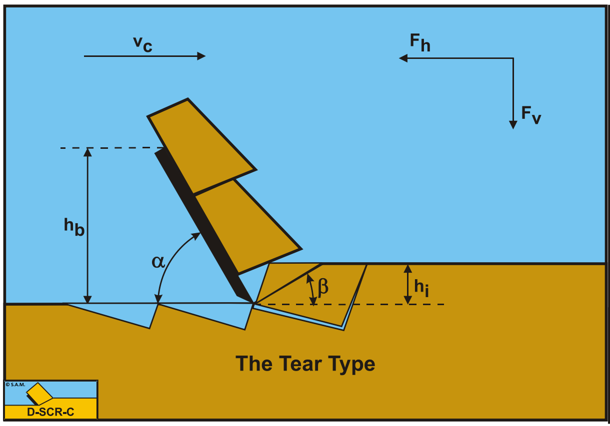

Figure 8-34: The Tear Type cutting mechanism in rock under hyperbaric conditions.

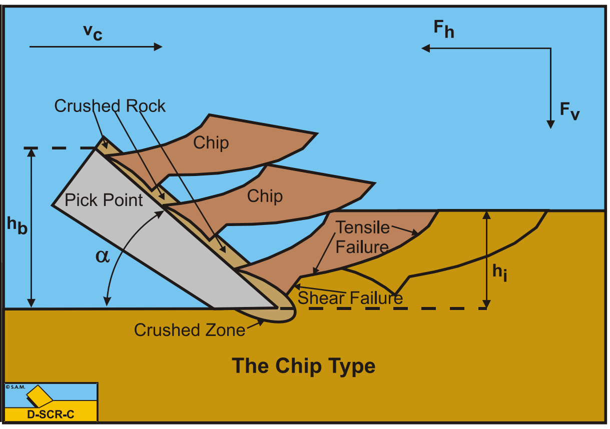

Figure 8-35: The Chip Type cutting mechanism in rock under hyperbaric conditions.

The radius **R** of the Mohr circle 1 can be found from the shear stress τ_{S1} by:

$$\mathrm{R} = \frac{\tau_{S1}}{\cos(\varphi)} \tag{8-119}$$

The center of the Mohr circle 1, σ_C, now follows from:

$$\begin{aligned}\sigma_C &= \sigma_{N1} + \mathrm{R}\cdot\sin(\varphi) = \sigma_{N1} + \tau_{S1}\cdot\tan(\varphi)\\ &= \sigma_{N1} + c\cdot\tan(\varphi) + \sigma_{N1}\cdot\tan^2(\varphi)\end{aligned} \tag{8-120}$$

The minimum principal stress σ_{min} equals the normal stress in the center of the Mohr circle σ_C minus the radius of the Mohr circle **R**:

$$\begin{aligned}\sigma_{min} &= \sigma_C - \mathrm{R}\\ &= \sigma_{N1} + c\cdot\tan(\varphi) + \sigma_{N1}\cdot\tan^2(\varphi) - \frac{c}{\cos(\varphi)} - \frac{\sigma_{N1}\cdot\tan(\varphi)}{\cos(\varphi)}\end{aligned} \tag{8-121}$$

Rearranging this gives:

$$\sigma_{min} = \sigma_{N1}\cdot\left(1+\tan^2(\varphi) - \frac{\tan(\varphi)}{\cos(\varphi)}\right) + c\cdot\left(\tan(\varphi) - \frac{1}{\cos(\varphi)}\right) \tag{8-122}$$

Substituting equation (8-111) for the normal stress on the shear plane gives:

$$\begin{aligned}\sigma_{min} = &\frac{-c\cdot\cos(\alpha+\beta+\delta)\cdot\cos(\varphi)}{\sin(\alpha+\beta+\delta+\varphi)}\cdot\left(1+\tan^2(\varphi) - \frac{\tan(\varphi)}{\cos(\varphi)}\right)\\ &+ c\cdot\left(\tan(\varphi) - \frac{1}{\cos(\varphi)}\right) > \sigma_T\end{aligned} \tag{8-123}$$

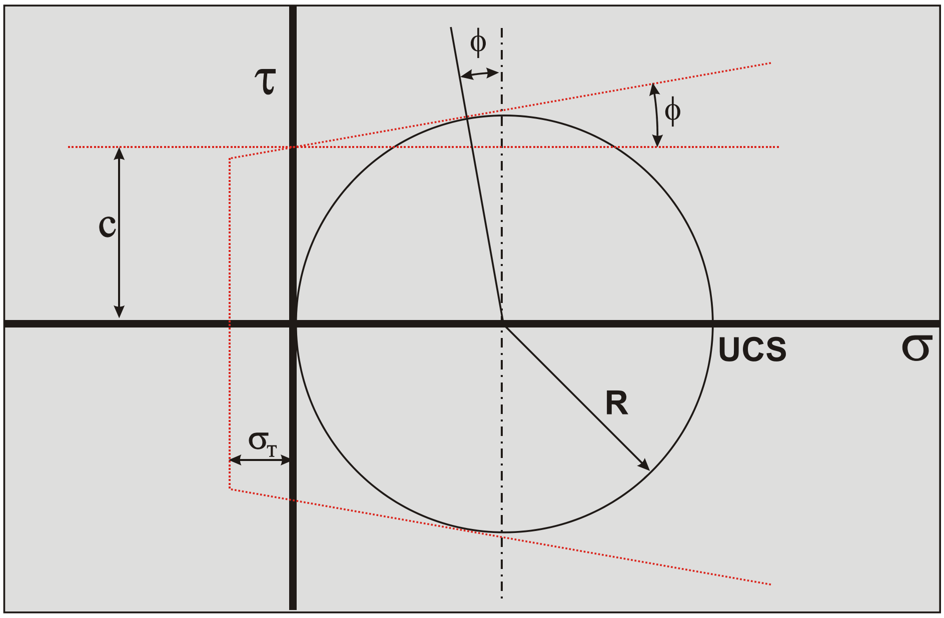

Figure 8-36: The Mohr circle for UCS and cohesion.

Now shear failure will occur if the minimum principal stress $\boldsymbol{\sigma_{min}}$ is larger than the tensile strength $\boldsymbol{\sigma_T}$, thus:

$$\sigma_{min} > \sigma_T \tag{8-124}$$

If equation (8-124) is true, shear failure will occur. Keep in mind however, that the tensile strength $\boldsymbol{\sigma_T}$ is a negative number. Of course if the minimum normal stress σ_{min} or in the graph, Figure 8-38, σ_T / c is positive, tensile failure can never occur. Equation (8-124) can be transformed to:

$$\frac{\sigma_T}{c} < -\frac{\cos(\alpha+\beta+\delta)}{\sin(\alpha+\beta+\delta+\varphi)} \cdot \left(\cos(\varphi) - \tan(\varphi) + \tan(\varphi)\cdot\sin(\varphi)\right) + \tan(\varphi) - \frac{1}{\cos(\varphi)} \tag{8-125}$$

Substituting equation (8-108) for the shear angle **β** gives:

$$\frac{\sigma_T}{c} < \frac{\sin\left(\frac{\alpha+\delta-\varphi}{2}\right)}{\cos\left(\frac{\alpha+\delta+\varphi}{2}\right)} \cdot \left(\cos(\varphi) - \tan(\varphi) + \tan(\varphi)\cdot\sin(\varphi)\right) + \tan(\varphi) - \frac{1}{\cos(\varphi)} \tag{8-126}$$

This can be transformed to:

$$\frac{\sigma_T}{c} < \left(\frac{\sin\left(\frac{\alpha+\delta-\varphi}{2}\right)}{\cos\left(\frac{\alpha+\delta+\varphi}{2}\right)} - 1\right) \cdot \left(\frac{1-\sin(\varphi)}{\cos(\varphi)}\right) \tag{8-127}$$

A mobilized cohesive shear strength $\mathbf{c_m}$ can be defined, based on the tensile strength $\boldsymbol{\sigma_T}$, by using the equal sign in equation (8-127). With this mobilized cohesive shear strength Mohr circle 2 can be constructed.

$$c_m = \frac{\sigma_T}{\left(\frac{\sin\left(\frac{\alpha+\delta-\varphi}{2}\right)}{\cos\left(\frac{\alpha+\delta+\varphi}{2}\right)}-1\right)\cdot\left(\frac{1-\sin(\varphi)}{\cos(\varphi)}\right)} \qquad \textbf{(8-128)}$$

Substituting equation (8-128) in the equations (8-109) and (8-110) gives for the cutting forces:

$$F_h = \frac{2\cdot c_m\cdot h_i\cdot w\cdot\cos(\varphi)\cdot\sin(\alpha+\delta)}{1+\cos(\alpha+\delta+\varphi)} = \lambda_{HT}\cdot\sigma_T\cdot h_i\cdot w \qquad \textbf{(8-129)}$$

$$F_v = \frac{2\cdot c_m\cdot h_i\cdot w\cdot\cos(\varphi)\cdot\cos(\alpha+\delta)}{1+\cos(\alpha+\delta+\varphi)} = \lambda_{VT}\cdot\sigma_T\cdot h_i\cdot w \qquad \textbf{(8-130)}$$

Figure 8-38 shows the pseudo cohesive shear strength coefficient σ_T / c from equation (8-127). Below the lines the cutting process is ductile (the **Flow Type**) or brittle (the **Shear Type**), while above the lines it is brittle (the **Tear Type**). It is clear from this figure that an increasing blade angle $\boldsymbol{\alpha}$ and an increasing internal friction angle $\boldsymbol{\varphi}$ suppresses the occurrence of the **Tear Type**. The coefficients $\boldsymbol{\lambda_{HT}}$ and $\boldsymbol{\lambda_{VT}}$ are shown in Figure 8-42 and Figure 8-43 for a range of blade angles $\boldsymbol{\alpha}$ and internal friction angles $\boldsymbol{\varphi}$.

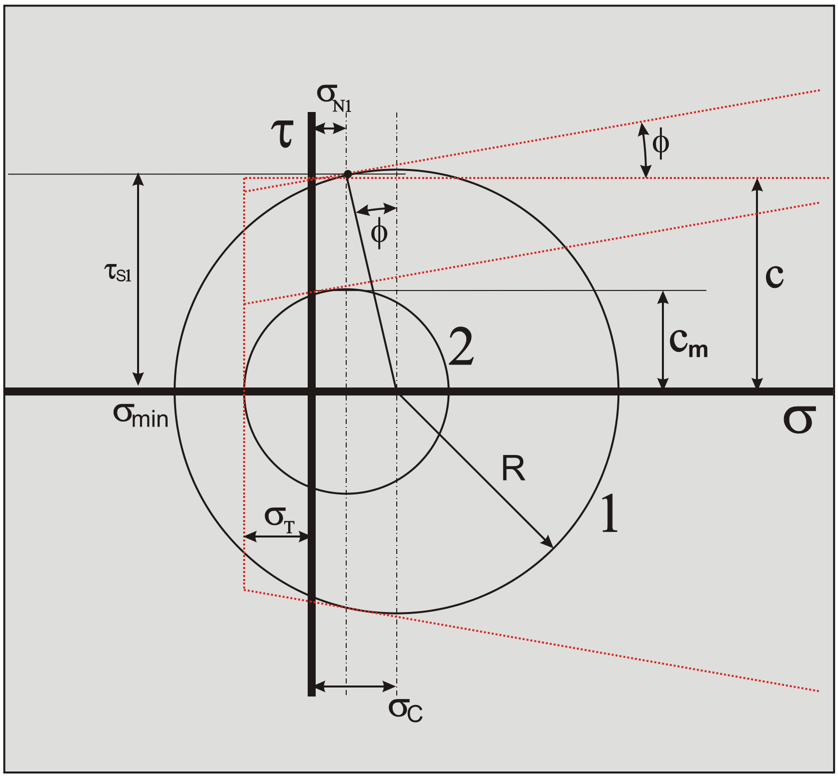

Figure 8-37: The Mohr circles of the Tear Type.

Equation (8-129) gives for the specific energy $\mathbf{E_{sp}}$:

$$E_{sp} = \lambda_{HT}\cdot\sigma_T \qquad \textbf{(8-131)}$$

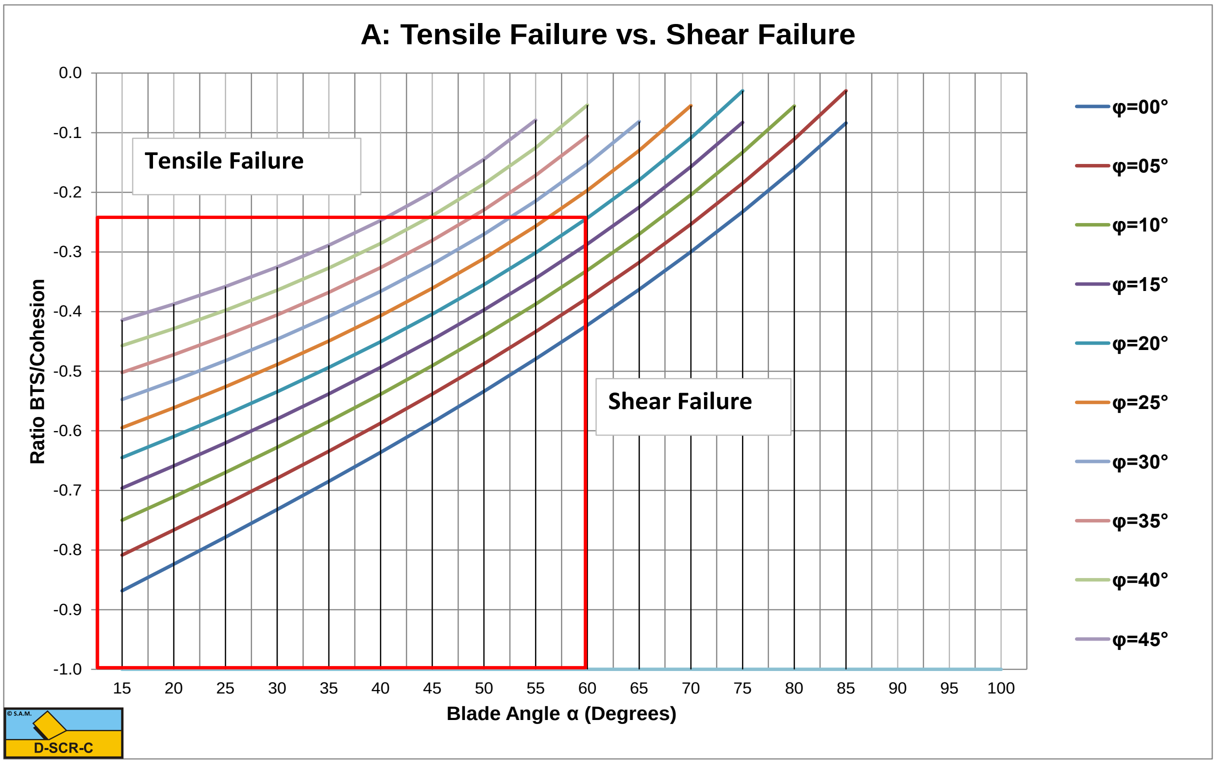

Figure 8-38: Below the lines (equation (8-125)) the cutting process is brittle (shear failure); above the lines it is brittle (tensile failure).

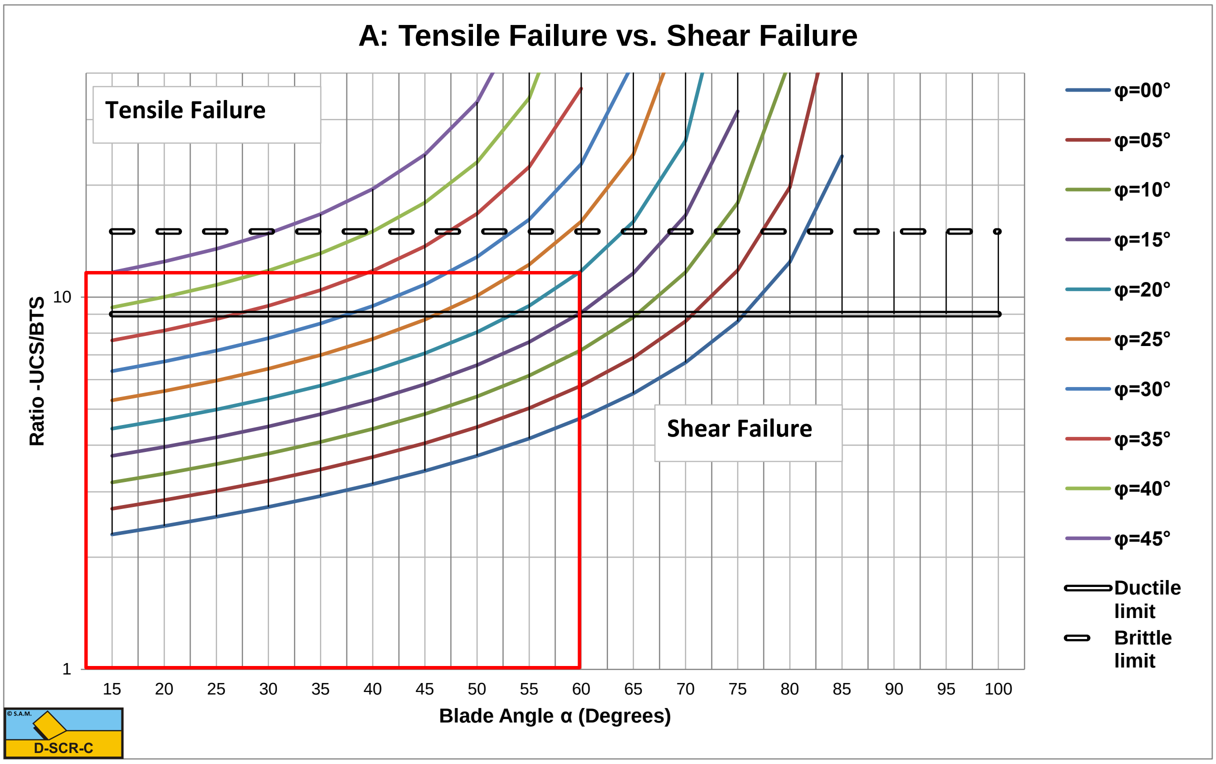

Figure 8-39: The ratio UCS/BTS, below the lines there is brittle (shear failure), above the lines it is brittle (tensile failure).

To determine the cutting forces in rock under atmospheric conditions the following steps have to be taken:

1. Determine whether the cutting process is based on the **Flow Type** or the **Tear Type**, using Figure 8-38.
2. If the cutting process is based on the **Flow Type**, use Figure 8-31 and Figure 8-32 to determine the coefficients λ_{HF} and λ_{VF}. Use equations (8-109) and (8-110) to calculate the cutting forces. Optionally a factor 0.3-0.5 may be applied in case of brittle shear failure, to account for average forces, power and specific energy.
3. If the cutting process is based on the **Tear Type**, use Figure 8-42 and Figure 8-43 to determine the coefficients λ_{HT} and λ_{VT}. Use equations (8-129) and (8-130) to calculate the cutting forces. A factor 0.3-0.6 should be applied to account for average forces, power and specific energy.

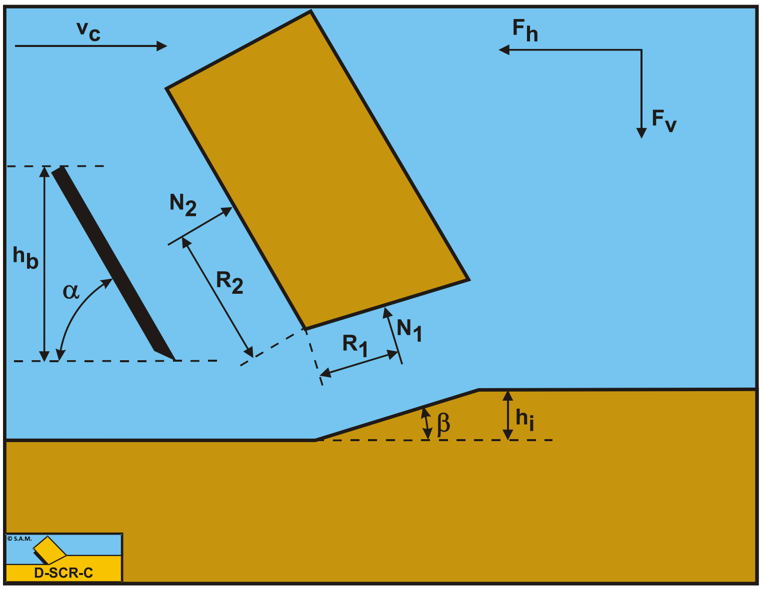

Figure 8-40: The moments on the layer cut.

For completeness, Figure 8-40 shows the moments on the layer cut.

Based on equation (8-127) and (8-117) the ratio UCS/BTS can also be determined. Gehking (1987) stated that below a ratio of 9 ductile failure will occur, while above a ratio of 15 brittle failure will occur. In between these limits there is a transition between ductile and brittle failure, which is also in accordance with the findings of Fairhurst (1964). Figure 8-39 shows that the ductile limit of 9 is possible for blade angles **α** between 45° and 60° corresponding with internal friction angles **φ** of 25° and 15°. For the same blade angles, the corresponding internal friction angles **φ** are 35° and 25° at the brittle limit of 15. These values match the blade angles as used in dredging and mining and also match the internal friction angle of commonly dredged rock. Figure 8-39 shows that in general a higher internal friction angle **φ** and a bigger blade angle **α** suppress tensile failure.

$$\frac{UCS}{BTS}=\frac{2}{\left(\frac{\sin\left(\frac{\alpha+\delta-\varphi}{2}\right)}{\cos\left(\frac{\alpha+\delta+\varphi}{2}\right)}-1\right)\cdot\left(\frac{1-\sin(\varphi)}{\cos(\varphi)}\right)^{2}} \tag{8-132}$$

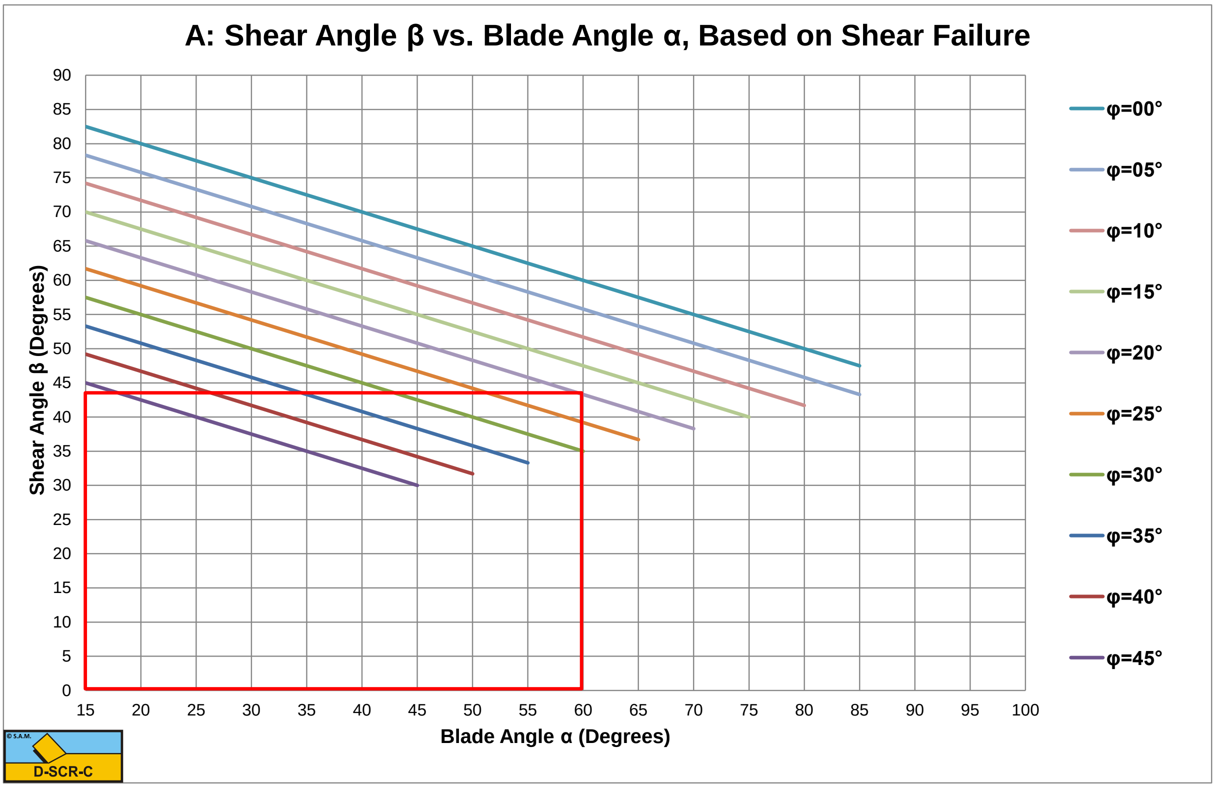

Figure 8-41: The shear angle with limitation.

Figure 8-41 shows the shear angle with limitations. The limitations occur because at a certain sum of the blade angle, the shear angle and the angle of internal friction, a positive tensile strength would be required to get brittle tensile failure, which is physically impossible. Compressive stresses are defined positive and tensile stresses negative, so a positive tensile stress would in fact be a compressive stress. Beyond this limitation only brittle shear can exist, or if the sum of the angles is to high, probably another mechanism like the wedge mechanism.

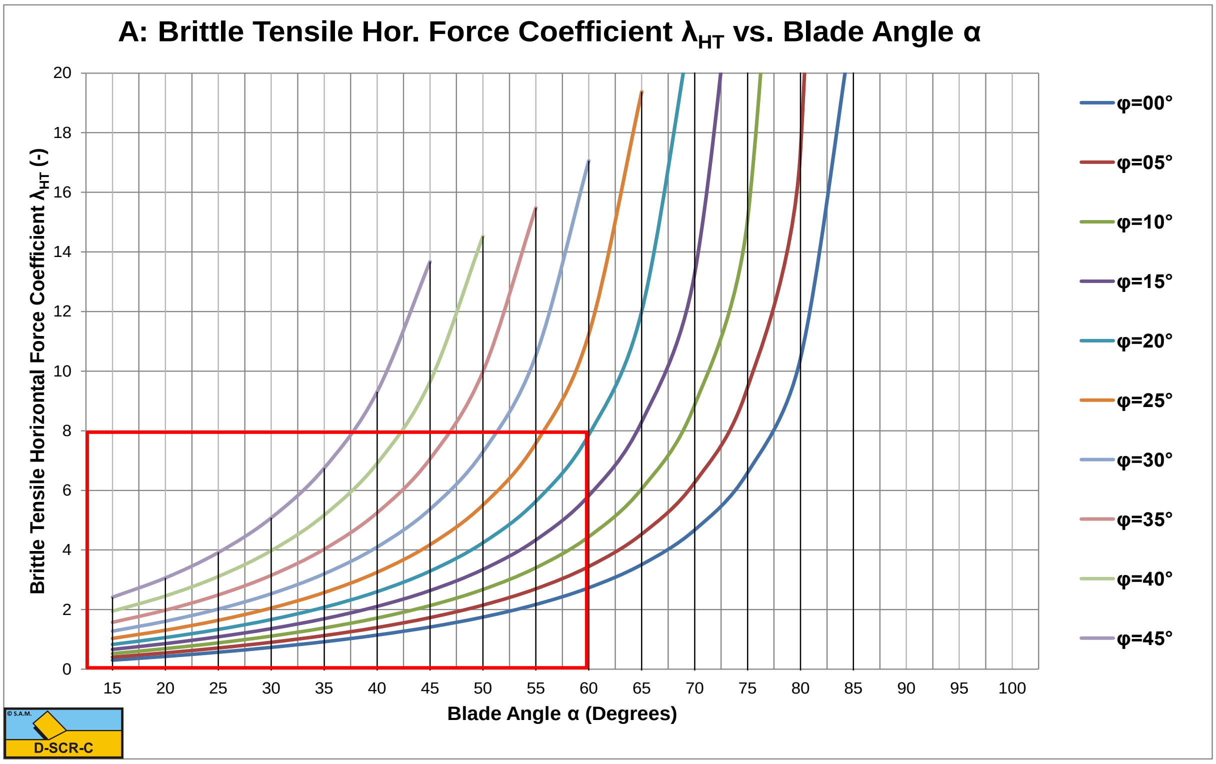

Figure 8-42: The brittle (tensile failure) horizontal force coefficient λ_{HT}.

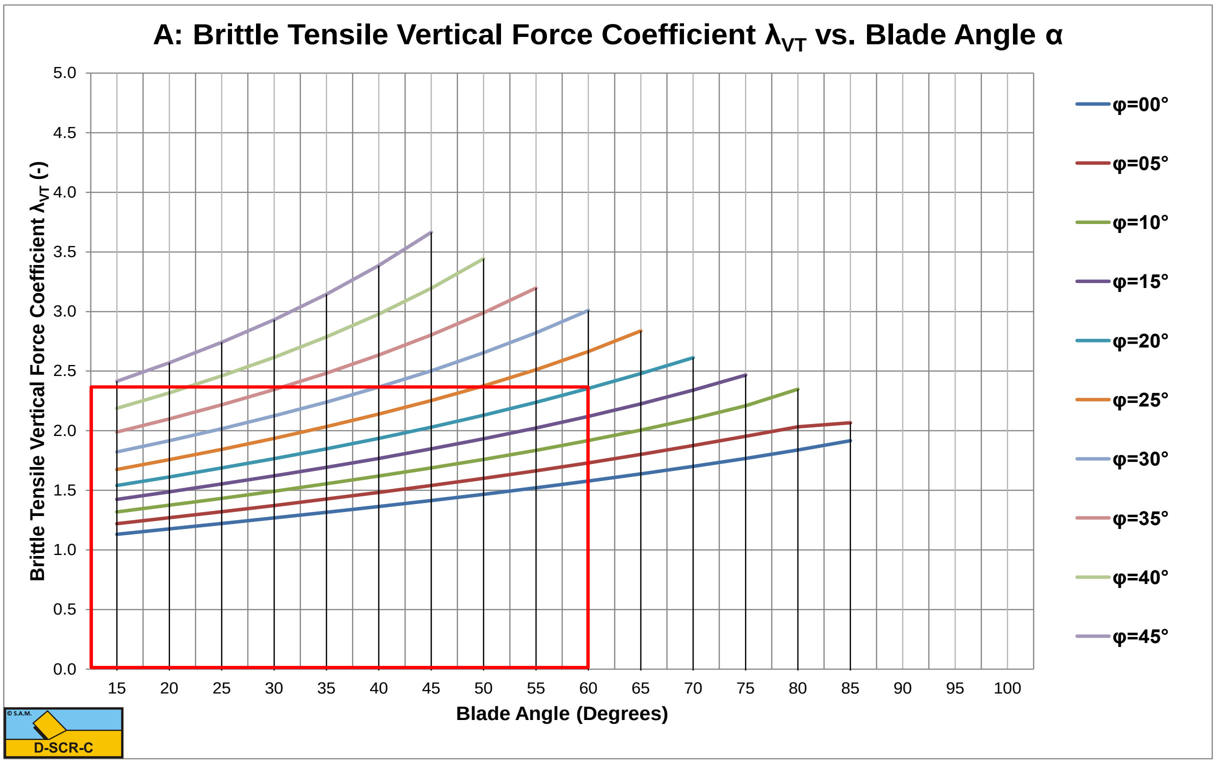

Figure 8-43: The brittle (tensile failure) vertical force coefficient λ_{VT}.

8.7. Correction on the Tear Type and the Chip Type.

The equations for the **Tear Type** are derived based on the shear angle **β** of the **Flow Type**. It is however a question whether this is correct under all circumstances. At the moment of transition of **Flow Type** to **Tear Type** this may be the case, but far away from this transition there may be another optimum shear angle **β**. Combining equations (7-68), (7-69) and (7-88) with the shear angle **β** as a variable and determining the minimum horizontal force, gives a different value for the shear angle **β**.

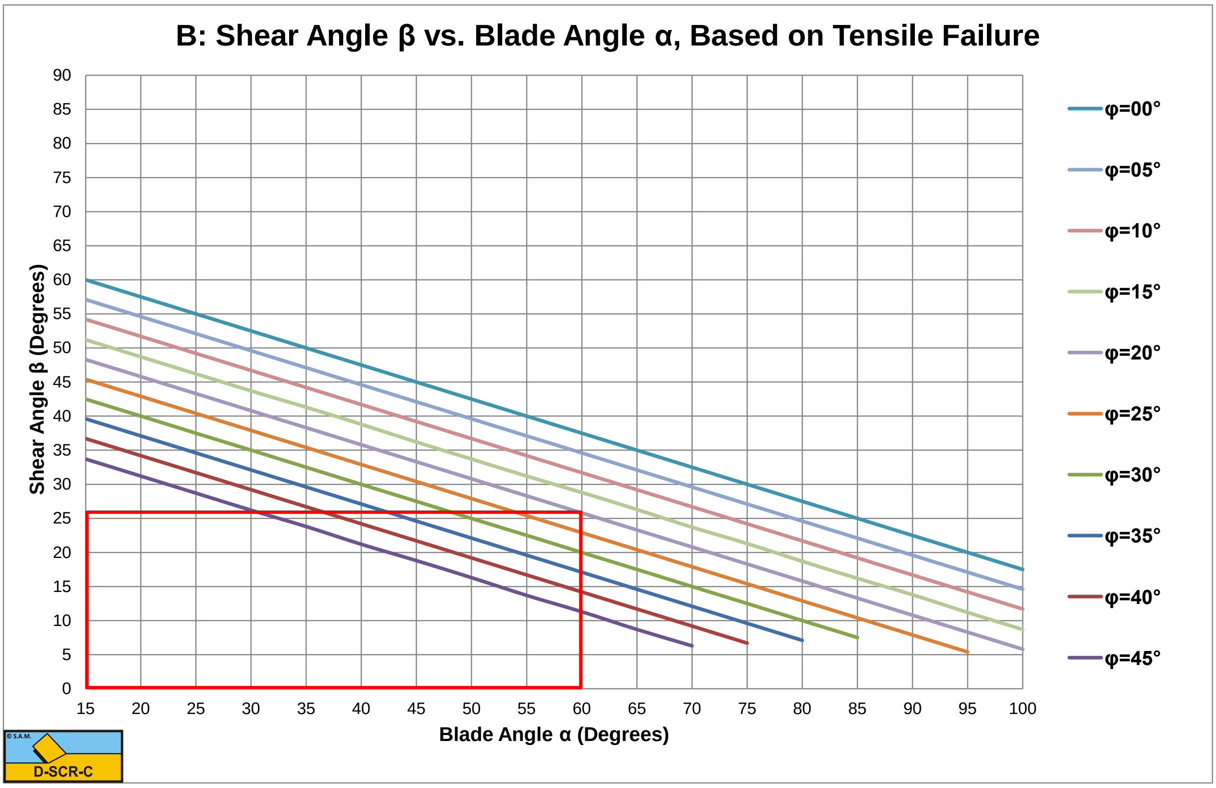

Figure 8-44: The shear angle β as a function of the blade angle α and the internal friction angle φ.

A shear angle **β** is found, exactly 22.5° smaller than the shear angle **β** of the **Flow Type** (see Figure 8-44).

$$\beta = \frac{\pi}{2} - \frac{\pi / 4 + \alpha + \delta + \varphi}{2} \tag{8-133}$$

Figure 8-45 and Figure 8-46 show the horizontal and the vertical cutting force coefficients which are slightly smaller than the horizontal and vertical cutting force coefficients in Figure 8-42 and Figure 8-43. Now there exists a set of parameters where both shear failure and tensile failure give a possible solution. In this range of parameters shear failure will not give tensile stresses that exceed the tensile strength while tensile failure would lead to smaller forces. The occurrence of the **Flow Type** or the **Tear Type** will depend on the history of the cutting process.

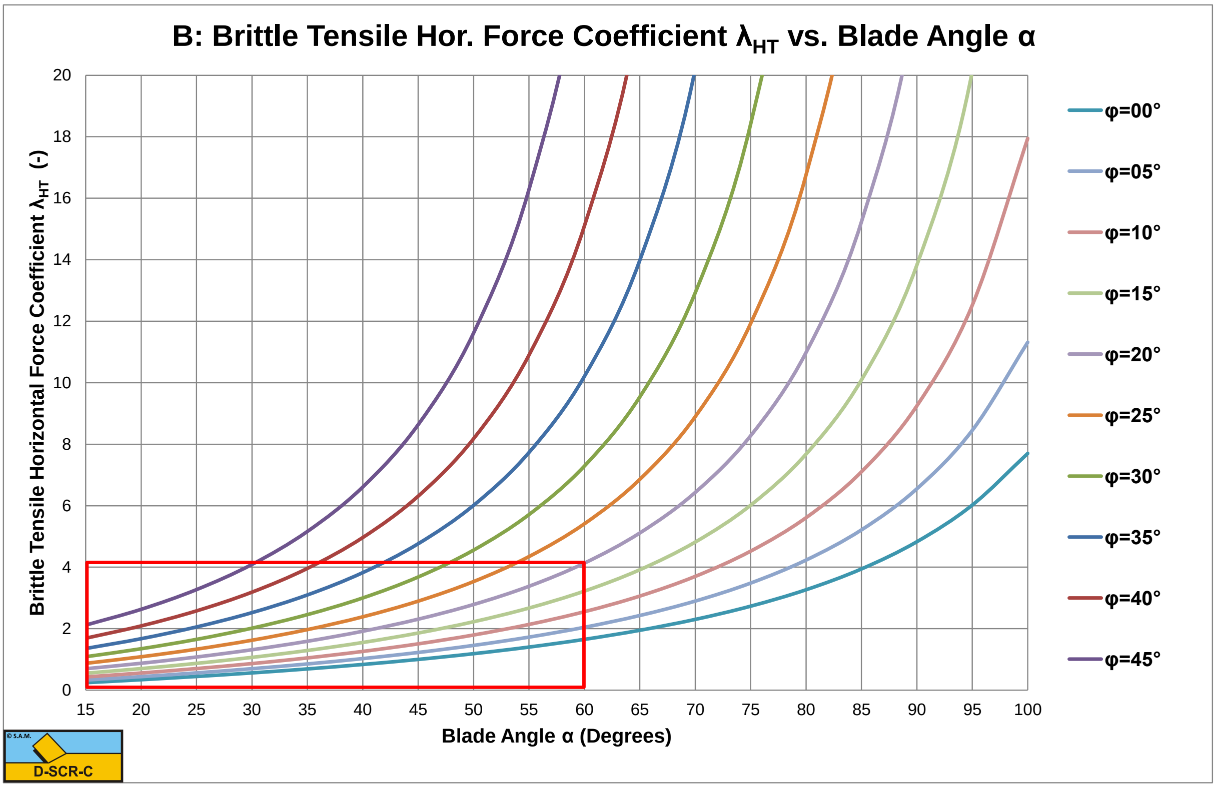

Figure 8-45: The brittle (tensile failure) horizontal force coefficient λ_{HT}.

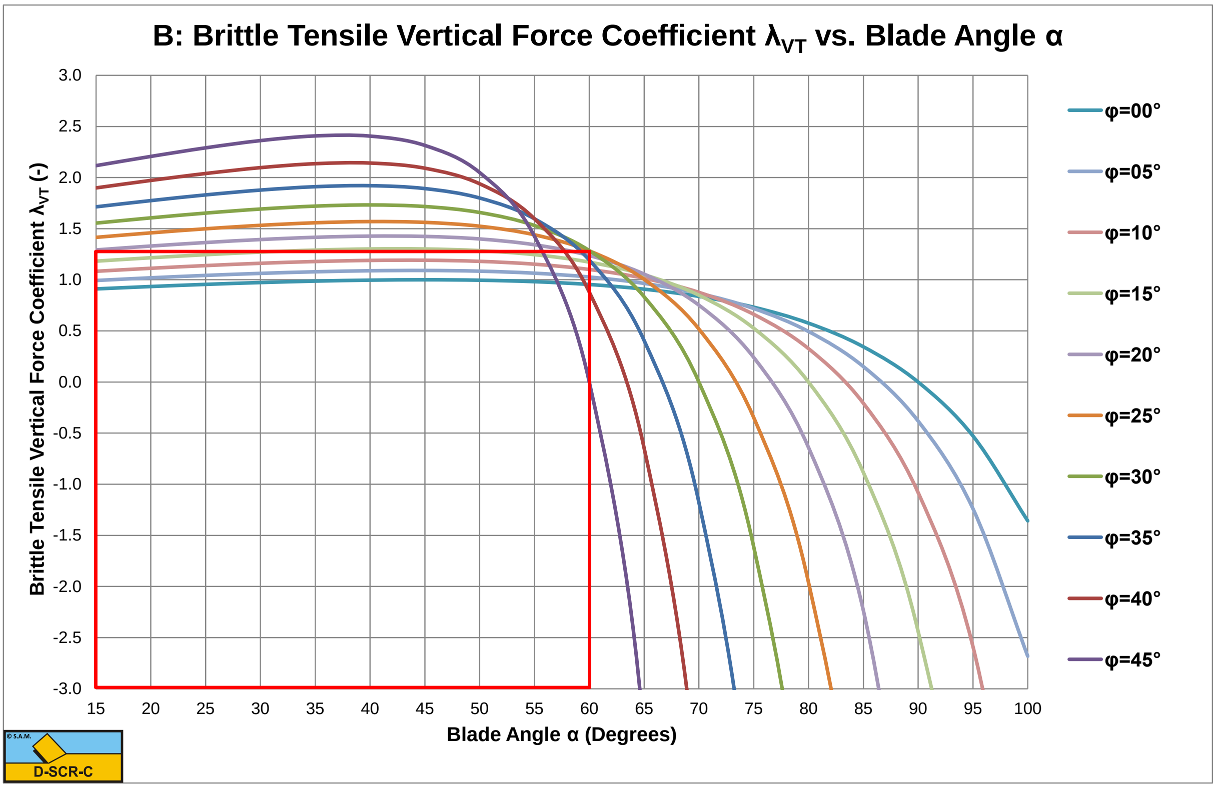

Figure 8-46: The brittle (tensile failure) vertical force coefficient λ_{VT}.

Substituting the corrected shear angle gives for the mobilized shear strength:

$$c_m = \frac{\sigma_T}{\left(\frac{\sin\left(\frac{\alpha + \delta - \varphi - \pi/4}{2}\right)}{\cos\left(\frac{\alpha + \delta + \varphi - \pi/4}{2}\right)} - 1 \right) \cdot \left(\frac{1 - \sin(\varphi)}{\cos(\varphi)} \right)} \tag{8-134}$$

Now the cutting forces can be determined with:

$$F_h = \frac{2 \cdot c_m \cdot h_i \cdot w \cdot \cos(\varphi) \cdot \sin(\alpha + \delta)}{\cos(\pi/4) + \cos(\alpha + \delta + \varphi)} = \lambda_{HT} \cdot \sigma_T \cdot h_i \cdot w \tag{8-135}$$

$$F_v = \frac{2 \cdot c_m \cdot h_i \cdot w \cdot \cos(\varphi) \cdot \cos(\alpha + \delta)}{\cos(\pi/4) + \cos(\alpha + \delta + \varphi)} = \lambda_{VT} \cdot \sigma_T \cdot h_i \cdot w \tag{8-136}$$

8.8. Specific Energy.

For the cases as described above, cutting with a straight blade with the direction of the cutting velocity $\mathbf{v_c}$ perpendicular to the blade (edge of the blade), the specific cutting energy $\mathbf{E_{sp}}$ is:

$$E_{sp} = \frac{F_h \cdot v_c}{h_i \cdot w \cdot v_c} = \frac{F_h}{h_i \cdot w} \tag{8-137}$$

The specific energy of the **Flow Type** or **Crushed Type** of cutting mechanism can be written as:

$$E_{sp} = \lambda_{HF} \cdot c \tag{8-138}$$

The specific energy of the **Tear Type** or **Chip Type** of cutting mechanism can be written as:

$$E_{sp} = \lambda_{HT} \cdot \sigma_T \tag{8-139}$$

Since the specific energy equations are based on the maximum horizontal cutting forces, where the cutting process is most probably either brittle shear or brittle tensile, the average cutting forces will be smaller. How much smaller depends on the type of rock, but literature mentions reductions by 30% to 70%. Since the specific energy is based on the average cutting forces, the values found with the above equations should be multiplied by a factor of 0.3-0.7.

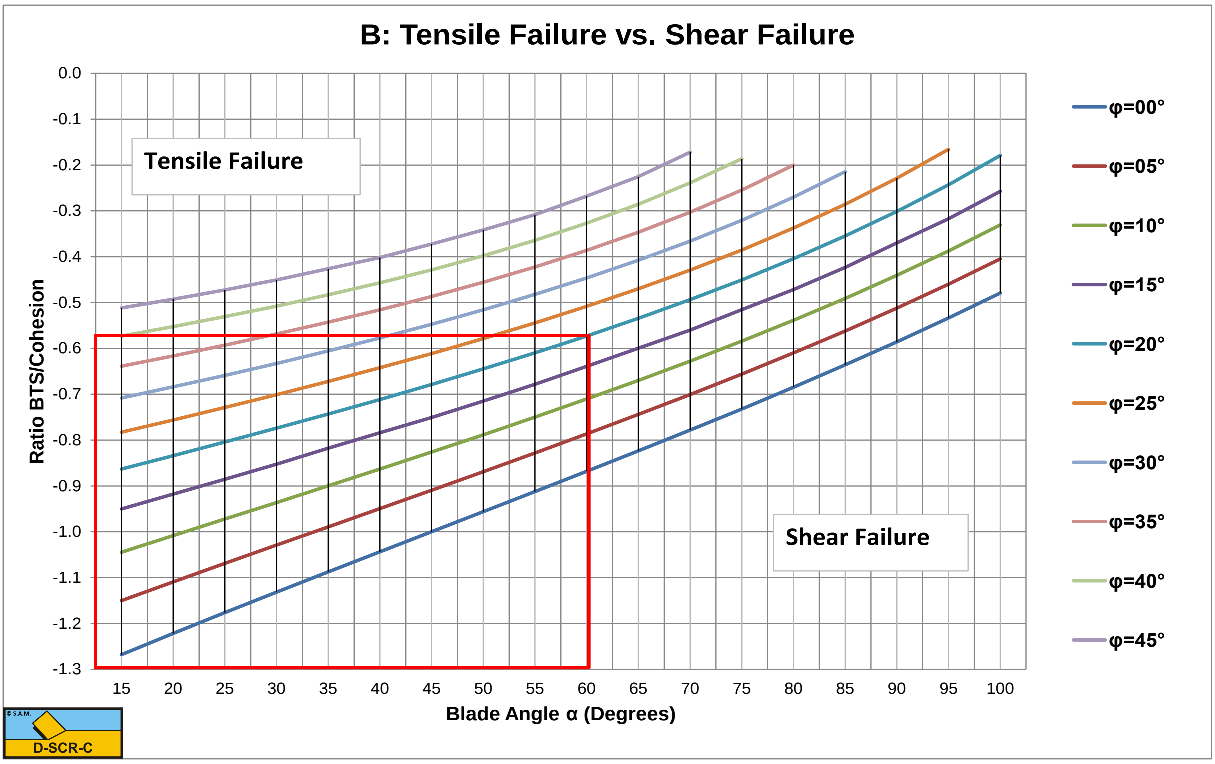

Figure 8-47: Below the lines (equation (8-125)) the cutting process is brittle (shear failure); above the lines it is brittle (tensile failure).

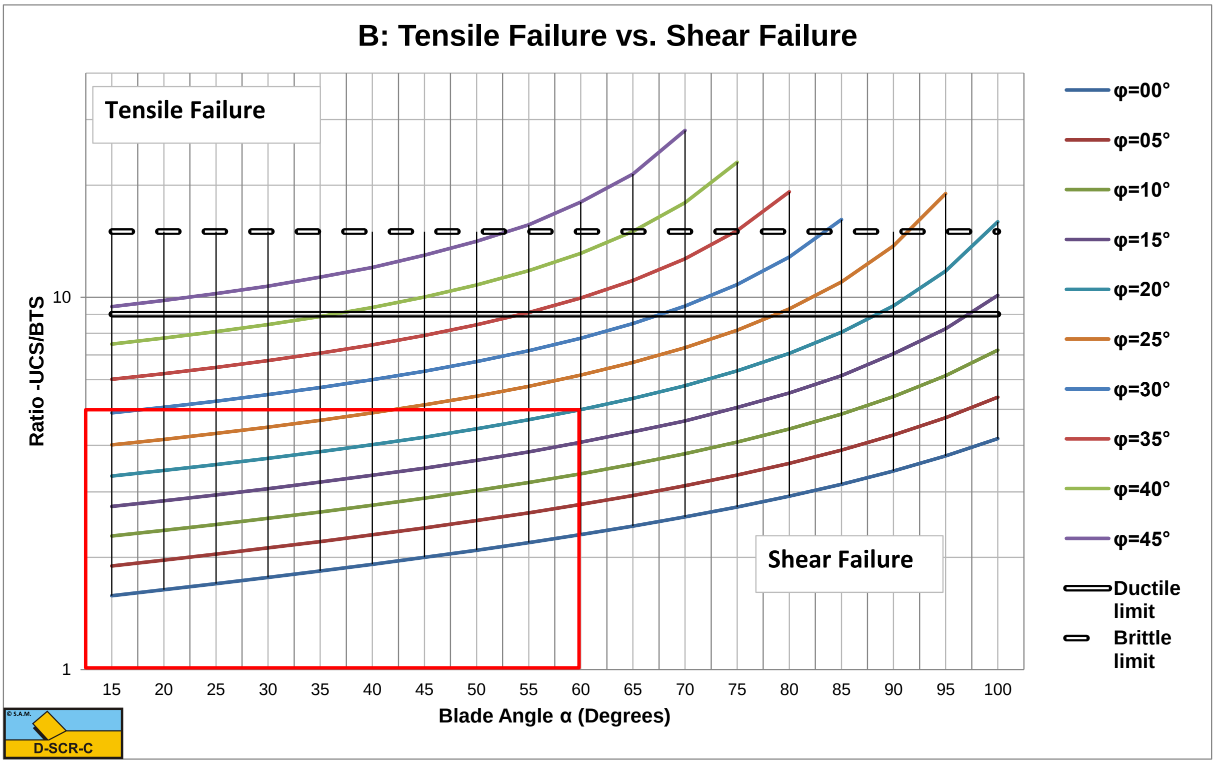

Figure 8-48: The ratio UCS/BTS, below the lines there is brittle (shear failure), above the lines it is brittle (tensile failure).

8.9. Resulting Forces & Mohr Circles.

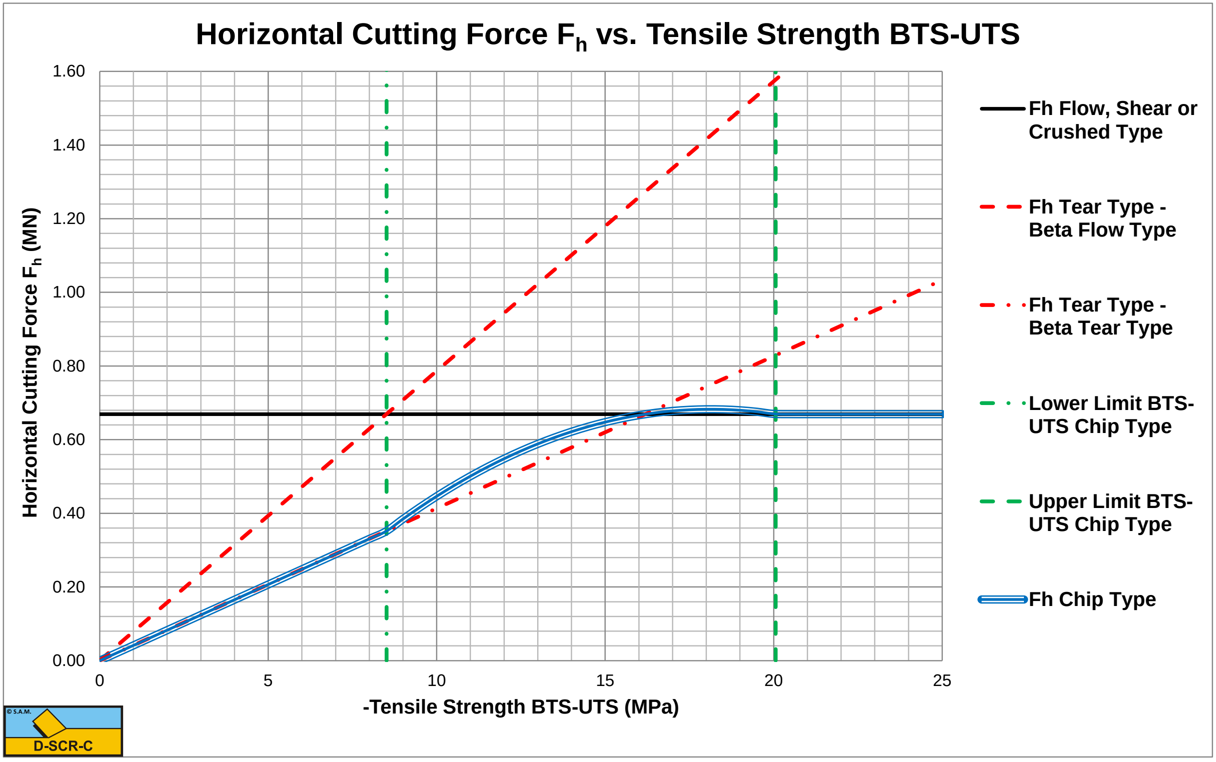

Figure 8-49: Horizontal cutting force: α=60 º, UCS=100 MPa, φ=20º, h_i=0.1 m & w=0.1 m.

Figure 8-50: Vertical cutting force: α=60 º, UCS=100 MPa, φ=20º, h_i=0.1 m & w=0.1 m.

Figure 8-49 and Figure 8-50 show the horizontal and vertical cutting forces. The transition tensile failure/shear failure occurs at a tensile strength of about -8.5 MPa, so 8.5% of the UCS value. From a tensile strength of -8.5 MPa (8.5% UCS) to -20 MPa (20% UCS), both tensile failure and shear failure are possible. Below a tensile strength of -20 MPa (20% UCS) only shear failure is possible. Figure 8-51 and Figure 8-52 show the Mohr circles for tensile strengths of -8.5 MPa (8.5% UCS) and -20 MPa (20% UCS). One can see that with a tensile strength of

-8.5 MPa both tensile failure and shear failure are possible, with a tensile strength of -20 MPa also both tensile failure and shear failure are possible. It should be mentioned here that the forces shown are peak forces, so average forces may reduce to 50%-60%. So the two limiting cases are shown.

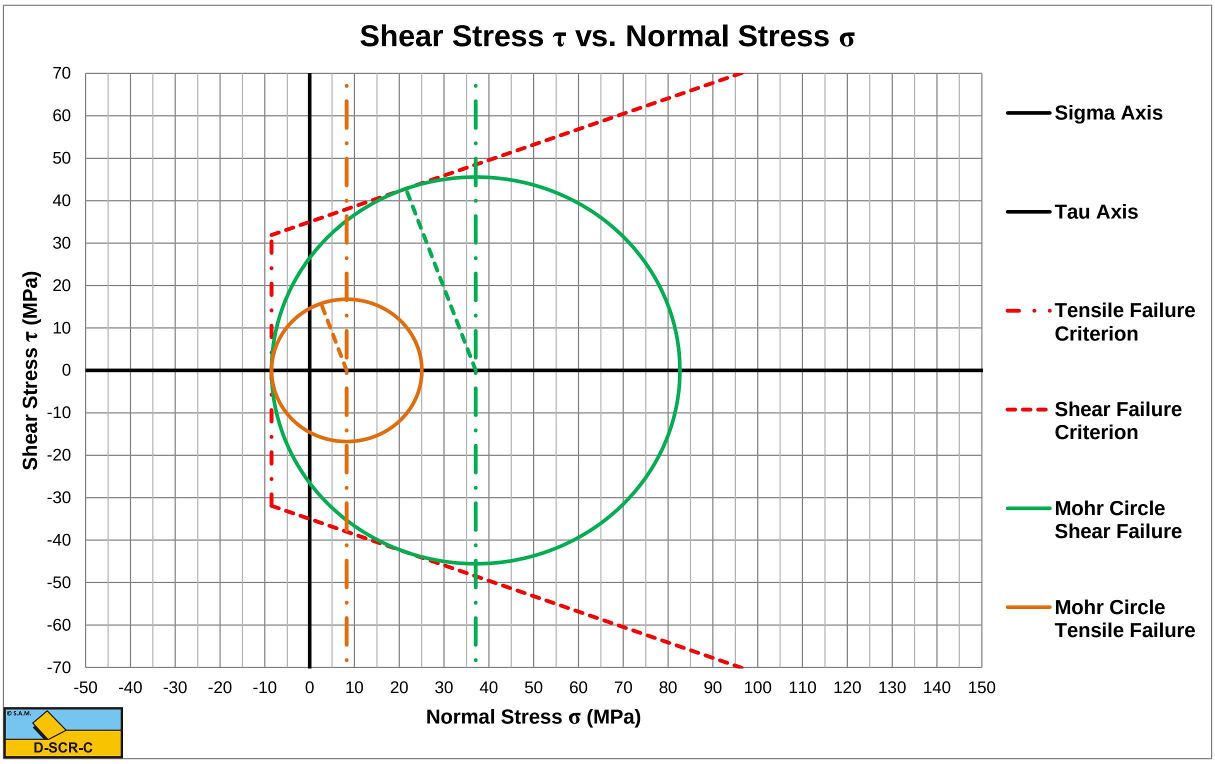

Figure 8-51: Mohr circles tensile strength -8.5 MPA.

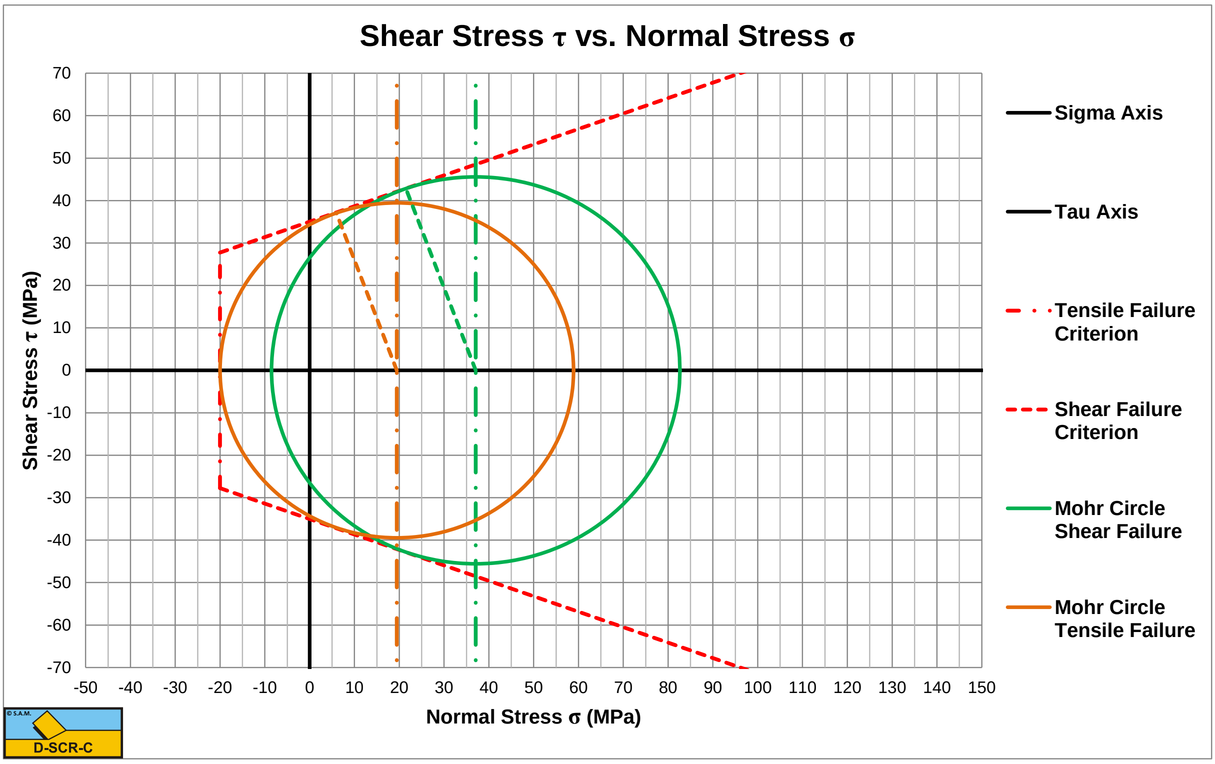

Figure 8-52: Mohr circles tensile strength -20 MPa.

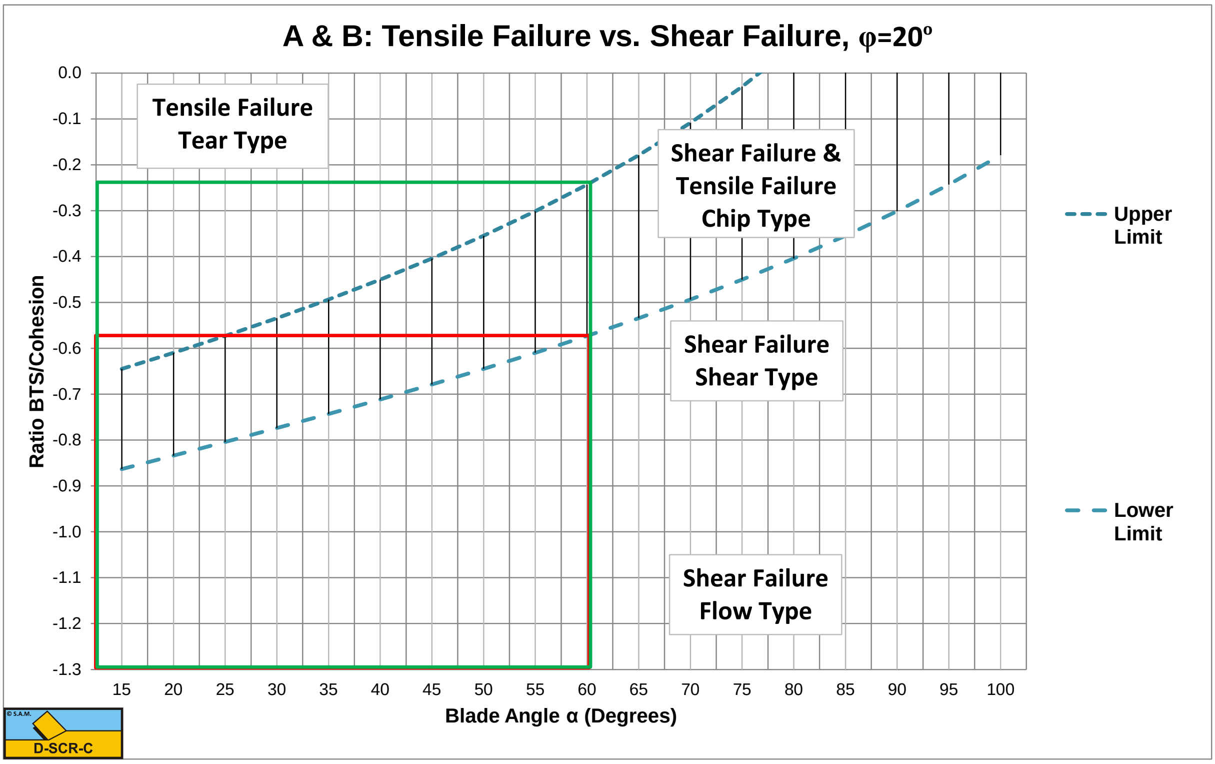

Figure 8-53: The tensile vs. shear failure range
based on the BTS to cohesion ratio.

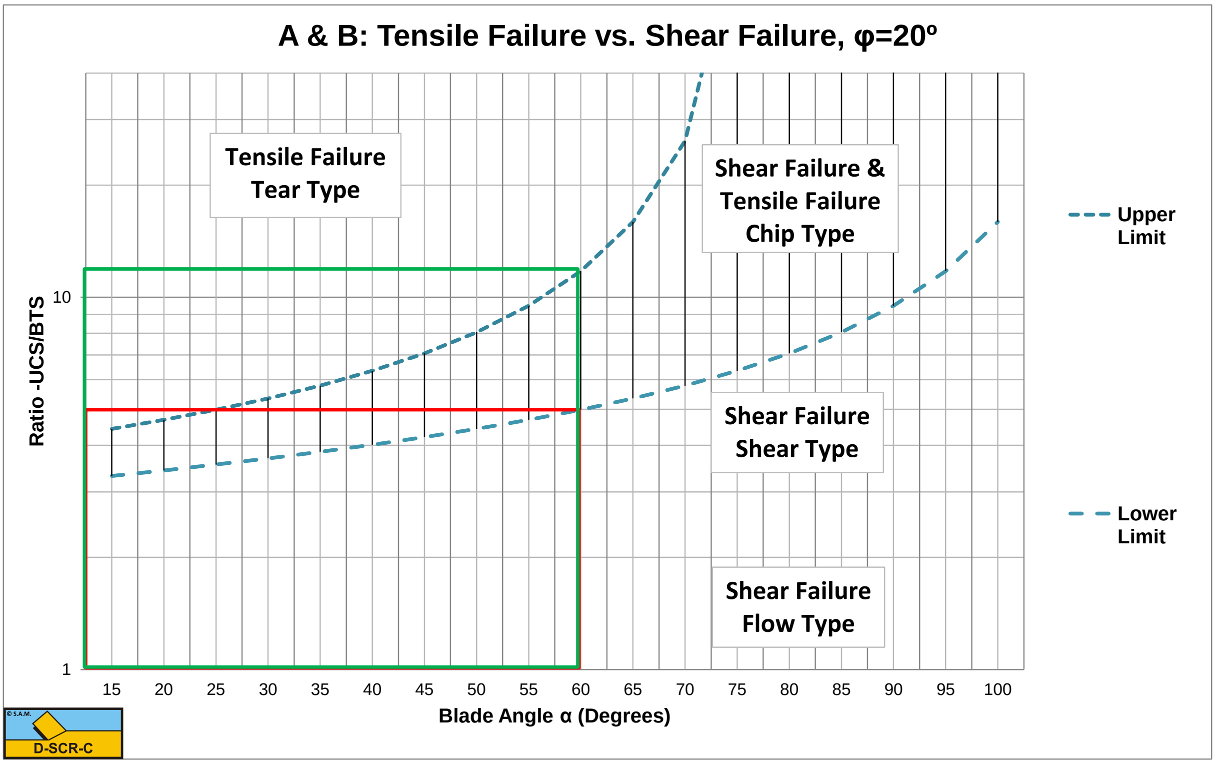

Figure 8-54 The tensile vs. shear failure range
based on the UCS to BTS ratio.

8.10. Example.

In this chapter and in Appendix W many graphs are given with a red or green rectangle giving the value of the different parameters for an **α=60º** blade and an internal friction angle **φ=20º**. The external friction angle is assumed to be **δ=2/3·φ**. Most graphs are dimensionless, but Figure 8-49, Figure 8-50, Figure 8-51 and Figure 8-52 are based on a compressive strength **UCS=100 MPa**, a blade width **w=0.1 m** and a layer thickness **h_i=0.1 m**.

8.10.1. Step 1: Brittle Shear.

The the shear angle **β=43.3º**, horizontal force coefficient **λ_{HF}=1.912**, the verticle force coefficient **λ_{VF}=0.572** and the **E_{sp}/UCS ratio=0.669**. This gives a horizontal force **F_h=0.669 MN**, a vertical force **F_v=0.200 MN** and a specific energy of **E_{sp}=66.9 MPa**. These values are peak values, but for comparison reasons these values will be used.

8.10.2. Step 2: The Transition Brittle Shear/Brittle Tensile.

The transitions brittle shear/brittle tensile occur for **UCS/BTS=4.985** and **UCS/BTS=11.75**. This can also be written as **BTS=0.085·UCS** and **BTS=0.2·UCS**, so **BTS=8.5 MPa** and **BTS=20 MPa**. **BTS** or **UTS** are considered positive numbers, while tensile strength is considered to be negative in this book.
This means that below the **Lower Limit BTS=8.5 MPa** brittle shear failure cannot exist, so there is always brittle tensile failure. Above the **Upper Limit BTS=20 MPa** brittle tensile failure cannot exist, so there is always brittle shear failure. In between, both can exist , even at the same time, according to Figure 8-19 the **Chip Type**. Figure 8-49 and Figure 8-50 show the horizontal and vertical cutting forces as a function of the tensile strength for the case considered. Interpolation curves are shown, simulating the simultaneous occurrence of brittle shear and brittle tensile failure according to the **Chip Type**. For this interpolation the following method is used:

First define a factor **f** according to:

$$\mathrm{BTS} < \mathrm{LowerLimit\ BTS} \quad \Rightarrow \mathrm{f} = 1$$

$$\mathrm{BTS} > \mathrm{UpperLimit\ BTS} \quad \Rightarrow \mathrm{f} = 0$$

$$\begin{array}{l} \mathrm{BTS} > \mathrm{LowerLimit\ BTS} \\ \qquad\qquad \Rightarrow \mathrm{f} = \left(\dfrac{\mathrm{UpperLimit\ BTS} - \mathrm{BTS}}{\mathrm{UpperLimit\ BTS} - \mathrm{LowerLimit\ BTS}} \right)^{p} \\ \mathrm{BTS} < \mathrm{UpperLimit\ BTS} \end{array} \tag{8-140}$$

Now the resulting cutting forces can be determined with:

$$\begin{aligned} F_h &= F_{h,\mathrm{TearType}} \cdot f + F_{h,\mathrm{ShearType}} \cdot (1-f) \\ F_v &= F_{v,\mathrm{TearType}} \cdot f + F_{v,\mathrm{ShearType}} \cdot (1-f) \end{aligned} \tag{8-141}$$

The power **p** used in Figure 8-49 and Figure 8-50 is **p=1**, a linear transition from tensile failure to shear failure, the **Chip Type**.

8.10.3. Step 3: Applying Tensile Strengths of -5 MPa, -10 MPa and -25 MPa.

From Figure 8-49 and Figure 8-50 the horizontal and vertical peak forces can be determined. They are given in the following table. Between brackets estimated average values, based on a 60% ratio between average and peak values.

Table 8-3: Resulting forces and specific energy.

Tensile Strength	**F_h (N)**	**F_v (MN)**	**E_{sp} (MPa)**	**E_{sp}/UCS (%)**
-5 MPa	0.207 (0.124)	0.062 (0.037)	20.7 (12.4)	20.7 (12.4)
-10 MPa	0.446 (0.268)	0.134 (0.080)	44.6 (26.8)	44.6 (26.8)
-25 MPa	0.669 (0.401)	0.200 (0.120)	66.9 (40.1)	66.9 (40.1)

The **UCS/BTS** ratio of 10 matches the findings of Roxborough (1987) giving a specific energy of about 25% of the **UCS** value.

$$E_{sp} = 0.25 \cdot U.C.S. + 0.11 \qquad \textbf{(8-142)}$$

8.11. Nomenclature.

a, τ_a	Adhesive shear strength	kPa
A	Adhesive force on the blade	kN
BTS	Brazilian Tensile Strength	kPa
c, τ_c	Cohesive shear strength	kPa
c_m	Mobilized cohesive shear strength	kPa
C	Cohesive force on shear plane	kN
E_{sp}	Specific energy	kPa
F	Force	kN
F_c	Cutting force on chisel Evans model	kN
F_n	Normal force on chisel Evans model	kN
F_{ch}	Horizontal force component Evans model	kN
F_{cv}	Vertical force component Evans model	kN
F_h	Horizontal cutting force	kN
F_v	Vertical cutting force	kN
g	Gravitational constant (9.81)	m/s^2
G	Gravitational force	kN
h_i	Initial thickness of layer cut	m
h_b	Height of the blade	m
K_1	Grain force on the shear plane	kN
K_2	Grain force on the blade	kN
I	Inertial force on the shear plane	kN
n	Power in Nishimatsu model	-
N_1	Normal grain force on shear plane	kN
N_2	Normal grain force on blade	kN
p	Stress in shear plane Nishimatsu model	kPa
p_0	Stress at tip of chisel Nishimatsu model	kPa
P_c	Cutting power	kW
Q	Production	m^3
r	Radius in Evans model	m
r	Adhesion/cohesion ratio	-
r_1	Pore pressure on shear plane/cohesion ratio	-
r_2	Pore pressure on blade/cohesion ratio	-
R	Radius of Mohr circle	kPa
R	Force on chisel Evans model	kN

R_n	Normal force on chisel surface Evans model	kN
R_f	Friction force on chisel surface Evans model	kN
R_1	Acting point on the shear plane	m
R_2	Acting point on the blade	m
S_1	Shear force due to internal friction on the shear plane	kN
S_2	Shear force due to external friction on the blade	kN
T	Tensile force	kN
UCS	Unconfined Compressive Strength	kPa
v_c	Cutting velocity	m/s
w	Width of the blade	m
W_1	Force resulting from pore under pressure on the shear plane	kN
W_2	Force resulting from pore under pressure on the blade	kN
α	Blade angle	rad
β	Angle of the shear plane with the direction of cutting velocity	rad
ε	Angle of chisel with horizontal Evans model	rad
τ	Shear stress	kPa
τ_a, a	Adhesive shear strength (strain rate dependent)	kPa
τ_c, c	Cohesive shear strength (strain rate dependent)	kPa
τ_{S1}	Average shear stress on the shear plane	kPa
τ_{S2}	Average shear stress on the blade	kPa
σ	Normal stress	kPa
σ_C	Center of Mohr circle	kPa
σ_T	Tensile strength	kPa
σ_{min}	Minimum principal stress in Mohr circle	kPa
σ_{N1}	Average normal stress on the shear plane	kPa
σ_{N2}	Average normal stress on the blade	kPa
φ	Angle of internal friction	rad
δ	Angle of external friction	rad
λ	Distance in Nishimatsu model	m
λ_s	Strengthening factor	-
λ_1	Acting point factor on the shear plane	-
λ_2	Acting point factor on the blade	-
λ_{HF}	**Flow Type/Crushed Type** horizontal force coefficient	-
λ_{VF}	**Flow Type/Crushed Type** vertical force coefficient	-
λ_{HT}	**Tear Type/Chip Type** horizontal force coefficient	-
λ_{VT}	**Tear Type/Chip Type** vertical force coefficient	-
ω	Angle in Evans model	rad

Chapter 9: Rock Cutting: Hyperbaric Conditions.

9.1. Introduction.

For rock cutting in dredging and mining under hyperbaric conditions not much is known yet. The data available are from drilling experiments under very high pressures (Zijsling (1987), Kaitkay and Lei (2005) and Rafatian et al. (2009)). The main difference between dredging and mining applications on one side and drilling experiments on the other side is that in dredging and mining the thickness of the layer cut is relatively big, like 5-10 cm, while in drilling the process is more like scraping with a thickness less than a mm. From the drilling experiments it is known that under high pressures there is a transition from a brittle-shear cutting process to a ductile-flow cutting process. Figure 9-2 and Figure 9-3 from Rafatian et al. (2009) show clearly that with increasing confining pressure, first the specific energy $\mathbf{E_{sp}}$ increases with a steep curve, which is the transition brittle-ductile, after which the curve for ductile failure is reached which is less steep. The transition is completed at 690 kPa-1100 kPa, matching a water depth of 69-110 m.

The Carthage Marble has a UCS value of about 100 MPa and the Indiana Limestone a UCS value of 48 MPa. The cutter had a blade angle $\boldsymbol{\alpha}$ of 110º. Figure 9-29 shows the specific energy (according to the theory as developed in this chapter) as a function of the UCS value and the confining pressure (water depth). For the Carthage Marble a specific energy of about 400 MPa is found under atmospheric conditions for the ductile cutting process. For the brittle shear process 25%-50% of this value should be chosen, matching Figure 9-2 at 0 MPa. For a water depth of 65 m, matching 0.65 MPa the graph gives about 500 MPa specific energy, which is a bit lower than the measurements. For the Indiana Limestone a specific energy of about 200 MPa is found under atmospheric conditions for the ductile cutting process. Also here, for the brittle shear process, 25%-50% of this value should be chosen, matching Figure 9-3 at 0 MPa confining pressure. For a water depth of 65 m, matching 0.65 MPa the graph gives about 280 MPa specific energy, which is a bit lower than the measurements.
For deep sea mining applications this is still shallow water. Both graphs show an increase of the $\mathbf{E_{sp}}$ by a factor 2-2.5 during the transition brittle-shear to ductile-flow, which matches a reduction factor of 0.25-0.5 for the average versus the maximum cutting forces as mentioned before. Figure 9-22 and Figure 9-23 show the results of Zijsling (1987) in Mancos Shale and Figure 9-1 shows the results of Kaitkay & Lei (2005) in Carthage Marble.
The experiments of Kaitkay & Lei (2005) also show that the transition from brittle-shear to ductile-flow takes place in the first few hundreds of meters of water depth (from 0 to about 2.5 MPa). They also show a multiplication factor of about 3 during this transition. The experiments of Zijsling (1987) are not really suitable for determining the transition brittle-shear to ductile-flow because there are only measurements at 0 MPa and about 10 MPa, so they do not show when the transition is completed, but they do show the increase in forces and $\mathbf{E_{sp}}$.

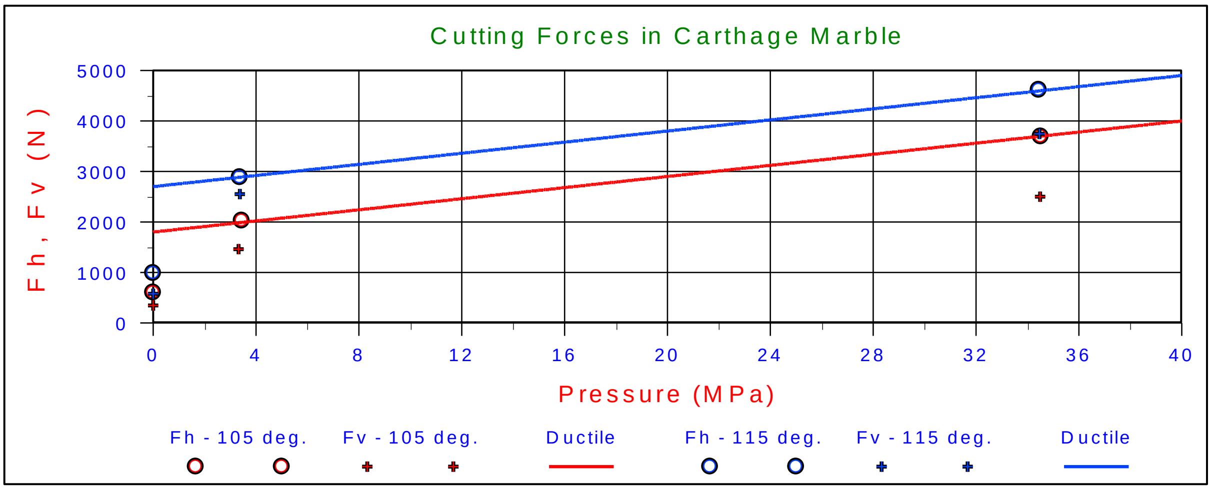

Figure 9-1: Variations of average cutting forces with hydrostatic pressure, Kaitkay & Lei (2005).

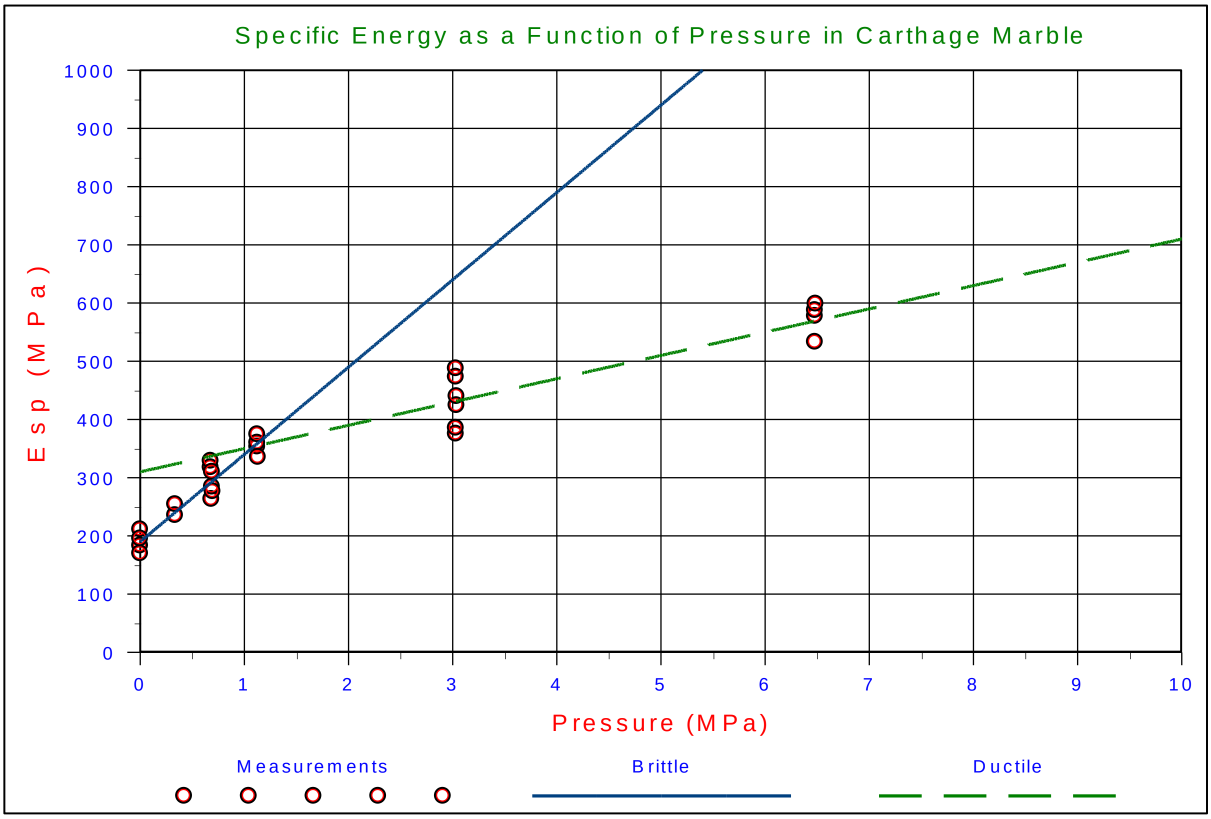

Figure 9-2: MSE versus confining pressure for Carthage marble in light and viscous mineral oil, Rafatian et al. (2009).

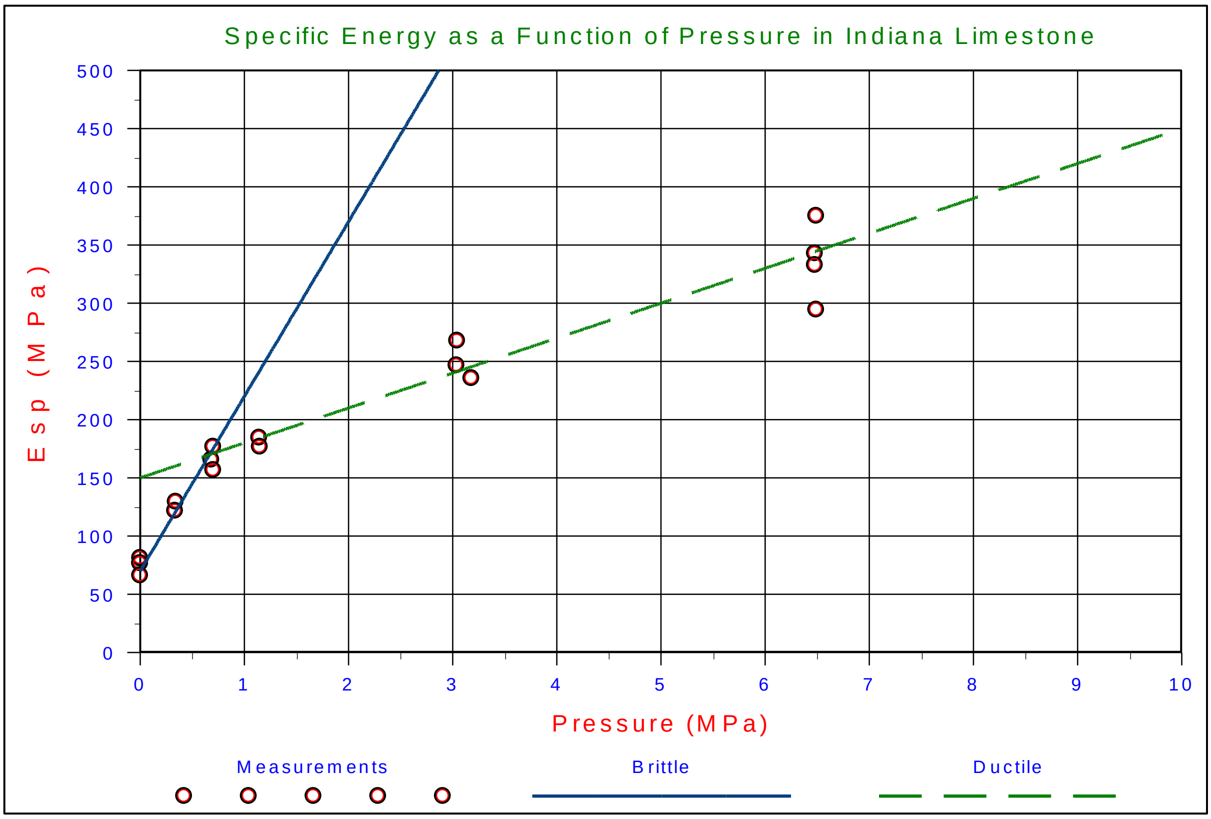

Figure 9-3: MSE versus confining pressure for Indiana limestone in light mineral oil, Rafatian et al. (2009).

The explanation for the transition from brittle-shear to ductile-flow is, according to Zijsling (1987), the dilatation due to shear stress in the shear plane resulting in pore under pressures, similar to the cutting process in water saturated sand as has been described by Miedema (1987 September). Zijsling however did not give any mathematical model. Detournay & Atkinson (2000) use the same explanation and use the Merchant (1944) model (equations (8-109) and (8-110) for the flow type cutting process) to quantify the cutting forces and specific energy by adding the pore pressures to the basic equations:

$$F_h = \frac{2 \cdot h_i \cdot w \cdot \cos(\varphi) \cdot \sin(\alpha + \delta)}{1 + \cos(\alpha + \delta + \varphi)} \cdot \left(c + p_{1m} \cdot \tan(\varphi)\right) \qquad \textbf{(9-1)}$$

The difference between the bottom hole pressure (or hydrostatic pressure) and the average pressure $\mathbf{p_{1m}}$ in the shear plane has to be added to the effective stress between the particles in the shear plane **A-B.** Multiplying this with the tangent of the internal friction angle gives the additional shear stress in the shear plane **A-B**, see Figure 9-4.

So in the vision of Detournay & Atkinson (2000) the effect of pore water under pressures $\mathbf{p_{1m}}$ is like an apparent additional cohesion. Based on this they find a value of the external friction angle which is almost equal to the internal friction angle of 23º for the experiments of Zijsling (1987). Detournay & Atkinson (2000) however forgot that, if there is a very large pore water under pressure in the shear plane, this pore water under pressure has not disappeared when the layer cut moves over the blade or cutter. There will also be a very large pore water under pressures on the blade as has been explained by Miedema (1987 September) for water saturated sand in dredging applications. In the next paragraph this will be explained.

9.2. The Flow Type and the Crushed Type.

First of all it is assumed that the hyperbaric cutting mechanism is similar to the **Flow Type** as is shown in Figure 9-5. There may be 3 mechanisms that might explain the influence of large hydrostatic pressures:

1. When a tensile failure occurs, water has to flow into the crack, but the formation of the crack goes so fast that cavitation will occur.
2. A second possible mechanism that might occur is an increase of the pore volume due to the elasticity of the rock and the pore water. If high tensile stresses exist in the rock, then the pore volume will increase due to elasticity. Because of the very low permeability of the rock, the compressibility of the pore water will have to deal with this. Since the pore water is not very compressible, at small volume changes this will already result in large under pressures in the pores. Whether this will lead to full cavitation of the pore water is still a question.
3. Due to the high effective grain stresses, the particles are removed from the matrix which normally keeps them together and makes it a rock. This will happen near the shear plane. The loose particles will be subject to dilatation, resulting in an increase of the pore volume. This pore volume increase results in water flow to the shear plane, which can only occur if there is an under pressure in the pores in the shear plane. If this under pressure reaches the water vapor pressure, cavitation will occur, which is the lower limit for the absolute pressures and the upper limit for the pressure difference between the bottom hole or hydrostatic pressure and the pore water pressure. The pressure difference is proportional to the cutting velocity and the dilatation, squared proportional to the layer thickness and reversely proportional to the permeability of the rock. If the rock is very impermeable, cavitation will always occur and the cutting forces will match the upper limit.

Now under atmospheric conditions, the compressive strength of the rock will be much bigger than the atmospheric pressure; usually the rock will have a compressive strength of 1 MPa or more while the atmospheric pressure is just 100 kPa. Strong rock may have compressive strengths of 10's of MPa's, so the atmospheric pressure and thus the effect of cavitation in the pores or the crack can be neglected. However in oil drilling and deep sea mining at water depths of 3000 m nowadays plus a few 1000's m into the seafloor (in case of oil drilling), the hydrostatic pressure could easily increase to values higher than 10 MPa up to 100 MPa causing softer rock to behave ductile, where it would behave brittle under low hydrostatic pressures.

It should be noted that brittle-tear failure, which is tensile failure, will only occur under atmospheric conditions and small blade angles as used in dredging and mining. With blade angles larger than 90° brittle-tear will never occur (see Figure 8-38). Brittle-shear may occur in all cases under atmospheric conditions.

Now what is the difference between rock cutting under atmospheric conditions and under hyperbaric conditions? The difference is the extra pore pressure forces $\mathbf{W_1}$ and $\mathbf{W_2}$ on the shear plane and on the blade as will be explained next.

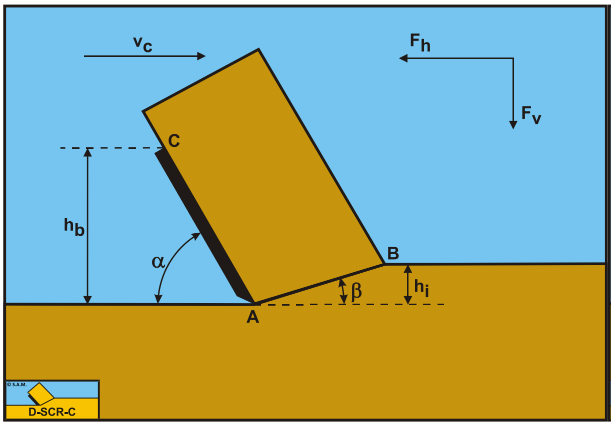

Figure 9-4: The definitions of the cutting process.

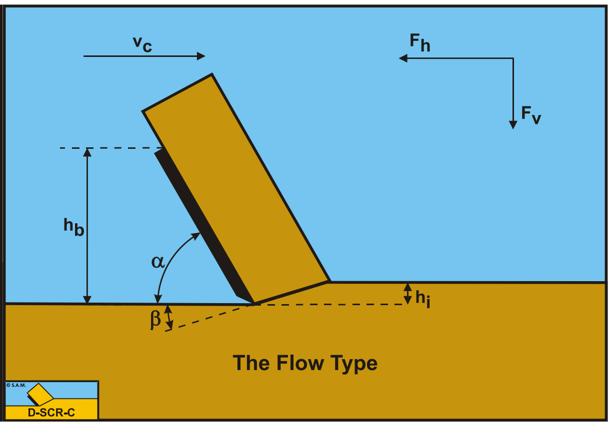

Figure 9-5: The Flow Type cutting mechanism.

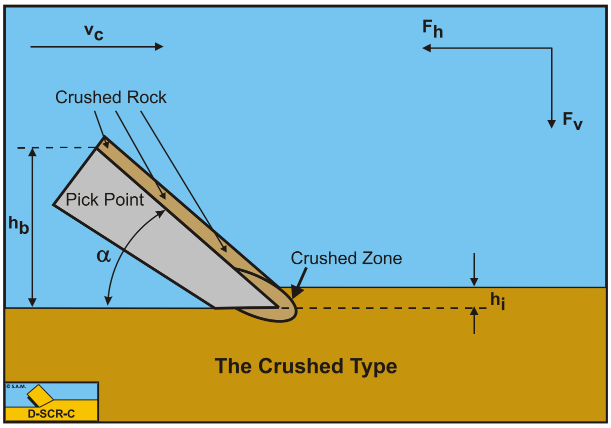

Figure 9-6: The Crushed Type cutting mechanism.

Figure 9-7 illustrates the forces on the layer of rock cut. The forces acting on this layer are:

1. A normal force acting on the shear surface **N_1** resulting from the grain stresses.
2. A shear force **S_1** as a result of internal friction **$N_1 \cdot \tan(\phi)$**.
3. A force **W_1** as a result of water under pressure in the shear zone.
4. A shear force **C** as a result of the cohesive shear strength **τ_c** or **c**. This force can be calculated by multiplying the cohesive shear strength **τ_c/c** with the area of the shear plane.
5. A force normal to the blade **N_2** resulting from the grain stresses.
6. A shear force **S_2** as a result of the external friction **$N_2 \cdot \tan(\delta)$**.
7. A shear force **A** as a result of pure adhesion between the rock and the blade **τ_a** or **a**. This force can be calculated by multiplying the adhesive shear strength **τ_a/a** of the rock with the contact area between the rock and the blade. In most rocks this force will be absent.
8. A force **W_2** as a result of water under pressure on the blade

The normal force **N_1** and the shear force **S_1** on the shear plane can be combined to a resulting grain force **K_1**.

$$K_1 = \sqrt{N_1^2 + S_1^2} \tag{9-2}$$

The forces acting on a straight blade when cutting rock, can be distinguished as:

1. A force normal to the blade **N_2** resulting from the grain stresses.
2. A shear force **S_2** as a result of the external friction **$N_2 \cdot \tan(\delta)$**.
3. A shear force **A** as a result of pure adhesion between the rock and the blade **τ_a** or **c**. This force can be calculated by multiplying the adhesive shear strength **τ_a/a** of the rock with the contact area between the rock and the blade. In most rocks this force will be absent.
4. A force **W_2** as a result of water under pressure on the blade

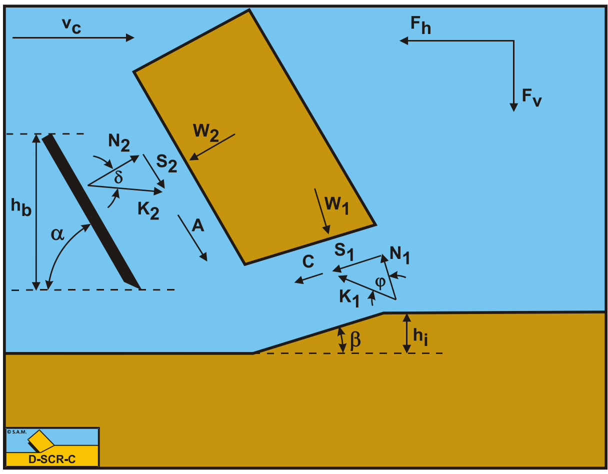

Figure 9-7: The forces on the layer cut in rock (hyperbaric).

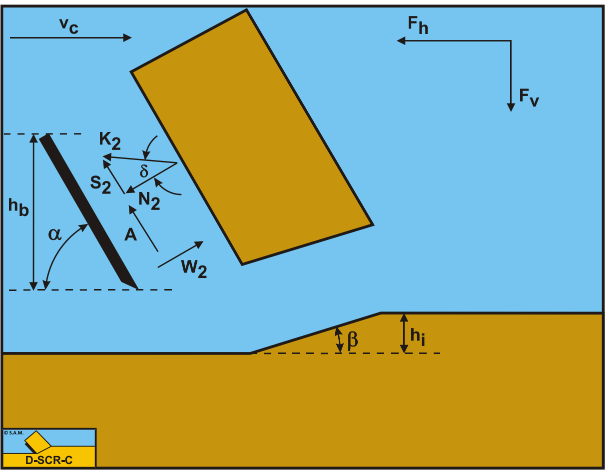

Figure 9-8: The forces on the blade in rock (hyperbaric).

These forces are shown in Figure 9-8. If the forces **N**$_2$ and **S**$_2$ are combined to a resulting force **K**$_2$ and the adhesive force and the water under pressures are known, then the resulting force **K**$_2$ is the unknown force on the blade. By taking the horizontal and vertical equilibrium of forces an expression for the force **K**$_2$ on the blade can be derived.

$$K_2 = \sqrt{N_2^2 + S_2^2} \tag{9-3}$$

The horizontal equilibrium of forces:

$$\begin{aligned}\sum F_h &= K_1 \cdot \sin(\beta + \varphi) - W_1 \cdot \sin(\beta) + C \cdot \cos(\beta) \\ &\quad - A \cdot \cos(\alpha) + W_2 \cdot \sin(\alpha) - K_2 \cdot \sin(\alpha + \delta) = 0\end{aligned} \tag{9-4}$$

The vertical equilibrium of forces:

$$\begin{aligned}\sum F_v &= -K_1 \cdot \cos(\beta + \varphi) + W_1 \cdot \cos(\beta) + C \cdot \sin(\beta) \\ &\quad + A \cdot \sin(\alpha) + W_2 \cdot \cos(\alpha) - K_2 \cdot \cos(\alpha + \delta) = 0\end{aligned} \tag{9-5}$$

The force **K**$_1$ on the shear plane is now:

$$K_1 = \frac{W_2 \cdot \sin(\delta) + W_1 \cdot \sin(\alpha + \beta + \delta) - C \cdot \cos(\alpha + \beta + \delta) + A \cdot \cos\left(\delta\right)}{\sin(\alpha + \beta + \delta + \varphi)} \tag{9-6}$$

The force **K**$_2$ on the blade is now:

$$K_2 = \frac{W_2 \cdot \sin(\alpha + \beta + \varphi) + W_1 \cdot \sin(\varphi) + C \cdot \cos(\varphi) - A \cdot \cos\left(\alpha + \beta + \varphi\right)}{\sin(\alpha + \beta + \delta + \varphi)} \tag{9-7}$$

From equation (9-7) the forces on the blade can be derived. On the blade a force component in the direction of cutting velocity **F**$_h$ and a force perpendicular to this direction **F**$_v$ can be distinguished.

$$F_h = -W_2 \cdot \sin(\alpha) + K_2 \cdot \sin(\alpha + \delta) \tag{9-8}$$

$$F_v = -W_2 \cdot \cos(\alpha) + K_2 \cdot \cos(\alpha + \delta) \tag{9-9}$$

The normal force on the shear plane is now:

$$N_1 = \frac{W_2 \cdot \sin(\delta) + W_1 \cdot \sin(\alpha+\beta+\delta)}{\sin(\alpha+\beta+\delta+\varphi)} \cdot \cos(\varphi) + \frac{-C \cdot \cos(\alpha+\beta+\delta) + A \cdot \cos(\delta)}{\sin(\alpha+\beta+\delta+\varphi)} \cdot \cos(\varphi) \tag{9-10}$$

The normal force on the blade is now:

$$N_2 = \frac{W_2 \cdot \sin(\alpha+\beta+\varphi) + W_1 \cdot \sin(\varphi)}{\sin(\alpha+\beta+\delta+\varphi)} \cdot \cos(\delta) + \frac{+C \cdot \cos(\varphi) - A \cdot \cos(\alpha+\beta+\varphi)}{\sin(\alpha+\beta+\delta+\varphi)} \cdot \cos(\delta) \tag{9-11}$$

The pore pressure forces can be determined in the case of full-cavitation or the case of no cavitation according to:

$$W_1 = \frac{\rho_w \cdot g \cdot (z+10) \cdot h_i \cdot w}{\sin(\beta)} \quad \text{or} \quad W_1 = \frac{p_{1m} \cdot h_i \cdot w}{\sin(\beta)} \tag{9-12}$$

$$W_2 = \frac{\rho_w \cdot g \cdot (z+10) \cdot h_b \cdot w}{\sin(\alpha)} \quad \text{or} \quad W_2 = \frac{p_{2m} \cdot h_b \cdot w}{\sin(\alpha)} \tag{9-13}$$

The forces **C** and **A** are determined by the cohesive shear strength **c** and the adhesive shear strength **a** according to:

$$C = \frac{c \cdot h_i \cdot w}{\sin(\beta)} \tag{9-14}$$

$$A = \frac{a \cdot h_b \cdot w}{\sin(\alpha)} \tag{9-15}$$

The ratio's between the adhesive shear strength and the pore pressures with the cohesive shear strength can be found according to:

$$r = \frac{a \cdot h_b}{c \cdot h_i}, \; r_1 = \frac{p_{1m} \cdot h_i}{c \cdot h_i} \quad \text{or} \quad r_1 = \frac{\rho_w \cdot g \cdot (z+10) \cdot h_i}{c \cdot h_i}, \; r_2 = \frac{p_{2m} \cdot h_b}{c \cdot h_i} \quad \text{or} \quad r_2 = \frac{\rho_w \cdot g \cdot (z+10) \cdot h_b}{c \cdot h_i} \tag{9-16}$$

Finally the horizontal and vertical cutting forces can be written as:

$$F_h = \lambda_{HF} \cdot c \cdot h_i \cdot w \tag{9-17}$$

$$F_v = \lambda_{VF} \cdot c \cdot h_i \cdot w \tag{9-18}$$

Figure 9-9, Figure 9-10 and Figure 9-11 show the horizontal and vertical cutting force coefficients and the shear angle as a function of the ratio of the hydrostatic pressure to the shear strength of the rock **r_z** for a 60 degree blade and full cavitation. If this ratio equals 1, it means the hydrostatic pressure equals the shear strength. At small ratios the resulting values approach atmospheric cutting of rock. Also at small ratios the shear angle approaches the theoretical value for atmospheric cutting. Figure 9-12 shows the **E_{sp}/UCS** ratio, which is very convenient for production estimation.

The vertical cutting force coefficient **λ_{VF}** is positive downwards directed. From the calculations it appeared that for a 60 degree blade, the **Curling Type** will already occur with an **$h_b/h_i=1$**. For a 110 degree blade it requires an **$h_b/h_i=4-5$**, depending on the internal friction angle. The transition at small **h_b/h_i** ratios, between the **Flow Type** and the **Curling Type,** will occur at blade angles between 60 and 90 degrees. So its important to determine the cutting forces for both mechanisms in order to see which of the two should be applied. This is always the mechanism resulting in the smallest horizontal cutting force.

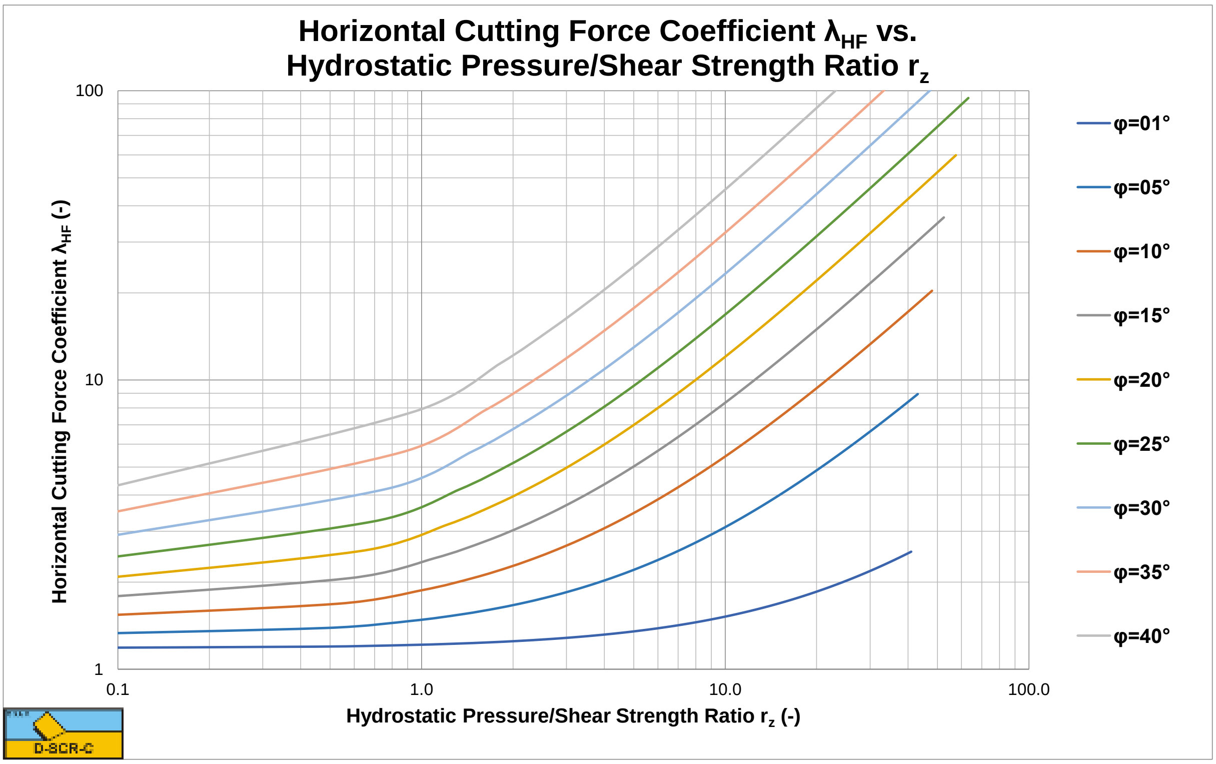

Figure 9-9: The horizontal cutting force coefficient λ_{HF} for a 60 degree blade, $h_b/h_i=1$.

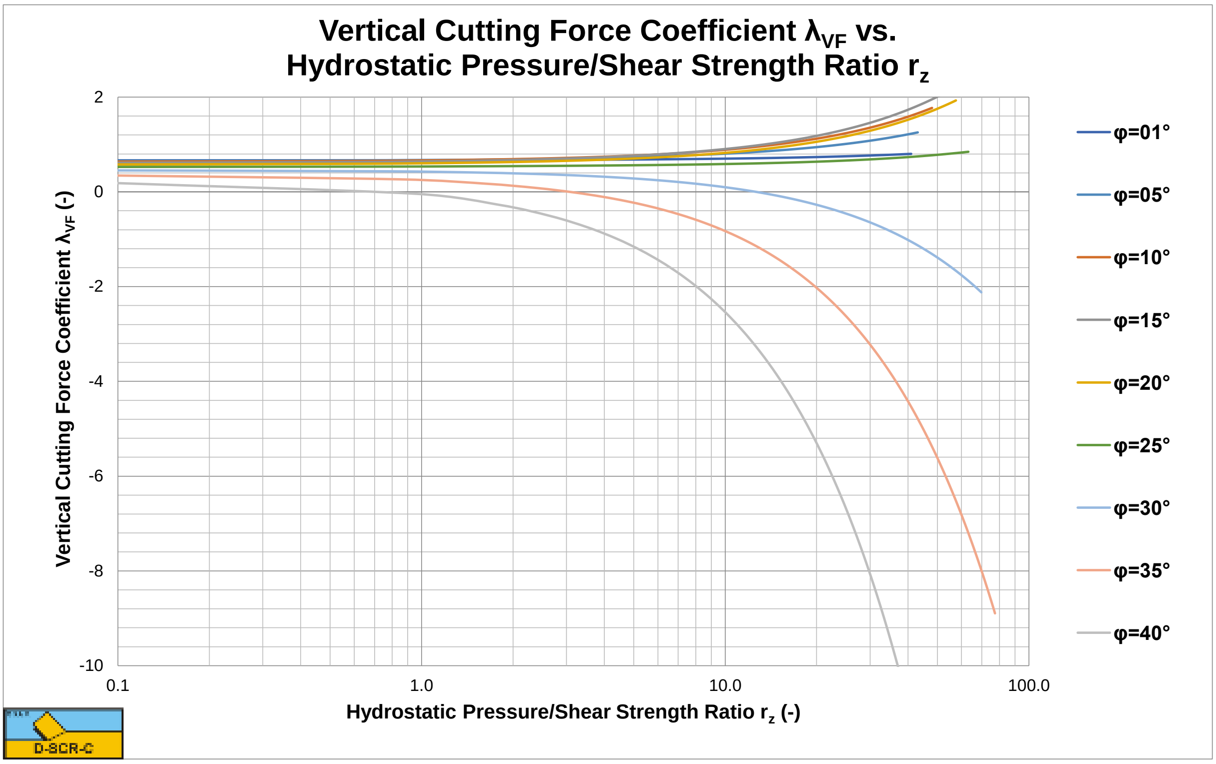

Figure 9-10: The vertical cutting force coefficient λ_{VF} for a 60 degree blade, $h_b/h_i=1$.

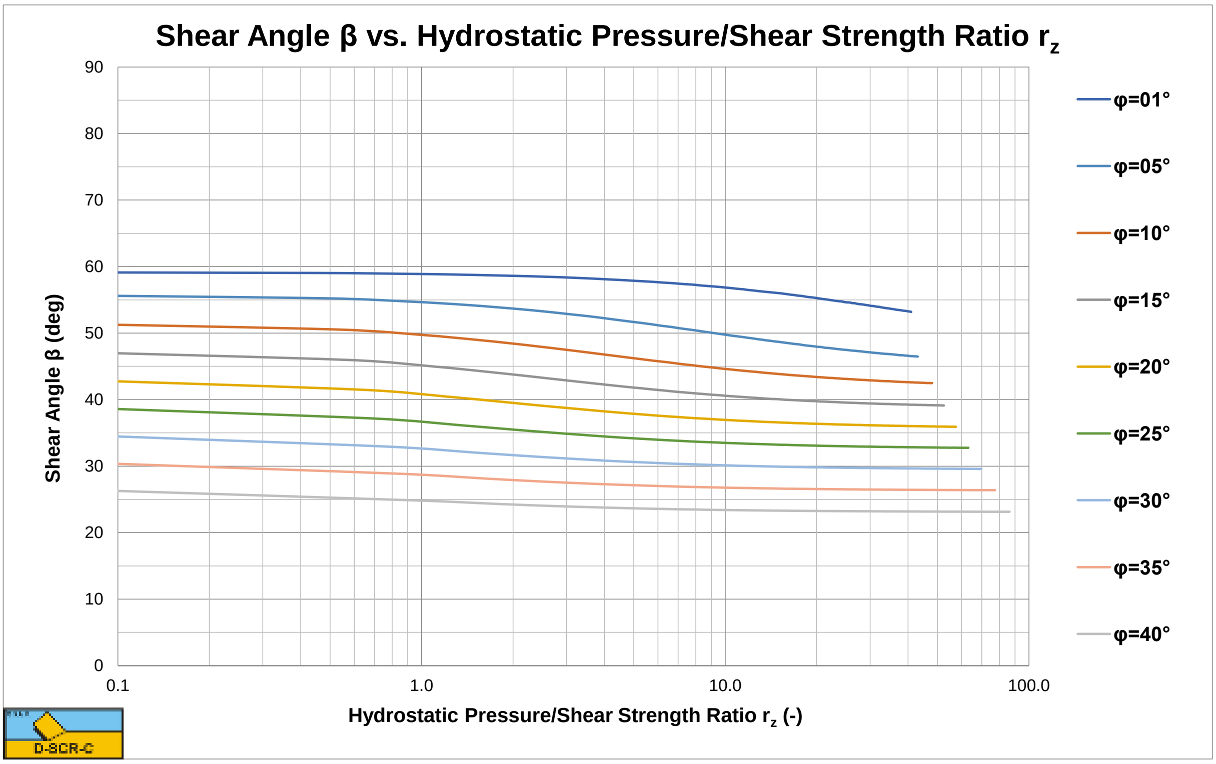

Figure 9-11:The shear angle β, for a 60 degree blade, $h_b/h_i=1$.

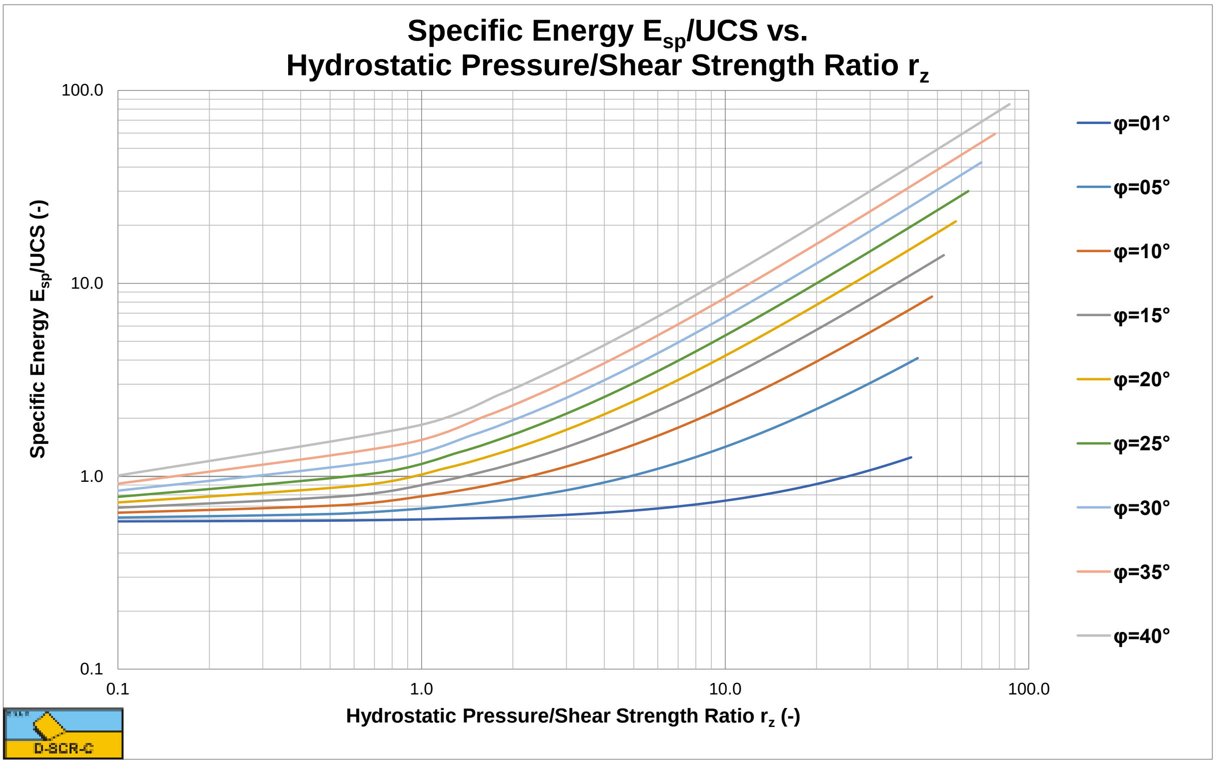

Figure 9-12: The E_{sp}/UCS ratio, for a 60 degree blade, $h_b/h_i=1$.

9.3. The Tear Type and the Chip Type.

Similar to the derivation of equation (8-127) for the occurrence of tensile failure under atmospheric conditions, equation (9-19) can be derived for the occurrence of tensile failure under hyperbaric conditions. Under hyperbaric conditions equation (9-19) will almost always be true, because of the terms with **r_1** and **r_2** which may become very big (positive). So tensile failure will not be considered for hyperbaric conditions.

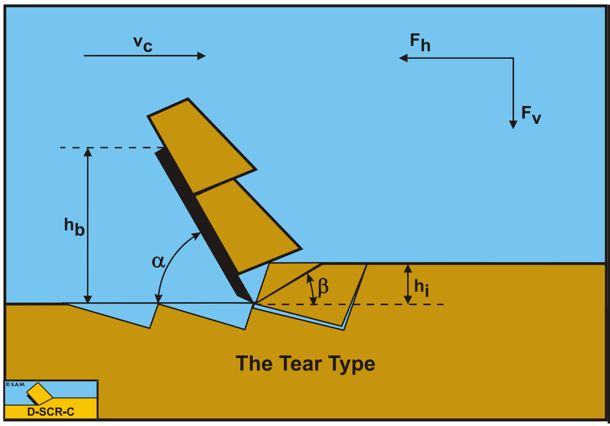

Figure 9-13: The Tear Type cutting mechanism in rock under hyperbaric conditions.

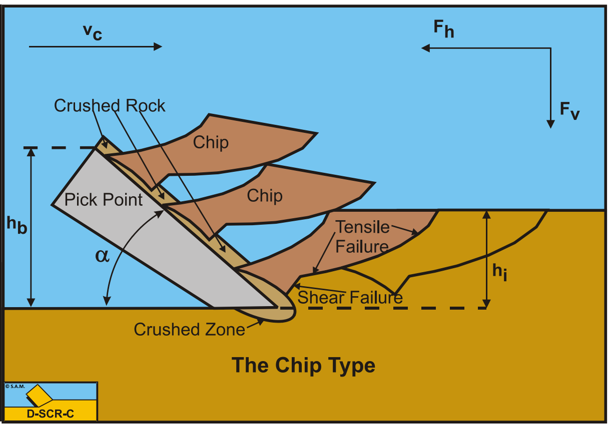

Figure 9-14: The Chip Type cutting mechanism in rock under hyperbaric conditions.

$$c\cdot\left(\begin{array}{l}\dfrac{r\cdot\dfrac{\sin(\beta)\cdot\cos(\delta)}{\sin(\alpha)}+r_2\cdot\dfrac{\sin(\beta)\cdot\sin(\delta)}{\sin(\alpha)}}{\sin(\alpha+\beta+\delta+\varphi)}\\ \\ +\dfrac{+r_1\cdot\sin(\alpha+\beta+\delta)}{\sin(\alpha+\beta+\delta+\varphi)}\\ \\ +\dfrac{-\cos(\alpha+\beta+\delta)-\sin(\alpha+\beta+\delta+\varphi)}{\sin(\alpha+\beta+\delta+\varphi)}\end{array}\right)\cdot\left(\frac{1-\sin(\varphi)}{\cos(\varphi)}\right)>\sigma_T \tag{9-19}$$

9.4. The Curling Type.

When cutting or scraping a very thin layer of rock, the **Curling Type** may occur. In dredging and mining usually the layer thickness is such that this will not occur, but in drilling practices usually the layer thickness is very small compared with the height of the blade. In the Zijsling (1987) experiments layer thicknesses of 0.15 mm and 0.30 mm were applied with a PDC bit with a height and width of about 10 mm. Under these conditions the **Curling Type** will occur, which is also named balling. Figure 9-15 shows this type of cutting mechanism.

Now the question is, what is the effective blade height **$h_{b,m}$**? In other words, along which distance will the rock cut be in contact with the blade? To solve this problem an additional condition has to be found. This condition is the equilibrium of moments around the blade tip as is shown in Figure 9-16. The only forces that contribute to the equilibrium of moments are the normal forces **N_1** and **N_2** and the pore pressure forces **W_1** and **W_2**. The acting points of these forces are chosen as fractions of the length of the shear plane **λ_1** and the blade length **λ_2**.

The equilibrium of moments around the blade tip is:

$$(N_1-W_1)\cdot R_1=(N_2-W_2)\cdot R_2 \tag{9-20}$$

For the acting points the following can be derived:

$$R_1 = \frac{\lambda_1 \cdot h_i}{\sin(\beta)}, \; R_2 = \frac{\lambda_2 \cdot h_{b,m}}{\sin(\alpha)} \tag{9-21}$$

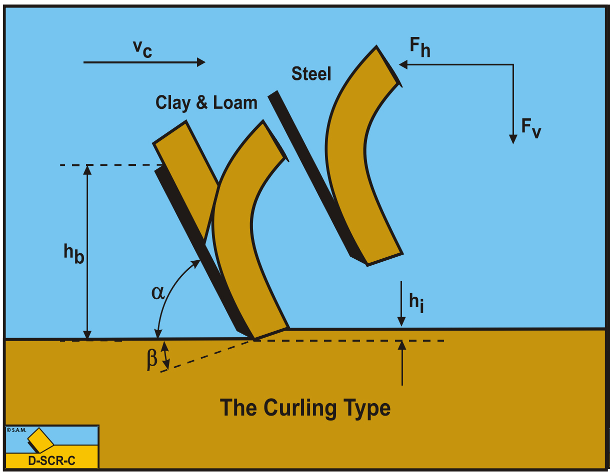

Figure 9-15: The Curling Type or balling.

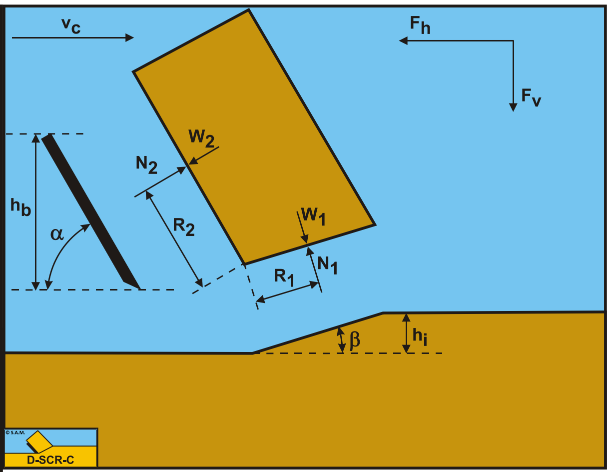

Figure 9-16: The equilibrium of moments on the layer cut in hyperbaric rock.

Substituting equations (9-10) and (9-11) into equation (9-20) gives:

$$\begin{aligned} &\left(\begin{array}{l} \dfrac{W_2 \cdot \sin(\delta) + W_1 \cdot \sin(\alpha+\beta+\delta)}{\sin(\alpha+\beta+\delta+\varphi)} \cdot \cos(\varphi) \\ \\ + \dfrac{-C \cdot \cos(\alpha+\beta+\delta) + A \cdot \cos(\delta)}{\sin(\alpha+\beta+\delta+\varphi)} \cdot \cos(\varphi) \\ \\ - W_1 \end{array} \right) \cdot \frac{\lambda_1 \cdot h_i}{\sin(\beta)} \\ = &\left(\begin{array}{l} \dfrac{W_2 \cdot \sin(\alpha+\beta+\varphi) + W_1 \cdot \sin(\varphi)}{\sin(\alpha+\beta+\delta+\varphi)} \cdot \cos(\delta) \\ \\ + \dfrac{+C \cdot \cos(\varphi) - A \cdot \cos(\alpha+\beta+\varphi)}{\sin(\alpha+\beta+\delta+\varphi)} \cdot \cos(\delta) \\ \\ - W_2 \end{array} \right) \cdot \frac{\lambda_2 \cdot h_{b,m}}{\sin(\alpha)} \end{aligned} \tag{9-22}$$

This can be written as a second degree function of the effective or mobilized blade height **$h_{b,m}$**:

$$\begin{gathered} A \cdot x^2 + B \cdot x + C = 0 \\ h_{b,m} = x = \frac{-B - \sqrt{B^2 - 4 \cdot A \cdot C}}{2 \cdot A} \end{gathered} \tag{9-23}$$

With:

$$\mathbf{A} = \frac{\lambda_2 \cdot p_{2m} \cdot \sin(\alpha+\beta+\delta+\varphi) - \lambda_2 \cdot p_{2m} \cdot \sin(\alpha+\beta+\varphi) \cdot \cos(\delta)}{\sin(\alpha) \cdot \sin(\alpha)}$$

$$+ \frac{+a \cdot \lambda_2 \cdot \cos(\alpha+\beta+\varphi) \cdot \cos(\delta)}{\sin(\alpha) \cdot \sin(\alpha)} \tag{9-24}$$

And:

$$\mathbf{B} = \frac{\lambda_1 \cdot p_{2m} \cdot \sin(\delta) \cdot \cos(\varphi) - \lambda_2 \cdot p_{1m} \cdot \cos(\delta) \cdot \sin(\varphi)}{\sin(\alpha) \cdot \sin(\beta)} \cdot h_i$$

$$+ \frac{-c \cdot \lambda_2 \cdot \cos(\delta) \cdot \cos(\varphi) + a \cdot \lambda_1 \cdot \cos(\varphi) \cdot \cos(\delta)}{\sin(\alpha) \cdot \sin(\beta)} \cdot h_i \tag{9-25}$$

And:

$$\mathbf{C} = \frac{\lambda_1 \cdot p_{1m} \cdot \sin(\alpha+\beta+\delta) \cdot \cos(\varphi) - \lambda_1 \cdot p_{1m} \cdot \sin(\alpha+\beta+\delta+\varphi)}{\sin(\beta) \cdot \sin(\beta)} \cdot h_i \cdot h_i$$

$$+ \frac{-c \cdot \lambda_1 \cdot \cos(\alpha+\beta+\delta) \cdot \cos(\varphi)}{\sin(\beta) \cdot \sin(\beta)} \cdot h_i \cdot h_i \tag{9-26}$$

If $\mathbf{h_{b,m}} < \mathbf{h_b}$ then the **Curling Type** will occur, but if $\mathbf{h_{b,m}} > \mathbf{h_b}$ the normal **Flow Type** will occur.

$$\begin{aligned} &\text{if } h_{b,m} < h_b \text{ then use } h_{b,m} \\ &\text{if } h_{b,m} \geq h_b \text{ then use } h_b \end{aligned} \tag{9-27}$$

Now in the case of full cavitation, the adhesion can be neglected and both arms are at 50% of the corresponding length. This simplifies the equations to:

$$\mathbf{A} = \frac{p_m \cdot \cos(\alpha+\beta+\varphi) \cdot \sin(\delta)}{\sin(\alpha) \cdot \sin(\alpha)}$$

$$\mathbf{B} = \frac{-p_m \cdot \sin(\varphi-\delta) - c \cdot \cos(\delta) \cdot \cos(\varphi)}{\sin(\alpha) \cdot \sin(\beta)} \cdot h_i \tag{9-28}$$

$$\mathbf{C} = \frac{-p_m \cdot \cos(\alpha+\beta+\delta) \cdot \sin(\varphi) - c \cdot \cos(\alpha+\beta+\delta) \cdot \cos(\varphi)}{\sin(\beta) \cdot \sin(\beta)} \cdot h_i \cdot h_i$$

Introducing the ratio $\mathbf{r_z}$ between the absolute hydrostatic pressure and the shear strength **c**:

$$r_z = \frac{\rho_w \cdot g \cdot (z+10)}{c} \tag{9-29}$$

Gives for the A, B and C:

$$\mathbf{A} = \frac{r_z \cdot \cos(\alpha+\beta+\varphi) \cdot \sin(\delta)}{\sin(\alpha) \cdot \sin(\alpha)}$$

$$\mathbf{B} = \frac{-r_z \cdot \sin(\varphi-\delta) - \cos(\delta) \cdot \cos(\varphi)}{\sin(\alpha) \cdot \sin(\beta)} \cdot h_i \tag{9-30}$$

$$\mathbf{C} = \frac{-r_z \cdot \cos(\alpha+\beta+\delta) \cdot \sin(\varphi) - \cos(\alpha+\beta+\delta) \cdot \cos(\varphi)}{\sin(\beta) \cdot \sin(\beta)} \cdot h_i \cdot h_i$$

The **B** term is always negative. The term **4·A·C** is also always negative. This results in a square root that will always be bigger than |**B**|. Since the sum of the angles in the arguments of the cosines will always be larger than 90 degrees, the cosines will give a negative result. So **A** will always be negative. This implies that the negative square root gives a positive answer, while the positive square root will give a negative answer. Since the mobilized blade height has to be positive, the negative square root should be used here.

Finally the horizontal and vertical cutting forces can be written as:

$$F_h = \lambda_{HC} \cdot c \cdot h_i \cdot w \tag{9-31}$$

$$F_v = \lambda_{VC} \cdot c \cdot h_i \cdot w \tag{9-32}$$

Figure 9-17 and Figure 9-18 show the ratio of the mobilized blade height to the layer thickness $\mathbf{h_{b,m}/h_i}$ and the shear angle **β** for a 60 degree blade. From Figure 9-17 it is clear that the **Curling Type** already occurs at normal $\mathbf{h_{b,m}/h_i}$ ratios. Especially at small internal friction angles this will be the case. Figure 9-19 and Figure 9-20 show the horizontal and vertical cutting force coefficients, which are not much different from the coefficients of the **Flow Type** and $\mathbf{h_{b,m}/h_i=1}$. . Figure 9-21 shows the $\mathbf{E_{sp}/UCS}$ ratio, which is very convenient for production estimation.

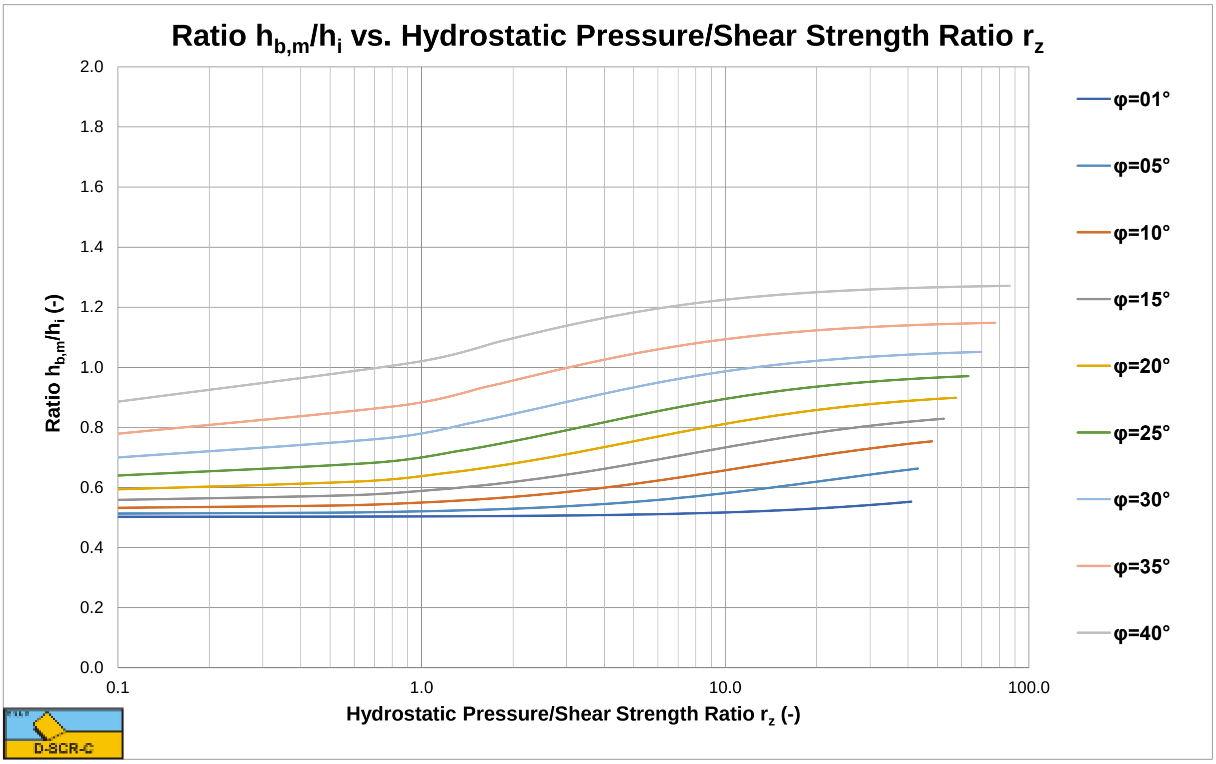

Figure 9-17: The ratio $h_{b,m}/h_i$ for a 60 degree blade.

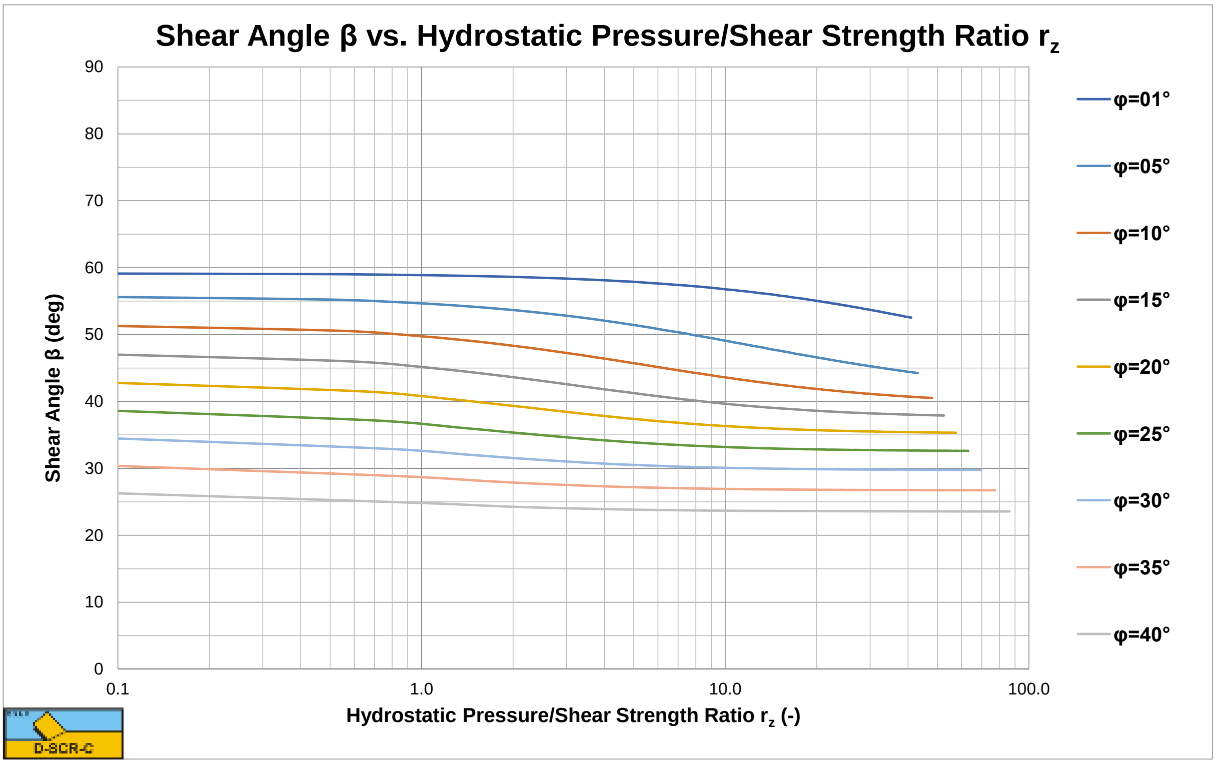

Figure 9-18:The shear angle β for a 60 degree blade

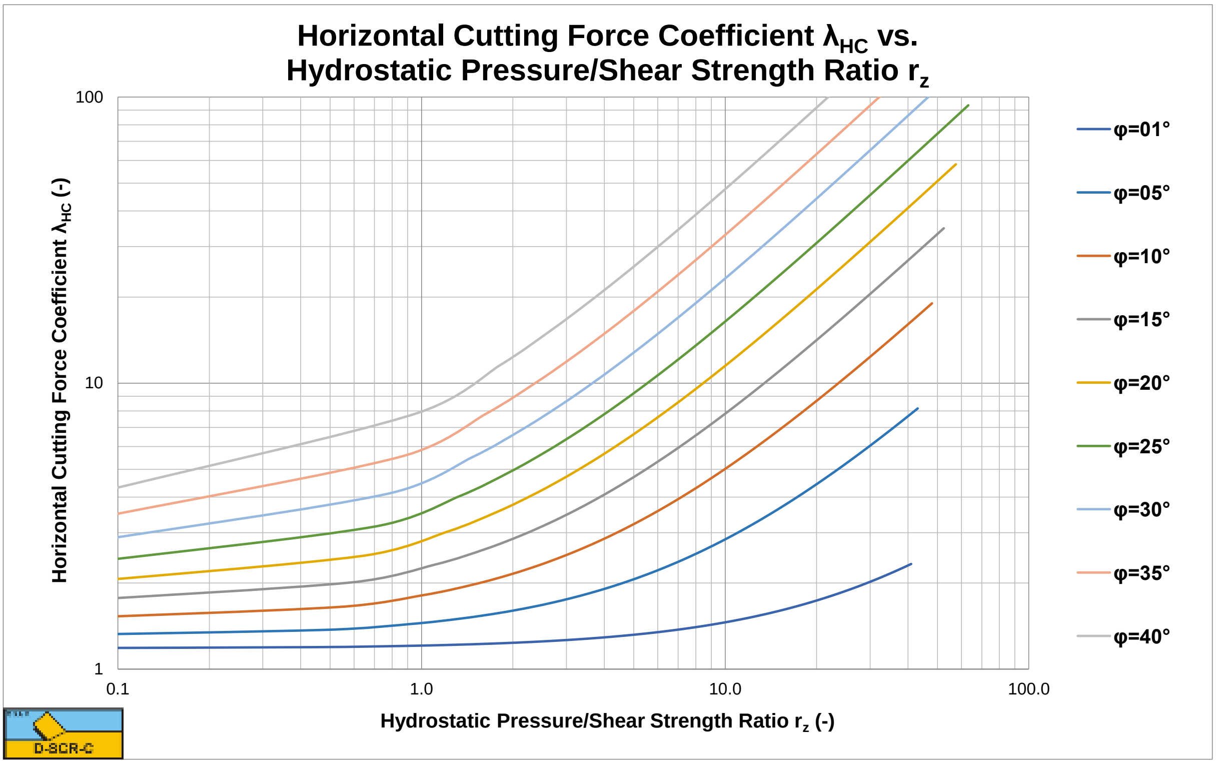

Figure 9-19: The horizontal cutting force coefficient λ_{HC} for a 60 degree blade.

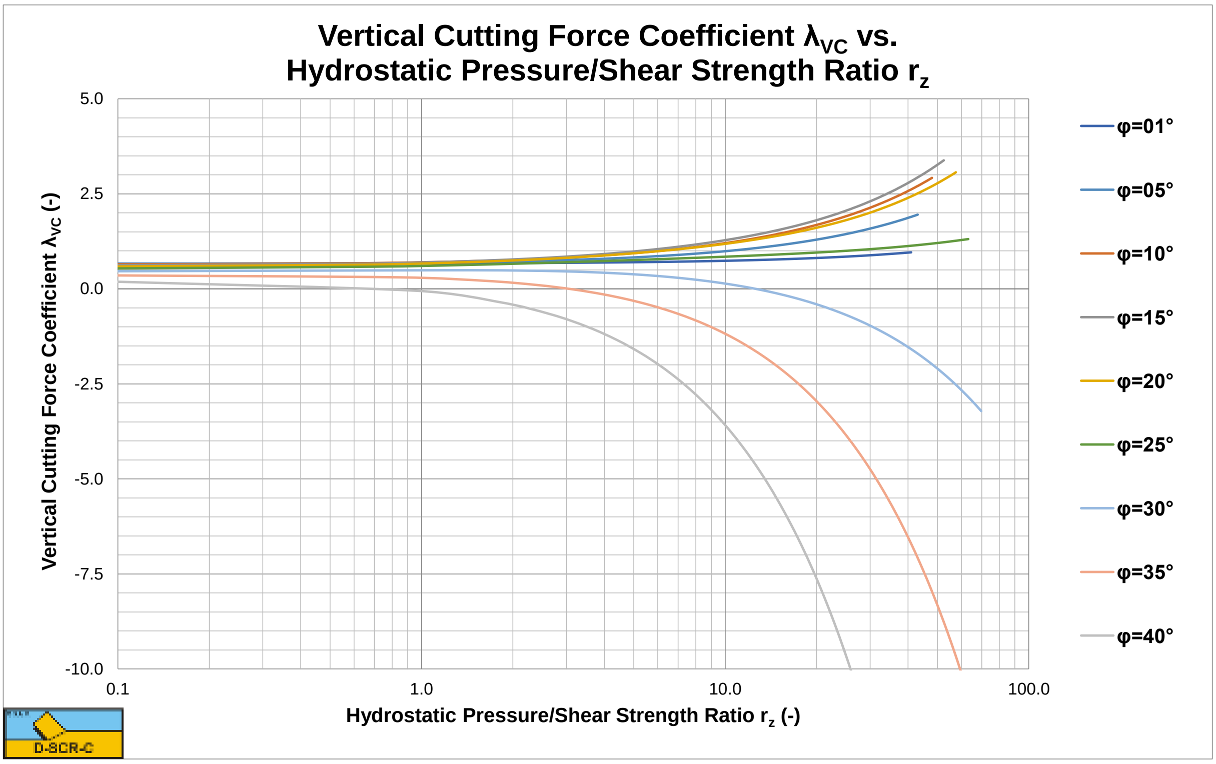

Figure 9-20: The vertical cutting force coefficient λ_{VC} for a 60 degree blade.
Positive downwards.

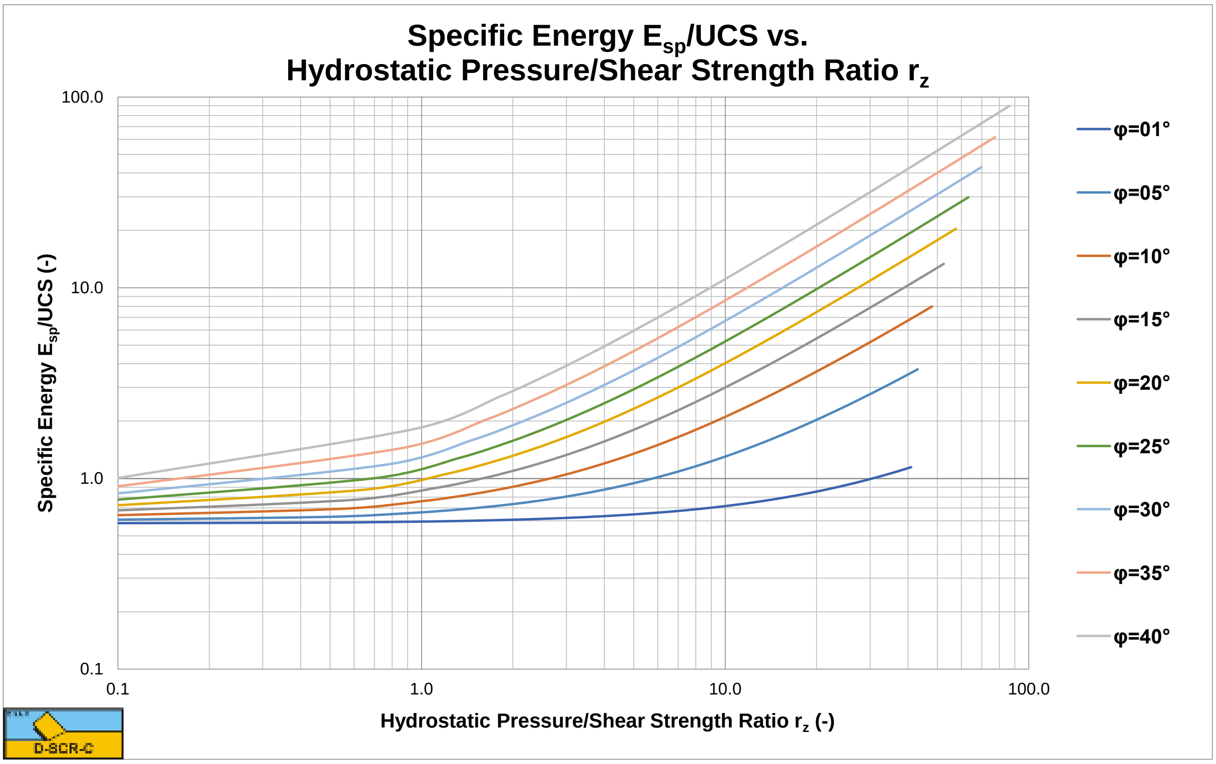

Figure 9-21: The E_{sp}/UCS ratio, for a 60 degree blade.

9.5. Experiments of Zijsling (1987).

The theory developed here, which basically is the theory of Miedema (1987 September) extended with the **Curling Type**, has been applied on the cutting tests of Zijsling (1987). Zijsling conducted cutting tests with a PDC bit with a width and height of 10 mm in Mancos Shale. This type of rock has a UCS value of about 65 MPa, a cohesive shear strength **c** of about 25 MPa, an internal friction angle **φ** of 23º, according to Detournay & Atkinson (2000), a layer thickness $\mathbf{h_i}$ of 0.15 mm and 0.30 mm and a blade angle **α** of 110º. The external friction angle **δ** is chosen at 2/3 of the internal friction angle **φ**. Based on the principle of minimum energy a shear angle **β** of 12º has been derived. Zijsling already concluded that balling would occur. Using equation (9-26) an effective blade height $\mathbf{h_{b,m}}$ = 4.04·$\mathbf{h_i}$ has been found**.** Figure 9-22 shows the cutting forces as measured by Zijsling compared with the theory derived here. The force **FD** is the force $\mathbf{F_h}$ in the direction of the cutting velocity and the force **FN** is the force $\mathbf{F_v}$ normal to the velocity direction. Figure 9-23 shows the specific energy $\mathbf{E_{sp}}$ and the so called drilling strength **S**. Figure 9-29 and Figure 9-30 show the specific energy $\mathbf{E_{sp}}$ as a function of the UCS value of a rock for different UCS/BTS ratio's and different water depths. Figure 9-29 shows this for a 110º blade as in the experiments of Zijsling (1987). The UCS value of the Mancos Shale is about 65 MPa. It is clear that in this graph the UCS/BTS value has no influence, since there will be no tensile failure at a blade angle of 110º. There could however be brittle shear failure under atmospheric conditions resulting in a specific energy of 30%-50% of the lowest line in the graph. Figure 9-29 gives a good indication of the specific energy for drilling purposes.

Figure 9-30 and Figure 9-31 show this for a 45º and a 60º blade as may be used in dredging and mining. From this figure it is clear that under atmospheric conditions tensile failure may occur. The lines for the UCS/BTS ratios give the specific energy based on the peak forces. This specific energy should be multiplied with 30%-50% to get the average value. Roxborough (1987) found that for all sedimentary rocks and some sandstone, the specific energy is about 25% of the UCS value (both have the dimension kPa or MPa). In Figure 9-30 and Figure 9-31 this would match brittle-shear failure with a factor of 30%-50% (R=2). In dredging and mining the blade angle would normally be in a range of 45º to 60º. Vlasblom (2003-2007) uses a percentage of 40% of the UCS value for the specific energy based on the experience of the dredging industry, which is close to the value found by Roxborough (1987). The percentage used by Vlasblom has the purpose of production estimation and is on the safe side (a bit too high). Both the percentages of Roxborough (1987) and Vlasblom (2003-2007) are based on the brittle shear failure. In the case of brittle tensile failure the specific energy may be much lower.

Resuming it can be stated that the theory developed here matches the measurements of Zijsling (1987) well. It has been proven that the approach of Detournay & Atkinson (2000) misses the pore pressure force on the blade and thus leads to some wrong conclusions. It can further be stated that brittle tensile failure will only occur with relatively small blade angles under atmospheric conditions. Brittle shear failure may also occur with large blade angles under atmospheric conditions. The measurements of Zijsling show clearly that at 0 MPa bottom hole pressure, the average cutting forces are 30%-50% of the forces that would be expected based on the trend. The conclusions are valid for the experiments they are based on. In other types of rock or with other blade angles the theory may have to be adjusted. This can be taken into account by the following equation, where **α** will have a value of 3-7 depending on the type of material.

$$\mathbf{F_{h,c} = F_h \cdot \left(1 - \frac{\alpha}{(z+10)}\right)} \qquad \mathbf{(9\text{-}33)}$$

At zero water depth the cutting forces are reduced to **α/10**, so to 30%-70% depending on the type of rock. At 90 m water depth the reduction is just 3%-7%, matching the Zijsling (1987) experiments, but also the Rafatian et al. (2009) and Kaitkay & Lei (2005) experiments. The equation is empirical and a first attempt, so it needs improvement.

Figure 9-24 and Figure 9-25 show the $\mathbf{h_{b,m}/h_i}$ ratio and the shear angle **β**. The Zijsling (1987) experiments match the curves of an internal friction angle of 25 degrees close. Since the blade height in these experiments was about 10 mm, the actual $\mathbf{h_{b,m}/h_i}$ ratio were 10/.15=66.66 and 10/.3=33.33. In both cases these ratios are much larger than the ones calculated for the **Curling Type**, leading to the conclusion that the **Curling Type** always occurs. So in offshore drilling, the **Curling Type** is the dominant cutting mechanism. On the horizontal axis, a value of 1 matches the shear strength of the rock, being about 25 MPa. A value of 4 matches the maximum hydrostatic pressure of 100 MPa as used in the experiments. The $\mathbf{h_{b,m}/h_i}$ ratio increases slightly with increasing hydrostatic pressure, the shear angle decreases slightly.

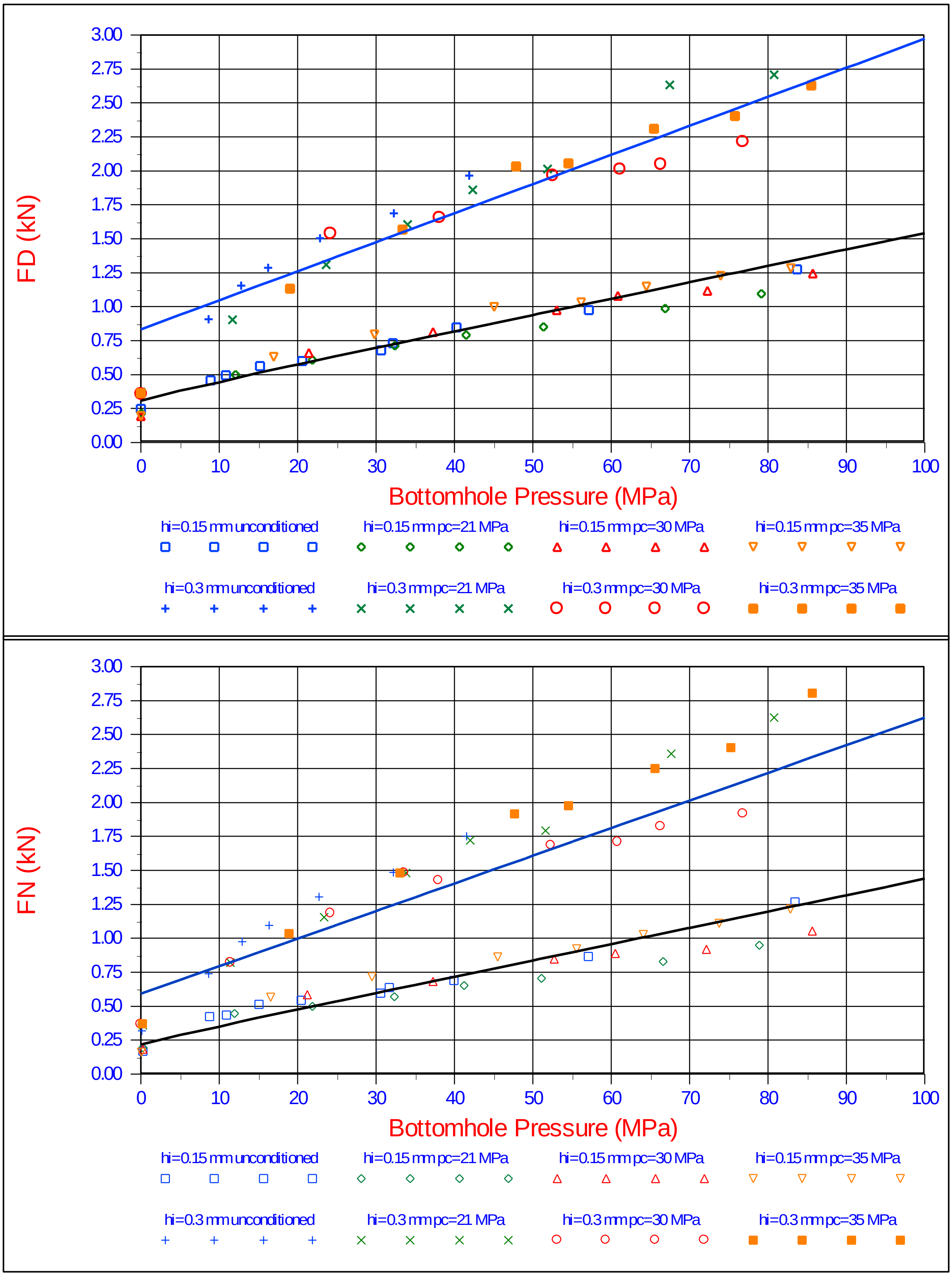

Figure 9-22: The theory of hyperbaric cutting versus the Zijsling (1987) experiments.

Blade angle **α** = 110º, blade width **w** = 10 mm, internal friction angle **φ** = 23.8º, external friction angle **δ** = 15.87º, shear strength **c** = 24.82 MPa, shear angle **β** = 12.00º, layer thickness $\mathbf{h_i}$ = 0.15 mm and 0.30 mm, effective blade height $\mathbf{h_b}$ = 4.04·$\mathbf{h_i}$.

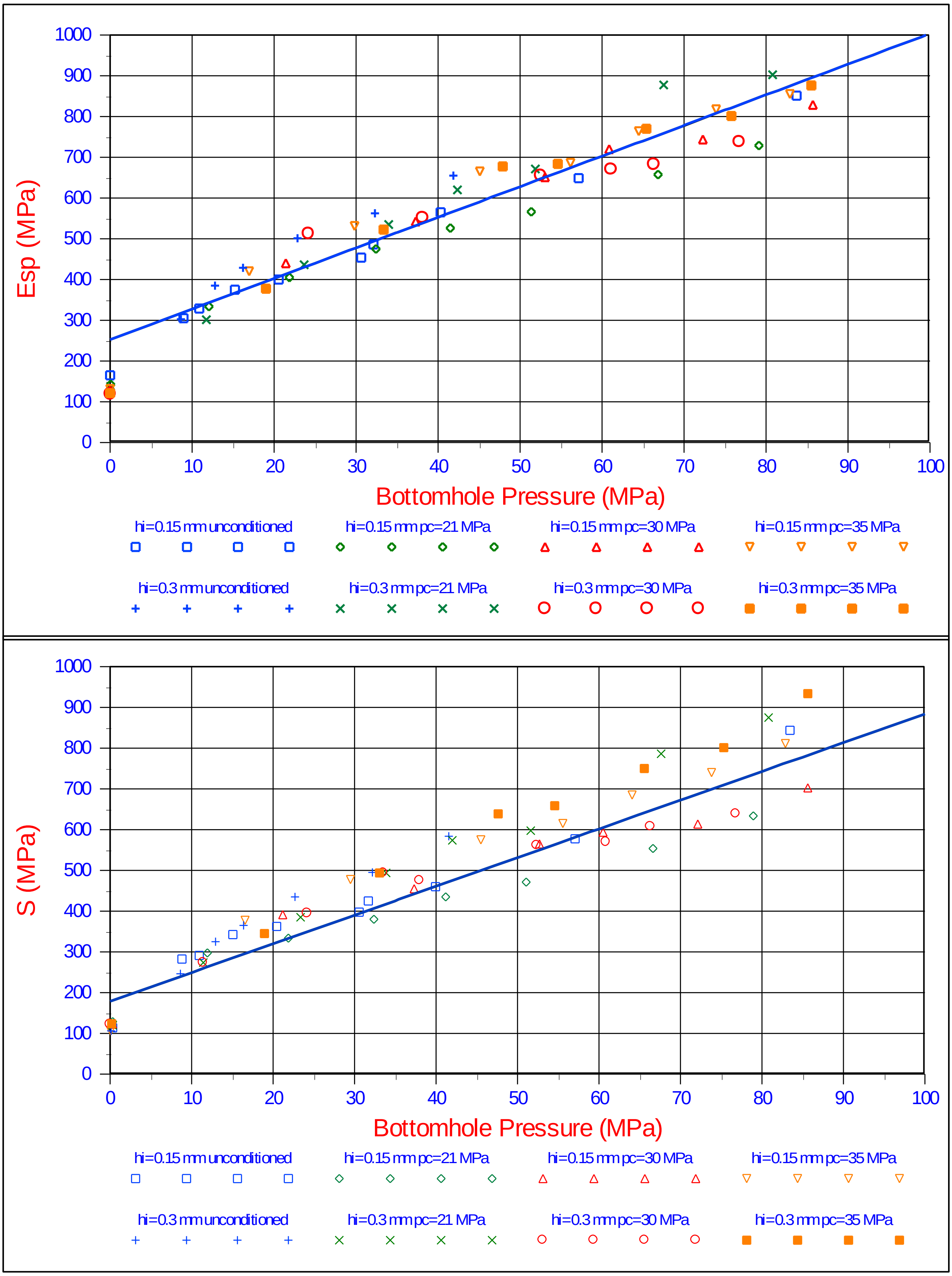

Figure 9-23: The specific energy E_{sp} and the drilling strength S, theory versus the Zijsling (1987) experiments.

Blade angle **α** = 110º, blade width **w** = 10 mm, internal friction angle **φ** = 23.8º, external friction angle **δ** = 15.87º, shear strength **c** = 24.82 MPa, shear angle **β** = 12.00º, layer thickness $\mathbf{h_i}$ = 0.15 mm and 0.30 mm, effective blade height $\mathbf{h_b} = 4.04 \cdot \mathbf{h_i}$.

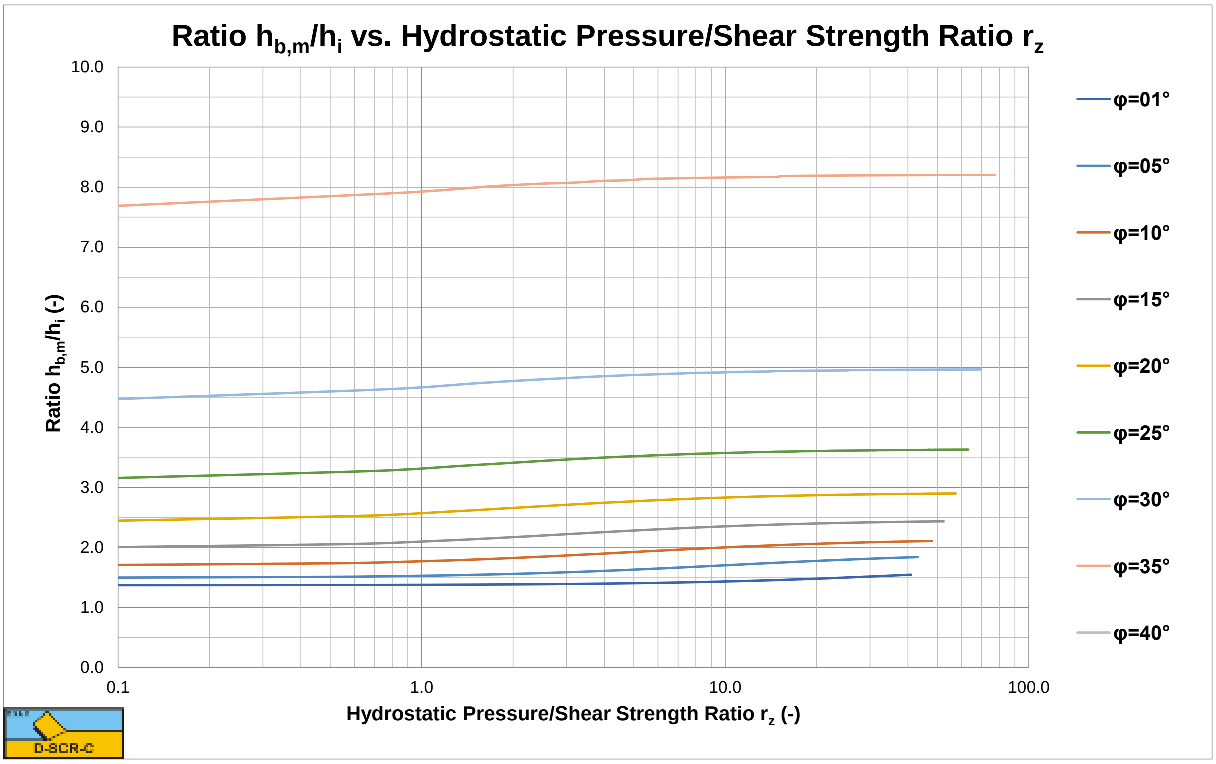

Figure 9-24: The ratio $h_{b,m}/h_i$ for a 110 degree blade.

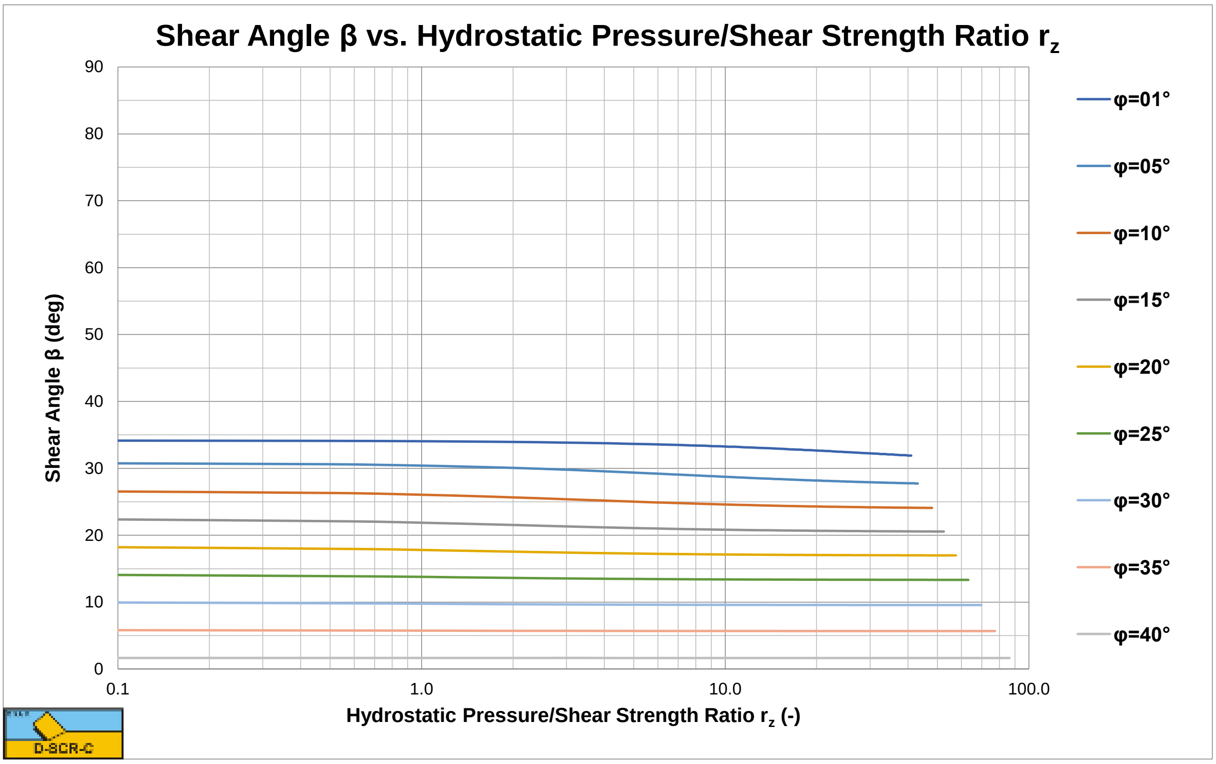

Figure 9-25:The shear angle β for a 110 degree blade.

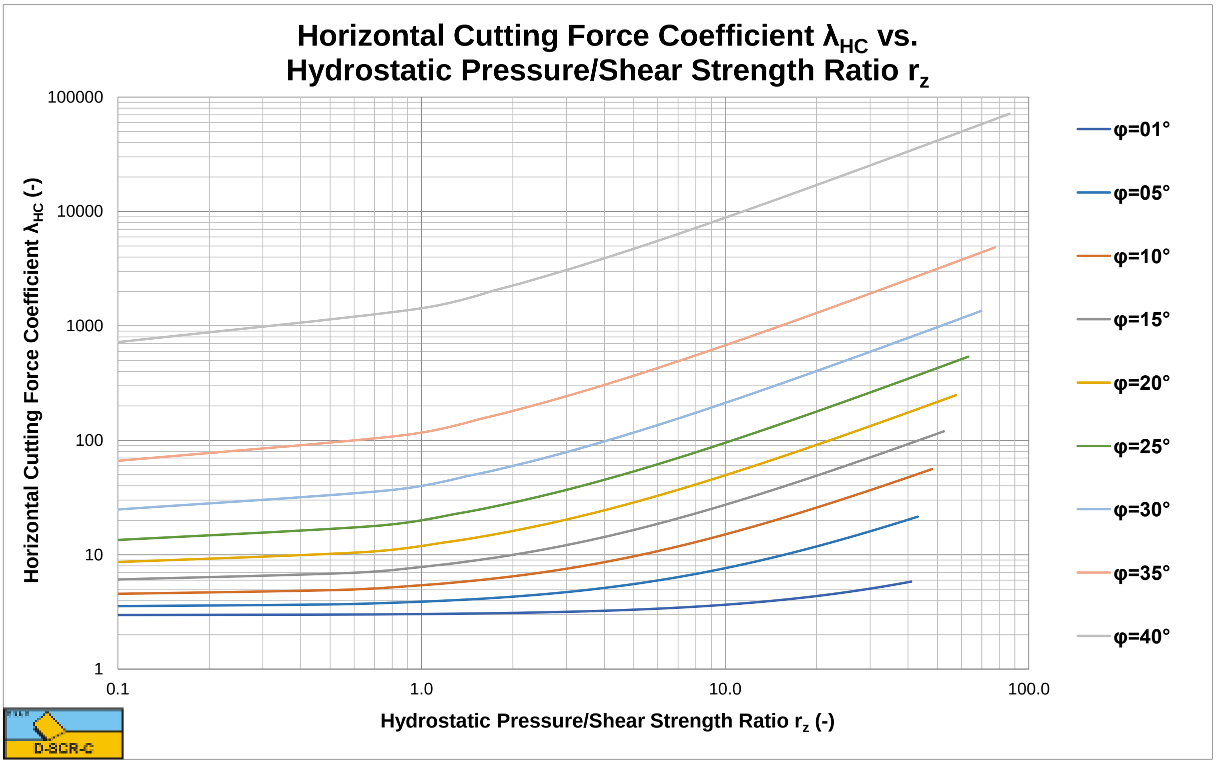

Figure 9-26: The horizontal cutting force coefficient λ_{HC} for a 110 degree blade.

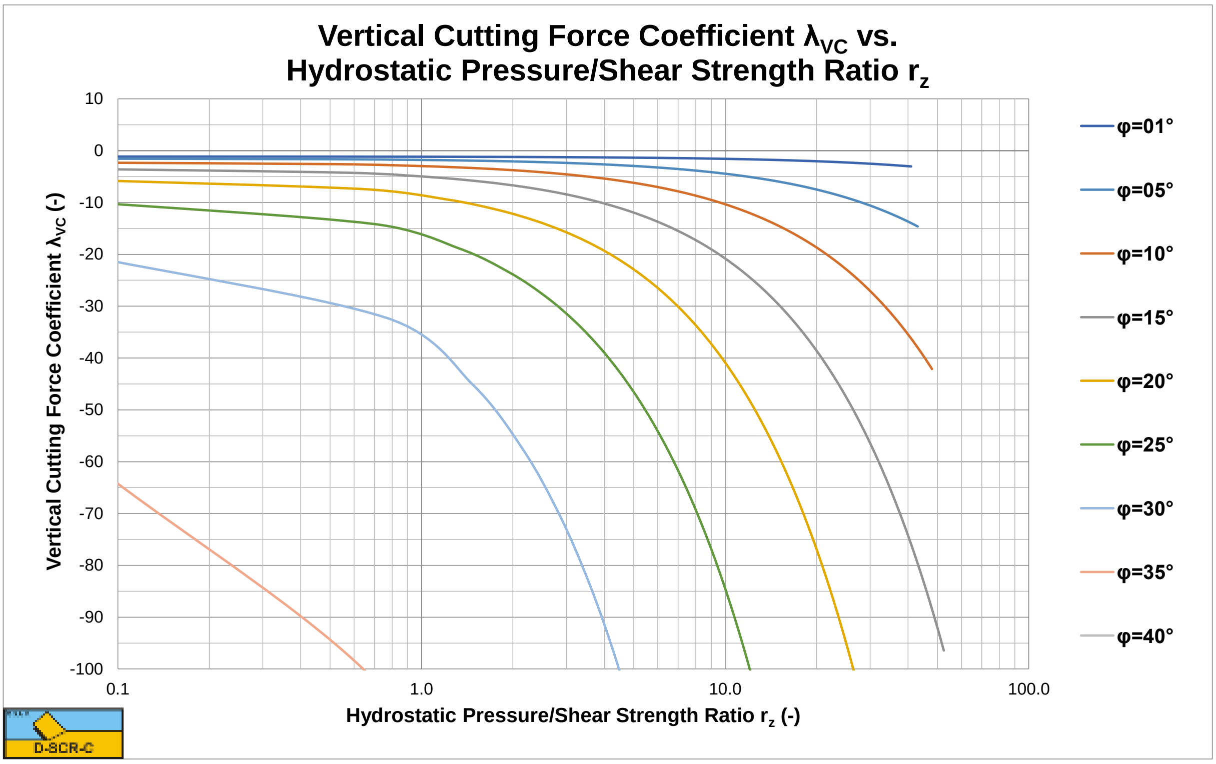

Figure 9-27: The vertical cutting force coefficient λ_{VC} for a 110 degree blade.
Positive upwards.

Figure 9-26 and Figure 9-27 show the horizontal and vertical cutting force coefficients. For a hydrostatic pressure of 100 MPa and an internal friction angle of 25 degrees the graphs give a horizontal cutting force coefficient of **λ_{HC}=45** and a vertical cutting force coefficient of **λ_{VC}=38** giving cutting forces of **F_h=F_D=3.25 kN** and **F_v=F_N=2.74 kN**, matching the experiments in Figure 9-22. Figure 9-28 shows the **E_{sp}/UCS** ratio, which is very convenient for production estimation.

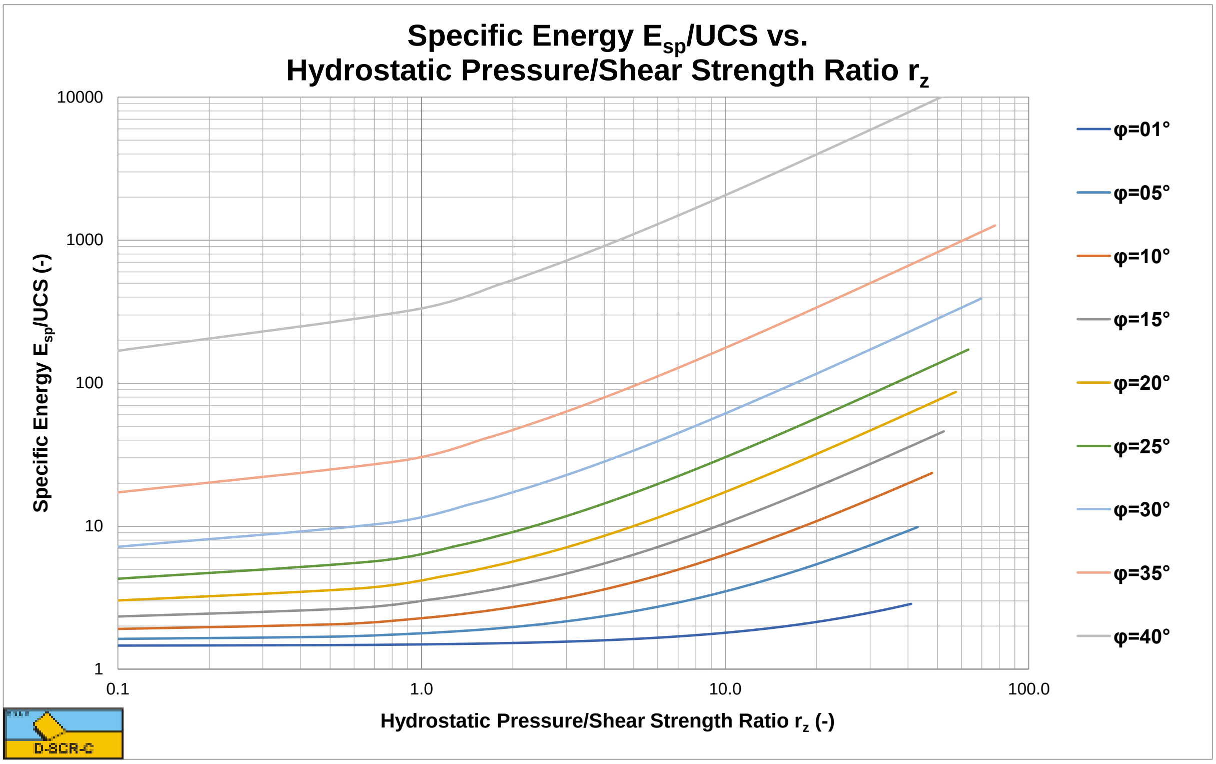

Figure 9-28: The E_{sp}/UCS ratio, for a 110 degree blade.

9.6. Specific Energy.

For the cases as described above, cutting with a straight blade with the direction of the cutting velocity $\mathbf{v_c}$ perpendicular to the blade (edge of the blade), the specific cutting energy $\mathbf{E_{sp}}$ is:

$$E_{sp} = \frac{F_h \cdot v_c}{h_i \cdot w \cdot v_c} = \frac{F_h}{h_i \cdot w} \tag{9-34}$$

The specific energy of the **Flow Type** of cutting mechanism can be written as:

$$E_{sp} = \lambda_{HF} \cdot c \tag{9-35}$$

The specific energy of the **Curling Type** of cutting mechanism can be written as:

$$E_{sp} = \lambda_{HC} \cdot c \tag{9-36}$$

Appendix X: Hyperbaric Rock Cutting Charts: Contains graphs for blade angles from 30 degrees up to 120 degrees, covering both dredging and offshore drilling applications.

9.7. Example.

In this chapter many graphs are given for an **α=60º** blade and different internal friction angles. Chosing **φ=20º**, like in chapter 8, gives the possibility to compare atmospheric and hyperbaric cutting of rock. The external friction angle is assumed to be **δ=2/3·φ**. Assume a blade width **w=0.1 m** and a layer thickness **h_i=0.1 m**, similar to chapter 8.

Also choosing UCS=100 MPa gives a specific energy to UCS ratio 0f 0.669 for very small hydrostatic pressure to UCS ratios, which is equal to the peak values found for atmospheric cutting. The atmospheric cutting process however is brittle shear failure in this case, resulting in lower average forces, while the hyperbaric process is supposed to be cataclastic or pseudo ductile. At very small hydrostatic pressures the behavior will still be brittle shear, but at larger water depths pseudo ductile.

Now suppose a rock with a UCS value of 10 MPa and water depths of 100 m, 1000 m and 3000 m. This results in the following forces and specific energies.

Table 9-1: Forces and specific energy example.

Water Depth z (m)	Hydrostatic Pressure/UCS Ratio	β (º)	$h_{b,m}/h_i$ (-)	λ_{HC} (-)	λ_{VC} (-)	E_{sp}/UCS (-)
0	0	43.23	0.584	1.94	0.58	0.68
100	0.1	42.33	0.602	2.20	0.60	0.77
1000	1.0	38.51	0.707	4.62	0.81	1.62
3000	3.0	36.50	0.800	10.17	1.12	3.56

The mobilized blade height $h_{b,m}$ is smaller than 1, which means that under normal circumstances the mobilized blade height is smaller than the actual blade height, resulting in the **Curling Type**. If the mobilized blade height is larger than the actual blade height, the **Flow Type** or **Crushed Type** will occur and the numbers in the above table will be different. Figure 9-17, Figure 9-18, Figure 9-19, Figure 9-20 and Figure 9-21 are used to determine the values in the above table.

9.8. Specific Energy Graphs.

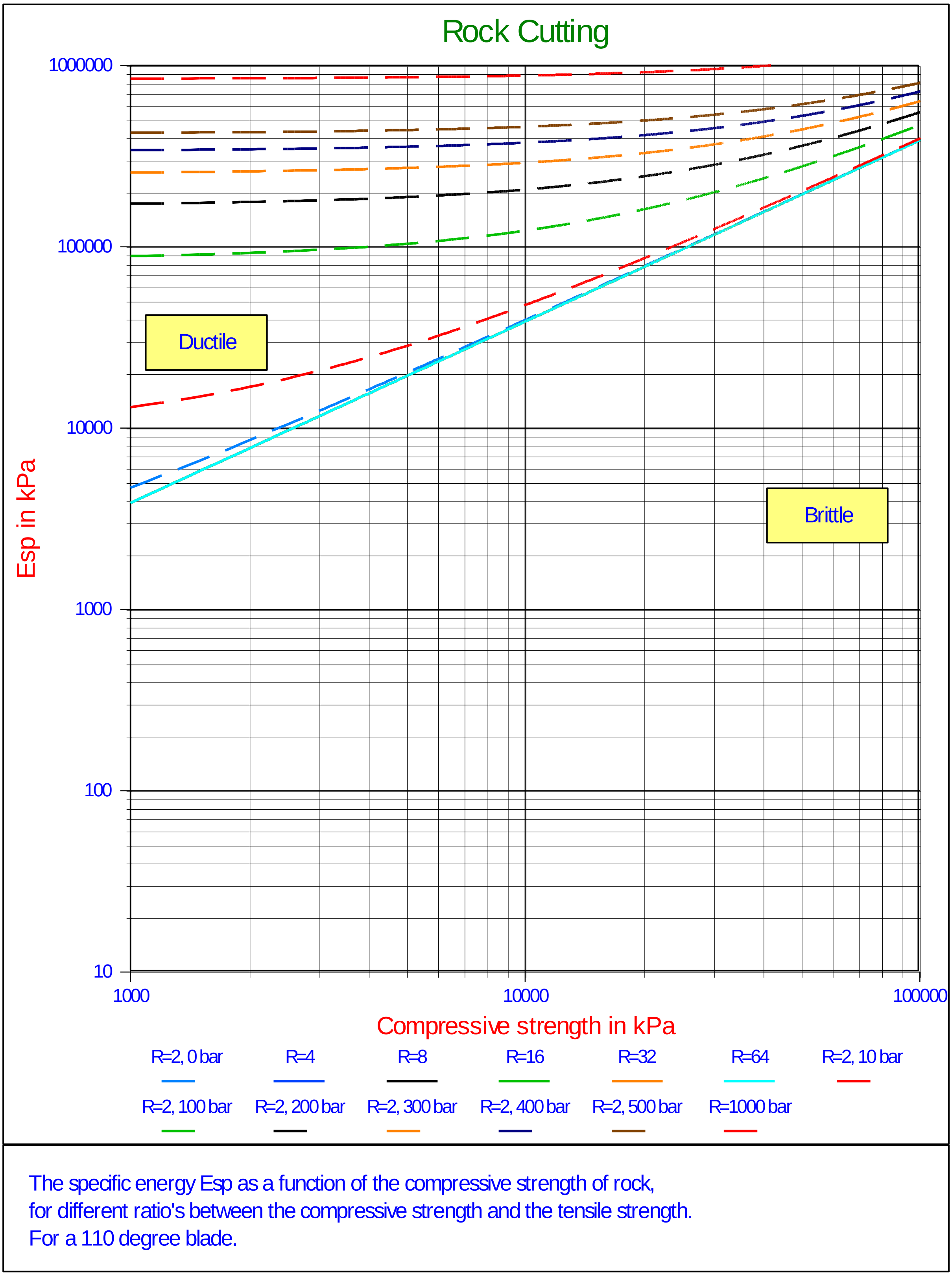

The specific energy Esp as a function of the compressive strength of rock,
for different ratio's between the compressive strength and the tensile strength.
For a 110 degree blade.

Figure 9-29: The specific energy E_{sp} in rock versus the compressive strength (UCS) for a 110° blade.

Blade angle **α** = 110°, layer thickness $\mathbf{h_i}$ = 0.00015 m, blade height $\mathbf{h_b}$ = 0.01 m, angle of internal friction **φ** = 23.80°, angle of external friction **δ** = 15.87°, shear angle **β** = 12.00°.

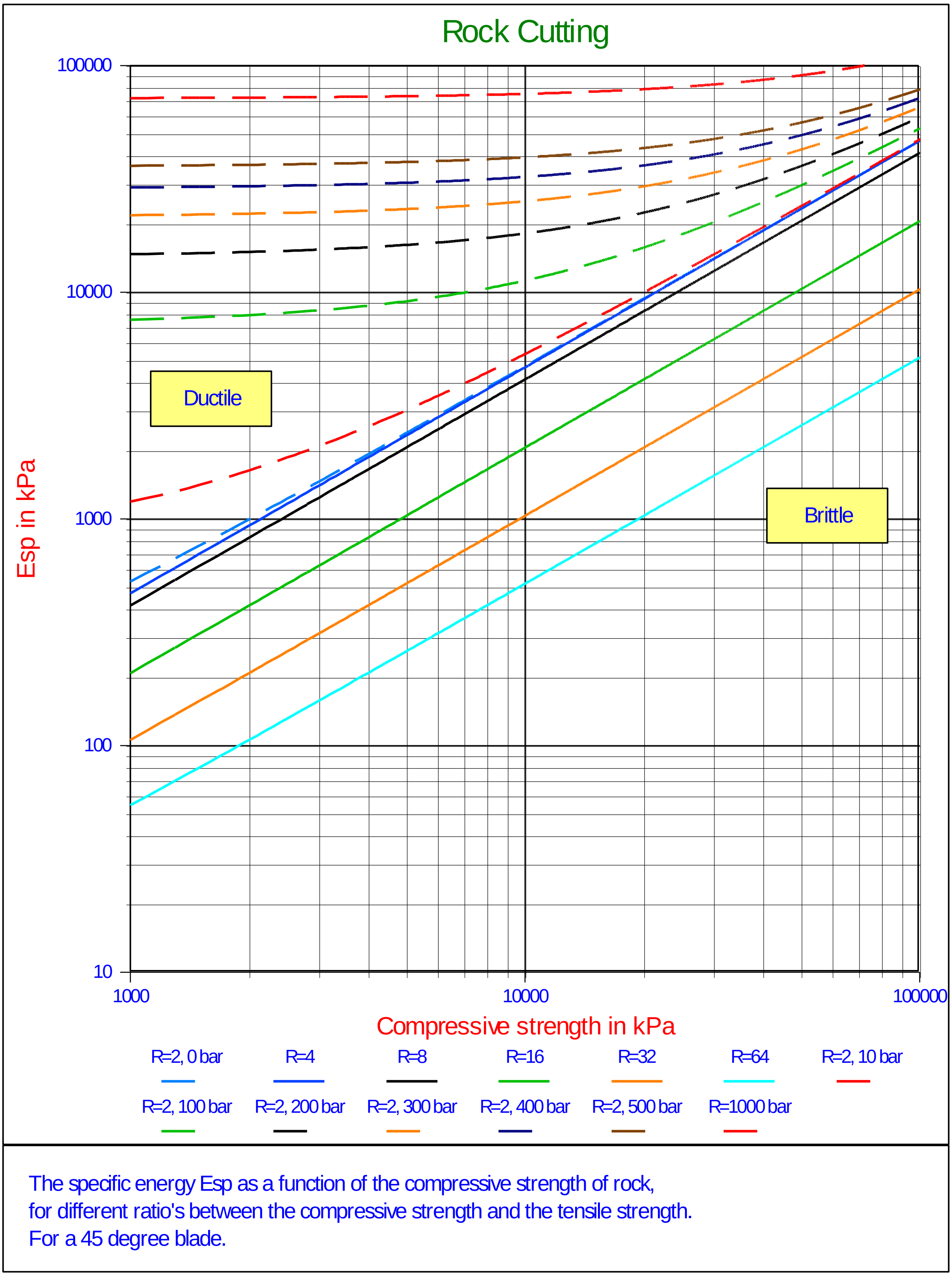

Figure 9-30: The specific energy E_{sp} in rock versus the compressive strength (UCS) for a 45º blade.

Blade angle **α** = 45º, layer thickness $\mathbf{h_i}$ = 0.05 m, blade height $\mathbf{h_b}$ = 0.1 m, angle of internal friction **φ** = 20.00º, angle of external friction **δ** = 13.33º, shear angle **β** = 40.00º.

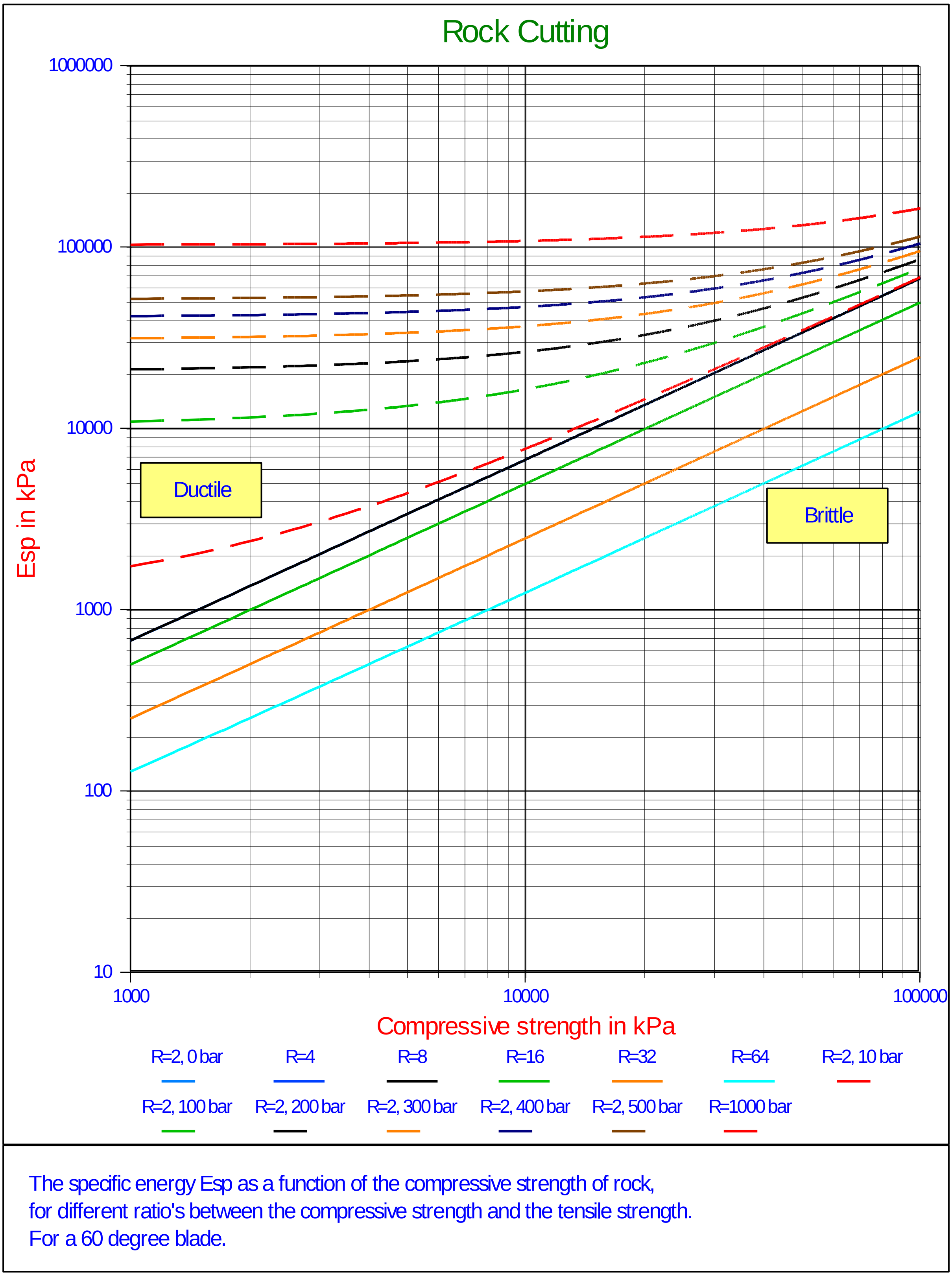

Figure 9-31: The specific energy E_{sp} in rock versus the compressive strength (UCS) for a 60º blade.

Blade angle **α** = 60º, layer thickness $\mathbf{h_i}$ = 0.05 m, blade height $\mathbf{h_b}$ = 0.1 m, angle of internal friction **φ** = 20.00º, angle of external friction **δ** = 13.33º, shear angle **β** = 40.00º.

9.9. Nomenclature.

a, τ_a	Adhesive shear strength	kPa
A	Adhesive force on the blade	kN
c, τ_c	Cohesive shear strength	kPa
c'	Pseudo cohesive shear strength	kPa
C	Cohesive force on shear plane	kN
E_{sp}	Specific energy	kPa
F	Force	kN
F_h	Horizontal cutting force	kN
FD	Drag force on chisel (horizontal force)	kN
F_v	Vertical cutting force	kN
FN	Normal force on chisel (vertical force)	kN
g	Gravitational constant (9.81)	m/s^2
G	Gravitational force	kN
h_i	Initial thickness of layer cut	m
h_b	Height of the blade	m
$h_{b,m}$	Mobilized height of the blade in case **Curling Type**	m
K_1	Grain force on the shear plane	kN
K_2	Grain force on the blade	kN
I	Inertial force on the shear plane	kN
N_1	Normal grain force on shear plane	kN
N_2	Normal grain force on blade	kN
p_{1m}	Pore pressure in the shear plane	kPa
p_{2m}	Pore pressure on the blade	kPa
P_c	Cutting power	kW
Q	Production	m^3
r	Adhesion/cohesion ratio	-
r_1	Pore pressure on shear plane/cohesion ratio	-
r_2	Pore pressure on blade/cohesion ratio	-
r_z	Ratio hydrostatic pressure to cohesion	-
R	Radius of Mohr circle	kPa
R_1	Acting point on the shear plane	m
R_2	Acting point on the blade	m
S_1	Shear force due to internal friction on the shear plane	kN
S_2	Shear force due to external friction on the blade	kN
T	Tensile force	kN
UCS	Unconfined Compressive Stress	kPa
v_c	Cutting velocity	m/s
w	Width of the blade	m
W_1	Force resulting from pore under pressure on the shear plane	kN
W_2	Force resulting from pore under pressure on the blade	kN
α	Blade angle	rad
β	Angle of the shear plane with the direction of cutting velocity	rad
τ	Shear stress	kPa
τ_a, a	Adhesive shear strength (strain rate dependent)	kPa
τ_c, c	Cohesive shear strength (strain rate dependent)	kPa
τ_{S1}	Average shear stress on the shear plane	kPa
τ_{S2}	Average shear stress on the blade	kPa
σ	Normal stress	kPa
σ_C	Center of Mohr circle	kPa
σ_T	Tensile strength	kPa
σ_{min}	Minimum principal stress in Mohr circle	kPa

σ_{N1}	Average normal stress on the shear plane	kPa
σ_{N2}	Average normal stress on the blade	kPa
φ	Angle of internal friction	rad
δ	Angle of external friction	rad
λ	Strengthening factor	-
λ_1	Acting point factor on the shear plane	-
λ_2	Acting point factor on the blade	-
λ_{HF}	**Flow Type/Crushed Type** horizontal force coefficient	-
λ_{VF}	**Flow Type/Crushed Type** vertical force coefficient	-
λ_{HT}	**Tear Type/Chip Type** horizontal force coefficient	-
λ_{VT}	**Tear Type/Chip Type** vertical force coefficient	-
λ_{HC}	**Curling Type** horizontal force coefficient	-
λ_{VC}	**Curling Type** vertical force coefficient	

Chapter 10: The Occurrence of a Wedge.

10.1. Introduction.

The cutting theories until now works well for small blade angles, however when the blade angle and the other angles involved increase, a problem with the model may occur. The basic equations contain a denominator with the sine of the sum of the blade angle, the shear angle, the internal friction angle and the external friction angle. So if the sum of these angles equals 180 degrees, the denominator is zero, meaning a division by zero giving infinity. Even worse, if the sum of these angles is greater than 180 degrees the sine gives a negative result, meaning the cutting forces become negative. But already if the sum of these angles approach 180 degrees the sine becomes very small and since it is in the denominator, the cutting forces would become very high. Now nature will normally choose the road of least resistance, nature will try to find another mechanism for the cutting process and this mechanism might be the occurrence of a wedge in front of the blade. This wedge will form a pseudo cutting blade **A-C** with a blade angle much smaller than the angle of the real blade. The probability of the occurrence of a wedge is large for sand and rock since all 4 angles mentioned play a role there. For clay the probability is much smaller, since in clay cutting normally the internal and external friction angles do not play a role.

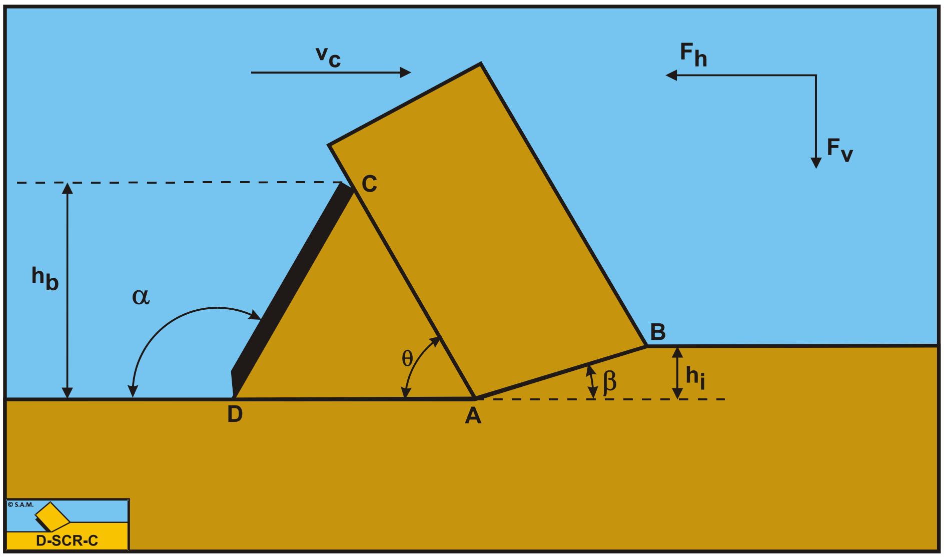

Figure 10-1: The occurrence of a wedge.

Now nature may choose another mechanism which will result in even smaller cutting forces, like the model of Hettiaratchi & Reece (1975), but their model is more complicated. The philosophy here is that if a mechanism can be found resulting in smaller cutting forces than the model used for small blade angles, this model will give a better prediction than the model for small blade angles. The wedge mechanism is such a mechanism, with the advantage that it is relatively simple to use and the cutting forces predicted with this model match the cutting forces from the experiments of Hatamura & Chijiiwa (1977B) pretty close. So from a pragmatic point of view this mechanism will be discussed for large blade angles.

Definitions:

1. **A**: The wedge tip.
2. **B**: End of the shear plane.
3. **C**: The blade top.
4. **D**: The blade tip.
5. **A-B**: The shear plane.
6. **A-C**: The wedge surface.
7. **A-D**: The wedge bottom.
8. **D-C**: The blade surface.
9. **h_b**: The height of the blade.
10. **h_i**: The thickness of the layer cut.
11. **v_c**: The cutting velocity.
12. **α**: The blade angle.
13. **β**: The shear angle.

14. **F_h**: The horizontal force, the arrow gives the positive direction.
15. **F_v**: The vertical force, the arrow gives the positive direction.

10.2. The Force Equilibrium.

Figure 10-2 illustrates the forces on the layer of soil cut. The forces shown are valid in general for each type of soil.

The forces acting on the layer **A-B** are:

1. A normal force acting on the shear surface **N_1**, resulting from the effective grain stresses.
2. A shear force **S_1** as a result of internal friction **$N_1 \cdot \tan(\varphi)$**.
3. A force **W_1** as a result of water under pressure in the shear zone.
4. A shear force **C_1** as a result of pure cohesion τ_c or shear strength. This force can be calculated by multiplying the cohesive shear strength τ_c with the area of the shear plane.
5. A gravity force **G_1** as a result of the weight of the layer cut.
6. An inertial force **I**, resulting from acceleration of the soil.
7. A force normal to the pseudo blade **N_2**, resulting from the effective grain stresses.
8. A shear force **S_2** as a result of the soil/soil friction **$N_2 \cdot \tan(\lambda)$** between the layer cut and the wedge pseudo blade. The friction angle λ does not have to be equal to the internal friction angle φ in the shear plane, since the soil has already been deformed.
9. A shear force **C_2** as a result of the mobilized cohesion between the soil and the wedge τ_c. This force can be calculated by multiplying the cohesive shear strength τ_c of the soil with the contact area between the soil and the wedge.
10. A force **W_2** as a result of water under pressure on the wedge.

The normal force **N_1** and the shear force **S_1** can be combined to a resulting grain force **K_1**.

$$K_1 = \sqrt{N_1^2 + S_1^2} \qquad \textbf{(10-1)}$$

The forces acting on the wedge front or pseudo blade **A-C** when cutting soil, can be distinguished as:

11. A force normal to the blade **N_2**, resulting from the effective grain stresses.
12. A shear force **S_2** as a result of the soil/soil friction **$N_2 \cdot \tan(\lambda)$**) between the layer cut and the wedge pseudo blade. The friction angle λ does not have to be equal to the internal friction angle φ in the shear plane, since the soil has already been deformed.
13. A shear force **C_2** as a result of the cohesion between the layer cut and the pseudo blade τ_c. This force can be calculated by multiplying the cohesive shear strength τ_c of the soil with the contact area between the soil and the pseudo blade.
14. A force **W_2** as a result of water under pressure on the pseudo blade **A-C**.

These forces are shown in Figure 10-3. If the forces **N_2** and **S_2** are combined to a resulting force **K_2** and the adhesive force and the water under pressures are known, then the resulting force **K_2** is the unknown force on the blade. By taking the horizontal and vertical equilibrium of forces an expression for the force **K_2** on the blade can be derived.

$$K_2 = \sqrt{N_2^2 + S_2^2} \qquad \textbf{(10-2)}$$

The forces acting on the wedge bottom **A-D** when cutting soil, can be distinguished as:

15. A force normal to the blade **N_3**, resulting from the effective grain stresses.
16. A shear force **S_3** as a result of the soil/soil friction **$N_3 \cdot \tan(\varphi)$**) between the wedge bottom and the undisturbed soil.
17. A shear force **C_3** as a result of the cohesion between the wedge bottom and the undisturbed soil τ_c. This force can be calculated by multiplying the cohesive shear strength τ_c of the soil with the contact area between the wedge bottom and the undisturbed soil.
18. A force **W_3** as a result of water under pressure on the wedge bottom **A-D**.

The normal force **N_3** and the shear force **S_3** can be combined to a resulting grain force **K_3**.

$$K_3 = \sqrt{N_3^2 + S_3^2} \qquad \textbf{(10-3)}$$

The forces acting on a straight blade **C-D** when cutting soil (see Figure 10-4), can be distinguished as:

19. A force normal to the blade $\mathbf{N_4}$**,** resulting from the effective grain stresses.
20. A shear force $\mathbf{S_4}$ as a result of the soil/steel friction $\mathbf{N_4 \cdot tan(\delta)}$.
21. A shear force **A** as a result of pure adhesion between the soil and the blade $\boldsymbol{\tau_a}$. This force can be calculated by multiplying the adhesive shear strength $\boldsymbol{\tau_a}$ of the soil with the contact area between the soil and the blade.
22. A force $\mathbf{W_4}$ as a result of water under pressure on the blade.

The normal force $\mathbf{N_4}$ and the shear force $\mathbf{S_4}$ can be combined to a resulting grain force $\mathbf{K_4}$.

$$K_4 = \sqrt{N_4^2 + S_4^2} \tag{10-4}$$

The horizontal equilibrium of forces on the layer cut:

$$\begin{aligned}\sum F_h =\; & K_1 \cdot \sin(\beta + \varphi) - W_1 \cdot \sin(\beta) + C_1 \cdot \cos(\beta) + I \cdot \cos(\beta) \\ & - C_2 \cdot \cos(\alpha) + W_2 \cdot \sin(\alpha) - K_2 \cdot \sin(\alpha + \lambda) = 0\end{aligned} \tag{10-5}$$

The vertical equilibrium of forces on the layer cut:

$$\begin{aligned}\sum F_v =\; & -K_1 \cdot \cos(\beta + \varphi) + W_1 \cdot \cos(\beta) + C_1 \cdot \sin(\beta) + I \cdot \sin(\beta) \\ & + G_1 + C_2 \cdot \sin(\alpha) + W_2 \cdot \cos(\alpha) - K_2 \cdot \cos(\alpha + \lambda) = 0\end{aligned} \tag{10-6}$$

The force $\mathbf{K_1}$ on the shear plane is now:

$$\begin{aligned}K_1 =\; & \frac{W_2 \cdot \sin(\lambda) + W_1 \cdot \sin(\alpha + \beta + \lambda) + G_1 \cdot \sin(\alpha + \lambda) - I \cdot \cos(\alpha + \beta + \lambda)}{\sin(\alpha + \beta + \lambda + \varphi)} \\ & + \frac{-C_1 \cdot \cos(\alpha + \beta + \lambda) + C_2 \cdot \cos(\lambda)}{\sin(\alpha + \beta + \lambda + \varphi)}\end{aligned} \tag{10-7}$$

The force $\mathbf{K_2}$ on the pseudo blade is now:

$$\begin{aligned}K_2 =\; & \frac{W_2 \cdot \sin(\alpha + \beta + \varphi) + W_1 \cdot \sin(\varphi) + G_1 \cdot \sin(\beta + \varphi) + I \cdot \cos(\varphi)}{\sin(\alpha + \beta + \lambda + \varphi)} \\ & + \frac{+C_1 \cdot \cos(\varphi) - C_2 \cdot \cos(\alpha + \beta + \varphi)}{\sin(\alpha + \beta + \lambda + \varphi)}\end{aligned} \tag{10-8}$$

From equation (10-8) the forces on the pseudo blade can be derived. On the pseudo blade a force component in the direction of cutting velocity $\mathbf{F_h}$ and a force perpendicular to this direction $\mathbf{F_v}$ can be distinguished.

$$F_h = -W_2 \cdot \sin(\alpha) + K_2 \cdot \sin(\alpha + \lambda) + C_2 \cdot \cos(\alpha) \tag{10-9}$$

$$F_v = -W_2 \cdot \cos(\alpha) + K_2 \cdot \cos(\alpha + \lambda) - C_2 \cdot \sin(\alpha) \tag{10-10}$$

The normal force on the shear plane is now:

$$\begin{aligned}N_1 =\; & \frac{W_2 \cdot \sin(\lambda) + W_1 \cdot \sin(\alpha + \beta + \lambda) + G_1 \cdot \sin(\alpha + \lambda)}{\sin(\alpha + \beta + \lambda + \varphi)} \cdot \cos(\varphi) \\ & + \frac{-I \cdot \cos(\alpha + \beta + \lambda) - C_1 \cdot \cos(\alpha + \beta + \lambda) + C_2 \cdot \cos(\lambda)}{\sin(\alpha + \beta + \lambda + \varphi)} \cdot \cos(\varphi)\end{aligned} \tag{10-11}$$

The normal force on the pseudo blade is now:

$$\begin{aligned} N_2 = {} & \frac{W_2 \cdot \sin(\alpha+\beta+\varphi) + W_1 \cdot \sin(\varphi) + G_1 \cdot \sin(\beta+\varphi)}{\sin(\alpha+\beta+\lambda+\varphi)} \cdot \cos(\lambda) \\ & + \frac{+I \cdot \cos(\varphi) + C_1 \cdot \cos(\varphi) - C_2 \cdot \cos(\alpha+\beta+\varphi)}{\sin(\alpha+\beta+\lambda+\varphi)} \cdot \cos(\lambda) \end{aligned} \tag{10-12}$$

Now knowing the forces on the pseudo blade A-C, the equilibrium of forces on the wedge A-C-D can be derived. The horizontal equilibrium of forces on the wedge is:

$$\begin{aligned} \sum F_h = {} & -A \cdot \cos(\alpha) + W_4 \cdot \sin(\alpha) - K_4 \cdot \sin(\alpha+\delta) + K_3 \cdot \sin(\varphi) \\ & + C_3 - W_2 \cdot \sin(\theta) + C_2 \cdot \cos(\theta) + K_2 \cdot \sin(\theta+\lambda) = 0 \end{aligned} \tag{10-13}$$

The vertical equilibrium of forces on the wedge is:

$$\begin{aligned} \sum F_v = {} & A \cdot \sin(\alpha) + W_4 \cdot \cos(\alpha) - K_4 \cdot \cos(\alpha+\delta) + W_3 - K_3 \cdot \cos(\varphi) \\ & - W_2 \cdot \cos(\theta) - C_2 \cdot \sin(\theta) + K_2 \cdot \cos(\theta+\lambda) + G_2 = 0 \end{aligned} \tag{10-14}$$

The unknowns in this equation are $\mathbf{K_3}$ and $\mathbf{K_4}$, since $\mathbf{K_2}$ has already been solved. Three other unknowns are the adhesive force on the blade **A**, since the adhesion does not have to be mobilized fully if the wedge is static, the external friction angle $\boldsymbol{\delta}$, since also the external friction does not have to be fully mobilized, and the wedge angle $\boldsymbol{\theta}$. These 3 additional unknowns require 3 additional conditions in order to solve the problem. One additional condition is the equilibrium of moments of the wedge, a second condition the principle of minimum required cutting energy. A third condition is found by assuming that the external shear stress (adhesion) and the external shear angle (external friction) are mobilized by the same amount. Depending on whether the soil pushes upwards or downwards against the blade, the mobilization factor is between -1 and +1. Now in practice, sand and rock have no adhesion while clay has no external friction, so in these cases the third condition is not relevant. However in mixed soil both the external shear stress and the external friction may be present.

The force $\mathbf{K_3}$ on the bottom of the wedge is now:

$$\begin{aligned} K_3 = {} & \frac{-W_2 \cdot \sin(\alpha+\delta-\theta) + W_3 \cdot \sin(\alpha+\delta) + W_4 \cdot \sin(\delta)}{\sin(\alpha+\delta+\varphi)} \\ & + \frac{K_2 \cdot \sin(\alpha+\delta-\theta-\lambda) + G_2 \cdot \sin(\alpha+\delta)}{\sin(\alpha+\delta+\varphi)} \\ & + \frac{A \cdot \cos(\delta) + C_3 \cdot \cos(\alpha+\delta) - C_2 \cdot \cos(\alpha+\delta-\theta)}{\sin(\alpha+\delta+\varphi)} \end{aligned} \tag{10-15}$$

The force $\mathbf{K_4}$ on the blade is now:

$$\begin{aligned} K_4 = {} & \frac{-W_2 \cdot \sin(\theta+\varphi) + W_3 \cdot \sin(\varphi) + W_4 \cdot \sin(\alpha+\varphi) + K_2 \cdot \sin(\theta+\lambda+\varphi) + G_2 \cdot \sin(\varphi)}{\sin(\alpha+\delta+\varphi)} \\ & + \frac{-A \cdot \cos(\alpha+\varphi) + C_3 \cdot \cos(\varphi) + C_2 \cdot \cos(\theta+\varphi)}{\sin(\alpha+\delta+\varphi)} \end{aligned} \tag{10-16}$$

This results in a horizontal force of:

$$F_h = -W_4 \cdot \sin(\alpha) + K_4 \cdot \sin(\alpha+\delta) + A \cdot \cos(\alpha) \qquad \textbf{(10-17)}$$

And in a vertical force of:

$$F_v = -W_4 \cdot \cos(\alpha) + K_4 \cdot \cos(\alpha+\delta) - A \cdot \sin(\alpha) \qquad \textbf{(10-18)}$$

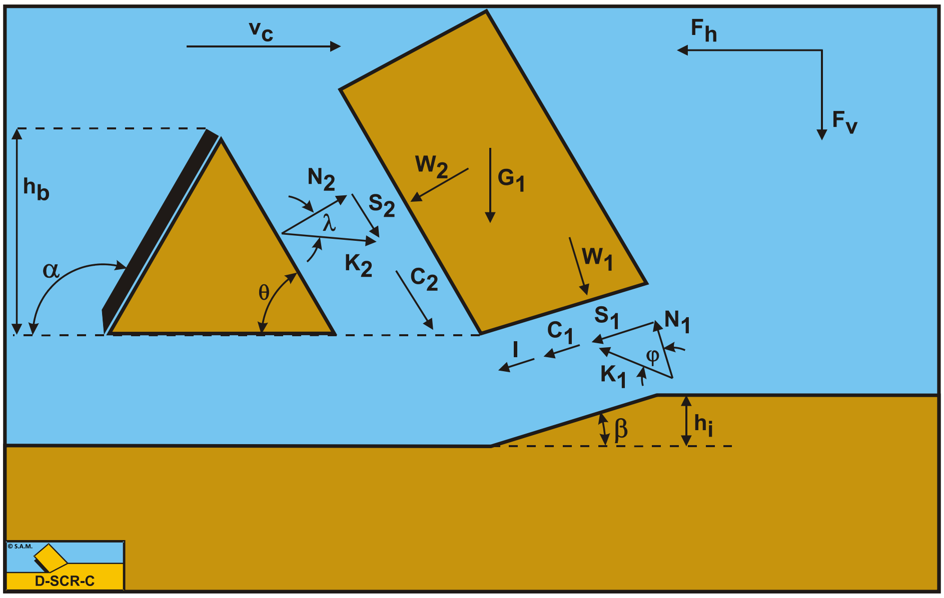

Figure 10-2: The forces on the layer cut when a wedge is present.

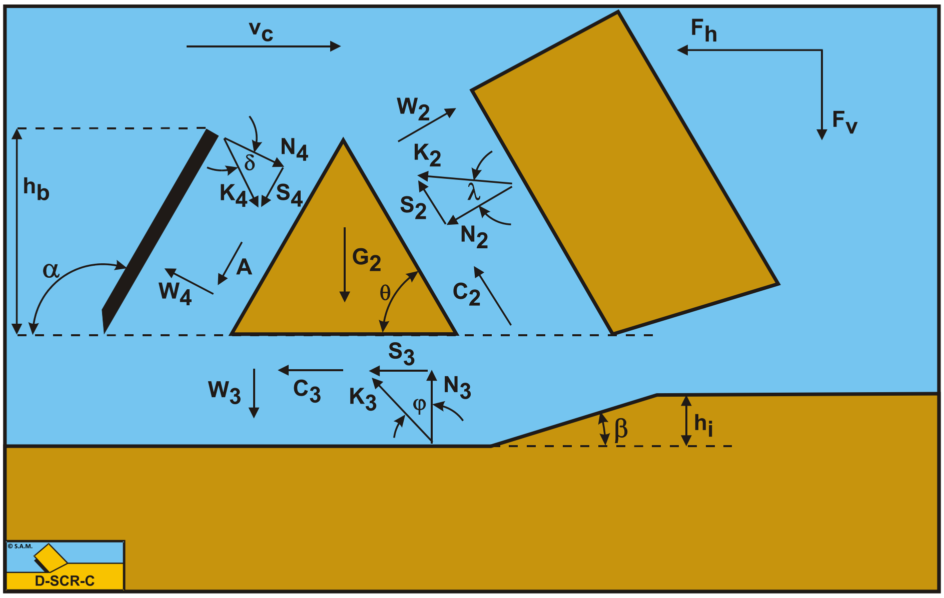

Figure 10-3: The forces on the wedge.

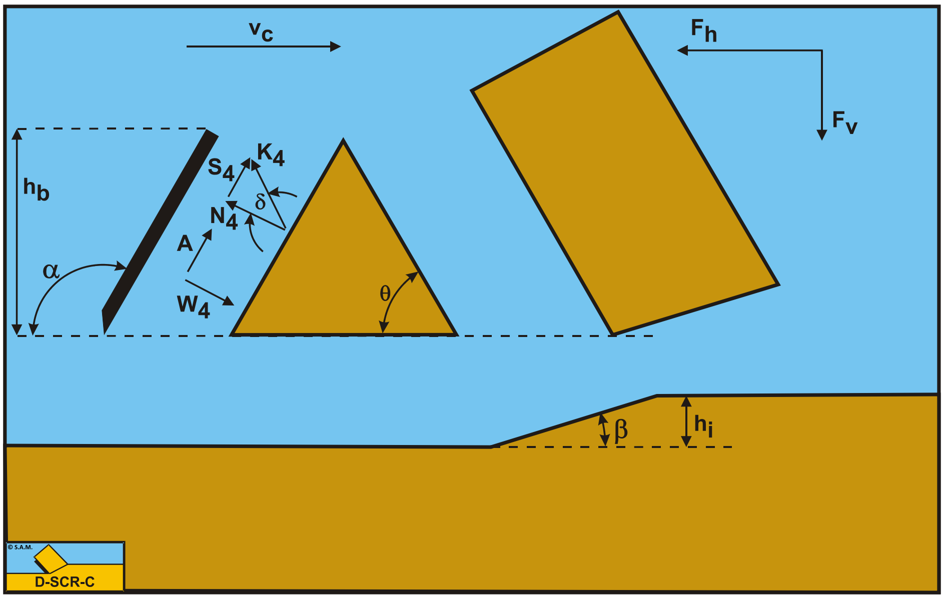

Figure 10-4: The forces on the blade when a wedge is present.

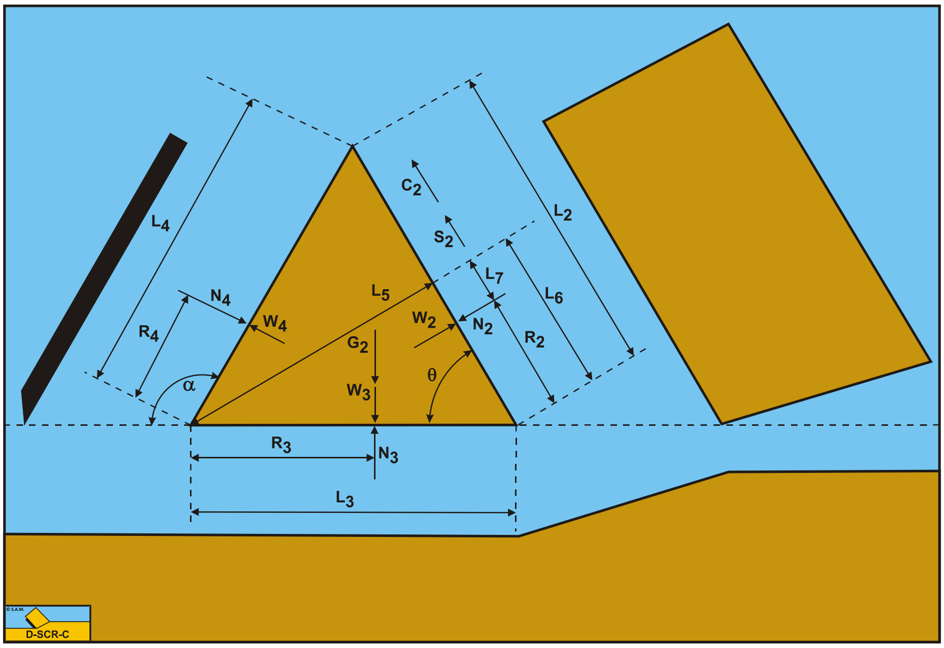

Figure 10-5: The moments on the wedge.

10.3. The Equilibrium of Moments.

In order to solve the problem, also the equilibrium of moments is required, since the wedge is not subject to rotational acceleration. The equilibrium of moments can be taken around each point of the wedge. Here the tip of the blade is chosen. The advantage of this is that a number of forces do not contribute to the moments on the wedge.

In order to derive the equilibrium of moments equation the arms of all the forces contributing to this equilibrium have to be known. Since these arms depend on the length of all the sides in the cutting process, first these lengths are determined. The length of the shear plane **A-B** is:

$$\mathbf{L_1 = \frac{h_i}{\sin(\beta)}} \tag{10-19}$$

The length of the pseudo blade **A-C** is:

$$\mathbf{L_2 = \frac{h_b}{\sin(\theta)}} \tag{10-20}$$

The length of the bottom of the wedge **A-D** is:

$$\mathbf{L_3 = h_b \cdot \left(\frac{1}{\tan(\theta)} - \frac{1}{\tan(\alpha)} \right)} \tag{10-21}$$

The length of the blade **C-D** is:

$$\mathbf{L_4 = \frac{h_b}{\sin(\alpha)}} \tag{10-22}$$

The length of the line from the tip of the blade to the opposite side of the wedge and perpendicular to this side is:

$$\mathbf{L_5 = L_3 \cdot \sin(\theta)} \tag{10-23}$$

The length of the line from point **A** to the intersection point of the previous line with side **A-C** is:

$$\mathbf{L_6 = L_3 \cdot \cos(\theta)} \tag{10-24}$$

The distance from the acting point of the pore pressure force on side **A-C** to the intersection point of the previous line with side **A-C** is:

$$\mathbf{L_7 = L_6 - R_2} \tag{10-25}$$

The values of the acting points $\mathbf{R_2}$, $\mathbf{R_3}$ and $\mathbf{R_4}$ follow from calculated or estimated stress distributions.

The equilibrium of moments is now:

$$\begin{aligned}\mathbf{\sum M} &= \mathbf{(N_4 - W_4) \cdot R_4 - (N_3 - W_3 - G_2) \cdot R_3} \\ &\quad \mathbf{+ (N_2 - W_2) \cdot L_7 - (S_2 + C_2) \cdot L_5 = 0}\end{aligned} \tag{10-26}$$

10.4. Nomenclature.

a, τ_a	Adhesion or adhesive shear strength.	**kPa**
A	Adhesive shear force on the blade.	**kN**
c, τ_c	Cohesion or cohesive shear strength.	**kPa**
C_1	Cohesive shear force on the shear plane.	**kN**
C_2	Cohesive shear force on the pseudo blade (front of the wedge).	**kN**
C_3	Cohesive shear force on bottom of the wedge.	**kN**
F_h	Horizontal cutting force.	**kN**
F_v	Vertical cutting force.	**kN**
G_1	Weight of the layer cut.	**kN**
G_2	Weight of the wedge.	**kN**
h_b	Blade height.	**m**
h_i	Layer thickness.	**m**
I	Inertial force on the shear plane.	**kN**
N_1	Normal force on the shear plane.	**kN**
N_2	Normal force on the pseudo blade (front of the wedge).	**kN**
N_3	Normal force on bottom of the wedge.	**kN**
N_4	Normal force on the blade.	**kN**
K_1	Sum of N_1 and S_1 on the shear plane.	**kN**
K_2	Sum of N_2 and S_2 on the pseudo blade (front of the wedge).	**kN**
K_3	Sum of N_3 and S_3 on bottom of the wedge.	**kN**
K_4	Sum of N_4 and S_4 on the blade.	**kN**
L_1	Length of the shear plane.	**m**
L_2	Length of the pseudo blade (front of the wedge).	**m**
L_3	Length of the bottom of the wedge.	**m**
L_4	Length of the blade.	**m**
L_5	Length of the line from the tip of the blade to the opposite side of the wedge and perpendicular to this side.	**m**
L_6	Length of the line from point **A** to the intersection point of the previous line with side **A-C.**	**m**
L_7	Distance from the acting point of the pore pressure force on side **A-C** to the intersection point of the previous line L_6 with side **A-C.**	**m**
R_1	Acting point forces on the shear plane.	**m**
R_2	Acting point forces on the pseudo blade (front of the wedge).	**m**
R_3	Acting point forces on the bottom of the wedge.	**m**
R_4	Acting point forces on the blade.	**m**
S_1	Shear (friction) force on the shear plane.	**kN**
S_2	Shear (friction) force on the pseudo blade (front of the wedge).	**kN**
S_3	Shear (friction) force on the bottom of the wedge.	**kN**
S_4	Shear (friction) force on the blade.	**kN**
W_1	Pore pressure force on the shear plane.	**kN**
W_2	Pore pressure force on the pseudo blade (front of the wedge).	**kN**
W_3	Pore pressure force on the bottom of the wedge.	**kN**
W_4	Pore pressure force on the blade.	**kN**
v_c	Cutting velocity.	**m/sec**
α	Blade angle.	**°**
β	Shear angle.	**°**
θ	Wedge angle.	**°**
φ	Internal friction angle.	**°**
δ	External friction angle.	**°**
λ	Internal friction angle on pseudo blade.	**°**

Chapter 11: A Wedge in Dry Sand Cutting.

11.1. Introduction.

The cutting theories until now works well for small blade angles, however when the blade angle and the other angles involved increase, a problem with the model may occur. The basic equations contain a denominator with the sine of the sum of the blade angle, the shear angle, the internal friction angle and the external friction angle. So if the sum of these angles equals 180 degrees, the denominator is zero, meaning a division by zero giving infinity. Even worse, if the sum of these angles is greater than 180 degrees the sine gives a negative result, meaning the cutting forces become negative. But already if the sum of these angles approach 180 degrees the sine becomes very small and since it is in the denominator, the cutting forces would become very high. Now nature will normally choose the road of least resistance, nature will try to find another mechanism for the cutting process and this mechanism might be the occurrence of a wedge in front of the blade. This wedge will form a pseudo cutting blade **A-C** with a blade angle much smaller than the angle of the real blade. The probability of the occurrence of a wedge is large for sand and rock since all 4 angles mentioned play a role there. For clay the probability is much smaller, since in clay cutting normally the internal and external friction angles do not play a role.

Now nature may choose another mechanism which will result in even smaller cutting forces, like the model of Hettiaratchi & Reece (1975), but their model is more complicated. The philosophy here is that if a mechanism can be found resulting in smaller cutting forces than the model used for small blade angles, this model will give a better prediction than the model for small blade angles. The wedge mechanism is such a mechanism, with the advantage that it is relatively simple to use and the cutting forces predicted with this model match the cutting forces from the experiments of Hatamura & Chijiiwa (1977B) pretty close. So from a pragmatic point of view this mechanism will be discussed for large blade angles.

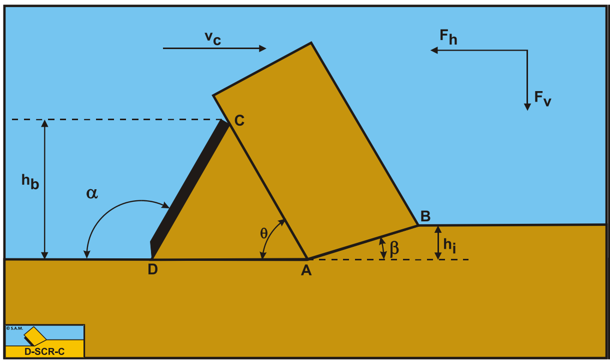

Figure 11-1: Definitions.

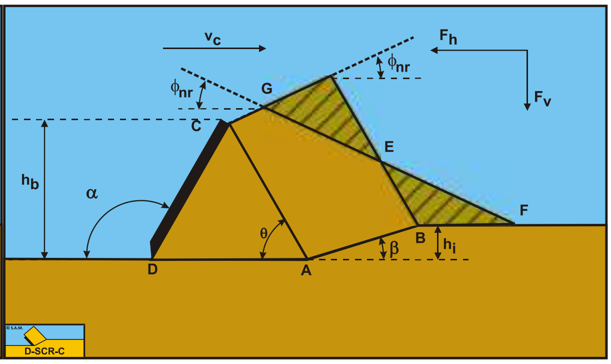

Figure 11-2: Alternative geometry of the layer cut.

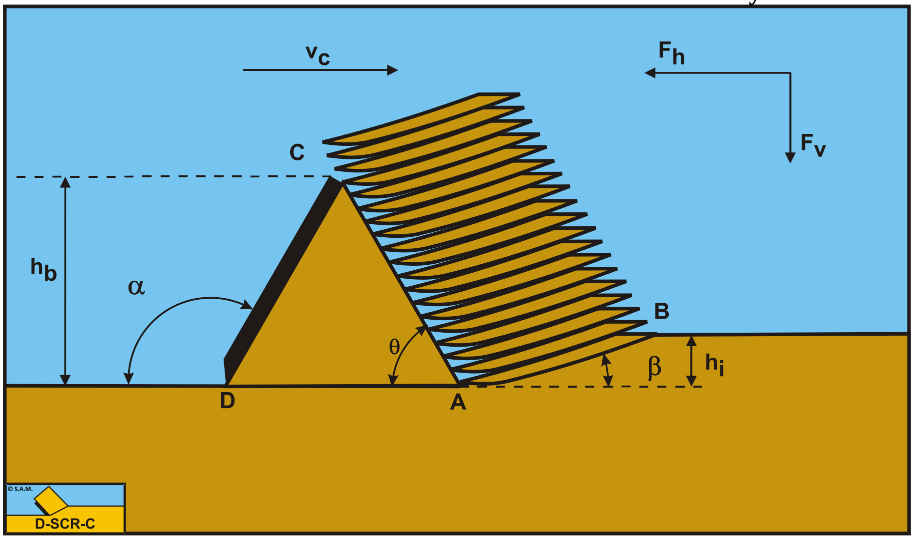

Figure 11-3: The cutting mechanism.

Definitions:

1. **A**: The wedge tip.
2. **B**: End of the shear plane.
3. **C**: The blade top.
4. **D**: The blade tip.
5. **A-B**: The shear plane.
6. **A-C**: The wedge surface.
7. **A-D**: The wedge bottom.
8. **D-C**: The blade surface.
9. $\mathbf{h_b}$: The height of the blade.
10. $\mathbf{h_i}$: The thickness of the layer cut.
11. $\mathbf{v_c}$: The cutting velocity.
12. **α**: The blade angle.
13. **β**: The shear angle.
14. $\mathbf{F_h}$: The horizontal force, the arrow gives the positive direction.
15. $\mathbf{F_v}$: The vertical force, the arrow gives the positive direction.

For the weight of the layer cut $\mathbf{G_1}$, see chapter 5: Dry Sand Cutting.

The weight of the wedge $\mathbf{G_2}$ is given by:

$$G_2 = \rho_s \cdot g \cdot \frac{h_b^2}{2} \cdot \left(\frac{1}{\tan(\theta)} - \frac{1}{\tan(\alpha)} \right) \cdot w \qquad \textbf{(11-1)}$$

11.2. The Force Equilibrium.

Figure 11-4 illustrates the forces on the layer of soil cut. The forces shown are valid in general for dry sand. The forces acting on the layer **A-B** are:

1. A normal force acting on the shear surface $\mathbf{N_1}$, resulting from the effective grain stresses.
2. A shear force $\mathbf{S_1}$ as a result of internal friction $\mathbf{N_1 \cdot tan(\varphi)}$.
3. A gravity force $\mathbf{G_1}$ as a result of the weight of the layer cut.
4. An inertial force **I**, resulting from acceleration of the soil.
5. A force normal to the pseudo blade $\mathbf{N_2}$, resulting from the effective grain stresses.
6. A shear force $\mathbf{S_2}$ as a result of the soil/soil friction $\mathbf{N_2 \cdot tan(\lambda)}$ between the layer cut and the wedge pseudo blade. The friction angle **λ** does not have to be equal to the internal friction angle **φ** in the shear plane, since the soil has already been deformed.

The normal force $\mathbf{N_1}$ and the shear force $\mathbf{S_1}$ can be combined to a resulting grain force $\mathbf{K_1}$.

$$K_1 = \sqrt{N_1^2 + S_1^2} \qquad \textbf{(11-2)}$$

The forces acting on the wedge front or pseudo blade **A-C** when cutting soil, can be distinguished as:

7. A force normal to the blade $\mathbf{N_2}$, resulting from the effective grain stresses.
8. A shear force $\mathbf{S_2}$ as a result of the soil/soil friction $\mathbf{N_2 \cdot tan(\lambda)}$) between the layer cut and the wedge pseudo blade. The friction angle **λ** does not have to be equal to the internal friction angle **φ** in the shear plane, since the soil has already been deformed.

These forces are shown in Figure 11-5. If the forces $\mathbf{N_2}$ and $\mathbf{S_2}$ are combined to a resulting force $\mathbf{K_2}$ and the adhesive force and the water under pressures are known, then the resulting force $\mathbf{K_2}$ is the unknown force on the blade. By taking the horizontal and vertical equilibrium of forces an expression for the force $\mathbf{K_2}$ on the blade can be derived.

$$K_2 = \sqrt{N_2^2 + S_2^2} \qquad \textbf{(11-3)}$$

The forces acting on the wedge bottom **A-D** when cutting soil, can be distinguished as:

9. A force normal to the blade $\mathbf{N_3}$, resulting from the effective grain stresses.
10. A shear force $\mathbf{S_3}$ as a result of the soil/soil friction $\mathbf{N_3 \cdot tan(\varphi)}$) between the wedge bottom and the undisturbed soil.

The normal force **N3** and the shear force **S3** can be combined to a resulting grain force **K3**.

$$K_3 = \sqrt{N_3^2 + S_3^2} \tag{11-4}$$

The forces acting on a straight blade **C-D** when cutting soil (see Figure 11-6), can be distinguished as:

11. A force normal to the blade **N4,** resulting from the effective grain stresses.
12. A shear force **S4** as a result of the soil/steel friction **N4·tan(δ)**.

The normal force **N4** and the shear force **S4** can be combined to a resulting grain force **K4**.

$$K_4 = \sqrt{N_4^2 + S_4^2} \tag{11-5}$$

The horizontal equilibrium of forces on the layer cut:

$$\sum F_h = K_1 \cdot \sin(\beta + \varphi) + I \cdot \cos(\beta) - K_2 \cdot \sin(\alpha + \lambda) = 0 \tag{11-6}$$

The vertical equilibrium of forces on the layer cut:

$$\sum F_v = -K_1 \cdot \cos(\beta + \varphi) + I \cdot \sin(\beta) + G_1 - K_2 \cdot \cos(\alpha + \lambda) = 0 \tag{11-7}$$

The force **K1** on the shear plane is now:

$$K_1 = \frac{G_1 \cdot \sin(\alpha + \lambda) - I \cdot \cos(\alpha + \beta + \lambda)}{\sin(\alpha + \beta + \lambda + \varphi)} \tag{11-8}$$

The force **K2** on the pseudo blade is now:

$$K_2 = \frac{G_1 \cdot \sin(\beta + \varphi) + I \cdot \cos(\varphi)}{\sin(\alpha + \beta + \lambda + \varphi)} \tag{11-9}$$

From equation (11-9) the forces on the pseudo blade can be derived. On the pseudo blade a force component in the direction of cutting velocity **Fh** and a force perpendicular to this direction **Fv** can be distinguished.

$$F_h = K_2 \cdot \sin(\alpha + \lambda) \tag{11-10}$$

$$F_v = K_2 \cdot \cos(\alpha + \lambda) \tag{11-11}$$

The normal force on the shear plane is now:

$$N_1 = \frac{G_1 \cdot \sin(\alpha + \lambda) - I \cdot \cos(\alpha + \beta + \lambda)}{\sin(\alpha + \beta + \lambda + \varphi)} \cdot \cos(\varphi) \tag{11-12}$$

The normal force on the pseudo blade is now:

$$N_2 = \frac{G_1 \cdot \sin(\beta + \varphi) + I \cdot \cos(\varphi)}{\sin(\alpha + \beta + \lambda + \varphi)} \cdot \cos(\lambda) \tag{11-13}$$

Now knowing the forces on the pseudo blade A-C, the equilibrium of forces on the wedge A-C-D can be derived. The horizontal equilibrium of forces on the wedge is:

$$\sum F_h = -K_4 \cdot \sin(\alpha + \delta) + K_3 \cdot \sin(\varphi) + K_2 \cdot \sin(\theta + \lambda) = 0 \tag{11-14}$$

The vertical equilibrium of forces on the wedge is:

$$\sum F_v = -K_4 \cdot \cos(\alpha + \delta) - K_3 \cdot \cos(\varphi) + K_2 \cdot \cos(\theta + \lambda) + G_2 = 0 \tag{11-15}$$

The unknowns in this equation are **K_3** and **K_4**, since **K_2** has already been solved. Two other unknowns are the external friction angle **δ**, since also the external friction does not have to be fully mobilized, and the wedge angle **θ**. These 2 additional unknowns require 2 additional conditions in order to solve the problem. One additional condition is the equilibrium of moments of the wedge, a second condition the principle of minimum required cutting energy. Depending on whether the soil pushes upwards or downwards against the blade, the mobilization factor is between -1 and +1.

The force **K_3** on the bottom of the wedge is now:

$$K_3 = \frac{K_2 \cdot \sin(\alpha + \delta - \theta - \lambda) + G_2 \cdot \sin(\alpha + \delta)}{\sin(\alpha + \delta + \varphi)} \qquad \textbf{(11-16)}$$

The force **K_4** on the blade is now:

$$K_4 = \frac{K_2 \cdot \sin(\theta + \lambda + \varphi) + G_2 \cdot \sin(\varphi)}{\sin(\alpha + \delta + \varphi)} \qquad \textbf{(11-17)}$$

This results in a horizontal force on the blade of:

$$F_h = K_4 \cdot \sin(\alpha + \delta) \qquad \textbf{(11-18)}$$

And in a vertical force on the blade of:

$$F_v = K_4 \cdot \cos(\alpha + \delta) \qquad \textbf{(11-19)}$$

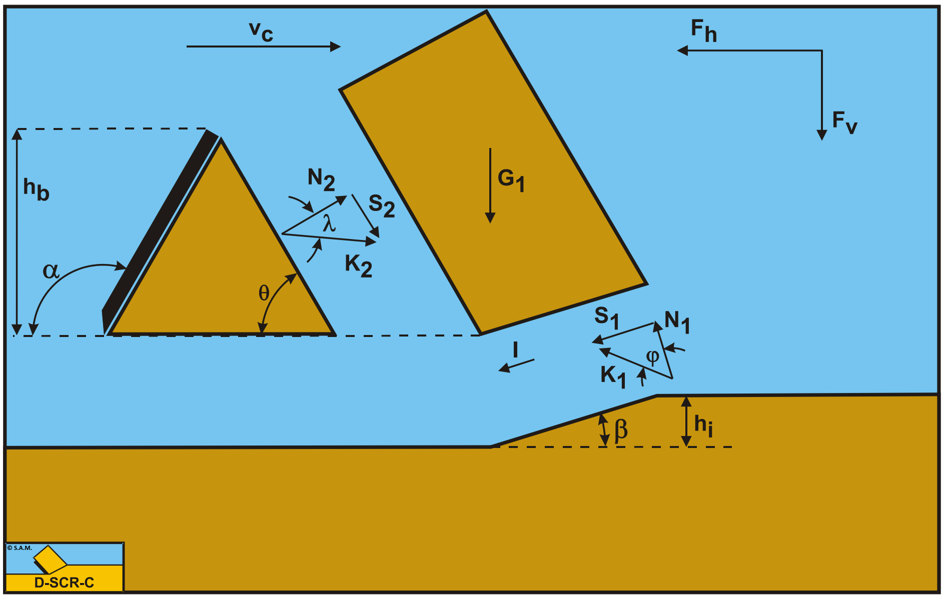

Figure 11-4: The forces on the layer cut when a wedge is present.

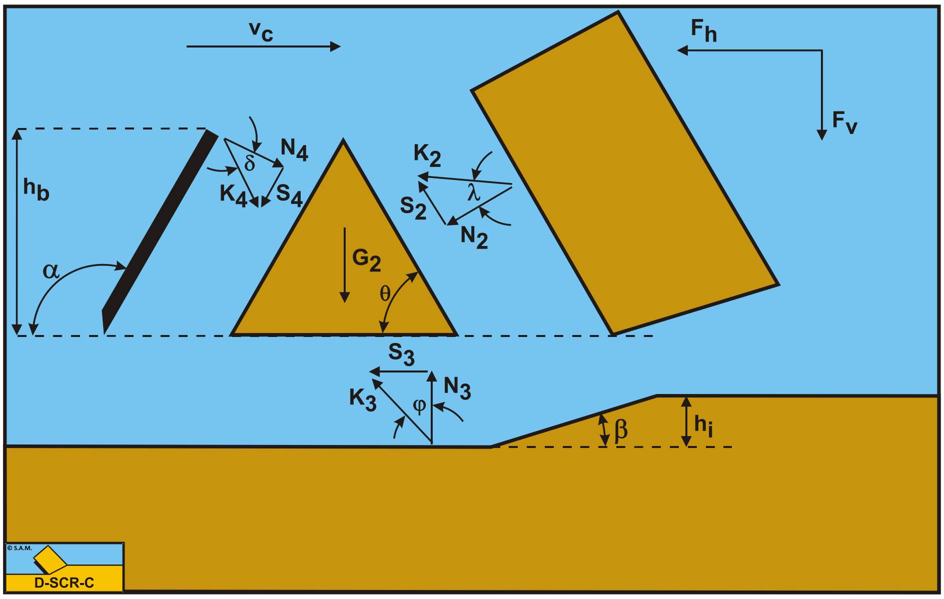

Figure 11-5: The forces on the wedge.

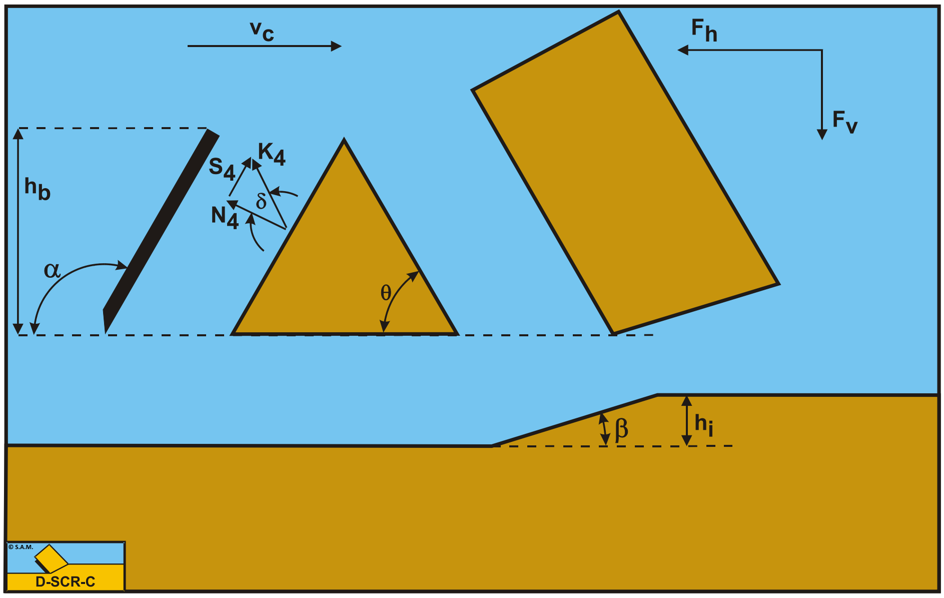

Figure 11-6: The forces on the blade when a wedge is present.

11.3. The Equilibrium of Moments.

In order to solve the problem, also the equilibrium of moments is required, since the wedge is not subject to rotational acceleration. The equilibrium of moments can be taken around each point of the wedge. Here the tip of the blade is chosen. The advantage of this is that a number of forces do not contribute to the moments on the wedge.

In order to derive the equilibrium of moments equation the arms of all the forces contributing to this equilibrium have to be known. Since these arms depend on the length of all the sides in the cutting process, first these lengths are determined. The length of the shear plane **A-B** is:

$$L_1 = \frac{h_i}{\sin(\beta)} \tag{11-20}$$

The length of the pseudo blade **A-C** is:

$$L_2 = \frac{h_b}{\sin(\theta)} \tag{11-21}$$

The length of the bottom of the wedge **A-D** is:

$$L_3 = h_b \cdot \left(\frac{1}{\tan(\theta)} - \frac{1}{\tan(\alpha)} \right) \tag{11-22}$$

The length of the blade **C-D** is:

$$L_4 = \frac{h_b}{\sin(\alpha)} \tag{11-23}$$

The length of the line from the tip of the blade to the opposite side of the wedge and perpendicular to this side is:

$$L_5 = L_3 \cdot \sin(\theta) \tag{11-24}$$

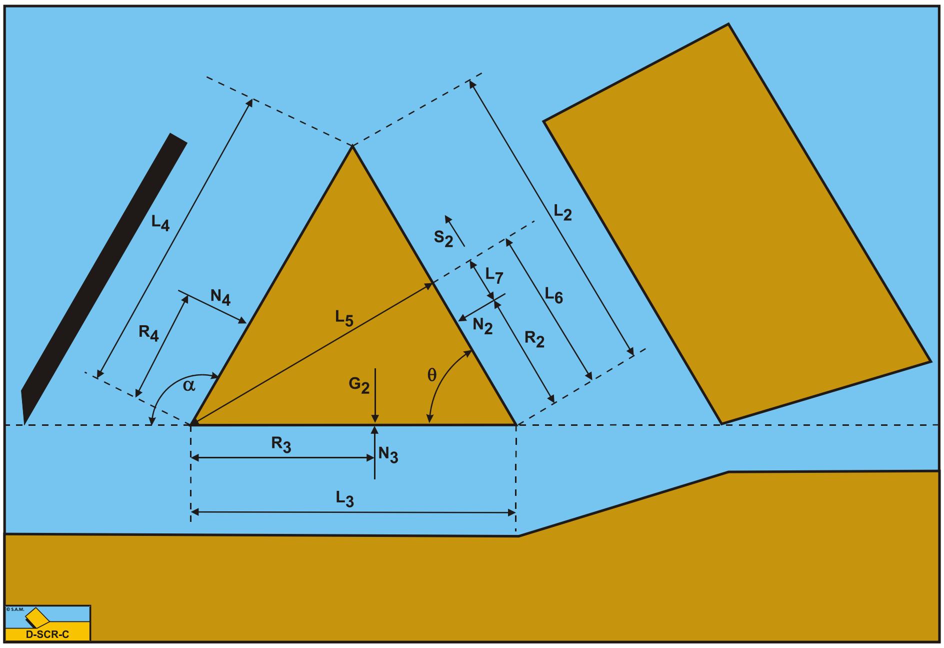

Figure 11-7: The moments on the wedge.

The length of the line from point **A** to the intersection point of the previous line with side **A-C** is:

$$L_6 = L_3 \cdot \cos(\theta) \tag{11-25}$$

The distance from the acting point of the pore pressure force on side **A-C** to the intersection point of the previous line with side **A-C** is:

$$L_7 = L_6 - R_2 \tag{11-26}$$

The values of the acting points $\mathbf{R_2}$, $\mathbf{R_3}$ and $\mathbf{R_4}$ follow from calculated or estimated stress distributions.

The equilibrium of moments is now:

$$\sum M = N_4 \cdot R_4 - (N_3 - G_2) \cdot R_3 + N_2 \cdot L_7 - S_2 \cdot L_5 = 0 \tag{11-27}$$

11.4. Results of some Calculations.

Since the wedge model depends on many parameters, some example calculations are carried out with the parameters as used by Hatamura & Chijiiwa (1977B). The calculations are carried out with a blade height **h_b=0.2 m**, a blade width **w=0.33 m**, an angle of internal friction **φ=38°**, an angle of internal friction **δ=2/3·φ**, an angle of internal friction on the pseudo blade of **λ=32°**, a dry density of **ρ_s=1.59 ton/m^3** and a cutting velocity of **v_c=0.05 m/sec**. The difference with the Hatamura & Chijiiwa (1977B) experiments is that here the blade height is constant, while in their experiments the blade length was constant. Further layer thicknesses of **h_i=0.066 m, 0.10 m and 0.20 m** are used in the calculations. Based on these and many more calculations an empirical equation has been found for the wedge angle **θ**.

$$\theta = (90 - \varphi)\cdot\left(0.73 + 0.0788\cdot\frac{h_b}{h_i}\right) \tag{11-28}$$

Figure 11-8, Figure 11-9 and Figure 11-10 show the shear angle, the mobilized external friction angle, the wedge angle, the total cutting force and the direction of the total cutting force.

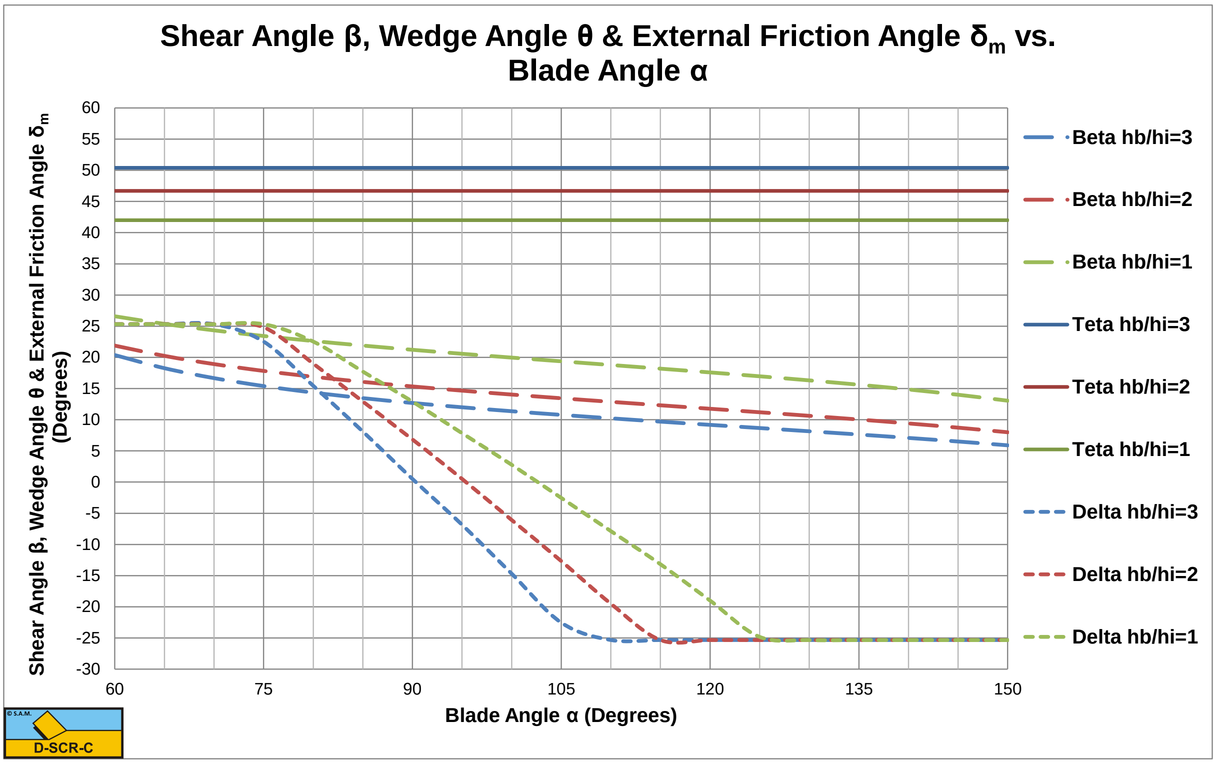

Figure 11-8: The shear angle, wedge angle and mobilized external friction angle calculated with wedge.

In the region where the mobilized external friction angle changes from plus the maximum to minus the maximum value, an equilibrium of moments exists. In the case considered this means that a wedge may exist in this region. When the mobilized external friction angle equals minus the maximum value there is no equilibrium of moments. In this region the total cutting force increases rapidly with an increasing blade angle in the calculations, but most probably another mechanism than the wedge mechanism will occur, so the values of the cutting forces in that region are not reliable. In the region of the mobilized external friction angle between plus the maximum to minus the maximum value the total cutting force is almost constant.

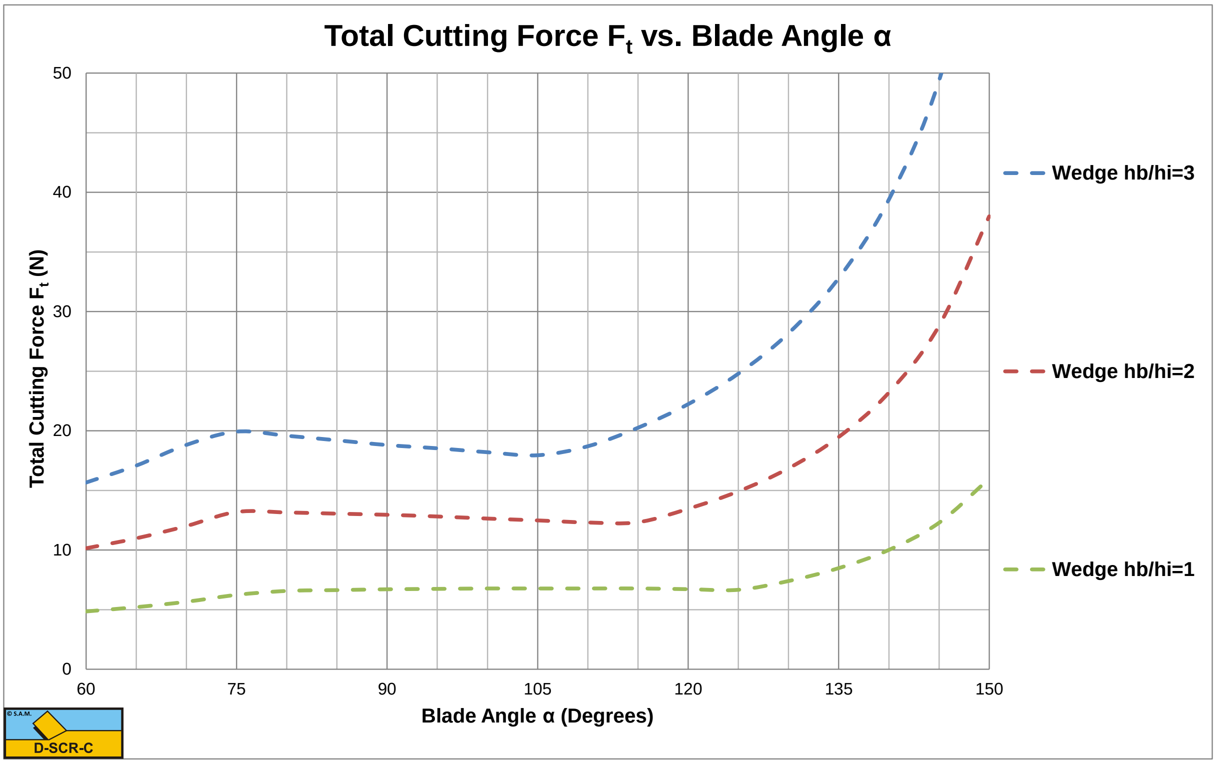

Figure 11-9: The total cutting force.

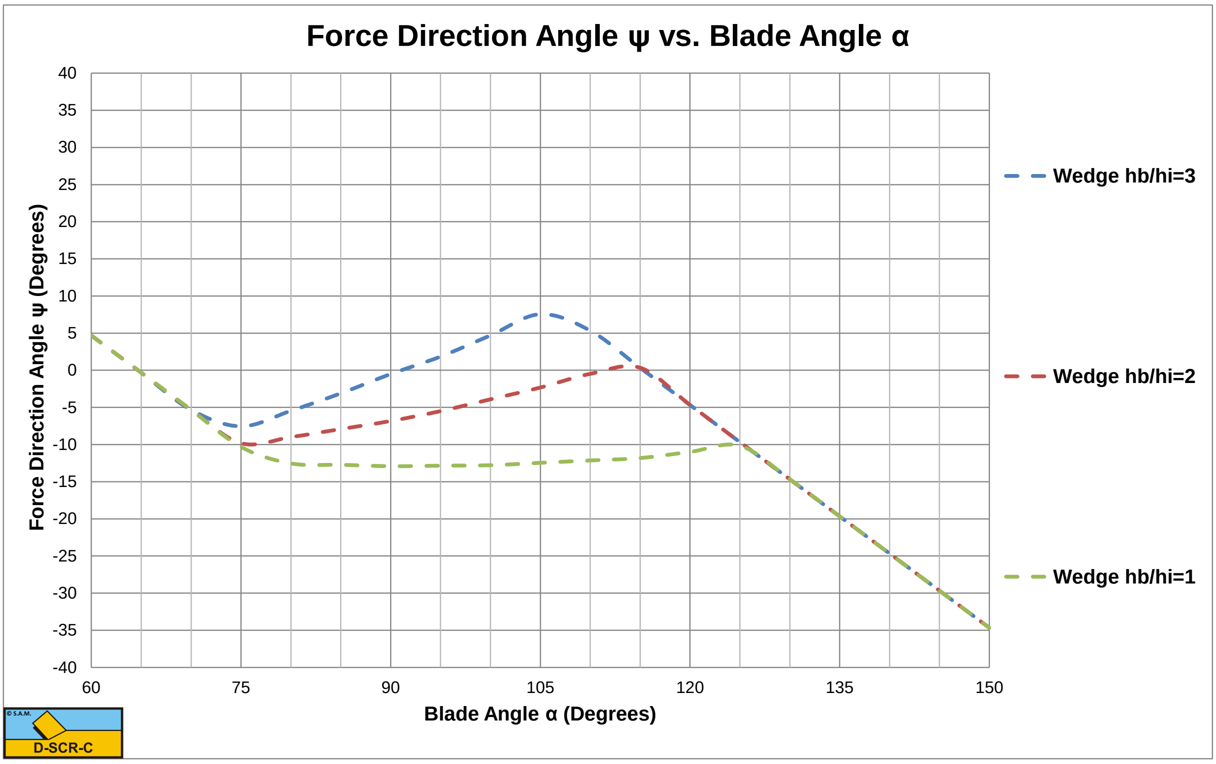

Figure 11-10: The direction of the total cutting force.

11.5. Experiments of Hatamura & Chijiiwa (1977B).

The experiments of Hatamura & Chijiiwa (1977B) were carried out with a blade length **L_4=0.2 m**, a blade width **w=0.33 m**, an angle of internal friction **φ=38°**, an angle of internal friction **δ=2/3·φ**, an angle of internal friction on the pseudo blade of **λ=32°**, a dry density of **ρ_s=1.46 ton/m^3** and a cutting velocity of **v_c=0.05 m/sec**.

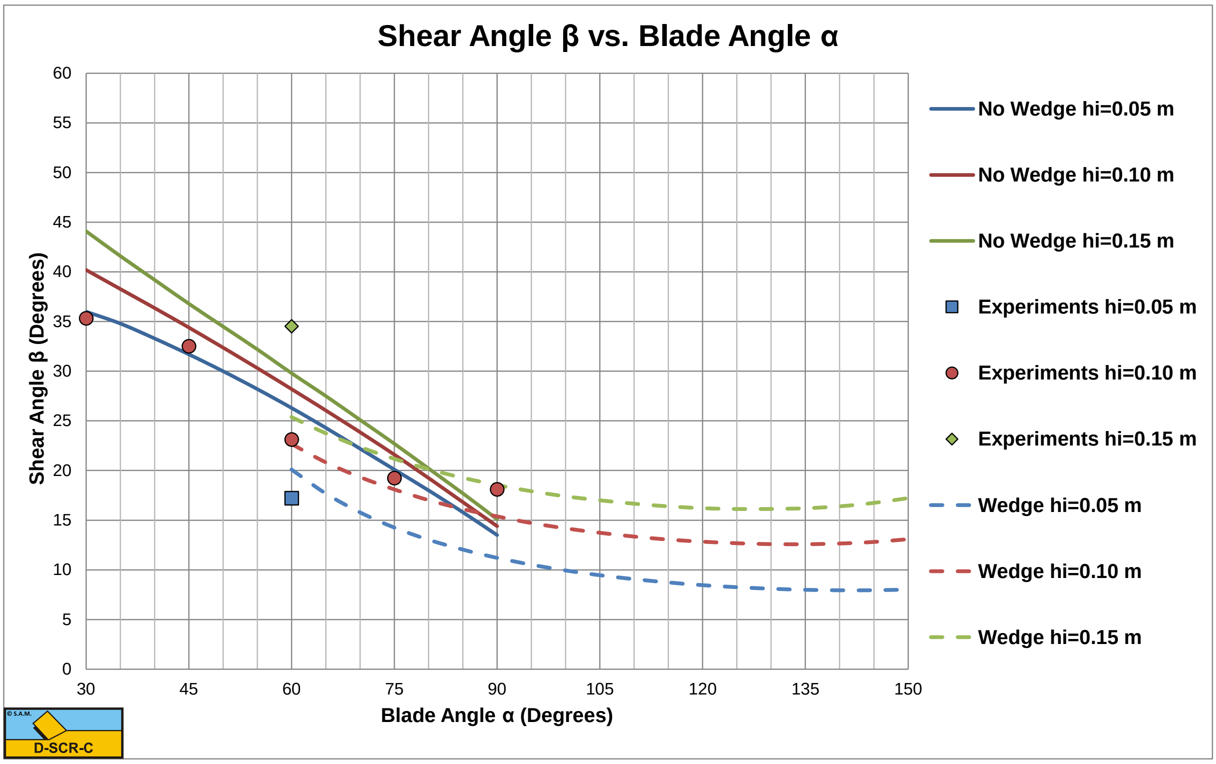

Figure 11-11: The shear angle of Hatamura & Chijiiwa (1977B) versus the calculated shear angles, with and without wedge.

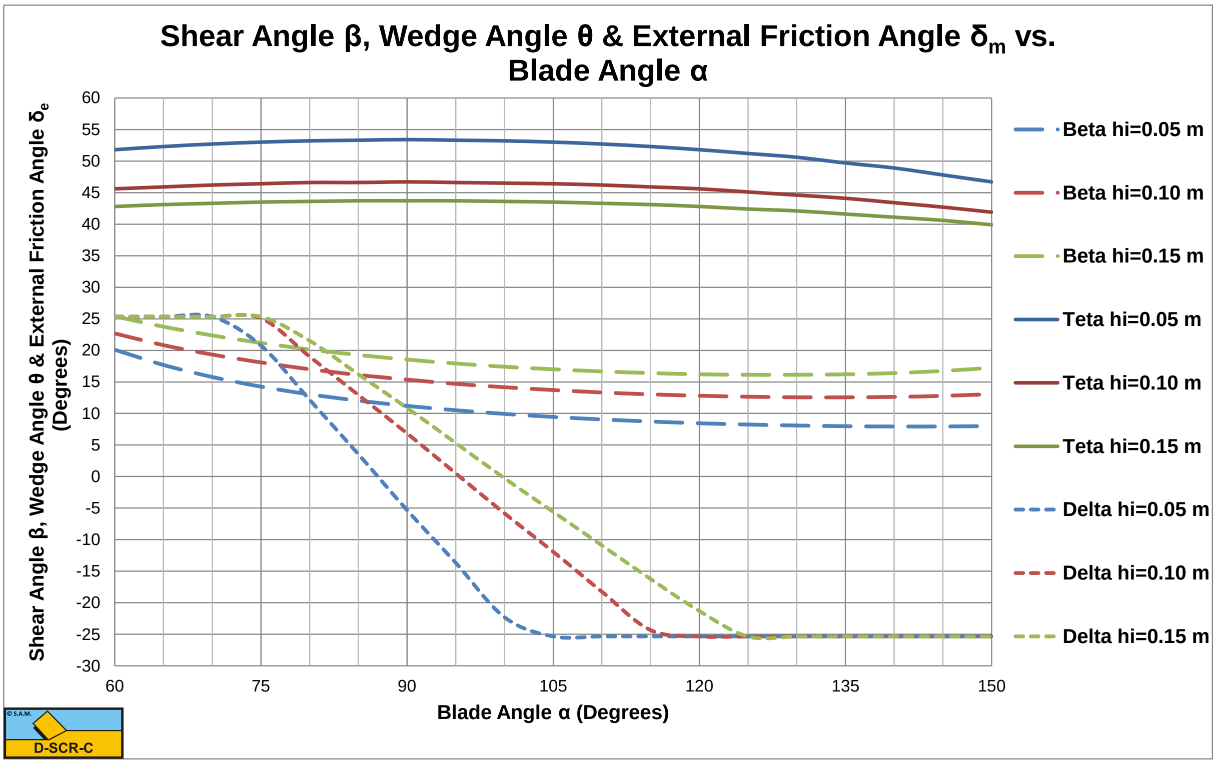

Figure 11-12: The shear angle, wedge angle and mobilized external friction angle calculated with wedge.

Although the number of experiments of Hatamura & Chijiiwa (1977B) is limited, both the shear angles and the total cutting forces tend to follow the wedge theory for blade angles of 75° and 90°. The direction of the total cutting force measured is more upwards directed (negative angle) than predicted with the wedge theory for the 90° blade. This could mean that the real mechanism is different from the wedge mechanism. The cutting forces however match well.

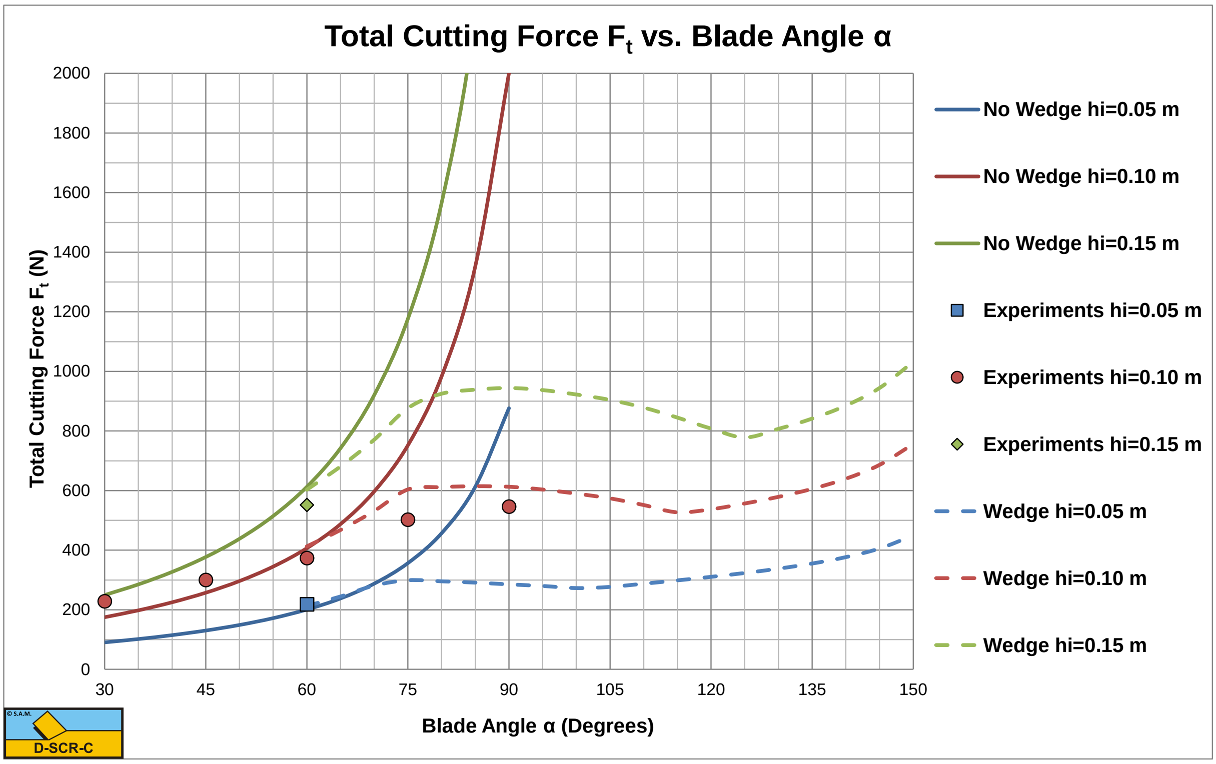

Figure 11-13: The total force of Hatamura & Chijiiwa (1977B) versus the calculated total force, with and without wedge.

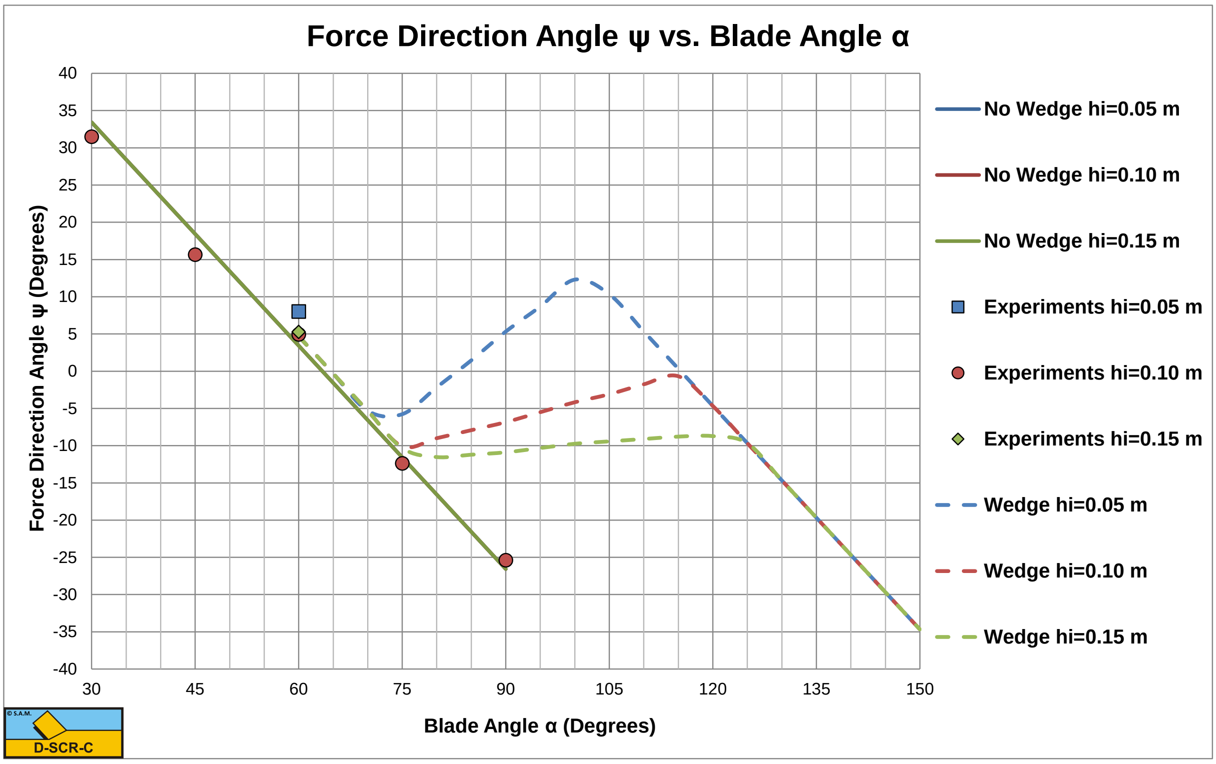

Figure 11-14: The direction of the cutting force of Hatamura & Chijiiwa (1977B) versus the calculated force direction, with and without wedge.

11.6. Nomenclature.

a, τ_a	Adhesion or adhesive shear strength.	**kPa**
A	Adhesive shear force on the blade.	**kN**
c, τ_c	Cohesion or cohesive shear strength.	**kPa**
C_1	Cohesive shear force on the shear plane.	**kN**
C_2	Cohesive shear force on the pseudo blade (front of the wedge).	**kN**
C_3	Cohesive shear force on bottom of the wedge.	**kN**
F_h	Horizontal cutting force.	**kN**
F_v	Vertical cutting force.	**kN**
G_1	Weight of the layer cut.	**kN**
G_2	Weight of the wedge.	**kN**
h_b	Blade height.	**m**
h_i	Layer thickness.	**m**
I	Inertial force on the shear plane.	**kN**
N_1	Normal force on the shear plane.	**kN**
N_2	Normal force on the pseudo blade (front of the wedge).	**kN**
N_3	Normal force on bottom of the wedge.	**kN**
N_4	Normal force on the blade.	**kN**
K_1	Sum of N_1 and S_1 on the shear plane.	**kN**
K_2	Sum of N_2 and S_2 on the pseudo blade (front of the wedge).	**kN**
K_3	Sum of N_3 and S_3 on bottom of the wedge.	**kN**
K_4	Sum of N_4 and S_4 on the blade.	**kN**
L_1	Length of the shear plane.	**m**
L_2	Length of the pseudo blade (front of the wedge).	**m**
L_3	Length of the bottom of the wedge.	**m**
L_4	Length of the blade.	**m**
L_5	Length of the line from the tip of the blade to the opposite side of the wedge and perpendicular to this side.	**m**
L_6	Length of the line from point **A** to the intersection point of the previous line with side **A-C.**	**m**
L_7	Distance from the acting point of the pore pressure force on side **A-C** to the intersection point of the previous line L_6 with side **A-C.**	**m**
R_1	Acting point forces on the shear plane.	**m**
R_2	Acting point forces on the pseudo blade (front of the wedge).	**m**
R_3	Acting point forces on the bottom of the wedge.	**m**
R_4	Acting point forces on the blade.	**m**
S_1	Shear (friction) force on the shear plane.	**kN**
S_2	Shear (friction) force on the pseudo blade (front of the wedge).	**kN**
S_3	Shear (friction) force on the bottom of the wedge.	**kN**
S_4	Shear (friction) force on the blade.	**kN**
W_1	Pore pressure force on the shear plane.	**kN**
W_2	Pore pressure force on the pseudo blade (front of the wedge).	**kN**
W_3	Pore pressure force on the bottom of the wedge.	**kN**
W_4	Pore pressure force on the blade.	**kN**
v_c	Cutting velocity.	**m/sec**
α	Blade angle.	**°**
β	Shear angle.	**°**
θ	Wedge angle.	**°**
φ	Internal friction angle.	**°**
δ	External friction angle.	**°**
λ	Internal friction angle on pseudo blade.	**°**

Chapter 12: A Wedge in Saturated Sand Cutting.

12.1. Introduction.

In the last decennia extensive research has been carried out into the cutting of water saturated sand. In the cutting of water-saturated sand, the phenomenon of dilatation plays an important role. In fact the effects of gravity, inertia, cohesion and adhesion can be neglected at cutting speeds in the range of 0.5 – 10 m/s. In the cutting equations, as published by Miedema (1987 September), there is a division by the sine of the sum of the blade angle, the shear angle, the angle of internal friction and the soil/interface friction angle. When the sum of these angle approaches 180°, a division by zero is the result, resulting in infinite cutting forces. This may occur for example for $\alpha=80°$, $\beta=30°$, $\phi=40°$ and $\delta=30°$. When this sum is greater than 180 degrees, the cutting forces become negative. It is obvious that this cannot be the case in reality and that nature will look for another cutting mechanism.
Hettiaratchi and Reece (1975) found a mechanism, which they called boundary wedges for dry soil. At large cutting angles a triangular wedge will exist in front of the blade, not moving relative to the blade. This wedge acts as a blade with a smaller blade angle. In fact, this reduces the sum of the 4 angles mentioned before to a value much smaller than 180°. The existence of a dead zone (wedge) in front of the blade when cutting at large cutting angles will affect the value and distribution of vacuum water pressure on the interface. He et al. (1998) proved experimentally that also in water saturated sand at large cutting angles a wedge will occur. A series of tests with rake angles 90, 105 and 120 degrees under fully saturated and densely compacted sand condition was performed by He et al. (1998) at the Dredging Technology Laboratory of Delft University of Technology. The experimental results showed that the failure pattern with large rake angles is quite different from that with small rake angles. For large rake angles a dead zone is formed in front of the blade, but not for small rake angles. In the tests he carried out, both a video camera and film camera were used to capture the failure pattern. The video camera was fixed on the frame which is mounted on the main carriage, translates with the same velocity as the testing cutting blade. Shown in the static slide of the video record, as in Figure 12-1, the boundary wedges exist during the cutting test. The assumption of an alternative failure mechanism is based on a small quantity of picture material, see Figure 12-1. It is described as a static wedge in front of the blade, which serves as a new virtual blade over which the sand flows away.

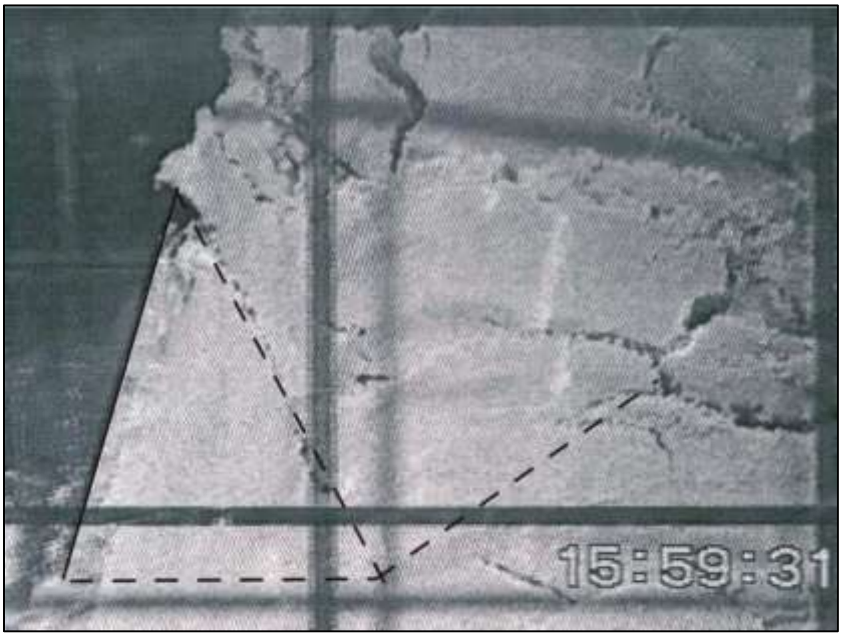

Figure 12-1: Failure pattern with rake angle of 120°.

Although the number of experiments published is limited, the research is valuable as a starting point to predict the shape of the wedge. At small cutting angles the cutting forces are determined by the horizontal and vertical force equilibrium equations of the sand cut in front of the blade. These equations contain 3 unknowns, so a third equation/condition had to be found. The principle of minimum energy is used as a third condition to solve the 3 unknowns. This has proved to give very satisfactory results finding the shear angle and the horizontal and vertical cutting forces at small cutting angles. At large cutting angles, a 4th unknown exists, the wedge angle or virtual blade angle. This means that a 4th equation/condition must be found in order to determine the wedge angle. There are 3 possible conditions that can be used: The principle of minimum energy, the circle of Mohr, The equilibrium of moments of the wedge. In fact, there is also a 5th unknown, the mobilized friction on the blade. New research carried out in the Dredging Engineering Laboratory shows that a wedge exists, but not always a static wedge. The sand inside the wedge is still moving, but with a much lower velocity then the sand outside the wedge. This results in fully mobilized friction on the blade. The bottom boundary of the wedge, which is horizontal for a static wedge, may have a small angle with respect to the horizontal in the new case considered.

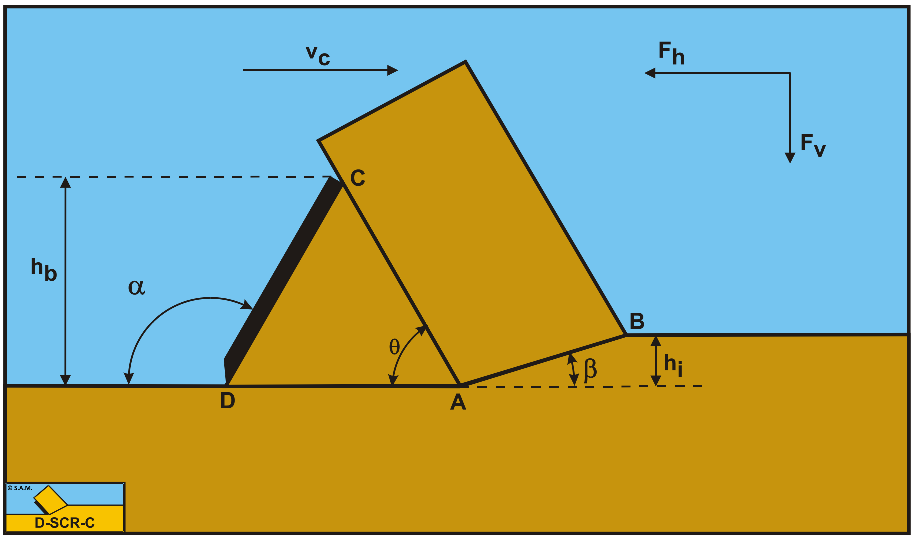

Figure 12-2: Sand cutting with a wedge, definitions.

Definitions:

1. **A**: The wedge tip.
2. **B**: End of the shear plane.
3. **C**: The blade top.
4. **D**: The blade tip.
5. **A-B**: The shear plane.
6. **A-C**: The wedge surface.
7. **A-D**: The wedge bottom.
8. **D-C**: The blade surface.
9. **h_b**: The height of the blade.
10. **h_i**: The thickness of the layer cut.
11. **v_c**: The cutting velocity.
12. **α**: The blade angle.
13. **β**: The shear angle.
14. **F_h**: The horizontal force, the arrow gives the positive direction.
15. **F_v**: The vertical force, the arrow gives the positive direction.

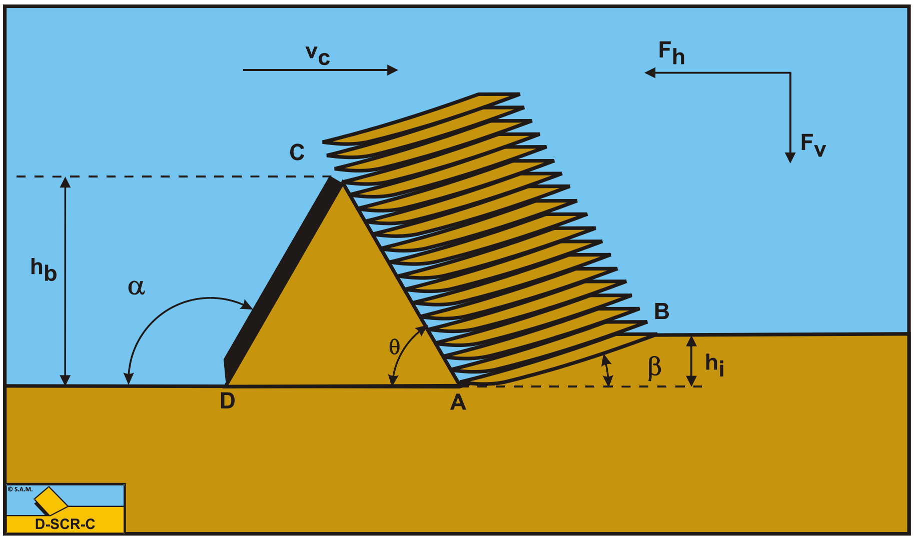

Figure 12-3: The cutting mechanism.

Figure 12-2 shows the definitions of the cutting process with a static wedge. A-B is the shear plane where dilatation occurs. A-C is the front of the static wedge and forms a pseudo cutting blade. A-C-D is the static wedge, where C-D is the blade, A-D the bottom of the wedge and A-C the pseudo blade or the front of the wedge.
The sand wedge theory is based on publications of Hettiaratchi and Reece (1975), Miedema (1987 September), He et al. (1998), Yi (2000), Miedema et al. (2001), Yi et al. (2001), Ma (2001), Miedema et al. (2002A), Miedema et al. (2002B), Yi et al. (2002), Miedema (2003), Miedema et al. (2003), Miedema (2004), Miedema et al. (2004), He et al. (2005), Ma et al. (2006A), Ma et al. (2006B), Miedema (2005), Miedema (2006A), Miedema (2006B).

12.2. The Equilibrium of Forces.

Figure 12-4, Figure 12-5 and Figure 12-6 show the forces occurring at the layer cut, the wedge and the blade, while Figure 12-18 shows the moments occurring on the wedge. The forces are:

The forces acting on the layer **A-B** are:

1. A normal force acting on the shear surface $\mathbf{N_1}$, resulting from the effective grain stresses.
2. A shear force $\mathbf{S_1}$ as a result of internal friction $\mathbf{N_1 \cdot tan(\varphi)}$.
3. A force $\mathbf{W_1}$ as a result of water under pressure in the shear zone.
4. A force normal to the pseudo blade $\mathbf{N_2}$, resulting from the effective grain stresses.
5. A shear force $\mathbf{S_2}$ as a result of the soil/soil friction $\mathbf{N_2 \cdot tan(\lambda)}$ between the layer cut and the wedge pseudo blade. The friction angle $\boldsymbol{\lambda}$ does not have to be equal to the internal friction angle $\boldsymbol{\varphi}$ in the shear plane, since the soil has already been deformed.
6. A force $\mathbf{W_2}$ as a result of water under pressure on the wedge.

The forces acting on the wedge front or pseudo blade **A-C** when cutting soil, can be distinguished as:

7. A force normal to the blade $\mathbf{N_2}$, resulting from the effective grain stresses.
8. A shear force $\mathbf{S_2}$ as a result of the soil/soil friction $\mathbf{N_2 \cdot tan(\lambda)}$) between the layer cut and the wedge pseudo blade. The friction angle $\boldsymbol{\lambda}$ does not have to be equal to the internal friction angle $\boldsymbol{\varphi}$ in the shear plane, since the soil has already been deformed.
9. A force $\mathbf{W_2}$ as a result of water under pressure on the pseudo blade **A-C**.

The forces acting on the wedge bottom **A-D** when cutting soil, can be distinguished as:

10. A force normal to the blade $\mathbf{N_3}$, resulting from the effective grain stresses.
11. A shear force $\mathbf{S_3}$ as a result of the soil/soil friction $\mathbf{N_3 \cdot tan(\varphi)}$) between the wedge bottom and the undisturbed soil.
12. A force $\mathbf{W_3}$ as a result of water under pressure on the wedge bottom **A-D**.

The forces acting on a straight blade **C-D** when cutting soil, can be distinguished as:

13. A force normal to the blade $\mathbf{N_4}$**,** resulting from the effective grain stresses.
14. A shear force $\mathbf{S_4}$ as a result of the soil/steel friction $\mathbf{N_4 \cdot tan(\delta)}$ between the wedge and the blade.
15. A force $\mathbf{W_4}$ as a result of water under pressure on the blade.

To determine the cutting forces on the blade, first the cutting forces on the pseudo blade have to be determined by taking the horizontal and vertical equilibrium of forces on the layer cut **B-A-C**. The shear angle $\boldsymbol{\beta}$ is determined by minimizing the cutting energy.

The horizontal equilibrium of forces:

$$\sum F_h = K_1 \cdot \sin(\beta + \varphi) - W_1 \cdot \sin(\beta) + W_2 \cdot \sin(\alpha) - K_2 \cdot \sin(\alpha + \lambda) = 0 \tag{12-1}$$

The vertical equilibrium of forces:

$$\sum F_v = -K_1 \cdot \cos(\beta + \varphi) + W_1 \cdot \cos(\beta) + W_2 \cdot \cos(\alpha) - K_2 \cdot \cos(\alpha + \lambda) = 0 \tag{12-2}$$

The force $\mathbf{K_1}$ on the shear plane is now:

$$K_1 = \frac{W_2 \cdot \sin(\lambda) + W_1 \cdot \sin(\alpha + \beta + \lambda)}{\sin(\alpha + \beta + \lambda + \varphi)} \tag{12-3}$$

The force $\mathbf{K_2}$ on the pseudo blade is now:

$$K_2 = \frac{W_2 \cdot \sin(\alpha + \beta + \varphi) + W_1 \cdot \sin(\varphi)}{\sin(\alpha + \beta + \lambda + \varphi)} \tag{12-4}$$

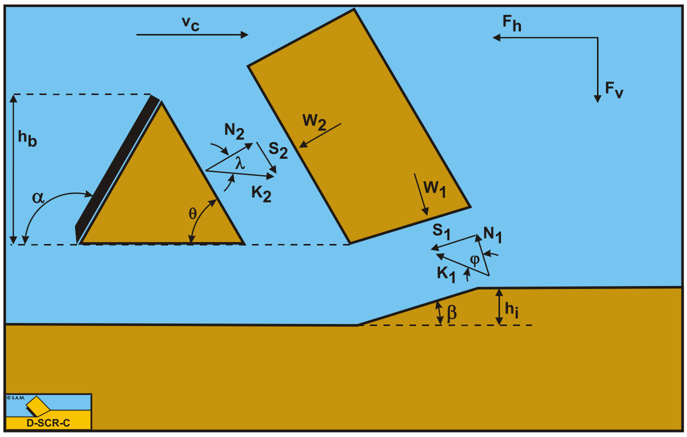

Figure 12-4: The forces on the layer cut in saturated sand with a wedge.

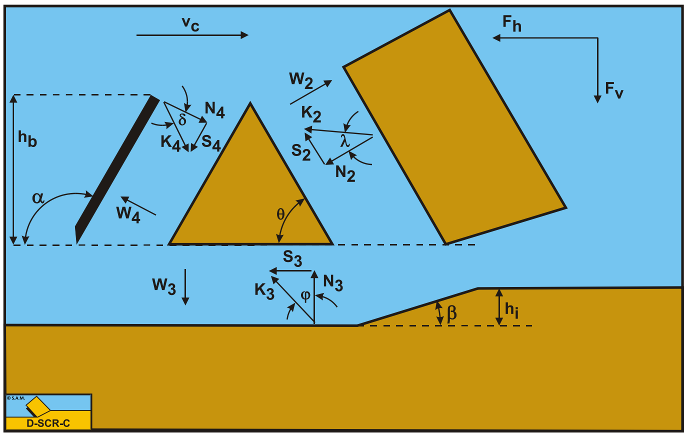

Figure 12-5: The forces on the wedge in saturated sand.

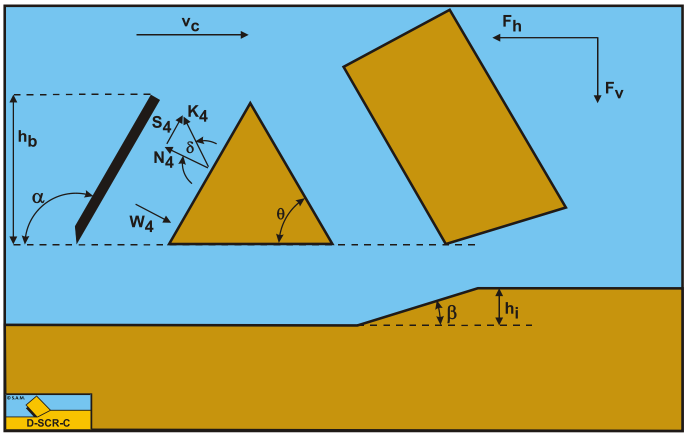

Figure 12-6: The forces on the blade in saturated sand with a wedge.

From equation (12-4) the forces on the pseudo blade can be derived. On the pseudo blade a force component in the direction of cutting velocity $\mathbf{F_h}$ and a force perpendicular to this direction $\mathbf{F_v}$ can be distinguished.

$$F_h = -W_2 \cdot \sin(\alpha) + K_2 \cdot \sin(\alpha + \lambda) \tag{12-5}$$

$$F_v = -W_2 \cdot \cos(\alpha) + K_2 \cdot \cos(\alpha + \lambda) \tag{12-6}$$

The normal force on the shear plane **A-B** is now:

$$N_1 = \frac{W_2 \cdot \sin(\lambda) + W_1 \cdot \sin(\alpha + \beta + \lambda)}{\sin(\alpha + \beta + \lambda + \varphi)} \cdot \cos(\varphi) \qquad \textbf{(12-7)}$$

The normal force on the pseudo blade **A-C** is now:

$$N_2 = \frac{W_2 \cdot \sin(\alpha + \beta + \varphi) + W_1 \cdot \sin(\varphi)}{\sin(\alpha + \beta + \lambda + \varphi)} \cdot \cos(\lambda) \qquad \textbf{(12-8)}$$

Now the force equilibrium on the wedge has to be solved. This is done by first taking the horizontal and vertical force equilibrium on the wedge **A-C-D**.

The horizontal equilibrium of forces:

$$\begin{aligned} \sum F_h = &+ W_4 \cdot \sin(\alpha) - K_4 \cdot \sin(\alpha + \delta_e) + K_3 \cdot \sin(\varphi) \\ &- W_2 \cdot \sin(\theta) + K_2 \cdot \sin(\theta + \lambda) = 0 \end{aligned} \qquad \textbf{(12-9)}$$

The vertical equilibrium of forces:

$$\begin{aligned} \sum F_v = &+ W_4 \cdot \cos(\alpha) - K_4 \cdot \cos(\alpha + \delta_e) + W_3 - K_3 \cdot \cos(\varphi) \\ &- W_2 \cdot \cos(\theta) + K_2 \cdot \cos(\theta + \lambda) = 0 \end{aligned} \qquad \textbf{(12-10)}$$

The grain force **K₃** on the bottom of the wedge is now:

$$\begin{aligned} K_3 = &\frac{-W_2 \cdot \sin(\alpha + \delta_e - \theta) + K_2 \cdot \sin(\alpha + \delta_e - \theta - \lambda)}{\sin(\alpha + \delta_e + \varphi)} \\ &+ \frac{+W_3 \cdot \sin(\alpha + \delta_e) + W_4 \cdot \sin(\delta_e)}{\sin(\alpha + \delta_e + \varphi)} \end{aligned} \qquad \textbf{(12-11)}$$

The grain force **K₄** on the blade is now:

$$\begin{aligned} K_4 = &\frac{-W_2 \cdot \sin(\theta + \varphi) + K_2 \cdot \sin(\theta + \lambda + \varphi)}{\sin(\alpha + \delta_e + \varphi)} \\ &+ \frac{+W_3 \cdot \sin(\varphi) + W_4 \cdot \sin(\alpha + \varphi)}{\sin(\alpha + \delta_e + \varphi)} \end{aligned} \qquad \textbf{(12-12)}$$

From equation (12-12) the forces on the pseudo blade can be derived. On the pseudo blade a force component in the direction of cutting velocity **F_h** and a force perpendicular to this direction **F_v** can be distinguished.

$$F_h = -W_4 \cdot \sin(\alpha) + K_4 \cdot \sin(\alpha + \delta_e) \qquad \textbf{(12-13)}$$

$$F_v = -W_4 \cdot \cos(\alpha) + K_4 \cdot \cos(\alpha + \delta_e) \qquad \textbf{(12-14)}$$

12.3. Pore Pressures.

If the cutting process is assumed to be stationary, the water flow through the pores of the sand can be described in a blade motions related coordinate system. The determination of the water vacuum pressures in the sand around the blade is then limited to a mixed boundary conditions problem. The potential theory can be used to solve this problem. For the determination of the water vacuum pressures it is necessary to have a proper formulation of the boundary condition in the shear zone. Miedema (1985A) derived the basic equation for this boundary condition. In later publications a more extensive derivation is published. If it is assumed that no deformations take place outside the deformation zone, then:

$$\left|\frac{\partial^2 p}{\partial x^2}\right| + \left|\frac{\partial^2 p}{\partial y^2}\right| = 0 \tag{12-15}$$

Making the boundary condition in the shear plane dimensionless is similar to that of the breach equation of Meijer and Van Os (1976). In the breach problem the length dimensions are normalized by dividing them by the breach height, while in the cutting of sand they are normalized by dividing them by the cut layer thickness. Equation (12-15) is the same as the equation without a wedge. In the shear plane **A-B** the following equation is valid:

$$\frac{k_i}{k_{max}} \cdot \left|\frac{\partial p}{\partial n'}\right|_1 + \left|\frac{\partial p}{\partial n'}\right|_2 = \frac{\rho_w \cdot g \cdot v_c \cdot \varepsilon \cdot h_i \cdot \sin(\beta)}{k_{max}} \quad \text{with:} \quad n' = \frac{n}{h_i} \tag{12-16}$$

This equation is made dimensionless with:

$$\left|\frac{\partial p}{\partial n}\right|' = \frac{\left|\dfrac{\partial p}{\partial n'}\right|}{\rho_w \cdot g \cdot v_c \cdot \varepsilon \cdot h_i / k_{max}} \tag{12-17}$$

The accent indicates that a certain variable or partial derivative is dimensionless. The next dimensionless equation is now valid as a boundary condition in the deformation zone:

$$\frac{k_i}{k_{max}} \cdot \left|\frac{\partial p}{\partial n}\right|_1' + \left|\frac{\partial p}{\partial n}\right|_2' = \sin(\beta) \tag{12-18}$$

The storage equation also has to be made dimensionless, which results in the next equation:

$$\left|\frac{\partial^2 p}{\partial x^2}\right|' + \left|\frac{\partial^2 p}{\partial y^2}\right|' = 0 \tag{12-19}$$

Because this equation equals zero, it is similar to equation (12-15). The water under-pressures distribution in the sand package can now be determined using the storage equation and the boundary conditions. Because the calculation of the water under-pressures is dimensionless the next transformation has to be performed to determine the real water under-pressures. The real water under-pressures can be determined by integrating the derivative of the water under-pressures in the direction of a flow line, along a flow line, so:

$$P_{calc} = \int_{s'} \left|\frac{\partial p}{\partial s}\right|' \cdot ds' \tag{12-20}$$

This is illustrated in Figure 12-7 and Figure 12-8. Using equation (12-20) this is written as:

$$P_{real} = \int_{s} \left|\frac{\partial p}{\partial s}\right| \cdot ds = \int_{s'} \frac{\rho_w \cdot g \cdot v_c \cdot \varepsilon \cdot h_i}{k_{max}} \cdot \left|\frac{\partial p}{\partial s}\right|' \cdot ds' \quad \text{with:} \quad s' = \frac{s}{h_i} \tag{12-21}$$

This gives the next relation between the real emerging water under pressures and the calculated water under pressures:

$$P_{real} = \frac{\rho_w \cdot g \cdot v_c \cdot \varepsilon \cdot h_i}{k_{max}} \cdot P_{calc} \tag{12-22}$$

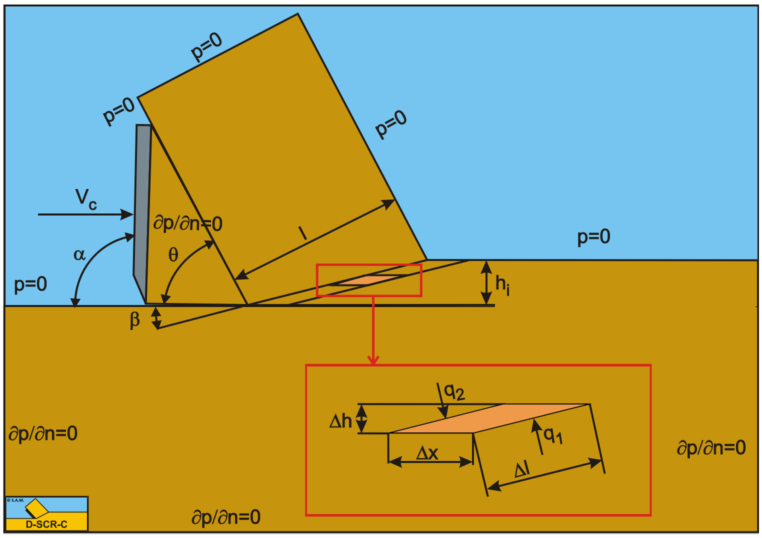

Figure 12-7: The volume balance over the shear zone.

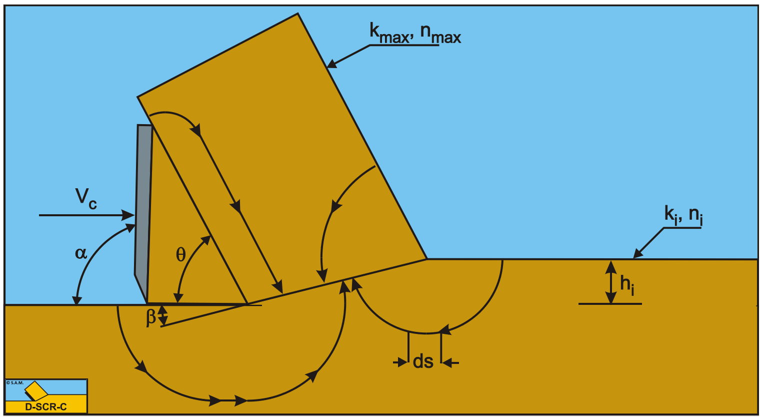

Figure 12-8: Possible flow lines.

To be independent of the ratio between the initial permeability $\mathbf{k_i}$ and the maximum permeability $\mathbf{k_{max}}$, $\mathbf{k_{max}}$ has to be replaced with the weighted average permeability $\mathbf{k_m}$ before making the measured water under pressures dimensionless.

The water vacuum pressures in the sand package on and around the blade are numerically determined using the finite element method. A standard FEM software package is used (Segal (2001)). Within this package and the use of the available "subroutines" a program is written, with which water vacuum pressures can be calculated and be output graphically and numerically. As shown in Figure 12-9, the SEPRAN model is made up of three parts, the original sand layer, the cut sand layer, and the wedge. The solution of such a calculation is however not only dependent on the physical model of the problem, but also on the next points:

1. The size of the area in which the calculation takes place.
2. The size and distribution of the elements
3. The boundary conditions

The choices for these three points have to be evaluated with the problem that has to be solved in mind. These calculations are about the values and distribution of the water under-pressures in the shear zone and on the blade, on the interface between wedge and cut sand, between wedge and the original sand layer. A variation of the values for point 1 and 2 may therefore not influence this part of the solution. This is achieved by on one hand increasing the area in which the calculations take place in steps and on the other hand by decreasing the element size until the variation in the solution was less than 1%. The distribution of the elements is chosen such that a finer mesh is present around the blade tip, the shear zone and on the blade, also because of the blade tip problem. A number of boundary conditions follow from the physical model of the cutting process, these are:

- For the hydrostatic pressure it is valid to take a zero pressure as the boundary condition.
- The boundary conditions along the boundaries of the area where the calculation takes place that are located in the sand package are not determined by the physical process.
- For this boundary condition there is a choice among:

1. A hydrostatic pressure along the boundary.

2. A boundary as an impermeable wall.
3. A combination of a known pressure and a known specific flow rate.

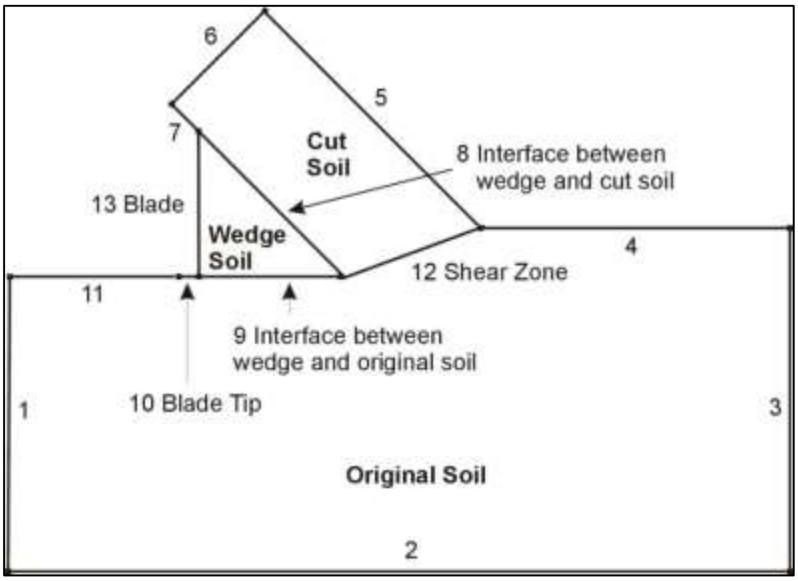

Figure 12-9: The boundaries of the FEM model.

None of these choices complies with the real process. Water from outside the calculation area will flow through the boundary. This also implies, however, that the pressure along this boundary is not hydrostatic. If, however, the boundary is chosen with enough distance from the real cutting process the boundary condition may not have an influence on the solution. The impermeable wall is chosen although this choice is arbitrary. Figure 12-14 and Figure 12-16 give an impression of the equipotential lines and the stream lines in the model area. Figure 12-10 show the dimensionless pore pressure distributions on the lines **A-B**, **A-C**, **A-D** and **D-C**. The average dimensionless pore pressures on these lines are named $\mathbf{p_{1m}}$, $\mathbf{p_{2m}}$, $\mathbf{p_{3m}}$ and $\mathbf{p_{4m}}$.

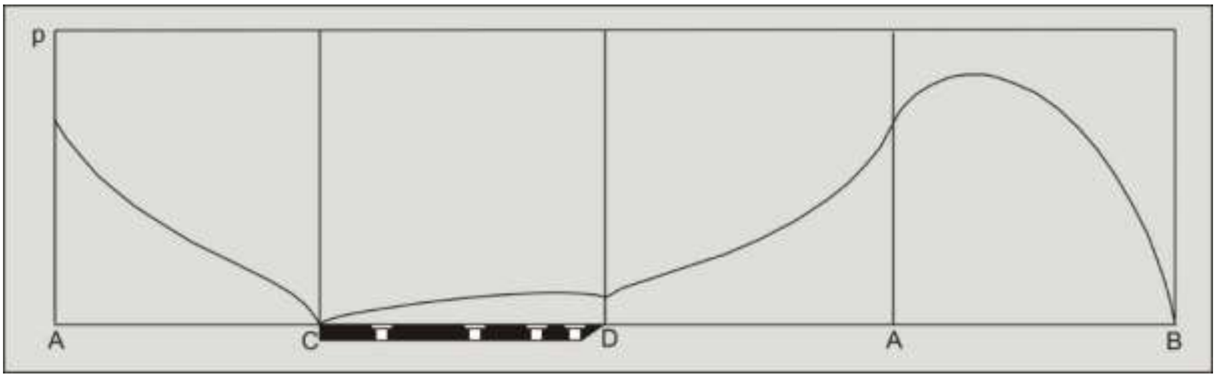

Figure 12-10: Pore pressure distribution on the shear plane A-B, the bottom of the wedge A-D, the blade D-C and the front of the wedge A-C.

If there is no cavitation the water pressures forces $\mathbf{W_1}$, $\mathbf{W_2}$, $\mathbf{W_3}$ and $\mathbf{W_4}$ can be written as:

$$W_1 = \frac{p_{1m} \cdot \rho_w \cdot g \cdot v_c \cdot \varepsilon \cdot h_i^2 \cdot w}{k_{max} \cdot \sin(\beta)} \tag{12-23}$$

And

$$W_2 = \frac{p_{2m} \cdot \rho_w \cdot g \cdot v_c \cdot \varepsilon \cdot h_i \cdot h_b \cdot w}{k_{max} \cdot \sin(\theta)} \tag{12-24}$$

And

$$W_3 = \frac{p_{3m}\cdot\rho_w\cdot g\cdot v_c\cdot\varepsilon\cdot h_i\cdot h_b\cdot w}{k_{max}}\cdot\left(\frac{\cos(\alpha)}{\sin(\alpha)}-\frac{\cos(\alpha)}{\sin(\alpha)}\right) \tag{12-25}$$

And

$$W_4 = \frac{p_{4m}\cdot\rho_w\cdot g\cdot v_c\cdot\varepsilon\cdot h_i\cdot h_b\cdot w}{k_{max}\cdot\sin(\alpha)} \tag{12-26}$$

In case of cavitation **W**$_1$, **W**$_2$, **W**$_3$ and **W**$_4$ become:

$$W_1 = \frac{\rho_w\cdot g\cdot(z+10)\cdot h_i\cdot w}{\sin(\beta)} \tag{12-27}$$

And

$$W_2 = \frac{\rho_w\cdot g\cdot(z+10)\cdot h_b\cdot w}{\sin(\theta)} \tag{12-28}$$

And

$$W_3 = \frac{\rho_w\cdot g\cdot(z+10)\cdot h_b\cdot w}{1}\cdot\left(\frac{\cos(\alpha)}{\sin(\alpha)}-\frac{\cos(\alpha)}{\sin(\alpha)}\right) \tag{12-29}$$

And

$$W_4 = \frac{\rho_w\cdot g\cdot(z+10)\cdot h_b\cdot w}{\sin(\alpha)} \tag{12-30}$$

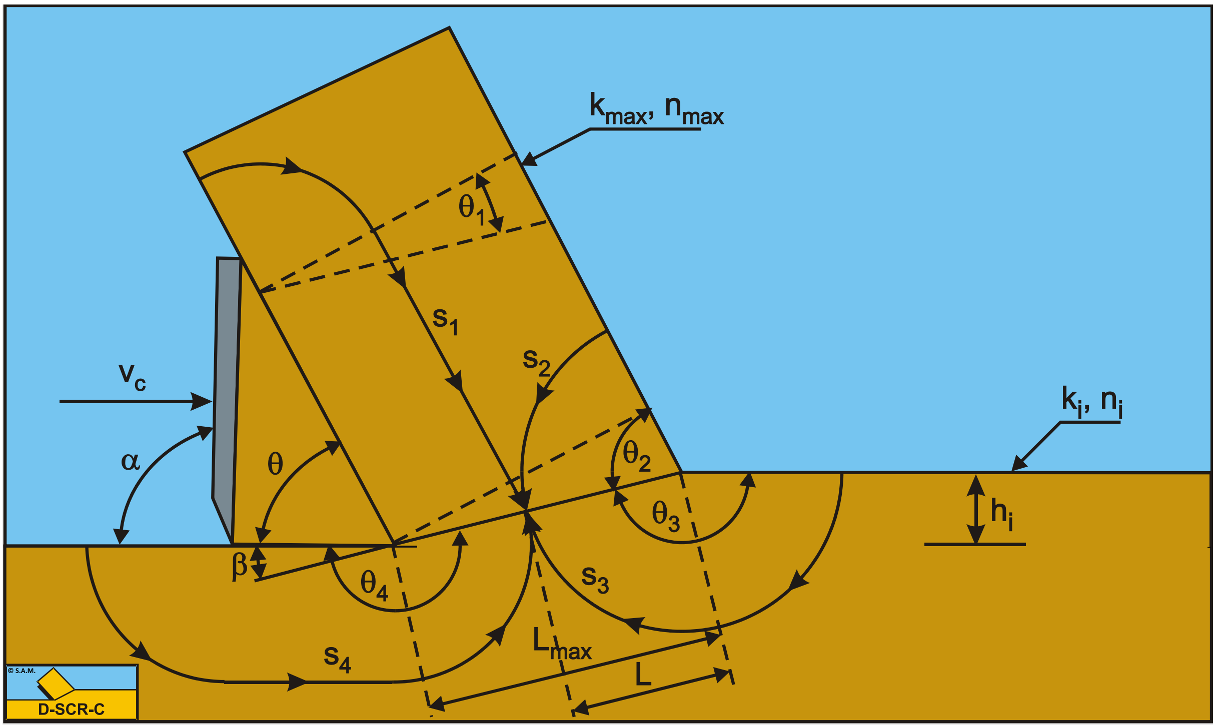

Figure 12-11: The parallel resistor method.

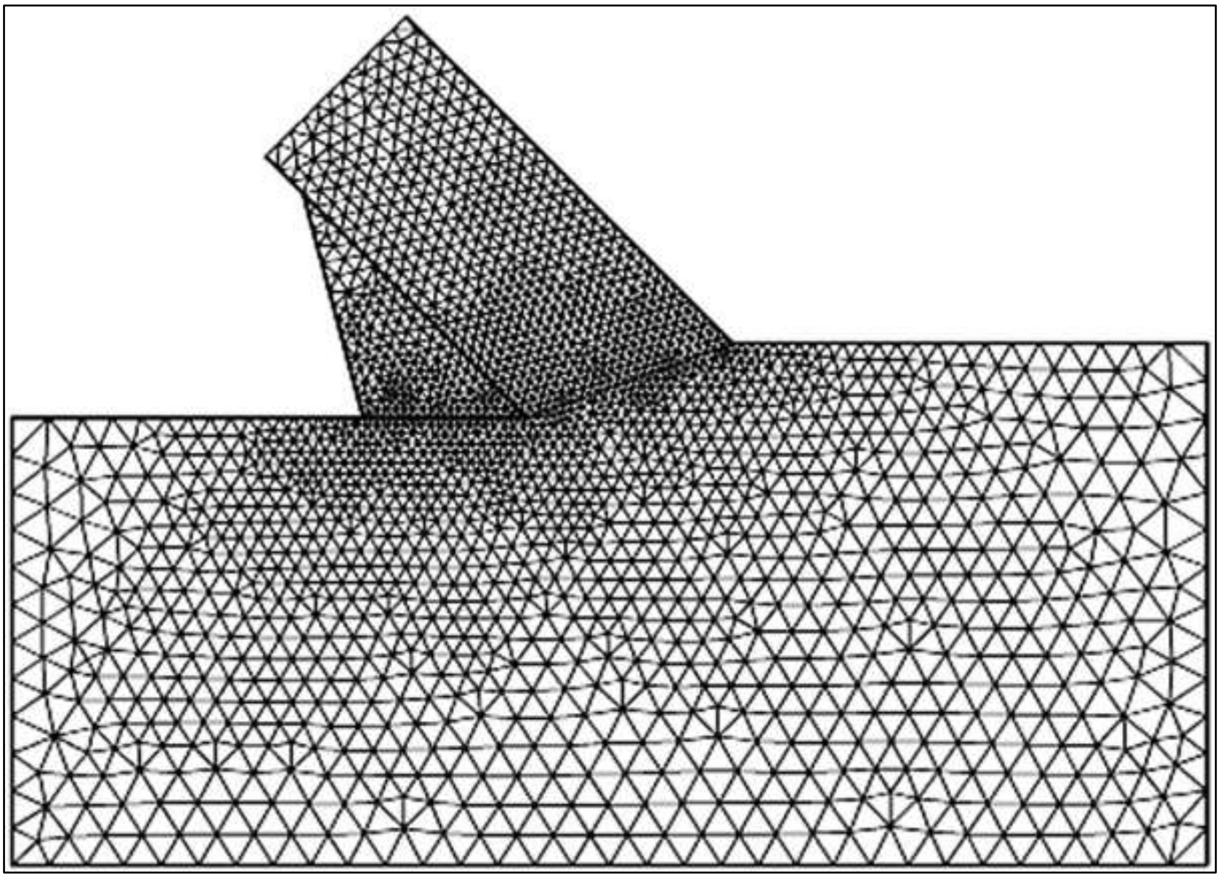

Figure 12-12: The coarse mesh.

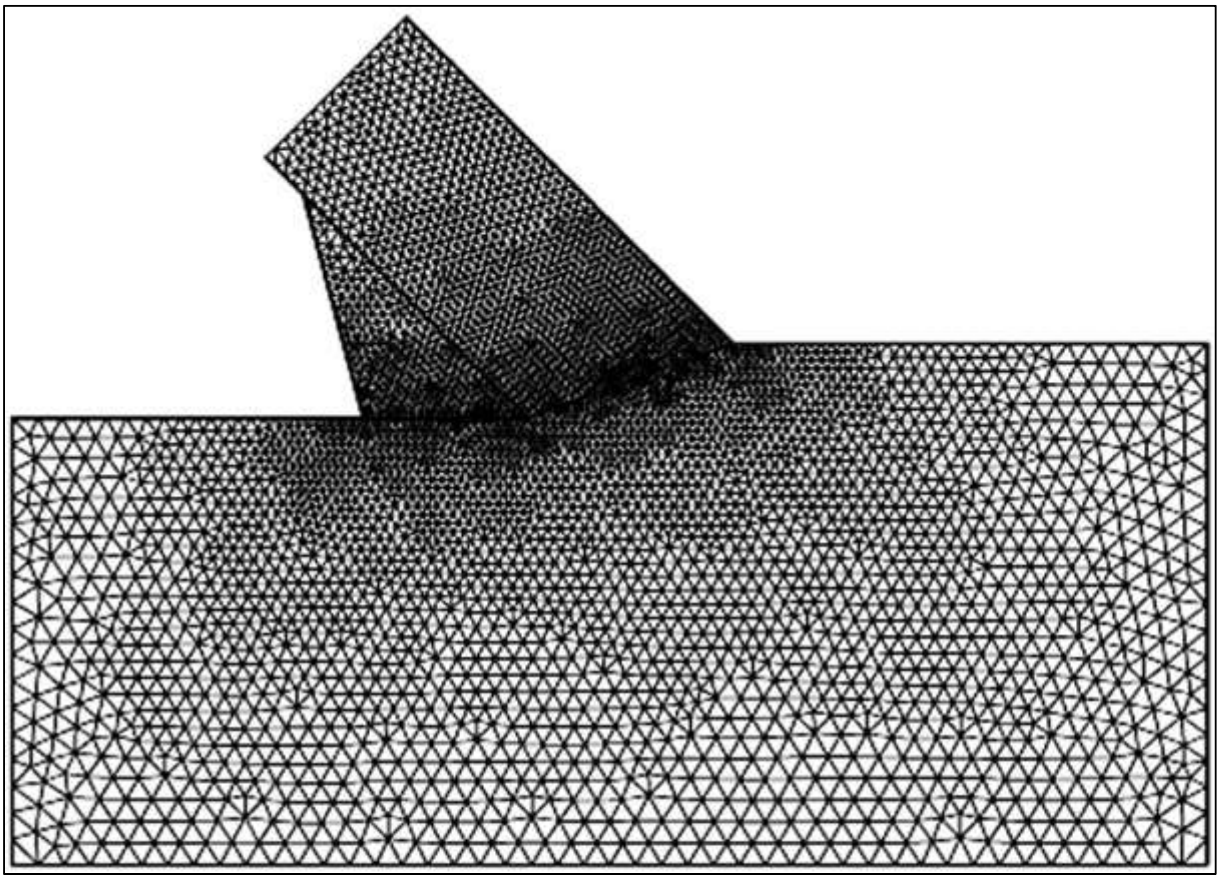

Figure 12-13: The fine mesh.

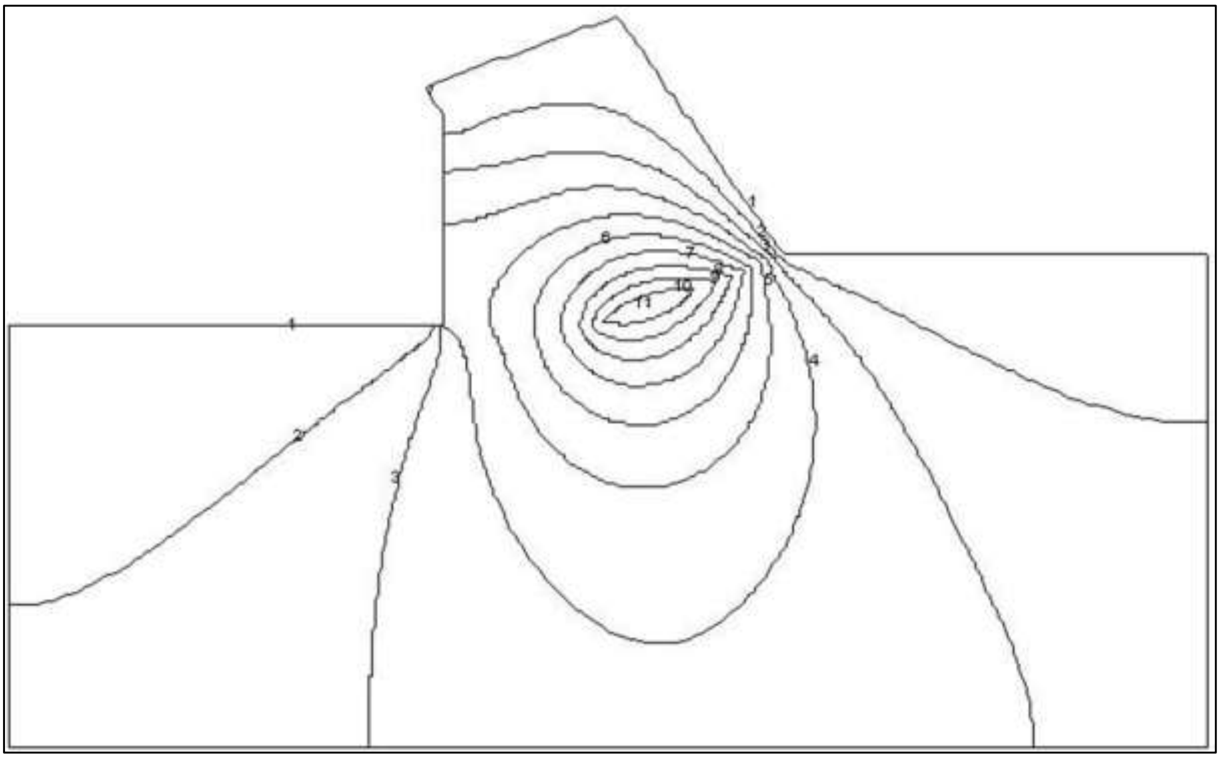

Figure 12-14: Equipotential lines of pore pressures.

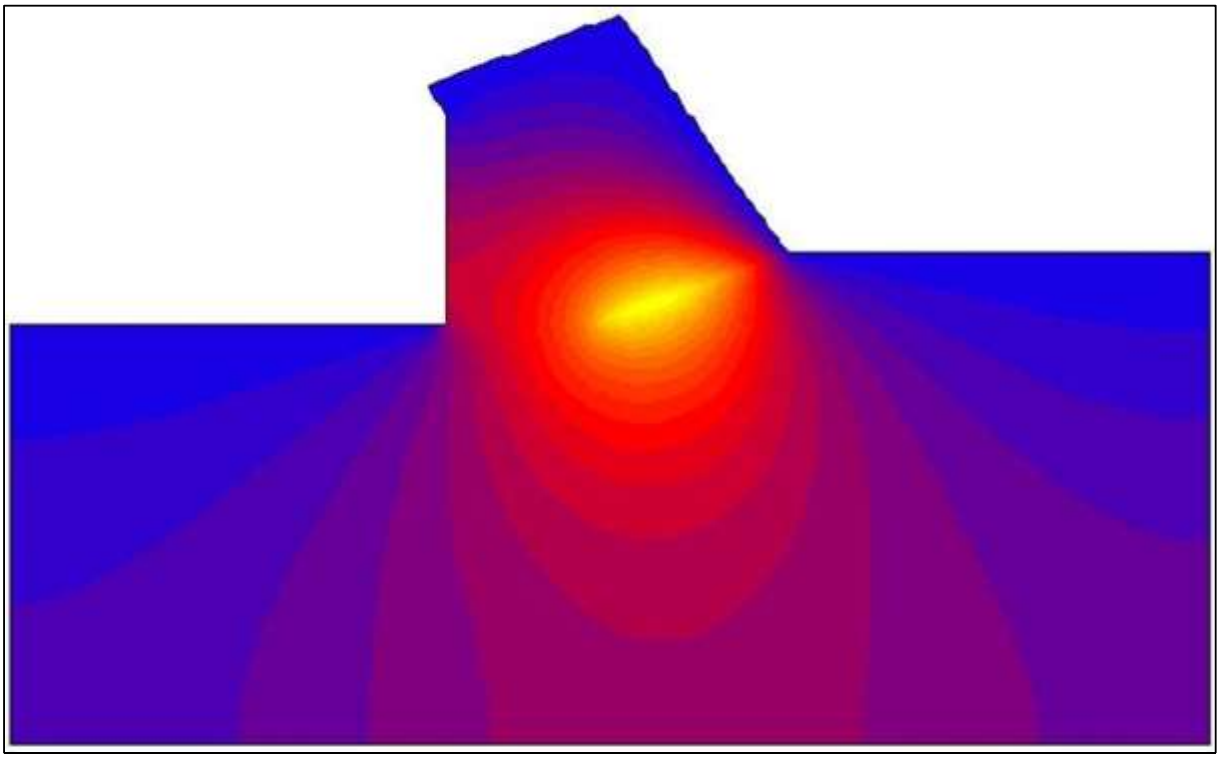

Figure 12-15: Equipotential distribution in color.

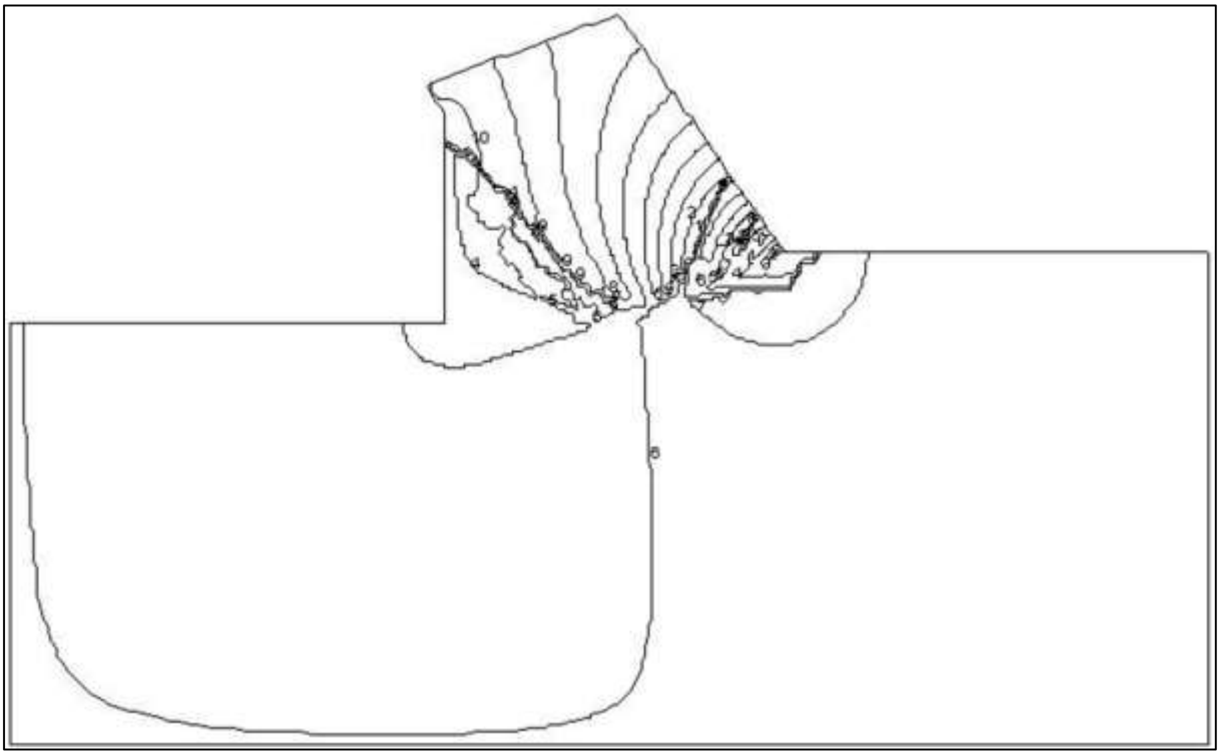

Figure 12-16: The flow lines or stream function.

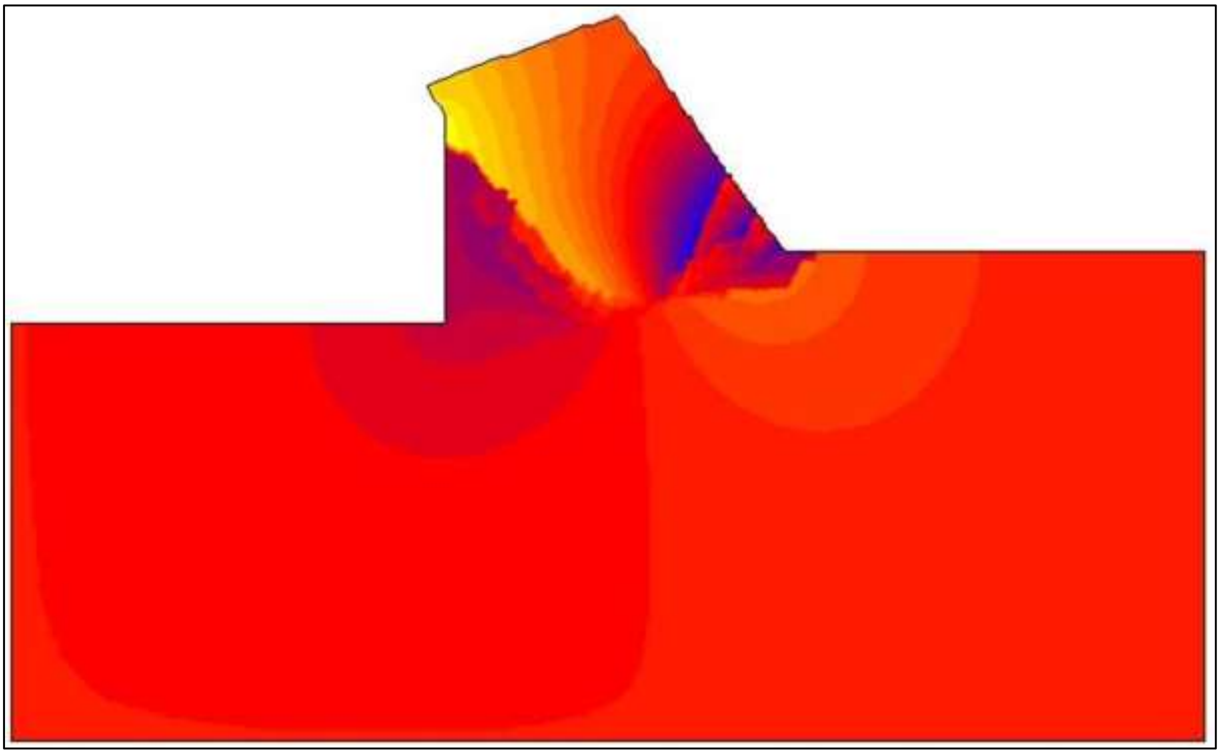

Figure 12-17: The stream function in colors.

12.4. The Equilibrium of Moments.

Based on the equilibrium of forces on the layer cut **B-A-C**, FEM calculations of pore water pressures and the minimum of cutting energy the forces $\mathbf{N_2}$, $\mathbf{S_2}$ and $\mathbf{W_2}$ are determined; see Miedema (1987 September). To determine the forces on the blade there are still a number of unknowns. $\mathbf{W_3}$ and $\mathbf{W_4}$ can be determined using FEM calculations of pore water pressures, given the wedge angle $\boldsymbol{\theta}$. Assuming $\boldsymbol{\lambda=\varphi}$ as a first estimate, the forces $\mathbf{K_3}$ and $\mathbf{K_4}$ depend on the wedge angle $\boldsymbol{\theta}$ and on the effective external friction angle $\boldsymbol{\delta_e}$. For a static wedge, meaning that there is no movement between the wedge and the blade, the effective external friction angle can have a value between + and – the maximum external friction angle $\boldsymbol{\delta}$, so $\boldsymbol{-\delta<\delta_e<\delta}$. Combining this with the minimum energy principle results in a varying $\boldsymbol{\delta_e}$ and a force $\mathbf{N_3}$ being equal to zero for a static wedge. The value of $\boldsymbol{\delta_e}$ follows from the equilibrium of moments. For small values of the blade angle $\boldsymbol{\alpha}$, smaller than about 60º**,** the effective external friction angle $\boldsymbol{\delta_e=\delta}$ and most probably there will not be a wedge. For intermediate values of the blade angle $\boldsymbol{\alpha}$ around 90º, there will be a static wedge and the effective external friction angle $\boldsymbol{\delta_e}$ will decrease from $\boldsymbol{+\delta}$ to $\boldsymbol{-\delta}$. For very large values of $\boldsymbol{\alpha}$**,** larger than about 120º, the effective external friction angle $\boldsymbol{\delta_e=-\delta}$ and $\mathbf{N_3}$ will have a positive value, meaning an upwards direction. Probably there will be a movement of soil under the blade. To find the value of the effective external friction angle first the equilibrium of moments has to be solved. Figure 12-18 shows the moments that occur on the wedge as a result of the forces and their acting points.

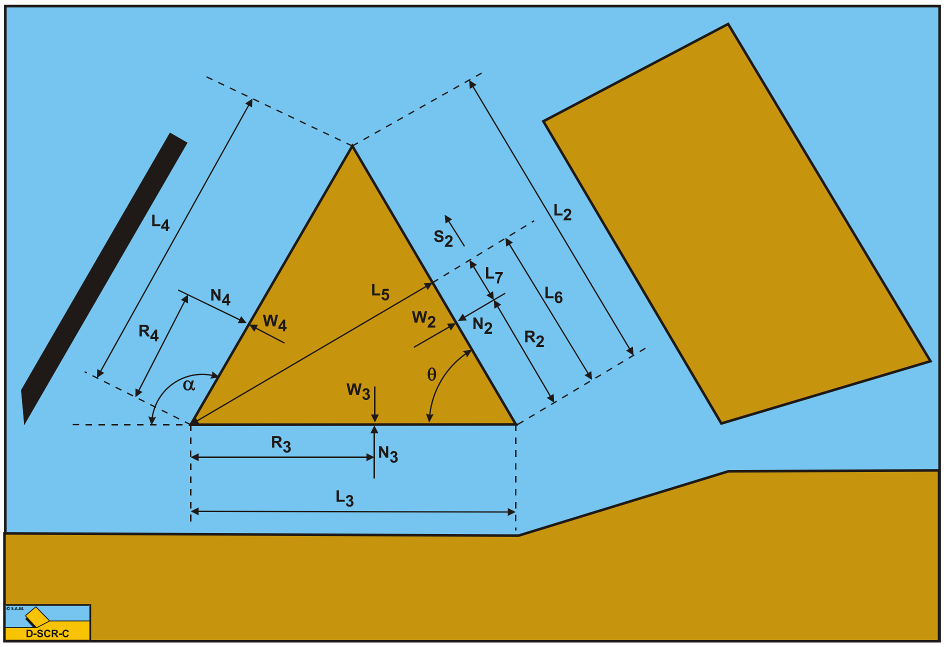

Figure 12-18: The equilibrium of moments on the wedge in water saturated sand.

To determine the moment on the wedge, first the different lengths and distances have to be determined. The length of the shear plane **A-B** is:

$$\mathbf{A-B=L_1=\frac{h_i}{\sin(\beta)}} \qquad \textbf{(12-31)}$$

The length of the pseudo blade or front of the wedge **A-C** is:

$$\mathbf{A-C=L_2=\frac{h_b}{\sin(\theta)}} \qquad \textbf{(12-32)}$$

The length of the bottom of the wedge **A-D** is:

$$\mathbf{A-D=L_3=h_b\cdot\left(\frac{1}{\tan(\theta)}-\frac{1}{\tan(\alpha)}\right)} \qquad \textbf{(12-33)}$$

The length of the blade **D-C** is:

$$D-C=L_4=\frac{h_b}{\sin(\alpha)} \tag{12-34}$$

The distance between the blade edge and the wedge side **A-C** (perpendicular) is:

$$L_5=L_3\cdot\sin(\theta) \tag{12-35}$$

The distance from point **A** and the line **L**$_5$ is:

$$L_6=L_3\cdot\cos(\theta) \tag{12-36}$$

The arm of the acting point of **N**$_2$ and **W**$_2$ is now:

$$L_7=L_6-R_2 \tag{12-37}$$

The equilibrium of moments can be determined using all those distances:

$$\sum M=(N_4-W_4)\cdot R_4-(N_3-W_3)\cdot R_3+(N_2-W_2)\cdot L_7-S_2\cdot L_5=0 \tag{12-38}$$

Equation (12-38) still contains the unknown arms **R**$_2$, **R**$_3$ and **R**$_4$. Based on the FEM calculations for the pore pressures, values of **0.35·L**$_2$, **0.55·L**$_3$ and **0.32·L**$_4$ are found, Ma (2001). Figure 12-19 shows the moments on the wedge with respect to the cutting edge as a function of the wedge angle **θ** for different values of the shear angle **β** and a blade angle **α** of 90º. The moment is zero for a wedge angle **θ** between 50º and 55º.

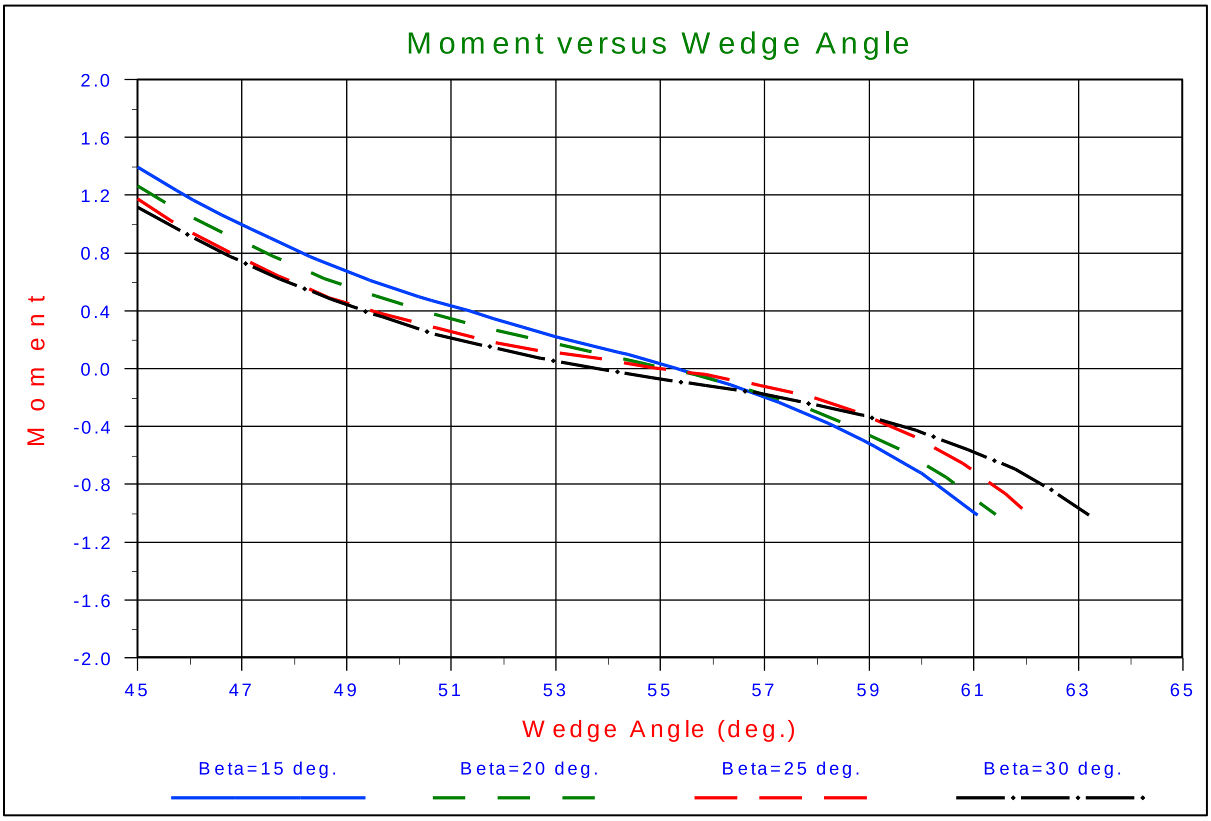

Figure 12-19: Moment versus wedge angle θ by using polynomial regression for: $\alpha=90^0$; $\beta=15^0,20^0,25^0,30^0$; $\delta=28^0$; $\varphi=42^0$; $h_i=1$; $h_b=3$; $k_i/k_{max}=0.25$

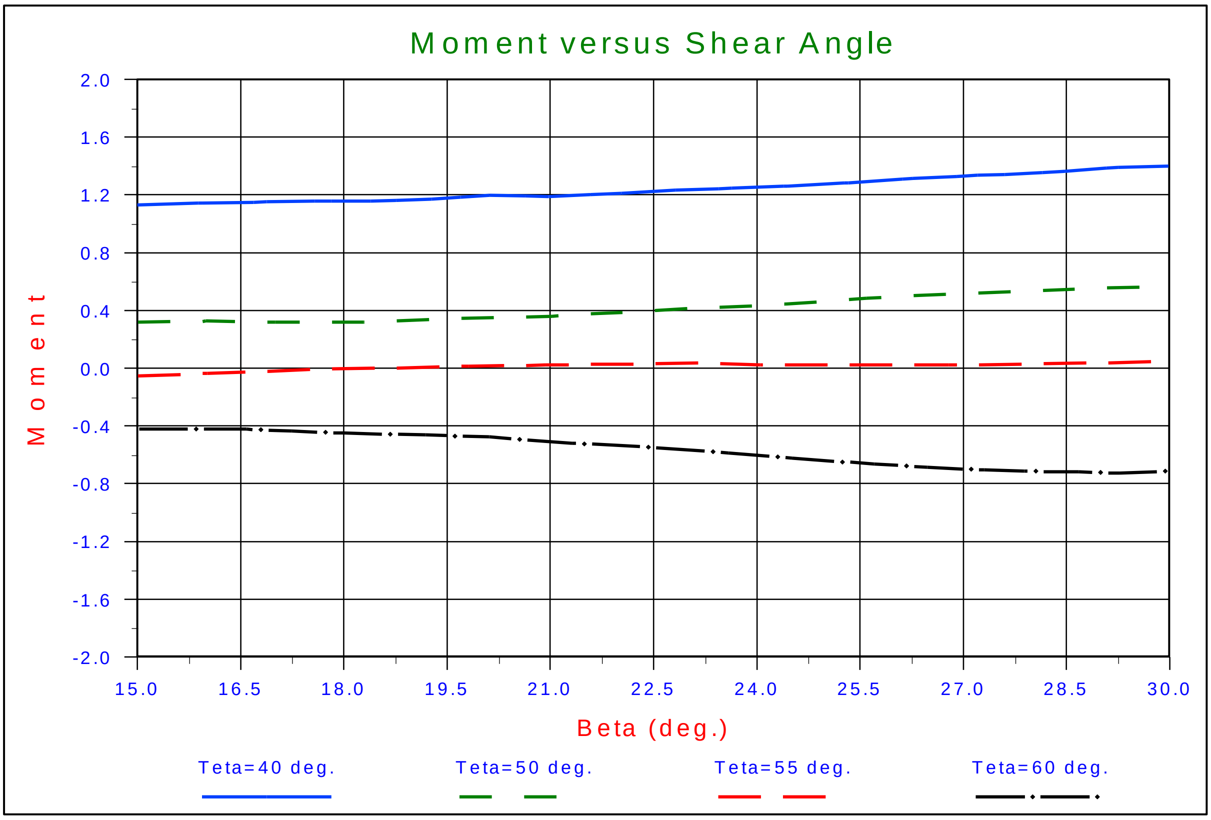

Figure 12-20: The moment versus the shear angle for 4 different wedge angles for: $\alpha=90^0$; $\delta=28^0$; $\varphi=42^0$; $h_i=1$; $h_b=3$; $k_i/k_{max}=0.25$

Figure 12-20 shows the moments as a function of the shear angle **β** for 4 values of the wedge angle **θ**. The moment is zero for the wedge angle **θ=55°** at a shear angle **β=18°**. It is clear from these figures that the shear angle where the moment is zero is not very sensitive for the shear angle and the wedge angle.

Figure 12-21 shows the force triangles on the 3 sides of the wedges for cutting angles from 60 to 120 degrees. From the calculations it appeared that the pore pressures on interface between the soil cut and the wedge and in the shear plane do not change significantly when the blade angle changes. These pore pressures $\mathbf{p_{1m}}$ and $\mathbf{p_{2m}}$, resulting in the forces $\mathbf{W_1}$ and $\mathbf{W_2}$, are determined by the shear angle **β**, the wedge angle **θ** and other soil mechanical properties like the permeability.
The fact that the pore pressures do not significantly change, also results in forces $\mathbf{K_2}$, acting on the wedge that do not change significantly, according to equations (12-4), (12-5) and (12-6). These forces are shown in Figure 12-21 on the right side of the wedges and the figure shows that these forces are almost equal for all blade angles. These forces are determined by the conventional theory as published by Miedema (1987 September). Figure 12-21 also shows that for the small blade angles the friction force on the wedge is directed downwards, while for the bigger blade angles this friction force is directed upwards.

$$\mathbf{R_2 = e_2 \cdot L_2}, \quad \mathbf{R_3 = e_3 \cdot L_3}, \quad \mathbf{R_4 = e_4 \cdot L_4} \qquad \textbf{(12-39)}$$

Now the question is, what is the solution for the cutting of water saturated sand at large cutting angles? From many calculations and an analysis of the laboratory research is described by He (1998), Ma (2001) and Miedema (2005), it appeared that the wedge can be considered a static wedge, although the sand inside the wedge still may have velocity, the sand on the blade is not moving. The main problem in finding acceptable solutions was finding good values for the acting points on the 3 sides of the wedge, $\mathbf{e_2}$, $\mathbf{e_3}$ and $\mathbf{e_4}$. If these values are chosen right, solutions exist based on the equilibrium of moments, but if they are chosen wrongly, no solution will be found. So the choice of these parameters is very critical. The statement that the sand on the blade is not moving is based on two things, first of all if the sand is moving with respect to the blade, the soil interface friction is fully mobilized and the bottom of the wedge requires to have a small angle with respect to the horizontal in order to make a flow of sand possible. This results in much bigger cutting forces, while often no solution can be found or unreasonable values for $\mathbf{e_2}$, $\mathbf{e_3}$ and $\mathbf{e_4}$ have to be used to find a solution.

So the solution is, using the equilibrium equations for the horizontal force, the vertical force and the moments on the wedge. The recipe to determine the cutting forces seems not to difficult now, but it requires a lot of calculations and understanding of the processes, because one also has to distinguish between the theory for small cutting angles and the wedge theory.

The following steps have to be taken to find the correct solution:

1. Determine the dimensionless pore pressures $\mathbf{p_{1m}}$, $\mathbf{p_{2m}}$, $\mathbf{p_{3m}}$ and $\mathbf{p_{4m}}$ using a finite element calculation or the method described by Miedema (2006B), for a variety of shear angles $\boldsymbol{\beta}$ and wedge angles $\boldsymbol{\theta}$ around the expected solution.
2. Determine the shear angle $\boldsymbol{\beta}$ based on the equilibrium equations for the horizontal and vertical forces, a given wedge angle $\boldsymbol{\theta}$ and the principle of minimum energy, which is equivalent to the minimum horizontal force. This also gives a value for the resulting force $\mathbf{K_2}$ acting on the wedge.
3. Determine values of $\mathbf{e_2}$, $\mathbf{e_3}$ and $\mathbf{e_4}$ based on the results from the pore pressure calculations.
4. Determine the solutions of the equilibrium equations on the wedge and find the solution which has the minimum energy dissipation, resulting in the minimum horizontal force on the blade.
5. Determine the forces without a wedge with the theory for small cutting angles.
6. Determine which horizontal force is the smallest, with or without the wedge.

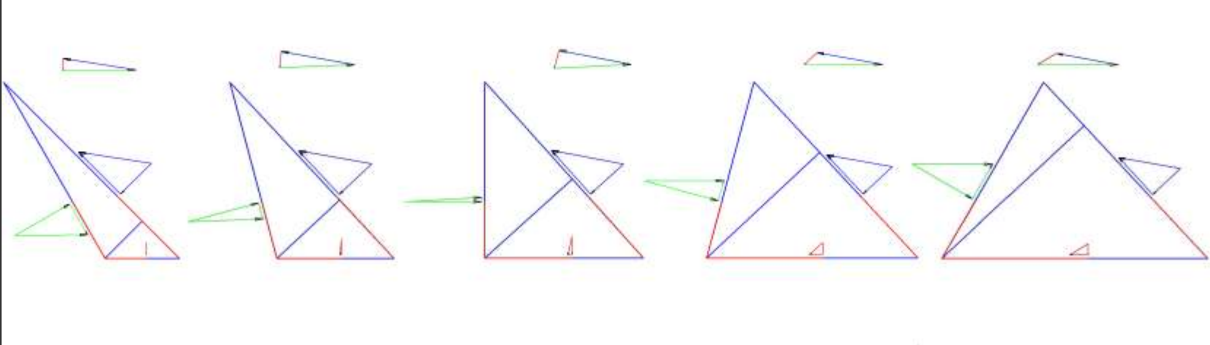

Figure 12-21: The forces on the wedges at 60°, 75°, 90°, 105° and 120° cutting angles.

12.5. The Non-Cavitating Wedge.

To illustrate the results of the calculation method, a non-cavitating case will be discussed. Calculations are carried out for blade angles $\boldsymbol{\alpha}$ of 65°, 70°, 75°, 80°, 85°, 90°, 95°, 100°, 105°, 110°, 115° and 120°, while the smallest angle is around 60° depending on the possible solutions. Also the cutting forces are determined with and without a wedge, so it's possible to carry out step 6.

The case concerns a sand with an internal friction angle $\boldsymbol{\varphi}$ of 30°, a soil interface friction angle $\boldsymbol{\delta}$ of 20° fully mobilized, a friction angle λ between the soil cut and the wedge equal to the internal friction angle, an initial permeability $\mathbf{k_i}$ of $6.2*10^{-5}$ m/s and a residual permeability $\mathbf{k_{max}}$ of $17*10^{-5}$ m/s. The blade dimensions are a width of 0.25 m and a height of 0.2 m, while a layer of sand of 0.05 m is cut with a cutting velocity of 0.3 m/s at a water depth of 0.6 m, matching the laboratory conditions. The values for the acting points of the forces, are $\mathbf{e_2=0.35}$, $\mathbf{e_3=0.55}$ and $\mathbf{e_4=0.32}$, based on the finite element calculations carried out by Ma (2001).

Figure 12-22 and Figure 12-23 show the results of the calculations. Figure 12-22 shows the wedge angle $\boldsymbol{\theta}$, the shear angle $\boldsymbol{\beta}$, the mobilized internal friction angle $\boldsymbol{\lambda}$ and the mobilized external friction angle $\boldsymbol{\delta_e}$ as a function of the blade angle $\boldsymbol{\alpha}$. Figure 12-23 shows the horizontal and vertical cutting forces, with and without a wedge.

The wedge angles found are smaller than $\mathbf{90°-\boldsymbol{\varphi}}$, which would match the theory of Hettiaratchi and Reece (1975). The shear angle $\boldsymbol{\beta}$ is around 20°, but it is obvious that a larger internal friction angle gives a smaller shear angle $\boldsymbol{\beta}$. The mobilized external friction angle varies from plus the maximum mobilized external friction angle to minus the maximum mobilized external friction angle as is also shown in the force diagrams in Figure 12-21.

Figure 12-23 shows clearly how the cutting forces become infinite when the sum of the 4 angles involved is 180° and become negative when this sum is larger than 180°. So the transition from the small cutting angle theory to the wedge theory occurs around a cutting angle of 70º, depending on the soil mechanical parameters and the geometry of the cutting process.

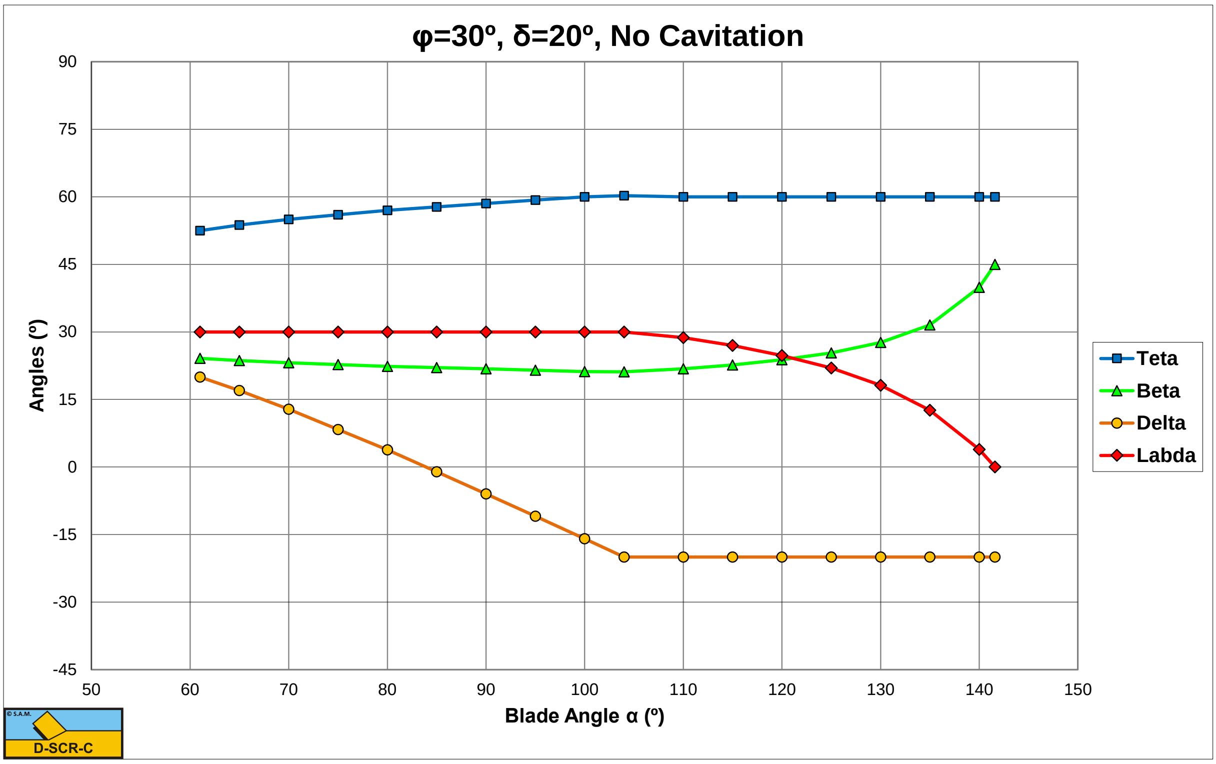

Figure 12-22: No cavitation, the angles θ, β, δ_m and λ as a function of the blade angle α for φ=30º and δ=20º.

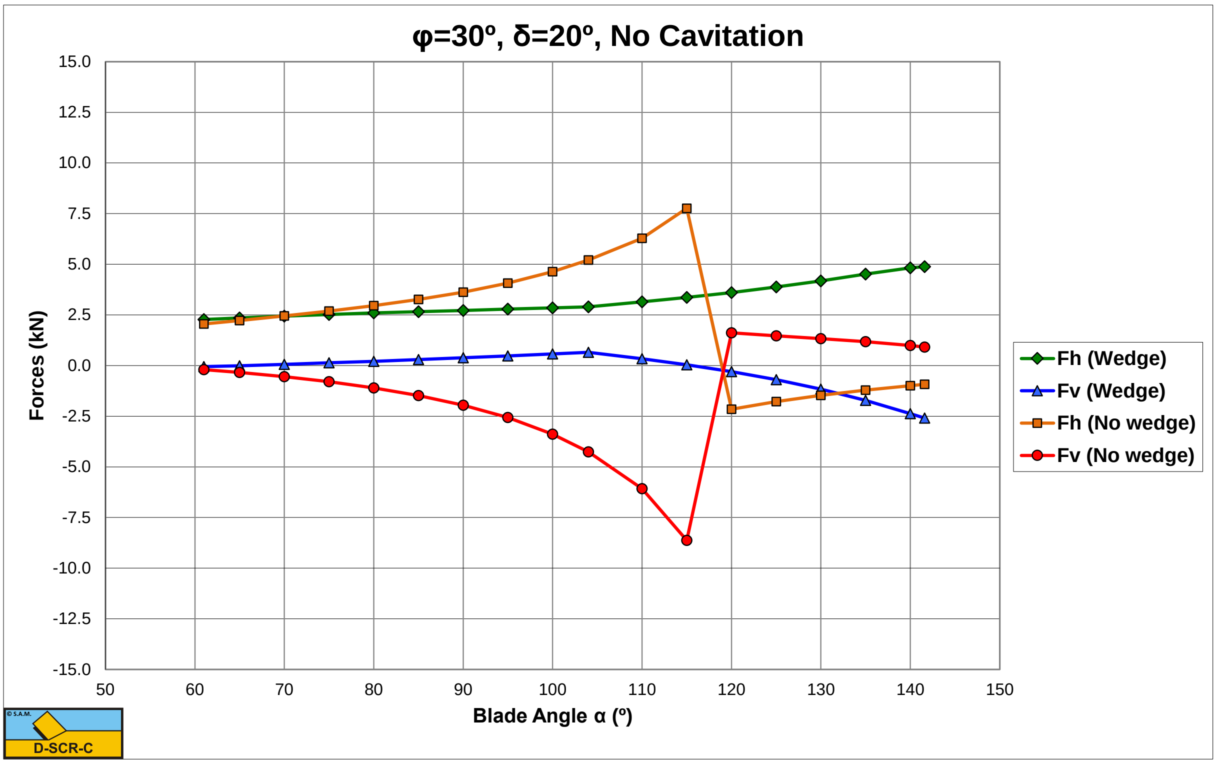

Figure 12-23: No cavitation, the cutting forces as a function of the blade angle α for φ=30º and δ=20º.

12.6. The Cavitating Wedge

Also for the cavitating process, a case will be discussed. The calculations are carried out for blade angles **α** of 65°, 70°, 75°, 80°, 85°, 90°, 95°, 100°, 105°, 110°, 115° and 120°, while the smallest angle is around 60º depending on the possible solutions. Also the cutting forces are determined with and without a wedge, so it's possible to carry out

step 6.

The case concerns a sand with an internal friction angle **φ** of 30°, a soil interface friction angle **δ** of 20° fully mobilized, a friction angle **λ** between the soil cut and the wedge equal to the internal friction angle, an initial permeability $\mathbf{k_i}$ of $6.2*10^{-5}$ m/s and a residual permeability $\mathbf{k_{max}}$ of $17*10^{-5}$ m/s. The blade dimensions are a width of 0.25 m and a height of 0.2 m, while a layer of sand of 0.05 m is cut with a cutting velocity of 0.3 m/s at a water depth of 0.6 m, matching the laboratory conditions. The values for the acting points of the forces, are $\mathbf{e_2=0.35}$, $\mathbf{e_3=0.55}$ and $\mathbf{e_4=0.32}$, based on the finite element calculations carried out by Ma (2001).

Figure 12-24 and Figure 12-25 show the results of the calculations. Figure 12-24 shows the wedge angle **θ**, the shear angle **β**, the mobilized internal friction angle **λ** and the mobilized external friction angle $\mathbf{\delta_e}$ as a function of the blade angle **α**. Figure 12-25 shows the horizontal and vertical cutting forces, with and without a wedge.

With the cavitating cutting process, the wedge angle **θ** always results in an angle of **90°-φ**, which matches the theory of Hettiaratchi and Reece (1975). The reason of this is that in the full cavitation situation, the pore pressures are equal on each side of the wedge and form equilibrium in itself. So the pore pressures do not influence the ratio between the grain stresses on the different sides of the wedge. From Figure 12-25 it can be concluded that the transition point between the conventional cutting process and the wedge process occurs at a blade angle of about 77 degrees.

In the non-cavitating cases this angle is about 70 degrees. A smaller angle of internal friction results in a higher transition angle, but in the cavitating case this influence is bigger. In the cavitating case, the horizontal force is a constant as long as the external friction angle is changing from a positive maximum to the negative minimum. Once this minimum is reached, the horizontal force increases a bit. At the transition angle where the horizontal forces with and without the wedge are equal, the vertical forces are not equal, resulting in a jump of the vertical force, when the wedge starts to occur.

12.7. Limits.

Instead of carrying out the calculations for each different case, the limits of the occurrence of the wedge can be summarized in a few graphs. Figure 12-26 shows the upper and lower limit of the wedge for the non-cavitating case as a function of the angle of internal friction **φ**. It can be concluded that the upper and lower limits are not symmetrical around 90º, but a bit lower than that. An increasing angle of internal friction results in a larger bandwidth for the occurrence of the wedge. For blade angles above the upper limit most probably subduction will occur, although there is no scientific evidence for this. The theory developed should not be used for blade angles above the upper limit yet. Further research is required. The lower limit is not necessarily the start of the occurrence of the wedge. This depends on whether the cutting forces with the wedge are smaller than the cutting forces without the wedge. Figure 12-28 shows the blade angle where the wedge will start to occur, based on the minimum of the horizontal cutting forces with and without the wedge. It can be concluded that the blade angle where the wedge starts to occur is larger than the minimum where the wedge can exist, which makes sense. For high angles of internal friction, the starting blade angle is about equal to the lower limit.

For the cavitating case the upper and lower limit are shown in Figure 12-27. In this case the limits are symmetrical around 90º and with an external friction angle of 2/3 of the internal friction angle it can be concluded that these limits are **90º+δ** and **90º-δ**. The blade angle where the wedge will start to occur is again shown in Figure 12-28.

The methodology applied gives satisfactory results to determine the cutting forces at large cutting angles. The results shown in this paper are valid for the non-cavitating and the cavitating cutting process and for the soils and geometry as used in this paper. The wedge angles found are, in general, a bit smaller then **90°-φ** for the non-cavitating case and exactly **90°-φ** for the cavitating case, so as a first approach this can be used.

The mobilized external friction angle δ_e varies from plus the maximum for small blade angles to minus the maximum for large blade angles, depending on the blade angle.

The cutting forces with the wedge do not increase much in the non-cavitating case and not at all in the cavitating case, when the cutting angle increases from 60° to 120°.

If the ratio between the thickness of the layer cut and the blade height changes, also the values of the acting points $\mathbf{e_2}$, $\mathbf{e_3}$ and $\mathbf{e_4}$ will change slightly.

It is not possible to find an explicit analytical solution for the wedge problem and it's even difficult to automate the calculation method, since the solution depends strongly on the values of the acting points.

Figure 12-26, Figure 12-27 and Figure 12-28 are a great help determining whether or not a wedge will occur and at which blade angle it will start to occur.

The theory developed can be applied to cutting processes of bulldozers, in front of the heel of a drag head, ice scour, tunnel boring machines and so on.

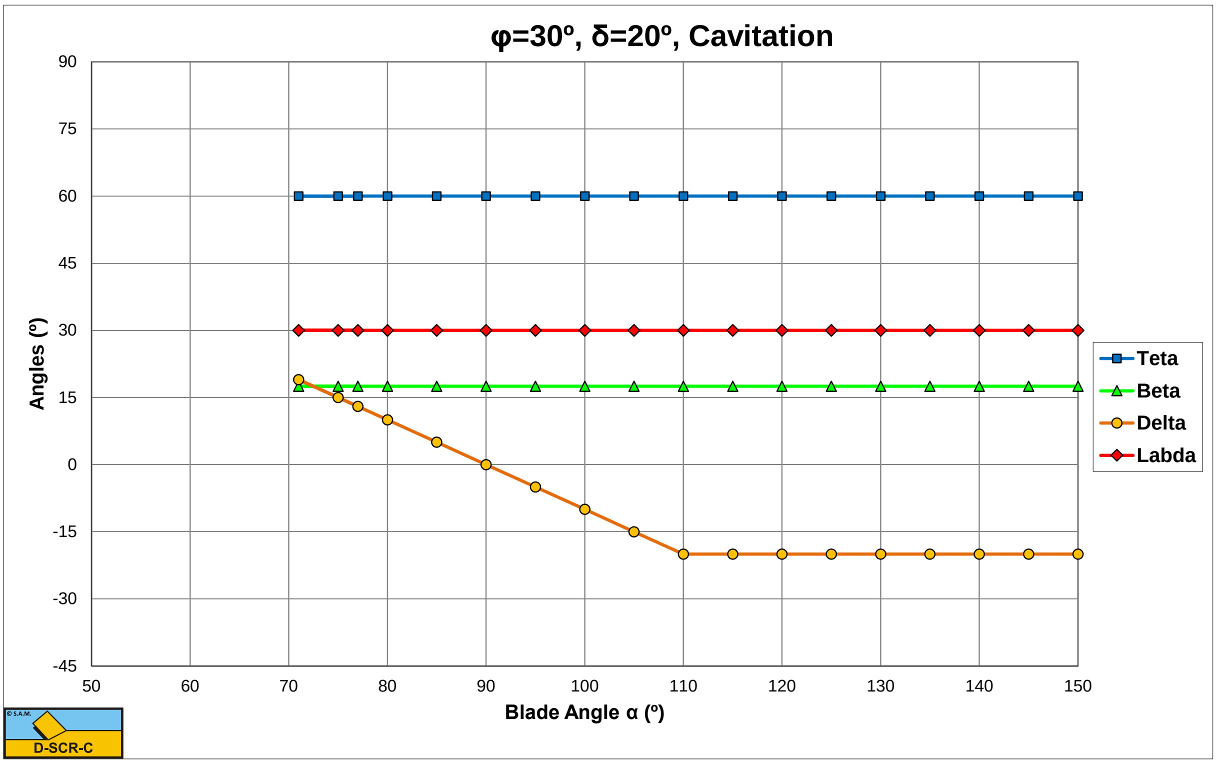

Figure 12-24: Cavitating, the angles θ, β, δ_m and λ as a function of the blade angle α for φ=30º and δ=20º.

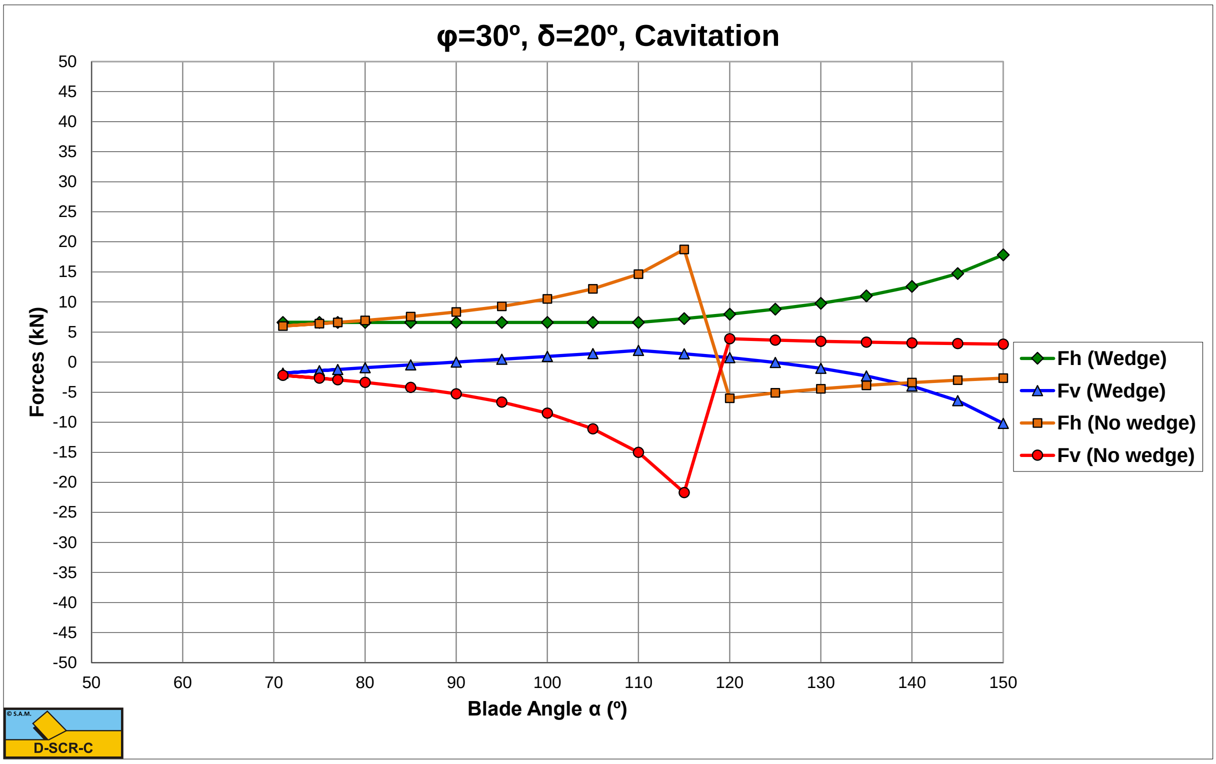

Figure 12-25: Cavitating, the cutting forces as a function of the blade angle α for φ=30º and δ=20º.

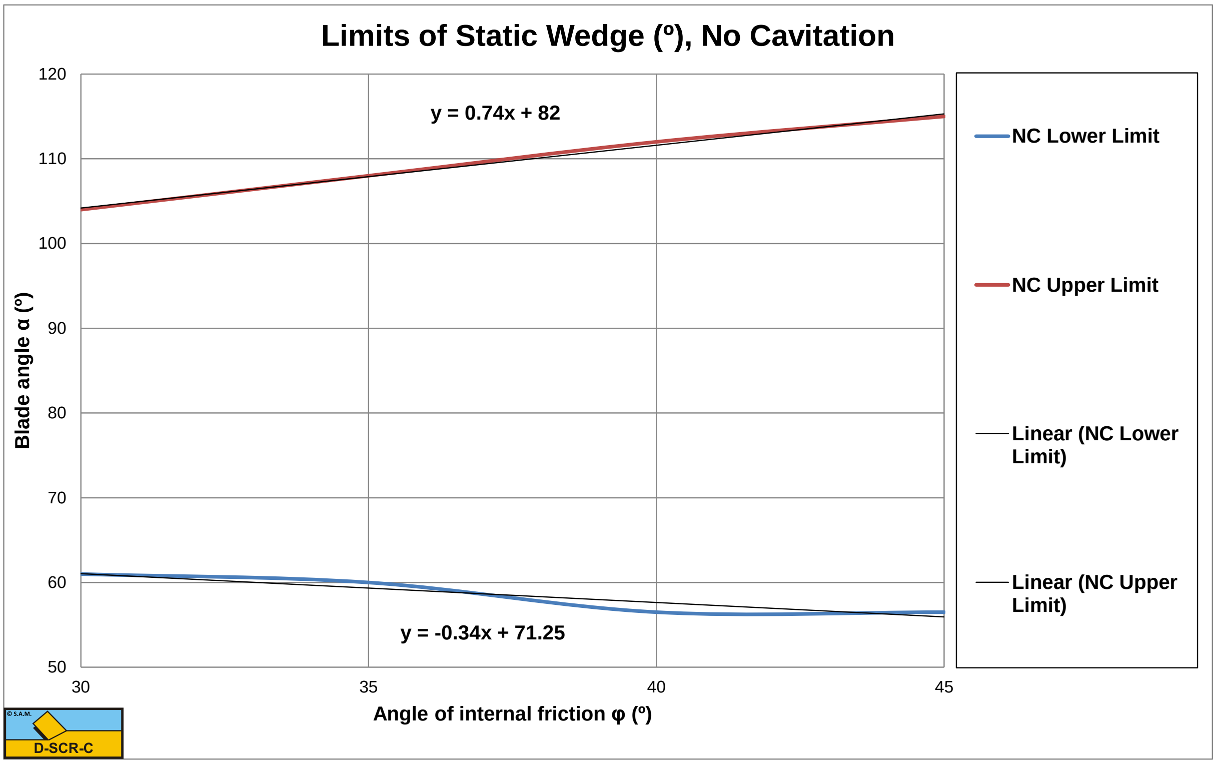

Figure 12-26: The lower and upper limit where a static wedge can exist for the non-cavitating cutting process.

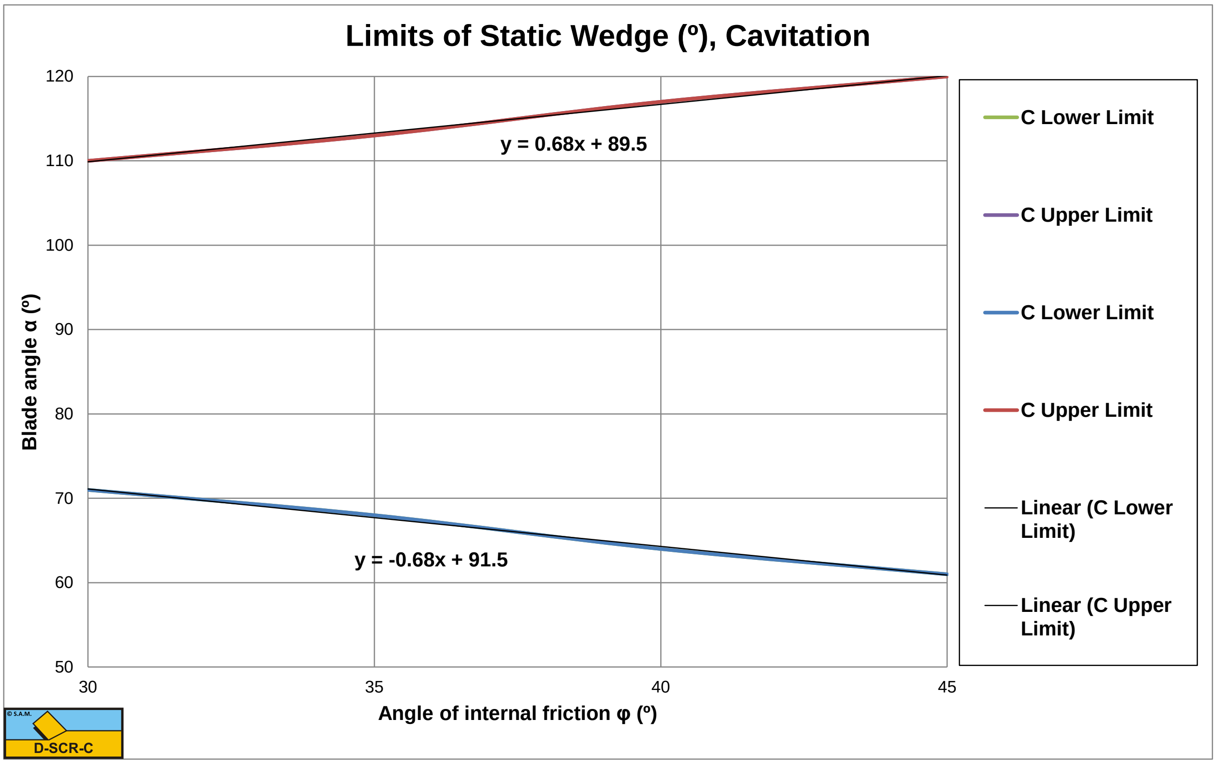

Figure 12-27: The lower and upper limit where a static wedge can exist for the cavitating cutting process.

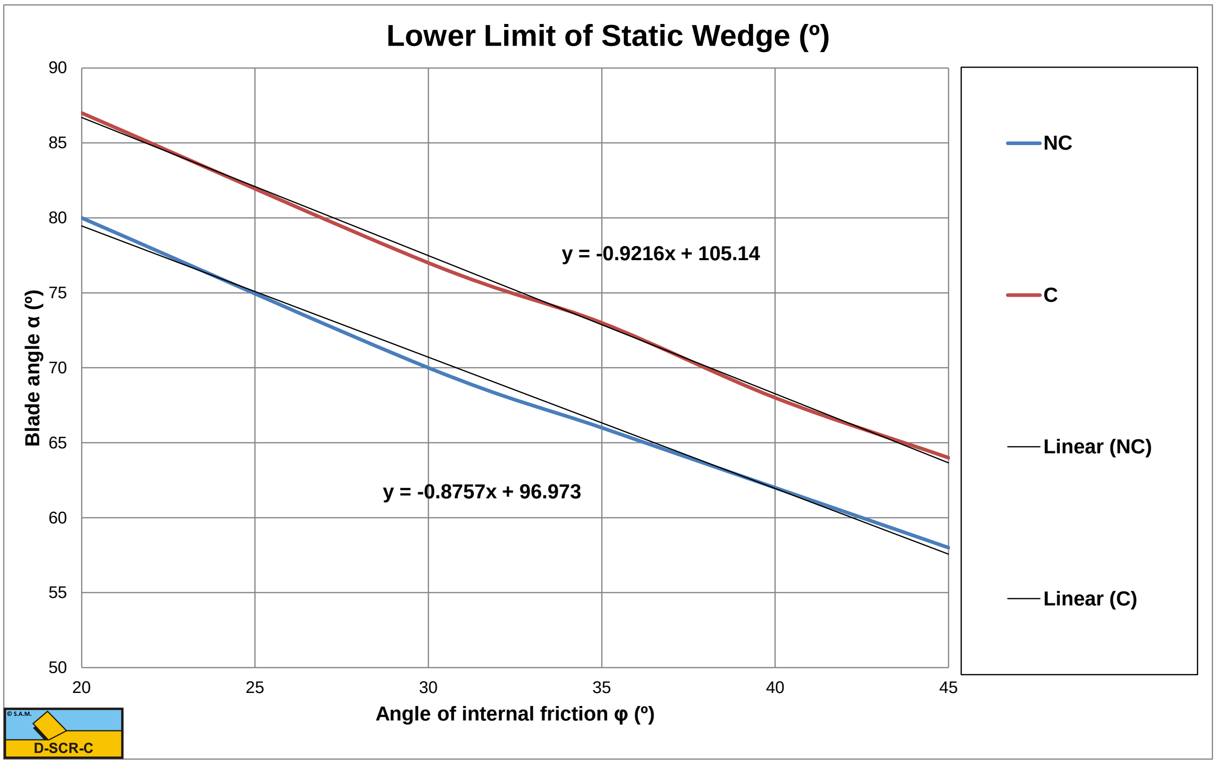

Figure 12-28: The lower limit where the wedge starts to occur.

12.8. Experiments.

Sand cutting tests have been carried out in the Laboratory of Dredging Engineering at the Delft University.

The cutting tank is a concrete tank with a length of 35 m, a width of 3 m and a depth of 1.5 m. The bottom of the tank is covered with a drainage system. Above the drainage system is a layer of about 0.7 m sand (0.110 mm). On top of the sand is a layer of 0.5 m water. Other soils than the 0.110 mm sand can be used in the tank. On top of the tank rails are mounted on which a carriage can ride with speeds of up to 1.25 m/s with a pulling force of up to 15 kN, or 2.5 m/s with a pulling force of 7.5 kN. On the carriage an auxiliary carriage is mounted that can be moved transverse to the velocity of the main carriage. On this carriage a hydraulic swell simulating system is mounted, thus enabling the cutting tools to be subjected to specific oscillations. Under the carriage dredging equipment such as cutter heads and drag heads can be mounted. The dredging equipment can be instrumented with different types of transducers such as force, speed and density transducers. The signals from these transducers will be conditioned before they go to a computer via an A/D converter. On the carriage a hydraulic system is available, including velocity and density transducers. A 25 kW hydraulic drive is available for cutter heads and dredging wheels. The dredge pump is driven by a 15 kW electric drive with speed control. With the drainage system the pore water pressures can be controlled. Dredged material is dumped in an adjacent hopper tank to keep the water clean for under water video recordings. In the cutting tank research is carried out on cutting processes, mixture forming, offshore dredging, but also jet-cutting, the removal of contaminated silt, etc.

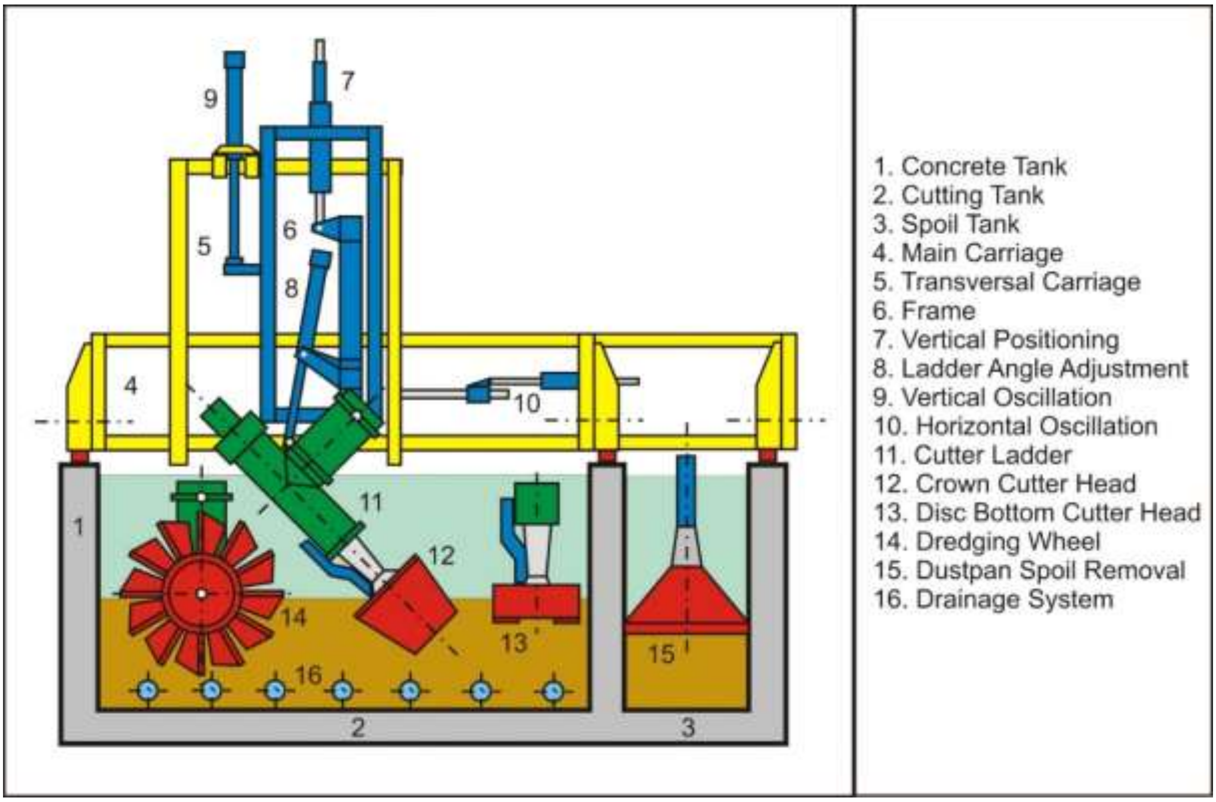

Figure 12-29: Cross section of the cutting tank.

The tests carried out in the Dredging Engineering Laboratory had the objective to find the failure mechanisms of a sand package under large cutting angles of 60°, 75° and 90°. Main goal of the tests was to visualize the total process in a 2-dimensional view. Besides, the behaviour of sand in front of the blade was to be investigated. As mentioned before, some wedge exists in front of the blade, but it was not clear until now whether this was a kinematic wedge or a dynamic wedge. Visualising the cutting process and visualising the velocity of the sand on the blade has to improve the understanding of the processes involved.

The existing testing facilities have been used to carry out the cutting tests. With these facilities cutting depths from 3 till 7 cm are tested, resulting in an (effective blade height)/(cutting depth) ratio of 2.5 to 6, for the various angles. Cutting velocities of the tests were from 0.1 m/s to 0.4 m/s for smaller and 0.2 m/s for the larger cutting depths. These maximum velocities are limited by the maximum electrical power of the testing facility. In the first series of tests the 2-dimensional cutting process is made visual by doing tests near the window in the cutting tank. The process is not completely 2-dimensional here, because the water pressures and sand friction are influenced by the window, but it gives a good indication of the appearing failure mechanism of the sand package. Figure 12-29 shows a cross-section of the cutting tank and the carriage under which the cutting tools are mounted, while Figure 12-30 shows a front view and Figure 12-31 shows the blades mounted under the carriage.

To visualise the behaviour of the sand package in front of the blade a Perspex window is made in the middle one of the 3 cutting blades. Here we expect the least side influences. The middle blade measures a height of 20 cm and a width of 25 cm. The camera is mounted at the back of the blade, in a cover, as seen in Figure 12-33. In Figure 12-32 you can see an underwater light, which is also mounted in the cover, shining on the camera. This construction gives a view of the process as can be seen in Figure 12-34 and Figure 12-35, at a height of 8 till 9 cm in the blade. The camera records with a frame rate of 25/sec. In the Perspex window, Figure 12-35, a scale of 1 cm is engraved. By tracing sand grains along the window a ratio is determined between the cutting velocity and the velocity along the window at the recorded height, for the angles of 75° and 90°. These ratios are respectively 0.3 and 0.15. At 60° this ratio can hardly be determined because it lies in the range of the cutting velocity and out of the range of the recorded frame rate.

Figure 12-30: Front view of the test facility.

With a dynamometer forces on the middle blade are measured. The horizontal cutting forces for the various angles are roughly in a ratio of 1:1.5:2, for 60°, 75°, 90° respectively. This indicates a changing failure mechanism for the 3 tested angles, which the videos from the tests along the glass also confirm.

Figures 9, 10 and 11 show the horizontal cutting forces as obtained from the experiments.

From the above results two main conclusions can be drawn. First of all, the sand is moving relative to the blade on the blade and secondly the cutting forces at a 90° blade are much smaller then would be expected from the cutting theory, Miedema (1987 September). As shown in Figure 12-1, He et al. (1998) and also observed according to Figure 12-39, a wedge exists in front of the blade, but apparently this is not a kinematic wedge, but a dynamic wedge.

To determine the flow pattern of the sand in the dynamic wedge, vertical bars of colored sand grains were inserted in the sand. These vertical bars had a length of about 10 cm. Since the maximum cutting depth was 7 cm, the full cutting process was covered by these bars. Figure 12 shows the cutting process with the vertical bars and it shows how the bars are deformed by the cutting process.

Figure 12-31: The blade mounted under the carriage

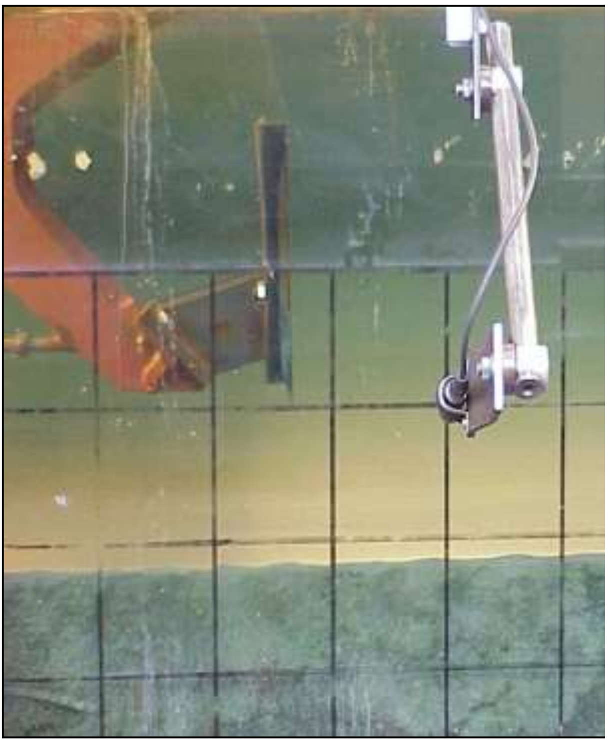

Figure 12-32: The camera in front of the window.

Figure 12-33: Cover with camera behind the blade.

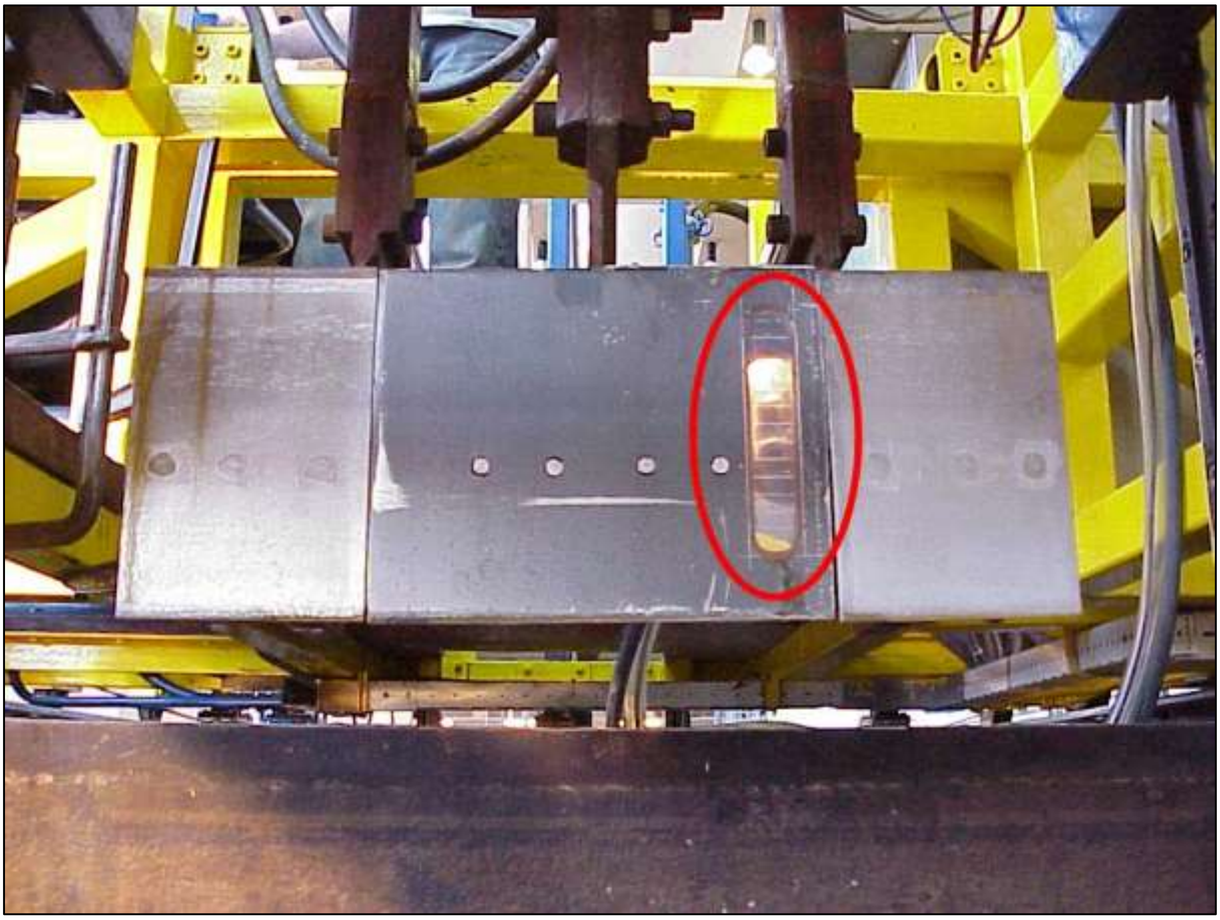

Figure 12-34: The Perspex window in the blade.

Figure 12-35: View of the cutting process through the Perspex window.

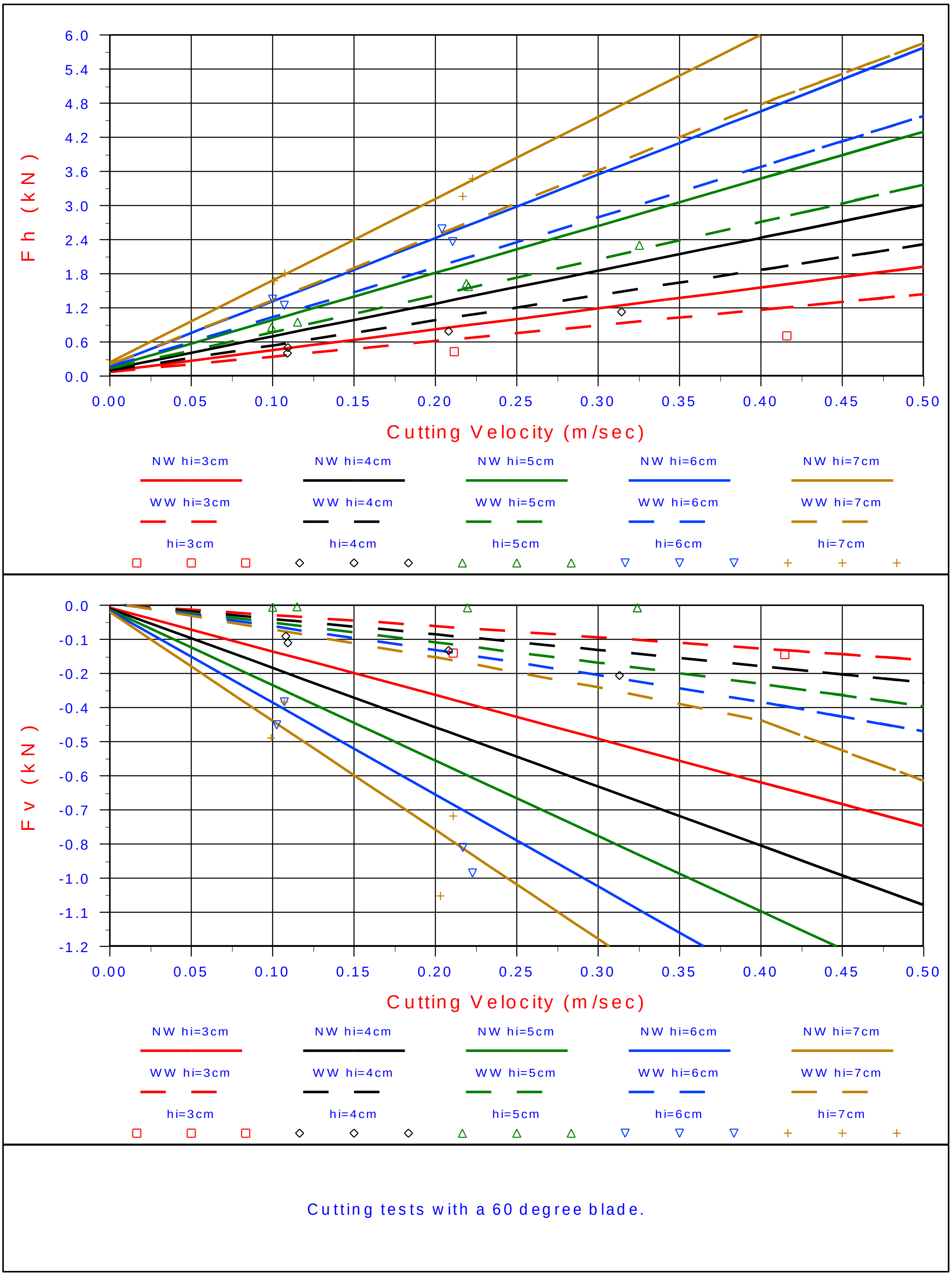

Figure 12-36: Cutting forces for cutting depths (h_i) from 3 to 7 cm; blade angle 60°.

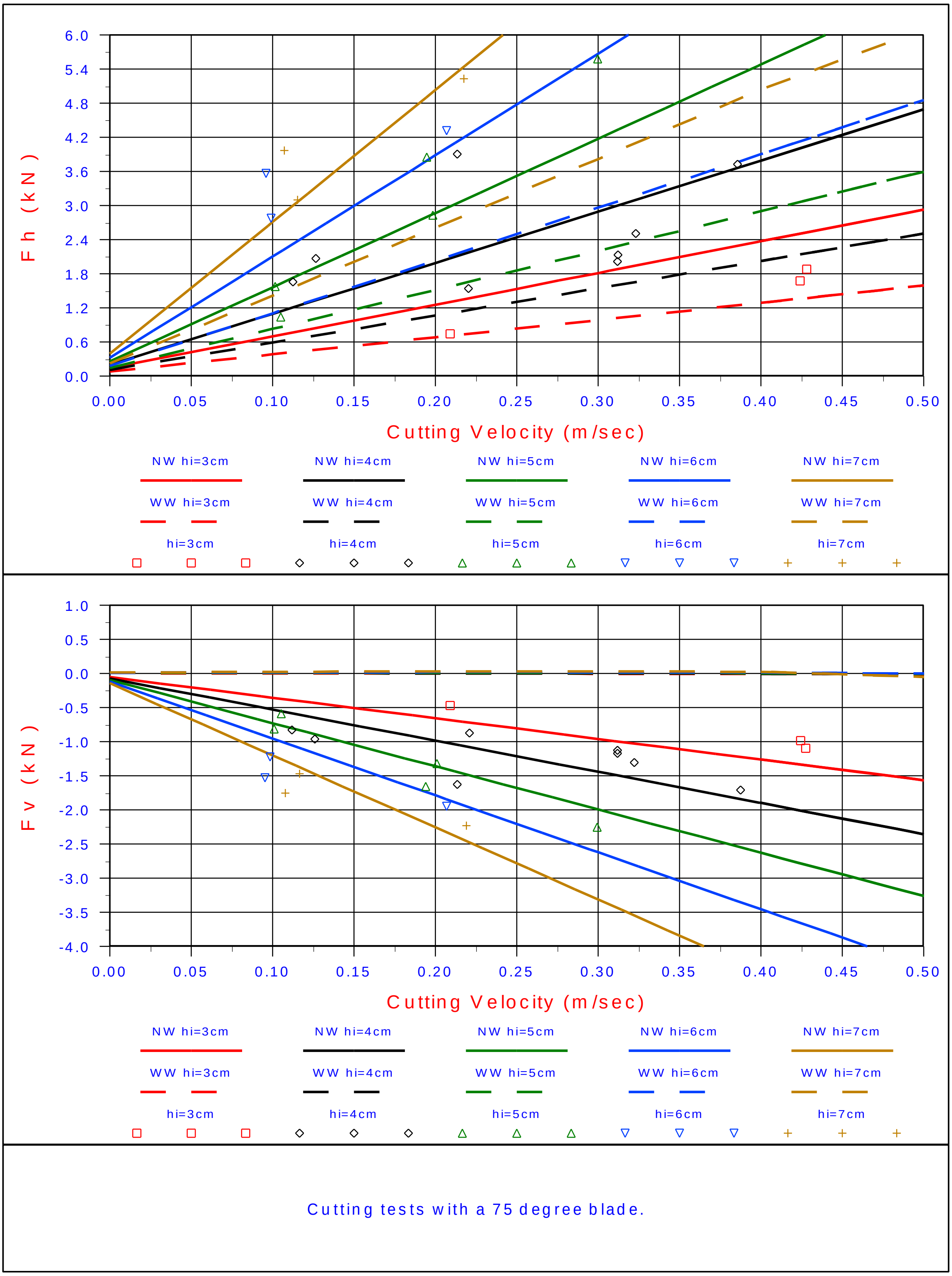

Figure 12-37: Cutting forces for cutting depths (h_i) from 3 to 7 cm; blade angle 75°.

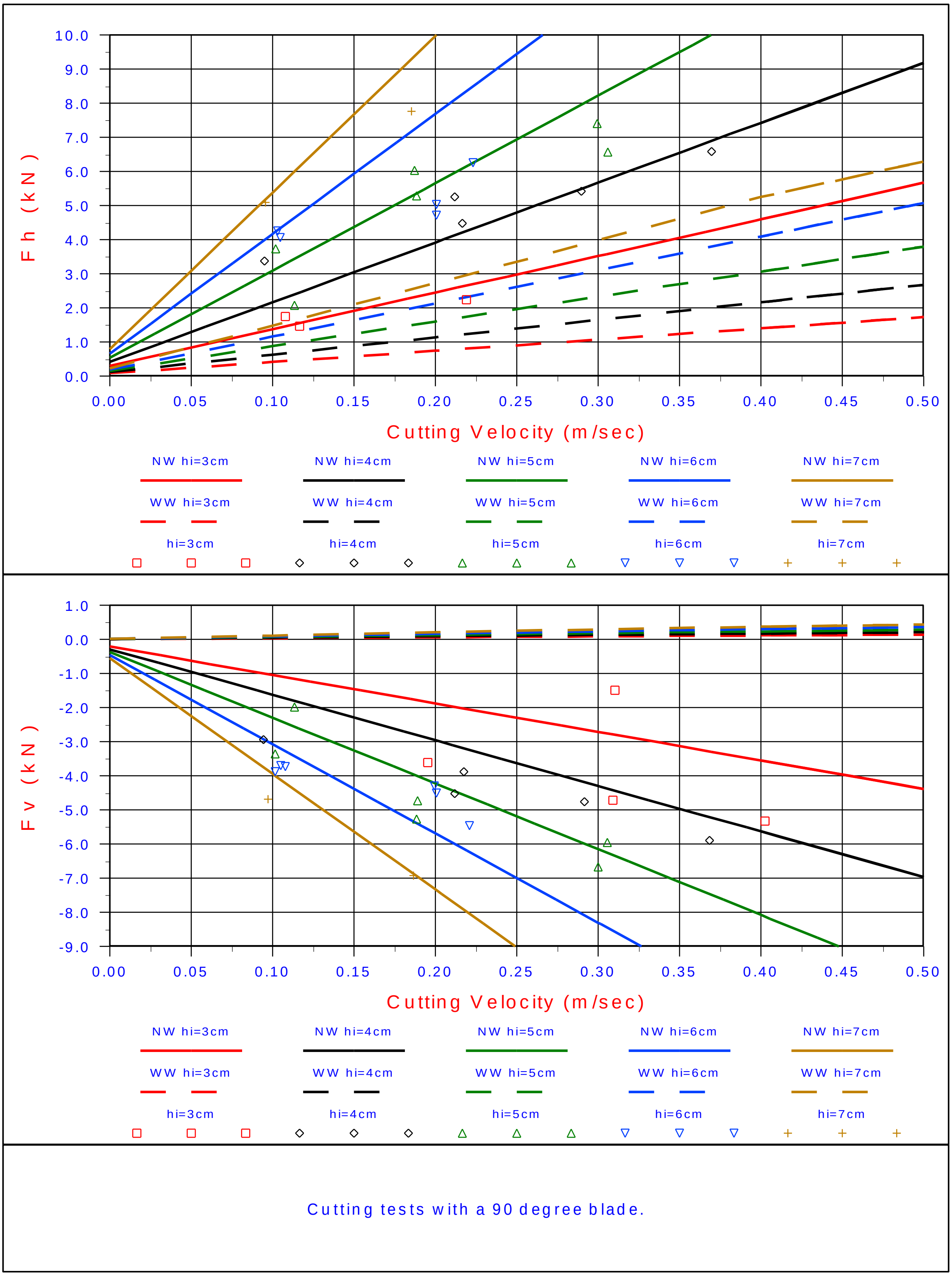

Cutting tests with a 90 degree blade.

Figure 12-38: Cutting forces for cutting depths (h_i) from 3 to 7 cm; blade angle 90°.

12.9. The Dynamic Wedge.

As discussed in the above paragraphs, the new research has led to the insight that the wedge in front of the blade is not static but dynamic. The aim of the new research was to get a good understanding of the mechanisms involved in the cutting at large cutting angles. To achieve this, vertical bars of about 10 cm deep with colored sand grains were inserted in the sand as is shown in Figure 12-39. When these bars are cut they will be deformed. If the wedge in front of the blade is a static wedge, meaning that the grains in the wedge have no velocity relative to the blade, then the colored grains from the bars will not enter the wedge. If however the colored grains enter the wedge, this means that the grains in the wedge move with respect to the blade. The research has shown that the colored grains have entered the wedge according to Figure 12-39. In the layer cut, the colored grains show a straight line, which is obvious, because of the velocity distribution in the layer cut. In fact the layer cut moves as a rigid body. In the wedge the colored grains show a curved line. Because of the velocity distribution in the wedge, the grains near the blade move much slower than the grains in the layer cut. Although Figure 12-39 shows a line between the layer cut and the wedge, in reality there does not exist a clear boundary between these two surfaces. The grains on both sides of the drawn boundary line will have (almost) the same velocity, resulting in an internal friction angle λ, which is not fully mobilized. The external friction angle on the blade however is fully mobilized. This contradicts the findings of Miedema et al. (2002A), from previous research. The value of this internal friction angle is between $\mathbf{0<\lambda<\varphi}$. Further research will have to show the value of $\boldsymbol{\lambda}$.

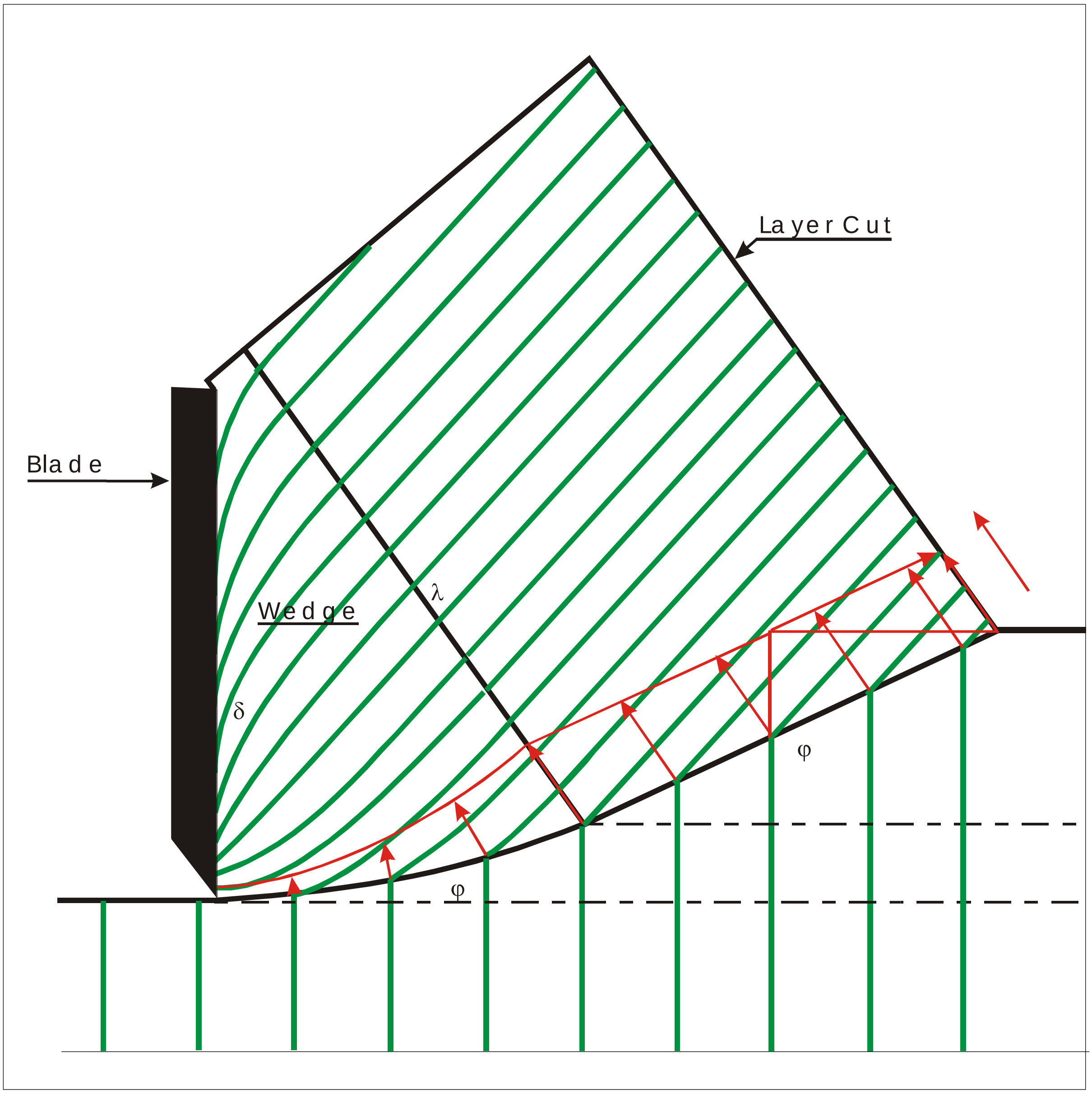

Figure 12-39: The dynamic wedge.

12.10. Nomenclature.

e_2, e_3, e_4	Acting point of cutting forces	-
F, F_h, F_v	Cutting force (general)	kN
g	Gravitation acceleration	m/s²
h_i	Initial layer thickness	m
h_b	Blade height	m
k_i	Initial permeability	m/s
k_{max}	Maximum permeability	m/s
$K_{1, 2, 3, 4}$	Grain force caused by grain stresses	kN
n_i	Initial pore percentage	%
n_{max}	Maximum pore percentage	%
$N_{1, 2, 3, 4}$	Normal force caused by grain stresses	kN
$p_{1m, 2m, 3m, 4m}$	Average pore pressure on a surface	-
$S_{1, 2, 3, 4}$	Force caused by shear stresses	kN
v_c	Cutting velocity perpendicular on the blade edge	m/s
w	Width of the blade of blade element	m
$W_{1, 2, 3, 4}$	Pore pressure forces	kN
z	Water depth	m
α	Blade angle	rad
β	Shear angle	rad
θ	Wedge angle	rad
ε	Volume strain	%
φ	Internal friction angle	rad
δ, δ_e	External friction angle, mobilized effective external friction angle	rad
ρ_w	Water density	ton/m³
λ	Angle of internal friction between wedge and layer cut	rad

Chapter 13: A Wedge in Clay Cutting.

13.1. Introduction.

Clay cutting is dominated by cohesive and adhesive forces. Pore pressure forces, gravitational forces and inertial forces do not play a role or can be neglected. Clay cutting is regarded to be an undrained process resulting in the **φ=0** concept, meaning that the internal and external friction angles can be considered to be zero. Because of the absence of internal and external friction angles, the sine of the sum of the 4 angles in the denominator of the equation for the cutting forces will less likely approach or exceed 180 degrees, resulting in very large or even negative forces. In clay only the blade angle and the shear angle play a role. Now the shear angle will in general be larger in the clay cutting process compared with the sand cutting process, still very large blade angles are required in order to approach the 180 degrees. The shear angle may have values of 30-50 degrees for a blade angle of 90 degrees, still not approaching the total of 180 degrees enough. Blade angles of around 150 degrees will be required to have a sum approaching 180 degrees. In normal dredging the blade angles will be up to about 60 degrees, but the front of a drag head of a trailing suction hopper dredge has an angle larger than 90 degrees, also in the problem of ice berg scour large angles may occur and usually tunnel boring machines have blades with large blade angles. So the problem of having large blade angles is relevant and the transition from the no-wedge mechanism to the wedge mechanism is of interest in engineering practice. Figure 13-1 shows the definitions of the wedge mechanism.

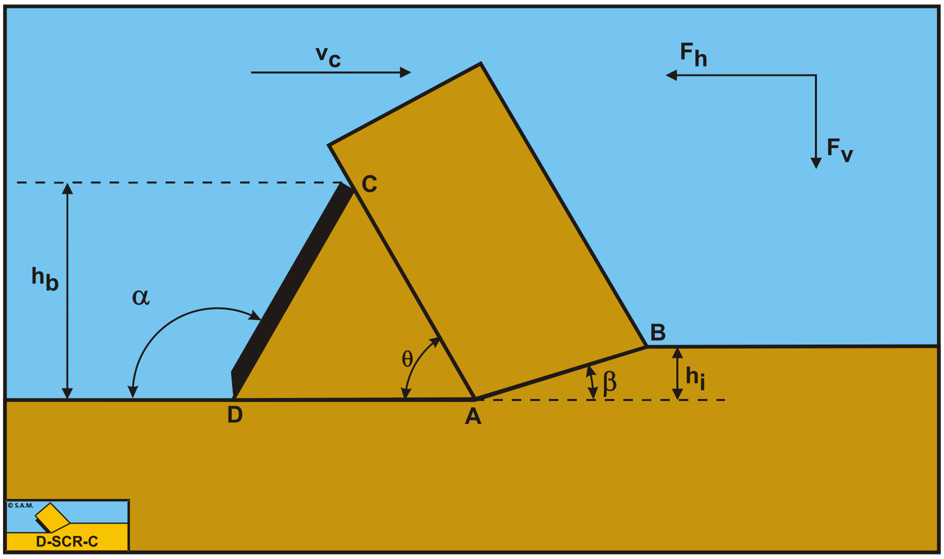

Figure 13-1: The occurrence of a wedge in clay cutting.

Definitions:

1. **A**: The wedge tip.
2. **B**: End of the shear plane.
3. **C**: The blade top.
4. **D**: The blade tip.
5. **A-B**: The shear plane.
6. **A-C**: The wedge surface.
7. **A-D**: The wedge bottom.
8. **D-C**: The blade surface.
9. h_b: The height of the blade.
10. h_i: The thickness of the layer cut.
11. v_c: The cutting velocity.
12. **α**: The blade angle.
13. **β**: The shear angle.
14. F_h: The horizontal force, the arrow gives the positive direction.
15. F_v: The vertical force, the arrow gives the positive direction.

13.2. The Equilibrium of Forces.

Figure 13-2 illustrates the forces on the layer of soil cut. The forces shown are valid for clay.

The forces acting on the layer **A-B** are:

1. A normal force acting on the shear surface **N_1**, resulting from the effective grain stresses.
2. A shear force **C_1** as a result of pure cohesion **τ_c** or shear strength. This force can be calculated by multiplying the cohesive shear strength **τ_c** with the area of the shear plane.
3. A force normal to the pseudo blade **N_2**, resulting from the effective grain stresses.
4. A shear force **C_2** as a result of the mobilized cohesion between the soil and the wedge **τ_c**. This force can be calculated by multiplying the cohesive shear strength **τ_c** of the soil with the contact area between the soil and the wedge.

The forces acting on the wedge front or pseudo blade **A-C** when cutting clay, can be distinguished as (see Figure 13-3):

5. A force normal to the blade **N_2**, resulting from the effective grain stresses.
6. A shear force **C_2** as a result of the cohesion between the layer cut and the pseudo blade **τ_c**. This force can be calculated by multiplying the cohesive shear strength **τ_c** of the soil with the contact area between the soil and the pseudo blade.

The forces acting on the wedge bottom **A-D** when cutting clay, can be distinguished as:

7. A force normal to the blade **N_3**, resulting from the effective grain stresses.
8. A shear force **C_3** as a result of the cohesion between the wedge bottom and the undisturbed soil **τ_c**. This force can be calculated by multiplying the cohesive shear strength **τ_c** of the soil with the contact area between the wedge bottom and the undisturbed soil.

The forces acting on a straight blade **C-D** when cutting soil (see Figure 13-4), can be distinguished as:

9. A force normal to the blade **N_4,** resulting from the effective grain stresses.
10. A shear force **A** as a result of pure adhesion between the soil and the blade **τ_a**. This force can be calculated by multiplying the adhesive shear strength **τ_a** of the soil with the contact area between the soil and the blade.

The horizontal equilibrium of forces on the layer cut:

$$\sum F_h = N_1 \cdot \sin(\beta) + C_1 \cdot \cos(\beta) - C_2 \cdot \cos(\alpha) - N_2 \cdot \sin(\alpha) = 0 \tag{13-1}$$

The vertical equilibrium of forces on the layer cut:

$$\sum F_v = -N_1 \cdot \cos(\beta) + C_1 \cdot \sin(\beta) + C_2 \cdot \sin(\alpha) - N_2 \cdot \cos(\alpha) = 0 \tag{13-2}$$

The force **N_1** on the shear plane is now:

$$N_1 = \frac{-C_1 \cdot \cos(\alpha + \beta) + C_2}{\sin(\alpha + \beta)} \tag{13-3}$$

The force **N_2** on the pseudo blade is now:

$$N_2 = \frac{+C_1 - C_2 \cdot \cos(\alpha + \beta)}{\sin(\alpha + \beta)} \tag{13-4}$$

From equation (13-4) the forces on the pseudo blade can be derived. On the pseudo blade a force component in the direction of cutting velocity **F_h** and a force perpendicular to this direction **F_v** can be distinguished.

$$F_h = +N_2 \cdot \sin(\alpha) + C_2 \cdot \cos(\alpha) \tag{13-5}$$

$$F_v = +N_2 \cdot \cos(\alpha) - C_2 \cdot \sin(\alpha) \tag{13-6}$$

Now knowing the forces on the pseudo blade A-C, the equilibrium of forces on the wedge A-C-D can be derived. The adhesive force does not have to be mobilized 100%, while this force could have both directions, depending on the equilibrium of forces and the equilibrium of moments. So for now the mobilized adhesive force $\mathbf{A_m}$ is used in the equations.

The horizontal equilibrium of forces on the wedge:

$$\sum F_h = N_4 \cdot \sin(\alpha) + A_m \cdot \cos(\alpha) - C_2 \cdot \cos(\theta) - N_2 \cdot \sin(\theta) - C_3 = 0 \tag{13-7}$$

The vertical equilibrium of forces on the wedge:

$$\sum F_v = N_4 \cdot \cos(\alpha) - A_m \cdot \sin(\alpha) - C_2 \cdot \sin(\theta) + N_2 \cdot \cos(\theta) - N_3 = 0 \tag{13-8}$$

To derive $\mathbf{N_4}$:

Multiply the horizontal equilibrium equation with **sin(α)**.

$$\begin{gathered} N_4 \cdot \sin(\alpha) \cdot \sin(\alpha) + A_m \cdot \cos(\alpha) \cdot \sin(\alpha) - C_2 \cdot \cos(\theta) \cdot \sin(\alpha) \\ -N_2 \cdot \sin(\theta) \cdot \sin(\alpha) - C_3 \cdot \sin(\alpha) = 0 \end{gathered} \tag{13-9}$$

Multiply the vertical equilibrium equation with **cos(α)**.

$$\begin{gathered} N_4 \cdot \cos(\alpha) \cdot \cos(\alpha) - A_m \cdot \sin(\alpha) \cdot \cos(\alpha) - C_2 \cdot \sin(\theta) \cdot \cos(\alpha) \\ +N_2 \cdot \cos(\theta) \cdot \cos(\alpha) - N_3 \cdot \cos(\alpha) = 0 \end{gathered} \tag{13-10}$$

Now add up the two resulting equations in order to get an expression for $\mathbf{N_4}$.

$$N_4 = C_2 \cdot \sin(\alpha + \theta) - N_2 \cdot \cos(\alpha + \theta) + C_3 \cdot \sin(\alpha) + N_3 \cdot \cos(\alpha) \tag{13-11}$$

The mobilized adhesive force $\mathbf{A_m}$ can be derived according to:

First multiply the horizontal equilibrium equation with **cos(α)**.

$$\begin{gathered} N_4 \cdot \sin(\alpha) \cdot \cos(\alpha) + A_m \cdot \cos(\alpha) \cdot \cos(\alpha) - C_2 \cdot \cos(\theta) \cdot \cos(\alpha) \\ -N_2 \cdot \sin(\theta) \cdot \cos(\alpha) - C_3 \cdot \cos(\alpha) = 0 \end{gathered} \tag{13-12}$$

Now multiply the vertical equilibrium equation with **sin(α)**:

$$\begin{gathered} N_4 \cdot \cos(\alpha) \cdot \sin(\alpha) - A_m \cdot \sin(\alpha) \cdot \sin(\alpha) - C_2 \cdot \sin(\theta) \cdot \sin(\alpha) \\ +N_2 \cdot \cos(\theta) \cdot \sin(\alpha) - N_3 \cdot \sin(\alpha) = 0 \end{gathered} \tag{13-13}$$

Subtracting the two resulting equations gives the equation for the mobilized adhesive force.

$$A_m = C_2 \cdot \cos(\alpha + \theta) + N_2 \cdot \sin(\alpha + \theta) + C_3 \cdot \cos(\alpha) - N_3 \cdot \sin(\alpha) \tag{13-14}$$

This can also be rewritten as an equation for the normal force $\mathbf{N_3}$ on the bottom of the wedge.

$$N_3 = N_4 \cdot \cos(\alpha) - A_m \cdot \sin(\alpha) - C_2 \cdot \sin(\theta) + N_2 \cdot \cos(\theta) \tag{13-15}$$

Since both the mobilized adhesive force $\mathbf{A_m}$ and the normal force on the bottom of the wedge $\mathbf{N_3}$ are unknowns, an additional condition has to be found. The wedge angle **θ** however is also an unknown, requiring an additional condition. Apparently $\mathbf{N_4}$ and $\mathbf{A_m}$ are independent of each other.

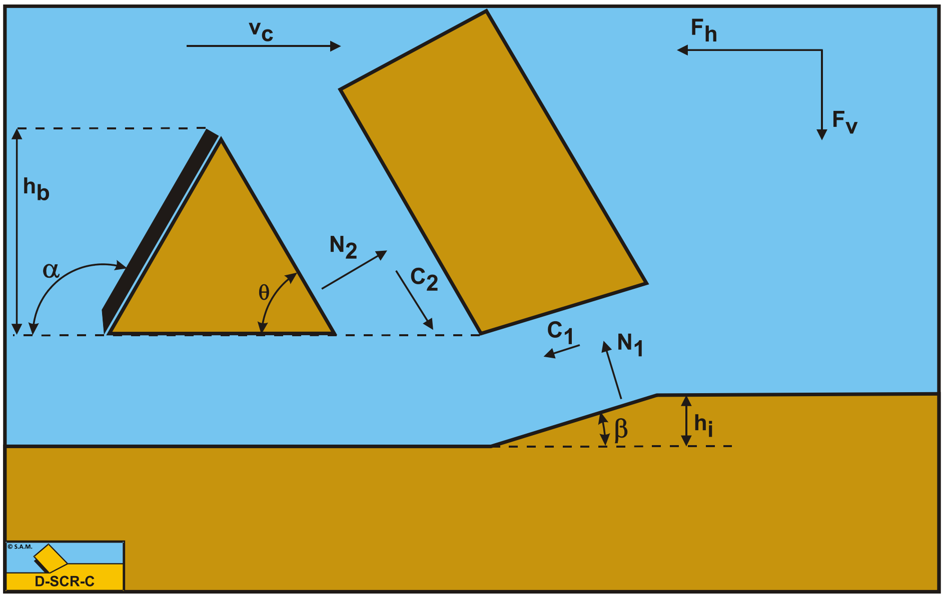

Figure 13-2: The forces on the layer cut in clay cutting with a wedge.

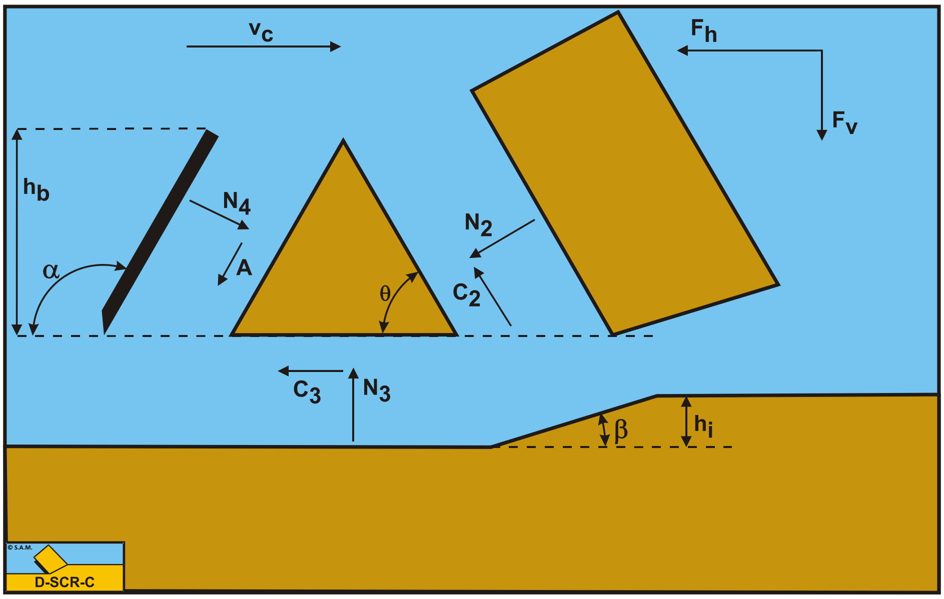

Figure 13-3: The forces on the wedge in clay cutting.

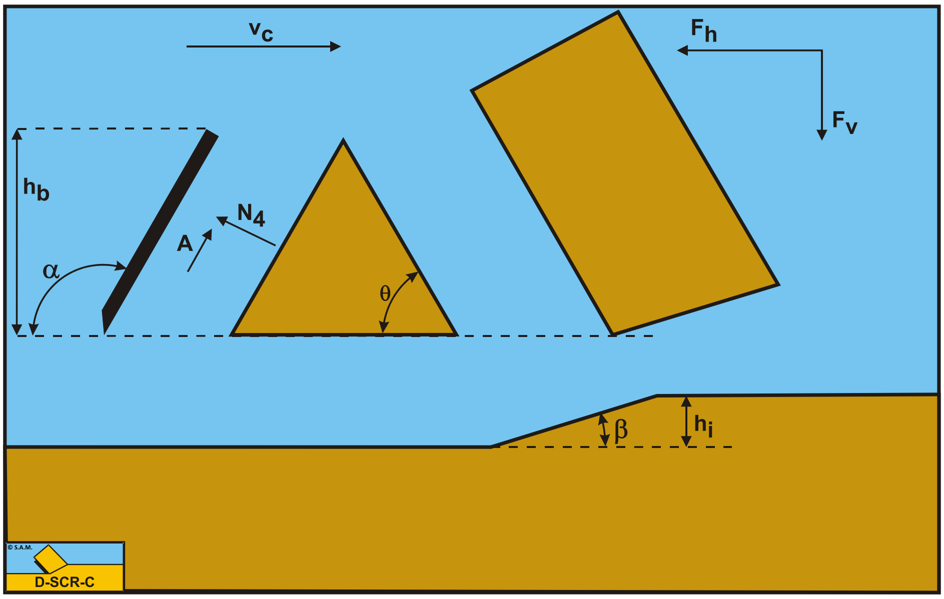

Figure 13-4: The forces on the blade when cutting clay with a wedge.

13.3. The Equilibrium of Moments.

The first additional condition is the equilibrium of moments of the wedge. Since the wedge is not subject to rotational accelerations in a stationary cutting process, the sum of the moments around any point on the wedge has to be zero. Here the tip of the blade is chosen for this point. First the equilibrium of moments is solved in order to find a relation between **N**$_3$ and **N**$_4$.

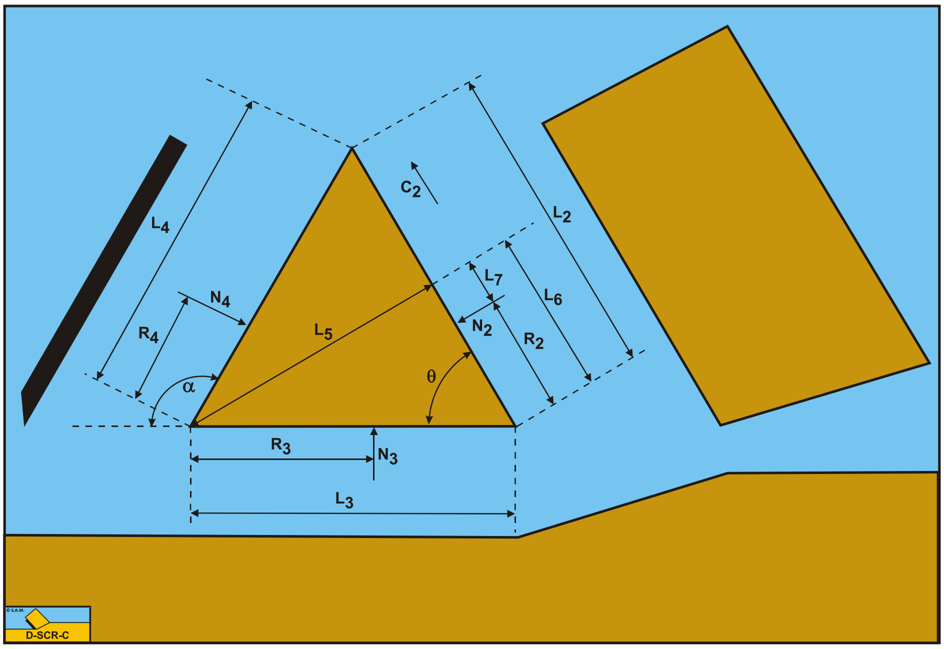

Figure 13-5: The equilibrium of moments on the wedge when cutting clay.

To solve the equilibrium of moments the lengths of the sides of the wedge and arms of the forces have to be determined.

The length of the shear plane **A-B** is:

$$L_1 = \frac{h_i}{\sin(\beta)} \tag{13-16}$$

The length of the front of the wedge **A-C** is:

$$L_2 = \frac{h_b}{\sin(\theta)} \tag{13-17}$$

The length of the bottom of the wedge **A-D** is:

$$L_3 = h_b \cdot \left(\frac{1}{\tan(\theta)} - \frac{1}{\tan(\alpha)} \right) \tag{13-18}$$

The length of the blade **C-D** is:

$$L_4 = \frac{h_b}{\sin(\alpha)} \tag{13-19}$$

The distance of the tip of the blade perpendicular to the front of the wedge is:

$$L_5 = L_3 \cdot \sin(\theta) \tag{13-20}$$

The distance from point **A** to the intersection point of the line going from the tip of the blade perpendicular to the front of the blade is.

$$L_6 = L_3 \cdot \cos(\theta) \tag{13-21}$$

The distance of the acting point of the force $\mathbf{N_2}$ to the intersection point of the line going from the tip of the blade perpendicular to the front of the blade is:

$$L_7 = L_6 - R_2 \tag{13-22}$$

$\mathbf{R_2}$ follows from the equilibrium of moments on the layer cut, assuming the forces on the shear plane act at half the length of the shear plane.

$$N_1 \cdot R_1 = N_2 \cdot R_2 \tag{13-23}$$

Now the equilibrium equation of moments can be derived according to:

$$\sum M = \frac{N_4 \cdot L_4}{2} - \frac{N_3 \cdot L_3}{2} + N_2 \cdot L_7 - C_2 \cdot L_5 = 0 \tag{13-24}$$

Both equation (13-11) and equation (13-24) don not contain the mobilized adhesive force $\mathbf{A_m}$, giving the possibility to solve the two unknowns $\mathbf{N_3}$ and $\mathbf{N_4}$. To solve the normal force $\mathbf{N_3}$ first an expression for the normal force $\mathbf{N_4}$ has to be derived based on the equilibrium of moments.

$$N_4 = \frac{2 \cdot (N_3 \cdot L_3 / 2 - N_2 \cdot L_7 + C_2 \cdot L_5)}{L_4} \tag{13-25}$$

Equation (13-11) and equation (13-25) should give the same result for the normal force $\mathbf{N_4}$, thus:

$$\begin{aligned} &\frac{2 \cdot (N_3 \cdot L_3 / 2 - N_2 \cdot L_7 + C_2 \cdot L_5)}{L_4} = \\ &C_2 \cdot \sin(\alpha + \theta) - N_2 \cdot \cos(\alpha + \theta) + C_3 \cdot \sin(\alpha) + N_3 \cdot \cos(\alpha) \end{aligned} \tag{13-26}$$

This can be written as:

$$N_3 \cdot \left(\frac{L_3}{L_4} - \cos(\alpha) \right) = N_2 \cdot \left(\frac{L_7}{2 \cdot L_4} - \cos(\alpha+\theta) \right)$$

$$+ C_2 \cdot \left(-\frac{L_5}{2 \cdot L_4} + \sin(\alpha+\theta) \right) + C_3 \cdot \sin(\alpha) \qquad \textbf{(13-27)}$$

Now **N3** can be expressed in a number of known variables according to:

$$N_3 = \frac{N_2 \cdot \left(\frac{L_7}{2 \cdot L_4} - \cos(\alpha+\theta) \right) + C_2 \cdot \left(-\frac{L_5}{2 \cdot L_4} + \sin(\alpha+\theta) \right)}{\left(\frac{L_3}{L_4} - \cos(\alpha) \right)}$$

$$+ \frac{+C_3 \cdot \sin(\alpha)}{\left(\frac{L_3}{L_4} - \cos(\alpha) \right)} \qquad \textbf{(13-28)}$$

Substituting equation (13-28) in equation (13-11) gives a solution for the normal force **N4**.

$$N_4 = C_2 \cdot \sin(\alpha+\theta) - N_2 \cdot \cos(\alpha+\theta) + C_3 \cdot \sin(\alpha) + N_3 \cdot \cos(\alpha) \qquad \textbf{(13-29)}$$

Substituting equation (13-28) in equation (13-14) gives a solution for the mobilized adhesion **Am**.

$$A_m = C_2 \cdot \cos(\alpha+\theta) + N_2 \cdot \sin(\alpha+\theta) + C_3 \cdot \cos(\alpha) - N_3 \cdot \sin(\alpha) \qquad \textbf{(13-30)}$$

This results in a horizontal force of:

$$F_h = N_4 \cdot \sin(\alpha) + A_m \cdot \cos(\alpha) \qquad \textbf{(13-31)}$$

And in a vertical force of:

$$F_v = N_4 \cdot \cos(\alpha) - A_m \cdot \sin(\alpha) \qquad \textbf{(13-32)}$$

Based on the experience with sand cutting it is assumed that the wedge angle **θ** can be determined by assuming that the horizontal force should be at a minimum for the angle chosen. It is very well possible that the mobilized adhesion is negative for large blade angles.

13.4. Nomenclature.

a, τ_a	Adhesion or adhesive shear strength.	**kPa**
A	Adhesive shear force on the blade.	**kN**
c, τ_c	Cohesion or cohesive shear strength.	**kPa**
C_1	Cohesive shear force on the shear plane.	**kN**
C_2	Cohesive shear force on the pseudo blade (front of the wedge).	**kN**
C_3	Cohesive shear force on bottom of the wedge.	**kN**
F_h	Horizontal cutting force.	**kN**
F_v	Vertical cutting force.	**kN**
G_1	Weight of the layer cut.	**kN**
G_2	Weight of the wedge.	**kN**
h_b	Blade height.	**m**
h_i	Layer thickness.	**m**
I	Inertial force on the shear plane.	**kN**
N_1	Normal force on the shear plane.	**kN**
N_2	Normal force on the pseudo blade (front of the wedge).	**kN**
N_3	Normal force on bottom of the wedge.	**kN**
N_4	Normal force on the blade.	**kN**
K_1	Sum of N_1 and S_1 on the shear plane.	**kN**
K_2	Sum of N_2 and S_2 on the pseudo blade (front of the wedge).	**kN**
K_3	Sum of N_3 and S_3 on bottom of the wedge.	**kN**
K_4	Sum of N_4 and S_4 on the blade.	**kN**
L_1	Length of the shear plane.	**m**
L_2	Length of the pseudo blade (front of the wedge).	**m**
L_3	Length of the bottom of the wedge.	**m**
L_4	Length of the blade.	**m**
L_5	Length of the line from the tip of the blade to the opposite side of the wedge and perpendicular to this side.	**m**
L_6	Length of the line from point **A** to the intersection point of the previous line with side **A-C.**	**m**
L_7	Distance from the acting point of the pore pressure force on side **A-C** to the intersection point of the previous line L_6 with side **A-C.**	**m**
R_1	Acting point forces on the shear plane.	**m**
R_2	Acting point forces on the pseudo blade (front of the wedge).	**m**
R_3	Acting point forces on the bottom of the wedge.	**m**
R_4	Acting point forces on the blade.	**m**
S_1	Shear (friction) force on the shear plane.	**kN**
S_2	Shear (friction) force on the pseudo blade (front of the wedge).	**kN**
S_3	Shear (friction) force on the bottom of the wedge.	**kN**
S_4	Shear (friction) force on the blade.	**kN**
W_1	Pore pressure force on the shear plane.	**kN**
W_2	Pore pressure force on the pseudo blade (front of the wedge).	**kN**
W_3	Pore pressure force on the bottom of the wedge.	**kN**
W_4	Pore pressure force on the blade.	**kN**
v_c	Cutting velocity.	**m/sec**
α	Blade angle.	°
β	Shear angle.	°
θ	Wedge angle.	°
φ	Internal friction angle.	°
δ	External friction angle.	°
λ	Internal friction angle on pseudo blade.	°

Chapter 14: A Wedge in Atmospheric Rock Cutting.

14.1. Introduction.

For completeness of the overview the equations for the cutting of the wedge mechanism for atmospheric rock are given here without further explanation.

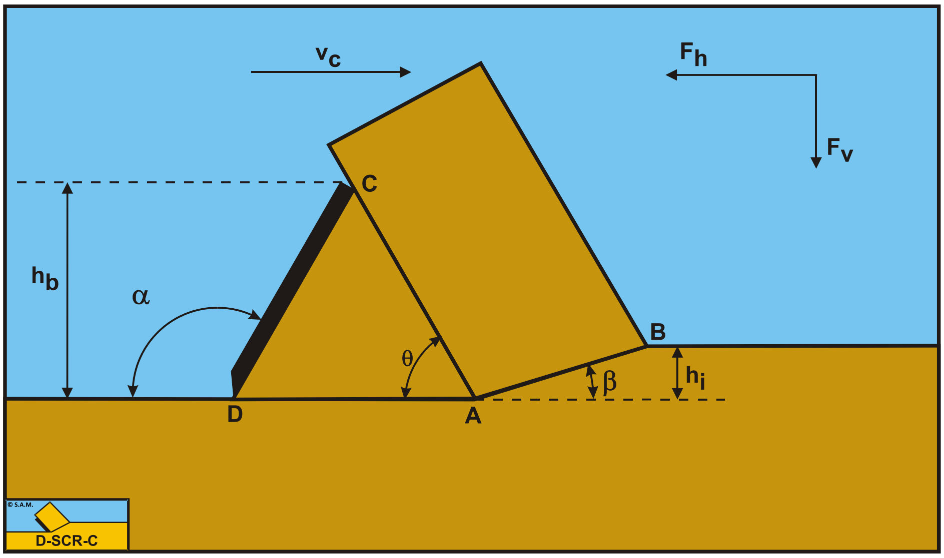

Figure 14-1: Definitions.

Definitions:

1. **A**: The wedge tip.
2. **B**: End of the shear plane.
3. **C**: The blade top.
4. **D**: The blade tip.
5. **A-B**: The shear plane.
6. **A-C**: The wedge surface.
7. **A-D**: The wedge bottom.
8. **D-C**: The blade surface.
9. **h_b**: The height of the blade.
10. **h_i**: The thickness of the layer cut.
11. **v_c**: The cutting velocity.
12. **α**: The blade angle.
13. **β**: The shear angle.
14. **F_h**: The horizontal force, the arrow gives the positive direction.
15. **F_v**: The vertical force, the arrow gives the positive direction.

14.2. The Equilibrium of Forces.

Figure 14-2 illustrates the forces on the layer of soil cut. The forces shown are valid in general for each type of soil.

The forces acting on the layer **A-B** are:

1. A normal force acting on the shear surface **N_1**, resulting from the effective grain stresses.
2. A shear force **S_1** as a result of internal friction **$N_1 \cdot \tan(\varphi)$**.
3. A shear force **C_1** as a result of pure cohesion τ_c or shear strength. This force can be calculated by multiplying the cohesive shear strength τ_c with the area of the shear plane.
4. A force normal to the pseudo blade **N_2**, resulting from the effective grain stresses.
5. A shear force **S_2** as a result of the soil/soil friction **$N_2 \cdot \tan(\lambda)$** between the layer cut and the wedge pseudo blade. The friction angle **λ** does not have to be equal to the internal friction angle **φ** in the shear plane, since the soil has already been deformed.

6. A shear force **C₂** as a result of the mobilized cohesion between the soil and the wedge τ_c. This force can be calculated by multiplying the cohesive shear strength τ_c of the soil with the contact area between the soil and the wedge.

The normal force **N₁** and the shear force **S₁** can be combined to a resulting grain force **K₁**.

$$K_1 = \sqrt{N_1^2 + S_1^2} \tag{14-1}$$

The forces acting on the wedge front or pseudo blade **A-C** when cutting soil, can be distinguished as:
7. A force normal to the blade **N₂**, resulting from the effective grain stresses.
8. A shear force **S₂** as a result of the soil/soil friction $N_2 \cdot \tan(\lambda)$) between the layer cut and the wedge pseudo blade. The friction angle λ does not have to be equal to the internal friction angle φ in the shear plane, since the soil has already been deformed.
9. A shear force **C₂** as a result of the cohesion between the layer cut and the pseudo blade τ_c. This force can be calculated by multiplying the cohesive shear strength τ_c of the soil with the contact area between the soil and the pseudo blade.

These forces are shown in Figure 14-3. If the forces **N₂** and **S₂** are combined to a resulting force **K₂** and the adhesive force and the water under pressures are known, then the resulting force **K₂** is the unknown force on the blade. By taking the horizontal and vertical equilibrium of forces an expression for the force **K₂** on the blade can be derived.

$$K_2 = \sqrt{N_2^2 + S_2^2} \tag{14-2}$$

The forces acting on the wedge bottom **A-D** when cutting soil, can be distinguished as:
10. A force normal to the blade **N₃**, resulting from the effective grain stresses.
11. A shear force **S₃** as a result of the soil/soil friction $N_3 \cdot \tan(\varphi)$) between the wedge bottom and the undisturbed soil.
12. A shear force **C₃** as a result of the cohesion between the wedge bottom and the undisturbed soil τ_c. This force can be calculated by multiplying the cohesive shear strength τ_c of the soil with the contact area between the wedge bottom and the undisturbed soil.

The normal force **N₃** and the shear force **S₃** can be combined to a resulting grain force **K₃**.

$$K_3 = \sqrt{N_3^2 + S_3^2} \tag{14-3}$$

The forces acting on a straight blade **C-D** when cutting soil (see Figure 14-4), can be distinguished as:
16. A force normal to the blade **N₄,** resulting from the effective grain stresses.
17. A shear force **S₄** as a result of the soil/steel friction $N_4 \cdot \tan(\delta)$.

The normal force **N₄** and the shear force **S₄** can be combined to a resulting grain force **K₄**.

$$K_4 = \sqrt{N_4^2 + S_4^2} \tag{14-4}$$

The horizontal equilibrium of forces on the layer cut:

$$\sum F_h = K_1 \cdot \sin(\beta + \varphi) + C_1 \cdot \cos(\beta) - C_2 \cdot \cos(\alpha) - K_2 \cdot \sin(\alpha + \lambda) = 0 \tag{14-5}$$

The vertical equilibrium of forces on the layer cut:

$$\sum F_v = -K_1 \cdot \cos(\beta + \varphi) + C_1 \cdot \sin(\beta) + C_2 \cdot \sin(\alpha) - K_2 \cdot \cos(\alpha + \lambda) = 0 \tag{14-6}$$

The force **K₁** on the shear plane is now:

$$K_1 = \frac{-C_1 \cdot \cos(\alpha + \beta + \lambda) + C_2 \cdot \cos(\lambda)}{\sin(\alpha + \beta + \lambda + \varphi)} \tag{14-7}$$

The force **K2** on the pseudo blade is now:

$$K_2 = \frac{+C_1 \cdot \cos(\varphi) - C_2 \cdot \cos(\alpha + \beta + \varphi)}{\sin(\alpha + \beta + \lambda + \varphi)} \tag{14-8}$$

From equation (14-8) the forces on the pseudo blade can be derived. On the pseudo blade a force component in the direction of cutting velocity **F_h** and a force perpendicular to this direction **F_v** can be distinguished.

$$F_h = K_2 \cdot \sin(\alpha + \lambda) + C_2 \cdot \cos(\alpha) \tag{14-9}$$

$$F_v = K_2 \cdot \cos(\alpha + \lambda) - C_2 \cdot \sin(\alpha) \tag{14-10}$$

The normal force on the shear plane is now:

$$N_1 = \frac{-C_1 \cdot \cos(\alpha + \beta + \lambda) + C_2 \cdot \cos(\lambda)}{\sin(\alpha + \beta + \lambda + \varphi)} \cdot \cos(\varphi) \tag{14-11}$$

The normal force on the pseudo blade is now:

$$N_2 = \frac{+C_1 \cdot \cos(\varphi) - C_2 \cdot \cos(\alpha + \beta + \varphi)}{\sin(\alpha + \beta + \lambda + \varphi)} \cdot \cos(\lambda) \tag{14-12}$$

Now knowing the forces on the pseudo blade A-C, the equilibrium of forces on the wedge A-C-D can be derived. The horizontal equilibrium of forces on the wedge is:

$$\begin{aligned} \sum F_h &= -K_4 \cdot \sin\left(\alpha + \delta\right) + K_3 \cdot \sin\left(\varphi\right) + C_3 \\ &\quad + C_2 \cdot \cos\left(\theta\right) + K_2 \cdot \sin\left(\theta + \lambda\right) = 0 \end{aligned} \tag{14-13}$$

The vertical equilibrium of forces on the wedge is:

$$\begin{aligned} \sum F_v &= -K_4 \cdot \cos\left(\alpha + \delta\right) - K_3 \cdot \cos\left(\varphi\right) \\ &\quad - C_2 \cdot \sin\left(\theta\right) + K_2 \cdot \cos\left(\theta + \lambda\right) = 0 \end{aligned} \tag{14-14}$$

The unknowns in this equation are **K_3** and **K_4**, since **K_2** has already been solved. Two other unknowns are, the external friction angle **δ**, since the external friction does not have to be fully mobilized, and the wedge angle **θ**. These 2 additional unknowns require 2 additional conditions in order to solve the problem. One additional condition is the equilibrium of moments of the wedge, a second condition the principle of minimum required cutting energy. Depending on whether the soil pushes upwards or downwards against the blade, the mobilization factor is between -1 and +1.

The force **K3** on the bottom of the wedge is now:

$$K_3 = \frac{+K_2 \cdot \sin\left(\alpha + \delta - \theta - \lambda\right) + C_3 \cdot \cos\left(\alpha + \delta\right) - C_2 \cdot \cos\left(\alpha + \delta - \theta\right)}{\sin\left(\alpha + \delta + \varphi\right)} \tag{14-15}$$

The force **K4** on the blade is now:

$$K_4 = \frac{+K_2 \cdot \sin\left(\theta + \lambda + \varphi\right) + C_3 \cdot \cos\left(\varphi\right) + C_2 \cdot \cos\left(\theta + \varphi\right)}{\sin\left(\alpha + \delta + \varphi\right)} \tag{14-16}$$

This results in a horizontal force on the blade of:

$$F_h = K_4 \cdot \sin(\alpha + \delta) \tag{14-17}$$

And in a vertical force on the blade of:

$$F_v = K_4 \cdot \cos(\alpha + \delta) \tag{14-18}$$

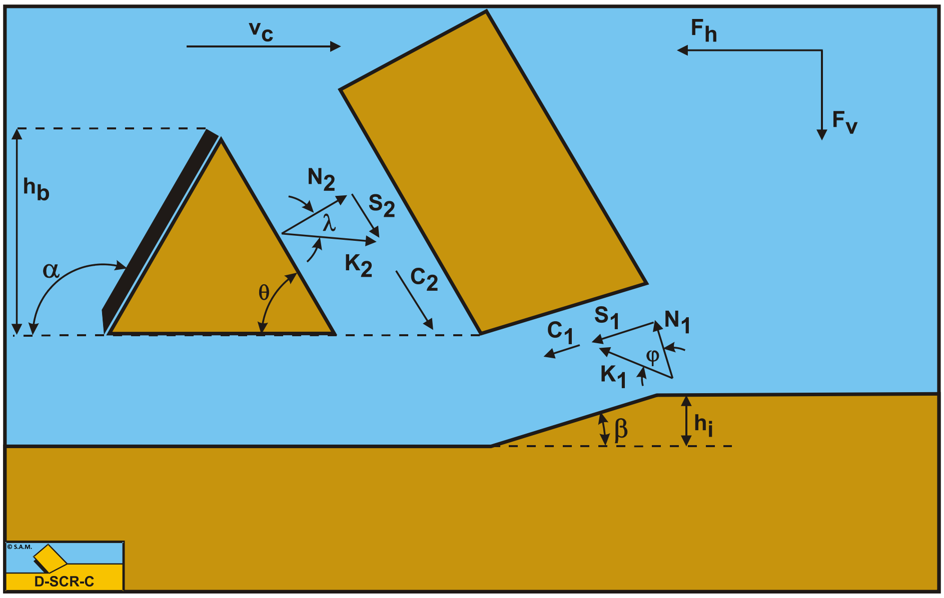

Figure 14-2: The forces on the layer cut when a wedge is present.

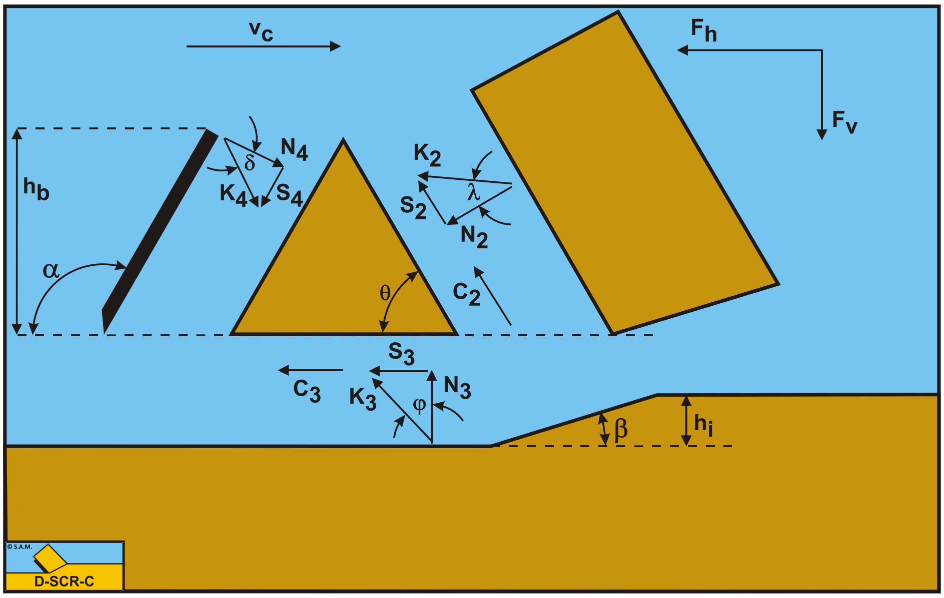

Figure 14-3: The forces on the wedge.

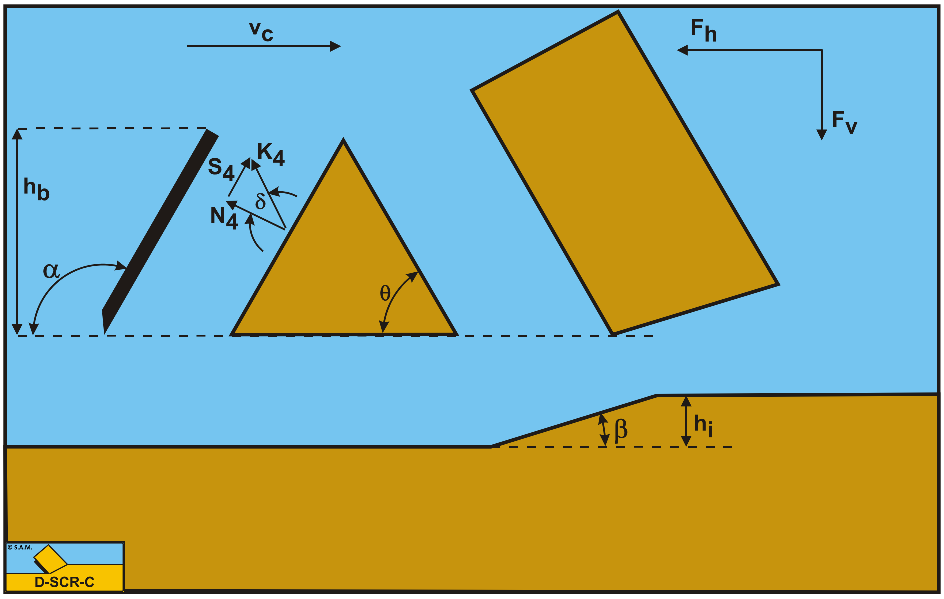

Figure 14-4: The forces on the blade when a wedge is present.

14.3. The Equilibrium of Moments.

In order to solve the problem, also the equilibrium of moments is required, since the wedge is not subject to rotational acceleration. The equilibrium of moments can be taken around each point of the wedge. Here the tip of the blade is chosen. The advantage of this is that a number of forces do not contribute to the moments on the wedge.

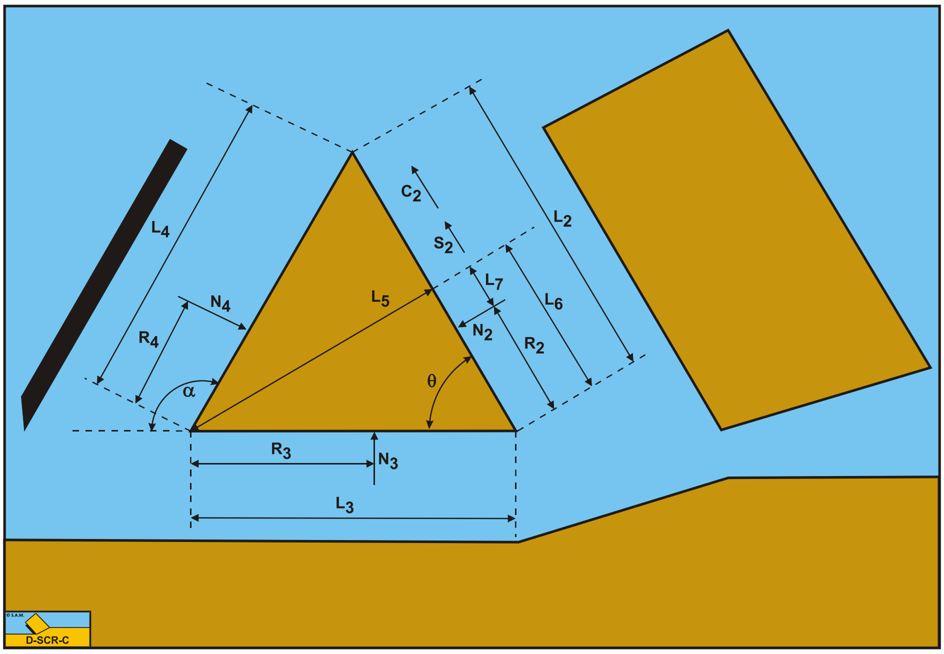

Figure 14-5: The moments on the wedge.

In order to derive the equilibrium of moments equation the arms of all the forces contributing to this equilibrium have to be known. Since these arms depend on the length of all the sides in the cutting process, first these lengths are determined. The length of the shear plane **A-B** is:

$$L_1 = \frac{h_i}{\sin(\beta)} \qquad \textbf{(14-19)}$$

The length of the pseudo blade **A-C** is:

$$L_2 = \frac{h_b}{\sin(\theta)} \tag{14-20}$$

The length of the bottom of the wedge **A-D** is:

$$L_3 = h_b \cdot \left(\frac{1}{\tan(\theta)} - \frac{1}{\tan(\alpha)} \right) \tag{14-21}$$

The length of the blade **C-D** is:

$$L_4 = \frac{h_b}{\sin(\alpha)} \tag{14-22}$$

The length of the line from the tip of the blade to the opposite side of the wedge and perpendicular to this side is:

$$L_5 = L_3 \cdot \sin(\theta) \tag{14-23}$$

The length of the line from point **A** to the intersection point of the previous line with side **A-C** is:

$$L_6 = L_3 \cdot \cos(\theta) \tag{14-24}$$

The distance from the acting point of the pore pressure force on side **A-C** to the intersection point of the previous line with side **A-C** is:

$$L_7 = L_6 - R_2 \tag{14-25}$$

The values of the acting points $\mathbf{R_2}$, $\mathbf{R_3}$ and $\mathbf{R_4}$ follow from calculated or estimated stress distributions.

The equilibrium of moments is now:

$$\sum M = N_4 \cdot R_4 - N_3 \cdot R_3 + N_2 \cdot L_7 - (S_2 + C_2) \cdot L_5 = 0 \tag{14-26}$$

14.4. Nomenclature.

a, τ_a	Adhesion or adhesive shear strength.	**kPa**
A	Adhesive shear force on the blade.	**kN**
c, τ_c	Cohesion or cohesive shear strength.	**kPa**
C_1	Cohesive shear force on the shear plane.	**kN**
C_2	Cohesive shear force on the pseudo blade (front of the wedge).	**kN**
C_3	Cohesive shear force on bottom of the wedge.	**kN**
F_h	Horizontal cutting force.	**kN**
F_v	Vertical cutting force.	**kN**
G_1	Weight of the layer cut.	**kN**
G_2	Weight of the wedge.	**kN**
h_b	Blade height.	**m**
h_i	Layer thickness.	**m**
I	Inertial force on the shear plane.	**kN**
N_1	Normal force on the shear plane.	**kN**
N_2	Normal force on the pseudo blade (front of the wedge).	**kN**
N_3	Normal force on bottom of the wedge.	**kN**
N_4	Normal force on the blade.	**kN**
K_1	Sum of N_1 and S_1 on the shear plane.	**kN**
K_2	Sum of N_2 and S_2 on the pseudo blade (front of the wedge).	**kN**
K_3	Sum of N_3 and S_3 on bottom of the wedge.	**kN**
K_4	Sum of N_4 and S_4 on the blade.	**kN**
L_1	Length of the shear plane.	**m**
L_2	Length of the pseudo blade (front of the wedge).	**m**
L_3	Length of the bottom of the wedge.	**m**
L_4	Length of the blade.	**m**
L_5	Length of the line from the tip of the blade to the opposite side of the wedge and perpendicular to this side.	**m**
L_6	Length of the line from point **A** to the intersection point of the previous line with side **A-C.**	**m**
L_7	Distance from the acting point of the pore pressure force on side **A-C** to the intersection point of the previous line L_6 with side **A-C.**	**m**
R_1	Acting point forces on the shear plane.	**m**
R_2	Acting point forces on the pseudo blade (front of the wedge).	**m**
R_3	Acting point forces on the bottom of the wedge.	**m**
R_4	Acting point forces on the blade.	**m**
S_1	Shear (friction) force on the shear plane.	**kN**
S_2	Shear (friction) force on the pseudo blade (front of the wedge).	**kN**
S_3	Shear (friction) force on the bottom of the wedge.	**kN**
S_4	Shear (friction) force on the blade.	**kN**
W_1	Pore pressure force on the shear plane.	**kN**
W_2	Pore pressure force on the pseudo blade (front of the wedge).	**kN**
W_3	Pore pressure force on the bottom of the wedge.	**kN**
W_4	Pore pressure force on the blade.	**kN**
v_c	Cutting velocity.	**m/sec**
α	Blade angle.	**°**
β	Shear angle.	**°**
θ	Wedge angle.	**°**
φ	Internal friction angle.	**°**
δ	External friction angle.	**°**
λ	Internal friction angle on pseudo blade.	**°**

Chapter 15: A Wedge in Hyperbaric Rock Cutting.

15.1. Introduction.

For completeness of the overview the equations for the cutting of the wedge mechanism for hyperbaric rock are given here without further explanation.

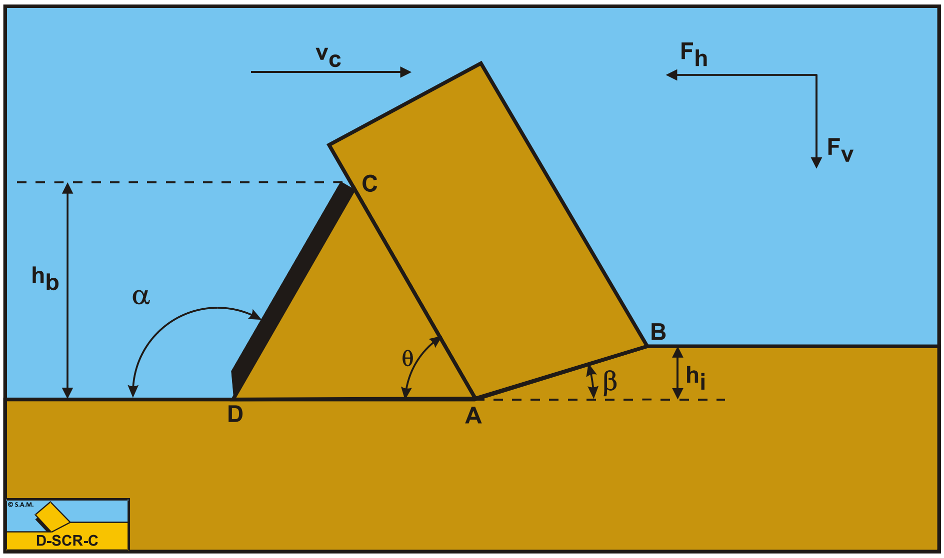

Figure 15-1: Definitions.

Definitions:

1. **A**: The wedge tip.
2. **B**: End of the shear plane.
3. **C**: The blade top.
4. **D**: The blade tip.
5. **A-B**: The shear plane.
6. **A-C**: The wedge surface.
7. **A-D**: The wedge bottom.
8. **D-C**: The blade surface.
9. **h_b**: The height of the blade.
10. **h_i**: The thickness of the layer cut.
11. **v_c**: The cutting velocity.
12. **α**: The blade angle.
13. **β**: The shear angle.
14. **F_h**: The horizontal force, the arrow gives the positive direction.
15. **F_v**: The vertical force, the arrow gives the positive direction.

15.2. The Equilibrium of Forces.

Figure 15-2 illustrates the forces on the layer of soil cut. The forces shown are valid in general for each type of soil.

The forces acting on the layer **A-B** are:

1. A normal force acting on the shear surface **N_1**, resulting from the effective grain stresses.
2. A shear force **S_1** as a result of internal friction **$N_1 \cdot \tan(\varphi)$**.
3. A force **W_1** as a result of water under pressure in the shear zone.
4. A shear force **C_1** as a result of pure cohesion **τ_c** or shear strength. This force can be calculated by multiplying the cohesive shear strength **τ_c** with the area of the shear plane.
5. A force normal to the pseudo blade **N_2**, resulting from the effective grain stresses.
6. A shear force **S_2** as a result of the soil/soil friction **$N_2 \cdot \tan(\lambda)$** between the layer cut and the wedge pseudo blade. The friction angle **λ** does not have to be equal to the internal friction angle **φ** in the shear plane, since the soil has already been deformed.

7. A shear force $\mathbf{C_2}$ as a result of the mobilized cohesion between the soil and the wedge τ_c. This force can be calculated by multiplying the cohesive shear strength τ_c of the soil with the contact area between the soil and the wedge.
8. A force $\mathbf{W_2}$ as a result of water under pressure on the wedge.

The normal force $\mathbf{N_1}$ and the shear force $\mathbf{S_1}$ can be combined to a resulting grain force $\mathbf{K_1}$.

$$K_1 = \sqrt{N_1^2 + S_1^2} \tag{15-1}$$

The forces acting on the wedge front or pseudo blade **A-C** when cutting soil, can be distinguished as:

9. A force normal to the blade $\mathbf{N_2}$, resulting from the effective grain stresses.
10. A shear force $\mathbf{S_2}$ as a result of the soil/soil friction $\mathbf{N_2 \cdot \tan(\lambda)}$) between the layer cut and the wedge pseudo blade. The friction angle λ does not have to be equal to the internal friction angle φ in the shear plane, since the soil has already been deformed.
11. A shear force $\mathbf{C_2}$ as a result of the cohesion between the layer cut and the pseudo blade τ_c. This force can be calculated by multiplying the cohesive shear strength τ_c of the soil with the contact area between the soil and the pseudo blade.
12. A force $\mathbf{W_2}$ as a result of water under pressure on the pseudo blade **A-C**.

These forces are shown in Figure 15-3. If the forces $\mathbf{N_2}$ and $\mathbf{S_2}$ are combined to a resulting force $\mathbf{K_2}$ and the adhesive force and the water under pressures are known, then the resulting force $\mathbf{K_2}$ is the unknown force on the blade. By taking the horizontal and vertical equilibrium of forces an expression for the force $\mathbf{K_2}$ on the blade can be derived.

$$K_2 = \sqrt{N_2^2 + S_2^2} \tag{15-2}$$

The forces acting on the wedge bottom **A-D** when cutting soil, can be distinguished as:

13. A force normal to the blade $\mathbf{N_3}$, resulting from the effective grain stresses.
14. A shear force $\mathbf{S_3}$ as a result of the soil/soil friction $\mathbf{N_3 \cdot \tan(\varphi)}$) between the wedge bottom and the undisturbed soil.
15. A shear force $\mathbf{C_3}$ as a result of the cohesion between the wedge bottom and the undisturbed soil τ_c. This force can be calculated by multiplying the cohesive shear strength τ_c of the soil with the contact area between the wedge bottom and the undisturbed soil.
16. A force $\mathbf{W_3}$ as a result of water under pressure on the wedge bottom **A-D**.

The normal force $\mathbf{N_3}$ and the shear force $\mathbf{S_3}$ can be combined to a resulting grain force $\mathbf{K_3}$.

$$K_3 = \sqrt{N_3^2 + S_3^2} \tag{15-3}$$

The forces acting on a straight blade **C-D** when cutting soil (see Figure 15-4), can be distinguished as:

17. A force normal to the blade $\mathbf{N_4}$**,** resulting from the effective grain stresses.
18. A shear force $\mathbf{S_4}$ as a result of the soil/steel friction $\mathbf{N_4 \cdot \tan(\delta)}$.
19. A force $\mathbf{W_4}$ as a result of water under pressure on the blade.

The normal force $\mathbf{N_4}$ and the shear force $\mathbf{S_4}$ can be combined to a resulting grain force $\mathbf{K_4}$.

$$K_4 = \sqrt{N_4^2 + S_4^2} \tag{15-4}$$

The horizontal equilibrium of forces on the layer cut:

$$\begin{aligned} \sum F_h =\; & K_1 \cdot \sin(\beta + \varphi) - W_1 \cdot \sin(\beta) + C_1 \cdot \cos(\beta) \\ & - C_2 \cdot \cos(\alpha) + W_2 \cdot \sin(\alpha) - K_2 \cdot \sin(\alpha + \lambda) = 0 \end{aligned} \tag{15-5}$$

The vertical equilibrium of forces on the layer cut:

$$\sum F_v = -K_1 \cdot \cos(\beta+\varphi) + W_1 \cdot \cos(\beta) + C_1 \cdot \sin(\beta)$$

$$+ C_2 \cdot \sin(\alpha) + W_2 \cdot \cos(\alpha) - K_2 \cdot \cos(\alpha+\lambda) = 0 \qquad (15\text{-}6)$$

The force **K1** on the shear plane is now:

$$K_1 = \frac{W_2 \cdot \sin(\lambda) + W_1 \cdot \sin(\alpha+\beta+\lambda) - C_1 \cdot \cos(\alpha+\beta+\lambda) + C_2 \cdot \cos(\lambda)}{\sin(\alpha+\beta+\lambda+\varphi)} \qquad (15\text{-}7)$$

The force **K2** on the pseudo blade is now:

$$K_2 = \frac{W_2 \cdot \sin(\alpha+\beta+\varphi) + W_1 \cdot \sin(\varphi) + C_1 \cdot \cos(\varphi) - C_2 \cdot \cos(\alpha+\beta+\varphi)}{\sin(\alpha+\beta+\lambda+\varphi)} \qquad (15\text{-}8)$$

From equation (15-8) the forces on the pseudo blade can be derived. On the pseudo blade a force component in the direction of cutting velocity **F**$_h$ and a force perpendicular to this direction **F**$_v$ can be distinguished.

$$F_h = -W_2 \cdot \sin(\alpha) + K_2 \cdot \sin(\alpha+\lambda) + C_2 \cdot \cos(\alpha) \qquad (15\text{-}9)$$

$$F_v = -W_2 \cdot \cos(\alpha) + K_2 \cdot \cos(\alpha+\lambda) - C_2 \cdot \sin(\alpha) \qquad (15\text{-}10)$$

The normal force on the shear plane is now:

$$N_1 = \frac{W_2 \cdot \sin(\lambda) + W_1 \cdot \sin(\alpha+\beta+\lambda)}{\sin(\alpha+\beta+\lambda+\varphi)} \cdot \cos(\varphi)$$

$$+ \frac{-C_1 \cdot \cos(\alpha+\beta+\lambda) + C_2 \cdot \cos(\lambda)}{\sin(\alpha+\beta+\lambda+\varphi)} \cdot \cos(\varphi) \qquad (15\text{-}11)$$

The normal force on the pseudo blade is now:

$$N_2 = \frac{W_2 \cdot \sin(\alpha+\beta+\varphi) + W_1 \cdot \sin(\varphi)}{\sin(\alpha+\beta+\lambda+\varphi)} \cdot \cos(\lambda)$$

$$+ \frac{+C_1 \cdot \cos(\varphi) - C_2 \cdot \cos(\alpha+\beta+\varphi)}{\sin(\alpha+\beta+\lambda+\varphi)} \cdot \cos(\lambda) \qquad (15\text{-}12)$$

Now knowing the forces on the pseudo blade A-C, the equilibrium of forces on the wedge A-C-D can be derived. The horizontal equilibrium of forces on the wedge is:

$$\sum F_h = W_4 \cdot \sin(\alpha) - K_4 \cdot \sin(\alpha+\delta) + K_3 \cdot \sin(\varphi)$$

$$+ C_3 - W_2 \cdot \sin(\theta) + C_2 \cdot \cos(\theta) + K_2 \cdot \sin(\theta+\lambda) = 0 \qquad (15\text{-}13)$$

The vertical equilibrium of forces on the wedge is:

$$\sum F_v = W_4 \cdot \cos(\alpha) - K_4 \cdot \cos(\alpha+\delta) + W_3 - K_3 \cdot \cos(\varphi)$$

$$- W_2 \cdot \cos(\theta) - C_2 \cdot \sin(\theta) + K_2 \cdot \cos(\theta+\lambda) = 0 \qquad (15\text{-}14)$$

The unknowns in this equation are **K₃** and **K₄**, since **K₂** has already been solved. Two other unknowns are, the external friction angle **δ**, since the external friction does not have to be fully mobilized, and the wedge angle **θ**. These 2 additional unknowns require 2 additional conditions in order to solve the problem. One additional condition is the equilibrium of moments of the wedge, a second condition the principle of minimum required cutting energy. Depending on whether the soil pushes upwards or downwards against the blade, the mobilization factor is between -1 and +1.

The force **K₃** on the bottom of the wedge is now:

$$K_3 = \frac{-W_2 \cdot \sin(\alpha+\delta-\theta) + W_3 \cdot \sin(\alpha+\delta) + W_4 \cdot \sin(\delta)}{\sin(\alpha+\delta+\varphi)} + \frac{+K_2 \cdot \sin(\alpha+\delta-\theta-\lambda) + C_3 \cdot \cos(\alpha+\delta) - C_2 \cdot \cos(\alpha+\delta-\theta)}{\sin(\alpha+\delta+\varphi)} \tag{15-15}$$

The force **K₄** on the blade is now:

$$K_4 = \frac{-W_2 \cdot \sin(\theta+\varphi) + W_3 \cdot \sin(\varphi) + W_4 \cdot \sin(\alpha+\varphi)}{\sin(\alpha+\delta+\varphi)} + \frac{+K_2 \cdot \sin(\theta+\lambda+\varphi) + C_3 \cdot \cos(\varphi) + C_2 \cdot \cos(\theta+\varphi)}{\sin(\alpha+\delta+\varphi)} \tag{15-16}$$

This results in a horizontal force on the blade of:

$$F_h = -W_4 \cdot \sin(\alpha) + K_4 \cdot \sin(\alpha+\delta) \tag{15-17}$$

And in a vertical force on the blade of:

$$F_v = -W_4 \cdot \cos(\alpha) + K_4 \cdot \cos(\alpha+\delta) \tag{15-18}$$

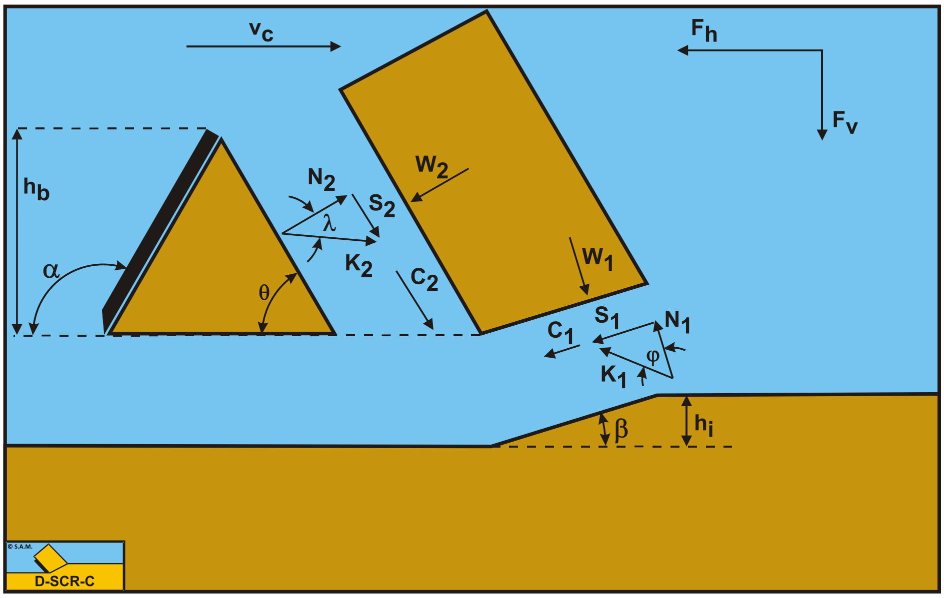

Figure 15-2: The forces on the layer cut when a wedge is present.

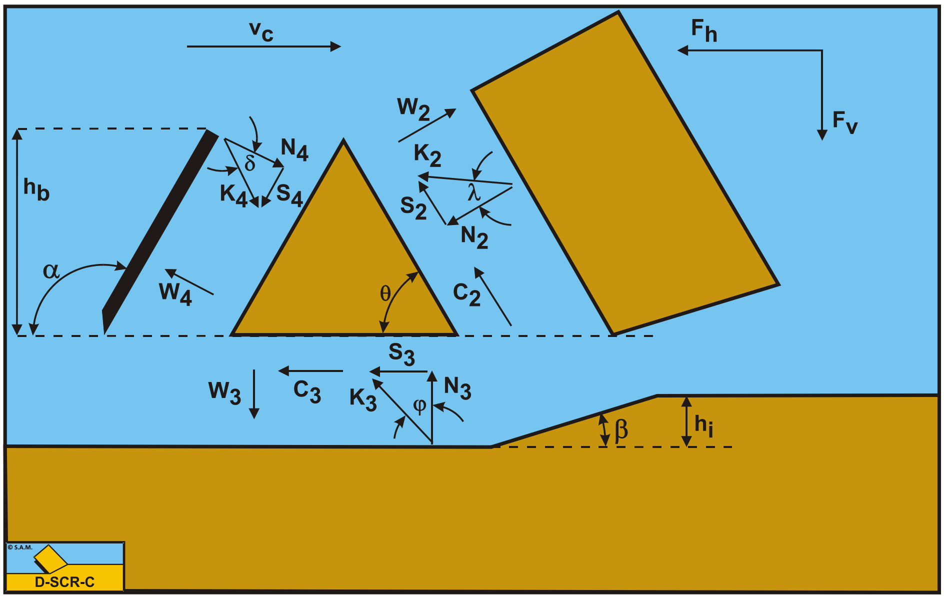

Figure 15-3: The forces on the wedge.

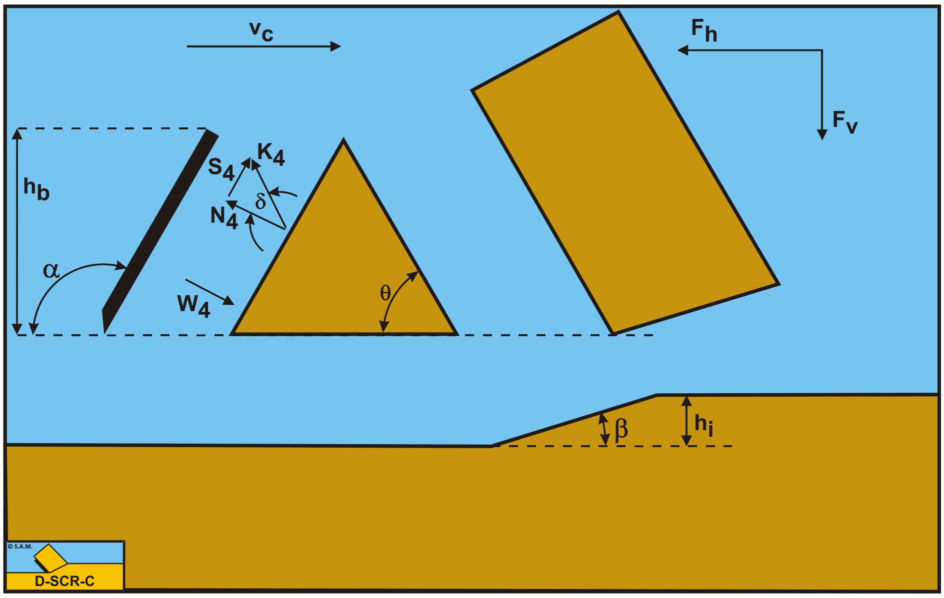

Figure 15-4: The forces on the blade when a wedge is present.

15.3. The Equilibrium of Moments.

In order to solve the problem, also the equilibrium of moments is required, since the wedge is not subject to rotational acceleration. The equilibrium of moments can be taken around each point of the wedge. Here the tip of the blade is chosen. The advantage of this is that a number of forces do not contribute to the moments on the wedge. In order to derive the equilibrium of moments equation the arms of all the forces contributing to this equilibrium have to be known. Since these arms depend on the length of all the sides in the cutting process, first these lengths are determined. The length of the shear plane **A-B** is:

$$L_1 = \frac{h_i}{\sin(\beta)} \tag{15-19}$$

The length of the pseudo blade **A-C** is:

$$L_2 = \frac{h_b}{\sin(\theta)} \tag{15-20}$$

The length of the bottom of the wedge **A-D** is:

$$L_3 = h_b \cdot \left(\frac{1}{\tan(\theta)} - \frac{1}{\tan(\alpha)} \right) \tag{15-21}$$

The length of the blade **C-D** is:

$$L_4 = \frac{h_b}{\sin(\alpha)} \tag{15-22}$$

The length of the line from the tip of the blade to the opposite side of the wedge and perpendicular to this side is:

$$L_5 = L_3 \cdot \sin(\theta) \tag{15-23}$$

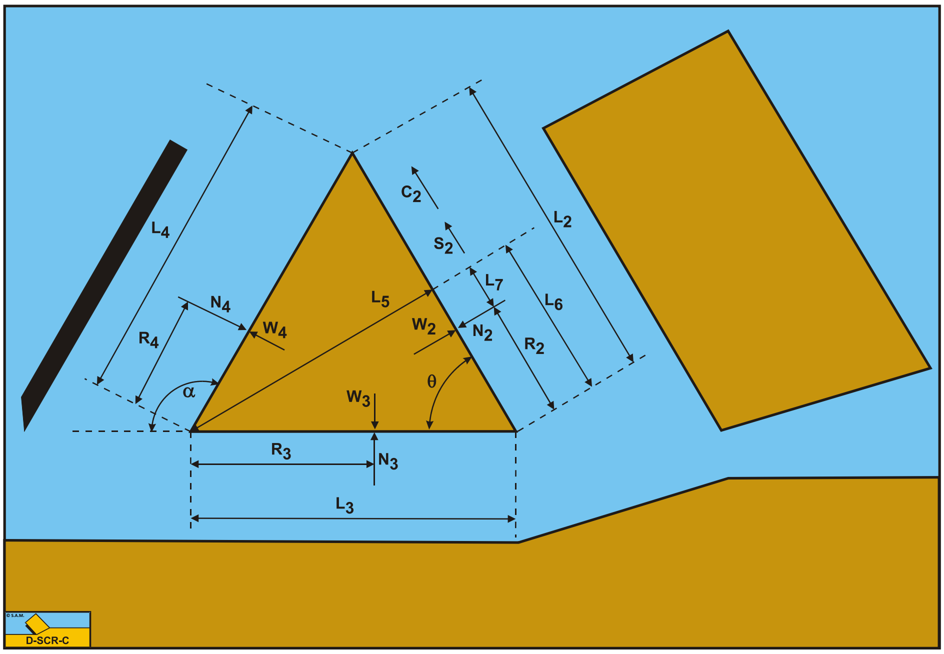

Figure 15-5: The moments on the wedge.

The length of the line from point **A** to the intersection point of the previous line with side **A-C** is:

$$L_6 = L_3 \cdot \cos(\theta) \tag{15-24}$$

The distance from the acting point of the pore pressure force on side **A-C** to the intersection point of the previous line with side **A-C** is:

$$L_7 = L_6 - R_2 \tag{15-25}$$

The values of the acting points **R**$_2$, **R**$_3$ and **R**$_4$ follow from calculated or estimated stress distributions.

The equilibrium of moments is now:

$$\begin{aligned} \sum M &= (N_4 - W_4) \cdot R_4 - (N_3 - W_3) \cdot R_3 \\ &+ (N_2 - W_2) \cdot L_7 - (S_2 + C_2) \cdot L_5 = 0 \end{aligned} \tag{15-26}$$

15.4. Nomenclature.

a, τ_a	Adhesion or adhesive shear strength.	**kPa**
A	Adhesive shear force on the blade.	**kN**
c, τ_c	Cohesion or cohesive shear strength.	**kPa**
C_1	Cohesive shear force on the shear plane.	**kN**
C_2	Cohesive shear force on the pseudo blade (front of the wedge).	**kN**
C_3	Cohesive shear force on bottom of the wedge.	**kN**
F_h	Horizontal cutting force.	**kN**
F_v	Vertical cutting force.	**kN**
G_1	Weight of the layer cut.	**kN**
G_2	Weight of the wedge.	**kN**
h_b	Blade height.	**m**
h_i	Layer thickness.	**m**
I	Inertial force on the shear plane.	**kN**
N_1	Normal force on the shear plane.	**kN**
N_2	Normal force on the pseudo blade (front of the wedge).	**kN**
N_3	Normal force on bottom of the wedge.	**kN**
N_4	Normal force on the blade.	**kN**
K_1	Sum of N_1 and S_1 on the shear plane.	**kN**
K_2	Sum of N_2 and S_2 on the pseudo blade (front of the wedge).	**kN**
K_3	Sum of N_3 and S_3 on bottom of the wedge.	**kN**
K_4	Sum of N_4 and S_4 on the blade.	**kN**
L_1	Length of the shear plane.	**m**
L_2	Length of the pseudo blade (front of the wedge).	**m**
L_3	Length of the bottom of the wedge.	**m**
L_4	Length of the blade.	**m**
L_5	Length of the line from the tip of the blade to the opposite side of the wedge and perpendicular to this side.	**m**
L_6	Length of the line from point **A** to the intersection point of the previous line with side **A-C.**	**m**
L_7	Distance from the acting point of the pore pressure force on side **A-C** to the intersection point of the previous line L_6 with side **A-C.**	**m**
R_1	Acting point forces on the shear plane.	**m**
R_2	Acting point forces on the pseudo blade (front of the wedge).	**m**
R_3	Acting point forces on the bottom of the wedge.	**m**
R_4	Acting point forces on the blade.	**m**
S_1	Shear (friction) force on the shear plane.	**kN**
S_2	Shear (friction) force on the pseudo blade (front of the wedge).	**kN**
S_3	Shear (friction) force on the bottom of the wedge.	**kN**
S_4	Shear (friction) force on the blade.	**kN**
W_1	Pore pressure force on the shear plane.	**kN**
W_2	Pore pressure force on the pseudo blade (front of the wedge).	**kN**
W_3	Pore pressure force on the bottom of the wedge.	**kN**
W_4	Pore pressure force on the blade.	**kN**
v_c	Cutting velocity.	**m/sec**
α	Blade angle.	**°**
β	Shear angle.	**°**
θ	Wedge angle.	**°**
φ	Internal friction angle.	**°**
δ	External friction angle.	**°**
λ	Internal friction angle on pseudo blade.	**°**

Chapter 16: Exercises.

16.1. Introduction.

This book is used for the courses OE4607 Introduction Dredging Engineering and OE4626 Dredging Processes I of the MSc program Offshore & Dredging Engineering of the Delft University of Technology. The exercises are questions of the exams. After each exam, the new questions will be added to this chapter.

16.2. Chapter 2: Basic Soil Mechanics.

16.2.1. MC: Mohr Circles.

Which of the following statements are true?
The **bold green** answers are true.

1. The Mohr circle gives the relation between normal stress and tensile stress.
2. In the **τ-σ** diagram for soil the positive horizontal axis gives tensile stress.
3. **In the τ-σ diagram for soil the positive horizontal axis gives compressive stress.**
4. **The Mohr circle gives the relation between normal stress and shear stress.**
5. In the **τ-σ** diagram for steel the positive horizontal axis gives compressive stress.
6. **In the τ-σ diagram for steel the positive horizontal axis gives tensile stress.**
7. **In the Mohr circle real angles are shown by a factor 2.**
8. In the Mohr circle real angles are shown by a factor 1/2.

16.2.2. MC: Active/Passive Soil Failure.

Which of the following statements are true?
The **bold green** answers are true.

1. **Passive soil failure is the failure where the soil is passive, the outside world is active.**
2. Active soil failure is the failure where the outside world is active, the soil is passive.
3. Passive soil failure is the failure where the soil is active, the outside world is passive.
4. **Active soil failure is the failure where the outside world is passive, the soil is active.**
5. **The stresses with passive failure are larger than with active failure.**
6. The stresses with active failure are larger than with passive failure.
7. Excavating soil in dredging is a typical example of active failure.
8. **Excavating soil in dredging is a typical example of passive failure.**

16.2.3. MC: Active/Passive Mode.

Which of the following statements are true? (Active mode means the horizontal stress is smaller than the vertical stress, passive mode means the horizontal stress is larger than the vertical stress).
The **bold green** answers are true.

1. **Settled or sedimented sand is in active mode.**
2. Settled or sedimented sand is in passive mode.
3. **Glacial sand, after the ice has melted is in passive mode.**
4. Glacial sand, after the ice has melted is in active mode.
5. **Glacial sand, when the layer of ice is the thickest is in active mode.**
6. Glacial sand, when the layer of ice is the thickest is in passive mode.
7. Sand with a building on top is in passive mode.
8. **Sand with a building on top is in active mode.**

16.2.4. MC: Active/Passive Soil Failure.

Which of the following statements are true? (Active failure means the horizontal stress is smaller than the vertical stress, passive failure means the horizontal stress is larger than the vertical stress).
The **bold green** answers are true.

1. The failure of a dike, because it's too high, is passive failure.
2. **At low tide a quay wall is pushed into to the water, this is active failure.**
3. A bulldozer pushes a hole in a dike, this is active failure.
4. **A very heavy truck drives over a dike. The dike collapses under the weight of the truck. This is active failure.**
5. Cutting processes in general are an example of active failure.
6. Forces occurring with active failure are always larger than with passive failure.
7. **The cutting process of a cutter head is a typical example of passive failure.**
8. The cutting process of a clamshell is a typical example of active failure.

16.2.5. MC: Mohr Circles.

Which of the following statements are true?
The **bold green** answers are true.

1. **The Mohr circle gives the relation between normal stress and shear stress.**
2. In the **τ-σ** diagram for soil the positive horizontal axis gives tensile stress.
3. In the **τ-σ** diagram for steel the positive horizontal axis gives compressive stress.
4. **On the plane of a principle normal stress there is no shear stress.**
5. **The largest shear stress is always on a plane with an angle of 45 degrees with respect to the principal stresses.**
6. **In the Mohr circle the angle between the two principal stresses is 180 degrees.**
7. Mohr circles can cross the failure line/curve.
8. Tensile failure occurs on a plane with an angle of 90 degrees with the plane with the largest shear stress.

16.2.6. Calc.: Bulldozer 1.

A bulldozer with a blade height of 0.5 m and a blade width of 3 m and a blade angle of 90 degrees is pushing sand. The internal friction angle of the sand is 45 degrees. The sand has no cohesion or adhesion and the friction between the sand and the blade is assumed to be zero, so a smooth blade. The bulldozer has a maximum forward speed of 1.5 m/sec.

1. What is the coefficient of passive failure for this sand?

$$K_p = \frac{1+\sin(\varphi)}{1-\sin(\varphi)} = \frac{1+\sin(\pi/4)}{1-\sin(\pi/4)} = 5.826 \quad \text{(-)}$$

2. What is the pushing force of the bulldozer?

The density of the dry sand ρ_s with 40% porosity is about 1.6 ton/m^3.

$$F = \frac{1}{2}\cdot\rho_s\cdot g\cdot h^2\cdot w\cdot K_p = \frac{1}{2}\cdot 1.6\cdot 9.81\cdot 0.5^2\cdot 3\cdot 5.826 = 34.3 \quad \text{(kN)}$$

3. What is the pushing power of the bulldozer?

$$P = F\cdot v = 34.3\cdot 1.5 = 51.45 \quad \text{(kW)}$$

4. Suppose a total efficiency of 1/3 of the whole drive system of the bulldozer, what is the installed power of the bulldozer.

$$P_{installed} = \frac{P}{\eta} = \frac{51.45}{0.3333} = 154.35 \quad \text{(kW)}$$

5. What is the coefficient of active failure of this sand?

$$K_a = \frac{1-\sin(\varphi)}{1+\sin(\varphi)} = \frac{1-\sin(\pi/4)}{1+\sin(\pi/4)} = 0.1716 \quad \text{(-)}$$

6. What is the force the bulldozer has to exert on the sand not to make it fail in active mode?

$$F = \frac{1}{2}\cdot\rho_s\cdot g\cdot h^2\cdot w\cdot K_a = \frac{1}{2}\cdot 1.6\cdot 9.81\cdot 0.5^2\cdot 3\cdot 0.1716 = 1.01 \quad \text{(kN)}$$

16.2.7. Calc.: Bulldozer 2.

A bulldozer with a blade height of 1.0 m and a blade angle of 90 degrees is pushing dry sand. The internal friction angle of the sand is 45 degrees. The sand has no cohesion or adhesion and the friction between the sand and the blade is assumed to be zero, so a smooth blade. The bulldozer has a maximum forward speed of 1.0 m/sec. The bulldozer has a maximum pushing force of 100 kN.

1. What is the coefficient of passive failure for this sand?

$$K_p = \frac{1+\sin(\varphi)}{1-\sin(\varphi)} = \frac{1+\sin(\pi/4)}{1-\sin(\pi/4)} = 5.826 \qquad (-)$$

2. What is the maximum width of the bulldozer blade?

The density of the dry sand ρ_s with 40% porosity is about 1.6 ton/m^3.

$$F = \frac{1}{2}\cdot\rho_s\cdot g\cdot h^2\cdot w\cdot K_p = 100\ \mathrm{kN}$$

$$w = \frac{100}{\frac{1}{2}\cdot\rho_s\cdot g\cdot h^2\cdot K_p} = \frac{100}{0.5\cdot 1.6\cdot 9.81\cdot 1^2\cdot 5.826} = 2.187\ \mathrm{m}$$

16.3. Chapter 3: The General Cutting Process..

16.3.1. MC: Cutting Mechanism.

The sine in the denominator of the generic cutting force equation has 4 angles in the argument. What happens if the sum of these 4 angles approaches 180 degrees?
The **bold green** answers are true.

1. **The cutting forces become very high.**
2. The cutting forces become negative.
3. **Nature will choose another cutting mechanism.**
4. The cutting force will be constant above a certain sum of the 4 angles.
5. The cutting process will be cavitating.
6. The adhesion will become zero.
7. The vertical cutting force will become negative.
8. The curling type will occur.

16.3.2. MC: The Snow Plough.

Which of the following statements is true?
The **bold green** answers are true.

1. The snow plough effect occurs when the sum of the 4 angles in the argument of the sine in the denominator of the generic cutting equation is larger than 180 degrees.
2. The snow plough effect occurs when the sum of the 4 angles in the argument of the sine in the denominator of the generic cutting equation is equal to 180 degrees.
3. **The snow plough effect will occur when the angle between the cutting velocity and the blade is not 90 degrees.**
4. **The snow plough effect will occur when the angle between the cutting velocity and the blade edge is smaller than 90 degrees.**
5. **The snow plough effect will occur when the angle between the cutting velocity and the blade edge is larger than 90 degrees.**
6. **The snow plough effect will push the blade sideways.**
7. The snow plough effect reduces the cutting forces strongly.
8. The snow plough effect increases the cutting forces strongly.

16.4. Chapter 4: Which Cutting Mechanism for Which Kind of Soil.

16.4.1. MC: Dry Sand Cutting.

Which of the following soil mechanical parameters play a dominant role in the cutting of dry sand?
The **bold green** answers are true.

1. **The density of the sand.**
2. **The angle of internal friction.**
3. The permeability of the sand.
4. The tensile strength of the sand.
5. **The porosity of the sand.**
6. The adhesion of the sand.
7. **The angle of external friction of the sand.**
8. The shear strength of the sand.

16.4.2. MC: Water Saturated Sand Cutting.

Which of the following soil mechanical parameters play a dominant role in the cutting of saturated sand?
The **bold green** answers are true.

1. The density of water.
2. **The angle of internal friction.**
3. **The permeability of the sand.**
4. The tensile strength of the sand.
5. **The porosity of the sand.**
6. The adhesion of the sand.
7. **The angle of external friction of the sand.**
8. The shear strength of the sand.

16.4.3. MC: Clay Cutting.

Which soil mechanical parameters dominate the cutting forces in clay?
The **bold green** answers are true.

1. The gravitational constant.
2. The density of the cutting blade.
3. **The internal shear strength or cohesion of the clay.**
4. The density of the clay.
5. The permeability of the clay.
6. **The external shear strength or adhesion of the clay.**
7. The porosity of the clay.
8. The angle of internal friction of the clay.

16.4.4. MC: Atmospheric Rock Cutting.

Which material properties play a dominant role in the atmospheric cutting of rock/stone?
The **bold green** answers are true.

1. **The external friction coefficient of the rock.**
2. The external shear strength or adhesion of the rock.
3. **The external friction angle of the rock.**
4. The density of the rock.
5. The permeability of the rock.
6. **The tensile strength of the rock.**
7. **The shear strength or cohesion of the rock.**
8. **The internal friction angle of the rock.**

16.4.5. MC: Hyperbaric Rock Cutting.

Which material/environmental properties play a dominant role in the hyperbaric cutting of rock/stone?
The **bold green** answers are true.

1. **The external friction coefficient of the rock.**
2. The external shear strength or adhesion of the rock.
3. **The external friction angle of the rock.**
4. **The hydrostatic pressure.**
5. The permeability of the rock.
6. The tensile strength of the rock.
7. **The shear strength or cohesion of the rock.**
8. **The internal friction angle of the rock.**

16.5. Chapter 5: Dry Sand Cutting.

16.5.1. MC: Soil Mechanical Parameters.

Which of the following statements is true? The cutting of dry sand is:
The **bold green** answers are true.

1. Dominated by pore pressures.
2. Dominated by adhesion and cohesion.
3. Dominated by the permeability of the sand.
4. **Dominated by the weight of the layer cut.**
5. **Influenced by the porosity of the sand.**
6. **Dominated by the inertial forces.**
7. **Influenced by the angle of external friction of the sand.**
8. Dominated by the shear strength of the sand.

16.5.2. MC: The Shear Angle.

Which of the following statements are true in the case only the weight of the soil is considered if dry sand is excavated with blade angles above 30°?
The **bold green** answers are true.

1. If the blade angle α increases, the shear angle β also increases.
2. If the angle of internal friction φ increases, the shear β angle also increases.
3. If the external friction angle δ increases, the shear β angle also increases.
4. **If the blade angle α increases, the shear angle β decreases.**
5. **If the angle of internal friction φ increases, the shear angle β decreases.**
6. **If the external friction angle δ increases, the shear angle β decreases.**

16.5.3. Calc.: The Shear Angle.

Suppose the cutting of dry sand is completely dominated by the inertial forces. Derive the analytical solution for the shear angle based on the minimum energy principle.

$$F_h = \rho_s \cdot v_c^2 \cdot h_i \cdot w \cdot \frac{\sin(\alpha)}{\sin(\alpha+\beta)} \cdot \frac{\cos(\varphi)}{\sin(\alpha+\beta+\delta+\varphi)} \cdot \sin(\alpha+\delta)$$

This is at a minimum when the denominator is at a maximum, so:

$$\frac{\partial}{\partial \beta}\left(\sin(\alpha+\beta)\cdot\sin(\alpha+\beta+\delta+\varphi)\right) = 0$$

$$\cos(\alpha+\beta)\cdot\sin(\alpha+\beta+\delta+\varphi) + \sin(\alpha+\beta)\cdot\cos(\alpha+\beta+\delta+\varphi) = \sin(2\cdot\alpha+2\cdot\beta+\delta+\varphi) = 0$$

$$2\cdot\alpha + 2\cdot\beta + \delta + \varphi = \pi$$

$$\beta = \frac{\pi}{2} - \frac{2\cdot\alpha+\delta+\varphi}{2}$$

16.6. Chapter 6: Water Saturated Sand Cutting.

16.6.1. MC: Soil Mechanical Parameters.

Which of the following soil mechanical parameters play a dominant role in the cutting of saturated sand?
The **bold green** answers are true.

1. The density of water.
2. **The angle of internal friction.**
3. **The permeability of the sand.**
4. The tensile strength of the sand.
5. **The porosity of the sand.**
6. The adhesion of the sand.
7. **The angle of external friction of the sand.**
8. The shear strength of the sand.

16.6.2. MC: Dilatation.

What is the definition of dilatation?
The **bold green** answers are true.

1. Dilatation is the increase of the pore volume of sand caused by gravitation.
2. Dilatation is the decrease of the pore volume of sand caused by shear stress.
3. Dilatation is the decrease of the pore volume of sand caused by dredging.
4. **Dilatation is the increase of the pore volume of sand caused by shear stress.**
5. Dilatation is the increase of the pore volume of sand caused by dredging.
6. Dilatation is the decrease of the pore volume of sand caused by gravitation.

16.6.3. MC: Cavitation.

Which statements are true?
The **bold green** answers are true.

1. **Cavitation is in fact the boiling of water.**
2. Cavitation at 10 degrees centigrade occurs at about 0.1 bar absolute pressure.
3. **At 100 degrees centigrade cavitation will occur at about 100 kPa.**
4. **Cavitation is the vaporization of water.**
5. **Cavitation at 10 degrees centigrade occurs at about 0.01 bar absolute pressure.**
6. **High in the mountains cavitation will occur at a temperature lower than 100 degrees centigrade.**
7. At an atmospheric pressure of 100 kPa cavitation occurs at 10 degrees centigrade.
8. High in the mountains cavitation will occur at a temperature higher than 100 degrees centigrade.

16.6.4. Calc.: Porosity.

If the porosity of sand is 42% before cutting (in situ) and 50% after cutting, what is the volume increase of the sand (grains + pores) as a fraction?

$$\varepsilon = \frac{n_{max} - n_i}{1 - n_{max}} = \frac{0.5 - 0.42}{1 - 0.5} = 0.16$$

16.6.5. Calc. : Density.

Assume a water density of 1.000 ton/m^3 and a quarts density of 2.650 ton/m^3. What is the density of a mixture with a volumetric concentration of 40% quarts (saturated sand)?

$$\rho_s = (1-n)\cdot\rho_q + n\cdot\rho_w = (1-0.4)\cdot 2.65 + 0.4\cdot 1.00 = 1.99 \qquad \text{(ton/m}^3\text{)}$$

16.6.6. Calc.: Permeability.

What is the value of the mean permeability k_m as used in the cutting equations for water saturated sand?
Consider a sand with the following properties:
Initial permeability: k_i=0.0001 m/sec
Maximum permeability: k_{max}=0.0004 m/sec

$$k_m = \frac{k_i + k_{max}}{2} = \frac{0.0001+0.0004}{2} = 0.00025 \qquad \text{(m/sec)}$$

16.6.7. Calc.: Dilatancy.

What is the value of the dilatancy ε?
Consider a sand with the following properties:
initial porosity: n_i=40%
Maximum porosity: n_{max}=50%

$$\varepsilon = \frac{n_{max} - n_i}{1 - n_{max}} = \frac{0.5-0.4}{1-0.5} = 0.20 \qquad (-)$$

16.6.8. Calc.: Transition Velocity.

Give the equation for the transition velocity from non-cavitating cutting to cavitating cutting.

$$v_c = \frac{d_1\cdot(z+10)\cdot k_m}{c_1\cdot h_i\cdot\varepsilon}$$

16.6.9. Calc.: Cutting Forces & Specific Energy.

Consider a sand with the following properties:
Angle of internal friction: φ=36º
Angle of external friction: δ=24º
Initial permeability: k_i=0.00005 m/sec
Maximum permeability: k_{max}=0.00025 m/sec
initial porosity: n_i=42%
Maximum porosity: n_{max}=50%

The cutting blade has the following properties:
The cutting angle: α=60º
The shear angle: β=20º
The blade height: h_b=0.2 m
The thickness of the layer to be cut: h_i=0.1 m
The width of the blade: w=1 m

Coefficients for the cutting equations:
The coefficient for non-cavitating cutting: c_1=0.35
The coefficient for cavitating cutting: d_1=4.5

General constants:
The density of water: ρ_w=1.025 tons/m^3
The gravitational constant: g=9.81 m/sec^2

A: What are the horizontal cutting forces at 0 m, 15 m and 30 m water depth for the non-cavitational cutting process at a cutting velocity of 0.5 m/s?

$$F_h = \frac{c_1 \cdot \rho_w \cdot g \cdot v_c \cdot h_i^2 \cdot \varepsilon \cdot w}{k_m} = \frac{0.35 \cdot 1.025 \cdot 9.81 \cdot 0.1^2 \cdot 0.16 \cdot 1}{0.00015} \cdot v_c$$

(kN)

$$= 37.54 \cdot v_c = 37.54 \cdot 0.5 = 18.77$$

The non-cavitational force does not depend on the water depth.

B: What are the horizontal cutting forces at 0 m, 15 m and 30 m water depths for the cavitational cutting process?

$$F_h = d_1 \cdot \rho_w \cdot g \cdot (z + 10) \cdot h_i \cdot w = 4.5 \cdot 1.025 \cdot 9.81 \cdot 0.1 \cdot 1 \cdot (z + 10)$$

$$= 4.52 \cdot (z + 10)$$

(kN)

This gives for 0 m water depth a force of **45.2 kN**, for 15 m water depth a force of **113 kN** and for 30 m water depth a force of **180.8 kN**.

C: At which velocities are the transitions between the cavitational and the non-cavitational cutting process at 0 m, 15 m and 30 m water depths?

$$37.54 \cdot v_c = 4.52 \cdot (z + 10) \quad \Rightarrow \quad v_c = 0.12 \cdot (z + 10)$$ **(m/sec)**

This gives for 0 m water depth a transition velocity of **1.2 m/sec**, for 15 m water depth a transition velocity of **3.0 m/sec** and for 30 m water depth a transition velocity of **4.8 m/sec**.

D: What is the specific energy at 0 m, 15 m and 30 m water depth at a cutting velocity of 1 m/s?

$$E_{sp} = \frac{F_h \cdot v_c}{h_i \cdot w \cdot v_c} = \frac{F_h}{h_i \cdot w} = \frac{F_h}{0.1 \cdot 1} = 10 \cdot F_h$$

(kPa)

At a cutting velocity of 1 m/sec the cutting process is non-cavitational at all 3 water depths, so in all 3 cases the specific energy is **375.4 kPa**.

E: What is the specific energy at a water depth of 0 m, 15 m and 30 m at a cutting velocity of 2 m/s?

At a cutting velocity of 2 m/sec, the cutting process at 0 m water depth is cavitating, giving a specific energy of **452 kPa**. At a water depth of 15 m the cutting process is non-cavitational giving a specific energy of **750.8 kPa**. At a water depth of 30 m the cutting process is also non-cavitational giving a specific energy of **750.8 kPa**.

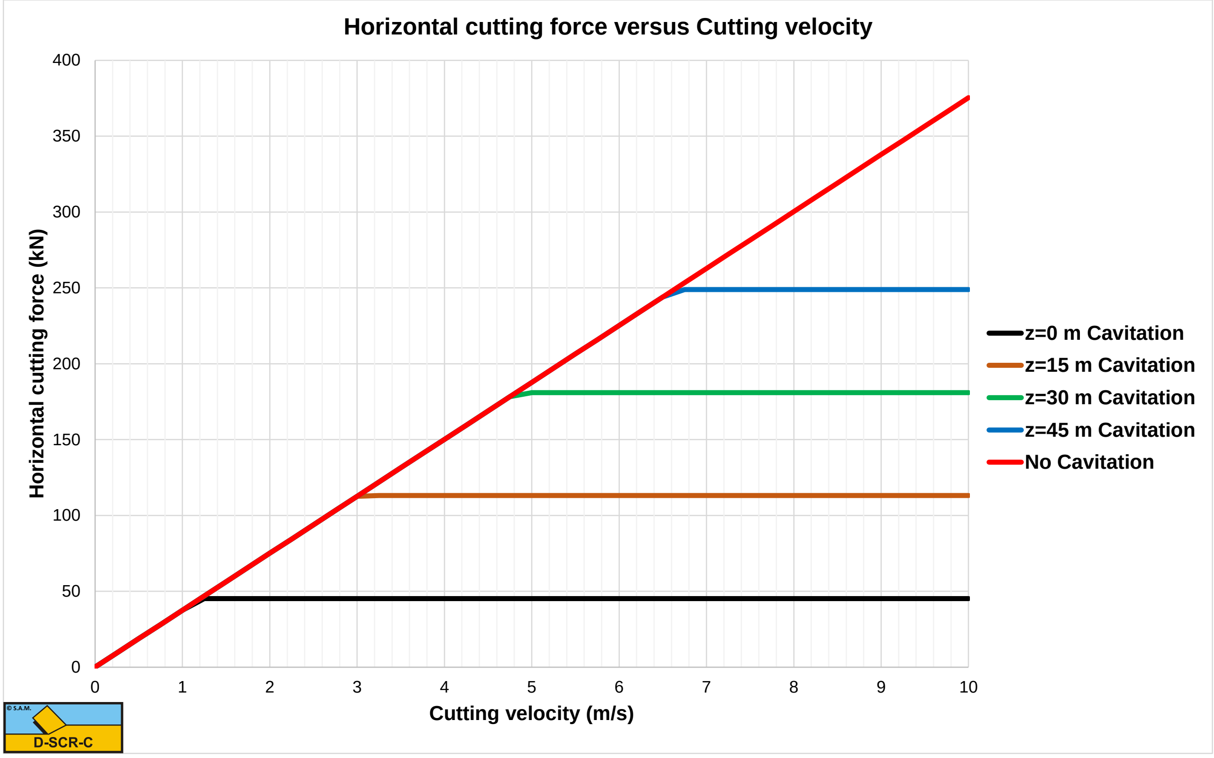

Figure 16-1: The horizontal cutting forces.

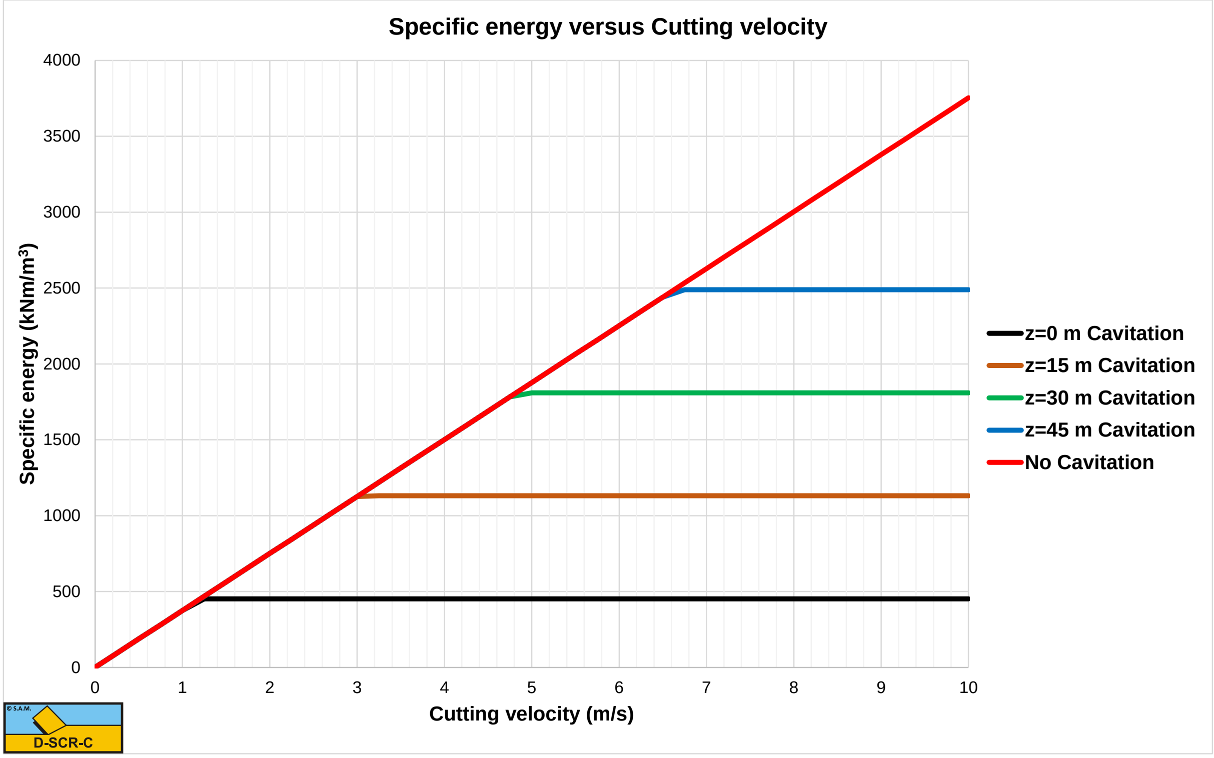

Figure 16-2: The specific energy.

F: Determine the pore pressure at the centre of the shear plane using the parallel resistor method for a cutting velocity of 0.5 m/sec.

First the 4 lengths have to be determined:

$$s_1 = \left(L_{max} - L\right)\cdot\left(\frac{\pi}{2} + \frac{\pi}{2} - \left(\alpha + \beta\right)\right) + \frac{h_b}{\sin\left(\alpha\right)} = 0.486$$

$$s_2 = 0.8\cdot L\cdot\left(\alpha + \beta\right) = 0.163$$

$$s_3 = 0.8\cdot L\cdot\left(\pi - \beta\right) = 0.327$$

$$s_4 = \left(L_{max} - L\right)\cdot\left(\pi + \beta\right) + 0.9\cdot h_i\cdot\left(\frac{h_i}{h_b}\right)^{0.5}\cdot\left(1.85\cdot\alpha\right)^2\cdot\left(\frac{k_i}{k_{max}}\right)^{0.4} = 0.636$$

Secondly the total resistance has to be determined:

$$\frac{1}{R_t} = \frac{1}{\left(\frac{s_1}{k_{max}}\right) + \left(\frac{s_2}{k_{max}}\right) + \left(\frac{s_3}{k_i}\right) + \left(\frac{s_4}{k_i}\right)} \quad \Rightarrow \quad R_t = 439$$

$$\Delta p = \rho_w\cdot g\cdot\varepsilon\cdot v_c\cdot\sin\left(\beta\right)\cdot R_t = 120.8\ (kPa)$$

Below which water depth will we have cavitation at this point?

An absolute pressure of **120.8 kPa** is reached at a water depth of **2.07 m**, so the point on the shear plane considered will cavitated for water depths below **2.07 m**.

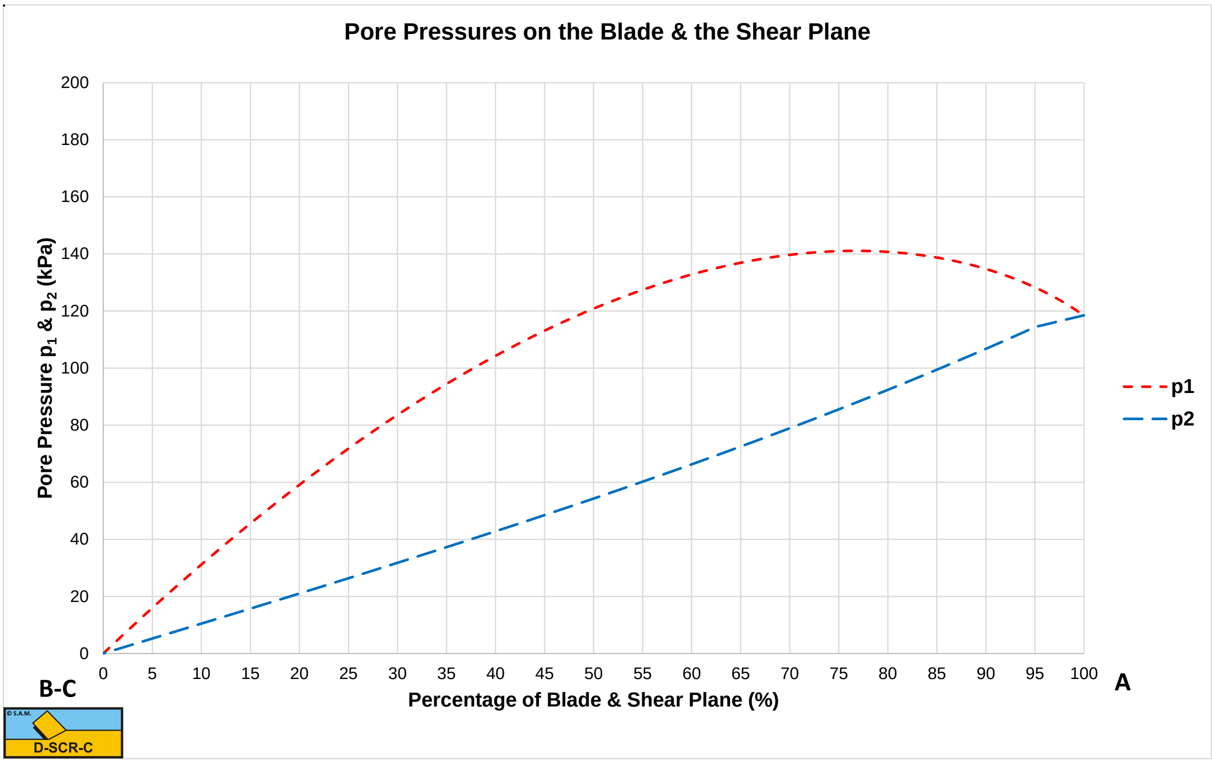

Figure 16-3: The pore pressures on blade and shear plane.

16.6.10. Calc.: Cutting Forces & Specific Energy.

Consider a sand with the following properties:
Angle of internal friction: φ=36º
Angle of external friction: δ=24º
Initial permeability: k_i=0.000025 m/sec
Maximum permeability: k_{max}=0.000125 m/sec
initial porosity: n_i=42%
Maximum porosity: n_{max}=50%

The cutting blade has the following properties:
The cutting angle: α=60º
The shear angle: β=20º
The blade height: h_b=0.2 m
The thickness of the layer to be cut: h_i=0.1 m
The width of the blade: w=1 m

Coefficients for the cutting equations:
The coefficient for non-cavitating cutting: c_1=0.45
The coefficient for cavitating cutting: d_1=5.5

General constants:
The density of water: ρ_w=1.025 tons/m^3
The gravitational constant: g=9.81 m/sec^2

A: What are the horizontal cutting forces at 0 m, 10 m and 20 m water depth for the non-cavitational cutting process at a cutting velocity of 1.5 m/s?

$$F_h = \frac{c_1 \cdot \rho_w \cdot g \cdot v_c \cdot h_i^2 \cdot \varepsilon \cdot w}{k_m} = \frac{0.45 \cdot 1.025 \cdot 9.81 \cdot 0.1^2 \cdot 0.16 \cdot 1}{0.000075} \cdot v_c \qquad \textbf{(kN)}$$

$$= 96.53 \cdot v_c = 96.53 \cdot 1.5 = 144.8$$

The non-cavitational force does not depend on the water depth.

B: What are the horizontal cutting forces at 0 m, 10 m and 20 m water depths for the cavitational cutting process?

$$F_h = d_1 \cdot \rho_w \cdot g \cdot (z+10) \cdot h_i \cdot w = 5.5 \cdot 1.025 \cdot 9.81 \cdot 0.1 \cdot 1 \cdot (z+10)$$

$$= 5.53 \cdot (z+10) \qquad \textbf{(kN)}$$

This gives for 0 m water depth a force of **55.3 kN**, for 10 m water depth a force of **110.6 kN** and for 20 m water depth a force of **165.9 kN**.

C: At which velocities are the transitions between the cavitational and the non-cavitational cutting process at 0 m, 10 m and 20 m water depths?

$$96.53 \cdot v_c = 5.53 \cdot (z+10) \quad \Rightarrow \quad v_c = 0.0573 \cdot (z+10) \qquad \textbf{(m/sec)}$$

This gives for 0 m water depth a transition velocity of **0.573 m/sec**, for 10 m water depth a transition velocity of **1.146 m/sec** and for 20 m water depth a transition velocity of **1.719 m/sec**.

D: What is the specific energy at 0 m, 10 m and 20 m water depth at a cutting velocity of 1 m/s?

$$E_{sp} = \frac{F_h \cdot v_c}{h_i \cdot w \cdot v_c} = \frac{F_h}{h_i \cdot w} = \frac{F_h}{0.1 \cdot 1} = 10 \cdot F_h \qquad \text{(kPa)}$$

At a cutting velocity of 1 m/sec the cutting process is non-cavitational at all z=0 m and non-cavitational at z=10 m and z=20 m, so in the specific energy is **553 kPa** at z=0 m and **965.3 kPa** at z=10 m and z=20 m.

E: What is the specific energy at a water depth of 0 m, 10 m and 20 m at a cutting velocity of 2 m/s?

At a cutting velocity of 2 m/sec, the cutting process at 0 m water depth is cavitating, giving a specific energy of **553 kPa**. At a water depth of 10 m the cutting process is cavitational giving a specific energy of **1106 kPa**. At a water depth of 20 m the cutting process is also cavitational giving a specific energy of **1659 kPa**.

F: Determine the pore pressure at the centre of the shear plane using the parallel resistor method for a cutting velocity of 1.5 m/sec.

First the 4 lengths have to be determined:

$$s_1 = \left(L_{max} - L\right) \cdot \left(\frac{\pi}{2} + \frac{\pi}{2} - (\alpha + \beta)\right) + \frac{h_b}{\sin(\alpha)} = 0.486$$

$$s_2 = 0.8 \cdot L \cdot (\alpha + \beta) = 0.163$$

$$s_3 = 0.8 \cdot L \cdot (\pi - \beta) = 0.327$$

$$s_4 = \left(L_{max} - L\right) \cdot (\pi + \beta) + 0.9 \cdot h_i \cdot \left(\frac{h_i}{h_b}\right)^{0.5} \cdot (1.85 \cdot \alpha)^2 \cdot \left(\frac{k_i}{k_{max}}\right)^{0.4} = 0.636$$

Secondly the total resistance has to be determined:

$$\frac{1}{R_t} = \frac{1}{\left(\frac{s_1}{k_{max}}\right) + \left(\frac{s_2}{k_{max}}\right) + \left(\frac{s_3}{k_i}\right) + \left(\frac{s_4}{k_i}\right)} \quad \Rightarrow \quad R_t = 878$$

$$\Delta p = \rho_w \cdot g \cdot \varepsilon \cdot v_c \cdot \sin(\beta) \cdot R_t = 725 \ \text{(kPa)}$$

Below which water depth will we have cavitation at this point?

An absolute hydrostatic pressure of **725 kPa** is reached at a water depth of **62.15 m**, so the point on the shear plane considered will cavitated for water depths below **62.15 m**.

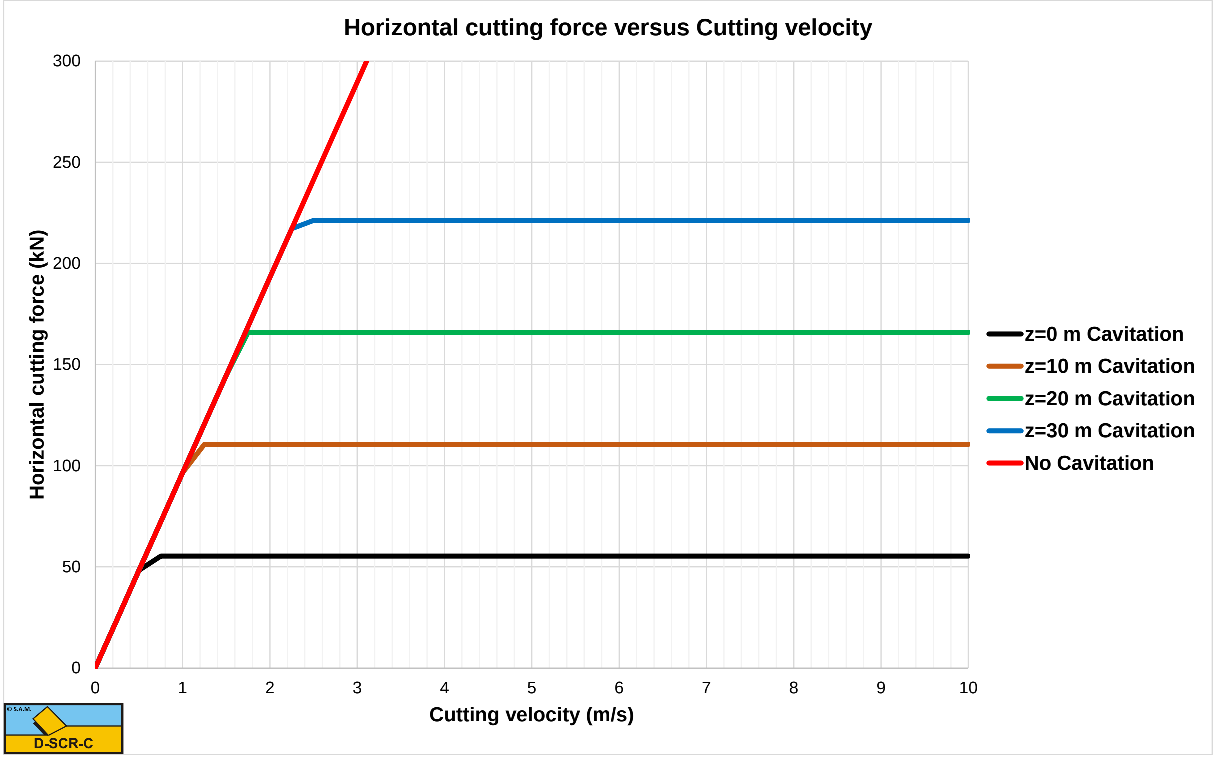

Figure 16-4: The horizontal cutting forces.

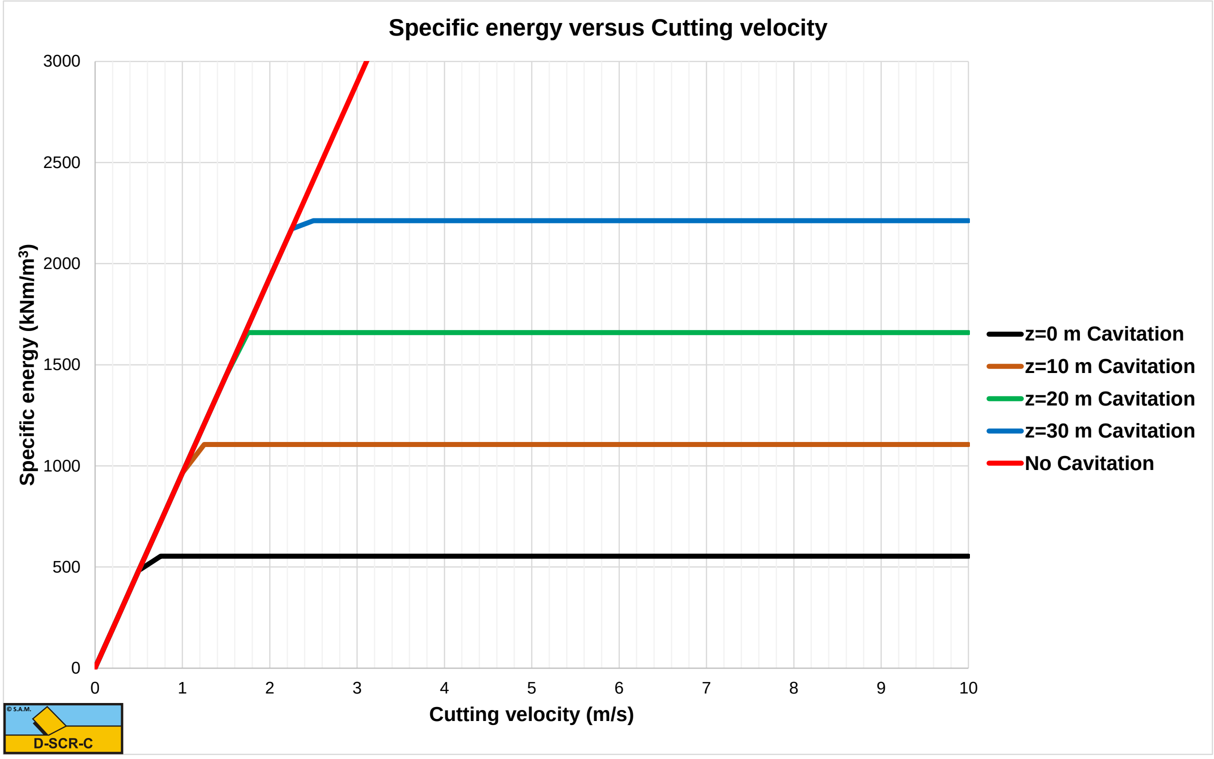

Figure 16-5: The specific energy.

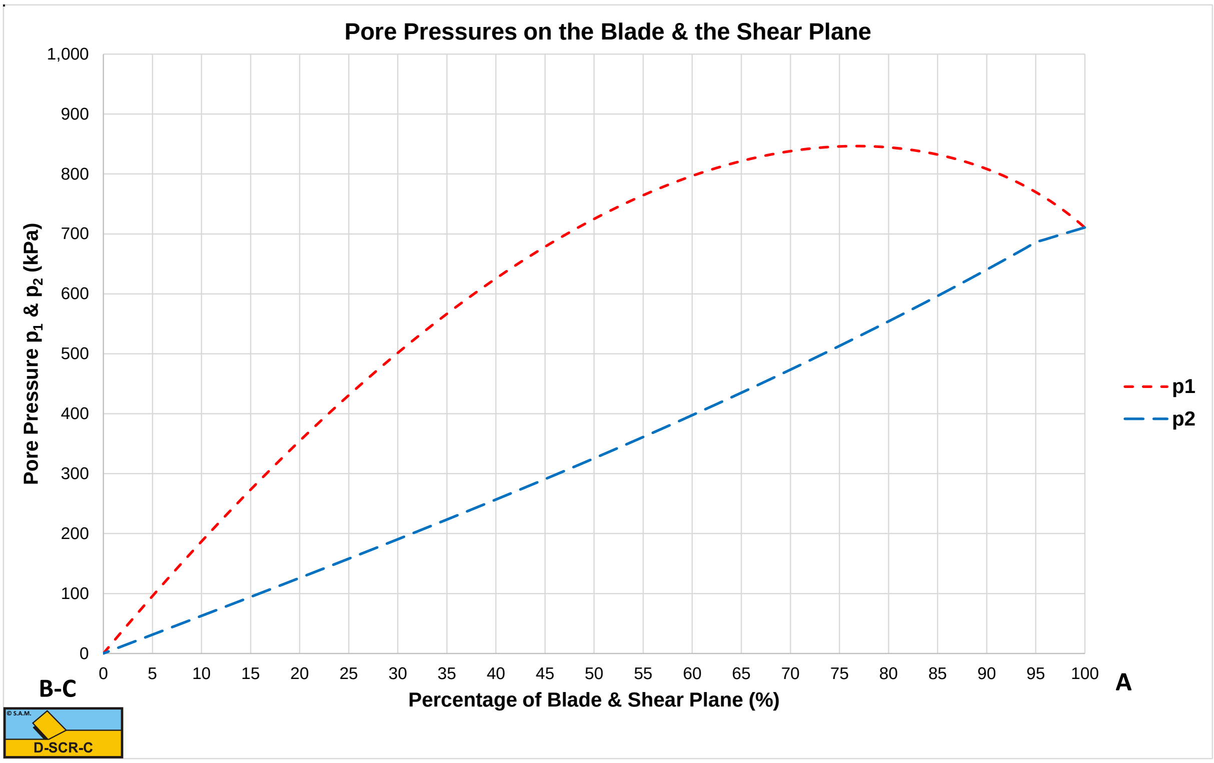

Figure 16-6: The pore pressures on blade and shear plane.

16.7. Chapter 7: Clay Cutting.

16.7.1. Calc.: Cutting Forces.

Consider clay with cohesion of 200 kPa and an adhesion of 50 kPa. The strengthening factor is 2. A blade angle of 55 degrees is used and a blade height of 0.1 m and blade width w=1 m. The layer thickness is 0.1 m. Assume the Flow Type.

What is the ac ratio r?

$$r = \frac{a \cdot h_b}{c \cdot h_i} = \frac{50 \cdot 0.1}{200 \cdot 0.1} = \frac{1}{4} \ (-)$$

What is the shear angle?

See Figure 7-21 (Figure 7.20, 1st edition), blade angle **α=55** degrees and **r=0.25** gives a shear angle **β** of about **57** degrees.

What are the horizontal and the vertical cutting forces?

Figure 7-23 (Figure 7.22, 1st edition) gives a horizontal cutting force coefficient **λ_{HF}** of about 1.3 and Figure 7-24 (Figure 7.23, first edition) gives a vertical cutting force coefficient **λ_{VF}** of 0.6. This gives for the **Flow Type**:

$$F_h = \lambda_s \cdot c \cdot h_i \cdot w \cdot \lambda_{HF} = 2 \cdot 200 \cdot 0.1 \cdot 1 \cdot 1.3 = 52 \text{ kN}$$

$$F_v = \lambda_s \cdot c \cdot h_i \cdot w \cdot \lambda_{VF} = 2 \cdot 200 \cdot 0.1 \cdot 1 \cdot 0.6 = 24 \text{ kN}$$

16.7.2. Calc.: Cutting Forces & Mechanisms.

Consider clay with cohesion of 200 kPa and an adhesion of 10 kPa. The strengthening factor is 2. A blade angle of 55 degrees is used and a blade height of 0.1 m and blade width w=1 m. The layer thickness is 0.1 m. Assume the Flow Type.

What is the ac ratio r?

$$r = \frac{a \cdot h_b}{c \cdot h_i} = \frac{10 \cdot 0.1}{200 \cdot 0.1} = \frac{1}{20} \ (-)$$

What is the shear angle?

See Figure 7-21 (Figure 7.20, 1st edition), blade angle **α=55** degrees and **r=0.05** gives a shear angle **β** of about **62** degrees.

What are the horizontal and the vertical cutting forces?

Figure 7-23 (Figure 7.22, 1st edition) gives a horizontal cutting force coefficient **λ_{HF}** of about 1.1 and Figure 7-24 (Figure 7.23, first edition) gives a vertical cutting force coefficient **λ_{VF}** of 0.7. This gives for the **Flow Type**:

$$F_h = \lambda_s \cdot c \cdot h_i \cdot w \cdot \lambda_{HF} = 2 \cdot 200 \cdot 0.1 \cdot 1 \cdot 1.1 = 44 \text{ kN}$$

$$F_v = \lambda_s \cdot c \cdot h_i \cdot w \cdot \lambda_{VF} = 2 \cdot 200 \cdot 0.1 \cdot 1 \cdot 0.7 = 28 \text{ kN}$$

If the tensile strength is -20 kPa, will we have the Tear Type or the Flow Type?

A tensile strength of -20 kPa gives a **σ_T/c** ratio of -0.1. With an **ac** ratio of r=0.05 this ratio should be below -0.5 according to Figure 7-27 (Figure 7-26, 1st edition) for the **Flow Type**, it is not, so we have the **Tear Type**.

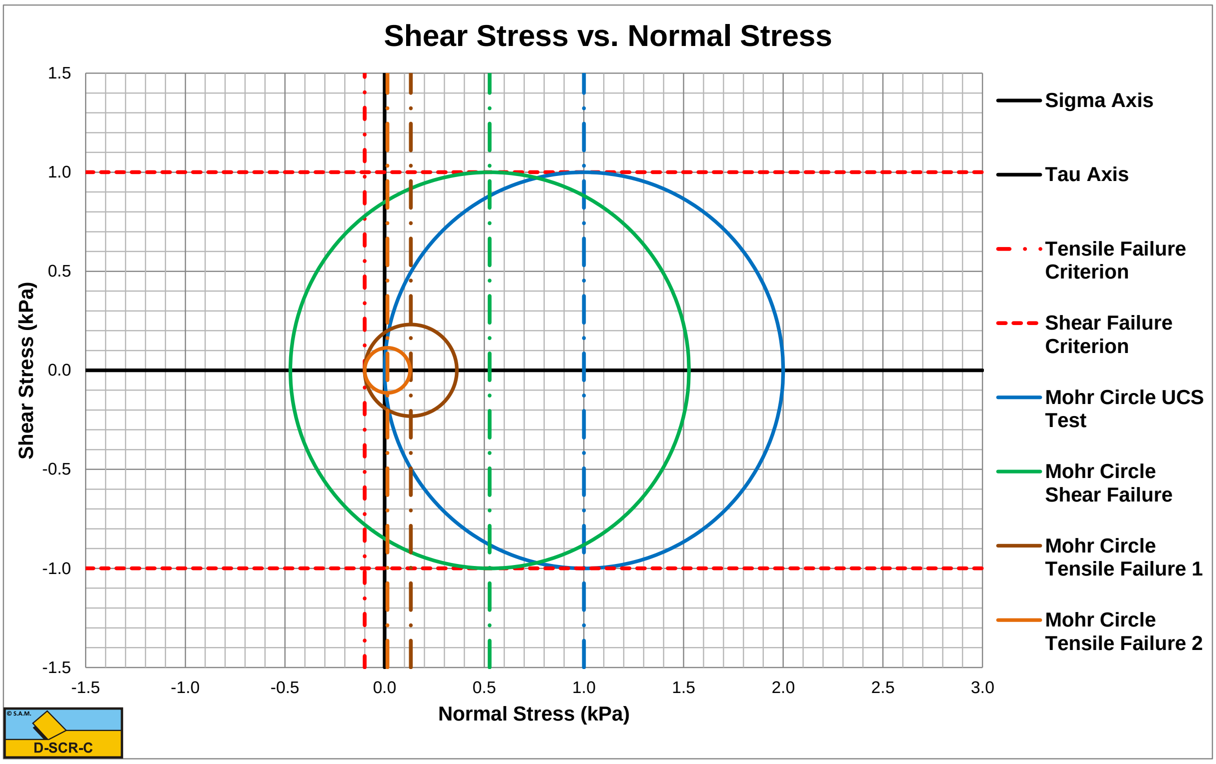

Figure 16-7: The Mohr circles.

16.8. Chapter 8: Atmospheric Rock Cutting.

16.8.1. Calc.: Cutting Forces & Mechanisms.

Consider a rock with a compressive strength of 30 MPa and a tensile strength of -2 MPa. The angle of internal friction is 18 degrees, the angle of external friction is 12 degrees. A blade angle of 55 degrees is used and a blade height of 0.2 m and blade width w=0.1 m. The layer thickness is 0.1 m.

Is the cutting process brittle shear or brittle tensile?

The cohesion or shear strength is:

$$c = \frac{UCS}{2} \cdot \left(\frac{1 - \sin(\varphi)}{\cos(\varphi)} \right) = 10.9 \text{ MPa}$$

According to Figure 8-38 (Figure 8.22, 1st edition) & (**φ=18°**), the BTS/Cohesion ratio should be above -0.3 for tensile failure, the ratio is -2/10.9=-0.183 which is above -0.3, so the process is brittle tensile failure.

If the tensile strength is -10 MPa, is the cutting process brittle shear or brittle tensile?

Now the ratio is -10/10.9=-0.92, which is below -0.3, so the process is shear failure, which is often related to ductile failure, but it is brittle shear failure.

What are the horizontal and the vertical cutting forces?

According to Figure 8-45 (Figure 8.28, 1st edition) the brittle horizontal coefficient λ_{HT} is about 3.07 and according to Figure 8-46 (Figure 8.29, 1st edition) the brittle vertical coefficient λ_{VT} about 1.30. This gives for a tensile strength of -2 MPa:

$$F_h = \lambda_{HT} \cdot \sigma_T \cdot h_i \cdot w = 3.07 \cdot 2000 \cdot 0.1 \cdot 0.1 = 61 \text{ kN}$$

$$F_v = \lambda_{VT} \cdot \sigma_T \cdot h_i \cdot w = 1.30 \cdot 2000 \cdot 0.1 \cdot 0.1 = 26 \text{ kN}$$

For the case with a tensile strength of -10 MPa, the following is found:

According to Figure 8-31 (Figure 8.16, 1st edition) the brittle shear horizontal coefficient λ_{HF} is about 1.61 and according to Figure 8-32 (Figure 8.17, 1st edition) the brittle shear vertical coefficient λ_{VF} about 0.68. This gives for a compressive strength of 30 MPa (cohesion about 10.9 MPa):

$$F_h = \lambda_{HF} \cdot c \cdot h_i \cdot w = 1.61 \cdot 10900 \cdot 0.1 \cdot 0.1 = 176 \text{ kN}$$

$$F_v = \lambda_{VF} \cdot c \cdot h_i \cdot w = 0.68 \cdot 10900 \cdot 0.1 \cdot 0.1 = 75 \text{ kN}$$

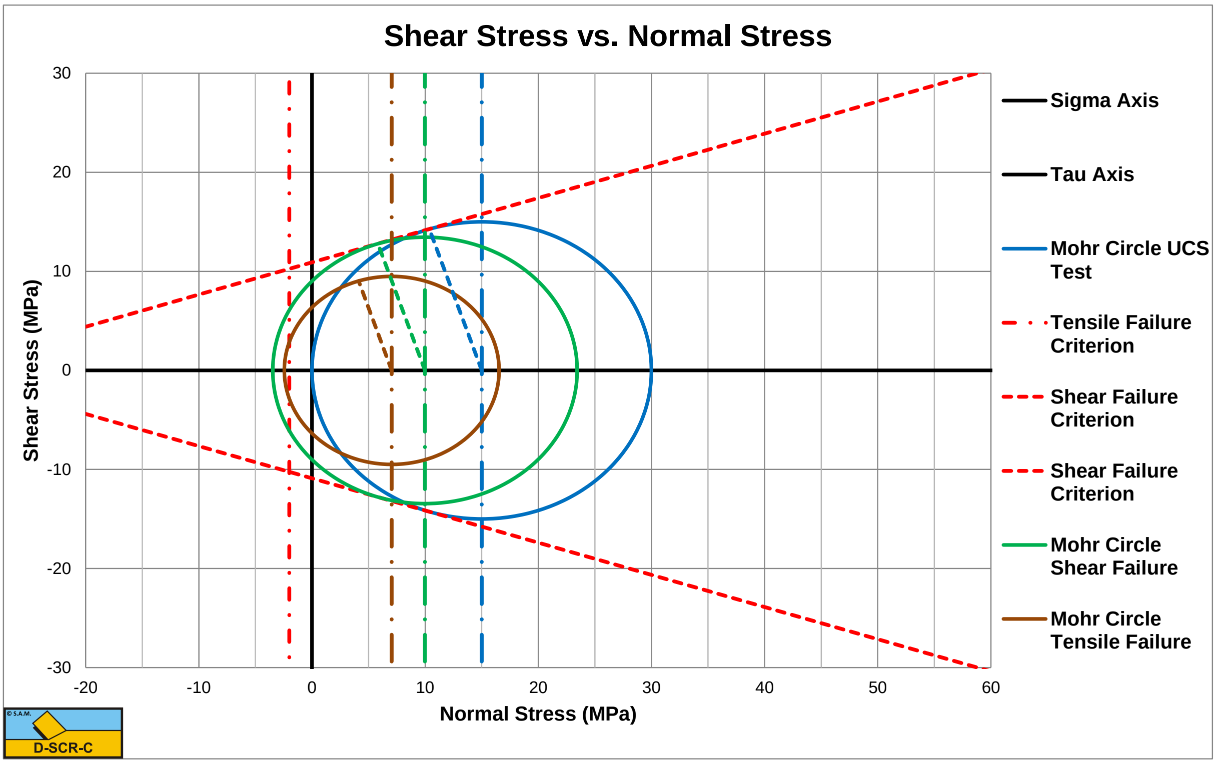

Figure 16-8: The Mohr circles for a tensile strength of -2 MPa. Tensile Failure.

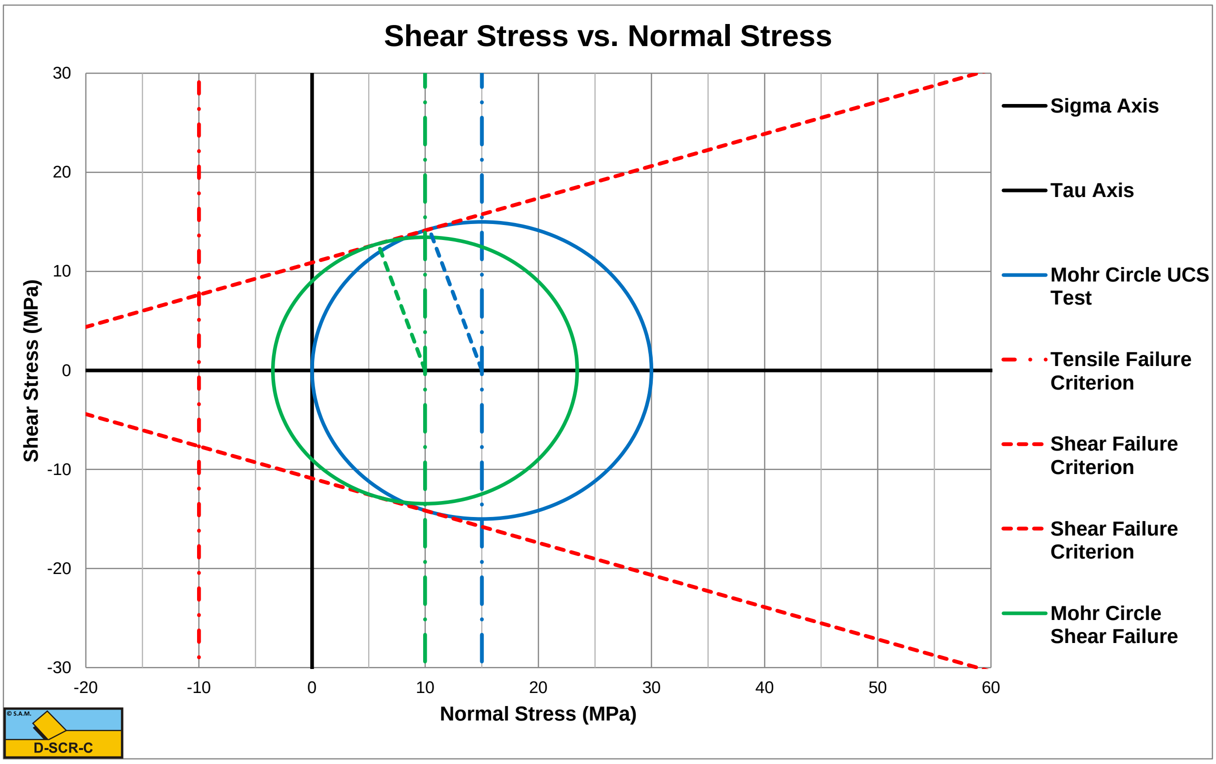

Figure 16-9: The Mohr circles for a tensile strength of -10 MPa. Shear Failure.

16.8.2. Calc.: Cutting Forces & Mechanisms.

Consider a rock with a compressive strength of 100 MPa and a tensile strength of -10 MPa. The angle of internal friction is 20 degrees, the angle of external friction is 13.33 degrees. A blade angle of 60 degrees is used and a blade height of 0.1 m and blade width w=1 m. The layer thickness is 0.1 m.

The shear angle is:

$$\beta = \frac{\pi}{2} - \frac{\alpha + \delta + \varphi}{2} = 43.33 \text{ degrees}$$

The cohesion or shear strength is:

$$c = \frac{UCS}{2} \cdot \left(\frac{1 - \sin(\varphi)}{\cos(\varphi)} \right) = 35 \text{ MPa}$$

The normal stress on the shear plane is:

$$\sigma_{N1} = \frac{-c \cdot \cos(\alpha + \beta + \delta)}{\sin(\alpha + \beta + \delta + \varphi)} \cdot \cos(\varphi) = 21.52 \text{ MPa}$$

The shear stress on the shear plane is:

$$\tau_{S1} = c + \sigma_{N1} \cdot \tan(\varphi) = 42.84 \text{ MPa}$$

The normal stress in the center of the Mohr circle is:

$$\sigma_C = \sigma_{N1} + \tau_{S1} \cdot \tan(\varphi) = 37.1 \text{ MPa}$$

The radius of this Mohr circle is now:

$$R = \frac{\tau_{S1}}{\cos(\varphi)} = 45.59 \text{ MPa}$$

The minimum principle stress of this Mohr circle is:

$$\sigma_{min} = \sigma_C - R = -8.48 \text{ MPa}$$

Since -8.48 MPa>-10 MPa there is no tensile failure but shear failure.

The horizontal force is now:

$$F_h = \frac{2 \cdot c \cdot h_i \cdot w \cdot \cos(\varphi) \cdot \sin(\alpha + \delta)}{1 + \cos(\alpha + \delta + \varphi)} = \lambda_{HF} \cdot c \cdot h_i \cdot w = 1.912 \cdot 35 \cdot 0.1 \cdot 1 = 6.691 \text{ MN}$$

The vertical force is now:

$$F_v = \frac{2 \cdot c \cdot h_i \cdot w \cdot \cos(\varphi) \cdot \cos(\alpha + \delta)}{1 + \cos(\alpha + \delta + \varphi)} = \lambda_{VF} \cdot c \cdot h_i \cdot w = 0.572 \cdot 35 \cdot 0.1 \cdot 1 = 2.0 \text{ MN}$$

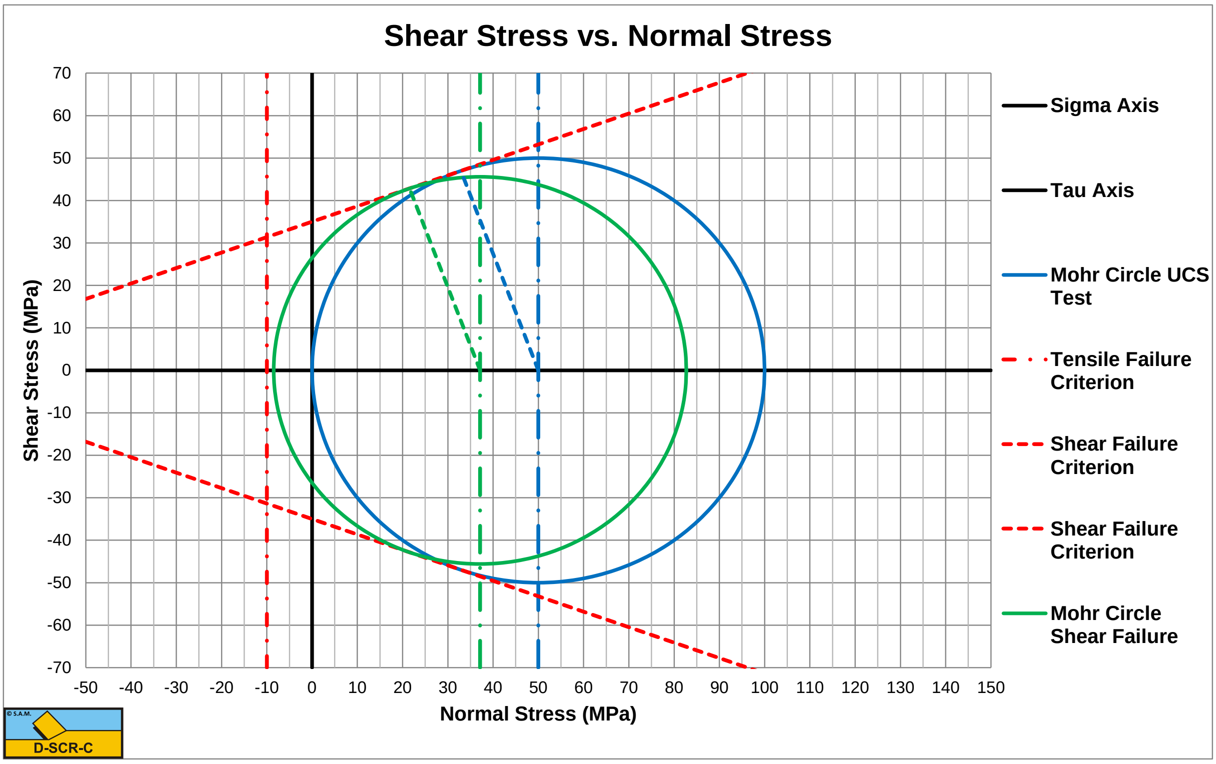

Figure 16-10: The Mohr circles with tensile strength of -10 MPa (UCS=100 MPa, φ=20°). Shear Failure.

16.8.3. Calc.: Cutting Forces & Mechanisms.

Consider a rock with a compressive strength of 100 MPa and a tensile strength of -5 MPa. The angle of internal friction is 20 degrees, the angle of external friction is 13.33 degrees. A blade angle of 60 degrees is used and a blade height of 0.1 m and blade width w=1 m. The layer thickness is 0.1 m.

The shear angle is:

$$\beta = \frac{\pi}{2} - \frac{\alpha + \delta + \varphi}{2} = 43.33 \text{ degrees}$$

The cohesion or shear strength is:

$$c = \frac{UCS}{2} \cdot \left(\frac{1 - \sin(\varphi)}{\cos(\varphi)} \right) = 35 \text{ MPa}$$

The normal stress on the shear plane is:

$$\sigma_{N1} = \frac{-c \cdot \cos(\alpha + \beta + \delta)}{\sin(\alpha + \beta + \delta + \varphi)} \cdot \cos(\varphi) = 21.52 \text{ MPa}$$

The shear stress on the shear plane is:

$$\tau_{S1} = c + \sigma_{N1} \cdot \tan(\varphi) = 42.84 \text{ MPa}$$

The normal stress in the center of the Mohr circle is:

$$\sigma_C = \sigma_{N1} + \tau_{S1} \cdot \tan(\varphi) = 37.1 \text{ MPa}$$

The radius of this Mohr circle is now:

$$R = \frac{\tau_{S1}}{\cos(\varphi)} = 45.59 \text{ MPa}$$

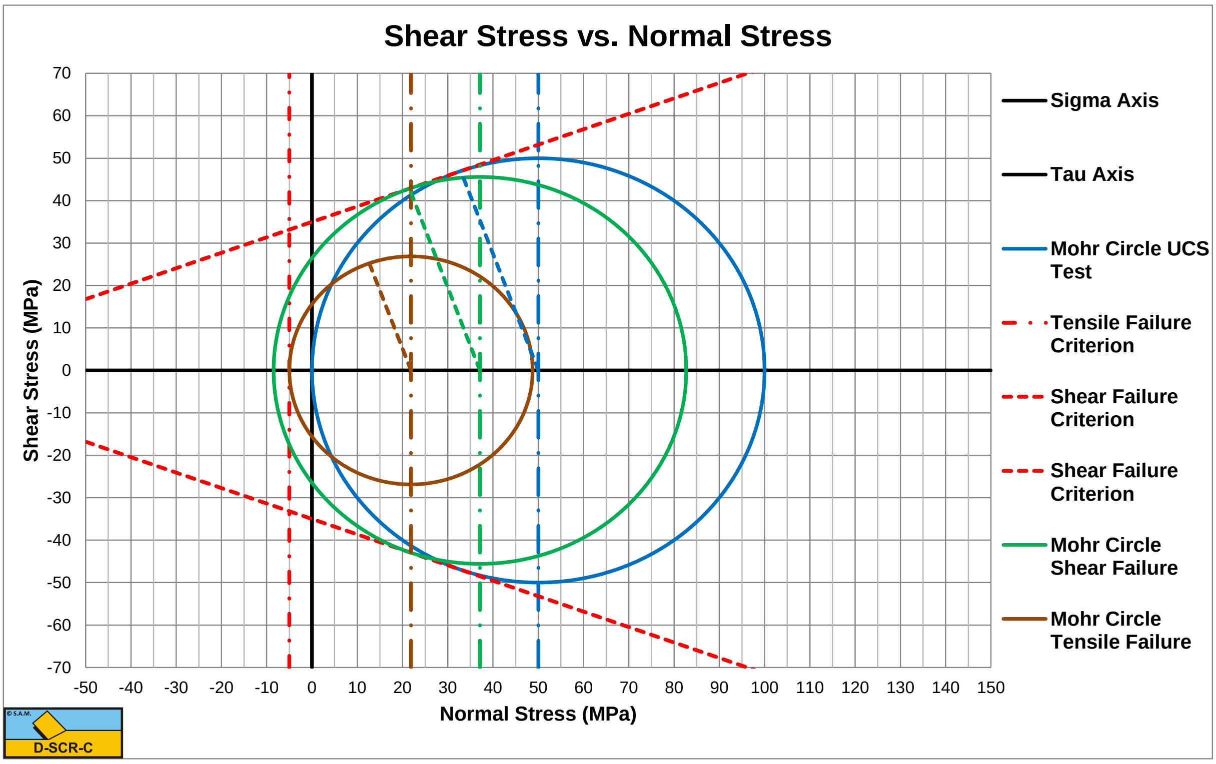

Figure 16-11: The Mohr circles with tensile strength of -5 MPa (UCS=100 MPa, φ=20°). Tensile Failure.

The minimum principle stress of this Mohr circle is:

$$\sigma_{min} = \sigma_C - R = -8.48 \text{ MPa}$$

Since -8.48 MPa<-5 MPa there is tensile failure but no shear failure. This results in another shear angle of 25.8°.

The horizontal force is now, Figure 8-45 (Figure 8.28, 1st edition):

$$F_h = \frac{2 \cdot c_m \cdot h_i \cdot w \cdot \cos(\varphi) \cdot \sin(\alpha + \delta)}{1 + \cos(\alpha + \delta + \varphi)} = \lambda_{HT} \cdot \sigma_T \cdot h_i \cdot w = 4 \cdot 5 \cdot 0.1 \cdot 1 = 2 \text{ MN}$$

The vertical force is now, Figure 8-46 (Figure 8.29, 1st edition):

$$F_v = \frac{2 \cdot c_m \cdot h_i \cdot w \cdot \cos(\varphi) \cdot \cos(\alpha + \delta)}{1 + \cos(\alpha + \delta + \varphi)} = \lambda_{VT} \cdot \sigma_T \cdot h_i \cdot w = 1.25 \cdot 5 \cdot 0.1 \cdot 1 = 0.625 \text{ MN}$$

16.8.4. Calc.: Cutting Forces & Mechanisms.

Consider a rock with a compressive strength of 60 MPa and a tensile strength of -10 MPa. The angle of internal friction is 20 degrees, the angle of external friction is 13.33 degrees. A blade angle of 60 degrees is used and a blade height of 0.1 m and blade width w=1 m. The layer thickness is 0.1 m.

The shear angle is:

$$\beta = \frac{\pi}{2} - \frac{\alpha + \delta + \varphi}{2} = 43.33 \text{ degrees}$$

The cohesion or shear strength is:

$$c = \frac{UCS}{2} \cdot \left(\frac{1 - \sin(\varphi)}{\cos(\varphi)} \right) = 21 \text{ MPa}$$

The normal stress on the shear plane is:

$$\sigma_{N1} = \frac{-c \cdot \cos(\alpha + \beta + \delta)}{\sin(\alpha + \beta + \delta + \varphi)} \cdot \cos(\varphi) = 12.9 \text{ MPa}$$

The shear stress on the shear plane is:

$$\tau_{S1} = c + \sigma_{N1} \cdot \tan(\varphi) = 25.7 \text{ MPa}$$

The normal stress in the center of the Mohr circle is:

$$\sigma_C = \sigma_{N1} + \tau_{S1} \cdot \tan(\varphi) = 22.27 \text{ MPa}$$

The radius of this Mohr circle is now:

$$R = \frac{\tau_{S1}}{\cos(\varphi)} = 27.35 \text{ MPa}$$

The minimum principle stress of this Mohr circle is:

$$\sigma_{min} = \sigma_C - R = -5.09 \text{ MPa}$$

Since -5.09 MPa>-10 MPa there is no tensile failure but shear failure.

The horizontal force is now:

$$F_h = \frac{2 \cdot c \cdot h_i \cdot w \cdot \cos(\varphi) \cdot \sin(\alpha + \delta)}{1 + \cos(\alpha + \delta + \varphi)} = \lambda_{HF} \cdot c \cdot h_i \cdot w = 1.912 \cdot 21 \cdot 0.1 \cdot 1 = 4.02 \text{ MN}$$

The vertical force is now:

$$F_v = \frac{2 \cdot c \cdot h_i \cdot w \cdot \cos(\varphi) \cdot \cos(\alpha + \delta)}{1 + \cos(\alpha + \delta + \varphi)} = \lambda_{VF} \cdot c \cdot h_i \cdot w = 0.572 \cdot 21 \cdot 0.1 \cdot 1 = 1.20 \text{ MN}$$

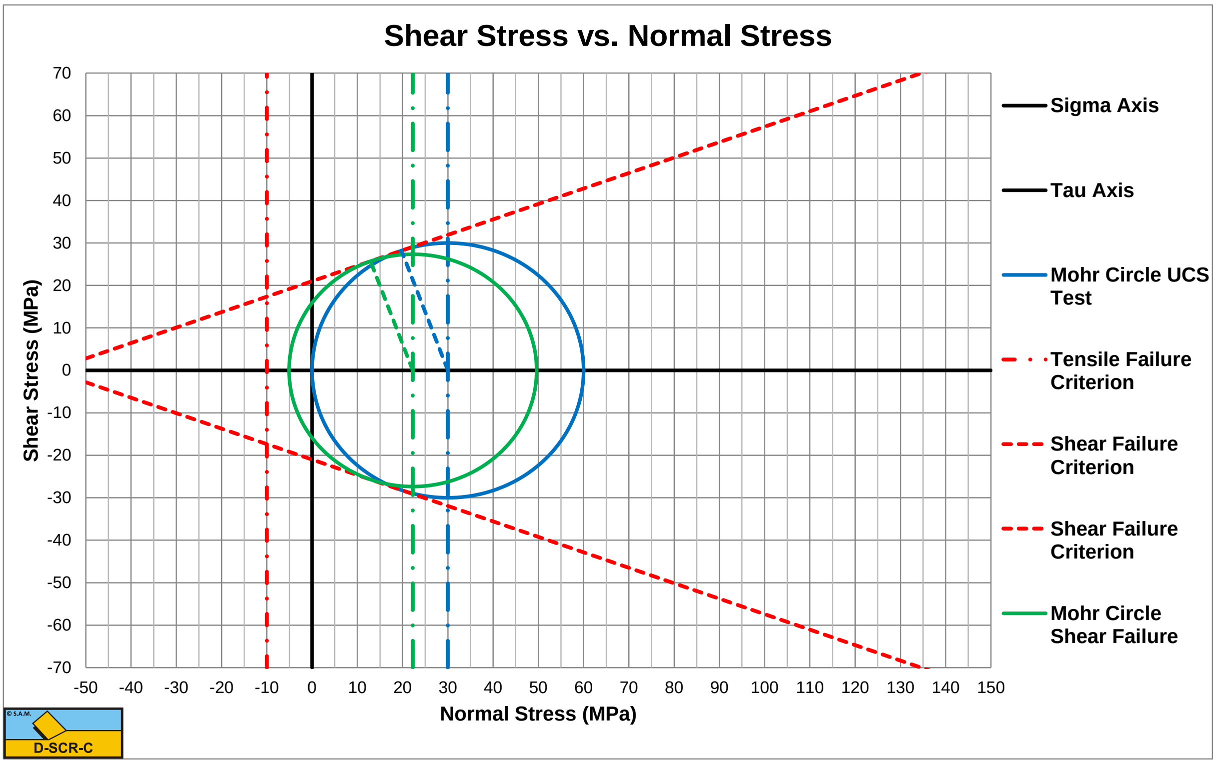

Figure 16-12: The Mohr circles with tensile strength of -10 MPa (UCS=60 MPa, φ=20°). Shear Failure.

16.8.5. Calc.: Cutting Forces & Mechanisms.

Consider a rock with a compressive strength of 60 MPa and a tensile strength of -3 MPa. The angle of internal friction is 20 degrees, the angle of external friction is 13.33 degrees. A blade angle of 60 degrees is used and a blade height of 0.1 m and blade width w=1 m. The layer thickness is 0.1 m.

The shear angle is:

$$\beta = \frac{\pi}{2} - \frac{\alpha + \delta + \varphi}{2} = 43.33 \text{ degrees}$$

The cohesion or shear strength is:

$$c = \frac{UCS}{2} \cdot \left(\frac{1 - \sin(\varphi)}{\cos(\varphi)} \right) = 21 \text{ MPa}$$

The normal stress on the shear plane is:

$$\sigma_{N1} = \frac{-c \cdot \cos(\alpha + \beta + \delta)}{\sin(\alpha + \beta + \delta + \varphi)} \cdot \cos(\varphi) = 12.9 \text{ MPa}$$

The shear stress on the shear plane is:

$$\tau_{S1} = c + \sigma_{N1} \cdot \tan(\varphi) = 25.7 \text{ MPa}$$

The normal stress in the center of the Mohr circle is:

$$\sigma_C = \sigma_{N1} + \tau_{S1} \cdot \tan(\varphi) = 22.27 \text{ MPa}$$

The radius of this Mohr circle is now:

$$R = \frac{\tau_{S1}}{\cos(\varphi)} = 27.35 \text{ MPa}$$

The minimum principle stress of this Mohr circle is:

$$\sigma_{min} = \sigma_C - R = -5.09 \text{ MPa}$$

Since -5.09 MPa<-3 MPa there is tensile failure but no shear failure. This results in another shear angle of 25.8°.

The horizontal force is now, Figure 8-45 (Figure 8.28, 1st edition):

$$F_h = \frac{2 \cdot c_m \cdot h_i \cdot w \cdot \cos(\varphi) \cdot \sin(\alpha + \delta)}{1 + \cos(\alpha + \delta + \varphi)} = \lambda_{HT} \cdot \sigma_T \cdot h_i \cdot w = 4.1 \cdot 3 \cdot 0.1 \cdot 1 = 1.24 \text{ MN}$$

The vertical force is now, Figure 8-46 (Figure 8.29, 1st edition):

$$F_v = \frac{2 \cdot c_m \cdot h_i \cdot w \cdot \cos(\varphi) \cdot \cos(\alpha + \delta)}{1 + \cos(\alpha + \delta + \varphi)} = \lambda_{VT} \cdot \sigma_T \cdot h_i \cdot w = 1.24 \cdot 3 \cdot 0.1 \cdot 1 = 0.371 \text{ MN}$$

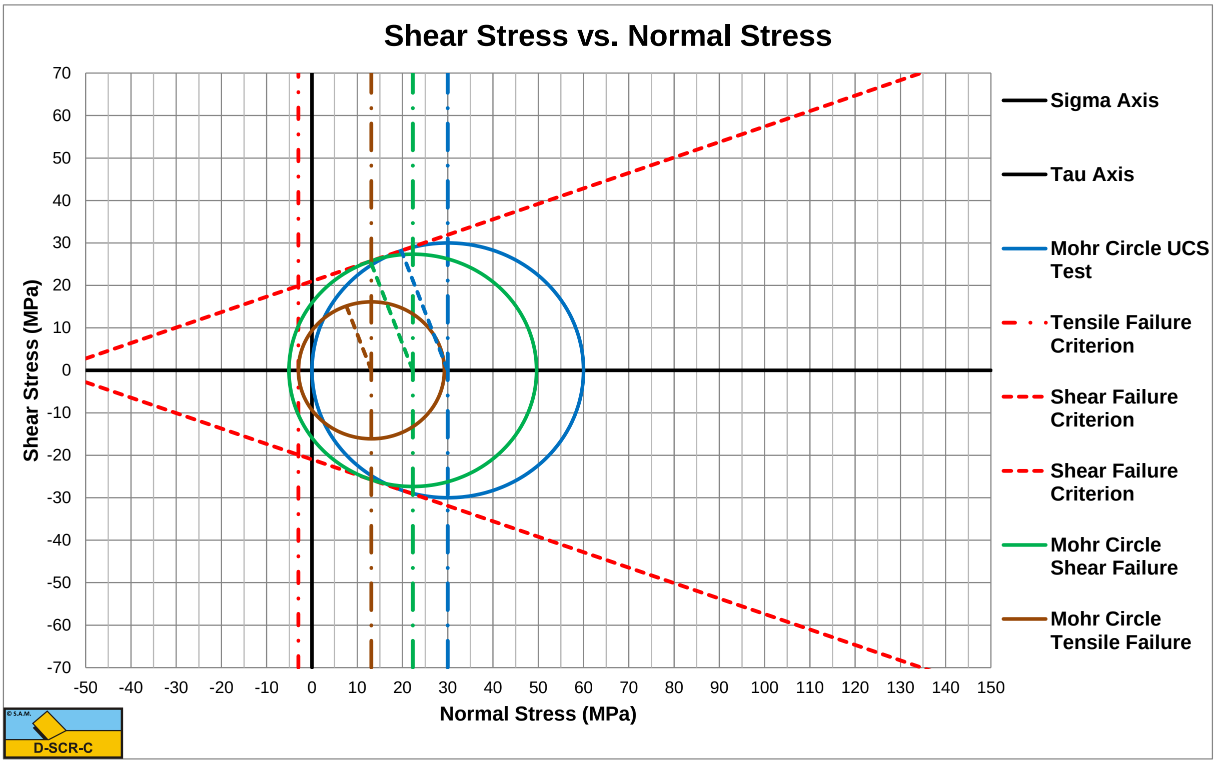

Figure 16-13: The Mohr circles with tensile strength of -3 MPa (UCS=60 MPa, φ=20º). Tensile Failure.

16.9. Chapter 9: Hyperbaric Rock Cutting.

16.9.1. MC: Soil Mechanical Parameters.

Which material/environmental properties play a dominant role in the hyperbaric cutting of rock/stone at high cutting velocities?
The **bold green** answers are true.

1. **The ratio of the hydrostatic pressure to the cohesion of the rock.**
2. The external shear strength or adhesion of the rock.
3. **The external friction angle of the rock.**
4. The hydrostatic pressure to adhesion ratio.
5. The permeability of the rock.
6. The tensile strength of the rock.
7. **The shear strength or cohesion of the rock.**
8. **The internal friction angle of the rock.**

1.1.1 Exercise 2.

Consider a rock with a compressive strength of 30 MPa and a tensile strength of -2 MPa. The angle of internal friction is 20 degrees, the angle of external friction is 13 degrees. A blade angle of 60 degrees is used and a blade height of 0.1 m and blade width w=0.05 m. The layer thickness is 0.01 m. The water depth is 1000 m.

What is the hydrostatic pressure to cohesion ratio **r_z**?

The cohesion or shear strength is according to equation (8-117) (eqn 8.77, 1st edition):

$$c = \frac{UCS}{2} \cdot \left(\frac{1 - \sin(\varphi)}{\cos(\varphi)} \right) = 10.5 \text{ MPa}$$

The hydrostatic pressure to cohesion ratio **r_z** is according to equation (9-29) (eqn 9-27, 1st edition):

$$r_z = \frac{\rho_l \cdot g \cdot (z + 10)}{c} = \frac{1.025 \cdot 9.81 \cdot (1000 + 10)}{10500} = 0.967$$

What is the mobilized blade height **$h_{b,m}$**?

The ratio **$h_{b,m}/h_i$=0.65**, see Figure 9-17 (Figure 9-16, 1st edition).

$$h_{b,m} = 0.65 \cdot h_i = 0.65 \cdot 0.01 = 0.0065 \text{ (m)}$$

So what is the cutting mechanism with the original blade height of 0.1 m?

Since the mobilized blade height **$h_{b,m}$** is smaller than the blade height **h_b**, the Curling Type will occur.

What are the horizontal and the vertical cutting forces?

The horizontal force coefficient is about 2.9 according to Figure 9-19 (Figure 9-18, 1st edition) and the vertical force coefficient is about 0.68 Figure 9-20 (Figure 9-19, 1st edition).

Horizontal $F_h = \lambda_{HC} \cdot c \cdot h_i \cdot w = 2.9 \cdot 10500 \cdot 0.01 \cdot 0.05 = 15.23$ **(kN)**
Vertical $F_v = \lambda_{VC} \cdot c \cdot h_i \cdot w = 0.68 \cdot 10500 \cdot 0.01 \cdot 0.05 = 3.57$ **(kN)**

What is the shear angle β?

The shear angle is **β=41°**, according to Figure 9-18 (Figure 9-17, 1st edition).

Chapter 17: Bibliography.

Abelev, A., & Valent, P. (2010). *Strain rate dependency of strength of soft marine deposits of the Gulf of Mexico.* Stennis Space Center, MS 39529, USA.: Naval Research Laboratory.

Becker, S., Miedema, S., Jong, P., & Wittekoek, S. (1992). On the Closing Process of Clamshell Dredges in Water Saturated Sand. *WODCON XIII* (p. 22 pages). Bombay, India: WODA.

Becker, S., Miedema, S., Jong, P., & Wittekoek, S. (1992, September). The Closing Process of Clamshell Dredges in Water Saturated Sand. *Terra et Aqua, No. 49*, 22 pages.

Biot, M. (1941). General theory of three dimensional consolidation. *Journal of Applied Physics, vol. 12.*, 155-164.

Bishop, A. (1966). The strength of soils as engineering materials. *Geotechnique, vol. 16, no. 2.*, 91-128.

Brakel, J. (1981). *Mathematisch model voor de krachten op een roterende snijkop van een in zeegang werkende snijkopzuiger.* Delft, Netherlands: Delft University of Technology - ScO/80/96.

Butterfield, R., & Andrawes, K. (1972). On the angles of friction between sand and plane surfaces. *Journal of Terramechanics, vol. 8, no. 4.*, 15-23.

Carman, P. (1937). Fluid flow through granular beds. *Transactions Institute Chemical Engineering, 15, 150.*

Carman, P. (1956). *Flow of gases through porous media.* London: Butterworths Scientific Publications.

Coulomb, C. (1776). Essai sur une application des regles des maximis et minimis a quelques problemes de statique relatifs a l'architecture. *Academie royale des sciences, Paris, Memoires de mathematique et de physique, vol. 7.*, 343-382.

Detournay, E., & Atkinson, C. (2000). Influence of pore pressure on the drilling response in low permeability shear dilatant rocks. *International Journal of Rock Mechanics & Mining Sciences, vol. 37.*, 1091-1101.

Evans, I. (1964). The force required to cut coal with blunt wedges. *Mining Research Establishment Isleworth*.

Evans, I., & Pomeroy, C. (1966). *The strength, fracture and workability of coal.* Pergamon Press.

Fairhurst, C. (1964). On the validity of the Brazilian test for brittle materials. *International Journal of Rock Mechanics & Mining Sciences, vol. 1.*, 535-546.

Geking, K. (1987). *Rock Testing Procedures at VA's Geotechnical Laboratory in Zeltweg.* Zeltweg, Austria.: Voest Alphine, International Report TZU 48.

Glasstone, S., Laidler, K., & Eyring, H. (1941). *The theory of rate processes.* New York: McGraw Hill.

Hansen, B. (1958). Line ruptures regarded as narrow rupture zones. *Earth Pressure Problems*, (pp. 39-48). Brussels.

Hatamura, Y., & Chijiiwa, K. (1975). Analyses of the mechanism of soil cutting, 1st report. *Bulletin of JSME, vol. 18, no. 120*, 619-626.

Hatamura, Y., & Chijiiwa, K. (1976A). Analyses of the mechanism of soil cutting, 2nd report. *Bulletin of the JSME, vol. 19, no. 131.*, 555-563.

Hatamura, Y., & Chijiiwa, K. (1976B). Analyses of the mechanism of soil cutting, 3rd report. *Bulletin of the JSME, vol. 19, no. 139.*, 1376-1384.

Hatamura, Y., & Chijiiwa, K. (1977A). Analyses of the mechanism of soil cutting, 4th report. *Bulletin of the JSME, vol. 20, no. 139.*, 130-137.

Hatamura, Y., & Chijiiwa, K. (1977B). Analyses of the mechanism of soil cutting, 5th report. *Bulletin of the JSME, vol. 20, no. 141.*, 388-395.

Hazen, A. (1982). Some physical properties of sands and gravels with special reference to their use in filtration. *24th Annual Report, Massachusetts State Board of Health, Pub. Doc. No. 34.*, 539-556.

He, J., & Vlasblom, W. (1998). Modelling of saturated sand cutting with large rake angles. *WODCON XV.* Las Vegas, USA: WODA.

He, J., Miedema, S., & Vlasblom, W. (2005). FEM Analyses Of Cutting Of Anisotropic Densely Compacted and Saturated Sand. *WEDAXXV/TAMU37.* New Orleans, Louisiana, USA: WEDA/TAMU.

Hettiaratchi, D. (1967A). The mechanics of soil cultivation. *AES, no. 3/245/C/28.*

Hettiaratchi, D., & Reece, A. (1967B). Symmetrical three-dimensional soil failure. *Journal of Terramechanics 4 (3).*, 45-67.

Hettiaratchi, D., & Reece, A. (1974). The calculation of passive soil resistance. *Geotechnique 24, no. 3.*, 289-310.

Hettiaratchi, D., & Reece, A. (1975). Boundary wedges in two dimensional passive soil failure. *Geotechnique 25, no. 2.*, 197-220.

Hettiaratchi, D., Witney, B., & Reece, A. (1966). The calculation of passive pressure in two dimensional soil failure. *Journal of Agriculture Engineering Resources 11 (2)*, 89-107.

Hoek, E., & Brown, E. T. (1988). The Hoek-Brown Failure Criterion - a 1988 Update. *15th Canadian Rock Mechanics Symposium.*, (pp. 31-38).

Joanknecht, L. (1973). *Mechanisch graaf onderzoek onder water.* Delft, Netherlands: Delft University of Technology.

Joanknecht, L. (1974). *Cutting forces in submerged soils.* Delft, Netherlands: Delft University of Technology.

Josselin de Jong, G. (1976). Rowe's stress dilatancy relation based on friction. *Geotechnique 26, no. 3*, 527-534.

Kaitkay, P., & Lei, S. (2005). Experimental study of rock cutting under external hydrostatic pressure. *Journal of Materials Processing Technology, vol. 159.*, 206-213.

Kelessidis, V., & Maglione, R. (2008). Yield stress of water bentonite dispersions. *Colloids and Surfaces A: Physicochemical Engineering Aspects 318.*, 217-226.

Kelessidis, V., Tsamantaki, C., & Dalamarinis, P. (2007). Effect of pH and electrolyte on the rheology of aqueous Wyoming bentonite dispersions. *Applied Clay Science 38.*, 86-96.

Kesteren, W. G. (1995). Numerical simulations of crack bifurcation in the chip forming cutting process in rock. In G. B. Karihaloo (Ed.), *Fracture of brittle disordered materials: concrete, rock and ceramics.* (pp. 505-524). London, UK.: E&FN Spon.

Koning, J. d., Miedema, S., & Zwartbol, A. (1983). Soil/Cutterhead Interaction under Wave Conditions. *WODCON X.* Singapore: WODA.

Kozeny, J. (1927). *Uber kapillare leitung des wassers in boden.* Wien: Sitzungsber. Akad. Wiss. Wien, Math. Naturwiss. Kl. Abt. 2a, 136, 271-306.

Lambe, T., & Whitman, R. (1979). *Soil mechanics, SI version.* New York: John Wiley & Sons.

Leussen, W. v., & Os, A. v. (1987 December). Basic research on cutting forces in saturated sand. *Journal of Geotechnical Engineering, vol. 113, no. 12.*, 1501-1516.

Leussen, W., & Nieuwenhuis, J. (1984). Soil mechanics aspects of dredging. *Geotechnique 34, no. 3.*, 359-381.

Lobanov, V., & Joanknecht, L. (1980). The cutting of soil under hydrostatic pressure. *WODCON IX.* Vancouver, Canada: WODA.

Ma, Y. (2001). *Mathematical model analysis for the saturated sand cutting with large cutting angles in the non-vavitation situation.* Delft, Netherlands: Delft University of Technology, Report: 2001.BT.5581.

Ma, Y., Ni, F., & Miedema, S. (2006A). Calculation of the Blade Cutting Force for small Cutting Angles based on MATLAB. *The 2nd China Dredging Association International Conference & Exhibition, themed Dredging and Sustainable Development.* Guangzhou, China: CHIDA.

Ma, Y., Ni, F., & Miedema, S. (2006B). Mechanical Model of Water Saturated Sand Cutting at Blade Large Cutting Angles. *Journal of Hohai University, ISSN 1009-1130, CN 32-1591.*

Meijer, K. (1981). *Berekening van spanningen en deformaties in verzadigde grond.* Delft, Netherlands: Delft Hydraulics Laboratory, Report R914 part 1.

Meijer, K. (1985). *Computation of stresses and strains in saturated soil, PhD Thesis.* Delft, Netherlands: Delft University of Technology.

Meijer, K., & Os, A. (1976). Pore pressures near a moving under water slope. *Geotechnical Engineering Division ASCE 102, no. GT4.*, 361-372.

Merchant, M. (1944). Basic mechanics of the metal cutting process. *Journal of Applied Mechanics, vol. 11A.*, 168-175.

Merchant, M. (1945A). Mechanics of metal cutting process, orthogonal cutting and a type 2 chip. *Journal of Applied Physics, vol. 16, no. 5.*, 267-275.

Merchant, M. (1945B). Mechanics of metal cutting, plasticity conditions in orthogonal cutting. *Journal of Applied Physics, vol. 16, no. 6.*, 318-324.

Miedema, S. (1981). *The soil reaction forces on a crown cutterhead on a swell compensated ladder.* Delft, The Netherlands: Delft University of Technology.

Miedema, S. (1982). The Interaction between Cutterhead and Soil at Sea. *Dredging Day November 19th* (p. 25 pages in Dutch). Delft, The Netherlands: Delft University of Technology.

Miedema, S. (1982). *The mathematical modeling of the soil reaction forces on a cutterhead and the development of the computer program DREDMO.* Delft, The Netherlands: Delft University of Technology.

Miedema, S. (1984A). *Mathematical Modeling of a Seagoing Cutter Suction Dredge.* Delft, The Netherlands: Delft University of Technology/KIVI.

Miedema, S. (1984B, October). The Cutting of Densely Compacted Sand under Water. *Terra et Aqua, No. 28*, 4-10.

Miedema, S. (1985A, September). Derivation of the Differential Equation for Sand Pore Pressures. *Dredging and Port Construction*, 35.

Miedema, S. (1985B, July). Mathematical Modeling of the Cutting of Densely Compacted Sand Under Water. *Dredging and Port Construction*, 22-26.

Miedema, S. (1986A). The Application of a Cutting Theory on a Dredging Wheel. *WODCON XI* (p. 14 pages). Brighton, UK: WODA.

Miedema, S. (1986B, June). Underwater Soil Cutting: a Study in Continuity. *Dredging and Port Construction*, 47-53.

Miedema, S. (1987 September). *The Calculation of the Cutting Forces when Cutting Water Saturated Sand, PhD Thesis.* Delft: Delft University of Technology.

Miedema, S. (1989). On the Cutting Forces in Saturated Sand of a Seagoing Cutter Suction Dredge. *WODCON XII* (p. 27 pages). Orlando, Florida, USA: WODA.

Miedema, S. (1989, December). On the Cutting Forces in Saturated Sand of a Seagoing Cutter Suction Dredge. *Terra et Aqua, No. 41*, 27 pages.

Miedema, S. (1992). New developments of cutting theories with respect to dredging, the cutting of clay. *WODCON XIII*. Bombay, India: World Dredging Association (WODA).

Miedema, S. (1994). On the Snow-Plough Effect when Cutting Water Saturated Sand with Inclined Straight Blades. *ASCE Dredging 94* (p. 24 pages). Orlando, Florida, USA: ASCE.

Miedema, S. (1995). Production Estimation Based on Cutting Theories for Cutting Water Saturated Sand. *WODCON IV* (p. 30 pages). Amsterdam, The Netherlands: WODA.

Miedema, S. (1999). Considerations on limits of dredging processes. *19th Annual Meeting & Technical Conference of the Western Dredging Association.* Louisville, Kentucky, USA: WEDA/TAMU.

Miedema, S. (2000). The modelling of the swing winches of a cutter dredge in relation with simulators. *Texas A/M 32nd Annual Dredging Seminar.* Warwick, Rhode Island, USA: WEDA/TAMU.

Miedema, S. (2003). The Existence of Kinematic Wedges at Large Cutting Angles. *CHIDA Dredging Days.* Shanghai, China: CHIDA.

Miedema, S. (2004). The Cutting Mechanisms of Water Saturated Sand at Small and Large Cutting Angles. *International Conference on Coastal Infrastructure Development - Challenges in the 21st Century.* Hongkong: ICCD.

Miedema, S. (2005). The Cutting of Water Saturated Sand, the FINAL Solution. *WEDAXXV/TAMU37.* New Orleans, Louisiana, USA: WEDA/TAMU.

Miedema, S. (2006A). The Cutting of Water Saturated Sand, the Solution. *CEDA African Section: Dredging Days.* Tangiers, Morocco: CEDA.

Miedema, S. (2006B). The Cutting of Water Saturated Sand, the Solution. *The 2nd China Dredging Association International Conference & Exhibition, themed Dredging and Sustainable Development.* Guangzhou, China: CHIDA.

Miedema, S. (2009). New Developments Of Cutting Theories With Respect To Dredging, The Cutting Of Clay And Rock. *WEDA XXIX/Texas A/M 40.* Phoenix, Arizona, USA: WEDA/TAMU.

Miedema, S. (2010). New Developments of Cutting Theories with respect to Offshore Applications. *ISOPE* (p. 8). Beijing, China.: ISOPE.

Miedema, S. A. (2014). *The Delft Sand, Clay & Rock Cutting Model.* (1st ed.). Delft: IOS Press, Delft University Press. doi:10.3233/978-1-61499-454-1-i

Miedema, S. A., & Zijsling, D. (2012). Hyperbaric rock cutting. *OMAE International Conference on Ocean, Offshore and Arctic Engineering* (p. 14). Rio de Janeiro, Brazil: ASME.

Miedema, S., & Becker, S. (1993). The Use of Modeling and Simulation in the Dredging Industry, in Particular the Closing Process of Clamshell Dredges. *CEDA Dredging Days* (p. 26 pages). Amsterdam, The Netherlands: CEDA.

Miedema, S., & Frijters, D. (2003). The Mechanism of Kinematic Wedges at Large Cutting Angles - Velocity and Friction Measurements. *23rd WEDA Technical Conference/35th TAMU Dredging Seminar* (p. 14 pages). Chicago, Illinois, USA: WEDA/TAMU.

Miedema, S., & Frijters, D. (2004). The wedge mechanism for cutting of water saturated sand at large cutting angles. *WODCON XVII.* Hamburg, Germany: WODA.

Miedema, S., & He, J. (2002B). The Existance of Kinematic Wedges at Large Cutting Angles. *WEDA XXII Technical Conference/34th Texas A/M Dredging Seminar* (p. 20 pages). Denver, Colorado, USA: WEDA/TAMU.

Miedema, S., & Ma, Y. (2002A). The Cutting of Water Saturated Sand at Large Cutting Angles. *ASCE Dredging 02* (p. 16 pages). Orlando, Florida, USA: ASCE.

Miedema, S., & Yi, Z. (2001). An Analytical Method of Pore Pressure Calculations when Cutting Water Saturated Sand. *Texas A/M 33nd Annual Dredging Seminar* (p. 18 pages). Houston, USA: WEDA/TAMU.

Mitchell, J. (1976). *Fundamentals of soil behavior.* John Wiley & Sons, Inc.

Mitchell, J., Campanella, R., & Singh, A. (1968). Soil creep as a rate process. *Journal SMFD, vol. 94, no. 1, ASCE.*

Mogi, K. (1966). Pressure dependence of rock strength and transition from brittle fracture to ductile flow. *Bulletin Earthquake Res. Inst. Japan, Vol. 44.*, 215-232.

Nishimatsu, Y. (1972). The mechanics of rock cutting. *International Journal of Rock Mechanics & Mining Science, vol. 9.*, 261-270.

Os, A. G. (1976). Snelle deformatie van korrelvormig materiaal onder water. *PT-P31, no. 12*, 735-741.

Os, A. G. (1977A). Behavior of soil when excavated under water. In *International course on modern dredging.* The Hague, Netherlands.

Os, A. G. (1977B). Snelle deformatie van korrelvormig materiaal onder water. *PT-B32, no. 8.*, 461-467.

Osman, M. (1964). The mechanics of soil cutting blades. *J.A.E.R. 9 (4)*, 313-328.

Palmer, A. (1999). Speed effects in cutting and ploughing. *Geotechnique 49, no. 3.*, 285-294.

Raalte, G., & Zwartbol, A. (1986). Disc bottom cutterhead, a report on laboratory and field tests. *WODCON XI.* Brighton, UK: WODA.

Rafatian, N., Miska, S., Ledgerwood III, L., Hughes, B., Ahmed, R., Yu, M., & Takach, N. (2009). Experimental study of MSE of a single PDC cutter under simulated pressurized conditions. *SPE/IADC 119302 Drilling Conference & Exhibition.* Amsterdam, Netherlands: SPE International.

Reece, A. (1965). The fundamental equation of earth moving machinery. *Symposium Earth Moving Machinery.* London: Institute of Mechanical Engineering.

Rhee, C., & Steeghs, H. (1991 June). Multi blade ploughs in saturated sand, model cutting tests. *Dredging & Port Construction*.

Roberts, J., Jepsen, R., Gotthard, D., & Lick, W. (1998). Effects of particle size and bulk density on erosion of quartz particles. *Journal of Hydraulic Engineering*, 1261-1267.

Rowe, P. (1962). The stress dilatancy relation for static equilibrium of an assembly of particles in contact. *Proceedings Royal Society A269.* (pp. 500-527). Royal Society.

Roxborough, F. (1987). The role of some basic rock properties in assessing cuttability. *Seminar on Tunnels - Wholly Engineered Structures* (pp. 1-21). Canberra, Australia: AFCC.

Schrieck, G. (1996). *Introduction to Dredging Engineering.* Delft, the Netherlands: Delft University of Technology.

Segal, G. (2001). *Sepra analysis programmers guide, standard problems and users manual.* Leidschendam, Netherlands: Ingenieursbureau Sepra.

Sohne, W. (1956). Some basic considerations of soil mechanics as applied to agricultural engineering. *Grundlagen der landtechnik (7).*, 11-27.

Soydemir, C. (1977). Potential models for shear strength generation in soft marine clays. *International Symposium on Soft Clay*. Bangkok, Thailand.

Stam, P. (1983). *Analyse ten behoeve van het ontwerp van een klei snijdende sleepkop, CO/82/129.* Delft, Netherlands: Delft University of Technology.

Steeghs, H. (1985A). Snijden van zand onder water, part I. *Ports & Dredging no. 121*.

Steeghs, H. (1985B). Snijden van zand onder water, part II. *Ports & Dredging no. 123.*

Terzaghi, K., & Peck, R. (1964). *Soil mechanics in engineering practise.* New York: John Wiley & Sons.

Turnage, G., & Freitag, D. (1970). Effects of cone velocity and size on soil penetration resistance. *ASEA 69-670.*

Verhoef, P. (1997). *Wear of rock cutting tools: Implications for site investigation of rock dredging projects.* Delft, Netherlands: Balkema Rotterdam.

Verruijt, A. (1983). *Soil Mechanics.* Delft: DUM, Netherlands.

Vlasblom, W. (2003-2007). *Rock Cutting, Lecture Notes.* Delft, Netherlands: Delft University of Technology.

Vukovic, M., & Soro, A. (1992). Determination of hydraulic conductivity of porous media from grain size composition. *Water Resources Publications, Littleton, Colorado.*

Weijermars, R. (1997-2011). *Principles of rock mechanics.* Delft, Netherlands: Alboran Science Publishing.

Wismer, R., & Luth, H. (1972A). Performance of Plane Soil Cutting Blades. *Transactions of ASEA*.

Wismer, R., & Luth, H. (1972B). Rate effects in soil cutting. *Journal of Terramechanics, vol. 8, no. 3.*, 11-21.

Yi, Z. (2000). *The FEM calculation of pore water pressure in sand cutting process by SEPRAN.* Delft, Netherlands: Delft University of Technology, Report: 2001.BT.5455.

Yi, Z., & Miedema, S. (2001). Finite Element Calculations To Determine The Pore Pressures When Cutting Water Saturated Sand At Large Cutting Angles. *CEDA Dredging Days* (p. 20 pages). Amsterdam, The Netherlands: CEDA.

Yi, Z., & Miedema, S. (2002). Finite Element Calculations To Determine The Pore Pressures When Cutting Water Saturated Sand At Large Cutting Angles. *CEDA Dredging Days* (p. 20 pages). Amsterdam, The Netherlands: CEDA.

Zeng, D., & Yao, Y. (1988). Investigation on the relationship between soil metal friction and sliding speed. *2nd Asian Pacific Conference of ISTVS.* Bangkok, Thailand.

Zeng, D., & Yao, Y. (1991). Investigation on the relationship between soil shear strength and shear rate. *Journal of Terramechanics, 28 (1).*

Zijsling, D. (1987). Single cutter testing - a key for PDC bit development (SPE 16529). *Offshore Europe 87.* Aberdeen, Scotland.

Chapter 18: Figures & Tables.

18.1. List of Figures.

18.2. List of Figures in Appendices.

18.3. List of Tables.

18.4. List of Tables in Appendices.

Chapter 19: Appendices.

Appendix A: Active & Passive Soil Failure Coefficients.

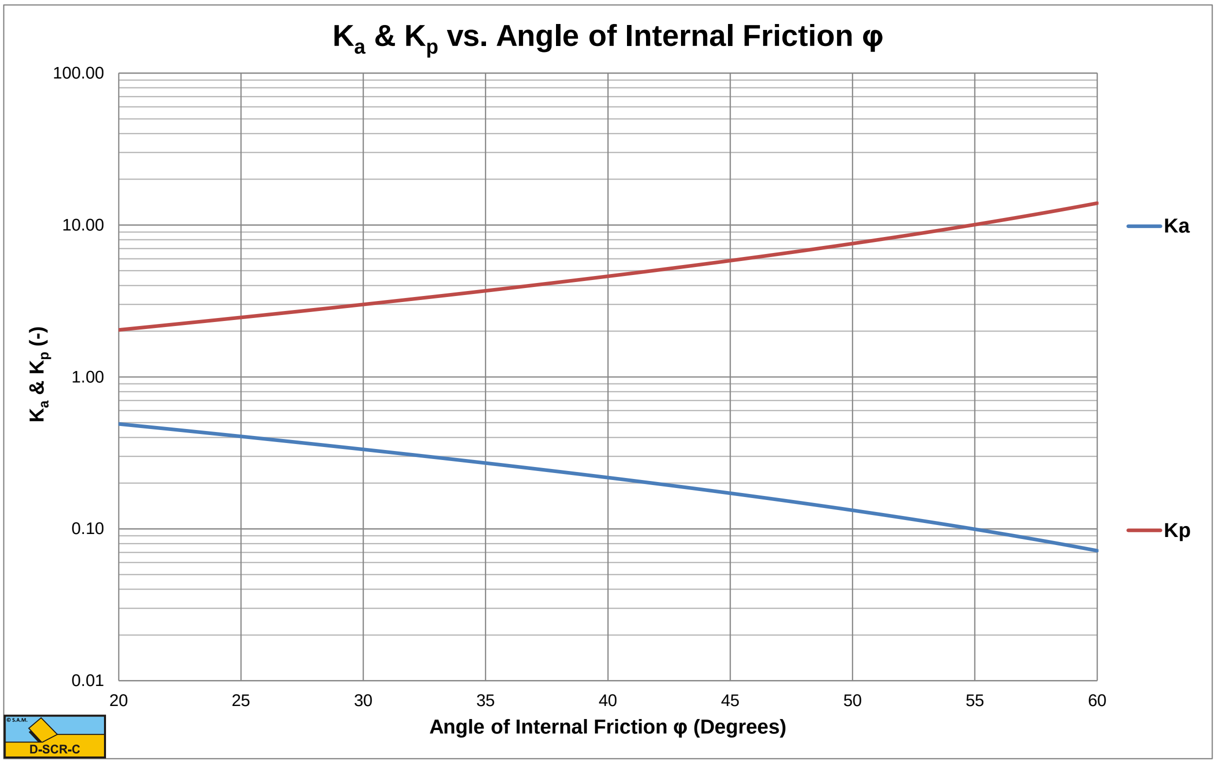

Figure A-1: The coefficients of active and passive soil failure K_a & K_p.

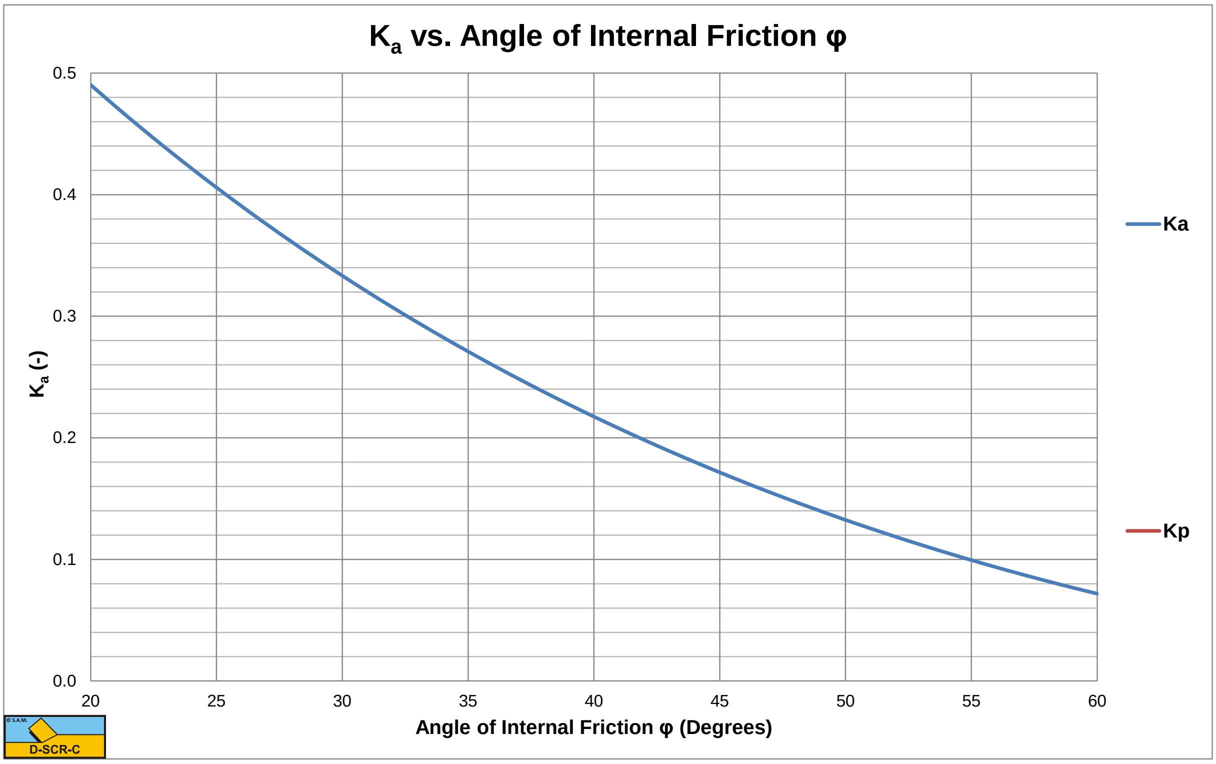

Figure A-2: The coefficient of active soil failure K_a.

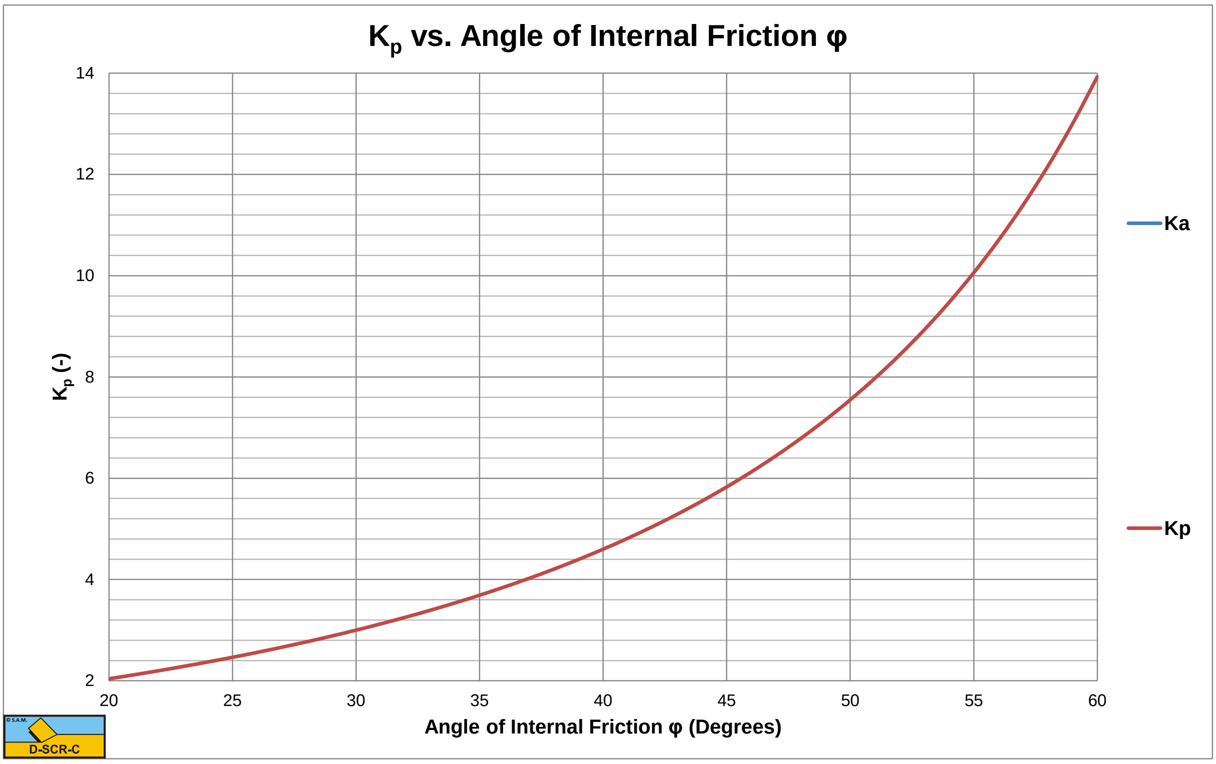

Figure A-3: The coefficient of passive soil failure K_p.

Appendix B: Dry Sand Cutting Coefficients.

B.1 Standard Configuration.

B.1.1 Standard h_b/h_i=1.

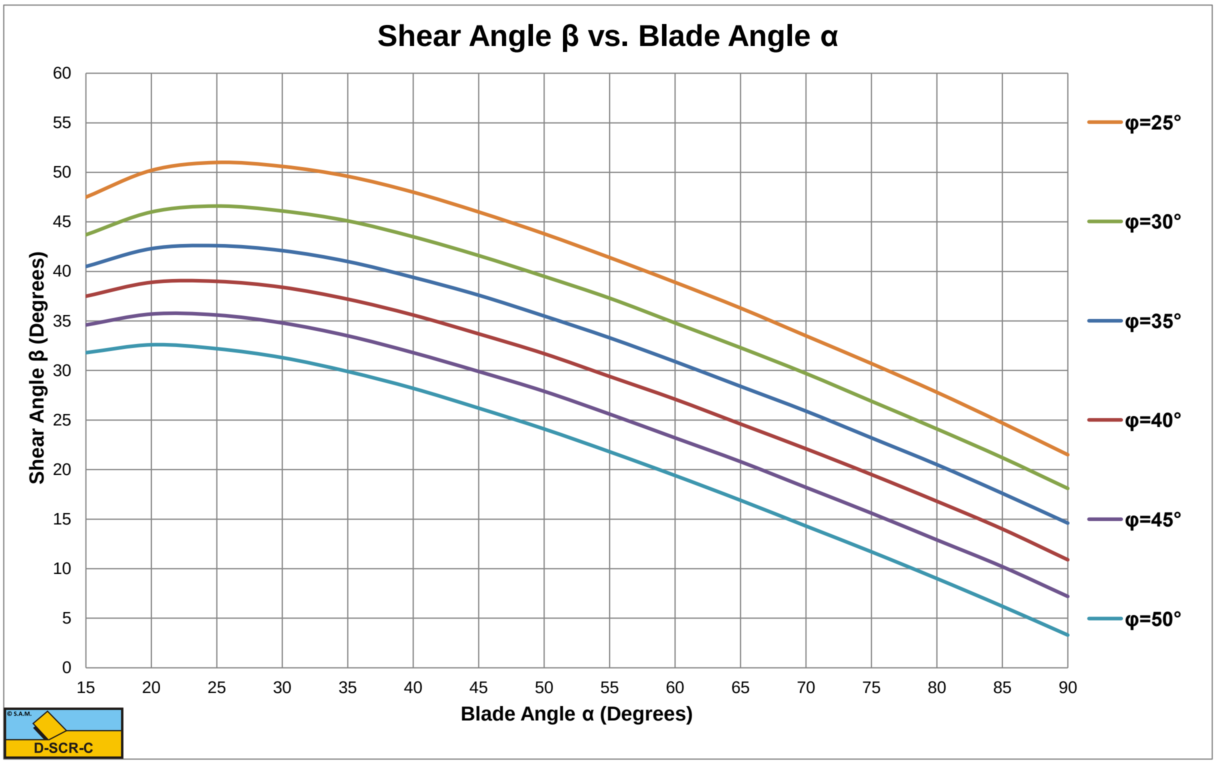

Figure B-1: The shear angle β as a function of the blade angle α for h_b/h_i=1.

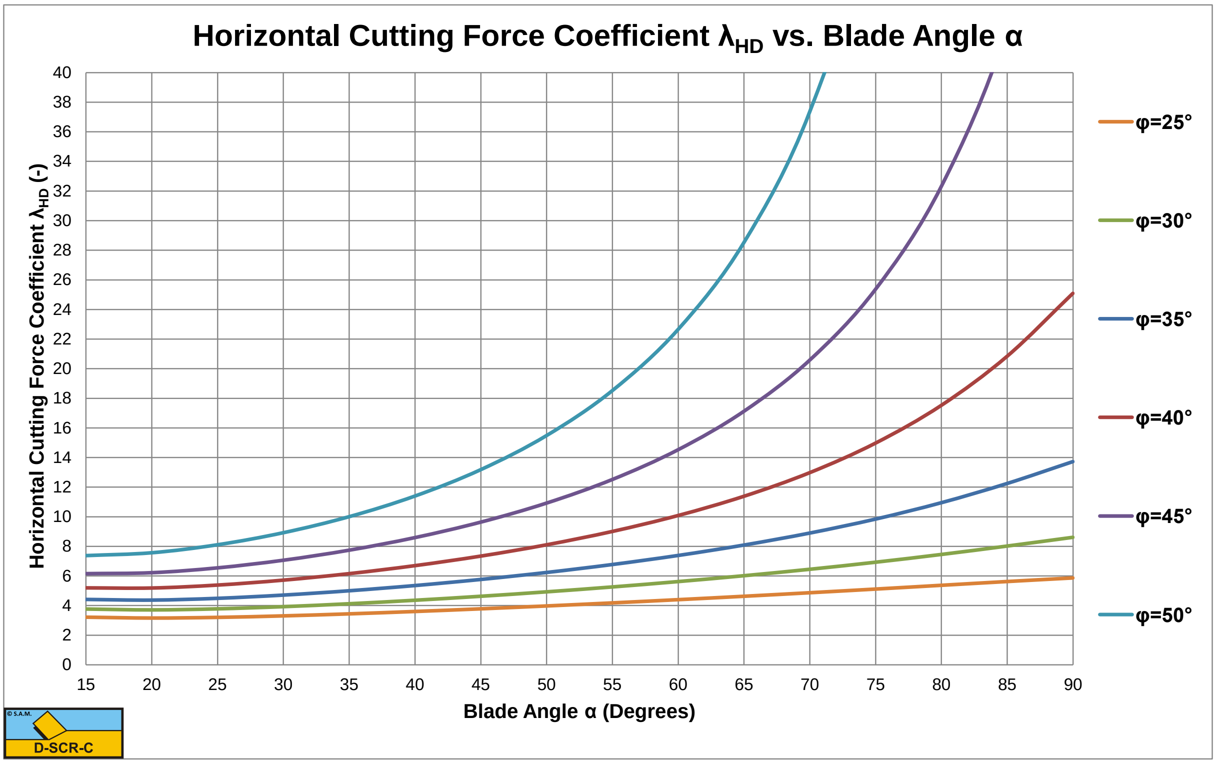

Figure B-2: The horizontal cutting force coefficient λ_{HD} as a function of the blade angle α for h_b/h_i=1.

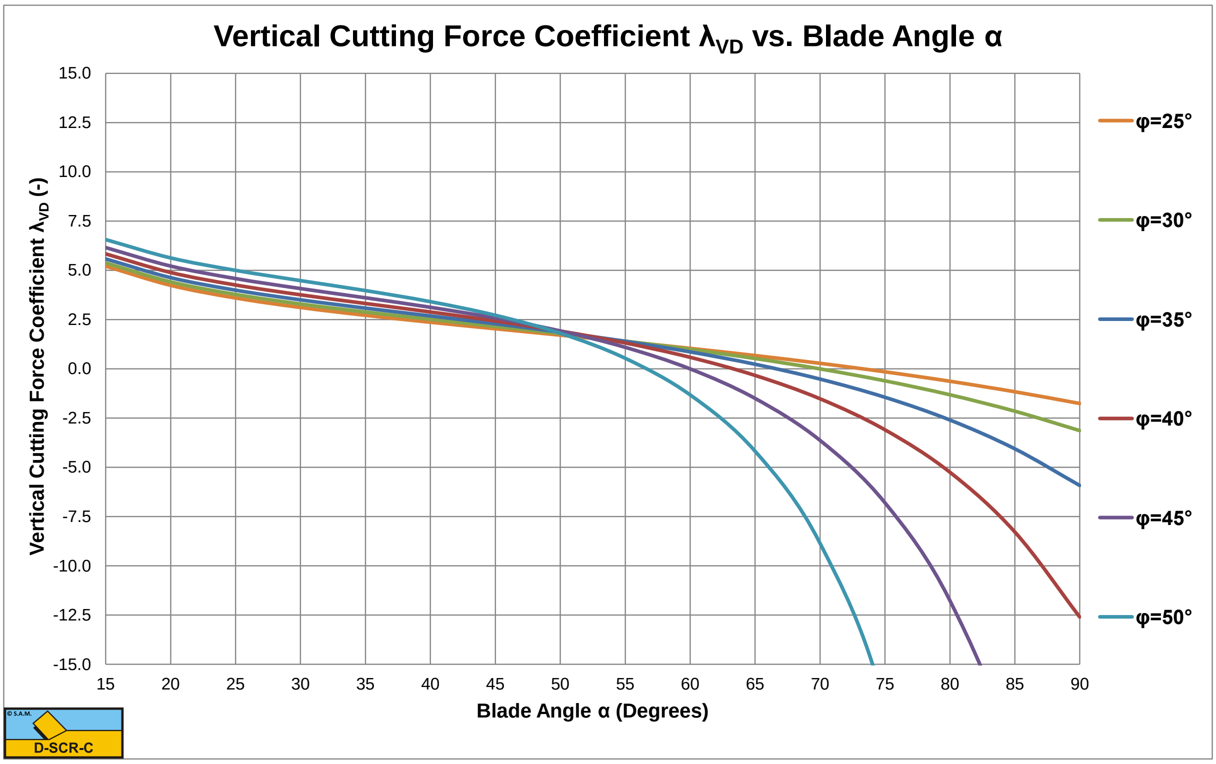

Figure B-3: The vertical cutting force coefficient λ_{VD} as a function of the blade angle α for h_b/h_i=1.

B.1.2 Standard h_b/h_i=2.

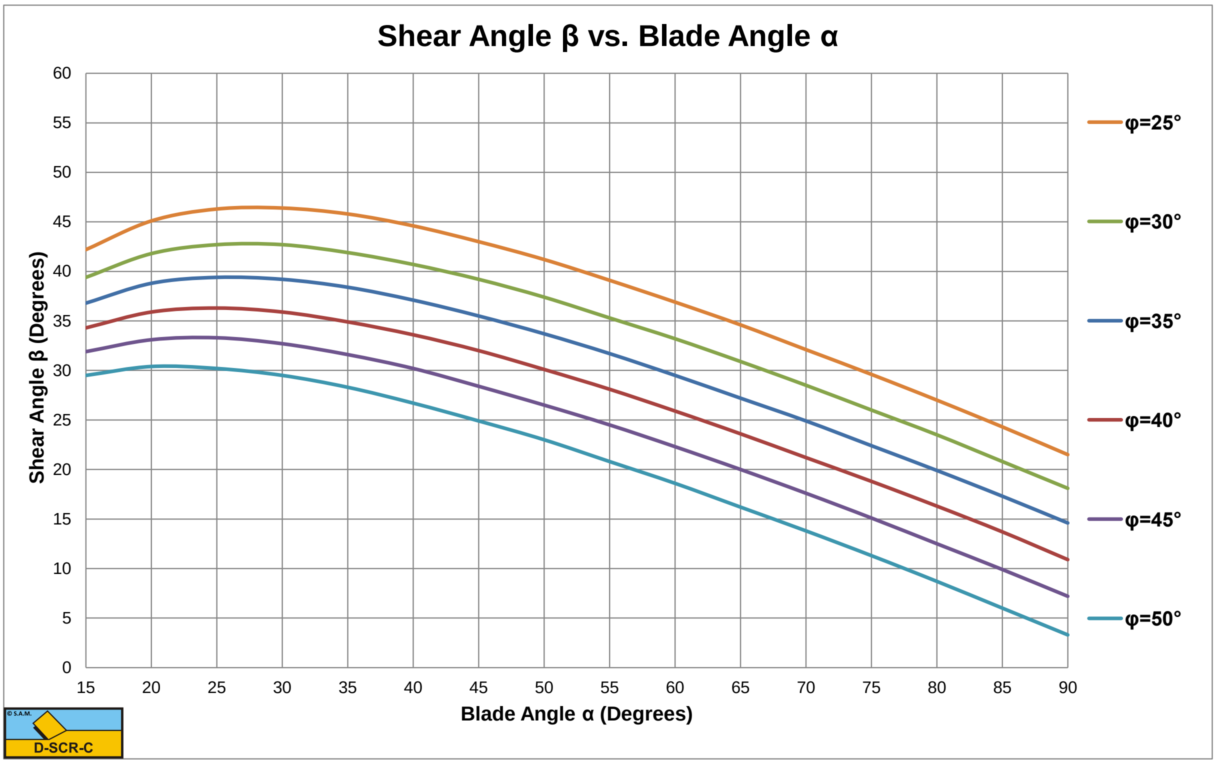

Figure B-4: The shear angle β as a function of the blade angle α for h_b/h_i=2.

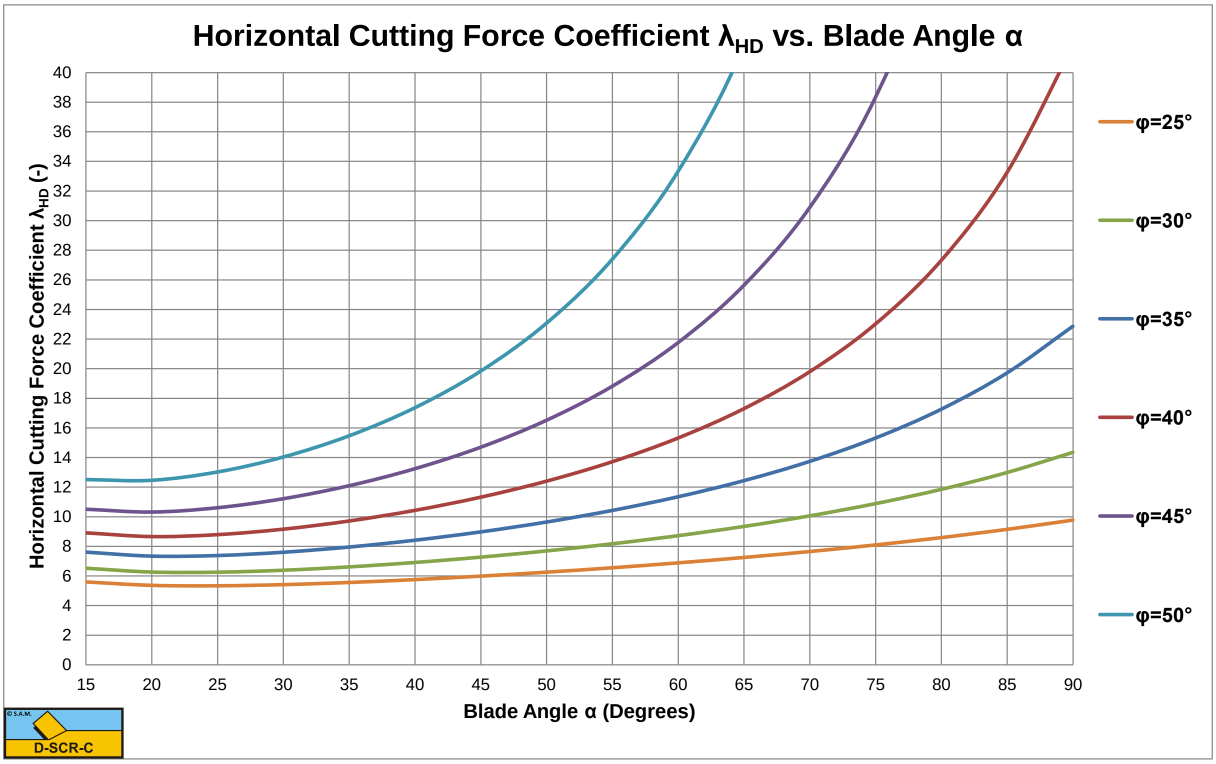

Figure B-5: The horizontal cutting force coefficient λ_{HD} as a function of the blade angle α for $h_b/h_i=2$.

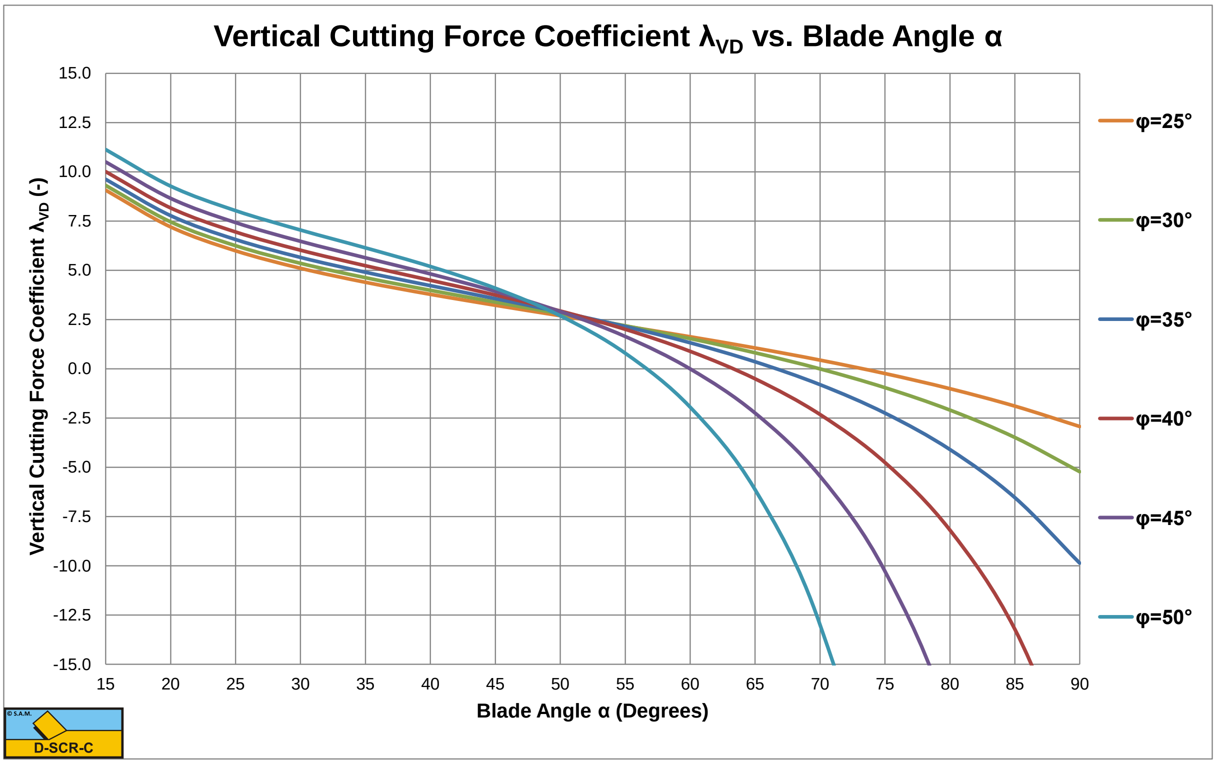

Figure B-6: The vertical cutting force coefficient λ_{VD} as a function of the blade angle α for $h_b/h_i=2$.

B.1.3 Standard h_b/h_i=3.

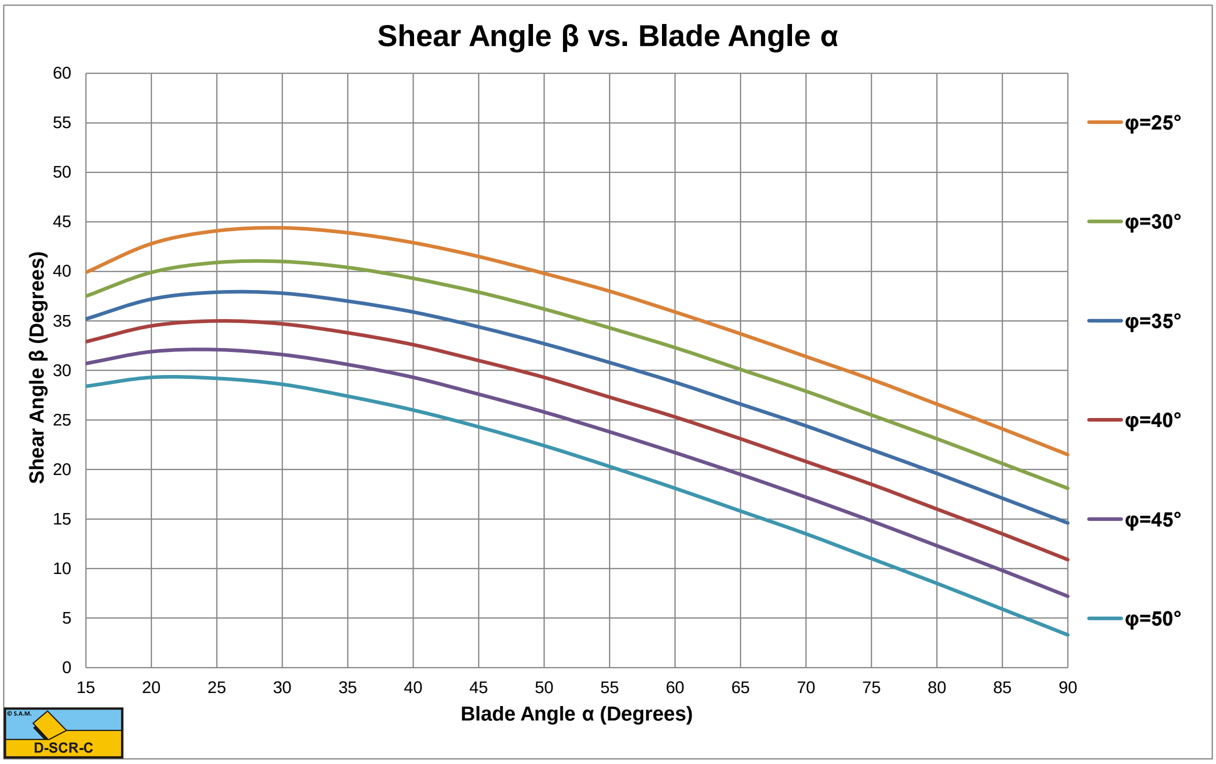

Figure B-7: The shear angle β as a function of the blade angle α for h_b/h_i=3.

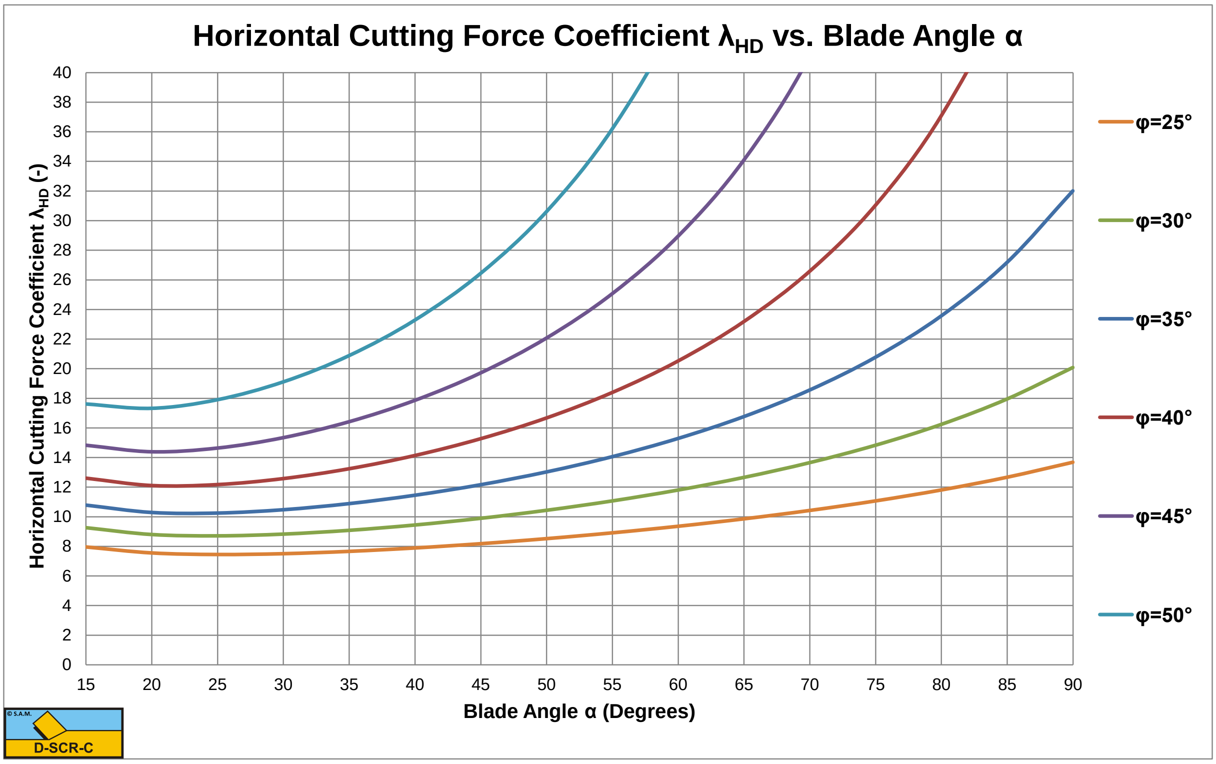

Figure B-8: The horizontal cutting force coefficient λ_{HD} as a function of the blade angle α for h_b/h_i=3.

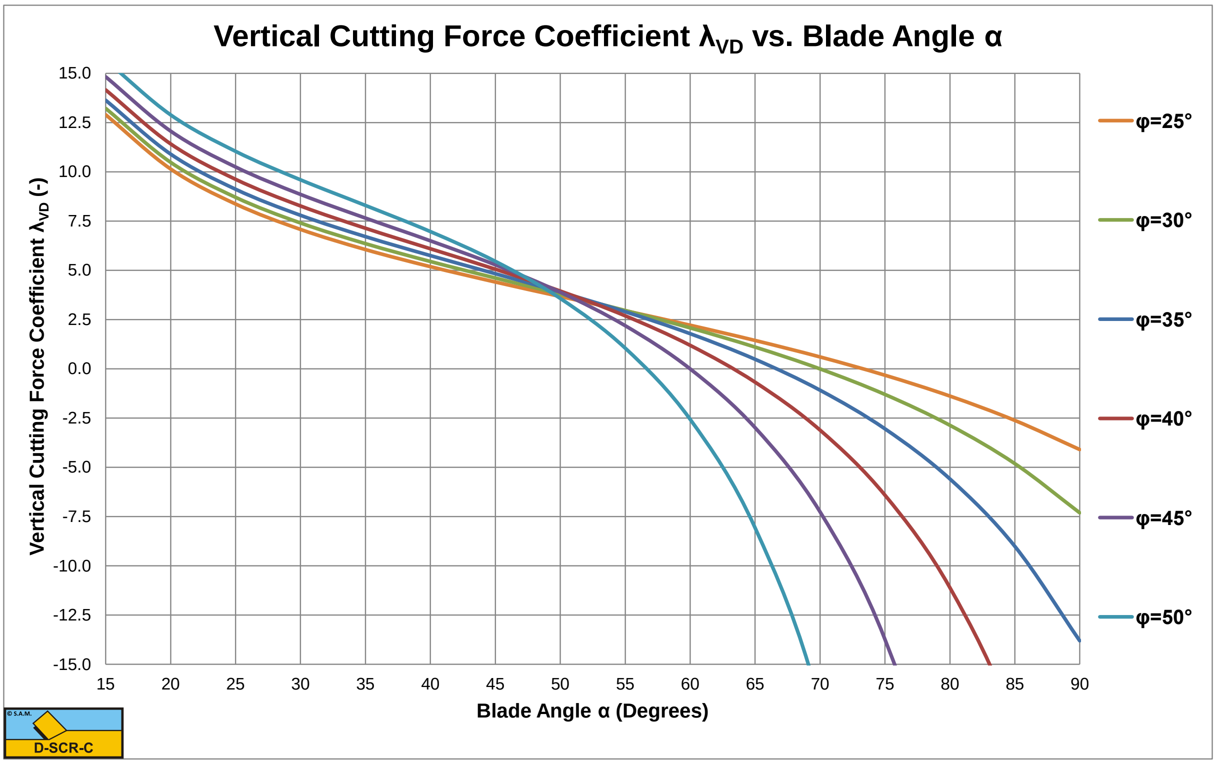

Figure B-9: The vertical cutting force coefficient λ_{VD} as a function of the blade angle α for h_b/h_i=3.

B.2 Alternative Configuration.

B.2.1 Alternative $h_b/h_i=1$.

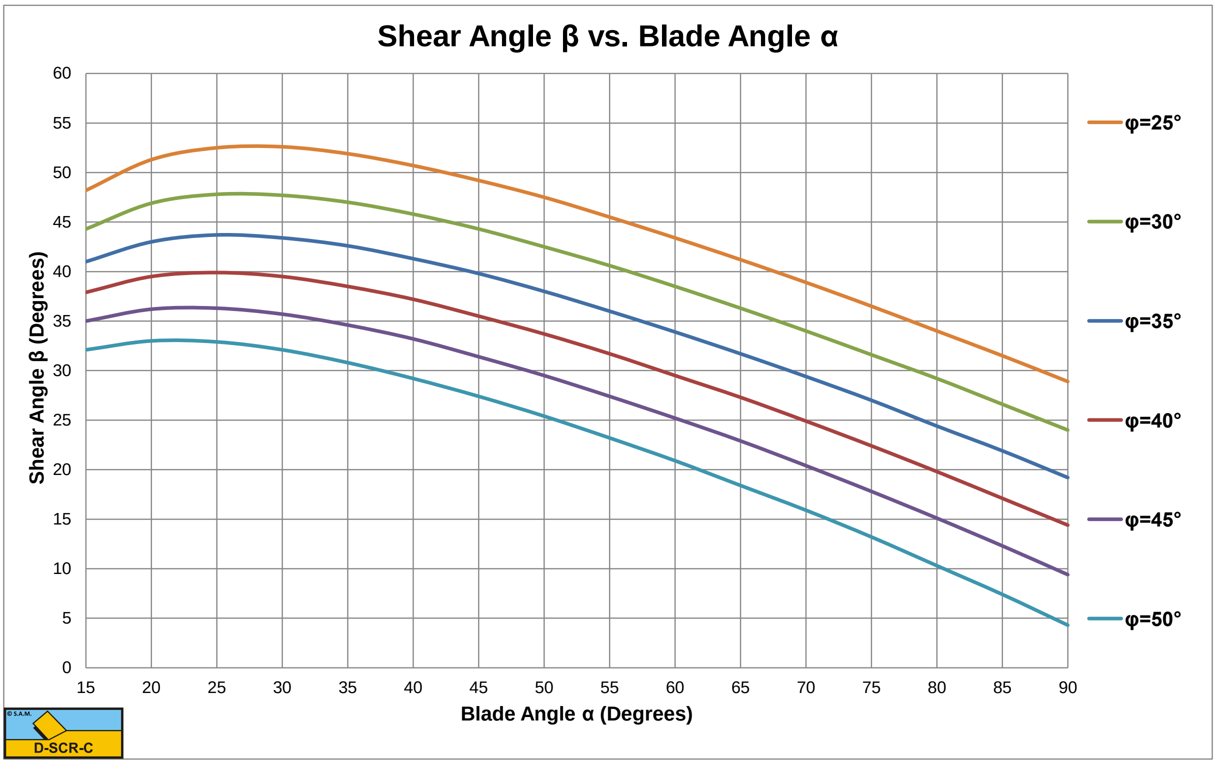

Figure B-10: The shear angle β as a function of the blade angle α for $h_b/h_i=1$.

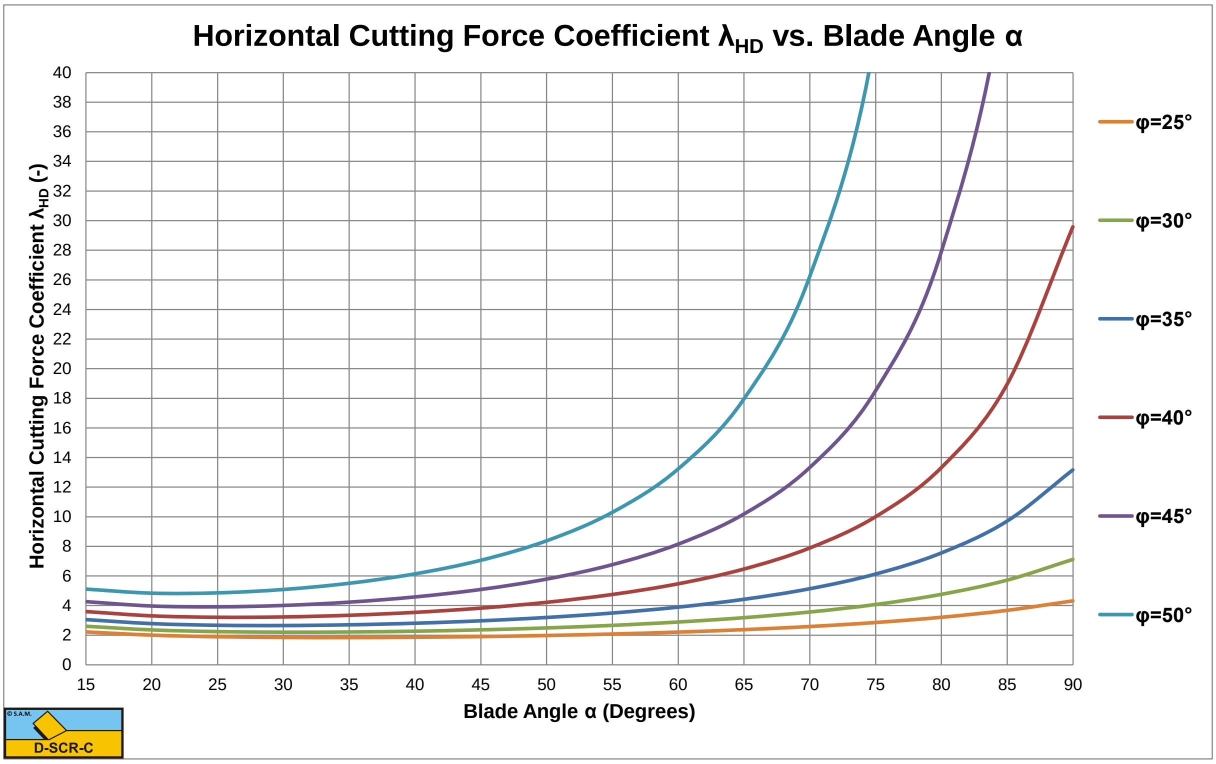

Figure B-11: The horizontal cutting force coefficient λ_{HD} as a function of the blade angle α for $h_b/h_i=1$.

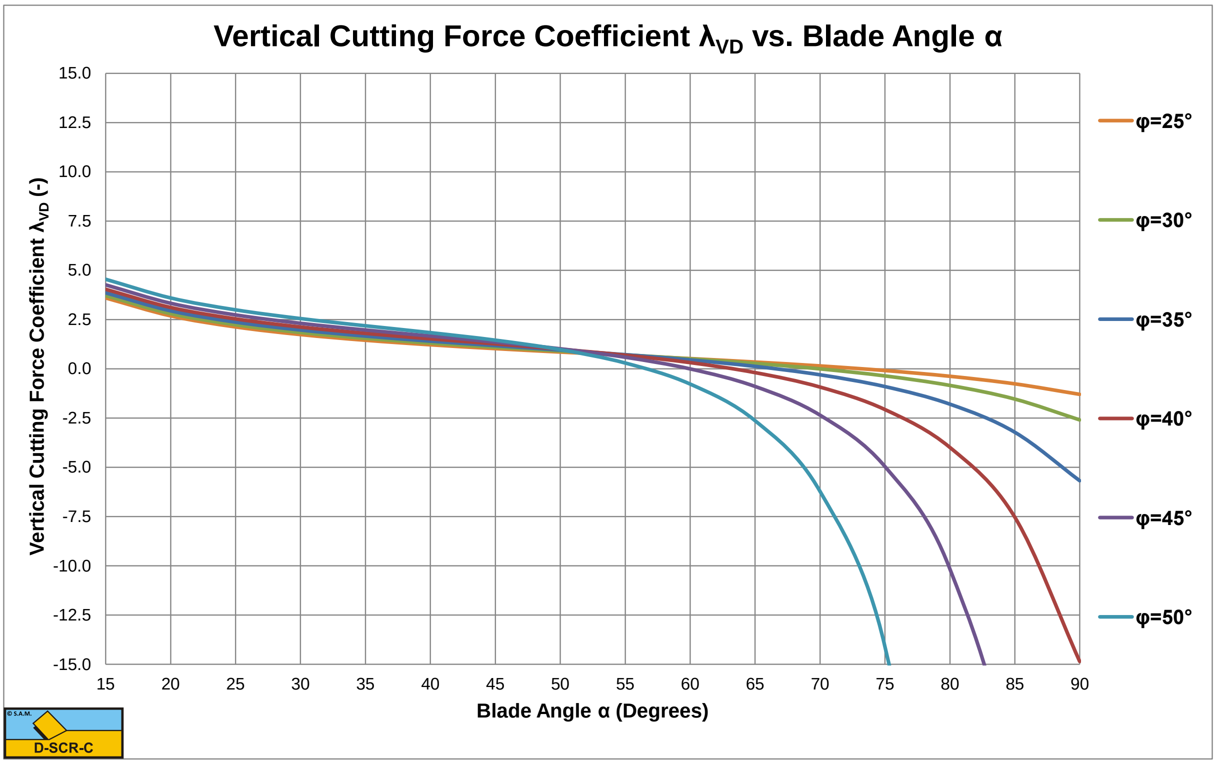

Figure B-12: The vertical cutting force coefficient λ_{VD} as a function of the blade angle α for $h_b/h_i=1$.

B.2.2 Alternative $h_b/h_i=2$.

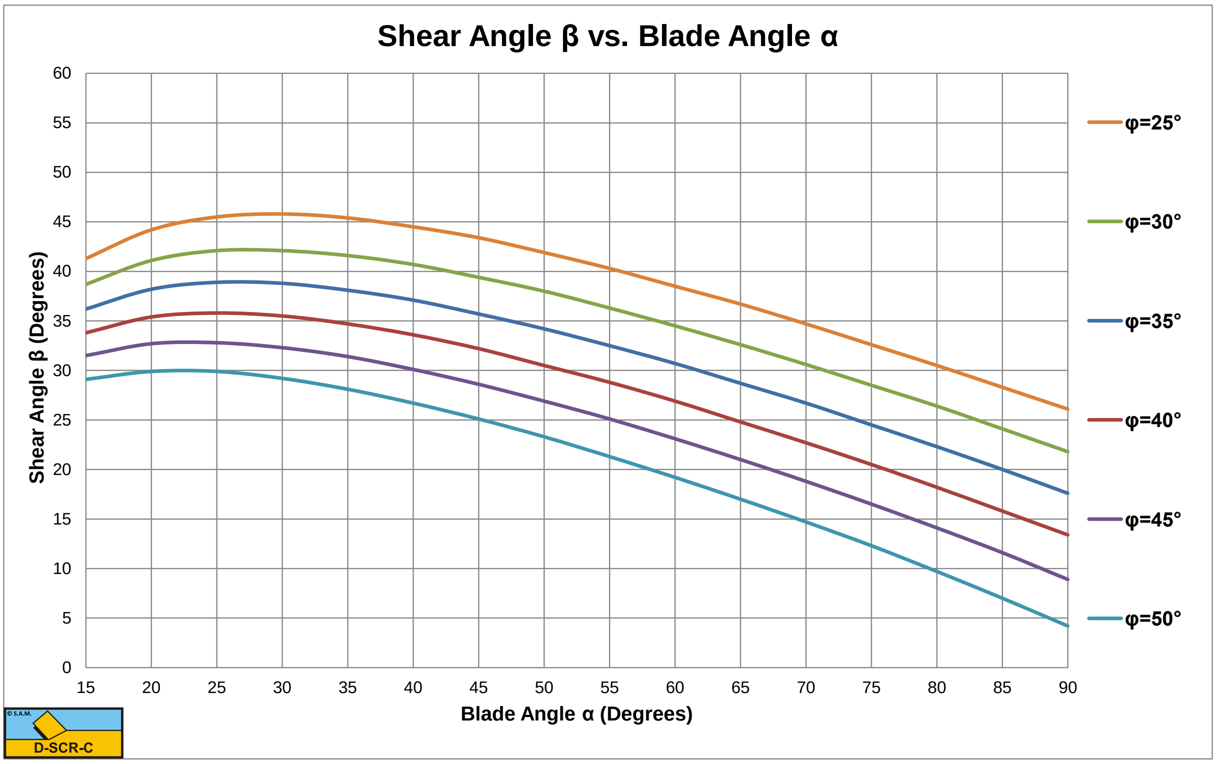

Figure B-13: The shear angle β as a function of the blade angle α for $h_b/h_i=2$.

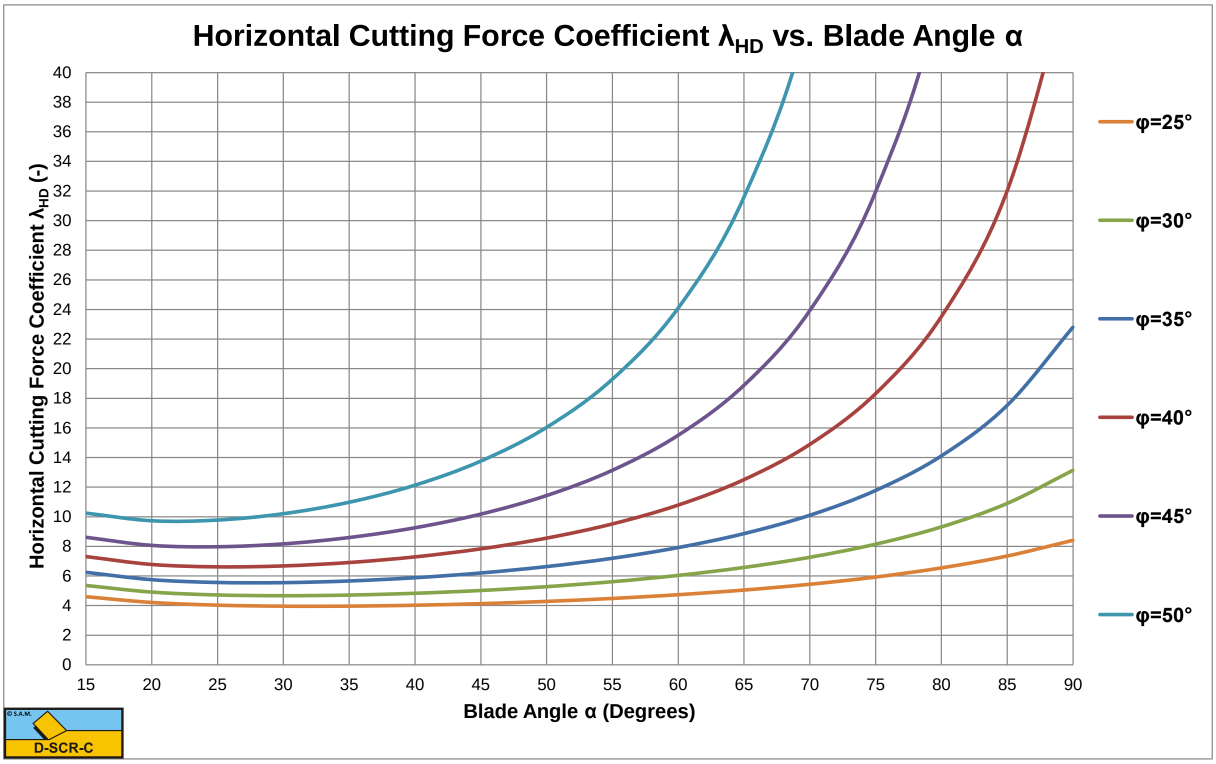

Figure B-14: The horizontal cutting force coefficient λ_{HD} as a function of the blade angle α for h_b/h_i=2.

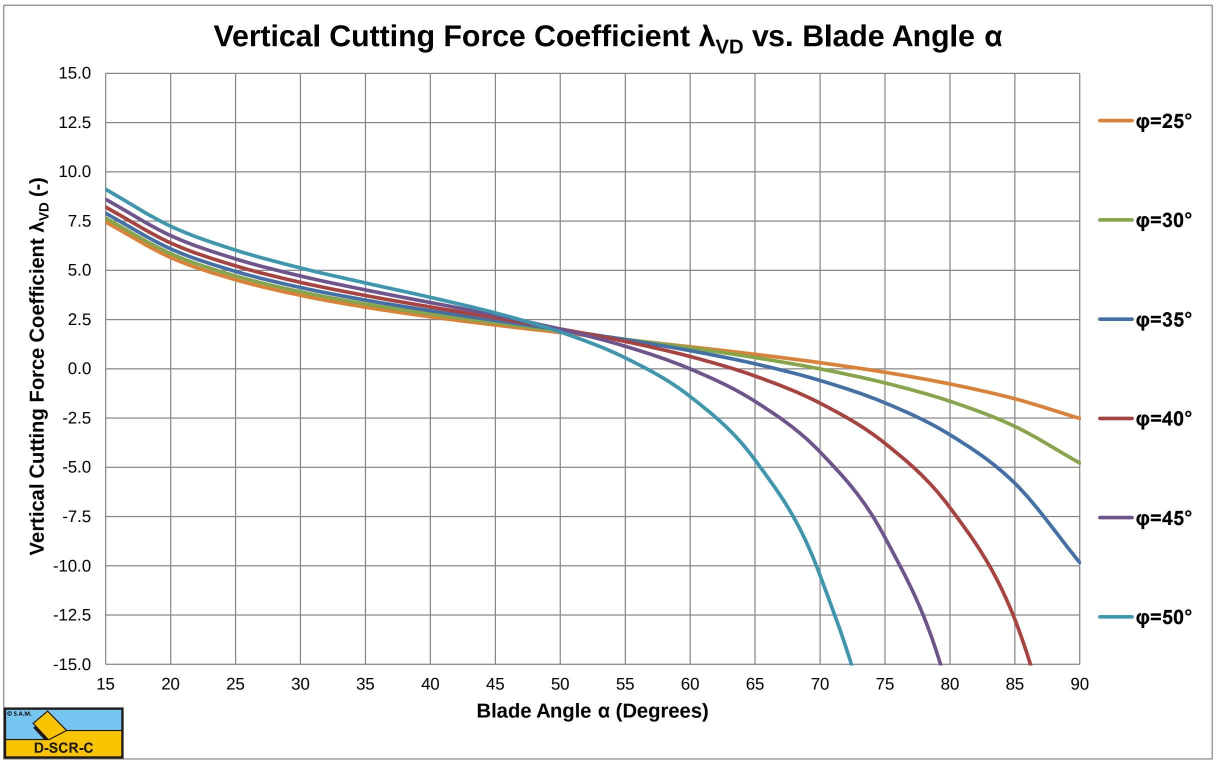

Figure B-15: The vertical cutting force coefficient λ_{VD} as a function of the blade angle α for h_b/h_i=2.

B.2.3 Alternative $h_b/h_i=3$.

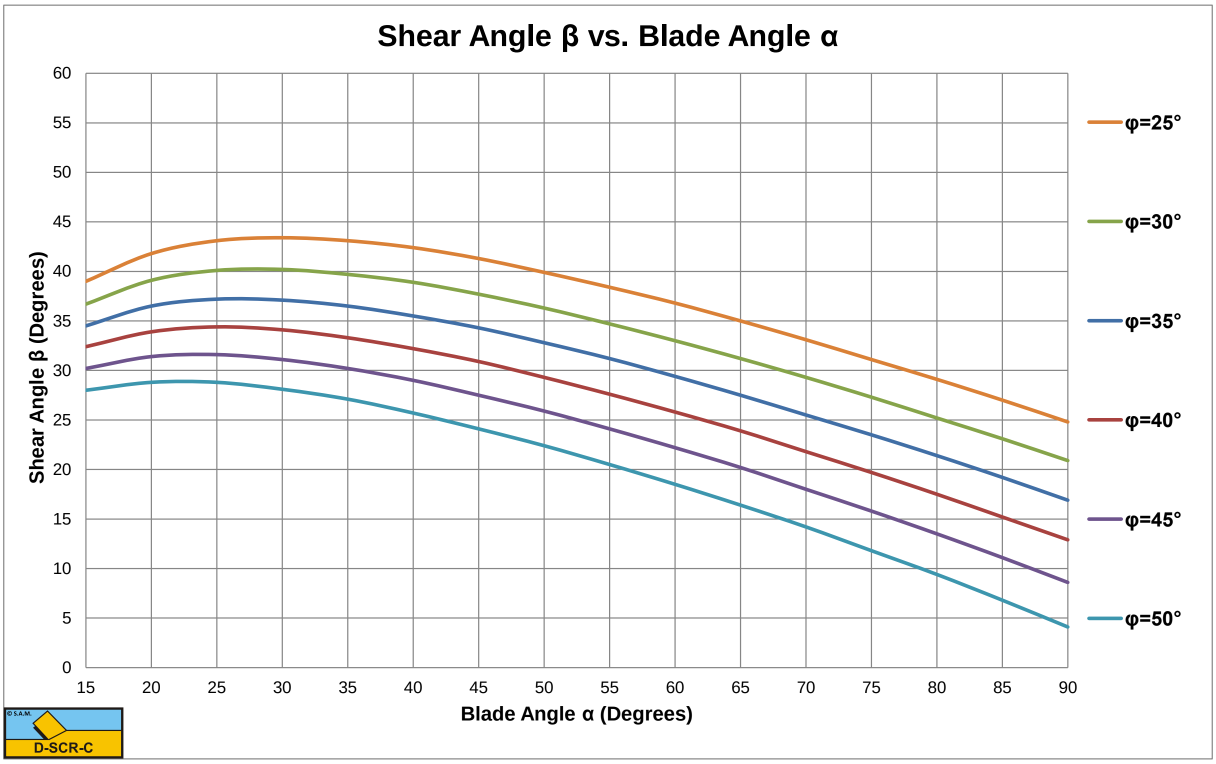

Figure B-16: The shear angle β as a function of the blade angle α for $h_b/h_i=3$.

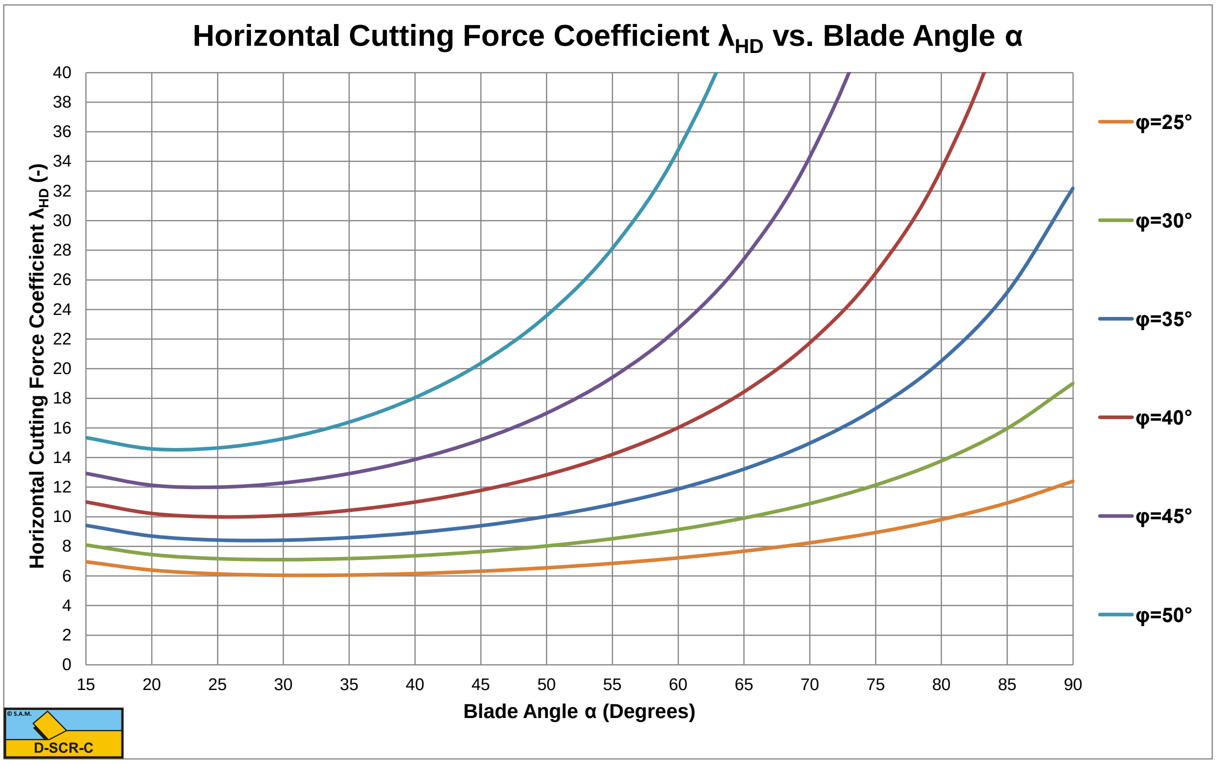

Figure B-17: The horizontal cutting force coefficient λ_{HD} as a function of the blade angle α for $h_b/h_i=3$.

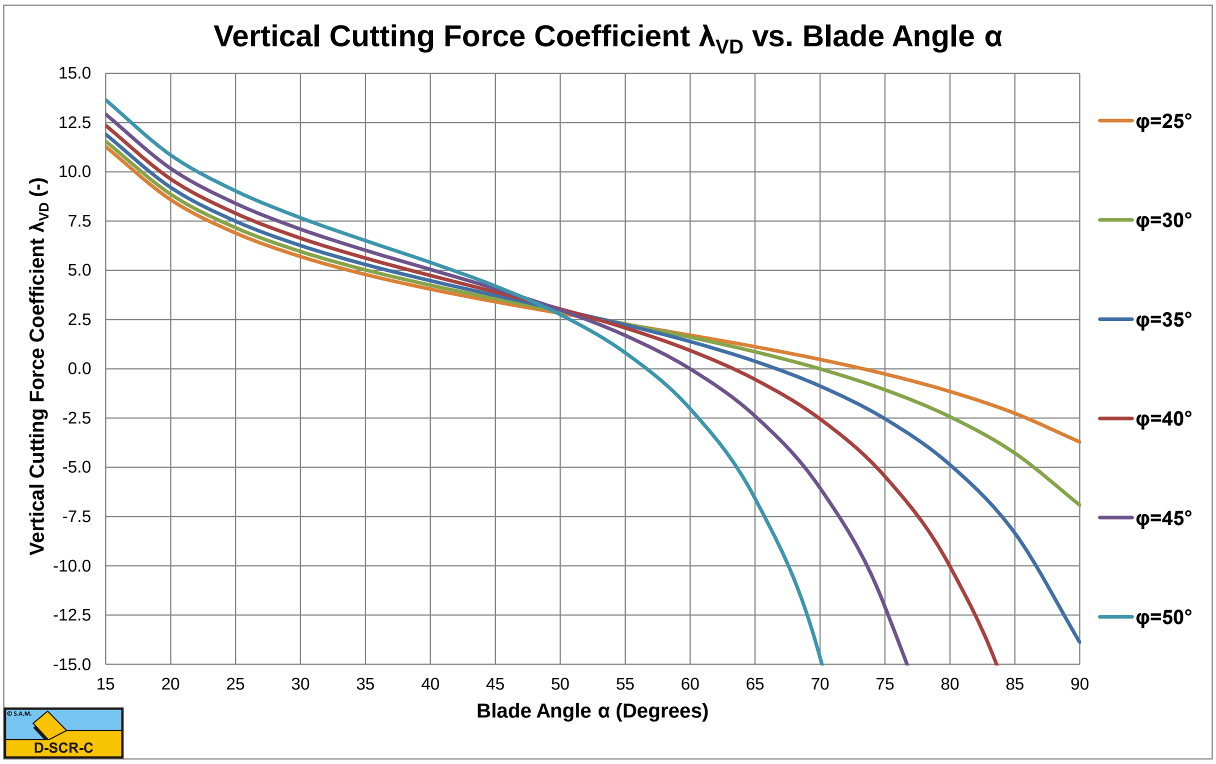

Figure B-18: The vertical cutting force coefficient λ_{VD} as a function of the blade angle α for $h_b/h_i=3$.

B.3 Percentage of Inertial Forces.

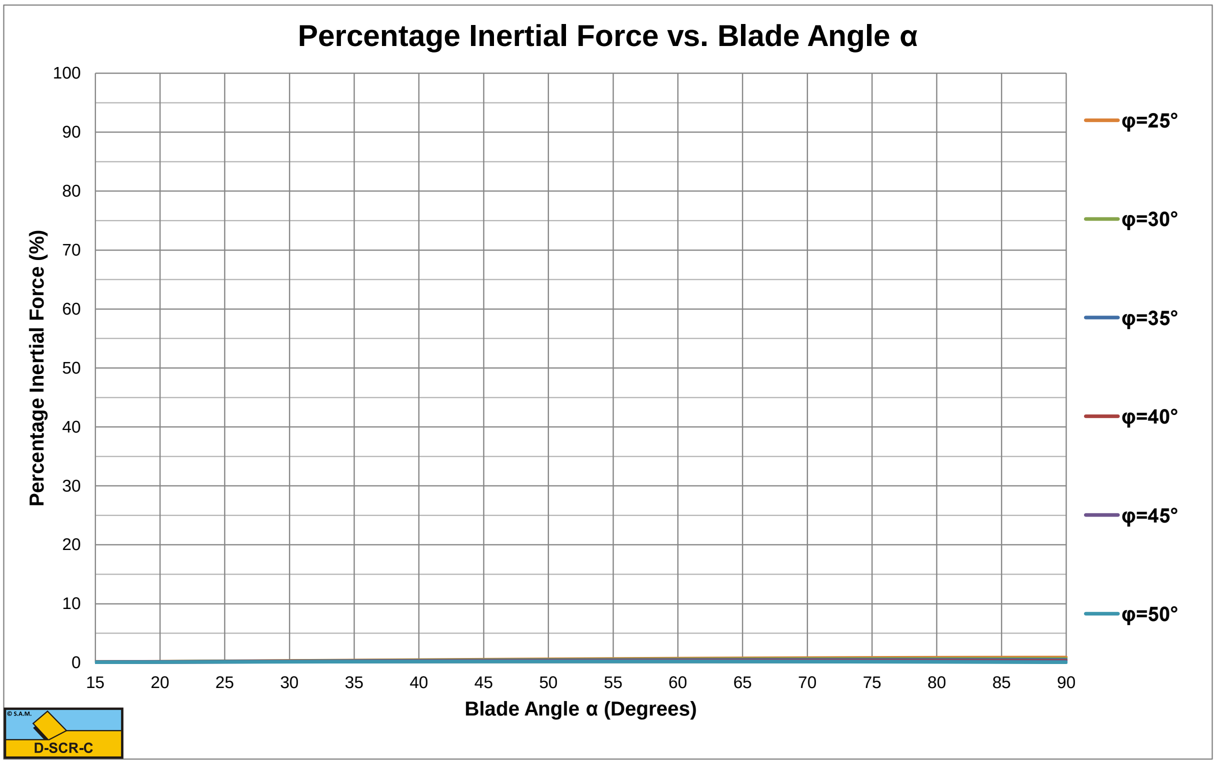

Figure B-19: The percentage inertial force for a dimensionless inertial effect parameter λ_i=0.025.

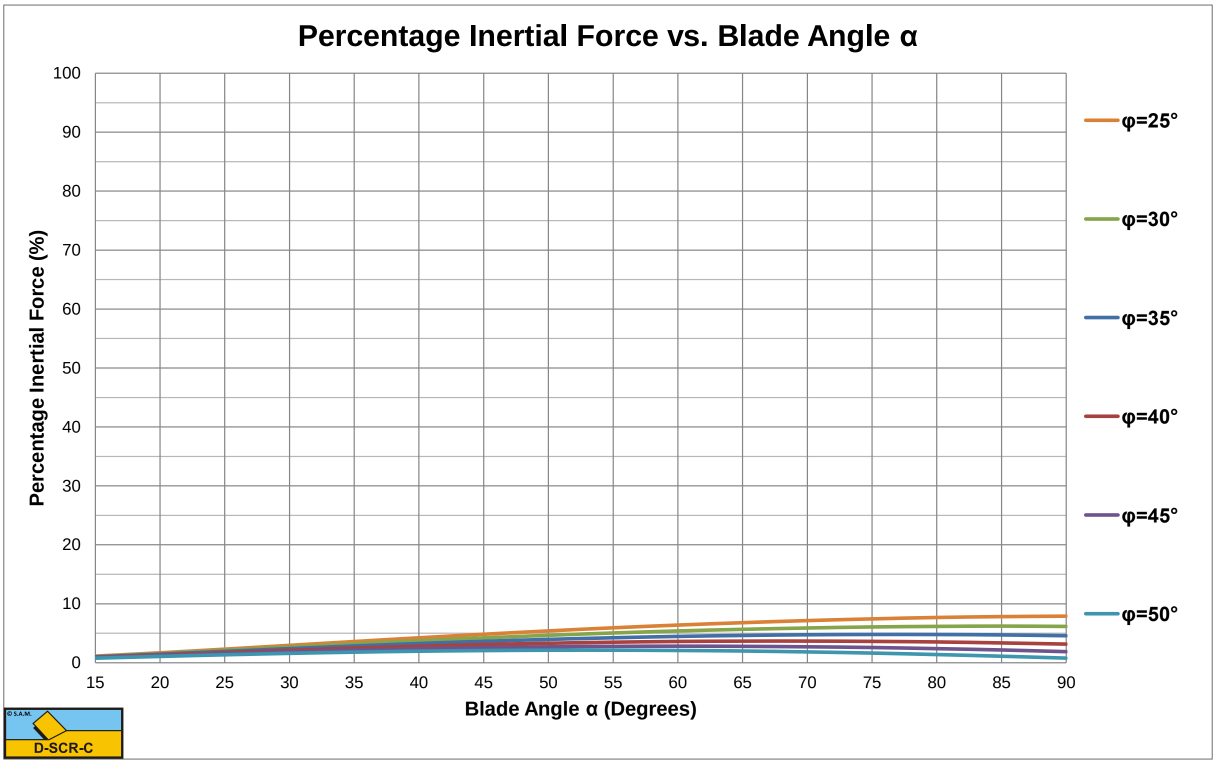

Figure B-20: The percentage inertial force for a dimensionless inertial effect parameter λ_i=0.25.

Figure B-21: The percentage inertial force for
a dimensionless inertial effect parameter λ_i=2.5.

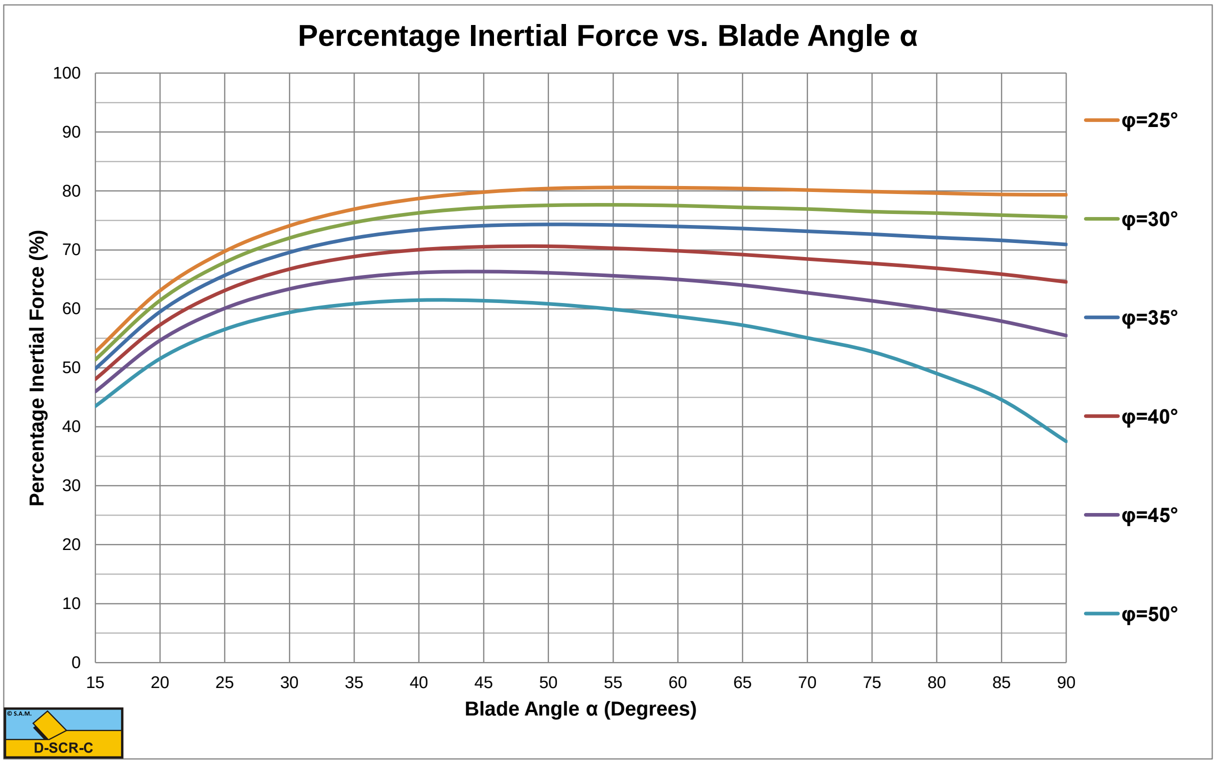

Figure B-22: The percentage inertial force for
a dimensionless inertial effect parameter λ_i=25.

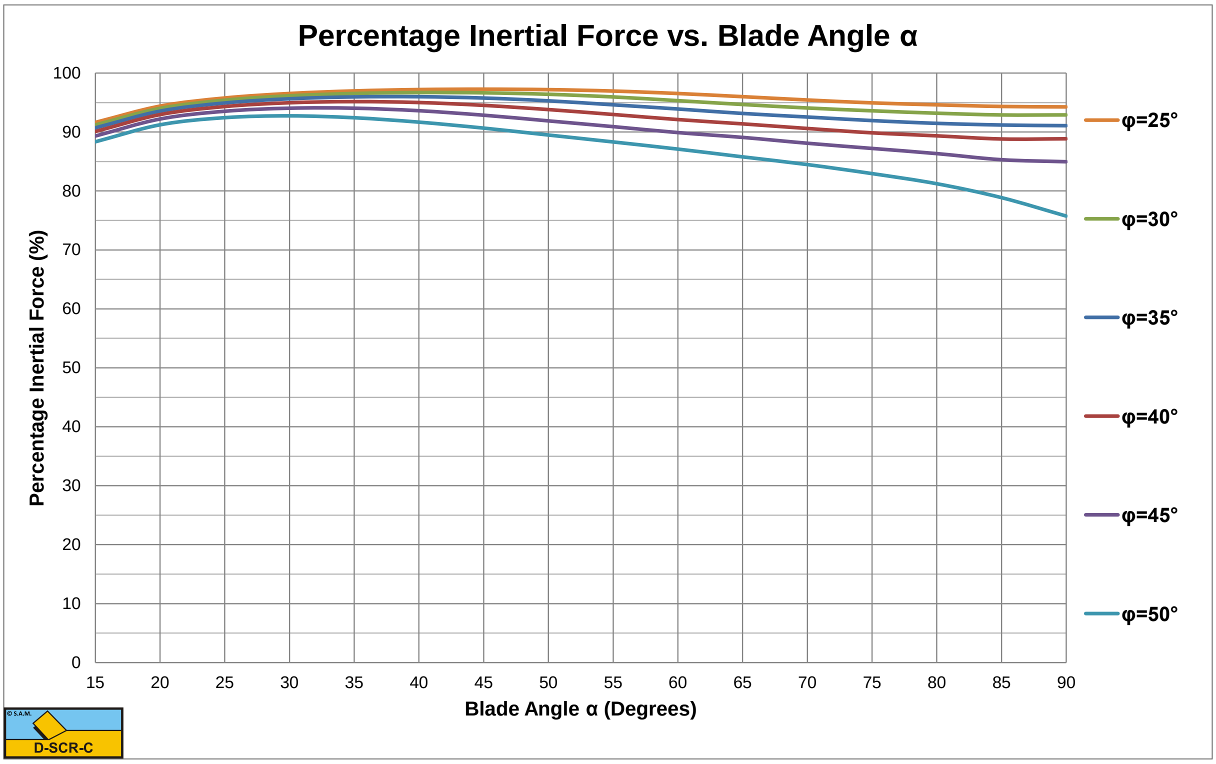

Figure B-23: The percentage inertial force for
a dimensionless inertial effect parameter λ_i=250.

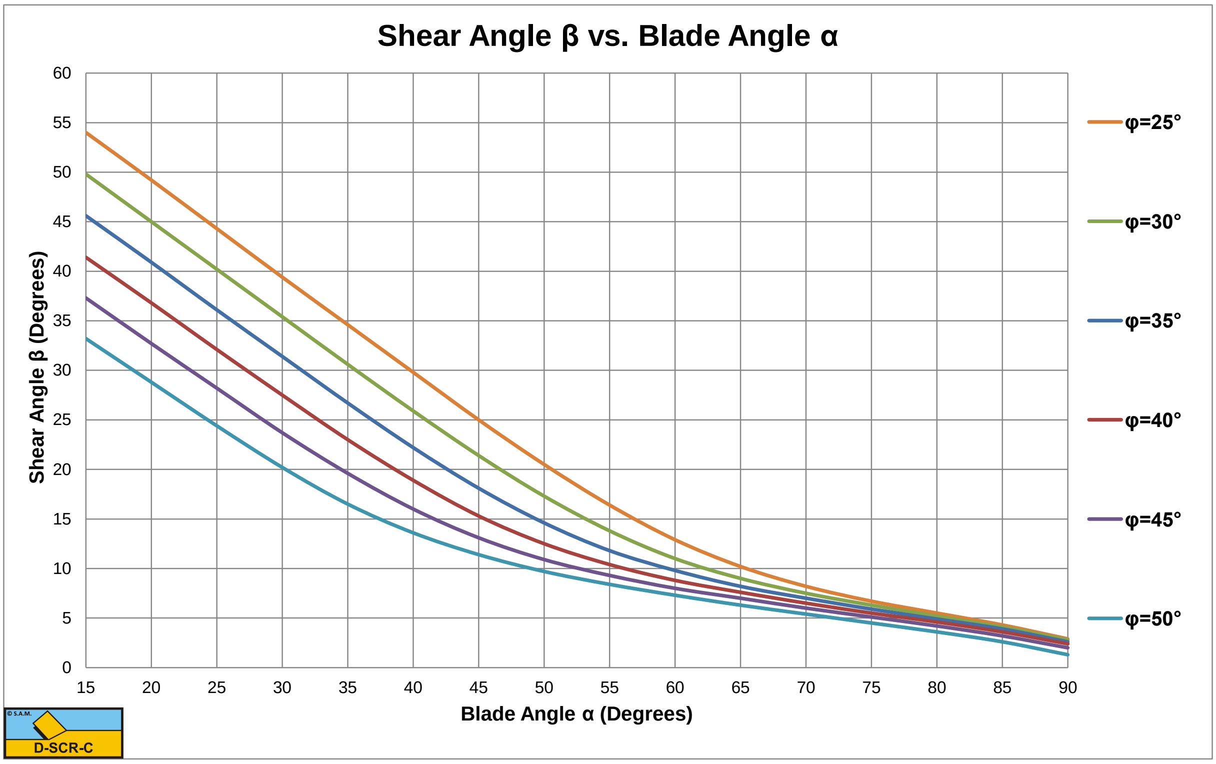

Figure B-24: The shear angle β, including the effect of inertial forces for
a dimensionless inertial effect parameter λ_i=250.

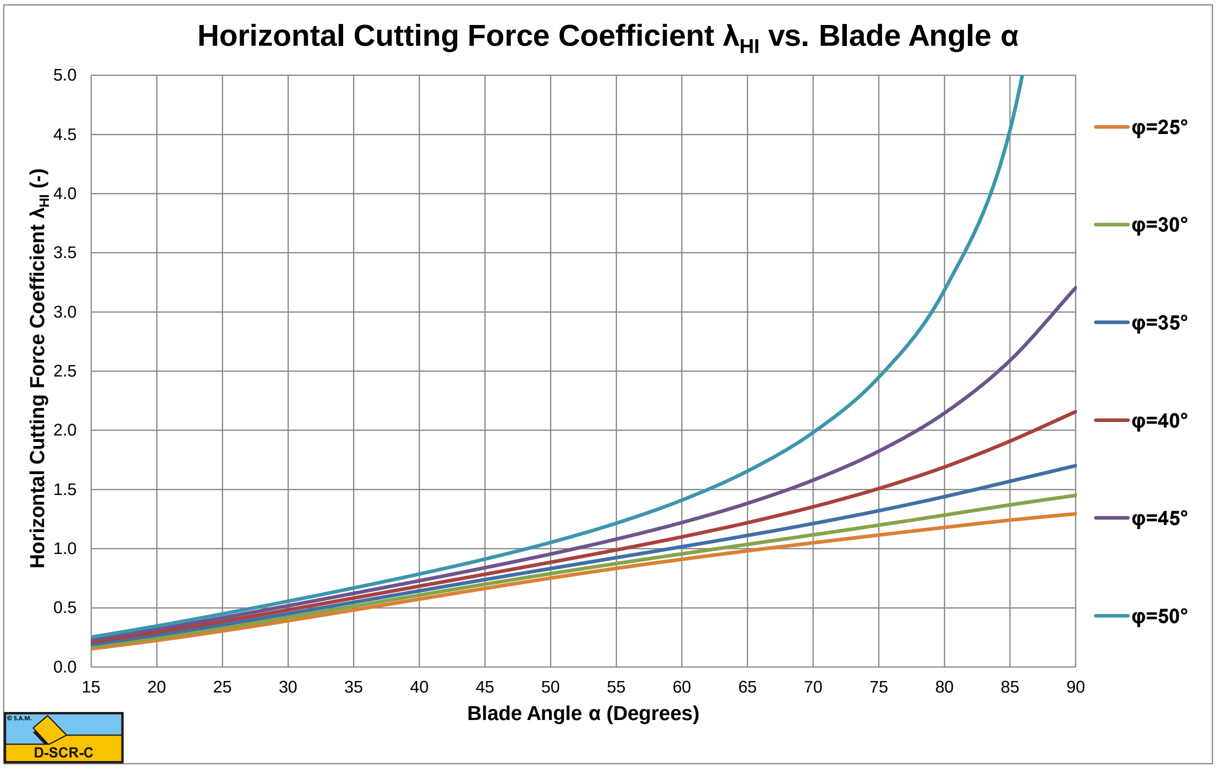

Figure B-25: The horizontal cutting force coefficient λ_{HI} for a dimensionless inertial effect parameter λ_i=250.

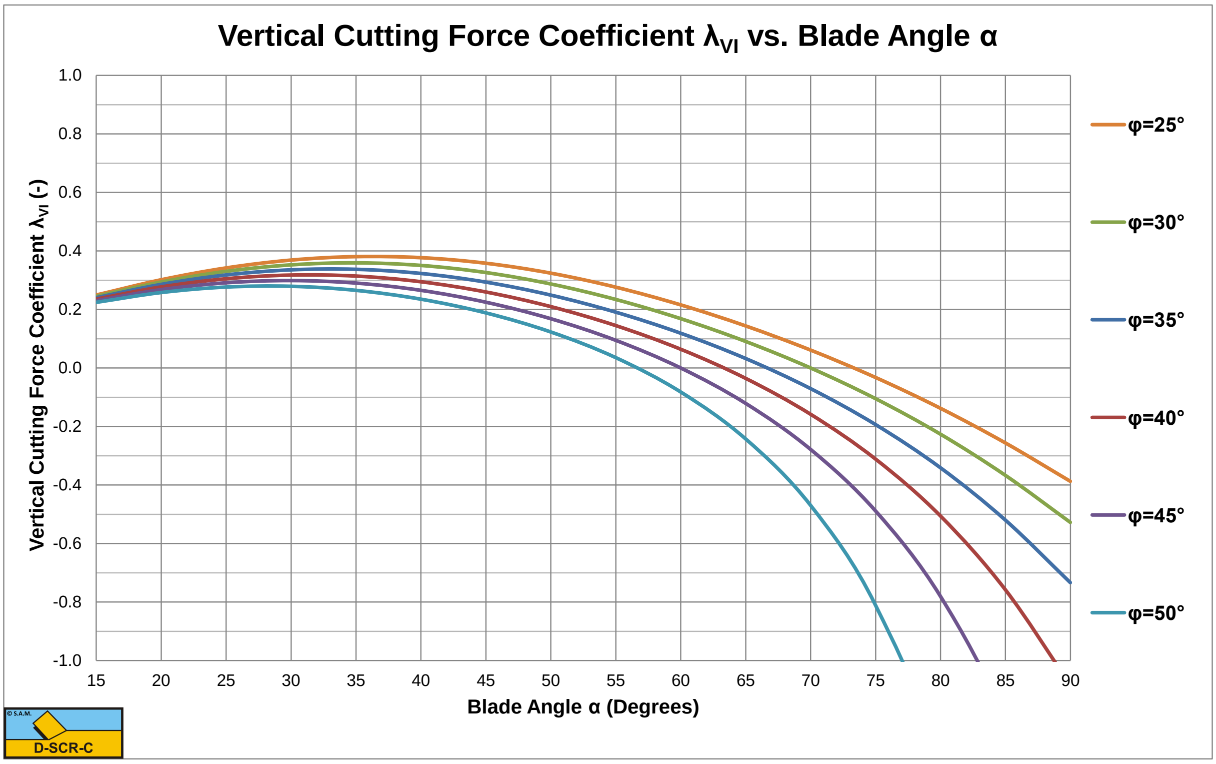

Figure B-26: The vertical cutting force coefficient λ_{VI} for a dimensionless inertial effect parameter λ_i=250.

Appendix C: Dimensionless Pore Pressures p_{1m} & p_{2m}.

Table C-1: The dimensionless pore pressures.

	h_b/h_i	k_i/k_{max}=1			k_i/k_{max}=0.25		
		β =30 °	37.5 °	45 °	30 °	37.5 °	45 °
α =15 °	1 (s)	0.156	0.168	0.177	0.235	0.262	0.286
	2 (s)	0.157	0.168	0.177	0.236	0.262	0.286
	3 (s)	0.158	0.168	0.177	0.237	0.262	0.286
	1 (b)	0.031	0.033	0.035	0.054	0.059	0.063
	2 (b)	0.016	0.017	0.018	0.028	0.030	0.032
	3 (b)	0.011	0.011	0.012	0.019	0.020	0.021
		β =25°	30°	35°	25°	30°	35°
α =30 °	1 (s)	0.178	0.186	0.193	0.274	0.291	0.308
	2 (s)	0.179	0.187	0.193	0.276	0.294	0.310
	3 (s)	0.179	0.187	0.193	0.277	0.294	0.310
	1 (b)	0.073	0.076	0.078	0.126	0.133	0.139
	2 (b)	0.049	0.049	0.049	0.084	0.085	0.086
	3 (b)	0.034	0.034	0.033	0.059	0.059	0.059
		β =20°	25°	30°	20°	25°	30°
α =45 °	1 (s)	0.185	0.193	0.200	0.289	0.306	0.325
	2 (s)	0.190	0.198	0.204	0.304	0.322	0.339
	3 (s)	0.192	0.200	0.205	0.308	0.325	0.340
	1 (b)	0.091	0.097	0.104	0.161	0.174	0.187
	2 (b)	0.081	0.082	0.083	0.146	0.148	0.151
	3 (b)	0.067	0.065	0.063	0.120	0.116	0.114
		β =15°	20°	25°	15°	20°	25°
α =60 °	1 (s)	0.182	0.192	0.200	0.278	0.303	0.324
	2 (s)	0.195	0.204	0.211	0.314	0.339	0.359
	3 (s)	0.199	0.208	0.214	0.327	0.350	0.368
	1 (b)	0.091	0.103	0.112	0.158	0.184	0.205
	2 (b)	0.100	0.106	0.109	0.182	0.196	0.204
	3 (b)	0.094	0.095	0.093	0.174	0.176	0.174

The dimensionless pore pressures $\mathbf{p_{1m}}$ in the shear zone (s) and $\mathbf{p_{2m}}$ on the blade surface (b) as a function of the blade angle **α**, de shear angle **β**, the ratio between the blade height $\mathbf{h_b}$ and the layer thickness $\mathbf{h_i}$ and the ratio between the permeability of the situ sand $\mathbf{k_i}$ and the permeability of the sand cut $\mathbf{k_{max}}$, with a wear zone behind the edge of the blade of $0.2\cdot\mathbf{h_i}$.

Appendix D: The Shear Angle β Non-Cavitating.

Table D-1: β for $h_b/h_i=1$, non-cavitating.

$h_b/h_i=1$	ϕ	32°	37°	42°	47°	52°
α	δ					
15	15°	40.892	40.152	39.169	38.012	36.727
	18°	39.024	38.380	37.483	36.402	35.184
	21°	37.355	36.781	35.947	34.924	33.756
	24°	35.847	35.321	34.534	33.552	32.423
	27°	34.468	33.975	33.220	32.269	31.166
	30°	33.196	32.723	31.989	31.058	29.973
30	15°	37.967	36.937	35.707	34.334	32.854
	18°	36.187	35.250	34.100	32.795	31.372
	21°	34.564	33.696	32.606	31.353	29.974
	24°	33.072	32.255	31.209	29.994	28.648
	27°	31.690	30.907	29.893	28.705	27.382
	30°	30.401	29.640	28.646	27.476	26.166
45	15°	33.389	32.254	30.936	29.481	27.919
	18°	31.792	30.726	29.467	28.061	26.539
	21°	30.326	29.310	28.092	26.720	25.224
	24°	28.969	27.984	26.793	25.442	23.963
	27°	27.700	26.733	25.557	24.218	22.745
	30°	26.503	25.543	24.373	23.036	21.562
60	15°	28.220	26.928	25.482	23.917	22.253
	18°	26.813	25.569	24.160	22.623	20.978
	21°	25.500	24.287	22.901	21.379	19.742
	24°	24.264	23.067	21.692	20.174	18.535
	27°	23.091	21.897	20.522	18.999	17.350
	30°	21.967	20.767	19.382	17.845	16.177

The shear angle β as a function of the blade angle α, the angle of internal friction ϕ, the soil/interface friction angle δ, for the non-cavitating cutting process, for $\mathbf{h_b/h_i=1}$.

Table D-2: β for h_b/h_i=2, non-cavitating.

h_b/h_i=2	ϕ	32°	37°	42°	47°	52°
α	δ					
15°	15°	41.128	40.402	39.427	38.273	36.986
	18°	39.239	38.609	37.720	36.643	35.424
	21°	37.554	36.993	36.167	35.147	33.979
	24°	36.030	35.517	34.738	33.760	32.630
	27°	34.638	34.158	33.410	32.462	31.358
	30°	33.354	32.893	32.167	31.238	30.152
30°	15°	39.129	37.939	36.562	35.056	33.457
	18°	37.223	36.144	34.859	33.429	31.894
	21°	35.458	34.468	33.258	31.891	30.408
	24°	33.820	32.899	31.748	30.432	28.992
	27°	32.293	31.425	30.320	29.043	27.637
	30°	30.864	30.035	28.965	27.718	26.336
45°	15°	33.483	32.334	30.991	29.508	27.918
	18°	31.743	30.679	29.408	27.985	26.444
	21°	30.142	29.141	27.925	26.547	25.043
	24°	28.660	27.704	26.527	25.182	23.705
	27°	27.278	26.353	25.202	23.879	22.420
	30°	25.982	25.074	23.939	22.630	21.179
60°	15°	27.692	26.533	25.186	23.694	22.085
	18°	26.156	25.057	23.759	22.307	20.729
	21°	24.744	23.683	22.418	20.991	19.432
	24°	23.432	22.394	21.147	19.733	18.180
	27°	22.203	21.173	19.932	18.520	16.965
	30°	21.039	20.008	18.763	17.344	15.776

The shear angle β as a function of the blade angle α, the angle of internal friction ϕ, the soil/interface friction angle δ, for the non-cavitating cutting process, for **h_b/h_i=2**.

Table D-3: β for h_b/h_i=3, non-cavitating.

h_b/h_i=3	ϕ	32 °	37 °	42 °	47 °	52 °
α	δ					
15 °	15 °	42.346	41.502	40.418	39.164	37.786
	18 °	40.414	39.674	38.681	37.507	36.198
	21 °	38.673	38.010	37.086	35.973	34.718
	24 °	37.087	36.481	35.609	34.542	33.328
	27 °	35.631	35.064	34.230	33.197	32.013
	30 °	34.283	33.742	32.934	31.926	30.763
30 °	15 °	40.176	38.793	37.257	35.619	33.909
	18 °	38.242	36.978	35.537	33.977	32.331
	21 °	36.421	35.258	33.900	32.407	30.817
	24 °	34.711	33.631	32.341	30.906	29.364
	27 °	33.103	32.090	30.858	29.470	27.968
	30 °	31.590	30.631	29.444	28.095	26.625
45 °	15 °	35.406	33.895	32.248	30.509	28.703
	18 °	33.548	32.142	30.578	28.907	27.156
	21 °	31.788	30.472	28.981	27.368	25.665
	24 °	30.126	28.885	27.455	25.891	24.230
	27 °	28.557	27.376	25.996	24.474	22.845
	30 °	27.075	25.941	24.600	23.111	21.509
60 °	15 °	28.252	26.972	25.516	23.930	22.241
	18 °	26.613	25.406	24.010	22.472	20.823
	21 °	25.094	23.940	22.588	21.086	19.464
	24 °	23.677	22.560	21.238	19.760	18.156
	27 °	22.348	21.253	19.950	18.485	16.890
	30 °	21.092	20.008	18.713	17.254	15.600

The shear angle β as a function of the blade angle α, the angle of internal friction ϕ, the soil/interface friction angle δ, for the non-cavitating cutting process, for **h_b/h_i=3**.

Appendix E: The Coefficient c_1.

Table E-1: c_1 for $h_b/h_i=1$.

$h_b/h_i=1$	ϕ	32 °	37 °	42 °	47 °	52 °
α	δ					
15 °	15 °	0.104	0.118	0.132	0.146	0.162
	18 °	0.119	0.134	0.150	0.167	0.186
	21 °	0.133	0.150	0.169	0.189	0.210
	24 °	0.147	0.167	0.188	0.211	0.236
	27 °	0.162	0.184	0.209	0.235	0.264
	30 °	0.177	0.202	0.229	0.259	0.292
30 °	15 °	0.175	0.203	0.234	0.268	0.306
	18 °	0.195	0.227	0.261	0.300	0.343
	21 °	0.215	0.251	0.290	0.334	0.384
	24 °	0.236	0.276	0.320	0.370	0.427
	27 °	0.257	0.302	0.352	0.409	0.474
	30 °	0.279	0.329	0.385	0.450	0.525
45 °	15 °	0.254	0.304	0.360	0.425	0.502
	18 °	0.279	0.334	0.398	0.472	0.560
	21 °	0.305	0.367	0.438	0.523	0.624
	24 °	0.332	0.401	0.482	0.578	0.695
	27 °	0.360	0.437	0.529	0.639	0.774
	30 °	0.390	0.477	0.580	0.706	0.863
60 °	15 °	0.360	0.445	0.547	0.671	0.826
	18 °	0.393	0.488	0.604	0.746	0.928
	21 °	0.428	0.535	0.666	0.831	1.045
	24 °	0.466	0.587	0.736	0.928	1.180
	27 °	0.507	0.643	0.815	1.039	1.341
	30 °	0.553	0.707	0.905	1.169	1.534

The dimensionless force $\mathbf{c_1}$, in the direction of the cutting velocity, as a function of the blade angle α, the angle of internal friction ϕ, the soil/interface friction angle δ, for $\mathbf{h_b/h_i=1}$.

Table E-2: c_1 for h_b/h_i=2.

h_b/h_i=2	ϕ	32 º	37 º	42 º	47 º	52 º
α	δ					
15 º	15 º	0.106	0.119	0.133	0.148	0.163
	18 º	0.120	0.135	0.152	0.169	0.187
	21 º	0.135	0.152	0.171	0.191	0.213
	24 º	0.149	0.169	0.191	0.214	0.239
	27 º	0.164	0.187	0.211	0.237	0.267
	30 º	0.179	0.205	0.232	0.262	0.296
30 º	15 º	0.185	0.214	0.246	0.281	0.320
	18 º	0.207	0.240	0.276	0.317	0.362
	21 º	0.230	0.267	0.308	0.354	0.407
	24 º	0.254	0.296	0.342	0.395	0.455
	27 º	0.278	0.325	0.378	0.437	0.507
	30 º	0.303	0.356	0.415	0.483	0.563
45 º	15 º	0.282	0.335	0.396	0.466	0.547
	18 º	0.313	0.373	0.441	0.521	0.616
	21 º	0.345	0.412	0.490	0.582	0.692
	24 º	0.379	0.454	0.543	0.648	0.775
	27 º	0.414	0.499	0.600	0.721	0.869
	30 º	0.452	0.547	0.662	0.801	0.974
60 º	15 º	0.415	0.509	0.622	0.760	0.932
	18 º	0.458	0.565	0.693	0.853	1.056
	21 º	0.504	0.625	0.772	0.958	1.197
	24 º	0.554	0.690	0.860	1.077	1.362
	27 º	0.607	0.762	0.958	1.213	1.556
	30 º	0.665	0.843	1.070	1.372	1.787

The dimensionless force c_1, in the direction of the cutting velocity, as a function of the blade angle α, the angle of internal friction ϕ, the soil/interface friction angle δ, for h_b/h_i=2.

Table E-3: c_1 for $h_b/h_i=3$.

$h_b/h_i=3$	ϕ	32 °	37 °	42 °	47 °	52 °
α	δ					
15 °	15 °	0.105	0.119	0.133	0.148	0.164
	18 °	0.120	0.135	0.152	0.169	0.188
	21 °	0.135	0.152	0.171	0.192	0.214
	24 °	0.150	0.170	0.191	0.215	0.240
	27 °	0.165	0.188	0.212	0.239	0.268
	30 °	0.180	0.206	0.234	0.264	0.298
30 °	15 °	0.185	0.215	0.247	0.282	0.322
	18 °	0.208	0.241	0.278	0.318	0.364
	21 °	0.232	0.269	0.310	0.357	0.410
	24 °	0.256	0.298	0.345	0.398	0.459
	27 °	0.280	0.328	0.381	0.441	0.511
	30 °	0.306	0.359	0.419	0.488	0.569
45 °	15 °	0.290	0.345	0.408	0.480	0.565
	18 °	0.324	0.386	0.457	0.541	0.640
	21 °	0.359	0.429	0.511	0.607	0.722
	24 °	0.396	0.476	0.568	0.679	0.813
	27 °	0.436	0.525	0.631	0.758	0.914
	30 °	0.478	0.579	0.699	0.846	1.029
60 °	15 °	0.439	0.538	0.657	0.802	0.983
	18 °	0.489	0.601	0.737	0.906	1.120
	21 °	0.542	0.670	0.826	1.024	1.278
	24 °	0.599	0.744	0.926	1.157	1.461
	27 °	0.660	0.827	1.037	1.310	1.676
	30 °	0.728	0.918	1.163	1.487	1.933

The dimensionless force c_1, in the direction of the cutting velocity, as a function of the blade angle α, the angle of internal friction ϕ, the soil/interface friction angle δ, for $h_b/h_i=3$.

Appendix F: The Coefficient c_2.

Table F-1: c_2 for h_b/h_i=1.

h_b/h_i=1	ϕ	32 °	37 °	42 °	47 °	52 °
α	δ					
15 °	15 °	0.113	0.137	0.161	0.187	0.215
	18 °	0.110	0.134	0.159	0.186	0.215
	21 °	0.106	0.130	0.156	0.184	0.214
	24 °	0.101	0.126	0.152	0.181	0.213
	27 °	0.096	0.121	0.148	0.178	0.211
	30 °	0.090	0.116	0.143	0.174	0.208
30 °	15 °	0.117	0.146	0.177	0.211	0.249
	18 °	0.110	0.139	0.171	0.206	0.246
	21 °	0.103	0.132	0.164	0.200	0.241
	24 °	0.094	0.123	0.156	0.193	0.235
	27 °	0.084	0.114	0.147	0.184	0.228
	30 °	0.074	0.103	0.136	0.174	0.218
45 °	15 °	0.101	0.130	0.164	0.202	0.247
	18 °	0.090	0.119	0.152	0.191	0.237
	21 °	0.078	0.106	0.139	0.178	0.224
	24 °	0.064	0.092	0.124	0.162	0.208
	27 °	0.049	0.075	0.106	0.143	0.188
	30 °	0.032	0.056	0.085	0.120	0.164
60 °	15 °	0.060	0.084	0.112	0.146	0.189
	18 °	0.041	0.063	0.088	0.120	0.160
	21 °	0.021	0.039	0.061	0.088	0.124
	24 °	-0.003	0.011	0.028	0.050	0.078
	27 °	-0.030	-0.021	-0.011	0.003	0.021
	30 °	-0.061	-0.059	-0.057	-0.055	-0.053

The dimensionless force c_2, perpendicular to the cutting velocity, as a function of the blade angle α, the angle of internal friction ϕ, the soil/interface friction angle δ, for h_b/h_i=1.

Table F-2: c_2 for h_b/h_i=2.

h_b/h_i=2	ϕ	32 º	37 º	42 º	47 º	52 º
α	δ					
15 º	15 º	0.113	0.136	0.161	0.187	0.215
	18 º	0.109	0.133	0.159	0.186	0.216
	21 º	0.105	0.130	0.156	0.184	0.215
	24 º	0.101	0.126	0.153	0.182	0.214
	27 º	0.095	0.121	0.148	0.178	0.212
	30 º	0.089	0.115	0.143	0.174	0.209
30 º	15 º	0.113	0.143	0.174	0.209	0.249
	18 º	0.105	0.135	0.168	0.204	0.245
	21 º	0.096	0.126	0.160	0.197	0.239
	24 º	0.086	0.116	0.150	0.188	0.232
	27 º	0.075	0.105	0.139	0.178	0.223
	30 º	0.062	0.092	0.127	0.166	0.212
45 º	15 º	0.092	0.123	0.158	0.199	0.247
	18 º	0.078	0.109	0.144	0.185	0.234
	21 º	0.062	0.092	0.127	0.168	0.217
	24 º	0.044	0.073	0.107	0.148	0.197
	27 º	0.023	0.051	0.084	0.124	0.173
	30 º	0.001	0.027	0.058	0.096	0.143
60 º	15 º	0.042	0.068	0.099	0.137	0.184
	18 º	0.017	0.040	0.069	0.104	0.148
	21 º	-0.012	0.008	0.033	0.063	0.103
	24 º	-0.044	-0.029	-0.010	0.015	0.046
	27 º	-0.081	-0.071	-0.060	-0.045	-0.025
	30 º	-0.123	-0.121	-0.120	-0.118	-0.116

The dimensionless force **c_2**, perpendicular to the cutting velocity, as a function of the blade angle α, the angle of internal friction ϕ, the soil/interface friction angle δ, for **h_b/h_i=2**.

Table F-3: c_2 for h_b/h_i=3.

h_b/h_i=3	**ϕ**	**32 °**	**37 °**	**42 °**	**47 °**	**52 °**
α	**δ**					
15 °	**15 °**	**0.113**	**0.137**	**0.161**	**0.188**	**0.216**
	18 °	**0.110**	**0.134**	**0.159**	**0.187**	**0.216**
	21 °	**0.105**	**0.130**	**0.156**	**0.185**	**0.216**
	24 °	**0.101**	**0.126**	**0.153**	**0.182**	**0.214**
	27 °	**0.096**	**0.121**	**0.149**	**0.179**	**0.212**
	30 °	**0.090**	**0.116**	**0.144**	**0.175**	**0.210**
30 °	**15 °**	**0.113**	**0.142**	**0.174**	**0.209**	**0.248**
	18 °	**0.105**	**0.135**	**0.167**	**0.204**	**0.244**
	21 °	**0.096**	**0.126**	**0.159**	**0.196**	**0.239**
	24 °	**0.085**	**0.116**	**0.149**	**0.188**	**0.231**
	27 °	**0.074**	**0.104**	**0.138**	**0.177**	**0.222**
	30 °	**0.061**	**0.091**	**0.125**	**0.165**	**0.211**
45 °	**15 °**	**0.089**	**0.121**	**0.156**	**0.197**	**0.246**
	18 °	**0.073**	**0.105**	**0.140**	**0.182**	**0.232**
	21 °	**0.056**	**0.086**	**0.122**	**0.163**	**0.214**
	24 °	**0.035**	**0.065**	**0.100**	**0.141**	**0.192**
	27 °	**0.012**	**0.041**	**0.074**	**0.115**	**0.164**
	30 °	**-0.013**	**0.013**	**0.045**	**0.083**	**0.131**
60 °	**15 °**	**0.032**	**0.058**	**0.090**	**0.129**	**0.177**
	18 °	**0.002**	**0.026**	**0.055**	**0.091**	**0.136**
	21 °	**-0.031**	**-0.011**	**0.014**	**0.045**	**0.085**
	24 °	**-0.069**	**-0.054**	**-0.035**	**-0.011**	**0.021**
	27 °	**-0.112**	**-0.104**	**-0.093**	**-0.079**	**-0.059**
	30 °	**-0.162**	**-0.162**	**-0.162**	**-0.162**	**-0.162**

The dimensionless force **c_2**, perpendicular to the cutting velocity, as a function of the blade angle α, the angle of internal friction ϕ, the soil/interface friction angle δ, for **h_b/h_i=3**.

Appendix G: The Coefficient a_1.

Table G-1: a_1 for h_b/h_i=1.

h_b/h_i=1	ϕ	32 º	37 º	42 º	47 º	52 º
α	δ					
15 º	15 º	0.525	0.520	0.515	0.509	0.503
	18 º	0.520	0.516	0.510	0.505	0.498
	21 º	0.516	0.511	0.506	0.500	0.494
	24 º	0.511	0.507	0.502	0.496	0.490
	27 º	0.507	0.503	0.498	0.492	0.485
	30 º	0.503	0.498	0.493	0.487	0.481
30 º	15 º	0.526	0.522	0.517	0.512	0.506
	18 º	0.523	0.519	0.514	0.509	0.503
	21 º	0.520	0.516	0.511	0.506	0.500
	24 º	0.517	0.512	0.508	0.502	0.497
	27 º	0.514	0.509	0.504	0.499	0.493
	30 º	0.510	0.506	0.501	0.496	0.490
45 º	15 º	0.534	0.530	0.525	0.520	0.514
	18 º	0.531	0.527	0.522	0.517	0.511
	21 º	0.528	0.524	0.519	0.514	0.508
	24 º	0.525	0.521	0.516	0.511	0.505
	27 º	0.523	0.518	0.513	0.508	0.501
	30 º	0.520	0.515	0.510	0.504	0.498
60 º	15 º	0.535	0.528	0.521	0.513	0.505
	18 º	0.530	0.524	0.517	0.509	0.500
	21 º	0.526	0.519	0.512	0.504	0.494
	24 º	0.521	0.515	0.507	0.498	0.489
	27 º	0.517	0.510	0.502	0.493	0.483
	30 º	0.512	0.505	0.497	0.487	0.477

The weigh factor a_1, for the determination of the weighted average permeability k_m, as a function of the blade angle **α**, the angle of internal friction **φ**, the soil/interface friction angle **δ**, for h_b/h_i=1.

Table G-2: a_1 for $h_b/h_i=2$.

$h_b/h_i=2$	ϕ	32 °	37 °	42 °	47 °	52 °
α	δ					
15 °	15 °	0.522	0.518	0.513	0.507	0.501
	18 °	0.518	0.514	0.509	0.503	0.497
	21 °	0.514	0.510	0.505	0.499	0.493
	24 °	0.510	0.506	0.501	0.495	0.489
	27 °	0.506	0.502	0.497	0.491	0.485
	30 °	0.502	0.498	0.493	0.487	0.481
30 °	15 °	0.531	0.526	0.521	0.516	0.511
	18 °	0.527	0.523	0.518	0.513	0.508
	21 °	0.524	0.520	0.515	0.510	0.505
	24 °	0.521	0.517	0.512	0.507	0.501
	27 °	0.518	0.514	0.509	0.504	0.498
	30 °	0.514	0.510	0.506	0.500	0.495
45 °	15 °	0.554	0.550	0.546	0.541	0.536
	18 °	0.552	0.548	0.544	0.539	0.534
	21 °	0.550	0.546	0.542	0.537	0.532
	24 °	0.548	0.544	0.539	0.535	0.529
	27 °	0.546	0.542	0.537	0.532	0.527
	30 °	0.544	0.540	0.535	0.530	0.524
60 °	15 °	0.575	0.569	0.563	0.556	0.549
	18 °	0.571	0.566	0.559	0.552	0.545
	21 °	0.568	0.562	0.556	0.549	0.541
	24 °	0.565	0.559	0.552	0.545	0.536
	27 °	0.561	0.555	0.548	0.541	0.532
	30 °	0.558	0.552	0.544	0.536	0.527

The weigh factor $\mathbf{a_1}$, for the determination of the weighted average permeability $\mathbf{k_m}$, as a function of the blade angle **α**, the angle of internal friction **φ**, the soil/interface friction angle **δ**, for $\mathbf{h_b/h_i=2}$.

Table G-3: a_1 for h_b/h_i=3.

h_b/h_i=3	ϕ	32 °	37 °	42 °	47 °	52 °
α	δ					
15 °	15 °	0.522	0.517	0.512	0.507	0.501
	18 °	0.518	0.513	0.508	0.503	0.497
	21 °	0.514	0.509	0.504	0.499	0.493
	24 °	0.510	0.505	0.500	0.495	0.489
	27 °	0.506	0.501	0.497	0.491	0.485
	30 °	0.502	0.498	0.493	0.487	0.480
30 °	15 °	0.534	0.529	0.524	0.519	0.514
	18 °	0.531	0.526	0.521	0.516	0.511
	21 °	0.528	0.523	0.519	0.513	0.508
	24 °	0.525	0.520	0.516	0.511	0.505
	27 °	0.522	0.517	0.513	0.508	0.502
	30 °	0.519	0.514	0.510	0.504	0.499
45 °	15 °	0.552	0.548	0.544	0.540	0.536
	18 °	0.550	0.547	0.543	0.539	0.534
	21 °	0.549	0.545	0.541	0.537	0.532
	24 °	0.547	0.543	0.539	0.535	0.531
	27 °	0.545	0.542	0.538	0.533	0.529
	30 °	0.544	0.540	0.536	0.531	0.527
60 °	15 °	0.580	0.575	0.570	0.565	0.559
	18 °	0.578	0.573	0.568	0.563	0.557
	21 °	0.576	0.571	0.566	0.560	0.554
	24 °	0.573	0.569	0.564	0.558	0.551
	27 °	0.571	0.566	0.561	0.555	0.548
	30 °	0.569	0.564	0.558	0.552	0.545

The weigh factor $\mathbf{a_1}$, for the determination of the weighted average permeability $\mathbf{k_m}$, as a function of the blade angle **α**, the angle of internal friction **φ**, the soil/interface friction angle **δ**, for $\mathbf{h_b/h_i=3}$.

Appendix H: The Shear Angle β Cavitating.

Table H-1: β for $h_b/h_i=1$, cavitating.

$h_b/h_i=1$	ϕ	32 °	37 °	42 °	47 °	52 °
α	δ					
15 °	15 °	37.217	37.520	37.355	36.831	36.026
	18 °	34.461	34.854	34.790	34.370	33.669
	21 °	32.163	32.598	32.594	32.243	31.613
	24 °	30.212	30.661	30.689	30.379	29.796
	27 °	28.530	28.973	29.012	28.726	28.173
	30 °	27.060	27.483	27.520	27.243	26.707
30 °	15 °	39.766	39.060	38.014	36.718	35.232
	18 °	37.341	36.757	35.823	34.628	33.233
	21 °	35.196	34.696	33.844	32.725	31.399
	24 °	33.280	32.837	32.041	30.977	29.704
	27 °	31.554	31.145	30.387	29.363	28.127
	30 °	29.985	29.593	28.859	27.860	26.650
45 °	15 °	36.853	35.599	34.097	32.412	30.591
	18 °	34.768	33.616	32.202	30.594	28.839
	21 °	32.866	31.789	30.441	28.892	27.188
	24 °	31.119	30.094	28.794	27.288	25.623
	27 °	29.502	28.512	27.246	25.770	24.132
	30 °	27.996	27.026	25.781	24.325	22.705
60 °	15 °	31.992	30.395	28.608	26.683	24.654
	18 °	30.155	28.634	26.911	25.039	23.055
	21 °	28.444	26.979	25.303	23.471	21.520
	24 °	26.841	25.414	23.772	21.968	20.040
	27 °	25.330	23.927	22.306	20.520	18.605
	30 °	23.897	22.506	20.896	19.118	17.208

The shear angle β as a function of the blade angle α, the angle of internal friction ϕ, the soil/interface friction angle δ, for the cavitating cutting process, for $\mathbf{h_b/h_i=1}$.

Table H-2: β for $h_b/h_i=2$, cavitating.

$h_b/h_i=2$	ϕ	32°	37°	42°	47°	52°
α	δ					
15°	15°	28.724	29.560	29.957	29.994	29.733
	18°	26.332	27.162	27.586	27.670	27.472
	21°	24.420	25.221	25.643	25.747	25.582
	24°	22.849	23.608	24.014	24.120	23.968
	27°	21.528	22.240	22.621	22.716	22.566
	30°	20.396	21.059	21.407	21.485	21.329
30°	15°	33.398	33.367	32.937	32.198	31.215
	18°	30.972	31.019	30.677	30.027	29.134
	21°	28.922	29.011	28.721	28.131	27.299
	24°	27.161	27.265	27.004	26.451	25.659
	27°	25.622	25.725	25.476	24.944	24.177
	30°	24.259	24.349	24.101	23.576	22.823
45°	15°	32.378	31.721	30.741	29.516	28.100
	18°	30.207	29.642	28.751	27.610	26.271
	21°	28.308	27.801	26.970	25.887	24.605
	24°	26.624	26.149	25.357	24.314	23.070
	27°	25.110	24.652	23.881	22.862	21.643
	30°	23.736	23.280	22.518	21.512	20.306
60°	15°	28.906	27.806	26.445	24.886	23.174
	18°	26.993	25.974	24.686	23.194	21.540
	21°	25.276	24.309	23.072	21.626	20.014
	24°	23.716	22.781	21.576	20.159	18.574
	27°	22.283	21.364	20.176	18.776	17.204
	30°	20.955	20.038	18.855	17.461	15.892

The shear angle β as a function of the blade angle α, the angle of internal friction ϕ, the soil/interface friction angle δ, for the cavitating cutting process, for **$h_b/h_i=2$.**

Table H-3: β for $h_b/h_i=3$, cavitating.

$h_b/h_i=3$	φ	32°	37°	42°	47°	52°
α	δ					
15°	15°	24.046	25.019	25.609	25.872	25.856
	18°	21.976	22.900	23.476	23.751	23.765
	21°	20.350	21.217	21.763	22.030	22.053
	24°	19.031	19.838	20.348	20.596	20.615
	27°	17.932	18.680	19.150	19.374	19.381
	30°	16.996	17.687	18.117	18.313	18.303
30°	15°	29.286	29.575	29.466	29.038	28.353
	18°	26.992	27.319	27.267	26.908	26.297
	21°	25.100	25.435	25.410	25.090	24.525
	24°	23.504	23.828	23.811	23.511	22.973
	27°	22.130	22.433	22.410	22.116	21.592
	30°	20.928	21.202	21.165	20.867	20.346
45°	15°	29.236	28.919	28.257	27.325	26.179
	18°	27.101	26.853	26.266	25.411	24.339
	21°	25.277	25.065	24.524	23.719	22.699
	24°	23.690	23.493	22.977	22.203	21.215
	27°	22.288	22.091	21.584	20.825	19.857
	30°	21.031	20.823	20.315	19.561	18.600
60°	15°	26.619	25.832	24.754	23.450	21.967
	18°	24.711	23.995	22.987	21.750	20.329
	21°	23.037	22.362	21.398	20.206	18.826
	24°	21.543	20.889	19.951	18.785	17.431
	27°	20.193	19.545	18.617	17.464	16.121
	30°	18.958	18.303	17.374	16.222	14.880

The shear angle β as a function of the blade angle α, the angle of internal friction φ, the soil/interface friction angle δ, for the cavitating cutting process, for **$h_b/h_i=3$.**

Appendix I: The Coefficient d_1.

Table I-1: d_1 for $h_b/h_i=1$.

$h_b/h_i=1$	ϕ	32°	37°	42°	47°	52°
α	δ					
15°	15°	1.390	1.505	1.625	1.753	1.890
	18°	1.626	1.766	1.913	2.069	2.238
	21°	1.860	2.028	2.205	2.393	2.597
	24°	2.092	2.291	2.501	2.726	2.970
	27°	2.324	2.557	2.803	3.068	3.358
	30°	2.556	2.826	3.112	3.423	3.764
30°	15°	1.206	1.374	1.559	1.766	2.000
	18°	1.381	1.575	1.791	2.033	2.309
	21°	1.559	1.783	2.033	2.315	2.638
	24°	1.741	1.998	2.286	2.613	2.991
	27°	1.928	2.222	2.552	2.930	3.370
	30°	2.121	2.455	2.833	3.269	3.781
45°	15°	1.419	1.688	2.000	2.365	2.800
	18°	1.598	1.905	2.262	2.685	3.192
	21°	1.784	2.133	2.543	3.032	3.625
	24°	1.980	2.376	2.846	3.411	4.105
	27°	2.186	2.636	3.174	3.829	4.642
	30°	2.404	2.916	3.533	4.292	5.249
60°	15°	1.879	2.331	2.883	3.570	4.444
	18°	2.099	2.615	3.252	4.054	5.090
	21°	2.336	2.925	3.661	4.602	5.837
	24°	2.593	3.267	4.120	5.228	6.711
	27°	2.872	3.645	4.639	5.952	7.746
	30°	3.179	4.069	5.232	6.798	8.991

The dimensionless force $\mathbf{d_1}$, in the direction of the cutting velocity, as a function of the blade angle α, the angle of internal friction ϕ, the soil/interface friction angle δ, for $\mathbf{h_b/h_i=1}$.

Table I-2: d_1 for h_b/h_i=2.

h_b/h_i=2	ϕ	32 °	37 °	42 °	47 °	52 °
α	δ					
15 °	15 °	2.295	2.460	2.627	2.801	2.984
	18 °	2.683	2.889	3.098	3.315	3.545
	21 °	3.062	3.313	3.569	3.836	4.119
	24 °	3.435	3.735	4.042	4.364	4.707
	27 °	3.803	4.156	4.520	4.903	5.313
	30 °	4.169	4.579	5.005	5.455	5.941
30 °	15 °	1.729	1.934	2.156	2.401	2.674
	18 °	1.997	2.239	2.503	2.794	3.122
	21 °	2.267	2.550	2.860	3.205	3.593
	24 °	2.539	2.868	3.230	3.634	4.093
	27 °	2.815	3.195	3.614	4.085	4.625
	30 °	3.097	3.532	4.015	4.563	5.195
45 °	15 °	1.836	2.142	2.492	2.898	3.377
	18 °	2.093	2.447	2.854	3.330	3.897
	21 °	2.357	2.765	3.238	3.794	4.462
	24 °	2.631	3.100	3.646	4.296	5.084
	27 °	2.917	3.454	4.085	4.843	5.772
	30 °	3.217	3.830	4.558	5.442	6.541
60 °	15 °	2.269	2.764	3.364	4.104	5.038
	18 °	2.567	3.139	3.837	4.710	5.827
	21 °	2.883	3.543	4.357	5.388	6.728
	24 °	3.221	3.982	4.933	6.154	7.771
	27 °	3.586	4.464	5.578	7.031	8.995
	30 °	3.982	4.998	6.306	8.047	10.453

The dimensionless force $\mathbf{d_1}$, in the direction of the cutting velocity, as a function of the blade angle α, the angle of internal friction ϕ, the soil/interface friction angle δ , for $\mathbf{h_b/h_i=2}$.

Table I-3: d_1 for h_b/h_i=3.

h_b/h_i=3	ϕ	32 °	37 °	42 °	47 °	52 °
α	δ					
15 °	15 °	3.145	3.362	3.578	3.799	4.028
	18 °	3.672	3.945	4.218	4.497	4.789
	21 °	4.185	4.519	4.855	5.200	5.562
	24 °	4.687	5.087	5.492	5.910	6.351
	27 °	5.180	5.652	6.132	6.631	7.159
	30 °	5.667	6.216	6.778	7.366	7.993
30 °	15 °	2.216	2.458	2.717	3.000	3.312
	18 °	2.567	2.858	3.169	3.510	3.889
	21 °	2.919	3.262	3.632	4.038	4.492
	24 °	3.272	3.673	4.107	4.587	5.127
	27 °	3.629	4.093	4.599	5.162	5.799
	30 °	3.991	4.525	5.110	5.766	6.515
45 °	15 °	2.222	2.566	2.954	3.402	3.925
	18 °	2.549	2.951	3.408	3.938	4.562
	21 °	2.883	3.350	3.885	4.509	5.252
	24 °	3.228	3.768	4.391	5.123	6.004
	27 °	3.585	4.207	4.929	5.788	6.831
	30 °	3.958	4.671	5.508	6.513	7.750
60 °	15 °	2.632	3.170	3.817	4.610	5.605
	18 °	2.999	3.627	4.387	5.329	6.526
	21 °	3.387	4.116	5.008	6.128	7.572
	24 °	3.799	4.645	5.692	7.025	8.774
	27 °	4.240	5.222	6.453	8.044	10.175
	30 °	4.717	5.856	7.307	9.217	11.833

The dimensionless force $\mathbf{d_1}$, in the direction of the cutting velocity, as a function of the blade angle α, the angle of internal friction ϕ, the soil/interface friction angle δ , for $\mathbf{h_b/h_i=3}$.

Appendix J: The Coefficient d_2.

Table J-1: d_2 for $h_b/h_i=1$.

$h_b/h_i=1$	ϕ	32 °	37 °	42 °	47 °	52 °
α	δ					
15 °	15 °	0.409	0.608	0.816	1.037	1.274
	18 °	0.312	0.528	0.754	0.995	1.255
	21 °	0.205	0.436	0.680	0.939	1.220
	24 °	0.087	0.333	0.592	0.870	1.172
	27 °	-0.040	0.219	0.493	0.788	1.110
	30 °	-0.175	0.095	0.382	0.692	1.034
30 °	15 °	0.474	0.642	0.828	1.035	1.269
	18 °	0.412	0.588	0.782	1.000	1.249
	21 °	0.341	0.523	0.725	0.954	1.216
	24 °	0.261	0.447	0.657	0.895	1.169
	27 °	0.171	0.361	0.576	0.822	1.108
	30 °	0.071	0.264	0.483	0.735	1.031
45 °	15 °	0.398	0.553	0.733	0.945	1.196
	18 °	0.325	0.481	0.664	0.879	1.138
	21 °	0.241	0.396	0.579	0.797	1.061
	24 °	0.145	0.298	0.478	0.696	0.962
	27 °	0.037	0.183	0.358	0.572	0.836
	30 °	-0.086	0.051	0.217	0.421	0.678
60 °	15 °	0.195	0.317	0.465	0.650	0.885
	18 °	0.083	0.193	0.329	0.500	0.721
	21 °	-0.047	0.047	0.164	0.313	0.510
	24 °	-0.198	-0.126	-0.036	0.081	0.238
	27 °	-0.372	-0.331	-0.278	-0.208	-0.113
	30 °	-0.575	-0.574	-0.573	-0.572	-0.570

The dimensionless force $\mathbf{d_2}$, perpendicular to the cutting velocity, as a function of the blade angle α, the angle of internal friction ϕ, the soil/interface friction angle δ, for $\mathbf{h_b/h_i=1}$.

Table J-2: d_2 for h_b/h_i=2.

h_b/h_i=2	ϕ	32 °	37 °	42 °	47 °	52 °
α	δ					
15 °	15 °	-0.024	0.262	0.552	0.853	1.170
	18 °	-0.253	0.064	0.387	0.722	1.076
	21 °	-0.496	-0.151	0.202	0.569	0.959
	24 °	-0.752	-0.381	-0.001	0.396	0.820
	27 °	-1.018	-0.626	-0.221	0.204	0.660
	30 °	-1.294	-0.884	-0.458	-0.007	0.479
30 °	15 °	0.266	0.471	0.693	0.938	1.211
	18 °	0.136	0.354	0.592	0.854	1.149
	21 °	-0.008	0.222	0.473	0.752	1.067
	24 °	-0.165	0.074	0.337	0.631	0.965
	27 °	-0.336	-0.089	0.183	0.490	0.841
	30 °	-0.520	-0.268	0.011	0.327	0.693
45 °	15 °	0.216	0.393	0.595	0.830	1.107
	18 °	0.087	0.267	0.475	0.718	1.007
	21 °	-0.059	0.123	0.334	0.582	0.880
	24 °	-0.221	-0.040	0.170	0.420	0.723
	27 °	-0.401	-0.226	-0.020	0.227	0.529
	30 °	-0.600	-0.435	-0.240	-0.002	0.293
60 °	15 °	-0.009	0.124	0.285	0.484	0.735
	18 °	-0.182	-0.060	0.089	0.275	0.513
	21 °	-0.379	-0.274	-0.145	0.019	0.233
	24 °	-0.603	-0.523	-0.422	-0.293	-0.122
	27 °	-0.859	-0.812	-0.753	-0.676	-0.571
	30 °	-1.151	-1.151	-1.150	-1.148	-1.146

The dimensionless force $\mathbf{d_2}$, perpendicular to the cutting velocity, as a function of the blade angle α, the angle of internal friction ϕ, the soil/interface friction angle δ, for $\mathbf{h_b/h_i}$**=2**.

Table J-3: d_2 for $h_b/h_i=3$.

$h_b/h_i=3$	ϕ	32°	37°	42°	47°	52°
α	δ					
15°	15°	-0.552	-0.177	0.198	0.581	0.979
	18°	-0.921	-0.501	-0.080	0.350	0.800
	21°	-1.306	-0.846	-0.384	0.092	0.590
	24°	-1.703	-1.208	-0.708	-0.191	0.353
	27°	-2.111	-1.586	-1.053	-0.498	0.090
	30°	-2.528	-1.979	-1.417	-0.828	-0.201
30°	15°	0.020	0.263	0.522	0.805	1.118
	18°	-0.182	0.079	0.360	0.667	1.009
	21°	-0.402	-0.124	0.176	0.505	0.873
	24°	-0.638	-0.346	-0.030	0.319	0.711
	27°	-0.890	-0.588	-0.259	0.107	0.521
	30°	-1.158	-0.850	-0.511	-0.132	0.301
45°	15°	0.017	0.215	0.440	0.698	1.001
	18°	-0.171	0.034	0.267	0.537	0.856
	21°	-0.379	-0.171	0.068	0.346	0.677
	24°	-0.608	-0.400	-0.160	0.122	0.460
	27°	-0.858	-0.656	-0.420	-0.141	0.199
	30°	-1.133	-0.941	-0.717	-0.447	-0.114
60°	15°	-0.221	-0.076	0.097	0.310	0.578
	18°	-0.455	-0.321	-0.159	0.042	0.298
	21°	-0.718	-0.602	-0.460	-0.282	-0.052
	24°	-1.014	-0.925	-0.814	-0.673	-0.488
	27°	-1.349	-1.297	-1.231	-1.147	-1.034
	30°	-1.728	-1.727	-1.726	-1.724	-1.722

The dimensionless force d_2, perpendicular to the cutting velocity, as a function of the blade angle α, the angle of internal friction ϕ, the soil/interface friction angle δ, for $h_b/h_i=3$.

Appendix K: The Properties of the 200 µm Sand.

The sand in the old laboratory DE, with a **d_{50}** of 200 µm, is examined for the following soil mechanical parameters:

1. The minimum and the maximum density, Table K-1: Pore percentages.
2. The dry critical density, Table K-1: Pore percentages.
3. The saturated critical density, Table K-1: Pore percentages. The permeability as a function of the density, Table K-2: Permeability as a function of the porosity.
4. The angle of internal friction as a function of the density, Table K-4: The angle of internal friction as function of the pore percentage.
5. The **d_{50}** as a function of the time, Table K-3: The d_{50} of the sand as function of the time.
6. The cone resistance per experiment.
7. The density in the test stand in combination with the cone resistance.

The points 7 and 8 need some explanation. With the aid of a Troxler density measuring set density measurements are performed in situ, that is in the test stand. During each measurement the cone resistance is determined at the same position. In this way it is possible to formulate a calibration formula for the density as a function of the cone resistance. The result is:

$$\mathbf{n = \frac{65.6}{C_p^{0.082}} \quad with: \; n \; in \; \%, C_p \; in \; kPa} \qquad \textbf{(K-1)}$$

In which the cone resistance is determined in a top layer of 18 cm, where the cone resistance was continuously increasing and almost proportional with the depth. The value to be used in this equation is the cone resistance for the 18 cm depth.

With the aid of this equation it was possible to determine the density for each cutting test from the cone resistance measurements. The result was an average pore percentage of 38.53% over 367 tests.
By interpolating in Table K-2 it can be derived that a pore percentage of 38.53% corresponds to a permeability of 0.000165 m/s. By extrapolating in this table it can also be derived that the maximum pore percentage of 43.8% corresponds to a permeability of approximately 0.00032 m/s. At the start of the cutting tests the pore percentage was averaged 38%, which corresponds to a permeability of 0.00012 m/s.

Table K-1: Pore percentages.

Minimum density	43.8%
Maximum density	32.7%
Dry critical density	39.9%
Saturated critical density	40.7%-41.7%
Initial density	38.5%

Table K-2: Permeability as a function of the porosity.

Pore percentage	Permeability (m/s)
36.97%	0.000077
38.48%	0.000165
38.98%	0.000206
39.95%	0.000240
40.88%	0.000297
41.84%	0.000307
43.07%	0.000289
43.09%	0.000322

Table K-3: The d_{50} of the sand as function of the time.

Date	d_{50} (mm)
22-09-1982	0.175
17-12-1984	0.180
02-01-1985	0.170
08-01-1985	0.200
14-01-1985	0.200
21-01-1985	0.200
28-01-1985	0.195
04-02-1985	0.205
26-02-1985	0.210

Table K-4: The angle of internal friction as function of the pore percentage.

Pore percentage	Cell pressure kPa	Angle of internal friction
Dry		
43.8%	50	35.1°
41.2%	50	36.0°
39.9%	50	38.3°
Saturated undrained		
43.8%	100	30.9°
42.1%	10	31.2°
42.1%	50	31.2°
42.1%	100	31.6°
42.2%	100	32.0°
41.8%	10	33.1°
41.3%	10	31.9°
41.2%	50	32.2°
41.1%	50	30.1°
41.1%	100	31.3°
41.1%	100	33.7°
41.0%	100	35.2°
40.5%	10	33.8°
40.3%	50	33.7°
40.4%	100	33.1°
39.8%	10	34.1°
39.2%	10	33.8°
39.2%	50	33.8°
39.2%	100	33.9°
38.2%	10	35.2°
38.1%	50	35.3°
38.1%	100	35.0°
37.3%	10	37.4°
37.0%	10	38.6°
37.0%	50	37.3°
36.9%	100	36.8°
36.2%	100	38.0°

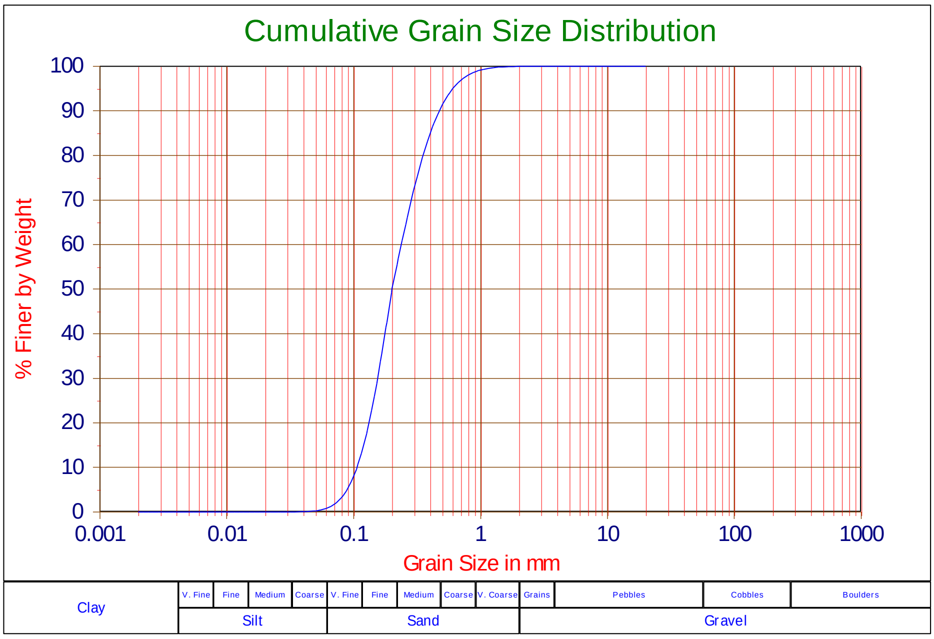

Figure K-1: The PSD of the 200 µm sand.

Appendix L: The Properties of the 105 µm Sand.

The sand in the new laboratory DE, with a $\mathbf{d_{50}}$ of 105 µm, is examined for the following soil mechanical parameters:

1. The minimum and the maximum density, Table L-1: Pore percentages, indicated are the average measured densities for the various blade angles.
2. The saturated critical density, Table L-1: Pore percentages, indicated are the average measured densities for the various blade angles.
3. The permeability as a function of the density, Table L-2: Permeabilities, indicated are the average permeabilities for the various blade angles.
4. The angle of internal friction as a function of the density, Table L-4: The angle of internal friction as a function of the pore percentage.
5. The $\mathbf{d_{50}}$ as a function of the time, Table L-3: The d50 of the sand as a function of time.
6. The cone resistance per test.
7. The density in the test stand in combination with the cone resistance.

The points 6 and 7 need some explanation. As with the 200 µm sand density measurements are performed in situ with the aid of a Troxler density measuring set. The calibration formula for the 105 µm sand is:

$$\mathbf{n = \frac{69.9}{C_p^{0.068}} \quad with:\ n\ in\ \%,\ C_p\ in\ kPa} \tag{L-1}$$

In which the cone resistance is determined in a top layer of 12 cm, where the cone resistance was continuously increasing and almost proportional with the depth. The value to be used in this equation is the cone resistance for the 12 cm depth.

With the aid of this equation it was possible to determine the density for each cutting test from the cone resistance measurements. As, however, new sand was used, the density showed changed in time. The sand was looser in the first tests than in the last tests. This resulted in different average initial densities for the different test series. The tests with a 45° blade were performed first with an average pore percentage of 44.9%. The tests with the 60° blade were performed with an average pore percentage of 44.2%. The tests with the 30° blade were performed with an average pore percentage of 43.6%. Because of the consolidation of the sand a relatively large spread was found in the first tests.
Table L-2 lists the permeabilities corresponding to the mentioned pore percentages. By extrapolation in Table L-2 a permeability of 0.00017 m/s is derived for the maximum pore percentage of 51.6%**.**
The sand bed is flushed after the linear tests because of the visibility in the water above the sand. In the tables it is indicated which soil mechanical parameters are determined after the flushing of the sand bed.

Table L-1: Pore percentages, indicated are the average measured densities for the various blade angles.

Minimum density	51.6%
Maximum density	38.3%
Initial density 30 °	43.6%
Initial density 45 °	44.9%
Initial density 60 °	44.2%
After the flushing	
Minimum density	50.6%
Maximum density	37.7%
Saturated critical density	44.5%

Table L-2: Permeabilities, indicated are the average permeabilities for the various blade angles.

Pore percentage	Permeability (m/s)
42.2%	0.000051
45.6%	0.000082
47.4%	0.000096
49.4%	0.000129
Initial	
43.6%	0.000062
44.2%	0.000067
44.9%	0.000075
After the flushing	
39.6%	0.000019
40.7%	0.000021
41.8%	0.000039
43.8%	0.000063
45.7%	0.000093
48.3%	0.000128

Table L-3: The d_{50} of the sand as a function of time.

Date	d_{50} (mm)
06-08-1986	0.102
06-08-1986	0.097
06-08-1986	0.104
06-08-1986	0.129
06-08-1986	0.125
06-08-1986	0.123
29-08-1986	0.105
29-08-1986	0.106
29-08-1986	0.102
16-09-1986	0.111
16-09-1986	0.105
16-09-1986	0.107

Table L-4: The angle of internal friction as a function of the pore percentage.

Pore percentage	Cell pressure kPa	Angle of internal friction
Saturated undrained		After the flushing
44.7%	100	33.5º
44.9%	200	33.3º
44.5%	400	32.8º
42.6%	100	35.0º
42.1%	200	35.5º
42.2%	400	34.8º
39.8%	100	38.6º
39.9%	200	38.3º
39.6%	400	37.9º

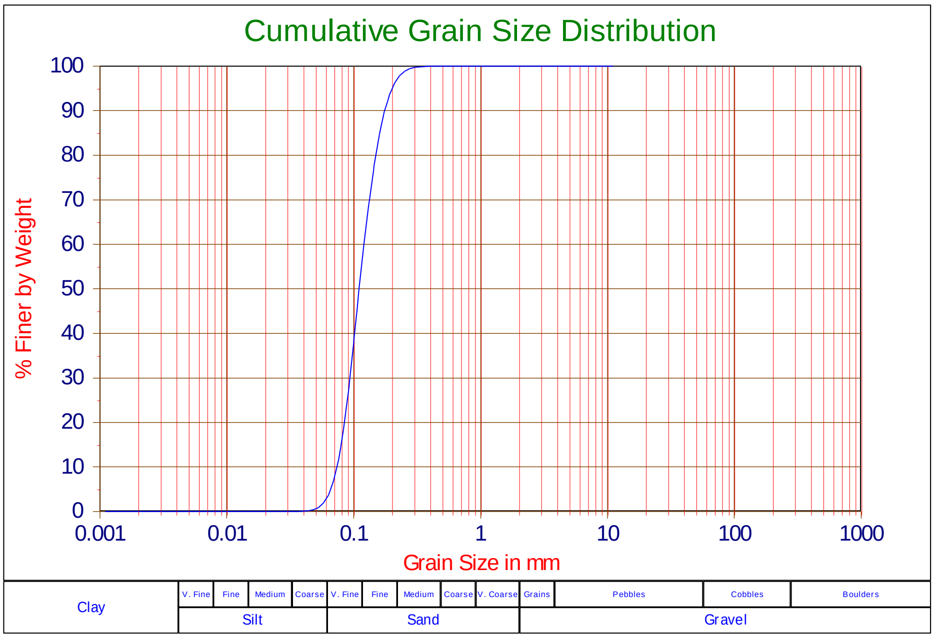

Figure L-1: The PSD of the 105 µm sand.

Appendix M: Experiments in Water Saturated Sand.

M.1 Pore pressures and cutting forces in 105 μm Sand

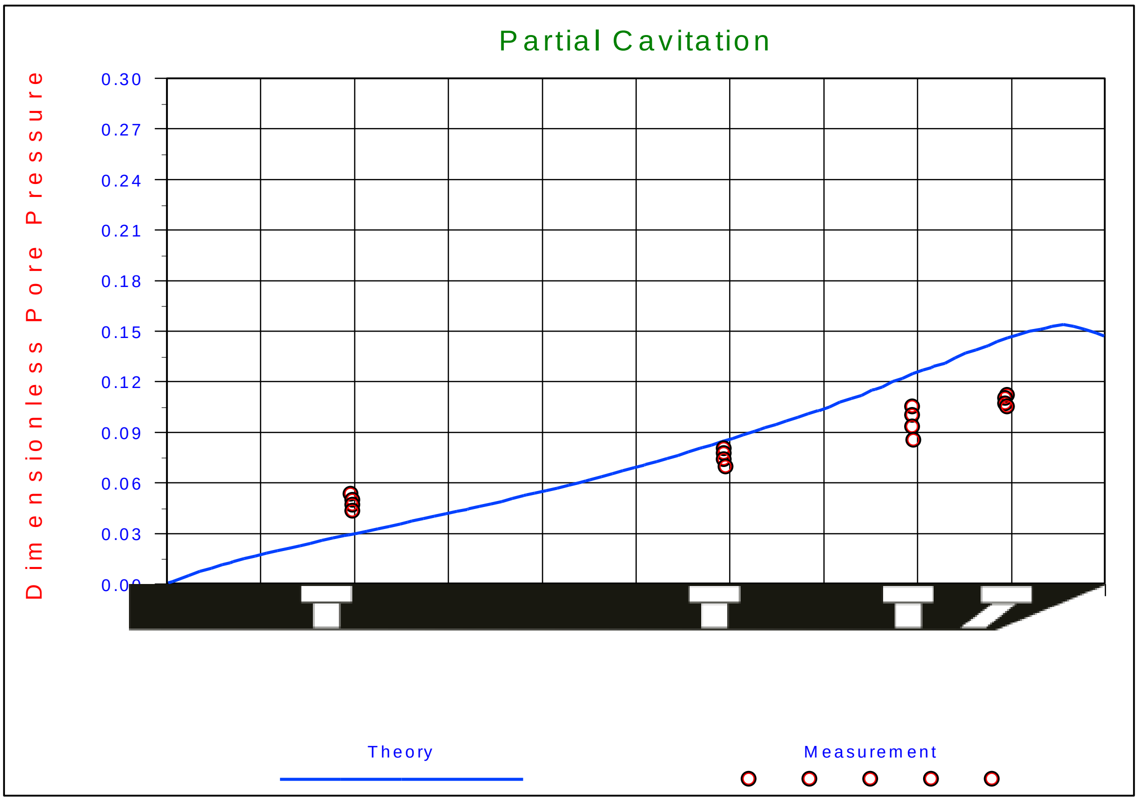

Figure M-1: Dimensionless pore pressures, theory versus measurements.

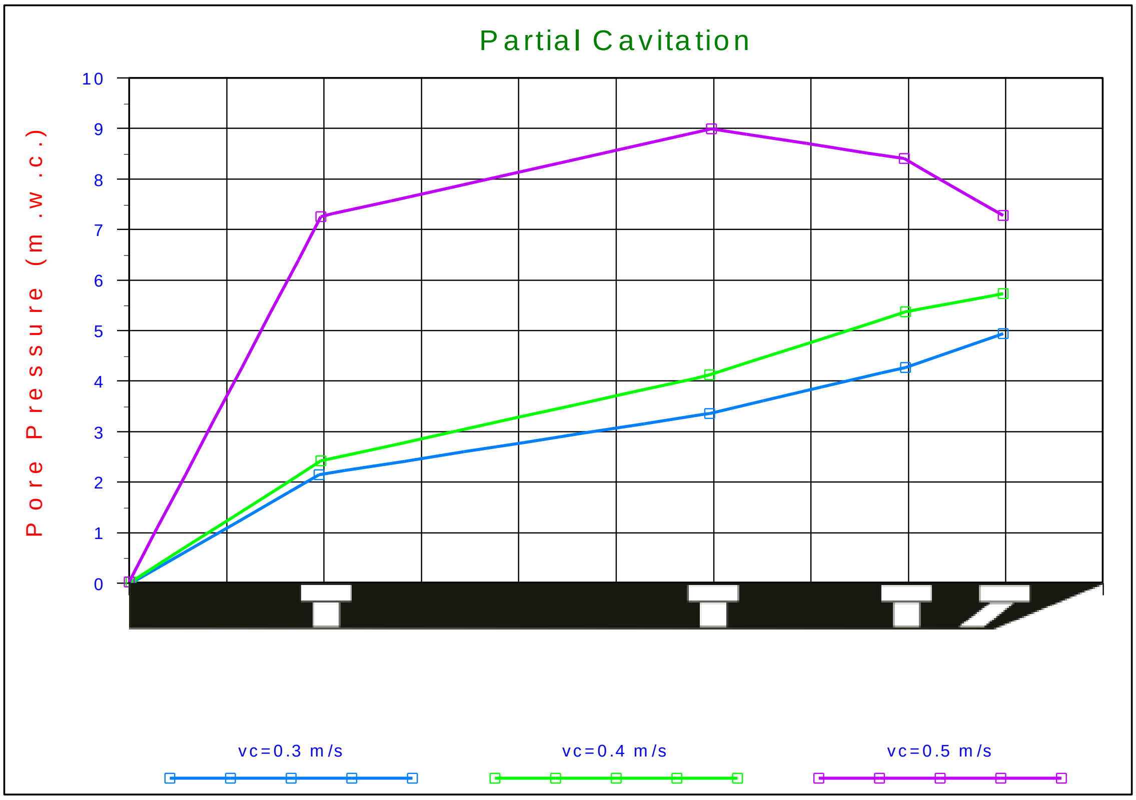

Figure M-2: Measured absolute pore pressures.

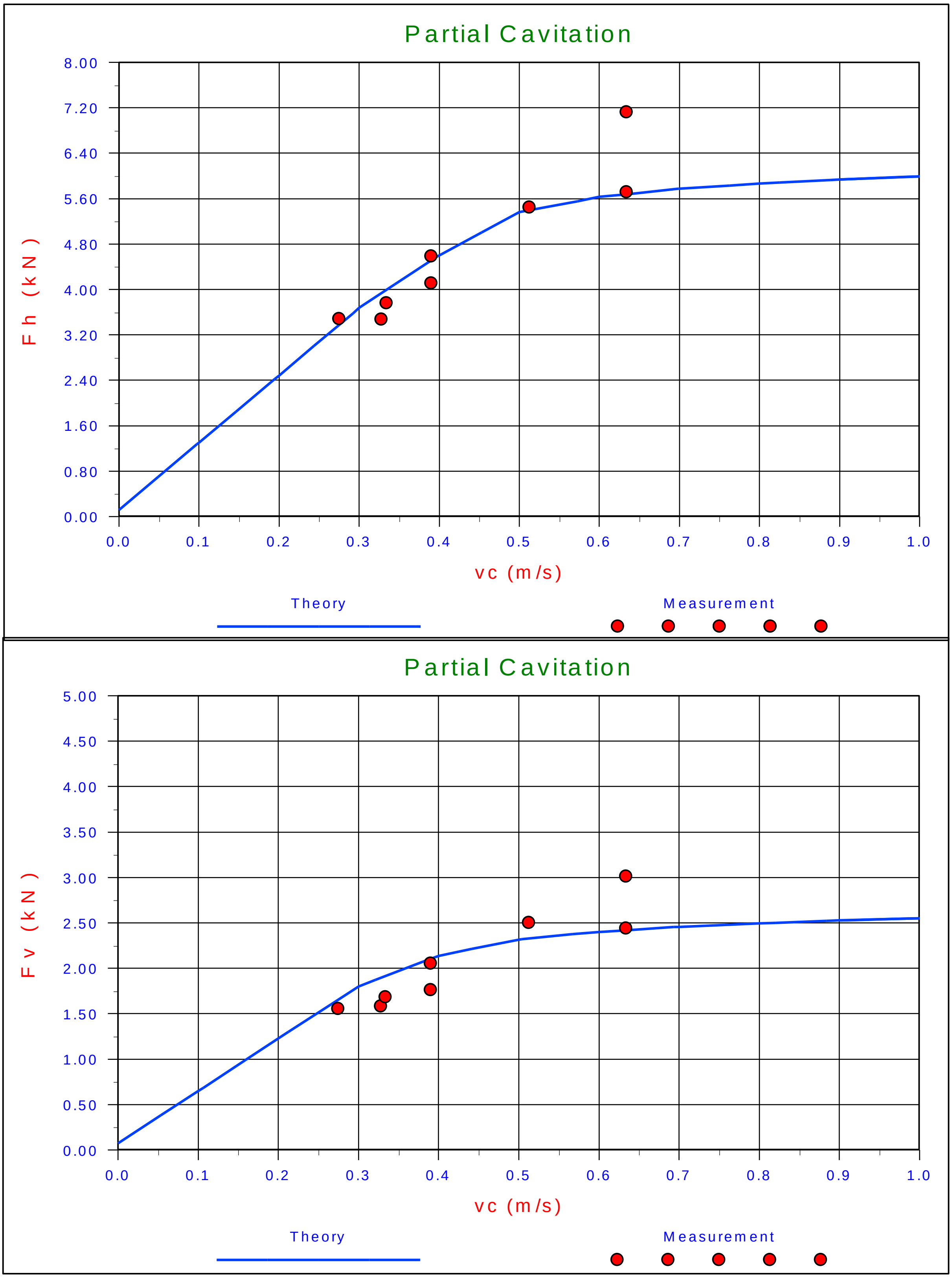

Figure M-3: The cutting forces F_h and F_v, theory versus measurement.

The cutting forces on the blade. Experiments in 105 μm sand, with **α**=30°, **β**=30°, **φ**=41°, **δ**=27°, $\mathbf{n_i}$=43.6%, $\mathbf{n_{max}}$=51.6%, $\mathbf{k_i}$=0.000062 m/s, $\mathbf{k_{max}}$=0.000170 m/s, $\mathbf{h_i}$=100 mm, $\mathbf{h_b}$=100 mm, **w**=0.2 m, **z**=0.6 m and a partial cavitating cutting process.

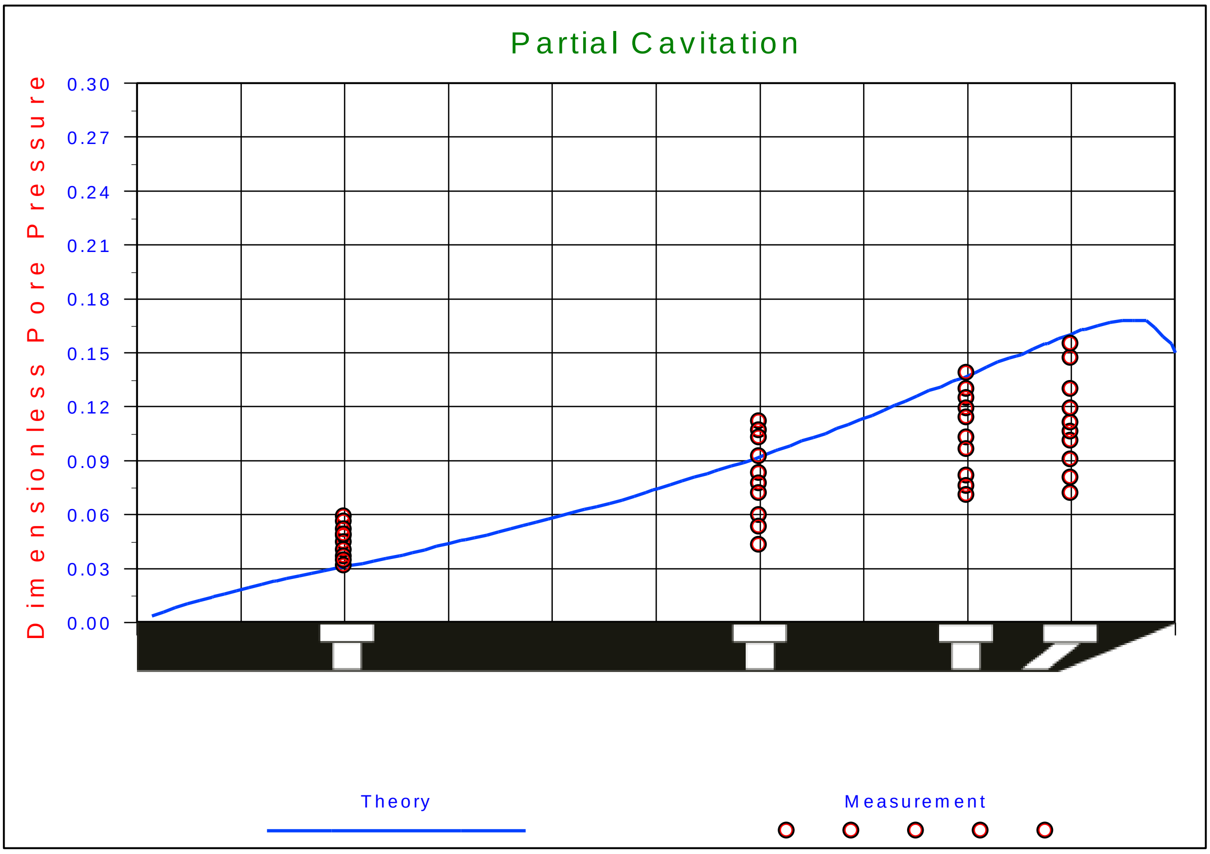

Figure M-4: Dimensionless pore pressures, theory versus measurements.

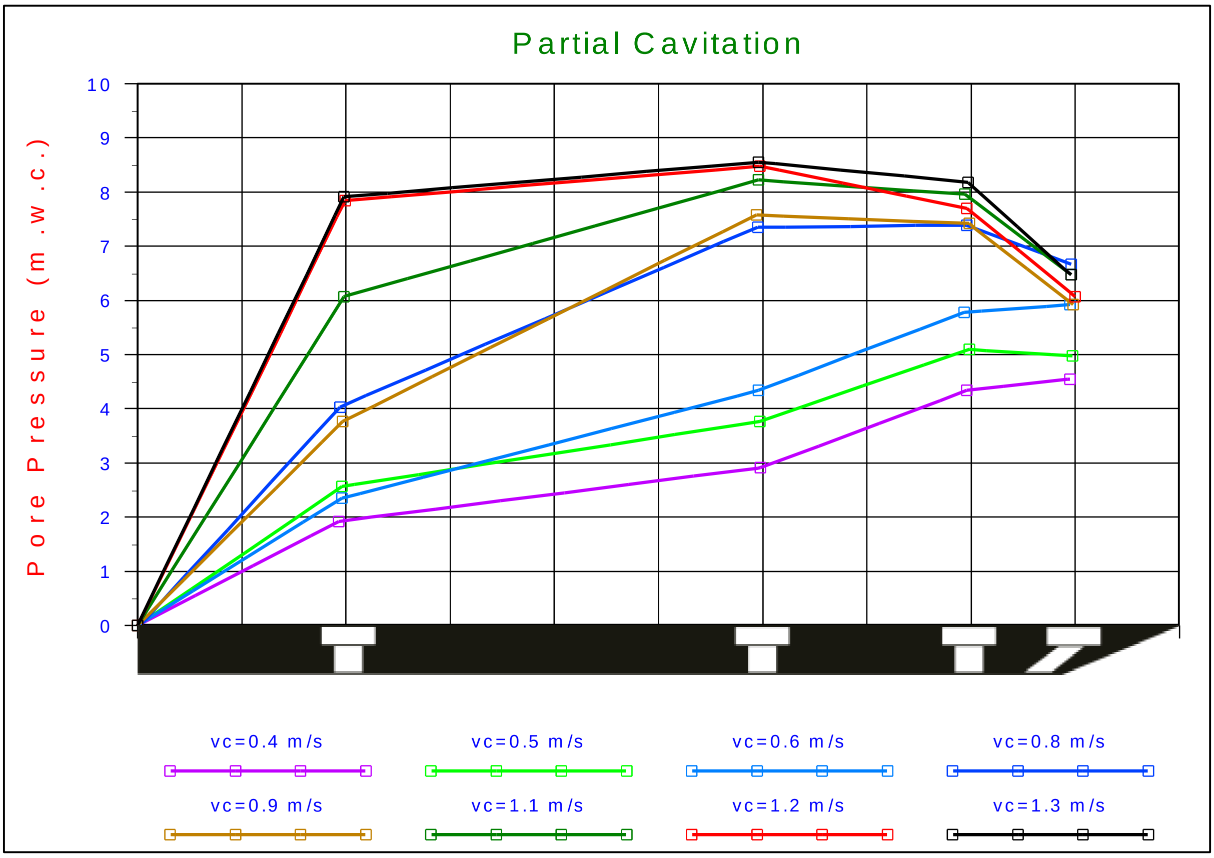

Figure M-5: Measured absolute pore pressures.

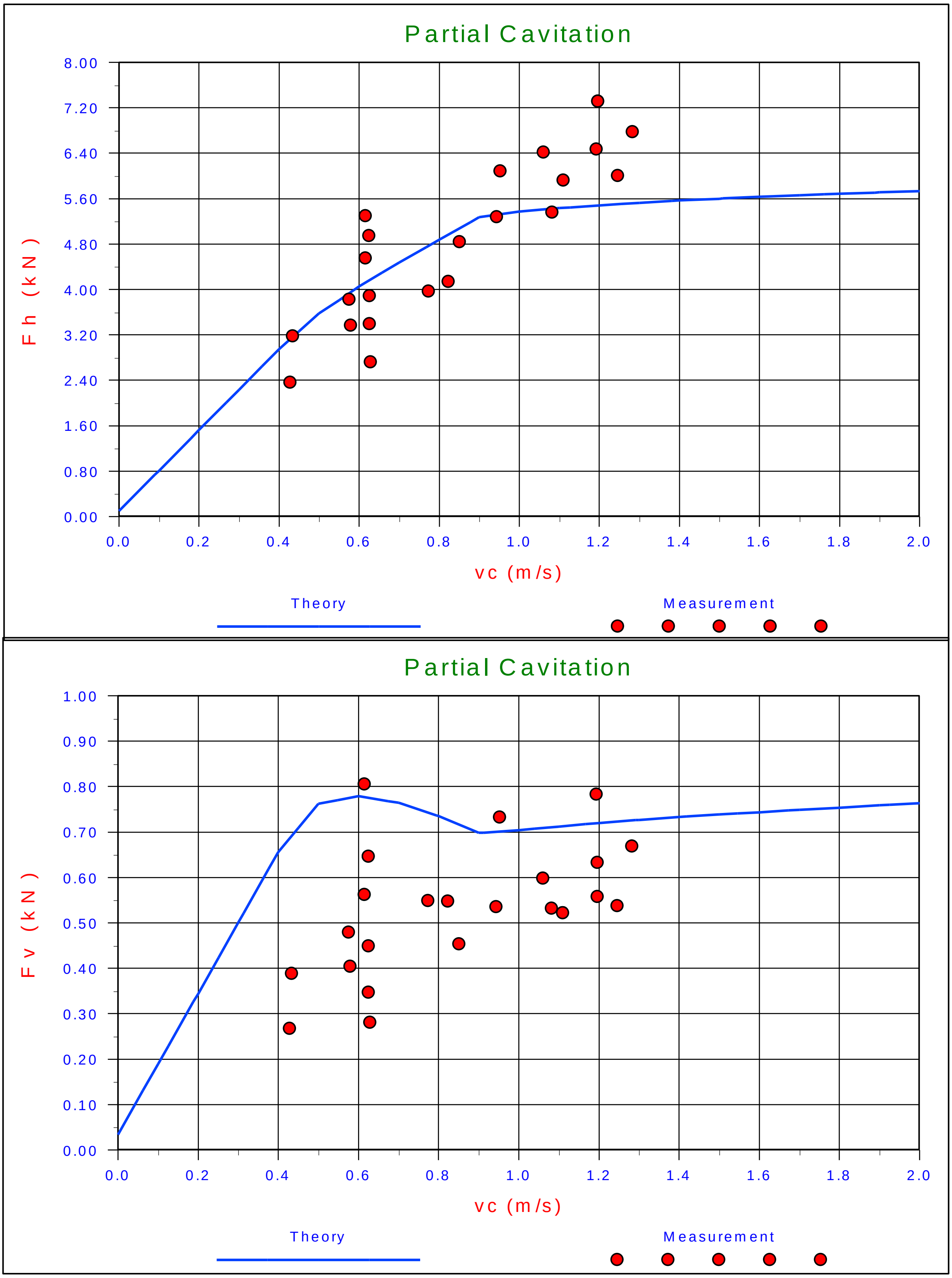

Figure M-6: The cutting forces F_h and F_v, theory versus measurement.

The cutting forces on the blade. Experiments in 105 μm sand, with **α**=45°, **β**=30°, **φ**=38°, **δ**=25°, $\mathbf{n_i}$=45.0%, $\mathbf{n_{max}}$=51.6%, $\mathbf{k_i}$=0.000075 m/s, $\mathbf{k_{max}}$=0.000170 m/s, $\mathbf{h_i}$=70 mm, $\mathbf{h_b}$=100 mm, **w**=0.2 m, **z**=0.6 m and a partial cavitating cutting process.

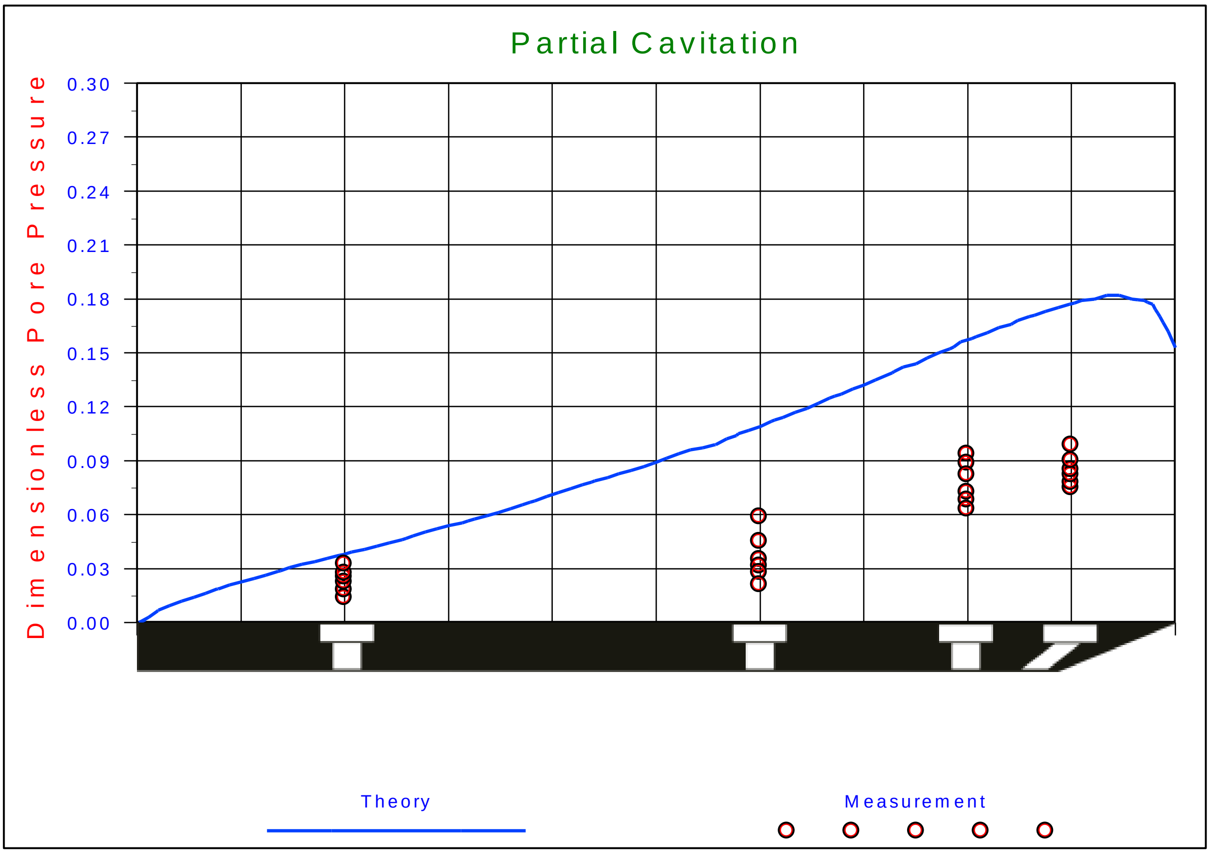

Figure M-7: Dimensionless pore pressures, theory versus measurements.

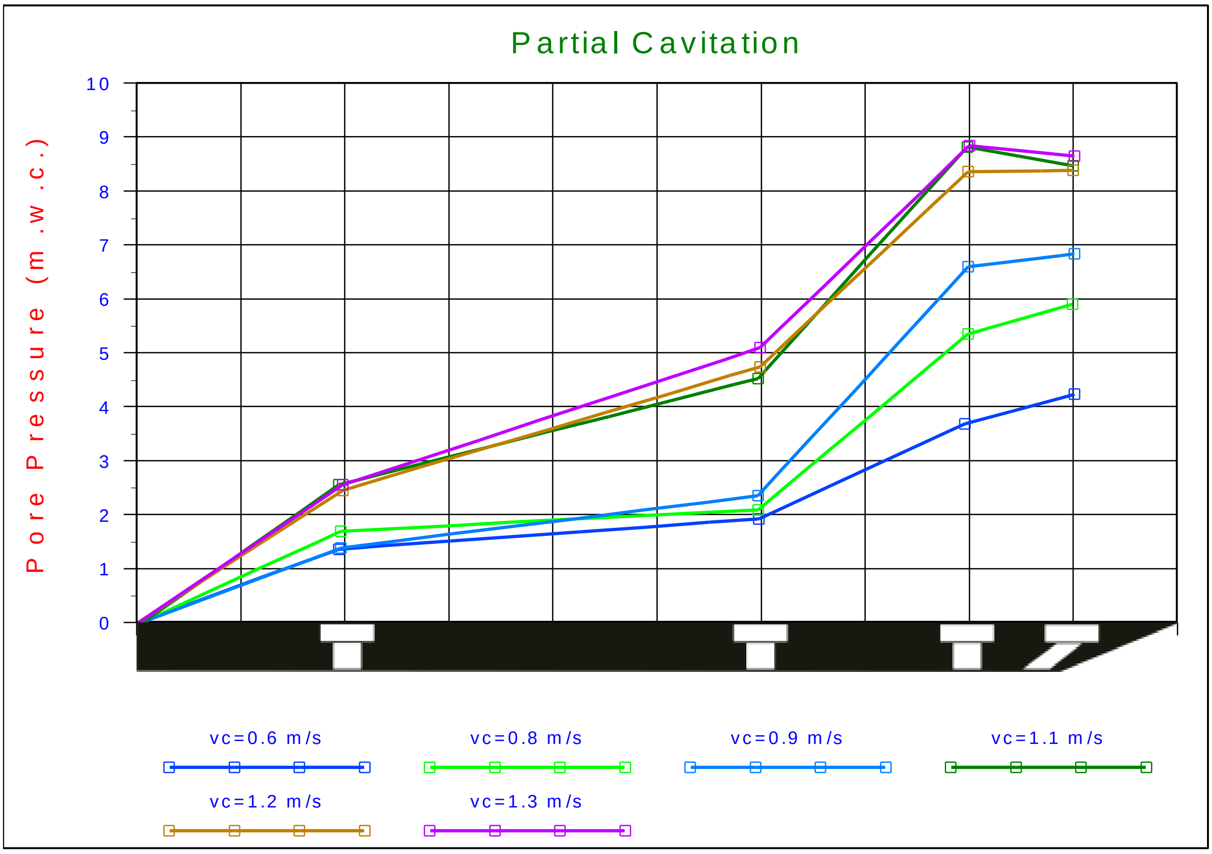

Figure M-8: Measured absolute pore pressures.

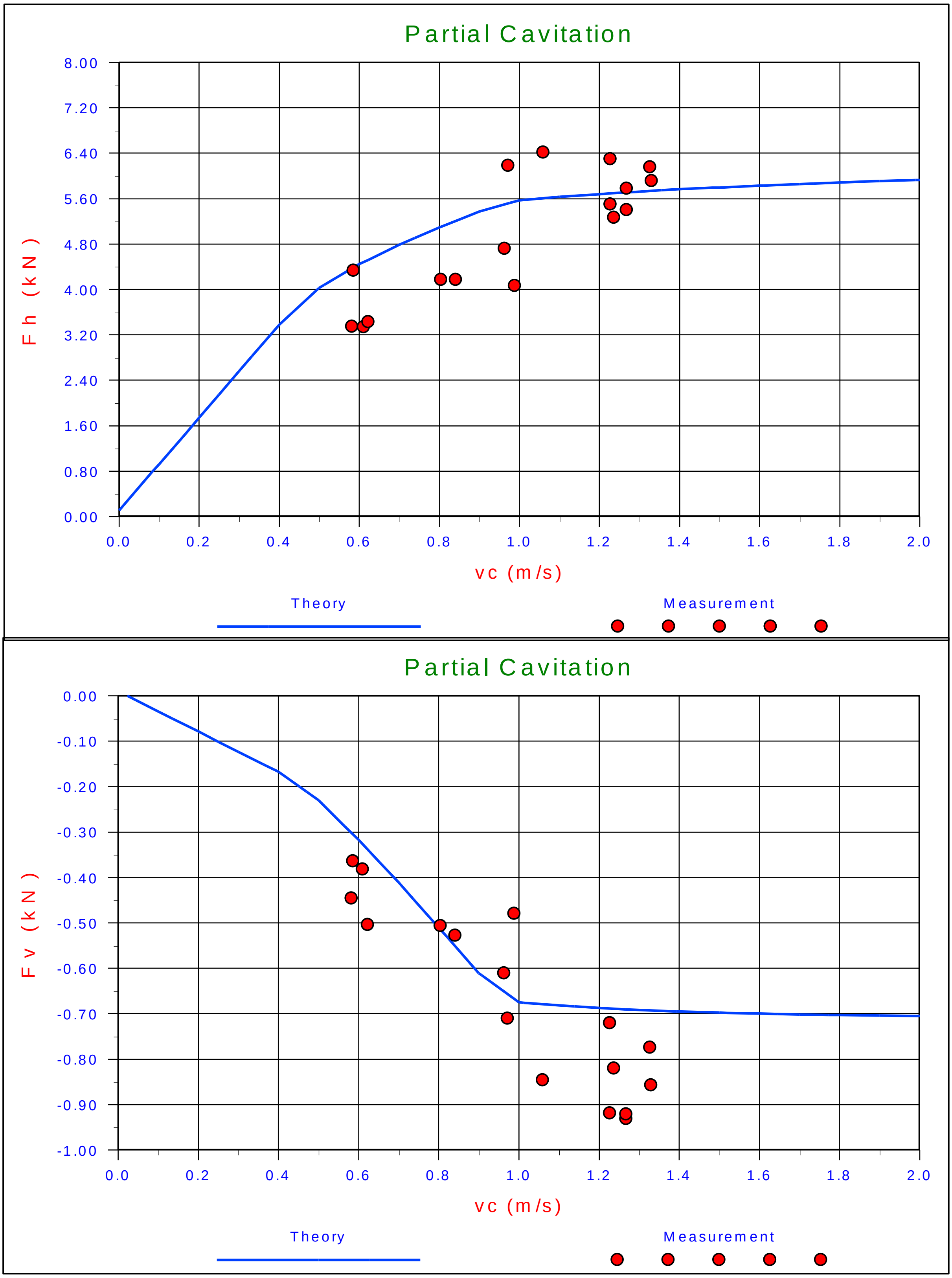

Figure M-9: The cutting forces F_h and F_v, theory versus measurement.

The cutting forces on the blade. Experiments in 105 μm sand, with α=60°, β=30°, φ=36°, δ=24°, n_i=44.3%, n_{max}=51.6%, k_i=0.000067 m/s, k_{max}=0.000170 m/s, h_i=58 mm, h_b=100 mm, w=0.2 m, z=0.6 m and a partial cavitating cutting process.

M.2 Pore Pressures in 200 μm Sand.

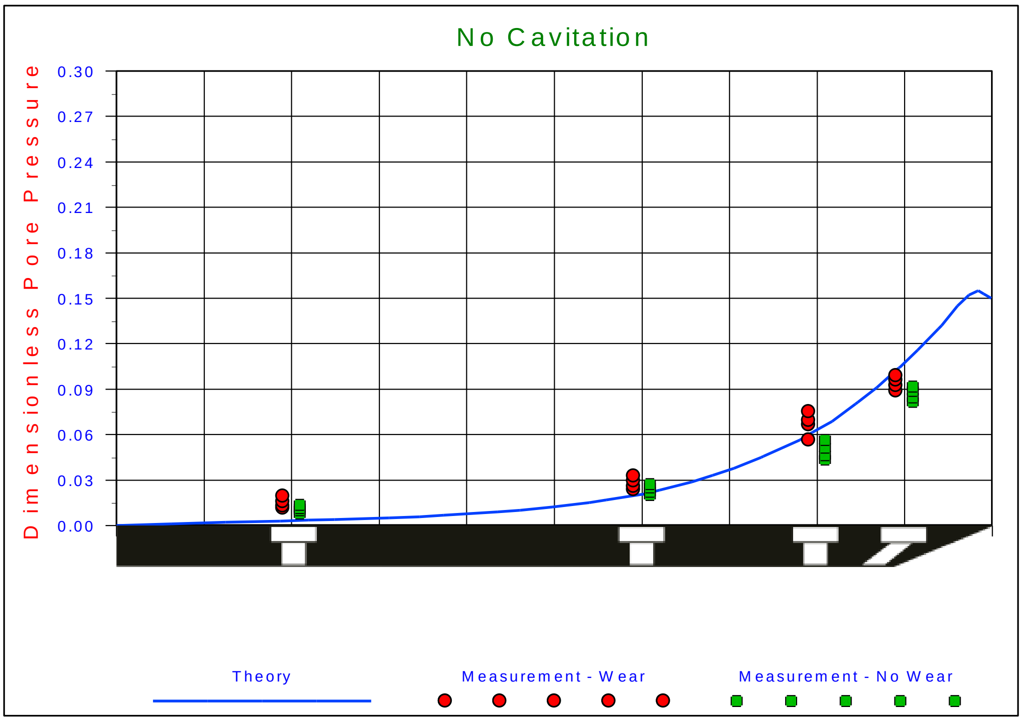

Figure M-10: α=30º, h_i=33 mm, h_b=100 mm.

The dimensionless water pore pressures on the blade. Experiments in 200 μm sand, with **α**=30°, **β**=30º, **φ**=38º, **δ**=30º, $\mathbf{n_i}$=38.53%, $\mathbf{n_{max}}$=43.88%, $\mathbf{k_i}$=0.000165 m/s, $\mathbf{k_{max}}$=0.000320 m/s, $\mathbf{h_i}$=33 mm, $\mathbf{h_b}$=100 mm, **w**=0.2 m, **z**=0.6 m and a non-cavitating cutting process.

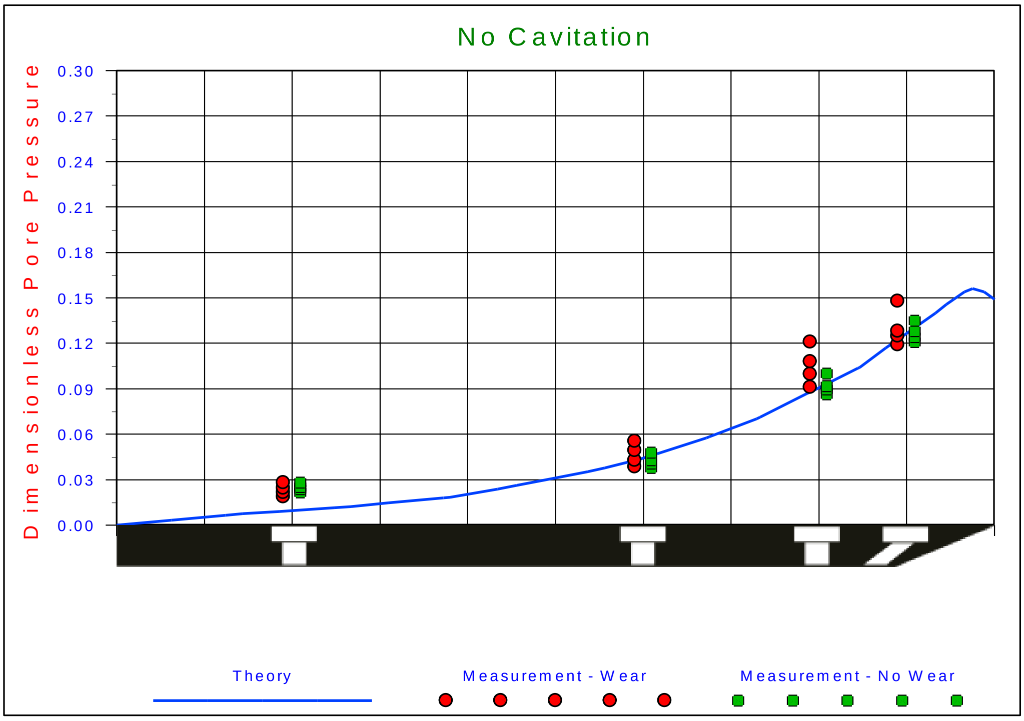

Figure M-11: α=30º, h_i=50 mm, h_b=100 mm.

The dimensionless water pore pressures on the blade. Experiments in 200 μm sand, with **α**=30°, **β**=29º, **φ**=38º, **δ**=30º, $\mathbf{n_i}$=38.53%, $\mathbf{n_{max}}$=43.88%, $\mathbf{k_i}$=0.000165 m/s, $\mathbf{k_{max}}$=0.000320 m/s, $\mathbf{h_i}$=50 mm, $\mathbf{h_b}$=100 mm, **w**=0.2 m, **z**=0.6 m and a non-cavitating cutting process.

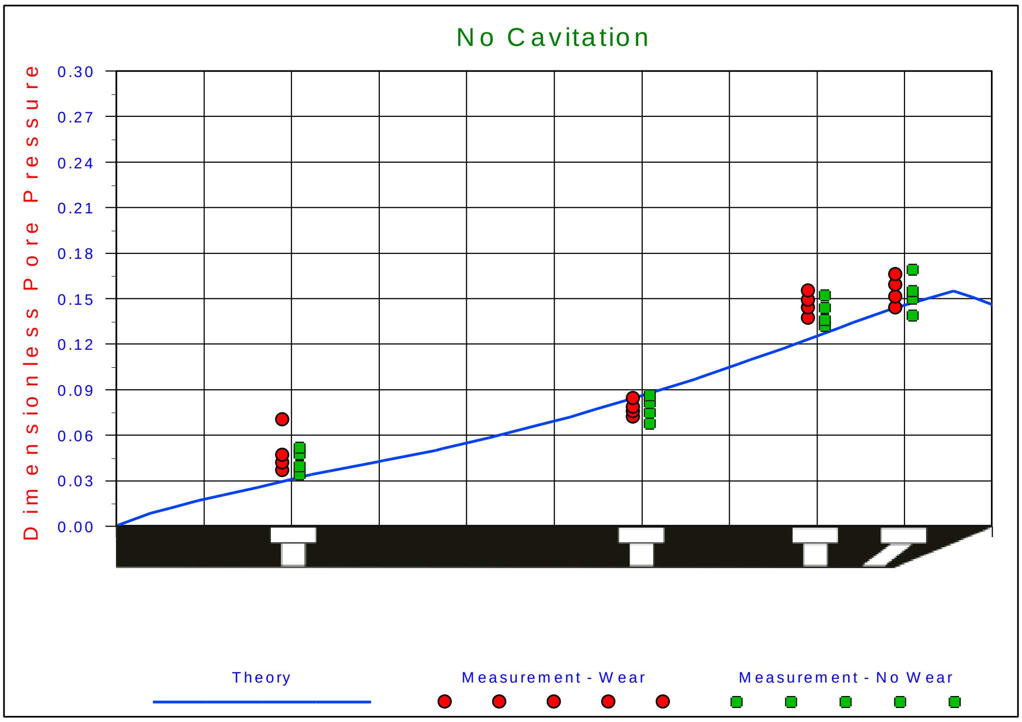

Figure M-12: α=30º, h_i=100 mm, h_b=100 mm.

The dimensionless water pore pressures on the blade. Experiments in 200 μm sand, with **α**=30°, **β**=29º, **φ**=38º, **δ**=30º, $\mathbf{n_i}$=38.53%, $\mathbf{n_{max}}$=43.88%, $\mathbf{k_i}$=0.000165 m/s, $\mathbf{k_{max}}$=0.000320 m/s, $\mathbf{h_i}$=100 mm, $\mathbf{h_b}$=100 mm, **w**=0.2 m, **z**=0.6 m and a non-cavitating cutting process.

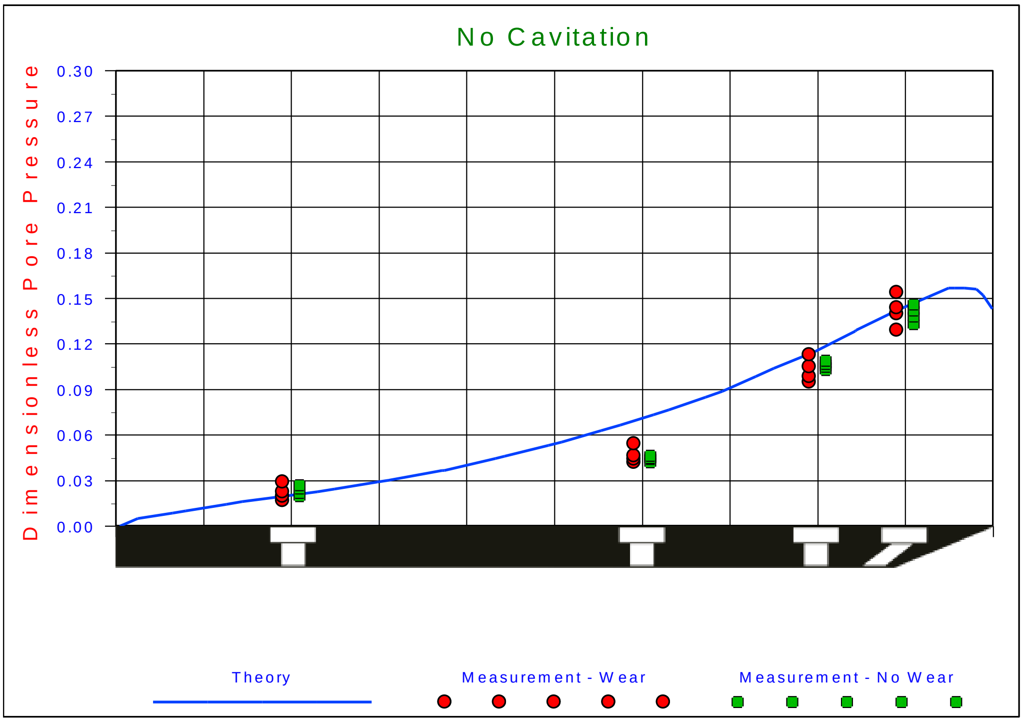

Figure M-13: α=45º, h_i=47 mm, h_b=141 mm.

The dimensionless water pore pressures on the blade. Experiments in 200 μm sand, with **α**=45°, **β**=25º, **φ**=38º, **δ**=30º, $\mathbf{n_i}$=38.53%, $\mathbf{n_{max}}$=43.88%, $\mathbf{k_i}$=0.000165 m/s, $\mathbf{k_{max}}$=0.000320 m/s, $\mathbf{h_i}$=47 mm, $\mathbf{h_b}$=141 mm, **w**=0.2 m, **z**=0.6 m and a non-cavitating cutting process.

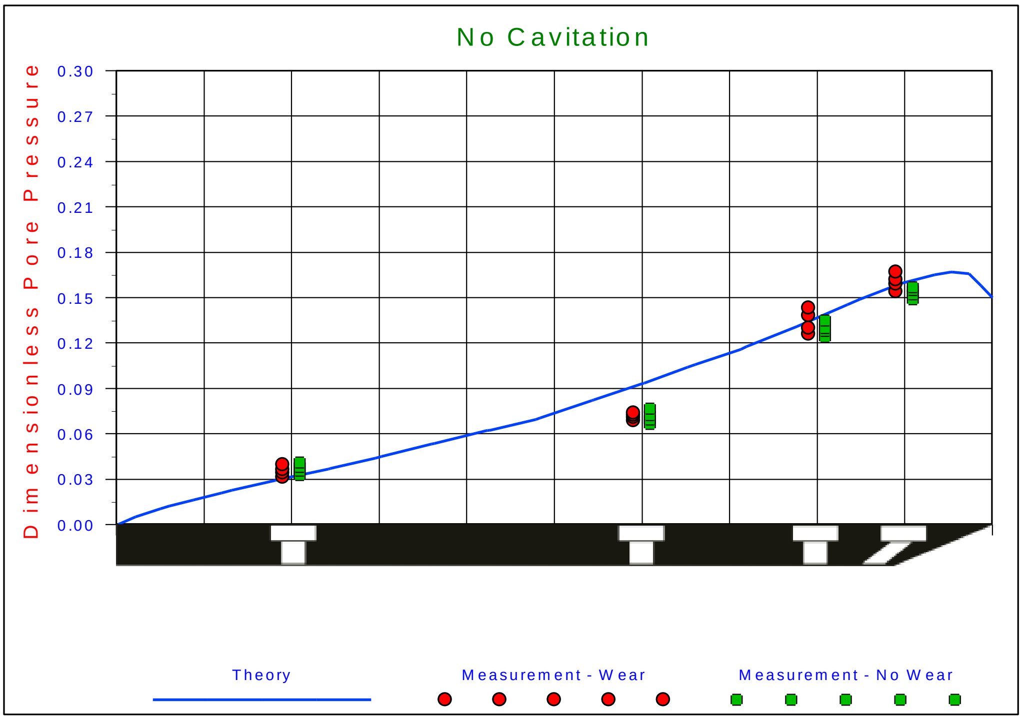

Figure M-14: α=45°, h_i=70 mm, h_b=141 mm.

The dimensionless water pore pressures on the blade. Experiments in 200 μm sand, with **α**=45°, **β**=24°, **φ**=38°, **δ**=30°, $\mathbf{n_i}$=38.53%, $\mathbf{n_{max}}$=43.88%, $\mathbf{k_i}$=0.000165 m/s, $\mathbf{k_{max}}$=0.000320 m/s, $\mathbf{h_i}$=70 mm, $\mathbf{h_b}$=141 mm, **w**=0.2 m, **z**=0.6 m and a non-cavitating cutting process.

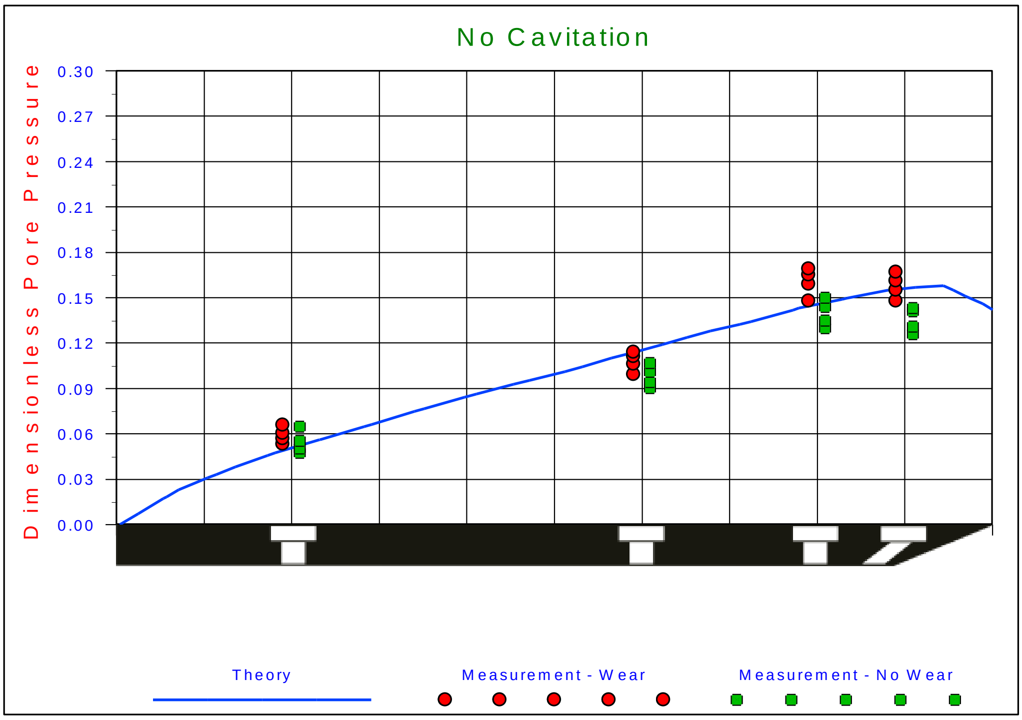

Figure M-15: α=45°, h_i=141 mm, h_b=141 mm.

The dimensionless water pore pressures on the blade. Experiments in 200 μm sand, with **α**=45°, **β**=25°, **φ**=38°, **δ**=30°, $\mathbf{n_i}$=38.53%, $\mathbf{n_{max}}$=43.88%, $\mathbf{k_i}$=0.000165 m/s, $\mathbf{k_{max}}$=0.000320 m/s, $\mathbf{h_i}$=141 mm, $\mathbf{h_b}$=141 mm, **w**=0.2 m, **z**=0.6 m and a non-cavitating cutting process.

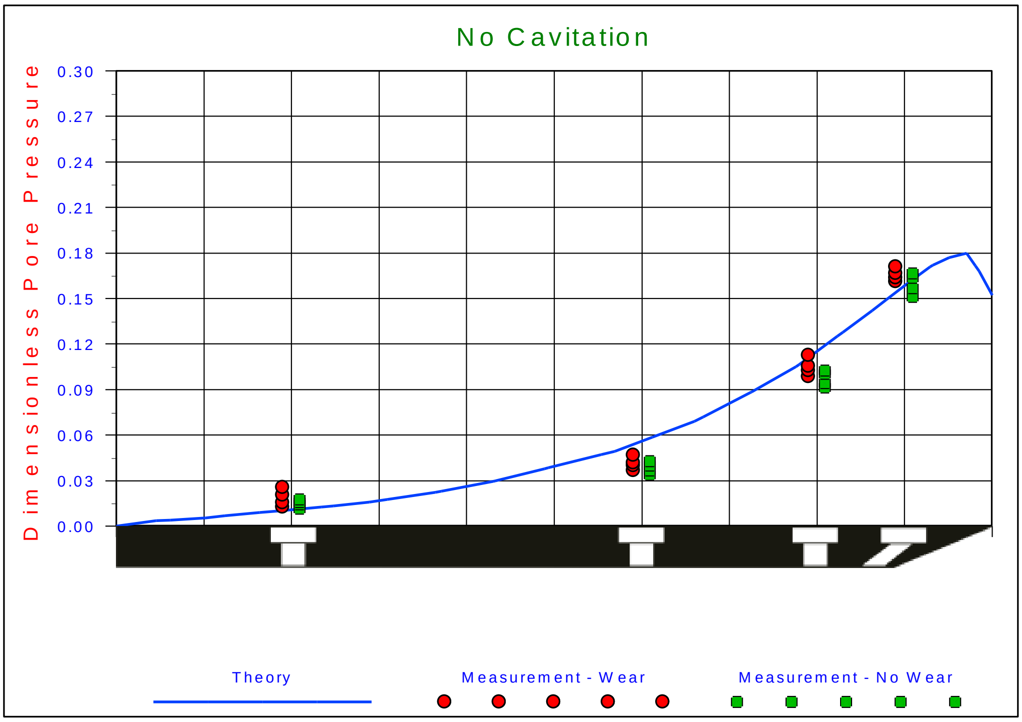

Figure M-16: α=60º, h_i=30 mm, h_b=173 mm.

The dimensionless water pore pressures on the blade. Experiments in 200 μm sand, with **α**=60°, **β**=19°, **φ**=38°, **δ**=30°, $\mathbf{n_i}$=38.53%, $\mathbf{n_{max}}$=43.88%, $\mathbf{k_i}$=0.000165 m/s, $\mathbf{k_{max}}$=0.000320 m/s, $\mathbf{h_i}$=30 mm, $\mathbf{h_b}$=173 mm, **w**=0.2 m, **z**=0.6 m and a non-cavitating cutting process.

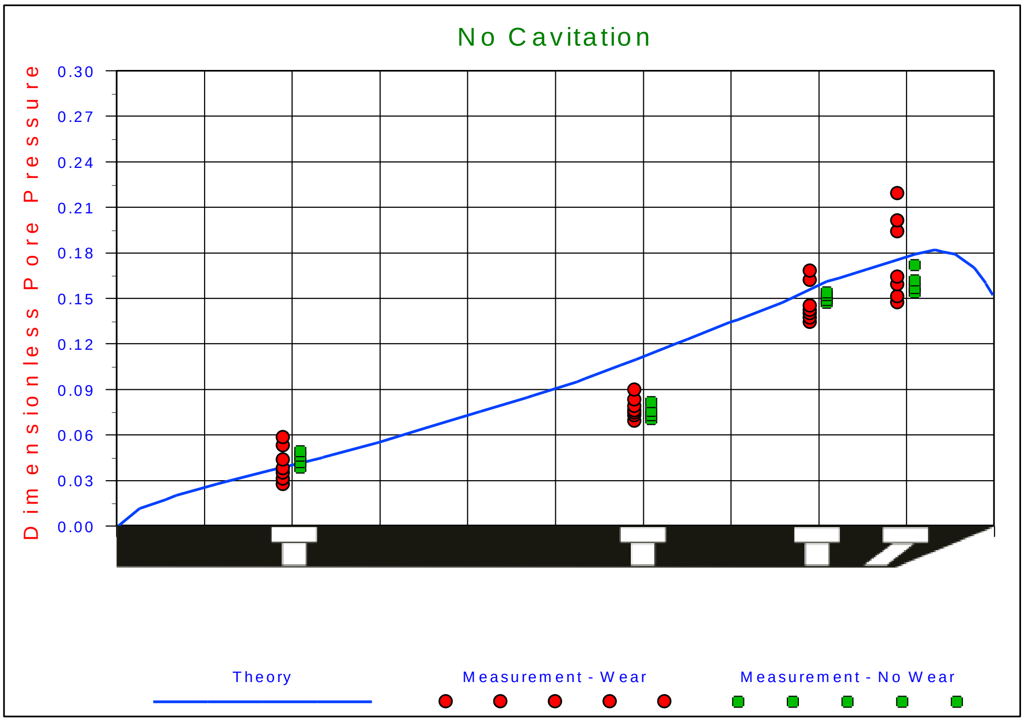

Figure M-17: α=60º, h_i=58 mm, h_b=173 mm.

The dimensionless water pore pressures on the blade. Experiments in 200 μm sand, with **α**=60°, **β**=19°, **φ**=38°, **δ**=30°, $\mathbf{n_i}$=38.53%, $\mathbf{n_{max}}$=43.88%, $\mathbf{k_i}$=0.000165 m/s, $\mathbf{k_{max}}$=0.000320 m/s, $\mathbf{h_i}$=58 mm, $\mathbf{h_b}$=173 mm, **w**=0.2 m, **z**=0.6 m and a non-cavitating cutting process.

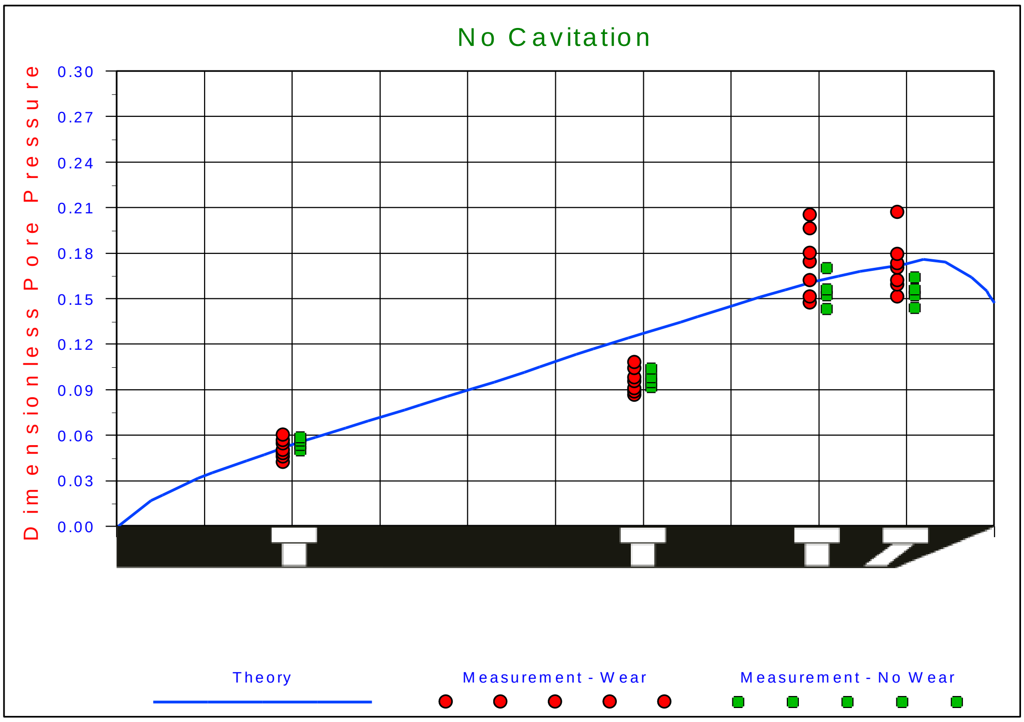

Figure M-18: α=60°, h_i=87 mm, h_b=173 mm.

The dimensionless water pore pressures on the blade. Experiments in 200 μm sand, with **α**=60°, **β**=19°, **φ**=38°, **δ**=30°, **n_i**=38.53%, **n_{max}**=43.88%, **k_i**=0.000165 m/s, **k_{max}**=0.000320 m/s, **h_i**=87 mm, **h_b**=173 mm, **w**=0.2 m, **z**=0.6 m and a non-cavitating cutting process.

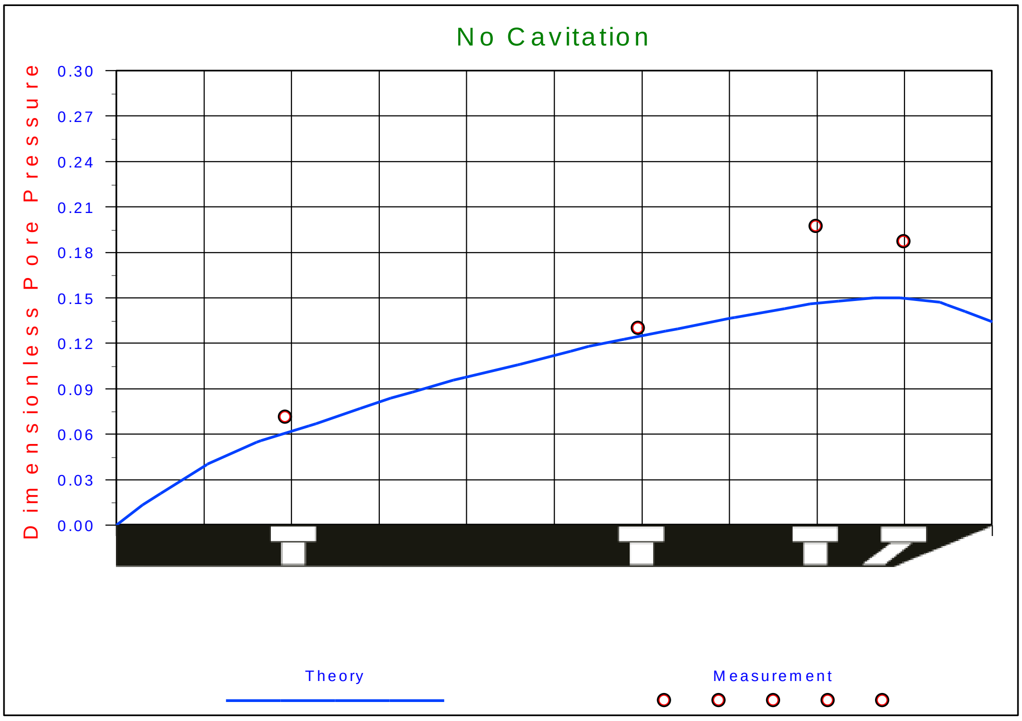

Figure M-19: α=60°, h_i=173 mm, h_b=173 mm.

The dimensionless water pore pressures on the blade. Experiments in 200 μm sand, with **α**=60°, **β**=20°, **φ**=38°, **δ**=30°, **n_i**=38.53%, **n_{max}**=43.88%, **k_i**=0.000165 m/s, **k_{max}**=0.000320 m/s, **h_i**=173 mm, **h_b**=173 mm, **w**=0.2 m, **z**=0.6 m and a non-cavitating cutting process.

M.3 Cutting Forces in 200 μm Sand.

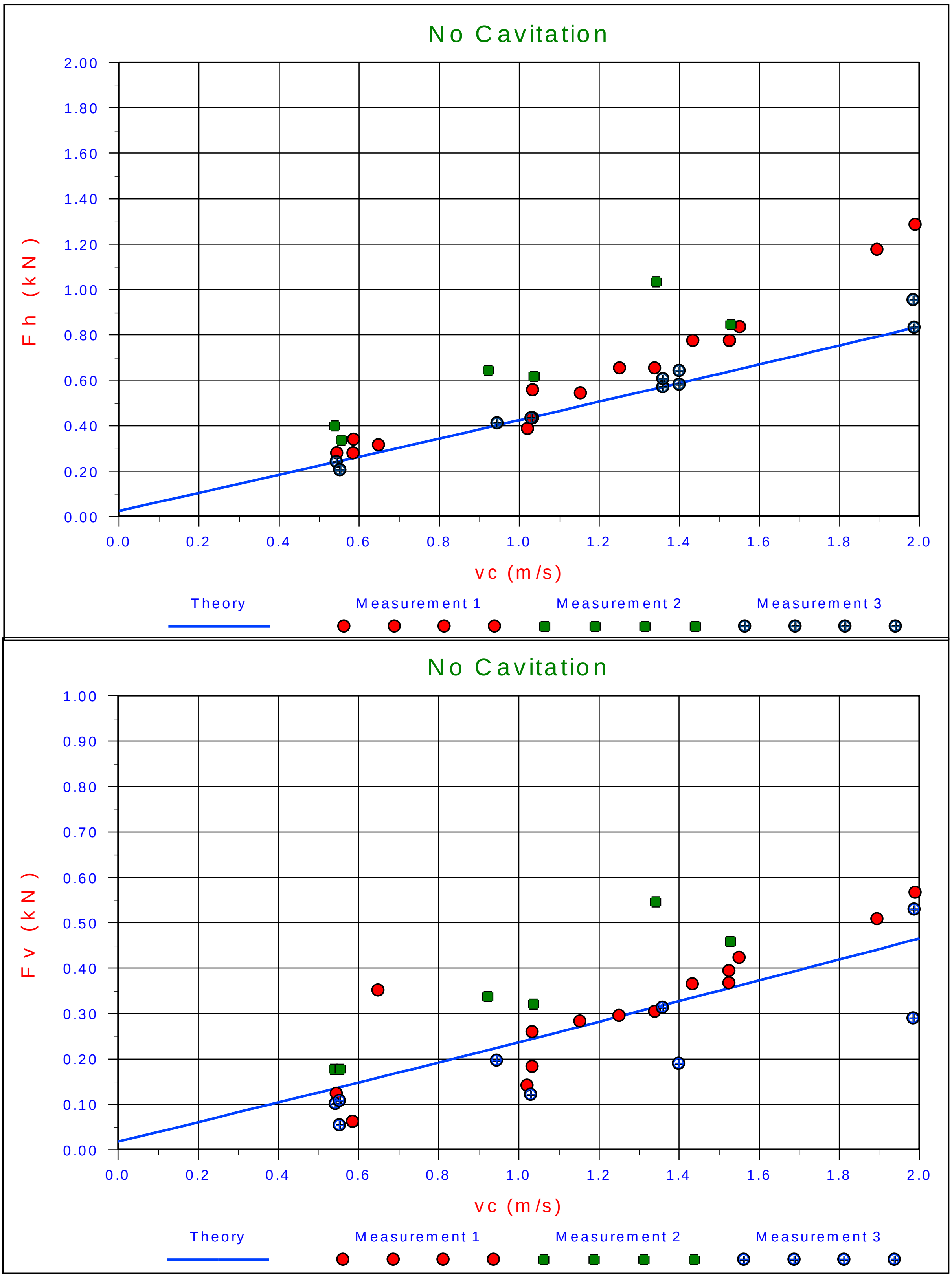

Figure M-20: α=30°, h_i=33 mm, h_b=100 mm.

The cutting forces $\mathbf{F_h}$ and $\mathbf{F_v}$ on the blade. Experiments in 200 μm sand, with $\boldsymbol{\alpha}$=30°, $\boldsymbol{\beta}$=30º, $\boldsymbol{\varphi}$=38º, $\boldsymbol{\delta}$=30º, $\mathbf{n_i}$=38.53%, $\mathbf{n_{max}}$=43.88%, $\mathbf{k_i}$=0.000165 m/s, $\mathbf{k_{max}}$=0.000320 m/s, $\mathbf{h_i}$=33 mm, $\mathbf{h_b}$=100 mm, **w**=0.2 m, **z**=0.6 m and a non-cavitating cutting process.

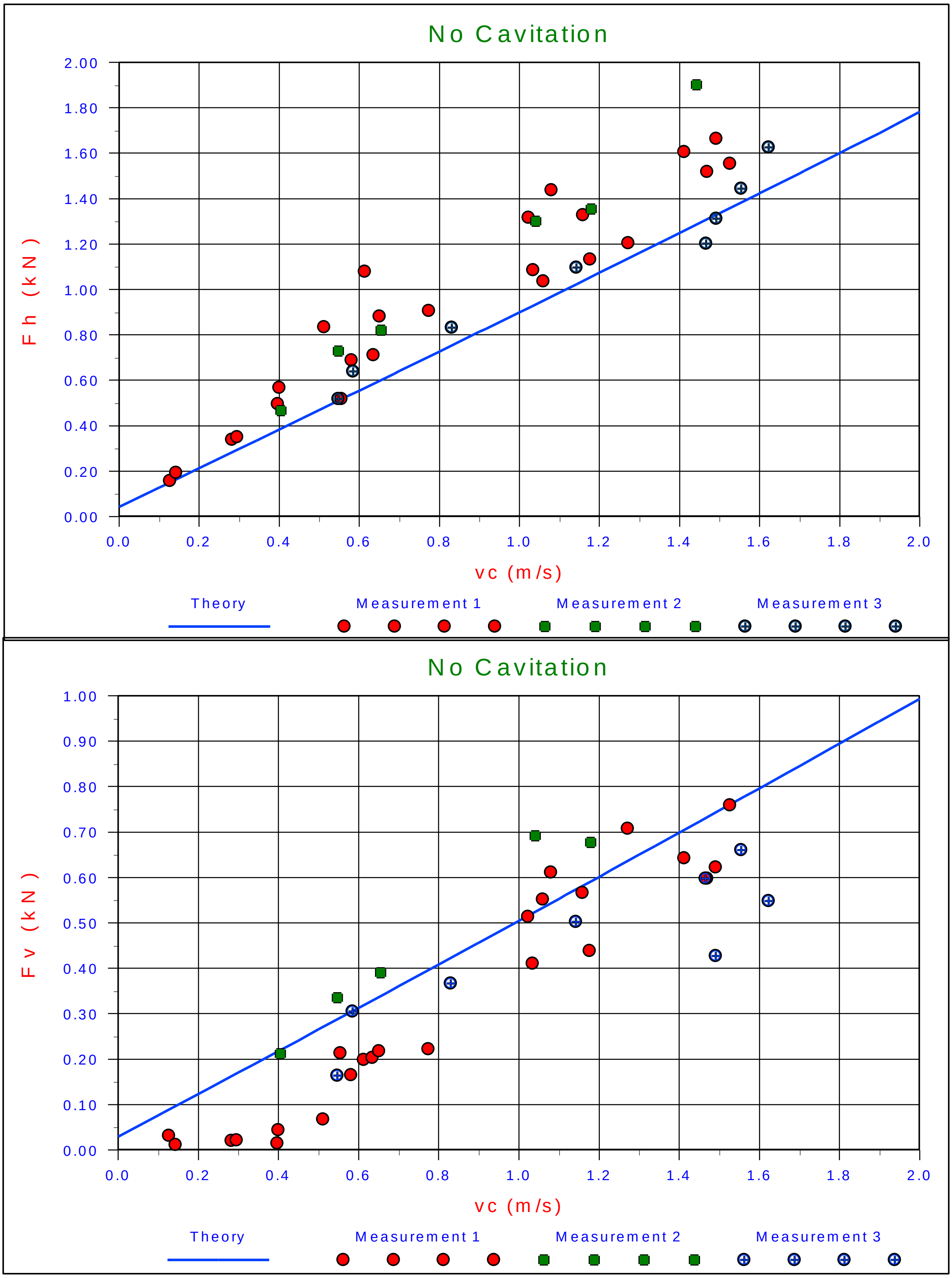

Figure M-21: α=30°, h_i=50 mm, h_b=100 mm.

The cutting forces $\mathbf{F_h}$ and $\mathbf{F_v}$ on the blade. Experiments in 200 μm sand, with **α**=30°, **β**=30º, **φ**=38º, **δ**=30º, $\mathbf{n_i}$=38.53%, $\mathbf{n_{max}}$=43.88%, $\mathbf{k_i}$=0.000165 m/s, $\mathbf{k_{max}}$=0.000320 m/s, $\mathbf{h_i}$=50 mm, $\mathbf{h_b}$=100 mm, **w**=0.2 m, **z**=0.6 m and a non-cavitating cutting process.

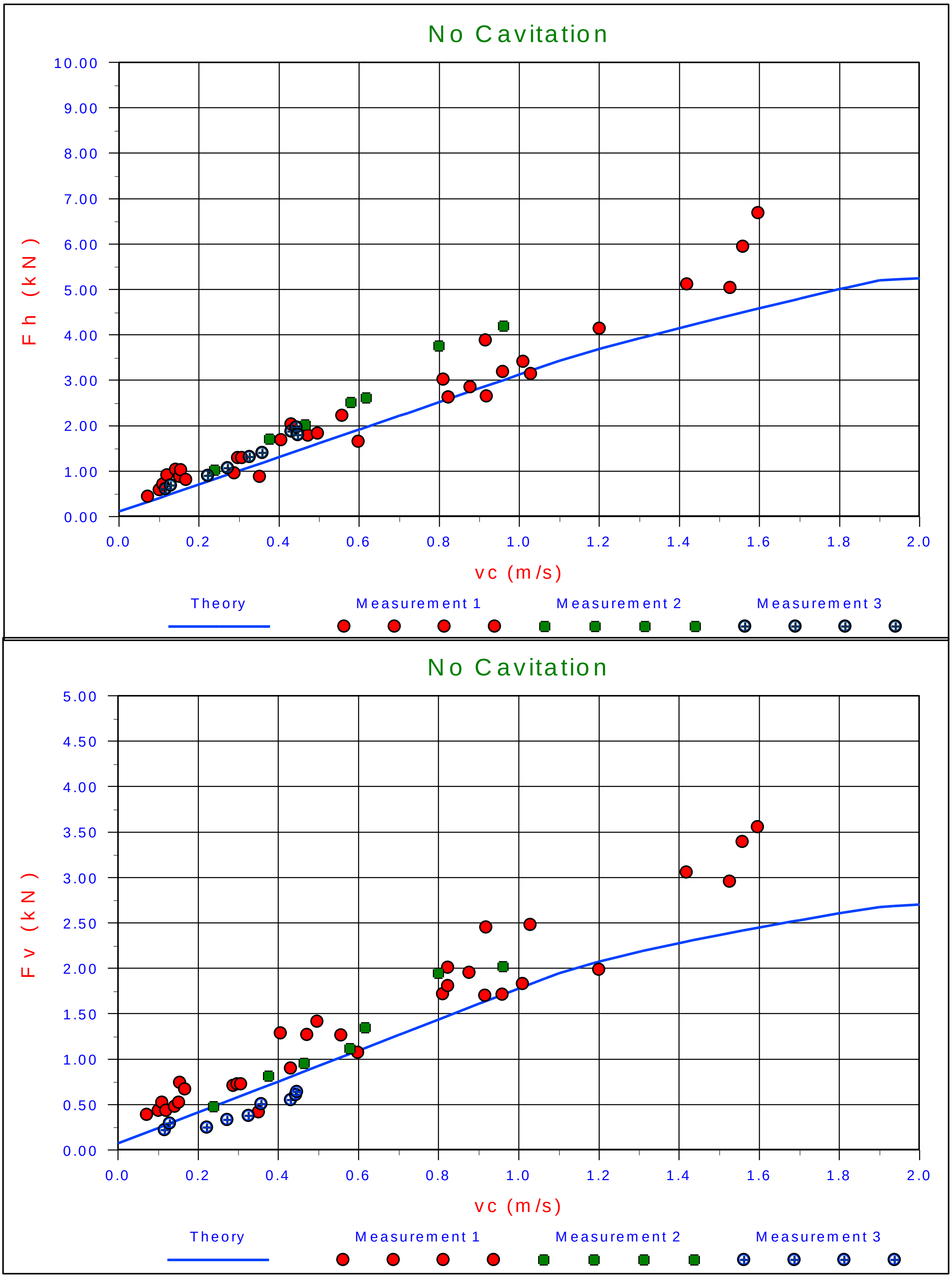

Figure M-22: α=30°, h$_i$=100 mm, h$_b$=100 mm.

The cutting forces **F$_h$** and **F$_v$** on the blade. Experiments in 200 μm sand, with **α**=30°, **β**=30º, **φ**=38º, **δ**=30º, **n$_i$**=38.53%, **n$_{max}$**=43.88%, **k$_i$**=0.000165 m/s, **k$_{max}$**=0.000320 m/s, **h$_i$**=100 mm, **h$_b$**=100 mm, **w**=0.2 m, **z**=0.6 m and a non-cavitating cutting process.

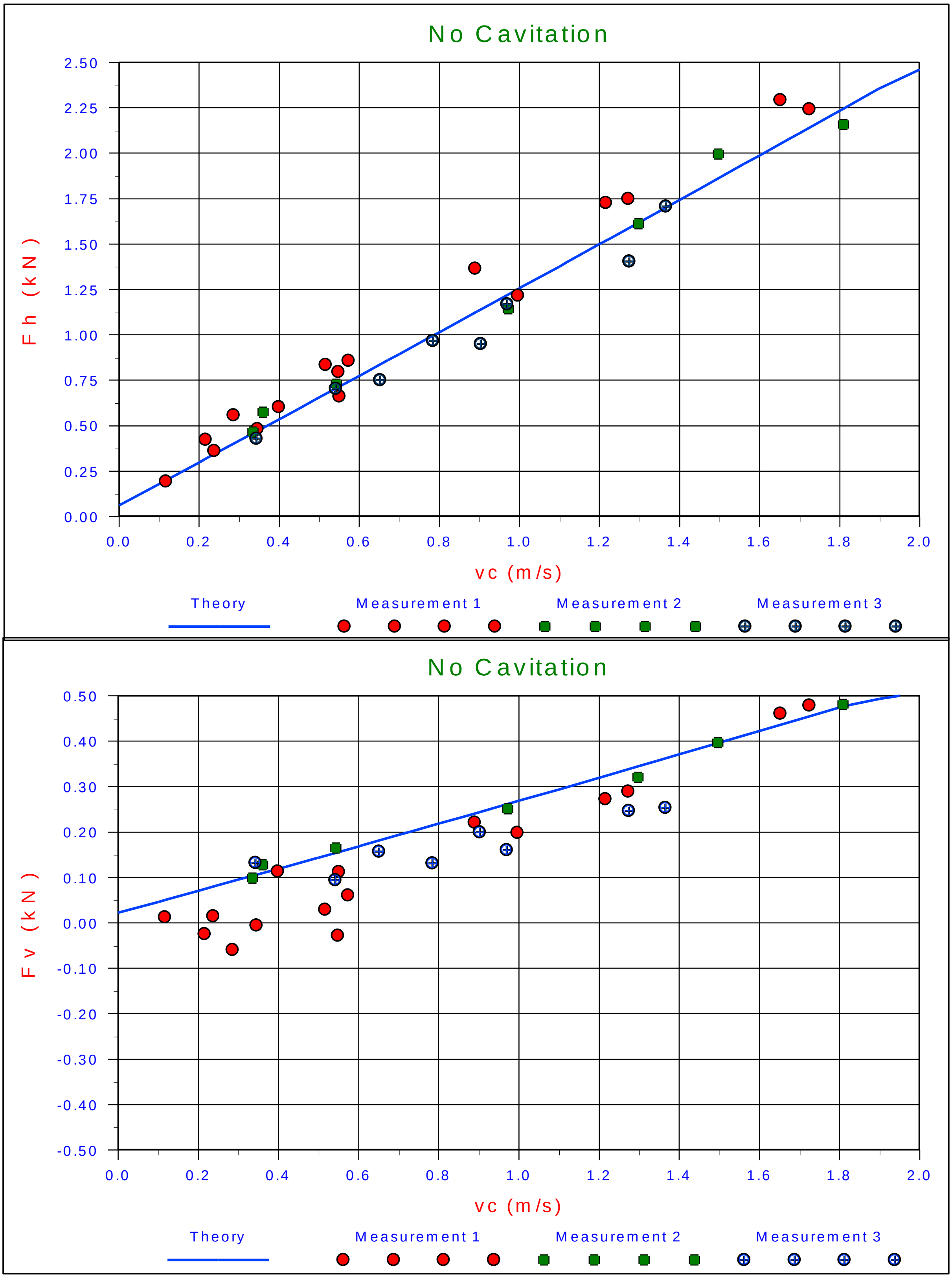

Figure M-23: α=45°, h_i=47 mm, h_b=141 mm.

The cutting forces $\mathbf{F_h}$ and $\mathbf{F_v}$ on the blade. Experiments in 200 μm sand, with **α**=45°, **β**=30º, **φ**=38º, **δ**=30º, $\mathbf{n_i}$=38.53%, $\mathbf{n_{max}}$=43.88%, $\mathbf{k_i}$=0.000165 m/s, $\mathbf{k_{max}}$=0.000320 m/s, $\mathbf{h_i}$=47 mm, $\mathbf{h_b}$=141 mm, **w**=0.2 m, **z**=0.6 m and a non-cavitating cutting process.

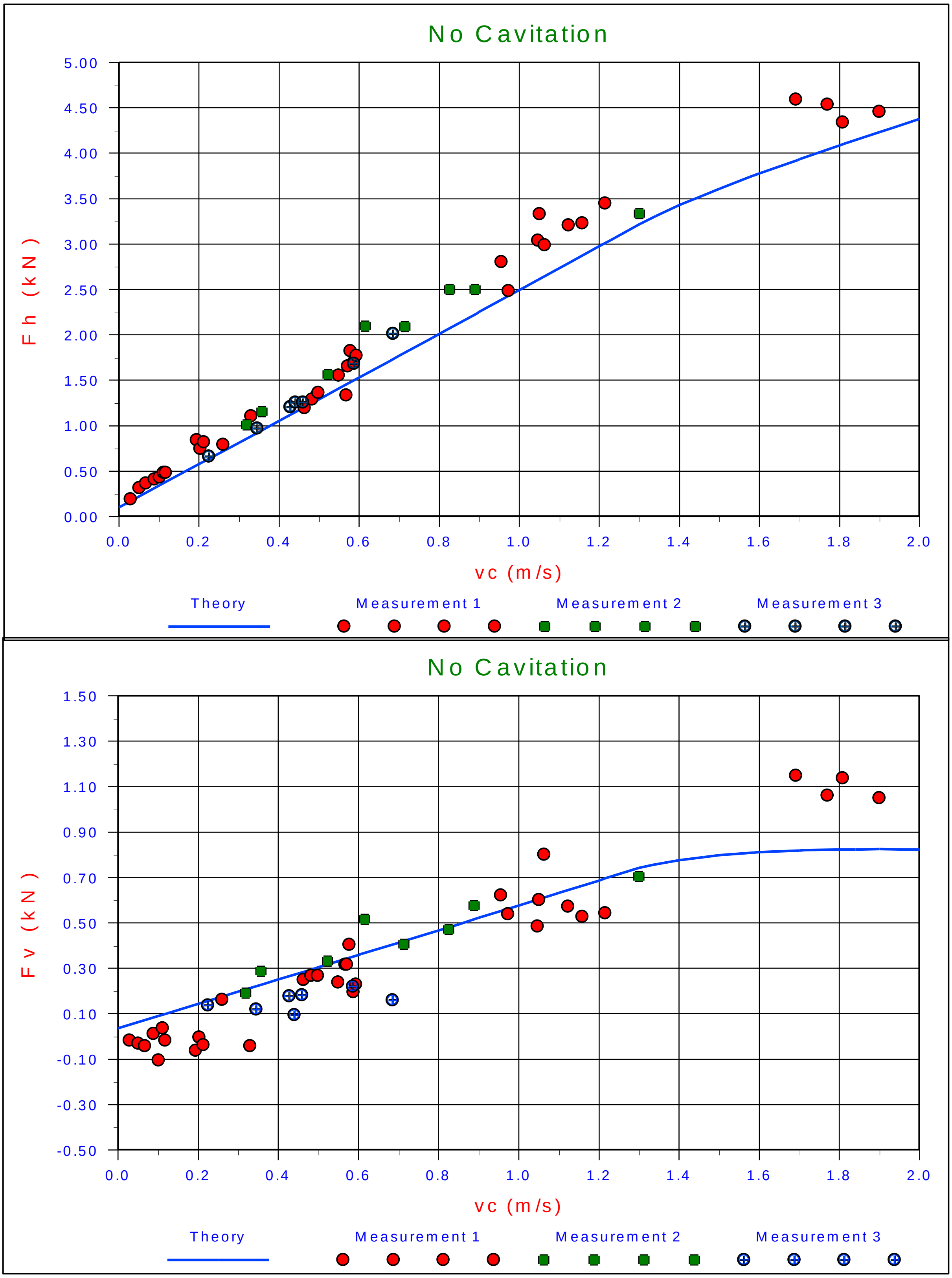

Figure M-24: α=45°, h_i=70 mm, h_b=141 mm.

The cutting forces $\mathbf{F_h}$ and $\mathbf{F_v}$ on the blade. Experiments in 200 μm sand, with **α**=45º, **β**=30º, **φ**=38º, **δ**=30º, $\mathbf{n_i}$=38.53%, $\mathbf{n_{max}}$=43.88%, $\mathbf{k_i}$=0.000165 m/s, $\mathbf{k_{max}}$=0.000320 m/s, $\mathbf{h_i}$=70 mm, $\mathbf{h_b}$=141 mm, **w**=0.2 m, **z**=0.6 m and a non-cavitating cutting process.

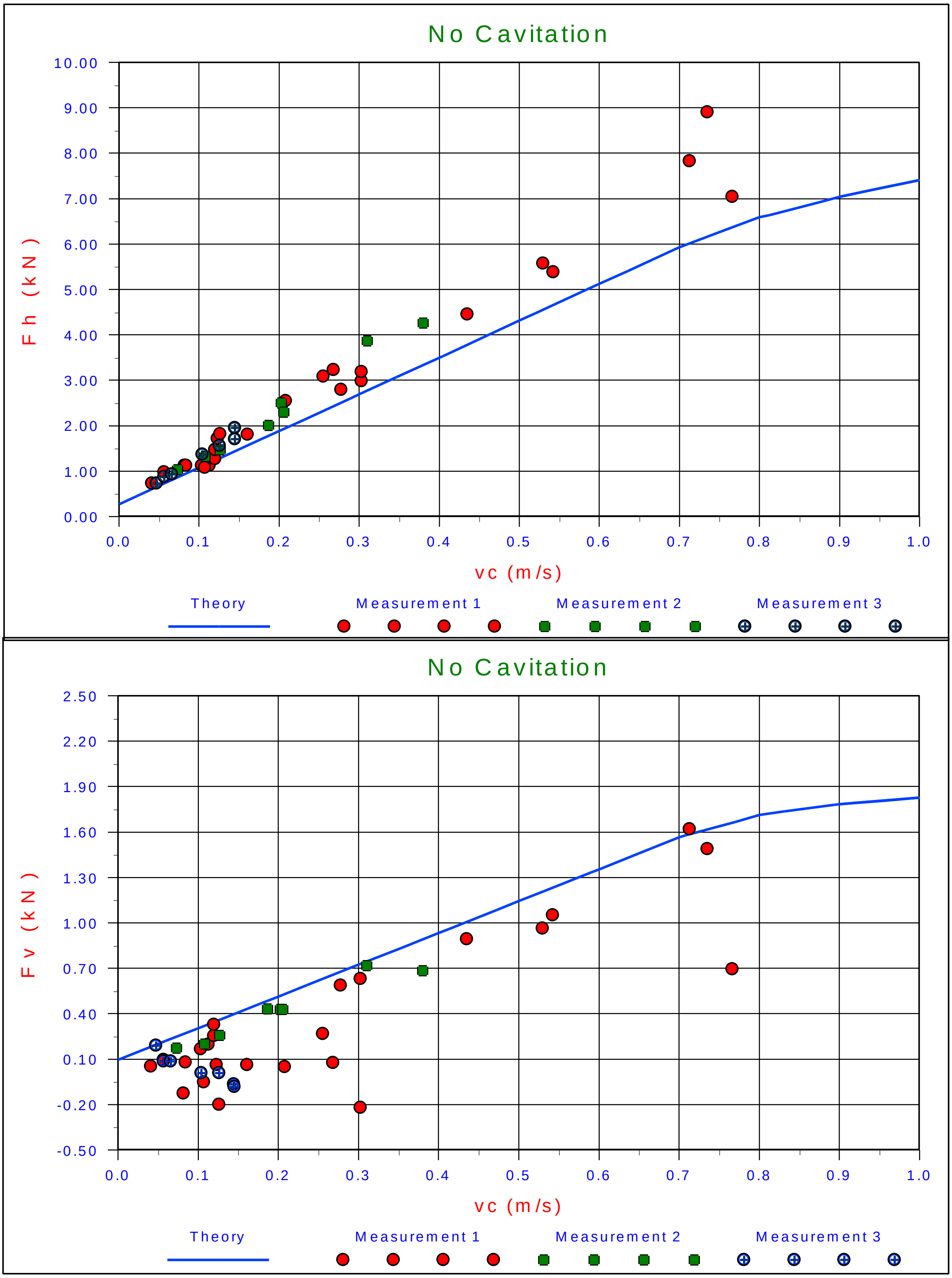

Figure M-25: α=45°, h_i=141 mm, h_b=141 mm.

The cutting forces $\mathbf{F_h}$ and $\mathbf{F_v}$ on the blade. Experiments in 200 μm sand, with $\boldsymbol{\alpha}$=45°, $\boldsymbol{\beta}$=30°, $\boldsymbol{\varphi}$=38°, $\boldsymbol{\delta}$=30°, $\mathbf{n_i}$=38.53%, $\mathbf{n_{max}}$=43.88%, $\mathbf{k_i}$=0.000165 m/s, $\mathbf{k_{max}}$=0.000320 m/s, $\mathbf{h_i}$=141 mm, $\mathbf{h_b}$=141 mm, **w**=0.2 m, **z**=0.6 m and a non-cavitating cutting process.

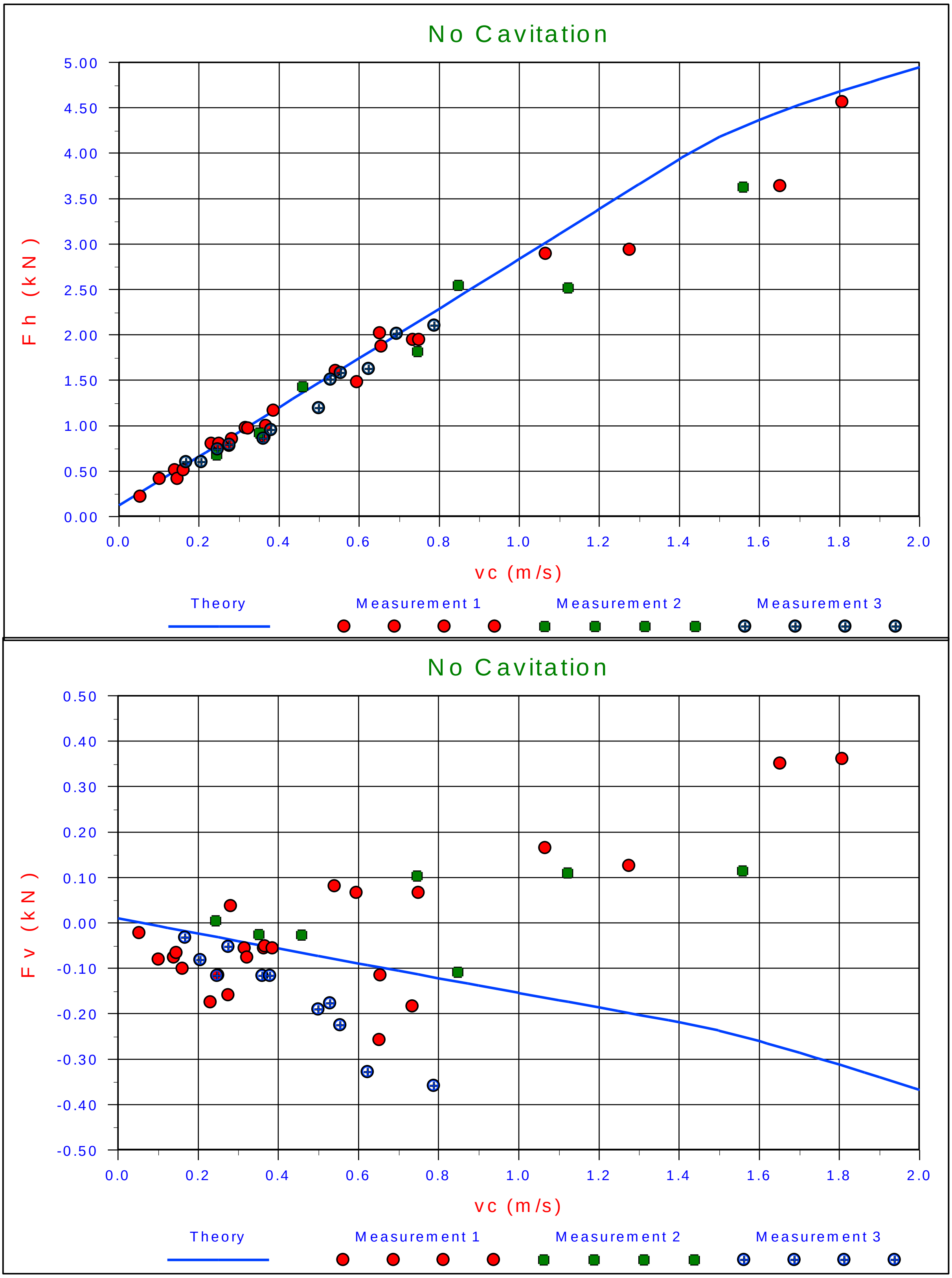

Figure M-26: α=60°, h_i=58 mm, h_b=173 mm.

The cutting forces $\mathbf{F_h}$ and $\mathbf{F_v}$ on the blade. Experiments in 200 μm sand, with **α**=45°, **β**=30°, **φ**=38°, **δ**=30°, $\mathbf{n_i}$=38.53%, $\mathbf{n_{max}}$=43.88%, $\mathbf{k_i}$=0.000165 m/s, $\mathbf{k_{max}}$=0.000320 m/s, $\mathbf{h_i}$=58 mm, $\mathbf{h_b}$=173 mm, **w**=0.2 m, **z**=0.6 m and a non-cavitating cutting process.

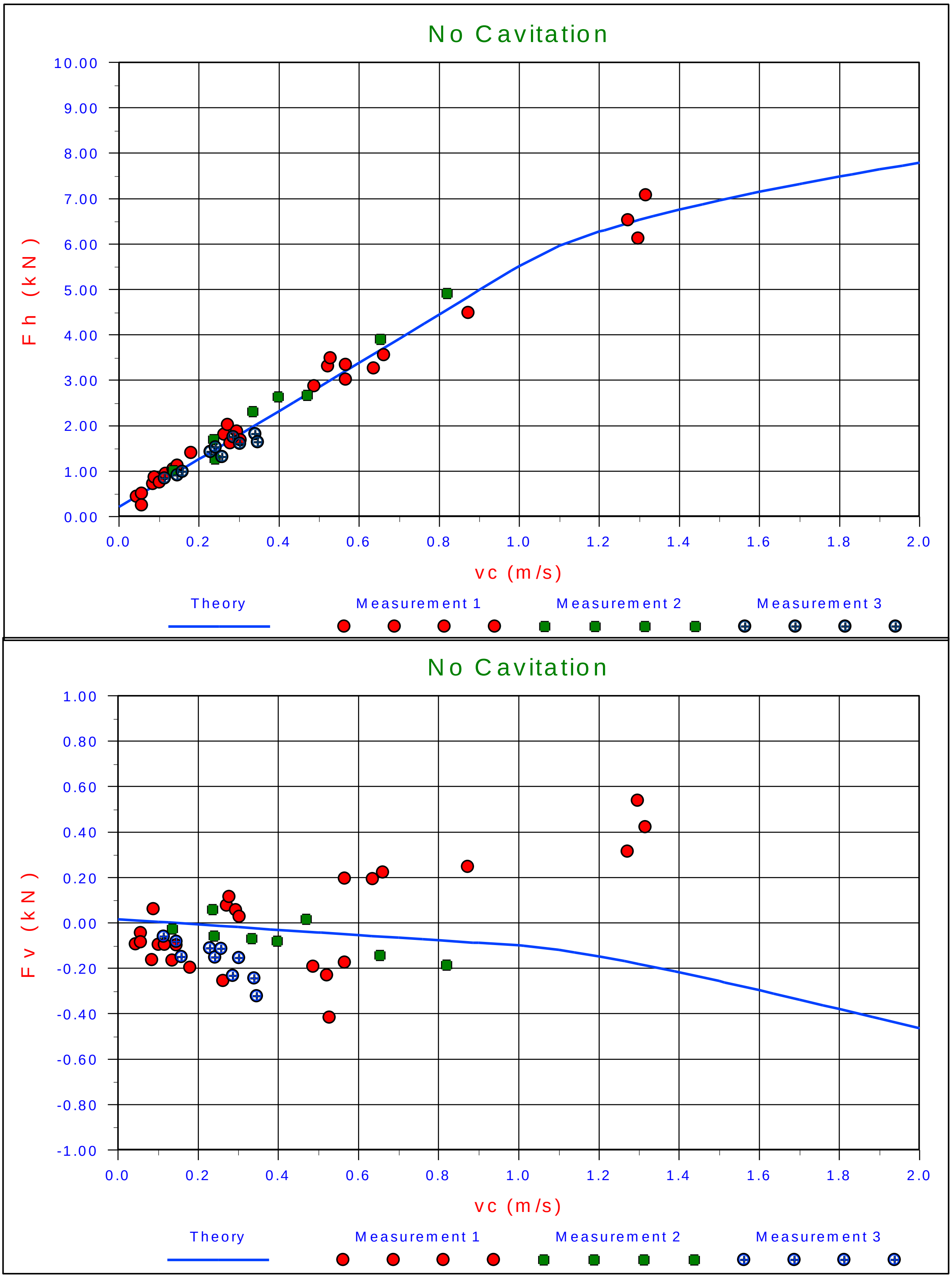

Figure M-27: α=60°, h_i=87 mm, h_b=173 mm.

The cutting forces $\mathbf{F_h}$ and $\mathbf{F_v}$ on the blade. Experiments in 200 μm sand, with **α**=45°, **β**=30º, **φ**=38º, **δ**=30º, $\mathbf{n_i}$=38.53%, $\mathbf{n_{max}}$=43.88%, $\mathbf{k_i}$=0.000165 m/s, $\mathbf{k_{max}}$=0.000320 m/s, $\mathbf{h_i}$=87 mm, $\mathbf{h_b}$=173 mm, **w**=0.2 m, **z**=0.6 m and a non-cavitating cutting process.

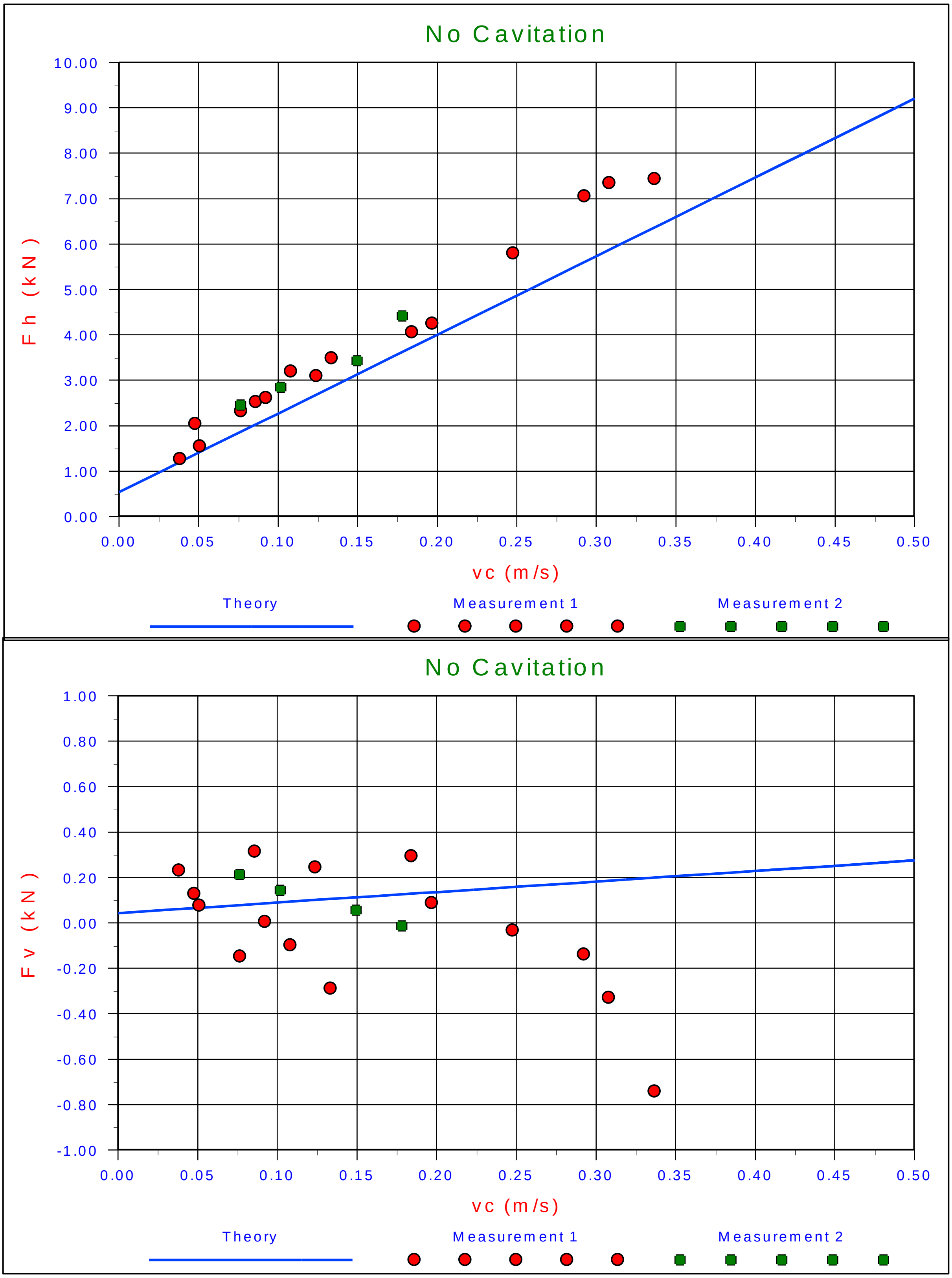

Figure M-28: α=60°, h_i=173 mm, h_b=173 mm.

The cutting forces $\mathbf{F_h}$ and $\mathbf{F_v}$ on the blade. Experiments in 200 μm sand, with **α**=45°, **β**=30º, **φ**=38º, **δ**=30º, $\mathbf{n_i}$=38.53%, $\mathbf{n_{max}}$=43.88%, $\mathbf{k_i}$=0.000165 m/s, $\mathbf{k_{max}}$=0.000320 m/s, $\mathbf{h_i}$=173 mm, $\mathbf{h_b}$=173 mm, **w**=0.2 m, **z**=0.6 m and a non-cavitating cutting process.

Appendix N: The Snow Plough Effect.

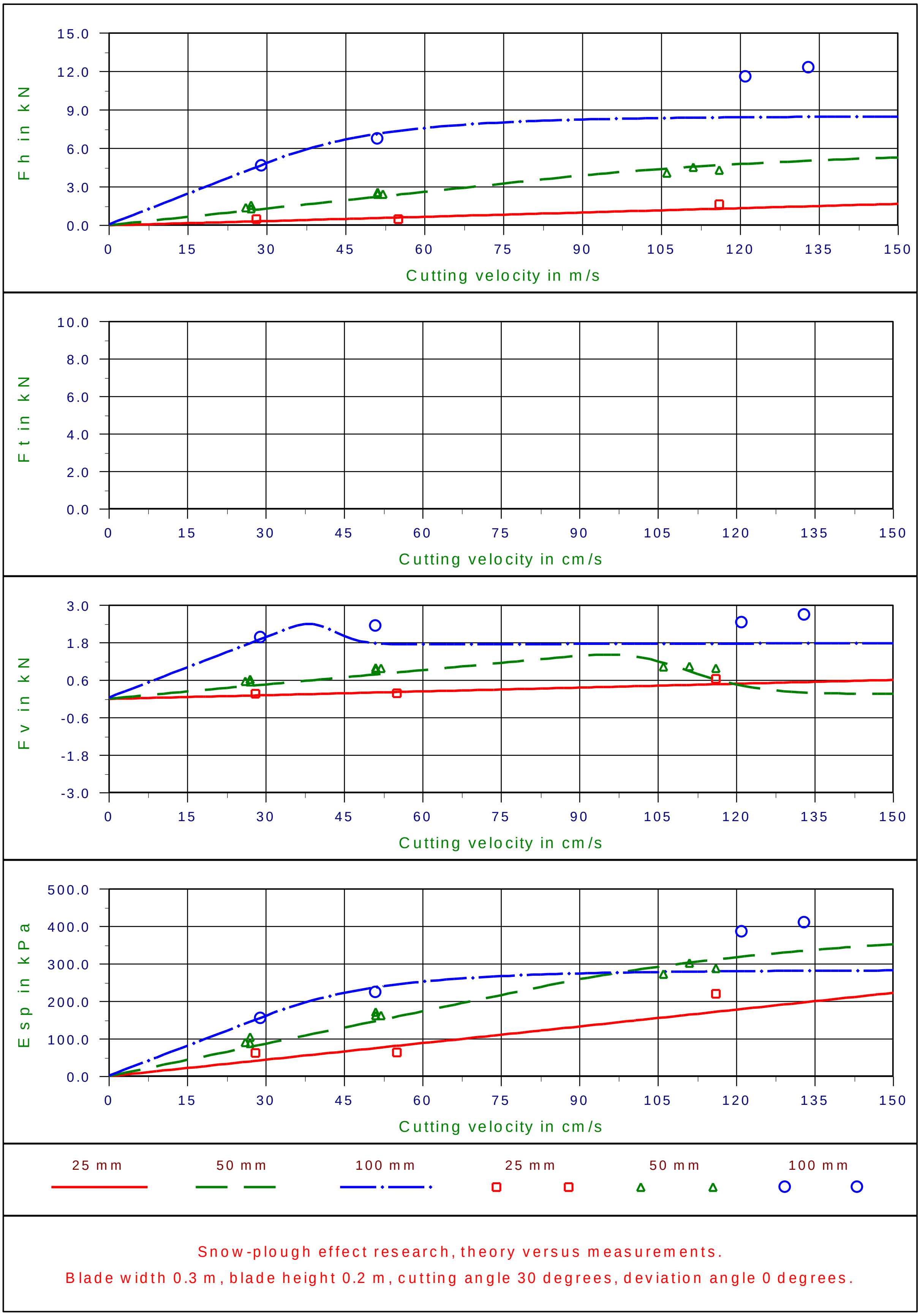

Snow-plough effect research, theory versus measurements.
Blade width 0.3 m, blade height 0.2 m, cutting angle 30 degrees, deviation angle 0 degrees.

Figure N-1: Blade angle 30 degrees – Deviation angle 00 degrees

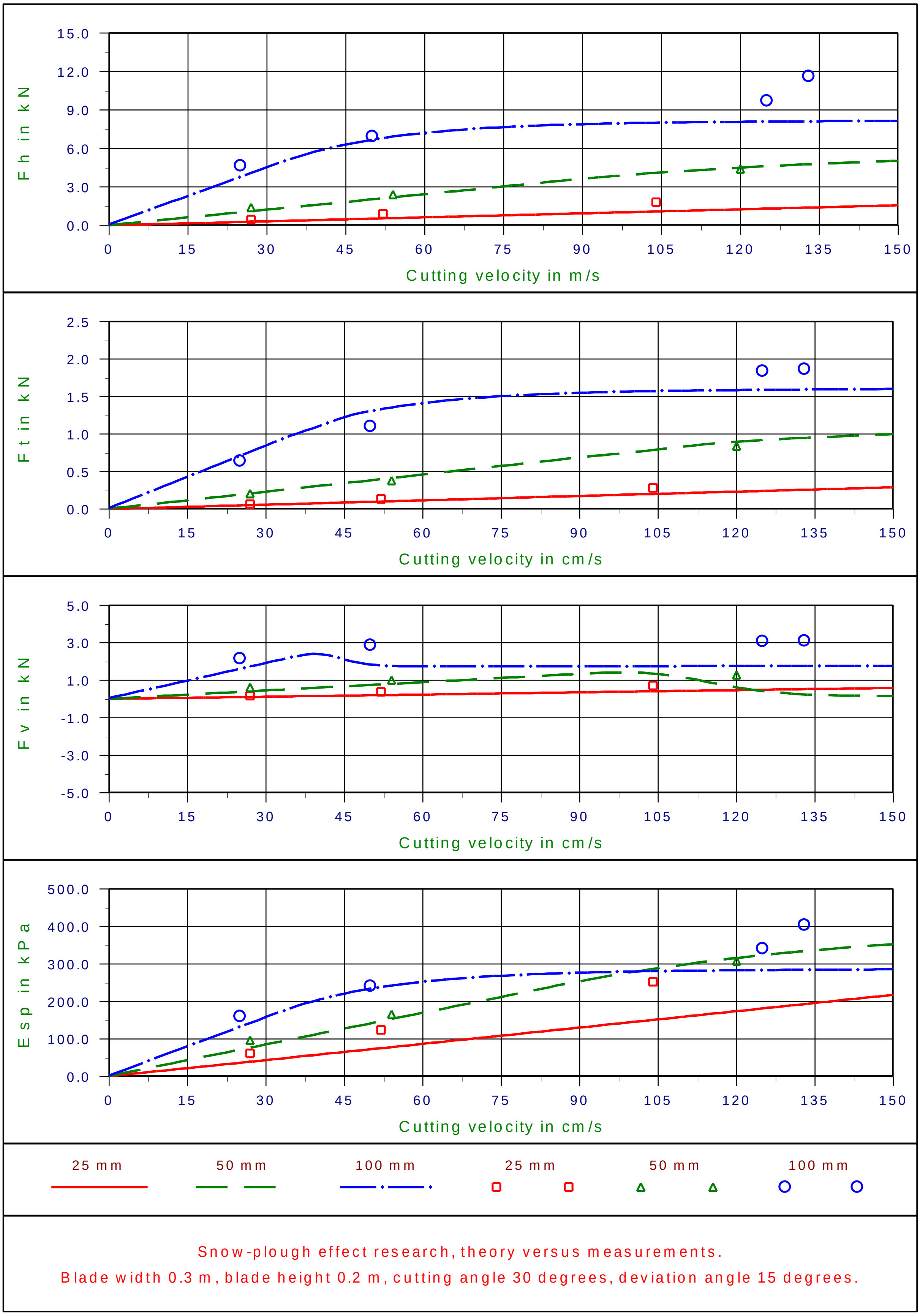

Figure N-2: Blade angle 30 degrees – Deviation angle 15 degrees

The 105 μm sand properties from Appendix L were used.

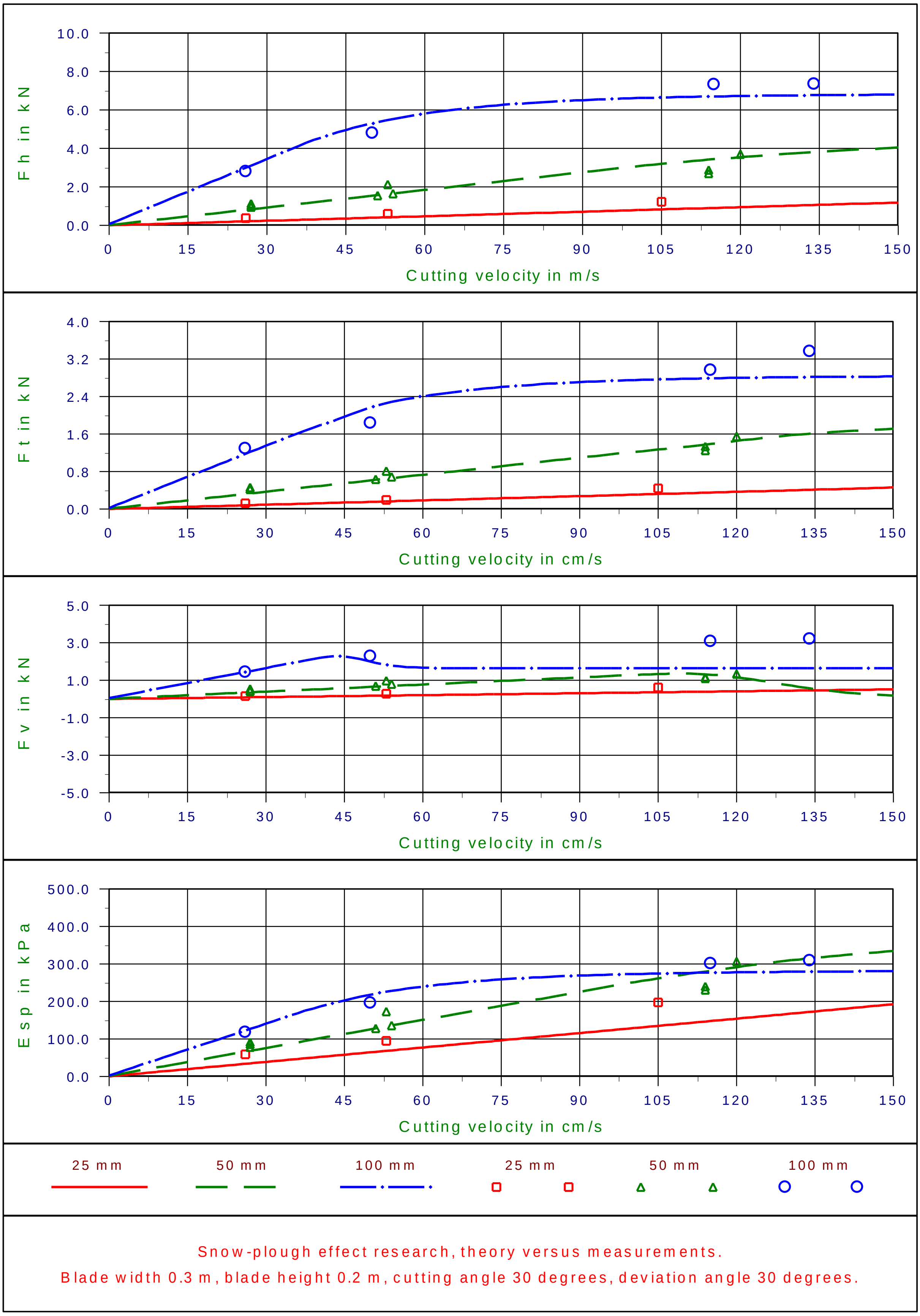

Snow-plough effect research, theory versus measurements.

Blade width 0.3 m, blade height 0.2 m, cutting angle 30 degrees, deviation angle 30 degrees.

Figure N-3: Blade angle 30 degrees – Deviation angle 30 degrees

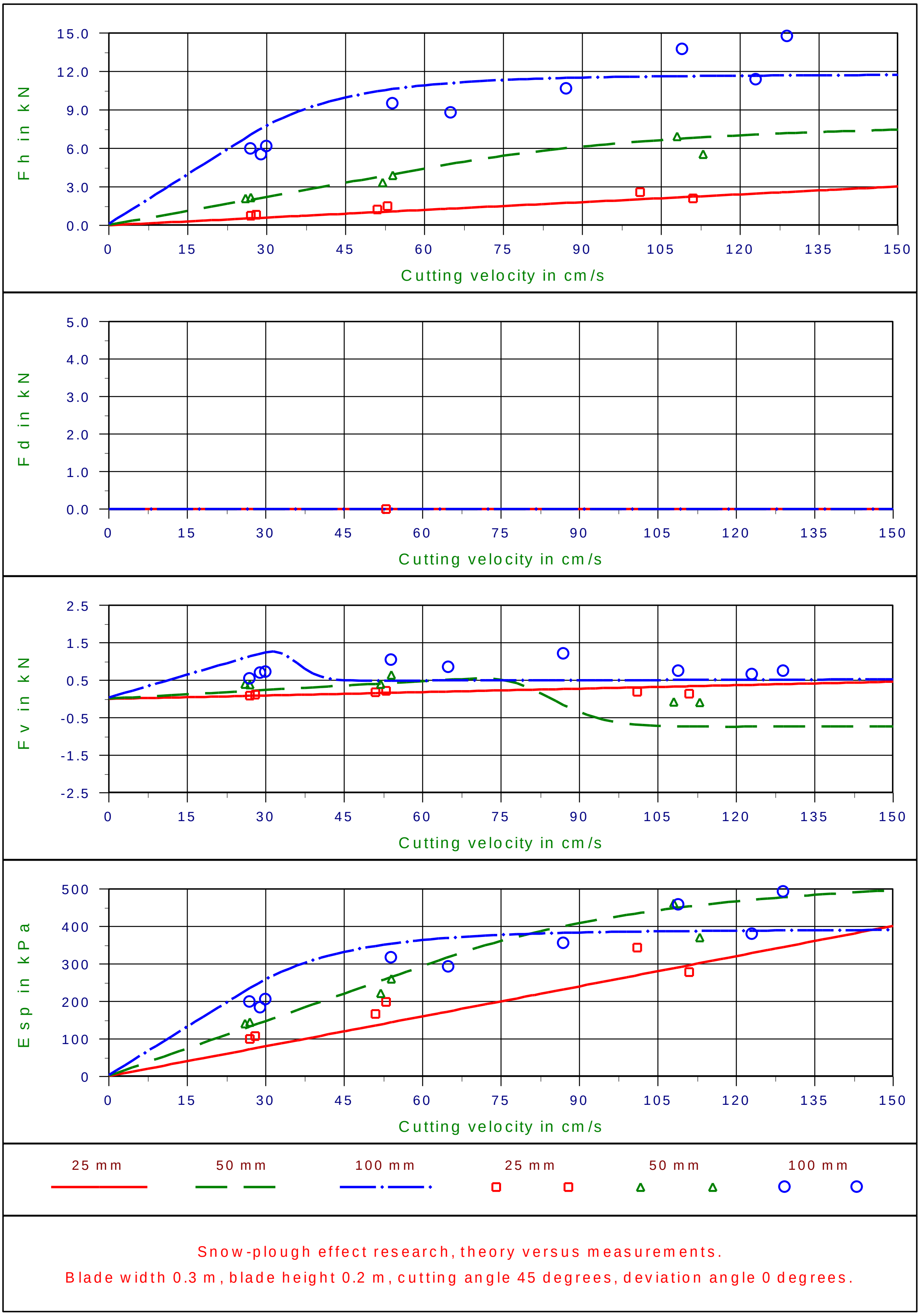

Snow-plough effect research, theory versus measurements.
Blade width 0.3 m, blade height 0.2 m, cutting angle 45 degrees, deviation angle 0 degrees.

Figure N-4: Blade angle 45 degrees – Deviation angle 00 degrees

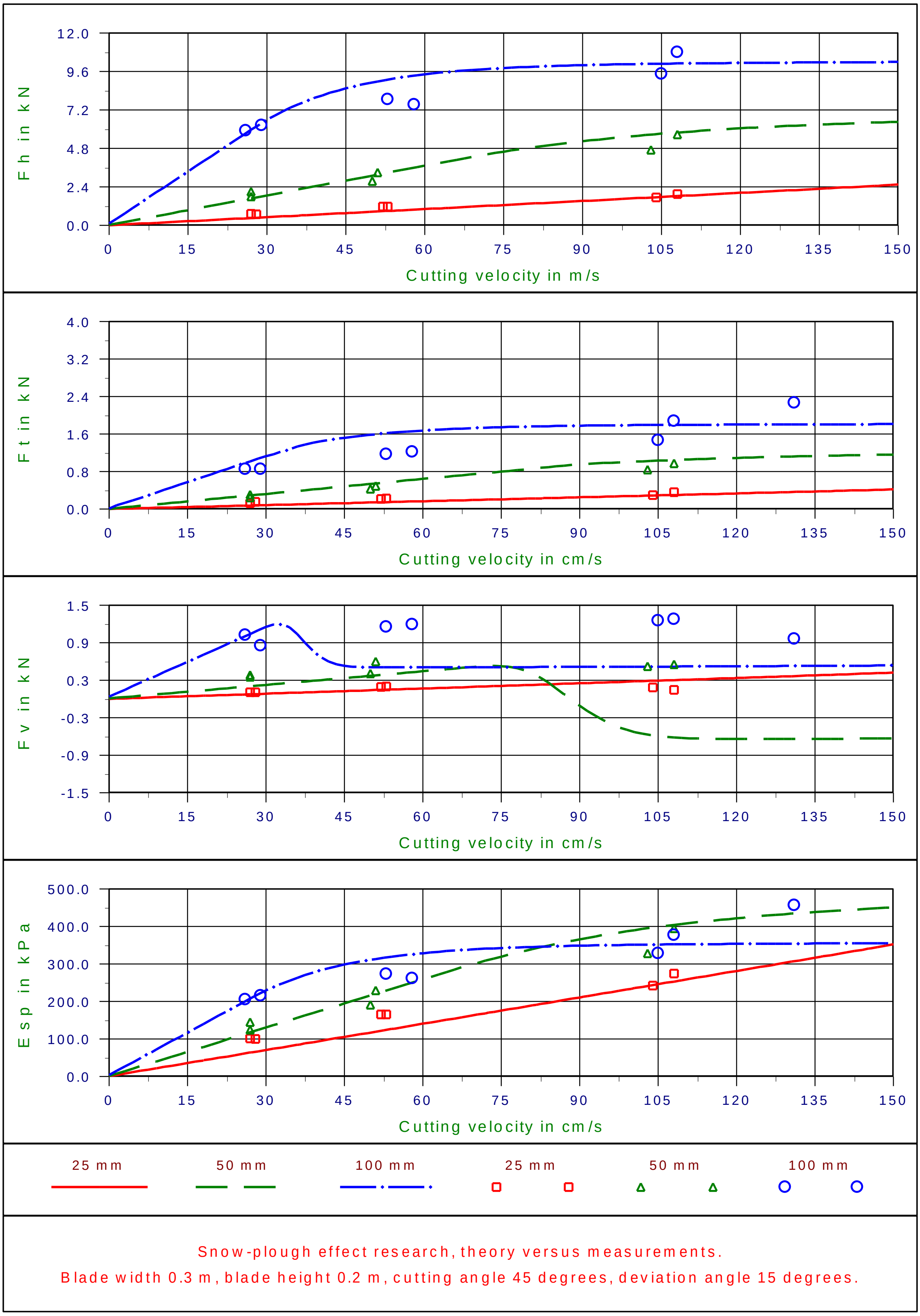

Figure N-5: Blade angle 45 degrees – Deviation angle 15 degrees

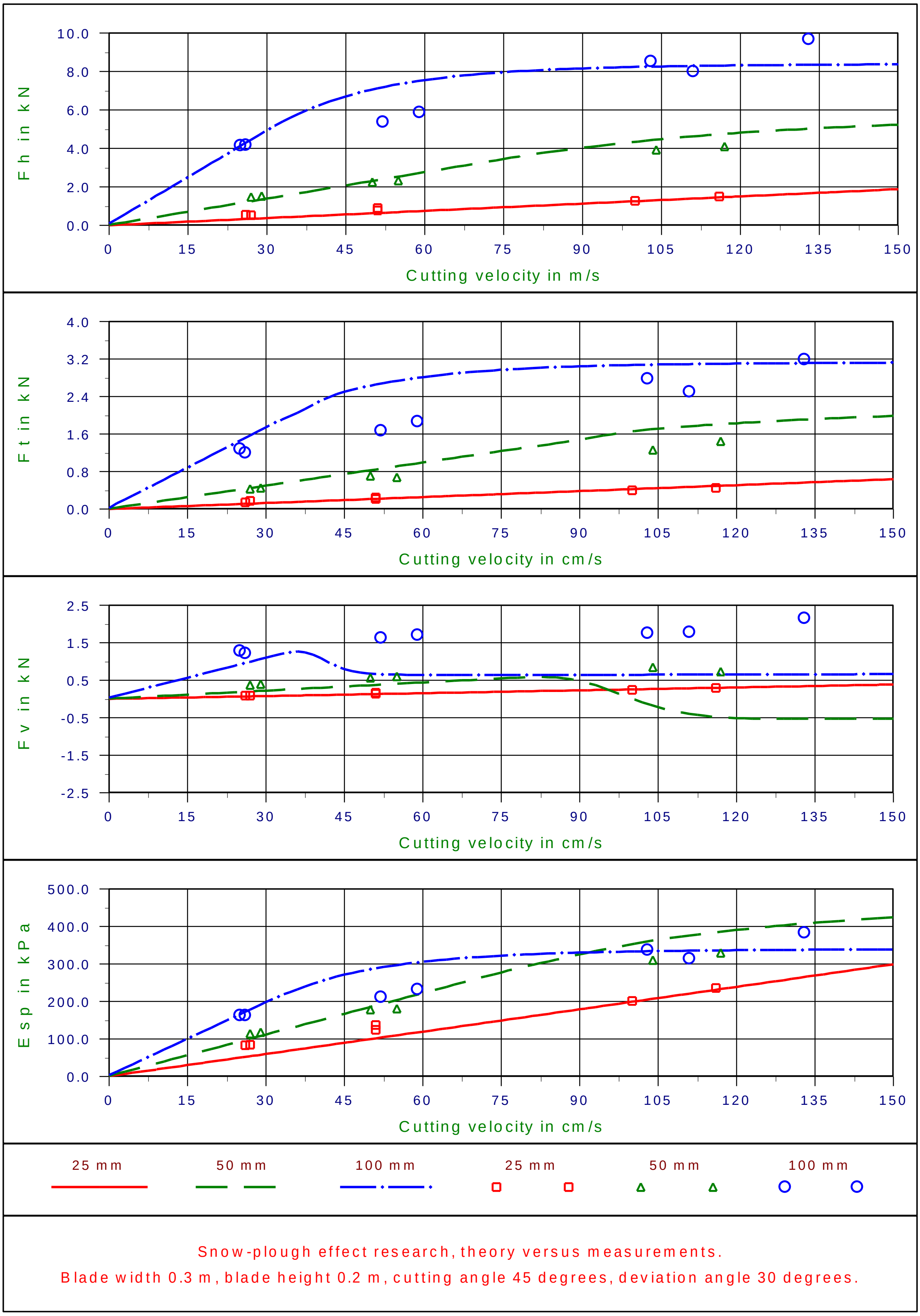

Figure N-6: Blade angle 45 degrees – Deviation angle 30 degrees

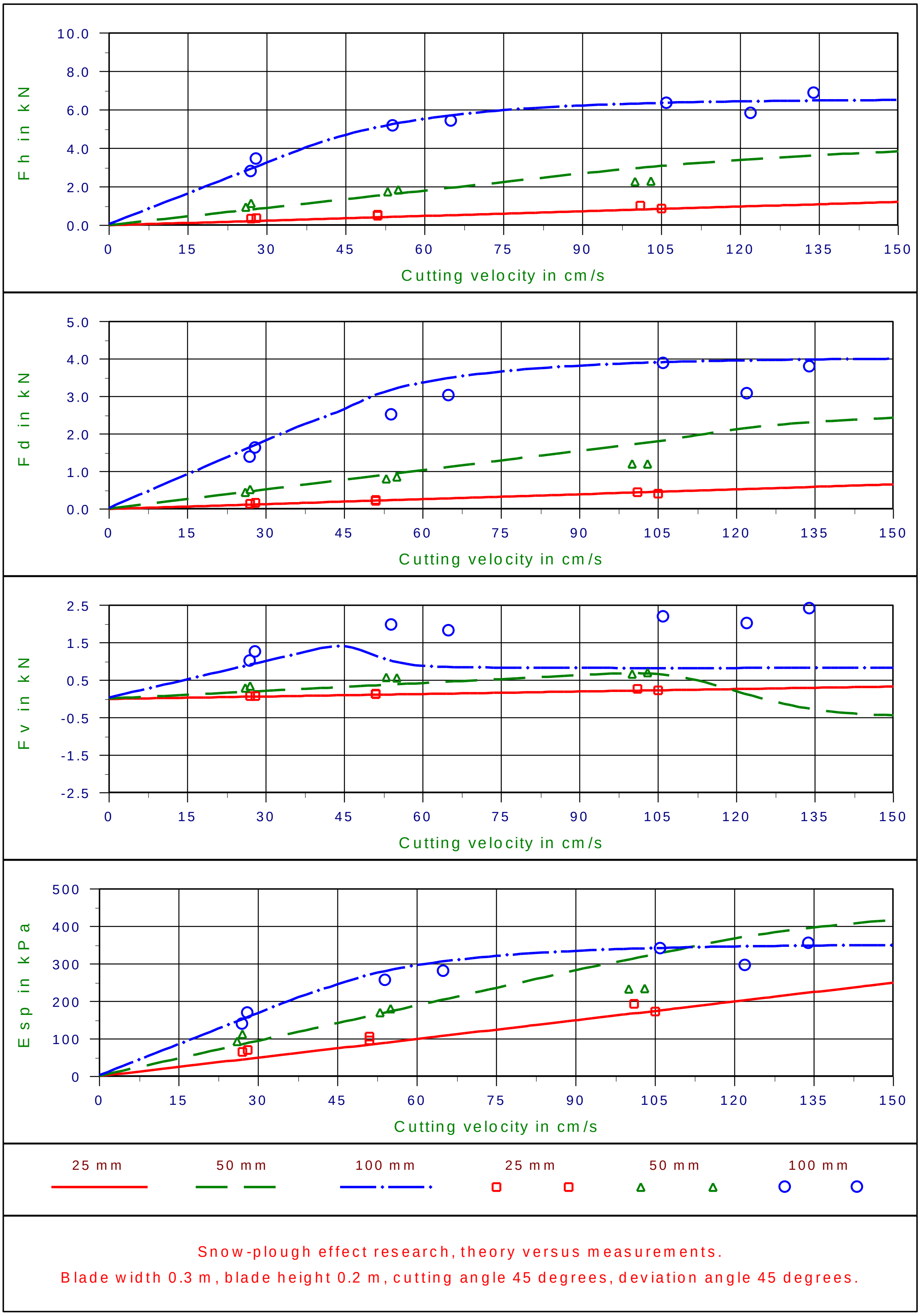

Figure N-7: Blade angle 45 degrees – Deviation angle 45 degrees

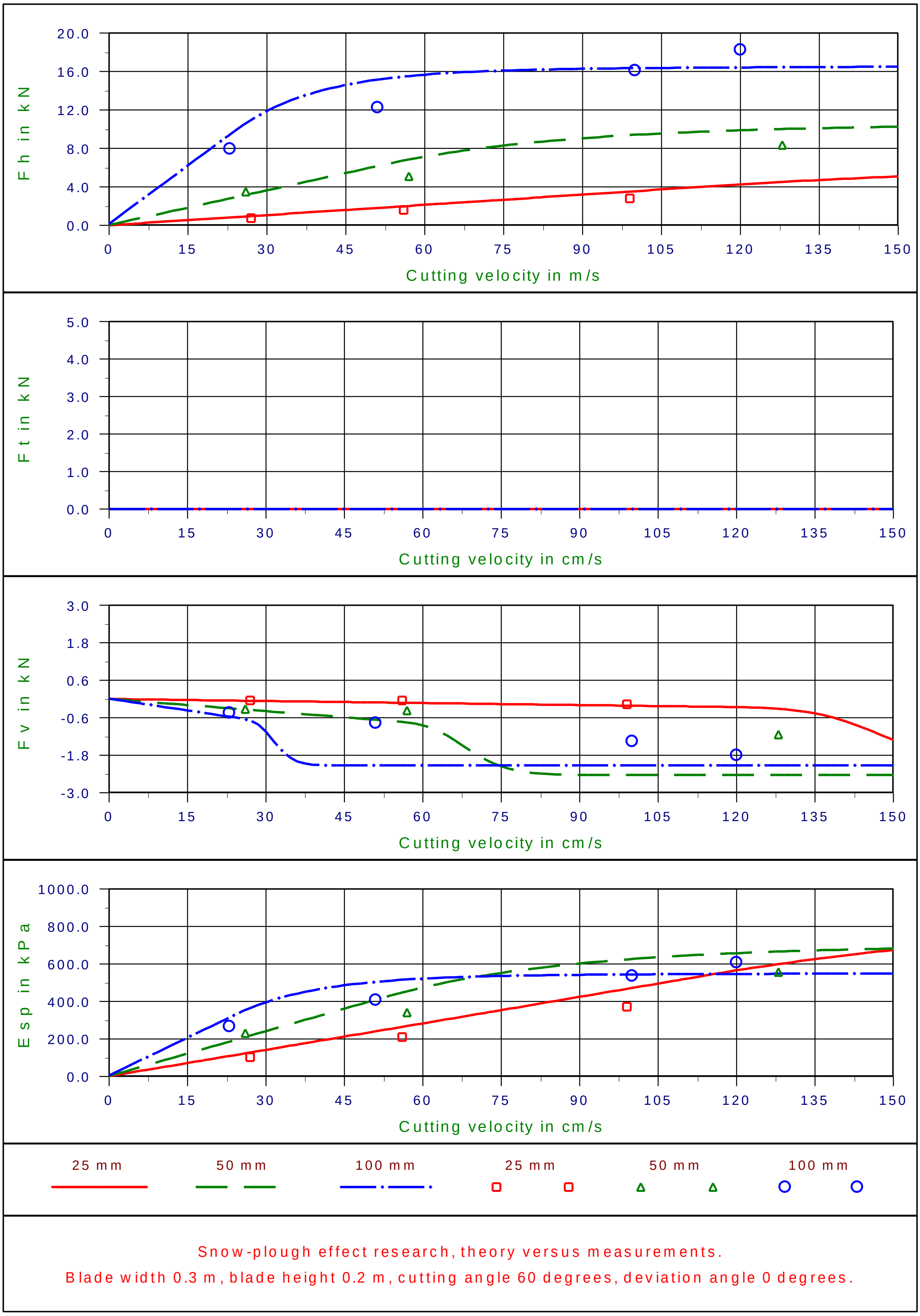

Figure N-8: Blade angle 60 degrees – Deviation angle 00 degrees

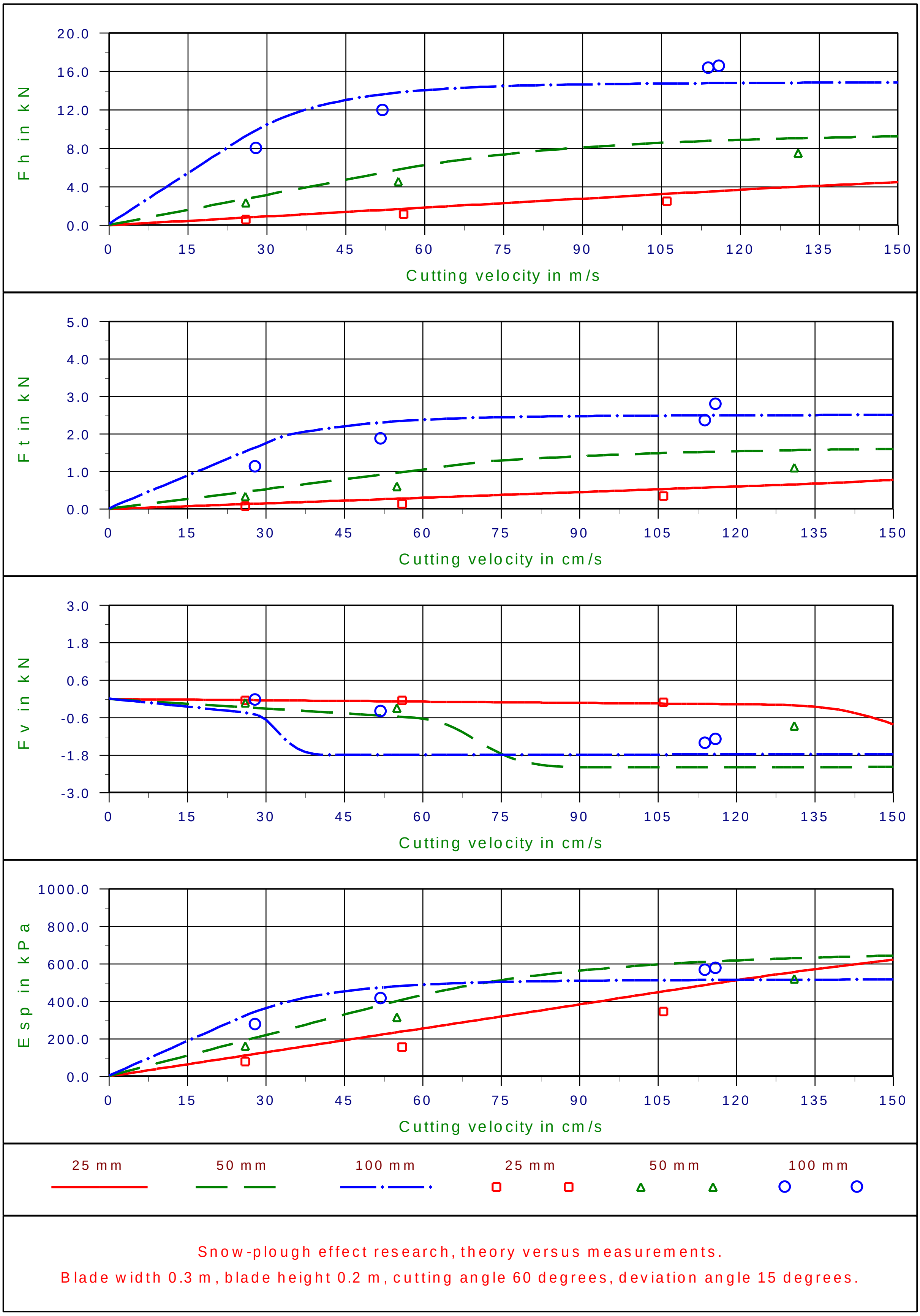

Figure N-9: Blade angle 60 degrees – Deviation angle 15 degrees

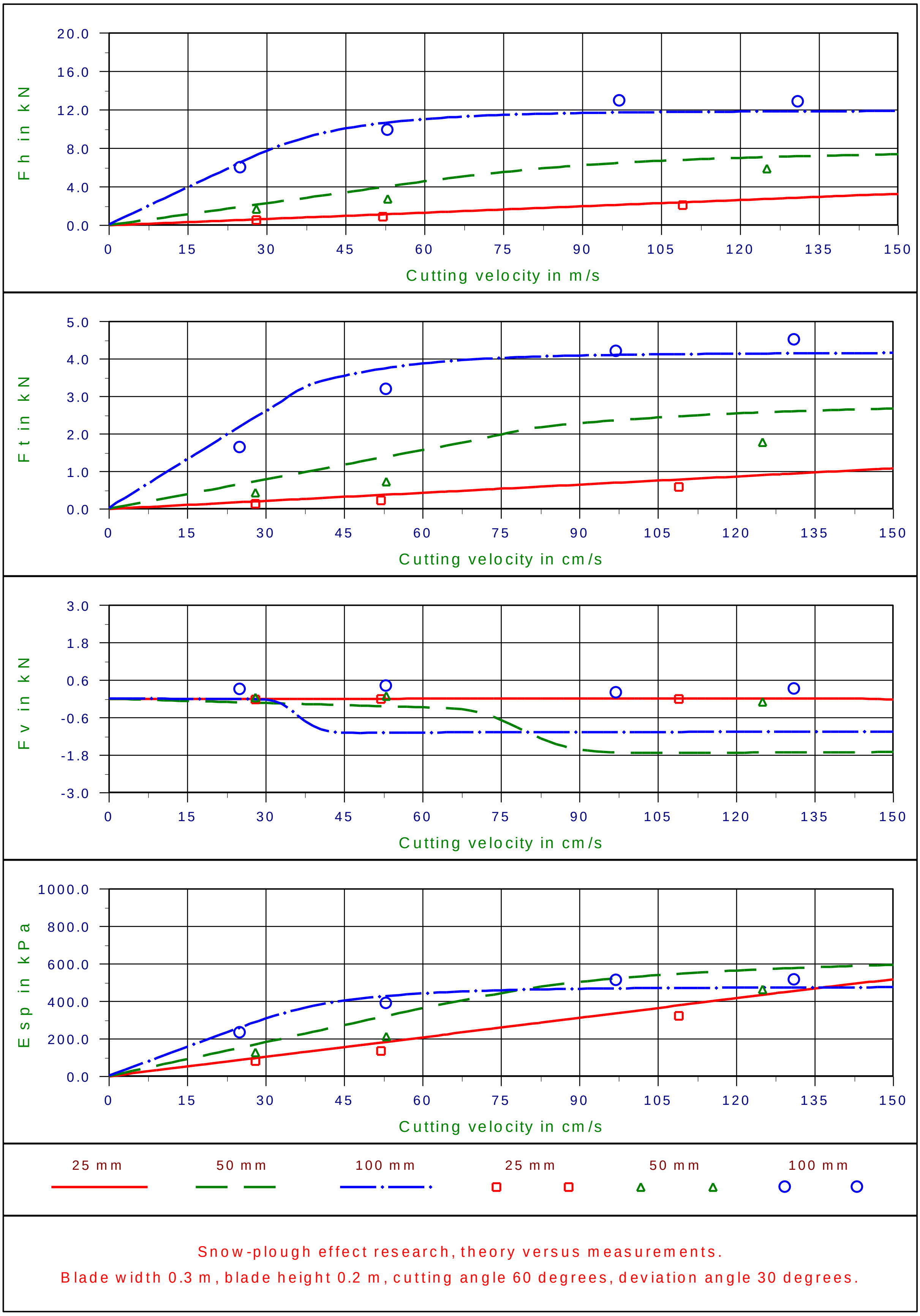

Snow-plough effect research, theory versus measurements.

Blade width 0.3 m, blade height 0.2 m, cutting angle 60 degrees, deviation angle 30 degrees.

Figure N-10: Blade angle 60 degrees – Deviation angle 30 degrees

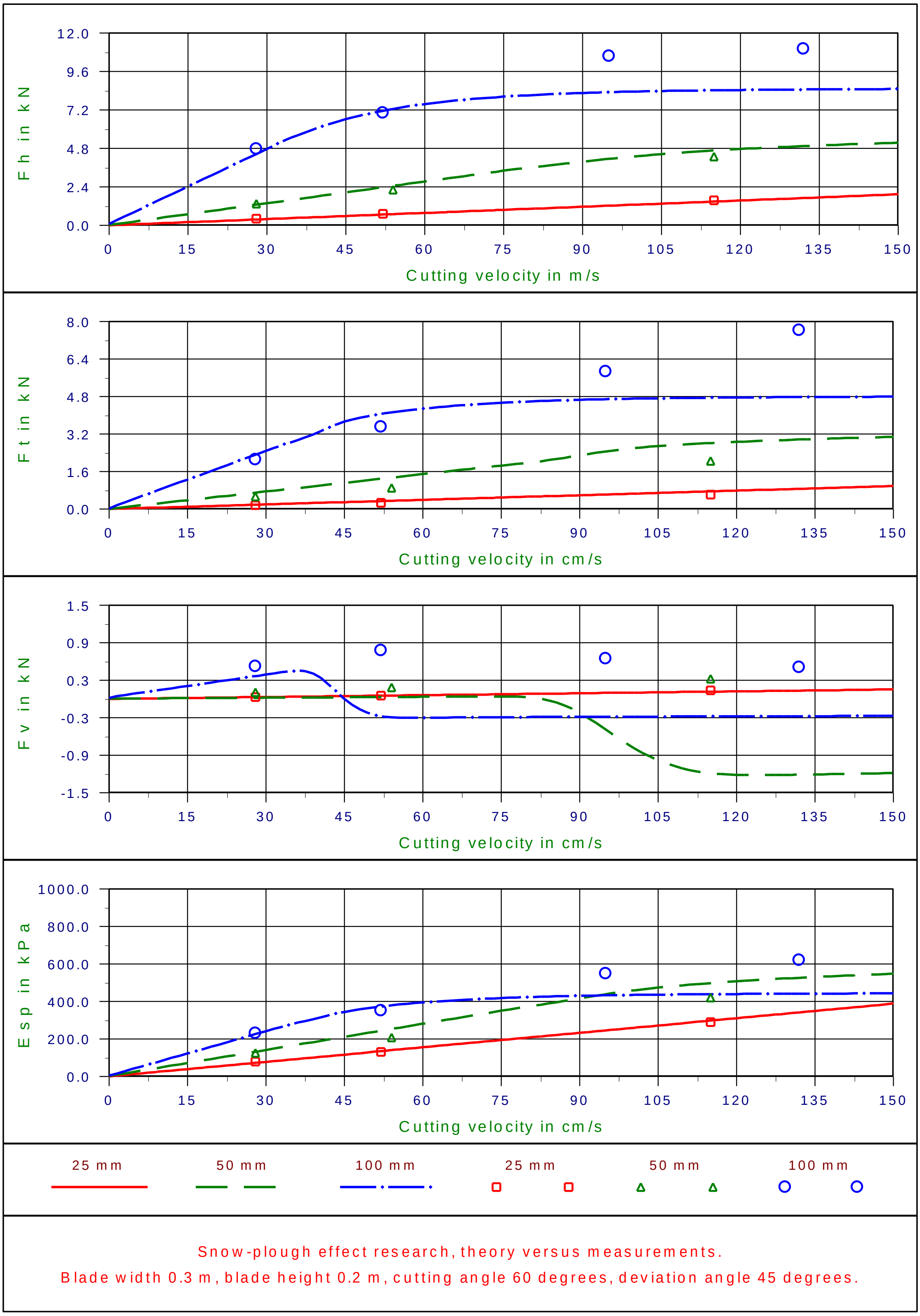

Figure N-11: Blade angle 60 degrees – Deviation angle 45 degrees

Appendix O: Specific Energy in Sand.

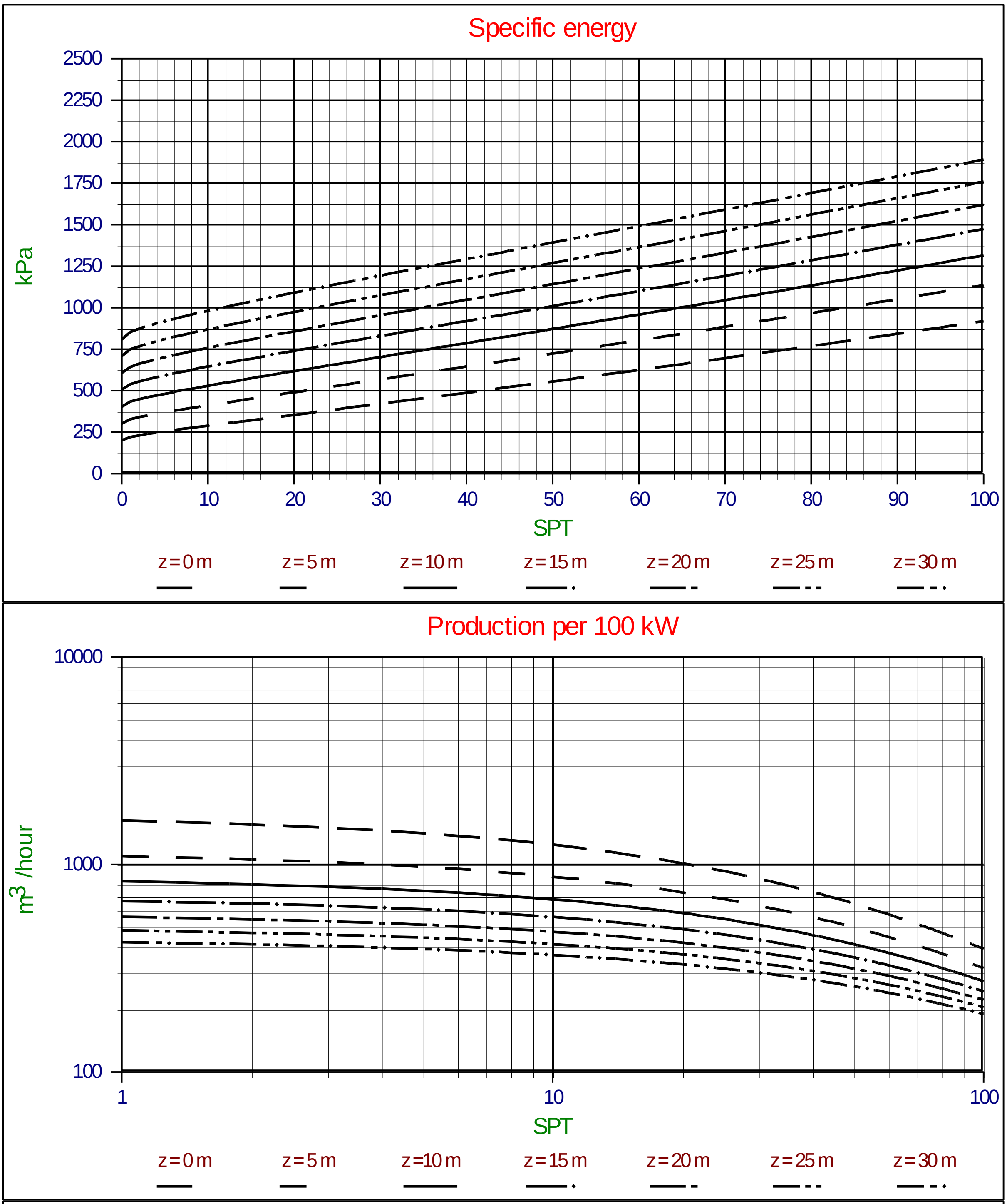

Specific energy and production for a 30 degree blade and a cavitating cutting process in sand as a function of the reduced SPT value.

Figure O-1: Specific energy and production in sand for a 30 degree blade.

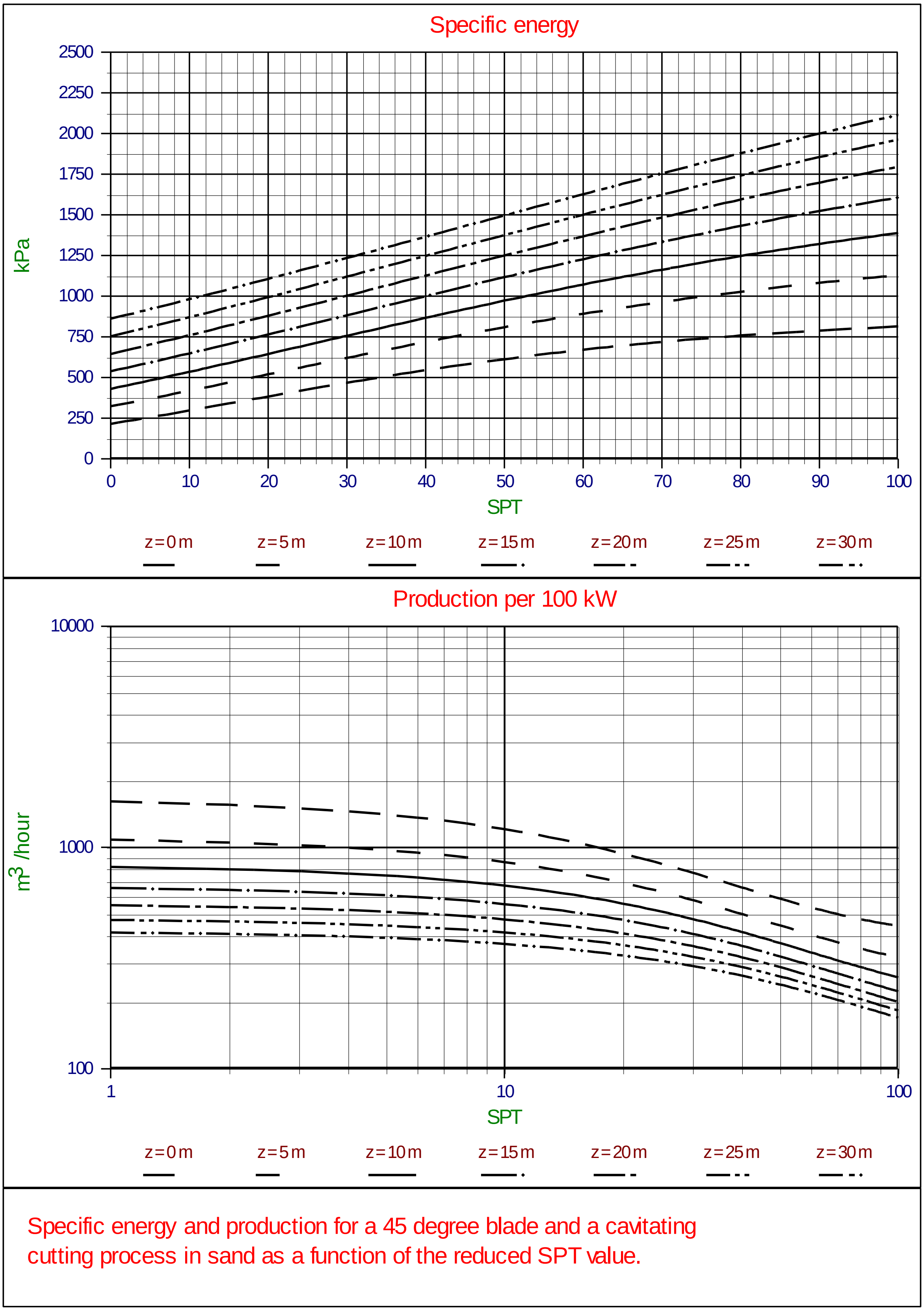

Figure O-2: Specific energy and production in sand for a 45 degree blade.

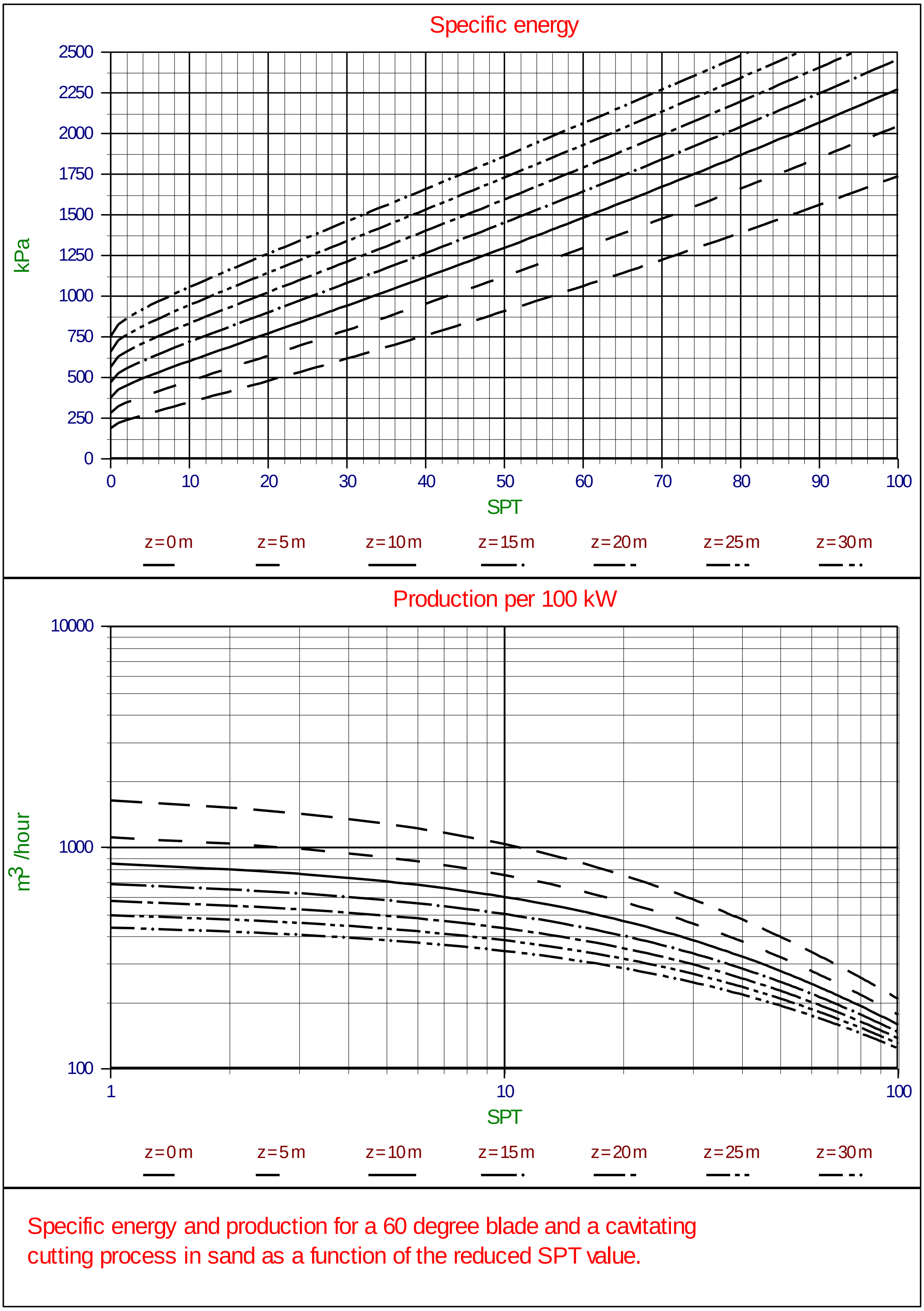

Figure O-3: Specific energy and production in sand for a 60 degree blade.

Appendix P: Occurrence of a Wedge, Non-Cavitating.

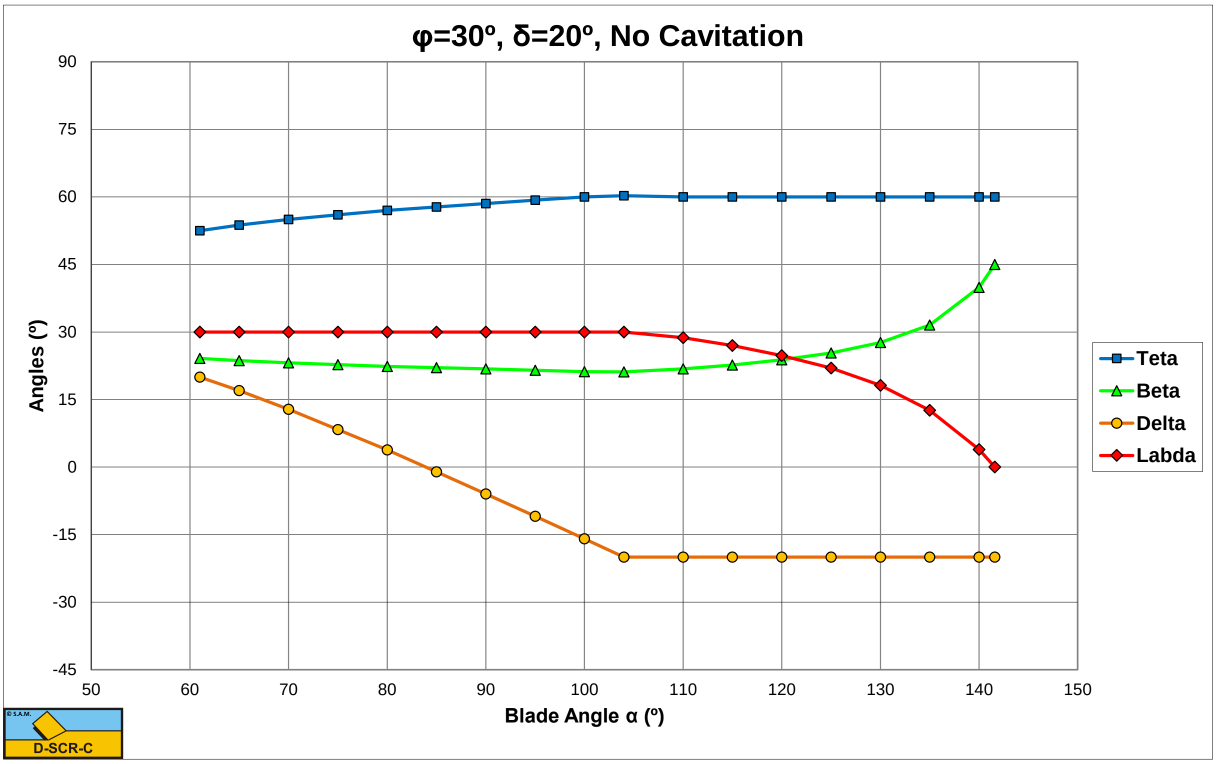

Figure P-1: No cavitation, the angles θ, β, δ_m and λ as a function of the blade angle α for φ=30º and δ=20º.

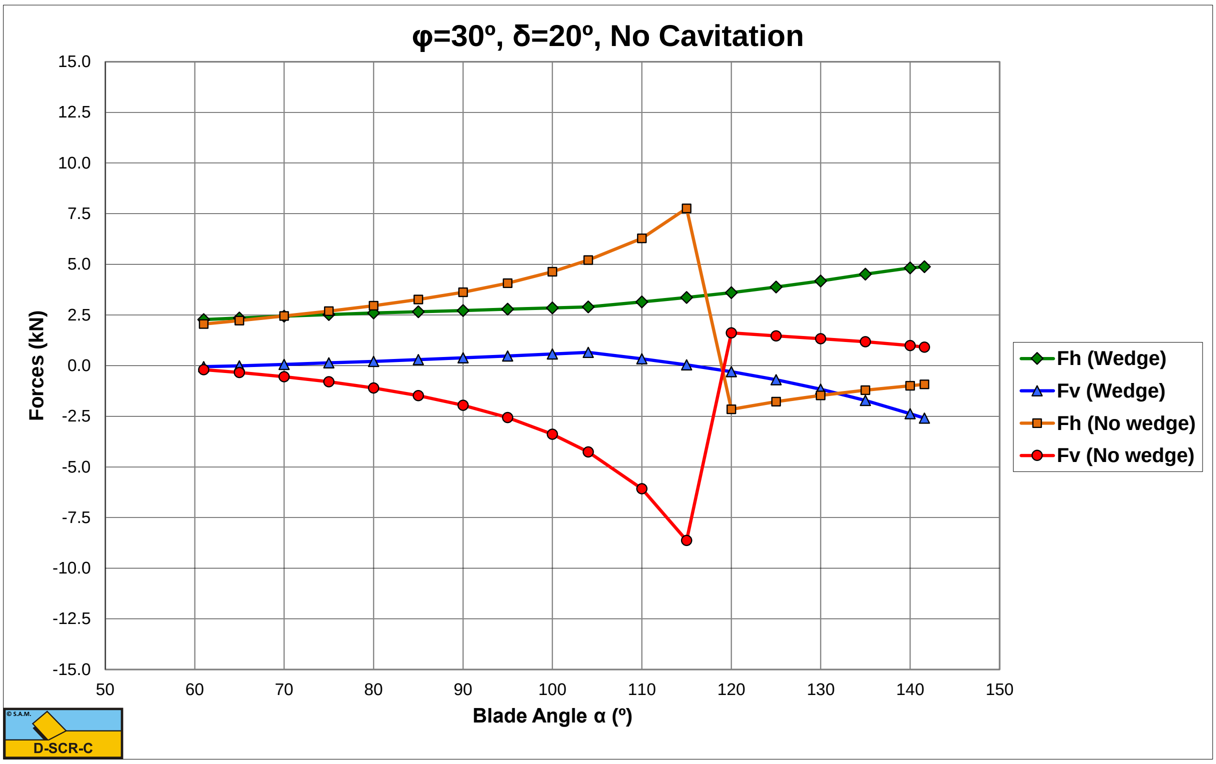

Figure P-2: No cavitation, the cutting forces as a function of the blade angle α for φ=30º and δ=20º.

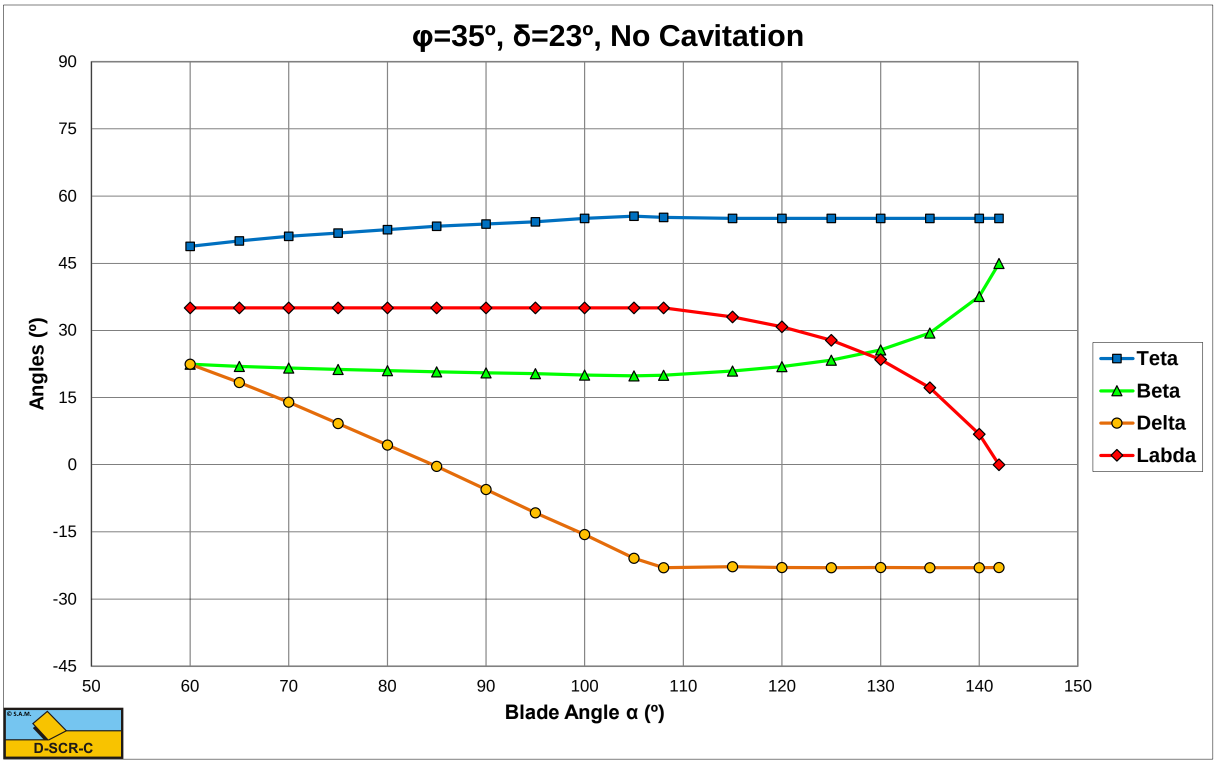

Figure P-3: No cavitation, the angles θ, β, δ_m and λ as a function of the blade angle α for φ=35º and δ=23º.

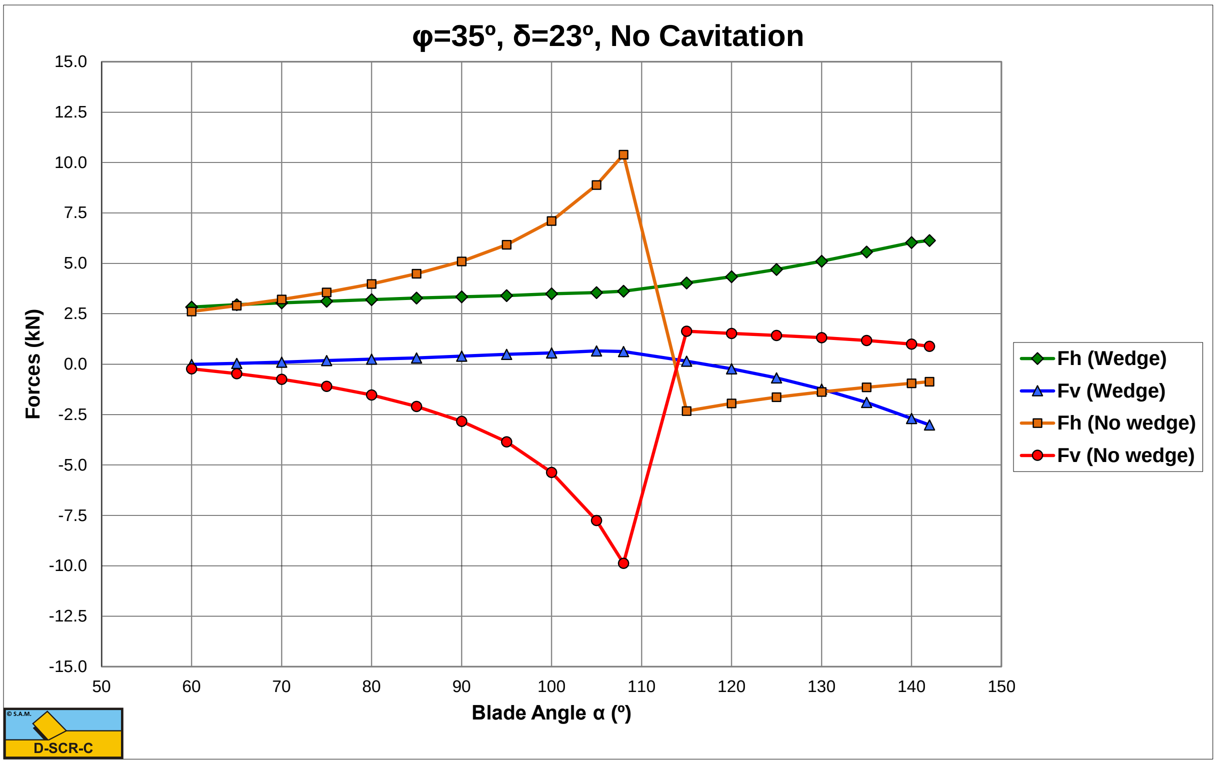

Figure P-4: No cavitation, the cutting forces as a function of the blade angle α for φ=35º and δ=23º.

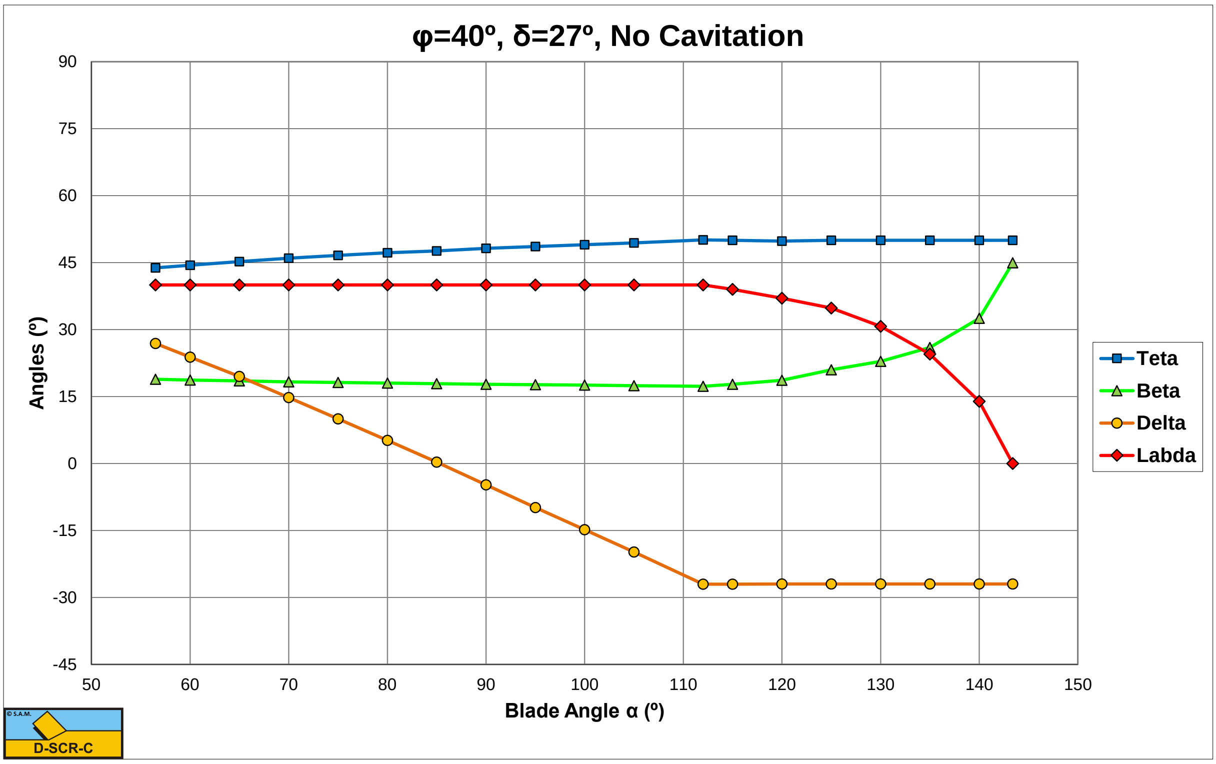

Figure P-5: No cavitation, the angles θ, β, δ_m and λ as a function of the blade angle α for φ=40º and δ=27º.

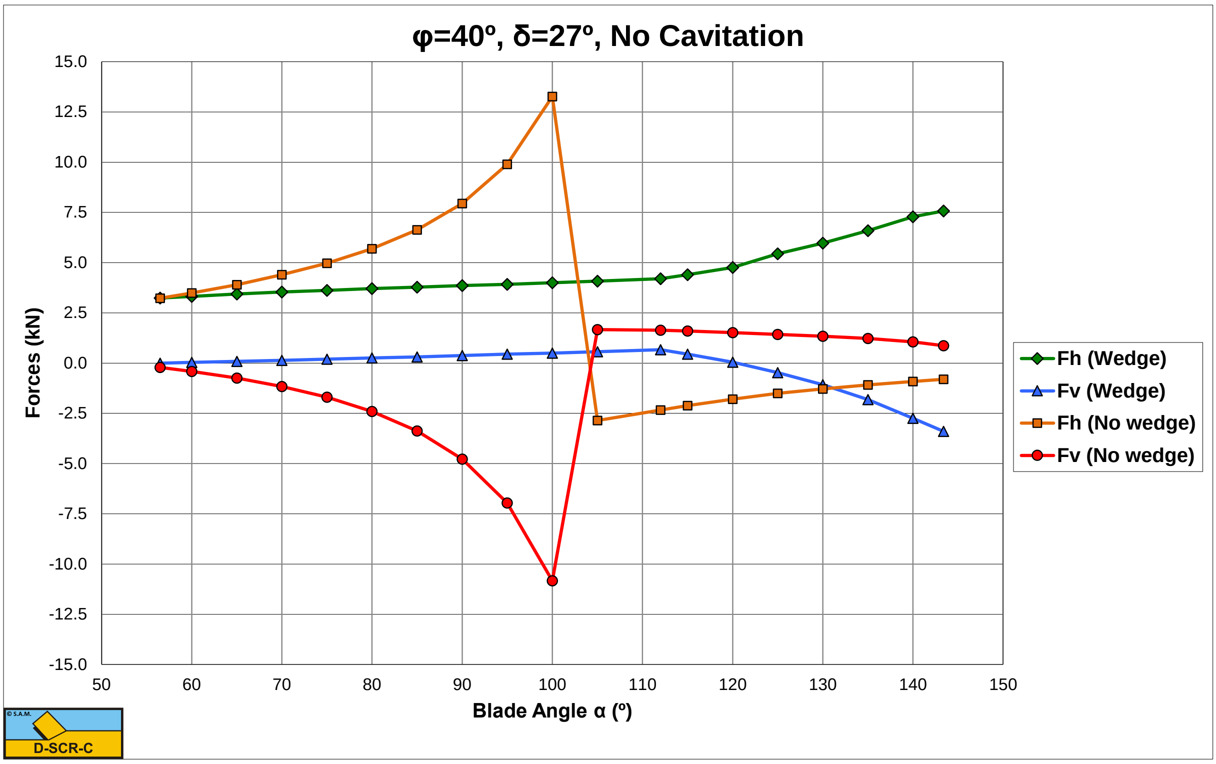

Figure P-6: No cavitation, the cutting forces as a function of the blade angle α for φ=40º and δ=27º.

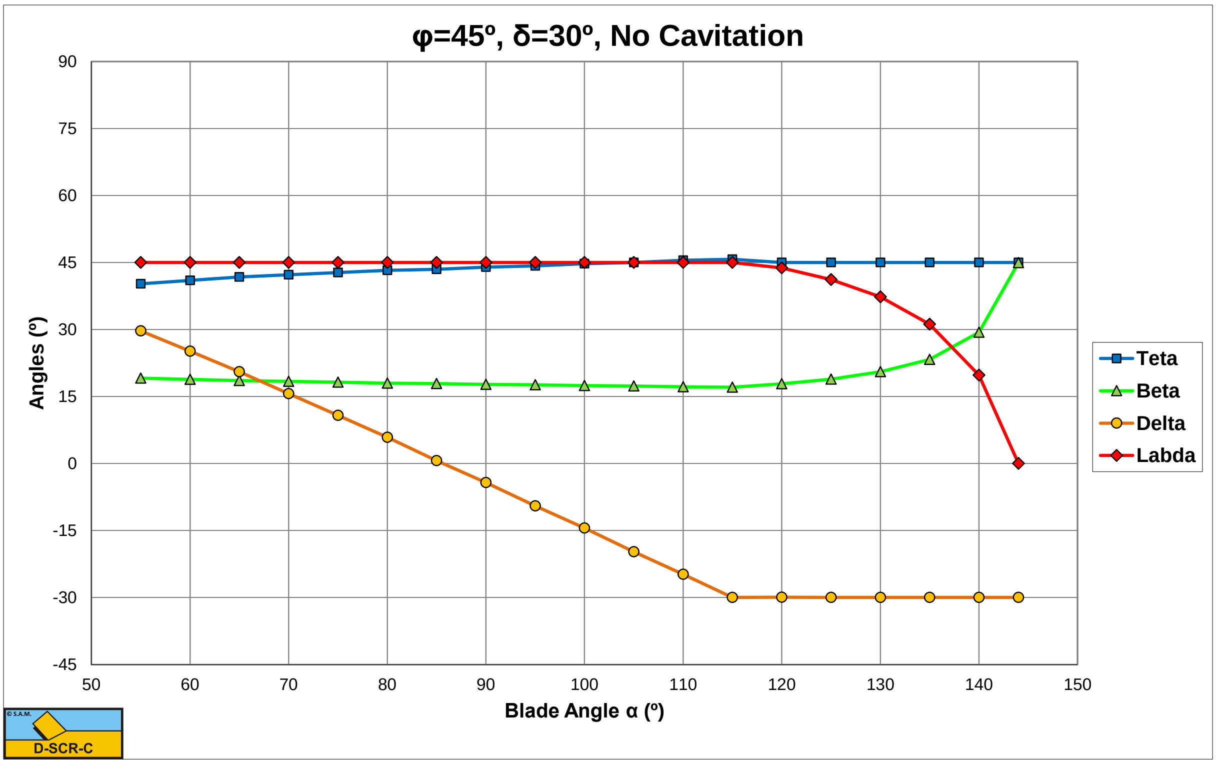

Figure P-7: No cavitation, the angles θ, β, δ_m and λ as a function of the blade angle α for φ=45º and δ=30º.

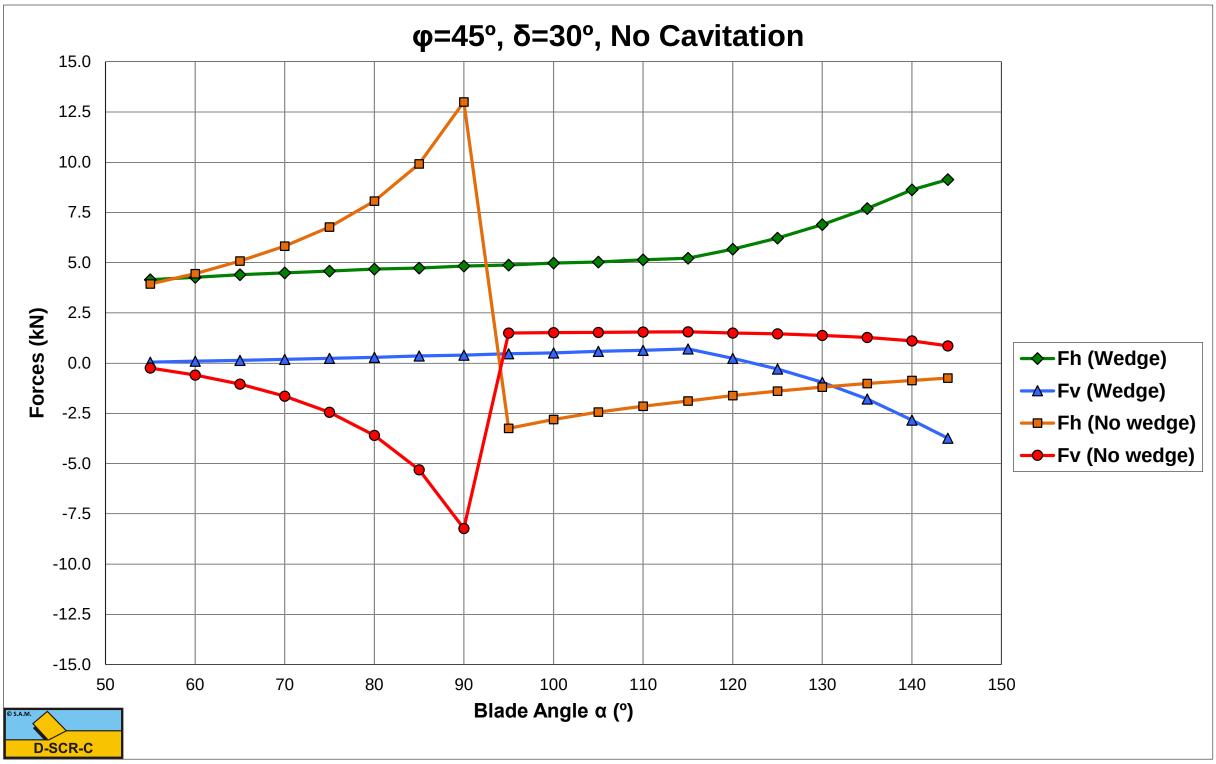

Figure P-8: No cavitation, the cutting forces as a function of the blade angle α for φ=45º and δ=30º.

Appendix Q: Occurrence of a Wedge, Cavitating.

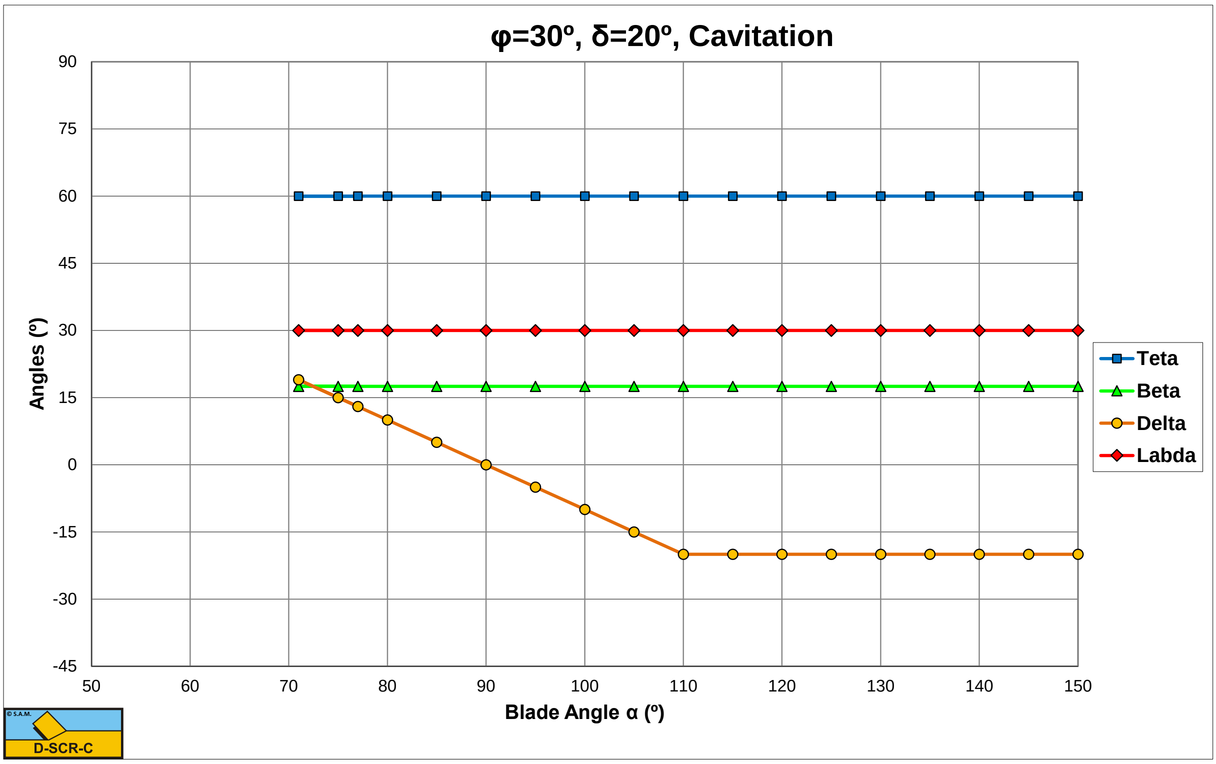

Figure Q-1: Cavitating, the angles θ, β, δ_m and λ as a function of the blade angle α for φ=30º and δ=20º.

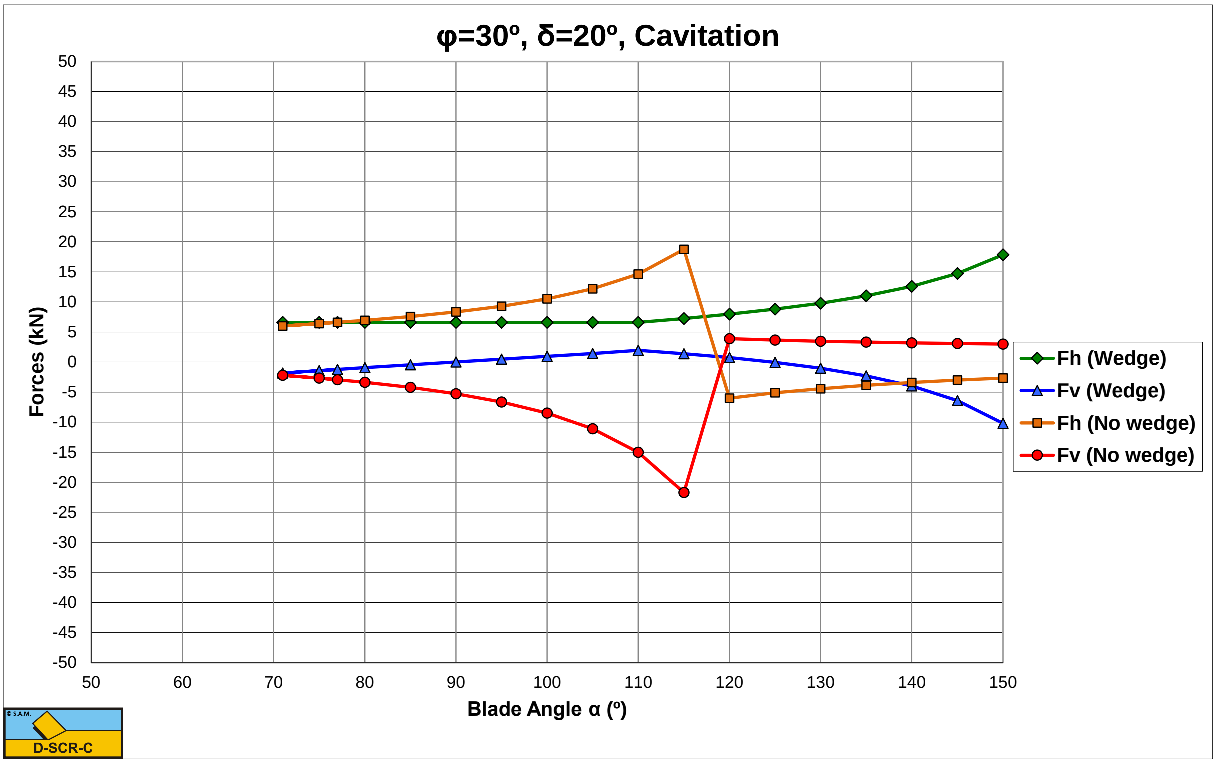

Figure Q-2: Cavitating, the cutting forces as a function of the blade angle α for φ=30º and δ=20º.

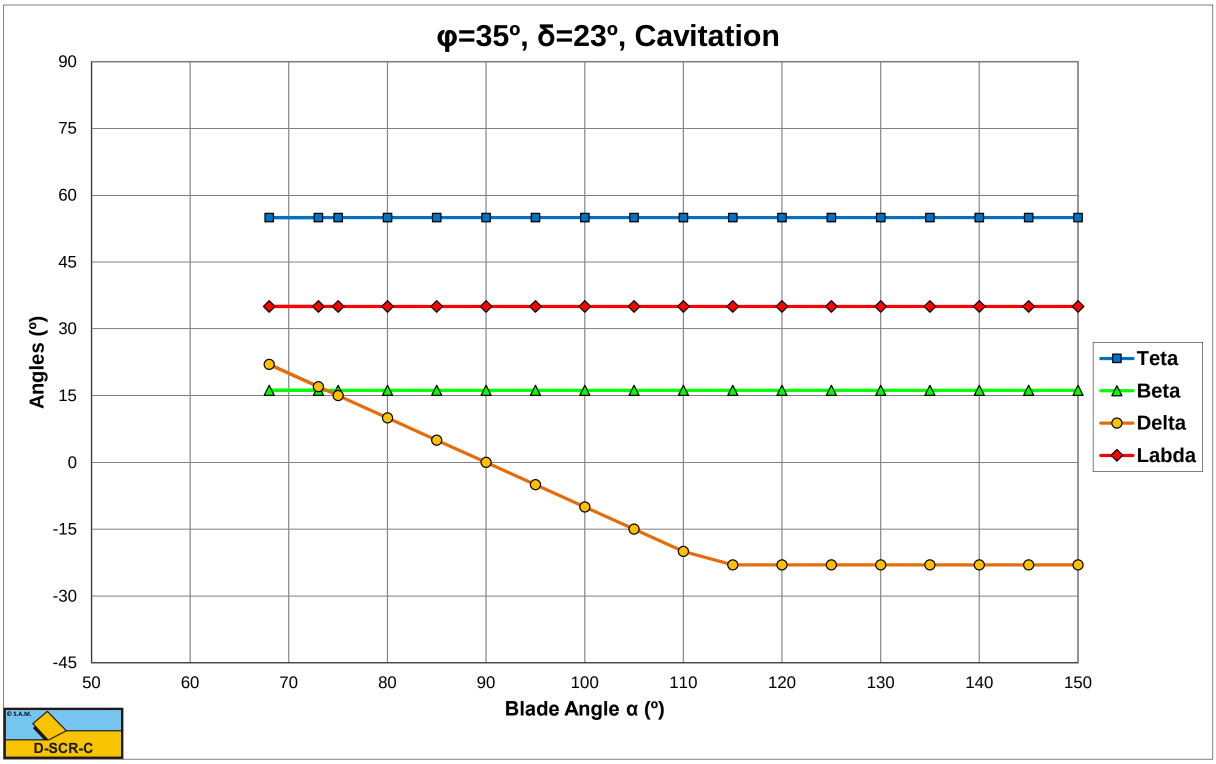

Figure Q-3: Cavitating, the angles θ, β, δ_m and λ as a function of the blade angle α for φ=35º and δ=23º.

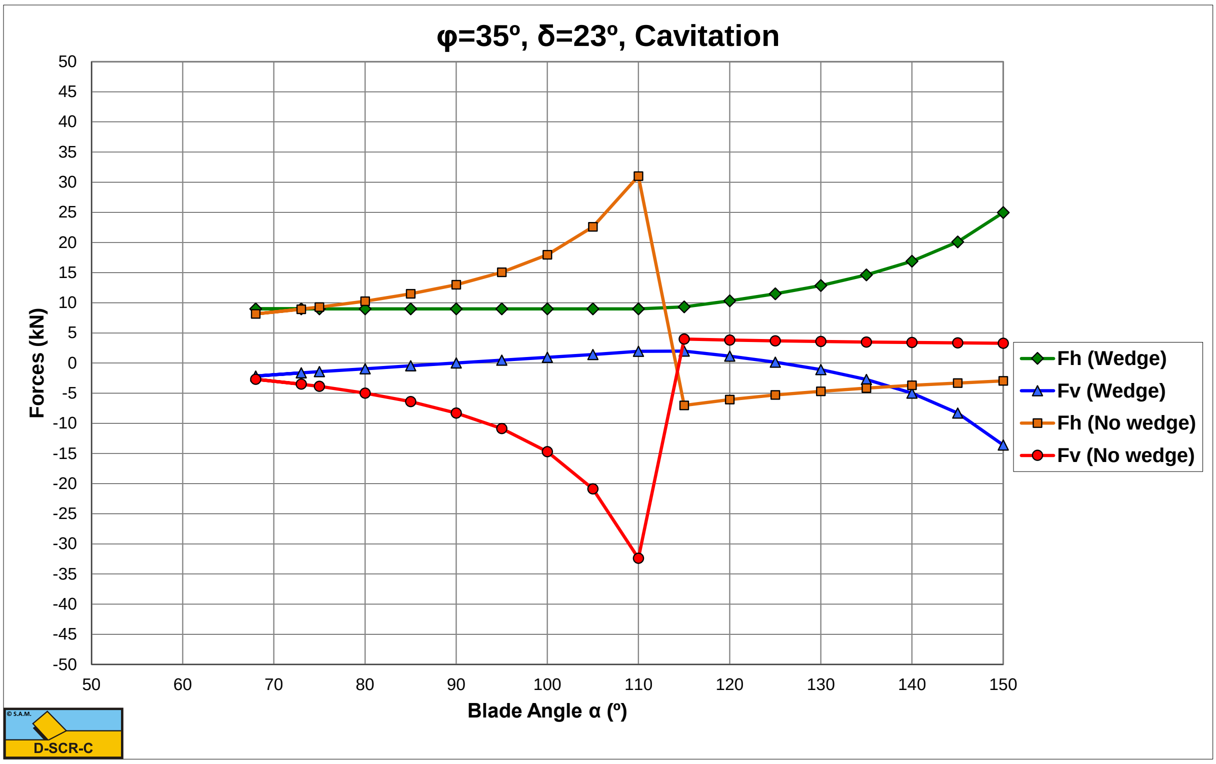

Figure Q-4: Cavitating, the cutting forces as a function of the blade angle α for φ=35º and δ=23º.

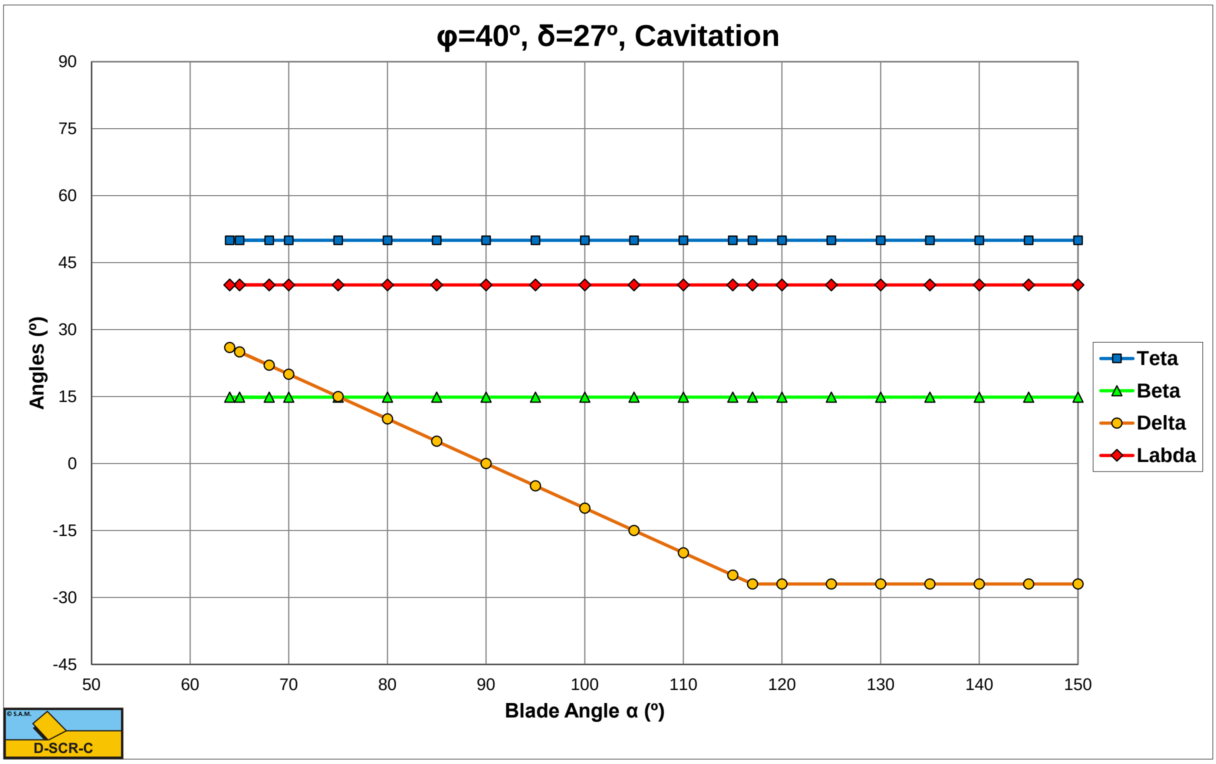

Figure Q-5: Cavitating, the angles θ, β, δm and λ as a function of the blade angle α for φ=40º and δ=27º.

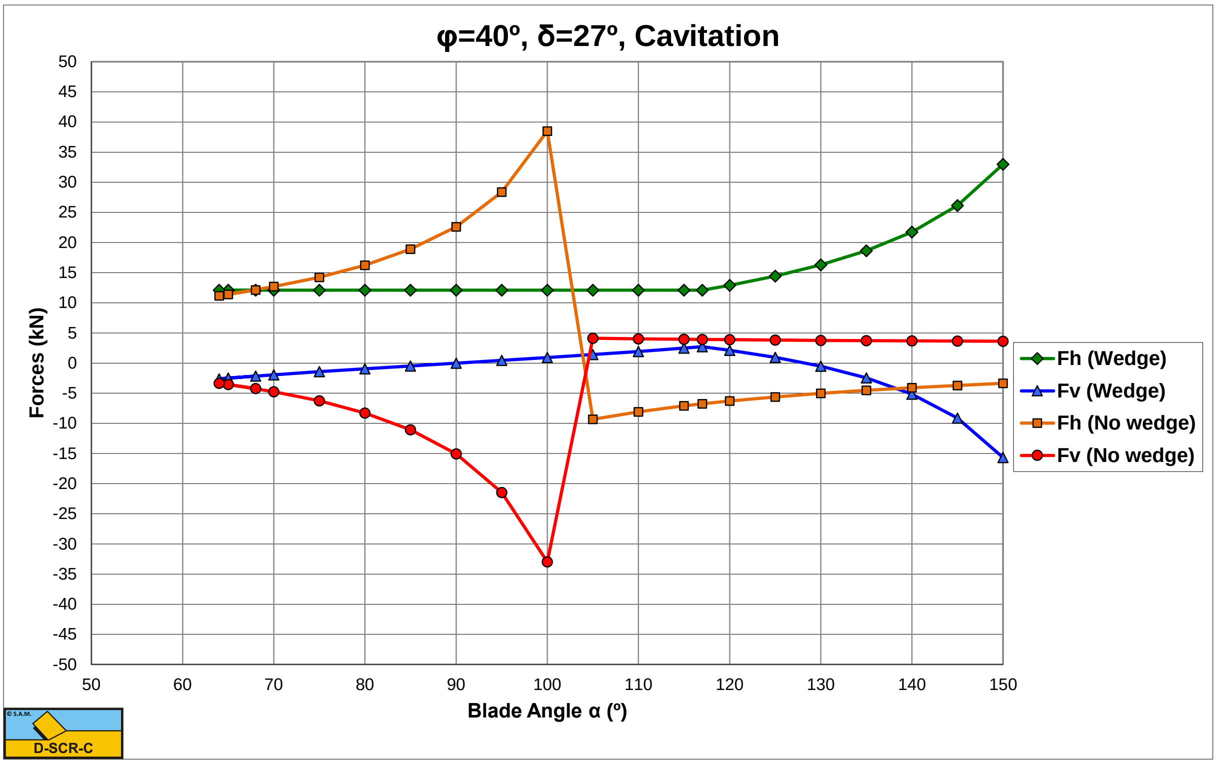

Figure Q-6: Cavitating, the cutting forces as a function of the blade angle α for φ=40º and δ=27º.

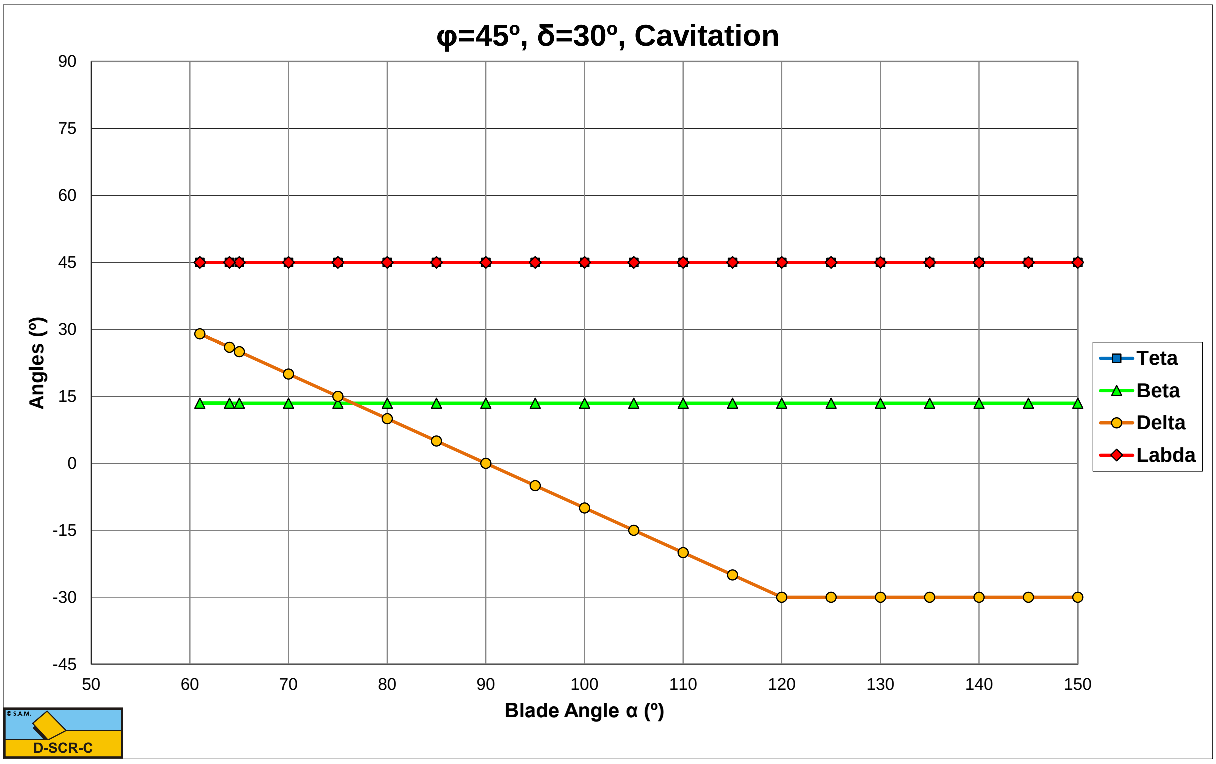

Figure Q-7: Cavitating, the angles θ, β, δ_m and λ as a function of the blade angle α for φ=45º and δ=30º.

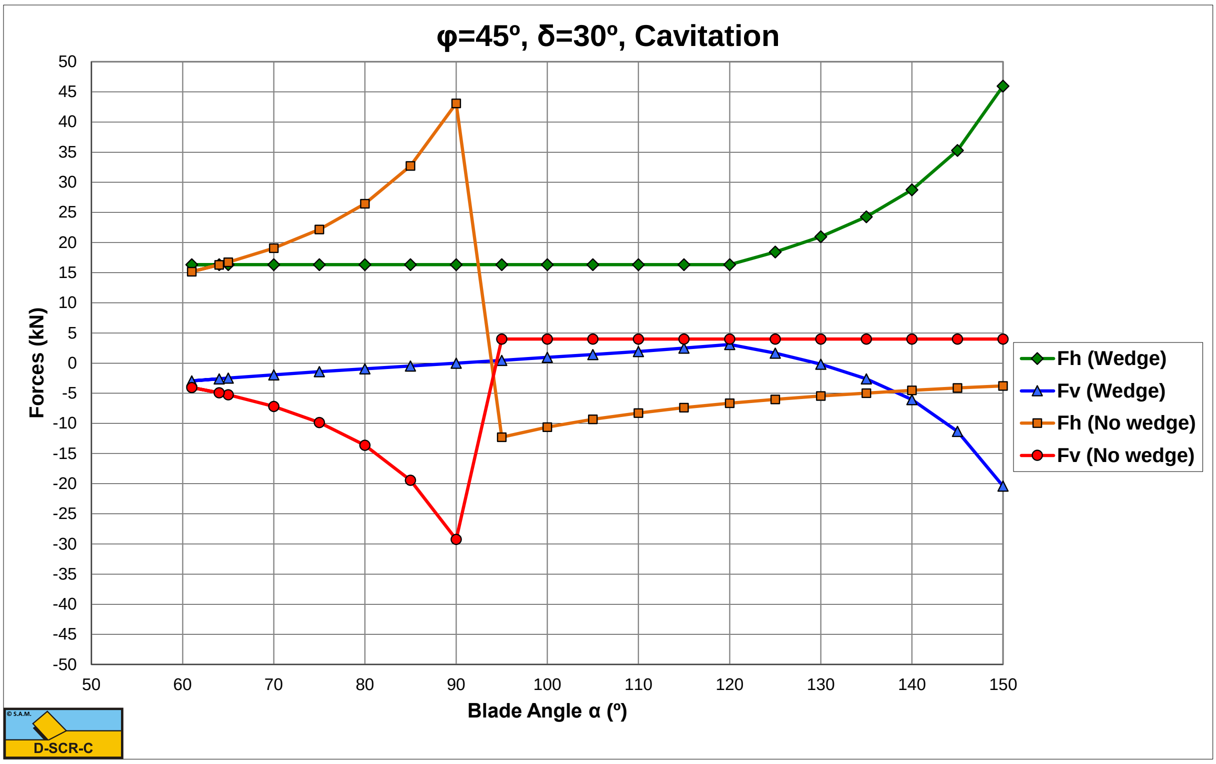

Figure Q-8: Cavitating, the cutting forces as a function of the blade angle α for φ=45º and δ=30º.

Appendix R: Pore Pressures with Wedge.

Table R-1: The average water pore pressure and total pressure along the four sides.

$\theta=30^0$	β		p_{1m}	p_{2m}	p_{3m}	p_{4m}
	15^0		0.2489	0.0727	0.1132	0.0313
	20^0		0.2675	0.0713	0.1133	0.0290
	25^0		0.2852	0.0702	0.1139	0.0268
	30^0		0.3014	0.0695	0.1149	0.0249
$\theta=40^0$	β		p_{1m}	p_{2m}	p_{3m}	p_{4m}
	15^0		0.2798	0.1040	0.1728	0.0688
	20^0		0.2980	0.1047	0.1788	0.0672
	25^0		0.3145	0.1036	0.1827	0.0640
	30^0		0.3291	0.1022	0.1859	0.0607
$\theta=50^0$	β		p_{1m}	p_{2m}	p_{3m}	p_{4m}
	15^0		0.3043	0.1338	0.2357	0.1141
	20^0		0.3240	0.1377	0.2523	0.1158
	25^0		0.3404	0.1373	0.2635	0.1134
	30^0		0.3544	0.1353	0.2722	0.1096
$\theta=55^0$	β		p_{1m}	p_{2m}	p_{3m}	p_{4m}
	15^0		0.3152	0.1492	0.2720	0.1392
	20^0		0.3367	0.1549	0.2967	0.1435
	25^0		0.3540	0.1549	0.3143	0.1422
	30^0		0.3684	0.1526	0.3284	0.1388
$\theta=59^0$	β		p_{1m}	p_{2m}	p_{3m}	p_{4m}
	15^0		0.3242	0.1626	0.3089	0.1607
	20^0		0.3481	0.1699	0.3436	0.1676
	25^0		0.3675	0.1705	0.3707	0.1679
	30^0		0.3838	0.1683	0.3922	0.1654

For $\alpha=60^0$; $h_i=1$; $h_b=3$; $k_i/k_{max}=0.25$.

Table R-2: The average water pore pressure and total pressure along the four sides.

$\theta=30^0$	β	p_{1m}	p_{2m}	p_{3m}	p_{4m}
	15^0	0.2499	0.0773	0.1071	0.0339
	20^0	0.2679	0.0735	0.1048	0.0292
	25^0	0.2854	0.0715	0.1041	0.0261
	30^0	0.3015	0.0704	0.1043	0.0240
$\theta=40^0$	β	p_{1m}	p_{2m}	p_{3m}	p_{4m}
	15^0	0.2825	0.1127	0.1622	0.0712
	20^0	0.2992	0.1088	0.1625	0.0651
	25^0	0.3152	0.1060	0.1634	0.0603
	30^0	0.3297	0.1039	0.1646	0.0564
$\theta=50^0$	β	p_{1m}	p_{2m}	p_{3m}	p_{4m}
	15^0	0.3088	0.1438	0.2160	0.1129
	20^0	0.3259	0.1422	0.2230	0.1086
	25^0	0.3414	0.1399	0.2283	0.1038
	30^0	0.3549	0.1373	0.2325	0.0992
$\theta=55^0$	β	p_{1m}	p_{2m}	p_{3m}	p_{4m}
	15^0	0.3175	0.1496	0.1994	0.1104
	20^0	0.3382	0.1556	0.2103	0.1128
	25^0	0.3547	0.1563	0.2156	0.1110
	30^0	0.3682	0.1548	0.2184	0.1076
$\theta=60^0$	β	p_{1m}	p_{2m}	p_{3m}	p_{4m}
	15^0	0.3300	0.1719	0.2720	0.1562
	20^0	0.3498	0.1745	0.2907	0.1567
	25^0	0..3664	0.1736	0.3043	0.1540
	30^0	0.3803	0.1710	0.3150	0.1497
$\theta=69^0$	B	p_{1m}	p_{2m}	p_{3m}	p_{4m}
	15^0	0.3474	0.1984	0.3369	0.1970
	20^0	0.3737	0.2066	0.3760	0.2050
	25^0	0.3953	0.2081	0.4060	0.2063
	30^0	0.4134	0.2062	0.4306	0.2041

For $\alpha=70^0$; $h_i=1$; $h_b=3$; $k_i/k_{max}=0.25$.

Table R-3: The average water pore pressure and total pressure along the four sides.

$\theta=30^0$	β	p_{1m}	p_{2m}	p_{3m}	p_{4m}
	15^0	0.2493	0.0738	0.0973	0.0279
	20^0	0.2679	0.0723	0.0966	0.0260
	25^0	0.2856	0.0712	0.0962	0.0242
	30^0	0.3018	0.0705	0.0964	0.0226
$\theta=40^0$	β	p_{1m}	p_{2m}	p_{3m}	p_{4m}
	15^0	0.2810	0.1058	0.1450	0.0595
	20^0	0.2992	0.1065	0.1481	0.0581
	25^0	0.3156	0.1055	0.1493	0.0555
	30^0	0.3302	0.1042	0.1501	0.0527
$\theta=50^0$	β	p_{1m}	p_{2m}	p_{3m}	p_{4m}
	15^0	0.3062	0.1352	0.1917	0.0967
	20^0	0.3257	0.1393	0.2010	0.0978
	25^0	0.3420	0.1393	0.2057	0.0954
	30^0	0.3557	0.1378	0.2085	0.0919
$\theta=55^0$	β	p_{1m}	p_{2m}	p_{3m}	p_{4m}
	15^0	0.3170	0.1495	0.2153	0.1167
	20^0	0.3378	0.1554	0.2284	0.1195
	25^0	0.3542	0.1560	0.2355	0.1176
	30^0	0.3678	0.1544	0.2400	0.1140
$\theta=60^0$	β	p_{1m}	p_{2m}	p_{3m}	p_{4m}
	15^0	0.3271	0.1639	0.2398	0.1375
	20^0	0.3493	0.1716	0.2572	0.1422
	25^0	0.3663	0.1728	0.2672	0.1411
	30^0	0.3799	0.1712	0.2739	0.1375
$\theta=70^0$	β	p_{1m}	p_{2m}	p_{3m}	p_{4m}
	15^0	0.3465	0.1944	0.2946	0.1820
	20^0	0.3727	0.2057	0.3231	0.1914
	25^0	0.3922	0.2082	0.3419	0.1923
	30^0	0.4070	0.2062	0.3549	0.1890

For $\alpha=80^0$; $h_i=1$; $h_b=3$; $k_i/k_{max}=0.25$.

Table R-4: The average water pore pressure and total pressure along the four sides.

$\theta=30^0$	β	p_{1m}	p_{2m}	p_{3m}	p_{4m}
	15^0	0.2494	0.0740	0.0917	0.0270
	20^0	0.2680	0.0726	0.0908	0.0252
	25^0	0.2857	0.0715	0.0902	0.0235
	30^0	0.3018	0.0708	0.0901	0.0220
$\theta=40^0$	β	p_{1m}	p_{2m}	p_{3m}	p_{4m}
	15^0	0.2813	0.1062	0.1358	0.0569
	20^0	0.2995	0.1070	0.1381	0.0556
	25^0	0.3159	0.1060	0.1387	0.0530
	30^0	0.3305	0.1047	0.1389	0.0504
$\theta=50^0$	β	p_{1m}	p_{2m}	p_{3m}	p_{4m}
	15^0	0.3067	0.1355	0.1782	0.0917
	20^0	0.3262	0.1397	0.1860	0.0926
	25^0	0.3424	0.1397	0.1893	0.0904
	30^0	0.3561	0.1383	0.1910	0.0871
$\theta=55^0$	β	p_{1m}	p_{2m}	p_{3m}	p_{4m}
	15^0	0.3175	0.1496	0.1994	0.1104
	20^0	0.3382	0.1556	0.2103	0.1128
	25^0	0.3547	0.1563	0.2156	0.1110
	30^0	0.3682	0.1548	0.2184	0.1076
$\theta=60^0$	β	p_{1m}	p_{2m}	p_{3m}	p_{4m}
	15^0	0.3276	0.1637	0.2209	0.1296
	20^0	0.3497	0.1713	0.2353	0.1338
	25^0	0.3666	0.1727	0.2428	0.1327
	30^0	0.3800	0.1713	0.2471	0.1292
$\theta=70^0$	β	p_{1m}	p_{2m}	p_{3m}	p_{4m}
	15^0	0.3464	0.1927	0.2670	0.1706
	20^0	0.3719	0.2038	0.2894	0.1780
	25^0	0.3907	0.2065	0.3027	0.1793
	30^0	0.4047	0.2049	0.3110	0.1759
$\theta=80^0$	β	p_{1m}	p_{2m}	p_{3m}	p_{4m}
	15^0	0.3658	0.2253	0.3216	0.2157
	20^0	0.3965	0.2400	0.3556	0.2289
	25^0	0.4185	0.2435	0.3776	0.2311
	30^0	0.4347	0.2411	0.3930	0.2277

For $\theta=90^0$; $h_i=1$; $h_b=3$; $k_i/k_{max}=0.25$.

Table R-5: Acting points for $\alpha=90^0$; $h_i=1$; $h_b=3$; $k_i/k_{max}=0.25$.

θ	β	E_2	E_3	E_4
60^0	15^0	0.36	0.56	0.40
60^0	20^0	0.36	0.56	0.40
60^0	25^0	0.35	0.56	0.39
60^0	30^0	0.34	0.57	0.39
55^0	15^0	0.35	0.56	0.40
55^0	20^0	0.34	0.56	0.40
55^0	25^0	0.33	0.57	0.39
55^0	30^0	0.33	0.57	0.39
50^0	15^0	0.34	0.58	0.40
50^0	20^0	0.34	0.58	0.40
50^0	25^0	0.33	0.59	0.40
50^0	30^0	0.33	0.59	0.40
40^0	15^0	0.32	0.61	0.40
40^0	20^0	0.31	0.62	0.40
40^0	25^0	0.30	0.62	0.40
40^0	30^0	0.29	0.63	0.39

Table R-6: Acting points for $\alpha=80^0$; $h_i=1$; $h_b=3$; $k_i/k_{max}=0.25$.

θ	β	E_2	E_3	E_4
60^0	15^0	0.36	0.54	0.39
60^0	20^0	0.35	0.54	0.39
60^0	25^0	0.35	0.55	0.38
60^0	30^0	0.34	0.56	0.37
55^0	15^0	0.35	0.55	0.40
55^0	20^0	0.34	0.55	0.39
55^0	25^0	0.33	0.56	0.39
55^0	30^0	0.33	0.57	0.38
50^0	15^0	0.35	0.57	0.40
50^0	20^0	0.34	0.57	0.40
50^0	25^0	0.33	0.58	0.39
50^0	30^0	0.32	0.58	0.39

Table R-7: Acting points for $\alpha=70^0$; $h_i=1$; $h_b=3$; $k_i/k_{max}=0.25$.

θ	β	E_2	E_3	E_4
60^0	15^0	0.36	0.53	0.36
60^0	20^0	0.35	0.53	0.35
60^0	25^0	0.34	0.54	0.34
60^0	30^0	0.34	0.54	0.34
55^0	15^0	0.35	0.54	0.37
55^0	20^0	0.34	0.54	0.37
55^0	25^0	0.33	0.54	0.36
55^0	30^0	0.33	0.54	0.35
50^0	15^0	0.34	0.55	0.38
50^0	20^0	0.33	0.55	0.38
50^0	25^0	0.32	0.56	0.37
50^0	30^0	0.31	0.56	0.36

Table R-8: Acting points for $\alpha=60^0$; $h_i=1$; $h_b=3$; $k_i/k_{max}=0.25$.

θ	β	E_2	E_3	E_4
55^0	15^0	0.34	0.52	0.34
55^0	20^0	0.32	0.52	0.33
55^0	25^0	0.31	0.52	0.32
55^0	30^0	0.30	0.52	0.31
50^0	15^0	0.33	0.54	0.35
50^0	20^0	0.32	0.54	0.34
50^0	25^0	0.31	0.54	0.34
50^0	30^0	0.31	0.54	0.33

Appendix S: FEM Calculations with Wedge.

S.1 The Boundaries of the FEM Model.

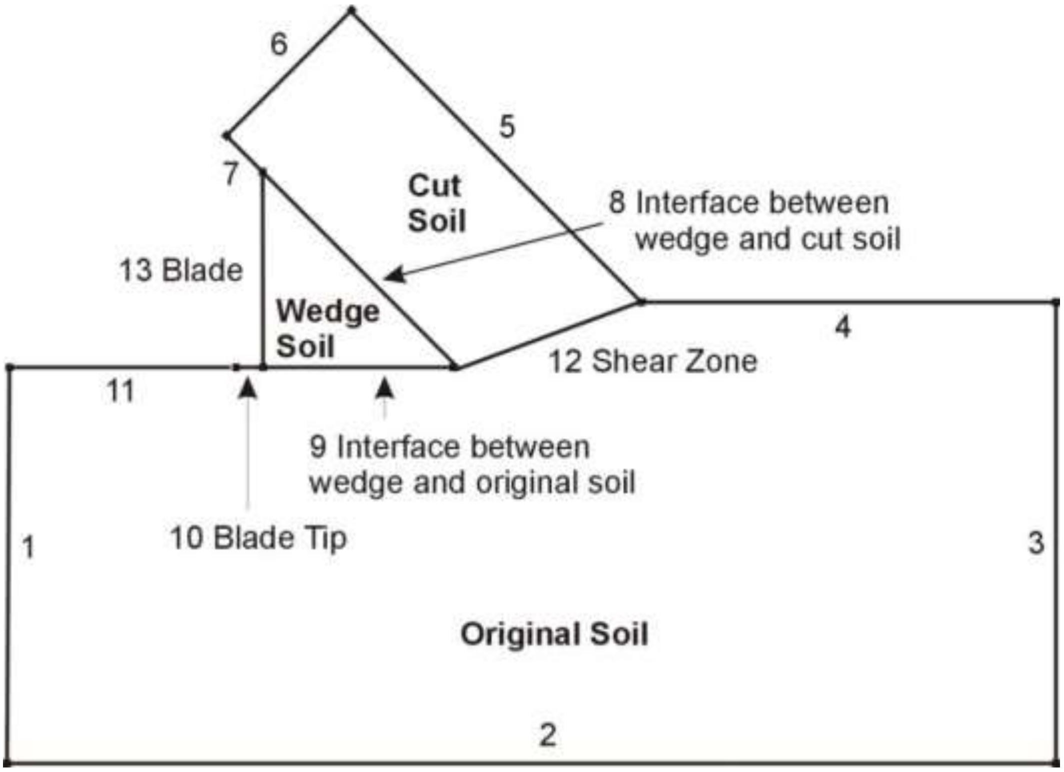

Figure S-1: The boundaries of the FEM model.

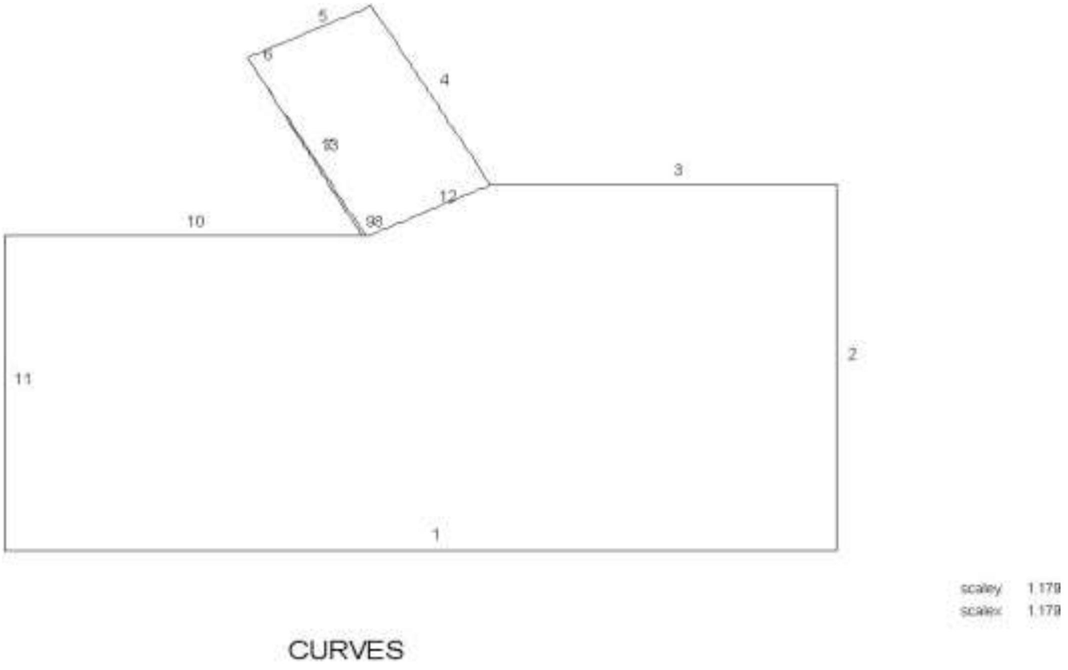

Figure S-2: The boundaries of the 60/59 degree calculations.

S.2 The 60 Degree Blade.

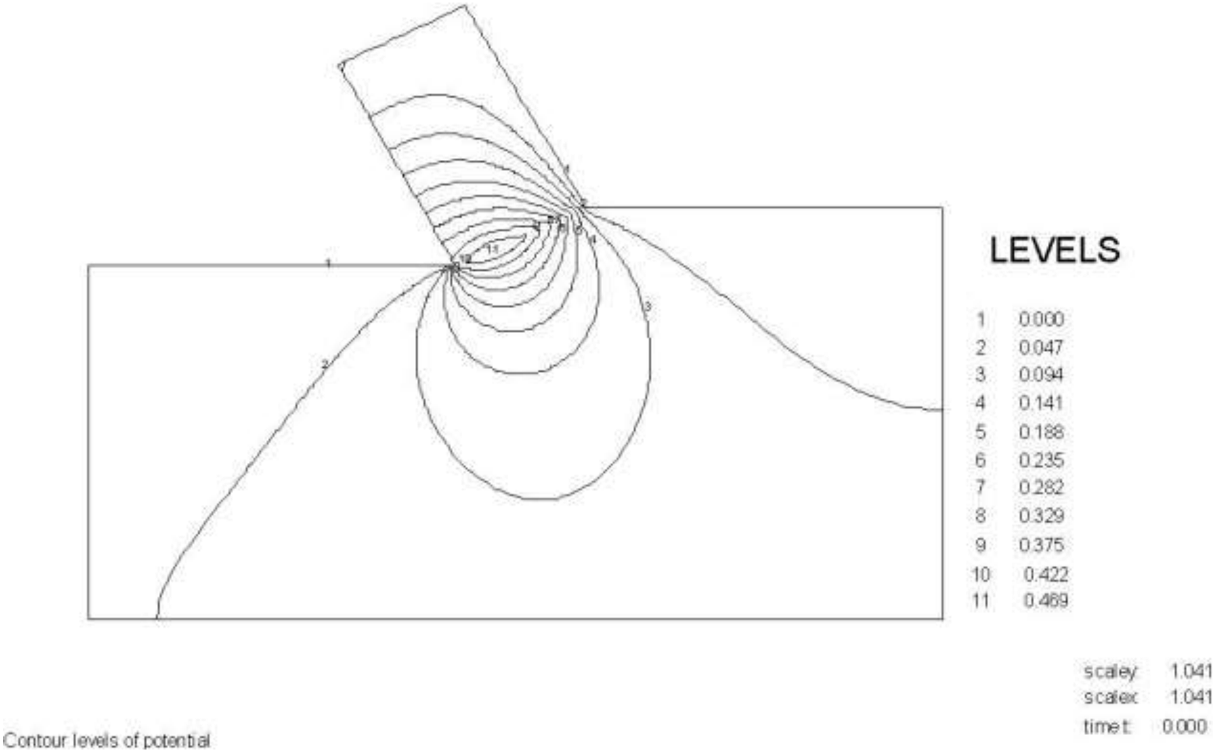

Figure S-3: The equipotential lines.

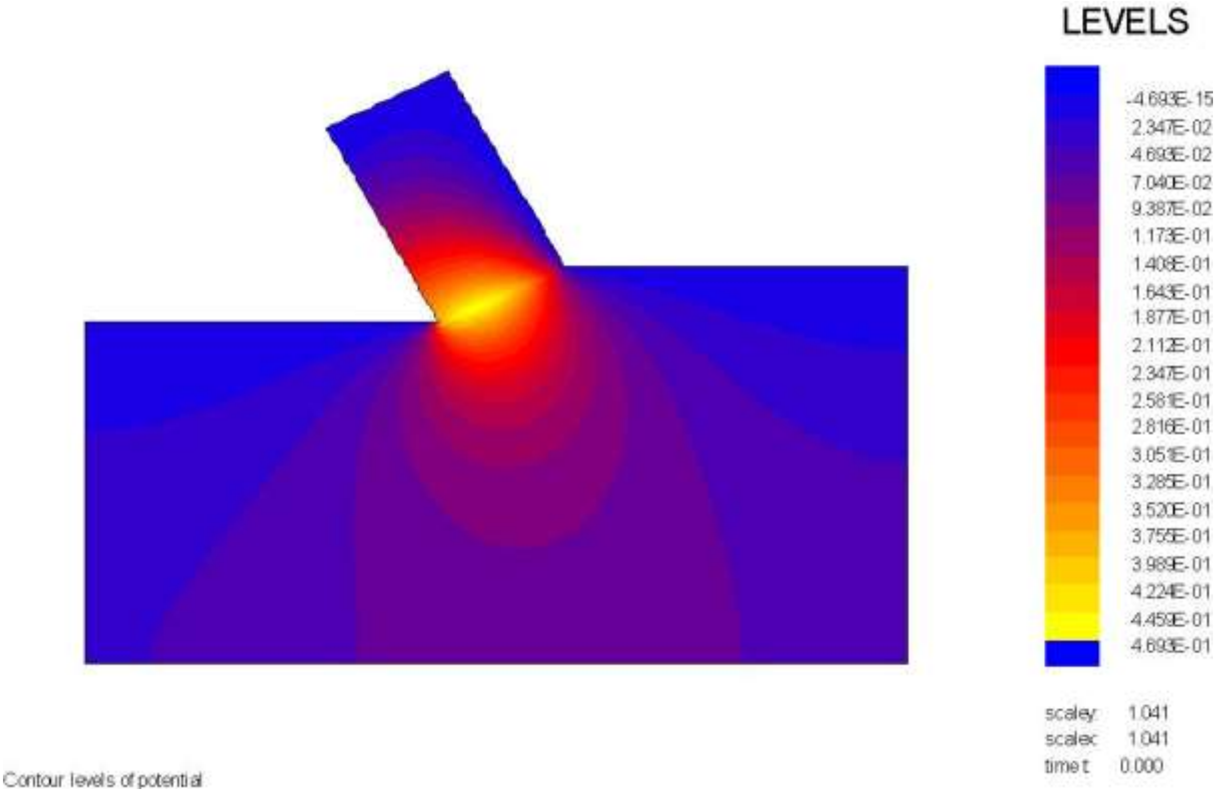

Figure S-4: The equipotential lines in color.

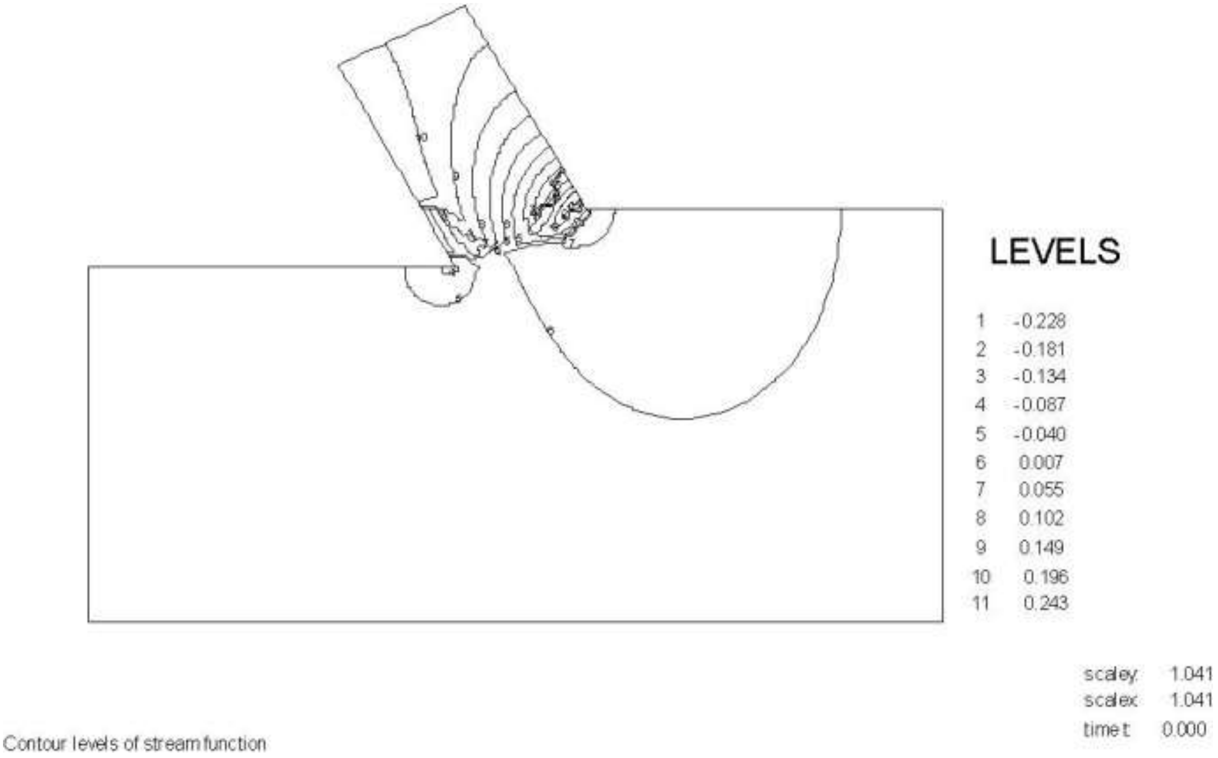

Figure S-5: The flow lines or stream function.

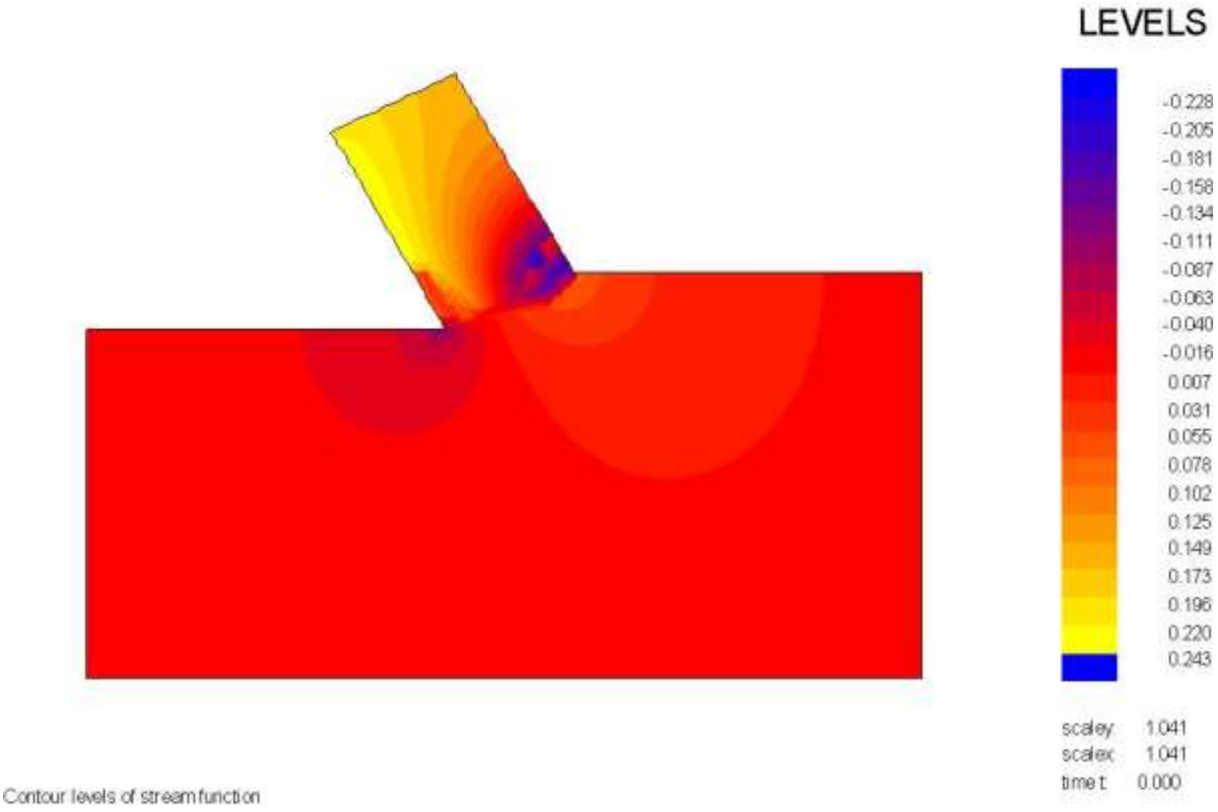

Figure S-6: The stream function in colors.

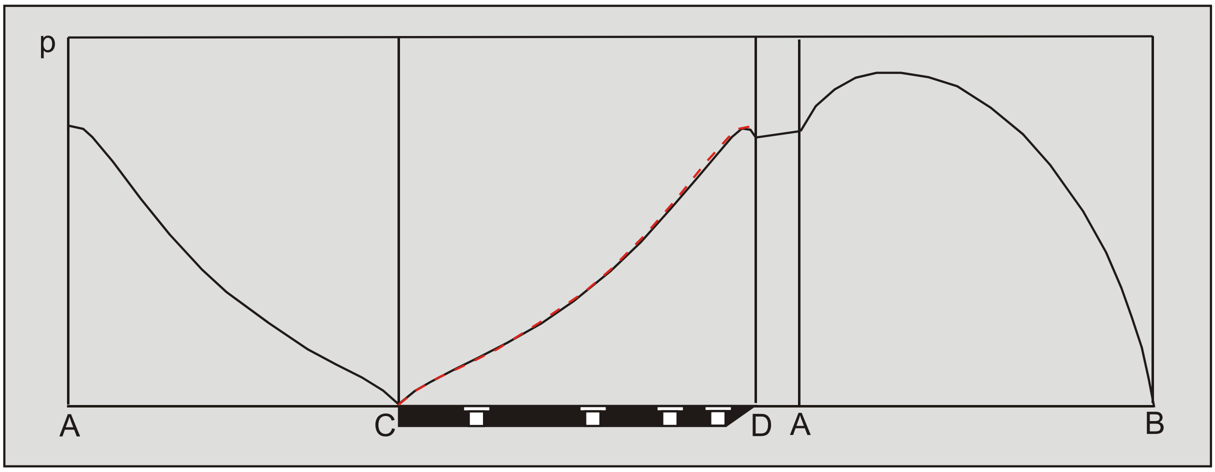

Figure S-7: The pore pressures in the shear zone A-B, at the bottom of the wedge A-D, on the front of the wedge C-A and on the blade C-D

The wedge angle in these calculations is 59 degrees. The pore pressures on the blade C-D are almost equal to the pore pressures on the front of the wedge A-C, which they should be with a blade angle of 60 degrees and a wedge angle of 59 degrees. The pore pressures on the front of the wedge C-A are drawn in red on top of the pore pressures on the blade C-A and match almost exactly.

S.3 The 75 Degree Blade.

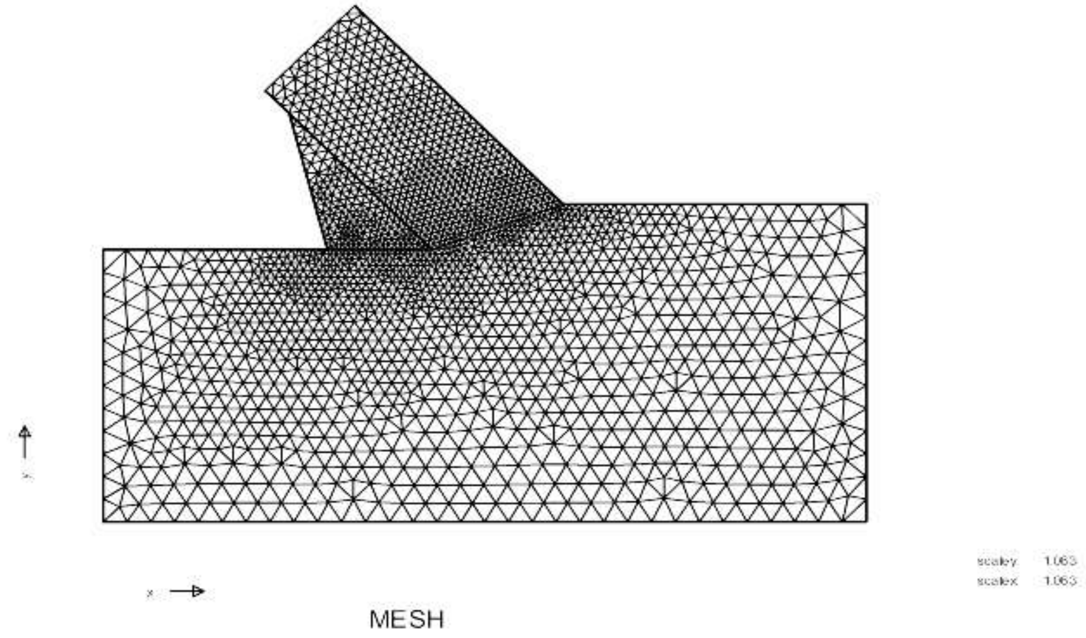

Figure S-8: The coarse mesh.

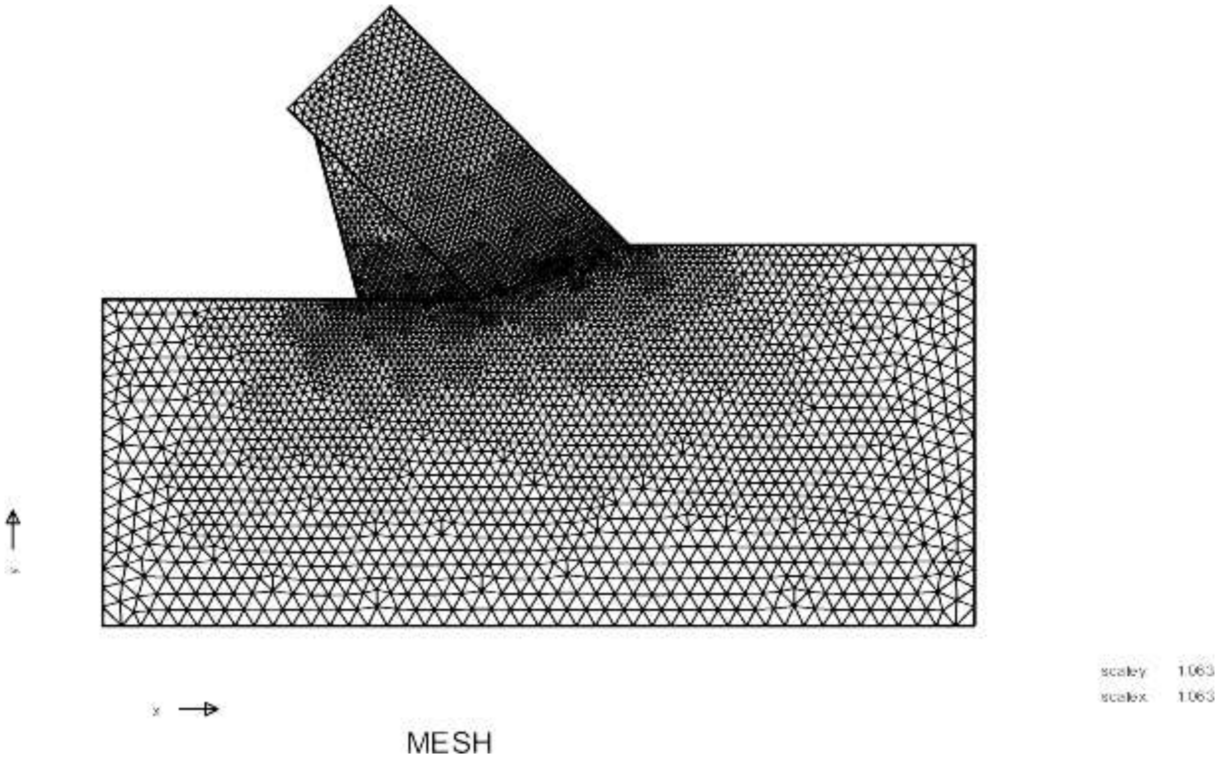

Figure S-9: The fine mesh.

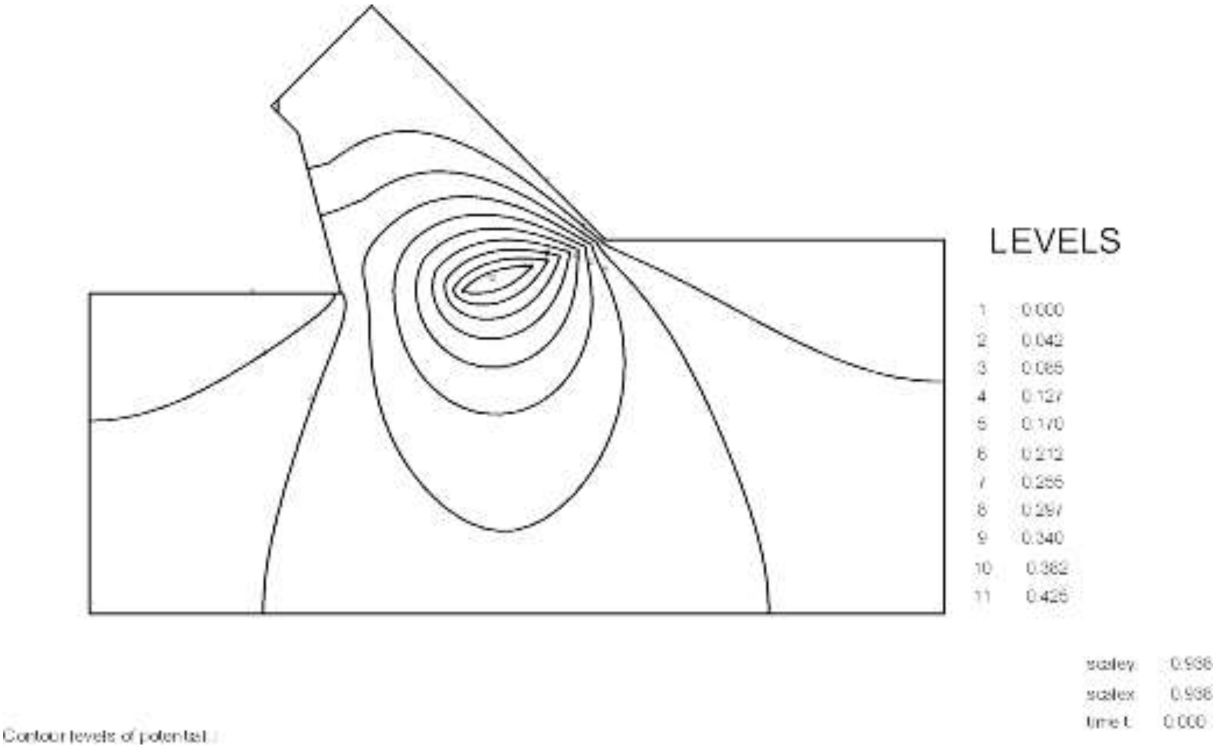

Figure S-10: The equipotential lines.

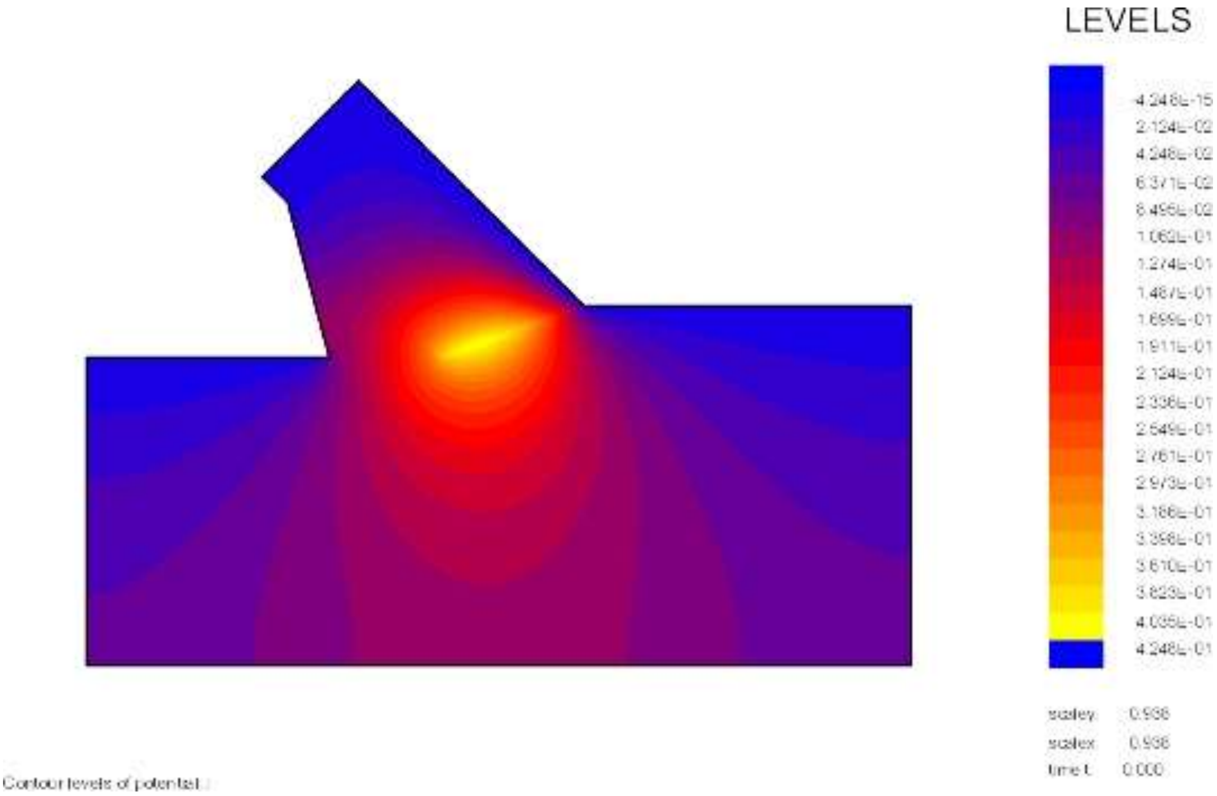

Figure S-11: The equipotential lines in color.

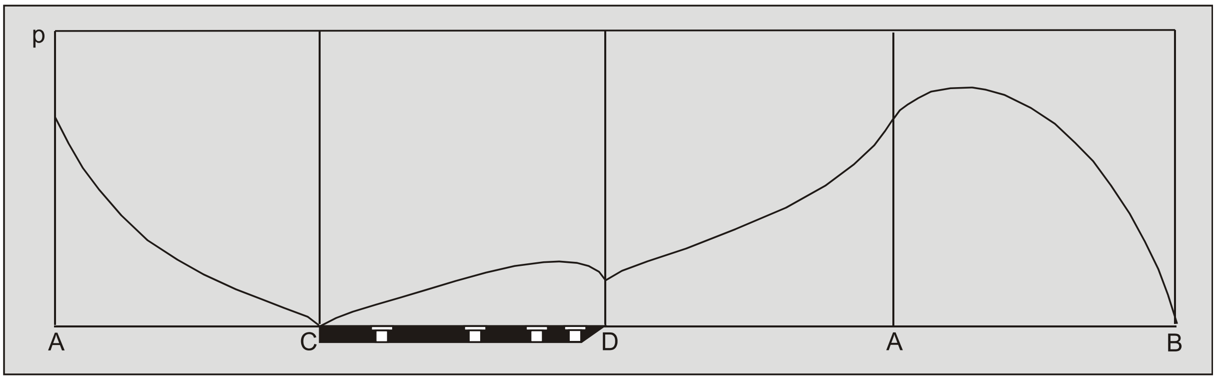

Figure S-12: Pore pressure distribution on the shear plane A-B, the bottom of the wedge A-D, the blade D-C and the front of the wedge A-C.

S.4 The 90 Degree Blade.

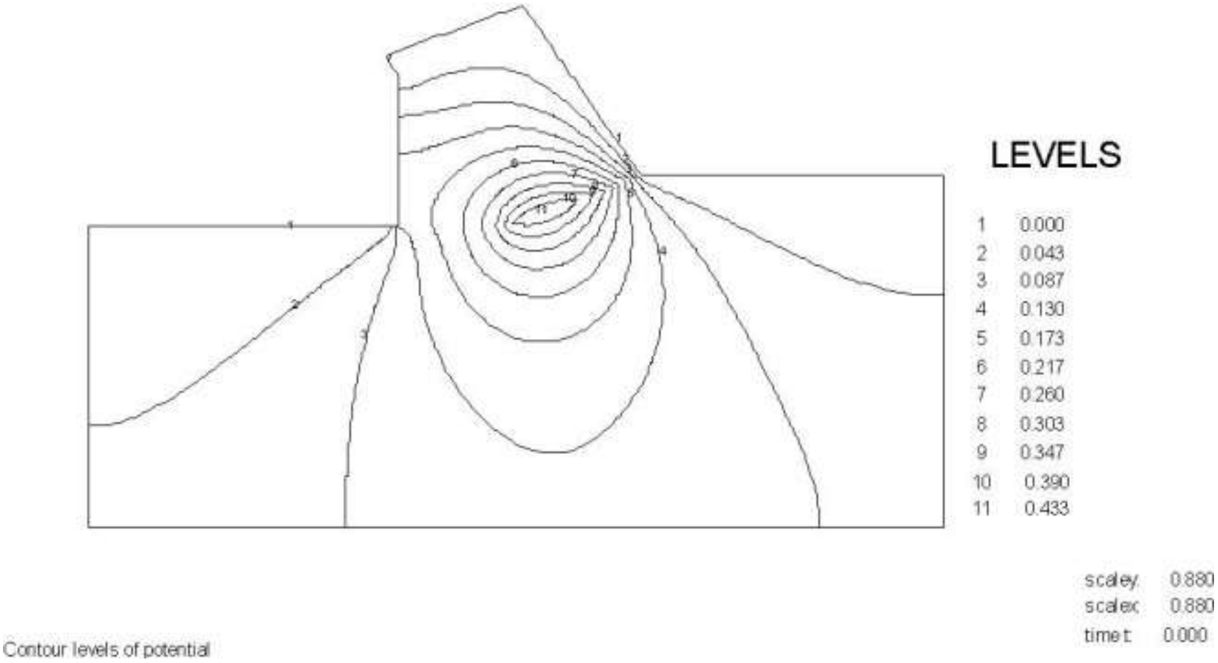

Figure S-13: Equipotential lines of pore pressures.

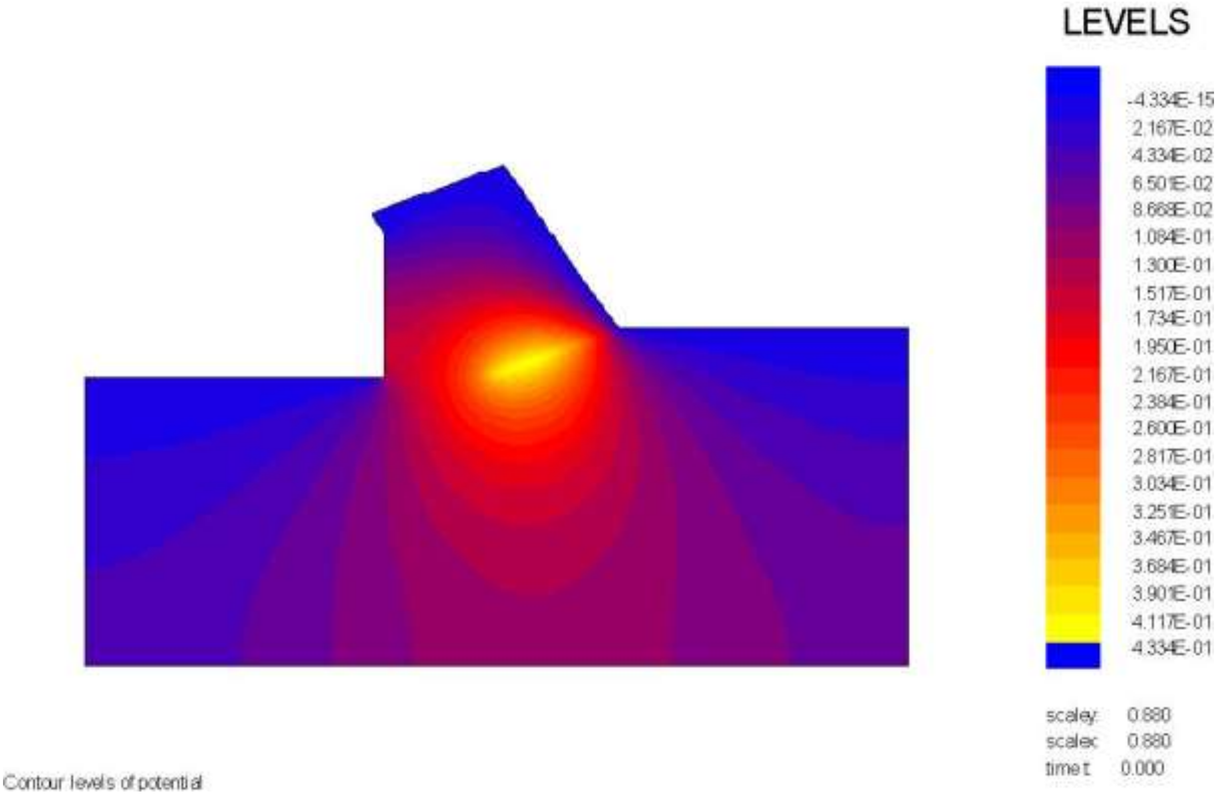

Figure S-14: Equipotential distribution in color.

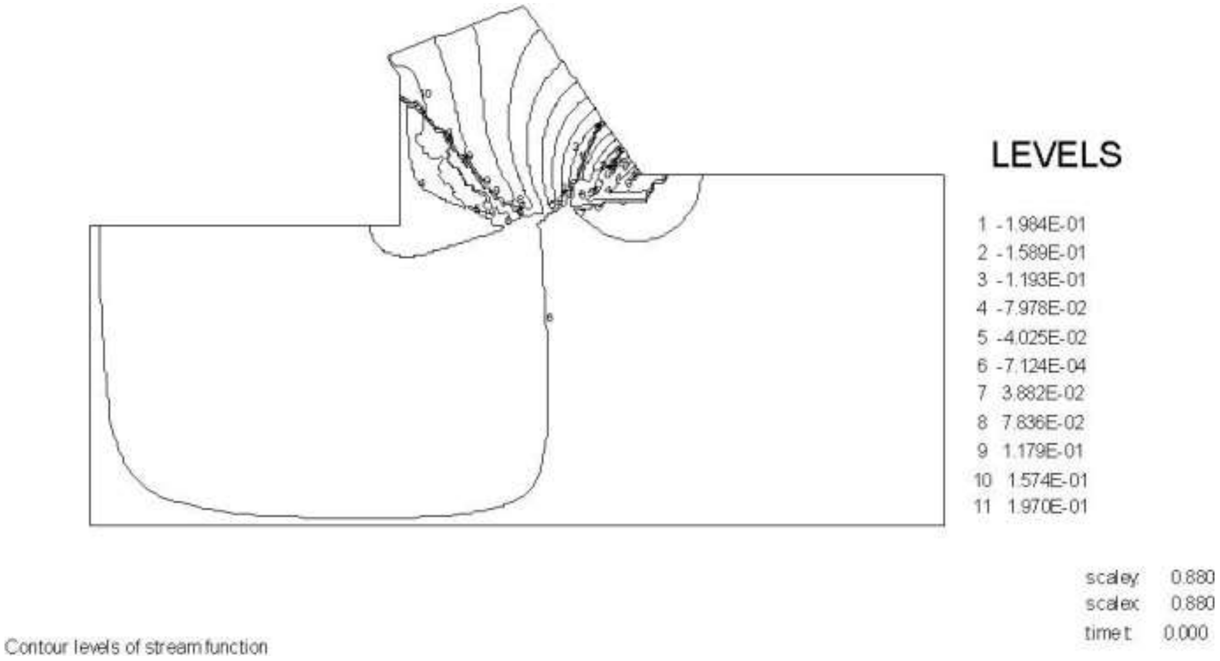

Figure S-15: The flow lines or stream function.

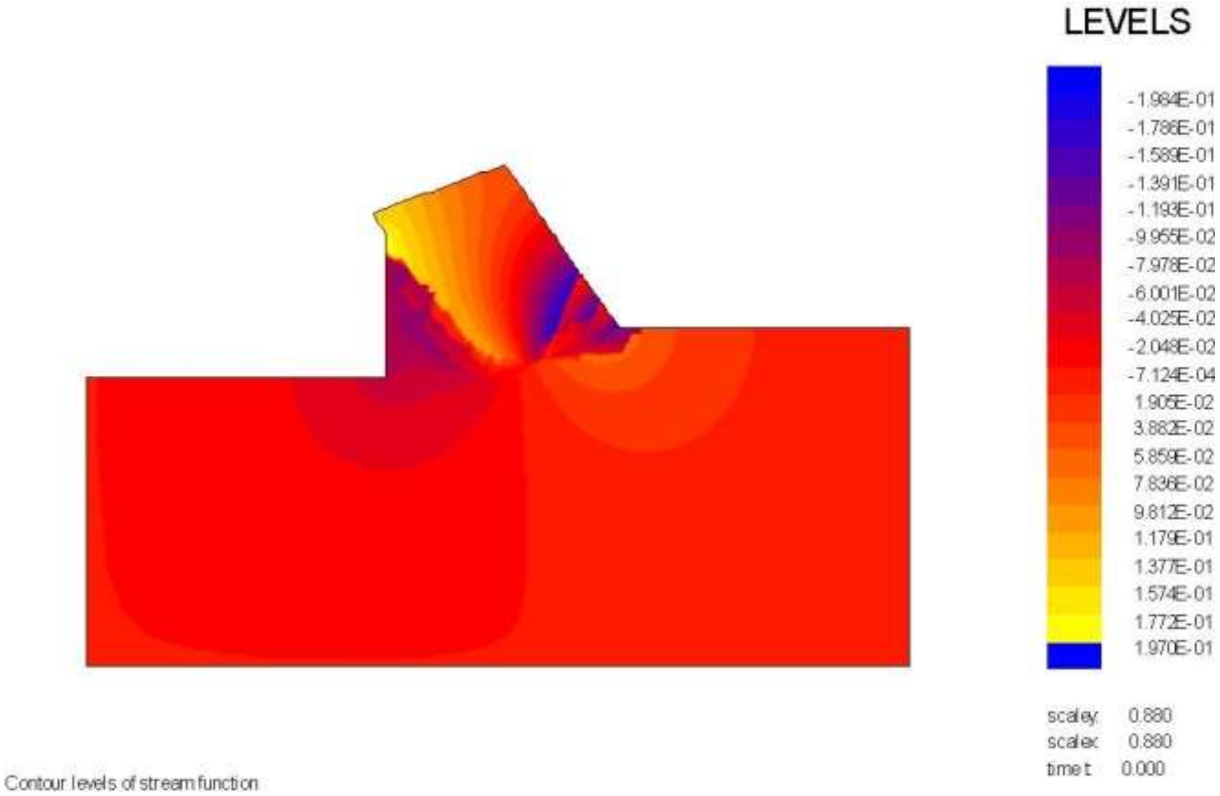

Figure S-16: The stream function in colors.

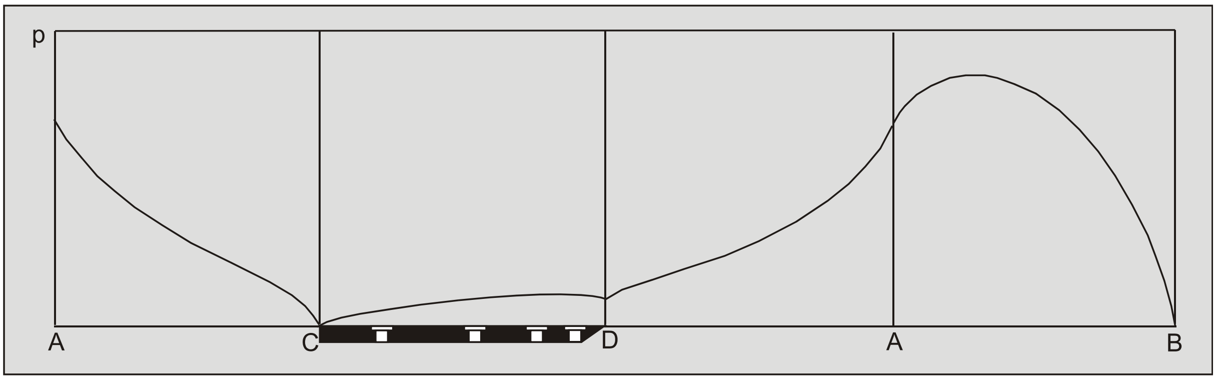

Figure S-17: Pore pressure distribution on the shear plane A-B, the bottom of the wedge A-D, the blade D-C and the front of the wedge A-C.

Appendix T: Force Triangles.

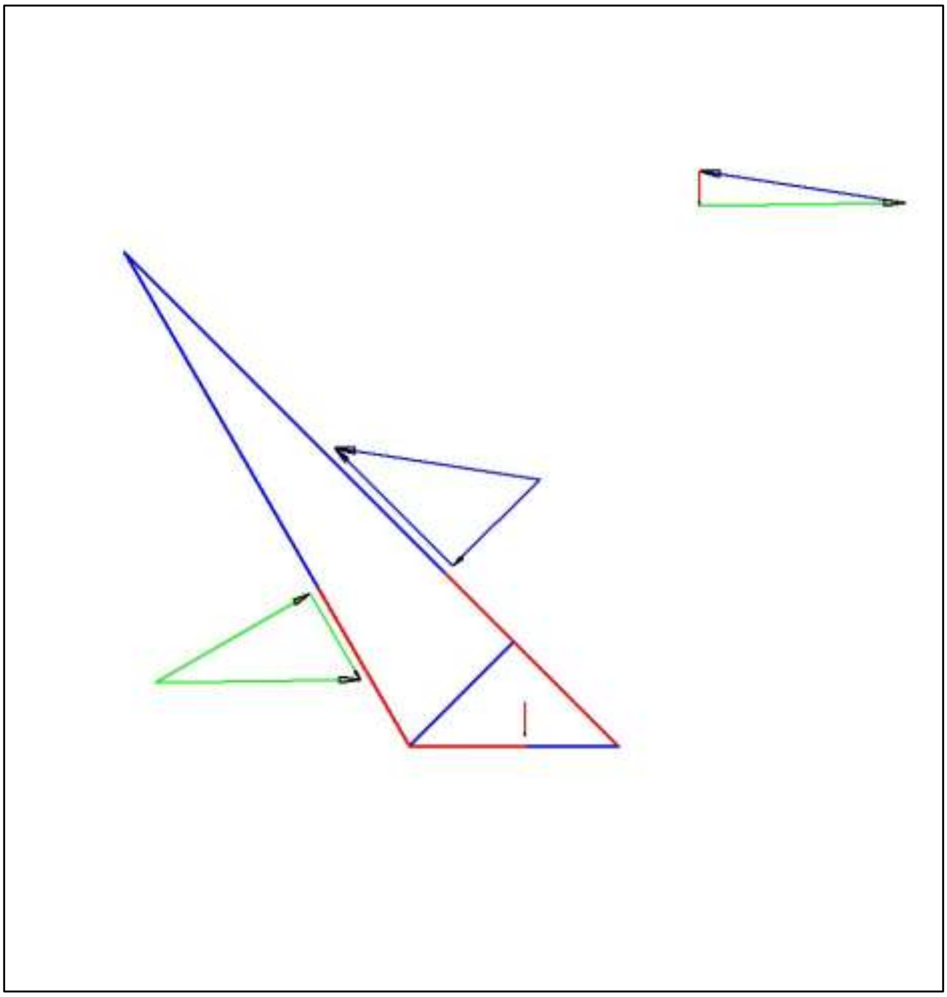

Figure T-1: The forces on the wedge for a 60º blade.

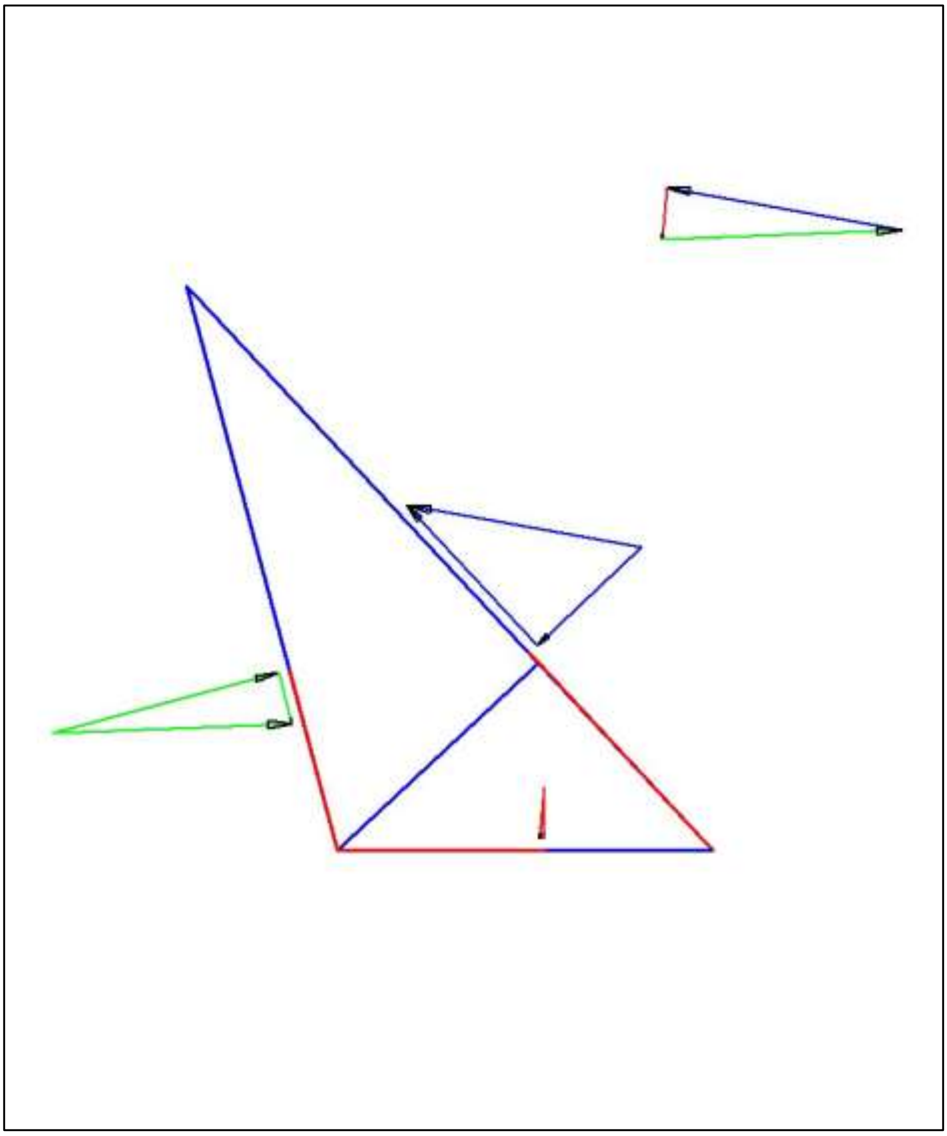

Figure T-2: The forces on the wedge for a 75° blade.

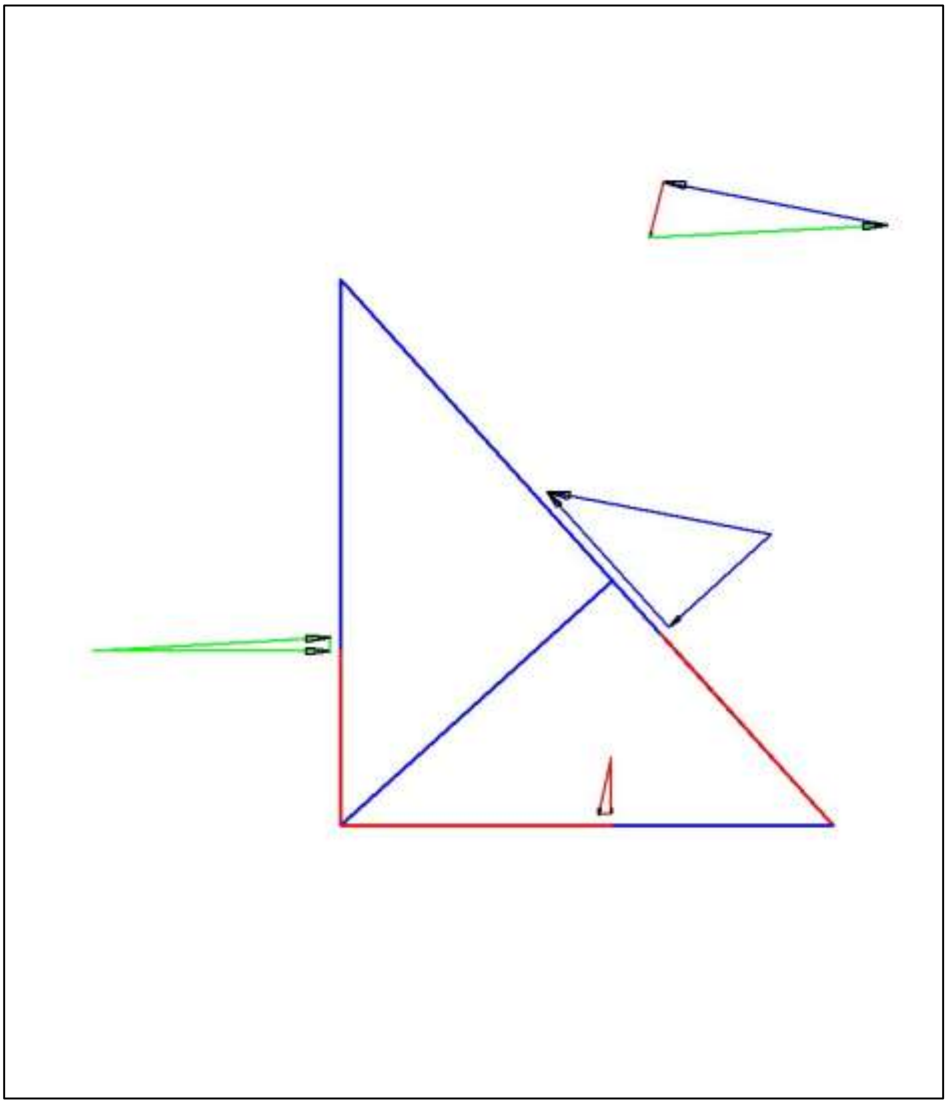

Figure T-3: The forces on the wedge for a 90° blade.

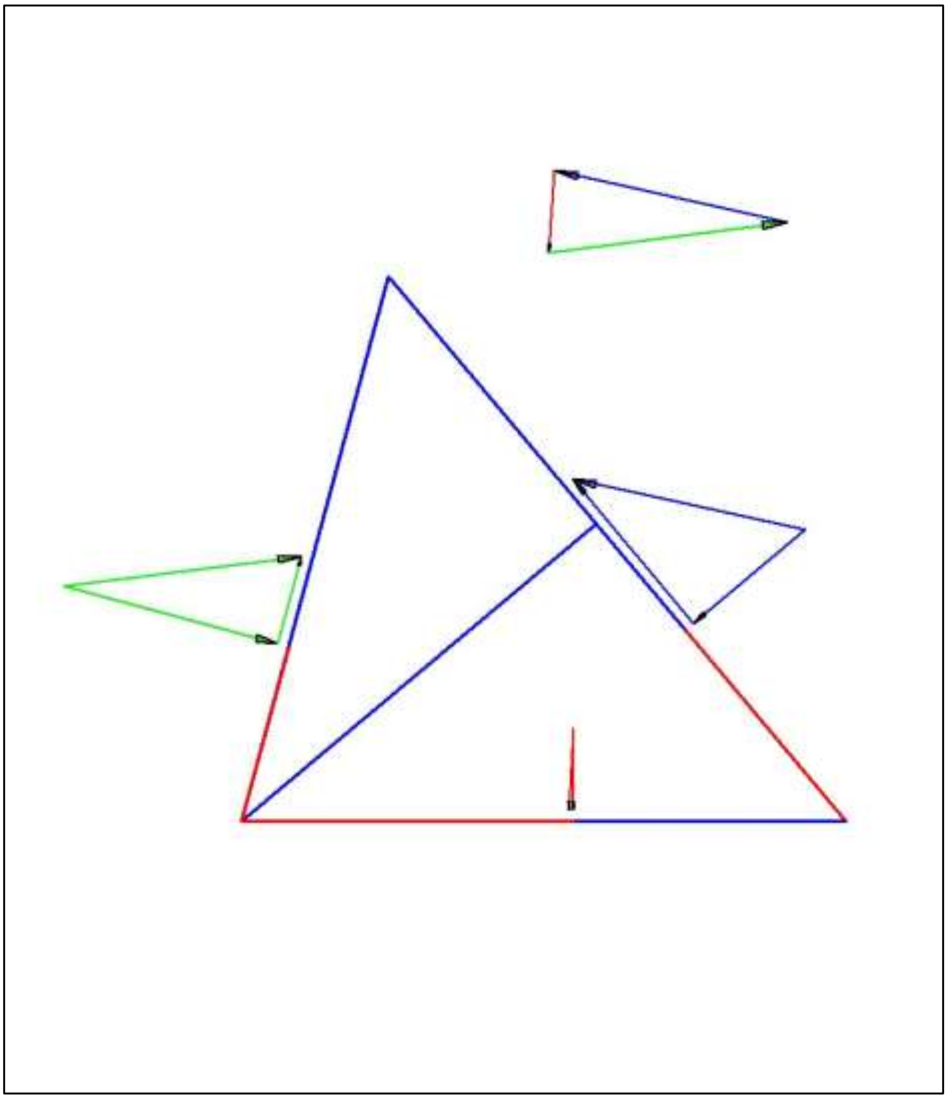

Figure T-4: The forces on the wedge for a 105º blade.

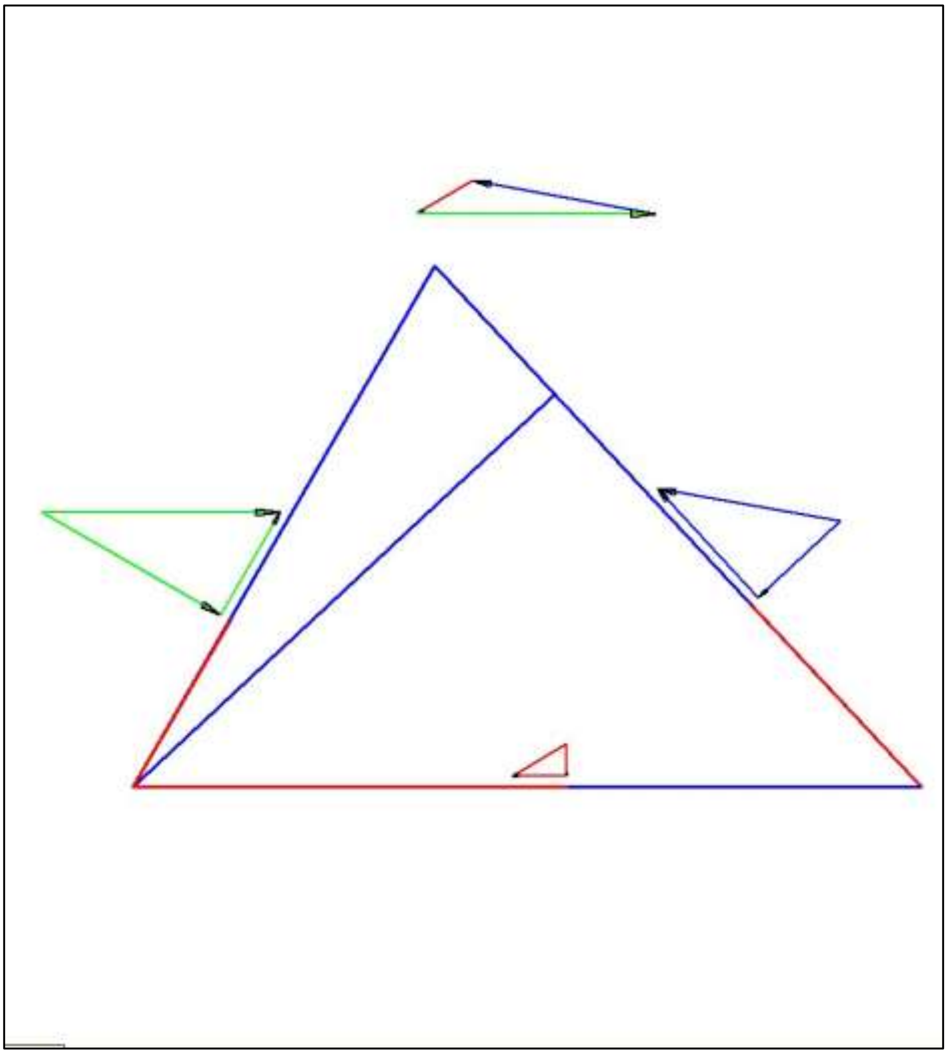

Figure T-5: The forces on the wedge for a 120º blade.

Appendix U: Specific Energy in Clay.

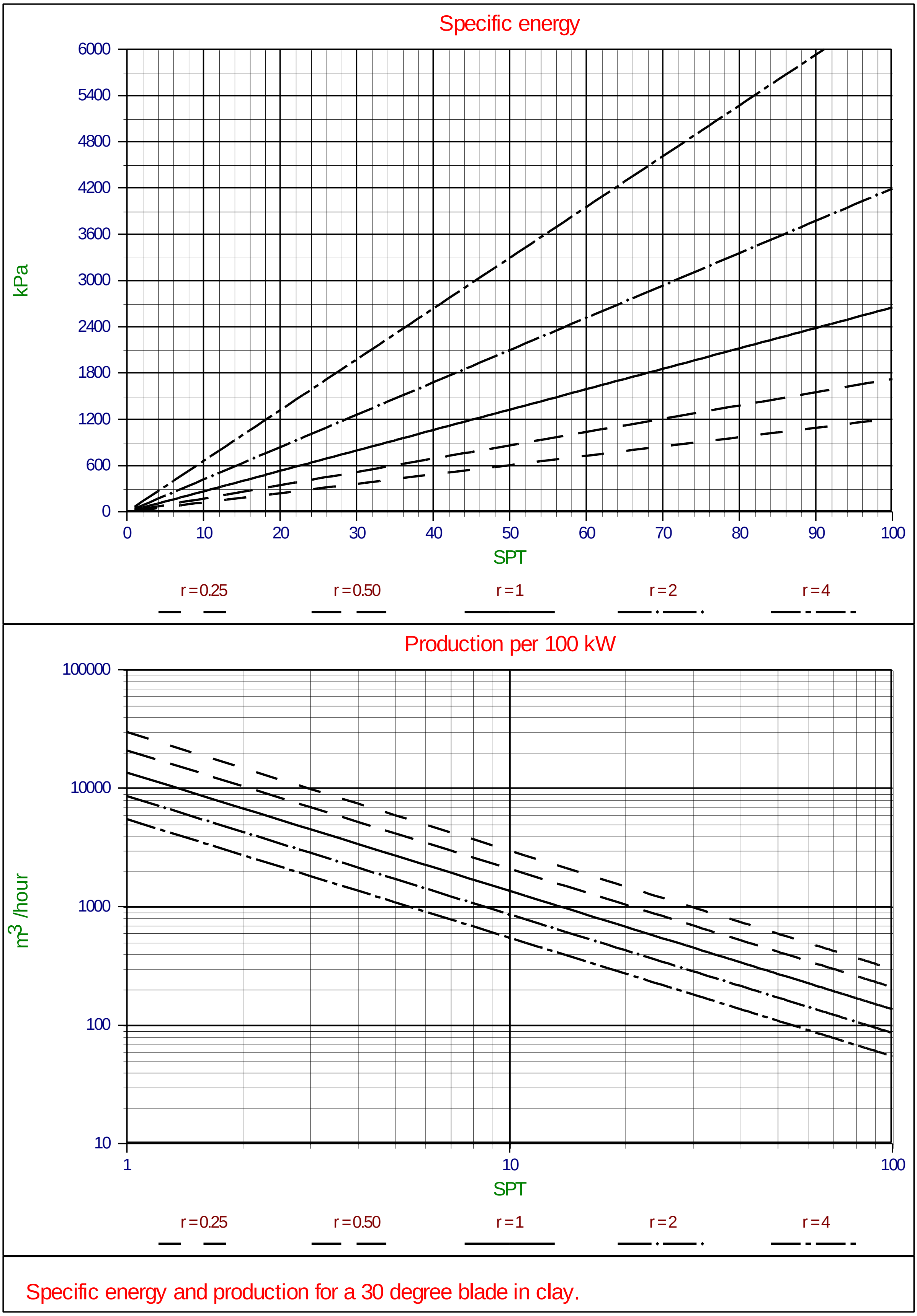

Figure U-1: Specific energy and production in clay for a 30 degree blade.

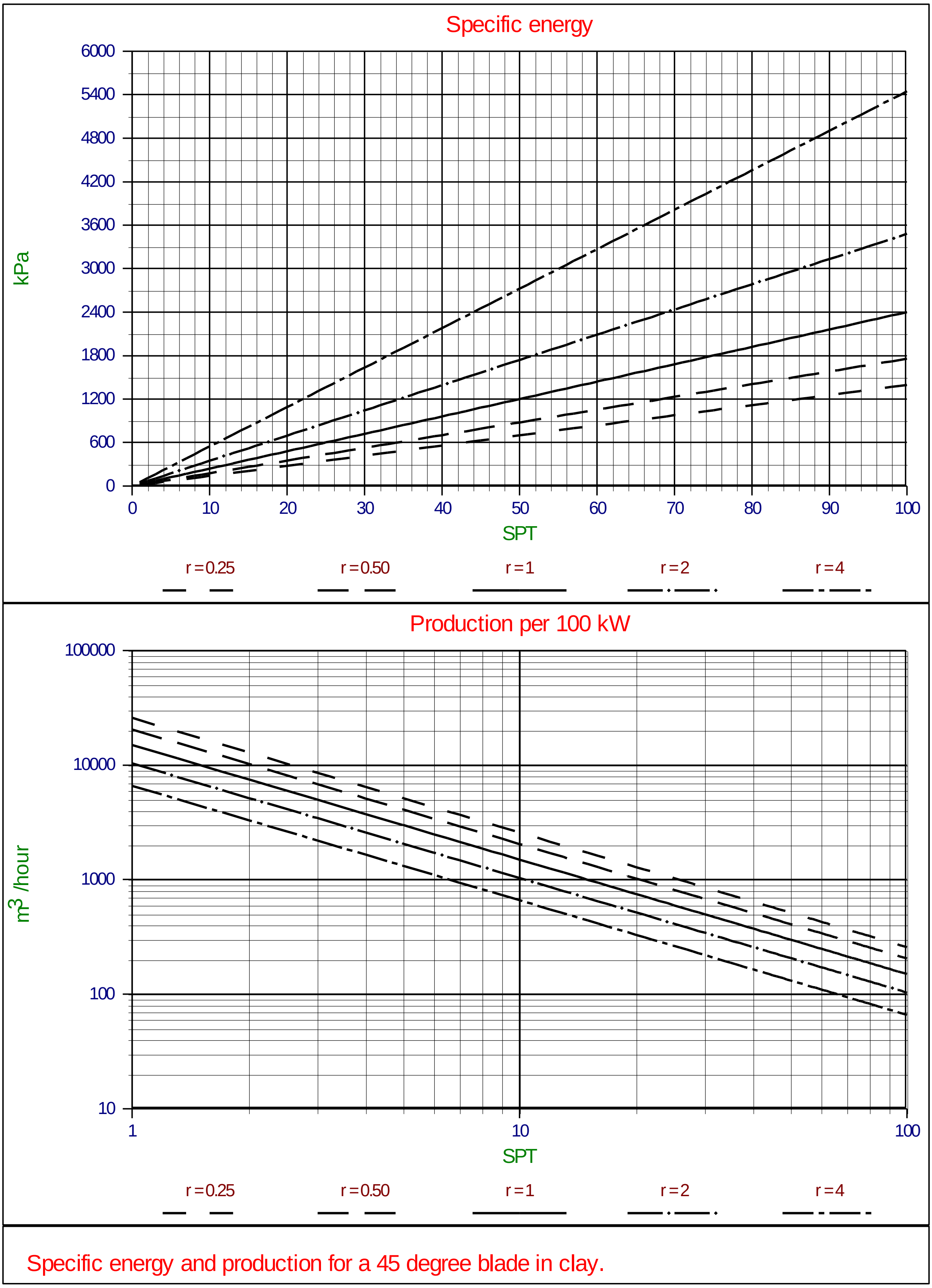

Figure U-2: Specific energy and production in clay for a 45 degree blade.

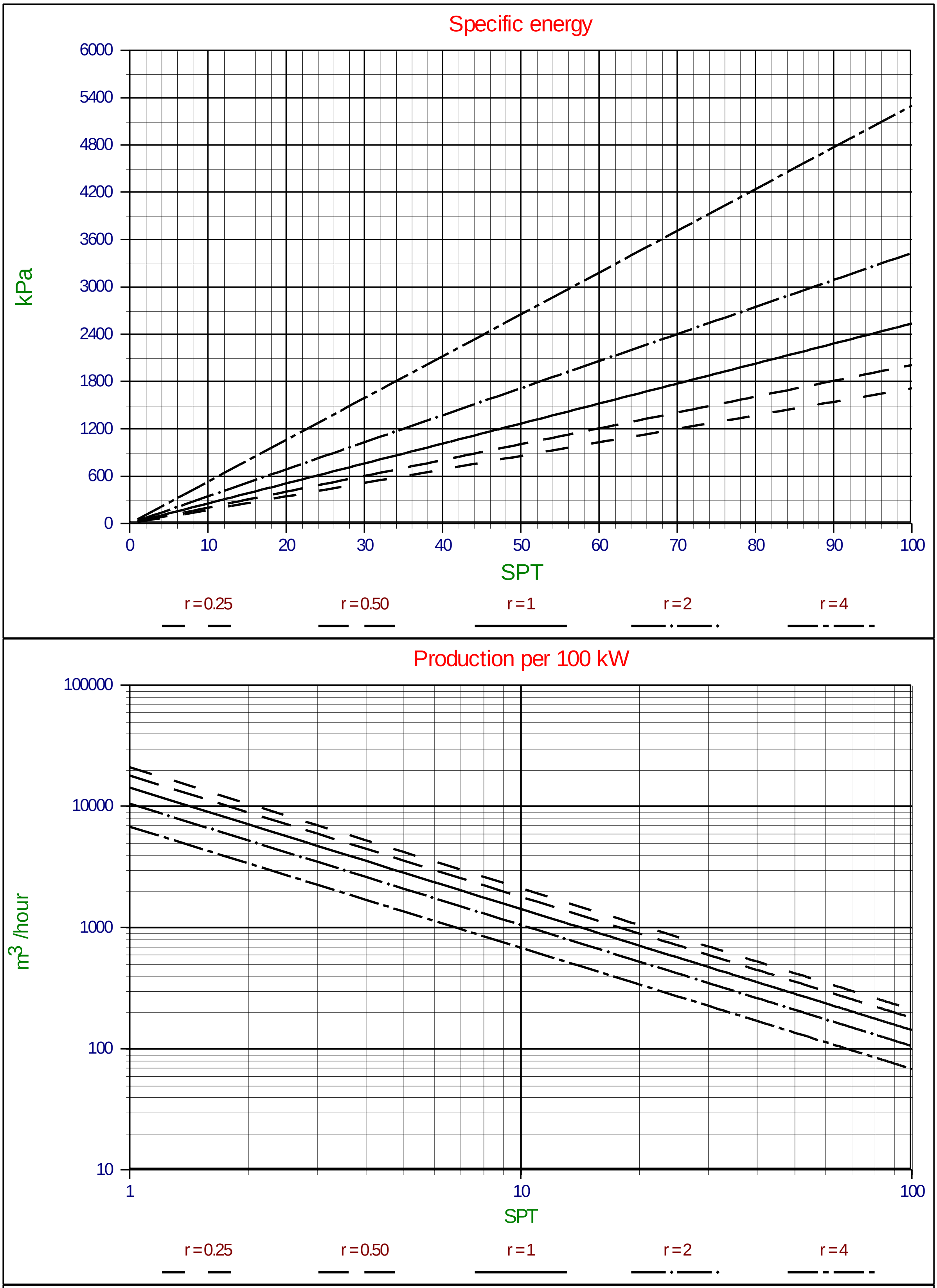

Specific energy and production for a 60 degree blade in clay.

Figure U-3: Specific energy and production in clay for a 60 degree blade.

Appendix V: Clay Cutting Charts.

V.1 The Flow Type.

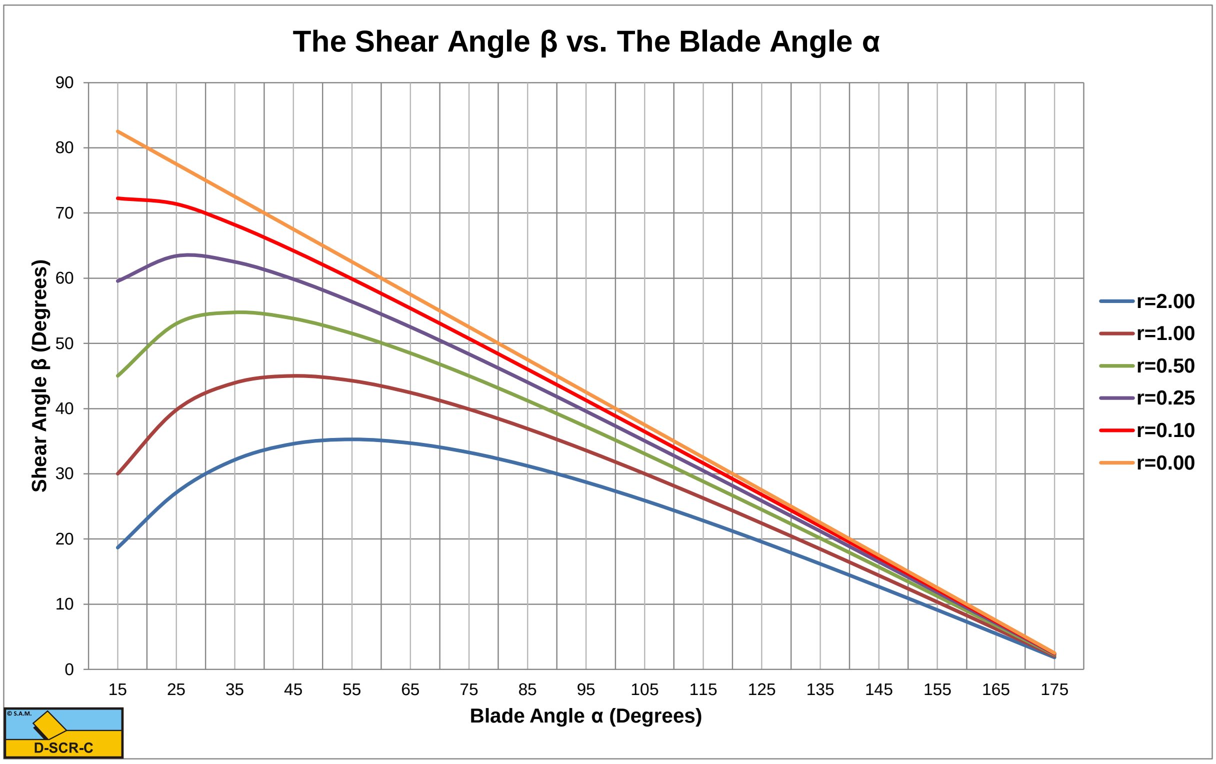

Figure V-1: The shear angle β as a function of the blade angle α and the ac ratio r.

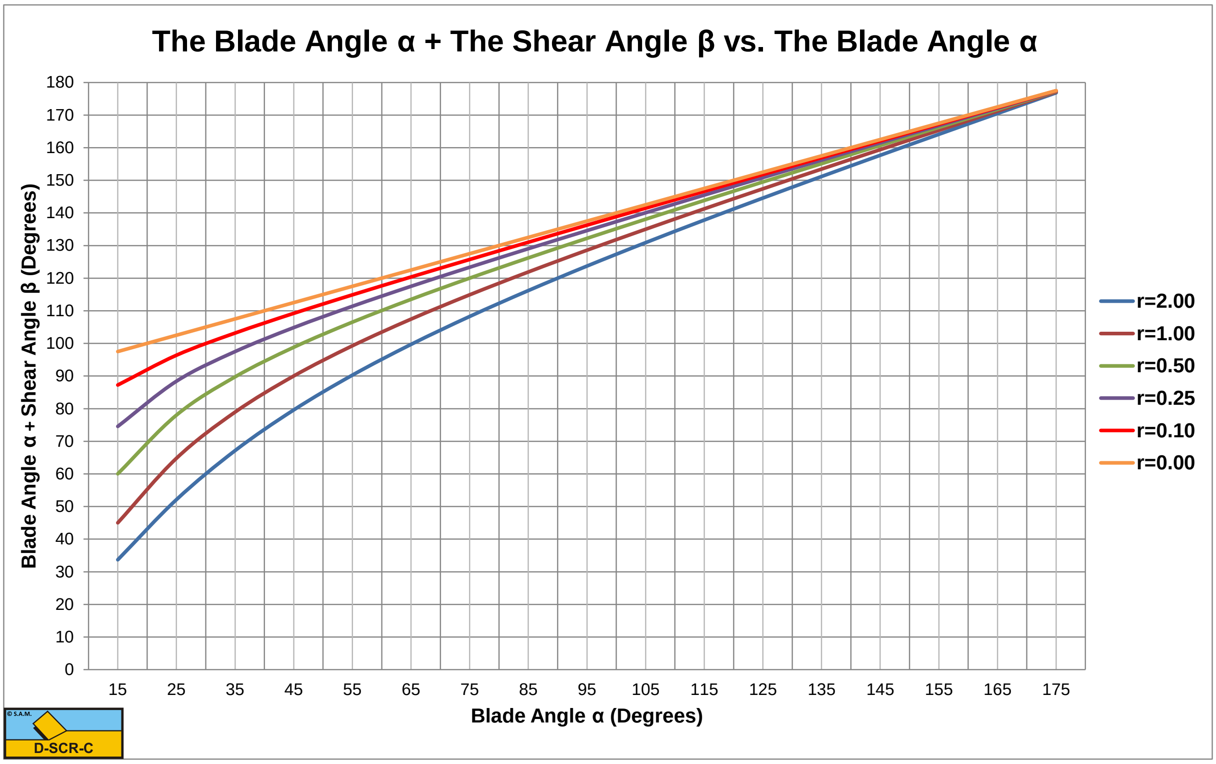

Figure V-2: The sum of the blade angle and the shear angle.

Shear angle and cutting forces for a layer thickness **h_i=0.1 m**, a blade width **w=1 m** and a strain rate factor **λ_c=1**.

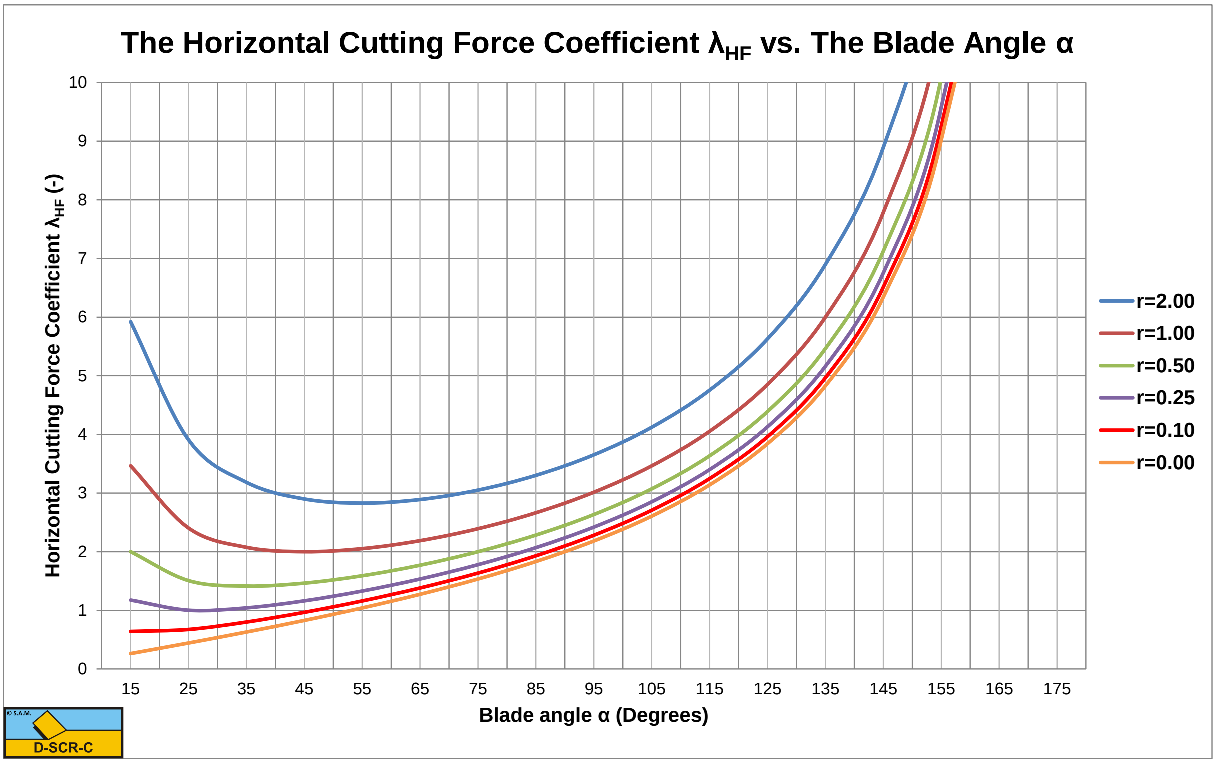

Figure V-3: The horizontal cutting force coefficient λ_{HF} as a function of the blade angle α and the ac ratio r.

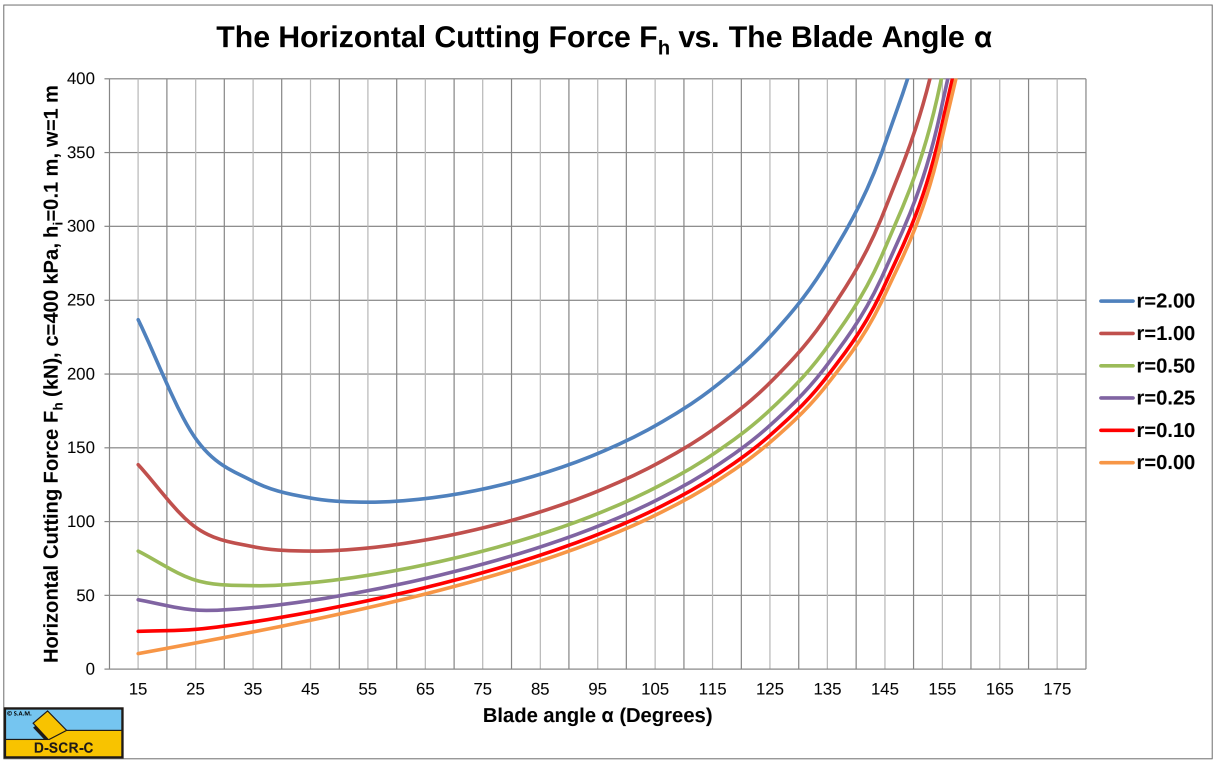

Figure V-4: The horizontal cutting force as a function of the blade angle α and the ac ratio r (c=400 kPa).

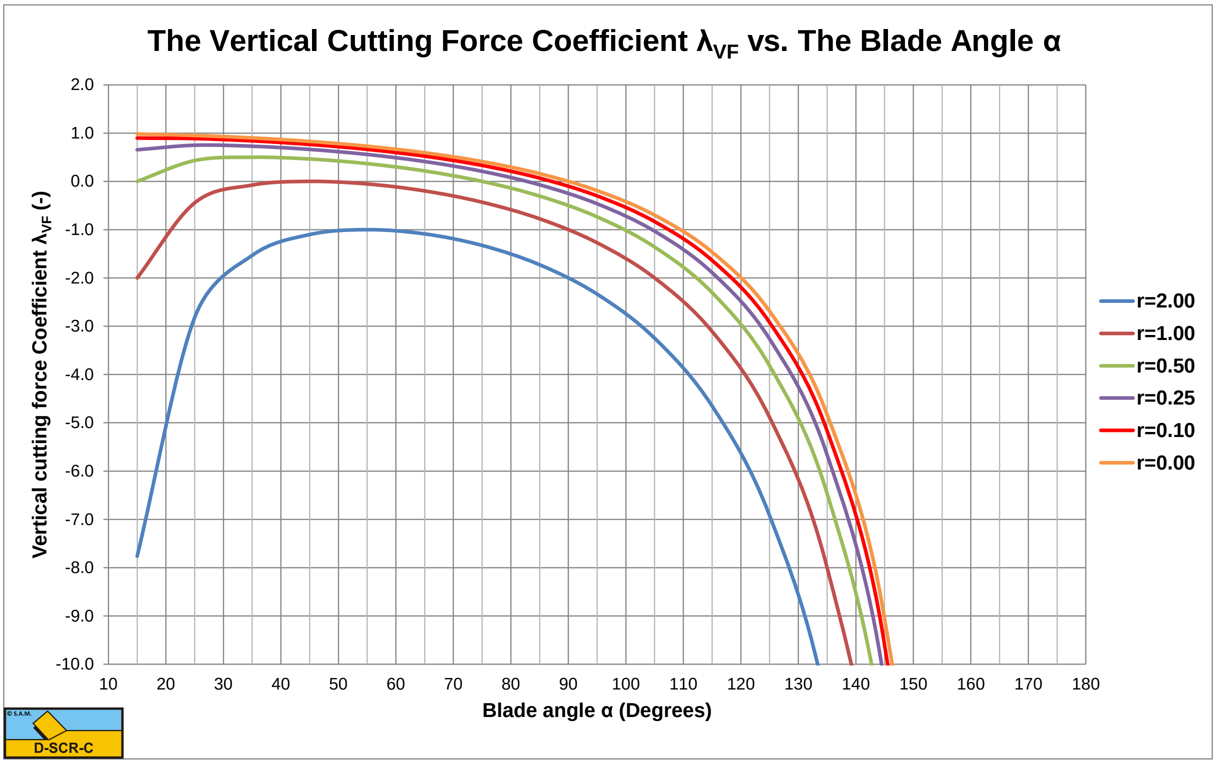

Figure V-5: The vertical cutting force coefficient λ_{VF} as a function of the blade angle α and the ac ratio r.

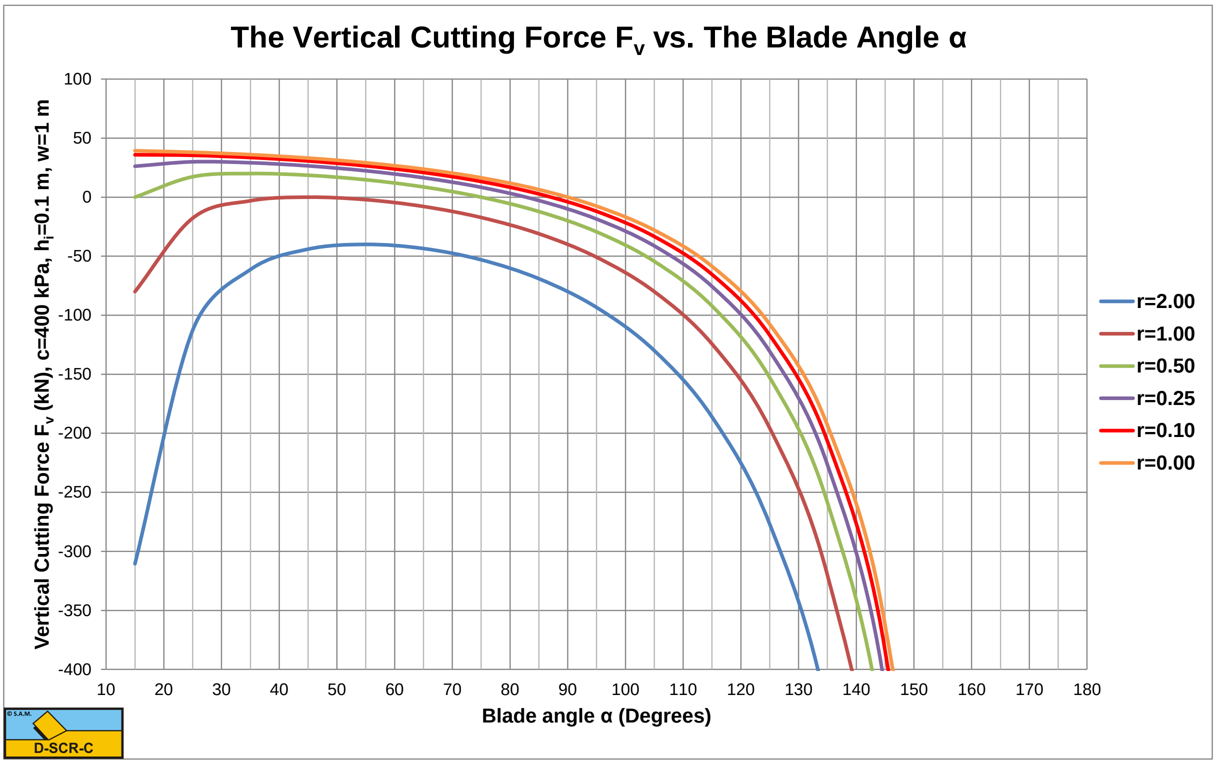

Figure V-6: The vertical cutting force as a function of the blade angle α and the ac ratio r (c=400 kPa).

V.2 The Tear Type.

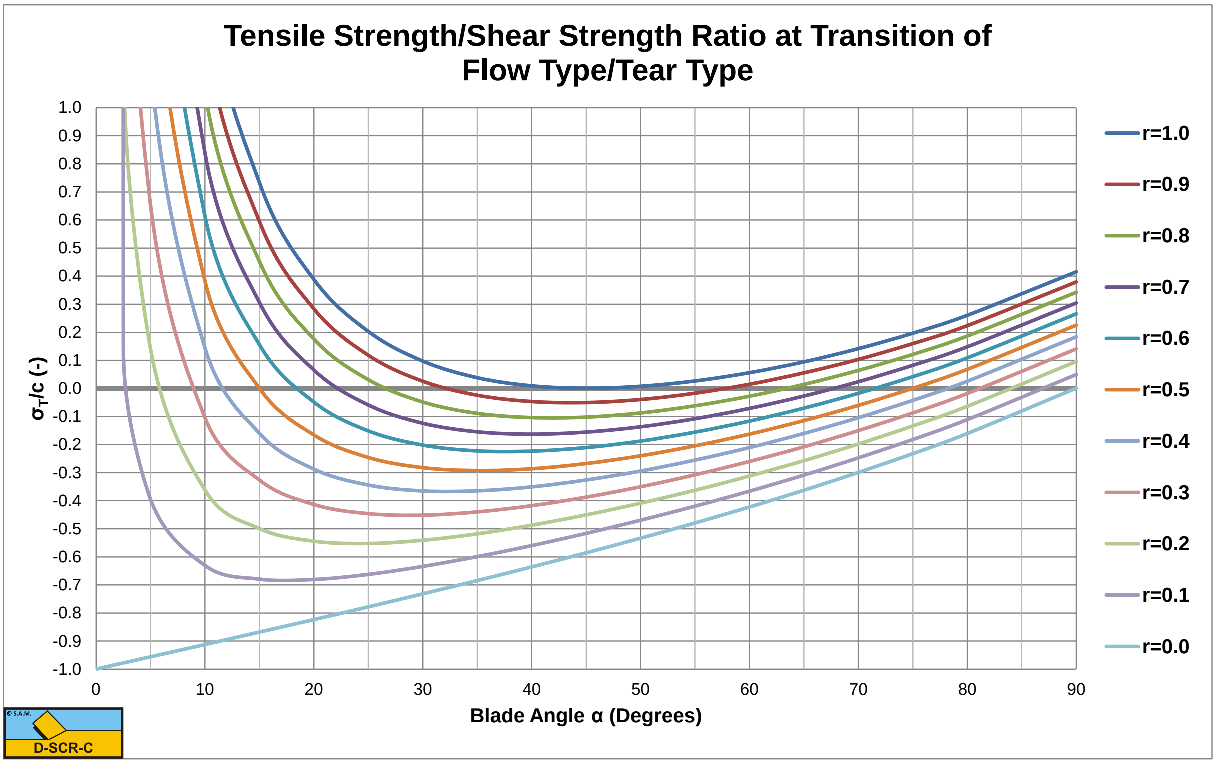

Figure V-7: The transition Flow Type vs. Tear Type.

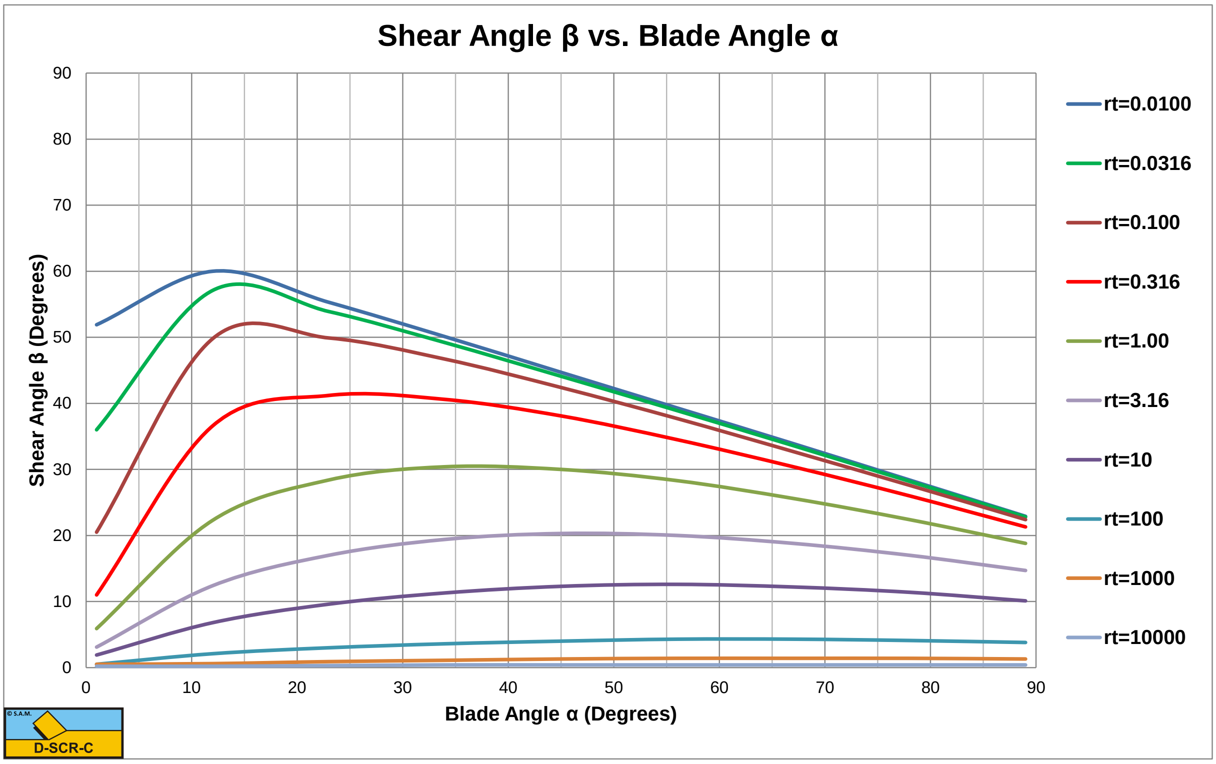

Figure V-8: The shear angle β vs. the blade angle α for the Tear Type.

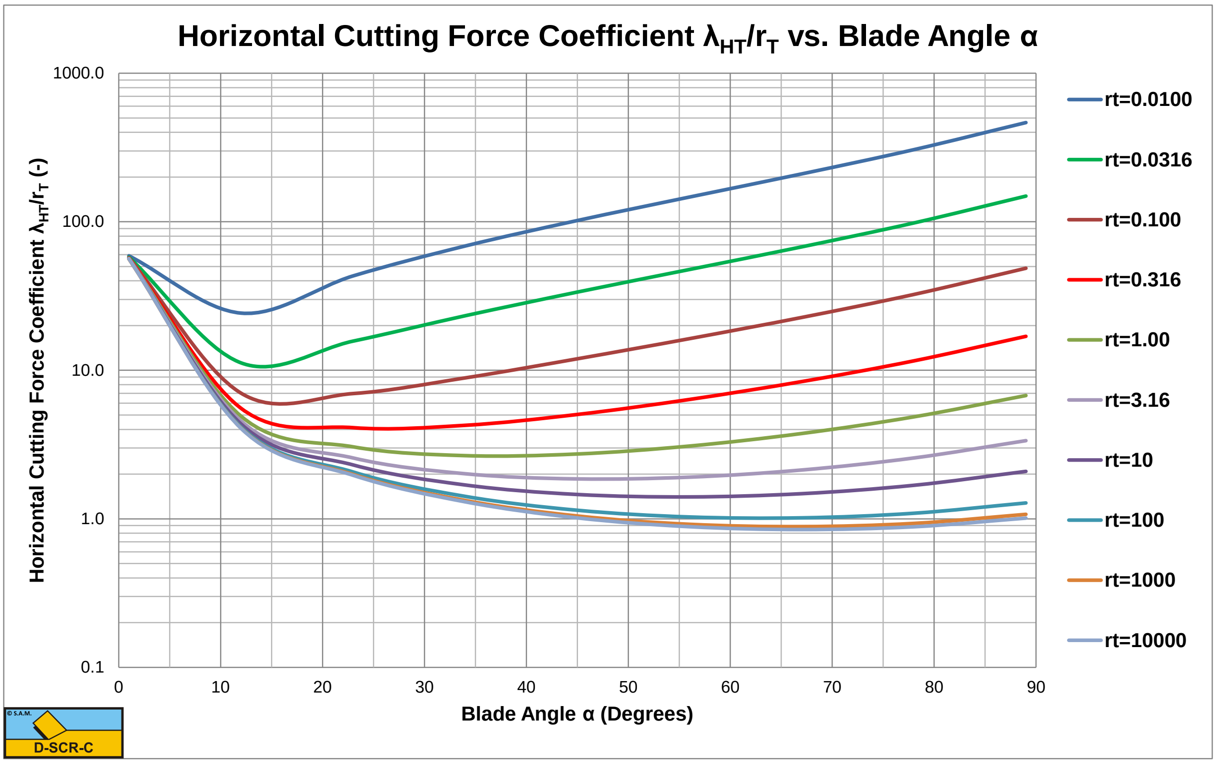

Figure V-9: The horizontal cutting force coefficient λ_{HT}/r_T.

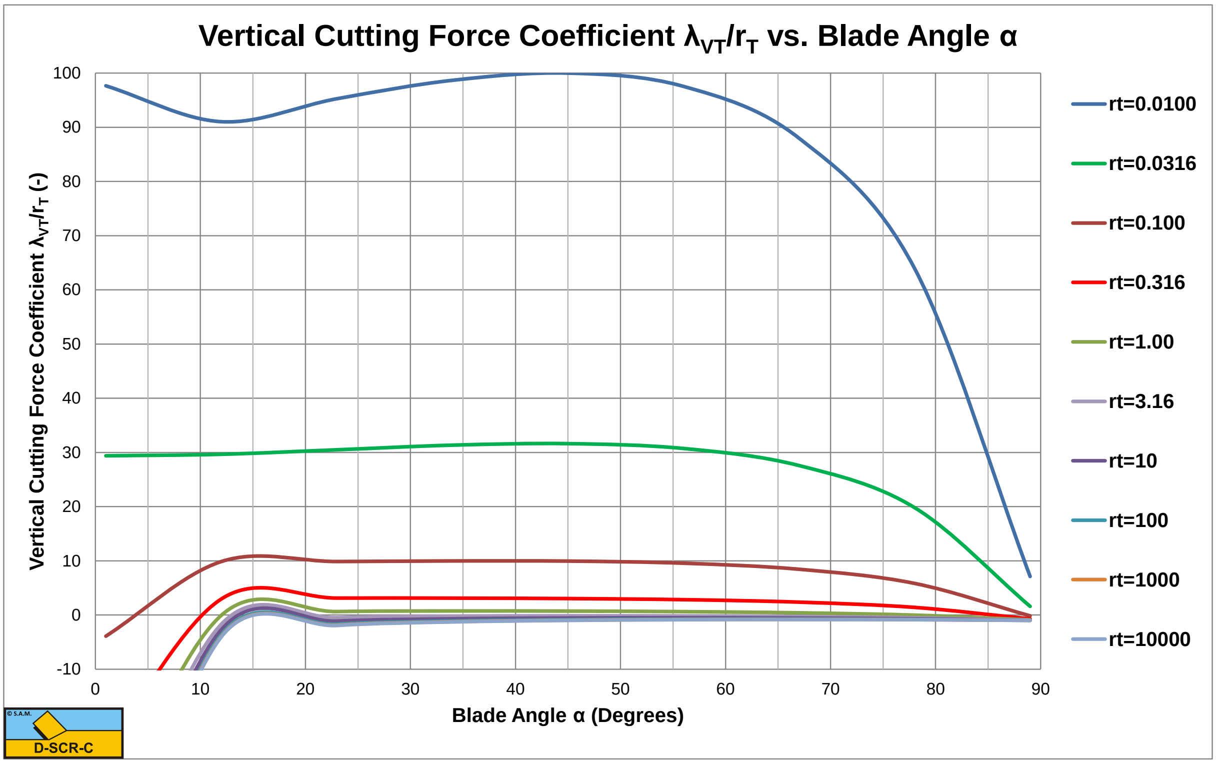

Figure V-10: The vertical cutting force coefficient λ_{VT}/r_T.

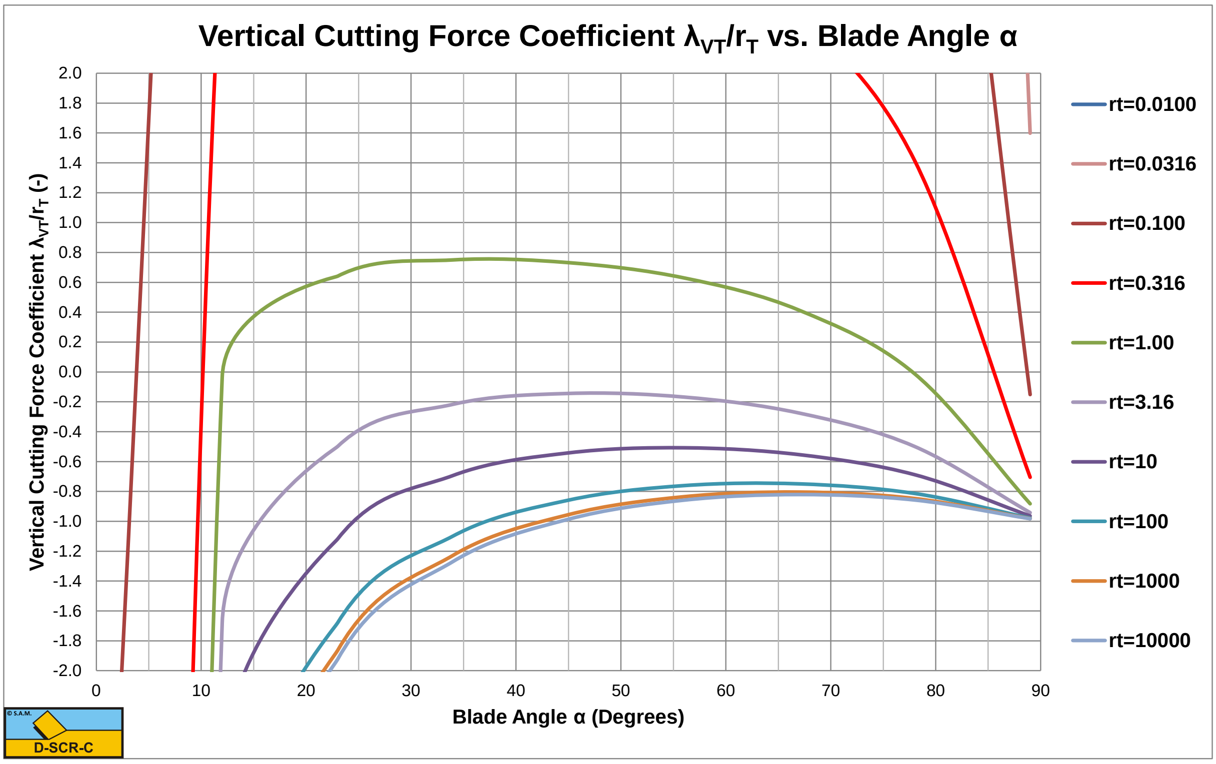

Figure V-11: The vertical cutting force coefficient λ_{VT}/r_T zoomed.

V.3 The Curling Type.

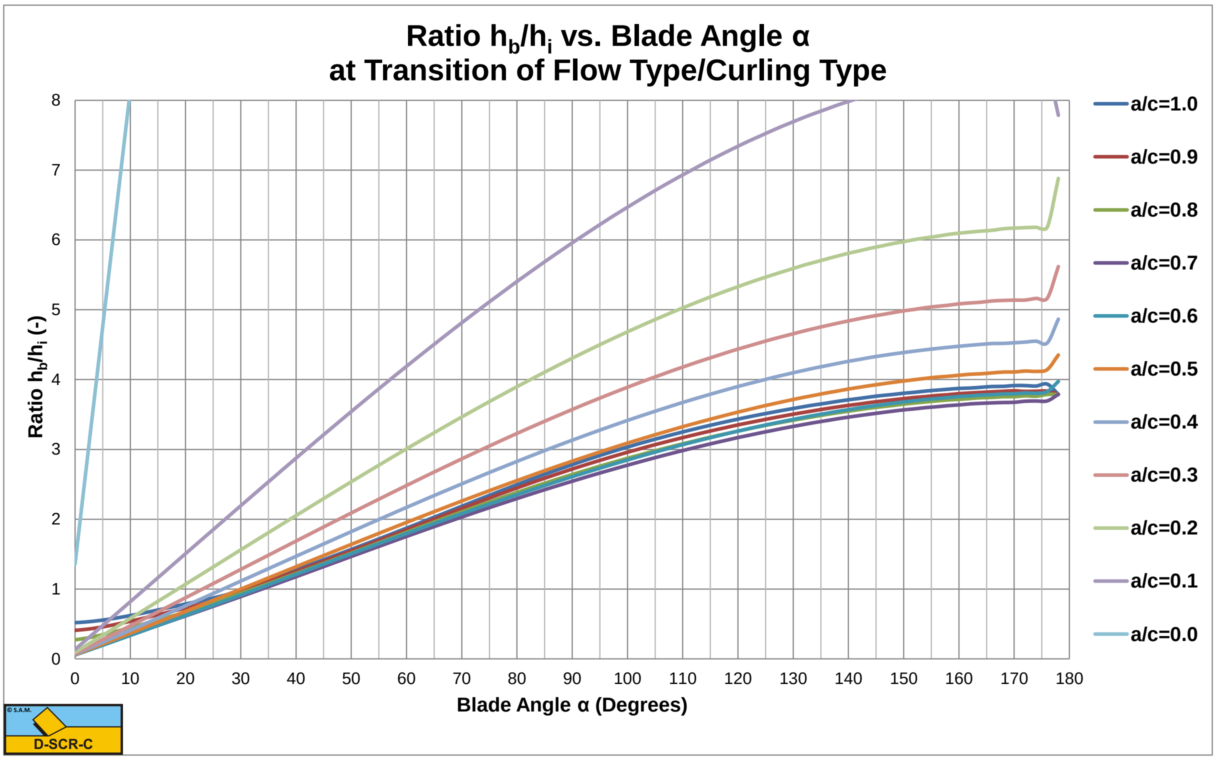

Figure V-12: The ratio h_b/h_i at the transition Flow Type/Curling Type.

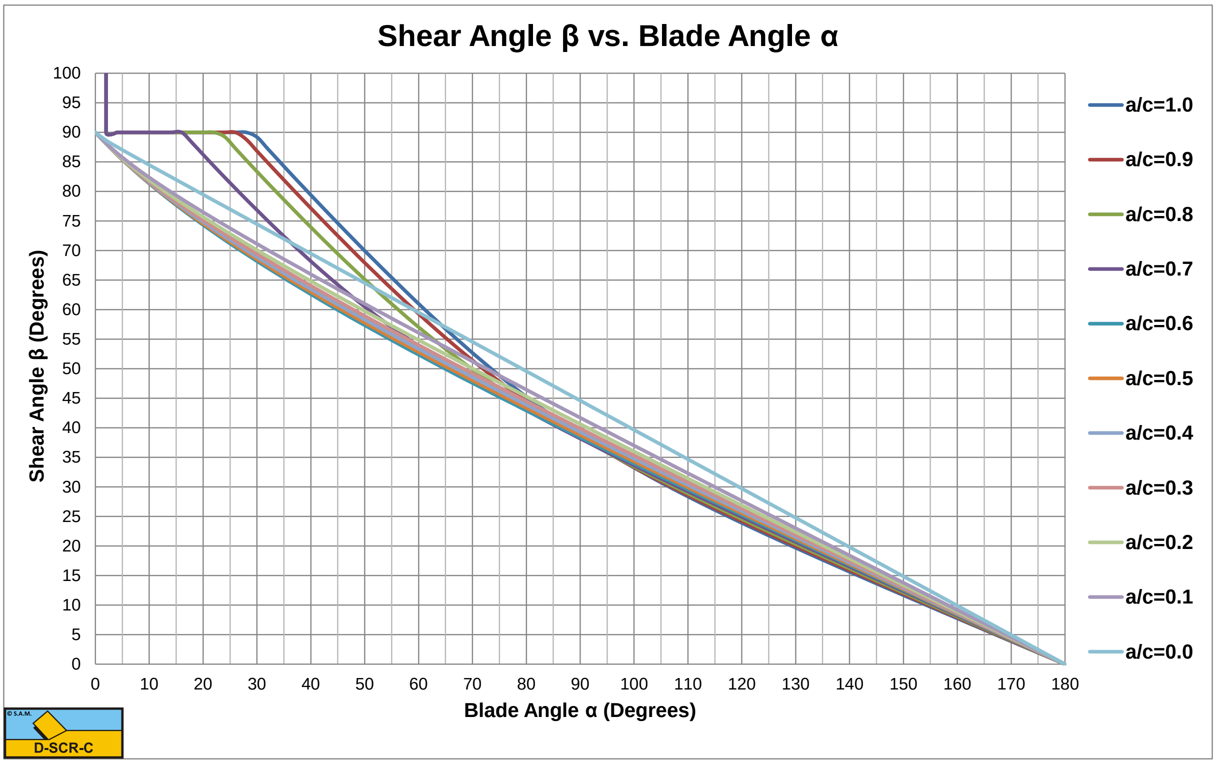

Figure V-13: The shear angle for the Curling Type

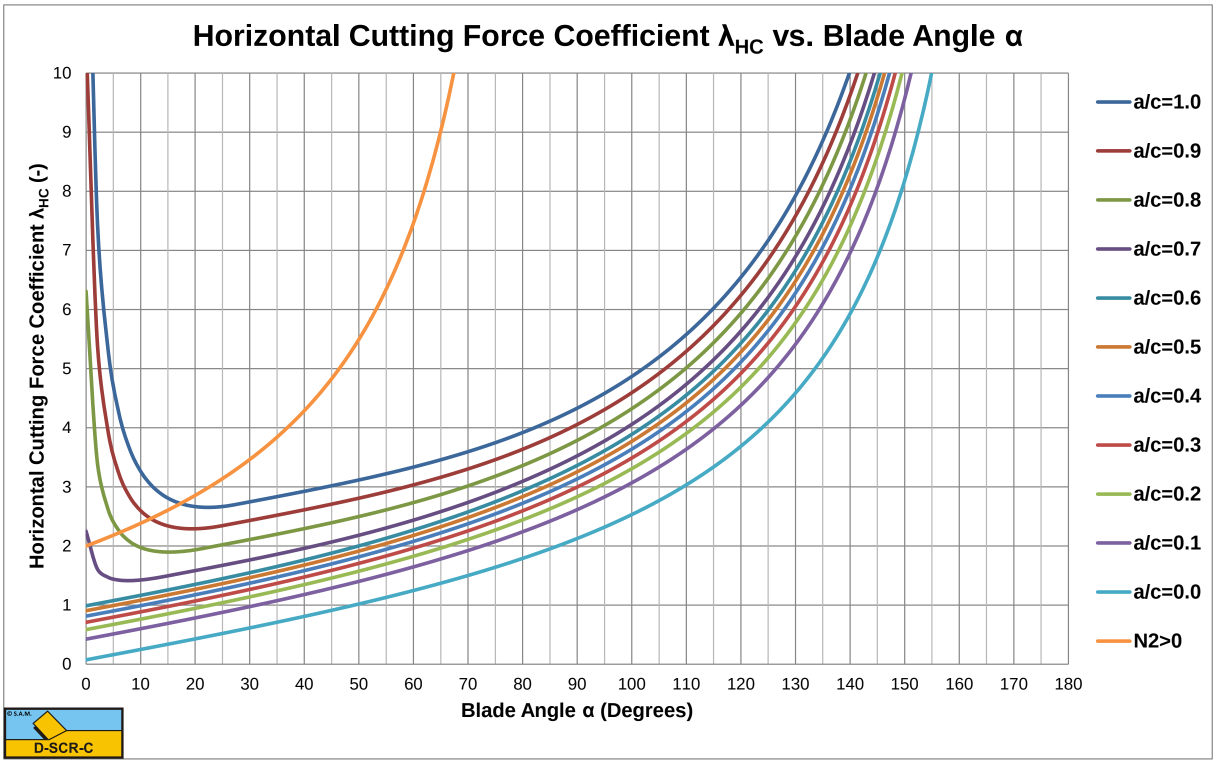

Figure V-14: The horizontal cutting force coefficient λ_{HC}.

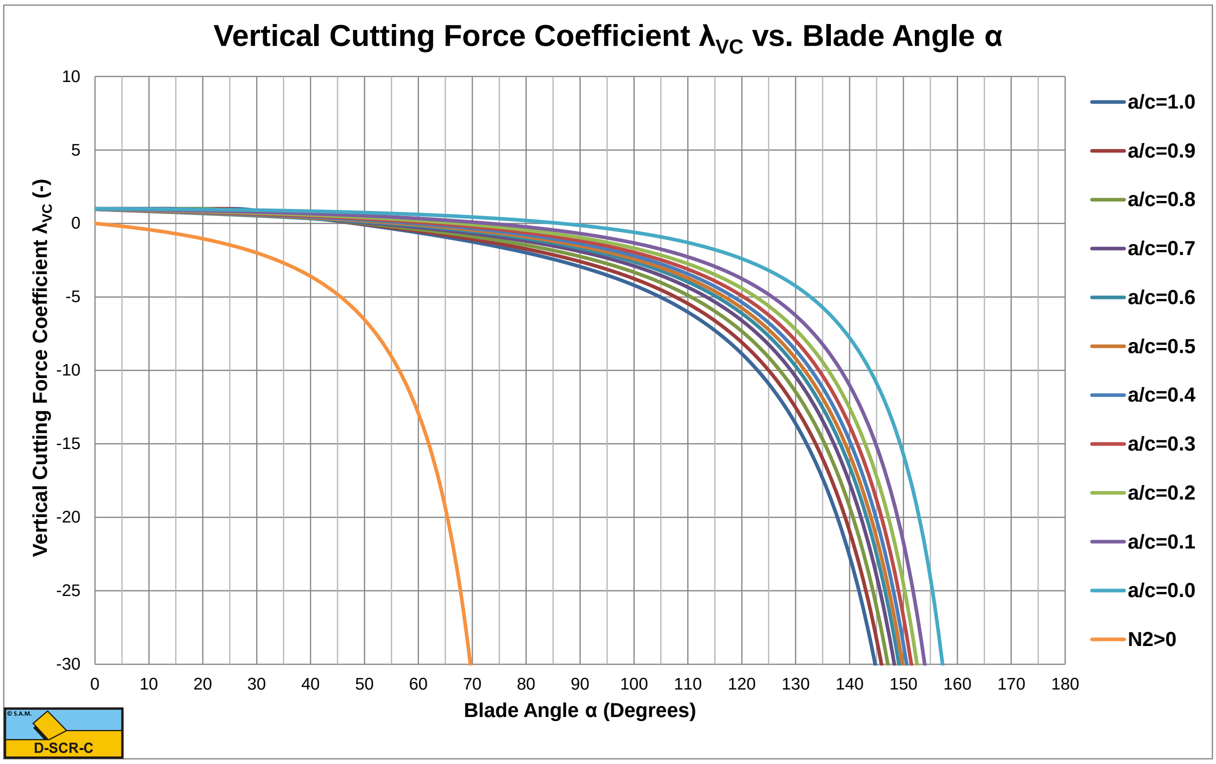

Figure V-15: The vertical cutting force coefficient λ_{VC}.

Appendix W: Rock Cutting Charts.

W.1 Brittle Shear.

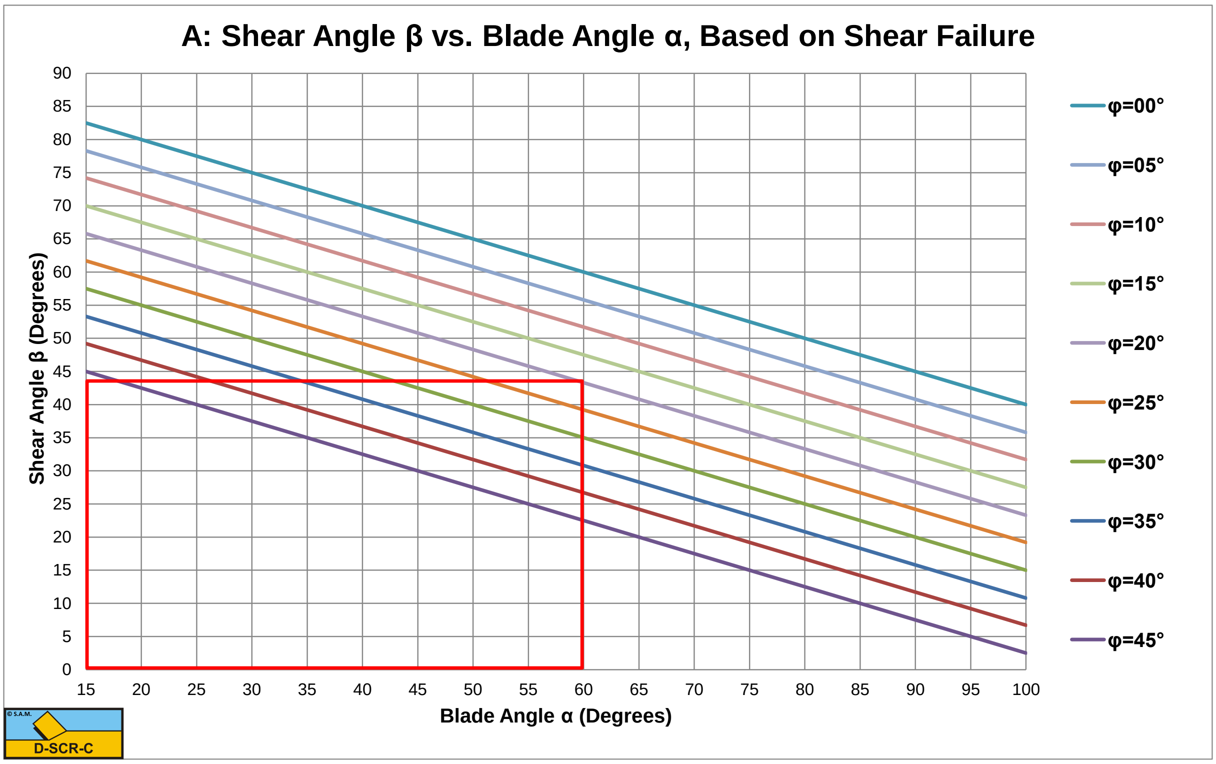

Figure W-1: The shear angle β as a function of the blade angle α and the internal friction angle φ for shear failure.

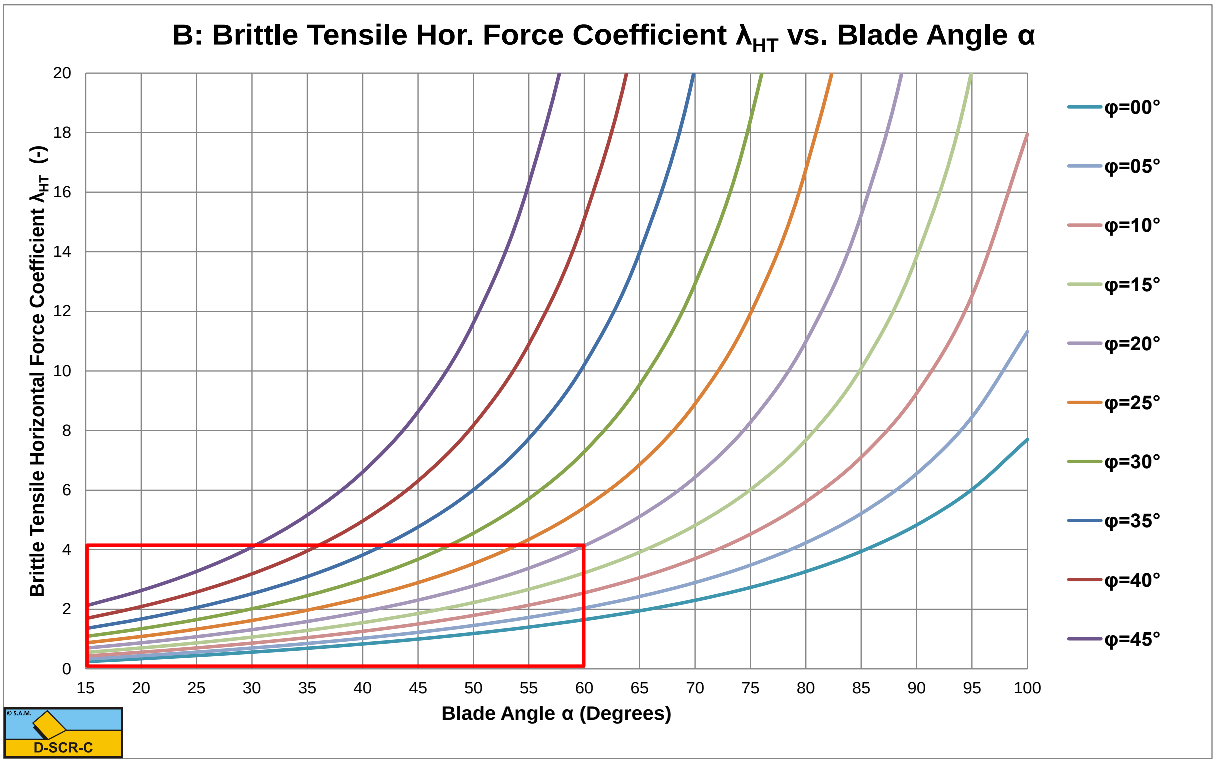

Figure W-2: The brittle (shear failure) horizontal force coefficient λ_{HF}.

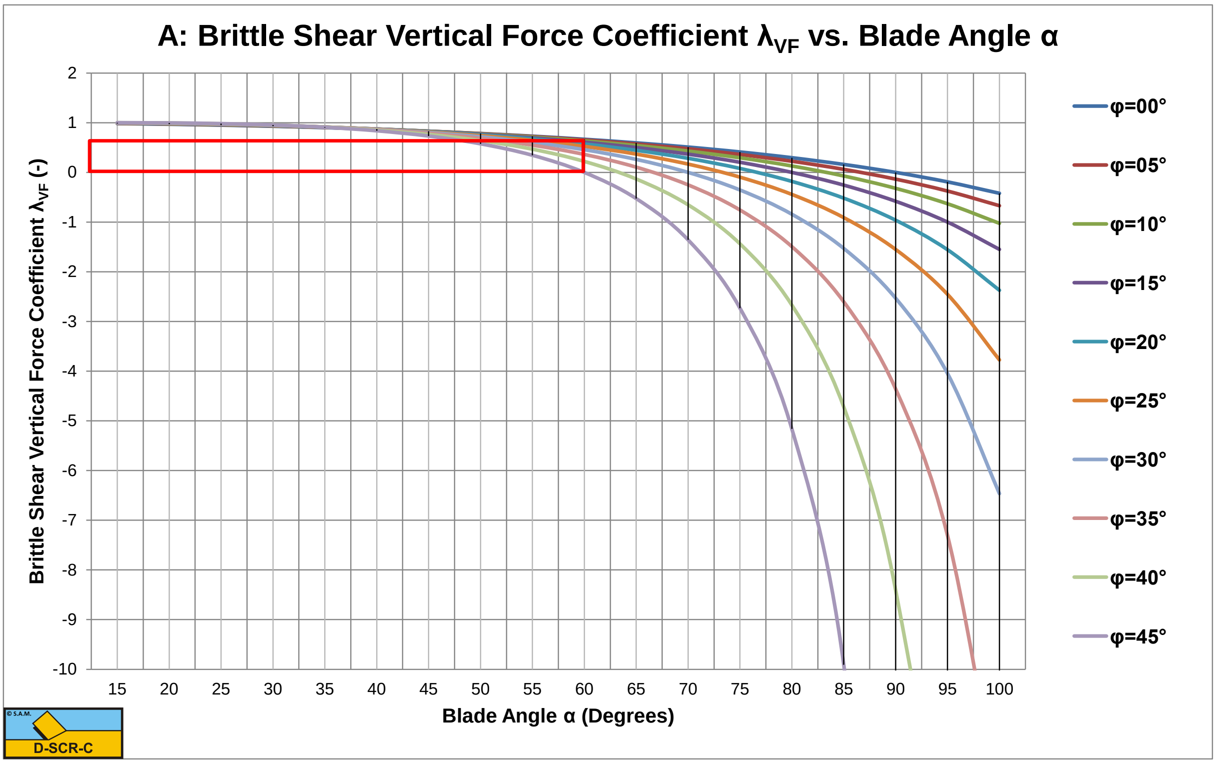

Figure W-3: The brittle (shear failure) vertical force coefficient λ_{VF}.

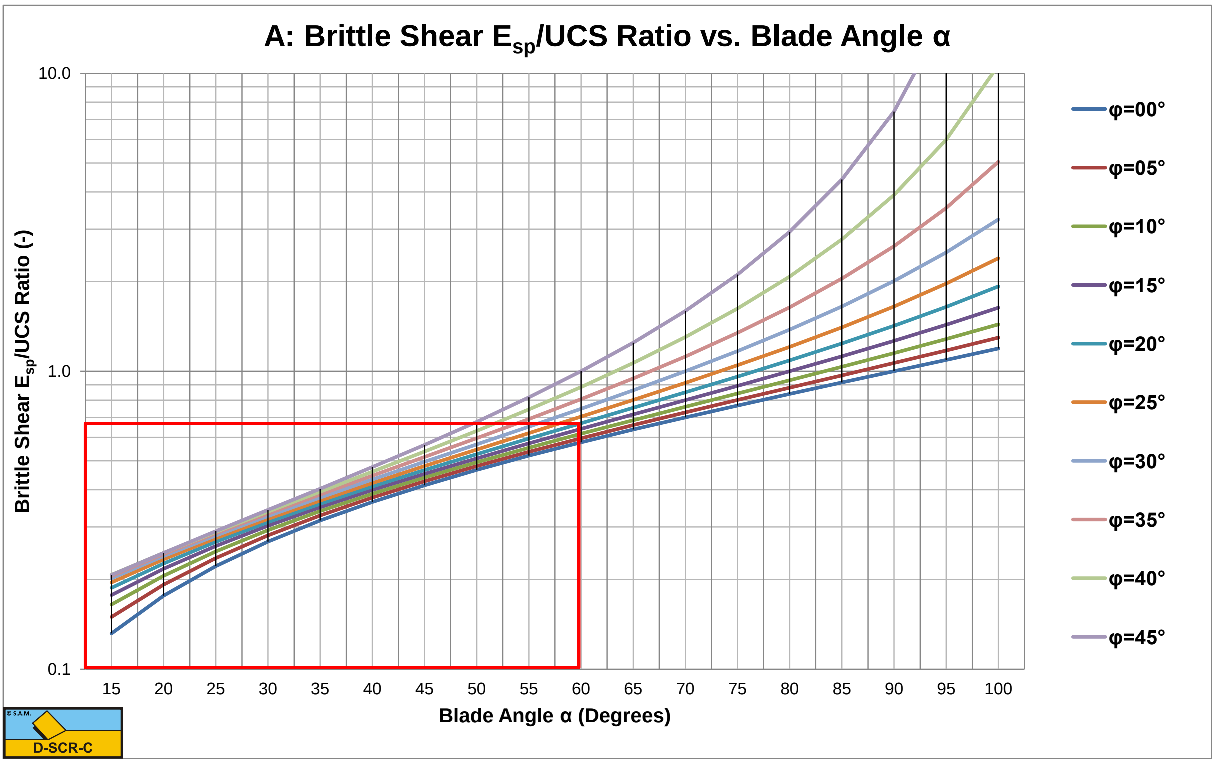

Figure W-4: The specific energy to UCS ratio.

In all figures an example is given for a 60° blade and an internal friction angle of 20°.

W.2 The Transition Brittle Shear/Brittle Tensile A.

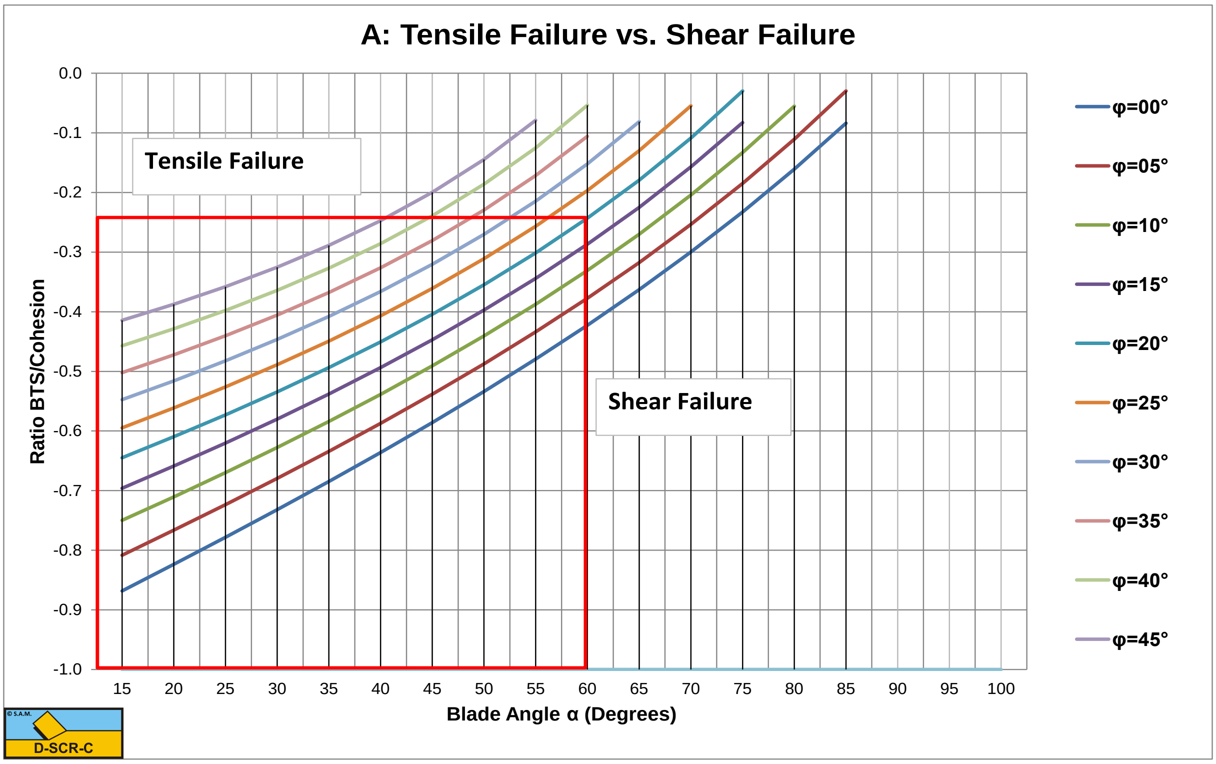

Figure W-5: The tensile/shear failure criterion based on BTS/Cohesion.

Below the lines the cutting process is subject to shear failure, above the lines to tensile failure. The curves are based on the shear angle resulting from shear failure.

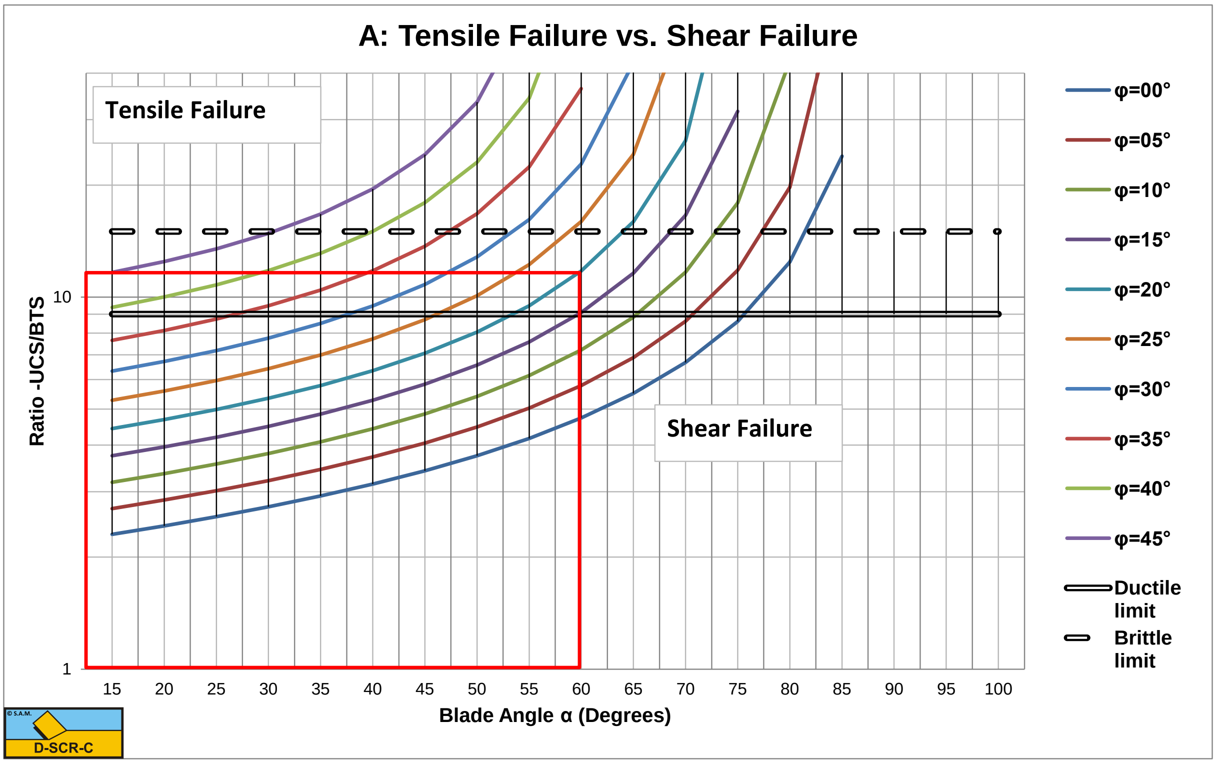

Figure W-6: The tensile/shear failure criterion based on UCS/BTS.

In all figures an example is given for a 60º blade and an internal friction angle of 20º.

W.3 The Transition Brittle Shear/Brittle Tensile B.

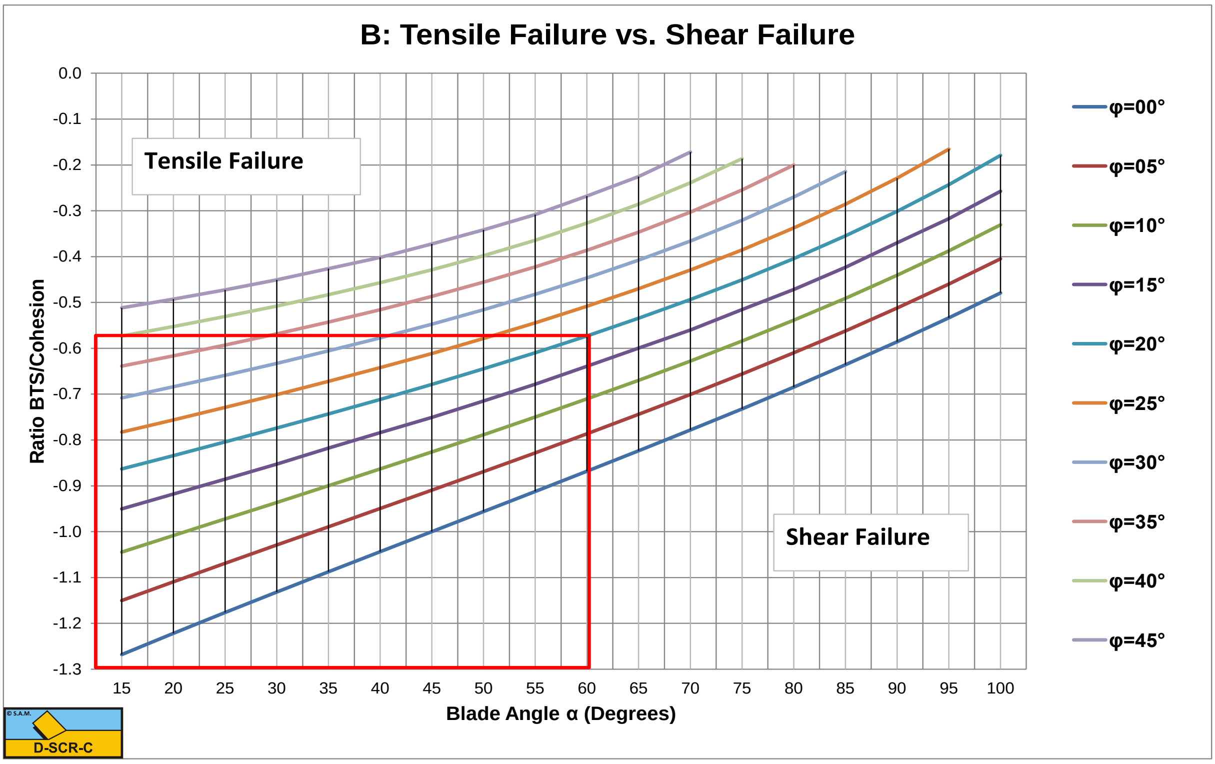

Figure W-7: The tensile/shear failure criterion based on BTS/Cohesion.

Below the lines the cutting process is subject to shear failure, above the lines to tensile failure. The curves are based on the shear angle resulting from tensile failure.

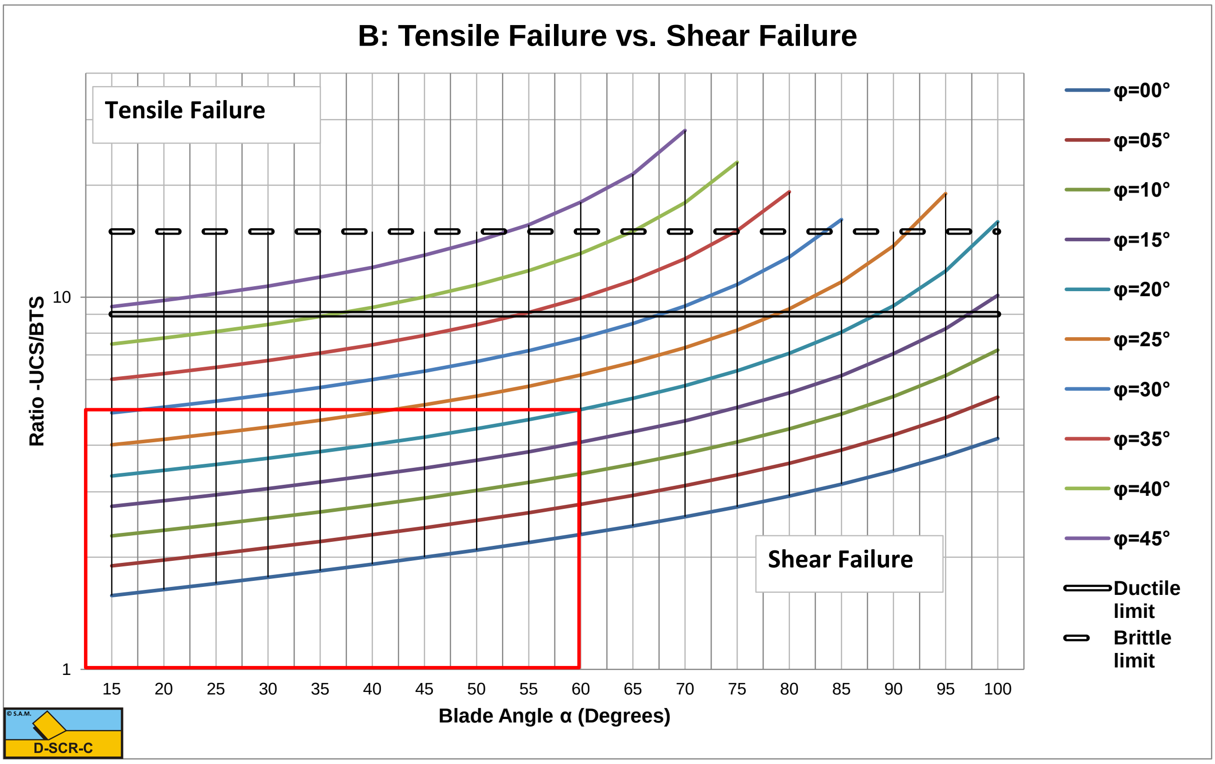

Figure W-8: The tensile/shear failure criterion based on UCS/BTS.

In all figures an example is given for a 60° blade and an internal friction angle of 20°.

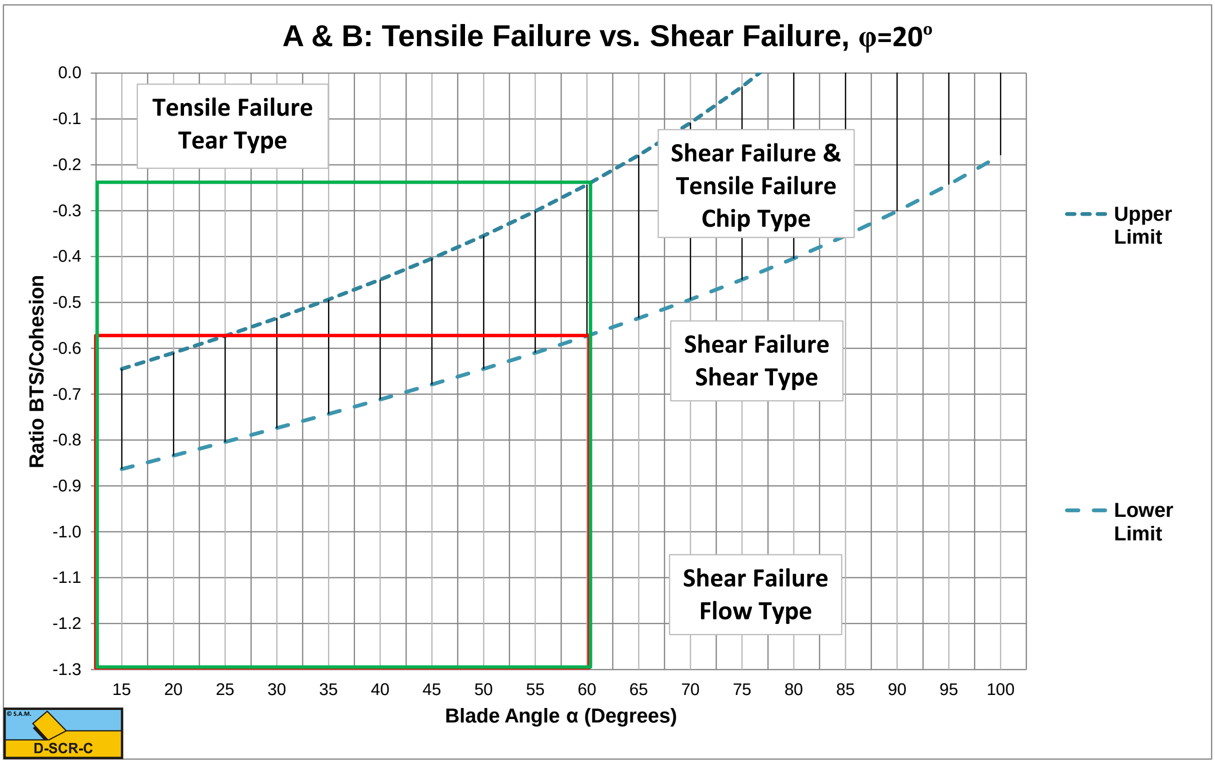

Figure W-9: The tensile/shear failure range based on BTS/Cohesion for φ=20º.

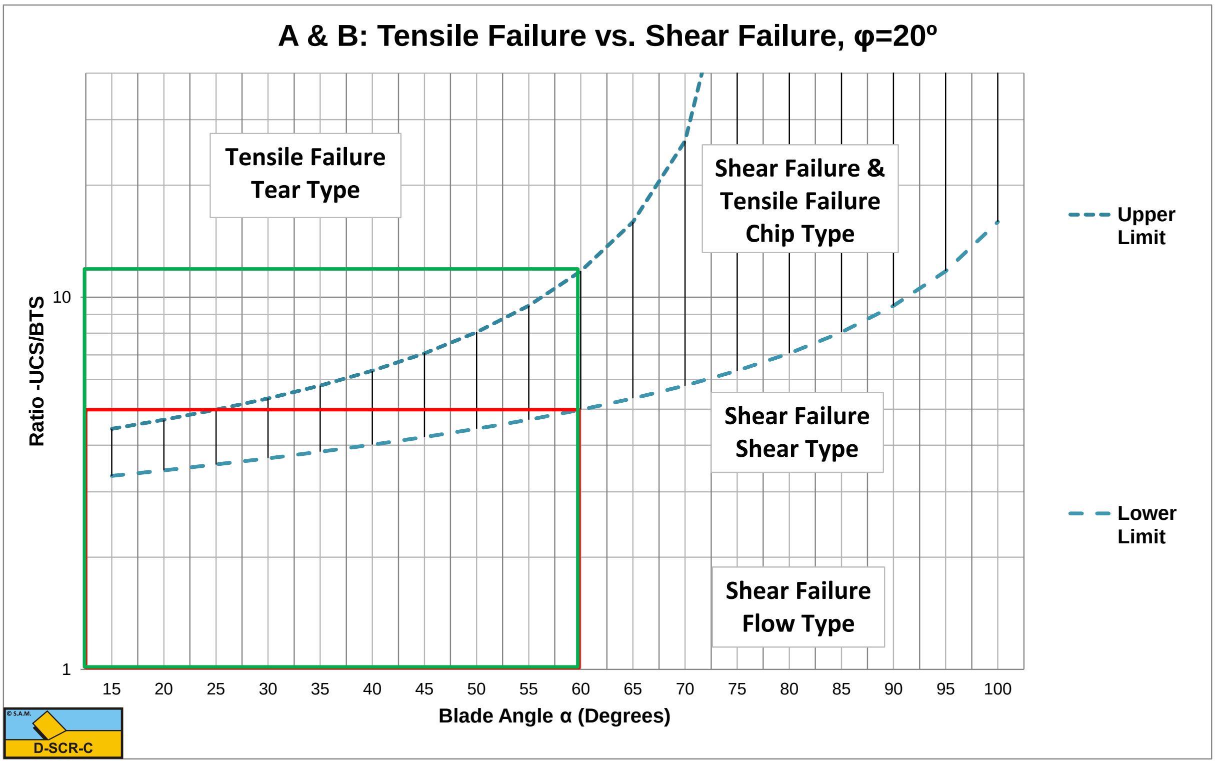

Figure W-10: The tensile/shear failure range based on UCS/BTS for φ=20º.

In all figures an example is given for a 60º blade and an internal friction angle of 20º.

W.4 Transition Ranges Brittle Shear/Brittle Tensile.

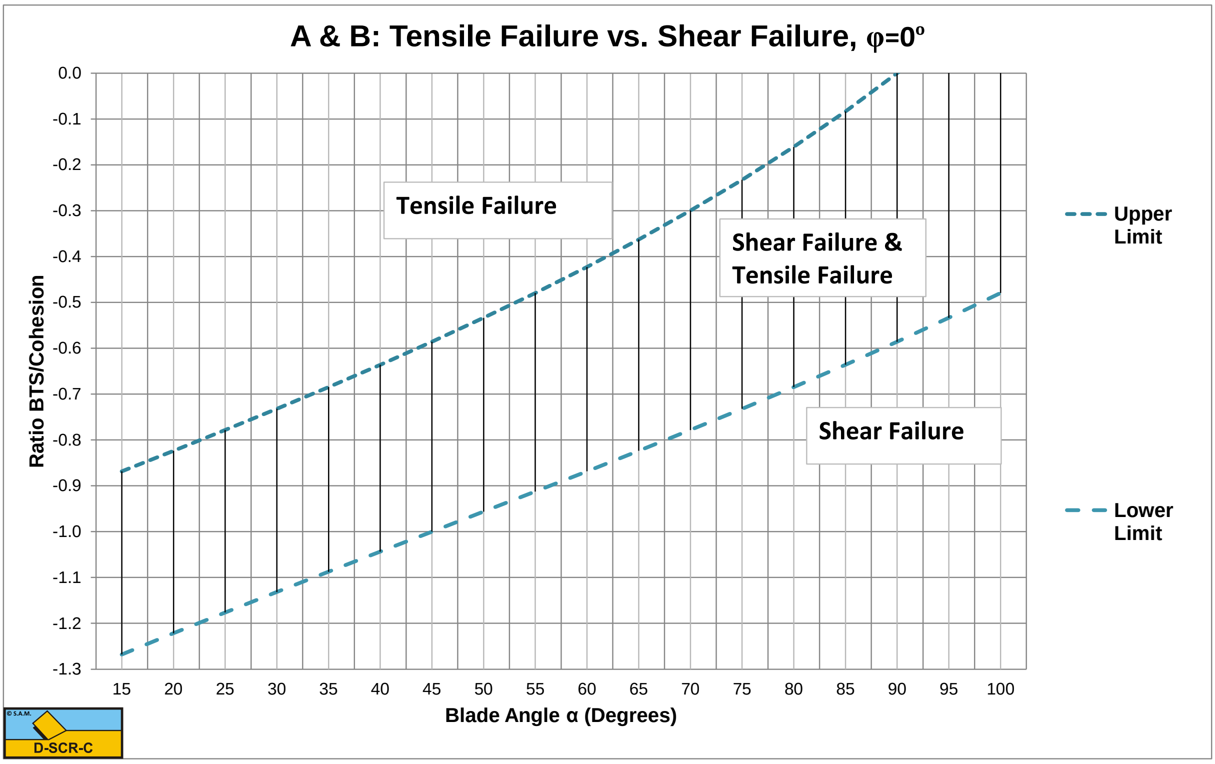

Figure W-11: The tensile/shear failure range based on BTS/Cohesion for φ=0°.

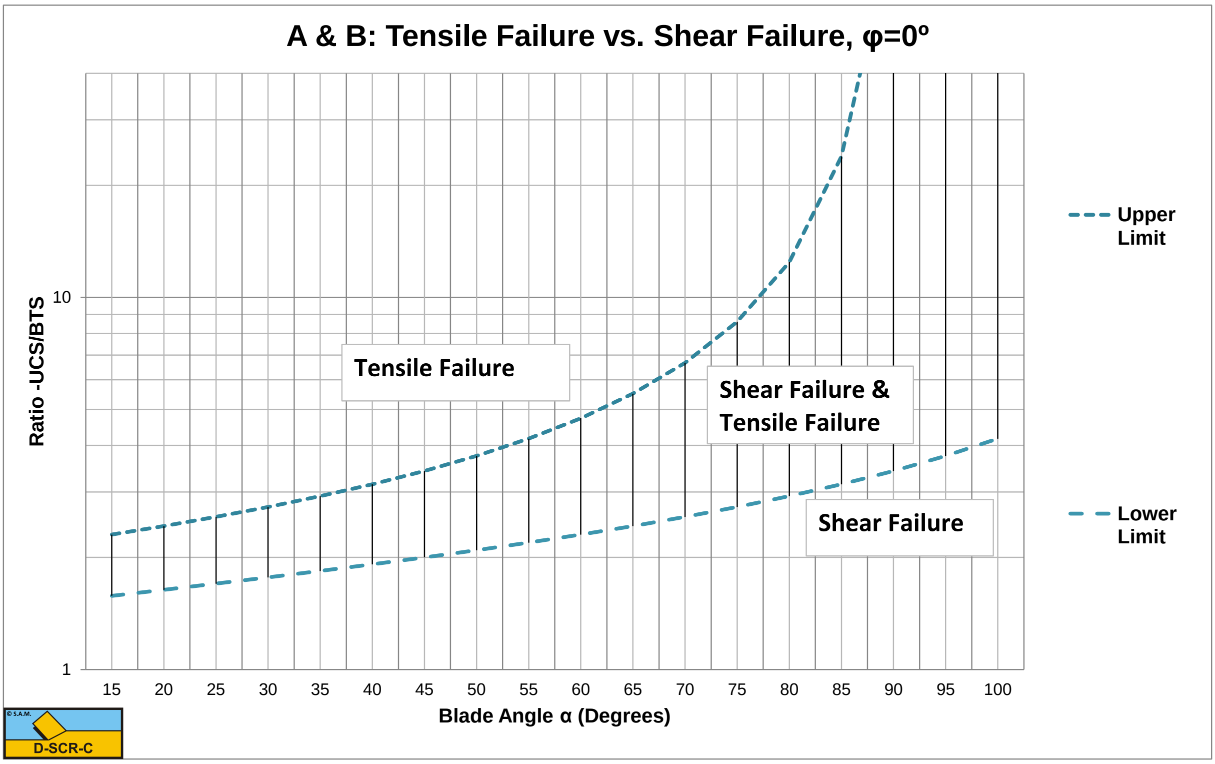

Figure W-12: The tensile/shear failure range based on UCS/BTS for φ=0°.

Figure W-13: The tensile/shear failure range based on BTS/Cohesion for φ=5º.

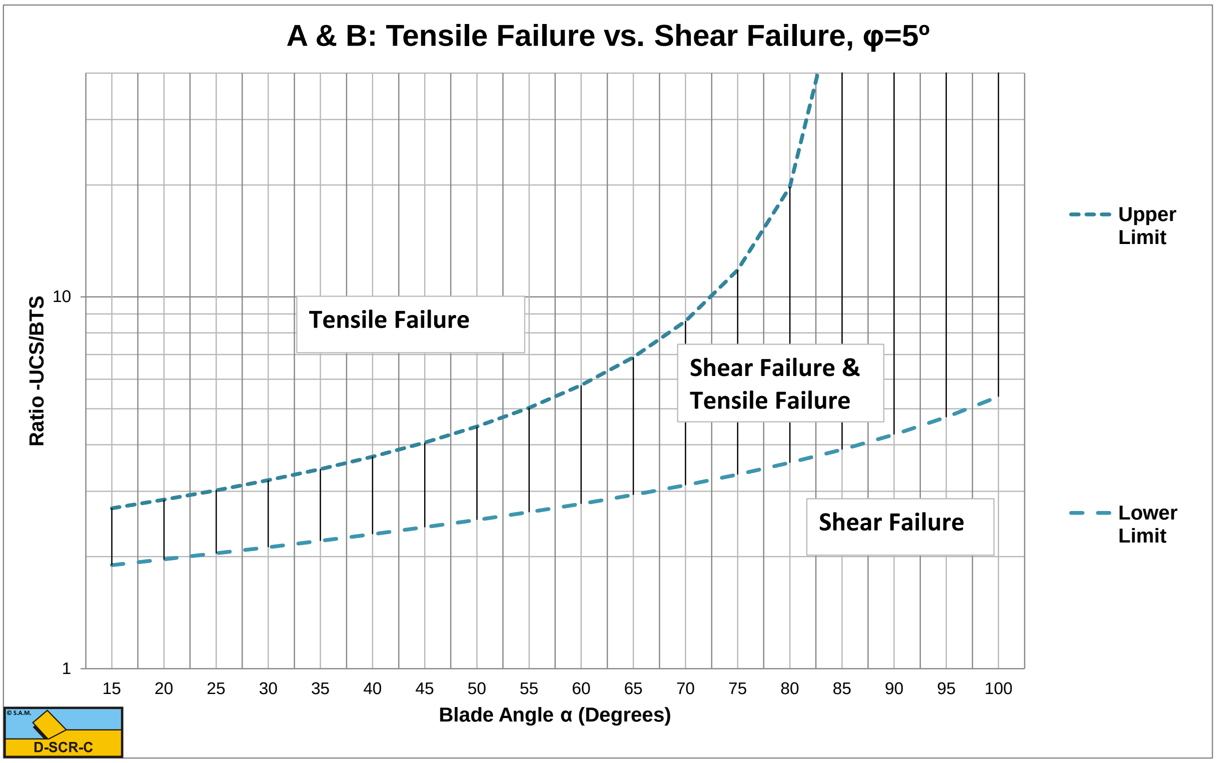

Figure W-14: The tensile/shear failure range based on UCS/BTS for φ=5º.

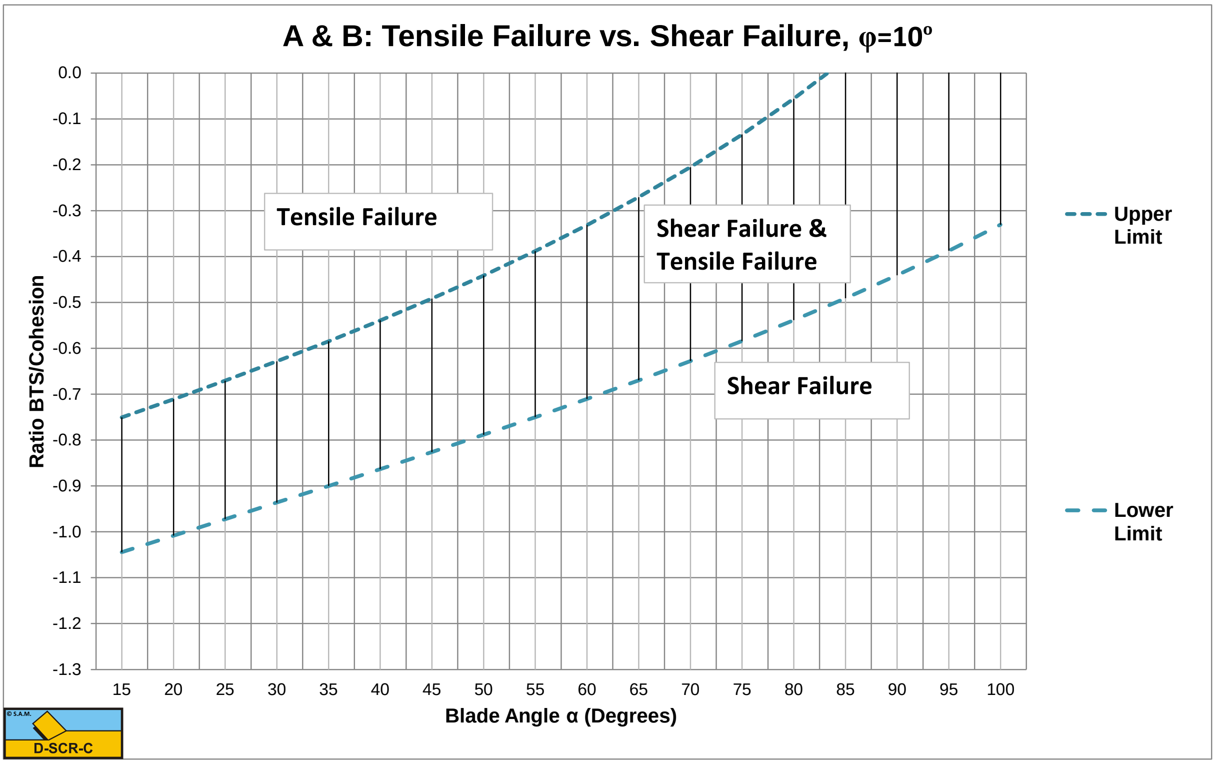

Figure W-15: The tensile/shear failure range based on BTS/Cohesion for φ=10º.

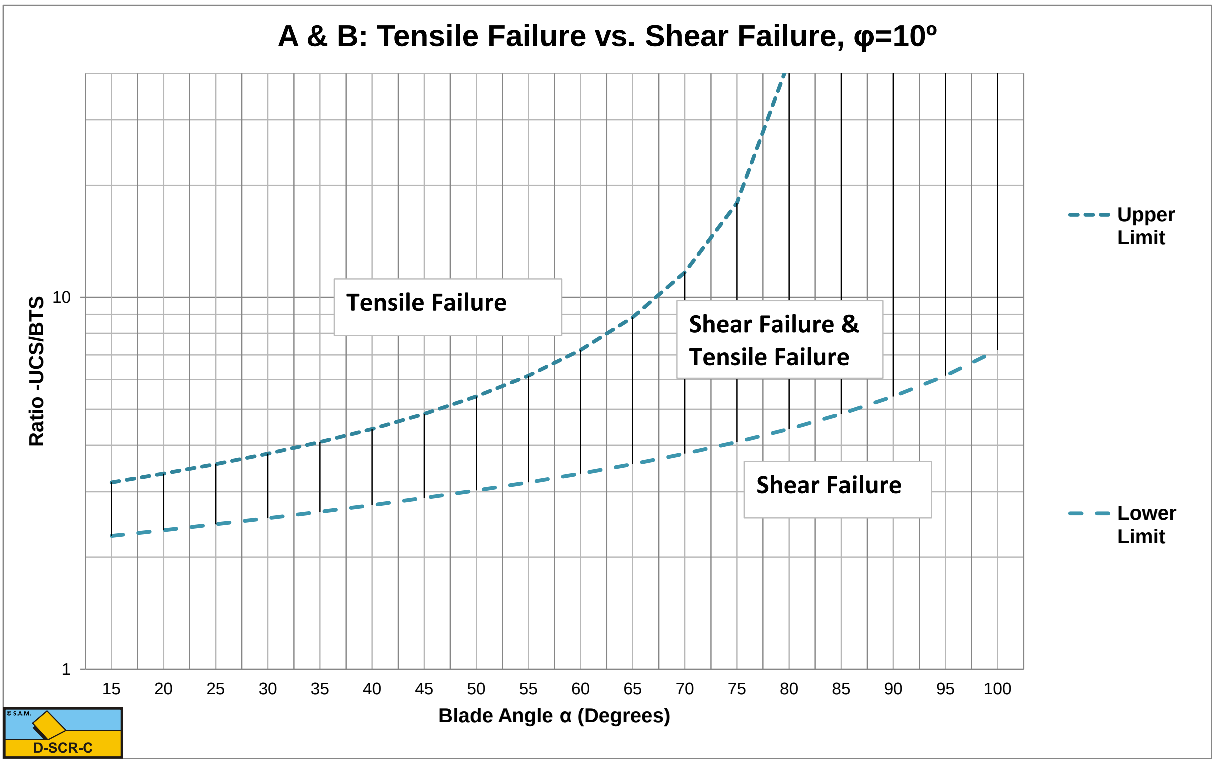

Figure W-16: The tensile/shear failure range based on UCS/BTS for φ=10º.

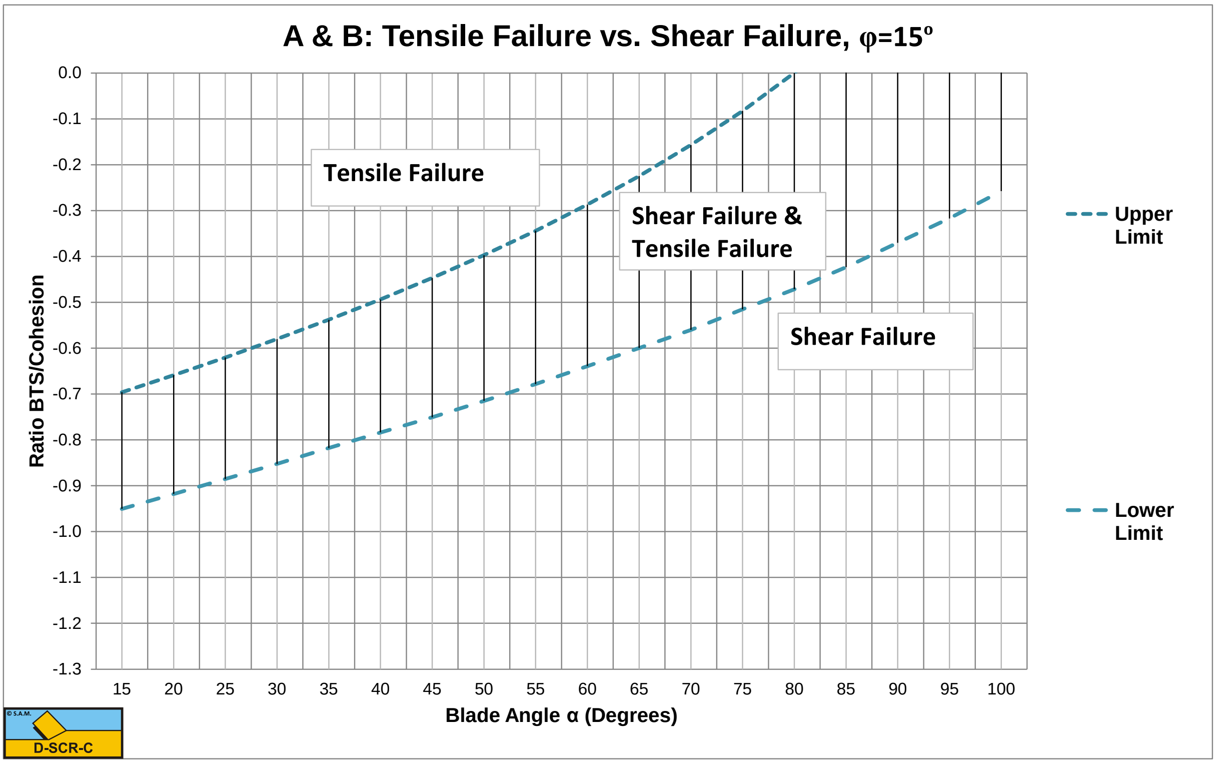

Figure W-17: The tensile/shear failure range based on BTS/Cohesion for φ=15º.

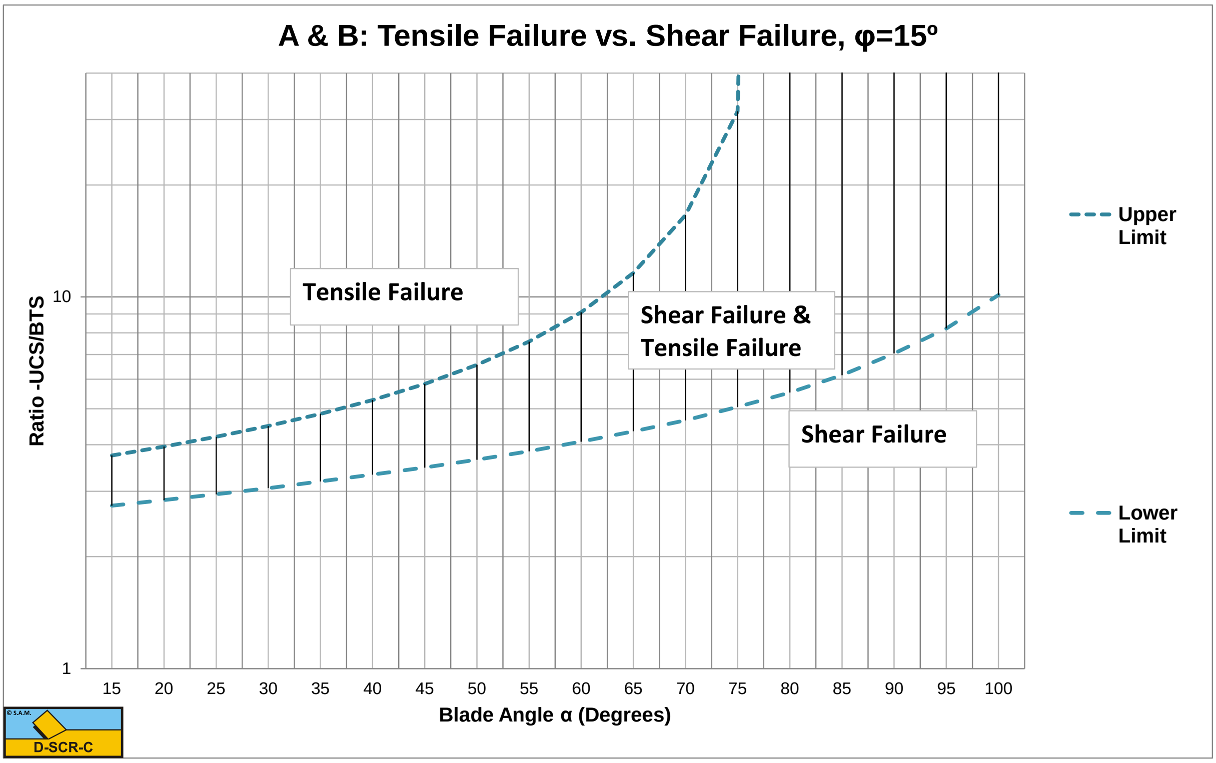

Figure W-18: The tensile/shear failure range based on UCS/BTS for φ=15º.

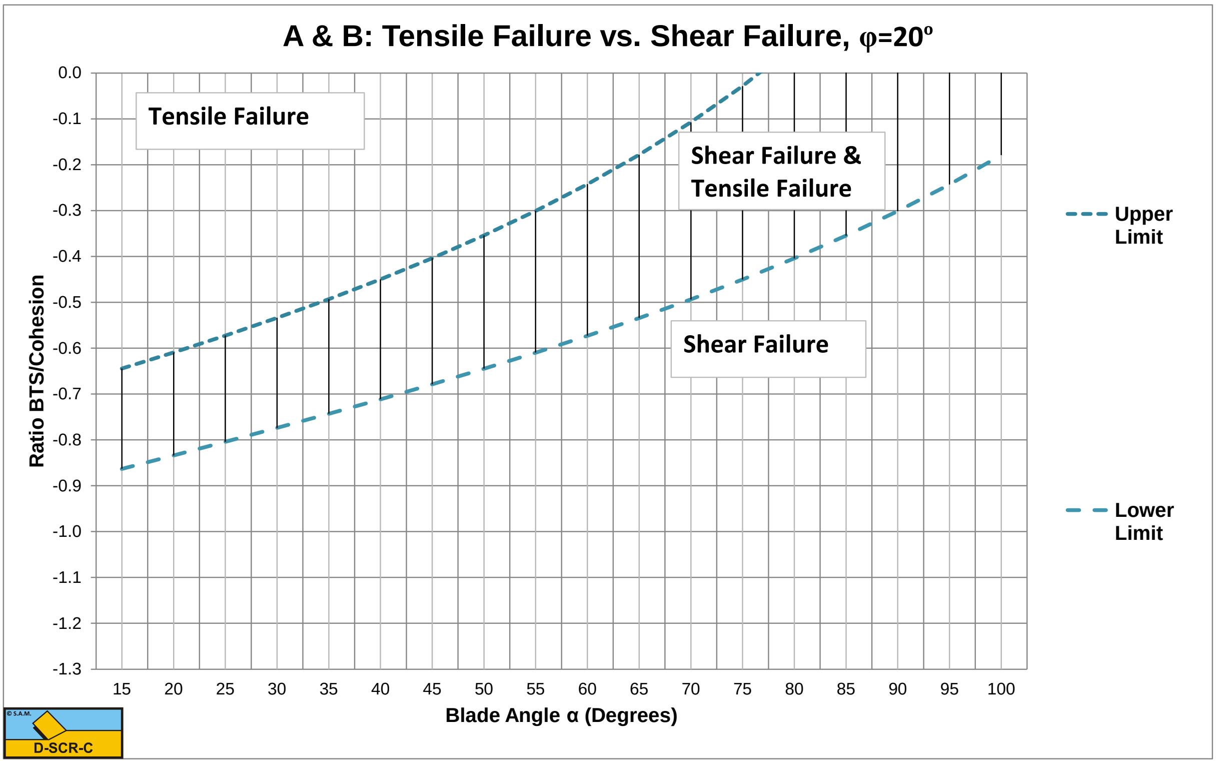

Figure W-19: The tensile/shear failure range based on BTS/Cohesion for φ=20º.

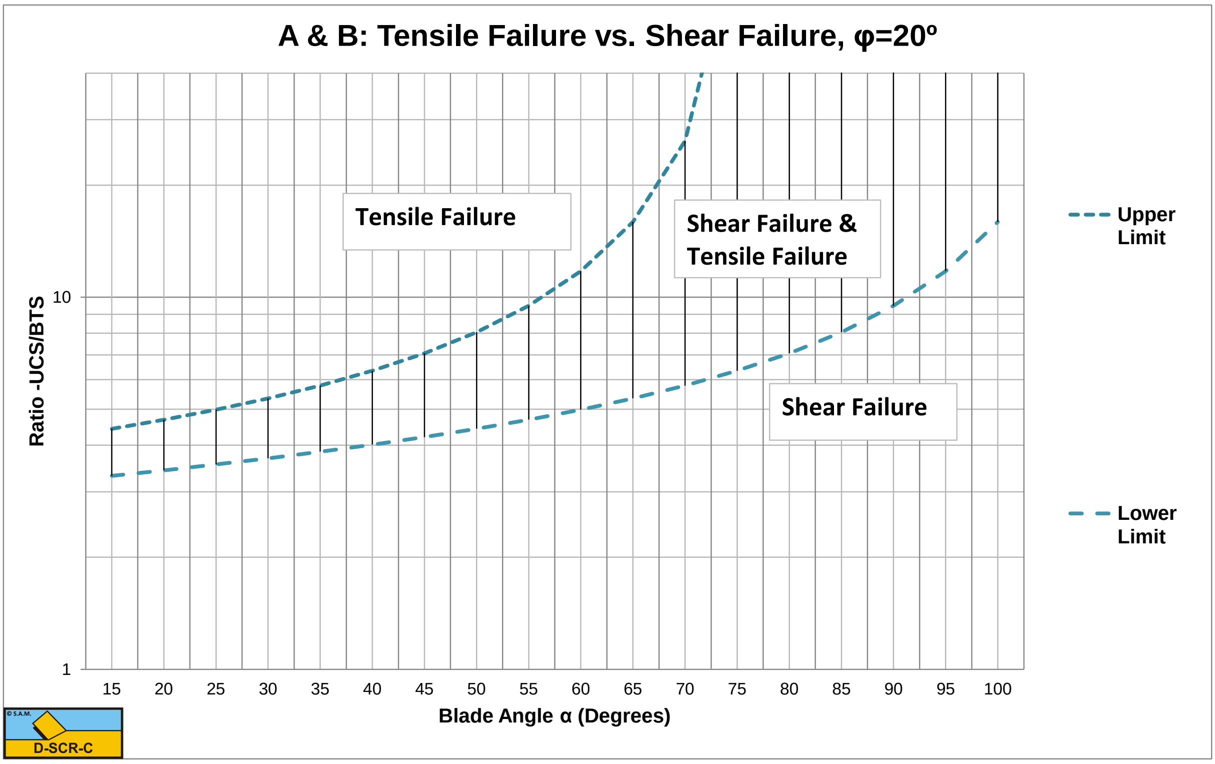

Figure W-20: The tensile/shear failure range based on UCS/BTS for φ=20º.

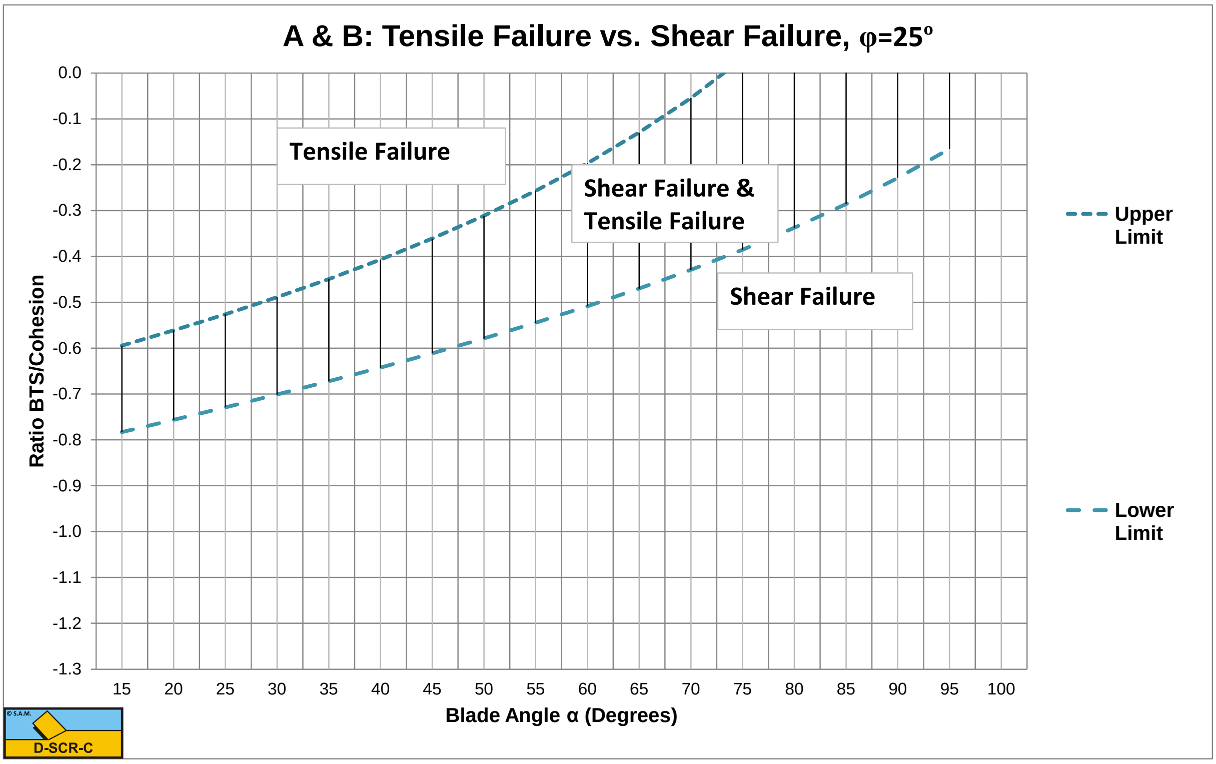

Figure W-21: The tensile/shear failure range based on BTS/Cohesion for φ=25º.

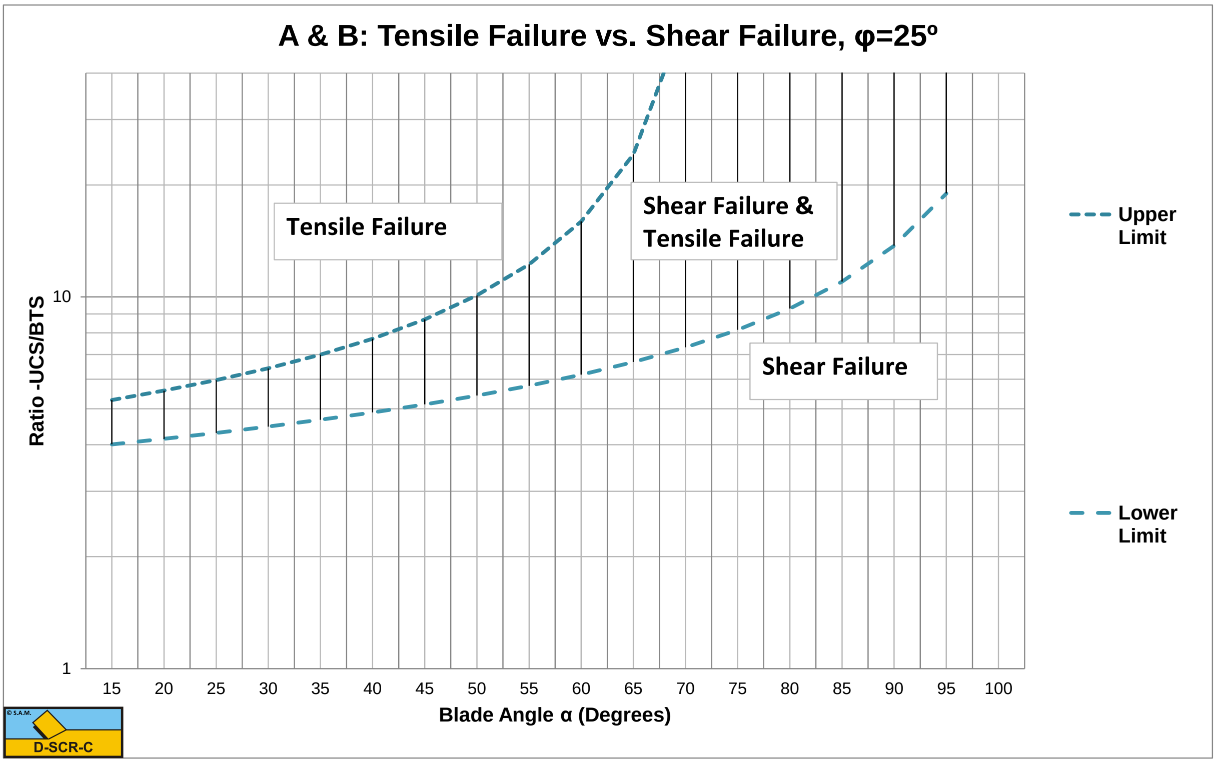

Figure W-22: The tensile/shear failure range based on UCS/BTS for φ=25º.

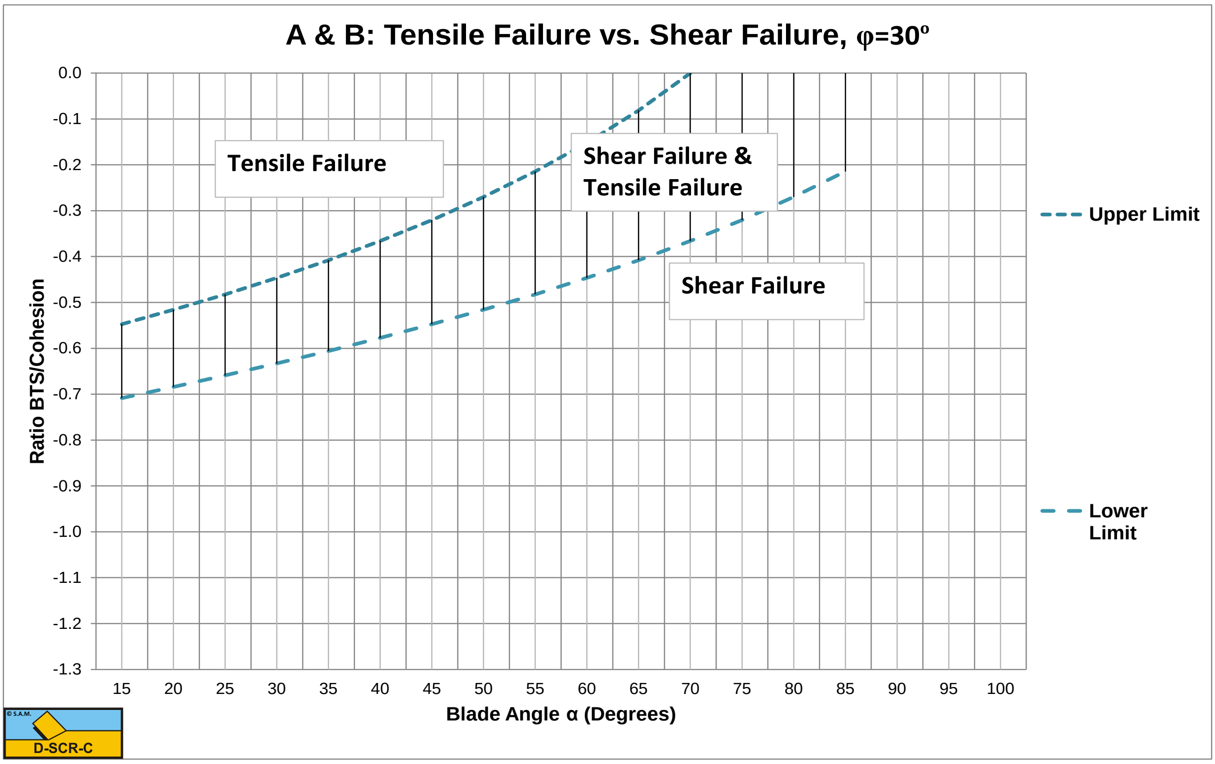

Figure W-23: The tensile/shear failure range based on BTS/Cohesion for φ=30º.

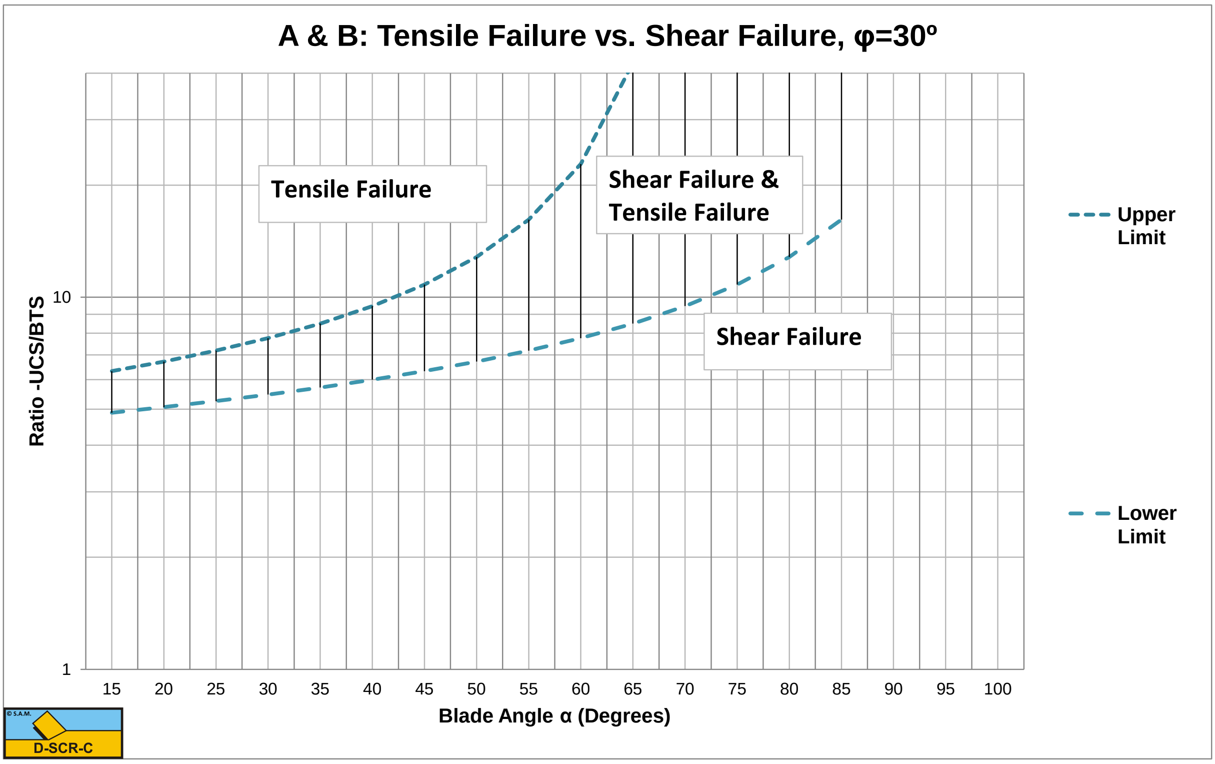

Figure W-24: The tensile/shear failure range based on UCS/BTS for φ=30º.

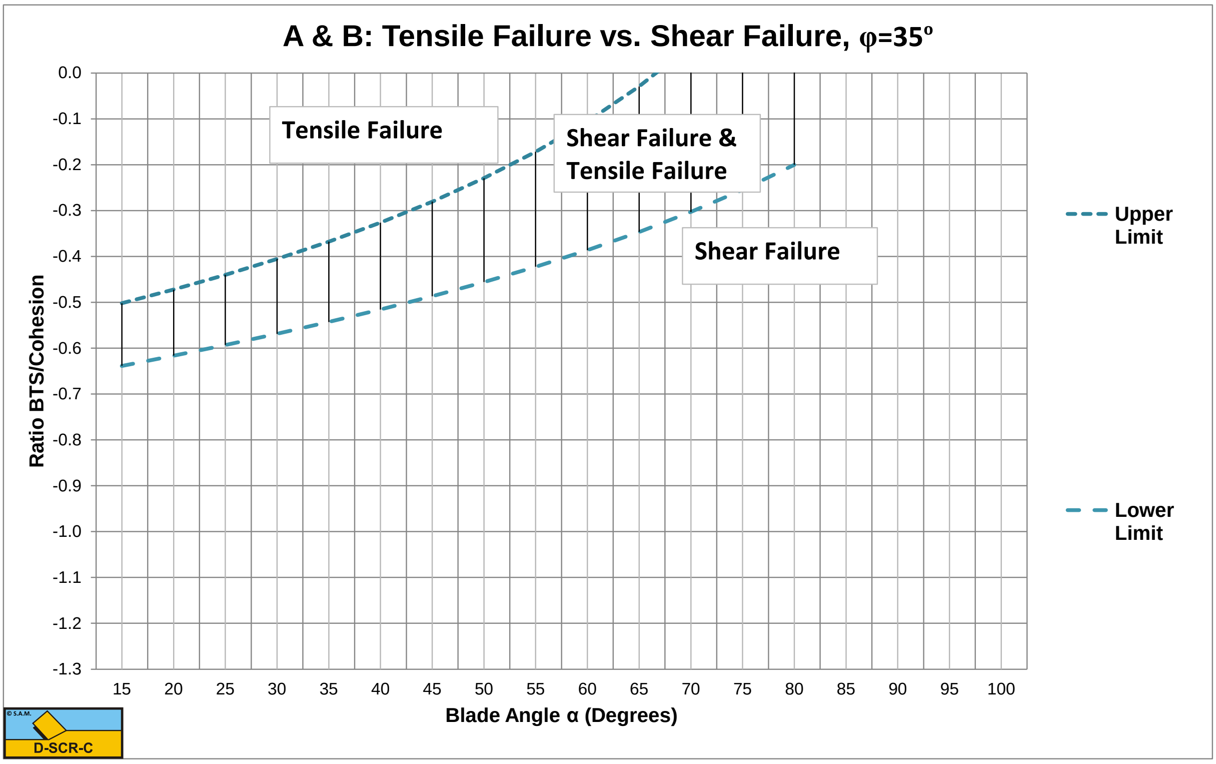

Figure W-25: The tensile/shear failure range based on BTS/Cohesion for φ=35º.

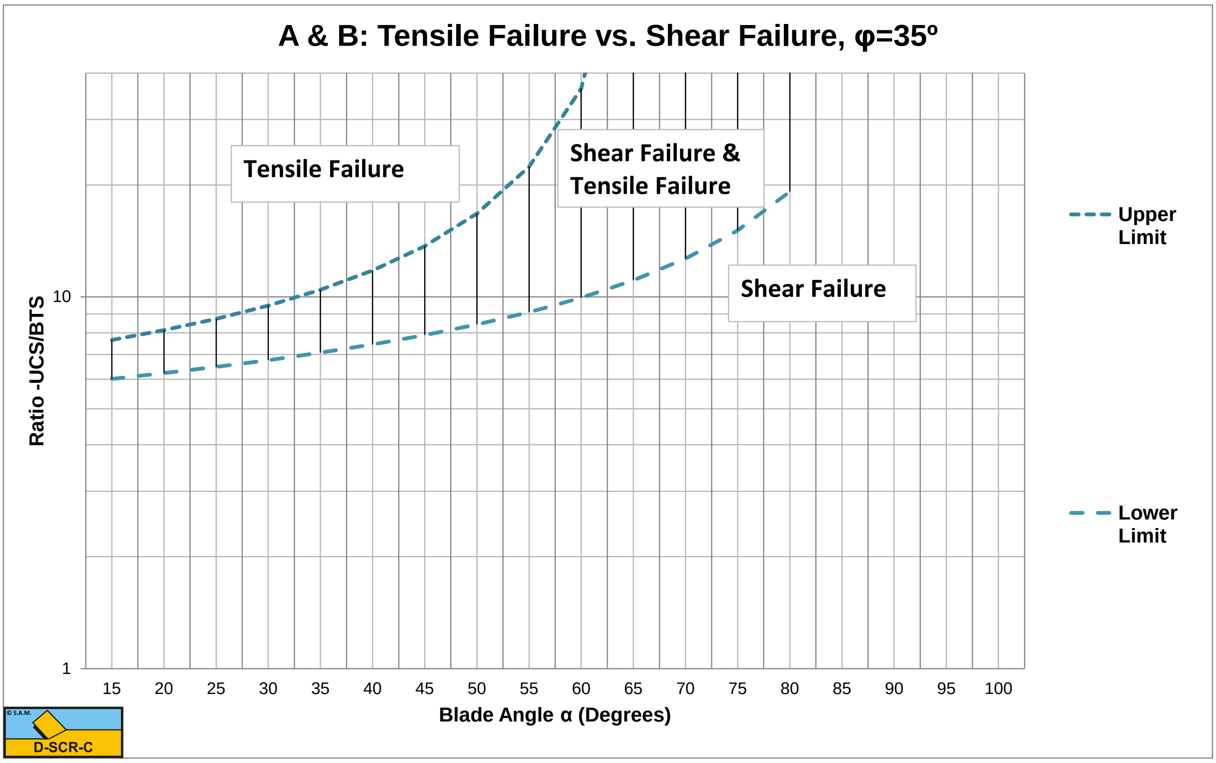

Figure W-26: The tensile/shear failure range based on UCS/BTS for φ=35º.

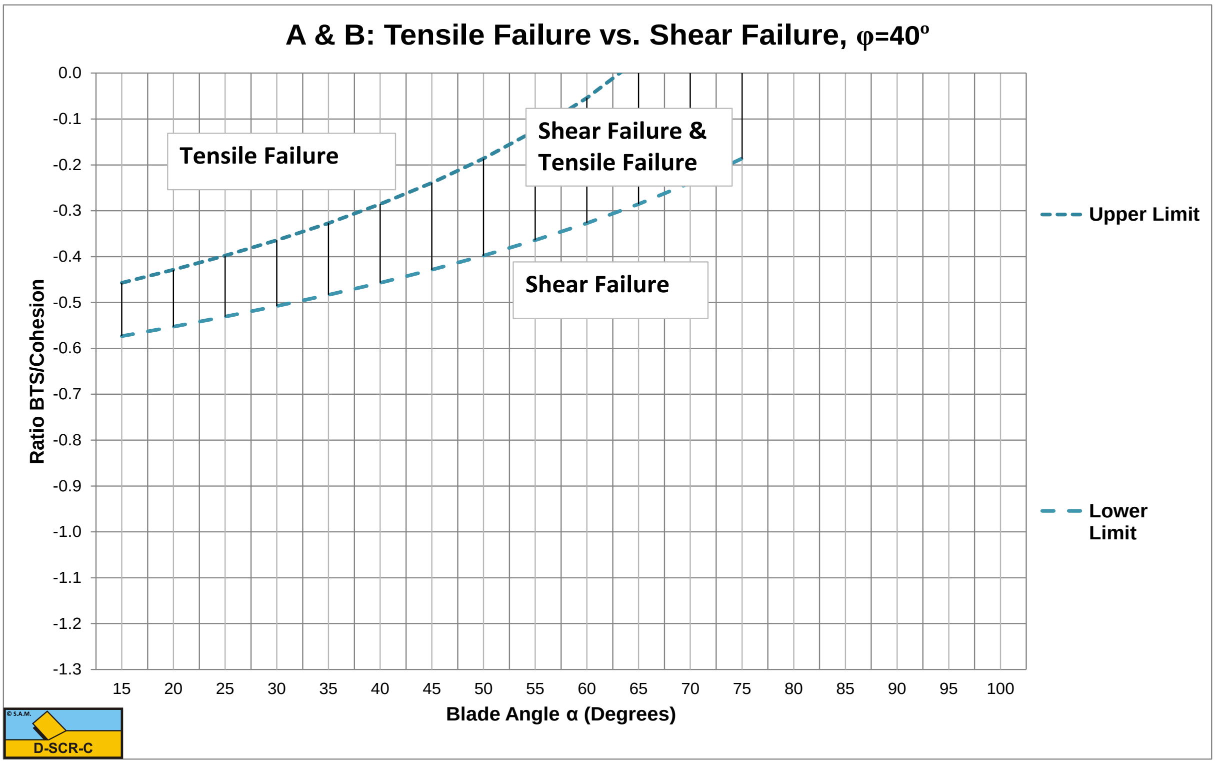

Figure W-27: The tensile/shear failure range based on BTS/Cohesion for φ=40º.

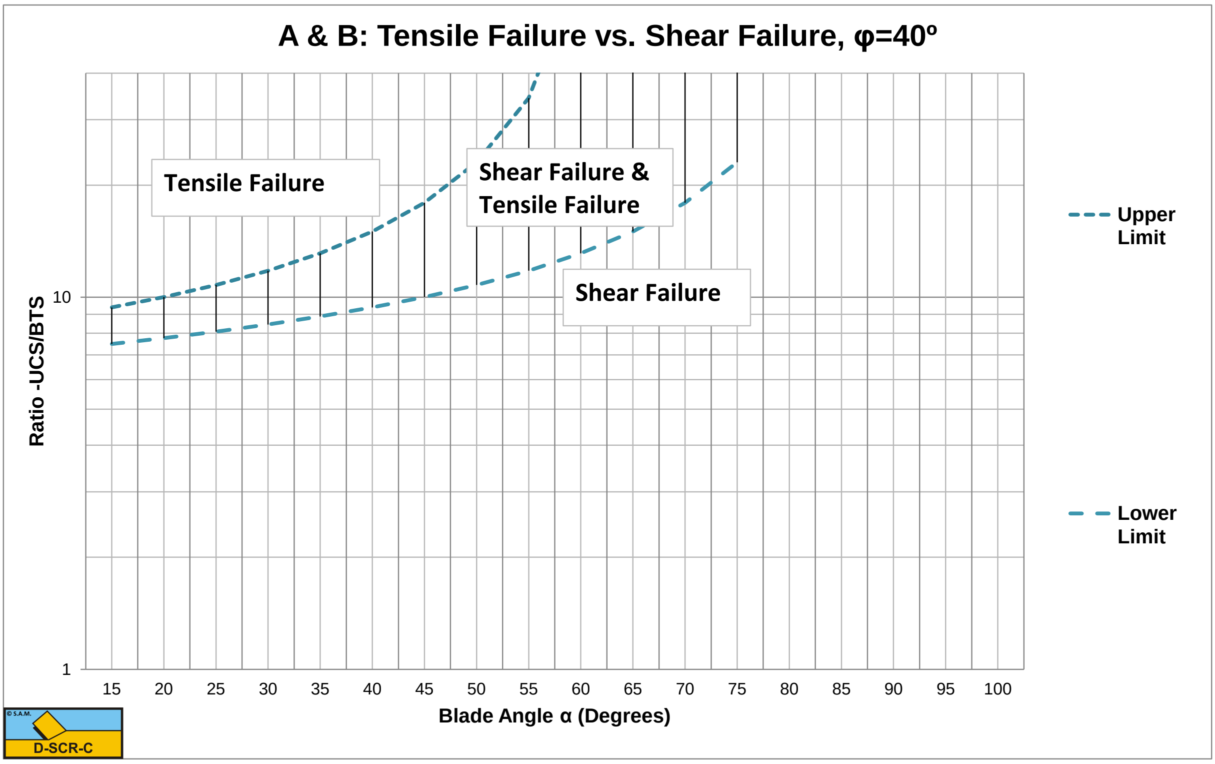

Figure W-28: The tensile/shear failure range based on UCS/BTS for φ=40º.

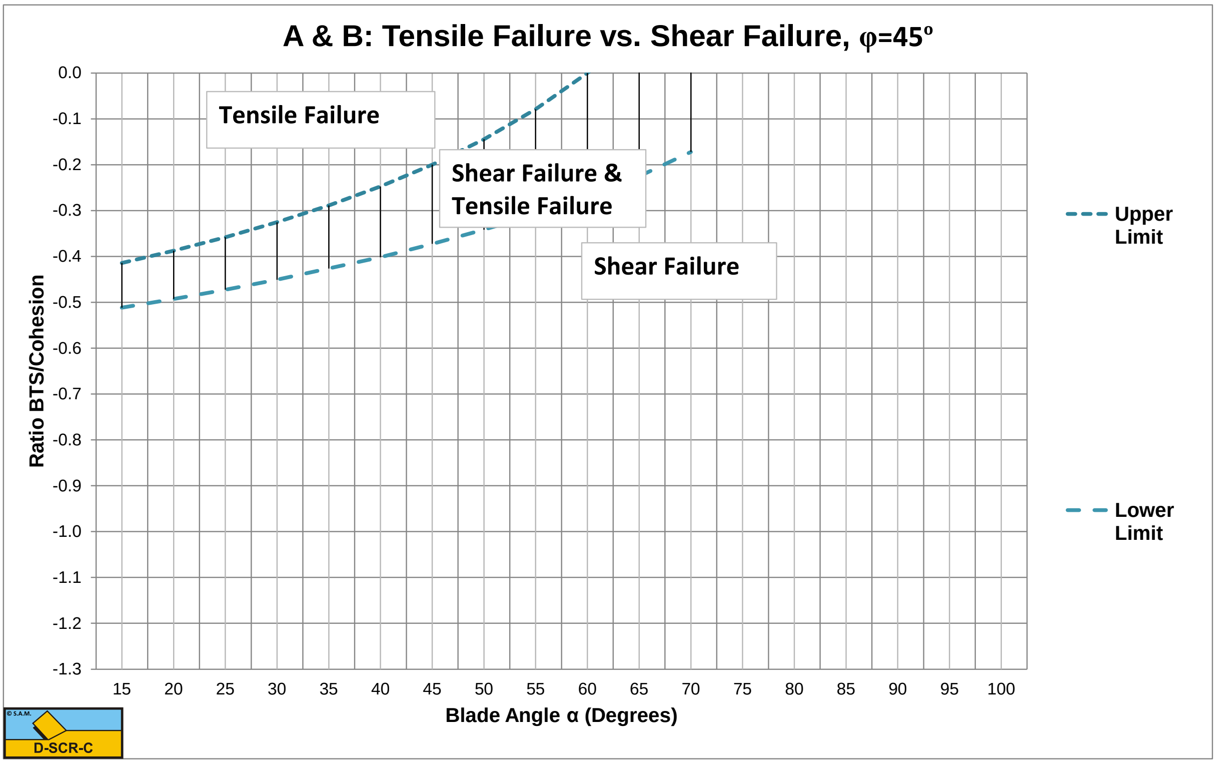

Figure W-29: The tensile/shear failure range based on BTS/Cohesion for φ=45º.

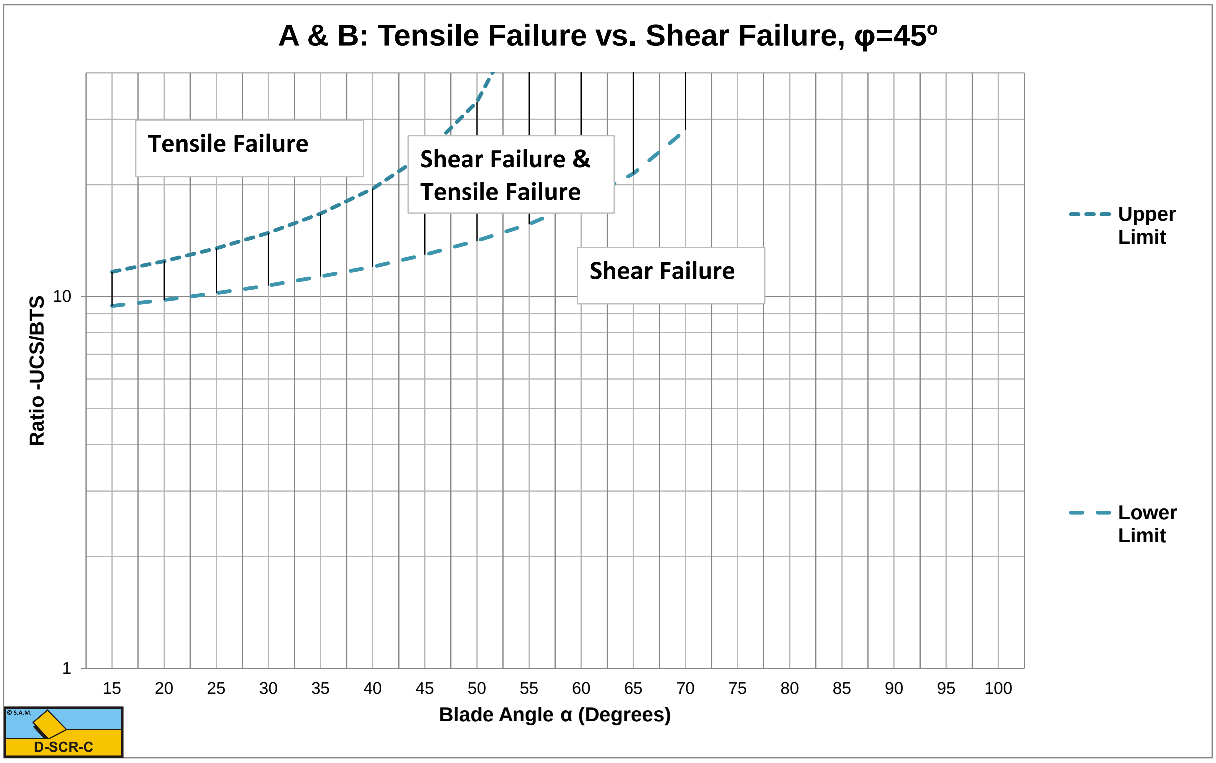

Figure W-30: The tensile/shear failure range based on UCS/BTS for φ=45º.

W.5 Brittle Tensile Failure based on Brittle Shear Shear Angle.

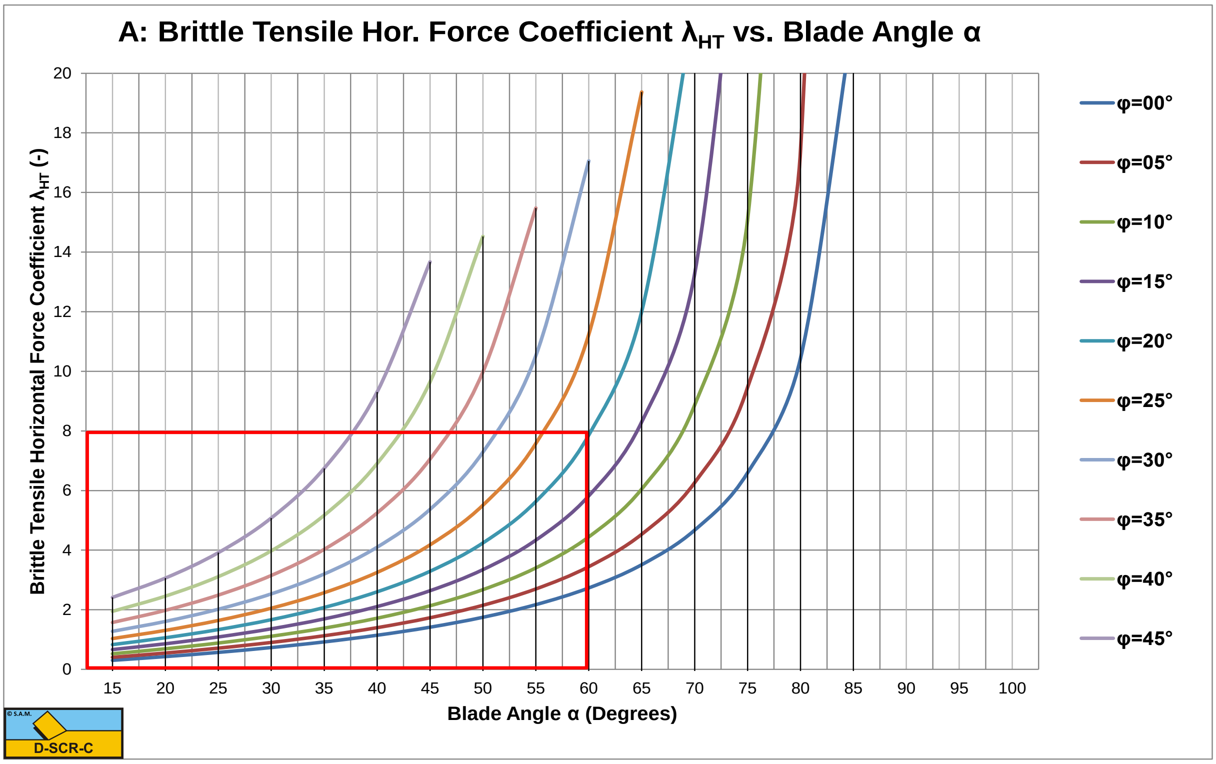

Figure W-31: The brittle (tensile failure) horizontal force coefficient λ_{HT}.

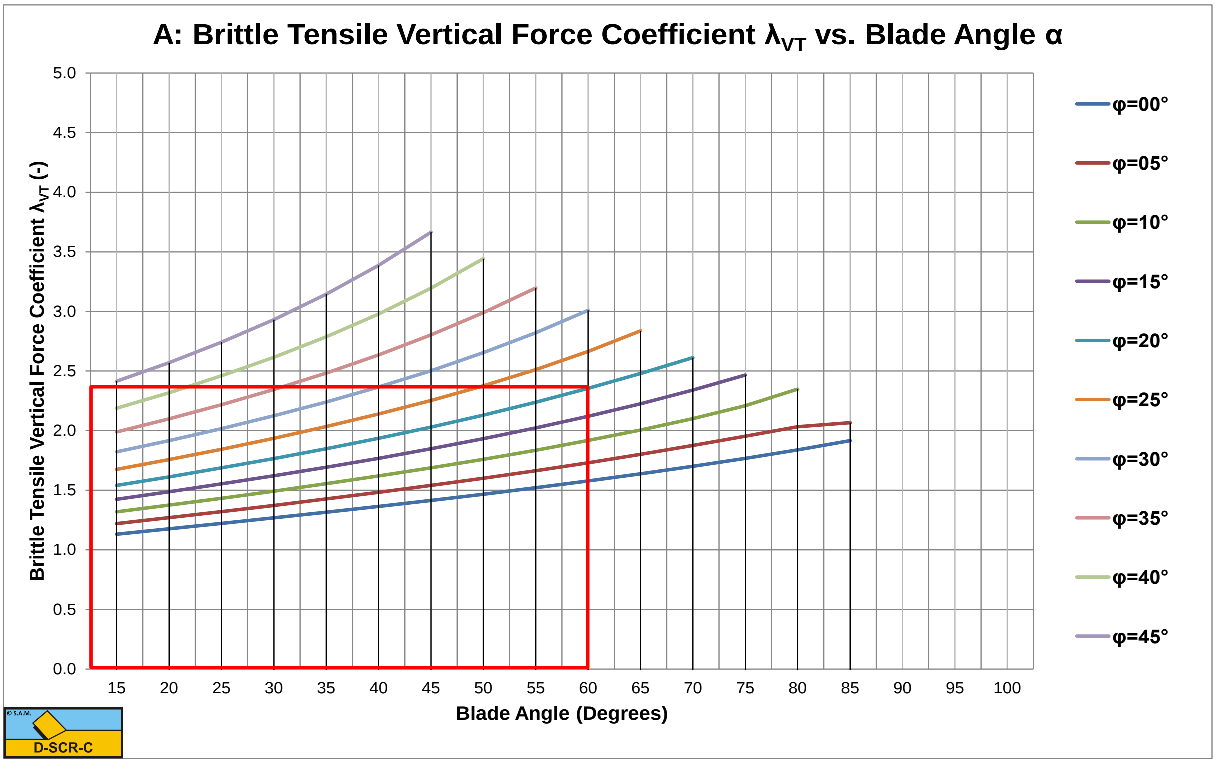

Figure W-32: The brittle (tensile failure) vertical force coefficient λ_{VT}.

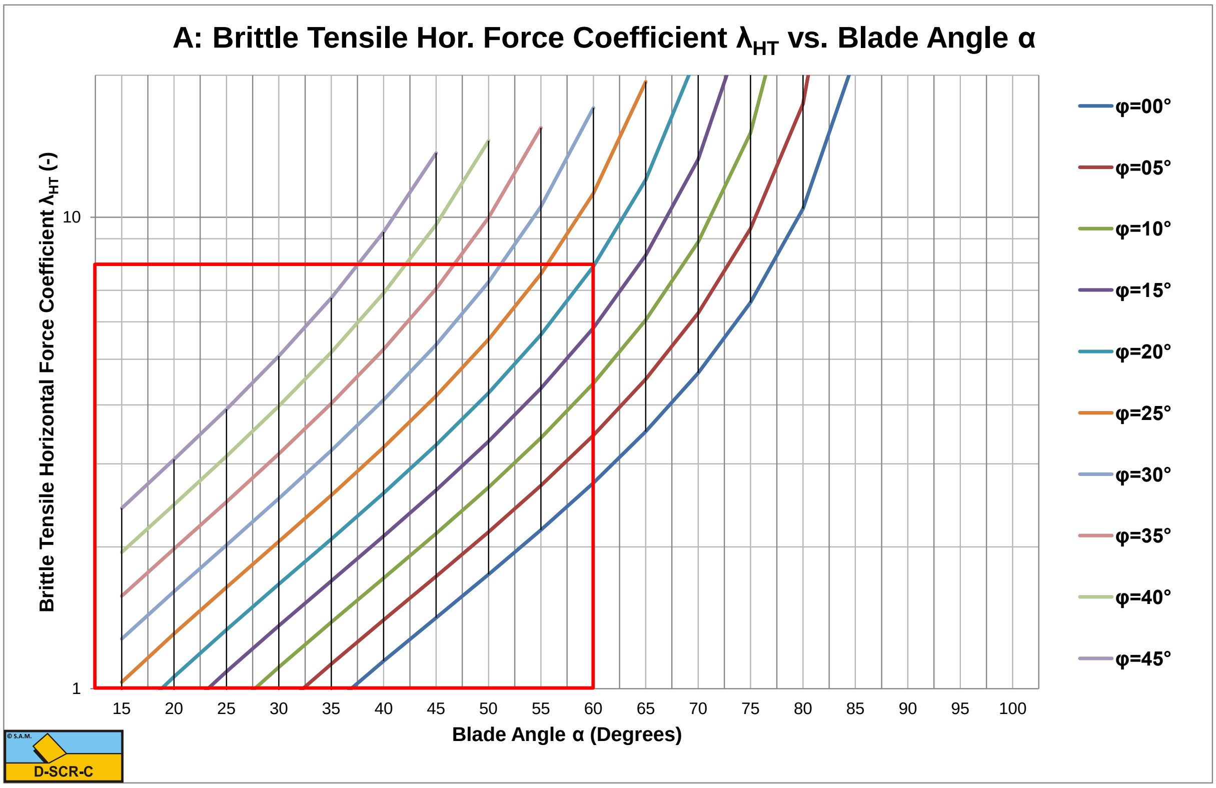

Figure W-33: The brittle (tensile failure) horizontal force coefficient λ_{HT} (DSCRCM, logarithmic).

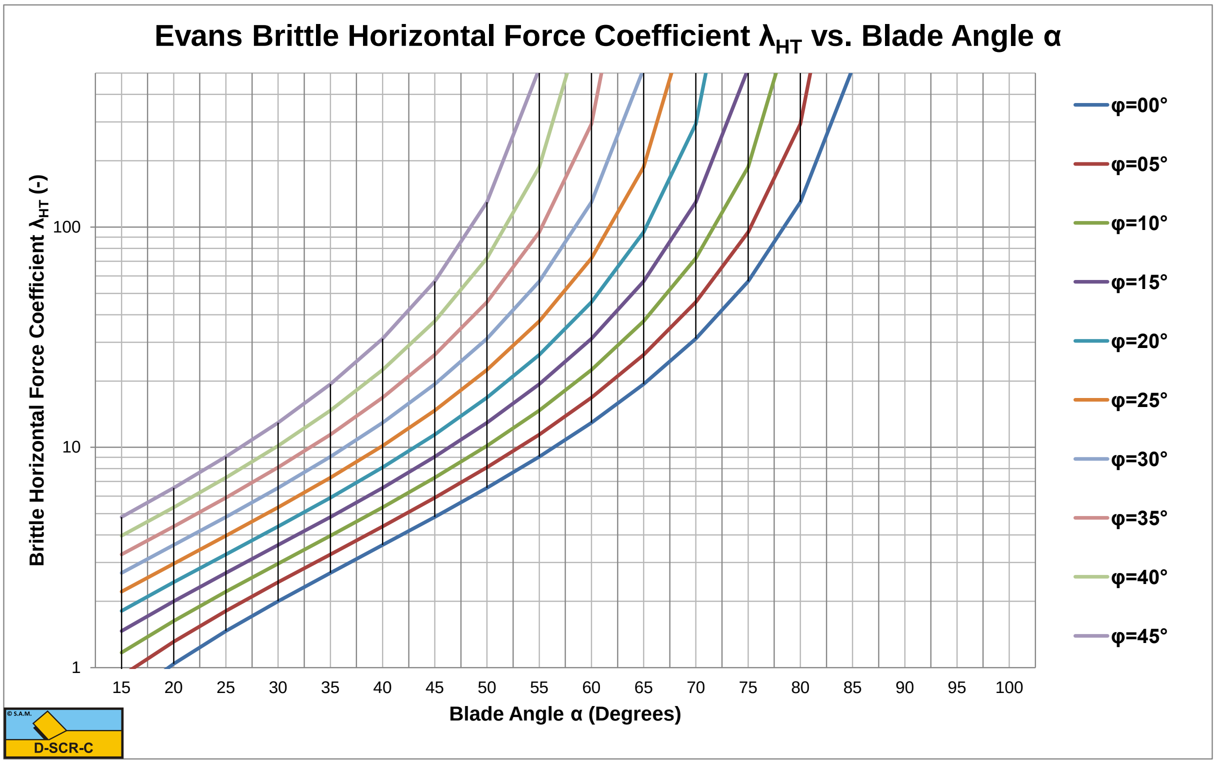

Figure W-34: The brittle (tensile failure) horizontal force coefficient λ_{HT} (Evans, logarithmic).

The Evans approach gives much higher values, since it is based on reaching the tensile strength in the whole failure plane. The DSCRCM model assumes reaching the tensile strength only at the start of the tensile crack.

W.6 Brittle Tensile Failure based on Brittle Tensile Shear Angle.

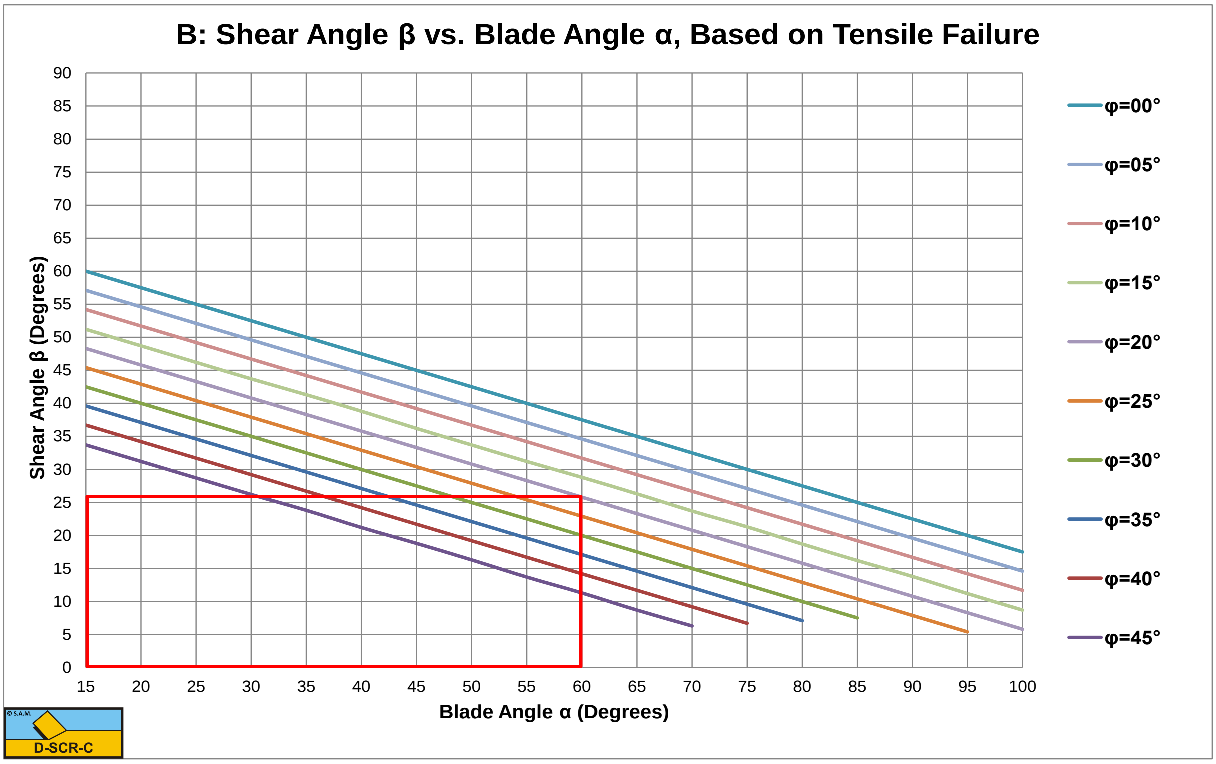

Figure W-35: The shear angle β as a function of the blade angle α and the internal friction angle φ for shear failure, corrected.

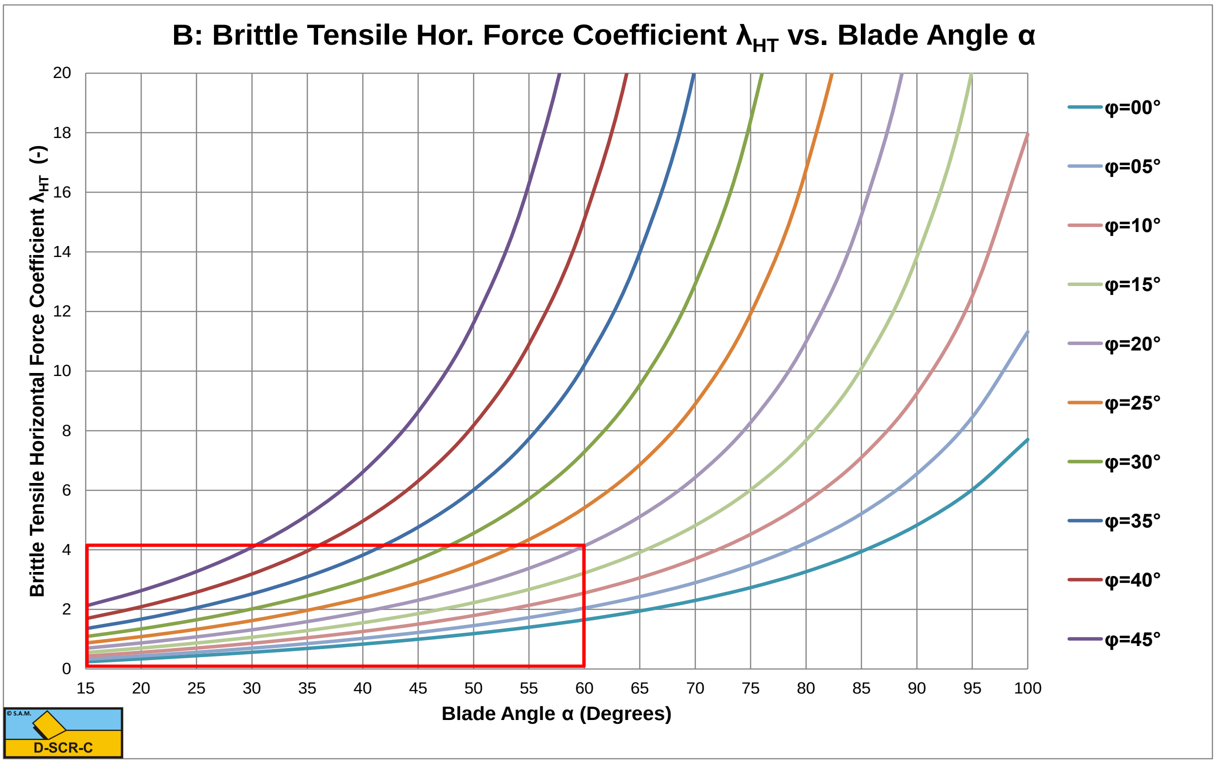

Figure W-36: The brittle (tensile failure) horizontal force coefficient λ_{HT}, corrected.

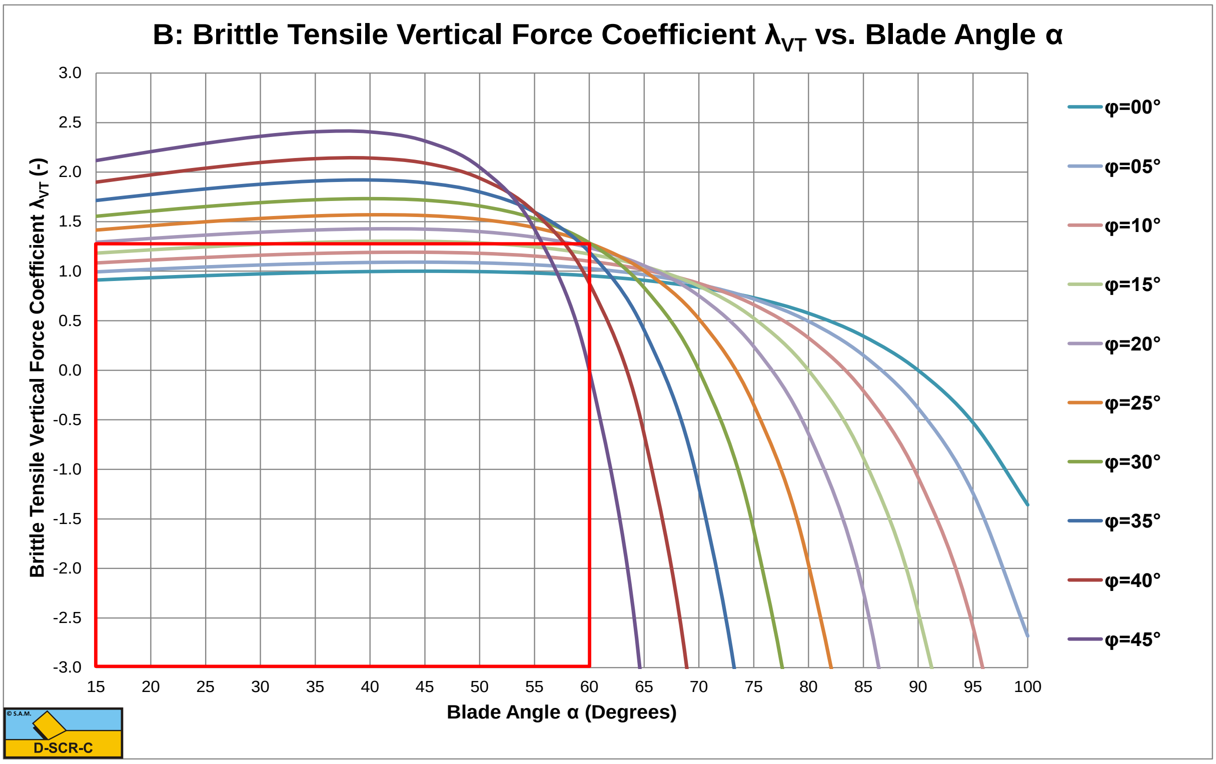

Figure W-37: The brittle (tensile failure) vertical force coefficient λ_{VT} , corrected.

Appendix X: Hyperbaric Rock Cutting Charts.

X.1 The Curling Type of the 30 Degree Blade.

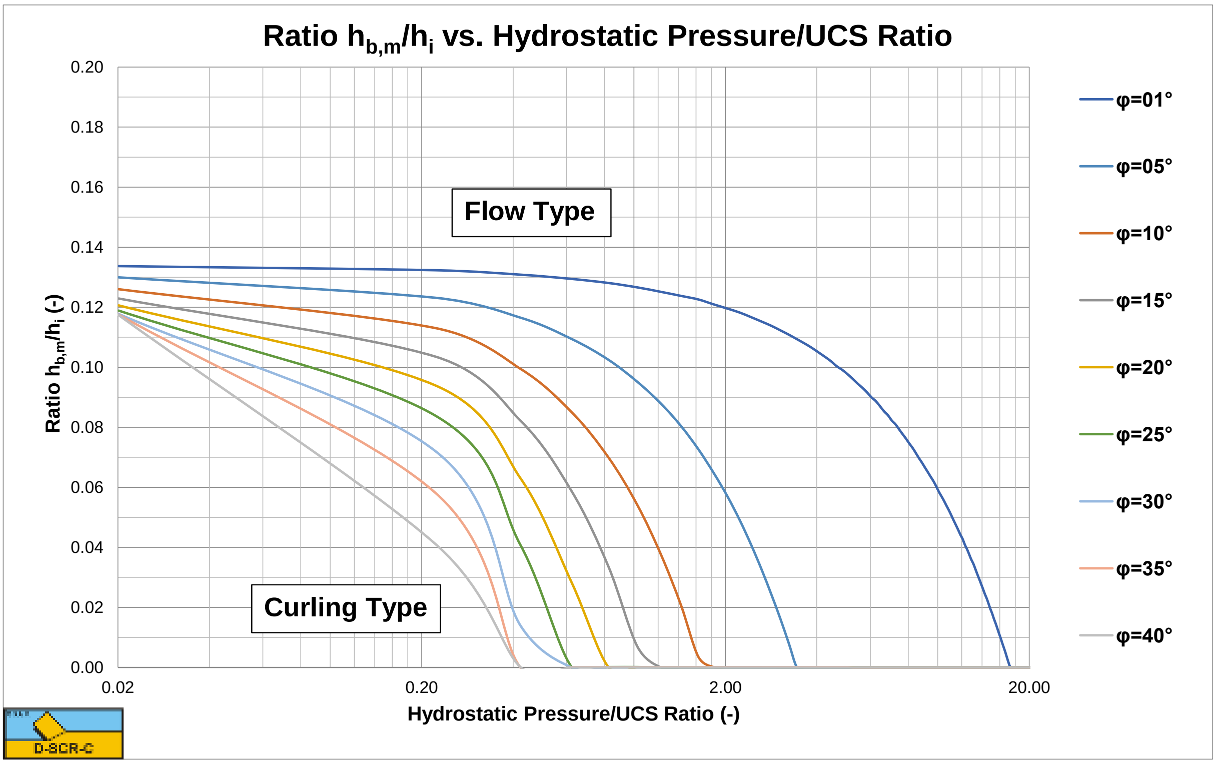

Figure X-1: The ratio $h_{b,m}/h_i$ for a 30 degree blade.

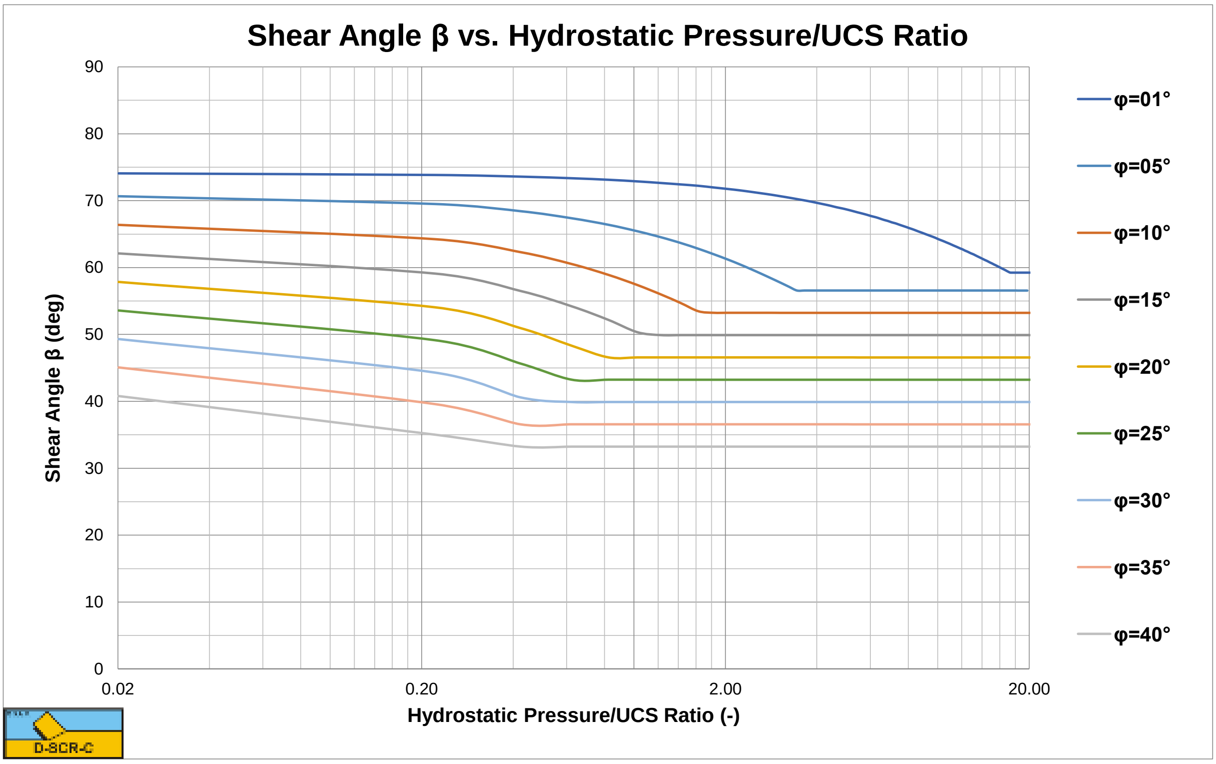

Figure X-2: The shear angle β for a 30 degree blade.

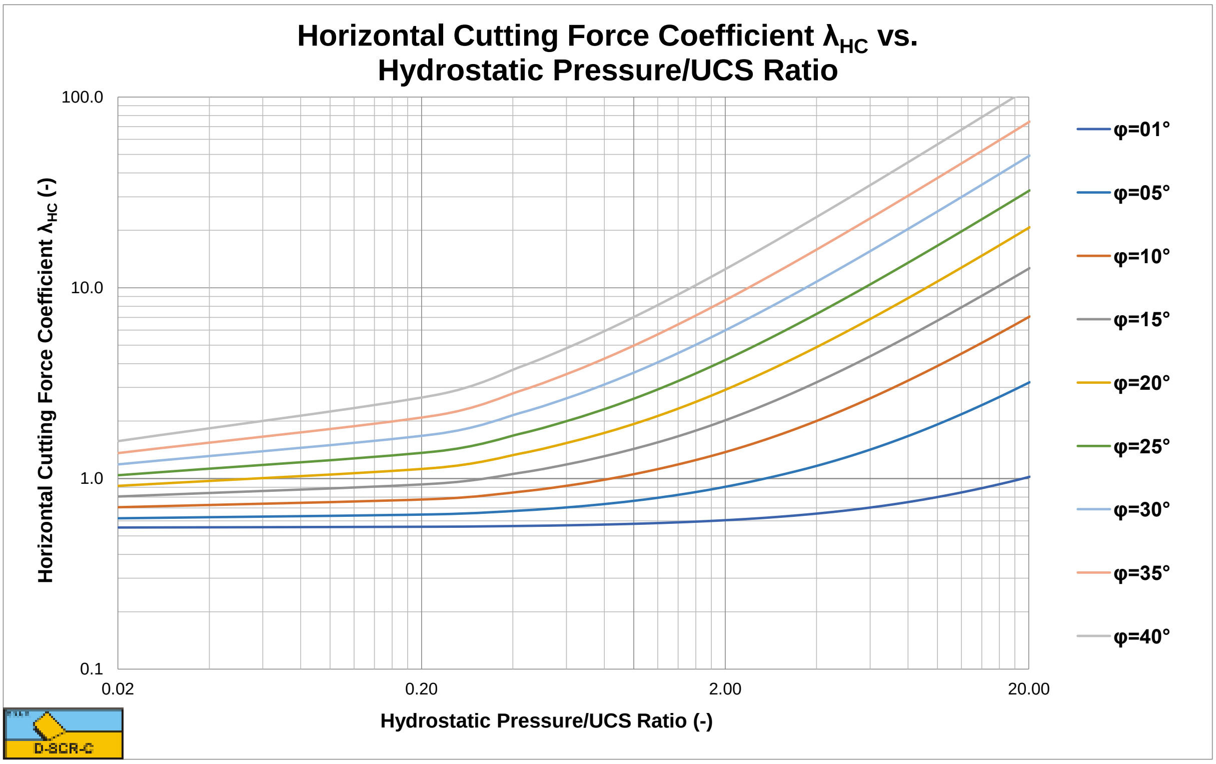

Figure X-3: The horizontal cutting force coefficient λ_{HC} for a 30 degree blade.

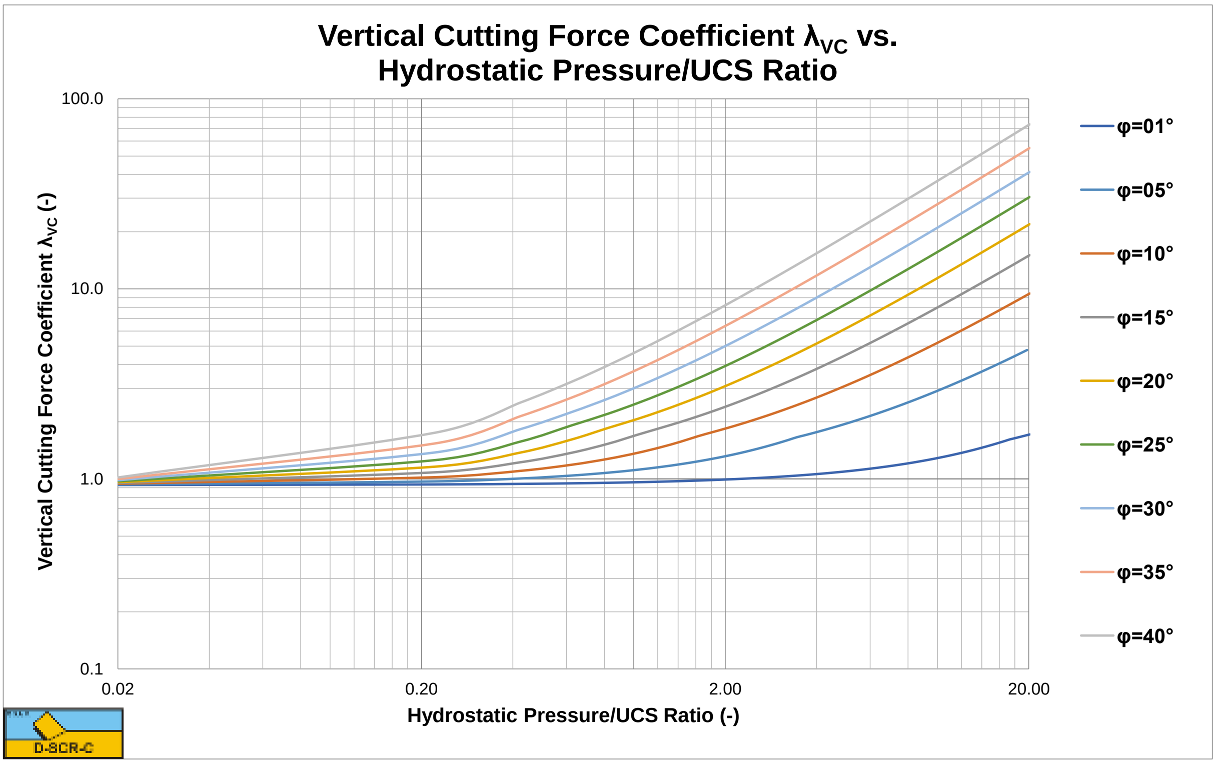

Figure X-4: The vertical cutting force coefficient λ_{VC} for a 30 degree blade.

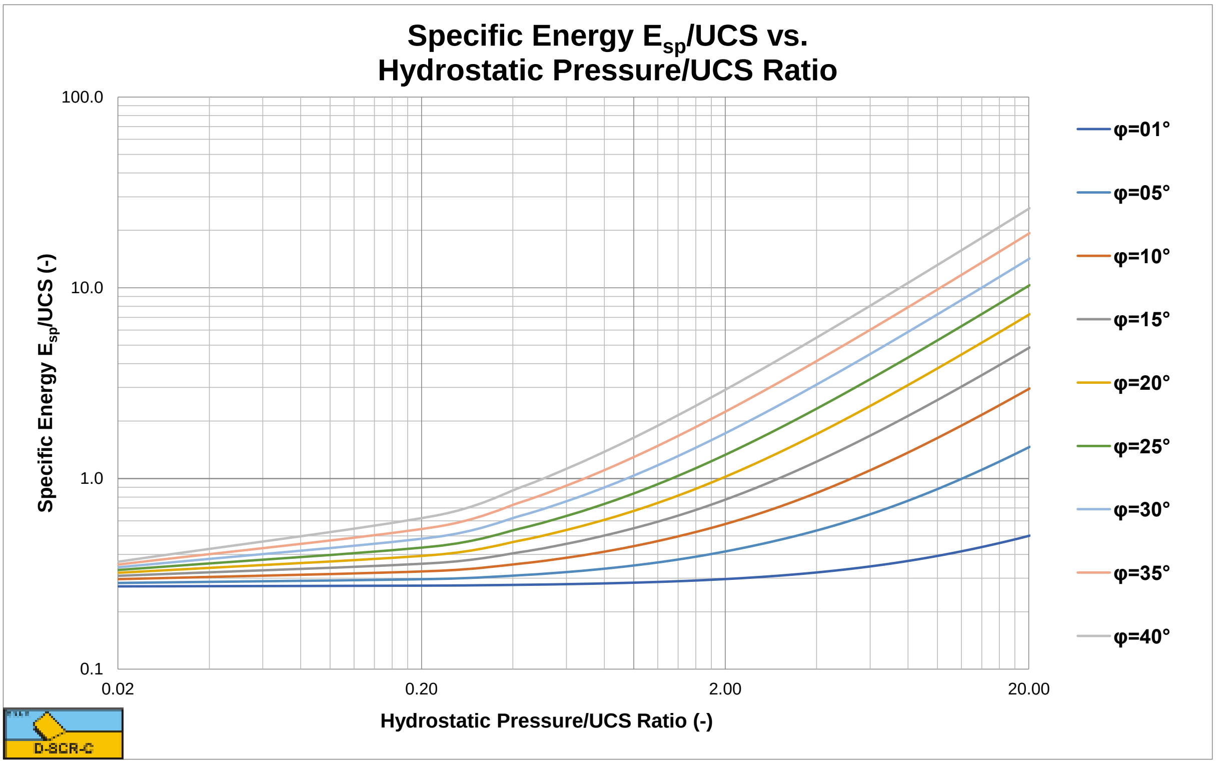

Figure X-5: The specific energy to UCS ratio for a 30 degree blade.

X.2 The Curling Type of the 45 Degree Blade.

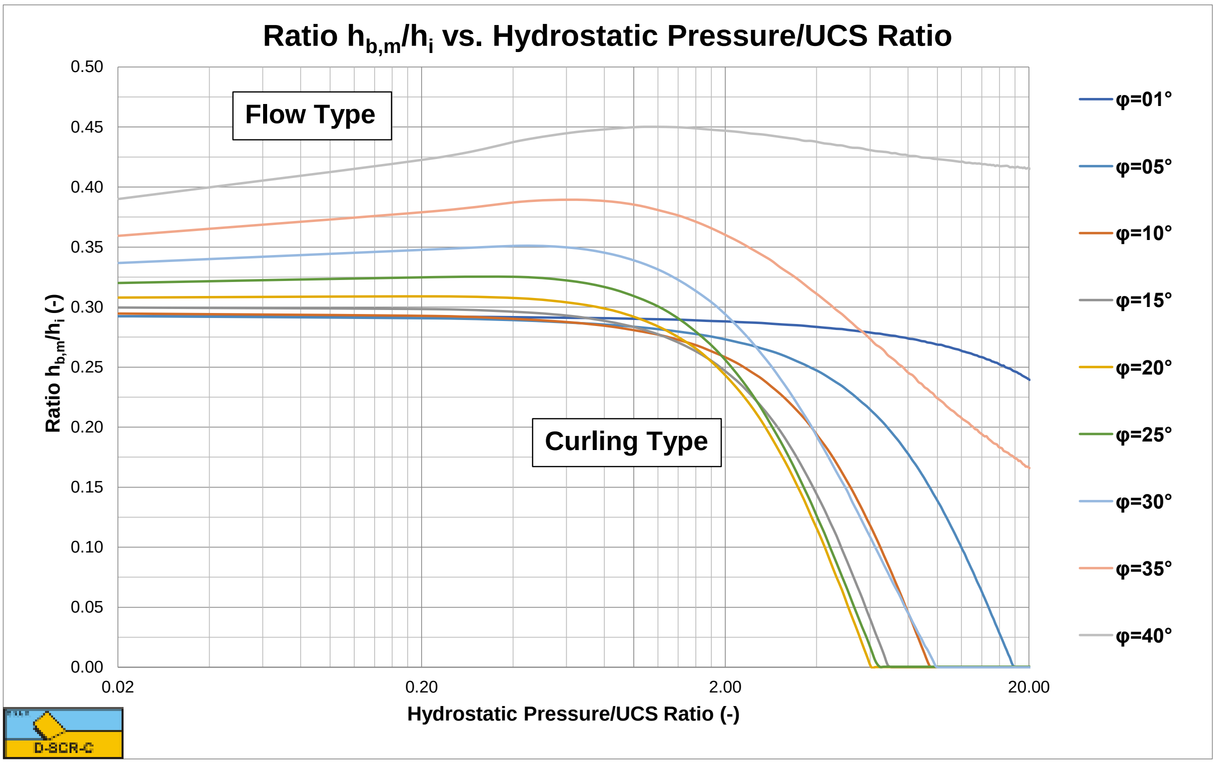

Figure X-6: The ratio $h_{b,m}/h_i$ for a 45 degree blade.

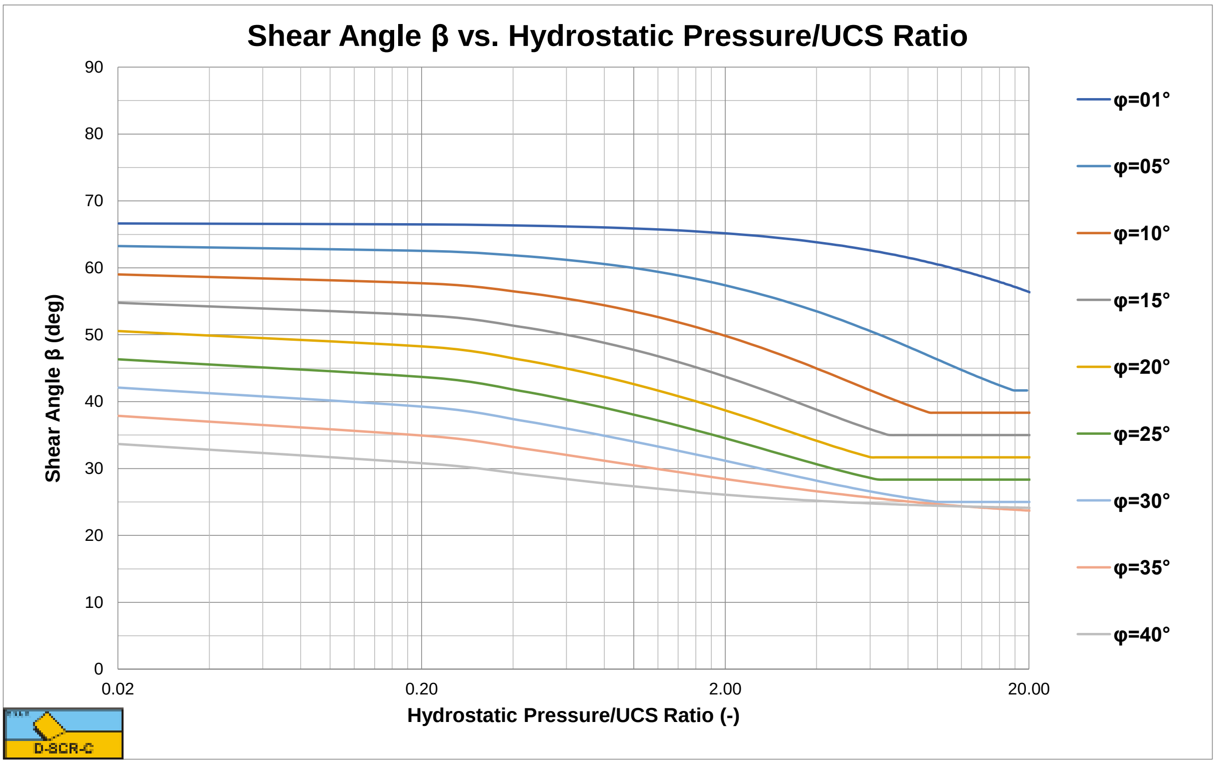

Figure X-7: The shear angle β for a 45 degree blade.

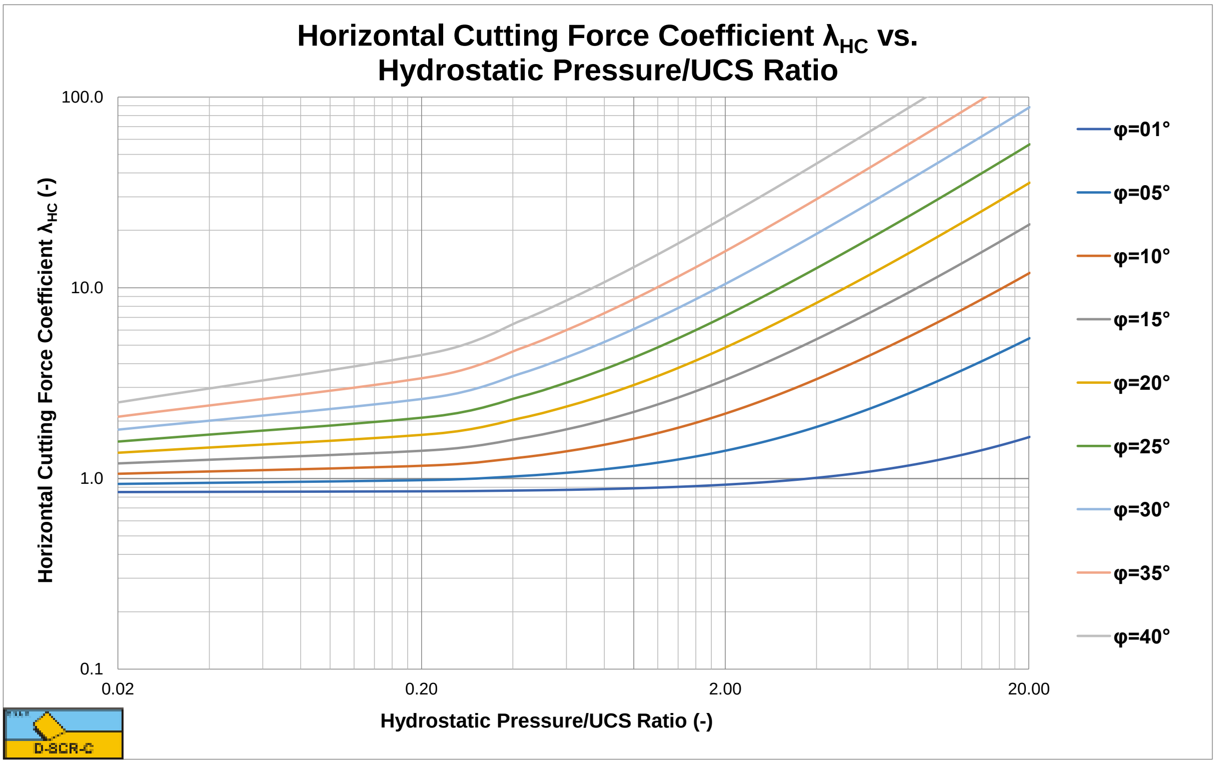

Figure X-8: The horizontal cutting force coefficient λ_{HC} for a 45 degree blade.

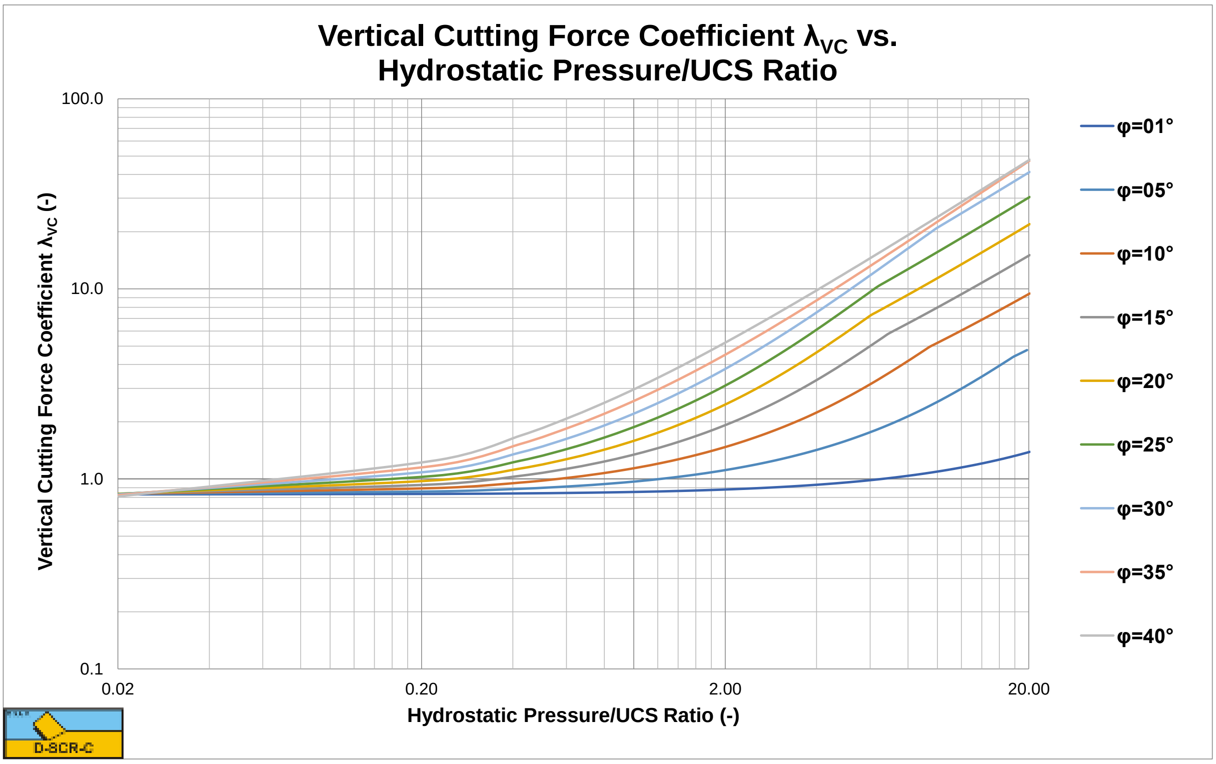

Figure X-9: The vertical cutting force coefficient λ_{VC} for a 60 degree blade.

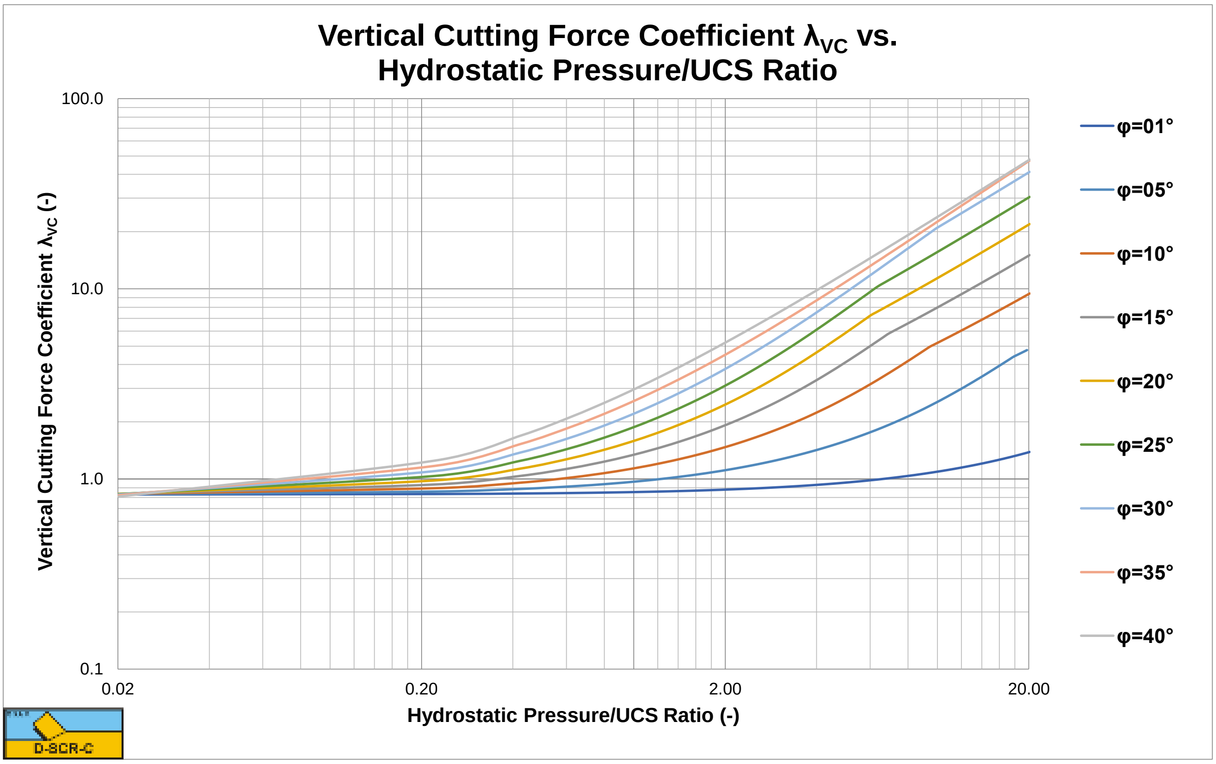

Figure X-10: The specific energy to UCS ratio for a 45 degree blade.

X.3 The Curling Type of the 60 Degree Blade.

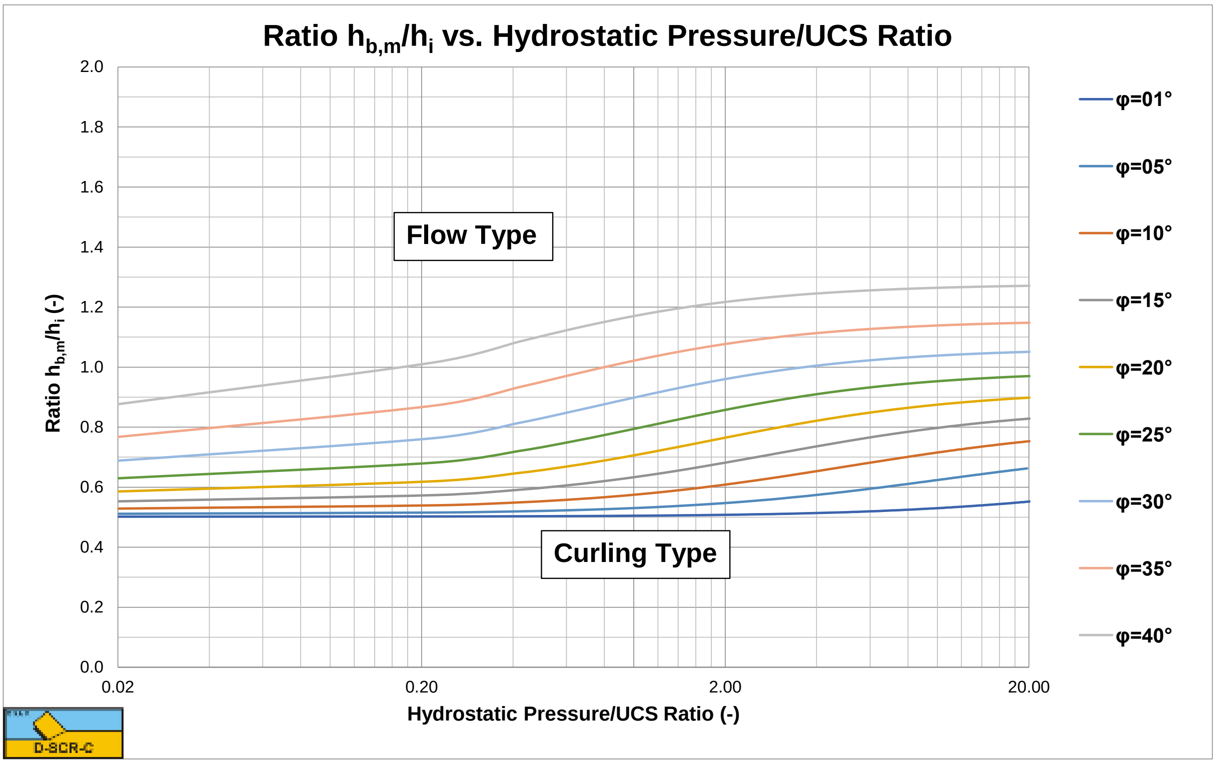

Figure X-11: The ratio $h_{b,m}/h_i$ for a 60 degree blade.

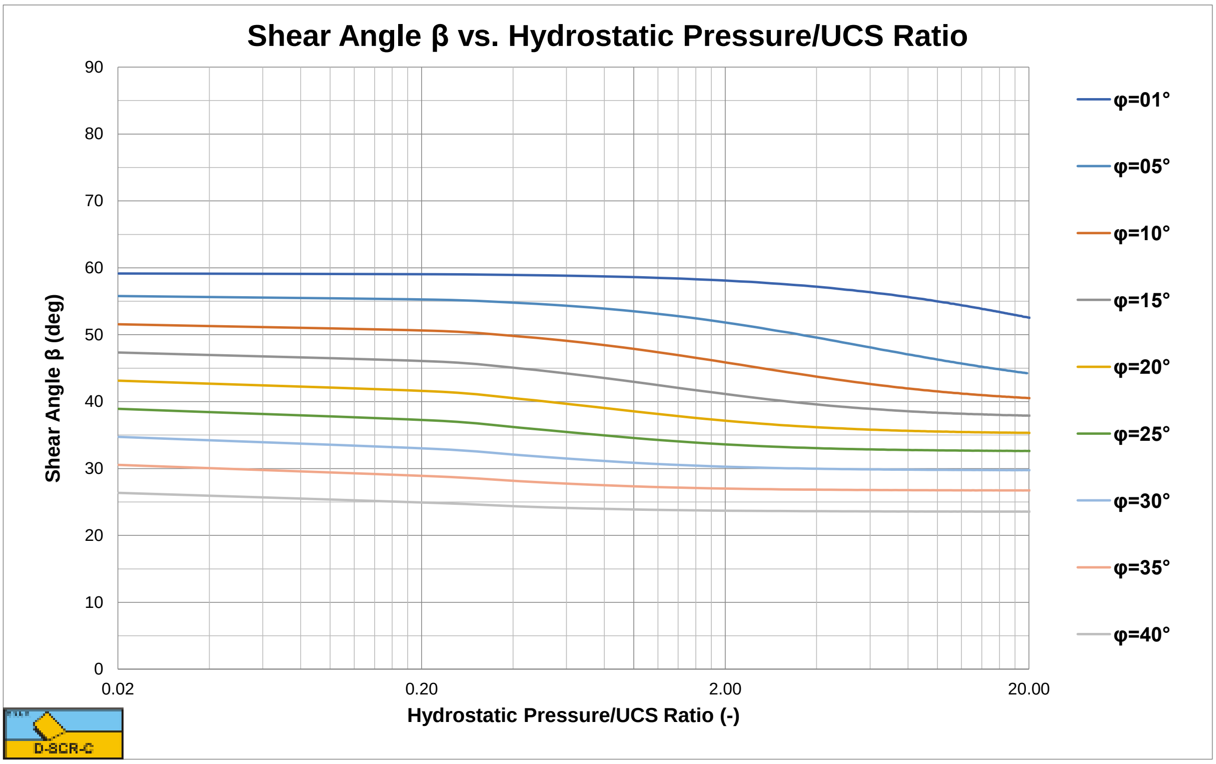

Figure X-12: The shear angle β for a 60 degree blade.

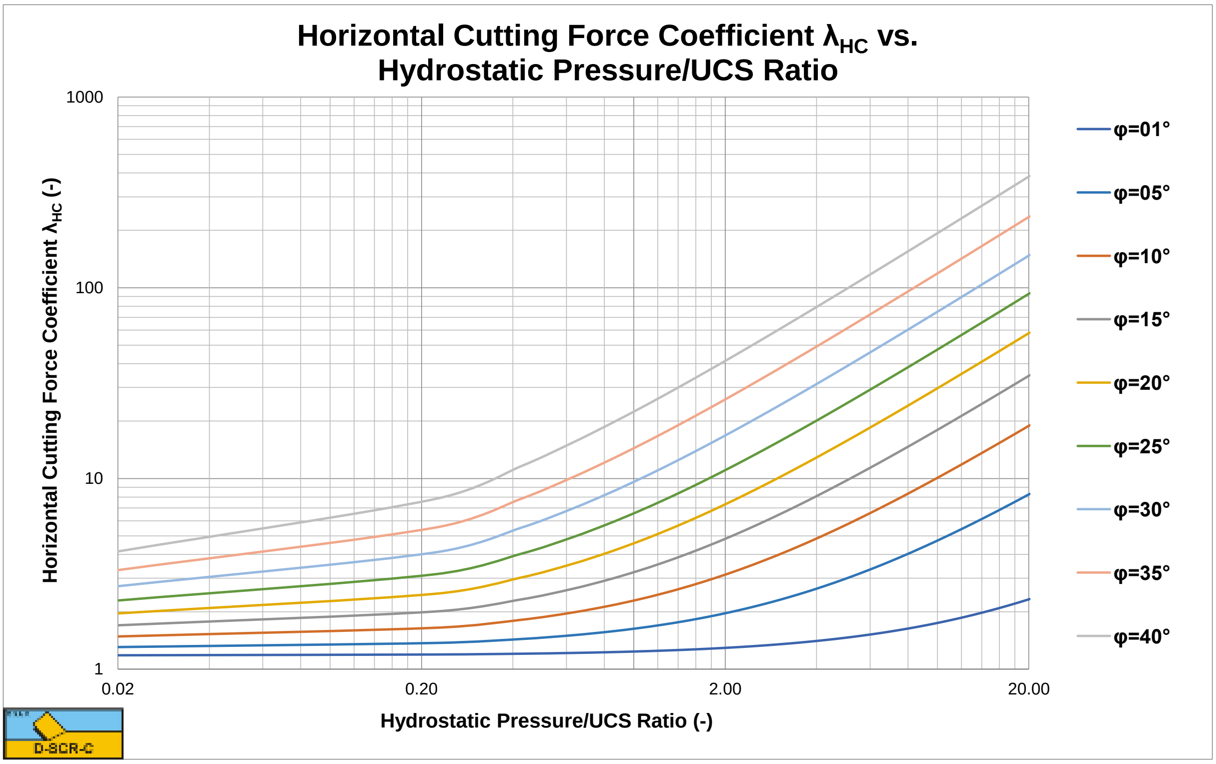

Figure X-13: The horizontal cutting force coefficient λ_{HC} for a 60 degree blade.

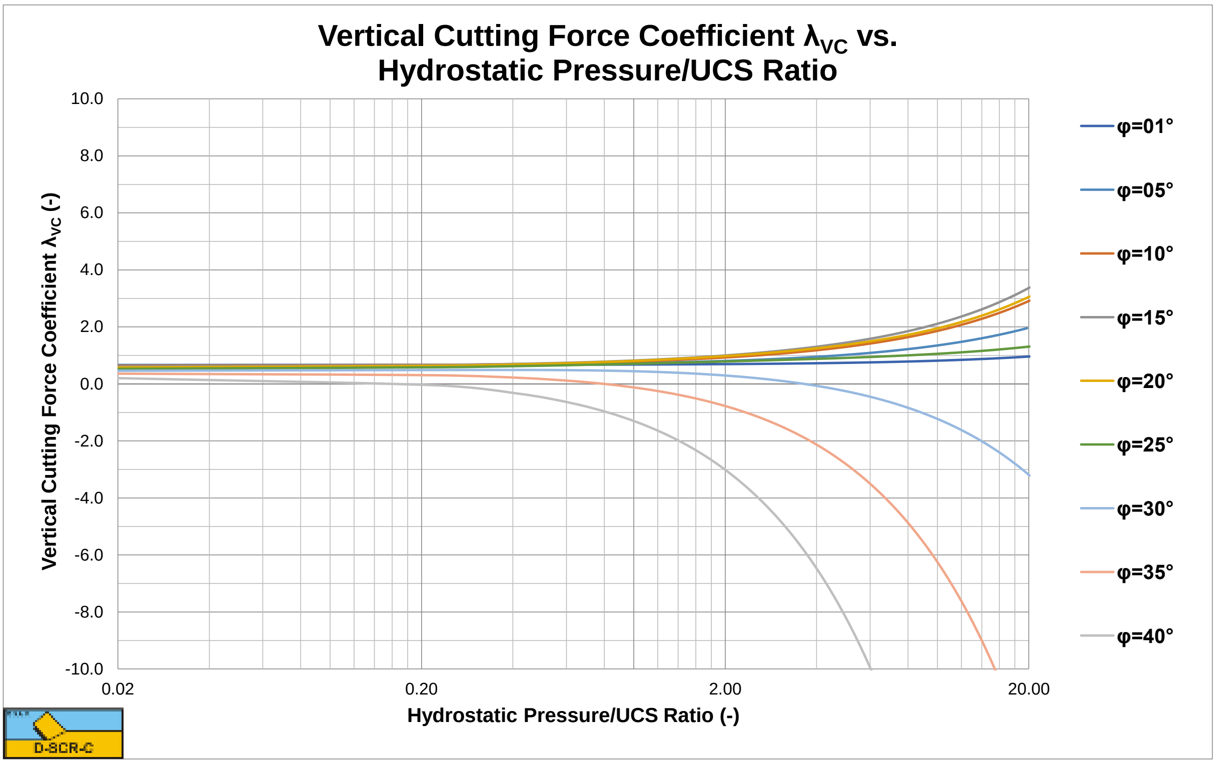

Figure X-14: The vertical cutting force coefficient λ_{VC} for a 60 degree blade.

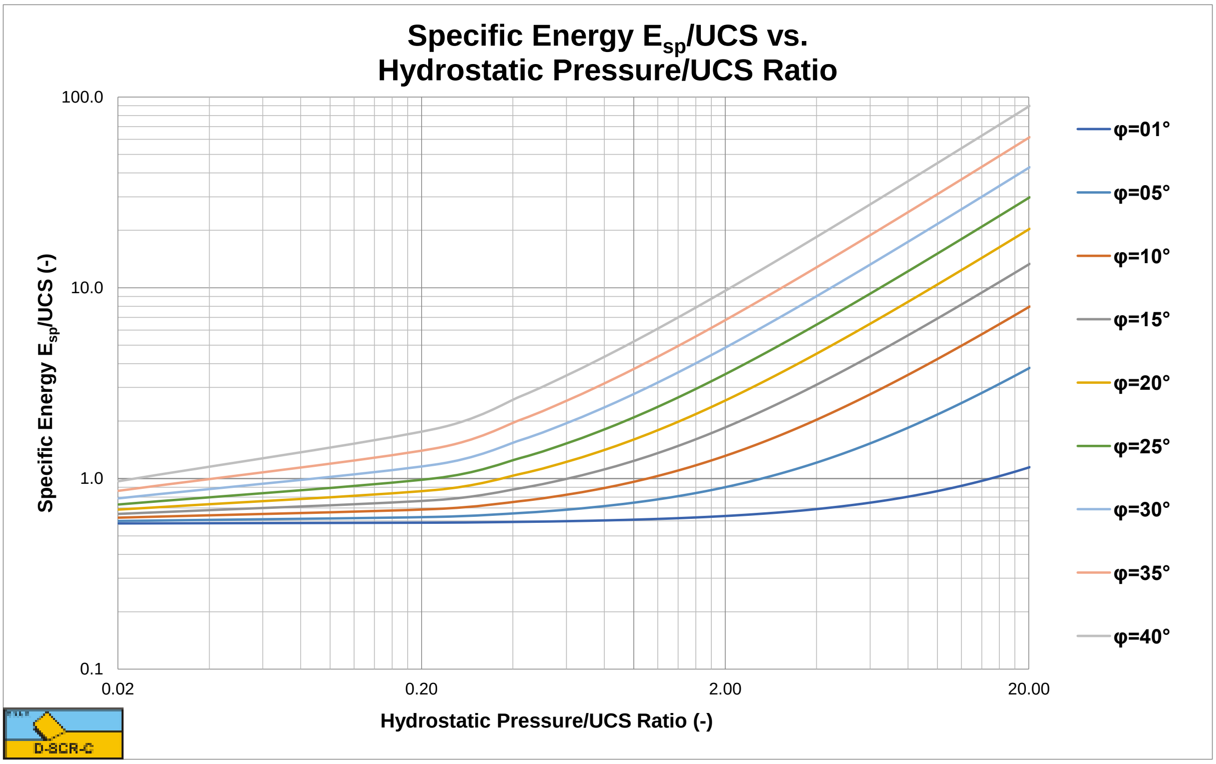

Figure X-15: The specific energy to UCS ratio for a 60 degree blade.

X.4 The Curling Type of the 75 Degree Blade.

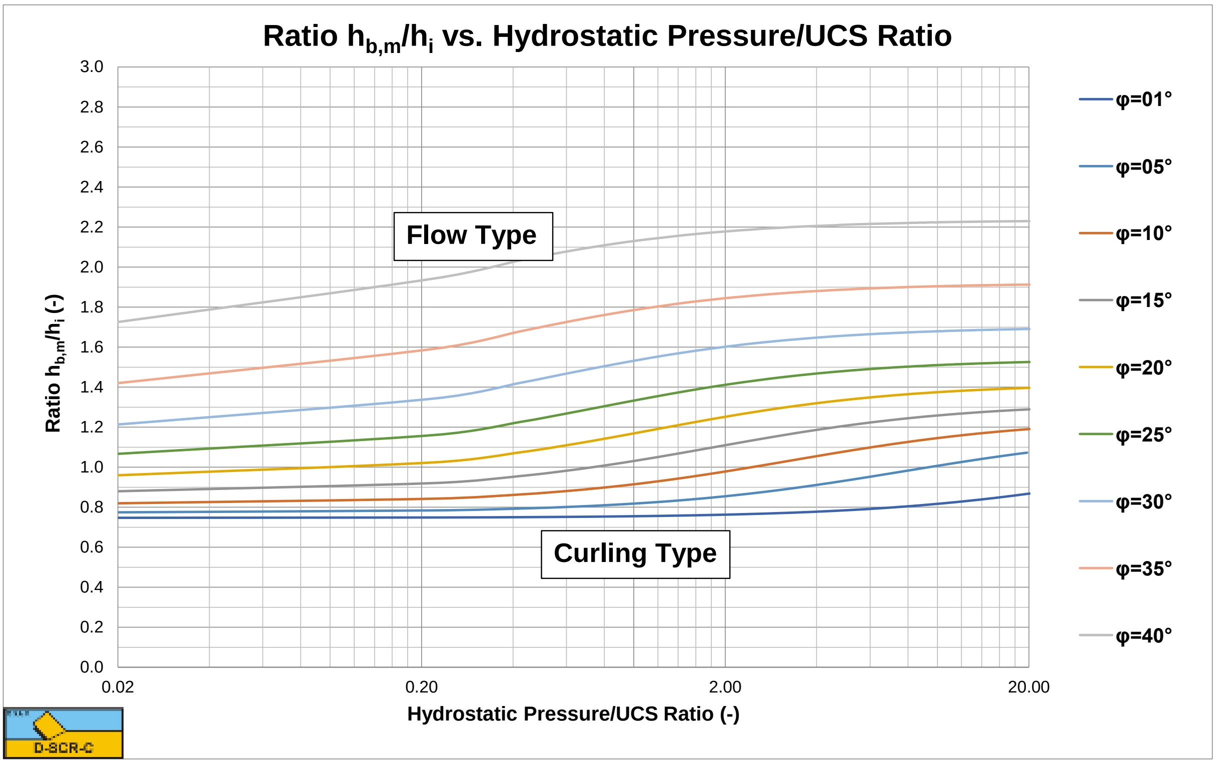

Figure X-16: The ratio $h_{b,m}/h_i$ for a 75 degree blade.

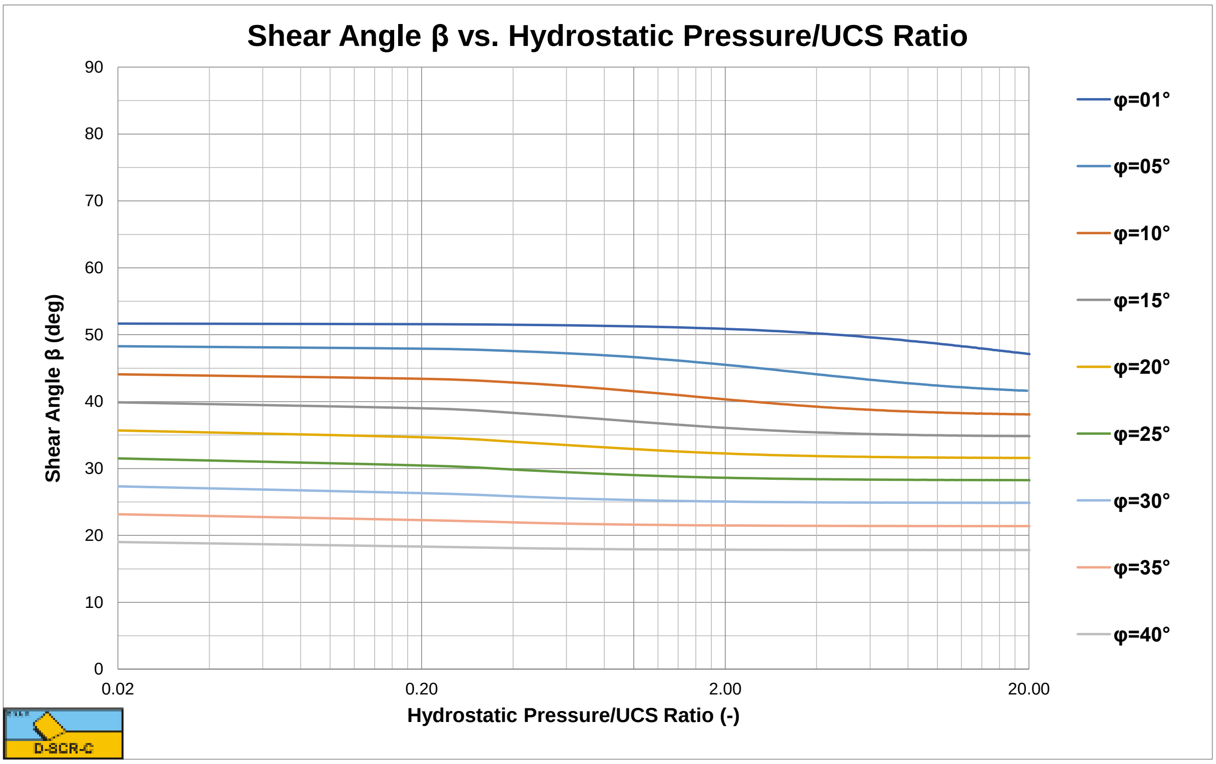

Figure X-17: The shear angle β for a 75 degree blade.

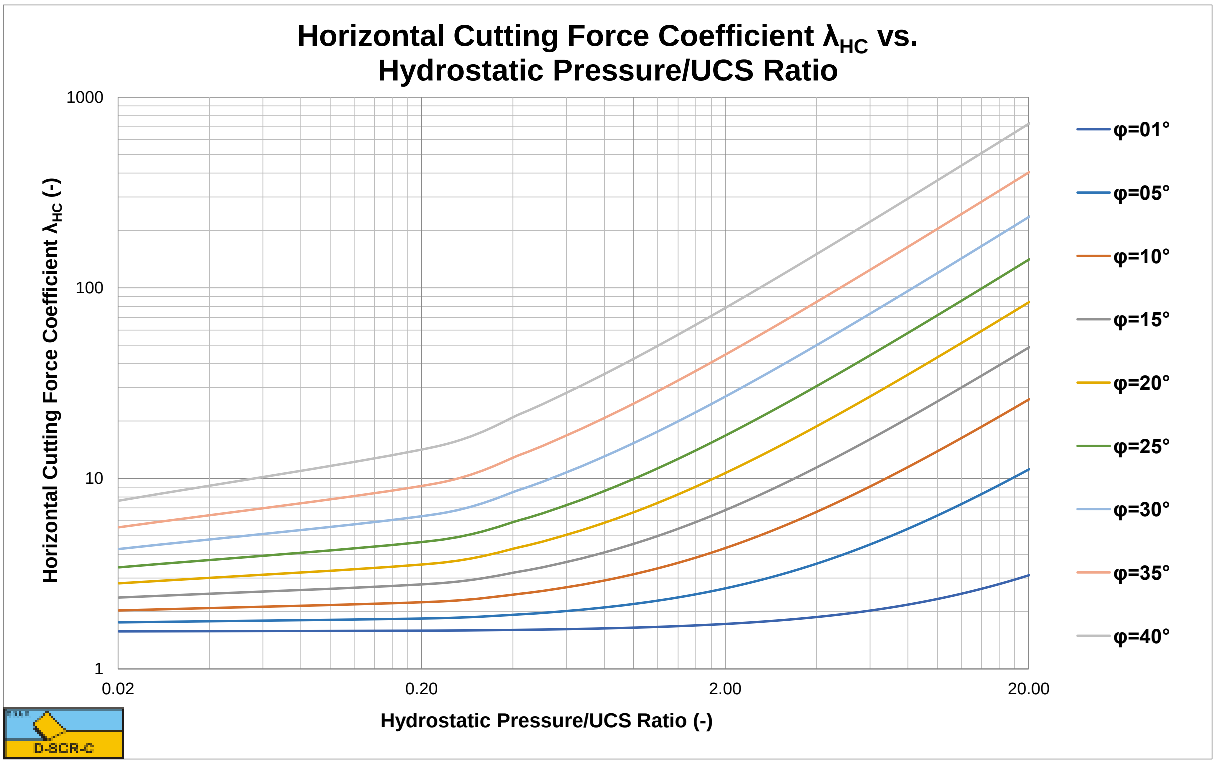

Figure X-18: The horizontal cutting force coefficient λ_{HC} for a 75 degree blade.

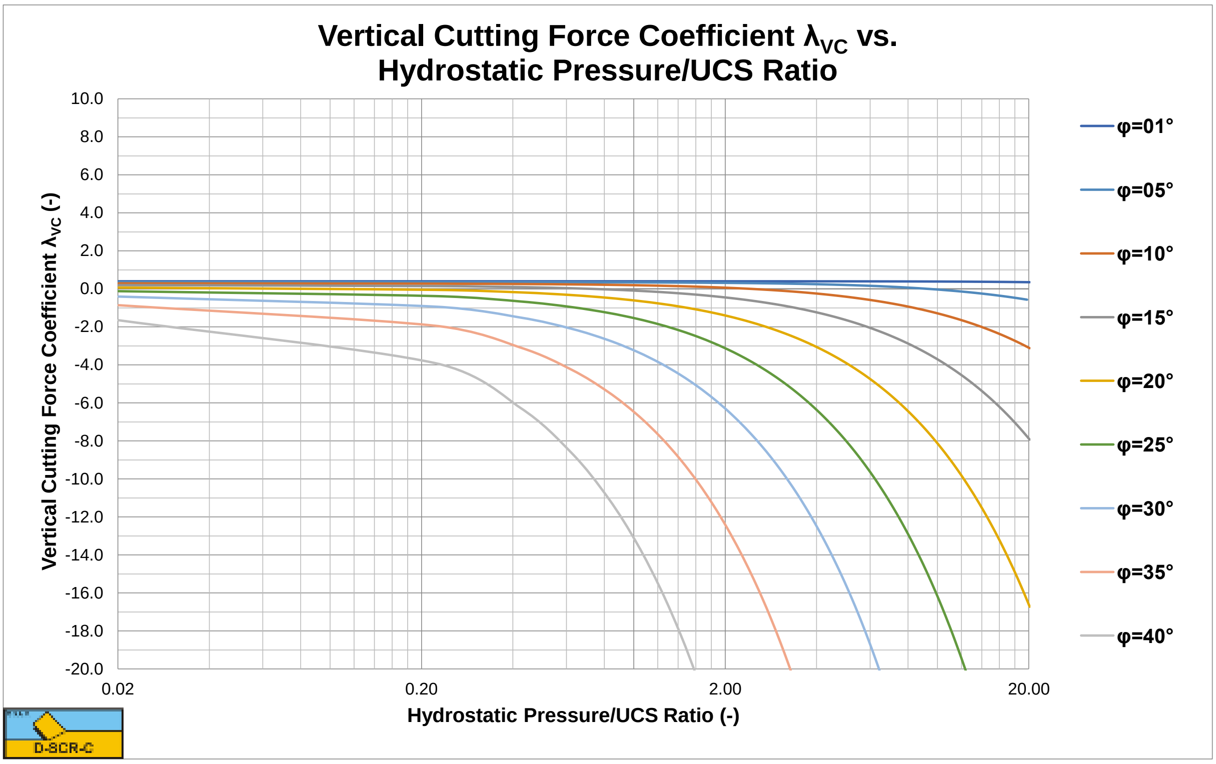

Figure X-19: The vertical cutting force coefficient λ_{VC} for a 75 degree blade.

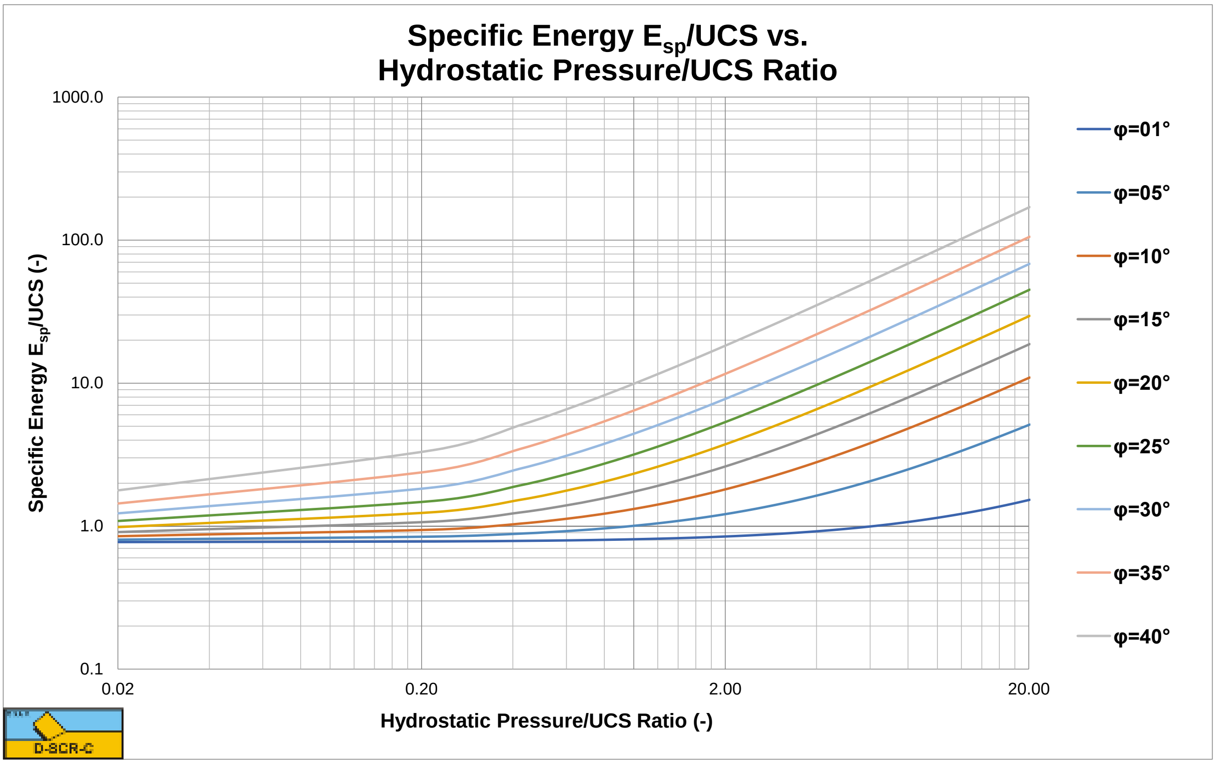

Figure X-20: The specific energy to UCS ratio for a 75 degree blade.

X.5 The Curling Type of the 90 Degree Blade.

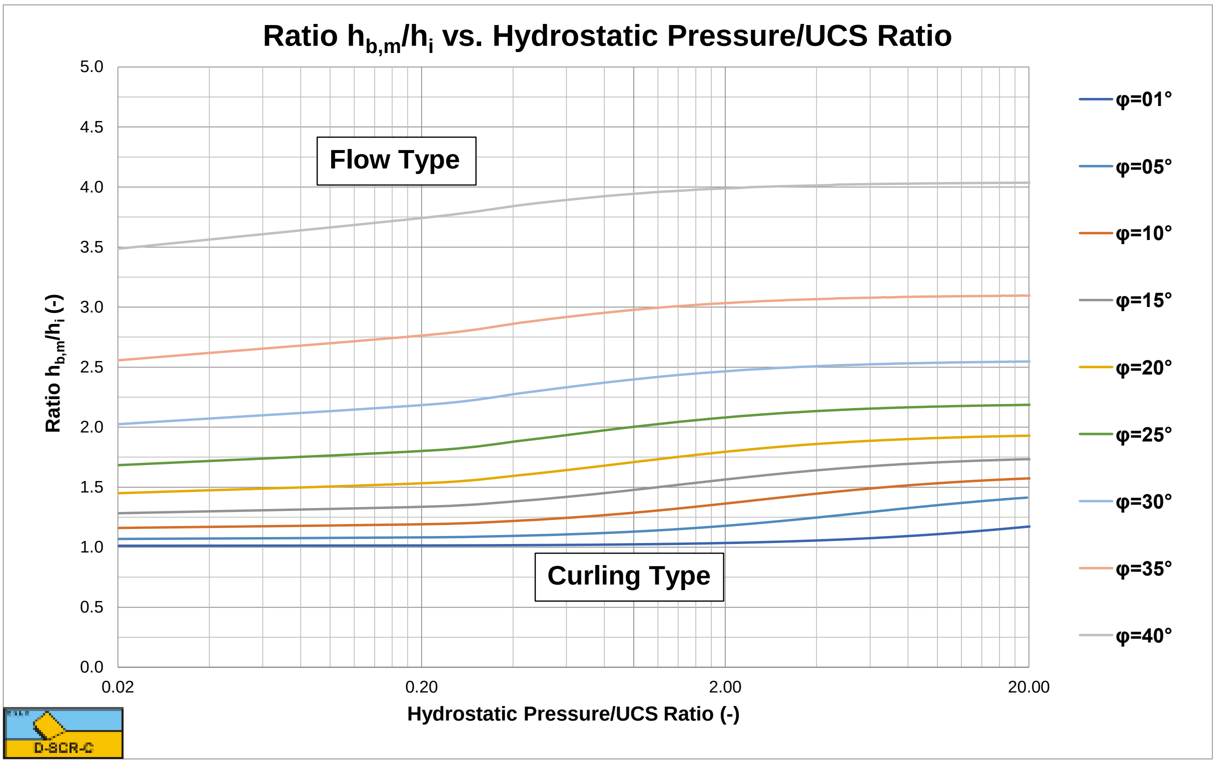

Figure X-21: The ratio $h_{b,m}/h_i$ for a 90 degree blade.

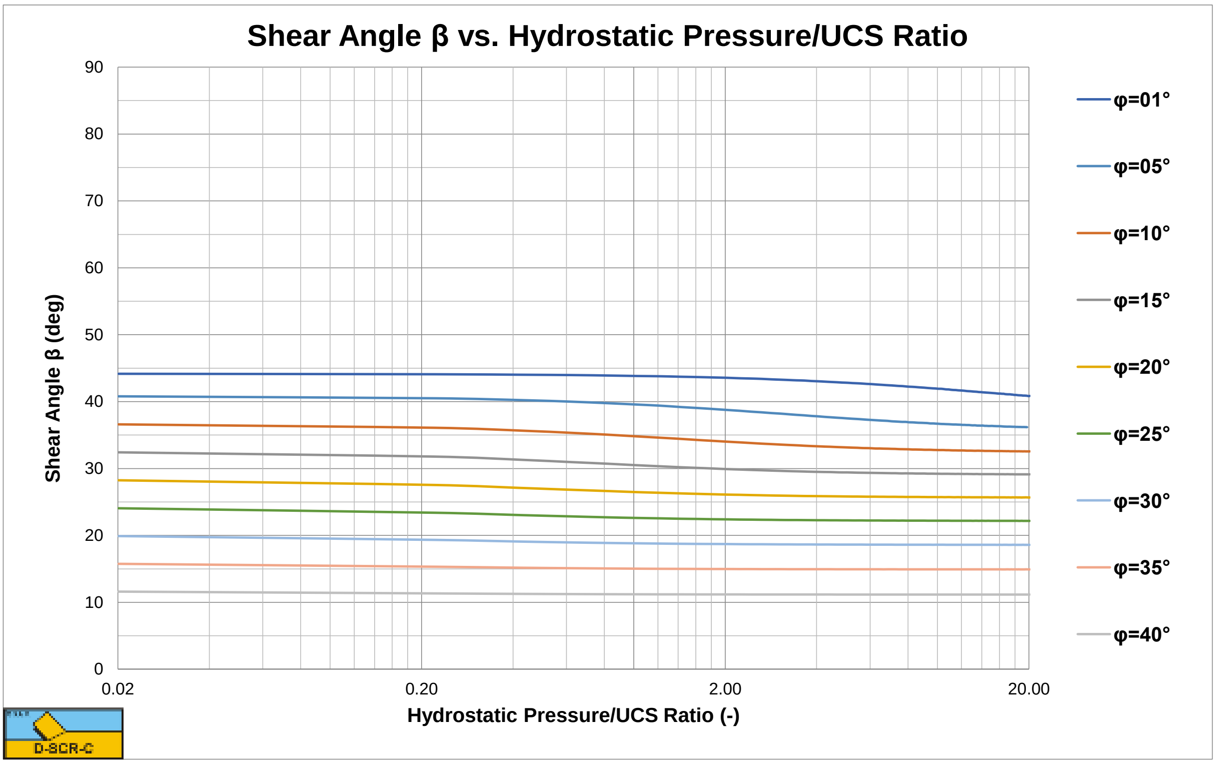

Figure X-22: The shear angle β for a 90 degree blade.

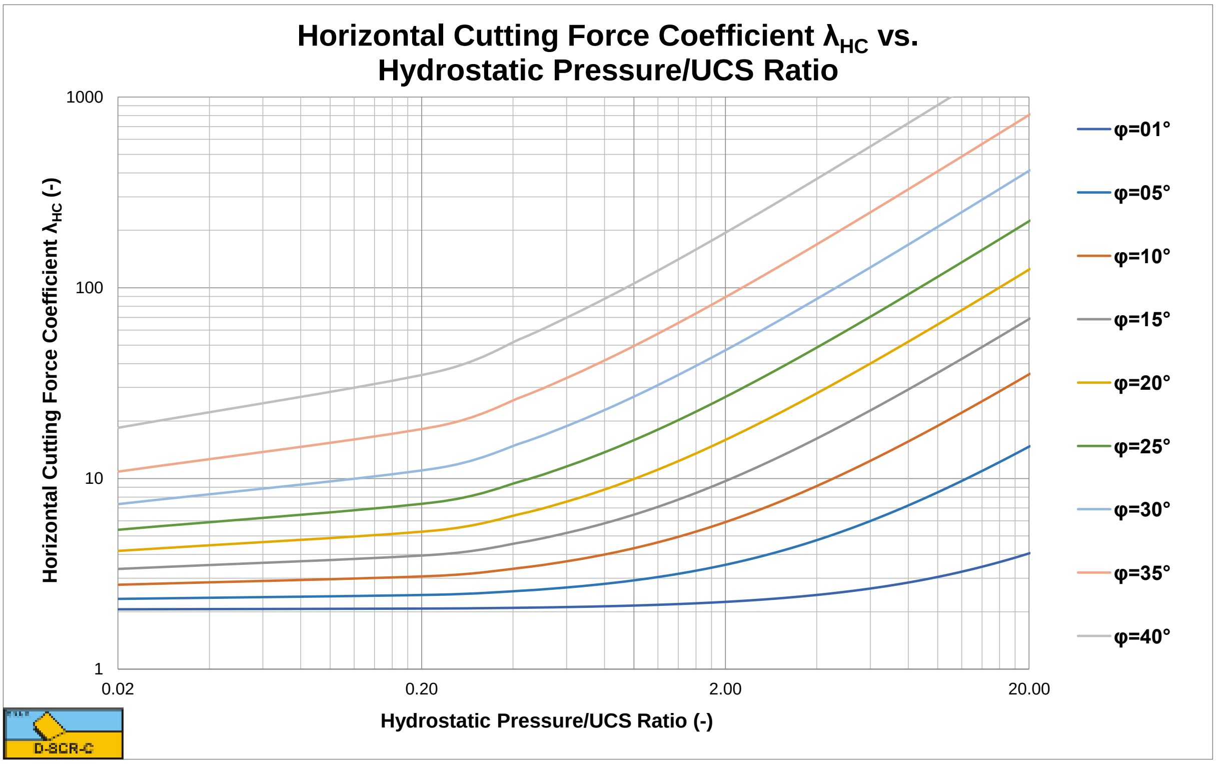

Figure X-23: The horizontal cutting force coefficient λ_{HC} for a 90 degree blade.

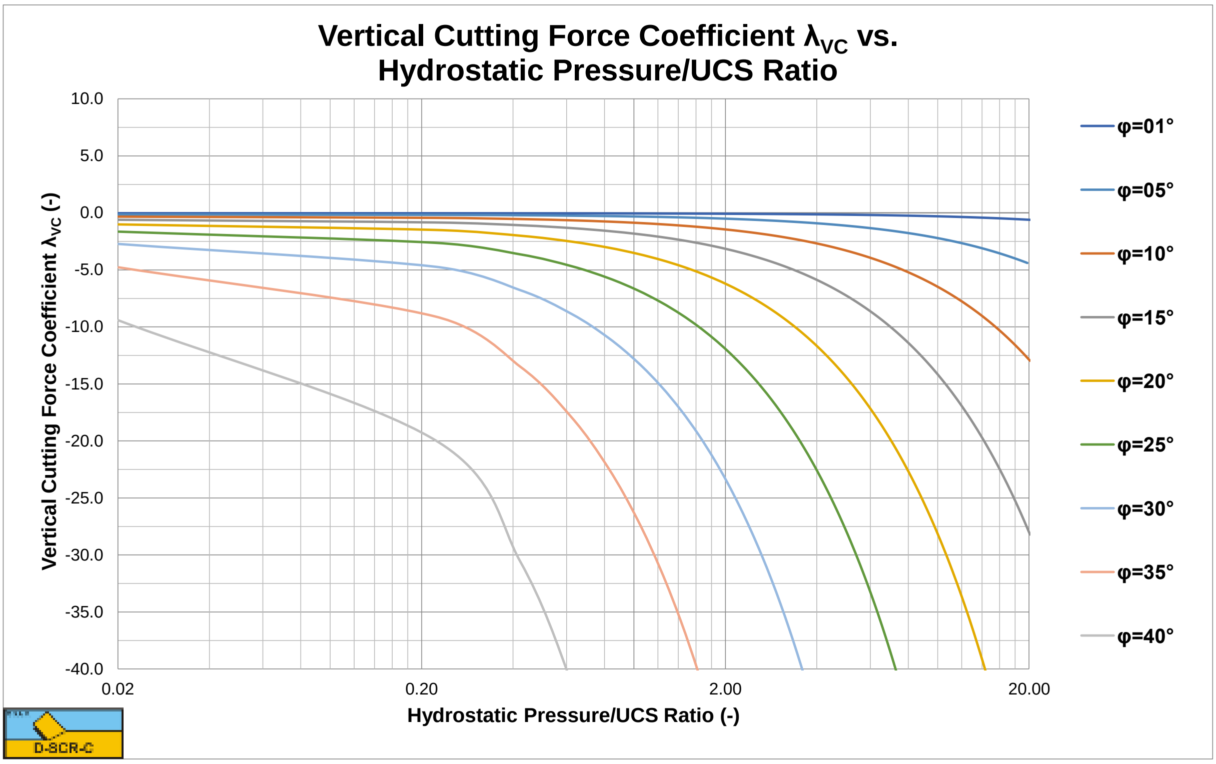

Figure X-24: The vertical cutting force coefficient λ_{VC} for a 90 degree blade.

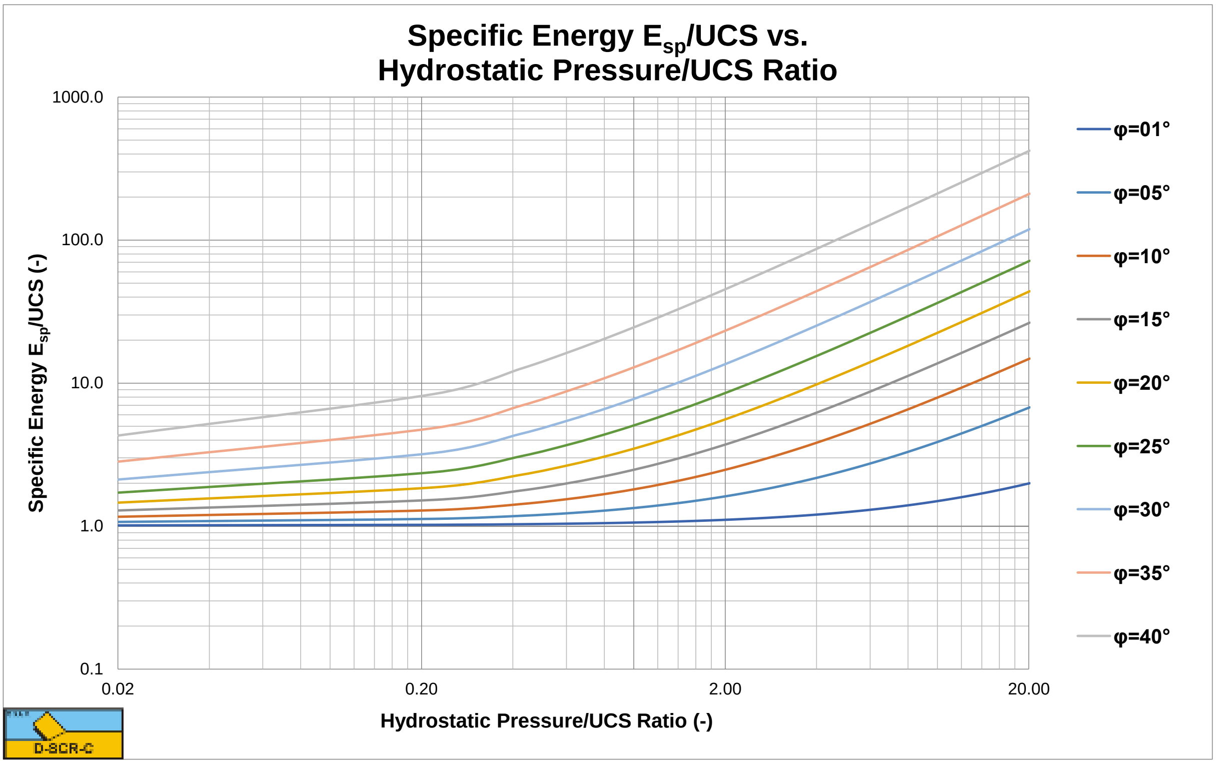

Figure X-25: The specific energy to UCS ratio for a 90 degree blade.

X.6 The Curling Type of the 105 Degree Blade.

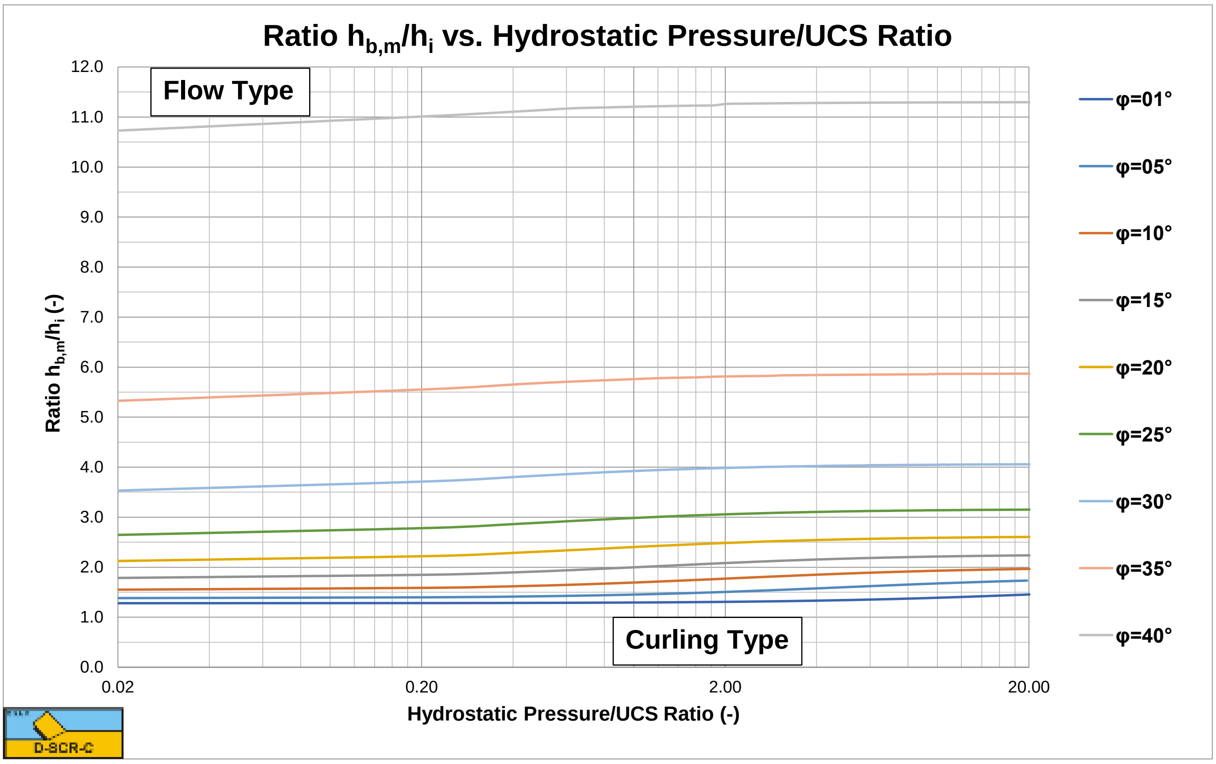

Figure X-26: The ratio $h_{b,m}/h_i$ for a 105 degree blade.

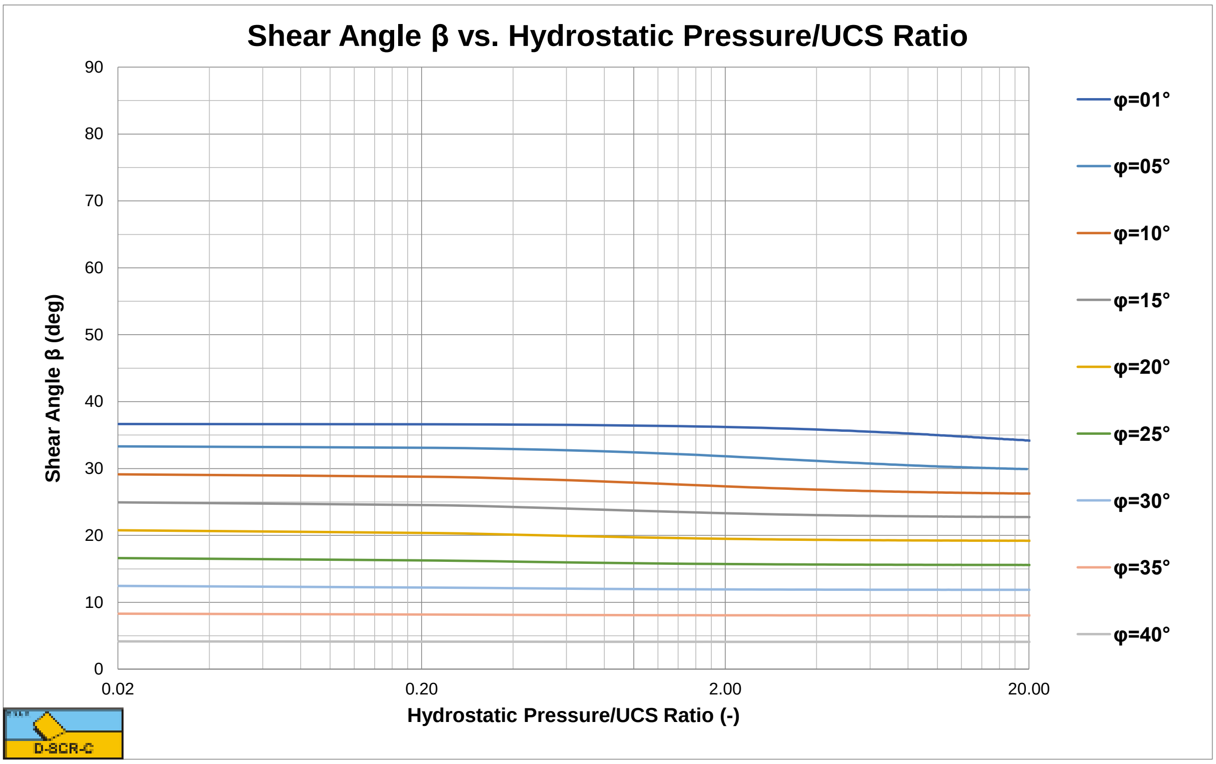

Figure X-27: The shear angle β for a 105 degree blade.

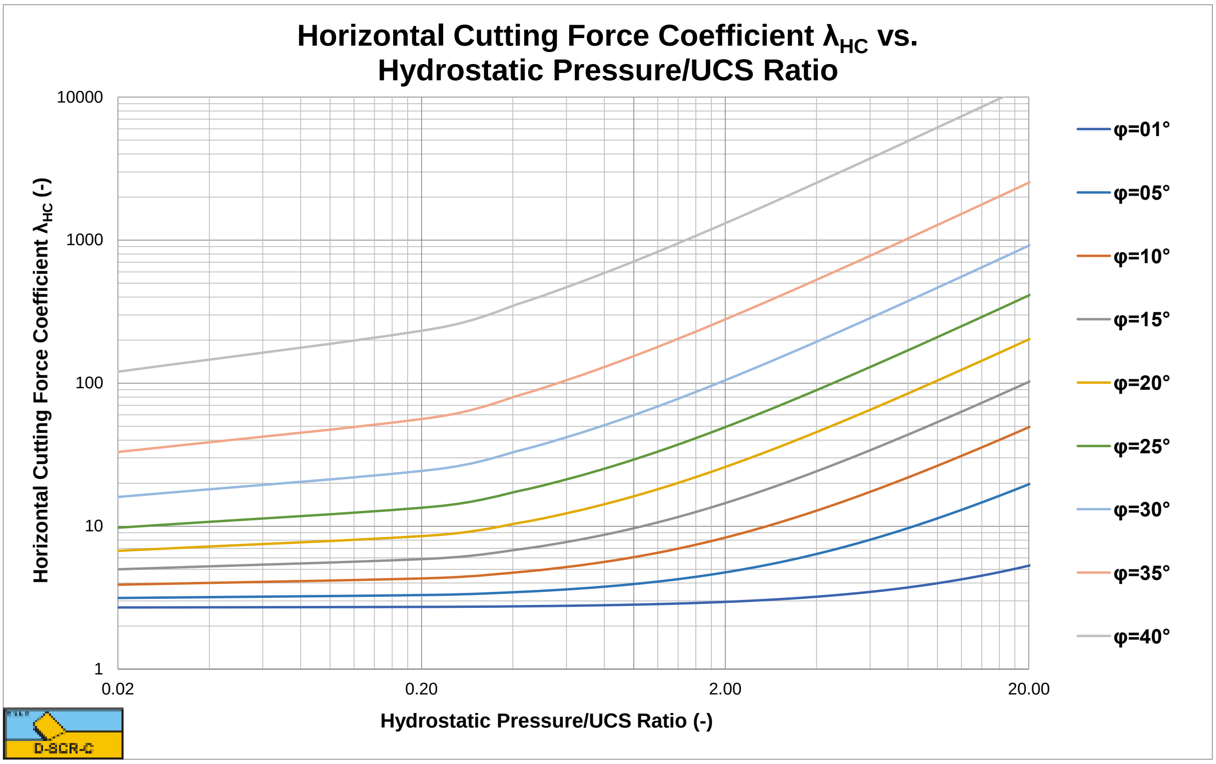

Figure X-28: The horizontal cutting force coefficient λ_{HC} for a 105 degree blade.

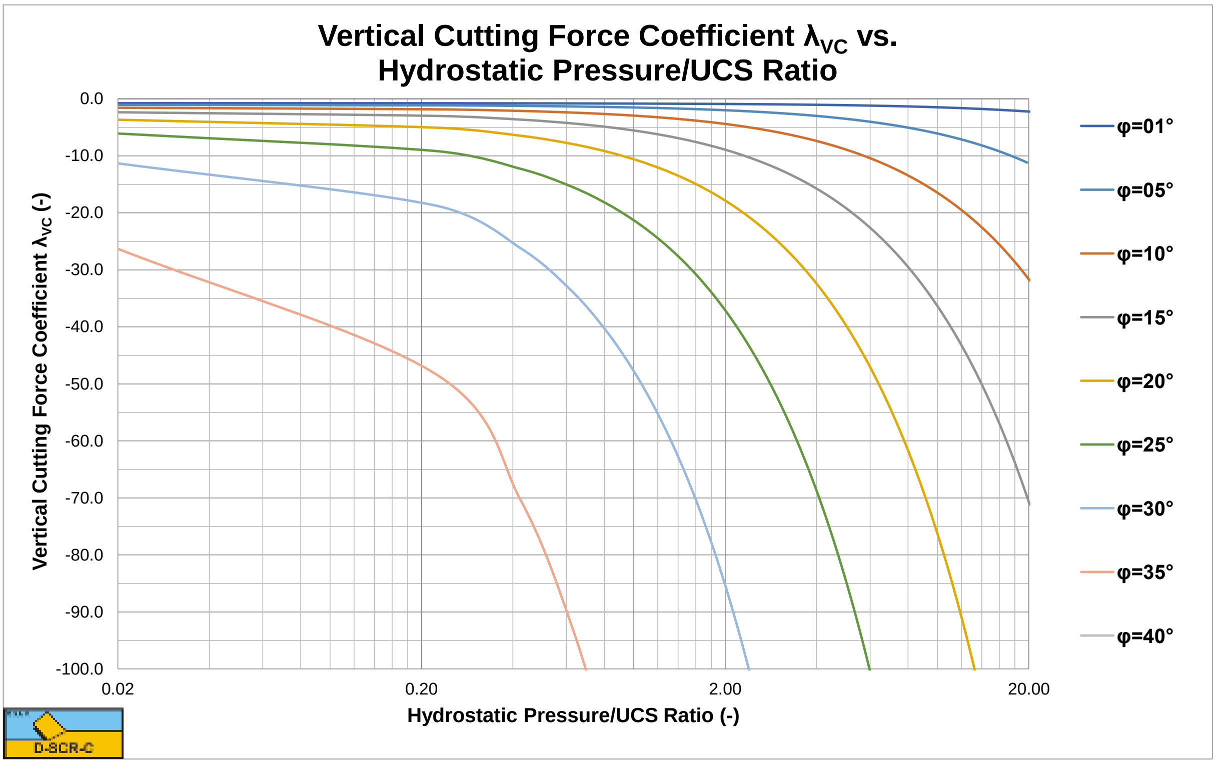

Figure X-29: The vertical cutting force coefficient λ_{VC} for a 105 degree blade.

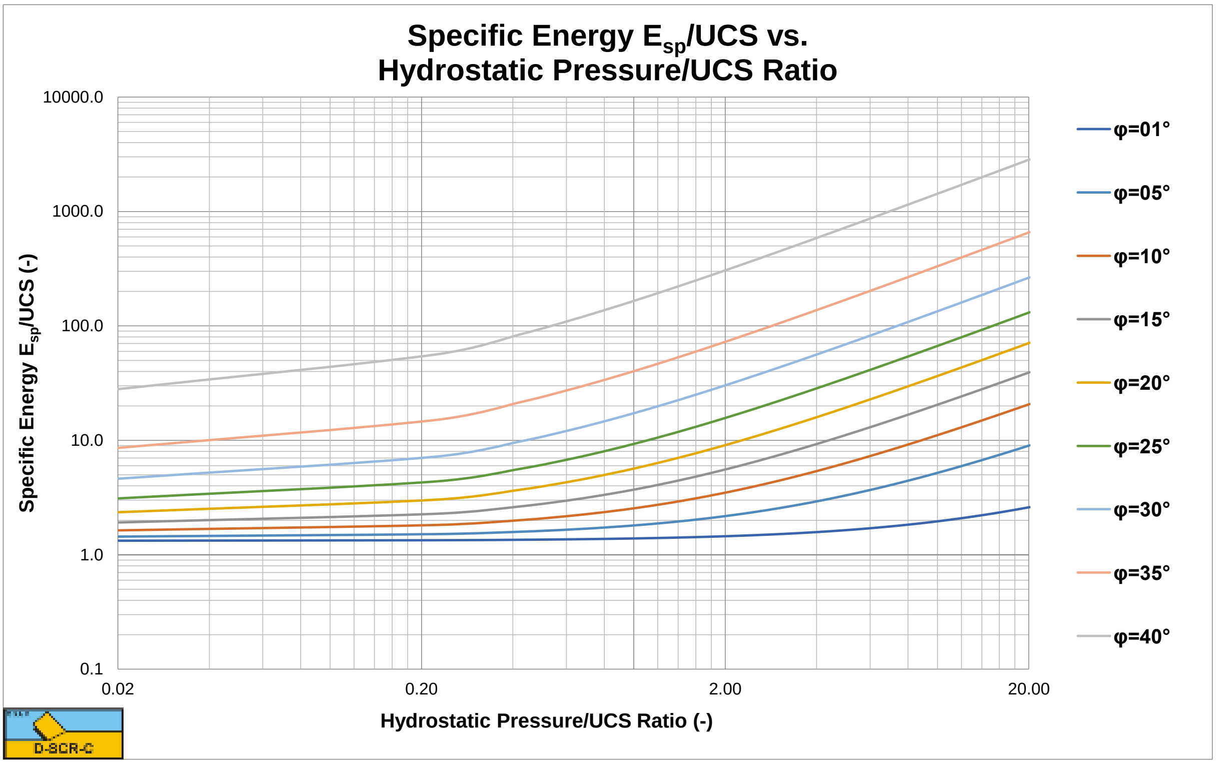

Figure X-30: The specific energy to UCS ratio for a 105 degree blade.

X.7 The Curling Type of the 120 Degree Blade.

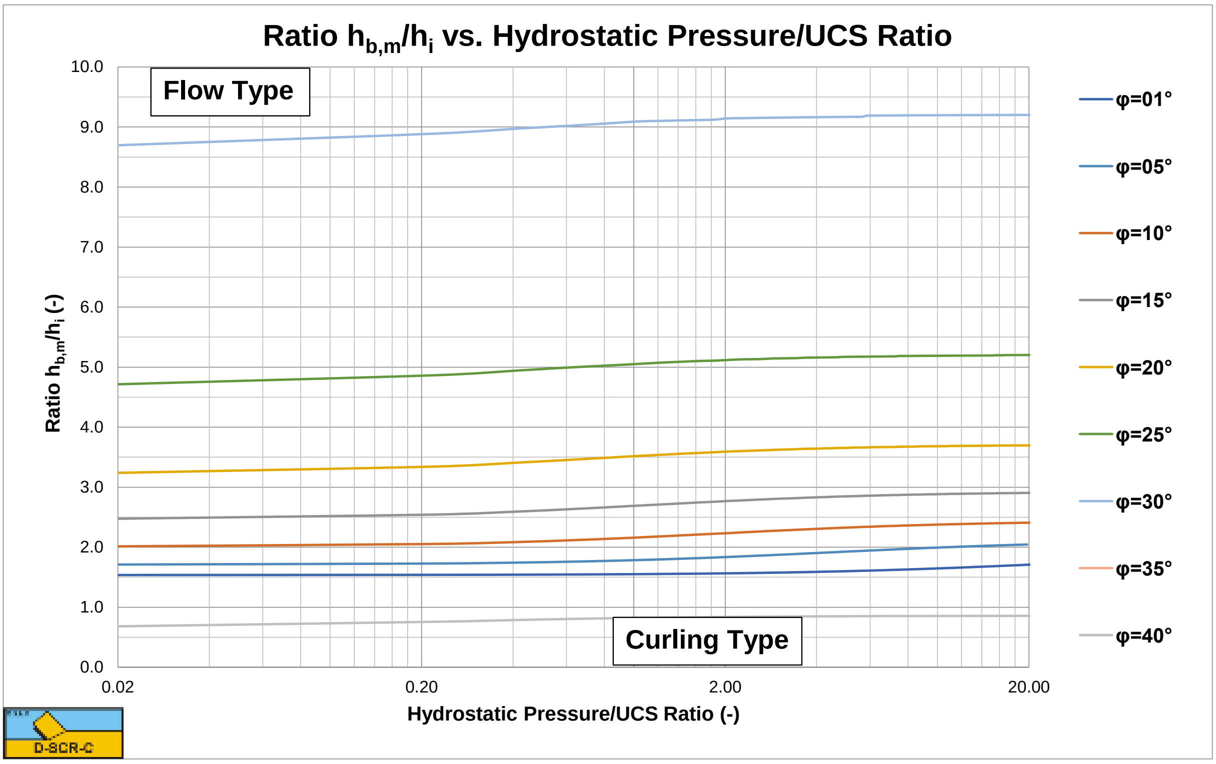

Figure X-31: The ratio $h_{b,m}/h_i$ for a 120 degree blade.

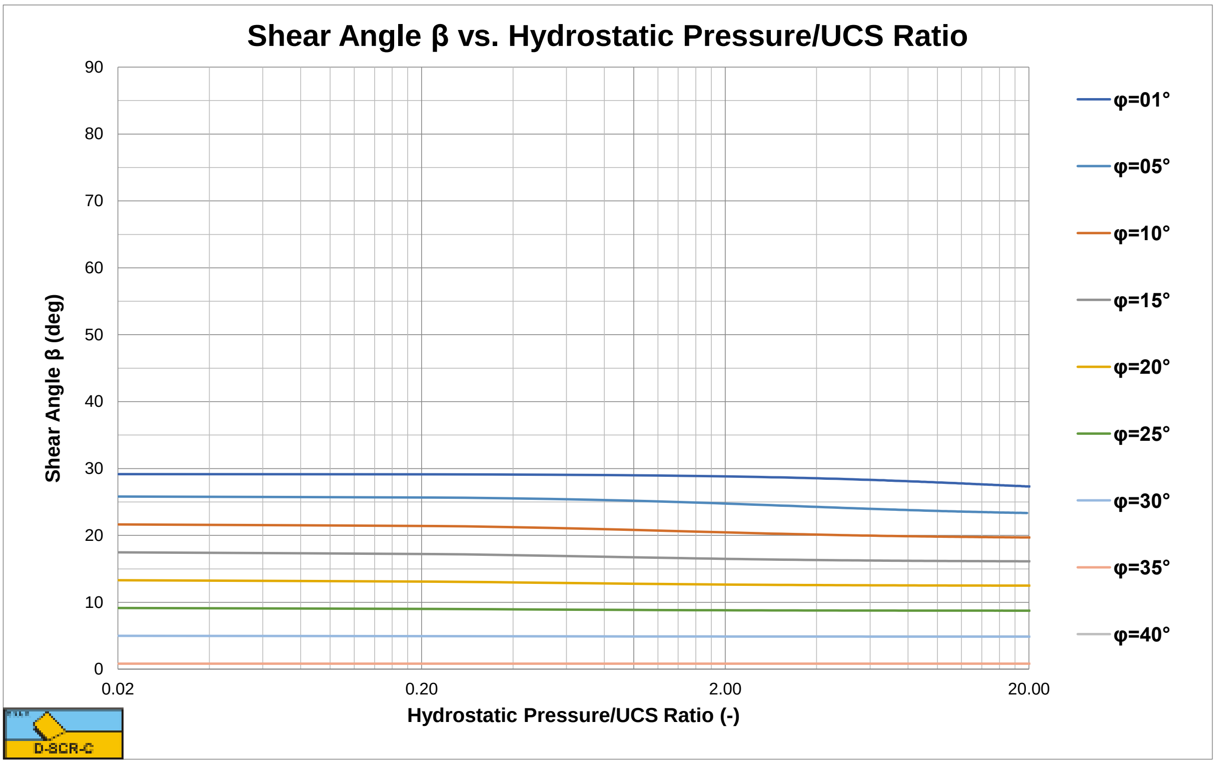

Figure X-32: The shear angle β for a 120 degree blade.

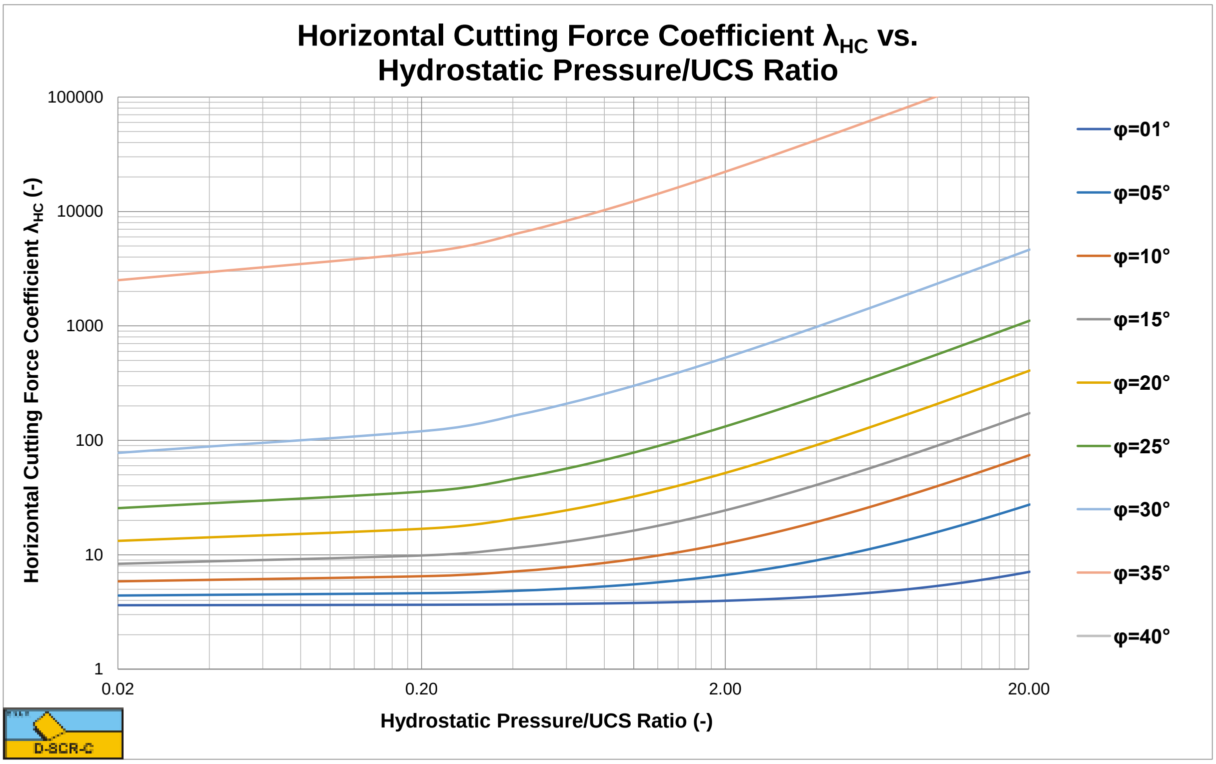

Figure X-33: The horizontal cutting force coefficient λ_{HC} for a 120 degree blade.

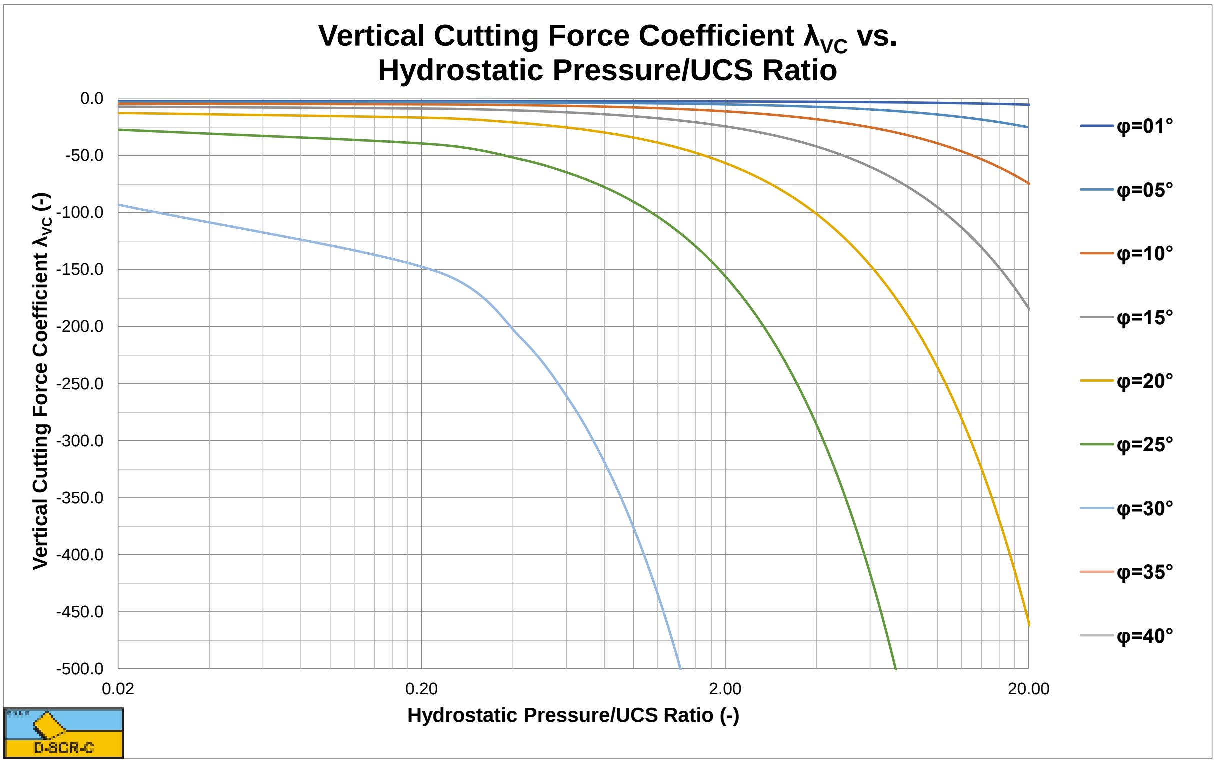

Figure X-34: The vertical cutting force coefficient λ_{VC} for a 120 degree blade.

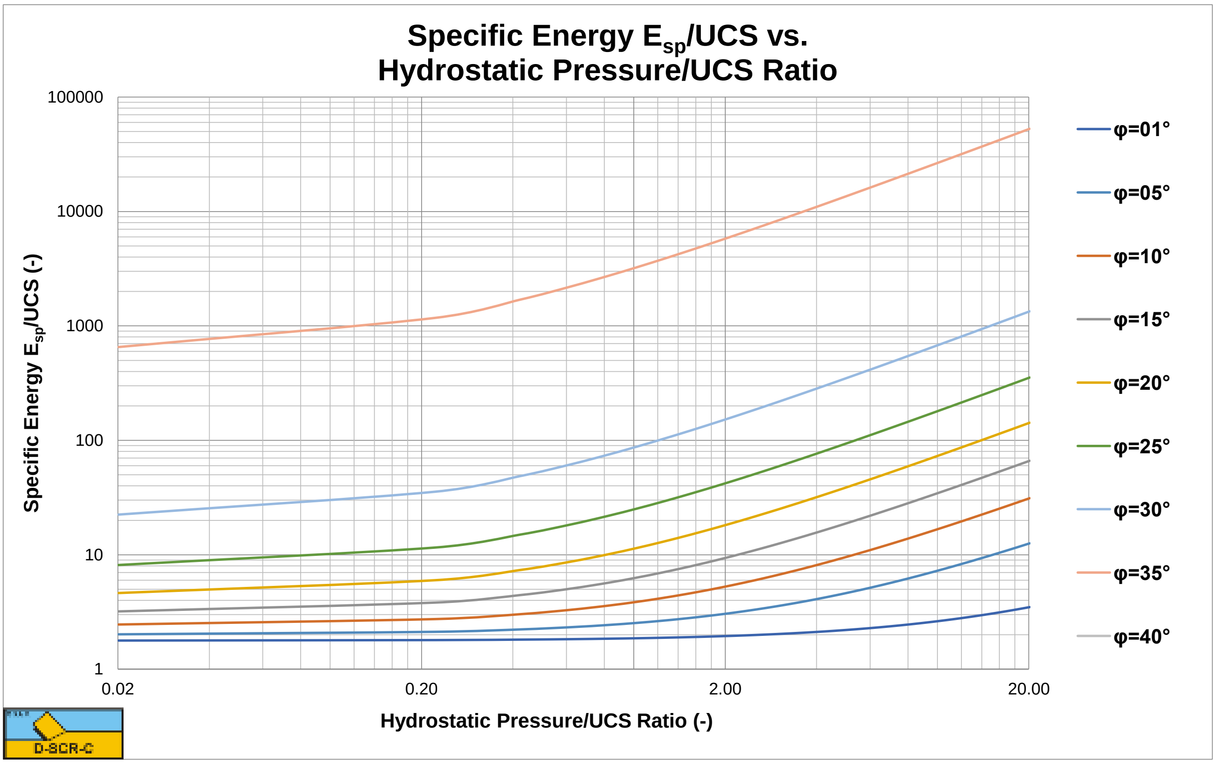

Figure X-35: The specific energy to UCS ratio for a 120 degree blade.

Appendix Y: Applications & Equipment.

Y.1 Historic Dredges.

Figure Y-1: Dredging machine 1760 (ARA, Staten van Holland 5675), patent of F. D’Arles de Liniere in 1761.

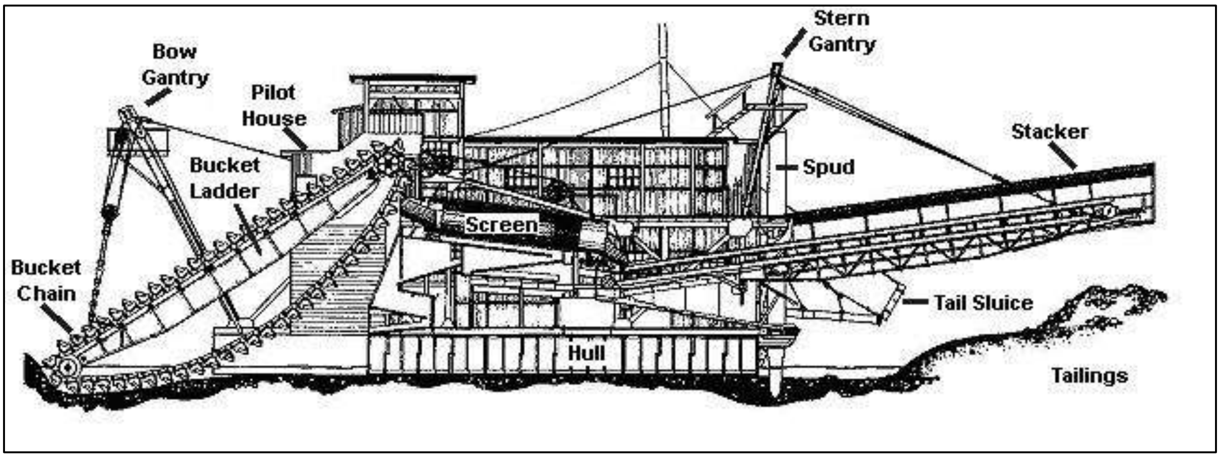

Figure Y-2: A gold dredging bucket ladder dredge (www.miningandmetallurgy.com).

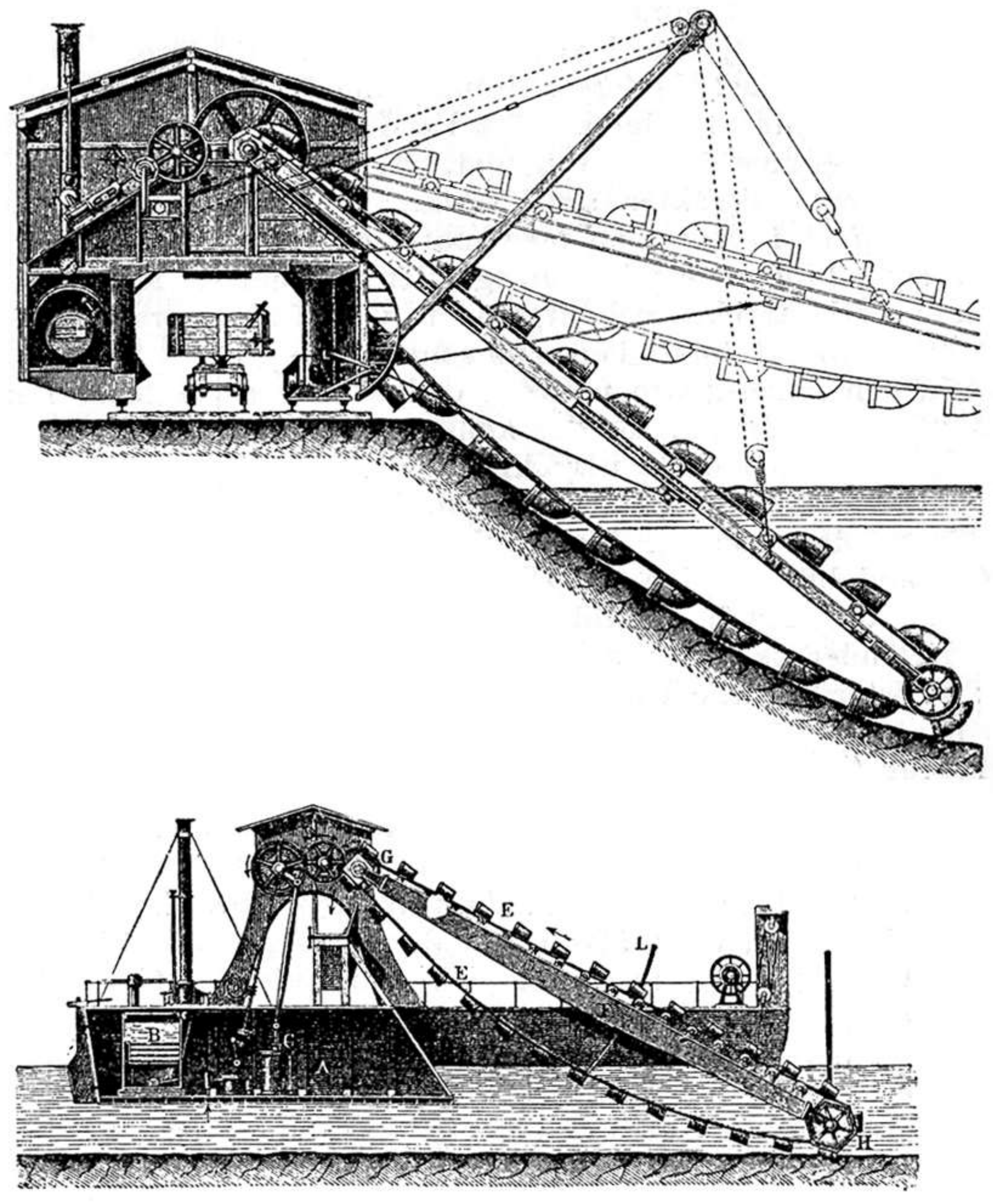

Figure Y-3: A dredge for canal works and a bucket ladder dredge (Swedish encyclopedia 1914).

Y.2 Bucket Ladder Dredges.

Figure Y-4: A bucket ladder dredge (IHC).

Figure Y-5: Bucket storage.

Figure Y-6: Garbage bucket dredge (Hamson Indonesia).

Figure Y-7: The buckets of a gold dredge.

Y.3 Cutter Suction Dredges.

Figure Y-8: The Mashour (Suez Canal Port Authorities, IHC).

Figure Y-9: The Crawlcat (IHC).

Figure Y-10: The d'Artagnan (28.200 kW, DEME group).

Figure Y-11: A model rock cutter head (Delft University of Technology).

Figure Y-12: A sand cutter head.

Figure Y-13: A rock cutter head.

Figure Y-14: A rock cutter head (van Oord).

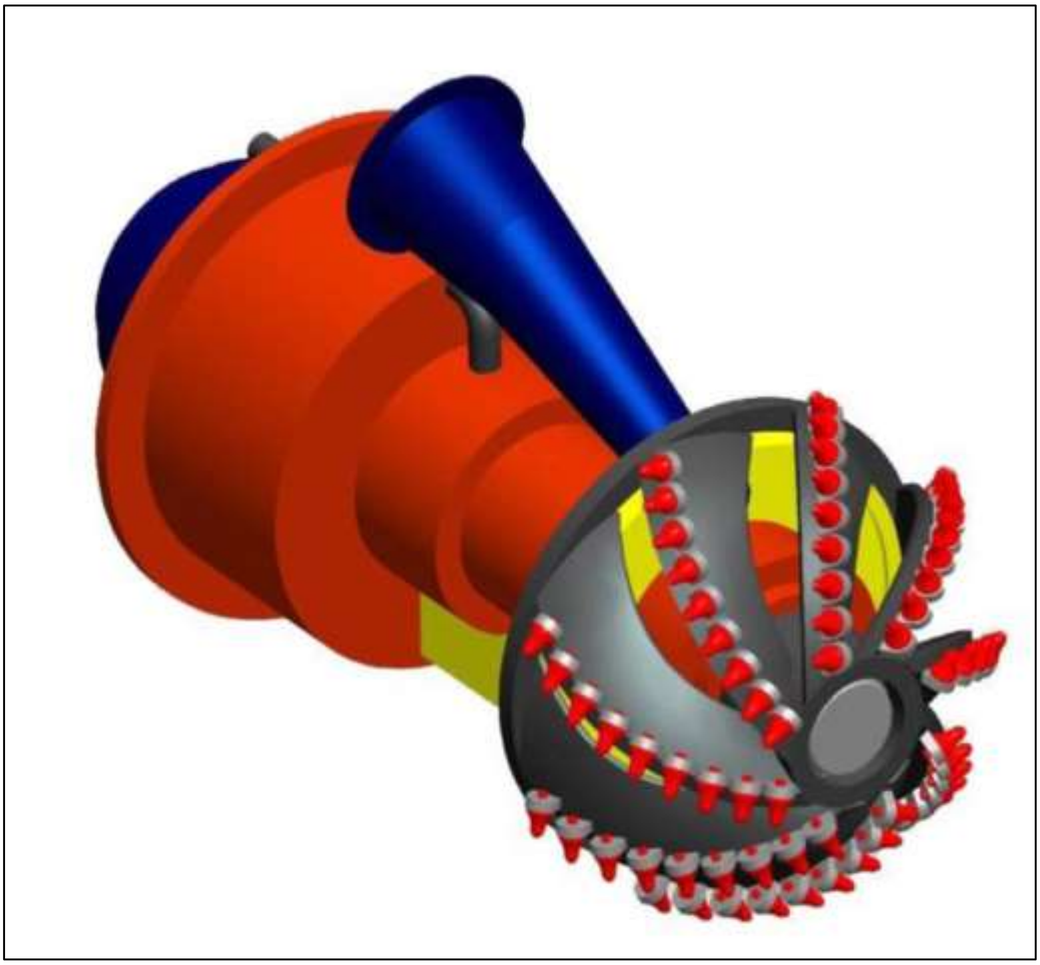

Figure Y-15: Cutterhead (IHC).

Figure Y-16: Rock cutterhead (IHC).

Y.4 Trailing Suction Hopper Dredges.

Figure Y-17: Gerardus Mercator (Jan de Nul, 18000 m^3).

Figure Y-18: The Gerardus Mercator (Jan de Nul, 18000 m^3) with one drag arm.

Figure Y-19: The Christobal Colon (Jan de Nul, 46.000 m^3).

Figure Y-20: The Volvox Terranova rainbowing (van Oord).

Figure Y-21: The Fairway (BosKalis, 35.000 m^3).

Figure Y-22: TSHD suction pipe (Jan de Nul).

Figure Y-23: Drag head (Damen Dredging).

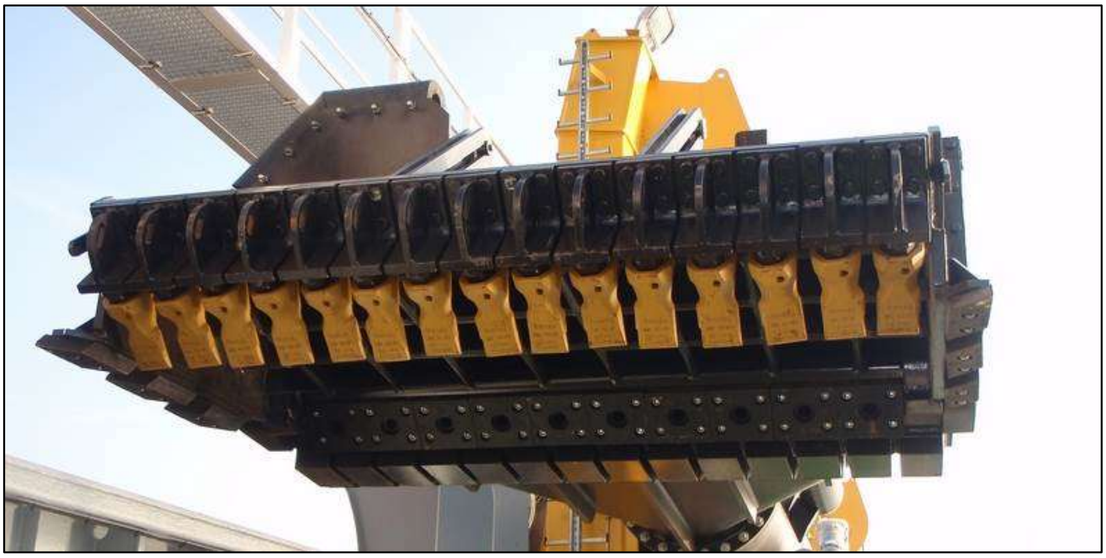

Figure Y-24: Drag head (Damen Dredging).

Figure Y-25: Drag head (Damen Dredging).

Y.5 Backhoe Dredges.

Figure Y-26: A large backhoe dredge.

Figure Y-27: A large backhoe dredge.

Figure Y-28: The Goliath (van Oord).

Figure Y-29: The New York (Great Lakes Dredge & Dock Company).

Y.6 Clamshell Dredges.

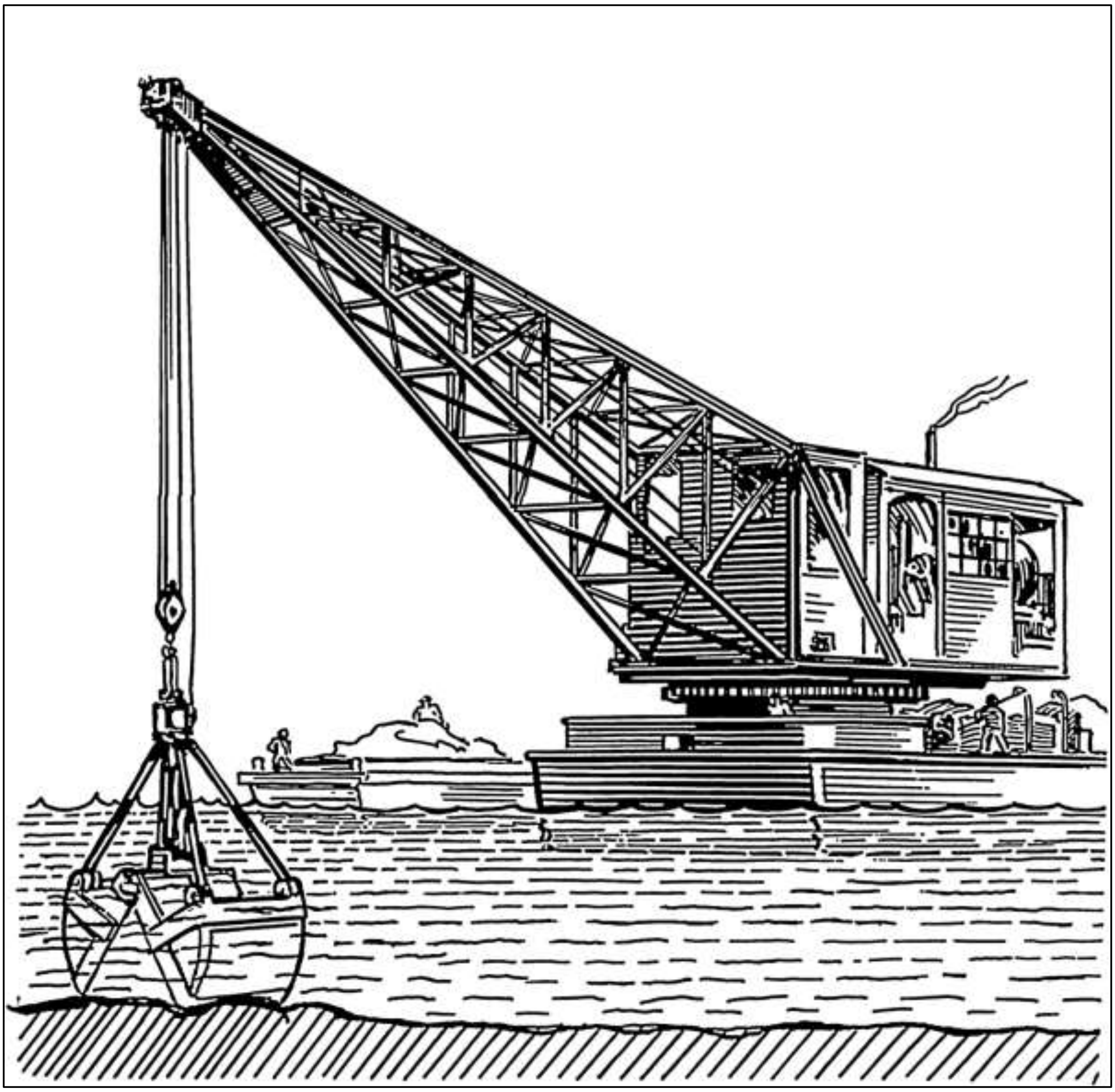

Figure Y-30: Line art drawing of a dredge (Pearson Scott Foresman).

Figure Y-31: The Chicago (Great Lakes Dredge & Dock Company).

Figure Y-32: The Chicago (Great Lakes Dredge & Dock company).

Figure Y-33: The biggest clamshell in the world.

Figure Y-34: The Chicago (Great Lakes Dredge & Dock Company).

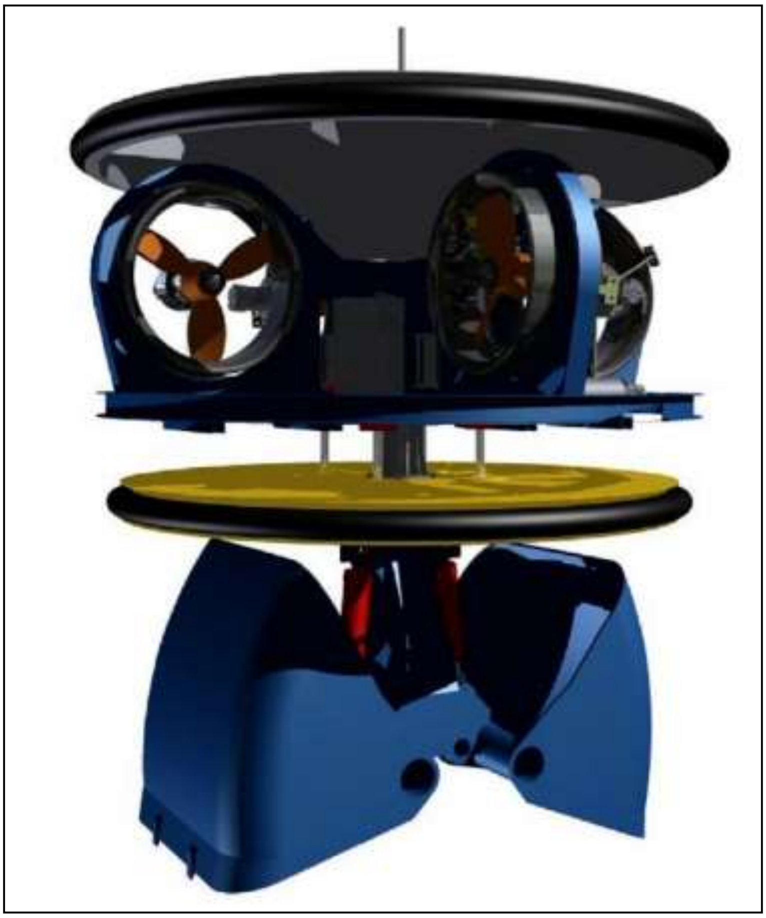

Figure Y-35: A deep sea mining clamshell (Seatools).

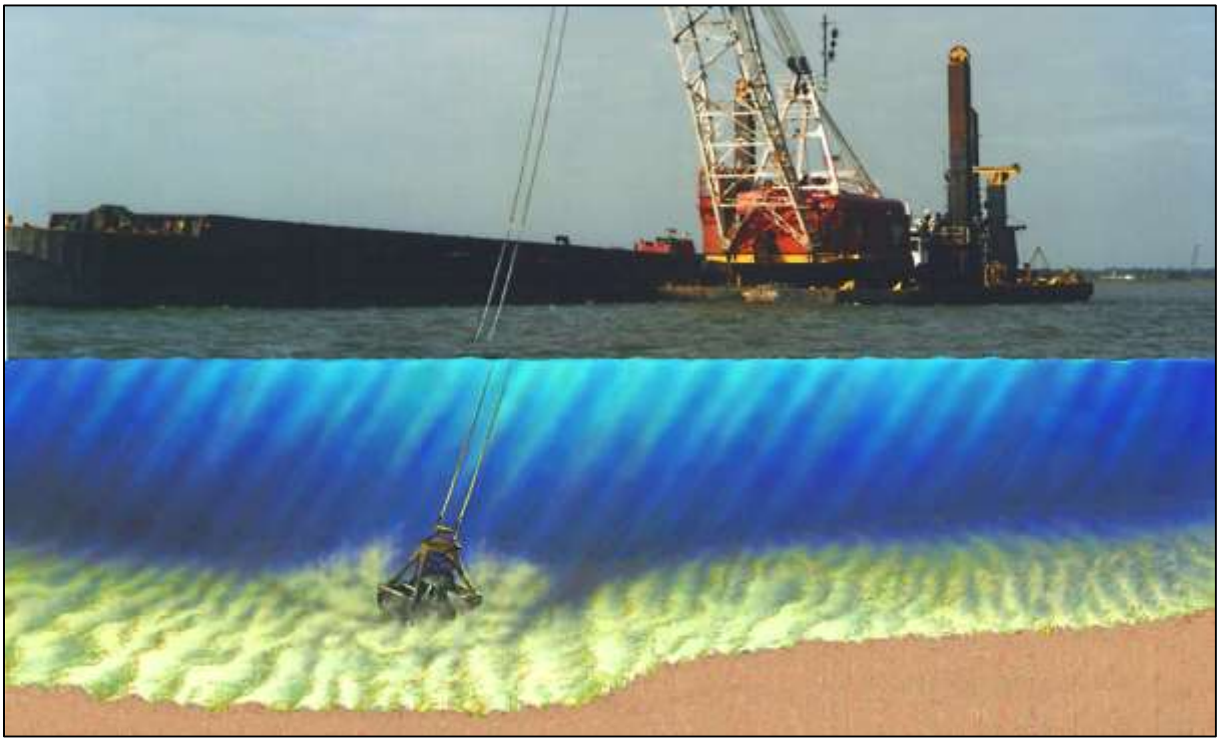

Figure_Apx Y-36: Artists impression of a clamshell operation.

Y.7 Bucket Wheel Dredges.

Figure Y-37: A bucket wheel dredge (IHC).

Figure Y-38: A bucket wheel dredge (China Hi Sea).

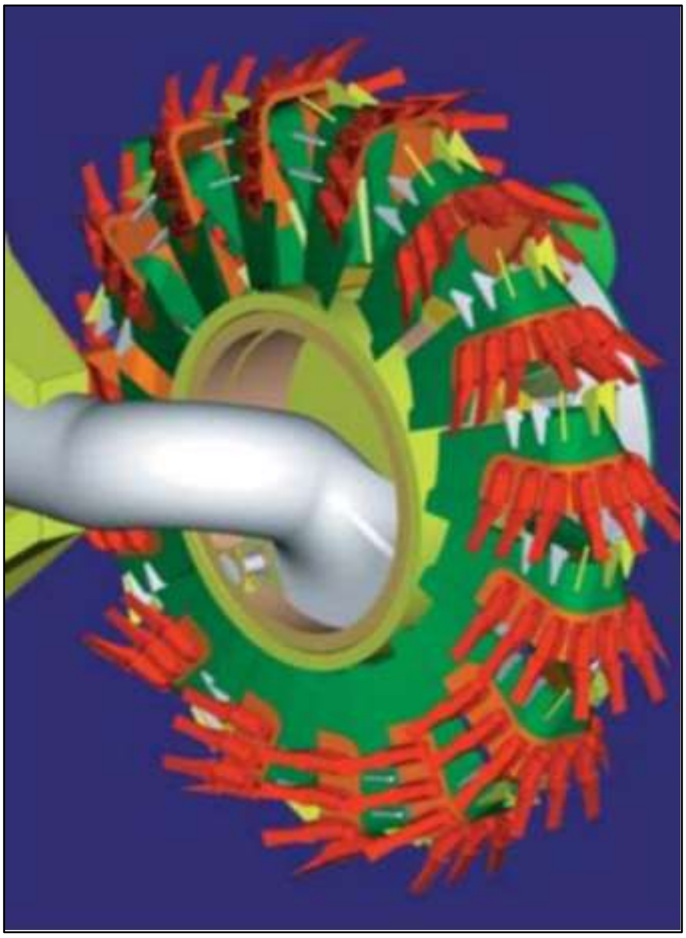

Figure Y-39: Dredging wheel (IHC).

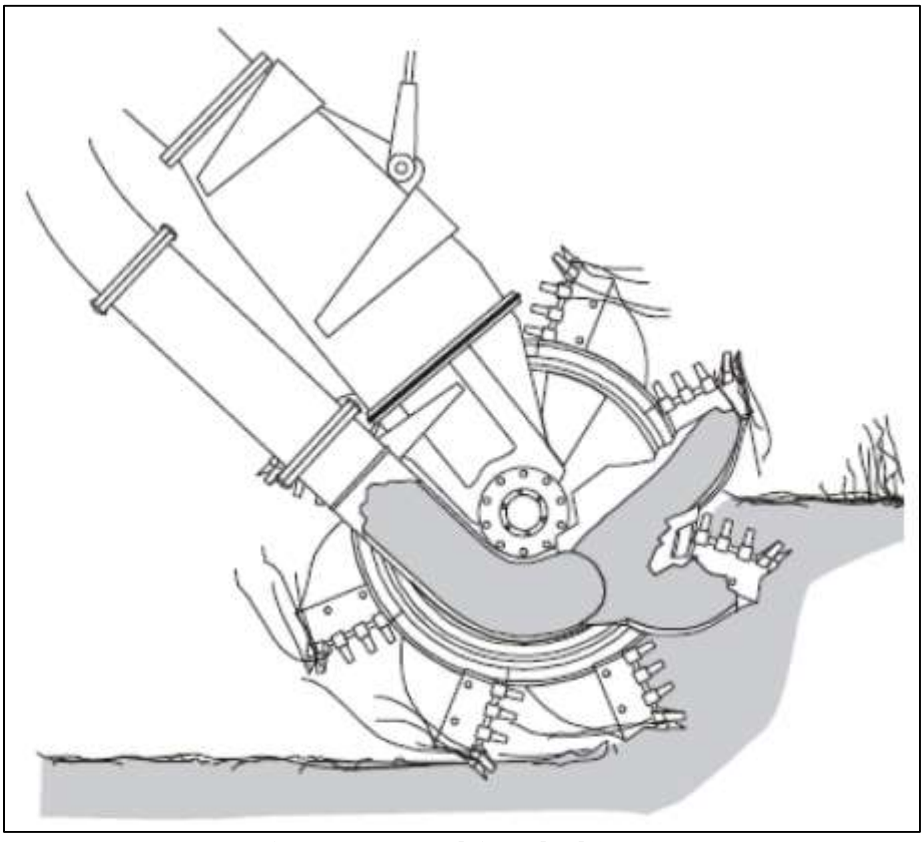

Figure Y-40: Dredging wheel (IHC).

Y.8 Braun Kohle Bergbau.

Figure Y-41: The world's largest excavator.

Figure Y-42: 95m high, 215m long, 45500 tons, \$100 million, 10 m/min, 76000 m^3/day.

Figure Y-43: A bucket wheel excavator (www.directindustry.com).

Figure Y-44: Giant bucket wheel excavator.

Y.9 Deep Sea Mining.

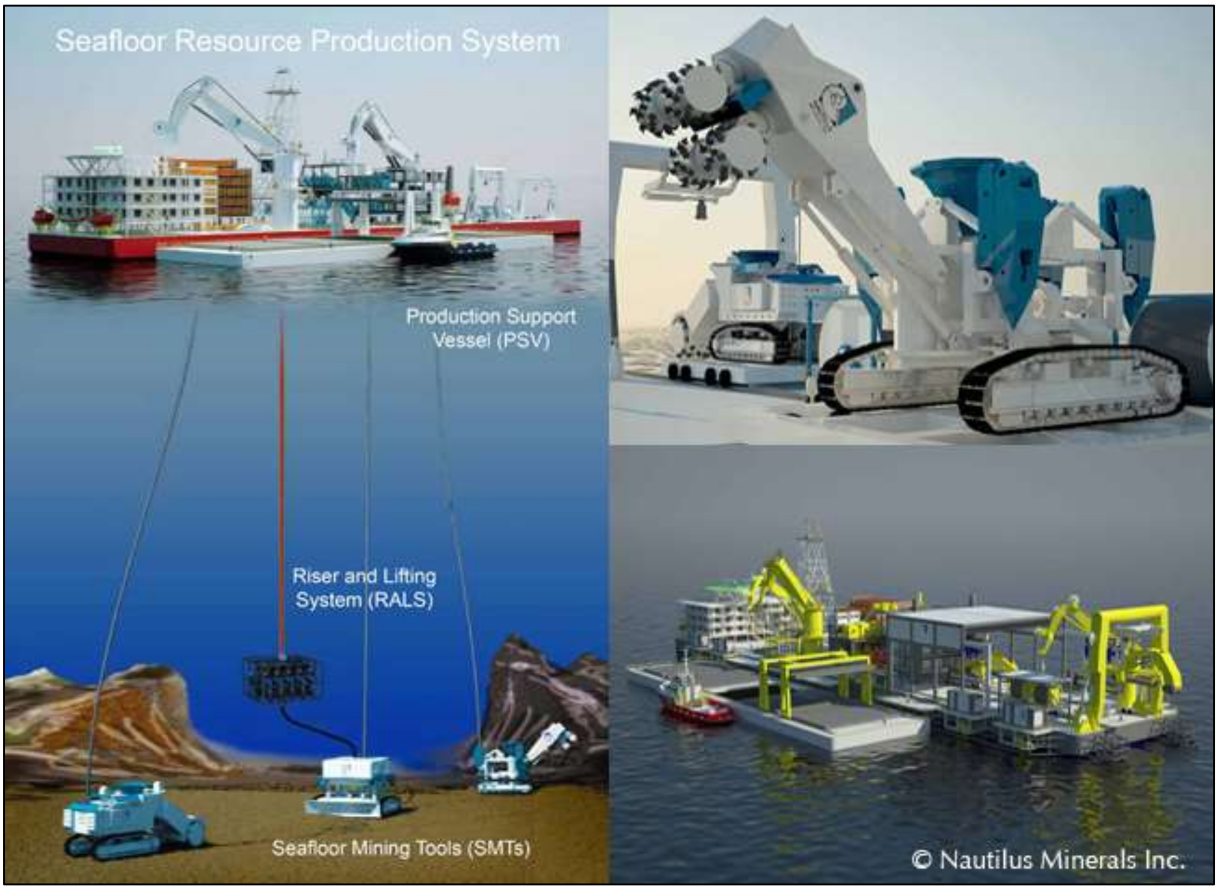

Figure Y-45: Deep sea mining, the Solwara Field.

Figure Y-46: A deep sea mining excavator (IHC).

Figure Y-47: Deep sea mining excavators (IHC).

Figure Y-48: Deep sea mining excavators.

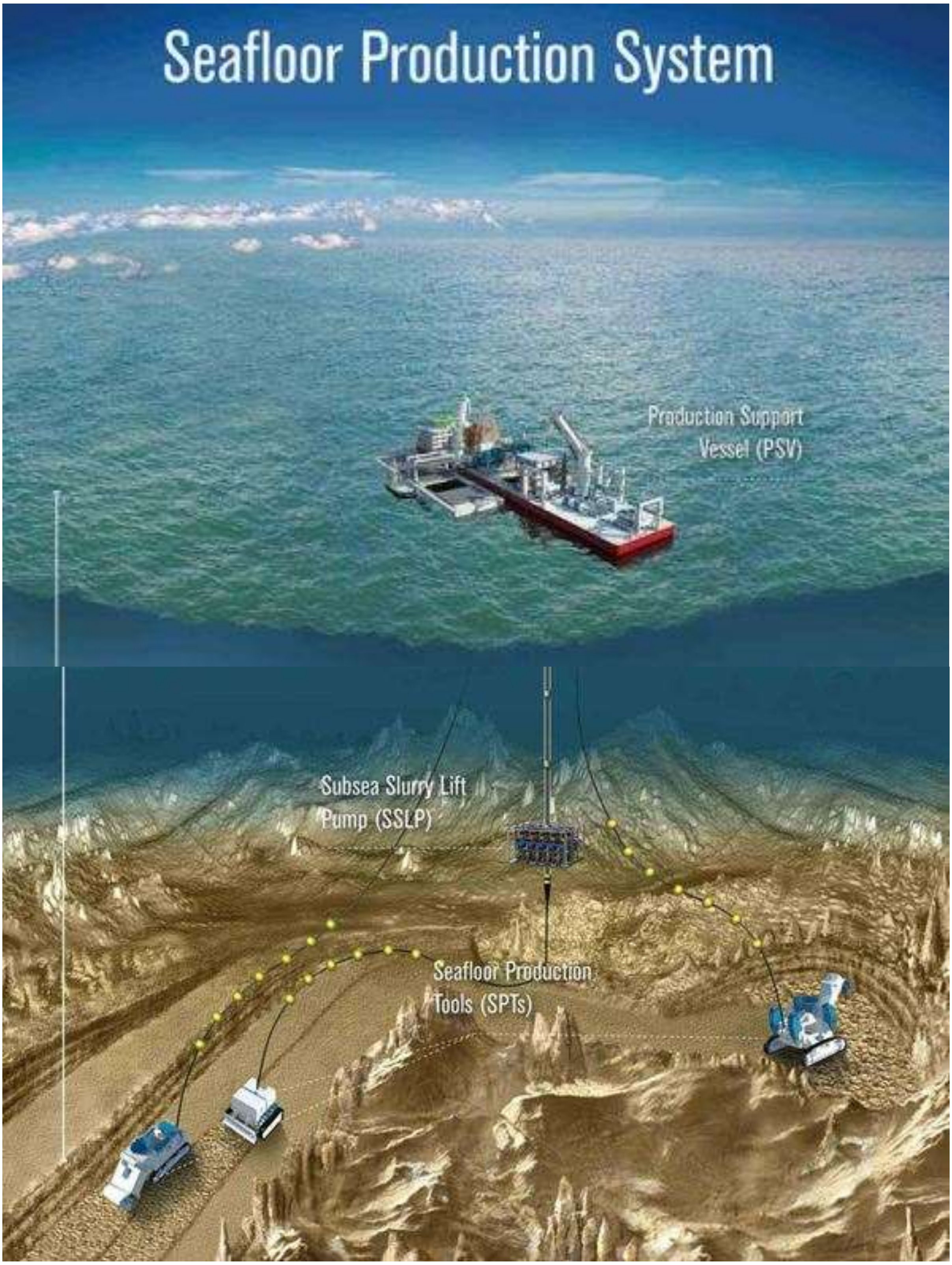

Figure Y-49: Sea floor production system.

Figure_Apx Y-50: An IHC excavator.

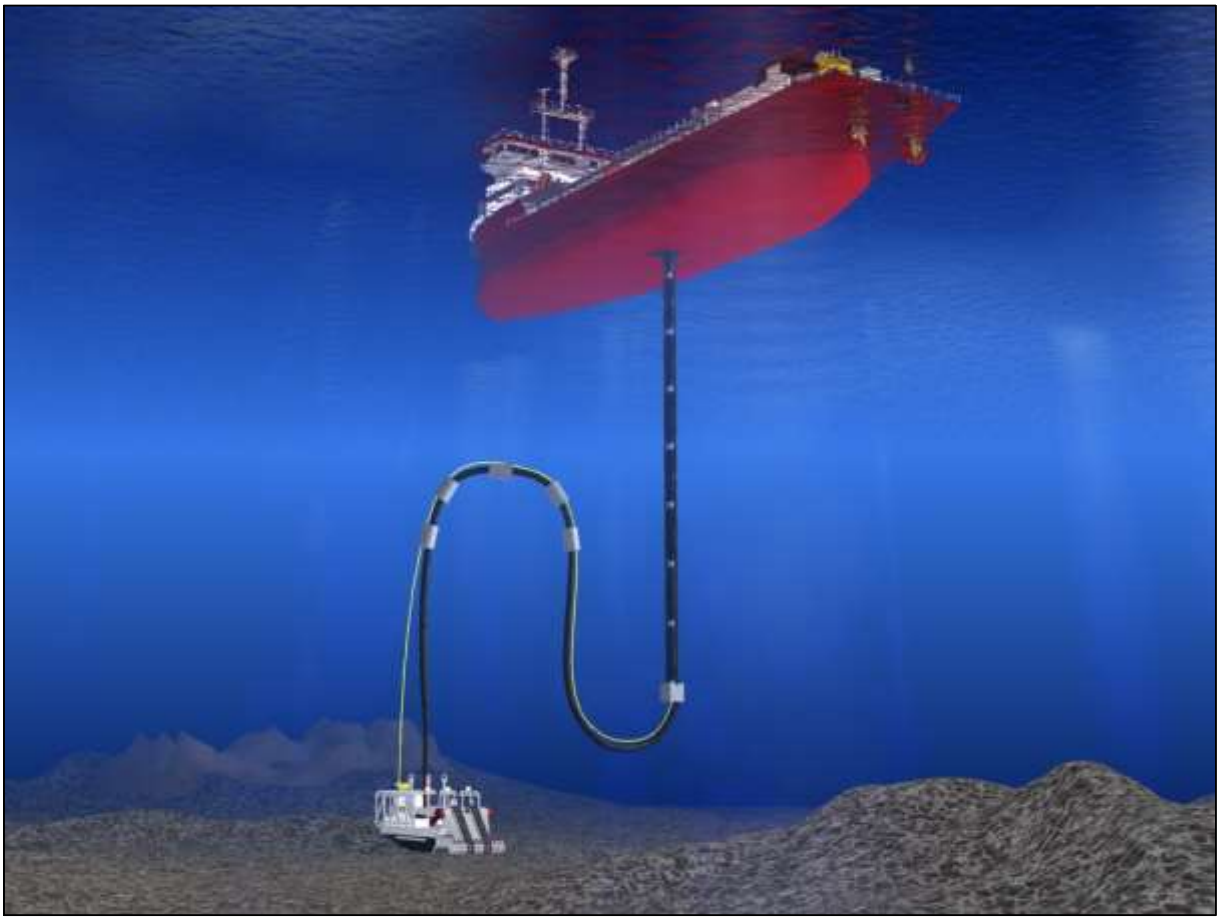

Figure Y-51: An artists impression of deep sea mining.

Y.10 Cable Trenching.

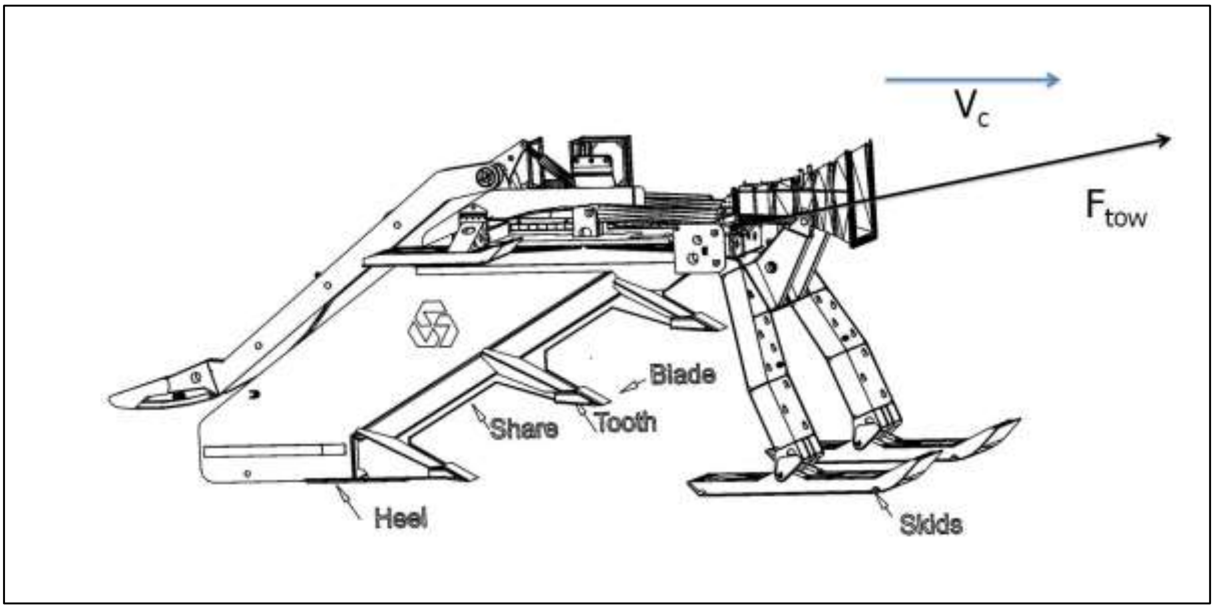

Figure Y-52: Subsea Cable Trench Plough Sea Stallion 4 (IHC).

Figure Y-53: The Sea Stallion Ormonde OWF (VSMC).

Figure Y-54: The Sea Stallion pulled by the mother ship.

Figure Y-55: The Sea Stallion.

Y.11 Offshore Pipeline Trenching.

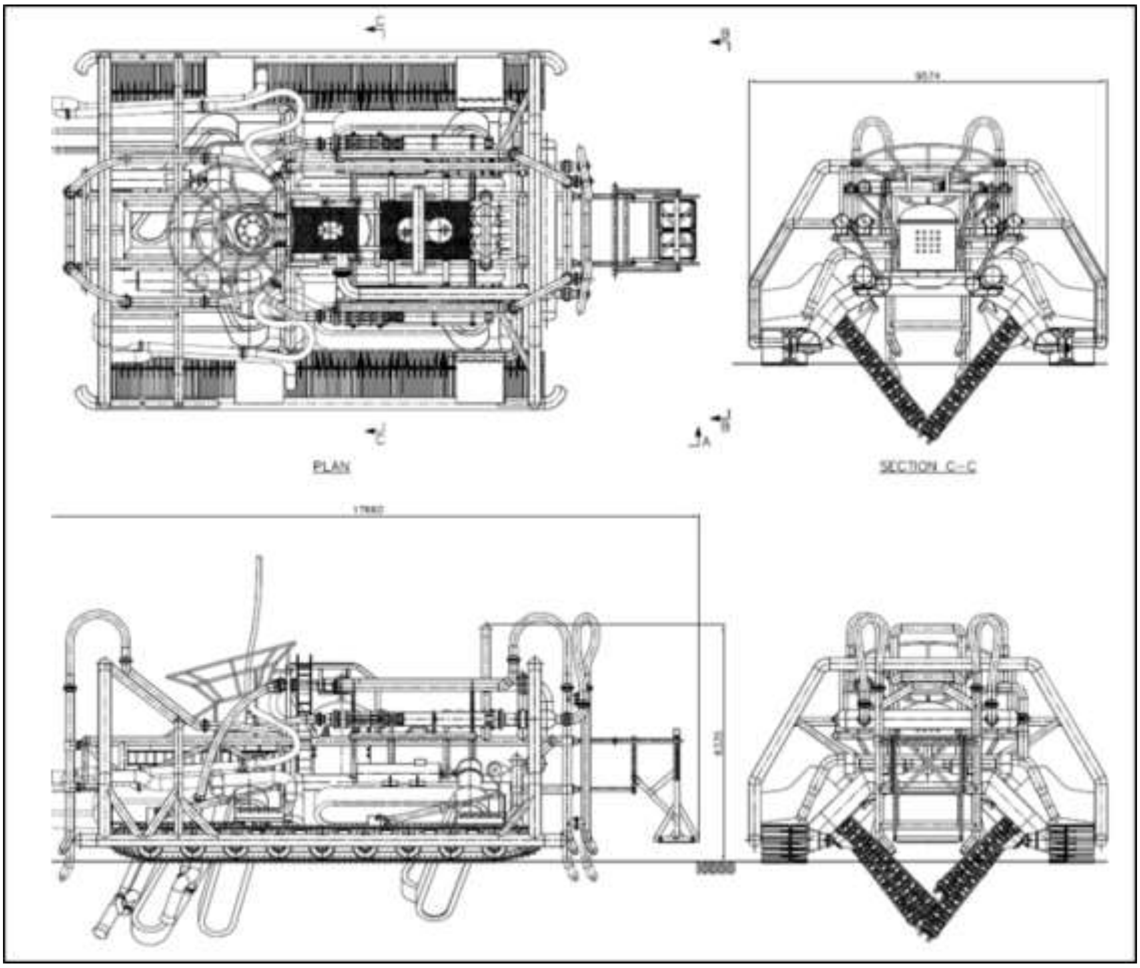

Figure Y-56: The Digging Donald (All Seas).

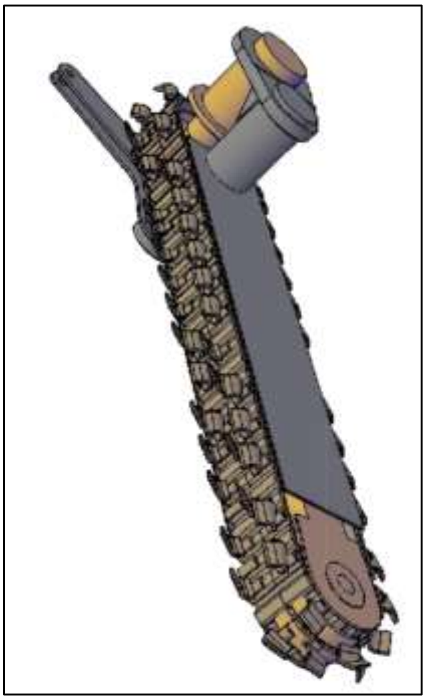

Figure Y-57: Arm with digging chain.

Figure Y-58: Reef Subsea trencher (www.dredgingtoday.com).

Figure Y-59: Seatools Arthopod 600.

Y.12 Dry Trenching.

Figure Y-60: Rock trencher (Rocksaw International).

Figure Y-61: Rock trencher (Rocksaw International).

Figure Y-62: NEPA pipeline trenching (lindeco.com).

Figure Y-63: NEPA pipeline trenching (lindeco.com).

Y.13 PDC Cutters (Oil & Gas Drilling).

Figure Y-64: A set of PDC cutters (HeJianShi FuLiang Dril Manufactury).

Figure Y-65: PDC bits.

PDC cutters (Polycrystalline Diamond Composite) are widely used in petroleum/oil field PDC bit, eological PDC exploration bits, gas exploration bits, PCD/PDC coal mining drill bits, ilfield drilling bits, currently, we developed new type of PDC cutters, and the length of the cutter is 32mm, with a round radius of the tungsten carbide substrate of the PDC cutter.

Figure Y-66: Percussion button bit and rotary drill bit (Varel International).

Figure Y-67: StaySharp premium PDC cutter technology.

Y.14 Bulldozers, Graders & Scrapers.

Figure Y-68: Catterpillar D11T (mining.cat.com).

Figure Y-69: Caterpillar 24M motor grader.

Figure Y-70: Caterpillar 631G tractor scraper.

Figure Y-71: Komatsu D85ex bulldozer.

Y.15 Dry Mining.

Figure Y-72: Double head drum cutter (www.drumcutters.com).

Figure Y-73: Tunnel Boring Machine (Shanghai Kemei El. Co.).

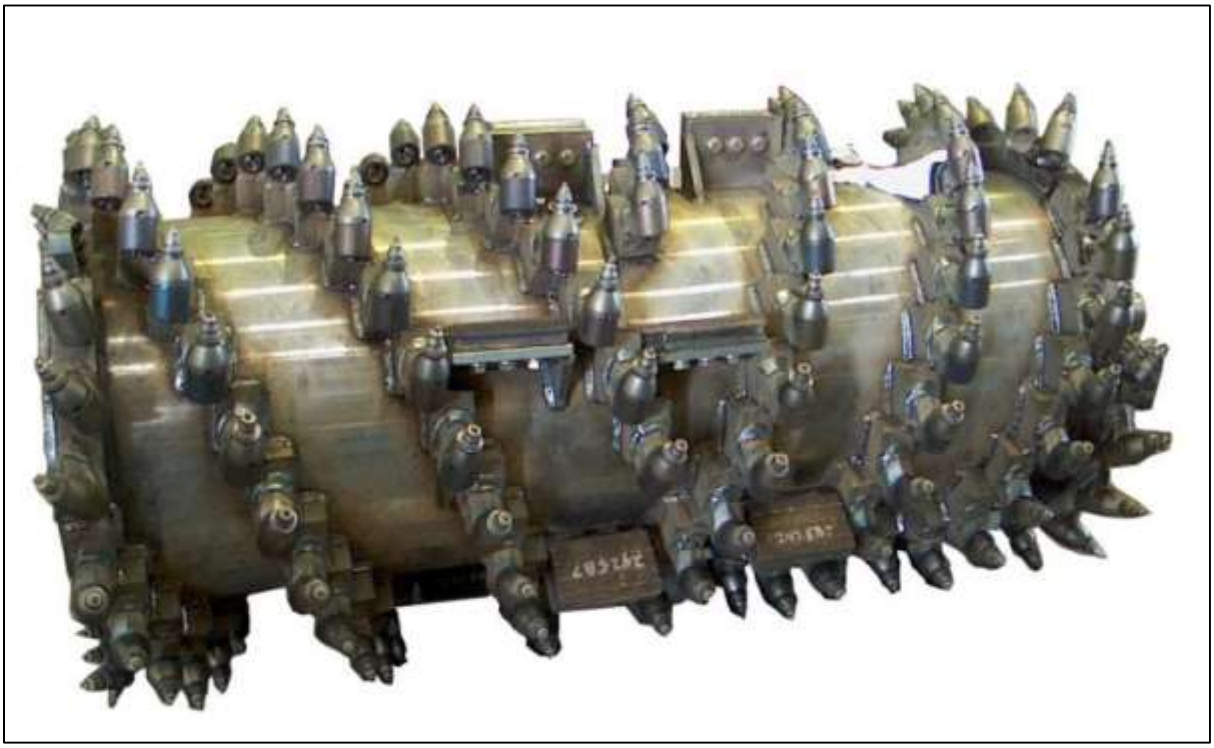

Figure Y-74: Drumcutter for dry mining applications.

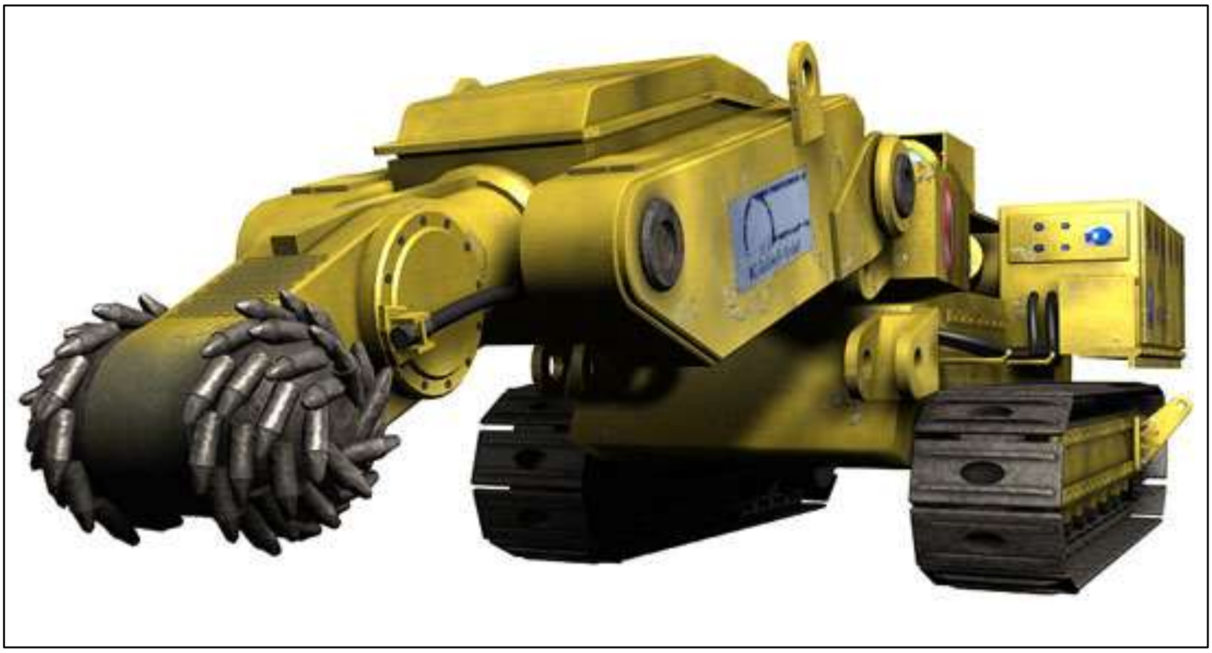

Figure Y-75: A tunnel boring machine.

Y.16 Tunnel Boring Machines.

Figure Y-76: An integrated TBM.

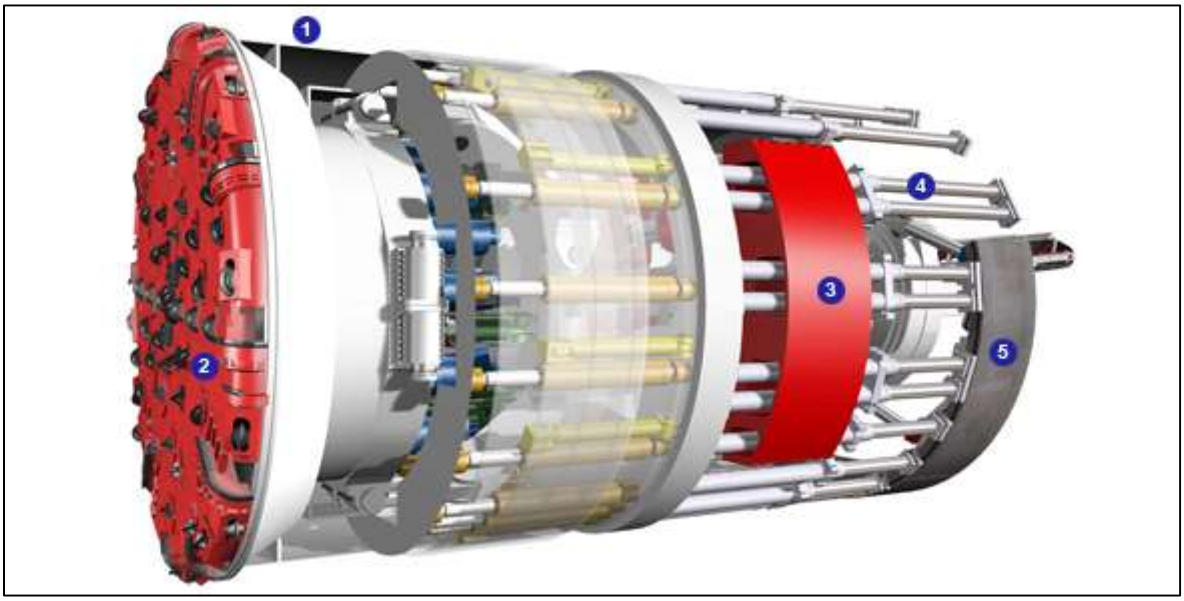

Figure Y-77: A TBM of Herrenknecht.

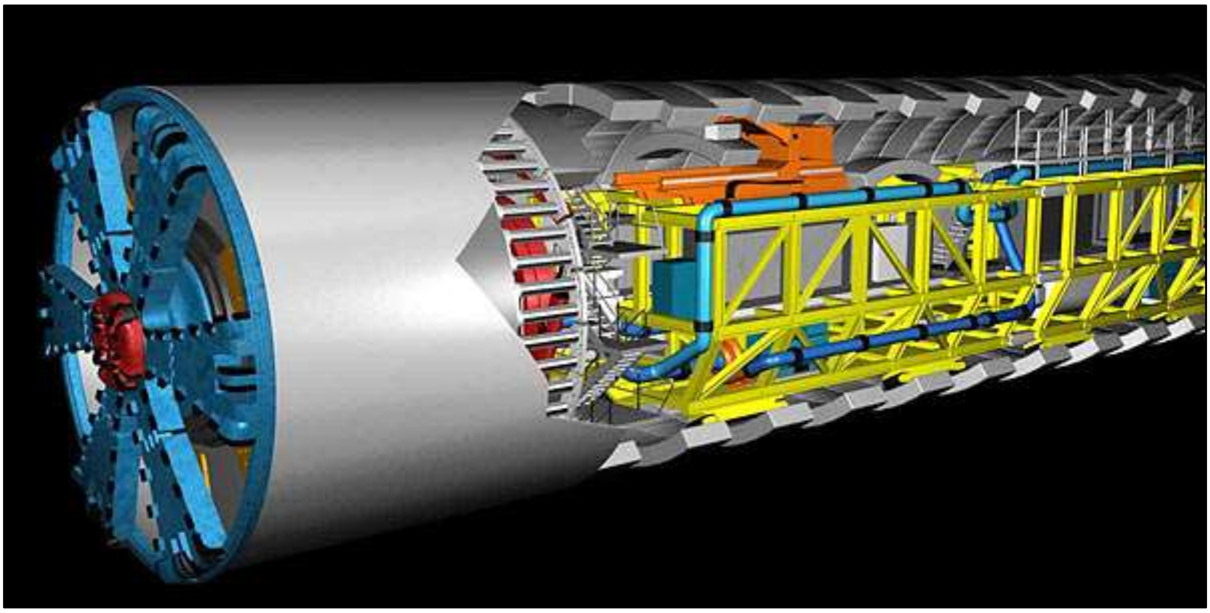

Figure Y-78: The WesterSchelde TBM.

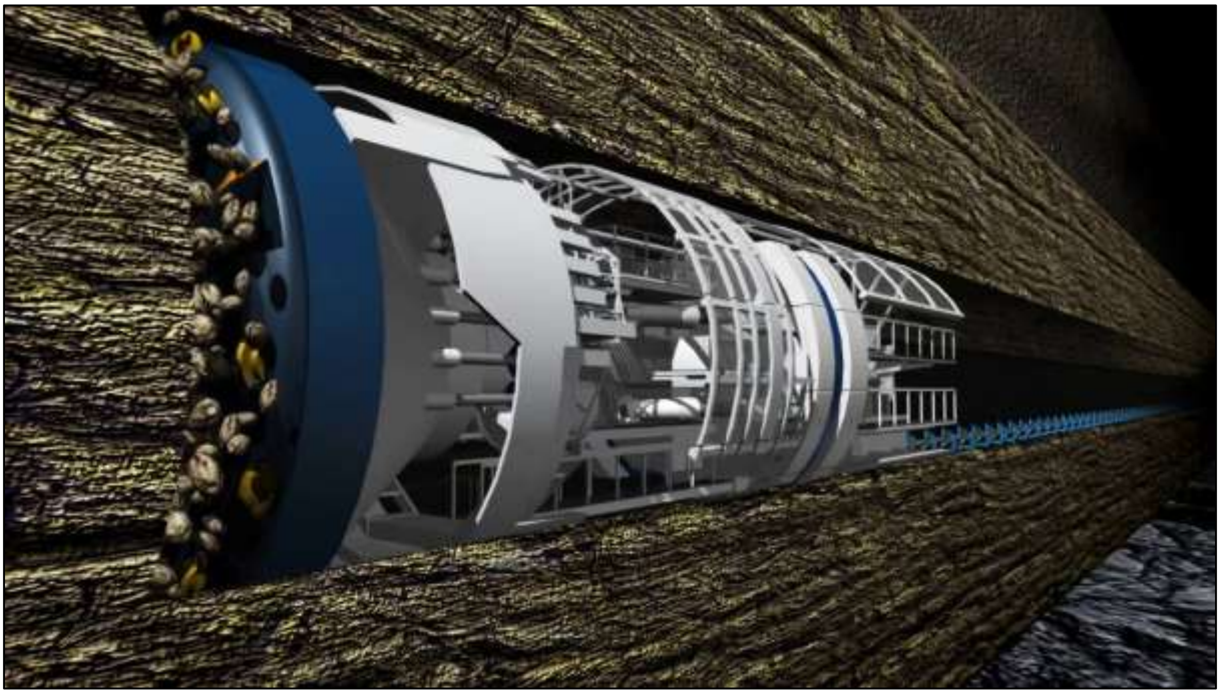

Figure Y-79: Tunnel Boring Machine (www.imaker.ca).

Appendix Z: Publications.

1. Miedema, S.A., "The soil reaction forces on a crown cutter head on a swell compensated ladder". LaO/81/97, Delft University of Technology, 1981, 36 pages.
2. Miedema, S.A., "Computer program for the determination of the reaction forces on a cutter head, resulting from the motions of the cutter head". Delft Hydraulics, 1981, 82 pages.
3. Miedema, S.A., "The mathematical modeling of the soil reaction forces on a cutter head and the development of the computer program DREDMO". CO/82/125, Delft University of Technology, 1982, with appendices 600 pages.
4. Miedema, S.A., "The Interaction between Cutter head and Soil at Sea" (In Dutch). Proc. Dredging Day November 19th, Delft University of Technology 1982.
5. Koning, J. de, Miedema, S.A., & Zwartbol, A., "Soil/Cutter head Interaction under Wave Conditions ". Proc. WODCON X, Singapore 1983.
6. Miedema, S.A., "Mathematical Modeling of a Seagoing Cutter Suction Dredge" (In Dutch). Published: The Hague, 18-9-1984, KIVI Lectures, Section Under Water Technology.
7. Miedema, S.A., "The Cutting of Densely Compacted Sand under Water ". Terra et Aqua No. 28, October 1984 pp. 4-10.
8. Miedema, S.A., "Mathematical Modeling of the Cutting of Densely Compacted Sand Under Water". Dredging & Port Construction, July 1985, pp. 22-26.
9. Miedema, S.A., "Derivation of the Differential Equation for Sand Pore Pressures". Dredging & Port Construction, September 1985, pp. 35.
10. Miedema, S.A., "The Application of a Cutting Theory on a Dredging Wheel ". Proc. WODCON XI, Brighton 1986.
11. Miedema, S.A., "Underwater Soil Cutting: a Study in Continuity". Dredging & Port Construction, June 1986, pp. 47-53.
12. Miedema, S.A., "The cutting of water saturated sand, laboratory research" (In Dutch). Delft University of Technology, 1986, 17 pages.
13. Miedema, S.A., "The forces on a trenching wheel, a feasibility study" (In Dutch). Delft, 1986, 57 pages + software.
14. Miedema, S.A., "Calculation of the Cutting Forces when Cutting Water Saturated Sand ". Basic Theory and Applications for 3-D Blade Movements and Periodically Varying Velocities for, in Dredging Commonly used Excavating Means. Ph.D. Thesis, Delft University of Technology, September 15th 1987.
15. Bakker, A. & Miedema, S.A., "The Specific Energy of the Dredging Process of a Grab Dredge". Delft University of Technology, 1988, 30 pages.
16. Miedema, S.A., "On the Cutting Forces in Saturated Sand of a Seagoing Cutter Suction Dredge". Proc. WODCON XII, Orlando, Florida, USA, April 1989. This paper was given the IADC Award for the best technical paper on the subject of dredging in 1989.
17. Miedema, S.A., "On the Cutting Forces in Saturated Sand of a Seagoing Cutter Suction Dredge". Terra et Aqua No. 41, December 1989, Elsevier's Scientific Publishers.
18. Miedema, S.A., "New Developments of Cutting Theories with respect to Dredging, the Cutting of Clay". Proc. WODCON XIII, Bombay, India, 1992.
19. Miedema, S.A. & Journee, J.M.J. & Schuurmans, S., "On the Motions of a Seagoing Cutter Dredge, a Study in Continuity". Proc. WODCON XIII, Bombay, India, 1992.
20. Becker, S. & Miedema, S.A. & Jong, P.S. de & Wittekoek, S., "On the Closing Process of Clamshell Dredges in Water Saturated Sand". Proc. WODCON XIII, Bombay, India, 1992. This paper was given the IADC Award for the best technical paper on the subject of dredging in 1992.
21. Becker, S. & Miedema, S.A. & Jong, P.S. de & Wittekoek, S., "The Closing Process of Clamshell Dredges in Water Saturated Sand". Terra et Aqua No. 49, September 1992, IADC, The Hague.
22. Miedema, S.A., "Modeling and Simulation of Dredging Processes and Systems". Symposium "Zicht op Bagger processen", Delft University of Technology, Delft, The Netherlands, 29 October 1992.
23. Miedema, S.A. & Becker, S., "The Use of Modeling and Simulation in the Dredging Industry, in Particular the Closing Process of Clamshell Dredges", CEDA Dredging Days 1993, Amsterdam, Holland, 1993.
24. Miedema, S.A., "On the Snow-Plough Effect when Cutting Water Saturated Sand with Inclined Straight Blades". ASCE Proc. Dredging 94, Orlando, Florida, USA, November 1994.
25. Miedema, S.A., "Production Estimation Based on Cutting Theories for Cutting Water Saturated Sand". Proc. WODCON IV, November 1995, Amsterdam, The Netherlands 1995.
26. Miedema, S.A. & Zhao Yi, "An Analytical Method of Pore Pressure Calculations when Cutting Water Saturated Sand". Texas A&M 33nd Annual Dredging Seminar, June 2001, Houston, USA 2001.

27. Zhao Yi, & Miedema, S.A., "Finite Element Calculations To Determine The Pore Pressures When Cutting Water Saturated Sand At Large Cutting Angles". CEDA Dredging Day 2001, November 2001, Amsterdam, the Netherlands.
28. Miedema, S.A., & Ma, Y., "The Cutting of Water Saturated Sand at Large Cutting Angles". Proc. Dredging02, May 5-8, Orlando, Florida, USA.
29. Miedema, S.A., & He, Y., "The Existence of Kinematic Wedges at Large Cutting Angles". Proc. WEDA XXII Technical Conference & 34th Texas A&M Dredging Seminar, June 12-15, Denver, Colorado, USA.
30. Miedema, S.A., Frijters, D., "The Mechanism of Kinematic Wedges at Large Cutting Angles - Velocity and Friction Measurements". 23rd WEDA Technical Conference & 35th TAMU Dredging Seminar, Chicago, USA, June 2003.
31. Miedema, S.A., "The Existence of Kinematic Wedges at Large Cutting Angles". CHIDA Dredging Days, Shanghai, China, November 2003.
32. Miedema, S.A. & Frijters, D.D.J., "The wedge mechanism for cutting of water saturated sand at large cutting angles". WODCON XVII, September 2004, Hamburg Germany.
33. Miedema, S.A., "THE CUTTING MECHANISMS OF WATER SATURATED SAND AT SMALL AND LARGE CUTTING ANGLES". International Conference on Coastal Infrastructure Development - Challenges in the 21st Century. Hong Kong, November 2004.
34. He, J., Miedema, S.A. & Vlasblom, W.J., "FEM Analyses Of Cutting Of Anisotropic Densely Compacted and Saturated Sand", WEDAXXV & TAMU37, New Orleans, USA, June 2005.
35. Miedema, S.A., "The Cutting of Water Saturated Sand, the FINAL Solution". WEDAXXV & TAMU37, New Orleans, USA, June 2005.
36. Miedema, S.A., "THE CUTTING OF WATER SATURATED SAND, THE SOLUTION". CEDA African Section: Dredging Days 2006 - Protection of the coastline, dredging sustainable development, Nov. 1-3, Tangiers, Morocco.
37. Miedema, S.A. & Vlasblom, W.J., "THE CLOSING PROCESS OF CLAMSHELL DREDGES IN WATER-SATURATED SAND". CEDA African Section: Dredging Days 2006 - Protection of the coastline, dredging sustainable development, Nov. 1-3, Tangiers, Morocco.
38. Miedema, S.A. "THE CUTTING OF WATER SATURATED SAND, THE SOLUTION". The 2nd China Dredging Association International Conference & Exhibition, themed 'Dredging and Sustainable Development' and in Guangzhou, China, May 17-18 2006.
39. Ma, Y, Ni, F. & Miedema, S.A., "Calculation of the Blade Cutting Force for small Cutting Angles based on MATLAB". The 2nd China Dredging Association International Conference & Exhibition, themed 'Dredging and Sustainable Development' and in Guangzhou, China, May 17-18 2006.
40. Miedema, S.A. , Kerkvliet, J., Strijbis, D., Jonkman, B., Hatert, M. v/d, "THE DIGGING AND HOLDING CAPACITY OF ANCHORS". WEDA XXVI AND TAMU 38, San Diego, California, June 25-28, 2006.
41. Ma Yasheng, Ni Fusheng, S.A. Miedema, "Mechanical Model of Water Saturated Sand Cutting at Blade Large Cutting Angles", Journal of Hohai University Changzhou, ISSN 1009-1130, CN 32-1591, 2006.
42. Miedema, S.A., Lager, G.H.G., Kerkvliet, J., “An Overview of Drag Embedded Anchor Holding Capacity for Dredging and Offshore Applications”. WODCON, Orlando, USA, 2007.
43. Miedema, S.A., "A Sensitivity Analysis of the Production of Clamshells". WEDA XXVIII & Texas A&M 39. St. Louis, USA, June 8-11, 2008.
44. Miedema, S.A., "A Sensitivity Analysis of the Production of Clamshells". WEDA Journal of Dredging Engineering, December 2008.
45. Miedema, S.A., "New Developments Of Cutting Theories With Respect To Dredging, The Cutting Of Clay And Rock". WEDA XXIX & Texas A&M 40. Phoenix Arizona, USA, June 14-17 2009.
46. Miedema, S.A., “New developments of cutting theories with respect to offshore applications, the cutting of sand, clay and rock”. ISOPE 2010, Beijing China, June 2010.
47. Miedema, S.A., “The influence of the strain rate on cutting processes”. ISOPE 2010, Beijing China, June 2010.
48. Abdeli, M., Miedema, S.A., Schott, D., Alvarez Grima, M., “The application of discrete element modeling in dredging”. WODCON XIX, Beijing China, September 2010.
49. Rahman, M., Schott, D.L., Miedema, S.A., Lodewijks, G., "Simulation of cutting process by hybrid granular and multi-body dynamics software". 3rd International Conference on Bulk solids. Glasgow, Scotland, September 9-10, 2010.
50. Rahman, M., Abdeli, M., Miedema, S.A., Schott, D., "Simulation of passive soil failure & cutting processes in sand. OMAE 2011 ASME, June 19-24, Rotterdam, the Netherlands.
51. Miedema, S.A., "Soil cutting processes, the cutting of water saturated sand". OMAE 2011 ASME, June 19-24, Rotterdam, the Netherlands.

52. Miedema, S.A., “THE BULLDOZER EFFECT WHEN CUTTING WATER SATURATED SAND”. OMAE 2012 ASME, June 10-15, Rio de Janeiro, Brazil.
53. Miedema, S.A., Zijsling, D., “HYPERBARIC ROCK CUTTING”. OMAE 2012 ASME, June 10-15, Rio de Janeiro, Brazil.
54. Kuiper, R.J., Miedema, S.A., Frumeau, J.C.L. & van Rhee, C., “Influence of the Hyperbaric Effect on Apparrent Material Strength of Fully Saturated Porous Rock”. OTC 2013, Houston, Texas, U.S.A., May 2013.
55. Helmons, R.I.J. & Miedema, S.A., “Cutting Through Hard Rock-Like Materials, A Review of the Process”. WODCON XX, Brussels, Belgium, June 2013.
56. Chen, X. & Miedema, S.A., “Porosity Calculation in Discrete Element Modeling of Sand Cutting Process”. WODCON XX, Brussels, Belgium, June 2013.
57. Chen, X. & Miedema, S.A., “Influence of Particle Geometry on the Simulation of Sand Cutting Process”. OMAE 2013, Nantes, France, June 2013.
58. Helmons, R.I.J. & Miedema, S.A., “Rock Cutting for Deep Sea Mining: an Extension into Poromechanics”. Poromechanics V © ASCE 2013.
59. Liefferink, D.M., Alvarez Grima, M., Miedema, S.A., Plat, R., Rhee, C. van, “Failure mechanism of cutting submerged frozen clay in an arctic trenching process”. OTC 2014. Houston, Texas, U.S.A., May 2014.
60. Chen, X., Miedema, S.A., “Numerical methods for modeling the rock cutting process in deep sea mining”. ASME-OMAE 2014, San Francisco, USA, June 2014.
61. Helmons, R.L.J., Miedema, S.A., Rhee, C. van, “A new approach to model hyperbaric rock cutting processes”. ASME-OMAE 2014, San Francisco, USA, June 2014.
62. Miedema, S.A., “A NEW APPROACH TO DETERMINE CUTTING FORCES IN BRITTLE ROCK UNDER HYPERBARIC CONDITIONS”. ASME-OMAE 2014, San Francisco, USA, June 2014.
63. Chen, X., Miedema, S.A. & Rhee, C. van, “Numerical modeling of excavation process in dredging engineering”. 7th World Congress on Particle Technology. Beijing, China, May 19-22, 2014.
64. Miedema, S.A., “The Delft Sand, Clay & Rock Cutting Model”. IOS Press, Delft University Press, Delft, The Netherlands, 2015.
65. Chen, X., Miedema, S.A. & Rhee, C. van, “Numerical modeling of excavation process in dredging engineering”. Procedia Engineering, Vol. 102, pp. 804-814, 2015.
66. Miedema, S.A., “The Delft Sand, Clay & Rock Cutting Model”. WEDA TAMU, Houston, Texas, USA, June, 2015.
67. Combe, Th., & Miedema, S.A., “The influence of adhesion on cutting processes in dredging”. WEDA TAMU, Houston, Texas, USA, June, 2015.
68. Alvarez Grima, M., Miedema, S.A., Ketterij, R.G. van de, Yenigul, N.B., Rhee, C. van, Ëffect of high hyperbaric pressure on rock cutting process”. Engineering Geology, Vol. 196, pp. 24-36, 2015.
69. Chen, X., Miedema, S.A., Rhee, C. van, “Sensitivity study of bond radius and energy dissipation in parallel bond method”. Joint Conference of 5th UK-China and 13th UK Particle Technology Forum, Leeds, UK, 2015.

The Delft Sand, Clay & Rock Cutting Model

3rd Edition

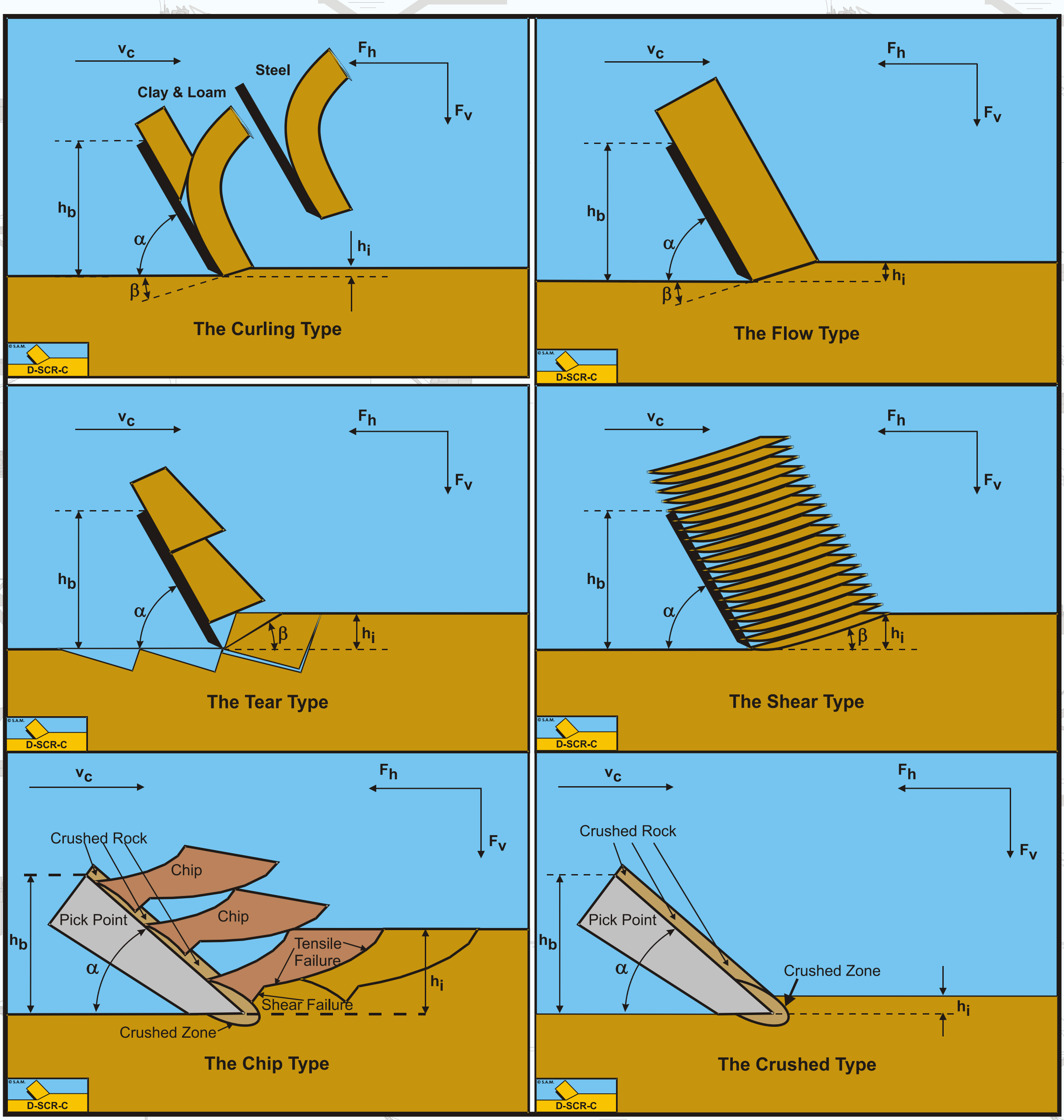

By

Sape A. Miedema

Sand, clay and rock have to be excavated for a variety of purposes, such as dredging, trenching, mining (including deep sea mining), drilling, tunnel boring and many other applications. Many excavations take place on dry land, but they are also frequently required in completely saturated conditions, and the methods necessary to accomplish them consequently vary widely.

This book provides an overview of cutting theories. It begins with a generic model, valid for all types of soil (sand, clay and rock), and continues with the specifics of dry sand, water-saturated sand, clay, atmospheric rock and hyperbaric rock. Small blade angles and large blade angles are discussed for each soil type, and for each case considered the equations/model for cutting forces, power and specific energy are given.

With models verified by laboratory research, principally from the Delft University of Technology, and data from other recognized sources, this book will prove an invaluable reference for anybody whose work involves major excavations of any kind.

by
Dr.ir. Sape A. Miedema